REPORT DOCUMENTATION PAGE

Form Approved
OMB No. 0704-0188

Public reporting burden for this collection of information is estimated to average 1 hour per response, including the time for reviewing instructions, searching existing data sources, gathering and maintaining the data needed, and completing and reviewing the collection of information. Send comments regarding this burden estimate or any other aspect of this collection of information, including suggestions for reducing this burden, to Washington Headquarters Services, Directorate for information Operations and Reports, 1215 Jefferson Davis Highway, Suite 1204, Arlington, VA 22202-4302, and to the Office of Management and Budget, Paperwork Reduction Project (0704-0188), Washington, DC 20503.

1. AGENCY USE ONLY (Leave blank)	2. REPORT DATE	3. REPORT TYPE AND DATES COVERED
	14 Jan 97	Final; 15 Apr 97 to 31 Dec 97

4. TITLE AND SUBTITLE
1997 Solid Freeform Fabrication Symposium Proceedings

5. FUNDING NUMBERS
G
N00014-97-1-0453

6. AUTHOR(S)
D.L. Bourell, J. Beaman, H.L. Marcus, R. Crawford, J. Barlow

7. PERFORMING ORGANIZATION NAME(S) AND ADDRESS(ES)
University of Texas at Austin
Mechanical Engineering
MC C2200
Austin TX 78712-1063

8. PERFORMING ORGANIZATION REPORT NUMBER

9. SPONSORING/MONITORING AGENCY NAME(S) AND ADDRESS(ES)
Office of Naval Research
Ballston Center Tower One
800 North Quincy Street
Arlington VA 22217-5660

10. SPONSORING/MONITORING AGENCY REPORT NUMBER

11. SUPPLEMENTARY NOTES

12a. DISTRIBUTION/AVAILABILITY STATEMENT
Approved for public release

DISTRIBUTION STATEMENT A
Approved for public release
Distribution Unlimited

12b. DISTRIBUTION CODE

13. ABSTRACT *(Maximum 200 words)*

The Eighth Solid Freeform Fabrication (SFF) Symposium, held at The University of Texas in Austin on August 11-13, 1997, was attended by 200 national and international researchers. Papers addressed SFF issues in computer software, machine design, materials synthesis and processing, and integrated manufacturing. Eighty-six presentations were made, 65 oral presentations and 21 poster presentations. The diverse domestic and foreign attendees represented industrial users, SFF machine manufacturers, universities, and government. We believe that documenting the constantly changing state of SFF art as represented by these Proceedings will serve both the people presently involved in this fruitful technical area as well as the large flux of new researchers and users entering the field. We are pleased to report that the SFF Symposium attracted a large number of young scientists this year. We had 51 students from 21 universities (4 international universities), approximately 25% of the entire meeting participants. The Organizing Committee has always valued the role of technical meetings as a venue for graduate students in research.

14. SUBJECT TERMS	15. NUMBER OF PAGES
Solid Freeform Fabrication, SFF, Rapid Prototyping	756
	16. PRICE CODE

17. SECURITY CLASSIFICATION OF REPORT	18. SECURITY CLASSIFICATION OF THIS PAGE	19. SECURITY CLASSIFICATION OF ABSTRACT	20. LIMITATION OF ABSTRACT
Unclassified	Unclassified	Unclassified	UL

Solid Freeform Fabrication Proceedings

September 1997

Solid Freeform Fabrication is an important and totally integrated approach to design, materials processing and manufacturing. Research results related to it are contained in this proceedings of the SFF Symposium held in Austin, Texas on August 11-13, 1997

SFF Topics covered in the Symposium include:

Processes/Process Development
Tooling
Materials
Modeling

DISTRIBUTION STATEMENT A
Approved for public release
Distribution Unlimited

David L. Bourell, Joseph J. Beaman
Richard H. Crawford, Harris L. Marcus
and Joel W. Barlow, Editors

DTIC QUALITY INSPECTED 3

© 1997 The University of Texas at Austin
All rights of reproduction in any form are protected by U.S. Copyright Laws.
Permission to copy, all or portions of the proceedings contents must be obtained
from the authors and The University of Texas at Austin.

Library of Congress ISSN 1053-2153

19980121 151

Table of Contents

Page

Preface ---- x

Organizing/Advisory Committee ---- xi

Processes/Process Development

Liquid Metal Jetting for Printing Metal Parts
John W. Priest[a], Charles Smith[a,b], Patrick DuBois[c], *[a]The University of Texas at Arlington, [b]Electrical Engineering, [c]Automation & Robotics Research Institute* ---- 1

Extrusion Freeform Fabrication of Bone-Like Mineralized Hydrogels and Muscle-Like Actuators
Paul Calvert and Zengshe Liu, *Arizona Materials Laboratories, Tucson AZ* ---- 11

A Layered-Manufacturing Process for the Fabrication of Glass-Fiber-Reinforced Composites
G. Zak, M.N. Sela, C.B. Park, B. Benhabib, *Computer Integrated Manufacturing Laboratory, Department of Mechanical and Industrial Engineering, University of Toronto* ---- 17

Recent Developments in Freeform Fabrication of Dense Ceramics From Slurry Deposition
Joseph Cesarano III[a], Thomas A. Baer[a], Paul Calvert[b], *[a]Sandia National Laboratories, [b]University of Arizona, Arizona Materials Laboratories* ---- 25

Direct-Write Fabrication of Integrated, Multilayer Ceramic Components
D. Dimos, P. Yang, T.J. Garino, M.V. Raymond, M.A. Rodriguez, *Sandia National Laboratories* ---- 33

Laser Aided Direct Rapid Prototyping
Robert Franceschini[a,c], Lee Napravnik[a,c], Amar Mukherjee[a,c], Srikanth Sankaranarayanan[b,c], Aravinda Kar[b,c], *[a]Department of Computer Science, [b]Center for Research and Education in Optics and Lasers, [c]University of Central Florida* ---- 41

Trussed Structures: FreeForm Fabrication Without the Layers
Joseph Pegna, David Messia, Woo Ho Lee, *Rensselaer Polytechnic Institute, Dept. of Mechanical Engineering, Aeronautical Engineering and Mechanics* ---- 49

Low-Cost Machine Vision Monitoring of the SLS Process
Ian Gibson, Ling Wai Ming, *Department of Mechanical Engineering, The University of Hong Kong* ---- 59

SLS Processing of Functionally Gradient Materials
L. Jepson, J. J. Beaman, D. L. Bourell and K. L. Wood, *University of Texas at Austin, Department of Mechanical Engineering* ---- 67

Direct Selective Laser Sintering and Containerless Hot Isostatic Pressing for High Performance Metal Components
Suman Das, Martin Wohlert, Joseph J. Beaman, David L. Bourell, *University of Texas at Austin, Department of Mechanical Engineering, Laboratory for Freeform Fabrication* ---- 81

DTIC QUALITY INSPECTED 3

Direct SLS of Powder Compositions Used for Self-Propagating High-Temperature Synthesis
I. V. Shishkovsky[a], A.G. Makarenko[b] and A.L. Petrov[a], [a]P.N. Lebedev *Physics Institute, Samara Branch, [b]Samara Technical University, SHS Laboratory* ---------- 91

Net Shape Functional Parts Using Diode Laser
Tariq Manzur[a,c], Chandra Roychoudhuri[a,c], Puneit Dua[a,c], Fahmida Hossain[d], Harris Marcus[b,c], *[a]Photonics Research Center, [b]Institute of Materials Science, [c]University of Connecticut, [d]Massachusetts Materials Research*---------- 99

Progress On Tooling by 3D Printing; Conformal Cooling, Dimensional Control, Surface Finish and Hardness
Emanuel Sachs, Samuel Allen, Honglin Guo, Javier Banos, Michael Cima, James Serdy, and David Brancazio, *Massachusetts Institute of Technology, Department of Mechanical Engineering*---------- 115

Measurement of Residual Stresses in Parts Created by Shape Deposition Manufacturing
N.W. Klingbeil, J.W. Zinn, J.L. Beuth, *Carnegie Mellon University, Department of Mechanical Engineering*---------- 125

Layered Manufacturing Material Issues for SDM of Polymers and Ceramics
John Kietzman[a], Alexander Cooper[a], Lee Weiss[b], Lawrence Schultz[b], John Lombardi[c], Fritz Prinz[a], *[a]Stanford University, [b]Carnegie Mellon University, [c]Advanced Ceramics Research*---------- 133

Statistical Process Control for Solid Freeform Fabrication Processes
Vito R. Gervasi, *Milwaukee School of Engineering, Rapid Prototyping Center*---------- 141

Net-Shape Composites Using SLA Tetracast* Patterns
Vito R. Gervasi, *Rapid Prototyping Center, Milwaukee School of Engineering* ---------- 149

Shrinkage and Deformation in Components Manufactured by Fused Deposition of Ceramics
Joseph J. McIntosh[a], Stephen C. Danforth[a], Vikram R. Jamalabad[b], *[a]Rutgers - The State University of New Jersey, Center for Ceramics Research, [b]AlliedSignal Research and Technology* ---------- 159

The Design and Construction of a Medical System to Optimize the Endoscopic Ultrasound Procedure
Darius P. Daruwala, Christopher M. Johnson and Donald R. Jacobsen, *Rapid Prototyping Center, Milwaukee School of Engineering* ---------- 167

Miscroscopic Flow Observation of Photopolymer by UV-Laser Beam Exposure
Yi Xu , Masato Imamura, Takeo Nakagawa, *Institute of Industrial Science, University of Tokyo* ---------- 177

Fused Deposition of Ceramics: Progress Towards a Robust and Controlled Process for Commercialization
R. Clancy[a], V. Jamalabad[a], P. Whalen[a], P. Bhargava[b], C. Dai[b], S. Rangarajan[b], S. Wu[b], S. Danforth[b], N.Langrana[b], A.Safari[b], [a]*AlliedSignal Research and Technology, Research and Technology,* [b]*Rutgers - The State University of New Jersey, Center for Ceramic Research* ---------- 185

FDM of ABS Patterns for Investment Casting
Paul Blake[a], Eric Fodran[b], Martin Koch[b], Unny Menon[b], Bill Priedeman[a], Stephen Sharp[b], [a]*Statasys,* [b]*California Polytechnic University* ---------- 195

Rapid Prototyping of Functional Metal and Ceramic Components by the Multiphase Jet Solidification (MJS) Process
Donald M. Kupp[a], Harald Eifert[a], Matthias Greul[b], Mattias Künstner[b], [a]*Fraunhofer Resource Center-Delaware,* [b]*Fraunhofer -Institute for Applied Materials Research-Bremen* ---------- 203

Bonding Methods for Laminated Tooling
Daniel F. Walczyk, Nathanael Y. Dolar, *Rensselaer Polytechnic Institute* ---------- 211

High Speed UV Laser Beam Scanning by Polygon Mirror
Kenji Yamazawa[a], Toshiki Niino[a], Seiji Hayano[b] and Takeo Nakagawa[c], [a]*The Institute of Physical and Chemical Research (RIKEN),* [b]*ASPECT Co.,* [c]*University of Tokyo* ---------- 223

Layered Micro-Wall Structures from Gas Phase
Joseph Pegna, David Messia, Woo Ho Lee, David DeAnqelis, *Rensselaer Polytechnic Institute, Department of Mechanical Engineering, Aeronautical Engineering and Mechanics* ---------- 231

Gas Phase SFF Control System for Silicon Nitride Deposition by SALD/SALDVI
Shay Harrison, Chris F. Costa, Kevin J. Jakubenas, James E. Crocker and Harris L. Marcus, *University of Connecticut, Institute of Materials Science* ---------- 241

Pre-LOM, LOM, and Post-LOM Processes for the Fabrication of SiC and SiC/SiC Components
Don Klosterman, Richard Chartoff, Nora Osborne, George Graves and Allan Lightman, *University of Dayton, Rapid Prototype Development Laboratory* ---------- 247

Automated Fabrication of Nonresorbable Bone Implants Using Laminated Object Manufacturing (LOM)
Cheri Steidle[a], Don Klosterman, Nora Osborne, George Graves and Richard Chartoff, *University of Dayton, Rapid Prototype Development Laboratory,* [a]*Chemical Engineering* ---------- 248

Rapid Fabrication of Disposable Fixtures for Correct Assembly of Split Build Rapid Prototyped Parts
Samit R. Kadakia[a], Andrei S. Novac[a], Mark D. Van Roosendaal[a], Charles L. Thomas[a], and Norman T. Smith[b], [a]*University of Utah, Department of Mechanical Engineering,* [b]*Ford Motor Company* ---------- 249

Tooling

Zirconium Diboride/Copper EDM Electrodes from Selective Laser Sintering
Brent Stucker, Walter Bradley, P. T. Eubank, Somchintana Norasetthekul and Bedri Bozkurt
Texas A&M University, Department of Mechanical Engineering ---------- 257

Thermal Effects on Accuracy in the 3D Keltool™ Process
Neil Hopkinson and Phill Dickens, *Dept. of Manufacturing Engineering & Operations Management, University of Nottingham, UK* ---------- 267

Sterolithographic Injection Molds for Direct Tooling
Suresh Jayanthi[a], Bronson Hokuf[a], Ronald McConnell, Robert J. Speer[b] and Paul S. Fussell[b], *[a]DuPont Somos Solid Imaging Materials, DuPont Somos Solid Imaging Group, [b]Aluminum Company of America, Alcoa Technical Center*---------- 275

Rapid Tooling by Powder Casting Transferred from R/P Model: Manufacturing Conditions Pursuing Zero Shrinkage
Hiroyuki Noguchi and Takeo Nakagawa, *University of Tokyo, Institute of Industrial Science* ---------- 287

Stereolithography Injection Mould Tools Failure Analysis
Sadegh Rahmati, Phill Dickens, *University of Nottingham, Department of Manufacturing Engineering and Operations Management*---------- 295

Deflection and the Prevention of Ingress within Laminated Tooling for Pressure Die-Casting
R. C. Soar, P. M. Dickens, *University of Nottingham, Department of Manufacturing Engineering and Operations Management*---------- 307

Injection Molds Behavior and Lifetime Characterization
N.P. Karapatis, J.-P.S. van Griethuysen and R. Glardon, *Swiss Federal Institute of Technology, Department of Mechanical Engineering* ---------- 317

Materials

Novel Liquid Crystal Resins for Stereolithography: Mechanical and Physical Properties
J. W. Schultz, J. S. Ullett, R. P. Chartoff, R.T. Pogue, *Rapid Prototype Development Laboratory and Ohio Rapid Prototype Process Development Consortium, University of Dayton*---------- 325

Novel Liquid Crystal Monomers for Stereolithography: Reaction Rates and Photopolymerization Conversion
Robert T. Pogue and Richard P. Chartoff, *Center for Basic and Applied Polymer Research and Rapid Prototype Development Laboratory, University of Dayton* ---------- 333

Silica Filled Resins for Rapid SLA Tools
Douglas Taft[a,c], Amod Ogale[a,c], Frank Paul[b,c], Elaine Hunt[b,c] and Said Ahzi[b,c], *[a]Department of Chemical Engineering, [b]Department of Mechanical Engineering, [c]Clemson University, Laboratory for the Advancement of Industrial Prototyping* ---------- 341

SL 5410: High Humidity, Water, and Heat Resistant Resin for Stereolithography
T. H. Pang[a], I. Figueroa[a], J. Fong[a], A. Melisaris[a], R. Wang[a], S. Hanna[b], H. Nguyen[b], M. Guertin[b] and C. Phan[b], *[a]Ciba Specialty Chemicals Corporation, [b]3D Systems Corporation* ---------- 349

Stereolithography of Ceramics
T. Himmer[a], T. Nakagawa[a,b], H. Noguchi[b], *[a]RIKEN Instrumentation Center, Saitama, Japan, [b]University of Tokyo, Institute of Industrial Science* ---------- 363

High Green Density Ceramic Components Fabricated by the Slurry-Based 3DP Process
Jason Grau, Jooho Moon, Scott Uhland, Michael Cima and Emanuel Sachs, *Massachusetts Institute of Technology, Department of Mechanical Engineering* ---------- 371

CAM-LEM Processing: Materials Flexibility
Z. E. Liu, T. C. Ko, J. Best, J. D. Cawley and A.H. Heuer, *Case Western Reserve University, Department of Materials Science and Engineering* ---------- 379

Multi-Material Processing by LENS
Michelle L. Griffith, Lane D. Harwell, J. Tony Romero, Eric Schlienger, Clint L. Atwood and John E. Smugeresky
Sandia National Laboratories ---------- 387

Shrinkage, Weight Loss and Crack Prevention During Binder Burn Out of Components Produced by Fused Deposition of Ceramics (FDC)
P. Bhargava[a], A. Bandyopadhyay[a], S. Rangarajan[a], G. Qi[a], C. Dai[b], S. Wu[a], S. Danforth[a] and A. Safari[a], *Rutgers - The State University of New Jersey, [a]Center for Ceramic Research, [b]Mechanical and Aerospace Engineering* ---------- 395

Processing of Novel Piezoelectric Transducers Via SFF
A. Safari S. C. Danforth, R K. Panda, T. F. McNulty, F. Mohammadi, A. Bandyopadhyay, *Rutgers - The State University of New Jersey, Center for Ceramic Research* ---------- 403

High Quality, Fully Dense Ceramic Components Manufactured Using Fused Deposition of Ceramics (FDC)
Cheng Dai[a,c], Gang Qi[b,c], Sriram Rangarajan[b,c], Suxing Wu[b,c], Noshir A. Langrana[a,c], Ahmad Safari[b,c] and Stephen C. Danforth[b,c], *[a]Mechanical and Aerospace Engineering, [b]Center for Ceramic Research, [c]Rutgers - The State University of New Jersey* ---------- 411

Properties of RU955 Si_3N_4 Filament for Fused Deposition of Ceramics
Gang Qi[a], Cheng Dai[b], Sriram Rangarajan[a], Suxing Wu[a], Amit Bandyopadhyay[a], Noshir Langrana, Ahmad Safari[a], and Stephen C. Danforth[a], *Rutgers - The State University of New Jersey, [a]Center for Ceramic Research, [b]Mechanical and Aerospace Engineering* ---------- 421

The Role of Materials Processing Variables in the FDC Process
Sriram Rangarajan[a], Gang Qi[a], Amit Bandyopadhyay[a], Cheng Dai[b], Joon W. Han[a], Parag Bhargava[a], Suxing Wu, , Ahmad Safari[a] and Stephen C. Danforth[a], *Rutgers - The State University of New Jersey, [a]Center for Ceramic Research, [b]Mechanical and Aerospace Engineering* ---------- 431

Soft Elastomers for Fused Deposition Modeling
Kurt Elkins[a,e], Howard Nordby[b,e], Christopher Janak[c,e], Robert W. Gray IV[d,e], Jan Helge Bøhn[c,e], Donald G. Baird[d,e], *[a]Department of Aerospace and Ocean Engineering, [b]Department of Materials Science and Engineering, [c]Department of Mechanical Engineering, [d]Department of Chemical Engineering, [e]Virginia Polytechnic and State University* ---------- 441

Effects of Processing Conditions on Prototypes Reinforced With TLCPs for Fused Deposition Modeling
Robert W. Gray IV, Donald G. Baird, Jan Helge Bøhn, *Department of Chemical Engineering, Department of Mechanical Engineering, Rapid Prototyping Laboratory and Polymer Materials and Interfaces Laboratory, Virginia Polytechnic Institute and State University* ---------- 449

Issues Associated With EFF & FDM Ceramic Filled Feedstock Formulation
John L. Lombardi[a], Robert A. Hoffman[a], Jason A. Waters[a], Dragan Popovich[a], Chad Souvignier[b] and Sajiv Boggavarapu[b]
[a]Advanced Ceramics Research, Inc., [b]University of Arizona, Arizona Materials Labs ---------- 457

Selective Laser Sintering of Quartz Powder
Hongyun Wang, David Bourell and Joseph J. Beaman Jr., *The University of Texas at Austin, Department of Mechanical Engineering* ---------- 465

Extrusion Freeforming of Nylon 6 Materials
John L. Lombardi[a], Paul D. Calvert[b], *[a]Advanced Ceramics Research, [b]Arizona Materials Laboratories, University of Arizona* ---------- 473

Fabrication of In-situ SiC/C Thermocouples by SALD
Lianchao Sun, Kevin J. Jakubenas, Jim Crocker, Shay Harrison, Leon L. Shaw, Harris L. Marcus, *Institute of Materials Science, The University of Connecticut* ---------- 481

SALDVI Optimization for the Tetramethylsilane - Silicon Carbide System
James E. Crocker, Kevin J. Jakubenas, Shay Harrison, Leon L. Shaw, and Harris L. Marcus, *Institute of Materials Science, University of Connecticut* ---------- 489

High Pressure Convectively-Enhanced Laser Chemical Vapor Deposition of Titanium
James Maxwell, Ramnath Krishnan, Suresh Haridas, *Institute for Micromanufacturing, Louisiana Tech University* ---------- 497

The LMP Process: Layered Metal Prototyping of Titanium from Condensed Thin-Films for Microelectromechanical Devices
James Maxwell, Sandesh Borse, *Institute for Micromanufacturing, Louisiana Tech University* ---------- 505

Properties of Near-Net Shape Metallic Components Made by the Directed Light Fabrication Process
Gary K. Lewis[a], John O. Milewski[a], Dan B. Thoma[a], Ron B. Nemec, *[a]Los Alamos National Laboratory, [b]SyntheMet Corporation* ---------- 513

Functional Gradient Metallic Prototypes through Shape Deposition Manufacturing
J.R. Fessler[a], A.H. Nickel[a], G.R. Link[a], F.B. Prinz[a], P. Fussell[b], *[a]Stanford University, [b]ALCOA Technical Center* ---------- 521

Laminated Object Manufacturing of Si_3N_4 with Enhanced Properties
Matthew J. Pope, Mark C.L. Patterson, Walter Zimbeck and Mark Fehrenbacher, *Ceramic Composites Inc.* ---------- 529

Automated Fabrication of Monolithic and Ceramic Matrix Composites via Laminated Object Manufacturing (LOM)
Don Klosterman, Richard Chartoff, Nora Osborne and George Graves, *University of Dayton, Rapid Prototype Development Laboratory* ---------- 537

Modeling

Rapid Prototyping Decision Support System
K. G. Jones and R. I. Campbell, *Department of Manufacturing Engineering and Operations Management, University of Warwick* ---------- 551

Empirical Similitude Method for the Functional Test with Rapid Prototypes
Uichung Cho and Kristin L. Wood, *University of Austin at Texas, Department of Mechanical Engineering* ---------- 559

The Clemson Intelligent Design Environment For Stereolithography - CIDES 2.0
Jill S. Kirschman[a,d], Charles F.Kirschman[b,d], Georges M. Fadel[c,d], Joel S. Greenstein[a,d], *[a]Industrial Engineering Department, [b]BPM Technology, Inc., [c]Mechanical Engineering Department, [d]Laboratory to Advance Industrial Prototyping, Center for Advanced Manufacturing, Clemson University* ---------- 569

An Analysis Technique for Layered Manufacturing Based on Quasi-Wavelet Transforms
Cheol H. Lee, Charles L. Thomas, *University of Utah, Department of Mechanical Engineering* ---------- 577

Using Adaptive Ruled Layers for Rapid Prototyping: Principles and First Results
P.J. de Jager, J.J. Broek and J.S.M. Vergeest, *Faculty of Industrial Design Engineering, Delft University of Technology* ---------- 585

Reverse Engineering: Algebraic Boundary Representations to Constructive Solid Geometry
S.F. Buchele[a], W.A. Ellingson[b], *[a]Computer Sciences Department, University of Texas, [b]Energy Technology Division, Argonne National Laboratory* ---------- 593

Reverse Engineering: Practical Considerations For Rapid Prototyping
Alair Griffin[a], Scott McMillin[a], Curtis Griffin[a], Charles Knox[b], *[a]Lone Peak Engineering, Inc., [b]Image3, LLC* ---------- 603

Solid Model Creation for Materially Graded Objects
Vinod Kumar, Debasish Dutta, *Department of Mechanical Engineering and Applied Mechanics, University of Michigan* ---------- 613

A Data Format Providing Side Wall Orientation and Adaptive Slicing for Use in Rapid Prototyping
Wei Fang, Chan Siang Ngooi, Haiqing Gong, *School of Mechanical and Production Engineering, Nanyang Technological University* ---------- 621

Build Style Decision Support for Stereolithography
J. McClurkin and D. Rosen, *Rapid Prototyping and Manufacturing Institute, Georgia Institute of Technology* ---------- 627

Validation of Rapid Prototyping Material for Rapid Experimental Stress Analysis
C. Schley, G. Smith-Moritz, G. C. Calvert, *University of Warwick, Rover Group, Advanced Power Train Technology*---------- 635

CAD and Control Technologies for Computer-Aided Manufacturing of Laminated Engineering Materials
Sangeun Choi[a,d], Ravi Hebbar[b,d], Yong Zheng[b,d], Wyatt S. Newman[c,d], *[a]Department of Mechanical Engineering, [b]Department of Electrical Engineering, Department of Electrical Engineering and Applied Physics, [d]Case Western Reserve University*---------- 643

Optimising Build Parameters and Hatch Style for Part Accuracy in Stereolithography
S.O. Onuh, K.K.B. Hon, *Rapid Prototyping Centre, Department of Industrial Studies, The University of Liverpool*---------- 653

An Integrated Software System for Process Planning for Layered Manufacturing
Anne L. Marsan, Seth Allen, Prashant Kulkarni, and Deba Dutta, *CAD/CAM Group, Department of Mechanical Engineering and Applied Mechanics, University of Michigan*---------- 661

The Use of VRML to Integrate Design and Solid Freeform Fabrication
Yanshuo Wang[a], Jian Dong[b] and H.L. Marcus[a], *[a]Institute of Materials Science, The University of Connecticut, [b]Space System Division, Boeing North American, Inc.*---------- 669

A Thermal Model for Laminated Object Manufacturing (LOM)
Lawrance Flach[a,c], Donald A. Klosterman[b,c], Richard P. Chartoff[b,c], *[a]Department of Chemical Engineering, [b]Rapid Prototype Development Laboratory and Ohio Rapid Prototype Process Development Consortium, [c]University of Dayton*---------- 677

Thermal Analysis of Fused Deposition
M. Atif Yardimci[a], Selcuk I. Guceri[a] and Stephen C. Danforth[b], *[a]University of Illinois at Chicago, [b]Rutgers - The State University of New Jersey, Center for Ceramic Research* ---------- 689

Simulation of Coarsening During Laser Engineered Net Shaping
Veena Tikare, Michelle Griffith, Eric Schlienger and John Smugeresky, *Sandia National Labs* ---------- 699

On Dimensional Stabilities: Modeling of the Bonus-Z During the SLS Process
Alexandre L. Papadatos, Said Ahzi, Carl R. Deckard and Frank W. Paul, *Clemson University, Laboratory to Advance Industrial Prototyping and Department of Mechanical Engineering*---------- 709

Rheology and Solid Freeform Fabrication: Modeling Material Flow in Deposition Techniques
R.S Crockett[a] and P.D. Calvert[b], *[a]Milwaukee School of Engineering, Rapid Prototyping, [b]University of Arizona, Arizona Materials Laboratories* ---------- 717

Modeling of Mechanical Behavior of SLA Parts
ZhanpingWu[a], Said Ahzi[a], Frank W. Paul[a], Elaine Hunt[a], and Amod A. Ogale[b], *Clemson University, Laboratory to Advance Industrial Prototyping, [a]Department of Mechanical Engineering, [b]Department of Chemical Engineering* ---------- 725

Reaction Heat Effect on Initial Linear Shrinkage of Stereolithography Resins
Hiroyuki Narahara[a],Fumiki Tanaka[b], Takeshi Kishinami[b], Satoru Igarashi[b], Katsumasa Saito[c], *[a]Department of Mechancial Systems Engineering, Kyushu Institute of Technology, [b]Hokkaido University, [c]Gunma Polytechnic College* ---------- 733

Keyword Index ---------- 741

Author/Attendee List ---------- 745

PREFACE

The Eighth Solid Freeform Fabrication (SFF) Symposium, held at The University of Texas in Austin on August 11-13, 1997, was attended by 200 national and international researchers. Papers addressed SFF issues in computer software, machine design, materials synthesis and processing, and integrated manufacturing. The continued growth in the research, application and development of SFF approaches was readily apparent from the increased participation over previous years and the diverse domestic and foreign attendees from industrial users, SFF machine manufacturers, universities, and government. The excitement generated at the Symposium reflects the participants' total involvement in SFF and the future technical health of this growing technology. The Symposium organizers look forward to its being a continuing forum for technical exchange among the expanding body of researchers involved in SFF.

The Symposium was again organized in a manner to allow the multi-disciplinary nature of the SFF research to be presented coherently, with various sessions emphasizing computer issues, machine topics, and the variety of materials aspects of SFF. We believe that documenting the constantly changing state of SFF art as represented by these Proceedings will serve both the people presently involved in this fruitful technical area as well as the large flux of new researchers and users entering the field.

The editors would like to extend a warm "Thank You" to Glorya Gutchess for her detailed handling of the logistics of the meeting and the Proceedings, as well as her excellent performance as registrar and problem solver during the meeting. We also acknowledge the support efforts of Cindy Pflughoft throughout. We would like to thank the organizing committee, the session chairmen, the attendees for their enthusiastic contributions, and the speakers both for their significant contribution to the meeting and for the relatively prompt delivery of the manuscripts comprising this volume. We look forward to the continued close cooperation of the SFF community in organizing the Symposium. We also want to thank ONR through Grant No. N00014-97-1-0453, DARPA, and The Minerals, Metals and Materials Society and the University of Connecticut at Storrs for co-sponsoring the Symposium with the Mechanical Engineering Department, Laboratory for Freeform Fabrication and the Center for Materials Science and Engineering at the University of Texas at Austin.

The editors.

Organizing Committee

Joel Barlow	University of Texas at Austin
Joseph Beaman	University of Texas at Austin
David Bourell	University of Texas at Austin
Richard Crawford	University of Texas at Austin
Harris Marcus	University of Connecticut at Storrs

Advisory Committee

Dr. Robert Brown	The Gillette Company
Dr. Michael Cima	Massachusetts Institute of Technology
Dr. William Coblenz	Advanced Research Projects Agency
Dr. Sam Drake	University of Utah
Dr. Steven Fishman	Office of Naval Research
Mr. Sean O'Reilly	Ford Motor Company
Dr. Fritz Prinz	Stanford University
Dr. Emanual Sachs	Massachusetts Institute of Technology
Mr. Greg Sanders	Lost Foam International
Dr. Susan Smyth	General Motors Corporation
Dr. Ralph Wachter	Office of Naval Research
Dr. Michael Wozny	National Institute of Standards and Technology



In Memoriam

Dick Aubin

Dick Aubin was a pioneer and leading spokesman for rapid prototyping and freeform fabrication. His involvement predates this symposium. In fact, Dick was instrumental in the creation and evolution of this technical forum through his comments and suggestions as a long-time member of the Advisory Committee. He was a regular participant and frequent author. Beyond this, Dick was a force for utilization of this technology in commercial settings, and his efforts led to the early introduction of SFF technologies. The successful result of his efforts at United Technologies was the creation and implementation of a most complete and accessible leading-edge facility. We appreciate and recognize Dick's contributions to solid freeform fabrication. Just last year, he was selected as part of an elite team to review the status of SFF worldwide.

Dick spoke prophetically with conviction and often conveyed a passion for the field and the directions of its evolution and maturity. Dick died unexpected this year. His contributions were acknowledged in the opening session of this Symposium, and it is fitting that his memory be preserved in this proceedings volume.

Liquid Metal Jetting for Printing Metal Parts

John W. Priest
The University of Texas at Arlington
Box 19017
Arlington, TX 76019

Charles Smith
The University of Texas at Arlington
Electrical Engineering
Box 19016
Arlington, TX 76019

Patrick DuBois
Automation & Robotics Research Institute
Box 19045
7300 Jack Newell Blvd.
South Ft. Worth, TX 76118

ABSTRACT

Liquid Metal Jetting (LMJ) is solid freeform fabrication process for producing metal mechanical parts and electronic interconnects. It is a technology similar to ink jet printing where individual molten droplets are accurately printed. LMJ will produce metal parts on demand from a CAD database with functional performance parameters similar to metal parts produced by machining or casting. By controlling solidification rates and metal alloy composition, LMJ is able to produce parts with unique properties such as metal matrices and functionally graded materials. This paper will review the current status of LMJ and future applications for this technology.

One emerging manufacturing technology that addresses many challenges in solid freeform fabrication (SFF) is liquid metal jet printing (LMJP). The process is based on technology analogous to ink-jet printing. This agile additive method dispenses individually controlled microballs of molten metals to precise locations. Unlike spray forming and spray deposition process which spray materials in an uncontrolled manner, LMJP dispenses and controls every "single molten droplet" of material to a specific location using digitally stored computer-aided design (CAD) data in a highly reproducible manner. The direct-write, additive nature of an LMJP system offers an agile approach. Potential applications for LMJP include the ability to rapidly fabricate 3-d mechanical parts and electronic circuitry. This paper discusses research issues in the development of liquid metal jet printing systems. The technical issues that affect jet operation and the quality of jetted materials are also discussed.

Background of Jetting Research

The Frenchman Nollet wrote in 1754 of observations made on a low-speed stream issuing from a small diameter nozzle [1]. He commented on the formation of drops, and the ability of a charged rod to deflect them. Lord Raleigh undertook the first thorough and accurate mathematical analysis of liquid jets in the 1870s [2,3]. Rayleigh's theoretical work explained the droplet disintegration mechanism as driven by surface tension induced instabilities. Basset [4] published a theory confirming the role of surface tension induced instabilities and the stabilizing effect of viscosity. Experimentalist A. Haenlein built a system to produce very long (up to 5 meter) water-, glycerin- and gasoline-air jets under positive pressures and no external oscillation in 1931 [5]. Weber [6,7], used the data and observations of Haenlein to generate the first cogent and useful analysis of a viscous cylindrical jet with both symmetric and transverse aerodynamic wave actions although the experimental results did not completely agree with the theory.

Electro-mechanical forced stimulation, was studied by Hansell [8] in the 1950's. This greatly broadened the application for jetting. Jet applications changed from fuel injection to rocket propulsion to ink-jet printing. Lee and Spencer [9] used fuel injection mechanisms with fairly broad nozzle length to diameter ratios in the generation of high speed photographic studies of liquid jets. McCormack et. al. [10] in 1965 described the essential elements of a modern forced oscillation experimental water jet system employing a vibrating PZT ceramic crystal

Jetting for building mechanical structures and parts, which is often called solid freeform fabrication (SFF), started with the use of wax and wax like materials. For example, a patent by Mitchell [11] discloses the generation of an object with liquid wax or similar type material using a jet printer. A later patent of Sanders Prototype shows a desktop jetting machine for generating wax parts. These systems used piezoelectric crystals which limited the systems to low melting point temperature waxes. Considerable research on solidification issues in jetting wax was performed by Gao and Sonin[12]. The jetting of molten metals became the natural next step for mechanical and electronic structures.

The field of liquid metal jet printing started in electronics with low temperature solder applications on a suggestion by IBM in 1972 [13]. Work during the 1980s by Heiber in solder jetting resulted in the first LMJP patent for Philips North American in 1989 [14]. The described drop on demand method utilized a lead zirconium titanate piezo-electric (PZT) crystal to generate

a pressure wave for controlled the droplet generation. Since PZT undergoes a phase change and loses its piezoelectricity at a finite temperature (i.e. Curie temperature), the technology described by the Heiber patent was initially useful up to approximately 200°C which limited the technique to very low melting point metals such as low temperature solder. As improved designs and PZT materials with higher operating temperatures became available, medium melting point metals such as 63/37 solder could be jetted.

Several research groups in the late 1980's and early 1990's such as Priest, Smith and DuBois at ARRI/UTA [15-21], Hayes and Wallace at MicroFab Technologies [22-25], and IBM [26] focused on solder jetting research to be used in electronic applications.

Rather than using a piezoelectric crystal to generate droplets, Ted Smith and Winstead at IBM took a different path and in 1993 filed for a patent on a electrodynamic pump for dispensing molten solder [34]. This pump uses a programmable current source with a magnetic coil to produce the jetting force. The pump has been shown to be reliable but is slower than piezoelectric crystal methods.

Several researchers in the early 1990's became interested in using liquid metal jetting to fabricate spherical balls (i.e. powder). Liquid metal jetting is an excellent method for ball generation. These spherical balls (i.e. powder) can be used in solder paste and powder metallurgy. Solder jetting has been reported to produce balls with 5% repeatability in volume. In a 1992 US patent filing, Chun and Passow proposes to charge the droplets to maintain their uniform size [27]. Filed in 1993, Hayes proposes a method for making solder compositions [23].

The benefits of using metal jet printing to directly fabricate 3-d metal parts and structures was obvious. During the early 1990's, research in liquid metal jet printing for manufacturing mechanical structures began. LMJP could produce metal parts on demand directly from a CAD database with functional performance parameters similar to or better than metal parts produced by machining or casting. By controlling solidification rates and metal alloy composition, LMJP can also produce 3 dimensional parts with unique properties such as metal matrices and functionally graded materials. The key material parameters affecting a materials ability to be jetted are the relationship between surface tension and viscosity. Analyses developed by Smith [28,29] and performed at The Automation & Robotics Research Institute at The University of Texas at Arlington have indicated that most molten metals can be jetted. Metals that have been jetted include copper, aluminum, tin, 63/37 solder, low melting point temperature solders, and mercury. In addition to Priest, Smith, and DuBois at ARRI/UTA, other groups led by Chun et.al. at MIT [30] and Orme at University of California at Irvine [31] are pursuing metal jet printing for building mechanical parts and producing uniformly sized metal balls. Chun and Passow developed a method called uniform spray deposition where the metal is jetted but individual droplets are not controlled (i.e. sprayed). In filings starting in 1990, Orme and Muntz has received a series of US patents on an apparatus for droplet stream manufacturing where the meta droplets are printed onto a collector of the shape of the desired product [32].

In addition to working on electronics and mechanical structure applications, several research groups started to examine methods for jetting higher melting point metals. Work done by Smith, Priest and DuBois at ARRI/UTA, IBM and Chun at MIT have resulted in several ideas

and US patents for jetting high melting point temperature metals such as Al, Cu, etc. [33,27]. In the patent filing, Chun suggested locating the lead metaniobate piezoelectric which is connected to a shaft and disk that extends to the molten metal. This keeps the crystal away from the heat.

In 1994, DARPA funded Texas Instruments and UTA/ARRI to build a prototype machine to jet high melting points metals such as copper, for a direct circuit write, environmentally friendly method for printed circuit boards.

The ARRI/UTA group worked on innovative methods for replacing the piezoelectric crystal with heat resistant methods for generating the force to produce droplets. Filed in 1993, the Smith, Priest, and DuBois patent [33] illustrated several innovative apparatus and methods for dispensing high temperature materials.

Liquid Metal Jet Printing System

There are two basic jetting methods: continuous and drop on demand. Continuous jetting is where the material is continuously jetted. Common applications for continuous jetting is high speed printing of patterns on bank checks, date labeling of products, and paper towels with printed designs. A thin liquid jet is considered to be continuous if the break up of the jet and resulting formation of droplets occurs a measurable distance down the jet away from the orifice from which the jet emanates. Such a continuous jet can be caused to breakup in a controlled way which is both uniform and periodic or random aperiodic as in the case of the natural break up of a viscous jet such as pouring syrup. A thin liquid jet is considered to be discontinuous if the break up of the jet and resulting formation of droplets occurs at the nozzle or orifice from which the jet emanates. Such a discontinuous jet is usually denoted as a 'drop on demand' jet and depending upon the exciting mechanism could be either periodic or aperiodic. A major difficulty in identification occurs when the discontinuous jet (i.e., drop on demand jet) is continuously excited in a periodic manner. The resulting drop on demand droplet stream appears identical to the droplet stream formed from a periodically excited continuous jet. A common application for this method is an ink jet printer for personal computers. The advantages of the continuos method is the faster droplet rates (10-100 KHz) and that less energy force is required to produce the droplets. The advantage of drop on demand is that there are no unused droplets. Table that shows the differences and for what applications?

Parameter	Drop on Demand	Continuous
Jet Speed (droplets per second)	less than 10 KHz	10 to 100 Khz in a cylindrical configuration and 5 to 20 Khz in a pump configuration
Droplet Size Relative to Orifice Size (diameter to diameter)	Same which is better for producing smaller drops	Droplet is 1.8 times larger than the oriface diameter which is better for producing larger drops.
Material Usage	Less	Must gutter unwanted droplets. This unused material can be reused in many applications
Generator Force/Energy Required	More	Less

The system for this discussion is a high speed, continuous metal jet printing system. The prototype system, shown in Figure 1, is divided into three distinct areas; 1) supply and head, 2) electrostatic charging and deflection area, and 3) target surface. The metal supply is melted in a pressurized container and the molten metal is forced through the tubing to the jet head. The droplet generator, which is housed in the jet head assembly, applies a pulsing mechanical force on the jet stream to stabilize the droplet formation. The liquid metal exits through an orifice attached to the solder jet head. This process results in the formation of a continuous stream of attached and elongated droplets. As a result of the mechanical excitation and surface tension, droplets break off from the molten metal stream. Generally the orifice diameter determines the size of the droplet, however, the droplet size can be changed within certain tolerances by modifying the force applied to the droplet generator.

The vertical shooter head is mounted to an precision X-Y positioning table. Using the a system shown in Figure 2, molten metals are applied in a precision pattern determined by CAD data. A CAD pattern information file is combined with jetting system knowledge base to develop the process commands. These commands include equipment control, environmental chamber control and numerical control (NC) code via a software package. At break up, a predetermined electrical charge is applied to the droplet according to the CAD data and a jet process knowledge base. The charged droplet is then directed to the target surface or to a catcher system by use of electric field deflection plates. A catcher is used to collect the unused droplets. To maintain a molten droplet and minimize oxidation, it is necessary to enclose the jet head and substrate in a heated, inert environment. A thermally controlled environmental chamber is incorporated for this purpose.

Jetted Materials Results

Jetting systems currently operational have produced output in the form of microballs (40 to125 μm in diameter), bumps on a substrate, individual wetted drops or splats on substrates, circuit lines, micro-diameter wires and three-dimensional cantilevered structures with very high aspect ratios (10:1).

Current Research Applications

On-going research efforts are being performed at the Automation & Robotics Research Institute at the University of Texas at Arlington, MicroFab Technologies, MIT, IBM, MPM, and The University of California at Irvine.

The ARRI/UTA research laboratory is located in Dallas/Ft.Worth and focuses on high temperature, high speed LMJP technology for mechanical 3-d parts, generating balls, and electronic manufacturing processes. Droplet speeds can be as high as 100 KHz although typical rate are in the order of 30 KHz. A LMJP prototype system is now being used to investigate how to deposit various high temperature metals such as aluminum and steel for building mechanical parts, aluminum printed circuit boards, and ball generation.

MicroFab Technologies Inc. is a company in Plano, Texas that has focused on commercializing solder jetting for surface mount technology in the electronics industry. This

research is led by Drs. Don Hayes and David Wallace. The three applications are fine pitch, ball grid arrays, and flip chip. Funding has been provided by the Advanced Technology Program of the US Department of Commerce. A drop on demand jet machine has been developed with Universal Instruments which produces 60 um diameter droplets with rates up to 2 KHz. It uses drop on demand generators which use piezoelectric crystals. Details and photographs can be found on their ISHM paper on the MicroFab web site [25]. Efforts are underway to integrate Microfab's demand mode technology with MPM's metal jet printing machine.

Research at the University of California at Irvine is being led by Dr. Melissa Orme. The research has focused on new forcing techniques which can modify droplet size and patterns, modeling of droplet collisions, and net form materials synthesis (i.e. rapid prototyping of mechanical parts) [32,35].

MIT has two different research groups in the Department of Mechanical Engineering that are working on jetting. One is led by Dr. Jung-Hoon Chun. Research by Chun has focused on modeling the droplet solidification process, generating balls and solid free form fabrication of mechanical parts [27,35,36,37,38]. Their method of producing metal parts is called uniform spray deposition (UDS). The other group is led by Dr. Sonin who has focused on modeling of the solidification process initially using wax materials [12].

Two other companies have been working on solder jet machines. These are IBM and MPM. The work at IBM (Austin) uses their patented pump and has focused on jetting solder for electronics assembly. Both IBM and MPM have produced prototypes for test and evaluation by several major electronics companies.

Summary

Current research has shown that a number of technical issues must be resolved prior to metal jet printing becoming a successful process in SFF. Major technical issues include:

1. process stability and reliability,
2. impact, solidification, and shape control
3. part and circuit performance.

Process Stability and Reliability

Process stability and reliability is a major problem due to the complexity of the jetting process. To date, liquid metal jet machine have not performed to the levels of quality that is required in industry. Key challenges include oxidation, material contamination, and thermal management and droplet generator reliability.

An important aspect of reliable operation of the jet is eliminating material contamination which can lead to clogging or leaching of contaminants into the molten metals. This means that the choice of both the construction materials used in the design and the filtering methods to

remove contaminants in the raw material are important aspects. The presence of particulate matter such as oxides or intermetallic phases can lead to clogging of the jet.

Impact, Solidification, and Shape Control

Investigations are underway by several research groups to study the impact of liquid metal droplets onto rigid substrates and other jetted droplets [30,31]. Material interaction depends on control of the entire jetting process which is a function of jet parameters such as velocity, perturbation wave frequency, and orifice diameter, material parameters such as absolute viscosity, surface tension, fluid density and temperature ,and the target parameters such as temperature, surface roughness, and wetting ability. The importance of each of these factors to the process and the extent to which these factors interact are questions that must be answered with careful experimentation.

A major challenge in solid freeform fabrication concerns fabricating part "features". Many features such as slots, overchangs, etc. will require fixturing. Tolerances for surface finish will also be hard to maintain. Reflowing or surface finishing the part after initial fabrication may be required.

Part and circuit performance

Long term performance and reliability testing of fabricated parts is needed. At this time, the operational testing emphasis has been on solder jetting for flip chip bumping and ball grid arrays using machines developed by MicroFab Technologies, IBM, and MPM.

Acknowledgments

This research was partially supported by ARPA/DSO contract Number MDA972-93-C-0035: "Liquid Metal Jetting: Alternative Printed Wiring Board Manufacturing Process", and four research grants from the Higher Educational Coordinating Board of the State of Texas. These are Fluid Jet of Liquid Solder, No. 365075; Development of a Production Prototype for Liquid Solder, No. 3656094; Fluid Jet for Dielectrics and Epoxies, No.3650109 and Liquid Metal Jet of All Aluminum Printed Wiring Board. Special thanks is given to the many students who have tirelessly worked in the Liquid Metal Jet Laboratory.

References

1. Techno-economic Study. 1978. The Business of Ink Jet Printing, The Research Association for the Paper and Board, Printing and Packaging Industries (PIRA).
2. J.W.S. Rayleigh. 1879. "On the Capillary Phenomena of Jets." Proceedings Roy. Soc., vol. xxix, pp. 71-97.
3. J.W.S. Rayleigh. 1892. "On the Instability of Cylindrical Fluid Surfaces." Phil. Mag., vol. 34, no. 207, pp. 177-180.
4. A.B. Basset. 1894. "Waves and Jets in a Viscous Liquid." American Journal of Math, vol. 16, no. 1, pp. 93-110.
5. A. Haenlein. 1933. "Disintegration of a Liquid Jet." NACA Technical Memorandum No. 659.

6. C. Weber. 1931. "Zum zerfall eines flussigkeitsstrahles." Ztschr f. angew. Math. und Mech., vol. 11, no. 2, pp. 136-154.
7. C. Weber. 1948. "On the Breakdown of a Fluid Jet." Ninth Progress Report, Project MX-833 (section II), University of Colorado, Boulder.
8. Hansell. 1950. U.S. Patent 2,512,743.
9. D.W. Lee and R.C. Spencer. 1932. "Photomicrographic Studies of Fuel Sprays." NACA Report No. 454.
10. P.D. McCormack, L. Crane and S. Birch. 1965. "Derivation of Jet Viscosity Modulation Caused by Injector Vibration." Brit. Journal Appl. Phys., vol. 16, pp. 1911-1912.
11. P. H. Mitchell. 1994. "Method and Apparatus for Manufacturing an Article using a Support Structure for Supporting an Article during Manufacture." US Patent 5362427. Assignee:inventor
12. F. Gao and A. A. Sonin. 1994. "Precise Deposition of Molten Microdrops: the Physics of Digital MicroFabrication" Proceedings of the Royal Society of Physics - London, vol 444. pp.533-554.
13. IBM, 1972 "Pulse Jet Solder Deposition". IBM Technical Disclosure Bulletin, vol. 14, pp. 2354-2355.
14. H. Hieber. 1989. "Method of Applying Small Drop Shaped Quantities of Metal Solder from a Nozzle to Surfaces to be Welted and Device for Carrying Out the Method." U.S. Patent 4,828,886. Assignee: US Philips.
15. J.W. Priest, H. Bordett, C. V. Smith, Jr., and P. DuBois. 1993. "Liquid Metal-Jetting: Its Application to SMT." Journal of Surface Mount Technology, vol. 6(4): pp. 4-10.
16. J.W. Priest, E. G. Jacobs, C. V. Smith, Jr., and Pat DuBois. 1993. "Liquid Metal-Jet Technology and its Application in Hybrids Microelectronics Manufacturing." Proceedings of International Symposium on Microelectronics, Dallas, Tx., pp. 120-125.
17. J.W. Priest, H. Bordett, C. V. Smith, Jr., and P. DuBois. 1993. "Liquid Metal Jetting". Proceedings of Surface Mount International, San Jose, CA., vol 1, pp.522-527.
18. J.W. Priest, H. Bordett, C. V. Smith, Jr., and P. DuBois. 1993. "A Process Overview: Dispensing Molten 63/37 Solder Using Liquid-Jet Technology." Proceedings of Printed Circuit World Convention, San Francisco, CA. pp. 3-8.
19. E. Jacobs, J.W. Priest, P. DuBois, and C.V. Smith. 1994. "Material Issues in Liquid Metal Jet Printing Technology." Proceedings of Annual Meeting of the Texas Academy of Science." Houston, Tx. pp.73-75.
20. J.W. Priest, E. Jacobs, C.E. Smith, et. al. 1994. "Liquid Metal-Jetting Technology: Application Issues for Hybrid Technology", International Journal of Microcircuits and Eletronic Packaging, Vol. 15(3), pp. 219-227.
21. J.W. Priest, C. Smith, P. DuBois, et.al. 1997. " Agile Manufacturing Using Liquid Metal Jet Technology", Proceedings of ICAM'97, Lafette, Louisiana.
22. D.B. Wallace. 1989. "Automated Electronic Circuit Manufacturing Using Ink-jet Technology", Transactions of the ASME Journal of electronic Packaging, vol. 111, no. 2, p. 108-111.
23. D.J. Hayes, et.al. 1993. "Method and Apparatus for Dispensing Spherical-Shaped Quantities of Liquid Solder", US Patent 529016. Assignee: MicroFab Technologies.

24. D.J. Hayes, D.B. Wallace, M.T. Boldman, and R.E. Marusak. 1993. "Picoliter Solder Droplet Dispensing." International Journal of Microcircuits and Electronic Packaging, vol. no., pp. 173-180.
25. MicroFab website 1997 "www.metronet.com/~dwallace".
26. IBM. 1994. "Demonstrations at SMTA Conference." San Jose, California, 1994.
27. J. Chun and C. H. Passow. 1993. "Production of Charged Uniformly Sized Metal Droplets", U.S. Patent 5266098.
28. C.V. Smith, Jr. 1974. "Analysis of Droplet Formation in Ink Jet Printers." Unpublished Research, The University of Texas at Arlington.
29. C.V. Smith, Jr. 1976. "Experimental Determination of Ink Fluid Parameter Variation Effect on Droplet Formation in Ink Jet Printing." Unpublished Research, The University of Texas at Arlington.
30. J.-H. Chun. 1997. " Proceess-Structure Relationships in the Uniform-Droplet Spray Process." Proceedings of the 1997 NSF Manufacturing anf Design Grantees Conference, pp.327-328.
31. M. Orme, C. Huang. 1997. "Advanced Materials Synthesis and Manufacturing Using Controlled Droplet Deposition" Proceedings of 1997 NSF Manufacturing and Design Grantees Conference, pp.377-378, website www.eng.uci.edu/maeadim.
32. M.E. Orme, et.al. 1994. "Method and Apparatus for Droplet Stream Manufacturing", US Patent 5340090 (continuation-in-part and divisions of US Patents 5259593, 55171360 and 5226948).
33. C.E. Smith, J.W. Priest, and P. N. DuBois. 1996. "Heat-Resistant Broad-Bandwidth Liquid Droplet Generators", U.S. Patent 5560543 , Assignee: The University of Texas System.
34. T.M. Smith, et. al. 1995. "Electrodynamic Pump for Dispensing Molten Solder", US Patent 5377961. Assignee: IBM
35. M. Orme. 1993. " A Novel Technique of Rapid Solidification Net-Form Material Synthesis". Journal of Materials Engineering and Performance, vol 2, pp. 399-405.
36. C.H. Passow, J.H. Chun, & T. Ando. 1993. "Spray Deposition of a Sn-40 wt pct Pb Alloy with Uniform Droplets," Metall. Trans. A, vol 24A, pp 1187-1193.
37. C.A. Chen, J.H. Chun, & T. Ando. 1994. "Microstructural Control by Uniform-Droplet Spray Forming," Advances in Powder Metallurgy and Particulate Materials, Toronto, Canada, May vol 6, pp. 227-234.
38. Y. Pyongwon, J.H. Chun. and T. Ando. 1996. "Production and Characterization of Mono-Sized Sn-Pb Alloy Balls", International Journal of Powder Metallurgy. vol 32 pp. 155.

EXTRUSION FREEFORM FABRICATION OF BONE-LIKE MINERALIZED HYDROGELS AND MUSCLE-LIKE ACTUATORS

Paul Calvert and Zengshe Liu
Arizona Materials Laboratories, Tucson AZ

Abstract

Extrusion freeform fabrication has been used to build shapes from agarose, polyacrylamide and polyacrylic acid hydrogels. Contraction and bending can be induced by pH change or application of a voltage between embedded electrodes. Mineral reinforcement can be induced by incorporating salts into the gels and allowing them to react.

Introduction

The growth of organisms normally occurs as the deposition of new material by a layer of cells at an external or internal surface in an aqueous supporting medium. The layerwise deposition makes the process quite analogous to freeform fabrication. The cells would, however, correspond to a highly parallel multiple head system rather than one with a single moving write head. As with some freeforming processes, the actual deposition is a chemical conversion of liquid to solid and the initial deposit may be later transformed to a harder or tougher structure. With this analogy in mind we have been exploring methods by which materials similar to biological tissues might be freeformed.

We have thus developed methods to make shapes from water-swollen hydrogels using extrusion freeform fabrication and have been exploring the application of this method to the production of synthetic bone and muscle-like actuators.

Extrusion Freeform Fabrication of Hydrogels.

A hydrogel is a cross-linked solution of a water-soluble polymer with properties similar to Jell-o [1]. Agarose is a polysaccharide that is used as an electrophoresis medium for biopolymer separation. A 5% solution in water melts at about 80°C and solidifies rapidly below 60°C to a strong gel. The solidification process is a phase transition to the formation of helical agglomerates of chains. Using our extrusion system, solids can be written using a heated syringe depositing material onto a cooled plate.

Polyacrylamide gels are much used as a medium for electrophoresis of proteins and are also used to retain water for houseplants. In this case a solution of acrylamide monomer and about 5% of methylenebisacrylamide crosslinking agent is polymerized by a free radical system. The solution reacts slowly at room temperature but polymerizes in 5-10 minutes at 60°C. Since the monomer solution is very fluid, it is necessary to add a gelling agent to render the solution pseudo plastic and thus allow the parts to hold their shape while polymerization occurs. This is achieved with the addition of 12 wt.% of fumed silica as a thickening agent.

It is also possible to form gels by writing into a liquid medium. A solution of acrylamide, bisacrylamide, potassium persulfate free radical catalyst and silica is deposited below the surface of an aqueous solution of tetramethylethylenediamine (TEMED) co-catalyst. As the monomer

solution contacts the TEMED solution, the TEMED reacts with the persulfate and initiates the polymerization. To prevent the two liquids from mixing, the TEMED solution is thickened with sodium carboxymethylcellulose. In these circumstances the hydrogel forms in a liquid support medium. It has, however, proved difficult to anchor the hydrogel and stop it drifting during the process. Osmotic pressure differences tend to lead to swelling of the gel so that good resolution is hard to achieve.

Gel muscles

Muscle functions by myosin crawling along an actin track driven by the energy of hydrolysis of ATP which induces a cyclic kinking and straightening of the myosin head group. Like a man running on a slippery floor, the force depends on the rate of reaction with ATP and there is no force in the absence of energy input. The electrical stimulation of excised muscle functions by inciting the cells to release ATP, not by directly powering the contraction.

Gel muscles depend on the contraction of cross-linked ionic gels as they change temperature, pH or solvent [2, 3]. These contractions can be large and the forces exerted are comparable to muscle but the response time is very long because water must diffuse from the gel as it contracts. Bending or contraction can also be induced electrically as the field drives ions into or out of the gel. The effect tends to be weak because it depends on establishing an ion concentration gradient within the gel or between the gel and its surroundings. Steep ion gradients cannot be established at the low fields that can be set up in aqueous media. A second problem with these gels is that they generally function immersed in water, which is incompatible with simple machinery.

We envisage using freeforming methods to make stacks of gels with interdigitated electrodes, both to speed the response and to provide internal reservoirs in which the extruded water can be stored. As a first step toward this, we have formed stacks of six layers of gels using both cross-linked polyacrylic acid and polyacrylamide. These have been tested for their response on transfer from acid to base and to field applied between electrodes placed between layers 2 and 3 and between layers 4 and 5.

Figure 1 shows the swelling response on being moved from acid solution to base of a series of 6-layer gels varying from all acrylamide to all acrylic acid via 1+5, 2+4 etc.. Acrylamide gels respond little to pH changes and acrylic acid gels swell strongly in base. It was expected that the mixed gels would curve very strongly as the acrylic acid side expanded. In fact they curved only slightly and the acrylamide portion of the mixed gels swelled equally in the x,y and z directions, driven by the acrylic acid. Apparently the strong swelling of the acrylic acid gel stretches the acrylamide along x and y. The concurrent swelling along z is interpreted as a Poisson's ratio of -1/2 for the acrylamide gel. Such anomalous Poisson's ratios have been previously found for gels [4, 5].

Electrical stimulation of similar multilayer stacks is being studied. Figure 2 shows the bending response of six layer stacks with one or two outer acrylamide gel layers either side of two or four acrylic acid gel layers. These samples are run in air with electrodes embedded between the outer acrylic acid layers and the acrylamide. We envision the acrylamide layers as providing a

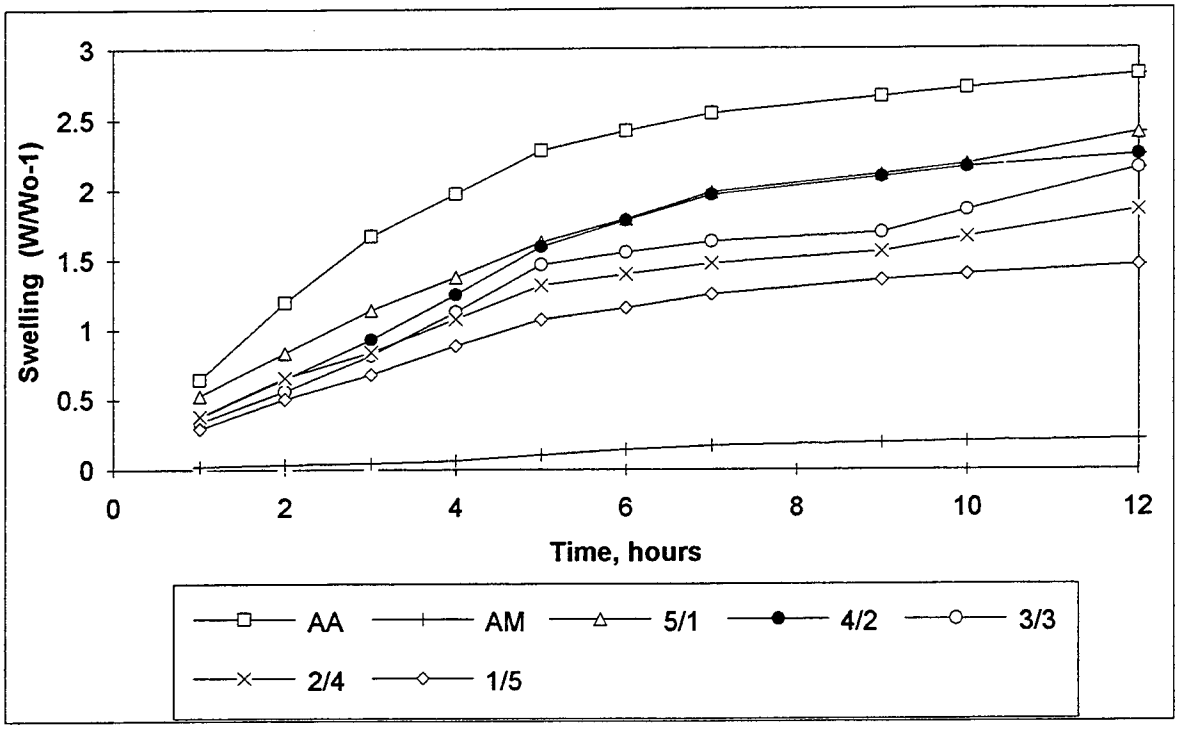


Figure 1) Water absorption by multilayer gel samples soaking in 0.1M NaOH after treatment in 0.1M HCl for 2 days. 6 layers: 0/6, 1/5,2/4,3/3,4/2,5/1,6/0 acrylamide gel/acrylic acid gel.

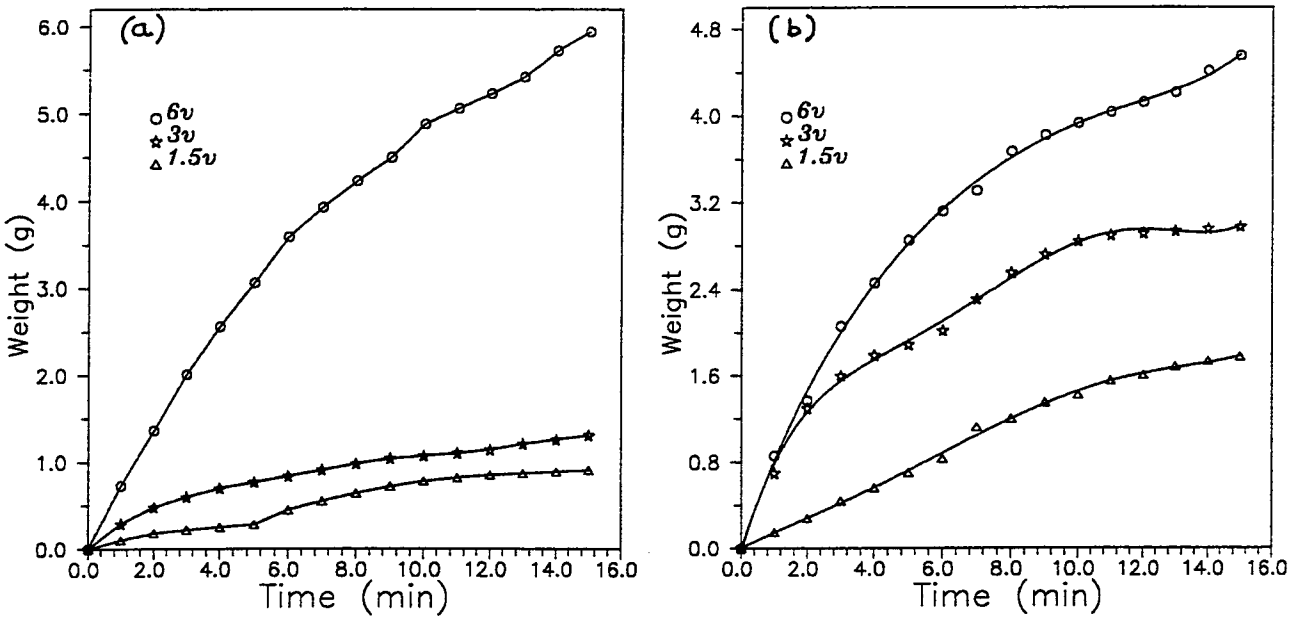


Figure 2 Force exerted by bending a 10 cm. long six layer gels when subjected to 1.5V, 3V or 6V across embedded electrodes. (a) MAAAAM: Acrylamide/electrode/acrylic acid x 4/electrode/acrylamide (b) MMAAMM: Acrylamide x 2/electrode/acrylic acid x 2/electrode/acrylamide x 2

passive reservoir for water and ions driven out of the contracting acrylic acid.

Gel bones

Bone is a composite material with 40-50 vol.% of a mineral, hydroxyapatite, embedded in a tough collagen matrix. Because the mineral grows in situ in the polymer, it is in the form of fine, highly oriented ribbons, which give bone remarkable stiffness and toughness for a particle-reinforced polymer. We hope to freeform similar materials, both for medical applications and as tough synthetic composites.

During puberty, the long bones grow by addition of new material to the "growth plate". This is a soft zone extended across the bone near one end. Here a layer of cells continuously forms new cartilage, which has a soft gel-like structure. As the cartilage thickens away from the cells, it becomes mineralized with hydroxyapatite and converts to bone over a distance of 5-10 microns from the cell front. In this way the bone progressively lengthens [6].

We hope to produce bone-like composites by a similar process of freeforming gel structures and then inducing mineralization. As a first step, agarose gels were freeformed with a high level of calcium chloride dissolved in the gel. These gels are then immersed in carbonate or phosphate solution to induce mineralization. In initial studies have focussed on carbonates because the precipitation chemistry is much simpler than for phosphate. When the carbonate solution is less concentrated than the calcium chloride in the gel, osmotic pressure drives solution into the gel, which mineralizes, as calcite, with little loss of calcium. In this way up to 14 wt.% mineral can be formed within the gel. While this fraction is too low to give a stiff structure, most of the mass of the composite is water and the mineral/polymer ratio is high. On drying, a hard bony structure with up to 70 wt.% mineral is formed, table 1.

To induce internal mineralization, multilayer gels have been formed with calcium and carbonate in alternating layers. Precipitation normally occurs uniformly in the layer with the higher initial ionic strength, rather than at the interface. The mineral content is limited by precipitation of the gel structure at high ionic strengths, especially with divalent anions. We are now reaching higher mineral contents by forming multiple layers containing dispersed powders of slightly soluble minerals, which then reprecipitate as calcium carbonate, leaving a soluble salt.

These studies raise a question that is, so far, unanswered. When bone forms, water is lost during mineralization. There is no obvious physical reason for this because the mineral forms inside the collagen fibers while the water is in a surrounding gel matrix. An understanding of this would help us drive the water out of our gels as they mineralize.

Conclusions

A freeformed gel matrix provides a medium within which subsequent or concurrent chemical processes can be used to make new materials with complex microstructures. There are many parallels between this approach and biological growth processes.

Acknowledgements

We would like to thank the Army Research Office for support of this work.

References

1. Dagani, R., "Intelligent Gels", *Chem. Eng. News* 26-37, June 9, 1997.
2. Osada, Y., Okuzaki, H. and Hori, H., *Nature* 355 , 242-244 , 1992.
3. Gong, J. P., Nitta, T. and Osada, Y. "Electrokinetic modeling of the contraction of polyelectrolyte gels." in *Proceedings of the Second International Conference on Intelligent Materials. ICIM '94 (1994)* (eds. Rogers, C.A. & Wallace, G.G.) (Technomic Publishing Co., Lancaster, PA, 1994) pp.556-564.
4. Li, C., Hu, Z. and Li, Y., "Poisson's ratio in polymer gels near the phase-transition point", *Phys. Rev. E* 48, 603-606, 1993.
5. Takigawa, T., Morino, Y., Urayama, K. and Masuda, T., "Osmotic Poisson's ratio and equilibrium stress of Poly(acrylamide) gels", *Polymer Journal* 28, 1012-1013, 1996.
6. Vaughan, J. A. *The physiology of bone.* 1-265 (Oxford : Clarendon Press, 1981).

Table 1

Calcium carbonate mineralization of agarose gels. Maximum possible carbonate content : 77 wt.% at 2M $CaCl_2$, 62 wt.% at 1M

$CaCl_2$ in gel, M	Na_2CO_3 in solution, M	wt.% $CaCO_3$, dry gel
2	0.5	42
	1	32
	1.5	41
	2	39
	2.5	36
	0.5 $NaHCO_3$	69
	1 $NaHCO_3$	72
1	0.5	46
	1	49
	1.5	54
	2	40
	2.5	30
	0.5 $NaHCO_3$	57
	1 $NaHCO_3$	59

A LAYERED-MANUFACTURING PROCESS FOR THE FABRICATION OF GLASS-FIBER-REINFORCED COMPOSITES

G. Zak M.N. Sela C.B. Park B. Benhabib

Computer Integrated Manufacturing Laboratory
Department of Mechanical and Industrial Engineering
University of Toronto
5 King's College Road, Toronto, Ontario, M5S 3G8
e-mail: beno@mie.utoronto.ca

ABSTRACT

In this paper, we present a rapid manufacturing process for the layered fabrication of polymer-based composite parts using short discontinuous fibers as reinforcements. In the recent past, numerous research efforts, similar to ours, have been made to produce fiber-reinforced plastic parts via layered manufacturing methods. However, most of these attempts have not resulted in the development of an effective commercially-viable manufacturing process. Our proposed fabrication process on the other hand has been experimentally verified to yield composite parts comparable in quality to pure polymer parts manufactured on a commercial stereolithography system.

This process uses a UV-laser-based system for the selective solidification of the composite liquid. The primary components of the prototype are: (1) fiber-resin mixing subsystem, (2) composite-liquid deposition subsystem, (3) liquid leveling subsystem, (4) laser-light delivery subsystem, and (5) contour-milling subsystem.

Extensive microscopic examination of composite parts, built by the proposed prototype system, has been conducted to evaluate the parts' layer quality. Results indicate that the prototype system can yield comparable layer quality, in terms of accuracy and uniformity, to that of pure-resin parts made by a photopolymer-based commercial system.

INTRODUCTION

Reinforcement of plastics by fibers has been used successfully for over fifty years as means of improving the mechanical properties of the manufactured products [1]. Combining high-modulus, high-strength fibers with a polymeric matrix produces a composite material with higher stiffness and strength, and lower thermal-expansion coefficient. The reinforcing fibers can be introduced either in continuous (long) or discontinuous (short) form. While continuous fibers provide greater relative improvement of the mechanical properties, they also significantly complicate composite-material processing. Short-fiber composites on the other hand can be easily manufactured by automated, and hence more economical, methods.

Since the late 1980's, several Rapid Layered Manufacturing (RLM) techniques have been investigated, and some commercially developed. These techniques allow free-form fabrication of complex-geometry parts directly from their CAD models [2]. The most commonly used RLM

technique for the production of plastic parts is Stereolithography (SL). As a building material, it employs a liquid photosensitive resin, which is selectively solidified by an ultraviolet (UV) laser beam. The SL technique is used as a basis for the rapid manufacturing of short-fiber reinforced parts proposed herein.

There has been some recent work performed on improving the mechanical properties of polymer-based parts produced by SL methods. For example, in [3], long fibers were added to the polymer matrix by stacking rings with arrays of parallel horizontal fibers stretched across, and then curing the polymer via a standard SL procedure. In another approach [4], continuous fibers were laid out by a dedicated apparatus before curing each layer of the part. Other approaches include using solid inserts within the polymer [5], or building fiber-reinforced shells around solidified resin part [6].

Feasibility studies were also reported regarding the use of discontinuous reinforcements in the form of either 10-15 mm chopped glass fiber bundles or 55 μm diameter glass microspheres [7, 8]. Composite samples several-layers thick were produced by manually spreading the glass fibers over the liquid resin on each layer. Fibers were not premixed due to the very high viscosity of the resulting mixture. Improvements of material mechanical properties were reported for fiber-based reinforcements, while no improvement was attained by using microspheres.

The above methods of reinforcement (especially those using medium-length or continuous fibers, as in [3, 4, 7, and 8]) are suitable for the rapid layered manufacturing of objects with relatively simple geometric shapes. However, significant difficulties may arise when applying these methods to the production of objects with small-scale features, thin walls or intricate shapes.

Thus, herein, we propose reinforcement of SL-made complex-geometry objects by short fibers introduced directly into the photopolymer matrix. The fact that the resin remains liquid at room temperature simplifies the process of adding the fibers, storing and handling the mixture, as well as controlling the amount of fibers added. Due to its transparency (for photo-curing) and relatively low cost [1], glass fiber was selected for reinforcement.

INCORPORATING FIBERS IN THE SL PROCESS

The benefits of reinforcements are limited by the maximum volume fraction that can be accommodated by the matrix. This limit is in turn governed by the uniformity of the fiber orientation and the fiber length. For uniformly oriented fibers, the concentration can reach 50-60% by volume; for randomly oriented fibers, the limit can be 10-40%, depending on the fiber length.

Below, we briefly review the suitability of the SL process for fabrication of *fiber-reinforced* parts.

(i) Mixture Viscosity

Adding fibers to the liquid resin creates a highly viscous liquid. When used in a standard SL process, such a liquid is likely to have difficulty in flowing to form an even layer after the part is

submerged. A subsequent wiping operation may also encounter problems because of the presence of fibers, as was confirmed in our preliminary investigation into the wiping of various fiber-resin mixtures.

(ii) Fiber Settling

Since the fiber density is more than twice that of a typical resin (2.54 g/cm^3 for glass vs. 1.13-1.15 g/cm^3 for resin), the fibers tend to sink if left undisturbed. For spheres in liquid, the terminal sinking velocity is given by [9]:

$$V = (\rho_s - \rho_l)\frac{gd^2}{18\mu} \tag{1}$$

where g is the gravitational acceleration, d sphere diameter, ρ_s density of sphere, ρ_l density of liquid, and μ viscosity of liquid. Using a typical resin viscosity of 200 cP, a fiber length of 1.5 mm and diameter of 15 μm, and calculating the diameter of a sphere equal to the fiber volume, yields a sinking rate of about 85 mm/hr. Thus, if the mixture was left undisturbed in a vat during part building, the fibers would settle continuously, which would lead to lower fiber concentration near the surface.

(iii) Fibers on the Part Surfaces

When short fibers are added to polymers as reinforcements in a typical manufacturing process (e.g., injection molding), the solidification of the matrix always takes place within a mold with solid boundaries surrounding the composite part. These boundaries guarantee that the fibers will not protrude from the surface of the finished part. On the other hand in our case, when the fiber-resin mixture is solidified by the laser beam, the boundary between the solid and the liquid will always fall across some fibers. Preliminary experiments showed that the parts produced by an SL method had protruding fiber filaments on their vertical surfaces.

THE NEW RAPID LAYERED MANUFACTURING PROCESS

One key novel feature distinguishes the proposed RLM process from the standard SL: the composite liquid is not stored in a vat but instead deposited from above for each layer (Figure 1). The primary fabrication steps of the current process are as follows:

(1) The composite liquid is continuously stirred in a separate container during the part building.

(2) A known volume of the composite liquid is deposited from above for each layer (Figure 1b).

(3) A wiper levels the liquid at the required height (Figure 1c).

(4) The layer is selectively cured by a UV laser (Figure 1d).

(5) A milling tool is used to remove the fibers protruding from the solidified walls of the current layer (Figure 1e).

(6) The part is lowered into the vat (Figure 1f), and the process steps 2 and 5 are repeated.

Once the part-building process is completed, the platform is raised, and the part is removed, cleaned, and post-cured.

This process solves all three primary problems addressed in the earlier section, namely, settling of fibers, spreading of a highly viscous composite liquid, and removing the fibers protruding from the finished part's vertical surfaces. The fiber-removal solution proposed herein is the use of a vertical milling tool. At each layer, a small-diameter, numerically controlled end-mill traces the perimeter of the part. The cut could be made to remove just a part of the solidified perimeter, thus assuring precise horizontal dimensions of the layer.

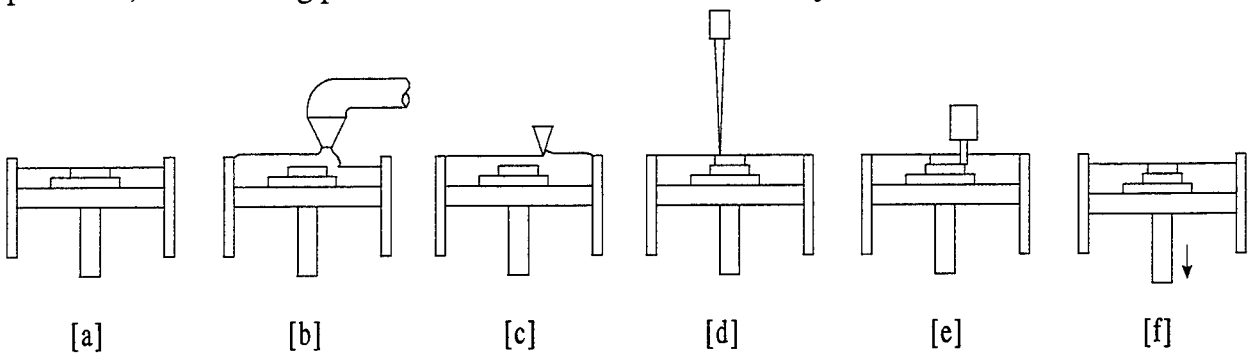


Figure 1: Steps of the Proposed RLM Process.

THE CURRENT EXPERIMENTAL SYSTEM

An experimental system was designed and built to serve as a tool for the process development. The first prototype was described briefly in [10]. The current prototype is capable of automatically building composite layered parts from the data provided by a CAD software. The main components of the system are (Figure 2):

(1) Fiber-resin mixing subsystem,

(2) Composite-liquid deposition subsystem,

(3) Liquid leveling subsystem,

(4) Laser-light delivery subsystem,

(5) Z-platform translation subsystem, and

(6) Milling subsystem.

The system is controlled by custom-written software running on an Intel-processor-based PC. The PC is interfaced to a motion controller, which drives four stepper motors, activates solenoid air valves, and receives feedback signals from several limit switches.

The *fiber-resin mixing subsystem* keeps the fibers in suspension throughout the building process. It consists of an open-top container and a helical-screw stirring device inserted into the container from above. The helical-screw arrangement achieves adequate mixing, when turning slowly, without causing agitation or foaming of the liquid.

The *composite-liquid deposition subsystem* delivers repeatable desired amounts of resin into the vat. This function is performed via a peristaltic pump, which uses rollers to squeeze the liquid through a flexible plastic tube. One end of the tubing is inserted into the container of the mixing subsystem; the other end is attached to the platform of the X-Y translator. The pumping action is combined with the simultaneous translation of the dispensing nozzle in front of the wiper to assure even spreading of the composite liquid. The advantages of delivery via a peristaltic pump are: (i) accurate metering of the liquid volume delivered, since the pump is of a positive displacement type and (ii) simplified system maintenance, since there is no contact between the pump mechanism and the liquid, and since the tubing is easily replaceable. Evaluation of the current version has shown significantly improved consistency of the liquid volume delivered, relative to our earlier system described in [10].

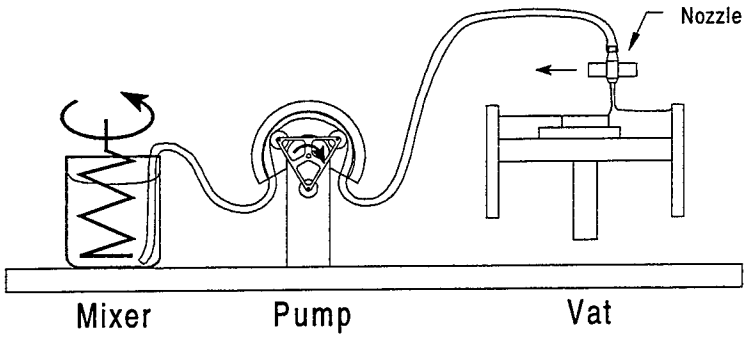


Figure 2: Current Version of Composite-Liquid Deposition and Fiber-Resin Mixing Subsystems.

The *liquid leveling subsystem* assures uniform spreading of the liquid over the vat's top surface to create a layer of consistent thickness. This is achieved by translating a wiper with a triangular edge profile. The wiper movement is actuated by a pneumatic cylinder. Two forward-and-return wiping stroke sequences are performed to form each layer: the first stroke sequence is carried out after the platform has been lowered by a depth of several layers, and the second stroke sequence when the platform has been raised back to the height one-layer lower than the last layer built.

The *laser-light delivery subsystem* delivers a focused beam of UV light to the surface of the composite liquid and moves the beam spot in the X-Y plane. The laser-light source is a 20 mW He-Cd UV laser, Omnichrome 3056-10M. The light is delivered via a fiber-optic cable. At the output end of the cable, a lens focuses the light beam. The X-Y motion of the beam is achieved by attaching the focusing lens and fiber-optic cable to an X-Y translator.

The *Z-platform subsystem* moves the supporting platform vertically. Since the height of the platform directly affects the layer thickness, its vertical displacement must be accurately controlled. To achieve the required accuracy, the Z platform is actuated by a stepper motor driving a micrometer attached to a vertical translation stage.

The *milling subsystem* removes surface fibers by a portable milling tool attached to the platform of the X-Y translator. The milling tool is driven remotely through a flexible shaft attached to an externally-mounted motor.

EXPERIMENTAL RESULTS

Since parts produced by an RLM process are formed out of individual layers, good surface quality and dimensional accuracy can be achieved only by building *high-quality individual layers.* The experimental system described above was therefore used to build a set of pure and composite rectangular parts (25×30×4.8 mm), and the layer cross-sectional profiles of these parts were then examined microscopically. The composite liquid comprised the 2202SF photopolymer by Allied Signal and 15% by volume 737BD 1.6 mm milled glass fibers by Owens Corning. It was noted that for 1.6 mm long fibers the maximum achievable volume fraction was about 15-20%. An additional pure-resin test part was built on a commercial SL machine (Sony JSC-2000 Solid Creator) from DeSolite SCR310 photopolymer. The measurements obtained from this part served as a benchmark for the layer quality of our own parts.

Several vertical sections of each part were made. Figure 3 shows the layer profiles for one section of the pure-resin part built on a commercial SL machine ("SL_PURE"). Figure 4 shows the layer profiles for sections of a pure-resin part ("RLM_PURE") and a composite part ("RLM_COMP") built on our prototype system. Ideally, the plots should consist of straight horizontal lines representing layer boundaries separated by the nominal layer thickness of 0.3 mm.

Statistical analysis of the observations from all sections of the above three parts was carried out after discarding the data for the first 8-10 layers in order to allow for process stabilization (Table 1). Three parameters are shown for each part: the average layer thickness, which is the mean of layer boundary separation values observed across all the part sections; the standard deviation within layers, which is a measure of the unevenness of the layers; and the standard deviation between layers, which is a measure of the layer-to-layer variability of the average layer thickness. The results show that our prototype is able to build layers with a mean thickness very close to the nominal value. Also, the variabilities in the building process of the layers are quite close to those obtained on the Sony machine, especially when one considers that our system is still in its prototype stage. The composite part layer variability is only slightly higher than that for the pure-resin part. Process refinements should reduce the difference even further.

Parts built on our prototype system have somewhat higher variability of the layer thickness than those built on a commercial SL machine. However, the standard deviation values are within the same order of magnitude. Also, note that the composite part layer variability is only slightly higher than that for the pure-resin part built on our prototype system. Process refinements should reduce the variability even further.

Table 1. Statistical Data for Layer Profiles of Multiple Sections.

	Average Layer Thickness (mm)	St. Dev. Within Layers (mm)	St. Dev. Between Layers (mm)
SL_PURE	0.313	0.008	0.002
RLM_PURE	0.306	0.016	0.007
RLM_COMP	0.315	0.021	0.010

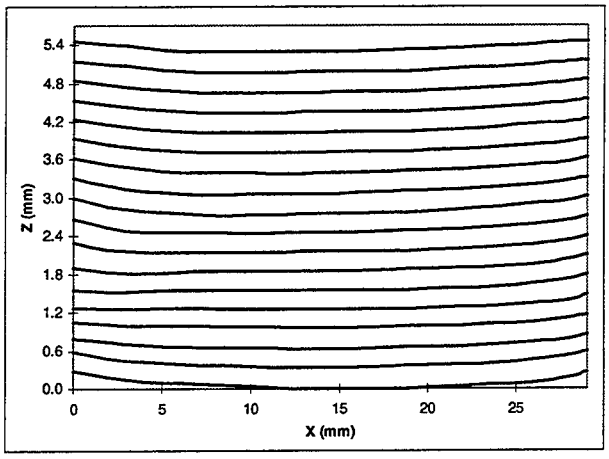
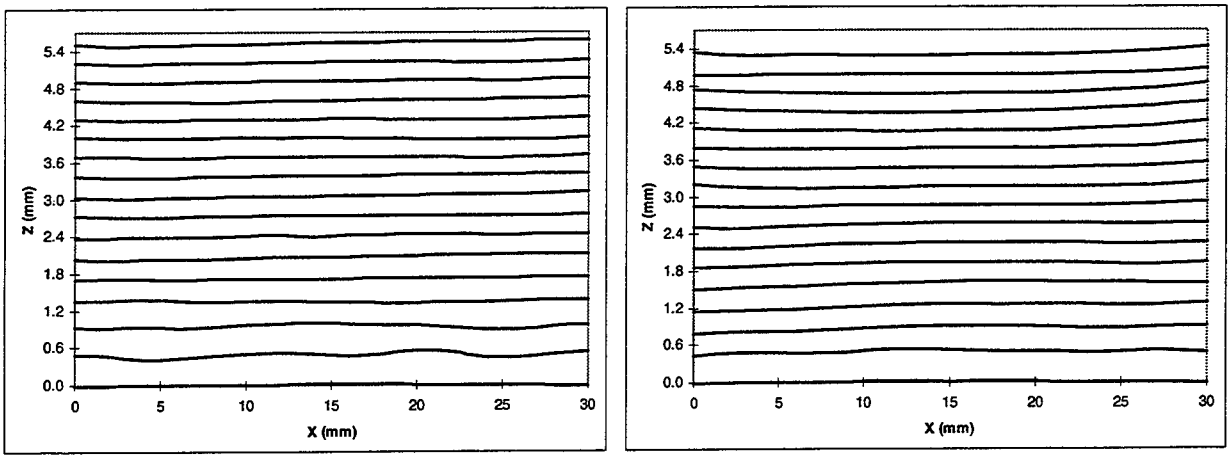


Figure 3. Layer Profiles for a Pure-Resin Part Made on a Commercial SL Machine.



(a) (b)

Figure 4: Layer Profiles for (a) a Pure-Resin and (b) a Composite Test Part.

CONCLUSIONS

This paper presented a new RLM process for the fabrication of glass-fiber-reinforced plastic composites. This process is based on a layer-by-layer selective solidification of composite liquids comprising photopolymers and glass-fibers. An experimental system was developed to verify the proposed RLM process and is currently capable of producing high quality glass-fiber-reinforced composite plastic parts.

REFERENCES

[1] M.R. Piggott, **Load-Bearing Fibre Composites**, Pergamon Press, New York, 1981.

[2] L.D. Schmidt, "How Chrysler is using stereolithography rapid prototyping survey results," *Proc., Fifth Int. Conf. on Rapid Prototyping*, June 1994, Dayton, Ohio, pp. 359-370.

[3] W.B. Barlage, C.C. Jara-Almonte, A. Bagchi, A.A. Ogale, R.L. Dodey, "Fiber/resin composite manufacturing using solid freeform fabrication," *Proc., Third Int. Conf. on Rapid Prototyping*, June 1992, Dayton, Ohio, pp. 15-24.

[4] R. Charan, T. Renault, A.A. Ogale, and A. Bagchi, "Automated fiber-reinforced composite prototypes," *Proc. Fifth Int. Conf. Rapid Prototyping*, June 1994, Dayton, Ohio, pp. 91-97.

[5] D.E. Reiff, D.W. Dorinski, and S.D. Hunt, "Method of manufacturing a three-dimensional plastic article," Motorola Inc., U.S. Patent 5173220, December 1992.

[6] S.W. Thomas, R.D. Key, K.G. Fluegel, W.K. Jackson, K.D. Elwell, and G.L. White, "Method for manufacturing fiber-reinforced parts utilizing stereolithography tooling," E-Systems Inc., U.S. Patent 5296335, March 1994.

[7] A.A. Ogale, T. Renault, R.L. Dooley, A. Bagchi, C.C. Jara-Almonte, "3-D photolithography for composite development: discontinuous reinforcements," *SAMPE Quarterly*, October 1991, pp. 28-38.

[8] T. Renault, and A.A. Ogale, "3-D photolithography: mechanical properties of glass and quartz fiber composites," *Proc., ANTEC 1992 - Conf. SPE*, Vol. 1, May 1992, pp. 745-747.

[9] G.K. Batchelor, **Introduction to Fluid Dynamics**, Cambridge University Press, 1967.

[10] G. Zak, N.M. Sela, C.B. Park, B. Benhabib, "A stereolithography method for the rapid manufacture of glass-fiber-reinforced composites," *Proc., 1996 ASME Winter Annual Meeting*, Atlanta, Georgia, November 17-22, 1996, DE-Vol.89, pp. 29-36.

Recent Developments in Freeform Fabrication of Dense Ceramics From Slurry Deposition

Joseph Cesarano III and Thomas A. Baer; Sandia National Laboratories, Albuquerque, NM. Paul Calvert; University of Arizona, Tucson, AZ.

Abstract

A freeform fabrication technique for dense ceramics and composites has been developed. The technique requires less than 2 volume percent of organic additives and relies on the principle of layerwise deposition of highly loaded colloidal slurries. Components can be manufactured into complex geometries with thick solid sections as well as with thin-walled sections with high aspect ratios. Process feasibility and quality is dependent on the processing parameters of solids loading, slurry rheology, deposition rate, and drying rate. These interrelated parameters must be controlled so that sintering defects are prevented and shape tolerance is maintained. A review of this freeform fabrication technique, called robocasting, will be discussed for fabrication of aluminum oxide parts. Recent developments for a finite element analysis technique for modelling the drying process will also be presented.

Introduction

Most of the techniques currently being developed for the freeform fabrication of dense structural ceramics revolve primarily around the sequential layering of ceramic loaded polymers/waxes or modified stereolithography using ceramic loaded ultraviolet curable resins. [1-3] For all of these techniques, pre-sintered parts typically have 45 - 60 vol% ceramic and 40 - 55 vol% polymer. In this regard, these techniques are analogous to powder injection molding of ceramics and require very long and complicated heat treatments to prevent cracking and produce a dense ceramic, free of organics. Consequently, while a part may be rapidly prototyped within a few hours, it may still take several days to densify the part. A typical heating rate is 0.2 ^{o}C per minute [4].

A new technique is being developed at Sandia National Laboratories for the freeform fabrication of dense ceramics that utilizes less than 2 volume percent organics. Therefore, a dense ceramic part may be freeformed, dried, and sintered in less than 24 hours. The process is based on the extrusion of highly loaded ceramic slurries that are typically 50 - 65 vol.% ceramic powder, < 1 vol.% organic additives, and 35 - 50 vol.% volatile solvent (usually water). This technique is useful for the near-net-shape fabrication of components with simple or complex shapes. Called robocasting, the technique uses robotics for computer controlled deposition of ceramic slurries through an orifice. The ceramic slurries are extruded in sequential layers. Any conceivable two-dimensional pattern may be "written" layer by layer into a three-dimensional shape (Figure 1). Orifice openings can range from several millimeters to tenths of millimeters. Robocasting is analogous to the ceramic near-net-shape processing techniques, slip casting [5] and gel casting [6]; however, robocasting is moldless and fabrication times are quicker. To maintain structural integrity while building a component, robocasting relies on the rheology of the deposited slurry and on partial drying of the individual layers. In contrast to gel casting and other freeform fabrication techniques, robocasting does not require organic polymerization reactions or solidification of a polymeric melt to maintain the shape of components.

Robocasting is no more conceptually complicated than chalking a bathtub. Except that, during robocasting, the substrate actually moves underneath the point where material is dispensed from a stationary orifice. While conceptually simple, transforming this concept into reality for the manufacture of ceramics requires a synergistic control of the : 1) percent solids in the ceramic powder slurry, 2) viscosity and rheology of the slurry, 3) dispensing rate of the slurry through the orifice, 4) drying kinetics of the dispensed bead of slurry, and 5) computer code for optimal machine instructions.

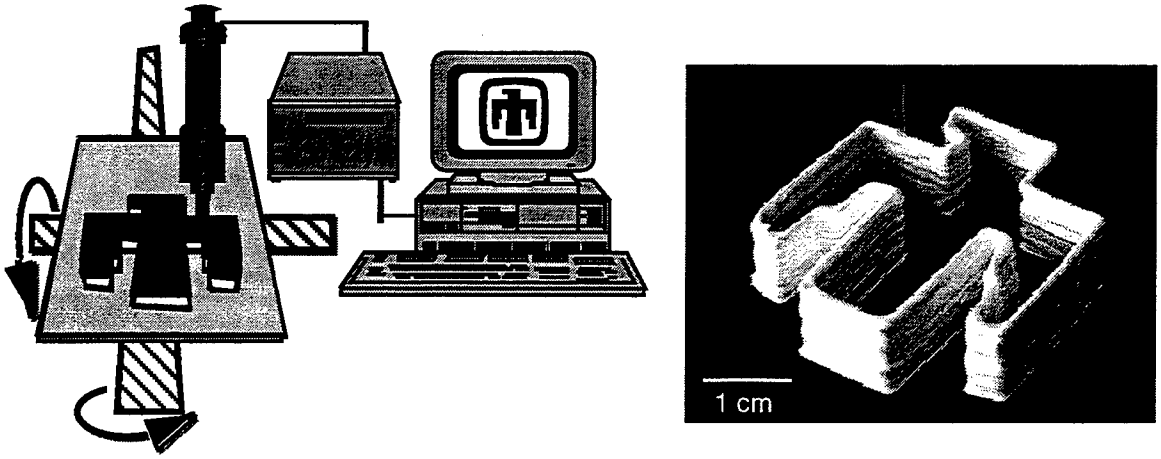


Figure 1. Schematic of the Robocasting process with an inset photo of an aluminum oxide thunderbird made in 20 layers and sintered crack-free to 96% theoretical density.

Experimental

The ceramic powder used was A-15 alumina from Alcoa Industrial Chemicals. The average particle size was 2.2 μm with a surface area of 4.3 m^2/g. Deionized water was used as the solvent and Darvan 821A (R.T. Vanderbilt Corp.) as the dispersant. The aqueous alumina slurries were made according to Cesarano, et al [7] and were 58 to 61 vol% alumina. The slurries were then aged for up to 20 days by gently mixing on a ball mill. The aging process made the slurry rheology suitable for robocasting.

The robotic slides used for the X, Y, Z and dispensing axes were purchased from Velmex, Inc. The slides were controlled with stepper motors and controllers from Arrick Robotics. When fabricating parts, typical table speeds were 0.5 to 1.2 cm/sec and typical slurry dispensing rates were 0.006 to 0.01 ml/sec. The slurry was dispensed onto a copper plate which was temperature controlled and maintained at temperatures ranging between 30 - 50 °C.

Rheological measurements were performed using a Brookfield DV-III programmable rheometer with a concentric cylinder attachment.

Modelling of the change in shape of dispensed beads of slurry with time was performed using GOMA. GOMA is a finite element analysis code for the fluid flow of free surfaces, developed at Sandia National Laboratories [8].

Results and Discussion

The slurry viscosity and the rheological dependence of viscosity with shear rate must be tailored during processing for optimal performance. During dispensing, the slurry will

experience high shear conditions while flowing through the orifice and as the moving substrate interacts with the dispensing slurry. However, immediately following this process, the slurry experiences a shear rate near zero. Therefore, in order to control the shape of dispensed beads, the slurry rheology must be extremely pseudoplastic so that the material can flow smoothly during dispensing but then solidify in place once shear stresses are removed (similar to paint). If the slurry is too fluid, beads will spread uncontrollably. If the slurry is too viscous, beads lay down like rope and maintain rounded tops. When the proper rheology is obtained, beads yield nearly rectangular cross sections with relatively straight walls and flattened tops (Figure 2A). Perfectly, rectangular cross sections would be optimal for filling space when additional layers are sequentially dispensed.

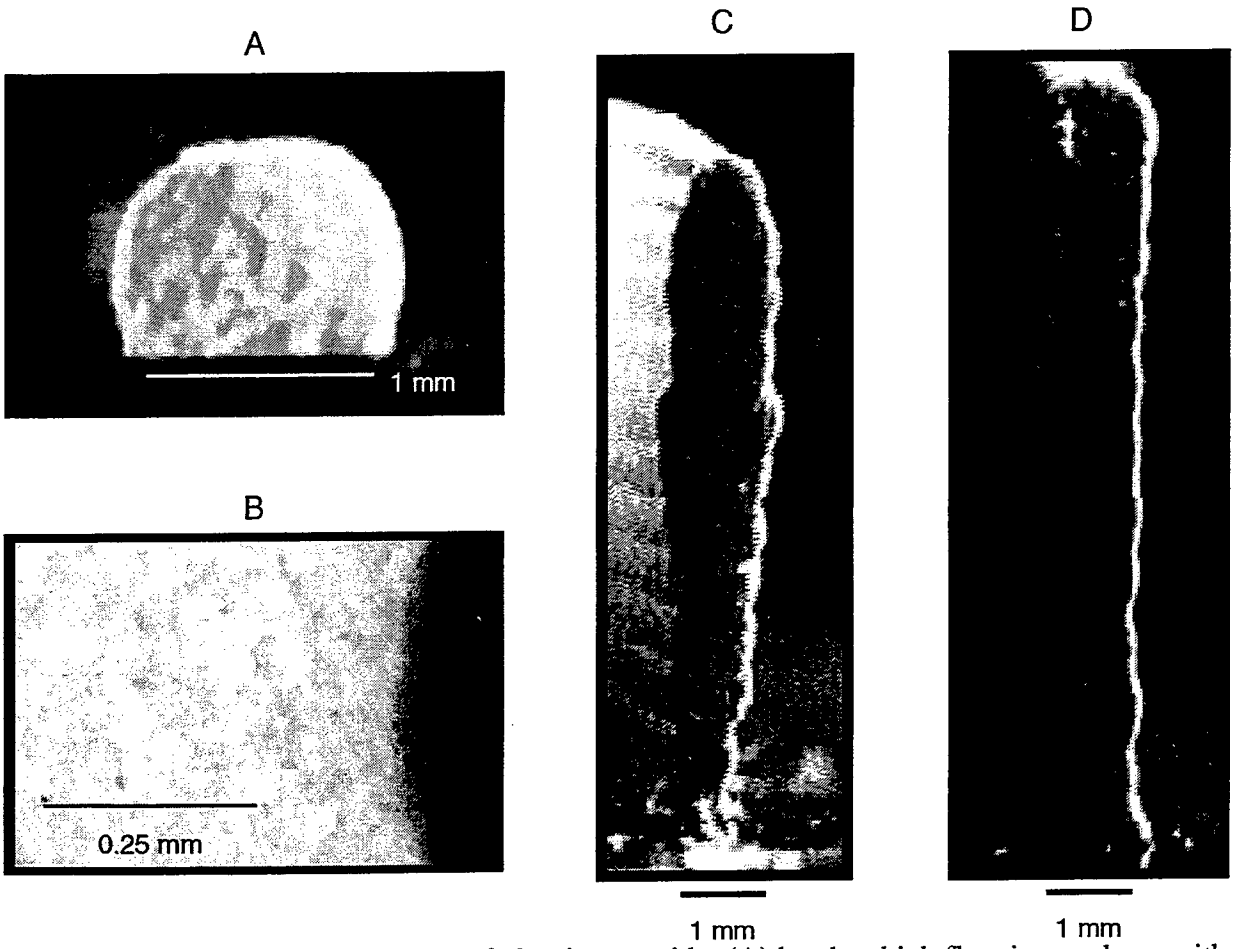


Figure 2. Cross sections of beads of aluminum oxide: (A) beads which flow into a shape with relatively straight walls and flat tops improve space filling; (B) properly dried layers mesh together without any defect detection using 10X optical microscopy; (C) Low viscosity and slow drying results in slumping of layers, forming nonuniform walls; (D) Proper rheology and drying yields beads which stack relatively straight and uniform.

Figure 3A shows the rheology for a slurry that yielded good behavior during robocasting. After 16 days of gentle mixing, a 61 vol% slurry exhibited the necessary yield stress and pseudoplastic rheology to make beads similar to those shown in Fig. 2A. Note that the 16 day old curve is practically level and that after the slurry begins to yield, only a very small increase in shear stress is required to induce substantial flow and large increases in shear rate. In practical terms, this slurry shows an appreciable resistance to flow but once flow has been initiated, the

viscosity decreases dramatically and there is very little resistance to flow. In fact, the viscosity of the 16 day old slurry decreases from nearly 1 million cP (at 0.07 s^{-1}) to 40,000 cP (at 1.7 s^{-1}). This is a very large decrease in viscosity over a small increase in shear rate. A typical shear rate through a robocasting orifice is 20 s^{-1}.

The rheology demonstrated in Fig. 3A is actually quite ideal for robocasting. The slurry will readily flow upon shear and then return to a state exhibiting a yield stress once shear has been removed. However, there are other factors that must be considered for multilayering and actual part fabrication. During multilayering, slumping may occur as a freshly dispensed bead is smeared over a previously dispensed bead. The smearing may induce a shear stress on the previously dispensed bead that exceeds the yield stress. Also, added weight due to multilayering may accumulate enough stress to induce flow in previously dispensed beads. Therefore, it is necessary to be able to permanently lock in the structure of a dispensed bead before smearing or weight build up can cause slumping. This may be accomplished by transforming the pseudoplastic slurry that behaves like a liquid into a dilatant mass that behaves like a solid. Typically, a ceramic slurry will start to behave like a dilatant solid once the solids loading is increased above approximately 64 vol%. Even though there is approximately 36 vol% water present, all of the water is entrapped in voids between the particles and particle mobility is restricted. If fact, as more stress is applied, particle mobility becomes even more unlikely and the structure of the solid/liquid mass is locked (i.e., dilatant). For robocasting this phenomenon is taken advantage of for "solidifying" beads of slurry before appreciable slumping can occur. For alumina slurries only minimal drying is required in order to increase the solids loading from 61 vol% solids to 64 vol% solids and transform the slurry rheology from pseudoplastic to dilatant. At this time, the shrinkage is virtually complete and shape changes are minimal as the remaining water is dried from the pores between the particles. The final dried density is typically 65 vol% alumina. The change in rheology due to the pseudoplastic to dilatant transition is shown schematically in Fig. 3B.

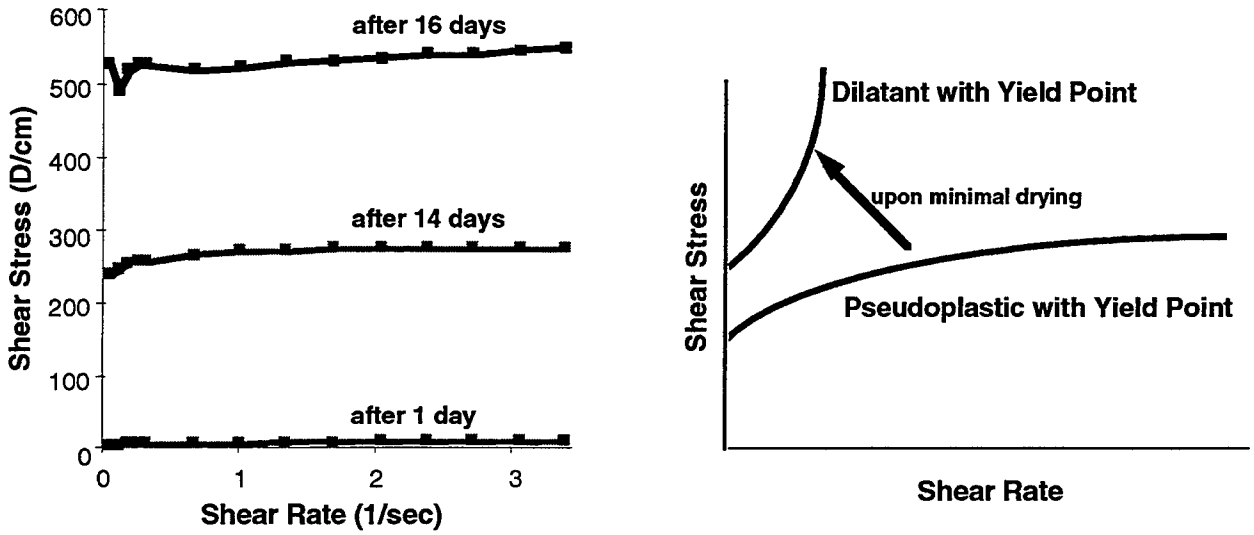


Figure 3. Shear stress vs. shear rate curves for pseudoplastic alumina slurries: A) 61 vol% alumina aged for 1, 14, and 16 days; B) schematic showing the transition of a pseudoplastic slurry into a dilatant slurry by drying.

The time that it takes to transform a dispensed bead of slurry into a stable dilatant mass is dependent on the size of the bead and the rate of drying. If the drying rate is too slow and the yield stress of the slurry too low then transformation to dilatancy may not occur until several layers have already been deposited. In this case, the added weight of slurry may induce

slumping. An example of this behavior is shown in Fig. 2C. Figure 2C shows a cross section of a wall built by multilayering 12 beads of slurry on a heated substrate. Above the fifth layer, appreciable slumping was observed. Heat transfer from the heated copper plate up through the beads of slurry was not great enough to sustain adequate drying kinetics on the freshly dispensed beads. Therefore, the slower drying beads in layers 5 through 11 did not have sufficient time to make the transformation from pseudoplasticity to dilatancy. As a result, the yield stress of these beads was exceeded and slumping occurred. Conversely, Fig. 2D shows that relatively uniform walls may be built with high aspect ratios when the drying kinetics can induce dilatancy before any external forces induce yielding and slumping of previously dispensed beads. However, if drying is forced to be too fast with respect to the rate of slurry deposition, warping, cracking, and delamination may occur.

When a functional balance between the bead dimensions, time between layers, and drying rate is achieved; not only can complicated shapes be fabricated but boundaries between layers disappear. Defect free boundaries are created under optimal drying conditions because fluid from freshly dispensed beads permeate into the partially dried bead that was previously deposited. The fluid transport naturally drags some powder particles with it and creates a finite interpenetrated region between the two beads that is free of defects or delaminations (Figure 2B).

Finite Element Analysis Of Drying

The drying process for dispensed beads of slurry is anisotropic and obviously very complicated with changes in solid content, dimensions, shape, and rheology all occurring simultaneously. The final structure is far from an equilibrium condition. However, in an effort to further understand the drying of slurries, we have started a study that utilizes a finite element analysis program, GOMA, developed at Sandia National Laboratories. [8] The GOMA program is being used to analyze the interplay between the mass transfer of water and fluid mechanics (viscosity) of the slurry to predict the size and shape of beads as a function of time. The time effects are not necessarily intuitive because the drying is anisotropic and the drying rate is dependent on the volume fraction of solids. Therefore, factors that need to be included in the finite element interaction calculations are changes in diffusivity and viscosity as the volume faction of solids increases. The changes in viscosity with increasing solid volume fraction is represented by

$$\mu = \mu_r (1-\emptyset/\emptyset_m)^n \qquad (1)$$

where μ is the viscosity of the slurry, μ_r is the viscosity of the solvent, $\emptyset$ is the solid volume fraction, $\emptyset_m$ is the maximum solid volume fraction, and n is an empirical exponent. [9] The diffusivity of the solvent through the slurry during drying is represented by an equation attributed to Batchelor [10]

$$D_s = [\kappa T/6\pi\mu_r A] (1+1.45\emptyset) \qquad (2)$$

where κ is Boltzmann constant and A is the average particle diameter. The drying rate of water from the free surface is controlled by the mass transfer coefficient of water (k) and the vapor pressure.

The GOMA model was used to simulate shape and dimensional changes of beads of ceramic slurry that contained 58 vol% solids at the beginning of drying. The diagrams in Fig. 4 represent the predicted shape of beads that have been drying for 5 minutes at three different

drying rates. Since the beads should be symmetric, each diagram is drawn as one-half of the cross section of the bead. Fig. 4A has a drying rate that is fast enough to cause the entire bead to exhibit the maximum viscosity within five minutes. The maximum viscosity is defined as the viscosity at the solid content $\emptyset_m$ (typically 64 vol%). In the case of Fig. 4A, the fast drying rate induces the formation of a very high viscosity shell that "freezes in" a rounded shape. The rounded shape is maintained until drying is complete. Conversely, Fig. 4C shows that for very slow drying rates, appreciable slumping can occur and the bead still doesn't form a shape preserving shell after 5 minutes. Under intermediate drying (Fig. 4B), high viscosity regions may form on the edges and cause the formation and maintenance of relatively straight walls. However, the formation of a high viscosity shell on the top of the bead is delayed so that appreciable flattening of the bead may occur during drying. This shape is similar to the shape observed experimentally in Fig. 2A and approaches the optimal rectangular shape that is best for space filling. With further study, this code may become a very useful tool for understanding the mechanisms in successful robocasting and for optimizing slurries and operational parameters to form optimally shaped beads.

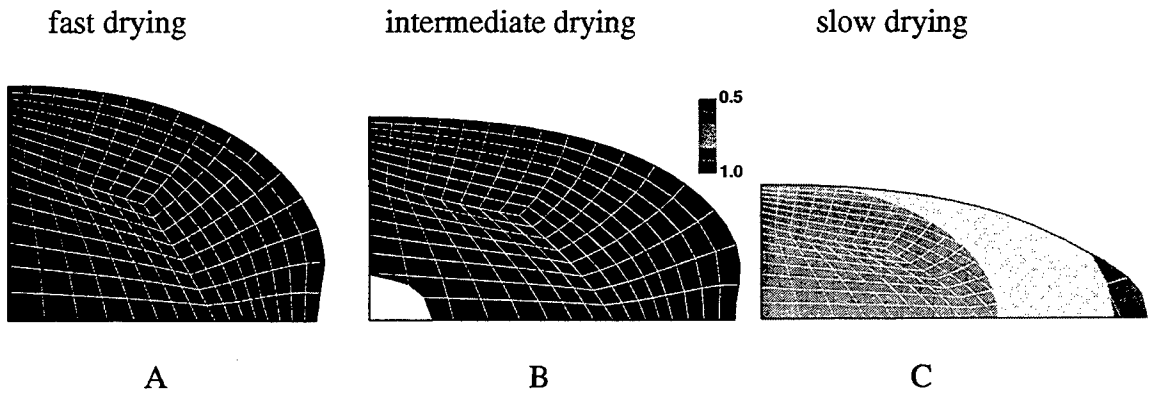


Figure 4 Finite element models of 58 vol% slurries that have been dried for five minutes at: A) fast drying rate, k = 0.001 cm/s, B) intermediate drying rate, k = 0.0001 cm/s, and C) slow drying rate, 0.00001 cm/s. The color scale represents the slurry viscosity throughout the grid. A viscosity of 1.0 indicates that the slurry has become dilatant.

Example Parts

In actual practice, when the materials issues discussed above are properly controlled, the processing window is quite large and forgiving and several different shapes have been robocasted from alumina slurries and sintered into relatively strong dense parts. Upon drying, the consolidated densities of aluminum oxide bodies are routinely approximately 65%. Upon sintering, crack-free alumina components have sintered densities greater than 95%. The entire process from fabrication through sintering may be completed in less than 24 hours. Components may be fabricated into bulk solids with large thicknesses unobtainable using slip casting; or, thin walled pieces made with aspect ratios greater than 20 and wall thicknesses less than 1 mm. Some examples of robocast alumina parts are shown in Fig. 5. Parts with overhangs up to 30 degrees have been built (Fig. 5A). The part with tailored porosity in Figure 5B is particularly interesting. It demonstrates the precision capability of robocasting and the possibilities for fabricating structures, with undercuts and closed porosity, that are not currently possible by traditional manufacturing methods. The part shown in Fig. 5B is actually an example of a substrate that is infiltrated with metal and used for fabricating graded ceramic/metal interlocking joints.

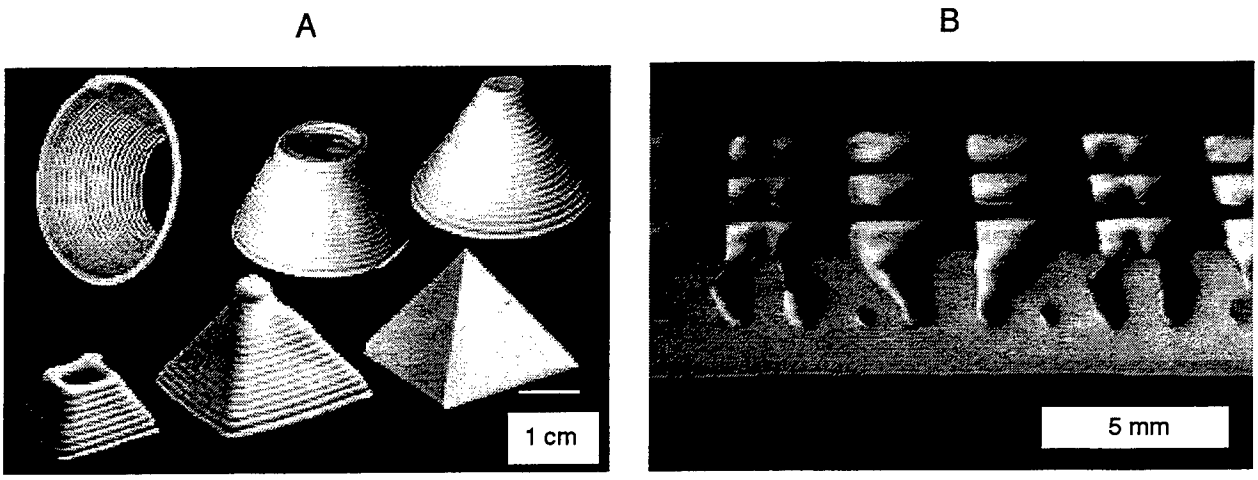


Figure 5 Examples of sintered aluminum oxide parts made by Robocasting: (A) Shows thin walled and solid parts. Notice that with minimal machining surfaces can be made smooth; (B) This cross section shows the symmetry and control that can be obtained in an intricate structure with tailored porosity. Due to regions with closed porosity and undercuts, this part could probably not be made by traditional molding or machining techniques.

Summary

It has been demonstrated that robocasting may be useful for the solid freeform fabrication of dense ceramic parts that may not be fabricated using traditional means. And, this near-net-shape technique is essentially binderless, utilizing less than 2 vol% organic processing aids. Successful robocasting requires controlled interactions among the solids loading of the slurry, the slurry rheology, the extrusion rate, the bead dimensions, and the drying rate. Finite element modelling of bead drying is yielding information for the understanding and optimization of extruded bead shape.

Sandia is now exploring the possibilities for multimaterial deposition for the moldless manufacture of intricately shaped composites and hybrid electronic packages. This task requires a significant effort in the development of computer software that can analyze a CAD file for a component and convert the file into a set of machine instructions that optimize processing parameters to produce high quality robocast components with precise control of feature resolution. Additionally, there is an effort to incorporate smart processing capabilities into robocasting with the aid of sensors and computer modeling. Sensors that monitor build conditions in real time are being incorporated into the system to provide closed loop sensor-based feedback for adjustment of build parameters during component fabrication.

Acknowledgment

Sandia is a multiprogram laboratory operated by Sandia Corporation, a Lockheed Martin Company, for the United States Department of Energy under Contract DE-AC04-94AL85000.

References

1) Agarwala, et al, American Ceramic Society Bulletin (1996), **75**, 11, 60-65.
2) Griffin, Mumm, and Marshall, American Ceramic Society Bulletin, (1996), **75**, 7, 65-68.
3) Griffith and Halloran, J. Am. Ceram. Soc., (1996), **79**, 10, 2601-08.
4) Heuer, Kernan, Baldwin, Ko, Liu, and Cawley, "Properties of Engineering Materials Made by CAM-LEM Technology, presented at the Solid Freeform Fabrication Symposium, University of Texas at Austin, August 11-13, 1997.
5) Reed, Introduction to the Principles of Ceramic Processing, John Wiley & Sons, (1988), chapter 22.
6) Omatete, Janney, and Strehlow, American Ceramic Society Bulletin (1991), **70**, 10, 1641-49.
7) Cesarano and Aksay, J. Amer. Ceram. Soc., (1988), **71**, 12, 1062-67.
8) Schunk, Sackinger, Rao, Chen, Cairncross, Baer, and Labreche, "GOMA - A Full-Newton Finite Element Program for Free Surface and Moving Boundary Problems with Coupled Fluid/Solid Momentum, Energy, Mass, and Chemical Species Transport: User's Guide," SAND95-2937, Sandia National Laboratories, Albuquerque, NM, January 1996.
9) Krieger, Adv. Colloid. Interface Sci., Vol. 3, 111-36, (1972).
10) Batchelor, J. Fluid Mech., Vol. 74, No. 1, (1976).

DIRECT-WRITE FABRICATION OF INTEGRATED, MULTILAYER CERAMIC COMPONENTS

D. Dimos, P. Yang, T.J. Garino, M.V. Raymond, M.A. Rodriguez
Sandia National Laboratories
Albuquerque, NM 87185

ABSTRACT

The need for advanced (electronic) ceramic components with smaller size, greater functionality, and enhanced reliability requires the ability to integrate electronic ceramics in complex 3-D architectures. For rapid prototyping and small-lot manufacturing, traditional tape casting and screen printing approaches are poorly suited. To address this need, we are developing a direct-write approach for fabricating highly integrated, multilayer components using a micropen to deposit slurries in precise patterns. With this technique, components can be constructed layer by layer, simplifying fabrication. It can also be used to produce structures combining several materials in a single layer. The parts are either cofired or sequentially fired, after each layer is deposited. Since differential shrinkage can lead to defects in these multilayer structures, we are characterizing the sintering behavior of individual layers. This technique has been used to fabricate devices such integrated RC filters, multilayer voltage transformers, and other passive components. The direct-write approach provides the ability to fabricate multifunctional, multimaterial integrated ceramic components (MMICCs) in an agile and rapid way.

INTRODUCTION

High reliability passive components (i.e., capacitors, resistors, and inductors) and packaging substrates are commonly made using multilayer ceramic constructions. However, the desire to achieve further miniaturization, greater functionality, and enhanced reliability in advanced electronic and microelectromechanical systems is driving the development of more highly integrated components based on combining different functional ceramics together into complex 3-D architectures. Currently there are numerous examples achieved by electronic ceramic manufacturers, in which various materials have been combined to produce monolithic, multilayer ceramics with sophisticated functionality, such as filters [1,2] and solid-state dc-dc converters [3]. Similarly, significant work is being done to permit embedding of passive components into low-temperature cofireable ceramic (LTCC) packages. This trend towards higher level integration, which is the passive component analog of an integrated circuit (IC), places increasing demand on fabrication processes and manufacturers.

The usual technique for making these multilayer, multi-material, integrated ceramics is based on cofiring of laminates made from layers of green tapes with screen printed features, such as conductor traces. This manufacturing method has been refined over decades of development, driven by the needs for low cost and high production volumes. While this approach works well for simple parts such as multilayer capacitors that contain only a single active ceramic, fabricating multifunctional components in complex geometries is a significantly more

challenging problem. Consequently, commercial development of sophisticated integrated ceramics has emphasized a highly empirical approach, making the technology impractical for low-volume, specialty components.

To overcome this limitation, we are developing a direct fabrication approach that simplifies the processing and provides greater flexibility than would otherwise be possible with tape casting and screen printing approaches. The goal is to provide a rapid prototyping and agile manufacturing approach to fabricating multifunctional, multimaterial integrated ceramic components (MMICCs). This work is based on the use of a commercial micropen system [4,5,6] for depositing electronic-grade slurries in precise patterns. In this paper, we discuss several specific issues that are critical to the direct fabrication of MMICCs by the micropen approach, such as the relationship between slurry rheology and print topology. Characterization of the sintering behavior of thick films, which is critical for assessing cofireability, has also been carried out using two different approaches. Finally, a number of specific devices that have been fabricated using the micropen are illustrated.

EXPERIMENTAL

Micropen

Direct deposition of precise patterns is being accomplished using a commercial Micropen system (Ohmcraft, Inc.), which is an automated printing device for ceramic slurries [5]. The micropen has a computer driven x-y stage that uses CAD file instructions, which permits easy on-line design changes in contrast to screen printing where a new screen is required for a pattern change. It is also inherently capable of laying down multiple materials in a single layer, which cannot be done with conventional tape casting techniques. The micropen utilizes nozzles with an inner orifice diameter as small as 1 mil and an outer diameter down to 2 mil for high definition patterns. A critical feature of the Micropen is the force feedback control on the pen tip, which is based on balancing the upward force on the pen due to the extruding slurry and the downward force applied by an electromagnet, as illustrated in Fig. 1. This control leads both to a very reproducible print topology and the ability to print over variations in the topography (i.e., height) of the workpiece. However, since the workpiece needs to support the force of the pen, any underlying slurry layer must be dried before printing on top of it.

The other critical feature of the system is the pump block, which uses two internal chambers to provide smooth, continuous delivery of slurry. The slurries are loaded into a syringe which screws into the pump block assembly. To get uniform and reproducible processing it is critical to eliminate air bubbles in the slurry, which is accomplished by centrifuging, and in the pump system, which is done by bleeding the pump block.

Materials

Commercial thick-film slurries were used to characterize the printing process and to fabricate components. The materials used in the work were: a crossover dielectric (Ferro 10-38N), a Ag conductor (Ferro 1039), and a RuO_2-based resistor (Ferro 87-102). Slurry viscosities were characterized using a Brookfield viscometer with a cone and plate attachment.

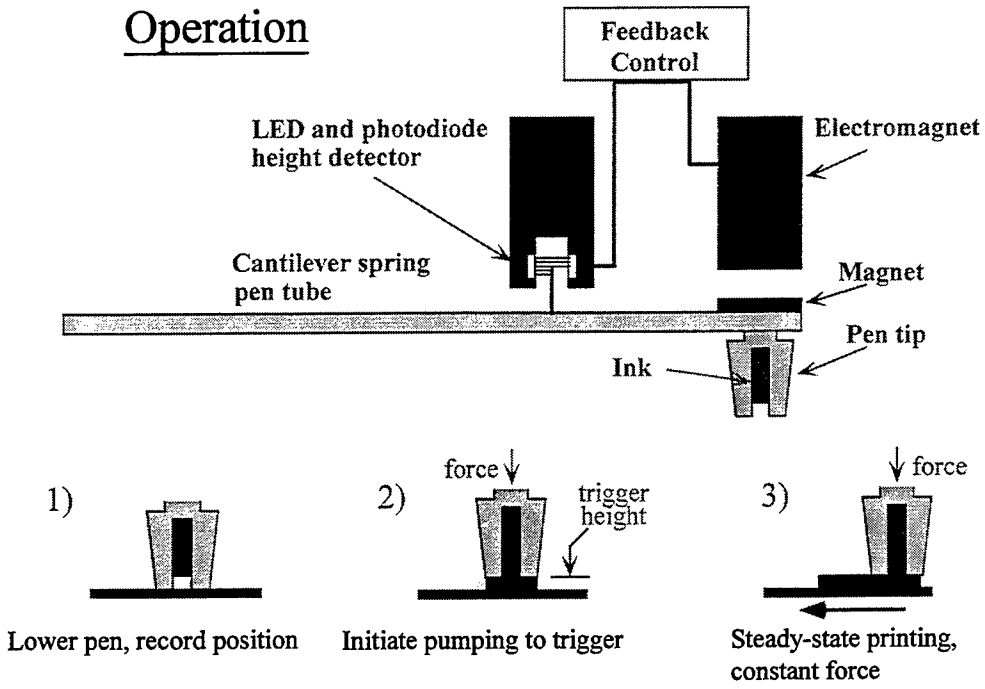


Figure 1. Schematic diagram of the micropen print head showing the photo detector system for height control and the electromagnet force balancing system. The lower drawings illustrate the steps to initiate slurry printing.

Sintering

Two different systems were developed to characterize the sintering behavior of individual thick film systems. While detailed descriptions will be published elsewhere [7], schematic diagrams of the two systems are given in Fig. 2.

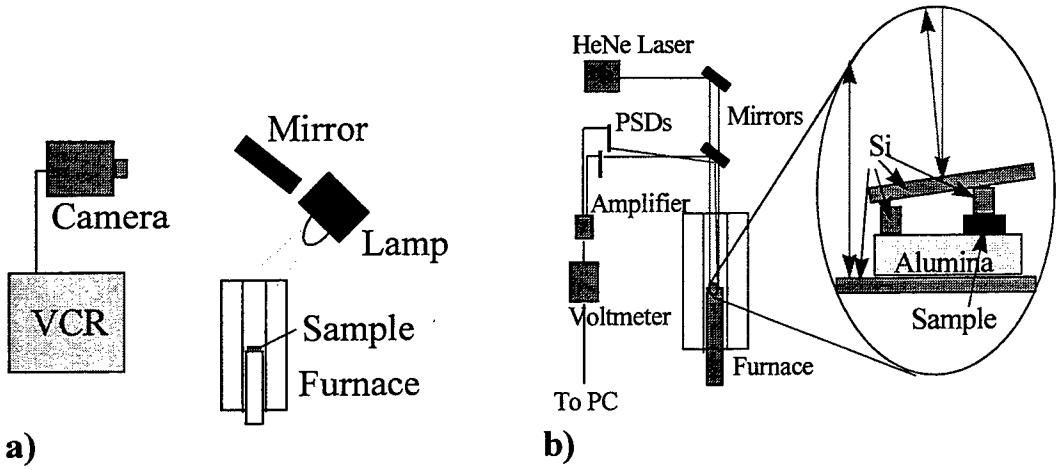


Figure 2. a) Schematic diagram of system for measuring (lateral) sintering behavior of free-standing films. b) Schematic diagram of system for measuring z-axis sintering behavior of laterally constrained films.

Figure 2a shows the arrangement used to determine the sintering behavior of unconstrained, free-standing thick films. Square samples were patterned with the micropen onto teflon or mylar substrates, so that the thick-film sample could be removed from the substrate producing a free-standing thick film piece with an area of 4mm x 4mm and a thickness of 75-100 μm (2-3 print layers). The samples were fired on top of a quartz setter, which did not react with the samples during the measurements. The sintering behavior was characterized by continuously monitoring the x-y dimensions of the sample with the video recorder during heating.

In contrast, Fig. 2b illustrates the arrangement for characterizing the sintering behavior of films constrained in the x-y plane. These measurements also used samples with an area of 4mm x 4mm and a thickness of 75-100 μm that were deposited onto alumina substrates. A dual laser beam system was used to determine the z-axis shrinkage of the film by comparing the deflection of a reference laser beam to the deflection of an incident parallel beam from a mirror positioned on the sample as shown in the inset of Fig. 2b. The laser beam deflections were continually monitored during heating using position-sensitive photodetectors. The optical path length from the sample mirror to the photodetector was ~1.5 m, which enabled small changes in the angular deflection of the sample mirror and, thus, very small changes in the sample thickness to be accurately determined. It should be noted that this system was developed after it was determined that a standard extensometer could not be used, since it applied enough pressure to the sample to locally deform it during firing.

RESULTS

Slurry viscosities as a function of shear rate are shown in Fig. 3, which demonstrate that all the thick film pastes are shear thinning. There is a wide range of viscosities for these materials at low shear rates. However, the range of viscosities converge at higher shear rates, which are typical of the printing process. The range of shear rates (dv/dr) typical of the printing process was

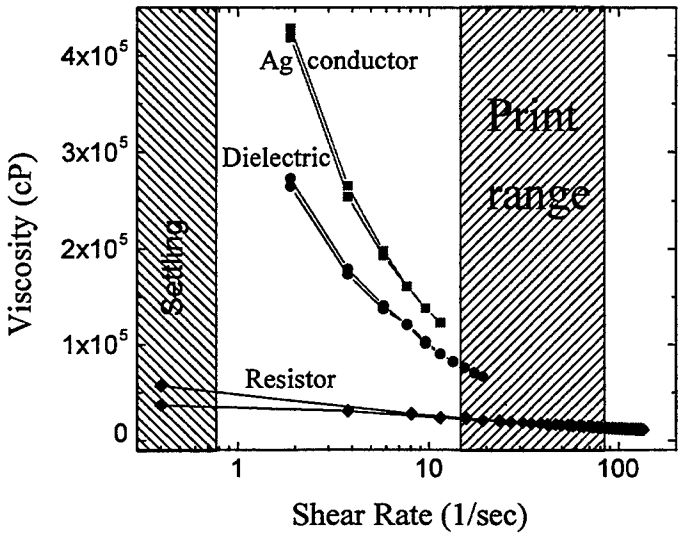


Figure 3. Viscosity vs shear rate behavior for the electronic thick films used.

estimated using the following equation for an incompressible, Newtonian fluid with no flow against the wall of the orifice:

$$dv/dr = (4/\pi)\,(Q/R^3)\ , \qquad (1)$$

where Q is the volumetric flow rate (typically ~ 10^{-5} cm^3/sec) and R is the inner orifice diameter (2-10 mil). The settling rates correspond to the high viscosity range.

An attractive feature of the Micropen is that the print topology is fairly insensitive to the slurry viscosity. This feature is illustrated in Fig. 4, which shows profilometry traces obtained on line prints of the dielectric, conductor, and resistor using identical print conditions. However, the slurry viscosity at the low shear rates is critical for optimizing materials for either high definition patterns or for filled regions. The most viscous slurry (Ag conductor) leads to sharply defined traces, whereas the more fluid resistor paste flows together to give a relatively smooth surface for filled areas, which are typical of thick-film resistors.

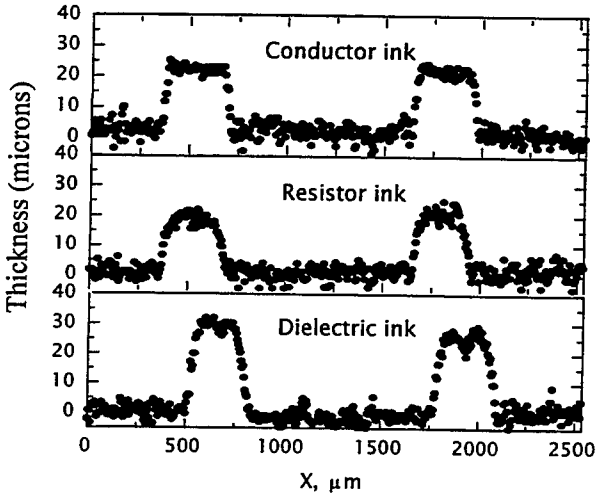


Figure 4. Profilometer traces showing that the print topologies for materials with different viscosities are very similar and good using identical print parameters.

Figure 5 illustrates the sintering behavior, at a constant heating rate of 20°C/hr, for the three thick-film systems. The Ag conductor sinters at a much lower temperature than the other two materials, which is not ideal for cofiring compatibility. The free sintering rate is also higher than the constrained sintering rate, which is commonly observed and is due to internal stresses in the constrained system [8]. The shrinkage curves for the dielectric and resistor systems both show a rather abrupt onset of sintering (at 725°-800°C), which is typical for liquid-phase sintering systems above the liquidus. The temperature compatibility also promotes good cofireability. In addition, the free and constrained shrinkage curves for these two materials are essentially identical, which is also consistent with a liquid-phase mechanism, since a liquid phase tends to limit stress buildup. It should also be noted that the total volume shrinkage is nearly equivalent for each material in both constrained and unconstrained sintering, which is anticipated and verifies good correlation between the two experimental methods.

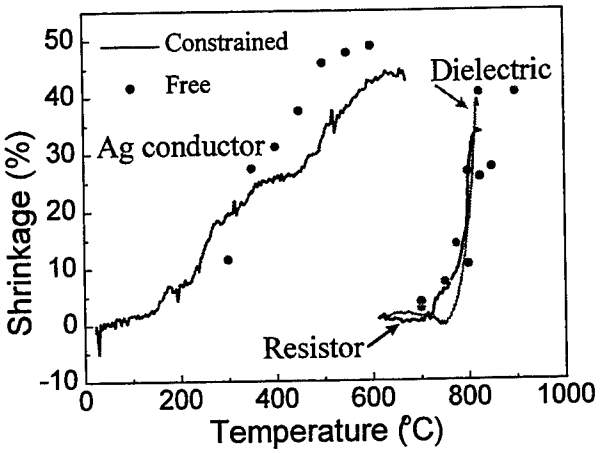


Figure 5. Measurements of the sintering behavior (% shrinkage vs temperature) at constant heating rate (20°C/hr) for three thick-film systems. Measurements were carried out with the two experimental setups to determine the constrained and unconstrained sintering behavior.

Prototype Components

The Micropen system has been used to prototype various electronic components. Figure 6a shows a R-C band reject filter fabricated with the micropen, based on the schematic circuit layout in Fig. 6b. The capacitors are parallel plate capacitors with a single (crossover) dielectric layer. The impedance response is shown in Fig. 6c, which indicates a 27 dB suppression at the reject frequency, which is given by $f_c = (\pi RC)/2$. The sharpness of the attenuation is given by achieving good matched values for the capacitors and resistors.

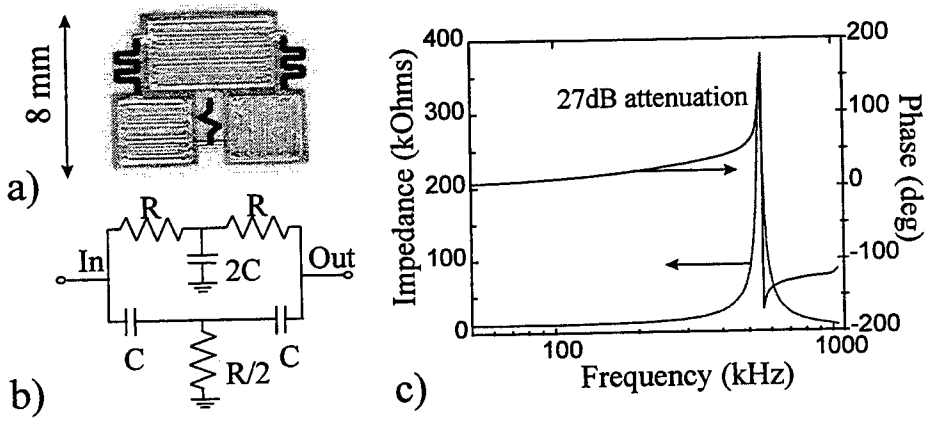


Figure 6. a) Photograph of 4-layer band reject filter fabricated with the micropen, b) schematic diagram of band reject filter, c) impedance response for a typical micropen band reject filter.

The capability of the Micropen to accommodate various topographies has also been utilized to build a multi-turn voltage transformer structure, as shown in Fig. 7a. The transformer is built with an outer winding of six turns and an inner winding of three turns so that the device can be used for 2:1 and 1:2 voltage conversion. This construction relies on the ability of the micropen to

print at a range of heights and would be extremely difficult to fabricate using standard tape/screen printing methods. This design works well, but the conversion efficiency (Fig. 7b) of the initial prototype is relatively poor since a low permeability dielectric was used for the prototyping, rather than a high permeability ferrite. In addition, we have successfully fabricated a flat eight turn solenoid (L ~ 1 μH), and a multitap voltage divider, which are shown in Figs 8a and 8b, respectively. While these devices are all printed on alumina substrates, the process has also been used to fabricate components on tapes and on mylar and teflon substrates that allow free standing components to be built.

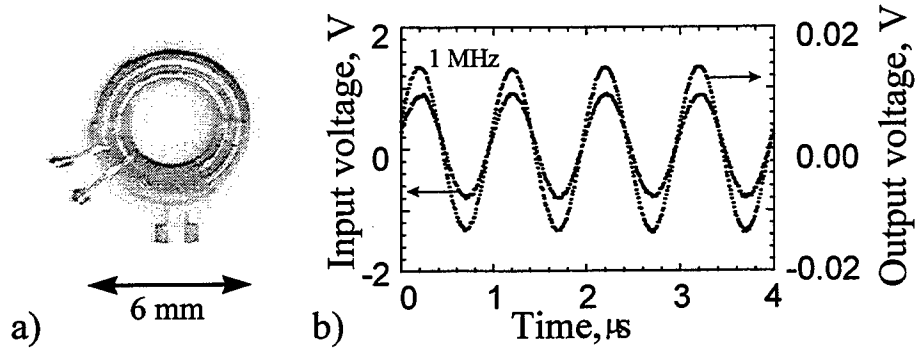


Figure 7. A) Picture of multiturn voltage transformer fabricated with independent Ag spiral windings (6 outer turns, 3 inner turns) and crossover dielectric. Plot of input vs output voltage for the transformer.

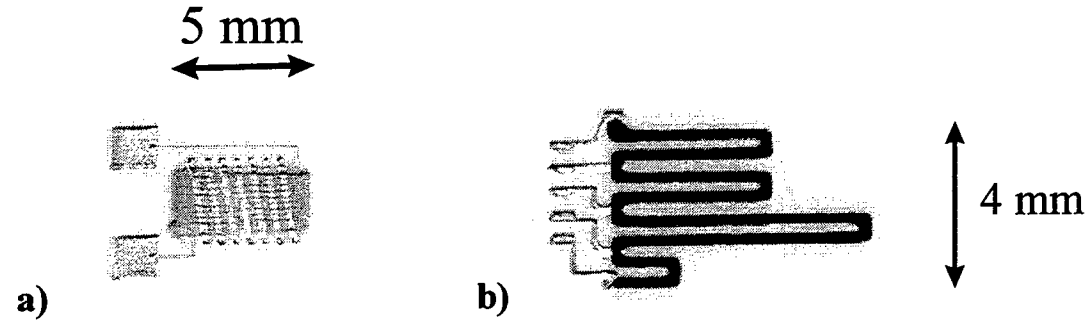


Figure 8. a) Flat solenoid fabricated by connecting lower half windings and upper half windings around thick-film dielectric (L(@ 1 MHz) ~ 1 μH), b) Multitap voltage divider for 10:1, 7:1, 4:1, and 2:1 voltage division. A 10kΩ/sq resistor with Ag electrodes is used.

CONCLUSIONS

We have demonstrated a direct-write approach for fabricating highly integrated, multilayer components using a micropen to deposit slurries in precise patterns. With this technique, components are constructed layer by layer, simplifying fabrication. The quality of print features depends on slurry viscosity; however, the micropen can use a wide range of slurry viscosities

with minimal optimization. Since differential shrinkage can lead to defects in these multilayer structures, we have developed two techniques for characterizing the sintering behavior of individual layers, which should help in assessing cofireability. Finally, the micropen technique has been used to fabricate devices such integrated RC filters, multilayer voltage transformers, and other passive components. The direct-write approach provides the ability to fabricate multifunctional, multimaterial integrated ceramic components (MMICCs) in an agile way with rapid turnaround.

ACKNOWLEDGMENTS

The authors would like to acknowledge excellent technical assistance from I. Alderete. This work was supported by the United States Department of Energy under Contract DE-AC04-94AL85000. Sandia is a multiprogram laboratory operated by the Sandia Corporation, a Lockheed Martin Company, for the United States Department of Energy.

REFERENCES

1. H. Hayashi, T. Ikeda, and S. Nishigaki, ISHM '91 Proceedings, 508-512 (1991).
2. H. Mandai, K. Wakino, H. Okamura, and J.P. Canner, Ceram. Trans., 15 (Mater. Processes Microelectron. Syst.), 391-404 (1990).
3. T. Minoru, Y. Mochizuki, A. Nakano, and H. Kobuke, ISHM '92 Proceedings, 269-274 (1992).
4. Micropen, Inc., Pittsford, NY.
5. C.E. Drumheller, ISHM '82 Proceedings (1982).
6. A. Dziedzic, J. Nijs, and J. Szlufcik, Hybrid Circuits, 30, 18-22 (1993).
7. T.J. Garino, P. Yang, D. Dimos, to be published.
8. T.J. Garino, H.K. Bowen, J. Am. Ceram. Soc., 73(2), 251-7 (1990).

Laser Aided Direct Rapid Prototyping

Robert Franceschini, Lee Napravnik, Amar Mukherjee
Department of Computer Science

Srikanth Sankaranarayanan, Aravinda Kar
Center for Research and Education in Optics and Lasers

University of Central Florida, Orlando, Florida 32816
{*francesc@cs, napravni@cs, amar@cs, srikanth@mail.creol, aravinda@mail.creol*}*.ucf.edu*

Abstract

We describe a multilevel design hierarchy applicable to the VLSI-like layered manufacturing technology of Solid Freeform Fabrication (SFF) called Laser Aided Direct Rapid Prototyping (LADRP). We discuss the interfaces between the abstraction levels and the requirements of the standard languages needed for the interfaces. We provide experimental verification for the thickness design rule and indicate other possible design rules applicable to this process. We then present a software tool called a **Slicer** *that takes a three-dimensional description of a solid body and creates 2.5D layers for the SFF process. Our current implementation is based on a boundary representation of solids described by the Unigrafix solid modeler.*

Keywords: Solid Freeform Fabrication, design hierarchy, layered fabrication, solid interchange format, slicer, LADRP (Laser Aided Direct Rapid Prototyping), design rules

1 Structured Design Methodology

VLSI design methodology has exploited multilevel design abstractions (viz. system, function, logic, circuit, and layout), each layer addressing the design issues specific to that layer with its associated synthesis and simulation tools. The communication between two layers takes place through a clean interface that encapsulates the constraints imposed by the lower layer in terms of simple rules to be observed by the layer above it. A "digital interface" between design and fabrication in the form of a set of design rules at the layout level allows processing steps to be defined independent of an object's geometry. For mechanical and electromechanical systems, the multilevel design hierarchy is much more complex due to energy transformation, function sharing of elemental components and because performance considerations are an integral part of the design process [16, 17]. The limits on geometric dimensions of the object and physical attributes of the material as they relate to correct function and performance of the object will be called *design constraints.* The design constraints are process independent and can be derived by experimental methods and mathematical modeling. This terminology is appropriate to distinguish between functionality and manufacturability of a part. For VLSI design, these two considerations can often be merged into a set of conservative geometric *design rules.* In practice, however, an additional set of design rules are followed which guarantees expected performance. An analogous set of design rules must also be discovered for the mechanical fabrication process. For the SFF process, at least four levels of design hierarchy can be identified. Figure 1 shows the design hierarchy beginning at the 3D geometry level.

- **Design level, including function, features, and properties:** At this high level, a formalism is needed to capture the functional behavior of the mechanical system from the physical parts without specifying the geometry information. The emerging international standard STEP [5, 15] will have facilities to specify the design at this high level of product definition.

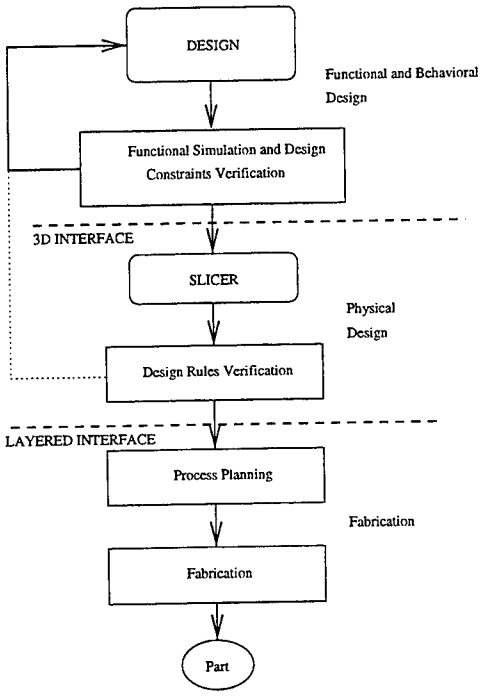


Figure 1: Design Hierarchy for Solid Freeform Fabrication

- **Three dimensional geometry level:** At this level, a completely process-independent representation of the system in terms of its geometrical shape and material in 3D has to be specified. We will call it a *design subsystem* which performs the traditional design by deriving the shape and geometry that achieves the desired functional specification. The design must satisfy a set of design constraints with respect to a set of relevant mechanical and physical properties of the material. The analysis and simulation tools verify the correctness of the design taking into account material strength, volumetric and surface properties, thermal and fluid flow properties if necessary [13].

  The design languages to be used for data exchange at the interfaces must be capable of expressing realistic three-dimensional objects. The SFF research community has given a name SIF (Solid Interchange Format) [11] to such a language. Such a language should probably be based on a solid modeling system such as CSG (Constructive Solid Geometry) or BREP (Boundary Representation), possibly augmented with non-uniform rational B-spline (NURBS) and quadric surfaces [2, 3, 12]. A large number of commercial and research solid modelers have been developed in the past [4] but none of these meet the requirements of SFF technologies.

- **Layered Level adapted to specific SFF technology:** The physical design phase uses specific knowledge of the process and its design rules to specify a layered description of the part. Ideally, like in VLSI which satisfies a layering paradigm with conservative design rules, this stage should be insensitive to an object's geometry.

  The translation of the 3-D geometry to layered geometry has to be done by a *Slicer* that will produce the layers, given its description in SIF. This description will form a digital interface between the physical design and the process planning stage [9, 11]. A key software tool at this level is a *Design Rules Checker*. The design rules specify the geometrical constraints on the dimensions of the layers that will conservatively guarantee reliable production of the part and its three-dimensional geometry (within limits of tolerances) by the underlying SFF fabrication process.

- **Process Planning and Fabrication:** This is the final stage of the hierarchy at the lowest physical level. If the design is validated by simulation and is free from both design constraints and design rules errors, the design is sent down to the process planning stage which generates the information for automatic sequencing of operations for the particular SFF process.

2 LADRP Process

2.1 Experimental setup

Laser Aided Direct Rapid Prototyping (LADRP) is used to develop 3-D metal parts by directly melting base metal powders using the laser source. The fabrication step takes the instructions from the process planning step and manipulates the robot arm to fabricate the part. In the LADRP process, the three main requirements are a laser beam, powder feed, and shielding gas. Experiments were conducted to formulate the design rules for fabrication. The detailed setup is shown in Figure 2. Since laser beams are inertialess and contactless tools, they are readily adaptable to automation. The CO_2 laser was run in CW mode with a maximum power output of 400 W. The laser beam was focused to a 406 micron spot size using a 5 inch lens and was triggered on/off using a controller interfaced with a computer. SS 304 type stainless steel powder of 150 micron size was fed to the focal spot of the laser beam using a volumetric powder feeder. The feed rate of the metal powder is one of the design criteria from the fabrication point of view.

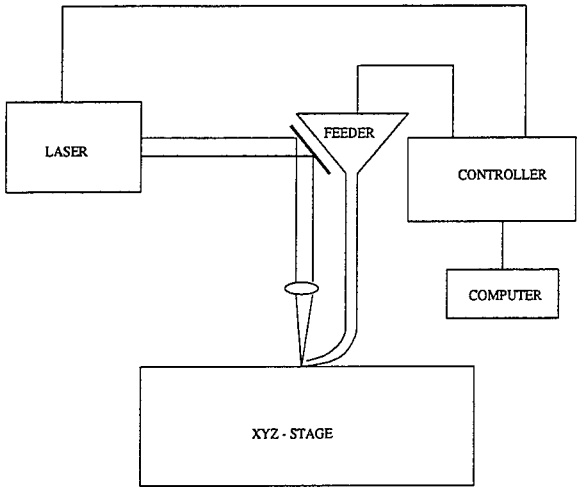


Figure 2: Laser-Aided Manufacturing of Multigraded Components

Three dimensional parts are fabricated by a layer by layer deposition method. The 3-D structure is stored in a computer and is replicated as a real part using a XYZ-Translational stage. The XYZ-stage is linked to the computer through a controller which has its own memory. One layer of the part is deposited as the XYZ stage translates in the XY plane. The next layer is deposited on top by giving an appropriate Z-axis displacement. Likewise the entire structure is formed by layer by layer deposition. The thickness of each layer depends on the speed of the XYZ stage, the Z-axis displacement, the powder feed rate, and the laser power. The interaction of the laser heated material and the surrounding air could cause oxide formation resulting in trapped oxide particles between adjacent layers which is detrimental to material quality. This was avoided using argon at the flow rate of 15 liters/min as a shielding gas. There are two outlets for the shielding gas, one through the laser head which also helps cooling the lens and the other through the powder delivery system which acts as a carrier gas for uniform powder deposition.

3 Design Rules for LADRP

The design rules specify a set of simple geometrical rules that a CAD designer must follow in a geometrical model so that the product is reliably produced by the process. Generic design rules such as VLSI's λ-based rules specifying minimum dimensions of transistors, separation and width of interconnecting wires [8], do not seem to exist for SFF processes. This can be attributed partly to the dependence of the functionality of the part on the particular material, geometry and fabrication technique used to produce the part. The dependence of the functionality of the part with its 3D geometry can be expressed in terms of a set of *design constraints* which are derived by designers using mathematical modeling of material properties and functional specification. Let us take a simple example of designing a bracket. It has a general shape but its actual dimensions will depend on the load specification. The same load-bearing capability of the bracket can be achieved by using various types of materials such as aluminum, iron, plastic, etc. But in each case, the dimensions will be different since the mechanical strengths of these materials are different. However, for all these materials, the strength and dimensions can be related by the same equation [14]. The next step is to verify whether the given manufacturing process is capable of fabricating the part. The limitations imposed by the process parameters on the manufacturability of the part are referred to as *design rules.* In a recent paper, Kar and Mukherjee [6] presented design rules that relate part dimensions with process parameters such as laser power, wire feed rate, temperature and thermophysical properties based on energy balance equation [1]. One of these rules, the thickness rule, states that given a set of process conditions and material, the thickness of a layer is proportional to the square root of the product of laser power and energy utilization factor. We will provide experimental verification of this design rule.

3.1 Experimental verification

The important process variables that affect the design rules are discussed below.

- Laser power - affects the energy input to the material.
- Laser beam radius - determines the radius of the material feed that can be melted. The beam radius depends on the focal length of the lens. The theoretically achievable smallest beam radius is given by the diffraction-limited spot size. For a given laser machine and beam focusing system, the beam radius can be computed by considering the propagation of the laser beam.
- Material (powder) feed rate - influences the rate of manufacturing the part. This process variable is usually selected on the basis of economic considerations.

The proposed thickness rule theory is verified using the experimental setup for LADRP shown in Figure 2. The various parameters like translational speed of the XYZ stage, the focal length, spot size, powder feed rate, and the shield gas were kept constant and the laser power was varied. The variation of layer thickness is plotted against the square root of laser power as shown in Figure 3. The linearity between the two quantities is evident. The same figure shows the linearity of the maximum thickness and the theoretical thickness for the various power levels. The various process parameters used are: Laser source - CW CO_2 Laser Maximum power level 400W: Focal Distance - 5 inch; Spot size - 460 micrometer;

Translational speed - 0.51 cm/sec; Shielding gas - Argon; Shielding gas flow rate- 15 l/min; Power level variation - 340 to 380 watts.

3.2 LADRP Fabrication Limits

Various process parameters like the spot size of the laser, the resolution of the XYZ translation stage, surface tension of the molten metal and orientation of the 3-D structure with respect to its fabrication

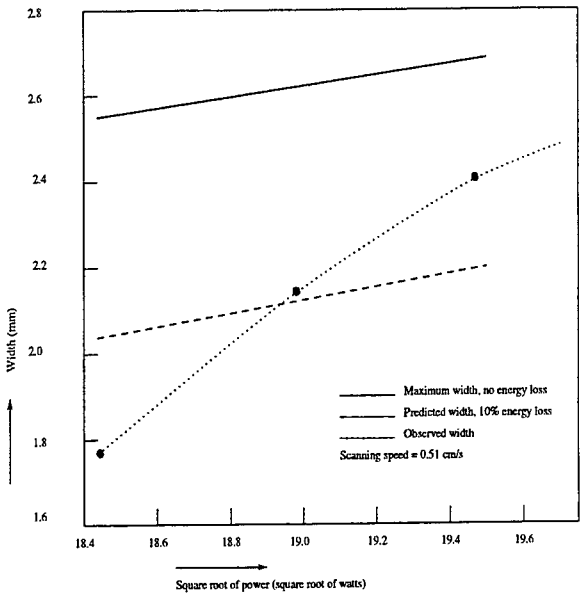


Figure 3: Experimental verification of the thickness rule

determine the limitations of the process. In our present work three kinds of limitations have been considered, namely angular resolution, cone tip resolution, and supportless structure formation.

1. **Angular resolution.** The large number of parameters influencing the process makes it difficult to formulate a mathematical expression for angular resolution. We have chosen instead to experimentally establish angular resolution criteria by building structures in the shape of triangles with various corner angles and determining the resolution of the angle by the quality. When using this technique, the measured values are affected by the XYZ stage resolution. The resolution of the XYZ stage was independently determined and was compared with the resolution of the process and the least of the two accounted for the observed value. The XYZ was found to have a resolution of about 1.71° below which it becomes difficult to distinguish between the lines with normal eyesight. The actual process has a much smaller resolution of about 11.3° only and hence structures with corner angles below this value become difficult to fabricate. For any two walls of thickness r meeting at an angle θ the length of the cross section is given by $\frac{r}{\sin\frac{\theta}{2}}$. Hence as the angle decreases the length of common region between the two walls increases. Below the angular resolution there is an overlap of the layers. In addition to this, at the corners the XYZ stage temporarily comes to rest. This results in more melting at the corners thus forming lumps. This can be avoided by reducing the powder feedrate at the corners or in similar positions where the stage experiences a temporary rest.

2. **Cone tip resolution.** Sharp points may be difficult to fabricate. This is due to the fabrication method of layer by layer deposition because corners tend to be more of a point than a layer. Various structures involve solid angles like a conical tip. Limitations of fabricating such features are established using the thickness rule criterion as discussed before. In case of a hollow cone the fabrication process starts from the base and a circular ring of thickness $2r$ forms the first layer. The second layer is deposited on top of the first with a slight offset and with a smaller diameter ring which accounts for the slant angle of the cone. The thickness $2r$ of the layer is determined by the thickness criterion. Again the slant angle is another design criterion fixed by surface tension of the liquid metal. Layer by layer deposition results in the conical structure of fixed dimension. The topmost layer decides on the tip resolution for the cone. Since the thickness of the layer is $2r$ which is the width of the layer w, the final top surface of the cone can be formed with no center gap i.e., with a diameter of $2w$. Hence the topmost surface of a

cone will have a finite area A_c and not a point as in case of an ideal cone. The area of the top cone surface is given by $A_c = w^2$ where w is the layer thickness given by the thickness criterion.

3. **Supportless structures.** For example, dome like structures can be fabricated without internal support with certain limitations on the angle of tilt of the dome. Only a certain maximum angle of tilt is allowed which is decided by the surface tension of the molten metal balanced by the weight of a single layer. Formation of supportless structures involves depositing layer by layer with a calculated offset which accounts for the angular dimension. However there is a limit to the extent of offset which is determined by the surface tension forces that act between the already solidified layer and the new liquid layer getting deposited. The area of interaction of surface tension forces are determined by the Z axis displacement of the stage and the translational speed. The surface tension forces balance the cosine component of the weight of the new layer being formed.

4 Slicer

In our project, we have chosen Unigrafix as a baseline for our 3D modeling language. Unigrafix (UG) is a boundary representation solid modeling language developed at the University of California at Berkeley [10]. UG uses simple BREP for its objects. This makes it easy to obtain the needed data for our slicer. Also it lends itself well to the joining together of the slices into a single unified object file. We are currently developing the 2.5D slicer so that we may express objects in an L-SIF language as described earlier.

The goal of this algorithm is to decompose a solid model into "slices" that can be suitably described to a Solid Freeform Fabrication system for manufacturing. Intuitively, the slicer we have implemented uses a "space-sweep" algorithm. The main idea is to sweep a plane oriented parallel to either the yz plane, xz plane, or xy plane (i.e., along the x, y, or z axis, respectively) through the solid model of the object. The plane stops at event points for processing. A sweep data structure is maintained that provides local information about the portion of the solid that has been swept so far that contributes to the current slice.

The inputs to the algorithm include the solid model (in Unigrafix boundary representation format), the axis (α) for the plane to sweep along (x, y, or z), and the width of each slice. Our initial implementation uses variable but prespecified slice widths; however, the implementation is easily extended to allow adaptive slicing by allowing an external process to supply slice widths.

In the first stage of the algorithm, an event queue is constructed using the solid model and the slice widths. Two types of events are added to the event queue: *vertex events* and *slice events*. Events are placed in the queue in increasing order of their corresponding values along the α axis (ordering of multiple events with the same α axis value is described below).

Vertex events are added to the event queue for each α axis value corresponding to a vertex in the solid model. Along with vertex events in the queue is a list of vertices that share the same event.

Slice events are added to the event queue at the location of each slice in the solid model. These locations are calculated by starting at the smallest vertex α value and adding successive slice widths. Note that although the current implementation fixes all slice widths before building the event queue, we only need to fix the width of one slice at a time; as a slice of the model is cut, we may request the next slice width and dynamically add a corresponding slice event to the queue.

If a slice event occurs at the same α axis value as one or more vertices in the solid model, then the slice event is placed after the vertex event for that α axis value.

In the second stage of the algorithm, the plane is swept along the α axis, stopping at each event point. A sweep data structure containing a boundary representation of the current slice of the solid is built as the plane sweeps through the solid. The processing at each event point is summarized below.

Vertex Event. In this case, all vertices at this α axis value are added to the sweep data structure along with any edges of the solid incident to these vertices that are not already within the slice model.

Slice Event. In this case, the sweep plane is intersected with the sweep data structure by intersecting it with the appropriate edges in the structure. The resulting "slice" is output by the algorithm. The top of the slice (the part cut by the sweep plane) is stored as the base of the next slice. The vertices within the sweep data structure that are below the sweep plane are removed, along with any edges below the sweep plane that have endpoints in vertices corresponding to this event.

An alternate algorithm is suggested in [7]. As part of our continued work, we intend to compare our approach with the algorithm given in [7] in order to develop a fairly general and efficient slicer.

4.1 Error Checking in Sliced Structures

All calculations within Unigrafix, and in particular the slicer, are done using floating point numbers. The properties and errors associated with floating point numbers are well known. These properties brought up the question of the potential for *gaps* within adjacent slice structures (i.e., a non-seamless intersection of a slice's ceiling and the floor of the slice above it).

The method used to find gaps was based on the following concept: The ceiling points of slice A should be identical, within some error range, to the floor points of the adjacent slice B, for all slices within the structure.

The floor/ceiling points of the respective slices are determined as being any points within some ϵ_1 of the floor/ceiling of the slice. When a slice is created, its floor points are determined and stored. If there exists a set of ceiling points from a previous slice, then a series of comparisons is made. Essentially, every new floor point is checked to see if it has a match in the corresponding ceiling. If a match is not found, then a gap has occurred between the two slices. A point (x, y, z) is tested as follows:

$$||\lfloor x \rfloor - \lceil x \rceil|| \leq \epsilon_2 \quad \text{and} \quad ||\lfloor y \rfloor - \lceil y \rceil|| \leq \epsilon_2 \quad \text{and} \quad ||\lfloor z \rfloor - \lceil z \rceil|| \leq \epsilon_2 \tag{1}$$

If the above condition is false, then a gap has occurred.

This test was run on a variety of structures with different epsilons. Sample ϵ_1 values were 0.5 to 0.1. Sample ϵ_2 values were 0.01, 0.001, 0.0001, 0.00001, and 0.000001. Sample structures included cubes, pyramids, dodecahedrons, and mixtures of several other forms. The results for all epsilons on all structures was 100% accuracy with no gaps.

These results are expected and are easily explained. When calculating line intersections, the same standard line equations were used for all slices. Also, only the original points from the slice are used for these calculations (i.e., no derived points are used to derive more points). And finally, the same precision was maintained throughout the code for all floating point numbers.

We expect to incorporate information about materials into our solid models in the near future. This will likely be done using tags indicating the type of material used for different parts of the solid. This presents several new constraints for the slicer algorithm, including how to slice an object made up of multiple materials (a consideration that may be important for some SFF processes) and anisotropy in density.

Our goal is to make our slicer general enough to be used with several different SFF processes. Although our current work is focused on one process (the LADRP process), we will attempt to make the output from our slicer conform to emerging standards and convey this output to other SFF sites.

5 Acknowledgment

The work has been supported by a National Science Foundation grant MIP-9625752.

References

[1] Sidney S. Charschan, editor. *Guide to Laser Materials Processing.* CRC Press, Boca Raton, Florida, 1993.

[2] Gerald Farin. *Curves and Surfaces for Computer Aided Geometric Design: A Practical Guide.* Academic Press, Inc., Boston, second edition, 1990.

[3] Christoph M. Hoffman. *Geometric & Solid Modeling: An Introduction.* Morgan Kaufmann Publishers, Inc., San Mateo, California, 1989.

[4] Spatial Technology Inc. ACIS geometric modeler: Technical overview, 1995.

[5] Haeseong J. Jee, Ram D. Sriram, and Mike Pratt, editors. *STEP-based Solid Interchange Format.* National Institute of Standards and Technology, US Department of Commerce, November 1996.

[6] A. Kar and A. Mukherjee. Design rules and digital interface for laser-aided direct rapid prototyping (LADRP). In *Proceedings of the NSF Workshop on Design Methodologies for Solid Freeform Fabrication*, 1995.

[7] Martti Mäntylä. *An Introduction to Solid Modeling.* Computer Science Press, Rockville, Maryland, 1988.

[8] C. Mead and L. Conway. *Introduction to VLSI Systems.* Addision-Wesley, 1980.

[9] National Science Foundation. *NSF Workshop on Design Methodologies for Solid Freeform Fabrication*, June 1995.

[10] C. H. Séquin and K. P. Smith. Introduction to the Berkeley UNIGRAFIX tools version 3.0. Technical Report UCB/CSD 90/606, Computer Science Division, University of California, Berkeley, 1990.

[11] Carlo H. Séquin and Sara McMains. What can we learn from the VLSI CAD revolution? In *Proceedings of the NSF Workshop on Design Methodologies for Solid Freeform Fabrication*, 1995.

[12] Jami J. Shah and Martti Mäntylä. *Parametric and Feature-Based CAD/CAM: Concepts, Techniques, and Applications.* John Wiley & Sons, Inc., New York, New York, 1995.

[13] Robert F. Sproull. Digital interfaces to fabrication. In *Proceedings of the NSF Workshop on New Paradigms for Manufacturing*, 1994.

[14] S.P. Timoshenko and J.N. Goodier. *Theory of Elasticity, International Student Edition.* McGraw-Hill, New York, third edition, 1982.

[15] G. Trapp. The emerging STEP standard for product-model data exchange. *Computer*, 26(2):85–87, February 1993.

[16] Herbert Voelcker. New paradigms for mechanical design and manufacturing. In *Proceedings of the NSF Workshop on New Paradigms for Manufacturing*, 1994.

[17] Daniel E. Whitney. Some differences between VLSI and mechanical design. In *Proceedings of the NSF Workshop on New Paradigms for Manufacturing*, 1994.

Trussed Structures: FreeForm Fabrication without the Layers

Joseph Pegna, David Messia, Woo Ho Lee

Department of Mechanical Engineering, Aeronautical Engineering and Mechanics
Rensselaer Polytechnic Institute
Troy, New York 12180-3590
U.S.A.
(518) 276-6030
Fax: (518) 276-2623
email: pegnaj@rpi.edu

Abstract: *Recent progress in 3D-LCVD have demonstrated the advantages of rod micro-fabrication, both from the point of view of the range of volumetric deposition rates —from 10^2 to 10^9 cubic micron per second— and from the point of view of processable materials.*

A method for fabricating trussed structures by LCVD of ethylene was tested, based upon scanning of the laser focus perpendicular to the laser axis during rod growth. Control of the process is achieved though feedback of the laser power. A closed loop system was designed, which maintains a constant volumetric deposition rate during growth.

Such capability, combined with previous results by the authors and other researchers in the field, open a new approach to free form fabrication without layers. Indeed, current results constitute a proof of concept for the fabrication of truss structures akin to a finite element mesh.

Keywords: *3-D LCVD, SALD, Process Control, Rod growth, tessellation.*

1 INTRODUCTION

A novel approach to freeform fabrication is explored in this paper. Rather than scanning the layers of a part, whereby the entire volume must be swept, we propose that a tessellated structure, akin to a finite element mesh can be fabricated by 3-D LCVD.

The premises for this novel approach lie in prior works by Maxwell, Pegna et al. [1-4], and the works of Stuke et al. [5,6]. Preliminary investigations of layered manufacturing using 3-D LCVD revealed that the order of volumetric deposition rates ranges from 10^2 $\mu m^3/s$ for direct write, up to about 10^9 $\mu m^3/s$ for rod growth. For wall deposition of carbon from ethylene edgewise on a 2-D substrate for example, Pegna et al. [7] recorded a volumetric deposition rate of the order of 0.5 $10^6 \mu m^3/s$. By this measure, it would take nearly two months to build a 3 cm^3 layered structure —about the size of a small watch! This is clearly not rapid prototyping.

Yet, LCVD remains attractive to many researchers for its wide range of processable materials, including functionally graded materials, as was demonstrated by Maxwell et al. [4] for Ni-Fe alloys. In order to magnify the volumetric deposition rates, researchers have used LCVD to fill interstitial voids in between powder particulates. This is essentially the basis for SALD-VI [8]. Alternatively, Stuke et al. [5] have demonstrated the fabrication of triangulated free-form surfaces by direct write onto a preform that was then dissolved. That work essentially demonstrated the

© 1997 Joseph Pegna, Dave V. Messia and Woo-Ho Lee, printed with permission.

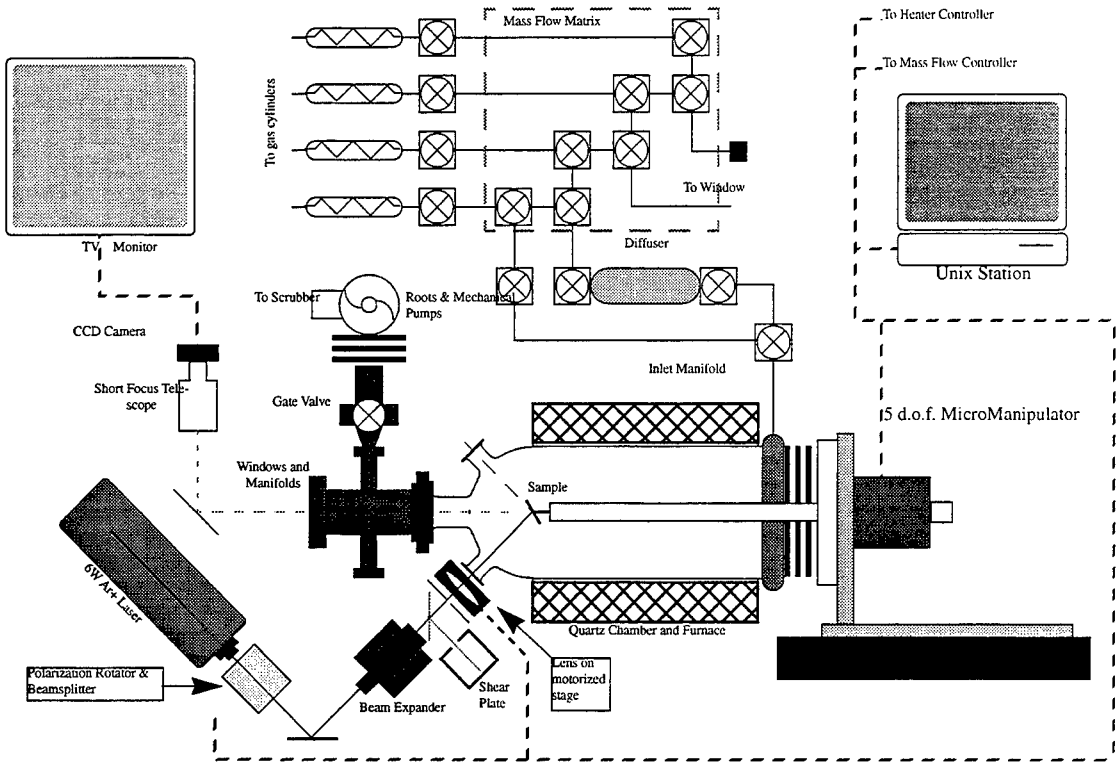


FIGURE 1. Schematic diagram of the 3-D LCVD reactor.

possibility of producing 3-D shapes about a millimeter in size using a process inherently slow (less than $10^4 \mu m^3/s$.) Most recently, Stuke et al. also demonstrated the feasibility of fabricating highly complex periodic rod microstructures by scanning a twin laser focus though a deposit transparent to the wavelength [6]. This experiment demonstrated for the first time the feasibility of using 3D-LCVD toward the fabrication of micromechanical photonic band gap devices not achievable by any other means. What makes this approach feasible for manufacturing purposes is that it capitalizes on the many folds increase in the order of magnitude of volumetric deposition rate in rod growth mode as opposed to direct write. Indeed assuming a conservative volumetric rate of 3. $10^5 \mu m^3/s$ —typical of high pressure LCVD of graphite [9]— and 0.6% volumetric fill —typical of a pyramidal tessellation 1 mm on the side with a ø20μm fiber— then the fabrication time of our sample $3 cm^3$ volume falls to 16 hours, or the equivalent of growing a 60 m fiber!

The above example shows that to be viable as a free form fabrication tool at the centimeter scale, 3-D LCVD must be exploited in rod growth mode to generate densely packed meshes. In order to achieve this result, the major obstacles to overcome are:

1. The ability to grow rods that are slanted with respect to the substrate and each other. This issue is addressed in Section 3.1, where two approaches will be pursued: One using a stationary laser tilted with respect to the substrate, and another by scanning the laser focus during rod growth. The latter revealed most promising and a series of experiments were carried out to determine the relationship between the angle and the scan rate for a number of different pressures.
2. The ability to join independently grown rods. This issue is covered in Section 3.2.
3. The ability to build trusses atop each other. This represents the current status of our work and

is covered in Section 3.3.
In addition, a preliminary result on braiding carbon fibers grown by 3-D LCVD is presented Section 3.4.

2 EXPERIMENTAL

2.1 Equipment

A schematic diagram of the Rensselaer 3D-LCVD system is shown in Figure 1 The 3D-LCVD reactor consists of a custom quartz tube with ports for viewing and laser input. The chamber is connected to a pumping station via a gate valve. The vacuum chamber and gas-delivery systems are enclosed within a ventilated hood for safety purposes. For the growth of pyrolytic graphite, 133 - 665 mbar (100-500 Torr) ranges of ethylene pressures were employed.

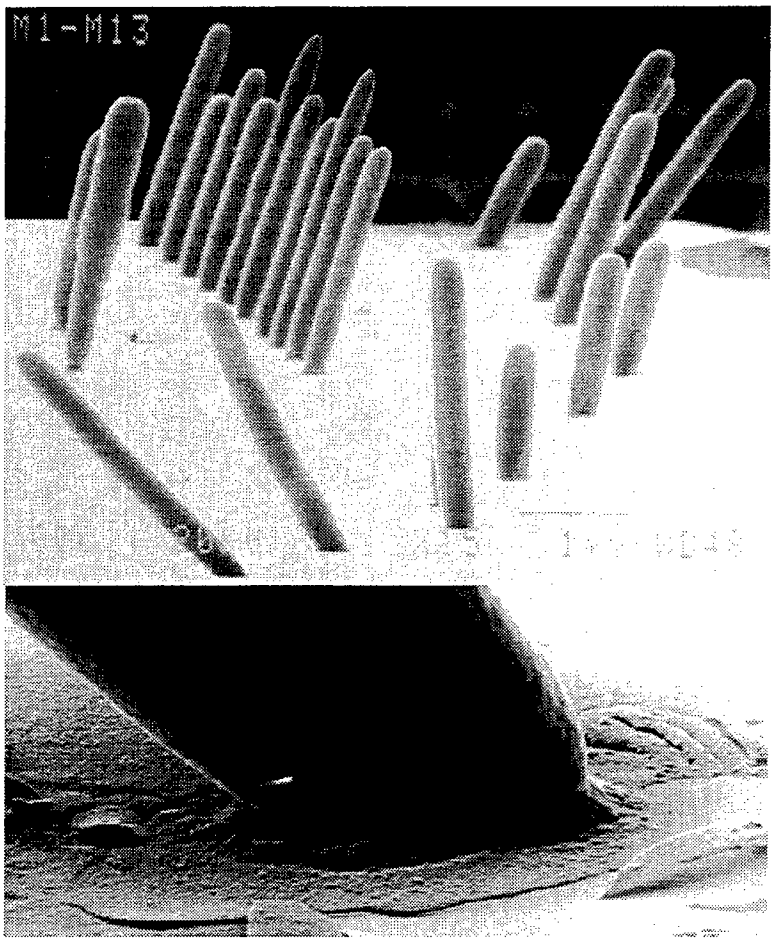


FIGURE 2. Top: Sample population of angled rod grown with a stationary laser at an angle to the substrate. Bottom: Sample rod base.

The beam source was a Coherent. model CR-18 argon ion laser with a maximum output of 12Watts (multi-mode) at the 488/514 nm primary lines. To vary the laser beam power, a liquid-crystal retarder and polarizing beam splitter were placed in series, allowing peak-to-peak power swings in under 200 ms. Incident powers reported herein represent total beam power at the deposit. Observation of the sample during growth and laser alignment is made with a custom-built short-focus telescope and CCD camera.

A photodetector, covered with narrow band filters, was mounted to one of the chamber windows, at a distance of roughly 200 mm from the sample. Using a two-decade pre-amplifier, the sensor could measure emissions as small as 0.25 mW at the substrate (at 656nm). The amplified signal was recorded by an Omega Nubus data acquisition system, with a typical sample period of 0.05-0.10 seconds, and was later time averaged as needed for real-time control.

At the core of the system is a precision five-degrees-of-freedom manipulator. This micromanipulator was designed to allow beam scanning not only in the plane of the substrate, but at any angle and orientation to the sample. This is effected through a computer-driven 5-axis micromanipulator. This tool allows sub-micron positioning with stepping motor control from outside the

vacuum chamber. The translational and angular resolutions of this micro-manipulator are 1 μm and 0.005° at the full step control mode.

The manipulator arm holds the sample within the chamber. The manipulator attaches to the vacuum chamber via a flexible bellows to limit vibrations transmitted to the sample. Both the manipulator and the laser lie on a vibration-isolated table, their relative position is fixed.

2.2 Trussed structure Fabrication Process Control

To fabricate the desired trussed structure, the laser power and motion of the manipulator need to be controlled during the process. A Macintosh computer with Omega Nubus data acquisition system and a custom C language program handle the entire process. The process sequence is as follows. The desired discretized trajectory of a path is generated by input data. Using this trajectory and calculated motion speed, the pulse trains of each stepping motor are generated. This pulse train signal is sent to the each stepping motor during the process. The laser power is controlled using the feedback signal, which is emitted during the deposition process as the substrate moves independently. Proportional-Integral-Derivative (PID) gains were fine-tuned to follow the desired reaction rate signal using the system response.

3 RESULTS AND DISCUSSION

3.1 Angular Rod Growth

3.1.1 Stationary Laser at an Angle to the Substrate: The most immediate approach to growing a rod at an angle to the substrate is to incline the orientation of a stationary laser. Figure 2 shows such sample rods at varied inclinations constructed by this method. In this configuration, growth is more difficult to initiate since reflection of the laser at the surface is increased. Nevertheless, angles up to 45° to the substrate were achieved with this technique. Once rod growth is initiated though, it becomes similar in all regards to regular stationary growth, exhibiting similar growth rates and rod morphology. These results demonstrate the practicality of this method for building needles at an angle. As we shall see in Section 3.2, however, this method will prove unpractical for truss building.

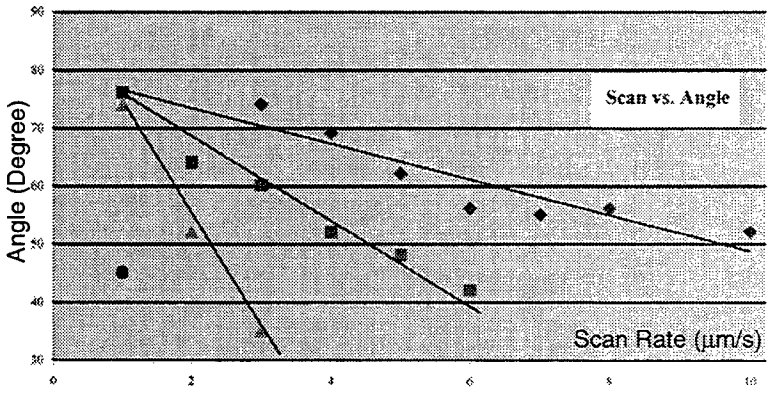


FIGURE 3. Rod angle with substrate as a function of scan rate for various precursor pressure. Laser power adjusted to maintain constant volumetric deposition rate. Deposit: carbon from ethylene. Substrate: quartz. Legend:

Index:	◆	■	▲
Pressure (Torr):	400	300	200
Em. Sign. (V)	0.1	0.1	0.1
Vol. Rate ($10^6 \mu m^3/s$)	2	1.5	0.8

3.1.2 Angular rod growth by laser scanning subject to constant volumetric deposition rate. A series of angular rod growth experiments were conducted to determine the dependence of the angle on pressure and scan rate. Figure 3 shows the results for constant volumetric deposition rate. The pressure ranged from 200 to 400 Torrs. For constant pressure the slope decreases with the

scan rate in a nearly linear fashion. This is to be expected. Let α be the angle between rod and substrate, V_s be the scanning speed, and R_o be the axial growth rate. As the axial growth rate is related to the scan rate by:

$$\cos\alpha = \frac{V_s}{R_o}, \qquad \text{(EQ 1)}$$

near α=90°, this relation appears approximately linear.

The graph shows that, for constant scan rate, the slope with respect to the substrate increases with pressure, which is consistent with prior results showing the increase of axial rate with pressure [3]. Finally, Figure 3 also shows the limit of vertical development for a given volumetric deposition rate. For example; it was found that, at the lower pressures, i.e.; 100 torr, only a very slow scan rate (1 µm/sec) resulted in a rod of any inclination, any faster rate resulted in direct write of a line on the substrate. The steepest angle achieved was 40° under the conditions of 200 Torr at 3 µm /sec.

Sample slanted rod structures grown by laser scanning under constant volumetric deposition rate are shown in Figure 4, along with their emission signature (representative of volumetric rate), controller input, and laser power. To achieve this growth, the laser power was modulated using the liquid crystal retarder in order to keep the emission signal at a set value of 0.07 Volts. Note the consistency of the growth over the two samples. Also mark the reduced power need once rod growth is initiated.

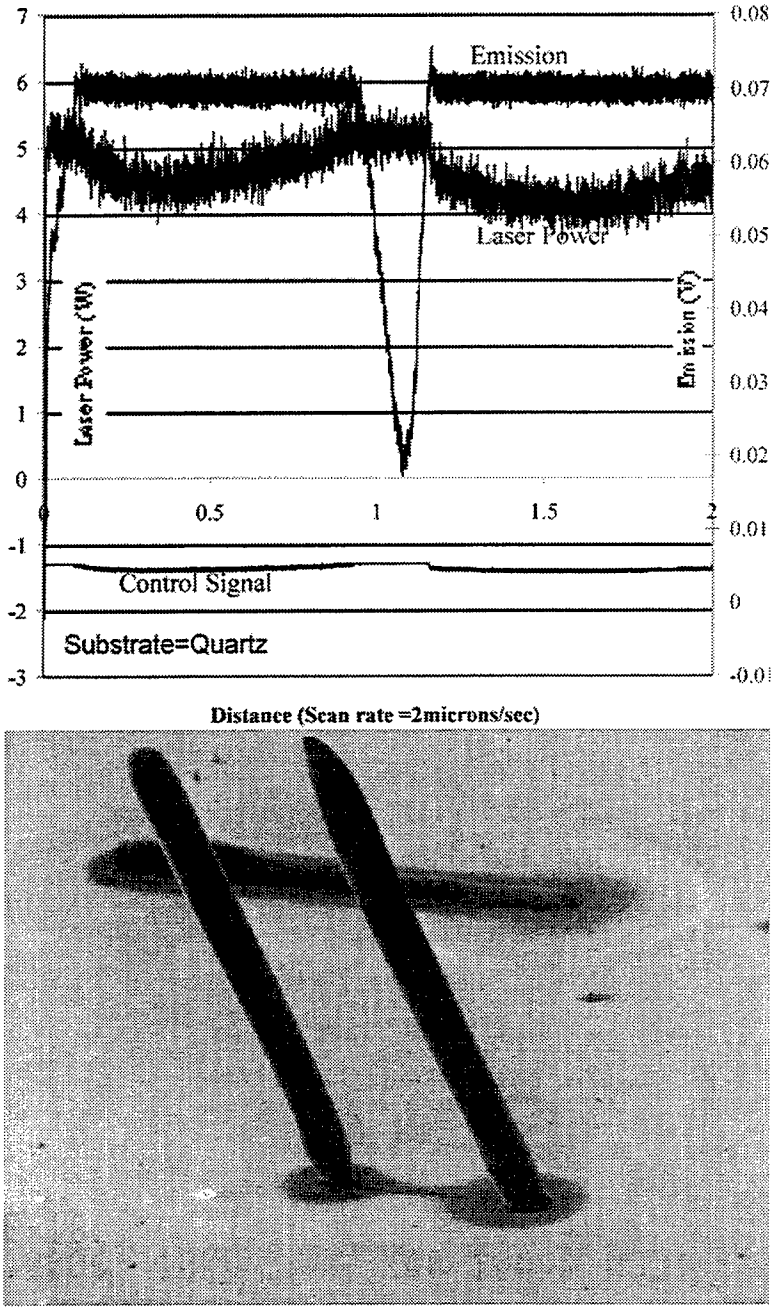


FIGURE 4. Sample constant volumetric rate rod growth for a constant scan rate of 2µm/s, Pressure: 250 Torr. Top: Emission signal and laser power. Bottom: Sample rod structures.

Slanted rods grown by scanning the laser focus over the substrate display a characteristic axial ridge on their posterior side (opposite the laser.) A close-up view of rods grown under such conditions is shown in Figure 5.

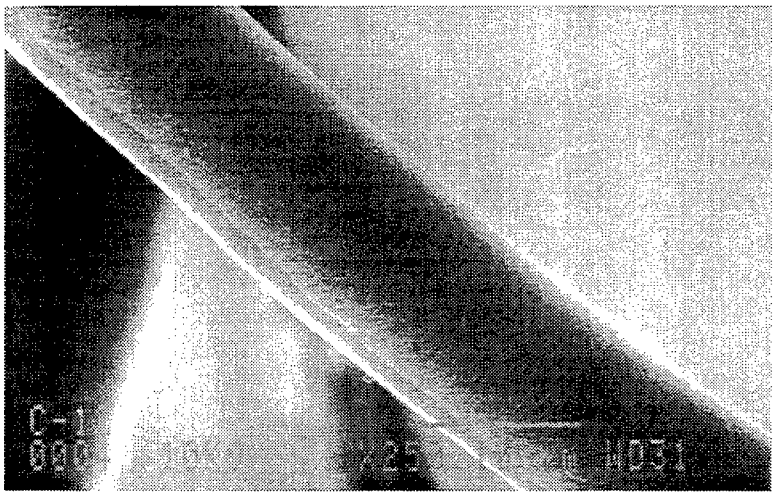


FIGURE 5. Close-up view of an angled rod showing the characteristic ridge on the posterior side.

Bending fracture of a typical angularly grown rod reveals an interesting morphology. The rod appears to be composed a two regions: An amorphous core and cylindrical graphitic skin. This is consistent with the results of Wallenberger and Nordine [9]. who showed that carbon fibers can be fabricated under high pressure LCVD of Methane.

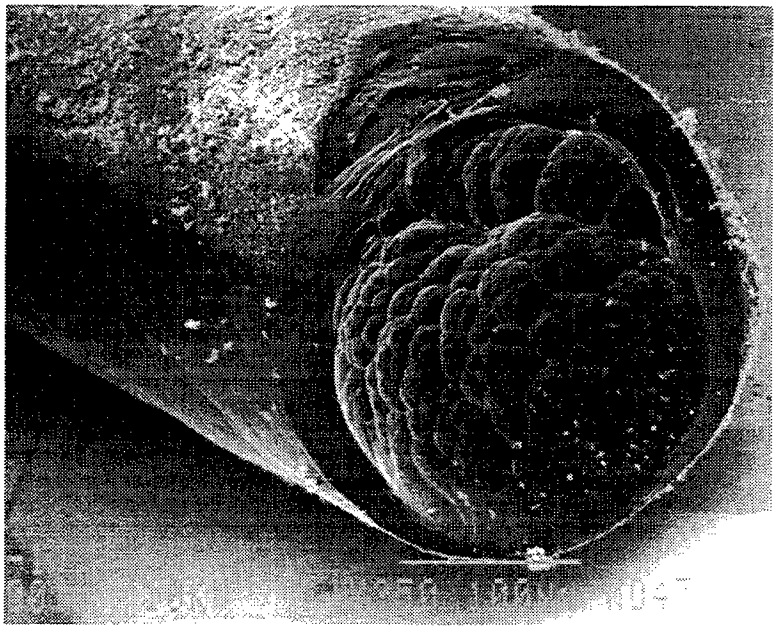


FIGURE 6. Close-up view of a fractured angled rod showing the uniform graphitic "skin", amorphous core, and axial ridge on the posterior side of the rod.

3.2 Weld Formation

The single critical step toward fabrication of micro-trusses for the purpose of rapid prototyping will be the ability to join fibers together at nodal points. This demonstration is critical to the proof of concept for the technique proposed herein. Experiments were thus designed with the aim of examining the feasibility of joining two needles together by each of the angular growth methods.

3.2.1 Stationary Laser: Experiments involving the growth of rods at an angle to the substrate and in such a manner that they would fuse at the tip proved inconclusive. In fact, they voided the concept. Let alone complications due to the accuracy requirements in positioning the laser with respect to the just completed rod, the method turned out to yield two main results:

1. The rod tip occluded the laser and the second rod grew out of the first, and
2. The rod tip was clear of the laser path and the two rod grew past each other.

These results are illustrated by Figure 7.

3.2.2 Scanning Laser: In addition to better trajectory control, rods obtained by the scanning laser approach avoid the occlusion problem discussed earlier in Section 3.2.1. Hence the next development attempted was to grow needles into each other directly so that they would meet at the

tip. While success rate is still low in this case, about 30 percent of the samples did interlock. Figure 8 shows a such successful attempts at meeting the needles at the tip. In addition, it was found that all the welded rods display a stronger attachment to the substrate and are able to sustain stronger loads than single rods, indicating a complete juncture.

3.3 Truss Building

The realization that a butt weld is possible with angled rod structure now open another avenue to free-from fabrication. Rather than scanning layers, the question becomes: Can we build a mesh akin to finite elements, whereby one could build a carbon fiber preform out of rods?

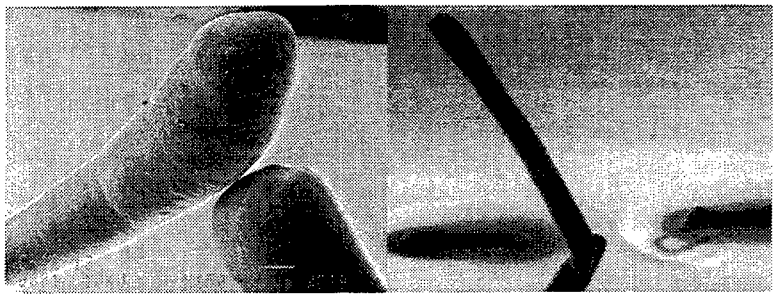


FIGURE 7. Typical joining problems with stationary laser growth. Left: First rod does not occult the laser and the rods grow past each other. Right: The first rod occults the laser and the second rod grows on top of the first one.

This section presents our preliminary answers to this question. Attempts at building micro-trusses were conducted, with mitigated results. Accurate location of the rod tip during fabrication remains a metrology challenge in this project, leading to a rather large amount of defects in the joining. Figure 9 shows sample micro-trusses structures obtained by the scanning laser method. It should be emphasized that there was no preform used in this construction and that the structure does not need to be optically transparent to the laser wavelength. These features differentiate this approach from the remarkable results obtained by Stuke et al. [6]. In addition, we demonstrated the possibility of constructing a multi-level truss with three-dimensional features.

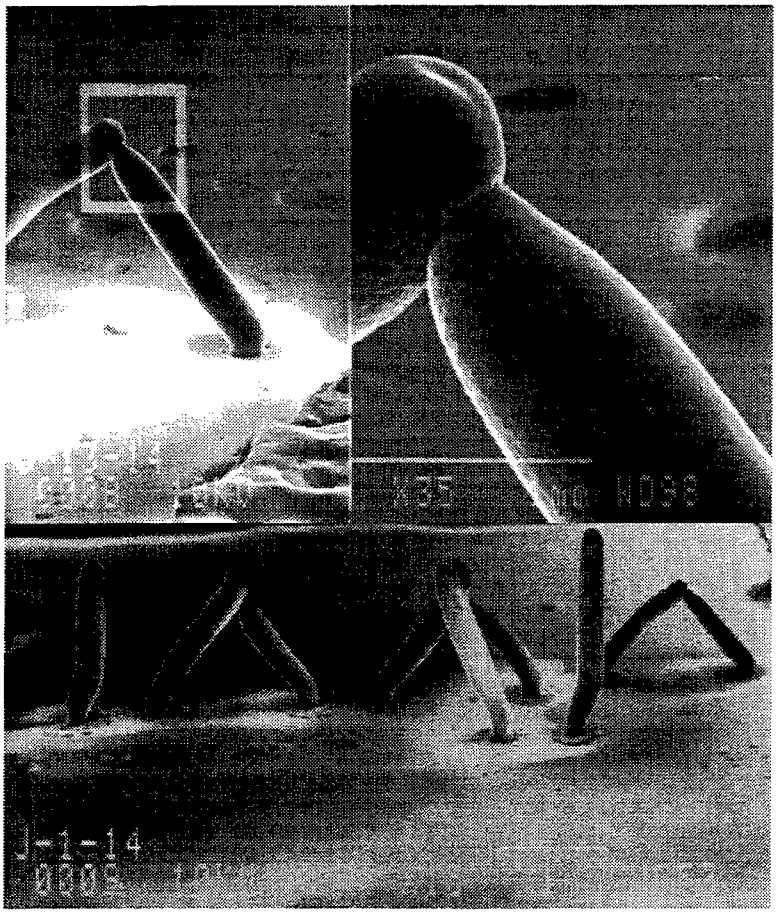


FIGURE 8. Sample rod welds.

3.4 Fiber Braiding

An aspect of fiber structure which is highly desirable in reinforcements is the ability to braid them. This option is compatible with both types of laser fabrication of angled rod, with the exception that the rod angle and direction is now required to change continuously. Pre-

liminary results for this line of work is shown in Figure 10 where a 3-fiber braid was initiated atop a l-level truss.

4 CONCLUSION

The main objective of the research exposed in this paper was to investigate the feasibility of fabricating trussed structures by means of 3-D LCVD. This approach is justified on the premise that rod growth is the only mode of LCVD with sufficient volumetric flow rate for free-form fabrication of centimeter size structures. The main issues addressed in this exploratory work were:

1. The ability to grow rods in arbitrary directions. This was achieved by scanning the laser focus parallel to the substrate during rod growth. Results pertaining to rod growth, scanning speed, angle and growth morphology were covered in Section 3.1.
2. The ability to butt-weld independently grown rods was demonstrated in Section 3.2. Though accurate location of the fiber tip remains a metrology challenge for this operation.
3. The ability to build meshes in a continuous fashion was explored in Section 3.3 with mitigated results. It appears though that this issue should be addressed with a better location system for the rod tip during growth.
4. Finally, the issue of braiding carbon fibers during growth was briefly investigated in Section 3.4.

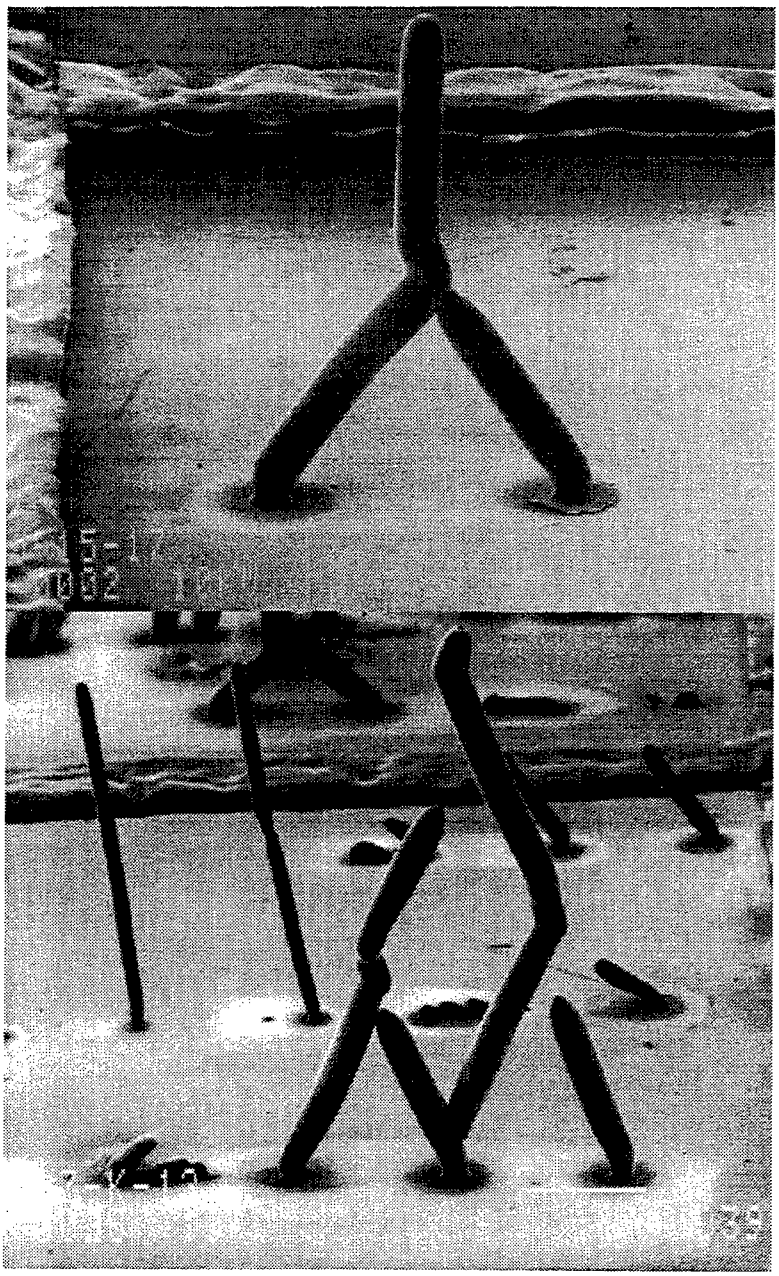


FIGURE 9. Sample micro-truss structures.

All the results exposed in this paper point to the fabrication of trussed structures using LCVD rod-growth as a viable approach to free-form fabrication of centimeter to possibly decimeter size objects.

The major interest of such an approach is in the material and size versatility of the process. About 80% of elements in the periodic table, as well as various intermetallic, oxides, and even functionally graded alloys can be deposited by LCVD. The wide range of volumetric deposition rates covers nearly 10 orders of magnitudes, thus allowing single stage fabrication of structures varying in size from micron to centimeter and possibly decimeter. Among its different operating modes (direct-write, rod growth, and SALD-VI) LCVD offers the prospect of a fully integrated, multi material, mesoscale fabrication.

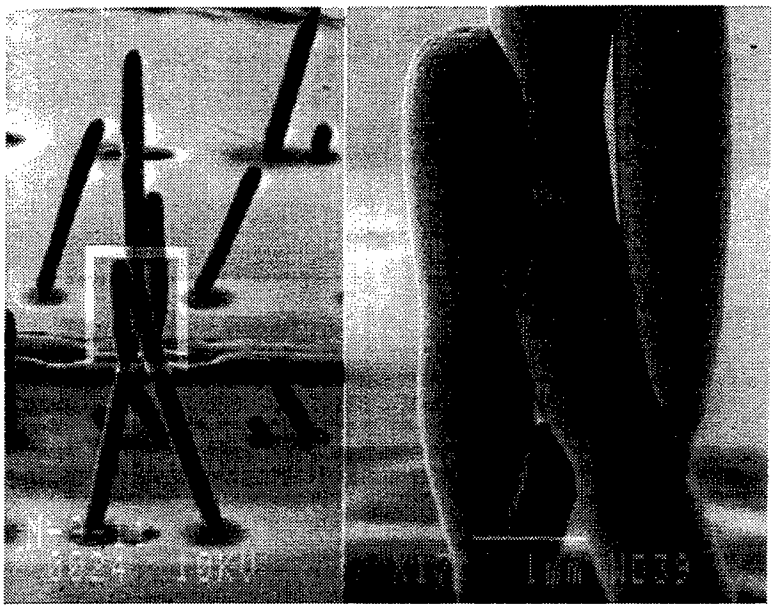


FIGURE 10. Sample 3-fiber braid atop a 1-level truss.

Support for this work was provided in part by the National Science Foundation under grants ECS-9314071 and DDM-9057059, and the Society of Manufacturing Engineers Education Foundation. Laboratory support was provided by Rensselaer's Center for Integrated Electronics and Electronics Manufacturing. All contributors to this project are gratefully acknowledged.

5 REFERENCES

[1] Maxwell, J. L., Ph.D. Thesis, Rensselaer Polytechnic Institute, (1996).

[2] Maxwell, J.L., Pegna, J., Messia, D.V., DeAngelis, D.A., *"Direct Feedback Control of Gas-Phase Laser-Induced Deposition,"* Proceedings of the 1996 Solid Freeform Fabrication Symposium, Austin, Tx, pp. 227-237 (1996)

[3] Maxwell, J.L., Pegna, J., and Messia, D.V., *"Real-time volumetric growth rate measurements and feedback control of three-dimensional laser chemical vapor deposition,"* To appear in Applied Physics A (1997)

[4] Maxwell, J.L., Pegna, J., DeAngelis, D., Messia, D.; "Three-Dimensional Laser Chemical Vapor Deposition of Nickel-Iron Alloys," Materials Research Society, Vol. 397, Advanced Laser Processing of Materials, pp. 601-606 (1996)

[5] Lehmann, O. and Stuke, M., *"Laser-Driven Movement of Three-Dimensional Microstructures Generated by Laser Rapid Prototyping,"* Science 270 (5242):1644 (8 Dec 1995)

[6] Wanke, M.C., Lehmann, O., Müller, K., Wen, Q., and Stuke, M., *"Laser Rapid Prototyping of Photonic Band-Gap Microstructures,"* Science 275 1284-1286 (28 Feb 1997)

[7] Pegna, J., Messia, D.V., and Lee, W.H., *"Layered Micro-Wall Structures from the Gas Phase,"* Proceedings of the Solid Freeform Fabrication Symposium, University of Texas at Austin, August 9-14, 1997.

[8] Harrison, S., Crocker, J.E., Manzur, T., Marcus, H.L., "Solid Freeform Fabrication at The University of Connecticut", Proceedings of the Solid Freeform Fabrication Symposium,

Ed. by D.L. Bourell, J.J. Beaman, H.L. Marcus, R.H. Crawford, and J. W. Barlow, The University of Texas at Austin, Texas, Aug. 12-14, 1996, pp. 345-348.

[9] Wallenberger, F.T., Nordine, P.C., and Boman, M.; *"Inorganic Fibers and Microstructures Directly from the Vapor Phase,"* Composite Science and Technology, v.51 pp 193-212 (1994)

Low-cost Machine Vision Monitoring of the SLS Process

Ian Gibson and Ling Wai Ming

Dept. Mechanical Engineering
The University of Hong Kong

Abstract

During the building of a part using SLS, it is common practice to adjust the temperature parameters. It is important to control these parameters because if they are too high then part breakout is difficult. If they are too low then parts have poor material properties. One method of controlling these parameters is by observation through the process chamber window. Any adjustment can be determined by examining the colour of the cross-section in process. By using a machine vision system to determine colour variation, it is possible to calculate temperature or laser power adjustments necessary to maintain consistent part quality.

Keywords: Selective Laser Sintering, Process control, Machine vision.

Introduction

One of the major advantages of Selective Laser Sintering (SLS) process is the wide range of materials capable of being processed. The majority of parts built using SLS use the nylon-based powders since these result in relatively, strong, durable components that can be made to have the appearance of many high volume, manufactured products. Nylon, being predominantly crystalline, has a very definite melting point which means that precise control of temperatures within the SLS machine is very important. Temperature is monitored in two particular areas in the machine. Powder temperature is monitored using thermocouples at the top of the powder feed chambers and the temperature of the part-bed is monitored using an infra-red (IR) sensor. These sensors are used to control the heaters in the machine to maintain constant settings.

There are two major problems in the use of the IR sensor to measure part-bed temperature. Firstly, the part-bed does not have a uniform temperaure across the entire surface. The closer to the perimeter of the part-bed, the cooler the powder at the surface. There is also likely to be a variation between the front and the back of the part-bed due to temperature losses through the process chamber door. The single IR sensor used in the SLS machine is focused on the centre of the part-bed and can only give an average readout for the bed temperature. Because of the temperature profile of the part-bed, Fine Nylon (LNF5000) can only be effectively processed within an 8" diameter cylinder at the centre of the bed.

The second problem relates to the geometry of the part being processed in the SLS machine. The solid part in the machine is hotter than the surrounding powder. If the part being built is relatively massive (which could be defined for one layer in terms of the ratio of the melted area to the

perimeter of the enclosing box) then there is a significant amount of stored energy in the part and it is sometimes necessary to reduce the feed temperatures to compensate. If this mass is in the centre of the platform then the IR sensor should be able to compensate automatically. However, parts that have some or all of the mass away from the centre may be difficult to control.

By placing a camera in such a way as to monitor the part-bed, it should be possible to obtain a localized measure of energy build up for a specific layer of a part. If this can be done accurately and effectively then it may be possible to automatically control the SLS process parameters according to the geometry of the part. The potential benefit of this is homogeneous mechanical properties or consistent part quality. This paper describes ongoing work at The University of Hong Kong using these techniques.

Use of Machine Vision with SLS

When first starting to use an SLS machine (and this is emphasized greatly during training at DTM) it is important to watch the process carefully. It is important to understand how part quality will vary according to different parameter settings. Eventually, experience takes over and after a short while it is possible to set the part build profile according to knowledge of the subtleties of the process and leave the machine to build the part automatically. However, it should be noted that even the most experienced operators may find difficulties with new geometries, requiring more than one attempt to produce an acceptable part. Since all rapid prototyping machines are designed to run unattended, it is often not until the build has finished that a fault is detected.

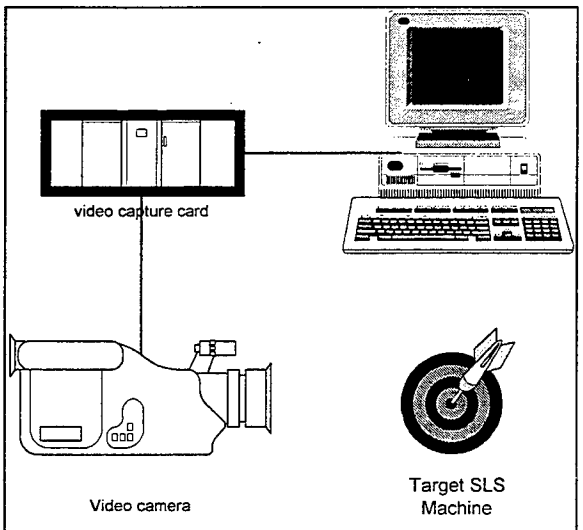


Figure 1
Hardware configuration

A machine vision system can make use of a camera placed in front of the process chamber window to see the same as the operator sees. According to the DTM materials manual [1], it is possible to observe a number of potential problems. Among these potential problems are in-build distortion (curling), short feed, ploughing, cracking and streaking. These will not always result in a bad part (except perhaps curling) and if detected in time can be adjusted to limit the effect. The most common problems are curling and short feed (critical mainly for large parts). It is suggested that machine vision can at least halt the process until manual intervention can make the decision to abort or continue (after action taken) and at best be linked into the process computer to adjust the parameters directly.

Initially, this project was approached as a final year undergraduate project and therefore it was important to minimize the cost of any additional equipment. A low cost machine vision system also has the attraction of being more practical for implementation into the existing SLS machine. The hardware configuration can be seen in figure 1. At the time, a video camera sampled through an image capture card offered the cheapest and most convenient solution.

Energy Principle

The general principle of SLS processing of nylon powders is to use the part-bed and powder heaters to raise the powder temperature close to melting point. Energy is then added to the powder from the laser in order to fully melt the powder. According to Nelson [2] the additional energy is constant for a set laser power, scan speed and scan spacing i.e.:-

$$\text{Energy density}(\text{cal/cm}^2) = \frac{P * f}{BS * SCSP}$$

Where P is laser power, BS is scan speed, SCSP is scan spacing, and f is a constant conversion factor. In order for the system to remain completely stable, this additional energy must be lost from the part before the next layer is melted. If not, then there will be a temperature build up that will eventually lead to growth, caking and other undesirable features. For massive parts, it may be prudent to allow a long delay between layers to allow the part-bed heater to control the part-bed temperature. This would result in much longer build times and so it may be more desirable to control the amount of energy put into the part, based on what has been observed to already exist in the part.

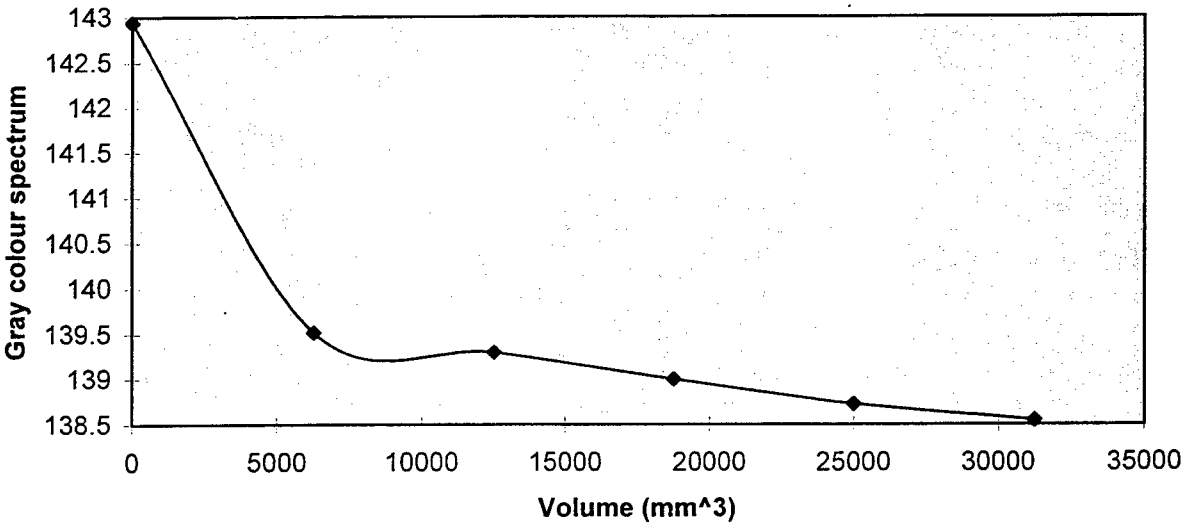


Figure 2 -grey colour against volume of a wedge-shape

Since the powder feed heaters are only very slightly affected by what goes on at the build platform, this implies that the only variable adjusted according to energy stored in the part is the part-bed heater. It has already been stated that the IR sensor focuses on the centre of the part-bed. If the part is not centred on the part-bed or the geometry of the part varies in some way then it is very difficult for this single measurement sensor to provide sufficient data for control of the energy within the part. This can be seen in figure 2. Under normal conditions, as a wedge shape is built (increasing volume), energy stored within the part changes the colour of the part.

Optical principle

The change in colour noted in figure 2 must correspond to a physical change in the powder. This physical change modified the optical properties of the powder in such a way as to look lighter or darker, dependent on the amount of energy supplied by the laser.

The camera used had automatic gain control (AGC) and focusing control disabled. The camera therefore did not attempt to compensate for any variation in the image. Similarly, the dominant lighting source was a stable, halogen lamp placed in close proximity to the camera, directed at the part-bed and not shining into the lens. The internal light source for the SLS machine was also disabled. However, although ambient variations must exist, it is the opinion of the authors that ambient conditions did not significantly affect results.

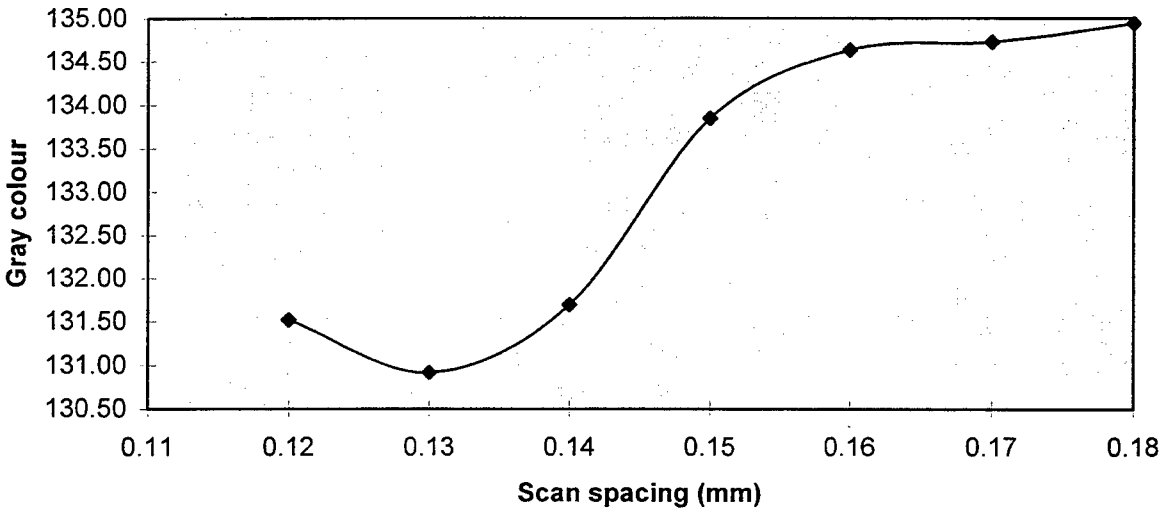


Figure 3 -grey colour against scan spacing

Figure 3 shows average grey colour measurements for a number of samples built using different scan spacings, varied around the optimum value. As the energy decreases, so the grey colour inside the boundary of the part shows a general increase making it appear lighter in colour. This can be explained in terms of the optical model used. As the energy increases, so the surface of the

part becomes smoother and more reflective. The inside of the chamber is relatively dark compared with the powder and so less light is reflected back to the camera. The most marked change is between scan spacing of 0.14mm and 0.15mm corresponding to the most significant change in the melt conditions. 0.15mm is the default setting for critical melting. A similar relationship was observed for variations of laser power around the optimum value.

Control Principle

It has been established that there is a relationship between observed grey scale value from the camera (G) and the part volume (V) and laser power (L).

$$G = f(V,L)$$

$$dG = \frac{dG}{dV} \cdot dV + \frac{dG}{dL} \cdot dL$$

Since volume distribution is determined by the geometry of the part, the above equation should be rearranged to determine the required laser power setting based on an observed change of grey scale and the change in volume between observations. A test experiment for a simple part geometry establishes a control equation based on grey scale and incremental heights (h) in the form:-

$$dL = \frac{dG + 1.562dh - 0.156hdh}{-1.817}$$

the figures derived in this equation assume linear relationships for grey scale vs. volume and grey scale vs. laser power. For a wedge-shaped part geometry, modifications to laser power were calculated and adjusted according to a grey scale set point which was monitored throughout the height of the wedge (figure 4). Laser power was considered easier to calculate than scan spacing, although the latter would probably allow finer resolution and stabilize more quickly. As can be seen, the grey scale and laser power variation tends to a constant value, probably related to the reduction in surface area of the wedge indicating again that massive components are more sensitive to this problem. Although difficult to see from the images below, the wedge shape under vision control showed a marked improvement in consistency compared with the other part.

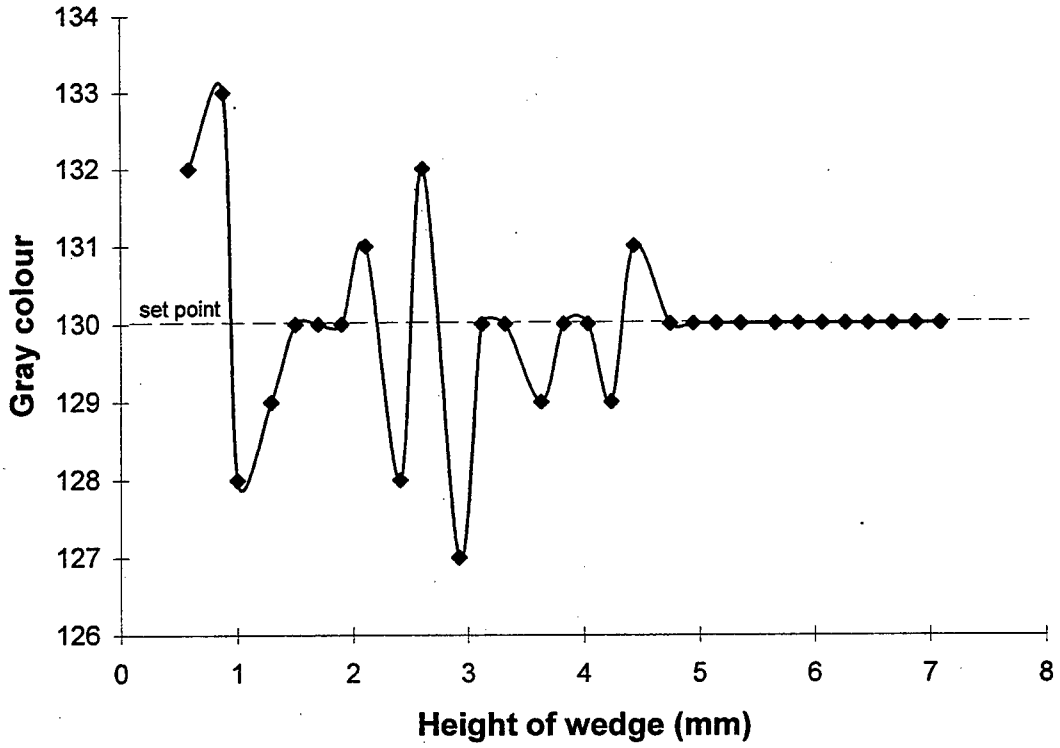


Figure 4 -grey colour against height of wedge

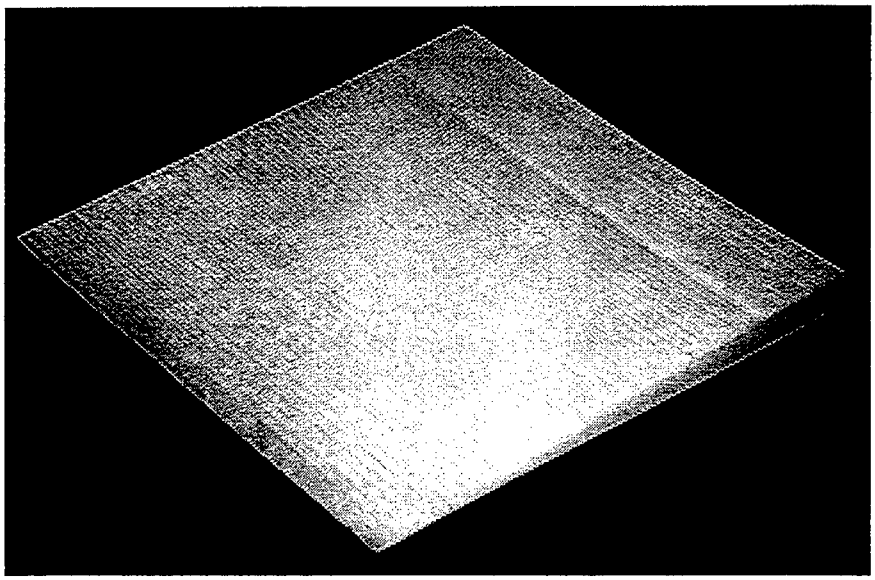


Photo 1 Wedge with vision control

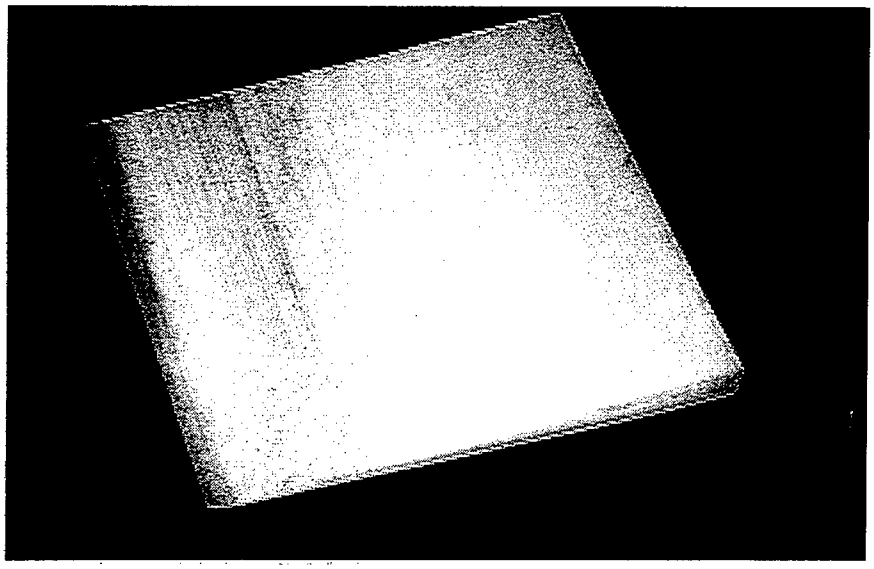


Photo 2 Wedge without vision control

Discussion and Further Work

These are only preliminary findings and require much additional work to verify and quantify. Work currently has been able to identify the following:-

- That there is a relationship between grey scale and part volume in terms of the energy build up within a massive part.
- That there is a relationship between grey scale and applied energy.
- That these relationships can be incorporated into a control function and applied to a simple geometry part.

There are also a number of problems that need to be overcome

- Vision processing on each layer: The data at the perimeter of each layer differs from inside the boundary and must be segmented out before calculation.
- A generalized control function needs to be extracted from the data, based on the height or volume of the part.
- Incorporation of process intelligence to compensate for variable feature geometry: Thin wall and thick wall structures may require different control strategies.
- Integration with the X-windows based SLS operating system to close the loop: Currently, the calculation is done off-line and entered manually.

These problems also need to be correlated with existing thermal models that describe the powder processing within the chamber of the SLS machine. Also, this process has been found to give a result that represents consistent quality within a part. Further work must identify methods to ensure optimum parameter settings. It may be possible to adjust these settings to give optimum performance according to different criteria (e.g. tensile strength, surface finish, density, etc.).

Future work is likely to involve a higher resolution camera. Whilst resisting the temptation to use thermal or other expensive camera systems, digital cameras with much higher resolutions are commonly available, allowing greater precision in calculation. Much more attention will also be devoted to improving the lighting arrangement to achieve consistent and stable lighting.

The indication is that this process can be applied as a form of adaptive control. Normally, a significant dwell time is used between each layer to allow the build temperature to stabilize. Using this method to control energy delivery through the laser power, it may be possible to significantly reduce this dwell time (perhaps down to zero). With the part-bed heater, the energy delivery can be a significant distance from the build surface.

Conclusions

For certain geometries of parts, the current SLS control model does not work satisfactorily. A method of using a camera with a digitally sampled image has been proposed. This image can be used to extract process information by observation through the process chamber window. This information relates to the amount of energy observed at each layer during the build process. From this the amount of energy required in order to build the next layer can be calculated in terms of an adjustment of the laser power. Initial studies using a simple experimental set-up indicate that this process can be used to control the quality of build throughout a simple geometry part.

References

1. The Sinterstation 2000 System Selective Laser Sintering Guide to Materials Optimizing and Understanding the Process - DTM Corporation
2. Selective Laser Sintering : A Definition Of the Process and an Empirical Sintering Model - Nelson, James Christian, UT-Austin, Ph.D. dissertation, UMI Dissertation Services, 1993

SLS Processing of Functionally Gradient Materials

L. Jepson, J. J. Beaman, D. L. Bourell, K. L. Wood
Laboratory for Freeform Fabrication
University of Texas at Austin

Abstract

A developing SLS process, known as Multiple Material Selective Laser Sintering, will allow the material composition of a component to be varied in a controlled manner. This process could allow the fabrication of functionally gradient materials (FGMs) in which a blended interface exists. Two potential applications of FGMs are the reduction of thermal stresses in metal/ceramic joints and the matching of material properties to functional requirements. A tungsten carbide/cobalt system has been examined in which the ceramic/metal ratio has been varied in an attempt to control the hardness/fracture resistance ratio. An FGM powder bed was manually fabricated using a discrete banding technique. Results of traditional SLS processing of this powder bed are presented.

1 Introduction

Due to the nature of the powder delivery subsystem in the current SLS process, fabricated components consist of only one material system. By altering the powder delivery subsystem, laser sintering of multiple materials may be achieved. This new SLS process, known as Multi-Material Selective Laser Sintering (M^2SLS) is currently under development. This process has the potential to create a geometrically complex component while varying the material composition in a controlled manner. The potential ability to control the material composition at an arbitrary interior point could allow the development of unique components whose material properties are tailored to functional requirements. The variation of the material composition could be discrete or gradual in nature. The primary focus of this work is the examination of components containing a gradual change in material composition, or Functionally Gradient Materials (FGMs).

2 Functionally Gradient Materials

2.1 FGMs: A Description

A traditional component containing multiple materials will have regions of distinctly different material compositions which have been joined together as the result of chemical and mechanical interactions. These interactions, or joining processes, create a material interface of between 50 and 200 micrometers, which is basically discontinuous on a

macroscopic scale. However, M^2SLS and other developing processes [1,2,3,4,5] allow the creation of a material interface where the material composition gradually changes from one material to another. For example, the bottom of a component could be a 100% metal alloy which gradually changes as one moves up through the component to a 100% ceramic composition at the top of the component. The ability to control the ratio of the two materials making up the FGM allows one to control the material composition and, therefore, the material properties at a given arbitrary interior point in the component. The gradual nature of an FGM also ensures that material properties will possess a continuous distribution throughout the interior of the component, and will not possess the discontinuous changes in material properties traditionally present in multiple material components.

2.2 Potential Applications of FGMs

The ability to control the material composition in an FGM allows one to match the material properties to the functional requirements demanded of the component at a given point. The control of material properties and the gradual nature of FGM interfaces also provide opportunities for increased bond strength, especially at metal/ceramic interfaces.

An example component in which material properties could be controlled is a tungsten carbide cutting tool in which the relative amounts of carbide and cobalt are varied. For this system, the material properties to be controlled are the fracture resistance and the ductility. In general, the cobalt provides ductility and resistance to brittle fracture, while the carbide constituent provides hardness and wear resistance. The functional requirements of the part demand high ductility in regions of stress concentration to prevent cracking and brittle failure while also demanding high hardness and wear resistance in regions such as the cutting edge. The example FGM component should possess relatively more cobalt in areas of stress concentration and more carbide in areas such as the cutting edge to provide a matching of material properties to functional requirements. The use of FGMs should result in an increase in cutting performance while maintaining or improving the fracture resistance of the component.

The nature of FGMs allow a blending of a material property across the interface between two materials. While a number of material properties could be controlled in this fashion, one of the most important properties with respect to bond formation is the coefficient of thermal expansion (CTE). The mismatch in CTEs normally present in a

discontinuous metal/ceramic bond lead to destructive thermal stresses during thermal cycling or thermal shock loading[6]. Metal/ceramic bonds are frequently created at an elevated temperature and then cooled. The large CTE mismatch coupled with this large change in temperature will create a residual thermal stress in the component which may weaken the bond. Additionally, metal/ceramic bonds operate at an elevated temperature, which results in thermal cycling during normal repeated use. These repeated large changes in temperature and the metal/ceramic CTE mismatch generate transient thermal stresses which, when coupled with the residual thermal stress generated during bond formation, may destroy the bond[6]. An FGM component allows the CTE value to change gradually from a low value to a high value. This distribution of CTE values will tend to spread thermal stresses out over a volume of material instead of concentrating them at the interface[1]. The maximum thermal stress developed in the bond will therefore become much smaller and the bond will possess lower residual stresses and a greater resistance to thermal cycling, which will act to increase the strength of the metal/ceramic bond.

3 Experimental

3.1 Development of Experiments

3.1.1 FGM Fabrication Via Traditional SLS

A experimental study of the use of laser sintering to produce FGMs is being undertaken during the conceptual design phase of the M^2SLS process. This study will examine the effect of various laser sintering parameters on the quality of the resulting FGM samples. The purposes of this study are to ensure that the formation of an FGM is physically possible using a laser sintering technique and to provide information regarding process behaviors which could impact design choices made during the development of the M^2SLS process. Additionally, this study provides insight into the fabrication of FGMs using laser sintering without the costs associated with the development of the M^2SLS process.

Therefore, the performance of this study consists of the fabrication of FGMs using traditional SLS processing. Since the distinguishing difference between traditional SLS and M^2SLS processing is the powder delivery subsystem, performance of this study will require an alteration in the method of powder delivery. In general, these alterations should be as simple as possible and must result in the fabrication of an FGM on the powder bed. The simplest method to create an FGM consists of a manual discrete banding technique.

This technique involves mixing powder blends with differing ratios of the two FGM materials and manually laying these blends out in bands to create a gradual change in material composition. This method produces an FGM with discrete steps which approximates a fully continuous FGM. The FGM powder bed examined in this study was fabricated using this technique and then laser sintered with the traditional SLS process. Another FGM fabrication technique would utilize vibration-induced segregation to create a fully continuous FGM. In this technique, a thin, sealable powder dish is filled with a one-to-one ratio mixture of the two FGM materials. This dish is placed on its side and vibrated to induce segregration of the two FGM materials. After segregation is achieved, the dish would be placed into an SLS workstation and laser sintering would proceed. The third FGM fabrication technique involves the creation of a vertical FGM in the powder side cylinder, either manually with discrete layers or using the vibration technique described above. As the SLS process proceeds, the roller would deposit material of a gradually changing composition on the part side piston. This technique would create a multilayer FGM sample in which the FGM would be oriented vertically. However, potential problems of segregation and mixing during roller transport of the material may be encountered with this technique.

3.1.2 Material Selection

The selection of the material system was based on the following criteria. First, the material system should be extensively documented in the literature so that the experimental FGM results can be compared to standard fabrication techniques. This comparison is required in order to gauge any improvements in the overall performance of a FGM component versus a standard component. Second, the material system should be commonly used to provide relevance to industrial applications. Third, the two material components in the system should be clearly identifiable with two distinct material properties which act independently to fulfill the functional requirements of the component.

The material system selected is the tungsten carbide system discussed earlier (Ref. Section 2.2). This system is very well documented in the literature with an extensive collection of data regarding its material properties and behavioral characteristics. Tungsten carbide is the most commonly used material system for the fabrication of the carbide cutting tool inserts found in practically all industrial machine shops. Finally, the cobalt matrix correlates with ductility to fulfill the functional requirement of preventing brittle

fractures in regions of stress concentration. The tungsten carbide constituent correlates with hardness and wear resistance to fulfill the functional requirement of maintaining a sharp and properly shaped cutting edge.

Tungsten carbide powder is available in two primary forms. The first form is a pre-alloyed powder in which each individual particle is made up of a cobalt matrix containing a tungsten carbide secondary phase. The other form is a powder mixture made up of individual particles of pure tungsten carbide and pure cobalt. The pre-alloyed powder is expected to provide a better microstructure since less migration of the molten cobalt is required to form a uniform cobalt matrix. However, the powder mixture form offers much more flexibility in the creation of custom blends of tungsten carbide with varying amounts of cobalt. A compromise choice of these two forms was made by choosing a 12% cobalt pre-alloyed powder as a base mixture. This base mixture was combined with a pure cobalt powder to create a series of powder blends with gradually increasing amounts of cobalt. This choice ensured a fairly uniform mixture of cobalt in each blend with little likelihood of cobalt depleted regions present in the mixture.

3.1.3 Experimental Parameters

The basic goal of this study is to examine the effect of different processing parameters on the quality of the resulting FGM coupons. Therefore, it was necessary to consider what the different processing parameters are and which parameters should be examined in this study. The potential parameters which could be examined are tabulated in Table 1 below.

An initial examination of the list of experimental parameters reveals that some of the parameters may be eliminated from the study based on the results of previous research on the direct SLS processing of cermet composite systems[7]. Results of previous work indicate the need for a high vacuum atmosphere and pre-heating of the powder bed for satisfactory sintering of metal systems to occur. Therefore, experiments to examine these parameters do not need to be conducted and they may be eliminated from the list of potential parameters. Additionally, an experimental examination of some of the parameters will require substantial process development. For example, the laser pre-heat and laser modulation parameters would require the development of a laser pre-heating system and a real-time laser power control system before an experimental examination of these parameters could occur. These more problematic parameters will be examined after experiments have been performed with respect to the other parameters.

Experimental Parameter	Description
Processing Atmosphere	Process in air versus high vacuum
Discreteness of FGM	Process discrete FGM created using the manual discrete banding technique versus continuous FGM created using the vibration-induced segregation technique
Pre-Heat	Process with versus without pre-heat
Laser Pre-Heat	Process with normal pre-heat versus pre-heat from laser
Scanning Speed	Process at different scanning speeds along fast axis
Laser Power	Process at different laser powers
Vector Density	Process at different scanning speeds along slow axis
Scanning Orientation	Process with vectors parallel to FGM versus perpendicular to FGM.
Laser Power Modulation	Process with real-time laser power modulation to match material composition.

Table 1: Experimental Parameters

The results of previous work and a desire to avoid excessive process development reduces the list of potential parameters to (1) Discreteness of FGM, (2) Scanning Speed, (3) Laser Power, (4) Vector Density, and (5) Scanning Orientation. The two parameters, Scanning Speed and Scanning Orientation, were chosen as the parameters to be examined in the initial set of experiments.

3.2 Experimental Preparation

The percentages of cobalt used in industrial environments generally range from approximately 3% to 12%. While the most industrially relevant choice would have been a series of roughly 10 blends ranging from 3% to 12% cobalt, the resulting material composition gradient would have been somewhat mild. A steeper gradient in which the percentage of cobalt ranges from roughly 10% to 100% will tend to reveal the effects of changes in the laser sintering parameters more strongly then a mild material composition gradient. Therefore, the composition of the different blends started from the 12% cobalt pre-alloy (Ref. Section 3.1.2) and increased in increments of roughly 10% up to a fully

100% cobalt metal blend (Ref. Table 2). The mixing of the pure cobalt powder with the 12% cobalt pre-alloy was performed using an industrial roller mixer for approximately 8 hours per blend.

Blend Number	% Cobalt	% Tungsten Carbide
1	12 %	88 %
2	24 %	76 %
3	36 %	64 %
4	48 %	52 %
5	60 %	40 %
6	72 %	28 %
7	84 %	16 %
8	100 %	------

Table 2: FGM Blends

The FGM sample size was chosen to be 0.5 inches square with a resulting band width of each blend of roughly 0.0625 inches as shown in Figure 1. This small size allowed several samples to be fabricated in one experimental run and yielded a more continuous FGM by forcing the bands widths to be narrow. In order to optimize the number of samples which could be fabricated, the FGM bands were oriented as shown in Figure 2. Note that the band labeled 'fgm' only contained the 24% Co to 84% Co blends since the 12% Co and 100% Co blends also acted as boundaries between the fgm bands. This arrangement allowed the processing of 12 samples per run and the raster scanning of samples both parallel and perpendicular to the FGM gradient.

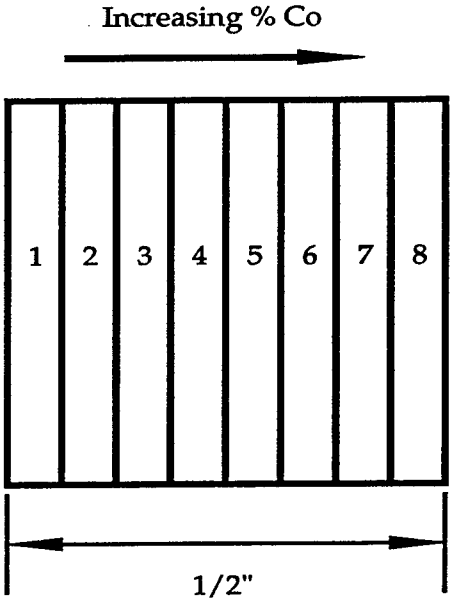


Figure 1: FGM Sample Coupon

Before scanning was initiated, the SLS chamber was brought to a high vacuum state and the powder bed was pre-heated to approximately 700°C. Proper alignment of the scanning location and the FGM bands was of critical importance to the fabrication of relevant FGM samples. An iterative process was used with a solid state positioning laser to confirm the scanning location prior to actual laser sintering. All of the samples were scanned using constant laser power with control of laser energy input achieved via changes in scanning speed.

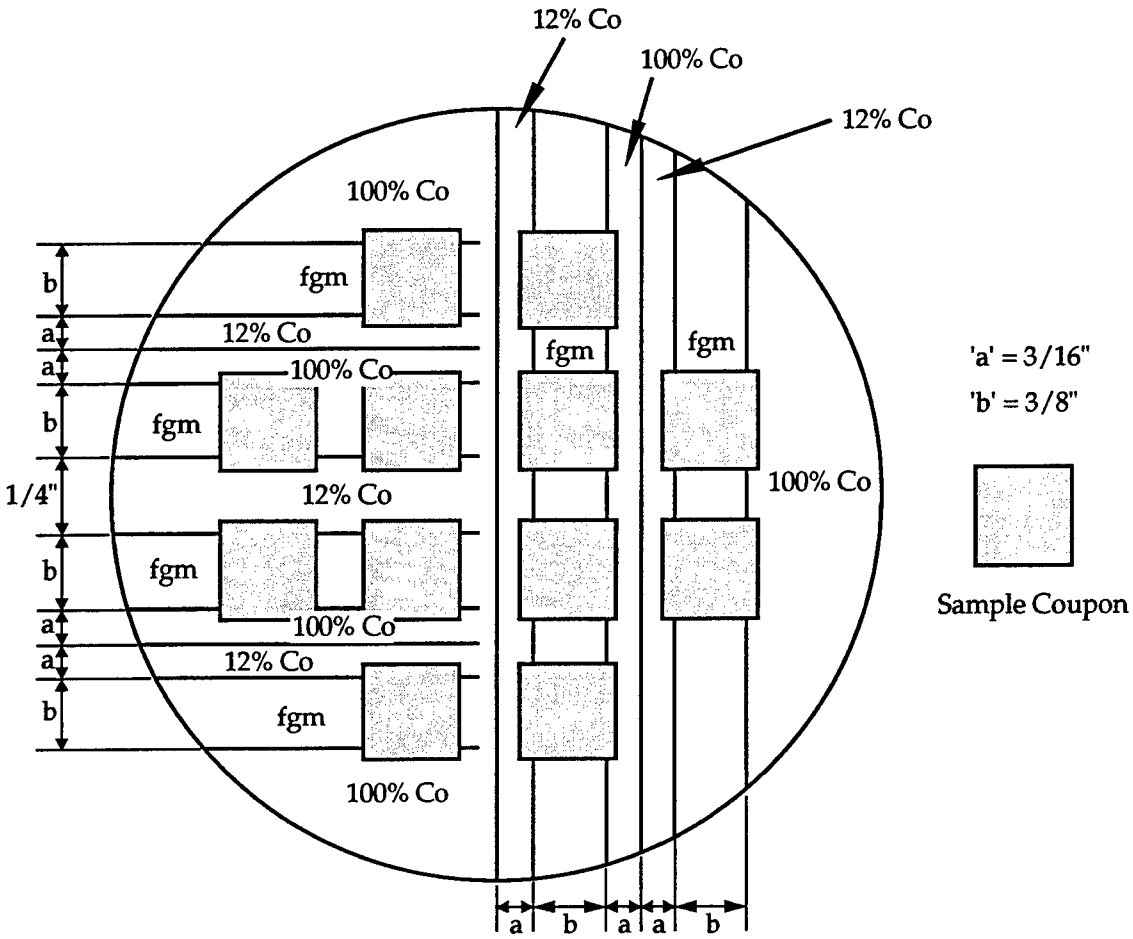


Figure 2: FGM Sample Placements

Laser power and scanning speed can be used to calculate the energy density, which is basically a description of the laser energy input per unit area. The energy density is calculated using the Andrew number equation[8] as shown below.

$$A_N = \frac{P}{\nu\,\delta}\left[\frac{\mathrm{J}}{\mathrm{in}^2}\right] \qquad (1)$$

where

P is the incident laser power (Watts)

ν is the scan speed (in/sec)

δ is the scan spacing (in)

Using the Andrew number equation generates the following three unique values of energy density: (1) 31.4 kJ/in^2, (2) 15.7 kJ/in^2, and (3) 10.5 kJ/in^2. Four samples were fabricated

for each of the three unique energy densities. Two samples for each density were scanned parallel to the FGM and the remaining two samples were scanned perpendicular to the FGM. This arrangement allowed three unique energy densities and two scanning orientations to be examined. Two samples were created for each of the six possible combinations of experimental parameters for a total of 12 samples. Scanning was initiated in the 12% cobalt region for all samples scanned parallel to the FGM.

3.3 Experimental Results

The results of the experiment must be examined with respect to the two experimental parameters studied. First, a comparison is made of those samples fabricated with the same energy density, but with different scanning orientations. This comparison indicates that a raster scan parallel to the FGM produces less cracking and balling then a raster scan perpendicular to the FGM (Ref. Figure 3) In Figure 3, the cobalt-rich region is at the top of the samples and scanning occurred in a vertical direction for those samples to the left while scanning occurred in a horizontal direction for those samples to the right. The cracking and balling of the samples on the right is most prevalent in the cobalt-rich region. The large percentage of cobalt in this region promotes the formation of melt pools that ball up due to

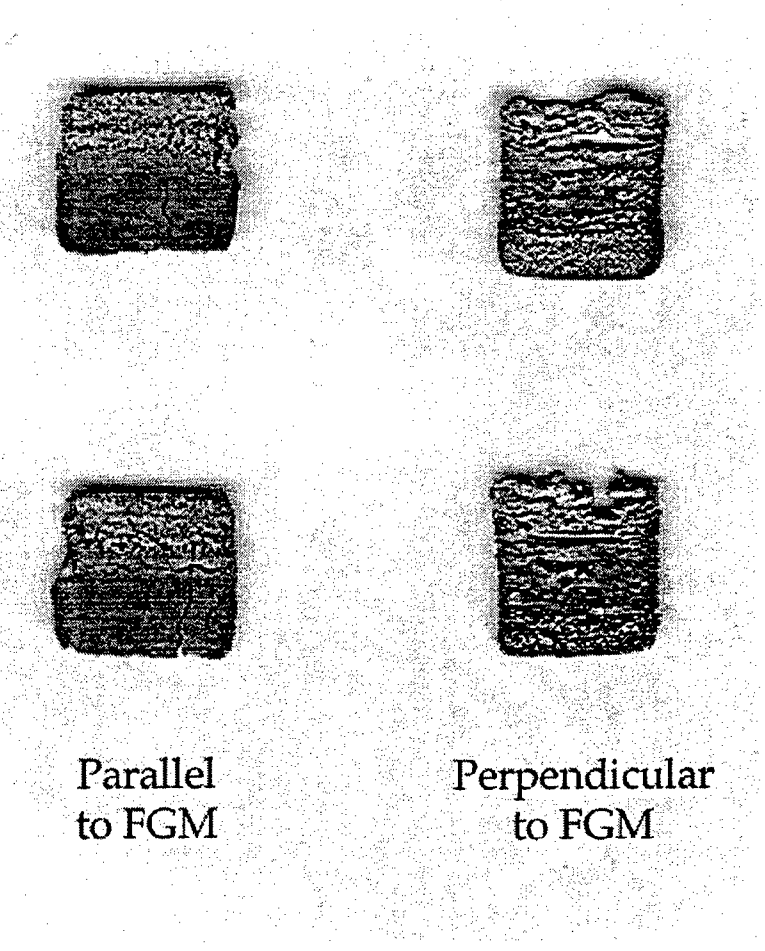


Figure 3: Results of FGM Scanning Orientation

surface tension and leave large cracks and voids in the sample. In the tungsten carbide-rich regions, less cobalt is present so that melt pools and associated balling and cracking does not occur. For scanning orientations parallel to the FGM, the laser will remain in the cobalt-rich region for a short time and then scan down into the tungsten carbide-rich region. By the time the laser has returned to the cobalt-rich region, the previously melted cobalt has partially resolidified so that only a small amount of cobalt remains in the liquid state. Therefore, the large amount of liquid cobalt required to form melt pools does not develop and the associated cracking and balling does not occur in the parallel scanning orientation.

Next, a comparison is made of those samples fabricated with the same scanning orientation, but with different energy densities. It was observed that increases in scanning speed reduced the amount of cracking and balling in those samples with a scanning pattern parallel to the FGM (Ref. Figure 4), however, no correlation between scanning speed and the amount of cracking and balling can be drawn for those samples fabricated with a scanning pattern perpendicular to the FGM. For the scanning pattern parallel to the FGM, faster scan speeds decrease the energy density and melt less of the cobalt during each vector scan. Therefore, at higher scan speeds, insufficient liquid cobalt is formed to develop melt pools and the associated balling and cracking behaviors are reduced. For the scanning pattern perpendicular to the FGM, increased scan speeds should also tend to reduce the amount of observed balling and cracking. However, the melt pools created by the perpendicular

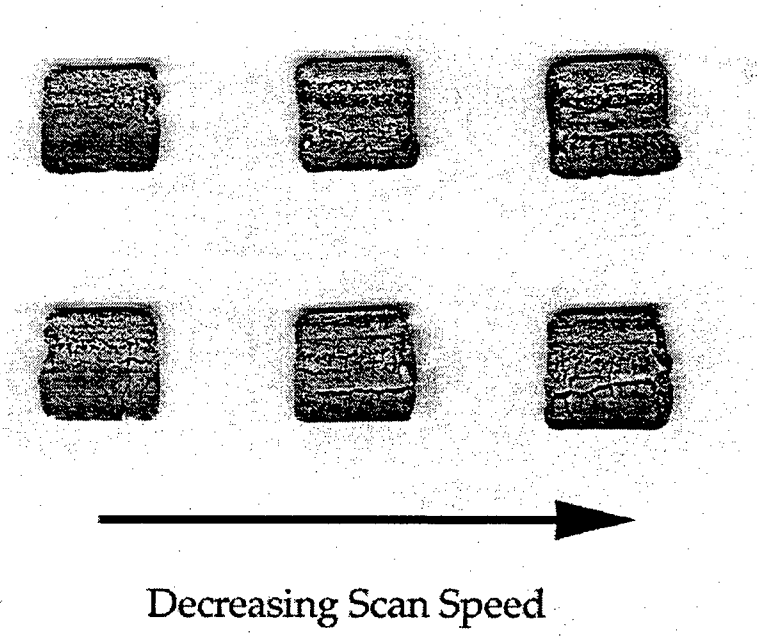


Figure 4: Effect of Scanning Speed (Parallel Scanning Pattern)

scanning orientation obscure this effect, and in general prevent the development of any correlation between scanning speed and the amount of balling and cracking. Therefore, the onset of balling and cracking is in general more sensitive to scanning orientation then to scanning speed. A large amount of sparking and off-gassing was also observed during processing which may be attributed to oxides and moisture contaminates in the powder.

4 Future Work

The immediate work to be completed is further testing and measurement of the samples presented above. These measurements include the development of micrographs to examine sample microstructures, and impact and hardness testing to determine the fracture resistance and hardness of the samples. Additional testing may include measurements of the sample density to determine the extent of porosity and SEM analysis to determine the material composition along the FGM. This analysis will check for disturbance of the FGM due to segregation or diffusion during the sintering process.

The next set of experiments to be conducted will duplicate the experiments described above with the following changes. First, an extensive bake-out of the powder for 12 to 14 hours at 500° C will be conducted to remove oxides and moisture from the powder before sintering. The experiments will be conducted at a higher pre-heat temperature of approximately 900° C. The higher pre-heat temperature will tend to reduce the extent of the balling by decreasing the surface tension and viscosity of the molten cobalt. Additionally, the increased temperature of the powder bed will cause an increase in the surface energy of the unmelted powder. In order to minimize the surface energy of the system, the area of the unmelted powder will tend to decrease so that increased wetting of the powder bed by the liquid cobalt will occur and the amount of balling will be reduced. These next set of experiments will also be conducted with a scanning orientation parallel to the FGM and at faster scan speeds based on the experimental results presented above (Ref. Section 3.3).

For a scanning pattern perpendicular to the FGM, additional experiments will orient the FGM so that scanning is initiated in the cobalt-rich region. It is expected that the amount of balling and cracking will increase due to the lack of powder bed pre-heat from previously sintering material. Future experimental work may examine the effect of real-time control of laser power during scanning of the FGM in an attempt to match laser

energy input to material composition. Additionally, attempts will be made to develop a more continuous FGM using the vibration-induced segregation technique described previously (Ref. Section 3.1.1).

5 Conclusions

These experiments represent one of the first attempts to produce FGMs using the traditional SLS process. FGMs were manually fabricated in a discrete configuration using a series of tungsten carbide and cobalt metal blends. Eight blends were used in which the percentage of cobalt varied from approximately 10% to 100%. SLS processing of the FGM was performed with scanning orientations parallel and perpendicular to the FGM and with three unique energy densities. Experimental results indicate that a raster scan parallel to the FGM and high scan speeds produce samples with the least amount of balling and cracking. The results also indicate that the onset of balling and cracking is in general more sensitive to scanning orientation then to scanning speed. The next set of experiments will include a pre-processing bake-out to reduce powder contamination, higher pre-heat to reduce the amount of balling, and faster scan speeds based on the results presented above.

6 Acknowledgments

Funding for this work was provided by the National Science Foundation Program Materials Processing and Manufacturing: NSF GOALIE under award number DMI 9622287.

References

[1] M. Niino and S. Maeda, "Recent development status of functionally gradient materials," *ISIJ International*, vol. 30, pp. 699-703, September 1990.

[2] M. Araki, M. Sasaki, S. Kim, S. Suzuki, K. Nakamura, and M. Akiba, "Thermal response experiments of SiC/C and TiC/C functionally gradient materials as plasma facing materials for fusion application," *Journal of Nuclear Materials*, vol. 212, pp. 1329-1334, September 1994.

[3] S. Kitaguchi, H. Hamatani, T. Saito, N. Shimoda, and Y. Ichiyama, "Development of functionally gradient materials (FGMs) of thermal relaxation type," *Nippon Steel Technical Report*, pp. 28-32, April 1993.

[4] T. Nagano and F. Wakai, "Fabrication of zirconia-alumina functionally gradient material by superplastic diffusion bonding," *Journal of Materials Science*, vol. 28, pp. 5793-5799, November 1993.

[5] G. Hilmas, J. Lombardi, R. Hoffman, and K. Stuffle, "Recent Developments in Extrusion Freeform Fabrication (EFF) Utilizing Non-Aqueous Gel Casting Formulations," *Solid Freeform Fabrication Symposium Proceedings 1996.* The University of Texas at Austin, pp. 443-450.

[6] M. Nicholas, *Joining of Ceramics.* London: Chapman and Hall, 1 ed., 1990.

[7] T. Fuesting, L. Brown, S. Das, N. Harlan, G. Lee, J. Beaman, D. Bourell, J. Barlow, K. Sargent, "Development of Direct SLS Processing for Production of Cermet Composite Turbine Sealing Components," *Solid Freeform Fabrication Symposium Proceedings 1996.* The University of Texas at Austin, pp. 39-55.

[8] J. Nelson, *Selective Laser Sintering: A definition of the process and empirical sintering model, Ph.D. dissertation.* Department of Chemical Engineering, The University of Texas at Austin, 1993. pp. 153.

Direct Selective Laser Sintering and Containerless Hot Isostatic Pressing for High Performance Metal Components

Suman Das, Martin Wohlert, Joseph J. Beaman, David L. Bourell
Laboratory for Freeform Fabrication
University of Texas at Austin

Abstract

A novel net shape manufacturing method known as SLS/HIP that combines the strengths of selective laser sintering (SLS) and hot isostatic pressing (HIP) is presented. Direct selective laser sintering is a rapid manufacturing technique that can produce high density metal components of complex geometry with an integral, gas impermeable skin. These components can then be directly post-processed to full density by containerless HIP. The advantages of *in-situ* HIP encapsulation include elimination of a secondary container material and associated container-powder interaction, reduced pre-processing time, a short HIP cycle and reduction in post-processing steps compared to HIP of canned parts. Results of research conducted on Inconel 625 superalloy, Ti-6Al-4V and Monel are presented. This research is funded by DARPA/ONR contract N00014-95-C-0139 titled "Low Cost Metal Processing Using SLS/HIP".

INTRODUCTION

Selective laser sintering (SLS) is a layered manufacturing technique that can produce freeform three-dimensional objects directly from their CAD models without part specific tooling or human intervention. Parts are built by selectively fusing layers of a powder material using a scanning laser beam. Details on this process are described elsewhere[1,2]. Selective laser sintering technology for prototyping parts in a variety of polymeric materials and for creating investment casting patterns has been commercially developed by DTM Corporation. More recently, RapidTool™ technology for creating prototype injection molding tooling has been introduced[3]. This process is an indirect SLS technique that involves the use of polymer coated metal powders to produce a produce a green shape that is subsequently post-processed by binder burnout and infiltration to produce a fully dense object[4,5,6,7,8,9]. Demand for low volume functional metal prototypes at reduced cost and short lead time has spurred the development of so-called direct fabrication processes. A number of such next-generation direct fabrication processes are under development. These processes typically use a concentrated energy source to consolidate and produce a fully dense or nearly fully dense shape directly from constituent materials. The next generation of selective laser sintering, i.e. direct fabrication of functional metal and cermet components and tooling is under development at the University of Texas[10,11,12]. To produce full density metal parts having complex geometry, a novel net shape manufacturing technique called SLS/HIP is under development at the University of Texas. The idea is to consolidate the interior of a component to 80% or higher density and to fabricate an integral gas impermeable skin or "can" at the part boundary *in-situ*. The SLS processed part can then be directly post-processed by containerless HIP to full density. A final machining step will result in a part having the desired geometry and mechanical properties.

BACKGROUND

The Department of Defense has a number of high value, high performance metal components in service that are produced by hot isostatic pressing. These parts are typically produced by conventional HIP of canned metal powders. Shaped metal cans are commonly used to encapsulate metal powders for HIP. The sheet metal container material is chosen so as to minimize interaction with the powder at processing temperatures. The container material must be removed by machining or by chemical methods after HIP post-processing. Properties of the can material including its melting temperature impose processing limits on the shaped metal encapsulation method.

Complex shapes are typically produced using the ceramic mold process[13] developed by Crucible Materials. This process is similar to investment casting in that dry powder instead of molten metal is poured into a ceramic mold. The production of a near net shape is advantageous because it minimizes scrap losses and machining steps. However, outgassing and heating cycles are long during this process because the ceramic mold is surrounded by a large volume of pressure transmitting medium[14]. The long cycle time and pre-processing steps necessary in the ceramic mold method make it a time consuming and expensive process. In addition, non-metallic contamination is also possible.

In the SLS/HIP process (Figure 1), the component is produced by selectively consolidating a metal powder with a laser beam layer by layer. While producing each layer, a gas impermeable high density skin (> 98% density) is formed at the boundaries of the part. The interior of the part is laser processed to a high density typically exceeding 80%. Thus, the part is shaped and canned *in-situ*. The encapsulated part is evacuated, sealed and post-processed by containerless HIP to full density. A final machining step may be applied if necessary.

SLS/HIP has several advantages over conventional HIP methods. Since an integral skin or "can" is formed of the same material as the part, a secondary canning step is not necessary. The part is directly post-processed by containerless HIP. Adverse container-powder interactions are eliminated and post-HIP container removal is not required. SLS/HIP allows production of complex shapes at reduced cost and shorter lead-times.

Based upon on a survey of several naval installations[15], four candidate materials have been selected for SLS/HIP process development. These are Inconel® 625, Ti-6Al-4V, 17-4PH stainless steel and Molybdenum. Table 1 below summarizes demonstration components and their applications.

Material	Component	Application
Inconel 625	Engine Vane	Aircraft turbine engine component
Ti-6Al-4V	Housing base	Tactical missile body component
17-4PH SS	Link assembly	Tactical missile launcher component
Molybdenum	Rotary valve	Torpedo component

Table 1 SLS/HIP demonstration components

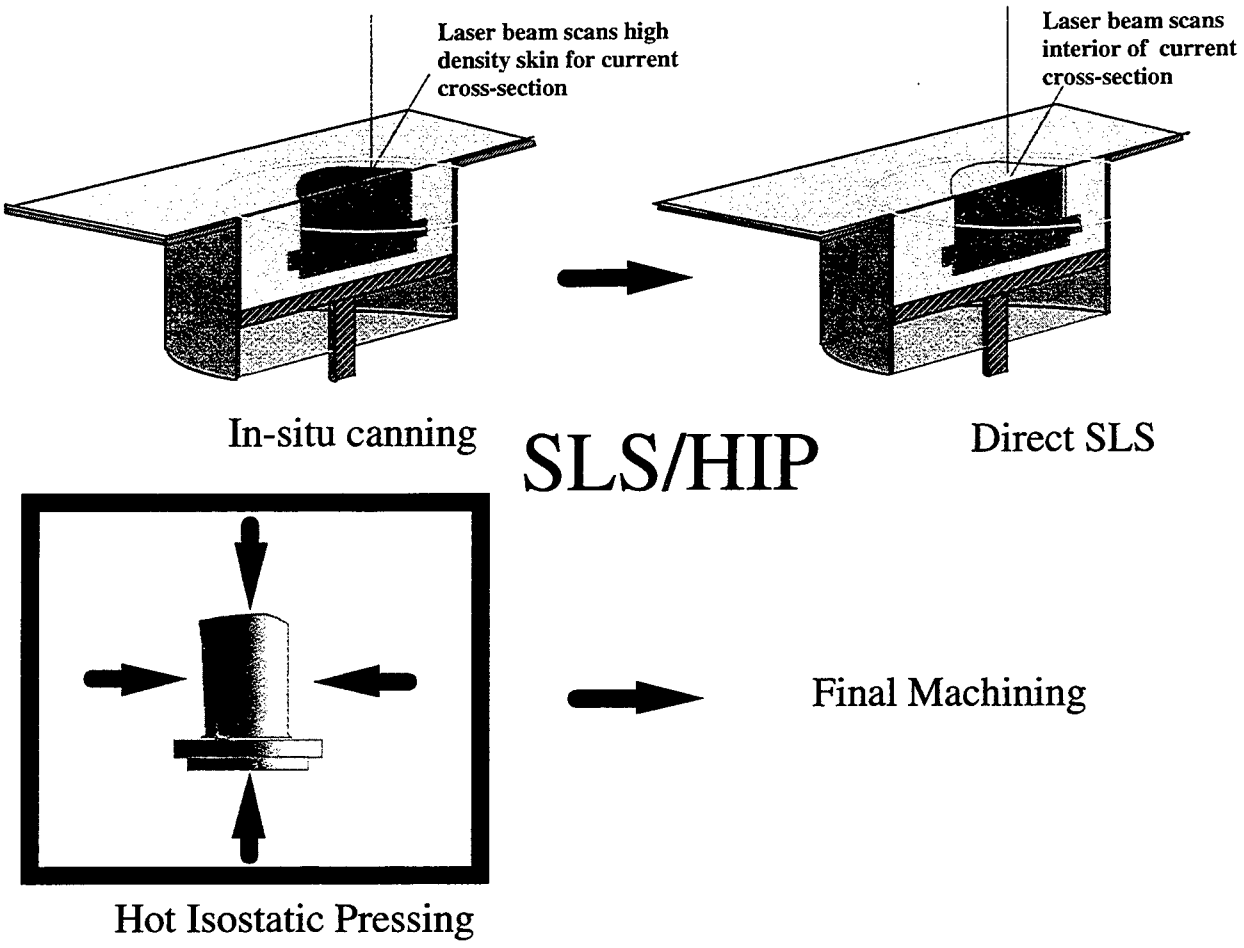


Figure 1 The SLS/HIP Process

EXPERIMENTAL

Candidate powders for screening trials were obtained from Anval Corp. and Nuclear Metals Inc. Anval provided Argon atomized Anval 625 alloy powder (16-44 μm). Ti-6Al-4V (37-74 μm) produced by the PREP method was provided by Nuclear Metals Inc. The compositions of Anval 625 and PREP Ti-6Al-4V are shown in Table 2 and Table 3 respectively.

C	Si	Mn	P	S	Cr	Ni	Mo	Ti	Nb	Al	Co	N	Fe
0.028	0.16	0.04	0.007	0.008	21.3	62.2	8.22	0.27	3.36	0.21	0.04	0.051	4.00

Table 2 Manufacturer's composition of Anval 625

Al	V	Fe	O	C	N	H	Y	Ti
6.35	4.19	0.19	0.19	0.02	0.01	< 0.01	< 0.001	Bal

Table 3 Manufacturer's composition of PREP Ti-6Al-4V

Characterization of the powders used in the SLS/HIP experiments included observation of the powder morphology by SEM and measurement of the powder surface area by gas adsorption surface area analysis (BET method).

Morphology

Both the Inconel 625 and Ti-6Al-4V powders were quite spherical, as would be expected for gas atomized and PREP powders. The high degree of sphericity provided excellent flow characteristics. A free flowing powder is important for SLS since the powder layers must be smooth and uniform. The presence of some particle rearrangement as material is drawn into the melt pool beneath the laser beam has also proven beneficial. The micrographs indicate a dendritic surface structure for both powders, but the presence of some segregation is not problematic since the material is melted and resolidified during the SLS process.

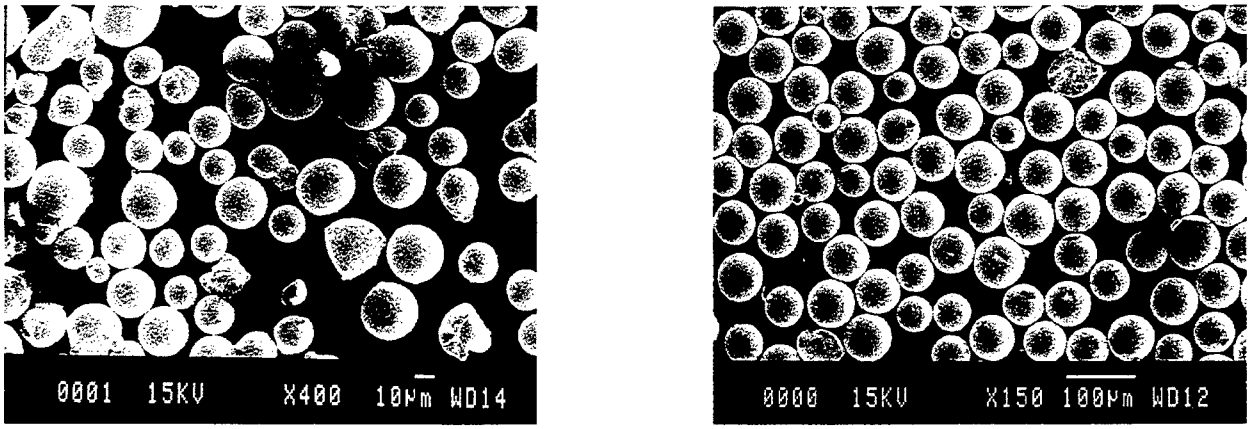


Figure 2 SEM micrographs of -325 mesh Anval 625 (left) and -200 mesh PREP Ti-6Al-4V (right)

Surface Area Analysis

The surface area of the powder is of greater concern, since the material must be thoroughly degassed prior to SLS processing. There are indications that the presence of oxide formation during SLS processing is a significant factor in influencing both the mechanical properties and the part density following the SLS stage. A 5-point BET surface area analysis (Table 4) was performed on the powder using a Micromeritics ASAP 2010 Surface area Analyzer. Samples of Inconel 625 and Ti-6Al-4V weighing 26 gm and 18 gm respectively were degassed at 350° C for 24 hours.

Material	Predicted Area (m^2/g)	Measured Area (m^2/g)
Inconel 625	0.035	0.052
PREP Ti-6Al-4V	0.034	0.0686

Table 4 BET Surface area analysis

Leak testing

To screen specimens produced by SLS for impermeability, a leak testing apparatus and procedure was adapted from the Metals handbook article on containerless HIP[16]. For a specimen to be acceptable for HIP, a gas impermeable barrier must be provided. A helium leak rate less than 1 X 10^{-9} standard cm^3/s is considered acceptable. Such low leak rates are required because the leak rate at typical a HIP pressure of 1000 atm (100 MPa) will be five orders of magnitude greater than that during leak testing at 1 atmosphere.

Feasibility demonstration

To demonstrate feasibility of constructing a thin walled can acceptable for HIP, a rectangular geometry was chosen. The procedure established to qualify specimens and to refine SLS processing parameters is shown in the flowchart of Figure 3. A schematic of the test geometry is shown in Figure 4.

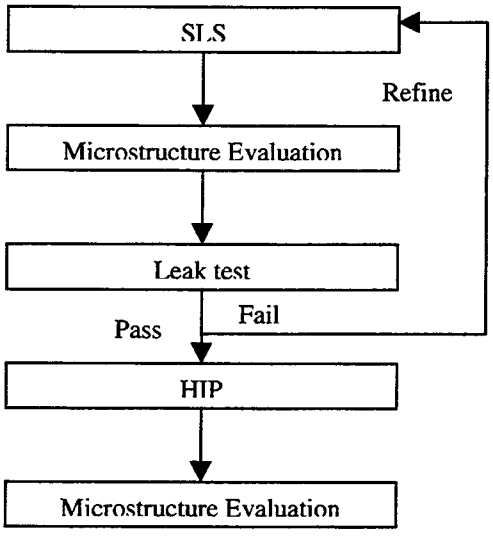


Figure 3 Specimen qualification procedure

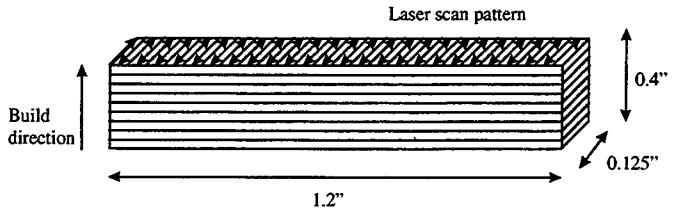


Figure 4 Thin wall specimen schematic

SLS apparatus

SLS trials were conducted on a high temperature selective laser sintering machine designed and built at the University of Texas. This machine is equipped with a 250 Watt Nd:YAG laser, powder preheating capability up to 600° C and controlled atmosphere.

HIP apparatus

HIP trials were conducted on a ABB model QIH-3 equipped with a graphite heating element. Temperatures up to 2000° C and pressures up to 200 MPa are attainable with the graphite element in inert atmosphere. Argon gas was used as the pressure transmitting medium.

RESULTS AND DISCUSSION

To demonstrate feasibility of constructing gas impermeable thin walls by SLS, specimens conforming to the geometry of Figure 4 were produced. These were then leak tested and screened according the procedure in Figure 3. Shown on the left in Figure 5 is the cross-section of a thin wall specimen produced by SLS. This specimen passed the leak test with a helium leak rate of less than 1 X 10^{-10} standard cm^3/s. This specimen was post-processed by a HIP cycle consisting of 1 hour at 1100 °C and 30 mTorr pressure followed by 45 minutes at 1100° C at 66 MPa. A cross-section of the HIPed specimen is shown on the right. Average porosity was measured over a metallographic montage in as SLS processed and HIPed specimens revealing a decrease in average porosity from 4.5% to 3.7%.

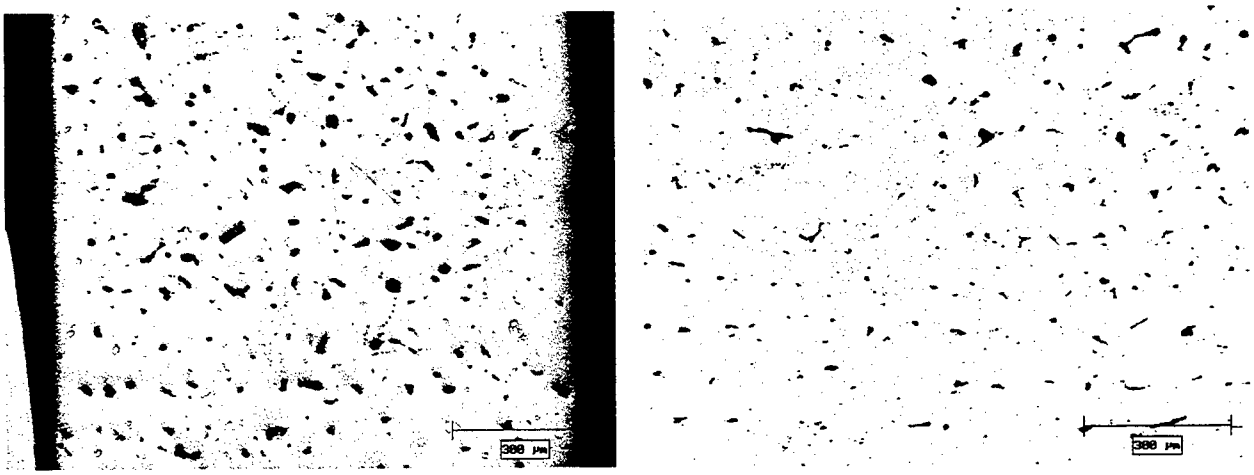


Figure 5 Inconel 625 Specimen 121496, as SLS processed (left) and HIP post-processed (right)

The next step in SLS/HIP process development was to demonstrate capability of constructing a simple shape. A 0.5 inch diameter, 0.5 inch long cylinder was chosen for this purpose. Shown in Figure 6 is an axial cross-section of an Inconel 625 cylinder processed by SLS to 98.5% density. This specimen was post-processed by a HIP cycle consisting of 3 hours at 1240 ° C and 25000 psi. This cycle resulted in nearly full densification to 99.5%. A cross-section of the HIPed specimen is shown in Figure 6 Specimen 051797, as SLS processed, 1.5% porosity . Temperature and pressure HIP maps (Ashby) were generated using software developed by one of the authors (Bourell). The objective was to correlate experimentally observed density with predicted density. These maps show that for Inconel 625 parts with initial density in excess of 98%, the dominant mechanism of densification at temperatures higher than 1100° C and pressures in excess of 100 MPa (15 ksi) is power law creep. The maps predict that HIPing conditions of 1100° C and 100 MPa should be sufficient to densify Inconel 625 in excess

of 98% density in 1 hour. To ensure full density, a more aggressive HIP cycle consisting of 3 hours at 1240° C and 165Mpa (25ksi) was employed.

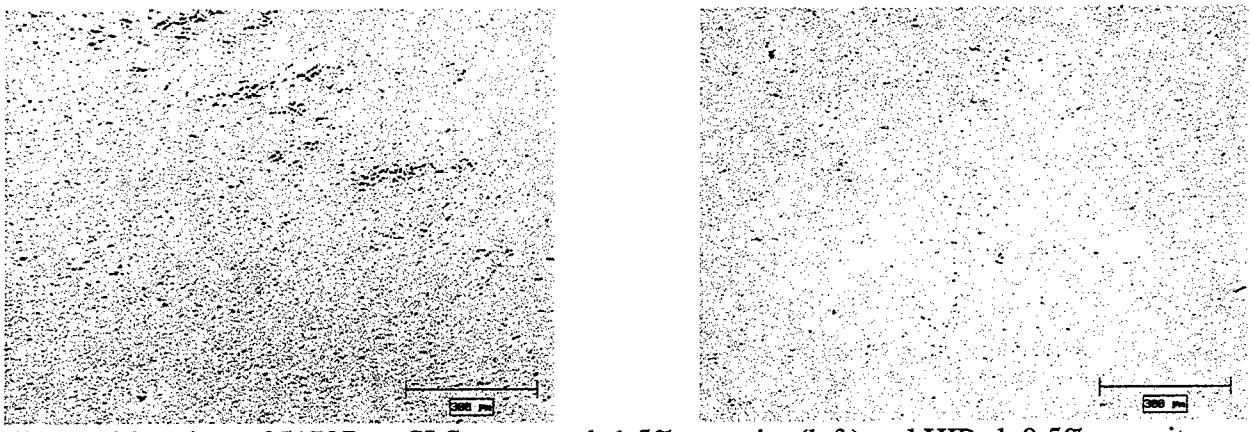


Figure 6 Specimen 051797, as SLS processed, 1.5% porosity (left) and HIPed, 0.5% porosity (right)

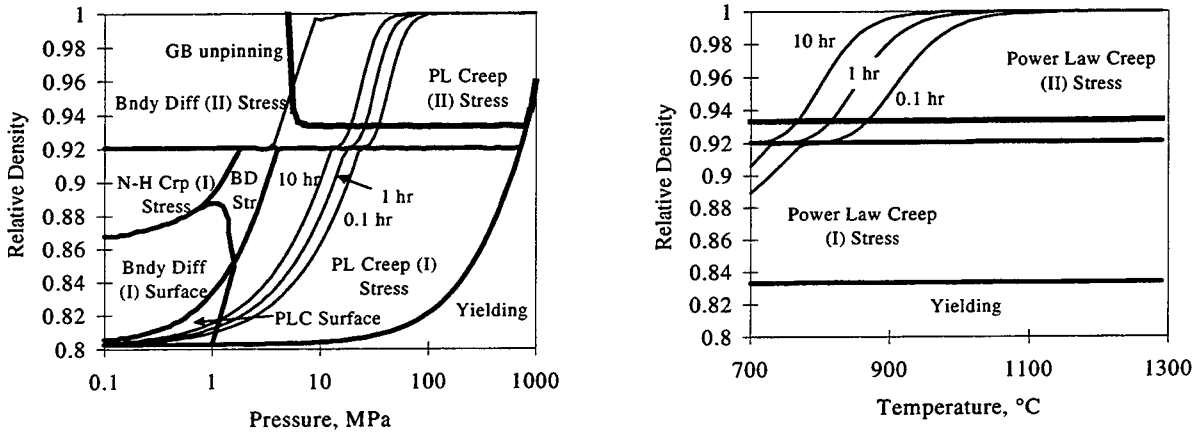


Figure 7 Pressure HIP map (at 1240° C) for Inconel 625 (left) and temperature HIP map (at 165 MPa) for Inconel 625 (right)

Single layer screening trials were conducted on candidate materials Ti-6Al-4V, Monel (65%Cu-35%Ni) and Ti-14Al-21Nb, a Titanium Aliminide. Shown in Figure 8 is a cross-section of a PREP Ti-6Al-4V single layer (0.15 cm thickness) produced by SLS. This specimen successfully passed the leak test with a helium leak rate less than 1 X 10^{-10} standard cm^3/s. Shown in Figure 9 are cross-sections of Ti-14Al-21Nb and Monel single layer specimens demonstrating full density capability.

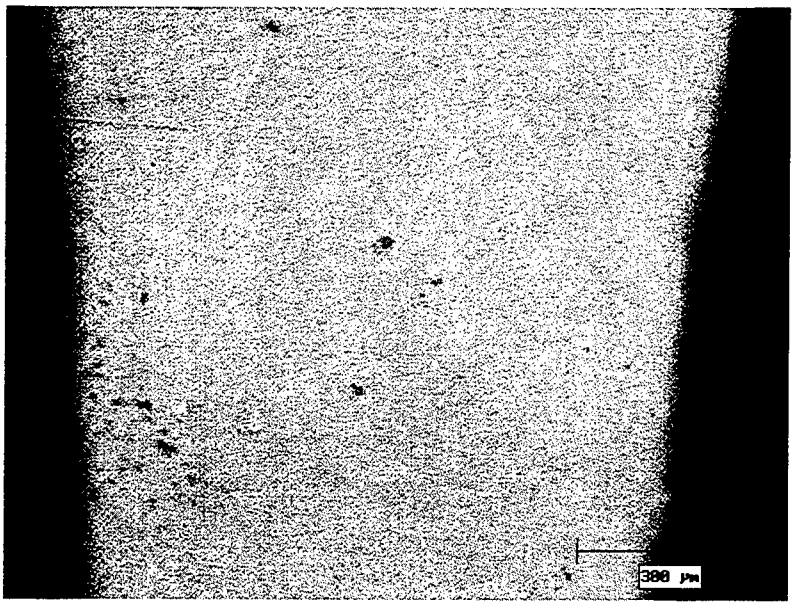


Figure 8 PREP Ti-6Al-4V, single layer, as SLS processed

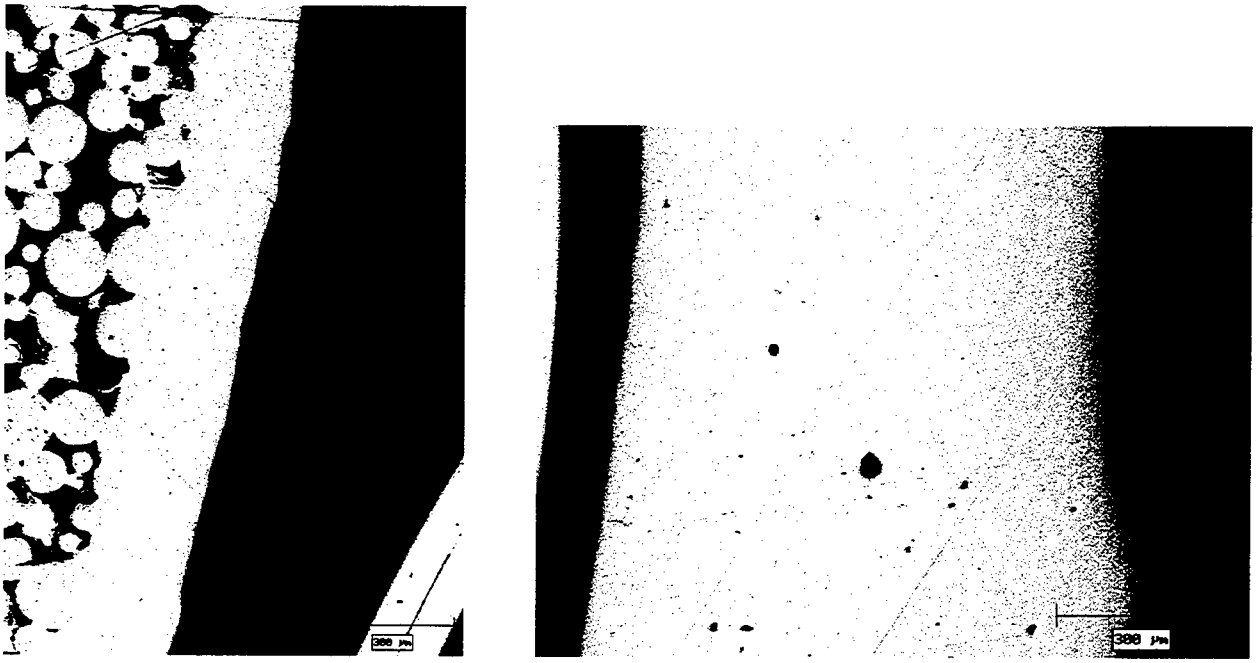


Figure 9 Single layer specimens of PREP Ti-14Al-21Nb (left) and Monel (right)

CONCLUSIONS

The feasibility of SLS/HIP has been successfully demonstrated for a simple cylindrical shape made of Inconel 625 superalloy. Preliminary screening trials on PREP Ti-6Al-4V indicate that a gas impermeable skin can be produced by SLS. Research is ongoing to qualify additional materials including Monel, Ti-14Al-21Nb, Molybdenum and 17-4PH stainless steel. The next step in SLS/HIP process development will be to demonstrate a complex geometry part. SLS/HIP has tremendous potential for rapid, net shape manufacture of high performance metal components at reduced cost and shorter lead times.

ACKNOWLEDGEMENTS

The Laboratory for Freeform Fabrication at the University of Texas gratefully acknowledges funding support provided by the Defense Advanced Research Projects Agency and The Office of Naval Research and under DARPA/ONR contract N00014-95-C-0139 titled "Low Cost Metal Processing Using SLS/HIP". Lockheed Martin Vought Systems is the contract program manager.

REFERENCES

[1] Beaman, Joseph J. and Deckard, Carl R., *Solid Freeform Fabrication and Selective Powder Sintering,* 15th NAMRC, North American Manufacturing Research Conference Proceedings, 1987, pp. 636-640.

[2] Deckard, C.R., Ph.D. Dissertation, Department of Mechanical Engineering, The University of Texas at Austin, 1988.

[3] *Rapid Prototyping and the Selective Laser Sintering Process : Tooling*, product literature, DTM Corporation, Austin, Texas.

[4] Vail, N.K., *Preparation and Characterization of Microencapsulated, Finely Divided Ceramic Materials for Selective Laser Sintering*, Ph.D. dissertation, Department of Chemical Engineering, The University of Texas at Austin, 1994.

[5] Vail, N. K., Barlow, J.W. and Marcus H.L., *Silicon Carbide Preforms for Metal Infiltration by Selective Laser Sintering of Polymer Encapsulated Powders*, Solid Freeform Fabrication Symposium Proceedings 1993, The University of Texas at Austin, pp. 204-214.

[6] Deckard, Lucy and Claar, Dennis T., *Fabrication of Ceramic and Metal Matrix Composites from Selective Laser Sintered Preforms*, Solid Freeform Symposium Proceedings 1993, The University of Texas at Austin, pp. 215-222.

[7] Stucker, Brent E., Bradley, Walter L., Norasetthekul, Somchin (Jiab) and Eubank, Phillip T., *The Production of Electrical Discharge Machining Electrodes Using SLS: Preliminary Results*, Solid Freeform Fabrication Symposium Proceedings 1995, The University of Texas at Austin, pp. 278-286.

[8] Bampton, C.C. and Burkett, R., *Free Form Fabrication of Metal Components and Dies*, Solid Freeform Fabrication Symposium Proceedings 1995, The University of Texas at Austin, pp. 342-345.

[9] Wohlert, M. and Bourell, D., *Rapid Prototyping of Mg/SiC Composites by a Combined SLS and Pressureless Infiltration Process,* Solid Freeform Fabrication Symposium Proceedings 1996, The University of Texas at Austin.

[10] Fuesting, T., L. Brown, S. Das, N. Harlan, G. Lee, J. J. Beaman, D. L. Bourell, J. W. Barlow and K. Sargent, *Development of Direct SLS Processing for Production of Cermet Composite Turbine Sealing Components-Part I,* Solid Freeform Fabriaction Symposium 1996 Proceedings, pp. 39-46.

[11] Fuesting, T., L. Brown, S. Das, N. Harlan, G. Lee, J. J. Beaman, D. L. Bourell, J. W. Barlow and K. Sargent, *Development of Direct SLS Processing for Production of Cermet Composite Turbine Sealing Components-Part I,* Solid Freeform Fabriaction Symposium 1996 Proceedings, pp. 47-55.

[12] Das, S., N. Harlan, J. J. Beaman and D. L. Bourell, *Selective Laser Sintering of High Performance High Temperature Metals,* Solid Freeform Fabrication Symposium 1996 Proceedings, pp. 89-95.
[13] *Hot Isostatic Pressing of Metal Powders,* Metals Handbook, Vol. 7, 9th Edition, pp. 425-426.
[14] Atkinson, H. V., and B. A. Rickinson, *Hot Isostatic Pressing*, Adam Hilger: Bristol, England, 1991, pp. 64-65.
[15] Knight, Ronald, Joe Wright, Joseph Beaman, and Douglas Freitag, *Metal Processing Using Selective Laser Sintering and Hot Isostatic Pressing (SLS/HIP),* Solid Freeform Fabrication Symposium 1996 Proceedings, pp. 349-353.
[16] *Hot Isostatic Pressing of Metal Powders,* Metals Handbook, Vol. 7, 9th Edition, pp. 436.

Direct SLS of powder compositions used for self-propagating high-temperature synthesis.

I.V. Shishkovsky, A.G. Makarenko+, A.L.Petrov.
P.N. Lebedev Physics Institute, Samara branch.
+Samara Technical University, SHS laboratory.
Novo-Sadovaja st. 221, 443011 Samara, Russia.
Fax: +7 (8462) 355600. E-mail: fian@transit.samara.ru

Abstract

The conditions of a direct selective laser sintering (SLS) were researched experimental in a volume and by layers for the eutectic and near-eutectic powder compositions, which usually used for the self-propagating high-temperature synthesis (SHS) technology. It was shown a possibility to realise during SLS process a control exothermic reaction of combustion exactly in the focus of cw-laser beam on Nd-YAG. The necessary parameters of a laser influence (a power, scan velocity and diameter of the laser beam), a dispersion and composition of the powder mixtures were determined for the such regime. The 3D parts from intermetallic compounds were created without any post-process procedures, that expands the functional opportunities of the sintering models.
Key words: direct SLS, eutectic powder compositions, self-propagating high-temperature synthesis (SHS), control exothermic reaction of combustion.

Introduction

The selective laser sintering (SLS) of powder compositions is a world-wide spread method of creation of 3D parts in the SFF technology. Initially developed for wax and plastic materials, today researchers are announcing about possibility directly to produce the volume parts from a polymer coating metal, bimetals and ceramic powder materials (see a pioneer work [1], Proceedings of SFF Symposiums and, at last, our works [2,3]).

Better results are obtained when applying a liquid phase sintering process, based on a mix of two or more powder materials, with a high and low melting point, respectively. During the part build, the phase with a low melt point fuses and binds a phase(s) with a high melt point. But conversation of a such 'green part' to a real metallic one is demand the post-processing techniques. There are procedures of powder preparation, a sintering in the special conditions (control of a bed temperature and around atmosphere), a post processing annealing in an oven and/or infiltration gives in the result a relatively long and complex process. It decreases the advantages of SLS method together with another its problems (a high porosity, a large shrinkage/distortion and etc.). No reject the all achievements the method of SLS at present time, we propose an alternative strategy of the research for the expansion of the uses opportunities of 3D parts and partial decision of above mention problems in the SLS process. It is a search of new powder compositions and a combination in a single technological process a some related processes. For example, the SLS can combine with a laser soldering [3], that allows to receive intermetallic compounds as in a paper [4] and for account of a high adhesion of the melt of a solder powder to non-melting phase to improve the properties of the volume models.

In this paper, the approach by the combination of the SLS process and a self-propagated high temperature synthesis (SHS) is examined. The investigated powder materials were a famous in SHS technology the mixtures on the basis Ni-Al and Ni-Ti in eutectic and near-eutectic compositions. A possibility of control exothermic reaction of combustion was

realised exactly in the focus of a laser beam during a selective laser scanning by the surface of those powder compositions.

Materials and equipment

The SLS process was conducted with use the scan laser beam from a computer controlled Nd-YAG. Laser worked in regimes with turn on (~ 3 kHz) and turn off (i.e., cw) an internal resonator modulation. On the laser the replaceable lenses are used with focus distances f = 149 and 336 mm (a diameter of laser spots was d = 50 and 100 mkm, accordingly). A laser power changed in a range 1-16 W and was supervised on the surface of powder with help of a measurement device. The control of laser beam with a computer had been used in a range of field 50x50 and 100x100 mm (i.e., 1024x1024 pixels) and had allowed to conduct a scan by any predefind counter, reproducing thus by layer a 3D part. The duration of a laser scanning determined the times of laser beam transition from point to point, a calm deflector in each point and could be changed by software over a wide range of values.

During SLS process the powders of the following marks are used (tabl.1). The size of powder fraction was determined with a help of the sieve analysis and an optical microscopy on NIOPHOT-30.

Table 1. Properties of used powder materials [2,5,6].

N / N	Type of powder materials	Particle size distribution, (mkm)	Density, ρ (g /cm³)	Solid density, ρ_s (g /cm³)	Void fraction, $\varepsilon=1-\rho/\rho_s$	Melt temperature, (T⁰C)	Latent heat of melt, (kJ/ mole)	Atom mass, (kg)	Stehiometric coefficient in SHS
1	Nickel powder (ПГСР4)	50-160	4,7	~8,8	0,47	~1200	17,5	58,6	3
2	Aluminium powder (АСД3,4)	10-50	1,25	2,7	0,54	660	10,8	27	↑1/3↓
3	Titanium powder	30-60	1,23	4,5	0,73	1668	15,5	47,9	1

There is important to take a size of particles no more than a laser spot, for account of we achieved an overlapping by the laser beam a few particles at once laser passage. A size of particles < 50 mkm was used. The following compositions were prepared for the realization of the next exothermic chemical reactions:

$$3Ni + Al \rightarrow Ni_3Al + Q_1, \quad (1)$$

$$Ni + 3Ti \rightarrow Ti_3Ni + Q_2. \quad (2)$$

It would occur to create the intermetallic compounds Ni_3Al and Ti_3Ni. That systems are selected as the model systems, which usually are using in the SHS technology. For those test systems the basis characteristics are known: an ignition temperature - T_i, energy activation of chemical reaction - E, a heat effect of reaction $Q_{1,2}$ on the one mole of Ni (see table 2 and fig.1).

Table 2.

Phase	T_i, (^{0}K)	E, (kJ/mole)	Q, (J/kg)
Ni_2Al_3	—	—	$1{,}9x10^6$
NiAl	910±25	135±27	$9{,}7x10^6$
Ni_3Al	925±16	115±25	$2{,}4x10^6$
Melt (Ni+Al)	—	48,24	$1{,}3x10^6$

Discussion

From the beginning, the powders are treated in a free pour volume, significantly more than a depth of a sintering mono-layer. We had been researched the conditions of combined SLS and control SHS processes for an one laser passage depend of a laser power, beam diameter, scan time and powder composition. Under control regime of the SHS we understood a realisation of the exothermic reaction of a combustion without a heat explosion and only in the zone of laser influence (i.e., in the so-called diffusion or kinetic regime of the SHS). It allows to determine the interval of sintering depths for the one laser passage under a minimal deformation on the layer.

Figures 2,3 show the experimental results of the laser influence on the Ni-Al powder equilibrium composition. Under a small laser power $P < 7$ W and a great velocity of laser beam $v > 25$ cm/s the sintering depths were a such little, that a sintered material looses from a touch. With an increasing of the power (fig.2) and decreasing of the beam velocity the depth of sintering stripe is growing. In the interval of laser powers among ~ 8,4-8,8 W (fig.2) and scan velocities ~ 2,9-8,6 cm/s visually we had been seen a control exothermic reaction combustion exactly in the zone of laser passage. At last, under values $P > 8{,}8$ W , $v = 25$ cm/s (fig.2) and $P = 8{,}8$ W, $v < 2{,}9$ cm/s (fig.3) an exothermic chemical reaction had been gone over to the regime of explosion and a front of combustion began to spread in the all directions independently without a laser influence. It can consider those regimes a critical. In according of SHS theory, a diffusion regime of combustion, which characterises of a stationary distribution of a synthesis wave, transforms to the regime of a heat explosion. It needs to remark (fig.1), that on the heating stage at the $T < T_e = 640$ ^{0}C only a Ni_2Al_3 (γ - phase) was arisen and diffusion grew on the contact surfaces of the Ni and Al particles. Then at the range 1132 ^{0}C $> T > T_e$, a NiAl (ε - phase) has been begun to create. When temperature is reached $T = 1638$ ^{0}C and would occur eutectic melt, then on the cooling stage from this melt an intermetallic NiAl and Ni_3Al (ε -phase) will crystallise. The laser influence parameters must be warm up so, that it would be sufficient a laser energy and a heat effect of exothermic reaction for the creation of those compounds.

An increasing of size particles in the Ni-Al mixtures was shown, the SLS process took place without SHS. As a result, for the laser spot $d = 100$ mkm an optimal interval (P,v) was changed for the combined SLS and SHS processes.

Also, we are investigated a near-eutectic Ni-Al powder compositions (mixtures - 1:1, 1:2, 1:4, 1:5). Deviation from an equilibrium composition sharply narrows the optimal interval of process's combination and practically a laser sintering was seen. Sintering mono-layers were a very brittle.

For the Ni-Ti powder composition (chemical reaction (2)) the combination SLS and SHS was realised also on the regimes with $v = 2{,}6$ cm/s and $P = 7{,}2$ - 8,8 W. However, the sintering monolayers were brittle although they had depths compare with before researched

powder composition NI-Al. Addition in Ni-Ti composition a material with a low melt temperature (braze powder) decreased a brittleness.

From our experimental results we can estimate a time — t_{LI} during which powder composition was under the laser influence and accomplished a transformation from the ignition regime to non-stationary a heat explosion regime. In the first case (fig.1, P > 8,8 W) $t_{LI} = d/v$ is equal 0,2 ms and in the second case (fig.2, P = 8,8 W) t_{LI} = 1,7 ms. A modern theory of ignition and explosion [8] allows to calculate the some parameters of SHS process, which a very closely describes a real situation. In the theory of ignition an important parameter is an adiabatic period of induction

$$t_{ind} = \frac{c}{Qk_0} * \frac{RT_i^2}{E} * \exp(\frac{E}{RT_i}), \qquad (3)$$

which by the sense corresponds our t_{LI}. In equation (3), k_0 - in front of exponent multiplier (it proportionate the number of molecule collisions during a chemical reaction (1)), c - a heat capacity, R - a gas constant (= 8, 3144 J/mole*K). A width of zone of exothermic chemical reaction in the moment of the ignition is equal

$$L_i = \left[\frac{\lambda}{Q\rho k_0} * \frac{RT_i^2}{E} * \exp(\frac{E}{RT_i}) \right]^{1/2}, \qquad (4)$$

where λ - a heat conductivity.

It would be interesting to compare the times t_{LI} with a prediction of the theory. A calculation by equation (3) gives for the NiAl system t_{ind} = 41 ms and for the Ni_3Al system — t_{ind} = 0,74 ms. Here we used the values from the Tables 1,2 and c_{Ni} = 462 J/kg*K, c_{Al} = 879 J/kg*K [7]; λ(NiAl) = 9±1 W/m*K, λ (Ni_3Al) = 20±2 W/m*K, $Q*k_0$(NiAl) = (14±2)x10^{16} W/kg, $Q*k_0(Ni_3Al)$ = (57±8)x10^{16} W/kg [5]. It is seen, that the calculated periods of induction by the order are agreed with the t_{LI}. Moreover, a t_{ind} for intermetallic compound Ni_3Al is located in an experimental interval 0,2-1,7 ms. So we proposed, there is a great probability to receive Ni_3Al phase. A calculation of the zone width (4) gives a next: L_i (NiAl) = 430 mkm, L_i (Ni_3Al) = 82,3 mkm. It is also a very important result, because a laser sintering process is demand a great selectivity. The pointed out values shown, that for the Ni_3Al phase a width of exothermic chemical reaction's zone is compared with a diameter of a laser spot d = 50 mkm and no more that two time greater than a size of powder particles. So we can consider, what a combination of SLS and SHS processes will exist successfully exactly by the counter of created 3D part. A time for period of induction for NiAl phase is not sufficient, then for the laser influence times a NiAl will not grow and a large L_i (NiAl) (which is order of 8-9 the laser beam diameters) could not be taken to attention. An X-rays analysis of treated powder compositions would be give a more exact result and we will plan to realise it.

The 3D parts a simple form (a cub, spheroid and etc.) were created from the (Ni-Al) powder composition of equilibrium mixture without any post-processes procedures. Investigations of properties of those 3D parts will plan in future also, but now can say, that their durability is more high then a sintered parts.

Conclusions

1. The combination of SLS and SHS processes in a single technological process was successfully realized for the eutectic and near-eutectic powder compositions on the basis of Ni-Al and Ni-Ti systems on the cw - Nd-YAG laser.

2. Optimal regimes of the laser influence were determined for the support of the control exothermic reaction of combustion exactly in the focus of the laser beam.
3. A compares of laser influence times — t_{LI} with a theoretical period on induction is present for experimental determined laser parameters (P,v,d). It is shown, that those t_{LI} are enough for synthesis of the intermetallic compound (Ni_3Al phase) exactly in the laser effected zone.
4. A good selectivity could be achieved during combination of SLS and SHS processes. A width of control exothermic reaction's zone — L_i (Ni_3Al) = 82,3 mkm is compared with a laser beam diameter.
5. The 3D parts of simple form had been obtained, which contended an intermetallic compound system without any post-processes procedures.

In a future research an attention must be given to investigate of intermetallic phases in the created 3D parts and those properties during the combination of SLS and SHS processes depend of laser influence parameters.

References

1. Bourell, D.L., Marcus, H.L., Barlow, J.W., Beaman, J.J. "Selective Laser Sintering of Metal and Ceramics", *The International Journal of Powder Metallurgy*, **28**, N4, pp. 369-381, 1992.
2. Shishkovsky, I.V., Kuprianov, N.L., Petrov, A.L. "Conditions of Monolayer Selective Sintering of Metal-Polymer Powder Compositions under Laser Influence", *Physics and Chemistry of Materials Treatment (Russian)*, N3, pp. 88-93, 1995.
3. Gureev, D.M., Petrov, A.L., Shishkovsky, I.V. "Selective Laser Sintering of Bimetal Powder Compositions", *ibid.*, 1997. (in the print)
4. Weiss, W.L., Bourell, D.L. "Selective Laser Sintering of Intermetallics", *Metallurgical Transaction A*, **24A**, N3, pp. 757-759, 1993.
5. Shiliaev, M.I., Borzyh, V.A., Dorohov, A.R. "To question of laser ignition of Ni-Al powder system", *Physics combustion and explosion (Russian)*, **30**, N 2, pp. 14-18, 1994.
6. Lapshiv, O.V., Ovcharenko, V.E. "Mathematical model of SHS of Ni_3Al in regime of heat explosion from pure powder mixture", ibid., **32**, N 3, pp. 68-76, 1996.
7. Tables of physical values. Handbook I.K. Kikoin, Moscow, Atomizdat, 1976, 1008 P.
8. Vilunov, V.N., Theory of ignition of condense materials. Novossibirsk, 1984, 190 P.

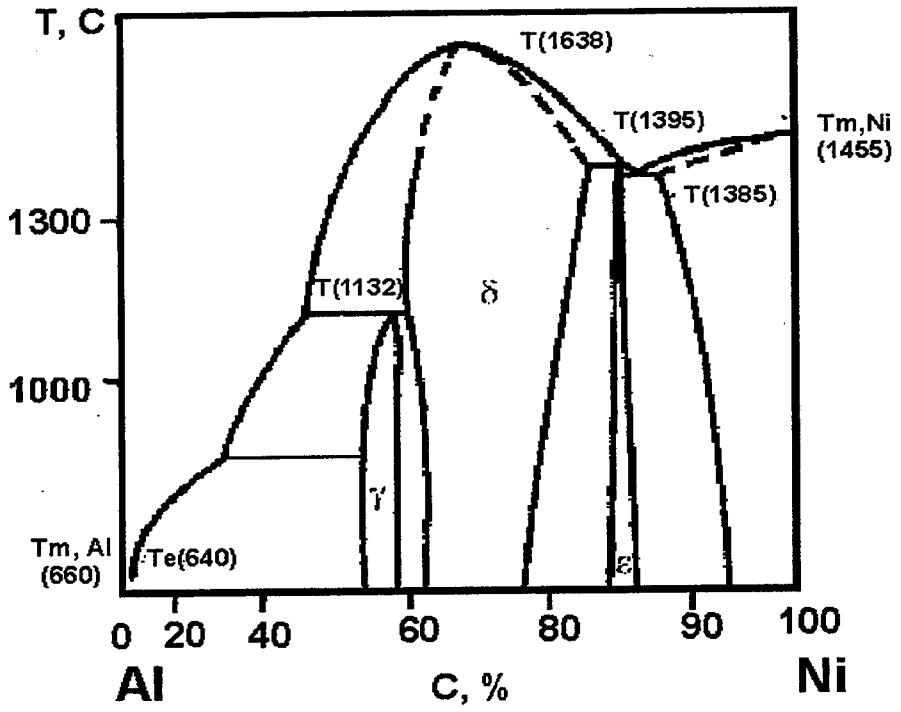


Figure 1. Equilibrium diagram of system Ni-Al.
(γ - phase Ni_2Al_3, δ - phase NiAl, ε - phase Ni_3Al)

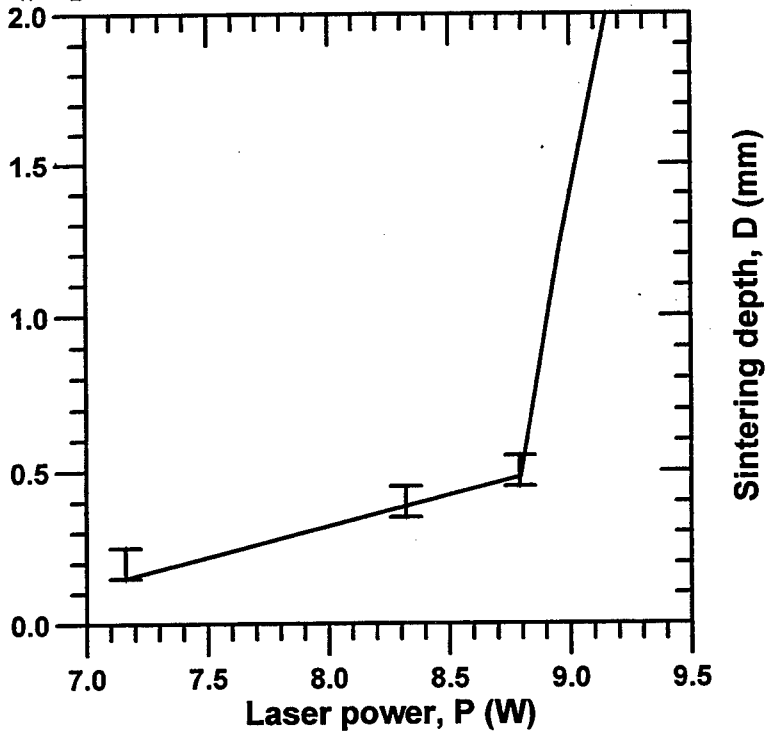


Figure 2. Effect of laser power on sintering depth. Powder mixture for chemical reaction (1). Laser scan velocity v = 25 cm/s, d = 50 mkm.

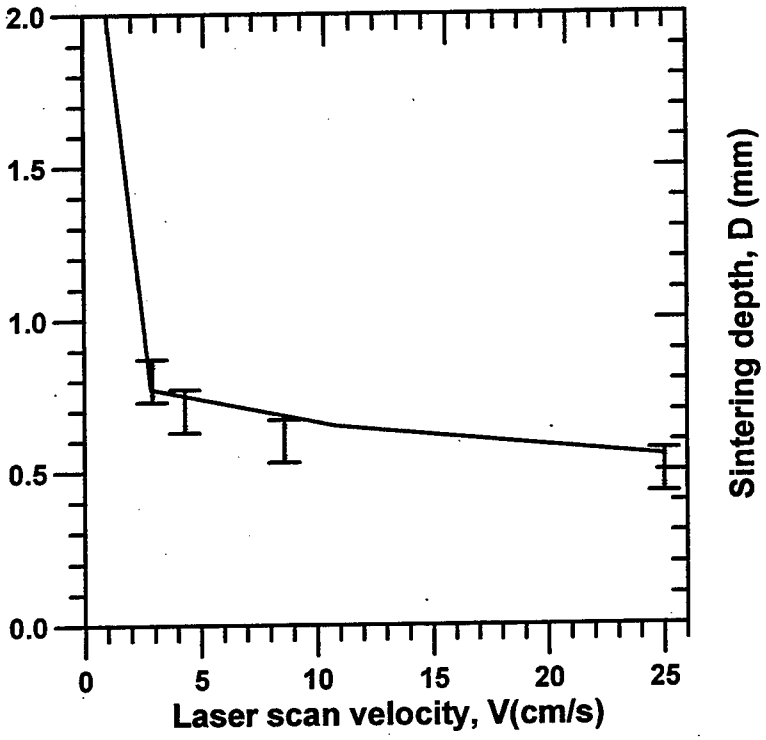


Figure 3. Effect of laser scan velocity on sintering depth. Powder mixture for chemical reaction (1). Laser power P = 8,8 W, d = 50 mkm.

Net shape Functional Parts Using Diode Laser

Tariq Manzur, Chandra Roychoudhuri and Puneit Dua
Photonics Research Center, University of Connecticut
Fahmida Hossain
Massachusetts Materials Research (MMR)
Harris Marcus
Institute of Materials Science, University of Connecticut

Manufacturing processes, such as cutting, drilling, soldering, marking, forming 3D-sintered parts from metal powders and laser vapor deposition, are now well established practices using matured high power lasers like Nd:YAG, CO_2 and Excimer lasers[1]. These lasers are bulky, inefficient and expensive. Semiconductor diode lasers, if wavelength is not a disadvantage, hold the potential of creating a major cost/convenience breakthrough in these and other new manufacturing processes such as growing integrated opto-electronics devices etc. They have the potential to initiate a mini industrial revolution because they are compact, have high wall-plug efficiency (50%) and above all, they can be mass produced (like computer chips). It is important to note that almost all laser material processing can be carried out if the intensity available can cover the range from 10^3 to 10^7 W/cm^2. Fortunately, microscopic as they may be, even low power diode lasers emit reliably at 10^6 W/cm^2. The hurdle that needs to be solved is coupling energy from a large number of diodes to obtain high total power without losing much of their inherent brightness and yet keep the system cost low. Price of high power laser diodes have already come down dramatically over the last five years; further reduction is expected as the volume market keeps increasing rapidly. Current commercial devices are mostly of two types: (1) fiber coupled arrays and (2) two-dimensional stacked arrays. We are using both types. We believe, the ultimate high brightness and high total power at low cost will be achieved by 2D array of broad area surface emitting lasers. We will present the results of our various activities using 30W (980 nm, spot size ~ 600 μm), 10 W (860 nm, spot size ~ 50 μm) and 60 W (810 nm, spot size ~ 700 μm) fiber-coupled cw diode laser and 50 W (930 nm spot size ~ 700 μm) free space diode lasers on: (1) fabricating 3D SLS parts directly from metal/ceramic powders using CAD/CAM design, (2) laser assisted selective area vapor phase deposition of amorphous SiC and Si_3N_4-rod, (3) Pb and Ag soldering of simple electronic parts, (4) surface hardening of stainless steel ribbon.

INTRODUCTION

At the University of Connecticut desk-top manufacturing (DTM) test bed uses diode laser to selectively sinter metal/ceramic powders without any polymeric binder at room temperature powder bed and laser assisted selective area metal organic chemical vapor deposition (LASAMOCVD) systems.

At present, solid free form fabrication (SFF) systems using CO_2 and Nd:YAG lasers are more flexible than alternative non-laser SFF technologies, but still have substantial shortcomings that sharply increase the total cost of fabricated parts. Among these shortcomings, existing laser based SFF systems are (a) expensive, with system costs between $300K and $2M and costs of delivered thermal power exceeding $200 per watt, (b) bulky, requiring large floor areas and room volume to accommodate high power CO_2 and Nd:YAG lasers and associated power supplies and cooling systems, inefficient in conversion of electrical energy to thermal energy - CO_2 producing 10-15% conversion of electrical to optical power but then not coupling this optical power efficiently into materials at the long 10.6 μm wavelength, and Nd:YAG producing only 1-3% conversion of electrical to optical power in the inexpensive flash lamp pumped units and achieving 15-20% efficiency only in much more expensive lasers.

Recent advances of diode laser technology makes it possible to deliver thermal energy in compact, efficient, low cost SFF systems, at costs of $30 or less per delivered watt, the cost of fabricated parts would drop rapidly and precision net shape micro parts manufacturers using this new technology would directly be benefited. Table 1 shows a cost analysis of variety of laser-processing systems performed with intensities in the range of 10^3 to 10^8 W/cm^2. Focused diode lasers, despite relatively low output power per stripe (~1W), emit 10^4 to 10^6 W/cm^2, a range suitable for many laser manufacturing jobs[2].

Table 1.Comparison Study of Diode Laser (DL) Mature Conventional Laser Technologies: Relative Performance & Cost

Laser Properties	CO_2	Nd:YAG	Diode Pump Nd:YAG	Excimer	Diode
Wavelength μm	9.6 to 10.6	1.06	1.06	0.19 to 0.35	0.67 to 0.98
Beam	CW Pulsed Single or Multi mode	CW Q-switched Single or Multi mode	CW Pulsed Single or Multi mode	Pulsed Single or Multi mode	CW Modulated Multi mode
Avg. Power	30 W to 10 kW	10 to 500 W	0.1 to 20 W	<150 W	20 to 200 W
Peak Power	10^{8-10} W	10^{8-10} W	10^{8-10} W	10^7 W	NA
Energy Joules	1 to 30	1 to 50	1 to 20	0.1 to 1	NA
Power Density W/cm^2	10^{6-10}	10^{4-9}	10^{3-8}	10^{4-7}	10^{2-6}
Spot size μm	10 to 500	5 to 300	5 to 300	20 to 800	150 to 800
Where Used	Light to Heavy Ind.	Light to Heavy Ind. High Precision	Tele-Com Applicati-on	High Precision	Light Ind.
Toxicity	No	No	No	Yes	No
High Voltage	Yes	Yes	No	Yes	No
RF	Yes	No	No	No	No
Absorption Metal Non-Metal	Small Moderate	Moderate Moderate	Moderate Moderate	Highly Highly	Good Good
Wall Plug-in Efficiency	~ 10%	~1%	~5%	<1%	40 - 50%
Cost of Laser	<$100/W	>$200/W	>$300/W	~$150/W	~$30/W

Sintering Systems

The apparatus used for the present experiment is an extension of a DTM Inc. system[3]. The apparatus includes power delivery system (diode laser), powder delivery system (PDS), oxidation prevention system, laser scan control system, data acquisition and transmission capabilities, in situ video monitoring, temperature measurement and feed back control system in a closed loop operation[4-5].

Solid freeform fabrication using laser sintering generates parts by selective sintered multiple layers of powder to build a three dimensional part in layer-by-layer manner. The way to feed powder will not only effect productivity but also will effect the quality of sintered product. In this experimentation system, a piston feeding system is designed with which powder can be fed manually. Automatic powder feeding can also be done if electric motors are connected. After sintering, a new layer is lay down on top of the sintered one, then layer-by-layer is deposited to form a 3-D structure. Layer thickness ranges between 200 to 500 μm for various powders. The layers of powder is traced with a computer controlled laser scanning system (Fig. 1). The laser beam diameter is on the order of 700 μm, working output power ranges between 5 to 60 watts, diode laser has been used in the initial selective laser sintering (SLS) system. The laser beam rasters the powder bed surfaces and raises the temperature of the powder it contacts, sintering the loose powder. The laser scan rate is of the order of 1 ~2 cm/s for metals and ceramic powders @ 15 watts cw power. At the end of first scan second layer of loose powder is deposited as described earlier and the process is repeated. We have also designed an extra piston which is used to pressure the powder to the sintered layer each time when a new layer of powder is added on. This increases the compactness of spread out powder.

CAD data transferring

Most rapid prototyping processes produce parts on a layer-by-layer basis. The first step of the rapid prototyping is to slice the geometric description of the part (CAD data) into layers. The slicing operation generates the contours of the part for each layer (Fig. 1). Each layer then can be further divided into many scanning paths. Three scanning paths is currently under studies. They are raster scanning in a single direction, unidirectional scanning, directional scanning and contour scanning. Most current RP processes are using raster scanning in a single direction to build each layer of the part. Unidirectional scanning will result in a large number of very short scanning vectors which requires very precise and sensitive motor to control laser beam.

Directional scanning results in smaller number of longer vectors. Longer vectors reduce the errors associated with laser toggling transients and repositioning of the laser beam, resulting in higher part accuracy. Contour scanning of the layer boundaries is expected to generate better surface quality. The form of the geometric description of mechanical parts to be produced by sintering process significantly affects the accuracy of the final part. Most current technologies consists of tessellating the surfaces of the geometric model into a mesh of non-overlapping triangular facets. The resulting geometry is transmitted in a standard file format, the so-called "STL" file format, developed by 3D Systems, Inc. (1988)[3].This format has been adopted by many CAD vendors and is readily available.

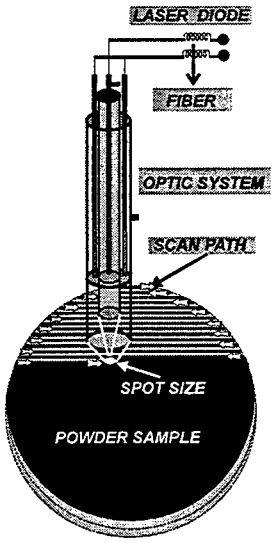


Fig.1 Computer Control Laser Scanning Path

Binding Mechanisms in SLS

Binding between powder particles takes place by laser induced localized heating. The duration of laser beam at any powder particle is short typically between 0.02 to 30 ms. Therefore the thermally-induced binding reactions must be kinetically rapid. Even at temperature approaching the melting point, metals and ceramics are very viscous and kinetic processes are very slow. For this reason, solid state binding mechanisms are not feasible for SFF technique. In SLS, the molten metal is often completely contained by loose powder rather than fully dense material. In this research we are developing two phase powder approach. In this approach the powder bed consists of two different powders of significantly disparate melting points. We are also working on the single phase powders sintering approach.

Computer Simulation

A distortion effect called "curl" is due to the material shrinkage force causing a bending moment perpendicular to the laser motion. As a result, mono-layers tend to bend horizontally from the test parts. Another effect responsible for part inaccuracies is the heat of polymerization evolving during the exothermal curing process. Mono layers tend to bend downwards on account of the inhomogeneous temperature distribution in their cross-section. The energy distribution of the laser spot on the surface of the powder sample is assumed to be Gaussian /Jacobs, with r being the Gaussian radius and where r may be a function of scanned time "t".

$$r = ((x(t) - x_0)^2 + (y(t) - y_0)^2)^{1/2}, \quad (1)$$

where x_0 and y_0 are the initial spot position.

Laser energy absorbed in the powder is given by the following equation:

$$dE/dz = eSE = -E_a; \quad (2)$$

where"e" being the absorptivity of the powder, "S" powder concentration and "E_a", is the energy absorbed by the powder. Computer simulation yields a deeper understanding of the physical, chemical and thermal processes occurring during SFF processes and are vital for an optimized finished 3-D part in terms of accuracy and quality.

MATERIALS

For SLS the materials used in the present study were Fe and Bronze-Fe and Bronze-Ni premixed powders. The powders were sieved and the particle sizes of the powders were 150 μm, 44 μm, 20 μm and 10 μm used in our experiment.

EXPERIMENTAL PROCEDURE

Several Bronze-Fe/Ni and Fe functional parts were made using SFF technique to determine the particle size effects and diode laser wave length effect on full density SLS parts. In this setup, the SFF device generates three-dimensional parts from CAD/CAM data files by selectively bonding multiple layers of powder using high-power diode lasers. For SFF requirements of the sintering experiments, the multi-mode fiber coupled power delivery system was attached with an optical re-imaging unit. The spot size of this unit using re-imaging unit is 700±70 μm. Both of these systems can deliver intensity up to $1x10^4$ W/cm^2 at the powder bed.

Two Phase Sintering:

Two phase sintering during the SLS process in Bronze-Fe system occurs insitu liquid phase sintering (LPS) of low melting temperature alloy in a system. In the Bronze-Fe system, the melting temperature of iron is 1535^O C. In the temperature range between 870^O C and 1030^O C, the mushy bronze flows around the iron powders and forms a continuous substrate of bronze with an island of Fe powders. As the temperature increases by increasing the laser power or by decreasing the scan speed, the bronze powder becomes more liquid, viscosity decreases and liquid solid diffusion increases. This enhances the densifications of the SLS parts. For SLS parts the powder spread out density is around 30%. To increase the sinter density from 30% to fully dense there must be a mechanism to feed the powder in, unless there will be a shrinkage of the SLS parts or large zones of voids. To solve this problem, optimization of laser processing parameters and powder size and shape distribution is very important.

Single Phase Sintering:

At present we are also working on single phase sintering of powder. In this process melting of the powder is done by the laser beam. The melted zone moves continuously as the laser scans over the surface. As the molten zone moves, the solid-liquid reaction takes place. This process increases the density of the fabricated parts from 40% (spread out density) to more than 90%.

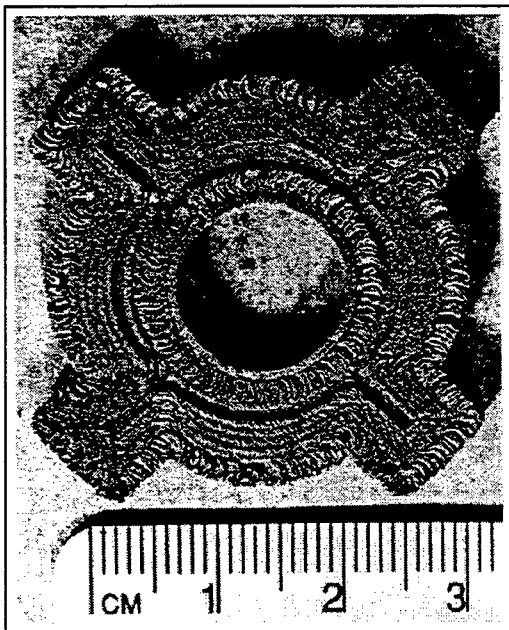
The strength and the surface finished of the sintered parts can be improved if the powder has the following properties:

1. **The particles must be well mixed and homogenized; particle size distribution within 10 μm.**
2. **The particle must not have any agglomerates and must be free of any contaminates.**
3. **The particle must have spherical morphology (equiaxed).**

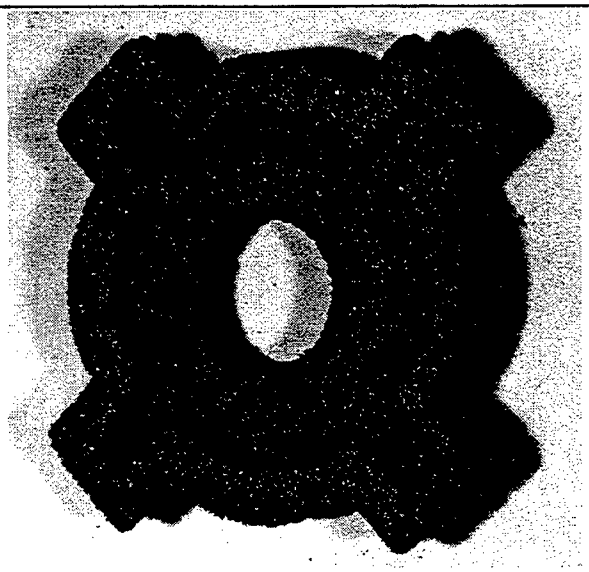
Figs. 2 & 3 shows the SFF functional parts made from Fe-Bronze premix powders. Figs. 2a & 2b-3a is from 44 μm and 150 μm particle size powders respectively. Fig. 3b is from 44 μm particle size Fe powder. Three Fe-based samples were fabricated which has relatively high melting temperature of 1100^{O} C (Fig. 4). In addition two other Fe-based samples (Fig. 4) were sintered using two different laser radiations. The laser parameters for SLS were observed to be a power between 12 to 15 watts cw, a scan speed in between 1 to 2 mm/sec and a layer thickness of 250 μm. The depth of image plane on the powder bed is $\pm$100 μm for λ = 980 and 810 nm. For both the laser the spot size is about 700$\pm$70 μm. During SLS the powder bed temperature varies between $50^{O} \sim 100^{O}$C.

RESULTS

Some examples of preliminary SSF sintered parts with multiple sintered layers made from Fe/Ni-Bronze premix powders are shown in Figs. 2 & 3. It reveals that sintered part from finer particle size powder has more dense packing. Fig. 4 shows near net shape

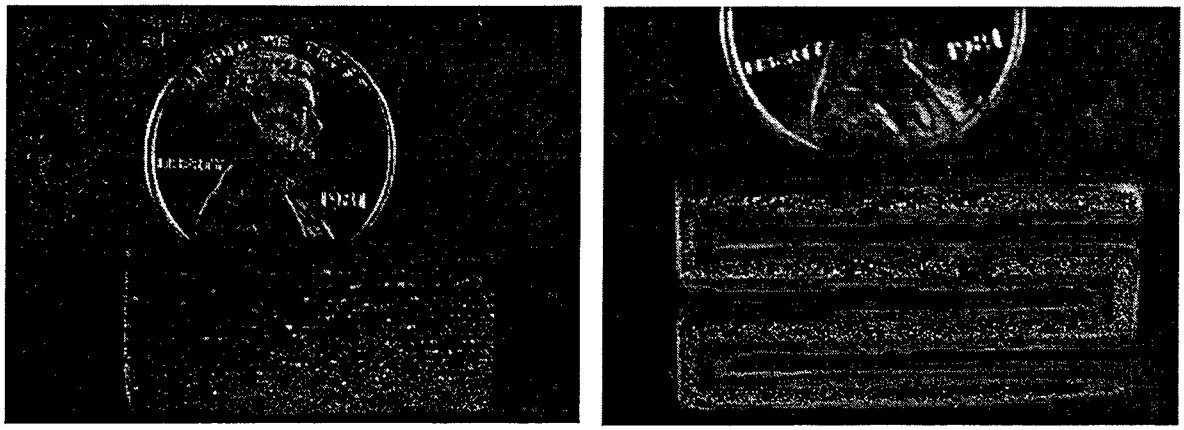


(a)



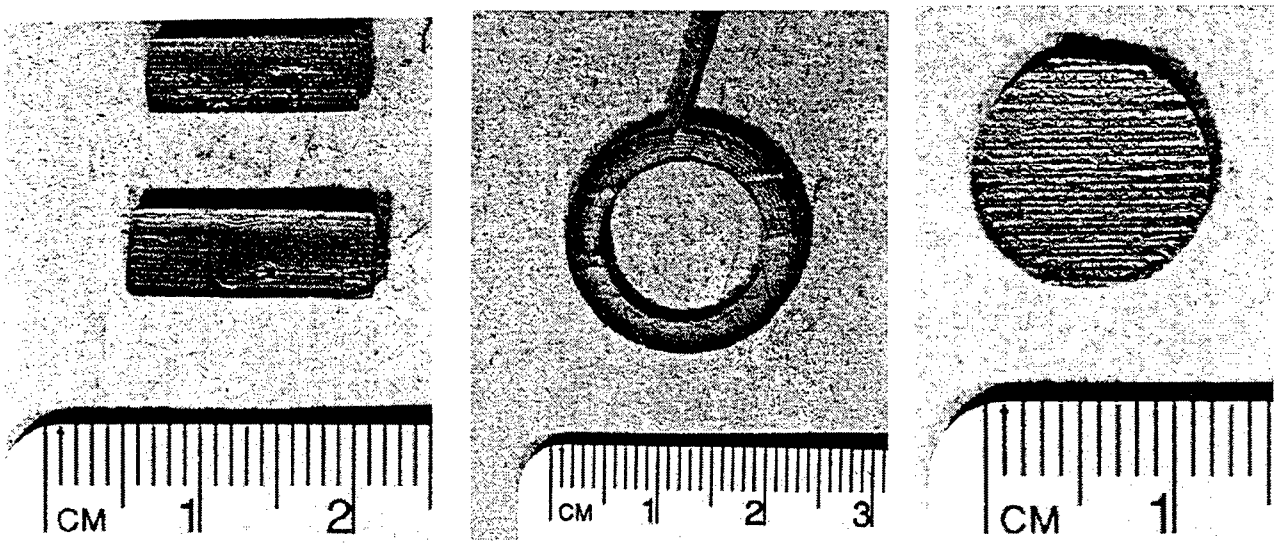
(b)

Figs. 2(a-b) The particle size effects of sintered samples made from iron-bronze premix powder in an argon atmosphere. As powder size decreases from left to right the resolution of SLS parts increases.
Figs. 2(a) Parameters used: λ = 980 nm, SS = 700$\pm$80 μm, SP = 1 mm/sec, Powder size = 44 μm, Power = 12 watts.
Fig. 2(b) Parameters used: λ = 980 nm, SS = 700$\pm$80 μm, SP = 1 mm/sec, Powder size = 150 μm, Power = 15 watts.



(a) (b)

Figs. 3(a-b) The wavelength effects of sintered samples made from iron/bronze premix powder and Fe powder in an argon atmosphere.
Fig. 3(a) Parameters used: λ = 810 nm, SS = 700$\pm$80 μm, SP = 1 mm/sec, Powder size = 150 μm Fe-Bronze, Power = 14 watts.
Fig. 3(b) Parameters used: λ = 980 nm, SS = 700$\pm$80 μm, SP = 1 mm/sec, Powder size = 150 μm Fe, Power = 14 watts.



(a) (b) (c)

Figs. 4(a-c) The SFF Fe parts melted from 44 μm Fe powder using 810 nm diode laser. The laser spot size was 700$\pm$70 μm carrying 15 watts cw power at a 1 mm/sec scanning speed.

fully dense functional parts. The SFF parts were sintered from 44 μm Fe powder with the aid of 810 nm diode laser. The influence of laser radiation wavelength on quality of sintered parts was also studied. The results are shown in Figs. 3(b) & 4. As the laser wavelength decreases the laser radiation absorbed by the powder increases. Fig. 4 shows complete melting and sintered ring of Fe powder using 810 nm diode laser compared to partial melting and partial sintering of Fe powder (Fig. 3b) where 980 nm laser was used.

Density of SLS Parts

The sintered (Figs. 2 & 3) Fe-Bronze SLS parts made from 44 μm powder, have density of approximately 80% of the theoretical density compared to about 50% density of the 150 μm Fe-Bronze sintered SLS parts. SLS near net shape functional parts (Fig. 4) prepared from 44 μm iron powder using 810 nm diode laser have 90% of the theoretical density.

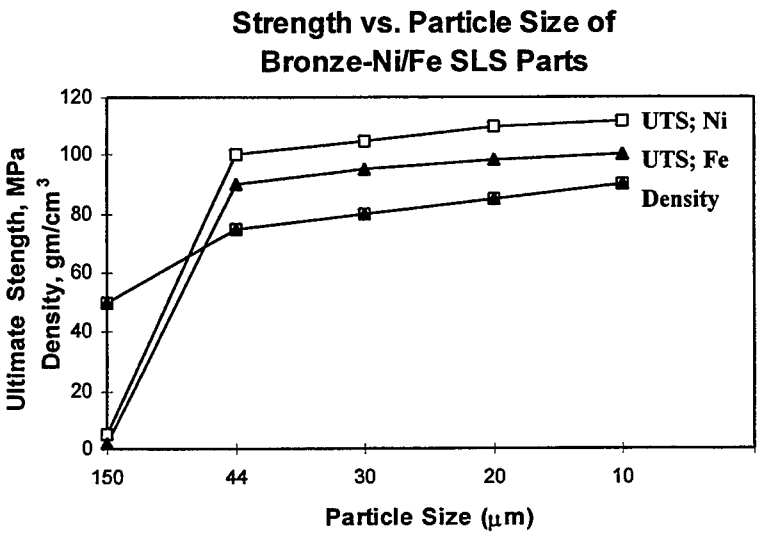


Fig. 5 Ultimate strength and density of Bronze-Ni/Fe powder as a function of particle size.

Strength of SLS Parts

Strength of SLS parts directly depends on the density or porosity. The dependency is similar to the profile which density exhibits with respect to processing parameters (laser scan speed, laser power, etc. Fig. 5). Fig. 5 shows an experimental result of ultimate strength as a function of particle size. From the figure it is evident that as the particle size of a powder decreases the ultimate strength of SLS parts increases. In Fig. 5 we have

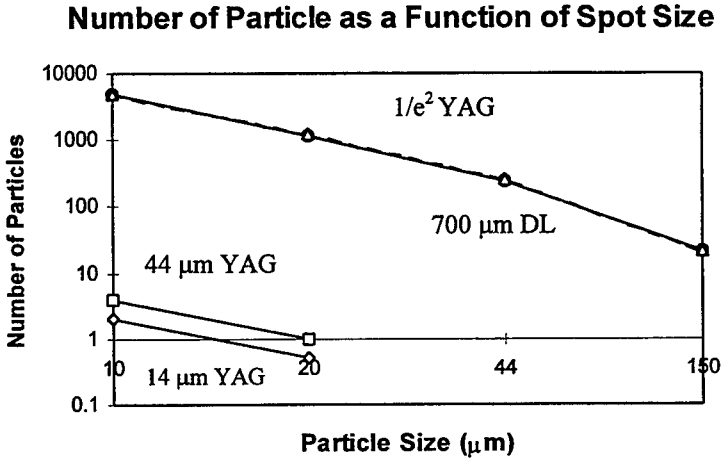


Fig. 6 Number of particles which can be accommodated within the spot area as a function of particle size.

also plotted density as a function of particle size. The density of SLS parts also increases as particle size decreases. Increase of pores reduce the load carrying capacity of the materials. Also pores or microcracks act as a site for stress concentrators for an effective crack's initiation site. Therefore, a SLS sample with density less than 100% is expected to have a strength less than that of a fully dense wrought material. Fractional density is also function of powder characteristics, such as particle size, size and shape distribution, etc. The following equation shows that strength is function of density:

$$\sigma = C\,\sigma_0\,f(\rho); \qquad (3)$$

where ρ is the fractional density of the SLS parts, σ is the strength and σ_0 is the strength for the wrought material. In general,

$$\sigma = C\,\sigma_0\,\rho^m; \qquad (4)$$

where C and m are the material empirical constants for the material.

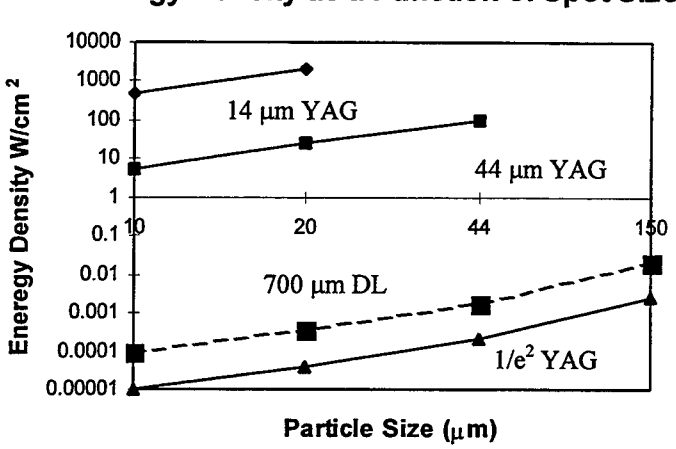


Fig. 7 Energy density per unit particle as a function of particle size

Curling of SLS Parts

In this research we did not observe any curling or bending of the Fe melted or sintered parts or any other Fe-Bronze sintered parts compared with the SLS parts fabricated by CO_2 or YAG lasers. Here we would like to address some of our findings of material photon interaction and their effects on materials properties. Fig. 6 is the calculated graph of total number of particles that can be accommodated inside an area. As the spot size decreases (14 μm YAG corresponds to 14 mm spot size at 10^7 W/cm^2 power density, 44 μm YAG corresponds to 44 μm spot size

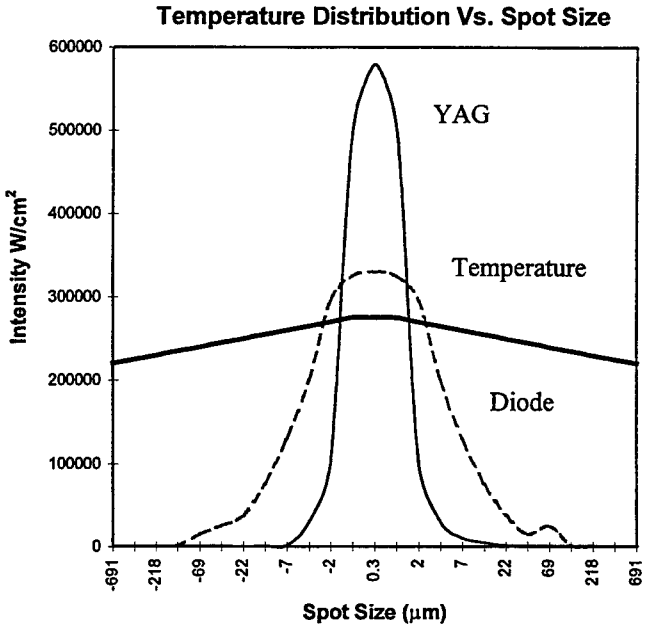


Fig. 8 Comparison of relative temperature distribution of YAG and diode laser as a function of a spot size.

at 10^6 W/cm^2 power density and 700 μm YAG corresponds to spot size at $1/e^2$ power density.), in case of an YAG laser the number of particles also decreases. The spread out powder particle density in an SLS process is about 30% of the calculated particle density. In Fig. 6 we also compared the spot size of a diode laser and the particle density. Fig. 7 is the calculated graph of an experimental value of an energy density. In this graph we are comparing the energy density per unit particle at different spot sizes. For YAG laser, energy density per particle increases as the spot size decreases. Fig. 8 is the relative comparison of temperature distribution of YAG and diode lasers. Diode laser having 700 μm spot size, is about 80% of its energy is within the spot area and just lies above the sintered temperature. If we compare the spot size of the YAG laser, the 80% energy corresponds to 44 μm spot size and the corresponding temperature is about twice higher. The large temperature gradient at the powder bed is the main cause of distortion of the sintered parts.

Energy Density

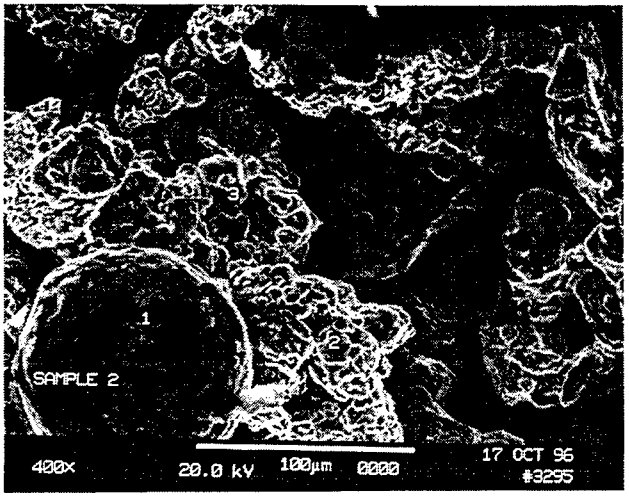
For a given power, density of the SLS Bronze-Fe parts increased as the scan speed and power size decreased. Also the density of the SLS parts is found to increase with increasing laser power for constant scan speed and power size. The higher density of the SLS part is achieved due to an increase of energy input to the per unit powder surface. The higher amount of energy per unit powder surface increases the temperature high enough to result in a large liquid phase formation of the low melting temperature alloy in two phase alloy systems. Bronze powder in a Bronze-Fe system melts incongruently between 870^O C (solidus) and 1030^O C (liquidus). A higher degree of liquid formation is observed as the temperature above the solidus increases. As the temperature increases the viscosity of the molten Bronze decreases which enhances the densification. However, at very high laser power and slow scan speed, significant amount of curling and warping phenomena was observed. Experiments had also been done to find the effect of the type of laser used to fabricate SLS parts. In this study diode (λ = 980 nm) and Nd:YAG (λ = 1060 nm) lasers had been used because both of them have very similar wavelengths. SLS parts fabricated using the YAG laser keeping all other parameters constant have shown significant amount of distortion and less densification compared to the parts fabricated by using the diode laser. There are two fold problems using the YAG laser. One is the wavelength disadvantage; YAG lasers have longer wavelength (1060 nm) compared to that of the diode lasers (810 nm). Which means that the diode laser energy is absorbed much more efficiently by the metallic powders compared to that of the YAG laser. Another one is the spot size disadvantage of the YAG laser over the diode laser. Due to this smaller spot size for YAG laser, powder particles are super-heated, and has large thermal gradient which is the main cause of the part's distortion. In this research we are using a new criterion to define usable energy delivered on per unit powder surface rather than per unit area on powder surface. Fig. 8 shows some temperature distribution of diode and YAG lasers with respect to sintered temperature. These new criteria will normalize the spot size effects between the two types of lasers. By optimizing the processing parameters it is possible to reduce the distortion.

MICROSTRUCTURE and QUALITATIVE MICRO-CHEMICAL ANALYSIS

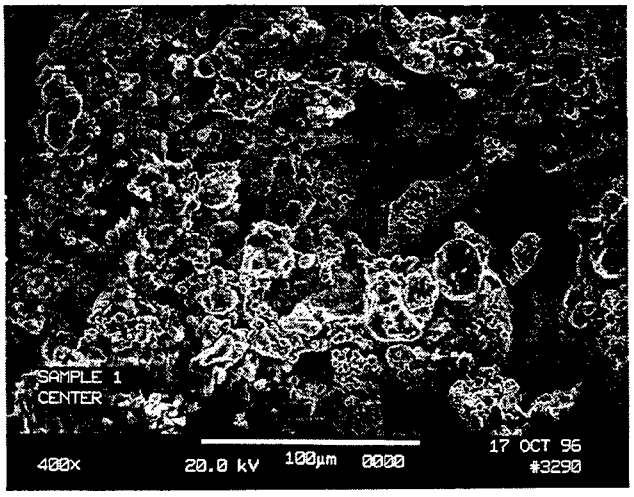
To study the microstructure and to perform qualitative micro-chemical analysis of Fe-Bronze sintered samples, a scanning electron microscope (SEM), model Amray 1830I, with EDS capability was used. Energy dispersive x-ray spectroscopy (EDS) is a qualitative micro-chemical analysis technique with use of equipment attached to the SEM. The EDS analysis was used on different sintered samples to evaluate the degree of homogeneity also.

SFF samples from a coarser (Fe-Bronze) powder with the same power density and wavelength shows less homogenization than the samples prepared from finer powder. Figs. 9(a & c) show typical microstructures of sintered samples made from 150 μm and 44 μm Fe-Bronze powder, respectively. Figs. 9(b & d) are their corresponding EDS spectrogram. The two EDS spectrograms in Fig. 9b were obtained from two different areas of Fig. 9a. Area 1 in Fig. 9a shows mostly copper (Cu) with trace amount of iron (Fe). Areas 2 & 3 in Fig. 9a revealed similar results; mostly iron (Fe) with trace amount of copper (Cu). Fig. 9d shows two other EDS spectrograms obtained from Fig. 9c.

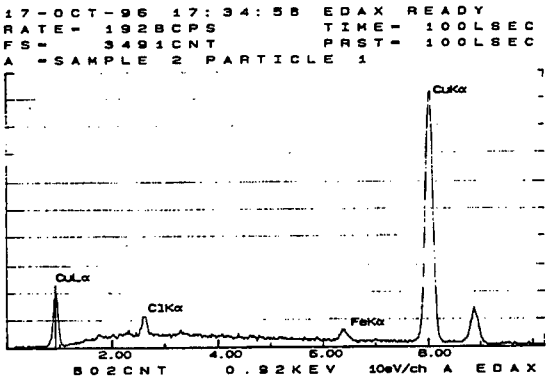
The spectrograms show that two different areas on the sample (Fig. 9c) has same amounts of Cu and Fe with a trace amount of Sn. The Cu-Sn phase diagram shows, prealloyed bronze powder with 6.97% Sn starts melting at around 800^{O} C. The complete melting of the system is at around 1000^{O} C. There is no existence of any binary or ternary phases in the Fe-Cu-Sn phase diagram. Comparisons of the spectrograms (Figs. 9b and 9d) reveal that finer powder shows more melting and homogenization compared to coarser pre-alloyed Fe-Bronze powder. In the coarse powder Fe and Cu stay separately.

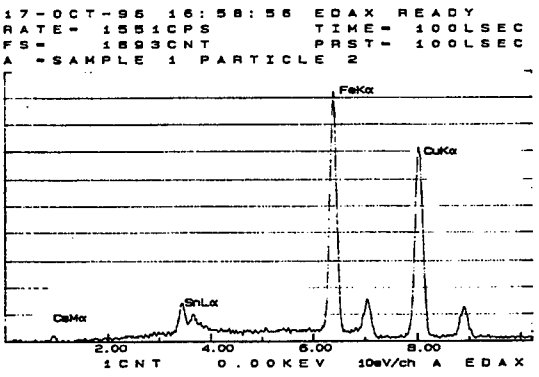


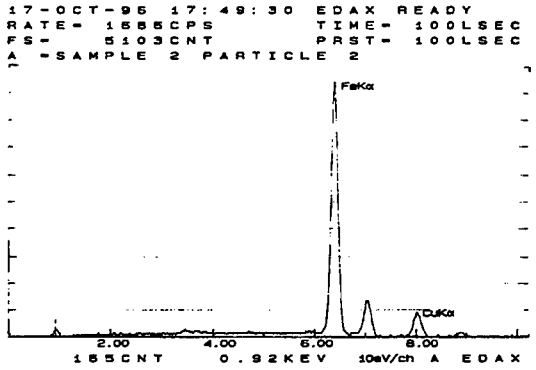
(a)



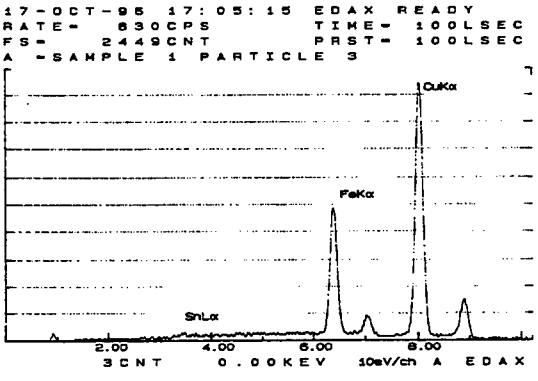
(c)







(b)



(d)

Fig. 9(a-d) is the SEM micrograph and EDAX of the Fe-Bronze premix powder at two different particle size.
Fig. 9(a) is the SEM micrograph of sintered Fe-Bronze parts. The powder size was 150 µm. Fig. 9(b) is the EDAX at two different particles of Fig. 9(a).
Fig. 9(c) is the SEM micrograph of sintered Fe-Bronze parts. The powder size was 44 µm. Fig. 9(d) is the EDAX at two different particles of Fig. 9(c).

OTHER RELATED WORKS

LASAMOCVD

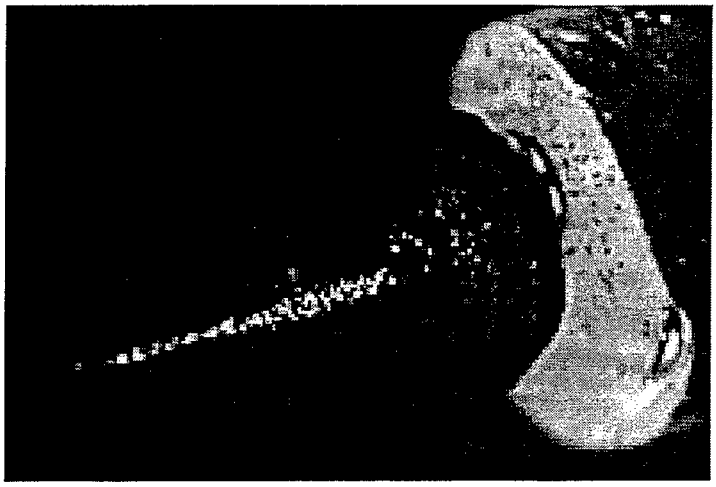


Fig. 10 SiC Rod Fabricated using LASAMOCVD techniques using diode laser, spot size = 600 μm, power cw = 12 watts, pressure = 25 torr TMS; time = 30 min, rod length = 10 mm, rod dia. at base = 700 μm and at top = 100 μm

Laser assisted selective area metal organic chemical vapor deposition (LASAMOCVD) is a locally controlled chemical vapor deposition (CVD) technique. There are two types LASAMOCVD, (1) pyrolytic and (2) photolytic. In pyroltic reaction, infrared diode laser beam interacts with the substrate to produce hot spot where thermally assisted chemical reactions take place. The film material is the decomposition product of the gas precursor. The film stick ton the substrate due to chemisorption processes. In the pyrolytic processes, the chemical reactions are usually takes place at the interface or just above the interface of the substrate. The selection of the precursors for LASAMOCVD is such that the decomposition temperature must be below the substrate melting temperature. The quality of the film or rod depends upon the precursor deposition temperature. Lower decomposition temperatures have a better film or rod quality. At DTM research lab at the University of Connecticut (Fig. 10), we had grown an amorphous and crystalline SiC, Si_3N_4 and graded SiC to Si_3N_4 rod of 1 to 2 mm diameter and 1 cm long. The volumetric deposition rate from $10^4 \sim 10^9$ micron/sec this corresponds to rod growth rate is of the order of mm/sec. For SiC rod fabrication, the gas precursor was tetramethylsilane (TMS) and for Si_3N_4, TMS and Ammonia (NH_4). Diode laser was used as a source of thermal energy for the decomposition of the gas. The solid decomposition products from the decomposition of the gas precursors by a laser beam in an atmospheric controlled chamber follow the laser beam profile. Therefore, the shape of the reaction products can be manipulated by beam steering, shaping, spot size controlling and beam scanning over the substrate on which deposition takes place. The decomposition of the gas takes place according to the following reactions:

For SiC: *Thermal Energy*

$$Si(CH_3)_4(g)[TMS] \xrightarrow{\text{Thermal Energy}} SiC(s) + 3CH_4$$

For Si_3N_4 *Thermal Energy*

$$3Si(CH_3)_4(g)[TMS] + 4NH_4\ [Ammonia] \xrightarrow{\text{Thermal Energy}} Si_3N_4 + 12CH_4 + 2H_2$$

Soldering

Laser beam soldered joints were made using Applied Optronics 30 watts cw (λ = 980 nm) fiber coupled diode laser, Fig. 11. The laser power and the soldering time were 7w and 1s, respectively. After soldering the joints were evaluated with binocular microscope to look for any damage or imperfections. Then a cross-section was cut and mounted in epoxy to facilitate optical microscope examination. No apparent damage was observed at a magnification of up to 500x. The microstructure and the wetting of the solder and substrate were good.

The microhardness of the bulk solder joint was measured using a knoop indentor, 20-gm load.

The values are:

Solder	Hardness Number
60Sn-40Pb	Knoop 18
97Sn-3Ag	Knoop 20

60Sn-40Pb (soft solder): The 60Sn-40Pb alloy has a two phase microstructure that consists of small dendrites of lead rich solid solution in a matrix of finer globular tin-lead eutectic. At a magnification of 500X there was no evidence of any intermetallic phase of Cu-Sn at the interface.

97Sn-3Ag: The microstructure consists of light color polygranular grains of tin-rich solid solution in a matrix of lamellar eutectic consisting of tin and Ag_3Sn intermetallic phase. There is no evidence of presence of any intermetallic phase of Cu-Sn in the microstructure. The micrographs revealed that there were no cracks, microcracks or pores present at the solder interfaces.

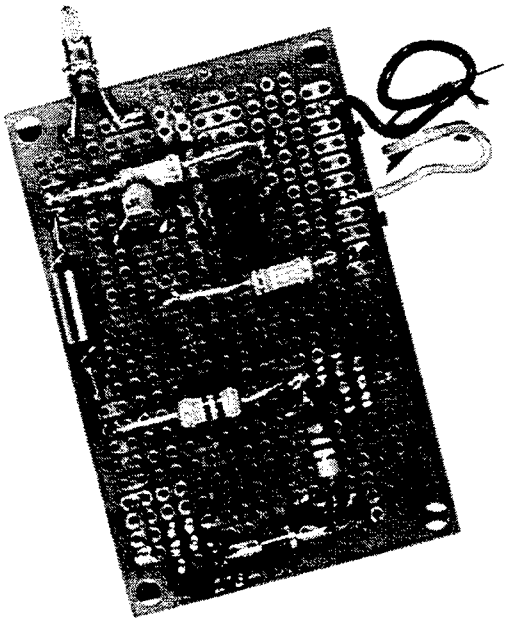


Fig. 11. High power diode laser soldering for electronic component assembly

Ultimate Breaking Strength (UBS)

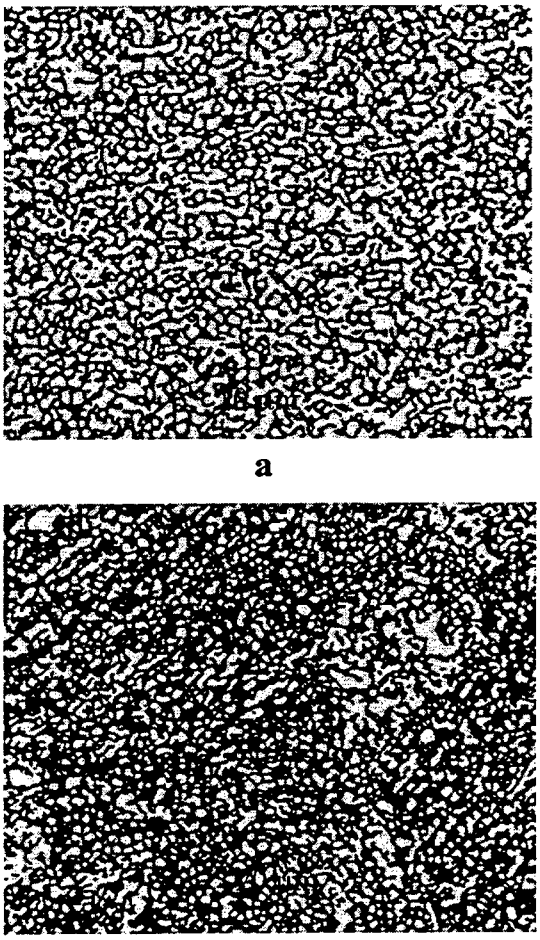
The ultimate breaking strength for both the samples were measured. The samples failed from the substrate-solder interface. For Sn-Pb sample UBS was 730 lb/cm^2 and that for Sn-Ag was 790 lb/cm^2.

Depending upon the demands of electronics applications the lower melting temperature can accommodate larger amount of strain due to mechanical or thermal stress. However,

where the dimensionality and stability of the joint is important the higher melting solder is better.

Transformation Hardening

Fig. 12 shows microstructutes of the stainless steel (a) before and (b) after laser irradiation which demonstrates successful transformation hardening. The phase was transformed from pearlite to martensite, with increased hardness from 30 to 70 in Rockwell C scale.



a

b

Fig.12 SEM micrograph of stainless steel: (a) before heat treatment, Pearlite phase; (b) after heat-treatment, Martensite phase[4]

CONCLUSION

The key success of DTM is the high brightness diode laser and to preserve this brightness when coupled to fiber delivery systems. At present all the commercial diodes use edge emitting technology edge emitting diode has high brightness of the order of 10^6 W/cm^2 at the facet but the coupling is very difficult. The commercial coupling underutilized both the cross section and the numerical aperture of the fiber, the brightness of the coupled power is significantly reduced compare to the original cluster. One high brightness approach is under development in our DTM laboratory, where our group has successfully demonstrated the useful intensity of the order of one to two orders of magnitude improvements. These approach uses one or two dimensional arrays of diode clusters and re-image it at fourrier transform plane to preserve the brightness of the individual clusters and then coupled it to a fiber[2]. Technique based on surface emitting distributed feedback (DFB) high brightness approach is under development at Hughes Danbury Optical Systems (Danbury, CT). At Hughes diode laser investigators have successfully demonstrated two orders of magnitude increase of useful intensity (10^6 W/cm^2) compare to current commercial technology (10^4 W/cm^2). At present our DTM lab has one such system. Power output of such diode laser has 10 watts cw into a spot size of 200 μm at 0.14 NA. By using 4:1 re-imaging unit we can reduce the spot size of the order of 50 μm at 0.5 NA.

Direct SLS of Bronze-Fe/Ni and Fe parts were studied by evaluating the density and microstructure of the parts as a function of processing parameters and powder size. We are particularly excited about our success with diode lasers in direct metal powder sintering, soldering, LASAMOCD for growing devices and other processes. The DTM technology will be capable of rapidly producing intricate, close-tolerance parts, a superior alternative to current prototyping techniques and in the near future will be used as a tool for rapid product development for desk-top manufacturing.

REFERENCES

1. Beam-material interaction spectrum, "Macro-materials processing". Proc. IEEE 70(6), 555-565(1982);C.M Banas and R. Webb.
2. Design Approaches for Laser-Diode Material-Processing Systems Using Fiber and Micro Optics; "Optical Engineering/Nov 1994/ Vol. 33, No. 11; W. Chen, Chandra Roychoudhuri.
3. "Solid Freeform Fabrication Symposium Proceedings 1990-95" Austin, Texas; Harris Marcus, David Bourell, Richard Crawford, Joel Barlow.
4. Potential Role of High power Laser Diode in Manufacturing, "SPIE Photonics West Conference", San Jose, Calofornia, Jan 27, 1996, pp 490/SPIE Vol. 2703; Tariq Manzur, Tony DeMaria, Weiquin Chen, Chandra Roychoudhuri.
5. SFF Using Diode Laser, "Solid Freeform Fabrication Symposium Proceedings 1996" Austin, Texas, pp 363-368; Tariq Manzur, Chandra Roychoudhuri, Harris Marcus.

Progress on Tooling by 3D Printing; Conformal Cooling, Dimensional Control, Surface Finish and Hardness

Emanuel Sachs, Samuel Allen, Honglin Guo, Javier Banos, Michael Cima, James Serdy, and David Brancazio

Massachusetts Institute of Technology
Rm. 35-134
77 Mass Ave
Cambridge, MA 02139
fax: (617) 253-0209
email: sachs@mit.edu

ABSTRACT

Three Dimensional Printing is being applied to the direct fabrication of tooling using metal powders. This paper presents progress updates in four areas: i) thermal management using conformal cooling and related work on enhanced heat transfer using surface textures, ii) data on dimensional control, iii)) improvements in surface finish, and iv) harder tooling.

Conformal cooling has demonstrated significantly improved performance in a production part geometry with simultaneous gains in production rate and part quality obtained as measured against conventional tooling. Surface textures printed on cooling channels have demonstrated 8X enhancement of heat transfer over smooth channels.

A set of 18 tooling inserts was fabricated using hardenable stainless steel powder with a resultant tooling hardness of 25-30 Rockwell C. Harder alloy systems are being designed with the aid of computational thermodynamic tools which allow accurate prediction of the interaction of powder and binder. Significant improvements in surface finish were obtained using improved printing technology. Dimensional control of tools conformed well to the expected result of being dominated by control of shrinkage and being predictable to within ±.25%.

INTRODUCTION

Goals

This work explores the fabrication of tooling directly from a CAD model using the Three Dimensional Printing Process. Following a brief review of the status of the technology, progress updates will be presented in 4 areas:

1) Data on a production application of conformal cooling
2) Data on dimensional control
3) Improvements in surface finish
4) Harder tooling

THREE DIMENSIONAL PRINTING OF TOOLING; TECHNOLOGY STATUS

Direct Printing of Tooling

Three Dimensional Printing involves the selective joining of powder within a layer by ink-jet printing of a binder material. Through the use of metal powders, 3D Printing can be used to create tooling directly from a computer model. The process has the potential to be scaled using multiple nozzle printing technology (an 8-jet printhead is in routine use at MIT) [Ref. 1: Sachs et al., "High Rate, High Quality 3D Printing through Machine Design, On-line Measurement, and Control", *International Journal of Machine Tools & Manufacture,* to be published].

Direct printing of tooling involves the following steps:

1) Print a polymeric binder into stainless or tool-steel powder. This step defines a green part within the powder bed.

2) Remove the loose powder, thereby revealing the green part.

3) Burn out the polymeric binder in a furnace and lightly sinter the part.

4) Infiltrate the part with a copper alloy in a second furnace operation, typically performed at 1100C. At this point, the part is fully dense.

5) Finish the tooling to achieve desired surface finish and dimensions as required.

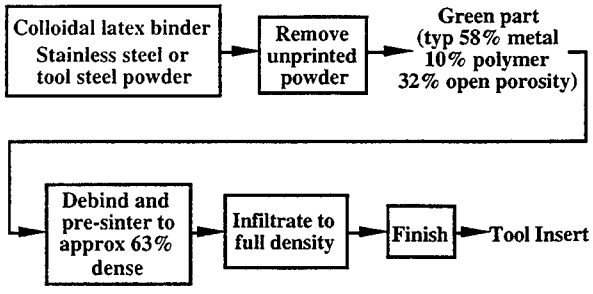


Figure 1. Process sequence for creating tooling directly by 3D Printing.

Recently Fabricated Tool Set

Periodically, a set of tools is fabricated for our industrial sponsors to serve as a benchmark for our process. The project is currently engaged in the fabrication of the third such set of tools. The results presented below and in this paper are derived from the second set of tools made. Figure 2 shows a "family portrait" of 14 of 22 tooling inserts made in the second set of tooling.

The tool inserts in the foreground have been finished and used to inject plastic parts. In materials including glass filled nylon and polycarbonite. Each tool set was designed by a different company and is typically relevant to a different industrial sector. Each company chose to finish the tool set in a different manner ranging from hand polishing to DDM. The tools toward the back of the photo are in earlier stages of processing and some are in the as infiltrated condition. A number of the tool inserts in this photo have conformal cooling channels within them (see section on Conformal Cooling below). All the tools were printed with 420 stainless steel powder and a bronze (90 copper, 10 tin) infiltrant. The hardness of these tool inserts is in the range of 25-30 HRC.



Figure 2. A set of tooling inserts printed for various industrial applications. All tools have been infiltrated and approximately half of the tools have been finished and used to inject parts. For scale, the tool in the lower left hand corner is 6" long.

PERFORMANCE OF CONFORMAL COOLING

In past papers [Ref 2: Sachs et al., "Production of Injection Molding Tooling with Conformal Cooling Channels using The Three Dimensional Printing Process", *Solid Freeform Fabrication Symposium Proceedings,* August 7-9, 1995, pp. 448-467] we have reported on the use of cooling

channels conformal to the molding cavity to improve the control of mold temperature and part dimensions in a simple mold cavity used to create a split ring part.

Recent work by an industrial sponsor has extended this approach to a high volume commercial product. Figure 3 shows the outline of the mold cavity with a representation of the serpentine conformal cooling channel printed in place (details are absent at the request of the sponsor). This cavity was run in controlled tests against the cavity used in production with the results summarized in bullet form below.

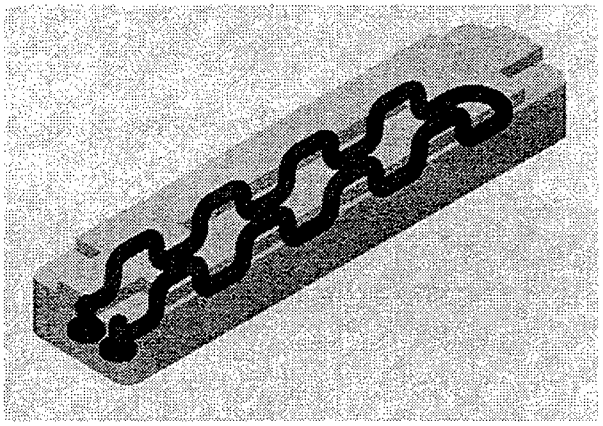


Figure 3. A cavity with a serpentine cooling channel.

- **At one set of molding conditions, a 15% improvement in cycle time was obtained using the 3D Printed cavity with conformal cooling SIMULTANEOUS with a 9% reduction in part distortion.** It was further noted that the factor limiting even further reduction in cycle time in the cavity with conformal cooling was freezing of the sprue and not the cavity itself, thus offering the potential of further cycle time reduction with a runner system redesign.
- **At a second set of molding conditions, a 37% reduction in part distortion was obtained using the 3D Printed cavity with conformal cooling with the same cycle time as the production tool.**

A development related to conformal cooling channels is the use of surface textures for heat transfer augmentation on the inside of channels. A variety of printed patterns were tested. The most successful was the "chevron" shaped ribs shown in Figure 4. It was found that channels printed with the chevron ribs exhibited significant improvements in heat transfer coefficients with water as the working fluid as compared with both as-printed and wire-EDM control channels. Over the full range of 1,500 - 15,000 Reynolds numbers the chevron ribbed showed an 8-fold increase in heat transfer coefficient as compared to the smooth EDM channel and a 4-fold increase as compared to the as-printed channel without ribs. This result is of significance as it would allow for effective cooling of a tool with flow in the laminar regime (with lower pumping requirements and pressures), whereas conventional wisdom dictates that turbulent flow must be maintained.

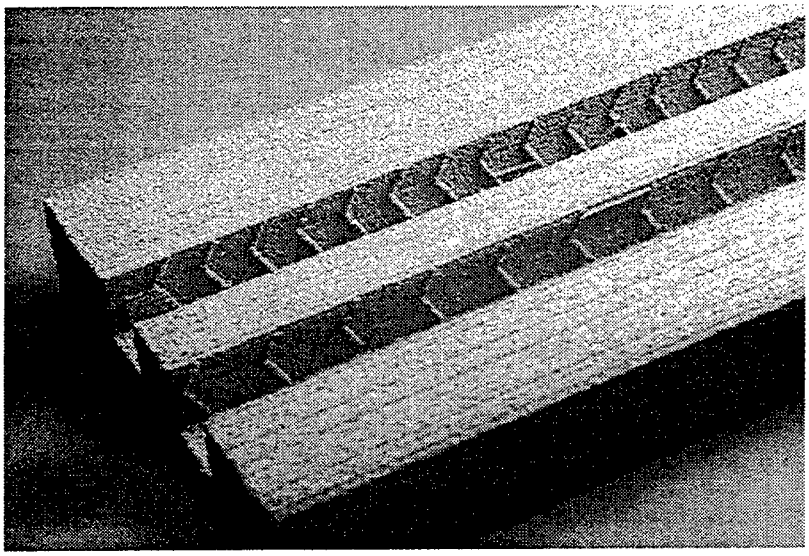


Figure 4. Printed ribs on the interior of 8 mm x 8mm channels for heat transfer augmentation. The ribs are approx. 200 microns high and 500 microns wide.

DIMENSIONAL CONTROL

The dimensional control of tooling made by 3D Printing is governed by the furnace processing steps and in particular by uncertainty in the shrinkage during the sintering operation. During the sintering operation there is some shrinkage of the part which is associated with the formation of a skeleton which can subsequently be infiltrated. The CAD file is "prestreched" by the amount of anticipated shrinkage. A green part is then printed and these green parts have been found to conform quite closely to the "prestreched" CAD dimensions. At the present time, the shrinkage during the sintering step is 1.8 ± .25 % (linear), which represents a nominal shrinkage of 1.8% and an uncertainty in shrinkage of .25%. While the nominal shrinkage can be anticipated by "prestretching" the CAD file, the uncertainty in shrinkage dictates a loss of dimensional control which scales with part dimension.

Based on previous observations, a specification range was created which contemplates a multiplicative error which is expected to scale with part size and an additive error which reflects uncertainty in the location of the edges of the part which is not expected to scale with part size. This spec range is illustrated as the trapezoidal shaded region in Figure 5 where the vertical axis is the error in linear dimension (deviation from desired dimension) of the infiltrated tool and the horizontal axis is the length of a particular dimension. The vertical intercepts represent the additive error while the slope of the top and bottom of the spec range represent the multiplicative error.

Based on previous observations, a specification range was created which contemplates a multiplicative error which is expected to scale with part size and an additive error which reflects uncertainty in the location of the edges of the part which is not expected to scale with part size. This spec range is illustrated as the trapezoidal shaded region in Figure 5 where the vertical axis is the error in linear dimension (deviation from desired dimension) of the infiltrated tool and the horizontal axis is the length of a particular dimension. The vertical intercepts represent the additive error while the slope of the top and bottom of the spec range represent the multiplicative error.

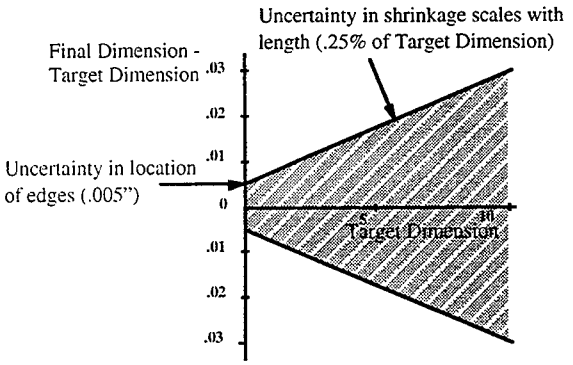


Figure 5. Illustration of the specification range for 3D Printed Tooling.

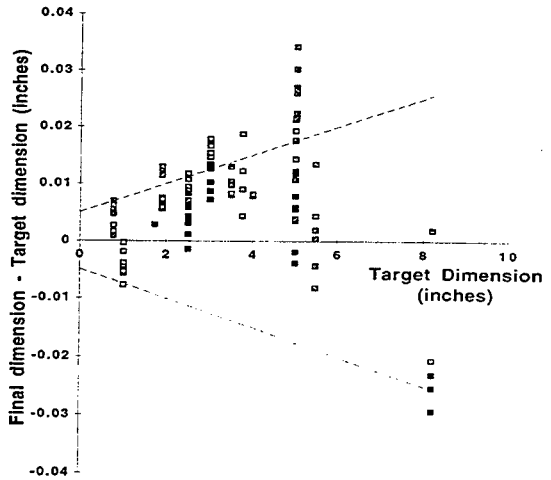


Figure 6. Data on dimensional control of 3D Printed tooling within the print plane.

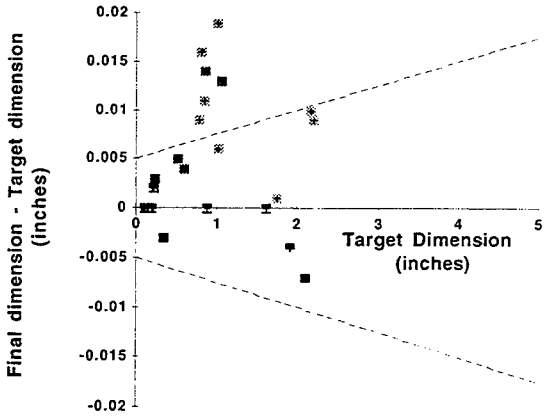


Figure 7. Data on dimensional control of 3D Printed tooling in the vertical axis.

Figure 6 shows data taken on 18 tools in both the fast and slow axes within the print plane. As can be seen, 81 of the 107 data points lie within the anticipated spec range. Figure 7 shows analogous data for the vertical axis. In this case less data is available but the ratio of 15 out of 21 points (on 6 tools) within the spec range is roughly comparable to the in plane print data. While the results were not quite as good as expected, it does seem that we have come close to defining a proper specification range which anticipates the dimensional control of our tooling. Further, it can

be noted that most of the data of Figures 6 and 7 has a positive bias, and so correction of this bias would further improve the results. Nonetheless, the dimensional control of our tooling is not sufficient for net shape tooling inserts (perhaps by a full order of magnitude). Thus, materials systems with substantially improved dimensional control are a major thrust for this project.

SURFACE FINISH

Figure 9 shows a detail area of the cavity geometry of Figure 8 created with two different printing approaches. The detail on the left was created 15 months ago, while the detail to the right was created more recently. The detail to the right illustrates a significant improvement in surface finish which has been achieved by control of the droplet landing position with 10 micron resolution in each of the two in-layer axes (contrast this with 10 micron x 150 micron resolution in the detail at the left). This achievement represents a combination of new printhead hardware, new software used to create the printing instructions from an .STL model and the integration of on-line measurement used to characterize and adapt to changes in the performance of the printhead [Ref. 1].

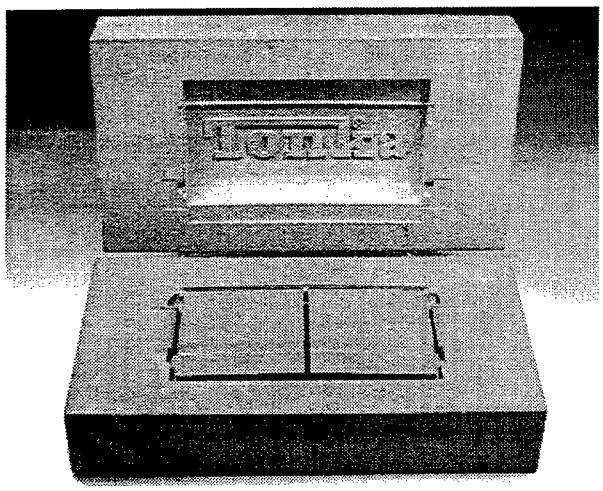


Figure 8. An infiltrated core and cavity set.

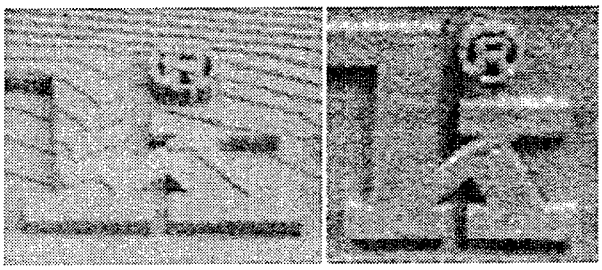


Figure 9. A detailed view of the "k" in the tool of Figure 8 with low resolution (left) and high resolution (right).

HARDER TOOLING

As noted earlier, the current tooling materials system is 420 stainless powder, infiltrated with bronze, a system which produces a Hardness of 25-30 on the Rockwell C scale. However, this hardness is actually the result of a composite system which has particles which are quite hard (HRC 50+) and infiltrant which is much softer (HRB scale).

A goal of the project is to develop materials systems with higher hardness and with greater uniformity of hardness between powder and infiltrant though the use of hardenable infiltrants. However, when the molten infiltrant contacts the powder, mutual solubility and fast the inter-diffusion at the infiltration temperatures can lead to changes in the composition of both powder and

infiltrant resulting in a loss of hardenability of both (as well as possible distortion). Thus, an important goal of the project is to understand the interaction of powder and infiltrant, design materials systems which minimize this interaction, and manage any remaining interaction. Toward this end, a computer-aided alloy design has been used in the 3DP material system selection. The computer modeling can simulate the thermodynamic interaction of the multi-component 3DP system at any temperature. The simulation results show the mole fraction of each phase and the composition of each phase at equilibrium state. In addition, the simulation can also show the melting point of the infiltrant, the phase transformation temperature and the effect of an additive element on the thermodynamic equilibrium.

Good agreement between the computer calculation and experimental result for the interaction of the 420 stainless/bronze system can be seen in the following tables. The tables show the composition of powder and infiltrant before furnace processing, and the changes in composition which are predicted and measured. This tool will now be used to design alloy systems.

Composition of the 420 stainless powder (wt%)

	Fe	Cr	C	Si	Mn	Cu	Ni	Sn
Before infiltration	85	14	0.47	0.37	0.29	-----	-----	-----
After infiltration (measured)	80	13	-----	-----	-----	2.5	3.5	0.15
After infiltration (calculated)	79	12	0.35	-----	-----	5.8	3.4	0.03

Composition of the bronze (Cu-10Sn) infiltrant (wt%)

	Fe	Cr	C	Si	Mn	Cu	Ni	Sn
Before infiltration	-----	-----	-----	-----	-----	85	9	6
After infiltration (measured)	2	0.3	-----	-----	0.2	88	2	7
After infiltration (calculated)	2.5	0.4	-----	-----	-----	89	0.7	7.5

CONCLUSIONS

Three Dimensional Printing is being applied to the fabrication of tooling directly from a computer model using metal powders. This paper presents progress updates in four area: i) harder tooling, ii) improvements in surface finish, iii) data on dimensional control, and iv) production application of conformal cooling. A set of 18 tooling inserts was fabricated using hardenable stainless steel powder with a resultant tooling hardness of 25-30 Rockwell C. Significant improvements in dimensional control were obtained using improved printing technology. Dimensional control of tools conformed well to the expected result of being dominated by control of shrinkage and being predictable to within ±.25%. Conformal cooling has demonstrated significantly improved performance in a production part geometry with simultaneous gains in production rate and part quality obtained. In one case, a simultaneous improvement of 15% in production rate and reduction of part distortion by 9% were obtained. Surface textures fabricated in channels show the potential for 8x improvement of heat transfer over smooth channels. Thermodynamic tools are being used to model the interaction of powder and binder and provide a method for the design of new, harder materials systems.

ACKNOWLEDGMENTS

Support for this work from the Technology Re-Investment Project, Cooperative Agreement (DMI - 9420964), members of the Three Dimensional Printing Industrial Consortium and the DARPA Solid Freeform Fabrication program is gratefully acknowledged.

Measurement of Residual Stresses in Parts Created by Shape Deposition Manufacturing

N.W. Klingbeil, J.W. Zinn and J.L. Beuth
Department of Mechanical Engineering
Carnegie Mellon University
Pittsburgh, PA 15213

Abstract

Residual stress build-up is a concern in any solid freeform fabrication process involving successive deposition of uncured or molten material, due to differential contractions caused by solidification or curing. The most detrimental effect of residual stresses is typically part warping, which can lead to unacceptable losses in part tolerance. In many processes residual stress build-up is a fundamental barrier to the consistent manufacture of high-quality artifacts. In this paper, two methods of measuring residual stresses in parts created by Shape Deposition Manufacturing (SDM) with microcasting are described. First, a technique for measuring warping in deposited plate-shaped specimens is detailed, which can be used to determine residual stress resultants as well as to quantify gross effects of processing changes on residual stress magnitudes. Next, x-ray diffraction procedures are described by which residual stresses in deposited layers can be measured at discrete in-plane locations as a function of depth. Measured results for 308L stainless steel deposits determined from each method are interpreted in the context of residual stress modeling results obtained numerically in a separate research effort. The measured results provide insight into the effects on residual stress of both the material deposition path and the discrete droplet-by-droplet nature of the microcasting deposition process. The insights provided here may also be applicable to other processes involving successive material deposition.

Introduction

The motivating application for this work is Shape Deposition Manufacturing (SDM), a layered manufacturing technique under development at Carnegie Mellon University (Merz *et al.*, 1994) and Stanford University (Fessler *et al.*, 1996). The SDM process involves successive deposition of layers of material and CNC machining of each layer. Applications of SDM include the manufacture of parts that have multiple materials, complex geometries that cannot be machined by conventional methods, and embedded electronic components. An advantage of SDM is that it can directly create fully-dense metal parts using materials such as stainless steel, copper and invar. Fully-dense metallic materials can be deposited in SDM by a number of different techniques, including microcasting, welding and laser deposition. Microcasting involves deposition of macroscopic droplets (1/8"-1/4" in diameter) of molten metal, and is the method of material deposition for which residual stresses are investigated in this study.

As discussed by Prinz *et al.* (1995) and Amon *et al.* (1997), there are a number of processing, thermal and mechanical issues associated with SDM. One of the most fundamental issues is the generation of residual stress, which is inherent in any process involving molten material deposition. Residual stress can lead to warping and loss of tolerance in SDM artifacts, and can also significantly reduce the structural reliability of finished parts. Thermomechanical numerical modeling of residual stress generation in microcasting has been investigated previously at Carnegie Mellon University (Chin *et al.* (1996a), Chin *et al.* (1996b), Chin *et al.* (1995)). In the current study, measurements of residual stress in 308L stainless steel microcast deposits are investigated and the results are interpreted in the context of the numerical modeling. The goals of this work include a better understanding of residual stress distributions in microcast layers, as well as insight into the effects of changes in process parameters on residual stress generation.

Residual stress measurements are obtained in this work by two different methods. The first method is the measurement of warping strains and curvatures in deposited plate structures. Somewhat similar measurements of warping deflections in laser deposited beam-shaped specimens have been described previously by Fessler *et al.* (1996). The procedures for measuring warping in plate specimens are relatively straightforward, and the results can be used to determine residual stress resultants for comparison with the numerical modeling, as well as to investigate gross effects of process changes on residual stress generation. The second (and substantially more complicated) method is x-ray diffraction, which directly determines residual stresses at discrete in-plane locations and depths into the deposit. The two methods are sufficiently independent that they are discussed and related to the numerical modeling separately herein, after which the common observations and the utility of the two methods are summarized. Results from both methods indicate that residual stress distributions in fully dense deposits reflect the droplet-by-droplet nature of the microcasting process.

Warping Measurements

In this section, techniques are discussed for the experimental measurement of warping in plate-shaped deposits. The test configuration is shown in Figure 1. A high temperature biaxial

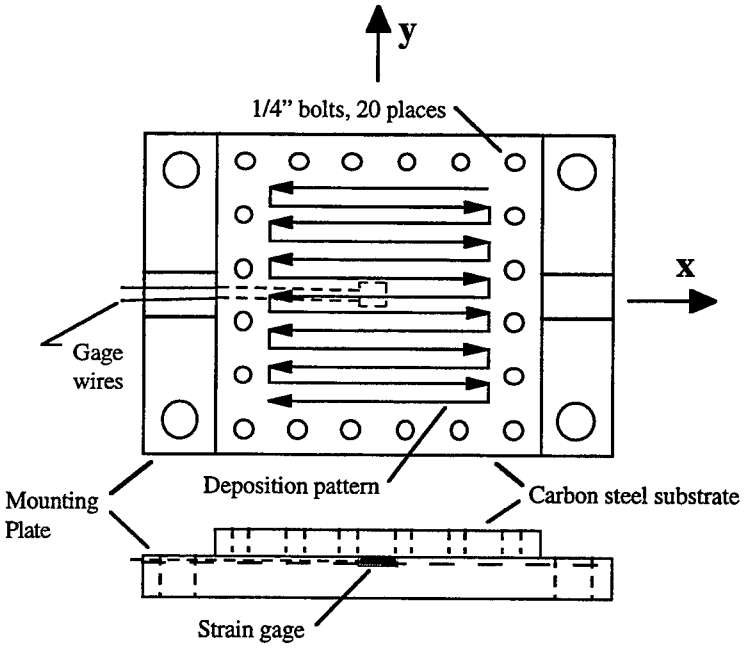


Figure 1. Warping Test Configuration

strain gage is centered on the bottom surface of a 6"x 6"x 1/2" fully-annealed 1018 carbon steel substrate. The steel substrate is then bolted near its edges to a 3/4" thick mounting plate, which is designed to allow for strain gage wires along the bottom of the substrate. The mounting plate is subsequently attached to a comparatively large pallet (not shown in Fig. 1) used in the SDM manufacturing process. The constraint of the pallet and mounting plate prevents warping of the specimen during manufacture. Material is then deposited in a 5" x 5" square onto the top surface of the substrate. For the test results discussed herein, the deposition path is as shown in Fig. 1, where the microcasting begins at the positive x,y corner and continues back and forth parallel to the x direction until ending in the negative x,y corner. Following material deposition, the specimen is allowed to cool to room temperature, and the deposit is machined flat to a thickness of 0.055". This thickness has been found by trial and error to render an essentially void-free deposit. Upon completion, the specimen is unbolted from the pallet and mounting plate, which results in residual

stress-induced warping. The resulting strains ε_x and ε_y in the x and y directions are recorded, and the warping deflections are measured using the coordinate measuring capabilities of the CNC milling machine (accurate to within ± 0.0005"). Deflection measurements are taken at 81 equally-spaced points forming a 4.0" x 4.0" grid centered on the surface of the deposit.

Although the initial residual stress state results from high temperature nonlinear material response, the warping of finished specimens is dominated by elastic unloading. As a result, specimen warping can be interpreted in the context of linear elastic plate theory. The plate curvatures $w_{,xx}$ and $w_{,yy}$ in the x and y directions are estimated by quadratic curve fits of the measured deflections. In the event that the effects of in-plane shrinkage are small compared to bending, the measured strains ε_x and ε_y are proportional to the curvatures and supply redundant information. The bending stress resultants per unit width M_x and M_y are related to the curvatures $w_{,xx}$ and $w_{,yy}$ by the plate theory relations

$$M_x = \frac{EI}{1-\nu^2}\left(w_{,xx}+\nu w_{,yy}\right),\ M_y = \frac{EI}{1-\nu^2}\left(w_{,yy}+\nu w_{,xx}\right), \qquad (1)$$

where E is the elastic modulus, ν is Poisson's ratio and I is the cross sectional moment of inertia per unit width. Application of eq. (1) assumes a negligible difference in elastic properties between the deposit and substrate, which is the case for stainless steel deposited onto carbon steel. Suitable relations for bending of layered plates composed of multiple dissimilar materials can be obtained as outlined by Pister and Dong (1952).

The procedures described above were used in obtaining sufficiently repeatable results for three specimens in which 308L stainless steel was microcast onto 1018 carbon steel substrates. A representative plot of measured specimen warping deflections is shown in Figure 2. Plots of the deflections taken through the center of the plate (along y = 0 and x = 0) are shown in Figure 3, from which quadratic curve fits were used to obtain the curvatures $w_{,xx}$ and $w_{,yy}$ in the x and y directions, respectively. A summary of the measured strains, curvatures and corresponding bending stress resultants for the three specimens is contained in Table 1. Note that the measured strains correspond well with the measured curvatures, indicating that the strains due to in-plane shrinkage are indeed small compared to the bending strains. Also, it is apparent from Table 1 that the calculated bending stress resultants M_x and M_y are relatively insensitive to variations in the measured curvatures, and are thus highly repeatable.

Some important insights into the effects of the material deposition path are evident from the test results. It is most noteworthy that for all three specimens, the strains and curvatures in Table 1 are larger in the x direction than in the y direction. In light of the deposition path shown in Fig. 1, this indicates that warping is more severe parallel to the direction of material deposition. This result suggests that for part geometries that are long in a particular direction, the maximum warping deflections might be reduced by depositing material in a path perpendicular to that direction. In addition, the curvature $w_{,xx}$ for the specimen of Fig. 2 was obtained as a function of y and was seen to decrease with decreasing values of y. In fact, the curvature $w_{,xx}$ at y = –2.0" was 20% less than its value at y = +2.0". Considering the deposition path of Fig. 1, it is apparent that warping in the direction of material deposition decreases as the total amount of deposited material increases. This result is in keeping with the expectation that substrate preheating occurring during material deposition tends to lessen the thermal mismatch, which ultimately leads to reduced warping. It is expected that alternative deposition paths could be used to achieve more uniform warping and/or reductions in part warping in critical directions.

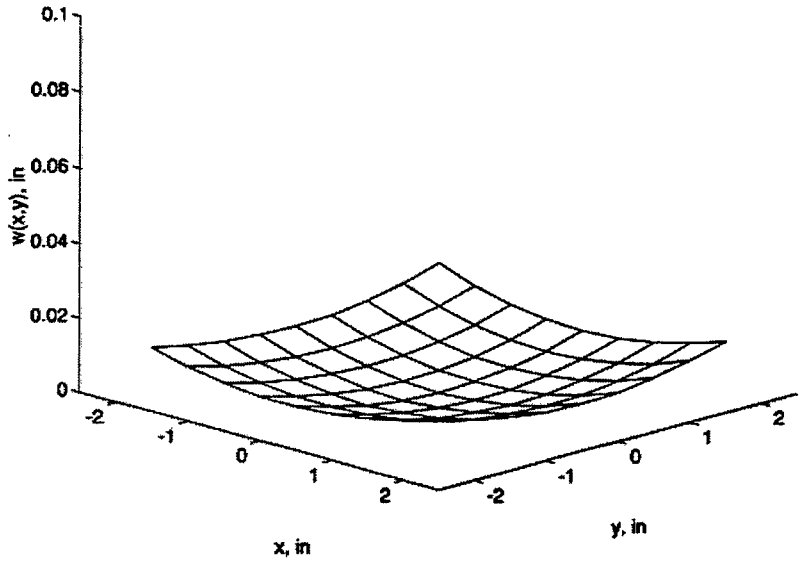


Figure 2. Measured Deflections for Specimen #1

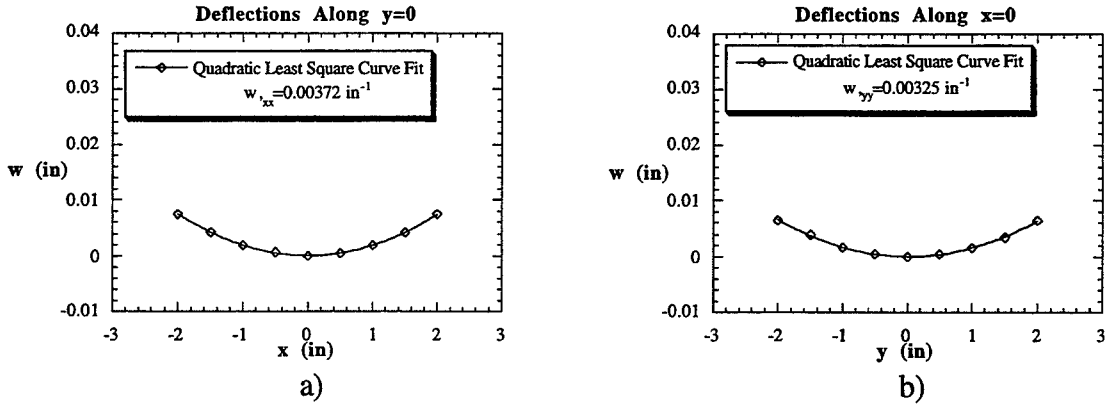


Figure 3. Quadratic Curve Fits for Specimen #1 Along a)y = 0 and b)x = 0

Table 1. Warping Test Results for Stainless Steel Microcast onto Carbon Steel

Specimen #	ε_x ($\mu\varepsilon$)	ε_y ($\mu\varepsilon$)	$w_{,xx}$ (in^{-1})	$w_{,yy}$ (in^{-1})	M_x ($in \cdot lb/in$)	M_y ($in \cdot lb/in$)
1	865	746	0.00372	0.00325	1.81×10^3	1.69×10^3
2	1010	697	0.00412	0.00295	1.93×10^3	1.62×10^3
3	931	703	0.00403	0.00322	1.93×10^3	1.71×10^3
Average Values	934	715	0.00395	0.00314	1.89×10^3	1.67×10^3

The warping measurements described above have been interpreted in the context of the 1-D thermomechanical residual stress modeling of Chin *et al.* (1996a). The 1-D results approximate the maximum residual stresses located along the centerline of a microcast droplet, away from the free edges. As a result, the 1-D results can be used to obtain an upper bound for the residual stress resultants corresponding to the case of an entire layer of material deposited at once. As discussed by Chin *et al.* (1996a), accurate high-temperature constitutive modeling is difficult, and the numerical results are merely estimates. However, 1-D numerical residual stress results for a geometry similar to that used in the experiments render a bending stress resultant equal to 3.94×10^3 in·lb/in, which corresponds to a curvature equal to 0.00681 in^{-1} and a strain on the substrate bottom equal to 1860 με. These values are on the order of twice the average measured values in Table 1. This result suggests that even in fully-dense microcast deposits, the effects of the droplet-by-droplet nature of the microcasting process are substantial, so that the average stress resultants are significantly less than those predicted by the 1-D model.

X-ray Diffraction Measurements

While plate warping measurements provide significant information regarding trends in residual stress resultants, they are unable to determine exact distributions of residual stresses in deposited layers. To this end, x-ray diffraction methods have also been used to measure residual stresses in deposited stainless steel. Determination of residual stress by x-ray diffraction is based on the measurement of changes in interplanar spacings between lattice planes in crystalline materials. In the interest of brevity, the details of x-ray diffraction theory are not addressed here. Background information on x-ray diffraction can be found in the book by Cullity (1978). The procedures for measurement of residual stress by x-ray diffraction are significantly more involved than those for measuring warping, and substantial care must be taken in both specimen preparation and calibration of the x-ray equipment. Standards for measurement of residual stress by x-ray diffraction include SAE J784a (1971) and ASTM E915-90 (1990).

In this study, a number of x-ray diffraction specimens were created to measure residual stress as a function of depth in microcast 308L stainless steel deposits. The results discussed in this section are for the specimen depicted in Figure 4. The specimen was cut from a larger deposit

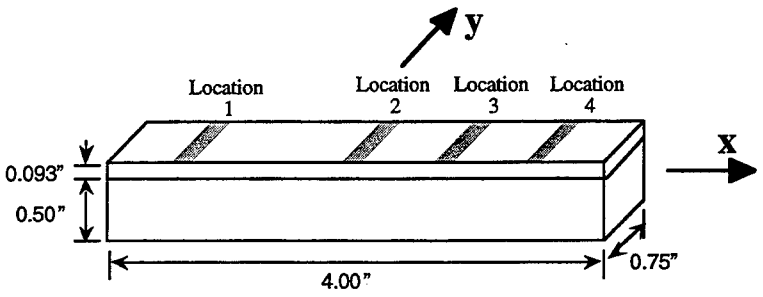


Figure 4. X-ray Diffraction Specimen Geometry

to in-plane dimensions of 0.75" x 4", with its length parallel to the direction of material deposition. The machined deposit surface was sanded, polished, and electropolished to remove all machining stresses. Electropolishing was conducted according to the guidelines in the *ASM Metals Handbook* (1973). Residual stresses parallel to the deposition direction were measured at 5 different depths into the deposited layer by removing thin layers of material through electropolishing. In order to investigate the possibility of local variations in residual stresses, results were obtained at 4 different locations along the length of the specimen.

Table 2 contains a summary of measured residual stresses at each depth for each location. As discussed in the previous section, a microcast deposit must be machined to roughly 0.055" in

order to be completely void free. In order to obtain stresses closer to the top of the deposit, this specimen was machined to a deposit thickness of approximately 0.0930" (which corresponds to a roughly 50% void-free surface) and then electropolished to Depth 1. Stresses were measured at Locations 1 and 3 for the first two depths, since these locations had no voids in the irradiated area. After the third depth, the specimen surface was over 80% void-free allowing stresses to be measured at Locations 1,2 and 4, which were more evenly spaced.

Table 2. X-ray Diffraction Measurements at Various Locations and Depths into the Deposit

Depth	Location 1		Location 2		Location 3		Location 4	
	Thickness,in	Stress,ksi	Thickness,in	Stress,ksi	Thickness,in	Stress,ksi	Thickness,in	Stress,ksi
Initial - 50% Voids	0.5915				0.5930			
Depth 1	0.5882	-95.6			0.5892	-58.6		
Depth 2	0.5871	-67.5			0.5880	-38.0		
Depth 3	0.5763	-21.5	0.5754	-33.3			0.5801	-45.0
Depth 4	0.5723	-10.6	0.5711	-8.56			0.5759	-25.8
Depth 5	0.5656	6.65	0.5647	15.9			0.5677	3.92

The general trend observed in the measured stresses at Locations 1, 2, 3, and 4, is that moving deeper beneath the surface of the deposit causes stresses to become more tensile and stress gradients to become less severe. Although there is some difference in stress magnitudes, there is generally good agreement between the stress gradients at the different locations. There is less in-plane variation in the measured stresses deeper into the deposit, which is likely due to the averaging of stresses by the overlapping of deposited droplets. The measured results indicate that there are two regimes of stress gradients in the deposit. Near the top of the deposit where high void concentrations exist, larger stress gradients of roughly -20,000 ksi/in are present. At greater depths where few voids are present, stress gradients of approximately -3,000 ksi/in are measured.

Figure 5 provides a plot of residual stresses as a function of depth at Location 1 as measured in the relaxed specimen and also as calculated for the same specimen with a bolted constraint. The bolted constraint on the substrate is modeled as a uniform edge moment, so that unbolting the substrate corresponds to the release of this moment. Thus, the stresses in the constrained deposit can be calculated by superimposing the measured stresses in the free specimen with the stresses produced by re-applying the released bending moment. The released moment M can be calculated from the curvature K using the beam-theory relationship $M = EIK$. A measured curvature equal to 0.005324 in^{-1} indicated a relaxed moment equal to 2082 $in \cdot lb$. Thus, bending stresses produced by a 2082 $in \cdot lb$ moment were added to the stresses measured in Layer I to obtain the stress distribution in the constrained specimen.

In addition to the 1-D numerical model previously discussed, a 2-D model for the distribution of residual stress resulting from the deposition of a single molten droplet is outlined in Chin *et al.* (1996a). The results for the 2-D model of a single deposited droplet on a clamped substrate predict high stress gradients along the droplet centerline, near the top of the droplet. The high stress gradients in the 2-D model result from the traction-free boundaries of the deposited droplet, which reduce the constraint applied to the droplet centerline. Figure 6 depicts representative 2-D numerical results for radial stresses along the centerline of a semi-spherical, stainless steel droplet deposited onto a 0.50 inch thick carbon steel substrate. Note the similarity between the gradients in the measured stresses of Fig. 5 and the gradients in the computed stresses

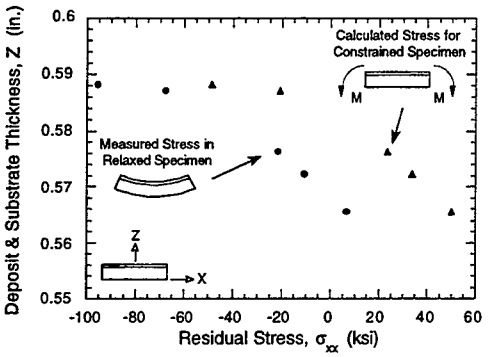


Figure 5. Measured Stress Distribution (Location 1)

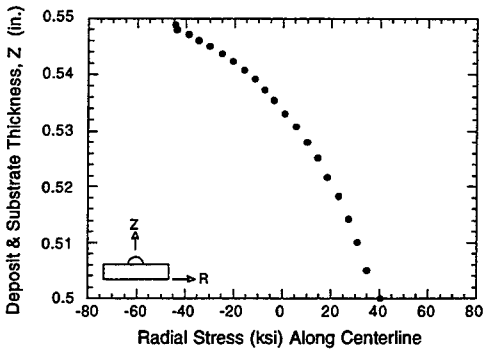


Figure 6. 2-D Model Stress Distribution

of Fig. 6. The numerical results predict stress gradients of -5,700 ksi/in in the top of the droplet and -2,700 ksi/in in the middle of the droplet. The measured stress gradients near the top of the deposit are higher than those predicted by the 2-D model, however the numerical predictions are comparable to the measured stress gradients at greater depths into the deposit. Thus, the stress gradients measured using x-ray diffraction indicate that the droplet-by-droplet nature of the microcasting process is reflected in the stress distributions of fully dense deposits, as was also seen in the warping test results of the previous section. This observation is also in keeping with the findings of Klingbeil and Beuth (1997), in which variations in interfacial fracture toughness were observed in microcast stainless steel/copper interfaces.

Conclusions

In this study, two methods for measuring residual stresses in microcast 308L stainless steel SDM deposits have been outlined. First, techniques for measuring warping in plate-shaped deposits have been described. These techniques are useful in determining gross effects of process changes on residual stress magnitudes, which is the focus of ongoing research. The results discussed in this paper indicate that warping is more severe parallel to the direction of material deposition, and that different material deposition paths might be used to decrease warping in critical directions or to obtain more uniform warping. The measured warping strains and curvatures are significantly lower than those predicted using results from a 1-D thermomechanical numerical model, which is likely a consequence of the droplet-by-droplet nature of the microcasting process. Residual stress measurements have also been obtained by x-ray diffraction. X-ray diffraction measurements have illustrated significant in-plane variations in residual stresses and residual stress gradients as a function of depth into the deposit. Good agreement has been observed between the measured stress gradients and those predicted by 2-D numerical modeling, which strongly suggests that the measured gradients are due to free-edge effects in deposited droplets. Thus, results from both the warping and x-ray diffraction testing suggest that effects of the droplet-by-droplet nature of the microcasting process exist even in fully dense microcast layers.

Acknowledgments

The authors gratefully acknowledge financial support from the Engineering Design Research Center, an Engineering Research Center of the National Science Foundation under Grant EEC-8943164, the National Science Foundation Graduate Research Traineeship Program under Grant EID-9256665 and the Office of Naval Research under Grant 96PR03703-00.

References

Amon, C.H., Beuth, J.L., Merz, R., Prinz, F.B. and Weiss, L.E., 1997, "Shape Deposition Manufacturing with Microcasting: Processing, Thermal and Mechanical Issues," submitted to the *Journal of Manufacturing Science and Engineering*.

ASM Metals Handbook, 1973, Vol. 8, T. Lyman *et al.*, eds., American Society for Metals.

ASTM Standard E915-90, 1990, *Annual Book of ASTM Standards*, Vol. 03.01, American Society for Testing Materials.

Chin, R.K., Beuth, J.L., and Amon, C.H., 1996a, "Thermomechanical Modeling of Molten Metal Droplet Solidification Applied to Layered Manufacturing," *Mechanics of Materials*, Vol. 24, pp. 257-271.

Chin, R.K., Beuth, J.L. and Amon, C.H., 1996b, "Thermomechanical Modeling of Successive Material Deposition in Layered Manufacturing," *Proc. 1996 Solid Freeform Fabrication Symposium* (D.L. Bourell, J.J. Beaman, H.L. Marcus, R.H. Crawford, and J.W. Barlow, eds.), Austin, August 1996, pp. 507-515.

Chin, R.K., Beuth, J.L. and Amon, C.H., 1995, "Control of Residual Thermal Stresses in Shape Deposition Manufacturing," *Proc. 1995 Solid Freeform Fabrication Symposium* (H.L. Marcus, J.J. Beaman, D.L. Bourell, J.W. Barlow and R.H. Crawford, eds.), Austin, August 1995, pp. 221-228.

Cullity, B.D., 1978, *Elements of X-Ray Diffraction*, 2nd Edition, Reading, Massachusetts, Addison-Wesley Publishing.

Fessler, J.R., Merz, R., Nickel, A.H. and Prinz, F.B., 1996, "Laser Deposition of Metals for Shape Deposition Manufacturing," *Proc. 1996 Solid Freeform Fabrication Symposium* (D.L. Bourell, J.J. Beaman, H.L. Marcus, R.H. Crawford, and J.W. Barlow, eds.), Austin, August 1996, pp. 117-124.

Klingbeil, N.W. and Beuth, J.L., 1997, "Interfacial Fracture Testing of Deposited Metal Layers Under Four-Point Bending," *Engineering Fracture Mechanics,* Vol. 56, No. 1, pp. 113-126.

Merz, R., Prinz, F.B., Ramaswami, K., Terk, M. and Weiss, L.E., 1994, "Shape Deposition Manufacturing," *Proc. 1994 Solid Freeform Fabrication Symposium* (H.L. Marcus, J.J. Beaman, J.W. Barlow, K.L. Bourell and R.H. Crawford eds.), Austin, August 1994, pp. 1-8.

Pister, K.S. and Dong, S.B., 1959, "Elastic Bending of Layered Plates," *ASCE Journal of the Engineering Mechanics Division*, Vol. EM 4, pp. 1-10.

Prinz, F.B, Weiss, L.E., Amon, C.H. and Beuth, J.L., 1995, "Processing, Thermal and Mechanical Issues in Shape Deposition Manufacturing," *Proc. 1995 Solid Freeform Fabrication Symposium* (H.L. Marcus, J.J. Beaman, D.L. Bourell, J.W. Barlow and R.H. Crawford, eds.), Austin, August 1995, pp. 118-129.

SAE J784a, 1971, *Residual Stress Measurement by X-Ray Diffraction*, prepared by the X-Ray Division of the SAE Fatigue Design and Evaluation Committee, Society of Automotive Engineers, Warrendale, PA.

Layered Manufacturing Material Issues for SDM of Polymers and Ceramics

J. W. Kietzman†, A. G. Cooper†, L. E. Weiss‡, L. Schultz‡, J. L. Lombardi§, F. B. Prinz†

†. Stanford University, Stanford CA
‡. Carnegie Mellon University, Pittsburgh PA
§. Advanced Ceramics Research, Tucson AZ

Abstract

Shape Deposition Manufacturing (SDM) is a solid freeform fabrication process which enables the manufacture of structural parts from engineering materials. This paper discusses the requirements and constraints for SDM part and sacrificial support materials, including chemical and physical compatibility, mutual adhesion, low shrinkage, machinability, and support material removability. Polymers and ceramics processed by SDM include polyurethanes, epoxies, polyurethane foams, photocurable acrylics, and green alumina ceramics. SDM compatible support materials include waxes, water-soluble polyacrylate soldermasks, and water-soluble thermoplastics. This paper details the selection of SDM part and support material combinations for the fabrication of polymer prototypes and polymer molds for ceramic prototypes.

Introduction: Shape Deposition Manufacturing and Mold SDM

Shape Deposition Manufacturing (SDM) is a layered manufacturing process involving an iterative combination of material addition and material removal [1,2]. A wide range of materials is available, including metals, polymers, and ceramic powders. These materials are deposited using a variety of deposition processes, depending on the materials. Material removal is accomplished with three-axis or five-axis milling, although other processes such as EDM can be used for conductive materials. SDM requires a part material and a sacrificial support material. The final object is made of part material. The sacrificial support material is used to support overhanging features while the object is being built, and is removed when the object is complete. SDM has been used to make metal and polymer parts through direct material deposition and shaping. Current research focuses on expanding the variety of materials processed by SDM.

A variant process called "Mold SDM" uses SDM to build molds for casting resins. In Mold SDM, a layered mold is fabricated. When the mold is complete, the support material is either dissolved or melted, leaving the mold. After casting, the mold is dissolved or melted, leaving the molded object. Postprocessing operations, including sprue removal, binder removal, or sintering, can be subsequently performed on the object. Figure 1 shows the steps required for the construction of simple parts processed by SDM and Mold SDM. Both polymer and green ceramic parts have been cast using polymer molds and the Mold SDM approach.

Figure 1A. Shape Deposition Manufacturing

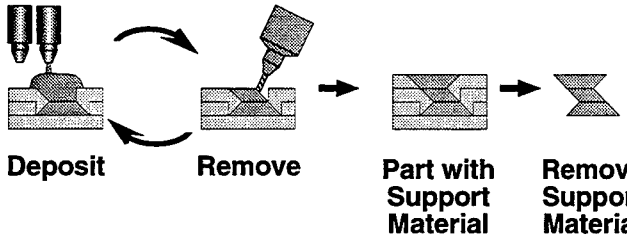
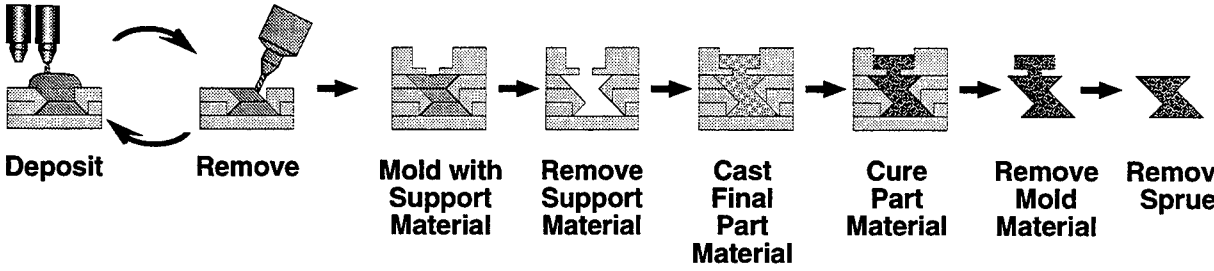


Figure 1B. Mold SDM



Material Requirements for SDM of Polymers

SDM requires compatible part and support materials, subject to the constraints of the deposition and removal processes. Extrusion and casting are the current polymer deposition methods for SDM. Part and support materials must be physically and chemically compatible. These materials must be deposited or cured at temperatures which do not damage previously shaped features. Part and support materials must have minimal intersolubility, and neither material may inhibit curing processes of the other.

In order to build strong parts using SDM, successive layers of part and support materials must exhibit high degrees of cohesion and adhesion. The part and support materials must solidify without the formation of defects, e.g. internal voids. Layers of cast material have the same intralayer properties as in any conventional casting application. Extruded material, however, may exhibit poorer mechanical properties within a layer due to interbead interfaces. To prevent voids during extrusion, either low viscosity material or high extrusion pressure is required to fill sharp interior corners and interbead gaps. In order to obtain high strength parts, the part material must also have good interlayer adhesion.

Distortion and warpage must be minimized to build accurate parts. Shrinkage is commonly encountered during layer solidification or curing, and it is often nonuniform. This shrinkage must be minimized to reduce residual stresses which can result in warpage or delamination [3]. Choosing amorphous rather than crystalline materials helps minimize shrinkage [4]. Preheating previous layers before depositing new material minimizes temperature differentials between old and new material, reducing differential shrinkage of new material as the layers cool. Coefficients of thermal expansion of part and support materials should be similar and as low as possible to reduce thermal distortion.

Besides the material constraints imposed by deposition processes, there are also constraints associated with support material removal. The support material must be removed carefully to avoid damage to the part material. If solvents are employed, they must induce minimal swelling of the support material before dissolving it, or dissolution stresses may crack the part. It is advantageous to use solvents to remove the support material from internal cavities.

Most of the aforementioned constraints on SDM are shared with the other SFF extrusion or jetting processes, e.g. FDM, BPM, Sanders, Actua, and Genisys. These other SFF processes, however, deposit material to net shape. Therefore, their materials' viscosity and solidification characteristics must be optimized for material to bond to previously deposited material while still maintaining its shape. SDM avoids some of these linked constraints by including a material shaping step. This requires the SDM part and support materials to have sufficient strength and stiffness to enable accurate machining. The support material must exhibit smooth surfaces after machining, since its surfaces will be replicated onto later-deposited part material. The part material must exhibit smooth surfaces after replication or machining.

The Mold SDM process has an additional material restriction. The mold material must also be compatible with the final part material cast into it. In particular, these materials must be chemically compatible, and no solidifying or curing part material may react with the mold material. The final part material is, however, not subject to all restrictions on normal SDM part materials. For example, the cast material need not adhere to itself or to the mold material. After casting is done, the mold material must be separable from the part. The need to have two different removable materials (support material and mold material) limits the possible material combinations for Mold SDM compared to conventional SDM. On the other hand, Mold SDM can make parts from materials which could not be processed directly via SDM.

Similar to other SFF processes, there are several practical manufacturing requirements which affect material selection. Cost, ease of use, and robustness must be considered. Deposition processes must produce well-controlled deposits over a wide range of material and process variations. Part throughput and process speed requirements encourage the use of rapid deposition processes with rapid solidification or curing as well as rapid machining rates. Inexpensive materials and simple deposition methods (with inexpensive deposition equipment) are preferable. SDM materials should have long shelf-lives, long pot-lives, as well as low toxicity. The support material and its removal solvents must have low toxicity.

All of the previous process constraints cannot necessarily be satisfied, and compromises must be made. The next section of this paper describes several complementary SDM material combinations. These material combinations have been used successfully in SDM, but material properties of the resulting parts have not yet been measured.

Types of Polymer Material Combinations Processable by SDM

Possible part and support material combinations for SDM of polymers can be categorized based on whether materials are thermoplastic or thermoset. As shown by the matrix in Table 1, there are four possible categories of materials for SDM. A discussion of each is presented below.

	Thermoplastic Support Material	Thermosetting Support Material
Thermoplastic Part Material	Category A Part: Polycarbonate Support: ACR 200	Category B Part: Wax Support: Soldermask
Thermosetting Part Material	Category C Part: Polyurethane Support: Wax	Category D Part: SLA Resin Support: Soldermask

Table 1. Example SDM Material Combinations

Category A: Thermoplastic Part Material and Thermoplastic Support Material

In SDM, heated thermoplastics are deposited by extrusion or casting. For optimal adhesion, surface remelting of previously deposited material is required. If bulk remelting occurs, then previously shaped geometry may be distorted. Materials with compatible melting and softening temperatures must therefore be chosen, and deposition temperatures must be carefully controlled. The support material can be removed by dissolving it or melting it at temperatures below the melting point of the part material.

One SDM material combination entails polycarbonate part material along with ACR 200 support material. ACR 200 is a proprietary non-ionic, water-soluble, machinable thermoplastic obtained from Advanced Ceramics Research in Tucson, AZ. Unfortunately, the high temperatures associated with the extrusion of polycarbonate tend to cause significant softening of ACR 200, producing replicated geometry with poor surface quality. Figure 2 shows an impeller wheel made via SDM using these materials.

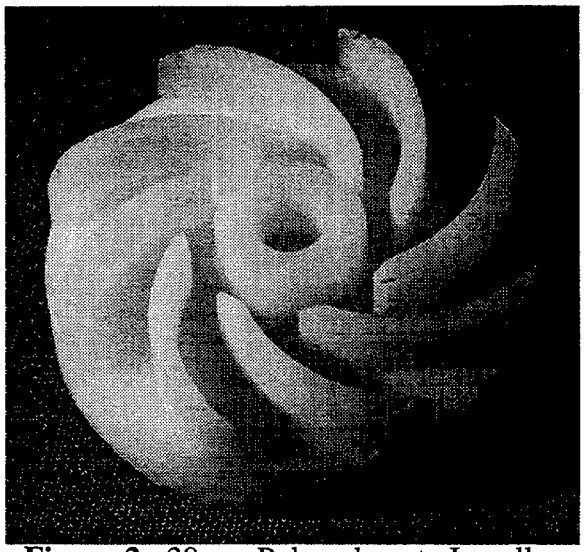


Figure 2. 38mm Polycarbonate Impeller

Category B: Thermoplastic Part Material and Thermosetting Support Material

In SDM, thermoset support material is deposited as a one-part ultraviolet-curing liquid. In this category, the thermosetting support material must be chosen so that its heat of polymerization does not melt the thermoplastic part material. Since thermoset resin does not melt, solvents are required for its removal.

One possible SDM material combination is wax part material and ultraviolet photo-polymerizable soldermask support material [5]. Soldermask is a commercial product used in the printed-circuit-board industry [6]. It is a highly-branched, lightly-crosslinked polymer which has high-temperature stability for short time periods. This makes it able to withstand deposition of hot thermoplastic. Long ultraviolet exposures are required to cure it sufficiently for machinability. Even when cured, this material is relatively brittle and prone to cracking. It is a water-soluble polymer, allowing easy support material removal. While this combination has been used to make molds for the Mold SDM process, it could also be used for polymer parts, e.g. investment-casting patterns.

In the Mold SDM process, wax molds are built using soldermask support material. When the molds are complete, the soldermask is dissolved in water. Gelcasting ceramic slurries [7] or thermoset resins are cast into the molds; these materials are cured with heat if required. The molds are then melted or dissolved. After mold removal, parts are ready for post-processing, e.g. binder burnout and sintering. This method has been used with alumina gelcasting slurries to make ceramic impeller wheels [Figure 3A]. These alumina parts were sintered to a final density of greater than 99%, measured through Archimedes' method. Polymer turbines have been made using castable polyurethane resins [Figure 3B]. These turbines consist of impellers free to spin on shafts.

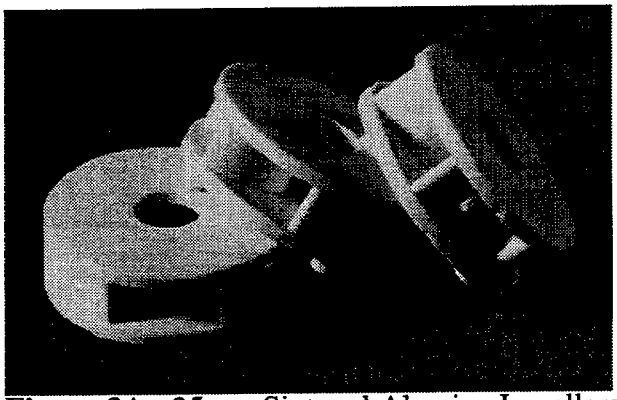


Figure 3A. 25mm Sintered Alumina Impellers



Figure 3B. 30mm Polyurethane Turbines

Category C: Thermosetting Part Material and Thermoplastic Support Material

This material combination has the same properties as the previous one, except that the thermoplastic support material can be removed by melting in lieu of dissolving. SDM materials in this category include two-part castable polyurethane or epoxy part material and wax support material. Either melting or heated solvents are utilized for support material removal. An advantage of this category of materials is the wide variety of castable thermoset resins commercially available for part fabrication. Many different polyurethane and epoxy resins are available, capable of producing parts having a variety of mechanical, chemical, or thermal properties. A limitation of this category of materials is the compromise between process speed and heat generation and shrinkage. Rapidly polymerizing resins are available, but it is difficult to control their polymerization exotherms. These resins exhibit greater shrinkage and severe remelting of the support material. Therefore most SDM parts have been fabricated from resins that polymerize at lower rates.

A series of wearable computers has been made using polyurethane part and wax support materials [8]. One is a waterproof computer which operates while fully immersed [Figure 4A]. Additional work has been done with metal-filled polyurethanes for improved heat transfer and polyurethane foams for improved insulation. Polyurethane and wax materials have been used to make assembled devices with movable parts, like sliding disks restrained by frames [Figure 4B].

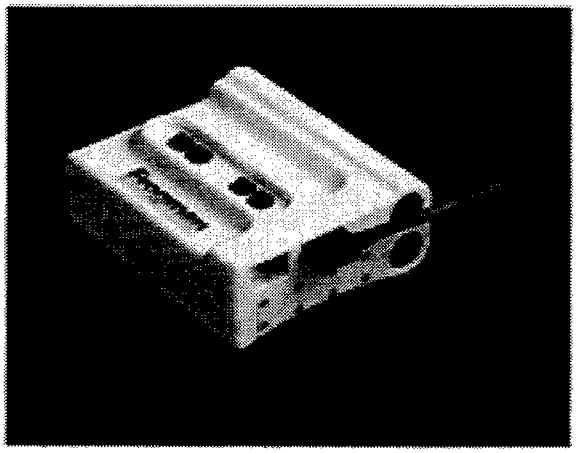


Figure 4A. "Frogman" Computer

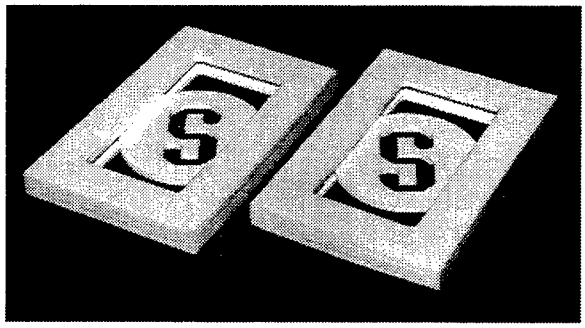


Figure 4B. 75 x 50mm Polyurethane Assemblies

Category D: Thermosetting Part Material and Thermosetting Support Material

In this category, the thermosetting part material must be more highly crosslinked than the support material so that the support material will be more easily swollen and subsequently removed from the part material. An SDM combination from this category is acrylic stereolithography resin part material with soldermask support material. DuPont SOMOS 2100, the part material, is machinable and somewhat flexible. This resin can be thermally postcured to increase its tensile strength, impact strength, and ductility [9]. While epoxy resins have been tested, epoxy part material is chemically incompatible with the acrylic-based soldermask support material. In the SDM process, part and support materials are both cured using ultraviolet flood lamps rather than lasers or other spot-curing light sources. This simplifies the equipment required, but eliminates the possibility of using different curing patterns to reduce shrinkage or tailor properties. An object made from SOMOS 2100 and soldermask is shown in Figure 5. This part duplicates an injection-molding tool made from stainless steel via SDM. A serpentine cooling channel is located in the middle of the part.

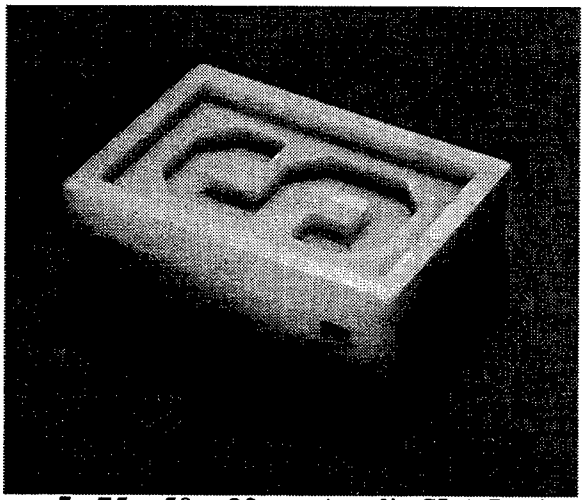


Figure 5. 75 x 50 x 20mm Acrylic SLA Resin Part

Conclusion

Several high quality polymer and ceramic green parts have been fabricated using the SDM and Mold SDM techniques. One successful material combination is castable polyurethane resin with wax support material. Both computer housings and mechanisms with movable parts have been made using these materials. Another successful combination involves wax part material with ultraviolet photo-polymerizable, water-soluble soldermask support material. These materials have been used to make molds for use in the Mold SDM process. Cast polyurethane assemblies and green alumina ceramic parts have been manufactured using this technique.

Current SDM polymer research efforts include both improving materials and interlayer interface quality. Several materials are limited by machinability and shrinkage, especially wax part and support materials. Waxes with good machinability tend to have high solidification shrinkage which causes delamination when building multilayer objects. Waxes with less solidification shrinkage tend to have worse machinability, limiting the achievable feature size. Alternate wax formulations with better compromises between these two properties are being investigated. Soldermask also has machinability limitations due to its brittleness. It often chips during machining unless cutting parameters are chosen carefully. Different curing cycles and improved soldermask formulations are being investigated to resolve this issue. The material combination of polyurethane and wax is also limited by interlayer adhesion; this has led to the use of modified building styles using partial embedding or temporary anchors. We believe that most of these materials issues can be resolved through the identification of improved materials or process steps.

SDM polymer interlayer interface quality is another limitation. For most applications, the issue is not inadequate bonding between layers, but surface finish defects at layer boundaries. Producing smooth surfaces by incrementally depositing and machining successive layers is challenging, especially when the part and support materials exhibit shrinkage upon deposition. Freshly deposited material can cause distortion in previously deposited and shaped material, often producing steps at layer interfaces. Lower-shrinkage materials and additional thermal pre-processing are under investigation in an attempt to alleviate this condition. Another possible solution is characterizing the distortion and modifying shaping processes to correct for it.

Current SDM ceramics research focuses on improving the Mold SDM process and investigating the direct production of green ceramic parts using extrusion processes. Most of the Mold SDM process improvement work revolves around improved materials for polymer molds, as discussed above. Process monitoring and automation are underway so that more repeatable material deposition and greater process throughput can be achieved. The direct deposition and shaping of green ceramic parts is also being investigated to complement the Mold SDM process. Ceramic-filled wax part material and water-soluble support material are being tested.

Acknowledgments

This work was supported by the Defense Advanced Research Projects Agency under contracts N00014-96-I-0625 and DABT63-95-C-0026. Additional support was provided by a National Defense Science and Engineering Graduate Fellowship and a Department of Energy Integrated Manufacturing Pre-Doctoral Fellowship. We would also like to thank Dr. Gennady Neplotnik, Dr. Greg Hilmas, Ronald Cipriani, Tom Hasler, Eric Chamness, and Dr. Robert Merz for their assistance.

Notes

[1] R. Merz, F. B. Prinz, K. Ramaswami, M. Terk, and L. E. Weiss, "Shape Deposition Manufacturing," *Proceedings of the 1994 Solid Freeform Fabrication Symposium,* The University of Texas at Austin, August 1994, pp. 1-8.

[2] F. Prinz and L. Weiss, "Method for Fabrication of Three-Dimensional Articles," U. S. Pat. No. 5,301,415, April 12, 1994.

[3] For a discussion of residual stresses resulting from solidification of metal droplets in SDM, see F. B. Prinz, L. E. Weiss, C. H. Amon, and J. L. Beuth, "Processing, Thermal and Mechanical Issues in Shape Deposition Manufacturing," *Proceedings of the 1994 Solid Freeform Fabrication Symposium,* The University of Texas at Austin, August 1994.

[4] There is a longer discussion of polymer shrinkage issues in J. J. Beaman, J. W. Barlow, D. L. Bourell, R. H. Crawford, H. L. Marcus, and K. P. McAlea, *Solid Freeform Fabrication: A New Direction in Manufacturing,* Dordrecht: Kluwer Academic Publishers, 1997, p. 94.

[5] We have categorized soldermasks as thermosets because they cure via ultraviolet light. Soldermasks are heavily branched and lightly crosslinked polymers which share characteristics of both thermoplastics and thermosets.

[6] Several ultraviolet-curable, water-soluble soldermasks are made commercially: ElectroLite (Danbury, CT) ELC-4497, Dymax (Torrington, CT) 9-20311F, and Tech Spray (Amarillo, TX) Wondermask W-UVA. The ElectroLite and Tech Spray products cure hard while the Dymax product cures soft; intermediate hardnesses are possible by mixing materials before curing them.

[7] M. A. Janney, "Method for Forming Ceramic Powders into Complex Shapes," U. S. Pat. No. 4,894,194, January 16, 1990.

[8] L. Weiss, F. Prinz, G. Neplotnik, K. Padmanabhan, L. Schultz, and R. Merz, "Shape Deposition Manufacturing of Wearable Computers," *Proceedings of the 1996 Solid Freeform Fabrication Symposium,* The University of Texas at Austin, August 1996, pp. 31-38.

[9] "SOMOS 2100 Family" Product Data, Version 1.26.93, DuPont SOMOS Group.

STATISTICAL PROCESS CONTROL FOR SOLID FREEFORM FABRICATION PROCESSES

Vito R. Gervasi
Rapid Prototyping Center,
Milwaukee School of Engineering

ABSTRACT

Statistical process control (SPC) has not been widely used for solid freeform fabrication (SFF) processes, primarily due to the wide diversity of geometries in builds. In addition, typical parts created on SFF platforms are not of simple, nor easy-to- measure geometries, which further complicates the application of SPC. A study is currently in progress to establish a method to apply SPC to SFF. Three SPC test parts were studied to determine the added build cost and accuracy improvement when SPC is applied to stereolithography. In this study, SPC was applied to X & Y shrinkage, and line-width-compensation factors over a period of time. If SPC can be effectively applied, it will alert the operator to otherwise unnoticed system changes before valuable build-time is lost.

INTRODUCTION

With the advent of Solid Freeform Fabrication (SFF) technologies, new manufacturing techniques are emerging. Users of SFF will continue to demand improved accuracy and repeatability for these new manufacturing techniques. Statistical process control (SPC) has not been widely used for SFF, but there is a rising competitive need to improve the quality of SFF processes.

Control-charts are one answer to quality improvement for SFF. Dr. Walter Shewhart of the Western Electric Company developed a control-chart to monitor the manufacture of fuses, heat coils, and station apparatus as early as 1924 [1]. Since this early control-chart, SPC has evolved, and is now widely used to monitor many modern manufacturing processes.

SFF is now being used in roles other than a conceptual three-dimensional printer; for example, it is being used for custom-manufacturing [2], rapid-tooling [3], and medical applications [4]. SFF materials and processes used vary considerably, but each technology has several distinct controllable variables that are key to optimizing quality. The ability to monitor and control these variables must be improved, if SFF is to move to a higher level of manufacturing quality.

In current SFF practice, quality control is accomplished by a periodic evaluation of build parameters by building specific diagnostic parts. For the Fused-Deposition-Modeling (FDM) process, a calibration box [5] is used to calibrate Z-offset. For the Stereolithographic (SLA) process, WINDOWPANES™ and CHRISTMAS-TREES™ [6,7] are used to adjust penetration depth (D_p), critical exposure (E_c), X/Y shrinkage compensation, and line-width-compensation (LWC). For the Laminated-Object-Manufacturing (LOM) Process, a Helisys test part is used to evaluate the build process. In addition to these technology-specific diagnostic parts, several RP-user parts have been developed to compare and evaluate different SFF technologies. Because these diagnostic

parts could be used for SPC, but were not designed for SPC, new SPC designs are needed. Other reasons why SPC charts have not been adopted for SFF include:

- Variation in part geometry from one build to the next.
- Cost of producing a measurable part on each build.
- Variations among SFF technologies.
- Variations in materials used in individual SFF machines.
- Variations in build styles in individual SFF machines.
- Operators and customers who are satisfied with the current quality level.

Since SFF technologies vary widely, SPC must focus on those variables that are critically related to build quality. For FDM, the density of a part may suggest something about the extrusion fusion quality. On the Selective Laser Sintering (SLS), perhaps the flexural modulus of a small nested sample would indicate part quality. For the SLA, the X/Y shrink-factors and LWC that can be monitored to improve accuracy, are the variables focused on in this paper. In the following sections the SPC approach, results, conclusions, and future SPC research are discussed.

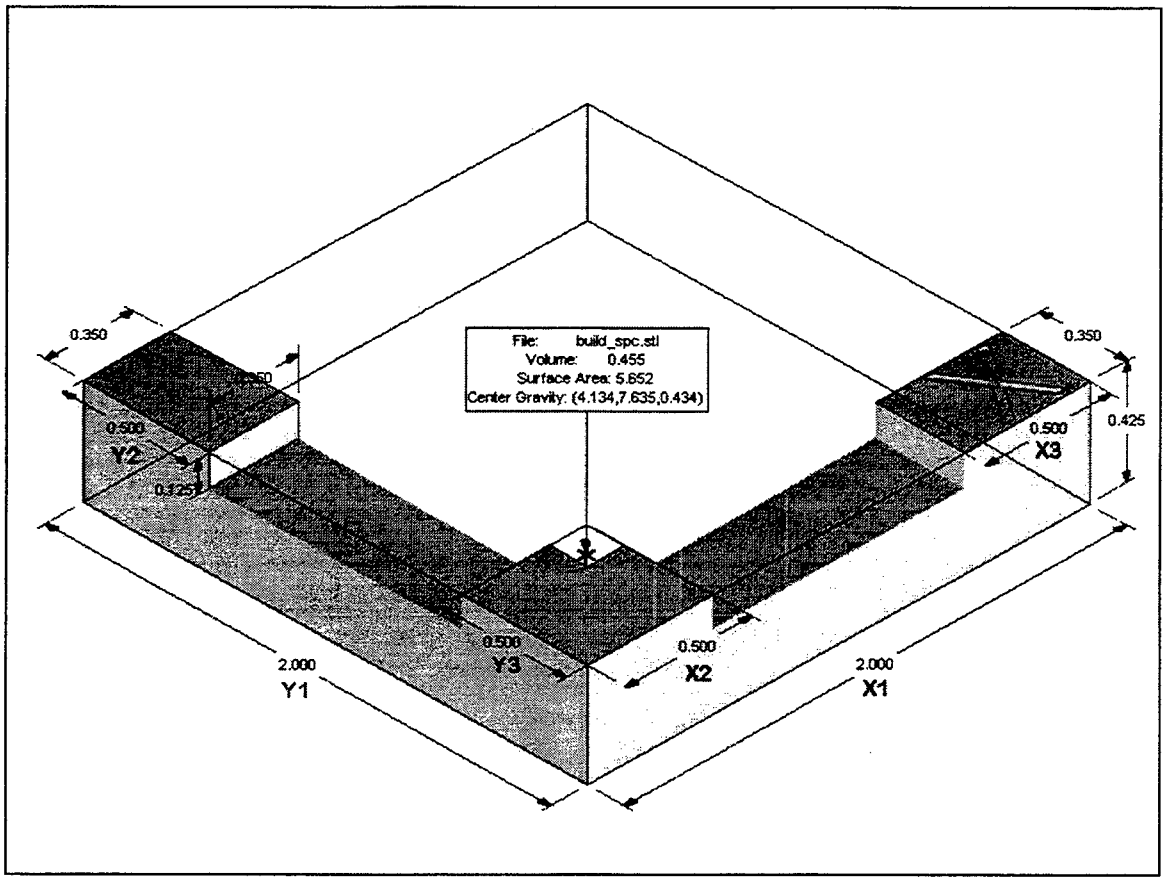


Figure 1. SPC L-block* (units in inches)

SPC APPROACH

The approach to applying SPC to stereolithography reported here, used an Exponential Weighted Moving Average (EWMA[8]) chart, to monitor both X/Y shrinkage-factors and line-width compensation factors. This chart was chosen over conventional X-bar & R charts, due to the EWMA chart's ability to use one test-block per build. The EWMA chart is able to smooth an inherently variant data set, to make trends more apparent. The L-block* shown in Figure 1, was designed to have minimal build volume, while being a fair representation of the entire build. In other words: if all parts on the build were created with the same LWC, layer thickness, and build style, one small L-block will accurately represent the quality of the entire build (neglecting part size and position).

The L-block was randomly positioned with the "X" leg parallel to the X-axis, placed anywhere. For this SPC experiment, the L-blocks were built with 0.006 inch layer-thickness builds, and typically only one copy was created per build. After the build was complete, the L-block was handled as if it were one of the actual parts to be post-processed. TPM and denatured alcohol were used for resin removal, followed by support removal, and ultraviolet light curing. Next, the L-block was measured for the EWMA charts. The following calculations were used to find X_t (the L-block X-axis result) from the average of three measured values of three dimensions (L-block, measurements, and CAD dimensions are illustrated in Figure 1). The target value for X_t was 3.000 inches.

$$X_t = 2\overline{X}_1 - (\overline{X}_2 + \overline{X}_3) \approx 3.000 \text{ inches (target)}$$

Next, the EWMA for X_E was calculated using the following formula:

$$X_E = \omega X_t + (1-\omega) X_{t-1}$$

Where X_E = Exponentially weighted moving average,
X_t = Measured value at time t,
and
ω = Constant for weighting (0 to 1)

After X_E was calculated for 30 L-blocks, the standard deviation and control limits were calculated for the X-axis as follows:

Standard deviation of raw measurements for X-axis calculation:

$$\sigma_E = \sigma_t \sqrt{\frac{\omega}{2-\omega}}$$

Where σ_E = Standard deviation of calculated data
and
σ_t = Standard deviation of raw measurements

Upper and lower control limits for X-axis calculation:

$$UCL = \mu + 3\sigma_E$$
and
$$LCL = \mu - 3\sigma_E$$

Where μ = the average of all X_t values,
UCL = upper control limit,
and
LCL = lower control limit

Next, X_t, X_m, UCL, LCL, and μ values were plotted on the EWMA chart (figures 2). As shown, the UCL, μ, LCL were drawn as straight lines.

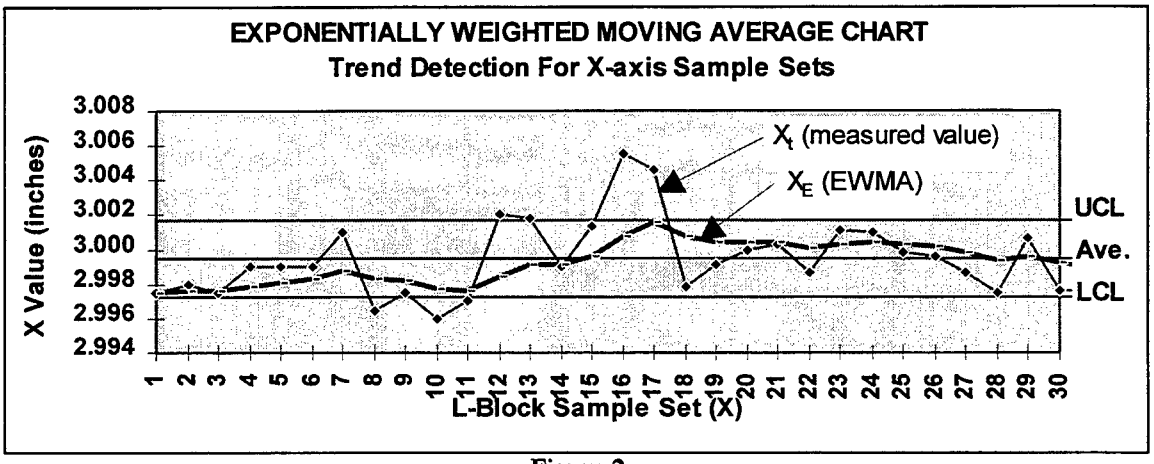


Figure 2

The calculations used to produce the chart for the X-axis measurements were repeated for Y-axis measurements, to generate Figure 3.

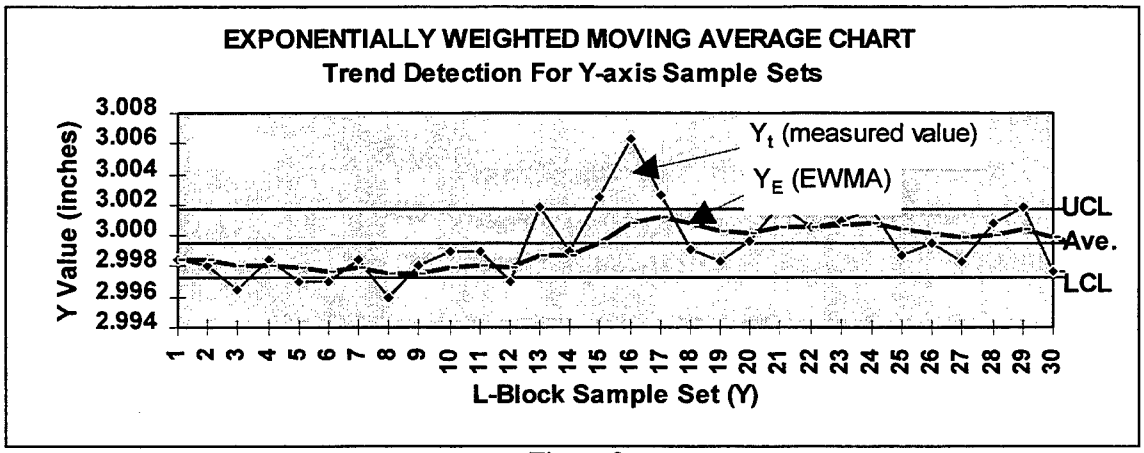


Figure 3

With the control-charts generated, with 30 points for X-axis & Y-axis the standard method for monitoring a control-chart was used. When a point or a series of points showed a trend, the X/Y shrink-factors or LWC were adjusted.

By using a spreadsheet to calculate EWMA, future LWC and shrink-factors were automatically predicted. When the EWMA indicated a trend, the next predicted shrink-factors and LWC (from trend-line) were used for the new settings. To calculate the LWC and shrink-factors the following equations were used:

Line-width-compensation (LWC) calculation:

$$\mathrm{LWC} = \frac{1}{6}(\overline{X}_2 + \overline{X}_3 + \overline{Y}_2 + \overline{Y}_3) - \frac{1}{12}(\overline{X}_1 + \overline{Y}_1) + \mathrm{LWC}_{\mathrm{now}}$$

Where $\mathrm{LWC}_{\mathrm{now}}$ = Current line-width compensation

X-axis shrink-compensation (X_{SC}) Calculation:

$$X_{sc} = 100\left[\left\{\frac{3\{(0.01X_{sc-now}) + 1\}}{\mathrm{X_E}}\right\} - 1\right]$$

X_{sc-now} = Current X shrink factor

Y-axis shrink-compensation (Y_{SC}) Calculation:

$$Y_{sc} = 100\left[\left\{\frac{3\{(0.01Y_{sc-now}) + 1\}}{\mathrm{Y_E}}\right\} - 1\right]$$

Y_{sc-now} = Current Y shrink factor

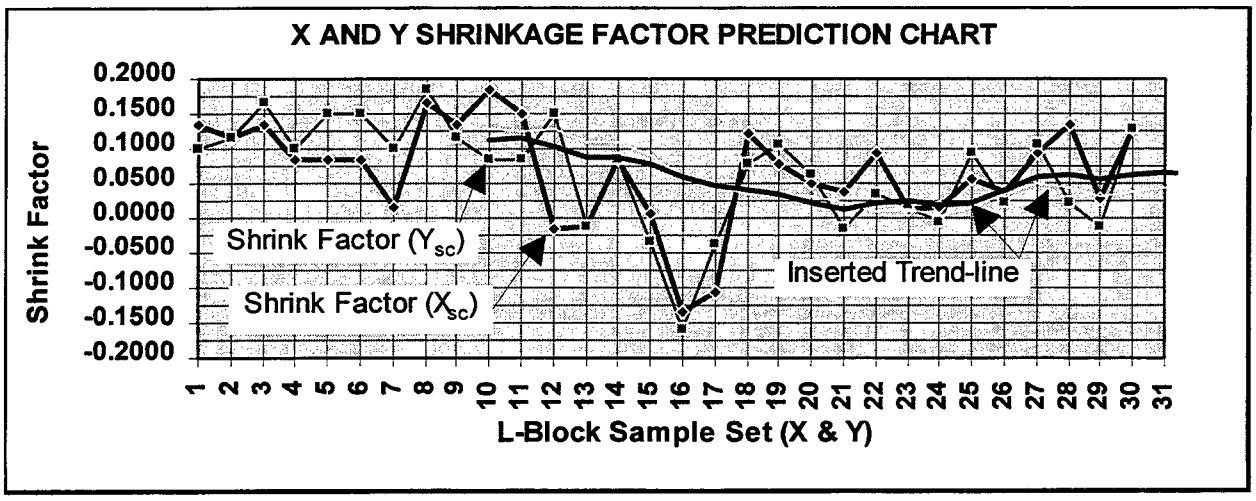


Figure 4

Thirty shrink factors (X & Y) and LWC's were plotted on separate charts as shown in figures 4 and 5. Moving average trend-lines were added to Xsc, Ysc, and LWC plots to predict the best X/Y shrink-factors and LWC for the next build. These numbers were only needed when a trend was detected, although, these values could be used more often to form a feed back loop.

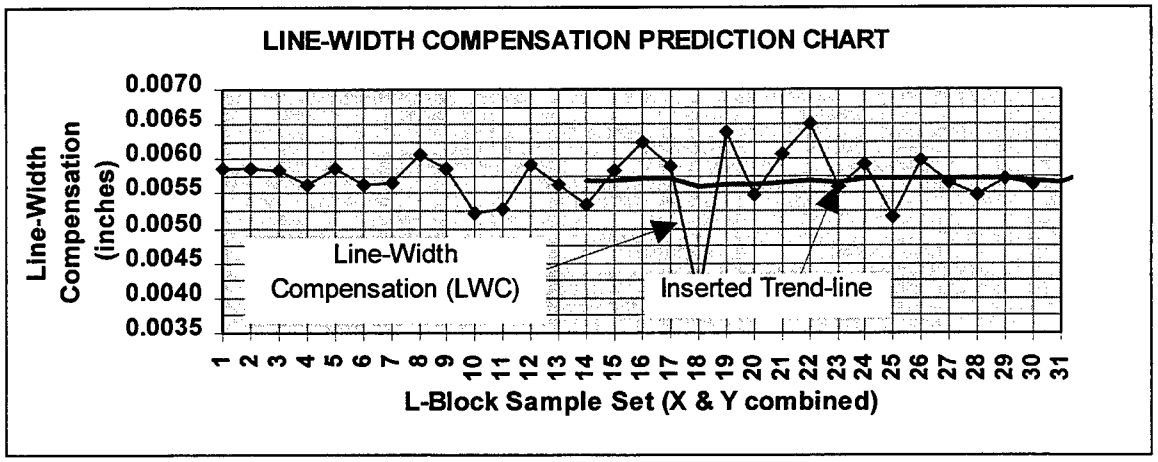


Figure 5

RESULTS/DISCUSSION

The first phase of this study focused on designing a reliable test block, generating 30+ data sets from that test block, applying EWMA chart techniques using the data, and finally predicting future SLA build parameters. A total of three block designs were studied and the final L-block shown in Figure 1 was used to generate the 30 data-sets. The data-sets were used to create the charts shown in figures 2,3,4&5. The results of the first phase of this multi-phase study are discussed below.

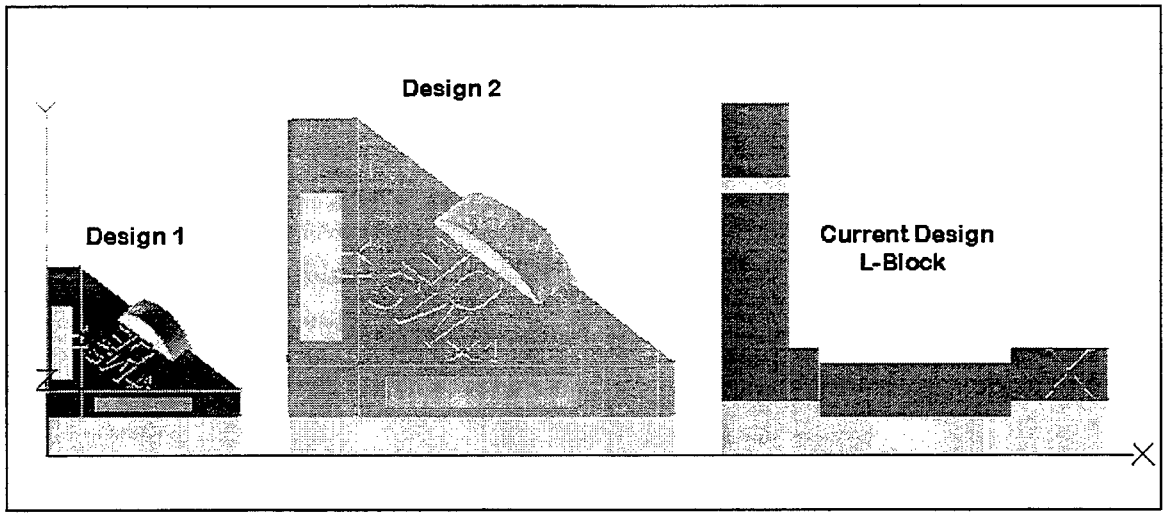


Figure 6. Three SPC Test-block Designs

The three test-block designs were tested for this experiment are illustrated in figure 6. The goal was to find a design that could be easily measured, have minimal volume, and have a minimal foot-print. Yet another important characteristic of the chosen test-block was to have similar results when measured by several people. The first design proved unreliable when different technicians took measurements. The small size caused shrinkage to become too small for accurate results. The second design satisfactory, but the volume and footprint were larger than desired. The L-block did have the best repeatability of measurements by different technicians. The total volume was approximately 0.5 in^3 with a footprint of 2 inches by 2 inches. The L-shaped foot-print worked well, and was easily fit into most builds.

The first two charts (figures 2 & 3) were generated to display the X_t & Y_t (measured) values, X_E & Y_E (EWMA) values, averages, and upper/lower control limits. A weighting constant (ω) of 0.20 was used for X_E and Y_E to produce the smoothed EWMA curves. The value of ω can be adjusted from 0 to 1 to obtain desired smoothing. Interestingly, both curves follow very similar paths. This similarity suggests that the L-block measurements are repeatable and that changes in build accuracy usually occurred in the X and Y simultaneously. The fluctuations of the two EWMA curves were also worth noting. The peak around data point 17, on both charts, apparently was caused by a variable that can be controlled. This may be due to fluctuations in laser power, humidity, resin properties, blade residue, and/or other factors. The main point in this example was that trends like this can be addressed.

The X and Y shrinkage factor prediction chart (Figure 4) was used when an EWMA curve shows a trend. A trend was detected around data set 17, but the trend-line value was very close to the current shrink factor, so no change was made. Again, it is worth noting that both trend lines are surprisingly similar.

The Line-width compensation prediction chart (Figure 5) is also used when an EWMA curve shows a trend. When the trend was detected at data set 17 on both charts a new LWC value was implemented. The previous LWC value was 0.005 inches replaced with 0.006. As shown in the succeeding EWMA chart values (sample sets 18 to 30) this adjustment was successful in increasing accuracy.

CONCLUSIONS/ FUTURE DIRECTION

Statistical Process Control can be used for SFF processes if the critical variables are identified and a means of monitoring these variables is used. In this particular SLA application of SPC it was shown, in one instance, that a trend can be detected and corrected. The EWMA control-chart does seem to fit this application, and perhaps other SFF processes will adopt SPC methods.

The next phase of this study will be to further verify that this SPC chart does signal significant changes in the build process and that they can be corrected. Changes in blade-gap, laser-power, build-style, Z-wait, build size, post-processing, humidity, resin viscosity, resin age, X/Y beam ratio, laser remelts, number of sweeps, and other variables will be studied. In addition, window panes and christmas trees will be performed to learn

whether calibrated Dp and Ec will improve accuracy over time, and to compare the current X/Y shrink-factors and LWC to those derived from the L-block results.

The third phase of this study will be to develop SPC models for several other SFF processes. SPC will be applied to LOM, FDM, and SLS as well as other important characteristics of the SLA. The development of user-friendly software programs and measurement systems will also be developed.

The objective of this SPC effort is to identify methods to improve product quality, and to improve the SFF industry in general.

ACKNOWLEDGEMENTS

The support of the National Science Foundation (EEC-9415345, Rapid Prototyping in Manufacturing Education: Research Based Modular Curriculum) is gratefully acknowledged.

The author would like to thank Dr. Jairus Warner of the Milwaukee School of Engineering for his technical assistance. In addition, appreciation to Sheku Kamara, Candy Barone, and the staff at the Rapid Prototyping Center at MSOE for their time and efforts on this project.

And special thanks to the Rapid Prototyping Consortium members for their involvement in this and other projects.

REFERENCES

1. Wadsworth, Harrison M., Kenneth S. Stephens, A. Blanton Godfrey, *Modern Methods for Quality Control and Improvement,* Malloy Lithographing, Inc, 1986, pp 253 - 256, 416

2. Kardos, Norma Jean, *NASUG Excellence award winner,* Pure Fluid Magic, 1997

3. Venus, Anthony D., Simon J. Van de Crommert, *Manufacturing of Injection Molds with SLS Rapid Tooling,* Rapid Prototyping, Volume 2, No. 3, SME/RPA, third quarter 1996, pp 1 - 5

4. Rovik, Joshua S., *An Additive Fabricator for High-Speed Production of Artificial Limbs*, Fifth International Conference on Rapid Prototyping, 1994, pp. 47-56

5. *FDM System Documentation*, Stratasys, Inc. Eden Prairie, MN, pg. F1650-13

6. *Improving Accuracy,* Rapid Prototyping Report, CAD/CAM Publishing, Inc, January 1993, pp. 4-7

7. *AccuMax™ Toolkit User Guide,* 3D Systems, Valencia, CA

8. Wortham, A.W., G.F. Heinrich, *A Computer Program for Plotting Exponentially Smoothed Average Control Charts,* Journak of Quality Technology, American Society for Quality Control, Vol. 5, No 2, April 1973, 84-90

---

* The L-block and related equations were developed at the Milwaukee School of Engineering Rapid Prototyping Center in March, 1997

NET SHAPE COMPOSITES USING SLA TETRACAST* PATTERNS

Vito R. Gervasi
Rapid Prototyping Center,
Milwaukee School of Engineering

ABSTRACT

Net-shape composites have been a focus of Solid Freeform Fabrication (SFF) for a number of years. A new method to achieve net-shape composites uses hollow Stereolithography (SLA) TetraCast* patterns. The TetraCast* pattern is injected with a filler material consisting of a matrix (typically epoxy) and reinforcement fibers, flakes, and/or particles. Upon solidification of the injected matrix, the net-shape composite is achieved.

Net-shape composites are ideal for custom manufacturing due to the virtually limitless geometry capabilities of SLA. Areas such as aerospace, medical, manufacturing, and others could someday benefit from this process.

Research to date has shown this composite structure to follow the "rule of mixtures." It has also been shown that heat-deflection, elastic-modulus, and tensile-strength can be enhanced and/or predicted in the composite material. Several areas of continuing research include: viscosity limitations, stair-step notch reduction, reinforcement combinations, shrinkage prediction, cooling methods, SLA skin removal, next-generation TetraCast* structures, wear-resistant coatings, process automation, and TetraCast* pattern fill methods.

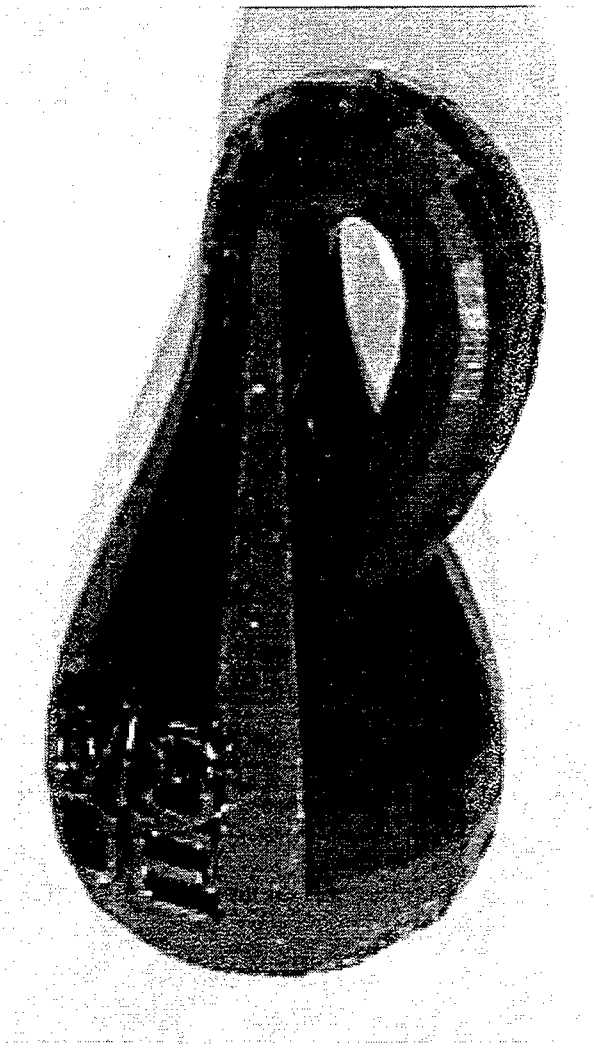


Figure 1. Composite 3D Representation of the Klein Bottle

INTRODUCTION

Net-shape and near-net-shape composite parts are and continue to be a goal of Solid Freeform Fabrication (SFF) technologies. Several methods have been studied to achieve net-shape or near-net-shape composite parts using Laminated Object Manufacturing (LOM) [1,2], Stereolithography (SLA) [3,4,5,6], Fused Deposition Modeling (FDM) [7,8], and other SFF technologies.

Rather than producing the composite directly from SFF, a new method uses SLA TetraCast* [9] patterns to initiate the Rapid Composite Process (RCP**). With this method, the TetraCast* pattern becomes part of the final composite, as it both defines the net-shape of the

desired geometry and embodies the composite material during matrix solidification. The composite material is introduced into the TetraCast* pattern as chopped fibers, flakes, and/or particles suspended in a liquid matrix (typically epoxy). After the TetraCast* pattern is completely filled, the matrix solidifies, resulting in a net-shape functional composite part.

Through this method, the composite material properties can be tailored to meet application requirements of the composite. Parts of virtually any geometry can be produced, as the Klein bottle shown in Figure 1 suggests. This three-dimensional representation of a Klein bottle has internal features, nearly impossible to build any other way, and has a wall thickness of only 0.1 inch. This process may be especially suited for custom-manufacturing of complex, one-of-a-kind, components for aerospace testing, medical equipment, satellite structures, and others.

The goal of this paper is to introduce RCP**, describe the composite formulation, summarize early research findings, and suggest RCP** applications.

RAPID COMPOSITE PROCESS

Figure 2 illustrates the process of generating a net-shape composite using a TetraCast* pattern and composite filler materials. The process consists of 8 steps starting with a CAD drawing and ending with composite finishing as follows:

Step 1. A .stl file is created using the traditional CAD method or reverse engineering via 3D scans.

Step 2. The hollow TetraCast* pattern of the model is then built on the SLA machine.

Step 3. Trapped resin is drained from the TetraCast* pattern by drilling small holes in the skin.

Step 4. The drain holes are sealed followed by a leak check and full ultraviolet light cure.

Step 5. The fill tube is placed into the liquid composite filler material and the system is evacuated.

Step 6. The liquid composite is forced into the vacuum-filled TetraCast* pattern by adding air pressure to the system.

Step 7. After the matrix solidifies the composite is thermally post-cured.

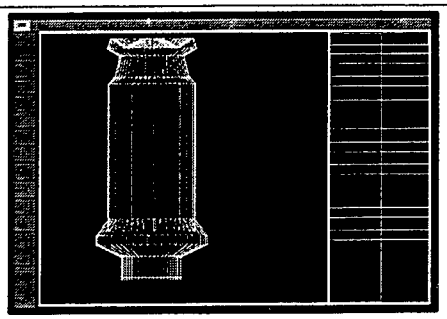
Step 8. Remove supports and finish the net-shape composite.

This process consists mainly of unattended curing time and can be completed in as little as 2 hours of labor including preparation, drainage, filling, and cleanup. In some cases this process can generate solid models in approximately half of the machine time of a solid ACES build (depending on wall thickness and other factors).

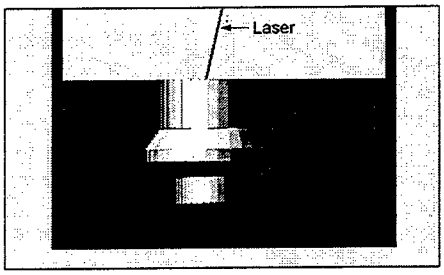
THE COMPOSITE MAKE-UP

The net-shape composite is made up of three main components including: the SLA TetraCast* pattern, resin matrix, and reinforcement. Typically, the resin matrix will be loaded to its limit, taking advantage of the resulting reinforcement mechanical properties.

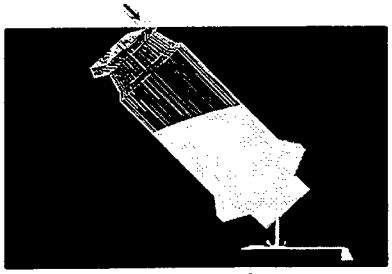
TetraCast* (Figure 3) is an SLA build style invented and developed for both RCP** applications and investment-casting applications. TetraCast* patterns have many of the same benefits and applications of QuickCast™ patterns. TetraCast* uses an internal three-dimensional tetrahedron structure modeled after the molecular bond geometry found in diamonds. The TetraCast* internal structure offers the SLA skin maximum support and



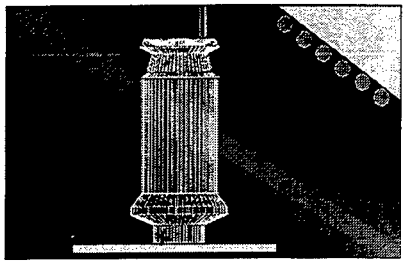
Step 1. Create .stl file



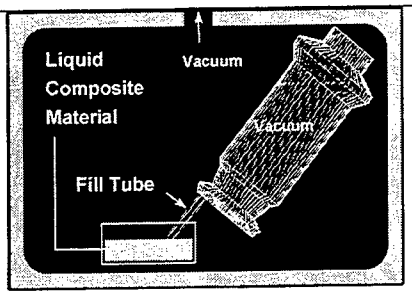
Step 2. Create Tetra Cast pattern on SLA



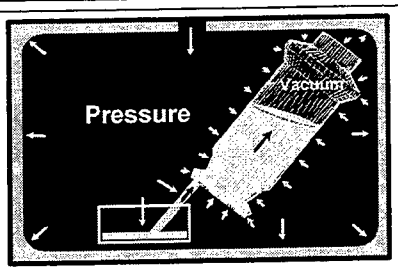
Step 3. Drain trapped photopolymer in T. C. pattern



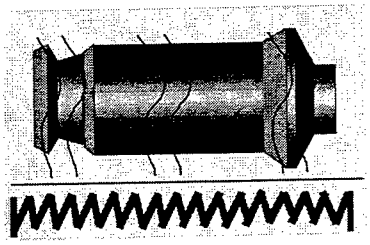
Step 4. Cure T. C. pattern with ultraviolet light and patch leaks



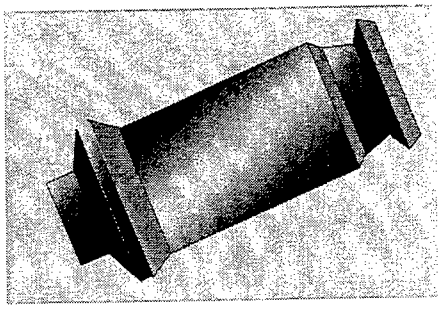
Step 5. Remove air from chamber and pattern to create a vacuum



Step 6. Pressurize chamber to force liquid composite material into T. C. pattern



Step 7. Heat solidified composite material to complete matrix curing process



Step 8. Clean up and finish

The resin matrix serves two main purposes: 1) suspension of the reinforcement during transport into the TC pattern; 2) solidification around the reinforcement to complete the composite. Typically, a two-part epoxy is used for the matrix, although polyurethane and other two-part plastics can be used. Epoxy was selected for its low viscosity level, excellent wetting characteristics, and reinforcement bonding capabilities. Factors that influence the type of epoxy to be used include: viscosity level, gel-time, exothermic characteristic, heat-deflection-temperature, tensile-strength, elastic-modulus, availability, shrinkage, post curing requirement, and notch sensitivity.

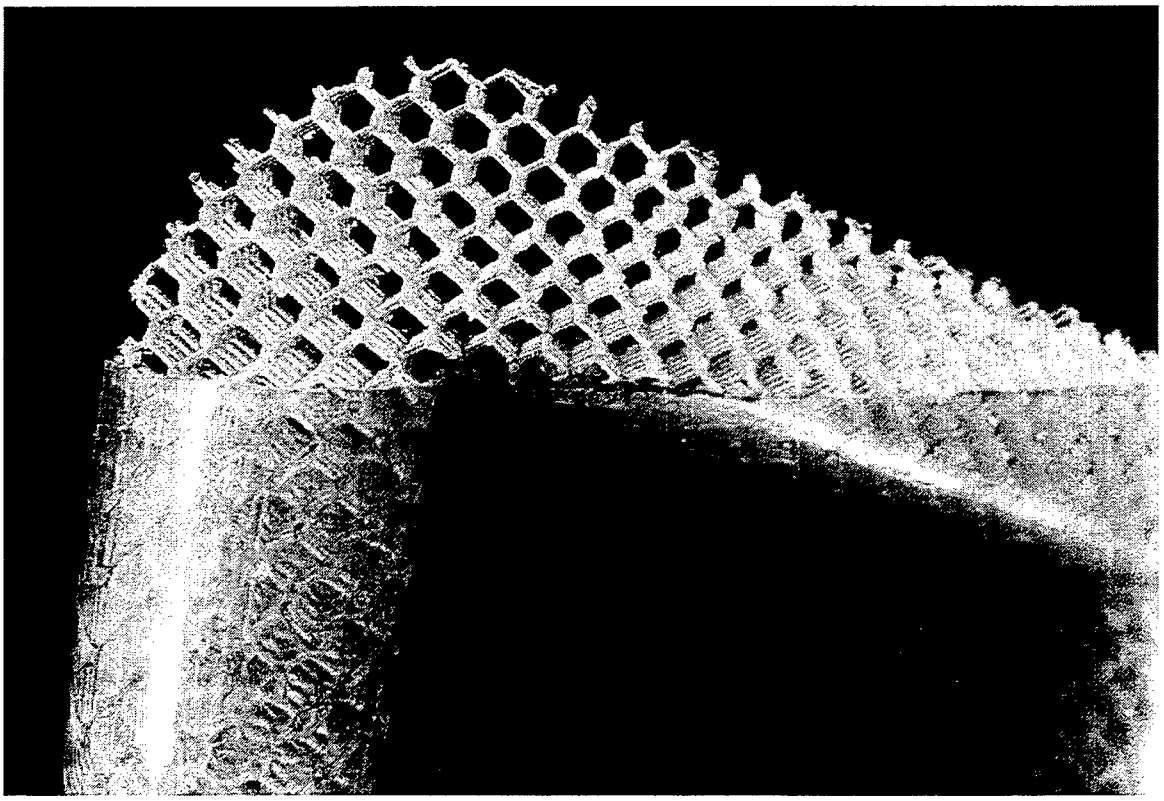


Figure 3. SLA TetraCast* Pattern with Exposed Tetrahedron Structure

By encapsulating various reinforcements in the epoxy matrix, enhanced mechanical properties can be achieved. These improved mechanical properties can exceed those of current SLA resins and also those of many engineering plastics. There are a large variety of reinforcement materials that can be used, but there are geometry limitations. Reinforcement materials include: glass, carbon, silicon carbide (whiskers), calcium carbonate, metal, aramid (Kevlar), and others. Those which are readily suspended in the liquid matrix material are ideal for RCP**. Reinforcement geometries include discontinuous fibers, flakes, particles and limited hand-placed filaments, as shown in Figure 4. Combinations of two or more of these reinforcement materials and/or geometries can be used to achieve desired physical or mechanical properties. Due to the random orientation of the reinforcement, composite structures will be nearly isotropic. Sizing can be used to enhance the bond between the reinforcement and the matrix.

PRELIMINARY RESEARCH FINDINGS

Beyond developing the RCP** process, we have studied the mechanical properties of simple composite combinations and confirmed that the rule of mixtures does apply. Mechanical properties including elastic-modulus, tensile-strength, and heat-deflection-temperature, have been investigated.

An early goal of developing RCP** was to determine whether the rule of mixtures does apply to this composite make-up. It was shown that the rule-of-mixtures [10] does apply to this composite system through two experiments (both experiments are shown in Figure 5). The earlier experiment included two composite volume ratios and two 100% samples of each material (epoxy photopolymer and straight epoxy). The later verification experiment included one composite sample and two 100% samples of each material. Both experiments showed this composite material to follow the rule of mixtures.

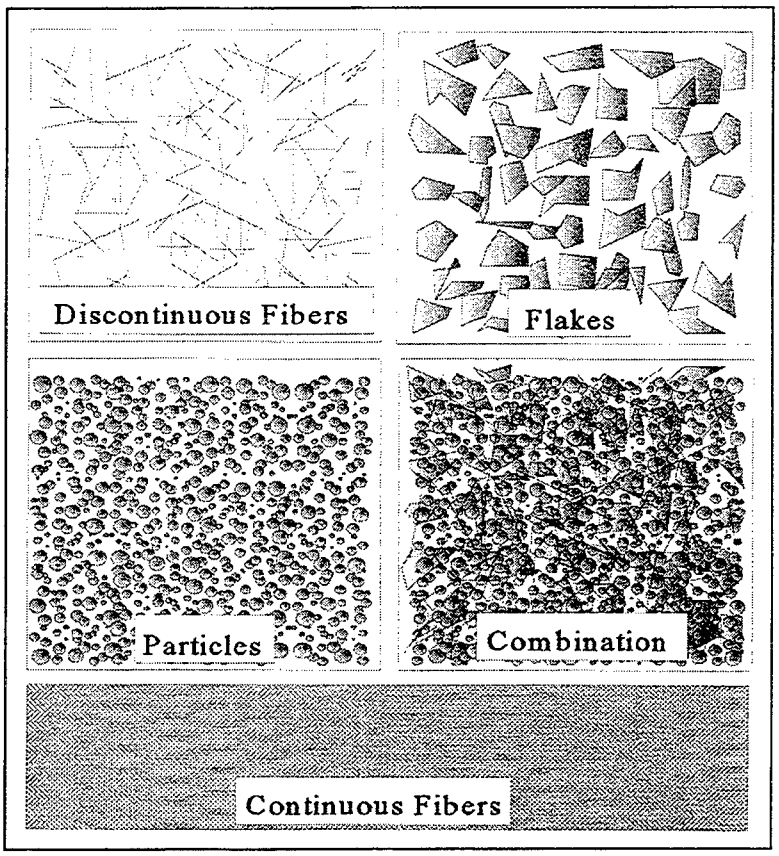


Figure 4. Reinforcements

Another early goal was to find a composite with a high elastic-modulus, well suited for rigid sand casting patterns. This goal was achieved by adding glass micro-spheres to the tensile samples [11, type III]. The first composite fillers included 10%, 17.5%, and 25% glass-in-epoxy by volume. These composite fillers were injected into the TC pattern and later tested. Figure 6 illustrates that the elastic-modulus is increased by increasing the volume ratio of glass. The elastic-modulus shown for 37.5% and 50% are predicted values.

Another research goal was to seek increased tensile-strength. It had been shown that by adding continuous-carbon-fiber as the reinforcement material, the tensile-strength can be increased to 30,000 psi (elastic-modulus of 2.0 M-psi). While this increased tensile strength is desirable, continuous fibers are not easily added. Discontinuous chopped-carbon-fiber additions increase viscosity making RCP** difficult. Milled-glass-fiber has shown much promise with up to 33% volume ratios achieved to date (not yet tested for mechanical properties). Particles and flakes have not been used to increase tensile-strength, but may be considered in the future.

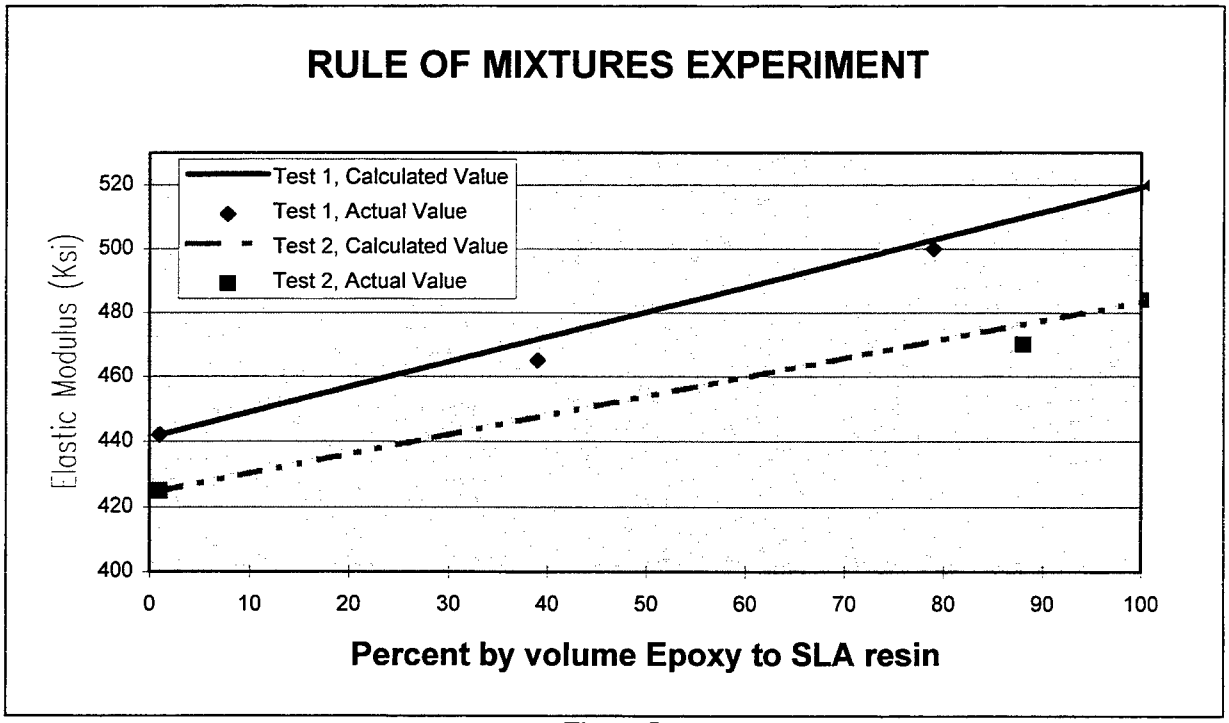


Figure 5.

Approaches to increasing heat-deflection-temperature is another area of preliminary investigation [9,12]. It has been shown that the composite materials have a significantly higher heat-deflection-temperature when compared to pure SLA epoxy. Figure 7 shows an increase of almost 50% when TC patterns loaded with calcium carbonate (CC) filled epoxy were tested. The epoxy matrix was the limiting factor in this experiment. If epoxy designed for higher

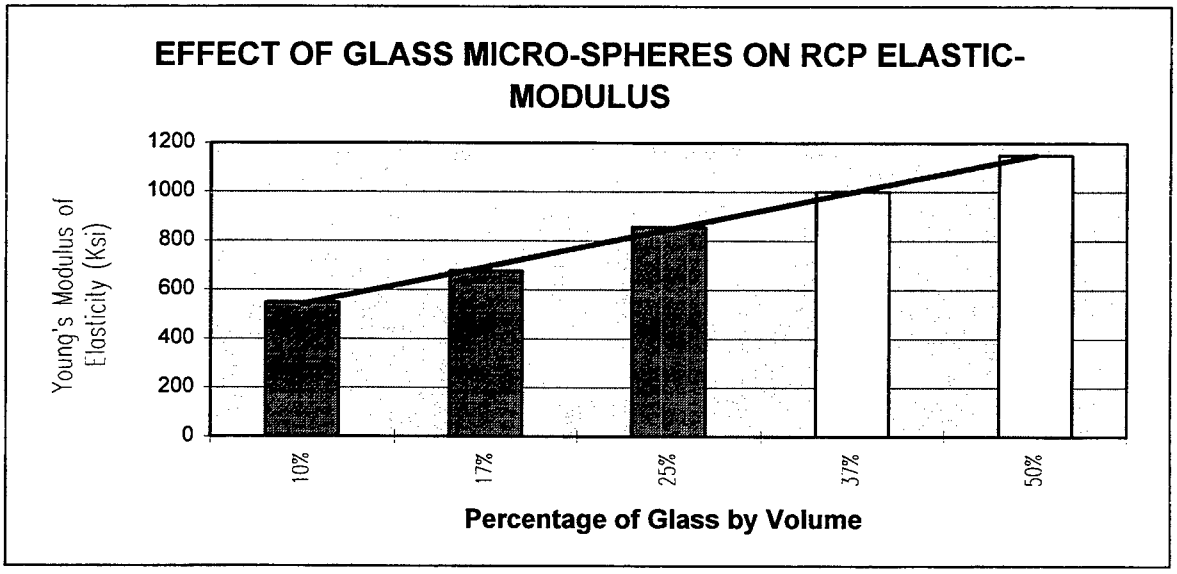


Figure 6.

temperature applications were used, the heat-deflection-temperature could be increased further. The SLA resin used has temperature limitations. Several new high temperature resins are being introduced which may extend the heat-deflection-temperature of RCP to above 300° F.

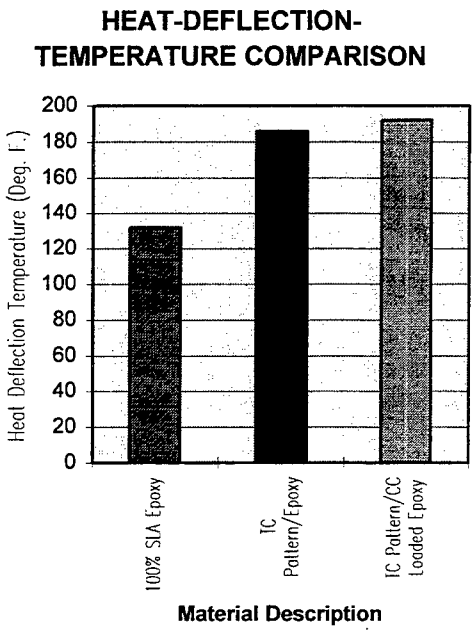


Figure 7.

CURRENT AND FUTURE RESEARCH

Several areas are currently being studied to better understand the limitations of RCP** and the parameters to work within. Areas currently being investigated include: viscosity limitations, stair-step notch reduction, shrinkage prediction, reinforcement combinations, cooling methods, and TC pattern fill methods. Areas of future study include next generation TC structures, process automation, SLA skin removal, wear-resistant coatings, and reinforcement sizing.

FUTURE APPLICATIONS

With any new technology, it is important to identify possible applications. Custom manufacturing of complex net-shape composites could be one application of this composite fabrication method. This would include areas such as aerospace, medical, prototyping, and manufacturing. With this method, composites of virtually any shape could be quickly produced with a wide spectrum of tailored physical and mechanical properties. Aerospace mechanical components could be rapidly and accurately produced at a significantly reduced cost. Applications ranging from custom test parts to custom ergonomic components could be produced using this process .

One-of-a-kind satellite and space-exploration components could be produced in line with NASA's 'Better, Faster, Cheaper' slogan. Housing components for miniaturized satellites might also find this process beneficial.

The medical applications of this process could include prosthetics, facial plates, and limited-production-equipment components. A RCP** vertebrae generated from a CT scan is shown in Figure 8.

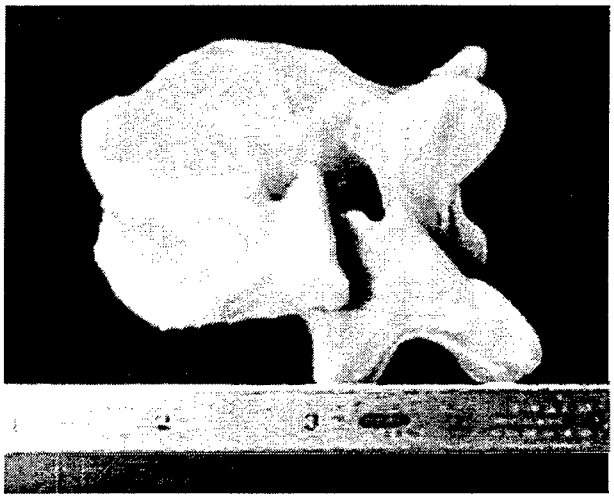


Figure 8. RCP Vertebrae**

Mechanical components that might be used on a prototype or manufacturing system could also be produced (Figure 9).

As this technology evolves, the applications will be extended, perhaps making new composite structures possible.

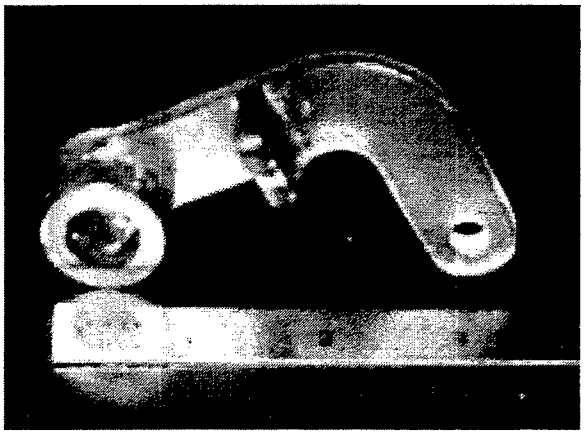


Figure 9. RCP Lever**

CONCLUSIONS

Net-shape composites can be achieved by using SLA TetraCast* patterns filled with a reinforcement loaded matrix. It has been shown that the rule of mixtures does apply to the resulting composite and that elastic-modulus, tensile-strength, and heat-deflection-temperature can be increased and/or predicted. Much research needs to be completed before the widened use of this process is realized.

ACKNOWLEDGMENTS

The support of the National Science Foundation (EEC-9415345, Rapid Prototyping in Manufacturing Education: Research Based Modular Curriculum) is gratefully acknowledged.

The author would like to thank Dr. Daniel A. Brandt for his guidance and support as principal investigator of the aforementioned grant.

The author would also like to thank Dr. Matthew Panhans and Jonathan McCray of the Milwaukee School of Engineering for efforts in technical assistance and process development. In addition, appreciation to the Advanced Rapid Prototyping Class and staff at the Rapid Prototyping Center at MSOE for their time and efforts on this project.

And special thanks to the Rapid Prototyping Consortium members for their involvement in this and other efforts.

REFERENCES

1. Klosterman, Don, Richard Chartoff, Nora Osborne, George Graves, Allen Lightman, Gyoowan Han, *Laminated Object Manufacturing (LOM) of Advanced Ceramics and Composites,* The 7th International Conference on Rapid Prototyping, 1997, pp. 43-50

2. Klosterman, Don, Brian Priore, Richard Chartoff, *Laminated Object Manufacturing of Polymer Matrix Composites,* The 7th International Conference on Rapid Prototyping, 1997, pp. 283-292

3. *Resin/Fiber Composite Manufacturing using Stereolithography,* Rapid Prototyping Report, Volume 2, Number 8, CAD/CAM Publishing, Inc., pp. 5-6

4. Bagchi, Amit, Robert Beesley, *Multi-Layered Composites using Photolithography,* Solid Freeform fabrication Symposium Proceedings 1994, pp. 234-241

5. Charan R., A. Bagchi, *Fabrication of Composite Prototypes by 3D Photolithography,* The 4th International Conference on Rapid Prototyping, 1993, pp. 15-23

6. Charan, R., T. Renualt, A.A. Ogale, A. Bagchi, *Automated Fiber Reinforced Composite Prototypes,* The 4th International Conference on Rapid Prototyping, 1993, pp. 91-97

7. Safari, A., S.C. Danforth, R.K. Panda, T.F. McNulty, F. Mohammadi, and A. Bandyopadhyay, *Fabrication of Piezoelectric Ceramics and Composites Using Rapid Prototyping Techniques,* The 7th International Conference on Rapid Prototyping, 1997, pp. 34-42

8. Calvert, Paul, Robert Crockett, John Lombardi, John O'Kelly, Kevin Struffle, *Extrusion Methods for Solid freeform Fabrication,* Solid Freeform fabrication Symposium Proceedings 1996, pp. 50-55

9. Gervasi, Vito R., Dr. Daniel A. Brandt, Steven D. Shaffer, King Lim, *TetraCast SLA Build Style,* The 7th International Conference on Rapid Prototyping, 1997, pp. 309-317

10. Gibson, Ronald F., *Principles of Composite Material Mechanics,* McGraw-Hill, 1994, pp. 70-71

11. *Standard Test Method for Tensile Properties of Plastics,* American Society for Testing and Materials, 1990, D638

12. *Standard Test Method for Deflection of Plastics Under Flexural Load,* American Society for Testing and Materials, 1990, D648

---

* TetraCast was developed at the Milwaukee School of Engineering Rapid Prototyping Center in October, 1995

** The Rapid Composite Process is similar to Rapid Composite Prototyping developed at the Rapid Prototyping Center at the Milwaukee School of Engineering in July of 1994

Shrinkage and Deformation in Components Manufactured by Fused Deposition of Ceramics

Joseph J. McIntosh, Stephen C. Danforth
Center for Ceramic Research,
Department of Ceramic and Materials Engineering,
Rutgers - The State University of New Jersey
Piscataway, NJ 08854

Vikram R. Jamalabad
AlliedSignal Research and Technology,
Morristown, NJ 07962

Abstract

Fused Deposition of Ceramics (FDC) presents a new processing technique that may contribute to anisotropic shrinkage and deformation, which are critical issues in the manufacture of ceramic components. The aim of this study is to identify and quantify key FDC parameters and their influence on shrinkage and deformation. The study was divided into two focus areas. The first was the effect of the FDC build parameters on the shrinkage of ceramic parts. The second focused on the interaction of the FDC build process with the geometrical features of a part. A series of experimental design techniques have been implemented in order to gain a thorough understanding of said parameters, as well as any possible interactions between parameters Studies have been conducted across each processing step, from the green manufacture of the part, through binder removal, and sintering. The data and knowledge gained from these experiments will allow us to redesign the original CAD component files to compensate for the shrinkage and deformation encountered when using the FDC technique.

Introduction

*S*olid *F*reeform *F*abrication is used to make three dimensional bodies from a computerized design (CAD file). Most SFF techniques use a wax or polymer system to fabricate parts. There have, however, been advances in the process of making metal as well as ceramic parts using established SFF processes. *S*elective *L*aser *S*intering (SLS), *L*aminated *O*bject *M*anufacturing (LOM), 3D-Printing, and *F*used *D*eposition (FD), show promise for the manufacturing of metal or ceramic components. The common factor between all these techniques is the layerwise building process. The computer reads in a CAD file and generates a series of continuous layers called slices, which when superimposed upon one another, recreate the three dimensional CAD file. The computer then sends the generated data to the tool which then physically builds the part one layer on top of another. These are all additive processes which differ largely from the normal subtractive process, by which a bulk part is machined to reach the desired shape. This process of material addition potentially imparts a unique set of defects and stresses which can result in warpage and anisotropic shrinkage in ceramic as well as metal parts, and is the focus of this research.[1]

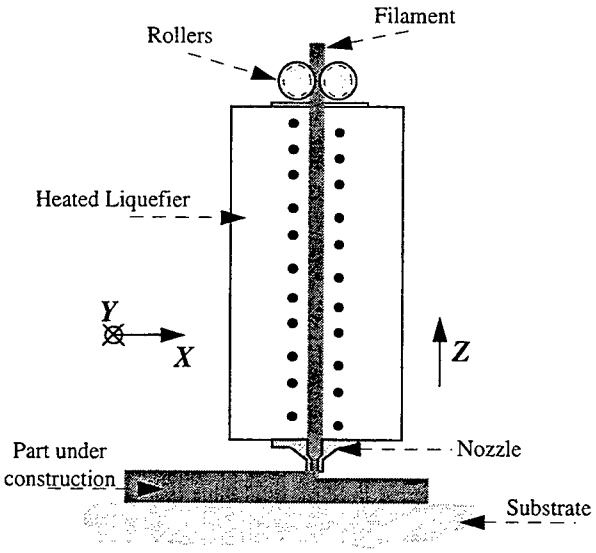


Figure 1: Schematic of Fused Deposition Liquefier

Ceramic feedstock for FDC is obtained by dispersing 55 vol% silicon nitride (GS-44) powder into an appropriate binder system.[2,3] Batch compounding occurs in a Haake torque rheometer where the surfactant coated powder is mixed with the molten binder.[4] The binder series used with GS-44 consists of approximately 20% elastomer, 15% tackifier, 30% wax, and 35% polymer.[2] The feedstock is extruded into a continuous filament 70 ± 1 mils in diameter.[3] Filament issues critical to successful FDC include flexibility, stiffness, viscosity, and adhesion or 'tack' behavior.[4] The filament is aged and spooled until ready for use. When ready, the filament is fed through two drive rollers into a liquefier where the binder material is melted, see Figure 1. The filament, which is continuously fed in, acts as a piston to drive the molten material through the liquefier. The liquefier moves in the X-Y direction and deposits material onto the substrate through a nozzle, generally 15 to 25 mils in diameter. In this manner, a singular layer is fabricated. The fill pattern of an individual layer can be manipulated during the setup of the computer file for the part. Once the layer is complete, the foam substrate is lowered and a new layer is built immediately over the previously built layer. The process continues until the entire part has been built. The binder is then removed and the part is sintered. The FDC process has been successfully demonstrated for silicon nitride, fused silica, aluminum oxide, lead-zirconate-titanate, stainless steel, and tungsten carbide cobalt.[2]

Procedure for Designed Experiments

Samples were fabricated using a modified Stratasys Inc. 3D Modeler™. The perimeter, contour, and rasters were made using a road width of 20 mils, and a slice thickness of 10 mils. A single contour was placed adjacent to the perimeter. The remainder of the layer was filled with rasters with the desired orientation. Negative offsets were used between adjacent roads, see Figure 2. The X-Y build speed was 500 mils per second. All other software values were held constant with the Quickslice™ default settings for ICW05, an investment casting wax developed by Stratasys for fused deposition modeling. Flow rate for the Modeler was set to 188%, and a nozzle with an inside diameter of 25 mils was used. The filament used was RU955, which is the RU9 binder system, at 55 volume % GS-44 silicon nitride powder.

The first series of experiments examined the effect of the FDC build parameters on the shrinkage of a rectangular bar 1"x ½"x ¼", see Figure 3. Liquefier temperature, modeling envelope temperature, and an aligned raster fill pattern of either 0° or 90°, relative to the long axis of the bar, were varied, see Table I. Parts were built directly on the foam substrate. Several samples were made with the conventional deposition method where alternating layers have roads aligned at 45°/-45° ("cross hatched" samples).

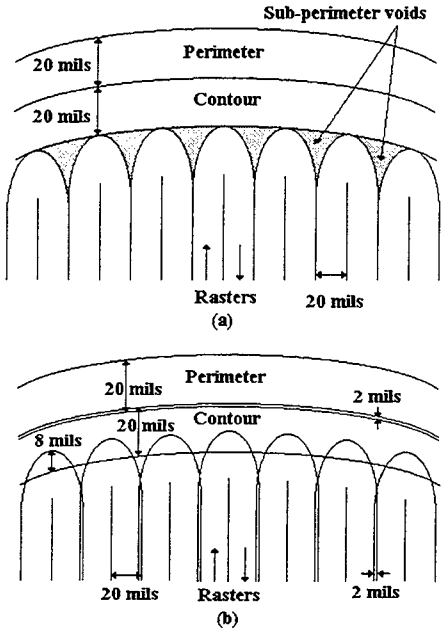


Figure 2: a) No offset b) Negative offset

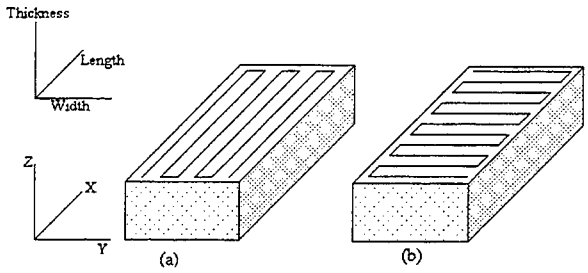
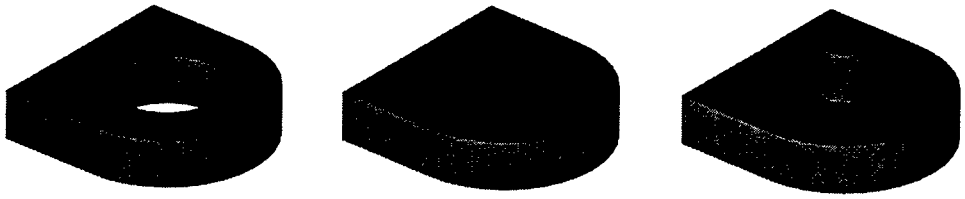


Figure 3: Fill patterns used a) 0° fill and b) 90° fill

Table I: FDC Build Parameters

	low	high
liquefier temperature	180° C	190° C
envelope temperature	40° C	50° C
road fill orientation	0°	90°

The second experiment investigated the effect of the FDC build process on geometrical features. The standard part geometry was a 1"x 1" plate, square on one side and hemispherical on the other, see Figure 4. To this standard plate was added in its center either a hole or a protrusion of diameter ¼" or ½". Build parameters were now held constant for all samples. The fill pattern used was a 45°/-45° cross hatch. Samples were built on a base five layers thick, which was removed prior to evaluation.



(a) (b) (c)

Figure 4: Various parts of the feature-based experimentation a) 1/2" or 1/4" hole, b) standard, c) 1/2" or 1/4" protrusion

Upon completion, all parts were stored in a low humidity chamber until ready for binder removal. Binder removal was accomplished in a tube furnace in a two stage process. In the first stage, parts were embedded in activated carbon and heated to 350° C in a nitrogen atmosphere. The second stage involved heating the samples to 450° C in an air environment.[5] The parts were then gas-pressure sintered under a schedule proprietary to AlliedSignal, Inc.

Characterization occurred in the green, brown (post binder removal), and sintered states. Measurements of length, width, thickness, and weight were taken. Shrinkage and weight loss percentage were calculated using the equation:

$$(X - X') / X * 100 = Y$$

where X is the original value, X′ is the new value, and Y is the percent change in the value. The experimental design program DOE KISS was used to analyze the results.

Results and Discussions

Experiment #1, CAD-Green

The Quickslice™ software generates an .sml file which the liquefier uses to direct its movement during the FDC build. In nearly all cases, it was found that the part was built larger than that specified by the .sml file, see Table II. Build direction was found to be the only factor tested which affected the dimensions in the build plane. The data shows the average shrinkage values calculated for both the 0° and 90° samples in the length and width direction. There are several phenomena which may account for the part being built larger than specified.

Table II: Cad-Green*

Build	0°		90°	
length	-0.26% ± 0.58		-1.65% ± 0.33	
width	-1.46% ± 0.61		-2.45% ± 1.48	
Liq Temp	180°	190°	180°	190°
thickness	-4.71% ± 1.15	-5.87% ± 2.22	-8.96% ± 1.93	-11.61% ± 2.97

* Note that a negative shrinkage indicates a final part dimensional larger than the .sml file

First, the part may be slumping due to insufficient stiffness while still in the modeling envelope. Too high a modeling envelope temperature may result in slumping. Within the temperature range tested here, 40° and 50° C, the modeling envelope temperature was not found to affect the green part size. Further testing at a broader temperature range may be required. The oversize in the samples may also have been due to the method used to eliminate sub perimeter voids. The mechanism of void filling employed was a single contour deposited just inside the perimeter of the sample which acts as a buffer layer into which rasters would plow, see Figure 2. There was a negative offset of 8 mils between the raster and contour fill which would provide excess material at their junction in order to prevent the formation of sub-perimeter voids. The large overlap would cause the rasters to plow into the semi-cool contour which would in turn push out into the perimeter and result in the perimeter being displaced outward from its original location. The perimeter will then cool in the new location resulting in a part with oversize X-Y dimensions.

The excess in size in X, Y, and Z, shown by the 90° parts, above that shown by the 0° parts, may have been due to the larger amount of excess material generated. The 90° samples required a larger number of roads to fill in the layer, as they had shorter path lengths. The higher number of roads contributed to more contour/raster interactions and resulted in even more excess material being deposited in the sub-perimeter region. With layer upon layer, this amount of extra material grew and would account for the 90° parts being oversized by a larger amount than the 0° parts. This was reinforced by the average original weights of the samples, 4.59g ± 0.09 for the 0° samples and 4.72g ± 0.09 for the 90° samples.

The data also shows that the length, or the 1" dimension, for both the 0° and 90° fill pattern was more accurate, or closer to the intended size, than the width, or ½" dimension. This was due to the greater effect of surface roughness on error when measuring the smaller dimension, and is reinforced by the data gathered for the cross hatched samples. They showed a similar effect, whereas the length had a shrinkage of -1.86% ± 0.15 and width a shrinkage of -3.15% ± 0.50.

The liquefier temperature was found to affect the part thickness, see Table II. At a liquefier temperature of 190°C, the deviation from theoretical was greater than at 180°C, and the cause for this is uncertain at present. From these results, we have determined that the present method of sub-perimeter void elimination is inadequate for the desired tolerances and contributes to a large variation in green part size dependent on the path length of the road, and the build pattern. Dog-earing, which alters the liquefier's path in the sub-perimeter region, will be revisited as an alternative to overfilling.[6]

Recall that all parts fabricated in this first experiment have an aligned raster pattern whereby all the roads in the part are deposited in the same direction. Normal FDM or FDC does not employ this type of fill, but instead uses a cross hatch pattern where the road direction is at 90° to the road direction of the previous layer. The rasters have been aligned in this study in order to gain an understanding of the effects of individual layers on shrinkage and warpage. This knowledge is vital when designing a part with very thin sections, high aspect ratios, or tight dimensional tolerances. One must be able to compensate in the CAD file for any differential shrinkage due to differences in the vector lengths of the fill.

All of the parts built, including the 0°, 90°, and cross hatched samples, were warped in the green state. Prior to removal from the foam substrate, it was evident that the parts were warped about an axis normal to that of the raster direction as indicated by the arrows in Figure 5. This may be inherent to the process by which a hotter layer is deposited onto a colder layer. On cooling, the hot layer is put in tension and the cold in compression due to both the higher thermal expansion of the hotter material, and its viscoelastic behavior. It is also possible that stresses are induced in the part by the repeated shearing of the deposited material. The liquefier increases its position by 10 mils for each new layer. Any excess material, above the 10 mil thickness will be sheared by the nozzle movement while depositing the next layer. With this material in its semi cool state, the shearing stresses may become significant. Warpage for the 90° samples was found to be 0.06%/in ± 0.28, while the 0° samples showed 0.53%/in ± 0.29. Extra samples were fabricated and green machined in order to eliminate the warpage found in the green state. They were then burnt out and sintered. There was no further warpage in the brown state, but after sintering it was apparent that some subsequent warpage had occurred. Future work will take a detailed

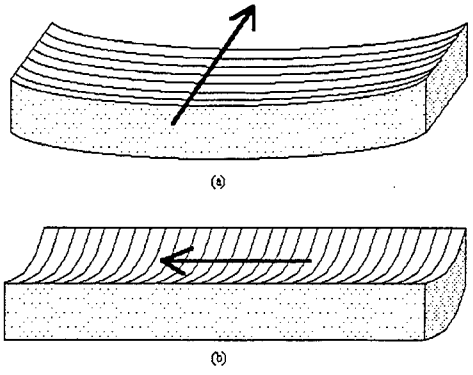


Figure 5: Warpage in a) 0° samples and b) 90° samples

look through each subprocess using sample geometries specifically designed to facilitate the study of warpage.

Green to Brown

Shrinkage in the X-Y plane was found to occur after binder removal, see Table III. It was found that more shrinkage occurred in the road direction than normal to it (within a given layer). This was contradictory to previous notion that the most shrinkage should occur in the direction normal to the roads. This notion stemmed from the hypothesis that there may be small density gradients found across a layer. The road center was thought to be slightly more dense than its edges, resulting in a less dense area between roads, which would shrink more upon binder removal and sintering. The fact that this is not the case suggests that reevaluation of the density gradients is required, or that there is yet unexplained phenomena occurring. A possible explanation is the relief of the viscoelastic tensions imparted to the roads during deposition, as described previously. DMA and thermal expansion tests will be carried out to understand the relaxation behavior of the RU955.

Table III: Green-Brown Shrinkage and Weight Loss

thickness	1.62% ± 0.83	
weight	19.39% ± 0.15	
Build	0°	90°
length	1.34% ± 0.31	0.97% ± 0.23
width	0.93 ± 0.40	1.31% ± 0.61

The cross hatched samples exhibited comparable brown shrinkage's of 1.32% ± 0.13 in the length and 1.22% ± 0.29 in the width. The anisotropy found in the aligned rasters was not visible here because the road directions were not isolated as before. The thickness showed a 1.62% ± 0.29 shrinkage.

Neither the liquefier temperature, environment temperature, or the build pattern was found to effect the shrinkage (from the green to brown state) in the build, or Z direction. The Z shrinkage was larger than either X or Y, however. This is common to parts made through layering processes and may stem from somewhat poorer bonding or lower densities between subsequent layers. At the conclusion of these experiments, it will be possible to compensate for this anisotropy in the software. The weight loss on burnout was also found to be independent of the three tested factors, as expected. Weight loss averaged 19.39% ± 0.15 for all parts tested.

Brown to Sinter

None of the FDC build factors tested had any effect on the shrinkage from the brown to the sintered state, see Table IV. The density of the samples was calculated by Archimedes' method to be 3.23 ± 0.06 g/cm^3, consistent with isopressed samples of GS-44 silicon nitride. There was some weight loss during sintering, which is typical for GS-44.

Table IV: Brown-Sintered Shrinkage and Weight Loss

length	16.10% ± 0.36
width	16.45% ± 0.53
thickness	18.06% ± 0.51
weight	0.85% ± 0.11

Table V: Bulk sample shrinkages through processing stages

	length	width	thickness
Green-Brown	0.95% ± 0.26	0.89% ± 0.48	0.97% ± 1.83
Brown-Sintered	16.14% ± 0.47	16.12% ± 0.40	17.65% ± 1.77
Green-Sintered	16.94% ± 0.50	16.85% ± 0.52	18.44 ± 1.12

Experiment #2

The second experiment examined the effect of various features on the bulk shape. This would provide information about the ability to hold tolerances on the critical features of complex parts. Samples were built with various features as shown in Figure 4. The goal of this experiment was first to determine whether or not a particular feature, such as a hole or a protrusion, would affect the shrinkage behavior of a known sample made by the FDC process. Second, the size dependence of the features was to be examined. The final objective was to observe the effect of the FDC processing parameters on the feature itself. Each subprocess was examined in a similar manner to the previous experiment.

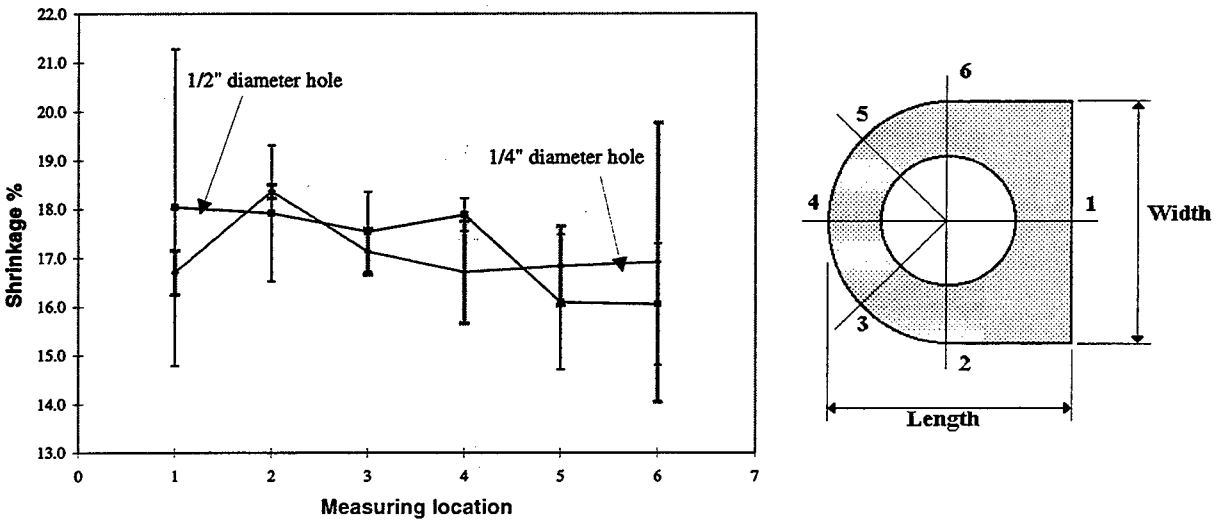


Figure 6: Dimensional variations from Green to Sintered stages for feature experiment samples, measurement location is shown to the right.

It was found that none of the geometric features employed significantly affected the shrinkage in the bulk part through any stage of processing. Data for the processes is shown in Table V. This is encouraging in that it suggests that if the part is fully dense in the green state, complex shapes are possible without the need for specific corrections according to feature shape. Figure 6 shows the shrinkage around the sample with the 1/4" and the 1/2" holes. Shrinkage's for both diameters were indistinguishable. The green holes themselves were smaller in diameter than designed, due once again to the overfilling as described previously. The 1/2" and the 1/4" diameter protrusion shrinkage's were also insignificantly different from one another. It was observed, however, that the base of the protrusion was slightly larger in diameter than regions above it. This enlargement affected only the first 3-5 layers of the protrusion. It is surmised that this may be another result of the subperimeter void fill method and further experimentation is ongoing.

Conclusions

Overfilling was determined to be a poor choice for use as a sub-perimeter void fill. It resulted in oversize parts and may have contributed to deformation at the base of some of the features. Road direction was found to influence shrinkage in the X-Y plane during binder removal. Shrinkage was larger in the road direction than normal to it. The FDC build parameters tested did not affect the shrinkage during the sintering stage. Warpage was found to occur in the green and sintered states and was about an axis normal to the direction of the roads. It was determined that geometrical features did not significantly affect the shrinkage of ceramic components manufactured by fused deposition. The samples tested do not, however, have features that approach the thickness of singular roads, nor the complexities possible with the 3D Modeler. Further studies will examine thinner cross section and more complex features.

Acknowledgments

We gratefully acknowledge the support of this research by DARPA and ONR under contract # N00014-94-0115, as well as the support and advice of R.B. Clancy and Dr. R. van Weeren at AlliedSignal, Inc., and Drs. P. Bhargava, C. Dai, S. Rangarajan, S. Wu, and A. Bandyopadhyay, A. Safari and the undergraduate staff at Rutgers University.

References

1. van Weeren, R., et. al., "Quality of Parts by Fused Deposition", *Proceedings of the SFF Symposium,* pgs. 314-321, H..Marcus, J.Beaman, D.Bourell, J.Barlow, and R.Crawford, editors © The University of Texas at Austin, Austin TX, August 1995.

2. Agarwala, M.K., et. al., "Fused Deposition of Ceramics and Metals", *Proceedings of the SFF Symposium,* pgs. 385-392 H..Marcus, J.Beaman, D.Bourell, J.Barlow, and R.Crawford, editors © The University of Texas at Austin, Austin TX, August 1996.

3. Agarwala, M.K., et. al.,"Fused Deposition of Ceramics for Structural Silicon Nitride Components", *Proceedings of the SFF Symposium,* pgs. 335-343 H..Marcus, J.Beaman, D.Bourell, J.Barlow, and R.Crawford, editors © The University of Texas at Austin, Austin TX, August 1996.

4. Agarwala M.K., et. al., "Filament Feed Materials for Fused Deposition Processing of Ceramics and Metals", *Proceedings of the SFF Symposium,* pgs. 451-456 H..Marcus, J.Beaman, D.Bourell, J.Barlow, and R.Crawford, editors © The University of Texas at Austin, Austin TX, August 1996.

5. Bhargava, P., et. al., " Shrinkage, Weight Loss and Crack Prevention during BBO of components produced by FDC" *Proceedings of the SFF Symposium*, Austin, TX, August 1997

6. Jamalabad, V. R., et. al., "Process Improvements in Fused Deposition of Ceramics (FDC): Progress Towards Structurally Sound Components", *The Proceedings of The 1996 ASME Design Engineering Technical Conference and Computers in Engineering Conference.* pgs. 18-22, August 1996, Irvine, CA.

The Design and Construction of a Medical System to Optimize the Endoscopic Ultrasound Procedure

Darius P. Daruwala
Christopher M. Johnson
Donald R. Jacobsen*

Rapid Prototyping Center, Milwaukee School of Engineering
*Medical College of Wisconsin

ABSTRACT

This project involved the use of rapid prototyping to produce a model of a section of the gastrointestinal (GI) tract which could be used for practice of the Endoscopic Ultrasound (EUS) procedure.

Computed Tomography (CT) scans were obtained from Dr. Donald Jacobsen, Assistant Professor of Radiology at the Medical College of Wisconsin in Milwaukee. Apart from the final testing, the entire project was performed at the Milwaukee School of Engineering's Rapid Prototyping Center. To convert the CT scans into files that are compatible with the rapid prototyping machines, a software developed by Materialise, N.V., was used. The rapid prototype models were used as master patterns for molds so that a polyurethane material with similar properties to human tissue could be used for actual simulation. Finally, these polyurethane models were placed in an enclosure and surrounded by a gelatin to simulate fatty abdominal tissue. The system was tested at Froedtert Memorial Lutheran Hospital under the supervision of Dr. Anthony Bohorfoush in conjunction with the Medical Physics Department of the Medical College of Wisconsin.

INTRODUCTION

The need for accurate models of the human body is greater in this age of rapid medical advancement. As new medical procedures and equipment are developed, few physicians and medical personnel have the knowledge and skills needed to use them effectively. Even the most skilled endoscopists have difficulty navigating the endoscope into the duodenum and targeting a specific organ. In addition, once the images are obtained, it is extremely difficult to interpret them due to the awkward orientation of the ultrasound transducer. Therefore, any system which will accurately simulate the human abdomen and allow physicians to practice EUS, will greatly increase the effectiveness of this relatively new medical procedure.

The purpose of this project was to develop a system that accurately simulated the human abdominal organs when subjected to the endoscopic ultrasound (EUS) procedure. Specifically, a model of the human stomach with the duodenum and an accurate simulation of the fatty tissue

that surrounds them were desired to allow physicians and radiologists to practice and teach the EUS procedure.

DISCUSSION

Rapid prototyping is a technique which is used to develop mechanical designs into a functional prototype within a few hours or days for physical or market testing. It can also be used to check the feasibility of new design concepts, to assess the fit of complex mechanisms, to make molds for wax cores in casting, and to use as a master pattern in silicon and epoxy molds.

In medicine, rapid prototyping can be used in a process called reverse engineering, where the structure already exists but does not have regular geometric properties, such as that of the human body. Three-dimensional models can be created using two-dimensional data from imaging devices such as CT or MRI scanners. These three-dimensional models provide the surgeon with tactical visibility and an acute understanding in some complicated cases. A physical model of the patient's anatomy is easier to interpret than a series of two-dimensional images. The models can be used in surgical planning where complex operating procedures can be tried out on the model, greatly reducing the time in the operating room. Physical models can also be used for communication of the patient's condition and expected outcome to members of the surgical team and for the patient's understanding of the treatment plan.

ENDOSCOPIC ULTRASONOGRAPHY

Endoscopic ultrasonography (EUS, sometimes simply called endoscopic ultrasound) is a relatively new technology that combines the features of two existing methods of obtaining structural information about the gastrointestinal tract and the tissues and organs immediately surrounding it. The combination of endoscopy and ultrasonography (ultrasound imaging) allows physicians to obtain information that is not available or is not as accurate by other non-invasive means.

With conventional ultrasound imaging, computed tomography (CT), and magnetic resonance imaging (MRI) already successfully in use, why was an invasive ultrasonography technique needed? CT, MRI, and transcutaneous ultrasonography all have limitations for resolving small structures within and surrounding the gastrointestinal tract. CT uses radiation and MRI is fairly expensive. Conventional ultrasonography may not provide adequate resolution of the structural details of the GI tract due to the low frequencies used to provide deep penetration. Since the EUS probe is actually placed in the GI tract, adjacent to the target area, higher frequencies can be used (little penetration required) resulting in better resolution of the tissues of the GI wall and of adjacent structures.

Conventional abdominal ultrasonography, CT, and MRI will continue to be an important part of the diagnostic procedures for patients with various gastrointestinal problems. However for several specific applications, EUS has proven itself superior to the other imaging methods. Diagnostic imaging with EUS is particularly valuable for examining endocrine tumors of the

pancreas. EUS has also been used to evaluate other pancreatic tumors, pancreatitis, and to find gall stones lodged in the common bile duct. In addition to pancreas abnormalities, EUS has allowed physicians to find and stage early gastrointestinal cancers more accurately, often preventing unnecessary surgery (to obtain biopsies). On occasions, when surgery is necessary, EUS can help to better prepare surgeons and patients for surgery. Ultimately, detection of cancers that are small and at an early stage will increase the chances of cure.

In the short number of years that the EUS procedure has been used, it has proven to be a valuable complement to conventional ultrasonography, CT, and MRI in the examination of the gastrointestinal tract and the surrounding organs.

DESIGN SPECIFICATIONS

The specification for the system was to accurately simulate the behavior of human abdominal organs during the EUS procedure. This requirement applied to the stomach, duodenum, and the fatty tissue that surrounds the internal organs. They had to be of similar size and shape of human organs and possess ultrasonic properties exhibited by human tissue.

The stomach and duodenum were required to be made of a soft, flexible material with nearly the same density as water. The human stomach is very flexible and is normally in a collapsed state, unless food or drink has just been consumed. It was also necessary that the stomach be watertight, as it is inflated with water during the EUS procedure. It was important for the stomach wall to have a uniform density in applications involving ultrasonic waves. Therefore, it was necessary to either utilize a molding technique that produced a casting as one complete part, or if cast in halves, develop a way to attach them without altering the density. The material selected for the stomach and duodenum from over twenty possibilities was a flexible polyurethane called *SKINFLEX* from BJB Enterprises. With this material, it was necessary to use platinum-based silicone as the molding material, since *SKINFLEX* will not cure correctly against tin-based silicones. After much deliberation, it was determined that the most effective method of producing the stomach was to cast it in halves and then glue the halves with the casting material.

In addition to the stomach and duodenum, it was also necessary to accurately simulate fatty tissue in the abdomen. The first requirement was that the material be extremely soft and flexible. Also, the tissue must accurately simulate the ultrasonic properties of human soft tissue. This again involved near water density, and material that simulated the attenuation effect of the cells and cell walls. It was determined that an organic gelatin could best provide the density and texture required. Also, mixing tiny graphite particles into the material would provide the ultrasonic attenuation due to cells. A gelatin-water mixture of approximately 7.5% gelatin to 100% distilled water provided the texture and hardness (firmness) closest to that of abdominal tissue.

The enclosure needed for the project was not one of the primary design focuses of the project. The only requirement of the enclosure was that it be approximately the size of an average human's abdomen and that it be able to hold the gelatin without deforming. A small

valve and tube were attached to the end of the duodenum to allow these organs to be filled with water and drained when needed. Four small plastic balls were placed in the gelatin to act as targets during ultrasound imaging. These balls were measured prior to placing them into the enclosure so they could be compared to measurements taken from the ultrasound images. Fishing line and washers were used to weight the balls down, and keep them in place until the gelatin solidified. Finally, a wire mesh screen was also placed in the enclosure to act as another target.

MATERIALS SELECTION

This project required the selection of two materials: (1) a material to simulate the stomach and the duodenum, and (2) a material to simulate the fatty tissue that surrounds the stomach and other internal abdominal organs. It was necessary that both materials be flexible and posses similar ultrasonic properties to the actual human organs.

The ultrasonic properties that were of primary importance were the attenuation and the speed of sound in these materials. The speed of sound is usually related directly to the density of the material. Therefore, materials with densities close to that of water (approximately 1.0 g/cm^3) were selected. Because the ultrasound transducer on the endoscope is placed in almost direct contact with the stomach wall, the attenuation and other ultrasonic properties of the stomach were important. The main requirement for the stomach was that it be of a uniform density. However for the fatty material that surrounds the stomach, acoustic impedence was of great importance. Therefore, in future models, very fine powdered graphite will be added to the gelatin to simulate the attenuation of human fatty tissue caused by cells,.

The major materials that were examined for these applications were epoxy, gelatin, latex, polyurethane, and silicone. Latex and epoxy were dropped from consideration early, because they break down in water, and material suppliers were difficult to locate. Numerous companies were contacted, and a great deal of information was gathered to allow the best decision between the remaining materials to be made. The following table summarizes the most appropriate offerings of companies contacted:

Table 1: Summary of Material Offerings of Companies Contacted.

Company	Materials Available	Application	Hardness
Air Products	Polyurethane	Stomach	45+ Shore A
BJB Enterprises	Polyurethane Polyurethane Gel	Stomach Fatty Surrounding	5+ Shore A Gelatin-Like
Ciba-Geigy	Polyurethane	Stomach	35+ Shore A
Eager Plastics	Polyurethane	Stomach	70+ Shore D
GE Silicones	Silicone	Stomach/Mold	14+ Shore A
Hapco	Polyurethane	Stomach	20+ Shore A
Vyse Gelatin	Gelatin	Fatty Surrounding	Gelatin-Like

After analyzing the literature and samples received, polyurethane emerged as the best material for the stomach and duodenum. Because of the wide range of physical properties available in polyurethanes, it was the material of choice. Polyurethane has a hardness that varies from "Shore A" to "Shore D". Also, polyurethane has a density close to the density of water. An extremely flexible polyurethane called *SKINFLEX* (BJB Ent.) was selected for the simulation of the stomach and the duodenum.

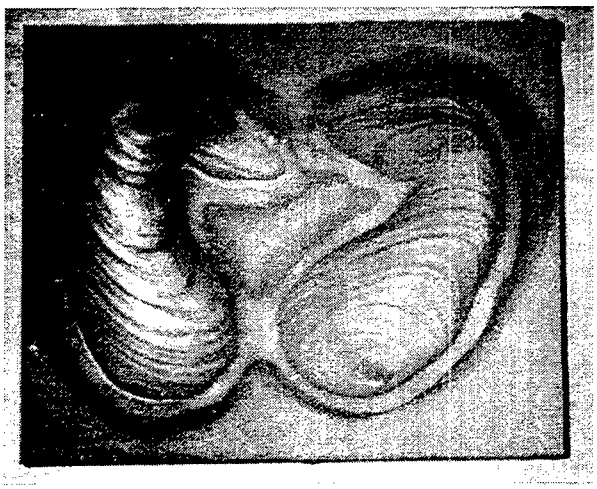


Figure 1: Silicone Rubber Mold of Two Stomach Halves

In addition to the polyurethane, gelatin was explored as a possible material to simulate the surrounding fatty tissue. With gelatin from the *Vyse Gelatin Company*, several samples were made. This gelatin produced a material with suitable hardness and density, but it was found to decompose when it was exposed to air. After several days in an open container, the gelatin samples grew fungus and dried up, becoming very brittle. However, after contacting the material vendor, it became clear that the addition of a preservative would increase the life of the system.

ASSEMBLY OF THE ENTIRE SYSTEM

After successfully producing the stomach model with the duodenum, the components had to be brought together to make a complete, usable system. The enclosure used was a simple plastic waste basket with a small valve fastened on the back side, near the bottom of the container. A small rubber tube was attached to the end of the duodenum and to the valve to allow the stomach and duodenum to be drained periodically. On the other end of the system, a larger rubber tube (1.0" I.D.) was attached. The stomach, duodenum and esophagus were positioned in the enclosure, and four small plastic balls were placed near the stomach and duodenum to act as targets during testing. A course wire mesh was also placed inside the

enclosure to act as an additional target. The system prior to the addition of gelatin is shown in **Figure 2**.

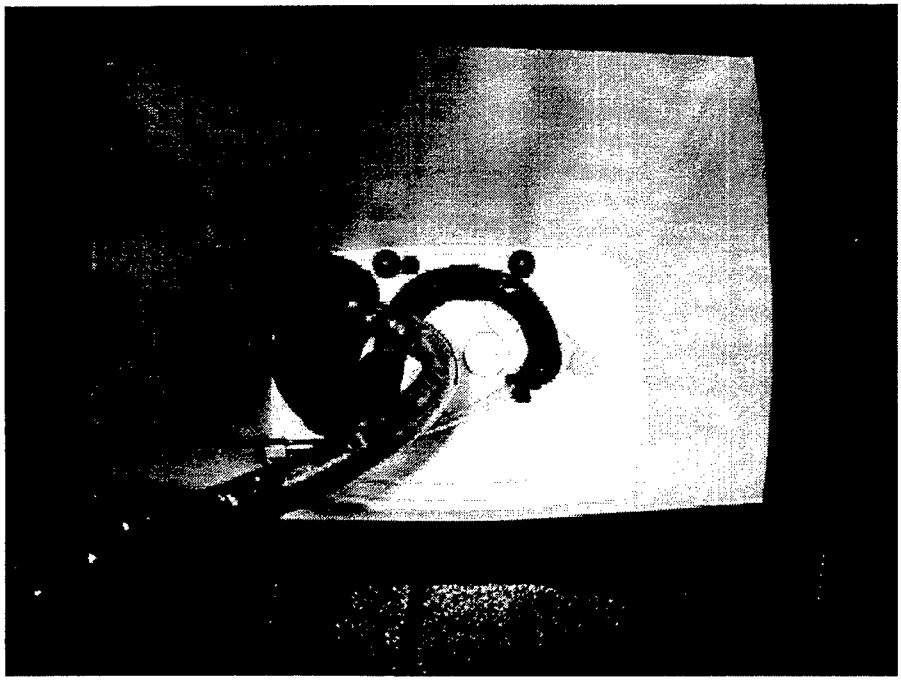


Figure 2: System prior to addition of gelatin.

Finally, the gelatin powder was mixed with six gallons of water at a 7.5% to 100% ratio and poured into the enclosure, around the internal organs. After several hours, the gelatin solidified.

TESTING THE SYSTEM

The final step of the project involved testing of the system with Dr. Anthony Bohorfoush at Froedtert Hospital. The probe was inserted into the stomach and the first portion of the duodenum ultrasound and video images were obtained.

The ultrasound images can be frozen, and printed at any time. **Figure 3** shows an image from one of the initial tests of the stomach. The main purpose of this initial test was to determine how well the material simulated the wall of a human stomach. The black half-ellipse on the top of the image is the ultrasound transducer, itself. In this case, the transducer is inside of the stomach, sending waves out. The top bright white line is where the ultrasound waves hit the inside of the stomach wall, while the lower white line shows the interface between the outside of the wall and the water (gelatin was not used in the initial test). After

looking at the images, Dr. Bohorfoush admitted that this material looked very much like a human stomach wall.

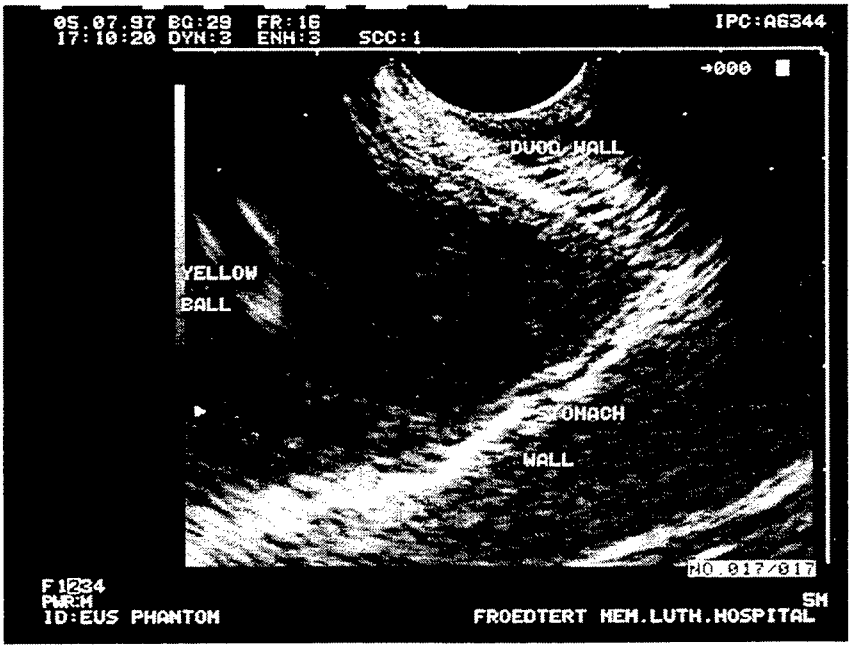


Figure 3: Ultrasound image of ball next to duodenum wall.

Figure 3 also shows one of the small balls placed under the stomach. The diameter of the ball and the distance from the transducer and the ball were measured and were within 5% of the actual values.

Another portion of the procedure involves real-time visual images. The images are displayed on a color video monitor and can help the endoscopist navigate through the organs, as well as see any deformities on the inner walls of the gastrointestinal tract. Like the ultrasound images, the visual images can be printed at any time, and the entire session can be recorded for review at a later date. **Figure 4**, on the following page, shows visual images obtained from inside of the stomach. The yellow ball can be clearly seen floating in the gelatin. The bright light of the scope makes it possible to see right through the stomach and gelatin.

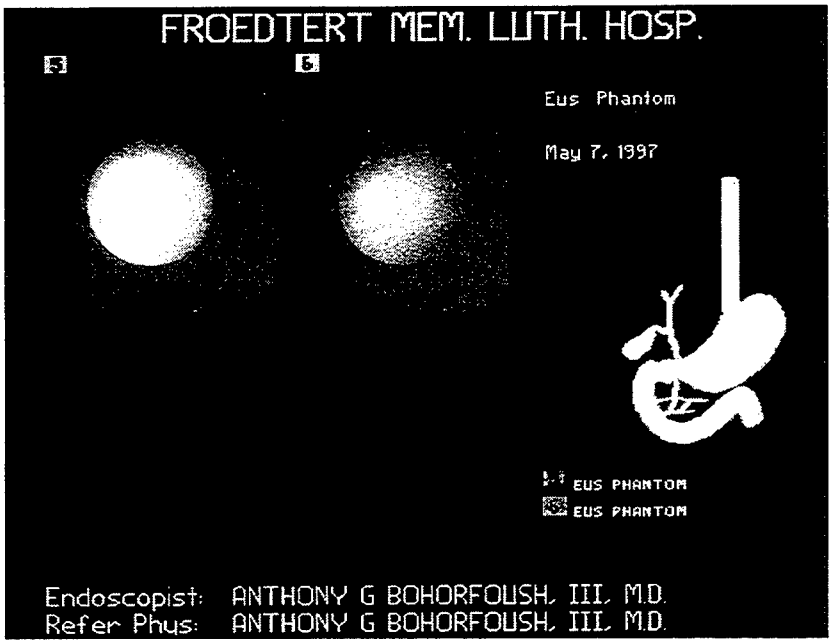


Figure 4: Images of yellow ball and duodenum entrance from inside stomach.

CONCLUSION

The medical system, developed in this project to allow physicians to practice and teach the endoscopic ultrasound procedure, was a great success. Rapid prototyping has proven to be a useful tool in surgical planning, as exemplified in this case. The doctors who tested the system were extremely pleased with the project, and commented numerous times on how similar the images obtained were to the images obtained from an actual patient. This system has exciting possibilities for training both new as well as experienced users in the performance of the procedure, and in the identification of abdominal anatomy as imaged with the EUS. The doctors, radiologists, and students at the medical colleges now have an invaluable tool at their disposal for practicing the EUS procedure.

BIBLIOGRAPHY

American Society of Gastrointestinal Endoscopy. *Understanding Upper GI Endoscopy.* Http://www.asge.com

American Society of Gastrointestinal Endoscopy. *Endoscopic Ultrasonography, Update February 1994.* Http://www.asge.com

Baker, T.M. *Integration of 3-D Medical Imaging and Rapid Prototyping to Create Stereolithographic Models.* Australian Physical & Engineering Sciences in Medicine, Vol. 16, No. 2. 1993.

Bohorfoush, Anthony G., M.D. *Advances in Imaging of Bile Ducts and Pancreas.* Grand Rounds at Froedtert Hospital. 1996.

Bronzino, Joseph D. *The Biomedical Engineering Handbook.* CRC Press, Inc. 1995.

Digestive Disease Center. *EUS (Endoscopic Ultrasound).* June 1995. Http://www.ddc.musc.edu/eus.

Eisner, Robin. *Endoscopic Ultrasound in Gastroenterology.* P&S Journal: Winter 1995, Vol. 15, No. 1.

Microscopic Flow Observation of Photopolymer by UV-Laser Beam Exposure

Yi XU, Masato IMAMURA, and Takeo NAKAGAWA
Institute of Industrial Science
University of Tokyo

ABSTRACT

Microscopic flow of liquid photopolymer around the cured polymer was observed during laser exposure. The maximum velocity was about 4 mm/s. The temperature raised by reaction heat, causes the density of liquid photopolymer to vary, resulting in this flow. This flow causes the nearby cured strands to sway and it decreases the accuracy of SL model.

1 INTRODUCTION

Stereolithography (SL) is a technology which directly creates 3D objects from digital data. Because SL offers the advantage of enabling models with complicated geometry to be created easily, it has been applied in numerous fields. Recent developments of SL focus on the applications of rapid tooling. For example, the SL model is used as the master model to create the die and model for small lot production. SL can also be employed to make die and mould of filler-in composite. All of these set high demands on the accuracy of the SL process. However, there is obviously a distance between the present available accuracy and such demands. The phenomena such as curl distortion and steps of models are factors which decrease the accuracy. To solve these problems, especially curl distortion, it is necessary to have a better understanding of the curing process of photopolymer. Numerous research works have pointed out that cure shrinkage and temperature are the potential factors which have influence on curl distortion. The attempts to quantify these factors are being made so as to control the curl distortion. Polymerization is exactly the transition of monomer from liquid phase to solid phase. Since the cured polymer has to be immersed in liquid photopolymer for a relatively long period, the liquid photopolymer should have certain effects on the curing process. As one of the liquid photopolymer's influences, swelling is a phenomenon where the cured polymer absorbs the monomer. It is known that swelling decreases the strength of the cured polymer[1] and induces curl distortion[2]. In addition to this, the flow of photopolymer during part building may decrease the accuracy. The possible causes of flow include the movement of the recoating system, flow induced by the heating system in the vat used for increasing the sensitivity of UV light. However , there is strong possibility for the generated heat or cure shrinkage to cause photopolymer flow. The purpose of this research is to observe the flow behavior of liquid photopolymer during laser exposure and clarify its causes so as to provide a clear understanding of the curing process.

2 PARTIAL MICROSCOPIC FLOW OF PHOTOPOLYMER

2.1. Experimental Details

In this experiment, a He-Cd laser (Output is 20mw) was used to cure the epoxy-based photopolymer HS-660 (Asahi Denka K.K).

In order to observe the photopolymer's flow, BN powder (average diameter is 1.5 μm) was used as the tracer (BN powder : photopolymer = 1 : 1400 in weight). The photopolymer was placed in a glass box (100x30x30). During laser exposure, a video camera was used to recorde the behavior of photopolymer and nearby cured strands from the top and front(Fig.1). This observation was carried out in spot and scan exposures by laser.

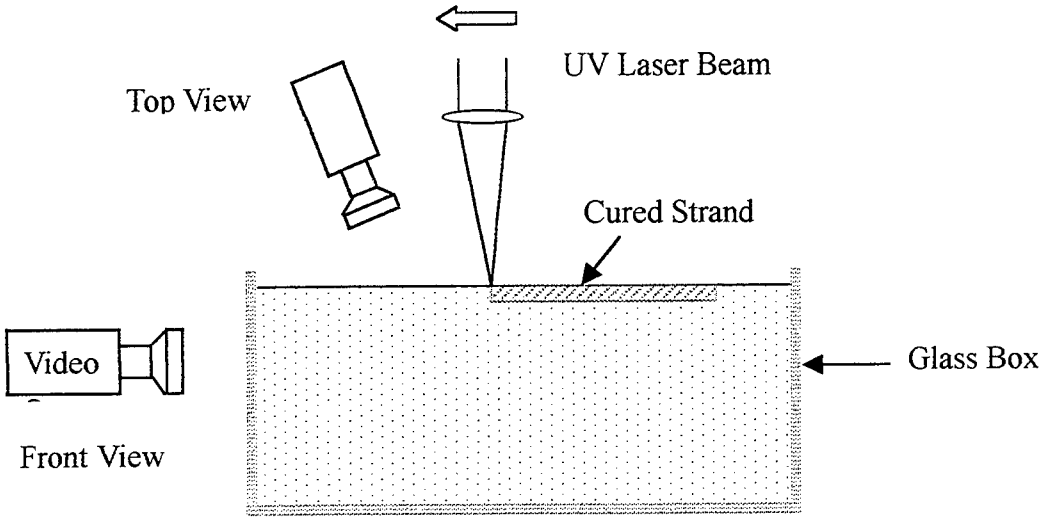


Figure 1 Observation of Flow during Laser Exposure

2.2 Behavior of Liquid Photopolymer Exposed by Laser Spot

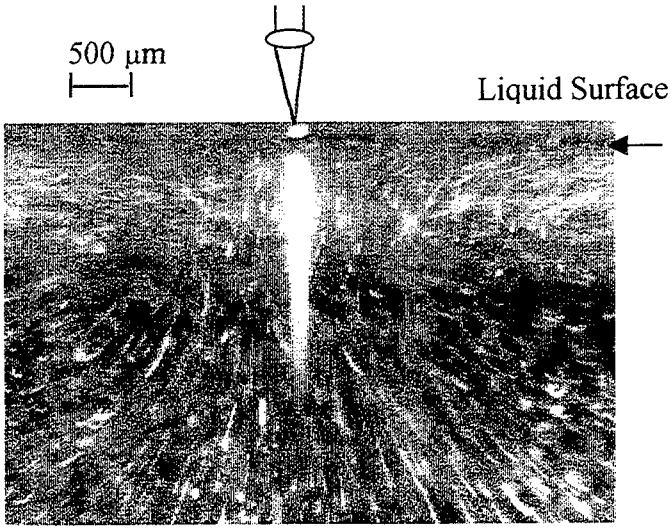


Figure 2 Partial Flow of Liquid Photopolymer During Laser Exposure

Fig. 2 shows the flow behavior of liquid photopolymer when spot exposed by UV laser spots to photopolymer, Once laser beam is projected onto the surface of the photopolymer, flow of the liquid photopolymer around the cured polymer results. At the beginning, the photopolymer under liquid surface moves away from the curing center. This is followed by movement along the solid boundary upward. Finally, circular movement of the photopolymer near the cured polymer results. When exposed by UV-laser, the curing area expands and the movement center of the flow moves away from the laser beam center.

2.2 Behavior of Liquid Photopolymer Exposed by Laser Scan

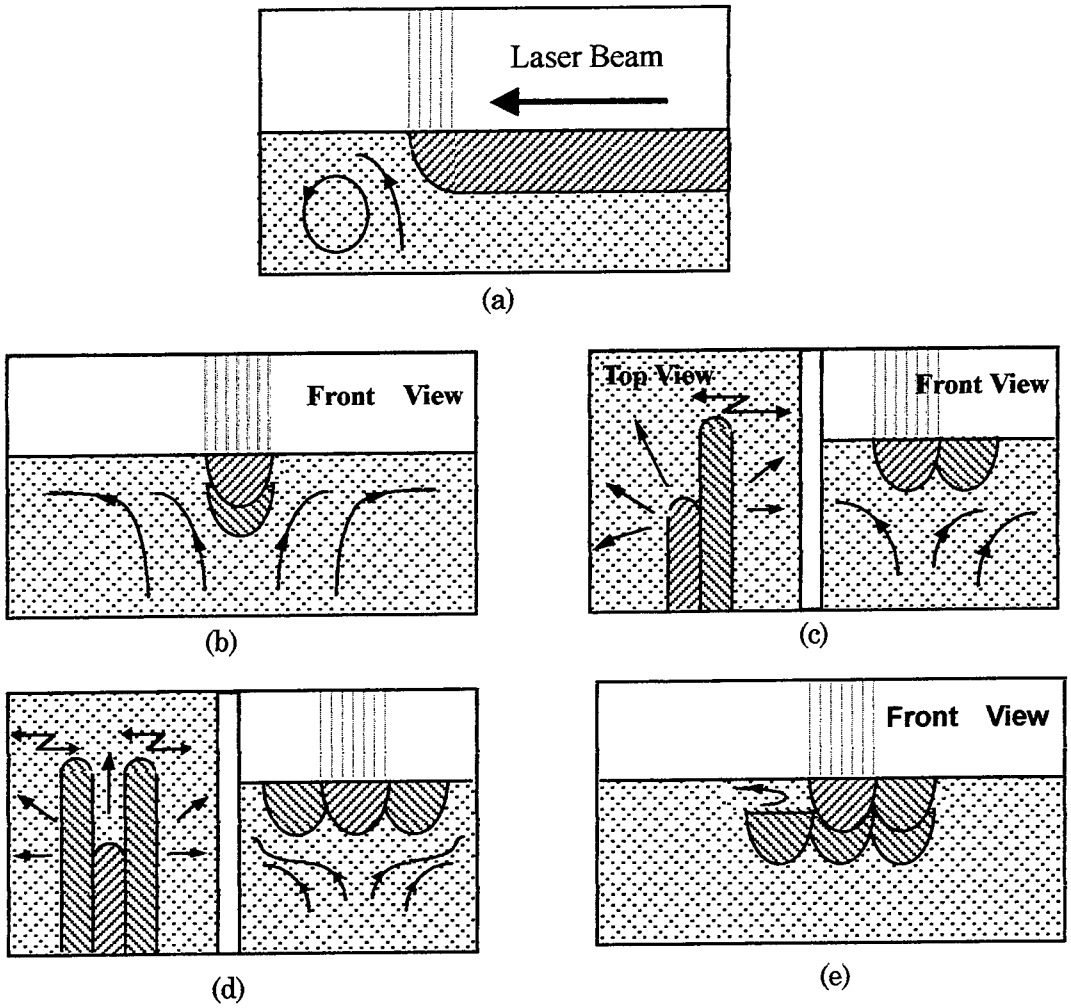


Figure 3 Flow Behavior of Photopolymer during Laser Scanning

When laser beam scans the surface of the photopolymer at a certain speed, a similar movement of photopolymer can be observed near the cured strand. The most active flow is in front of the laser beam center, and it moves with the laser beam. This movement is explained in Fig 3a.

When the laser beam scans the region where there are pre-cured strands nearby at two sides or at the lower level, the flow of photopolymer overruns these pre-cured strands

(Fig.3b,Fig3c,Fig3d). Even if the photopolymer is trapped by the pre-cured strands (Fig 3e), a slight flow is still observed.

2.3 Velocity of Flow

To express the flow precisely, it is necessary to know the velocity in any region of the liquid photopolymer as the functions of time and position. With this knowledge, it then becomes possible to know the impact applied on the nearby liquid photopolymer and cured polymer. To clarify the cause of this flow, it should be helpful to investigate the temperature distribution within this area. By using microcapsulized thermo sensing liquid crystal particles, the temperature and velocity can be measured[3]. In this experiment, the temperature was measured by an integrated thermocouple sensor[4]. Therefore, PTV (Particle Tracking Velocimetry)[5] was used to measure the velocity distribution of the liquid photopolymer. The principal of PTV is to directly track the tracers in the continuous images of video.

In this experiment, A laser beam with a speed of 10 mm/s was used to cure photopolymer. The movement of the tracer particles was consecutively recorded at a time interval of 1/30 s by a NTSC video format camera(Fig.4). A computer software modified from conventional image processor NEXUS 6400 was used to process the image and calculate the velocity of tracer particles.

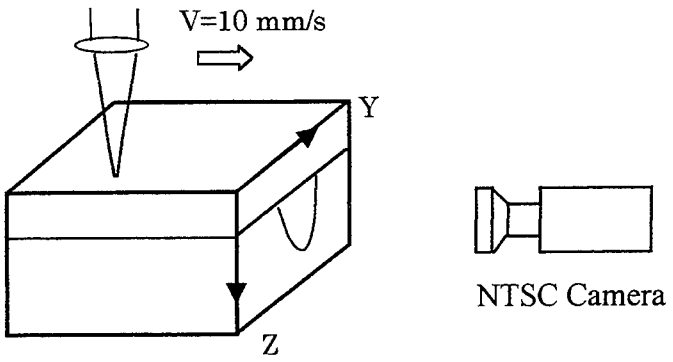


Figure 4 Measurement of Velocity of Flow

Fig.5 and Fig.6 show the velocity distribution of the flow of the photopolymer at the YOZ plane(Fig.4) at the initial moment of the flow induced by laser exposure.

When laser cures an individual strand, there is rapid flow around the strand. The maximum velocity reaches about 4 mm/s(Figure 5). The liquid photopolymer of the two sides of the cured strand flows rapidly (greater than 2 mm/s), but the liquid photopolymer under the strand flows slowly (smaller than 2 mm/s). This shows that source of the flow may lie in the upper region of the two sides of the strand. In general, the velocity is very high.

When the second strand is cured beside the first strand. The velocity shows a different trend (Figure 6). At the side of second strand, the velocity is as high as that shown in Figure 4. However, the velocity at the (right) side of the first strand is far lower than that at the left side.

It proves that the flow at the right side is induced by that one of the left side

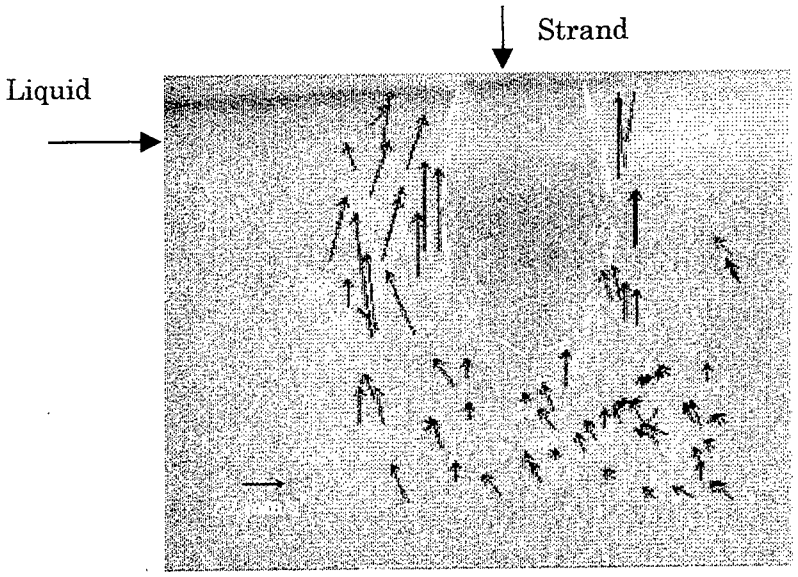


Figure 5 Velocity Distribution around Cured Strand

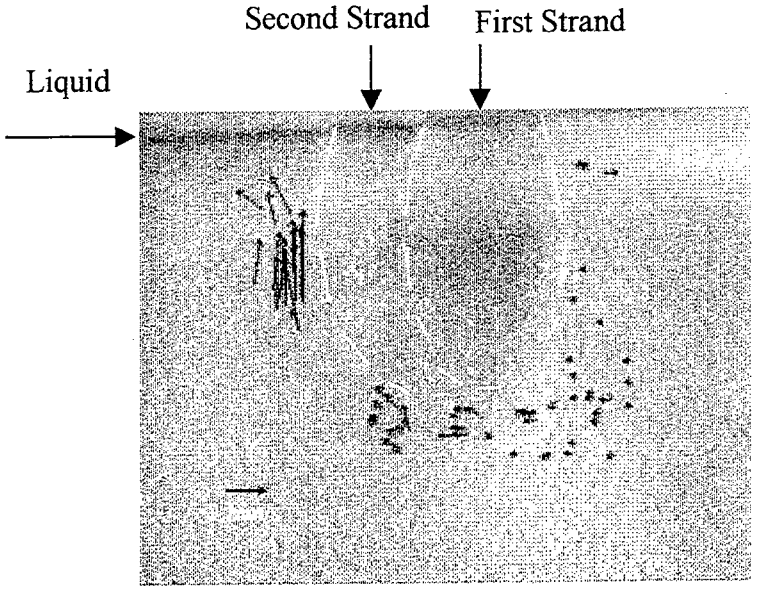


Figure 6 Velocity Distribution of Flow Influenced by Neighbor Cured Strand

2.4 Behavior of Cured Strands during Laser Scanning

The above measurement results show that the maximum velocity of the flow is as big as about 4 mm/s. It should have a very big impact on the nearby cured strands. From video observation, it was seen that the free ends of the cured strands sway if the laser beam scans near them. For investigating the impact from the flow, a sample was created as shown in Fig.7. This is a twin-cantilever sample with only one layer. The distance between the strands is twice the cured width. It means that the strands should disconnect each other completely. However, the free ends of the cantilever-strands have been connected together. When laser draws the

strands, the free ends sway due to the liquid photopolymer flow. Because the interval for laser to draw the next path is very short. The swaying free ends of the cured strands happen to be in the laser path. Finally, these free ends are connected. After several strands have been connected, there is a enough strength to resist the impact of flow. The connected free ends do not sway again. Then the group of connected free ends are formed by laser drawing. This is the reason why there are three groups of connected free ends.

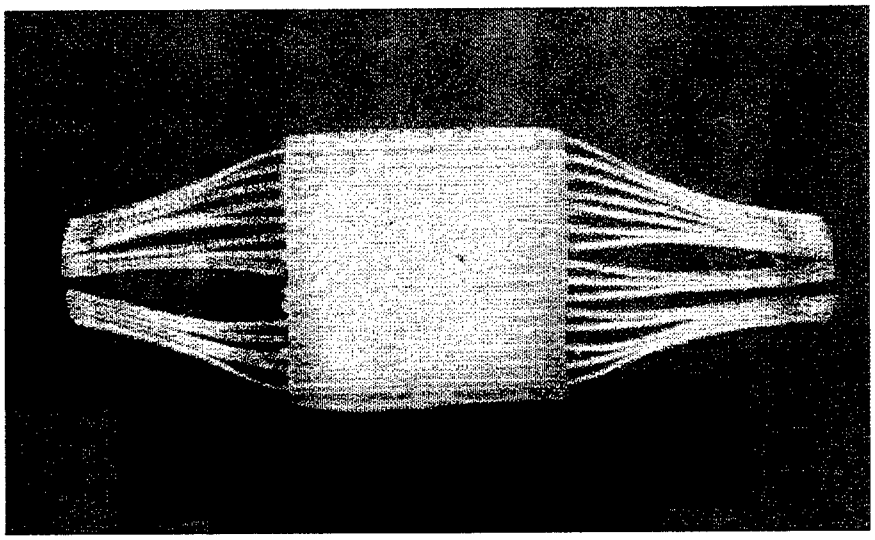


Figure 7 Connected Free Ends of Continuous Cured Strands

3 Cause of Photopolymer Flow

There are two potential factors which cause the flow of liquid photopolymer. One is the cure shrinkage and the other is temperature variation.

The maximum linear cure shrinkage of the photopolymer HS-660 used in this experiment is about 2.2%. If the profile of cross-section of the cured strand is assumed as a circle and its radius is 0.5 mm, the maximum linear shrinkage is about 0.01 mm. The velocity should be less than 0.01 mm/s because it takes about 100 seconds for cure shrinkage to reach its maximum. It is far less than the velocity in above measurement. In addition to this, the velocity should be in the radius direction if this flow caused by cure shrinkage which was obviously not the case with the observation result. Therefore, it can be concluded that cure shrinkage is a potential factor to cause flow but not the main one.

The inhomogeneous pressure and density distribution cause flow of the fluid[6]. For liquid photopolymer, heat is generated during laser exposure. Figure 8 shows the temperature distribution in the cured polymer and nearby liquid photopolymer. There is a temperature slope within the nearby liquid photopolymer. The high temperature leads to low density as shown in Fig.9 and there is a possibility for this inhomogeneous temperature to cause photopolymer flow.

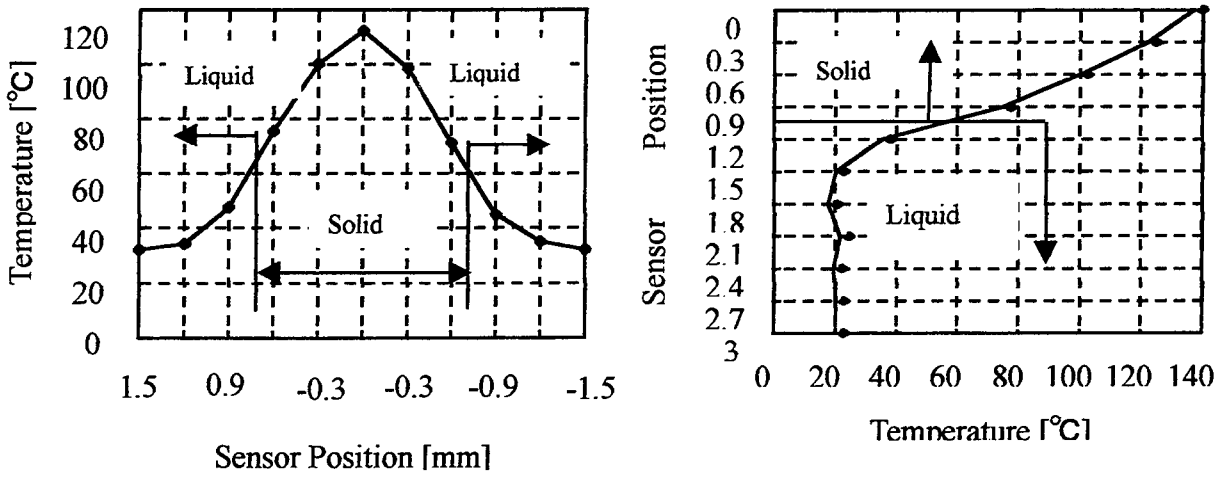


Fig. 8 Temperature Variation in Solid and Liquid Phases

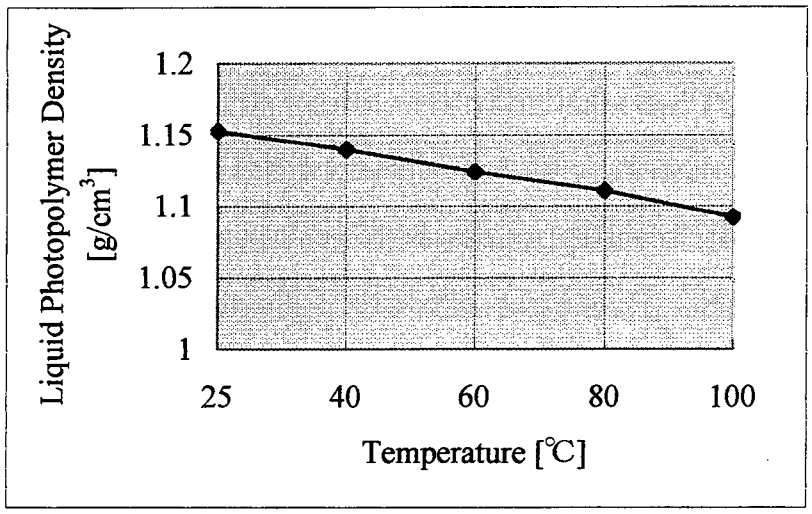


Figure 9 Relation of Density and Temperature of Photopolymer HS-660

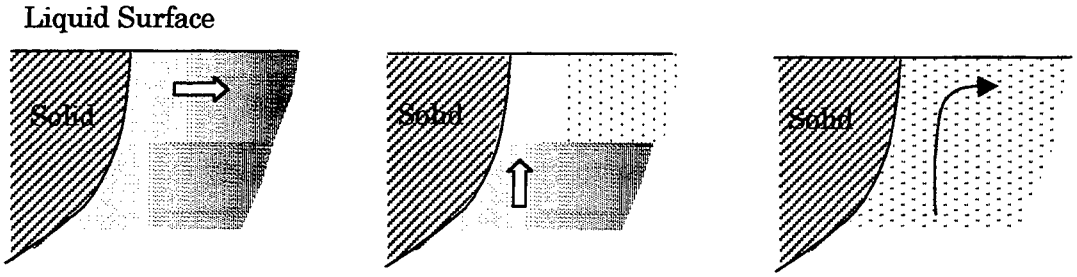


Figure 10 Enlarged Schematic Side View of Partial Microscopic Flow of Photopolymer during Laser Exposure

Under the liquid surface, there is a tendency for photopolymer to move to the right side because temperature is high near the solid boundary and the density is low. The photopolymer under this region trends also to occupy the space left by this right movement. These two tendencies causes the photopolymer to flow upward in the low region and to the right under the surface.

4.CONCLUSION

To investigate the influence of liquid photopolymer on cured polymer during laser exposure, experimental observation was carried out by means of a video camera. Partial microscopic flow of photopolymer was observed near the curing area. As soon as the laser spot projects on the surface of the liquid photopolymer, flow occurs. The velocity of the flow is very great. Measurements show that the maximum velocity reaches about 4 mm/s. Even though the neighbor cured polymer resists this flow, observations show that the flows overcomes this cured polymer and this flow causes the nearby pre-cured strands sway. This can been considered one of the sources of curl distortion. There is also a temperature variation near the curing area which varies the density of the photopolymer. This inhomogeneous density is the cause of photopolymer flow during laser exposure.

Acknowledgements

The authors wish to thank Mr.S.Segawa of IIS, University of Tokyo for his assistance in velocity measurement.

REFERENCE

1 Takeo Nakagawa and Yoji Marutani, Lamination Fabrication System, New Development of 3D Copy Technology, Association of Industrial Investigation, 1996,Tokyo.

2 E.J.Murphy, M.G. Sullivan, M.J.Bezdicek, Swelling Distortion in Stereolithography, Proceedings of The second International Conference on Rapid-Prototyping, June 23-26,1991,Dayton,pp.95-101.

3 Deoghee DOH, Toshio Kobayashi, Tetsuo Saga, Segeki Segawa, Development of 3D particle-Imaging Thermograph and Velocimetry (PITV), Proceeding of 70th Conference of JSM, Mar. 1993, pp.930-9

4 Yi Xu, Masato Imamura, Takeo Nakagawa, Heat Generation of Photopolymer by UV-Laser Exposure, Proceedings of The 7th International Conference on Rapid-Prototyping, Mar,1997,San Francisco,pp.122-129.

5 Kobayashi Lab.IIS,University of Tokyo, Experimental Report B of Science and Technology Department of Japan, 1995,pp.10-12.

6 Fluid Mechanics Handbook, Maruzen, 1987,p.475

Fused Deposition of Ceramics: Progress Towards a Robust and Controlled Process for Commercialization

R. Clancy, V. Jamalabad, P. Whalen
AlliedSignal, Inc. Research and Technology
Morristown, NJ 07962

P. Bhargava, C. Dai, S. Rangarajan, S. Wu, S. Danforth, N. Langrana, A. Safari
Center for Ceramic Research
Rutgers - The State University of New Jersey
Piscataway, NJ 08855

The feasibility of using the Fused Deposition of Ceramics (FDC) process to rapidly fabricate functional quality advanced ceramic components has been demonstrated[1-5]. *This direct manufacturing technique, by eliminating the need for costly tooling, dramatically reduces functional prototype development time. This makes it suitable for small quantity production runs and complex parts. The move from "feasibility" to a robust, reliable commercial fabrication tool requires that every aspect of the manufacturing be understood and brought under control. An overview of the five basic process steps in FDC: batch compounding, filament fabrication, fused deposition, binder burnout and sintering will be presented in light of this drive toward a robust process. Tools such as Statistical Process Control and Experimental Design techniques are being used to monitor, improve, and stabilize each step and sub-process. Hardware and software modifications have been made to the FD machine to effect the required changes. This paper will identify the remaining technical barriers to commercialization and our progress in addressing these issues.*

I. Introduction

Direct fabrication of ceramic components using SFF techniques has created an opportunity to reduce lead times and costs in the development of new products. The Fused Deposition of Ceramics process uses a ceramic/polymer filament as feed material to build a part from a CAD file by additive layering. The binder is then removed and the part is sintered to full density. In order to apply this process to existing commercial manufacturing needs, effort has been directed to reduce variability and increase robustness. A reproducible, predictable process creating final parts of specified dimensions and strength within 6σ deviation is crucial for commercialization.

Due to the sequential, "building block" nature of the FDC process, upstream material- or process-variability can result in major part defects such as voids, cracks, and warpage; this is a common issue for conventional ceramic processing. Batch-to-batch variability results in unpredictable filament quality, and operator responses to this deviation often introduce new process variables. It is difficult to isolate the root causes of technical hurdles, such as material contamination, filament buckling, voids and surface irregularities in the FDC parts, and irregular

shrinkage, without establishing a baseline process. However, due to time constraints of the program, many of these issues were attacked concurrently. Where the problems could not be eliminated or contained, they were quantified, possible root causes were identified, and experiments were planned.

The first step to process improvement was run-charting, tracking experimental data through time. This evolving database will yield Quality Control measures such as target and limits, introducing Statistical Process Control. Standard Operating Procedures were established to lessen operator-to-operator variability, and environmental controls were digitized. The FDC steps were characterized by measuring viscosity, modulus, and material content in each batch. The application of Design of Experiments (DoE) methodology to FDC sub-processes identified effective parameters and optimized conditions quickly.

II. Batch Compounding and Filament Fabrication[2,3]

The ceramic system employed in this study is an *in situ*-reinforced Si_3N_4, commercially supplied by AlliedSignal (Ceramic Components, Torrance, California) as GS-44. The powder is coated with a surfactant, oleyl alcohol, in a batch ball-milling process. The coated powder is compounded with the proprietary binder system, designated RU9 (Stratasys, Inc., Eden Prairie, Minnesota), in a torque rheometer. The compounded material is granulated and sieved, then fed into a single screw extruder with an attached torque rheometer. Continuous filament of nominal 0.070" +/- 0.001" diameter is extruded through a die and wound on spools for storage and use in the Fused Deposition process.

A homogeneous mix of powder, surfactant, and binder is crucial to ensuring a reproducible FDC process. As such, a number of process characterization techniques monitor the uniformity of the filament fabrication operation. Loss on Ignition (LOI) tests measure the amount of oleyl alcohol (after milling) and binder (after compounding). Torque values are monitored during compounding and extrusion. An Instron capillary rheometer measures viscosity and load by extrusion of the compounded material. The diameter of the filament is monitored by a laser micrometer as it is extruded.

The solvent drying step after ball milling causes a non-uniform distribution of oleyl alcohol, resulting in batch-to-batch variability. Mixing and sieving of six coated batches together increased homogeneity of the feedstock, as seen in **Figure 1**. LOI tests after mixing and subsequent compounding show reduced variability due to the mixing and sieving step. In addition, particle size analysis shows that the mixing and sieving step decreased agglomeration, from 50% (coated powder) to greater than 95% particles finer than 1 μm. This de-agglomeration reduced the torque variation during compounding and pressure variation in the capillary rheometer.

In order to increase the homogeneity of the filaments, a breaker plate and screen were inserted between the extrusion barrel and die in the single screw extruder. The plate and screen

reduce agglomeration and inclusions in the mix, and increase the pressure at the die entrance, leading to better mixing efficiency during filament fabrication.

	coated	compounded		
	LOI (% wt.loss) of powders	ave. compounding torque (m-g)	Instron load variation (N)	LOI (% wt.loss) of RU955
coated powders	2.93 ± 1.08	1071 ± 247	61	19.30 ± 0.33
mixed and sieved	2.86 ± 0.18	1033 ± 52	23	19.31 ± 0.12

Figure 1. Increased homogeneity due to mixing and sieving step.

III. Fused Deposition[1,3,4]

In the process of fused deposition, filament is continuously fed between a pair of motorized rollers into a heated liquifier, where the binder melts. The filament acts as both feedstock and piston, pushing the melt through the nozzle and onto the build platform. Software controls the translational motion of the liquifier/nozzle assembly and the height of the platform, thus "writing" the layered part out of extruded "roads". The extruded road hardens as the binder cools. Material is initially deposited as a perimeter, defining the boundary of each layer of the part, then as a fill pattern, either contours or rasters. The enclosed build envelope is maintained at a warm temperature in order to promote bonding between adjacent roads.

One of the most difficult tasks of this program has been the balance of filament properties required by the process: flexible (for spooling), yet stiff (as a piston), low viscosity (reduce shear in the liquifier) but high modulus. A major obstacle to FDC automation has been buckling of the filament under the rollers and above the liquifier. This is caused by low filament modulus, and is exacerbated by high viscosity reducing flow through the liquifier and heat transfer softening the binder. Direct cooling supplied by an air conditioner onto the filament at the rollers has raised the filament modulus in the necessary process location, and increased the robustness of the filament such that uninterrupted builds of 16 hours have been achieved. The cool air is recirculated in tubes, isolating the cooling process from the warm build envelope; this enables the operator to maintain independent warm and cool environments where they are required.

The nozzles supplied by Stratasys have an internal 0.070" channel, which tapers at the bottom to the particular nozzle tip diameter (0.015", 0.025") at a 118° angle. The liquifier flow channel is 0.073" diameter, thus creating two possible dead zones: at the liquifier-nozzle interface and at the nozzle channel-taper interface. The nozzles were redesigned (**Figure 2**) with a constant channel taper from 0.073" at the top to the tip diameter at the bottom, with the flow channel angle optimized (A. Yardimci, the University of Chicago) to maximize the flow rate for the specific tip diameters. Application of the machined nozzles lowered the motor torque driving the filament as well as the torque variability, and helped to eliminate nozzle clogging.

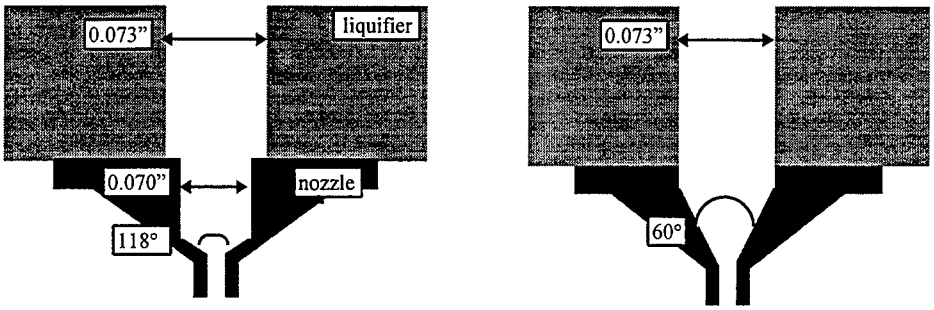


Figure 2. Nozzles re-designed with optimized internal angle and "dead zones" removed.

In order to accurately predict final part dimensions and reduce the necessity for machining, the build roads must be of consistent width and have no apparent seams or bulges at the joints. For contour and raster fills, inconsistent road widths and poor seams can cause internal voids which limit part strength. For perimeter roads, these issues cause sub-perimeter voids and poor surface quality. The parameters which affect flow in the start- and end- zones of the tool path were identified, and the process was optimized for constant width perimeters and controllable seams, as in **Figure 3**.

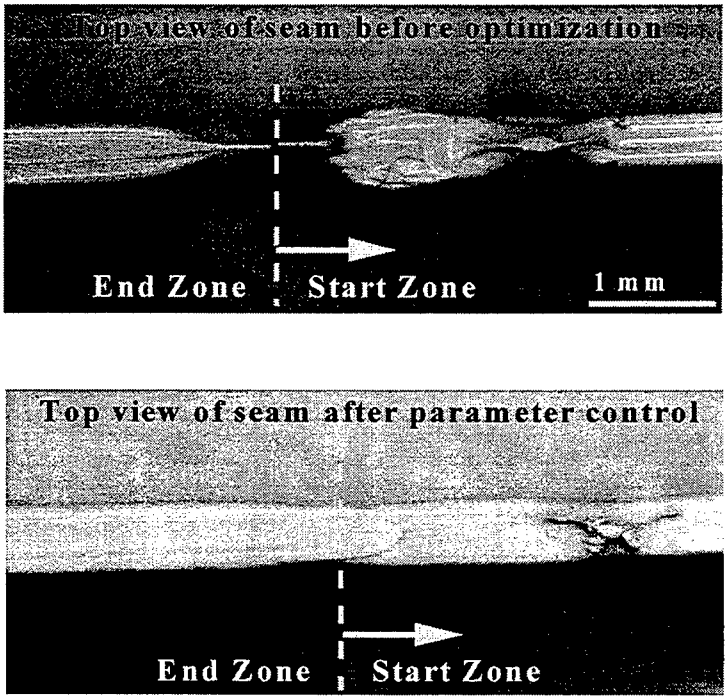


Figure 3. DoE identified critical parameters and optimized perimeter consistency.

Two locations of internal part voids[1,4] are inter-lamellar (between adjacent roads) and sub-perimeter (caused by deviation from the set toolpath, due to control limitations), **Figure 4**. Inter-lamellar voids have been addressed by offsetting the road location such that roads overlap by ~20% of their width. Sub-perimeter voids are also addressed by over-filling, either by raster offset (impinging the raster into a contour or perimeter by ~10% of the latter width) or toolpath alteration to fill the gaps at the corners of the raster turn ("dog-earing"). Figure 4 illustrates the results of experiments to optimize the internal fill of parts, ensuring full green density and consistent strengths.

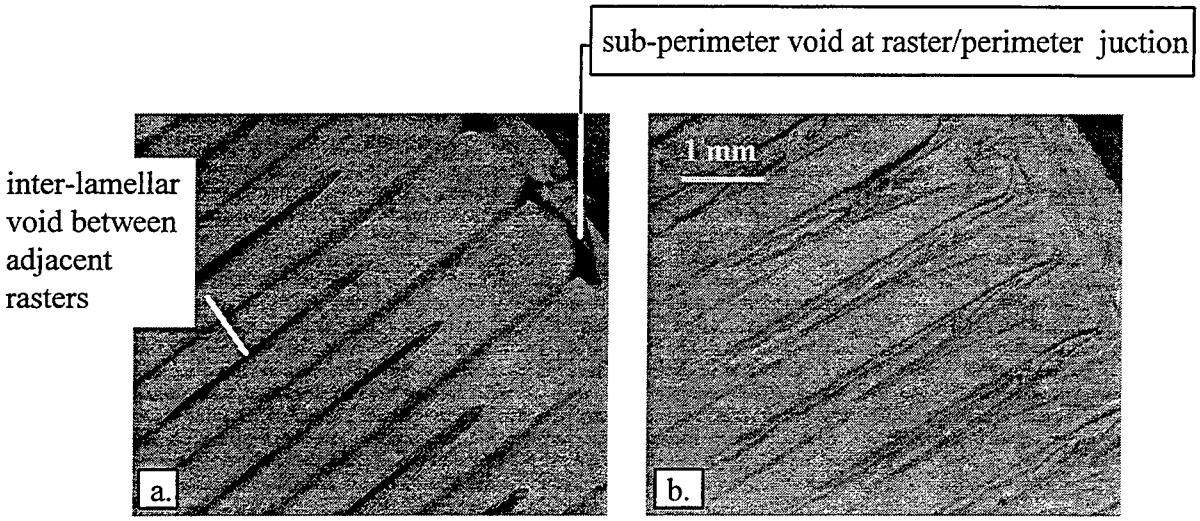


Figure 4. Internal voids reduced by flow control, off-setting, and toolpath alteration; (a.) standard build, (b.) build with inter-lamellar correction and dog-earing.

IV. Binder Burn-Out

The binder matrix must be removed from the green FDC parts before the ceramic particles can be sintered to full density. Thermal degradation occurs during Binder Burn-Out (BBO), a two stage process in which most of the binder is removed slowly at moderate temperatures in a N_2 atmosphere, followed by rapid degradation of residual carbon at higher temperature in air. The parts may crack if binder is removed too quickly, and reproducible shrinkage is critical for meeting final part dimensional specifications.

In order to characterize the critical temperatures in the binder removal process, draw trials were used to measure weight loss and shrinkage of samples soaked at incremental temperatures. The results in **Figure 5** show maximum shrinkage at low temperatures with minimal binder weight loss. This may be due to microstructural rearrangement toward ceramic particle-particle contact and void removal. At higher temperatures, less shrinkage occurs as more binder

volatilizes, creating residual pores. Draw trial results were incorporated into the BBO schedule (170° C dwell to maximize shrinkage) and a DoE (critical intermediate temperatures as binder degrades) which considered the effects of ramp rates, environment, and sample size on shrinkage and cracking. Results indicate that extended dwell times increase shrinkage and lower ramp rates eliminate cracks. The BBO schedule was optimized to ensure reproducible, predictable shrinkage with no part cracking.

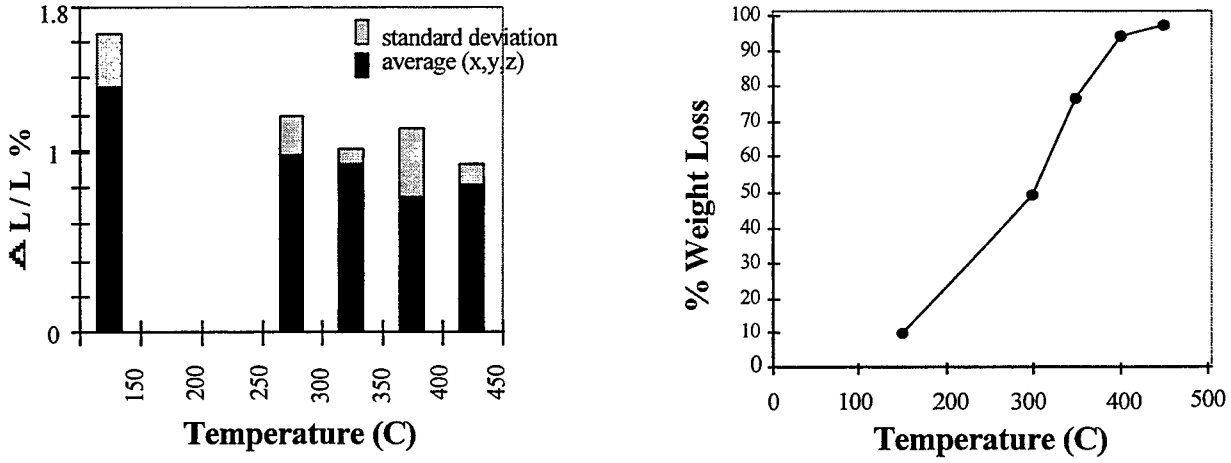


Figure 5. Draw trials of Binder Burn-Out process show critical temperatures.

The application of process improvement tools such as quality control and DoEs, from feedstock and filament fabrication through fused deposition and binder removal, have reduced shrinkage variability to ± 0.5%. This controlled, reproducible shrinkage from FDC to final sintered component (**Figure 6**) allows a more accurate CAD file estimation and reduces the need for machining of the part, which increases cost and can introduce damage.

V. Mechanical Properties of FDC Samples

In order to manufacture functional ceramic parts, strengths comparable to conventional ceramic processing are required. Also, the strengths must be reliable and predictable, with low variability. To evaluate the evolving FDC process, both 4-pt. bend strengths and toughness values are measured on fabricated bars. As the FDC process variability has been reduced, strengths have been consistently high (~900 MPa) with large standard deviation (~135 MPa). Fractography was used to identify large (~100 μm) pores as the root cause of low strengths. A Weibull distribution of the strengths, with samples segregated by failure mechanism, illustrates

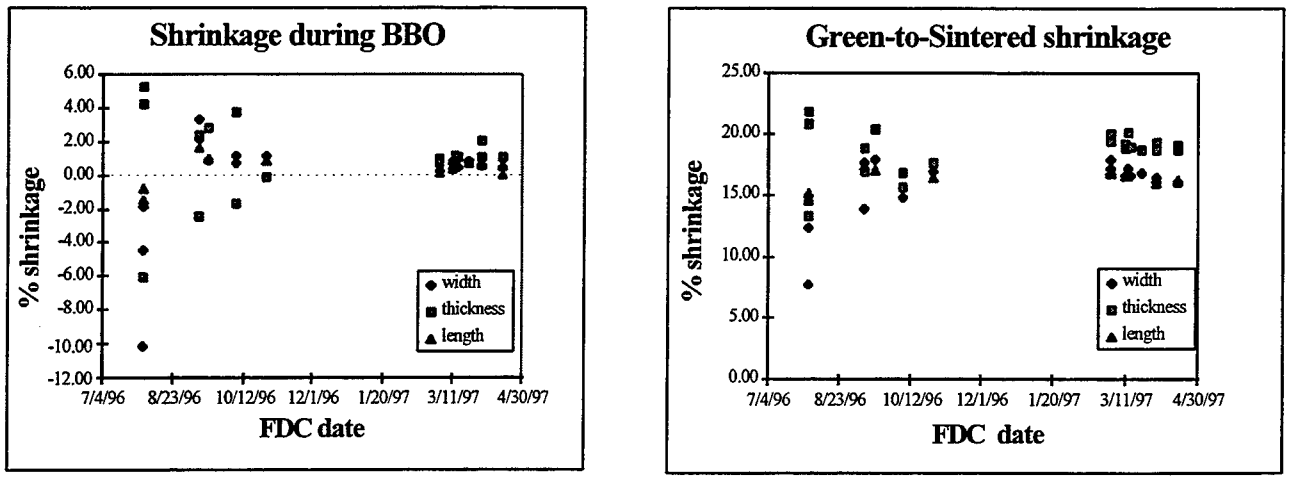


Figure 6. Application of process improvements decreased linear shrinkage variation to ± 0.5%.

the effect of the process improvements (**Figure 7**). "Vintage 1" samples were made before the topics in this paper were addressed, and "Vintage 2" samples were made as the results of quality control and DoEs were incorporated. "Vintage 2" samples which failed due to large pores have a Weibull modulus (slope of curve) of 4.2, comparable to the 5.6 modulus of "Vintage 1" samples. The distribution of "Vintage 2" samples which broke with no discernible root cause has a Weibull modulus of 15.1, which estimates the process potential if large pores could be eliminated (full sintered density).

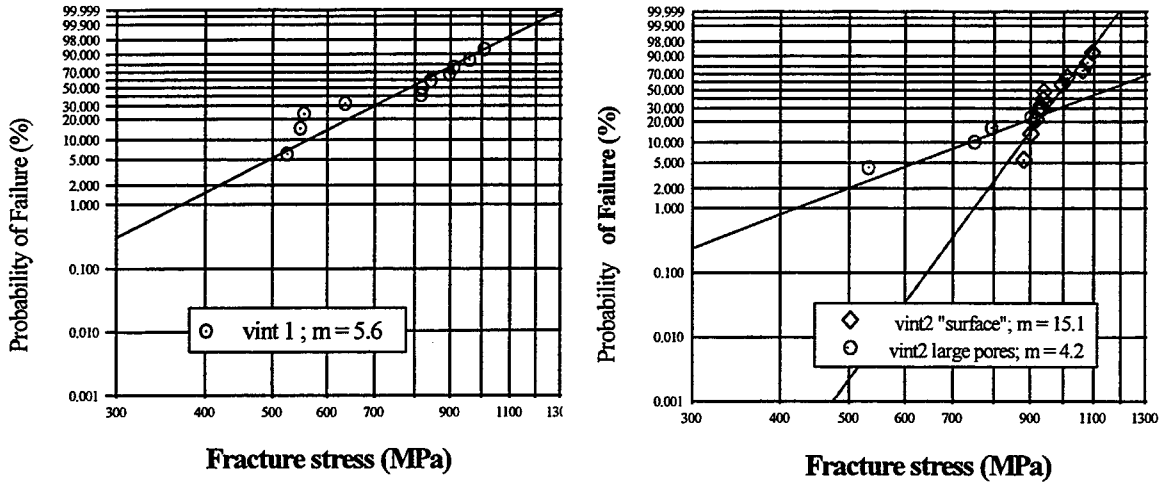


Figure 7. Weibull distributions of FDC bar strengths before current process improvement efforts ("Vintage 1") and during process control evolution ("Vintage 2").

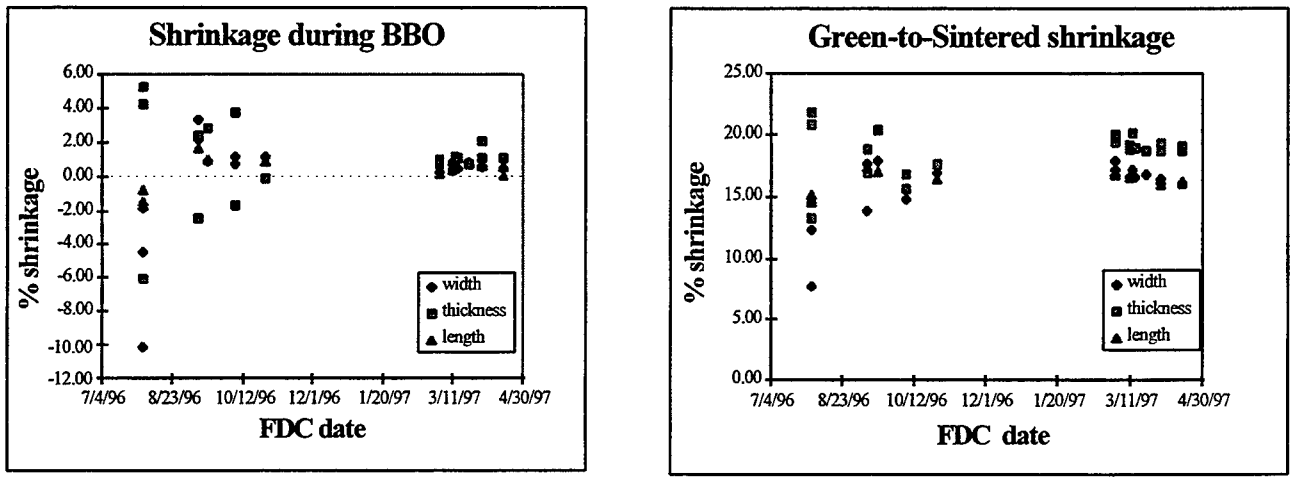


Figure 6. Application of process improvements decreased linear shrinkage variation to ± 0.5%.

the effect of the process improvements (**Figure 7**). "Vintage 1" samples were made before the topics in this paper were addressed, and "Vintage 2" samples were made as the results of quality control and DoEs were incorporated. "Vintage 2" samples which failed due to large pores have a Weibull modulus (slope of curve) of 4.2, comparable to the 5.6 modulus of "Vintage 1" samples. The distribution of "Vintage 2" samples which broke with no discernible root cause has a Weibull modulus of 15.1, which estimates the process potential if large pores could be eliminated (full sintered density).

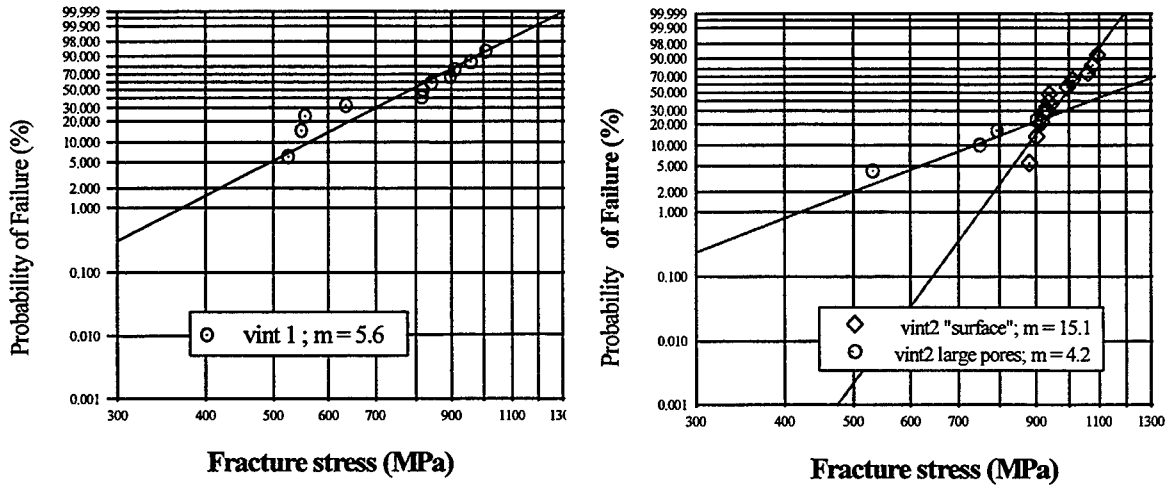


Figure 7. Weibull distributions of FDC bar strengths before current process improvement efforts ("Vintage 1") and during process control evolution ("Vintage 2").

VI. Remaining Technical Barriers to Commercialization

Efforts in the near future will focus on eliminating remaining obstacles to commercialization. Large pores must be eliminated from FDC parts to ensure high Weibull modulus and predictable strengths. Internal voids which occur due to insufficient bonding between adjacent roads will be addressed via dynamic, "on the fly" flow control, rather than by less precise off-setting. Sub-perimeter voids remain a problem at the high-incidence angle intersection of rasters and perimeter, as well as at start-stop zones of the raster fills, and flow control will be investigated in conjunction with off-setting. Statistical Process Control will be instituted to monitor deviation from process targets, and quality control feedback will track each feedstock batch through processing to final sintered part dimensions and strength and isolate aberrant samples.

Acknowledgments

We gratefully acknowledge the support of this research by DARPA and ONR under contract # N00014-94-0115, as well as the support and advice of Drs. John Pollinger and Charles Gasdaska of AlliedSignal, Inc., William R. Priedeman of Stratasys, Inc., and Drs. Amit Bandyopadhyay and Gang Qi of Rutgers University.

References

1. Agarwala, M. K., et. al., "Structural Quality of Parts Processed by Fused Deposition", *Rapid Prototyping Journal*, Vol. 2, No. 4, 1996, pp. 4-19.

2. Agarwala, M. K., et. al., "Filament Feed Materials for Fused Deposition Processing of Ceramics and Metals", *Proceedings of the Seventh Annual Solid FreeForm Symposium*, 12-14 August, 1996, Austin, TX, edited by David L. Bourell, et. al., © The University of Texas at Austin.

3. Agarwala, M. K., et. al., "FDC, Rapid Fabrication of Structural Components", *The American Ceramic Society Bulletin*, Vol. 75, No. 11, November 1996, pp. 60-65.

4. Jamalabad, V. R., et. al., "Process Improvements in Fused Deposition of Ceramics (FDC): Progress Towards Structurally Sound Components", *Proceedings of the 1996 ASME Design Engineering Technology Conference and Computers in Engineering Conference*, 18-22 August 1996, Irvine, CA.

5. van Weeren, R., et. al., "Quality of Parts Processed by Fused Deposition", *Proceedings of the Sixth Annual Solid FreeForm Symposium*, 12-14 August, 1995, Austin, TX, edited by David L. Bourell, et. al., © The University of Texas at Austin.

FDM of ABS Patterns for Investment Casting

By

Paul Blake[*] Eric Fodran[˘] Martin Koch[˘] Unny Menon[˘] Bill Priedeman[*]
Stephen Sharp[˘]

[*]STRATASYS
[˘]CALIFORNIA POLYTECHNIC STATE UNIVERSITY, SAN LUIS OBISPO

ABSTRACT

This paper will evaluate the suitability of fused deposition modeling (FDM) of acrylonitrile butadiene styrene (ABS) patterns for use in investment casting. The focus is on integration with existing foundry practices. It is a combined industry/university project with the case studies performed at the industrial sites with university produced patterns. Process parameters, ash handling and casting issues are addressed.

2 INTRODUCTION

Fused deposition modeling (FDM) has demonstrated the ability to reduce production time requirements in many applications. Like other forms of rapid prototyping, FDM provides a means of directly creating a tangible 3D object from a CAD/CAM image. On average when compared to machining, FDM has provided a method of verifying designs quickly and often, for a low relative cost. Additional decreases in production time can be obtained, if the FDM Acrylinitrile butadiene styrene (ABS) builds were used as the investment casting patterns. The feasibility of this is determined by addressing casting issues, ash handling, and process parameters, as well as, through thermal analysis and macroscopic examination.

3 GOALS

Our goals are to present casting guidelines for the average Investment Casting Foundry (IC) to use with the ABS patterns. These guidelines involve the use of simple techniques and common materials, and have generally resulted in successful castings.

4 CASTING ISSUES

In order for ABS casting patterns to reduce the investment casting time cycle, ABS must be easily useable with standard practices. Therefore, pattern preparation, gating and venting, investing, burn-out, ash removal, and casting must be considered when determining if ABS is a usable alternative to wax.

4.1 Pattern Preparation

The ABS patterns are robust and easy to work with. They sand well and can be machined. They can be modified with wax to improve surface finish, and combined with waxes to form composite patterns.

4.2 Gating and Venting

For ABS patterns, traditional gating and venting practices require some modifications. These changes can easily be adapted to IC, and must be followed in order to obtain adequate ash removal. It is during the gating and venting design process that the modifications are first introduced.

Ash removal will require low air pressure and water rinsing. Therefore, it is necessary to install additional vents on the pattern. This will improve the air and water feature penetration during the ash removal process. A fair amount of access to the interior of the mold structure is also gained by cutting open the gate end. This too will increase the efficiency and ease of the ash removal. Consequently, it is also important to design the investment tree with the idea that the gate and vent ends will be removed prior to the burn-out process.

Once the investment tree design has been established, standard IC technique is used to attach the gates and venting.

4.3 Investing

A cleaning/etching agent is normally applied to the investment tree prior to shelling. This provides a means of removing any release agents. Once the

cleaning/etching agent has dried, standard investment casting procedures are followed in producing the shell. Generally an FDM investment shell is composed of, first, three normal layers, followed by three layers with steel wire reinforcement, with a final seal coat then applied. The number of reinforcing layers can be increased to strengthen the shell when necessary.

After the final seal coat has dried, the tips of the vents are ground to expose the wax. The main sprue is also ground exposing the wax. This modified investing step, must be performed prior to the burn-out cycle.

4.4 Burn-Out

Two methods have demonstrated potential for removing Rapid Prototype (RP) patterns from an investment mold. Though both techniques have succeeded in reducing the pattern and associated material to ash, each has inherent drawbacks.

The autoclave / high temperature burn method is a two step process. First, the mold is placed in an autoclave to remove the majority of the wax from the mold. This step is considered the melt-out cycle, with temperatures ranging between 200 °F to 300 °F (94 °C to 150 °C) (Jacobs 1996). The mold is then transferred, in the second step, to a high temperature oven. At this stage the pattern material is reduced to ash and any residual wax is incinerated. During this stage, the burn-out temperature will range between 1,200 °F to 1400 °F (650 °C to 760 °C) (Jacobs 1996). A disadvantage with this method is that on occasion, the shelling has been reported to crack. This is due to the expansion of the RP material during the melt-out cycle and is addressed by using additional layers and reinforcement..

The temperature for the flash process, starts at 1600°F (871°C) and is elevated to as high as 1900°F (1038°C) for burn-out. This method reduces the RP pattern, as well as all associated tree material, to ash for easy removal. This method too has a drawback. All of the wax in this technique is incinerated, which creates additional smoke during the process.

Both methods have worked successfully with FDM ABS molds. Foundries should determine which method is preferred for their casting process.

4.5 Ash Removal

Removing the ash requires an additional step when casting with a FDM ABS pattern. After the shell has been blown-out with low pressure air and flushed with water, the open gate end and vent openings are resealed with shell repair cement.

4.6 Casting

Casting procedures for FDM ABS mold and traditional investment casting are the same. Standard filling methods and furnace temperatures are applicable.

5 CAST PATTERNS

ABS is the pattern material to be studied. It is the name given to a polymeric structure that represents a family of thermoplastic materials (Smith 1990). ABS is a mixture of three monomers: polyacrylonitrile, polybutadiene, and polystyrene. ABS is not a terpolymer though, it is based on blended copolymers of styrene-acrylonitrile

(70:30) and butadiene-acrylonitrile (65:35) and on graft interpolymers of styrene and acrylonitrile with polybutadiene (Smith 1990) (Sharp 1990). By adding modifiers to the basic ABS mixture, the material properties can be altered. Consequently, the ABS material being evaluated should be the same material that is used during the production of a FDM build.

6 THERMAL ANALYSIS

Thermogravimeteric Analysis Systems (TGA) have proven effective for temperature related polymeric degradation studies. The TGA is designed to measure the change in the sample's mass with respect to the temperature of its environment, even if that environment is altered (Kelen 1983). Several methods can be used to alter the environment: varying the temperature, introducing reactive gases into the sample chamber or a combination of these variables.

After determining the appropriate test parameters, two samples are selected for exposure. The first specimen is the actual sample material; contrarily, the other is inert to the test environment. The inert sample, known as the reference sample, provides a reference point during thermal analysis.

6.1 Graphical Interpretation

Most TGA systems also provide the derivative of the thermogravimeteric curve (DTG) and label the curve, the Differential Thermal Analysis (DTA). The DTA provides information on endothermic or exothermic reactions in the sample material. This is depicted by plotting the change in temperature measurements for the sample against the unaffected reference sample. The endothermic and exothermic points are then useful in determining the temperature at which deterioration of the material properties occurs (Kelen 1983).

7 MACROSCOPIC EXAMINATION

Macroscopic examination is one of the most basic forms of visual examination available. Often used as a prelude to microscopic studies, macroscopic inspection can also be used alone. In this case, inspection of the cast parts will be visually inspected, unless it is deemed necessary to examine a part in greater detail.

8 EXPERIMENTATION

Several builds were produced using the Stratysis 1600. These builds were then used as investment casting patterns and for thermal analysis. The two different types of builds produced were the 3D Systems "Nine-Wall" patterns, seen in figure 1, and the Stratysis "Turbine" pattern, seen in figure 2.

8.1 CASTING

Each sample requires some preparation work prior to casting. Sanding was not required, but a utility knife was used to shave plastic stringers and remove some of the ABS support material. A small screwdriver was also utilized to remove some of the ABS support material from the patterns. The final preparation requirement for each pattern

was to fill the small surface openings with paste wax. Approximately 20 minutes was required to prepare each pattern for investing.

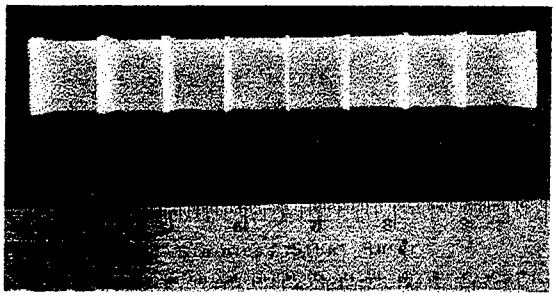


Figure 1 - FDM Nine-Wall ABS pattern

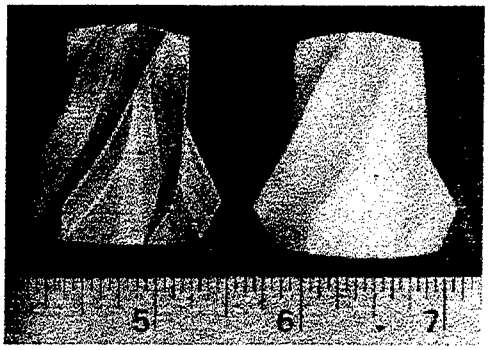


Figure 2 - The as cast turbine pattern on the left and ABS turbine pattern on the right

Some of the patterns were provided to Aurora Engineering for use as casting patterns. A design that would be capable of providing adequate access for ash removal was determined first. The investment tree design and venting arrangement are show in figure 3. The investment tree was composed of a styrofoam core with a wax coating. Addition venting is also evident in figure 3, from the increase in the bleeder wax, that is positioned around the ABS pattern.

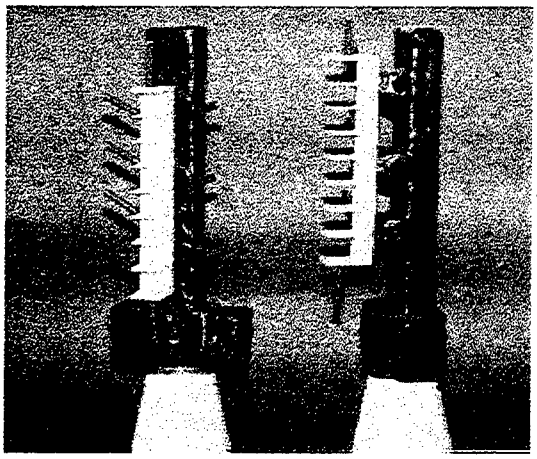


Figure 3 - Nine-Wall pattern ready for investing

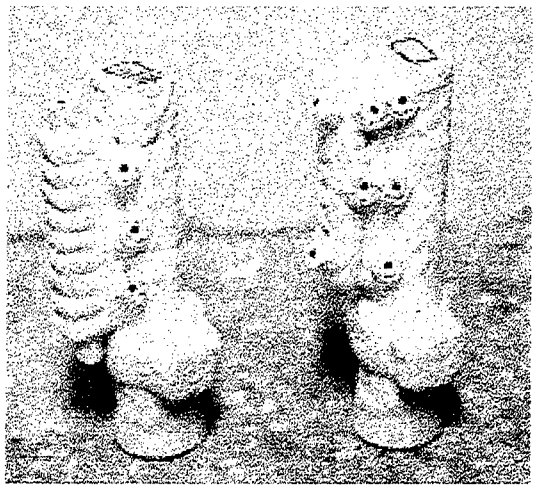


Figure 4 - Invested pattern with gate end and vents opened

The entire investment tree was sprayed with isopropyl alcohol and allowed to dry, in preparation for the investing process. Once the investment tree had dried, it was dipped in a coating solution a total of seven times: three normal coats, three coats with steel wire added, and then one final coat. The final invested pattern is shown in figure 4. The ends of the vents and gates have been removed to aid in subsequent ash removal. Burn-out was performed using the flash process. The molds were placed in a preheated

furnace at 1600°F(871°C), immediately raised to 1900°F (1038°C) and left for 90 minutes. After burn-out, the ash (a light white powder) was remove with low-pressure air and water. Mold repair cement was then used to reseal the vent and gate ends.

Standard casting procedures were then followed and aluminum was cast into the molds. The molds at the time of casting were preheated to 1200°F (649°F) and the aluminum was poured at 1285°F (696°C).

The molds were allowed to solidify and the shelling was removed. This produced the as cast structure that is seen in figure 5. After removing the excess material, the gating and venting contact points were ground smooth. The finished products are visible in figure 6, as well as in the Turbine Pattern comparison photograph labeled figure 2.

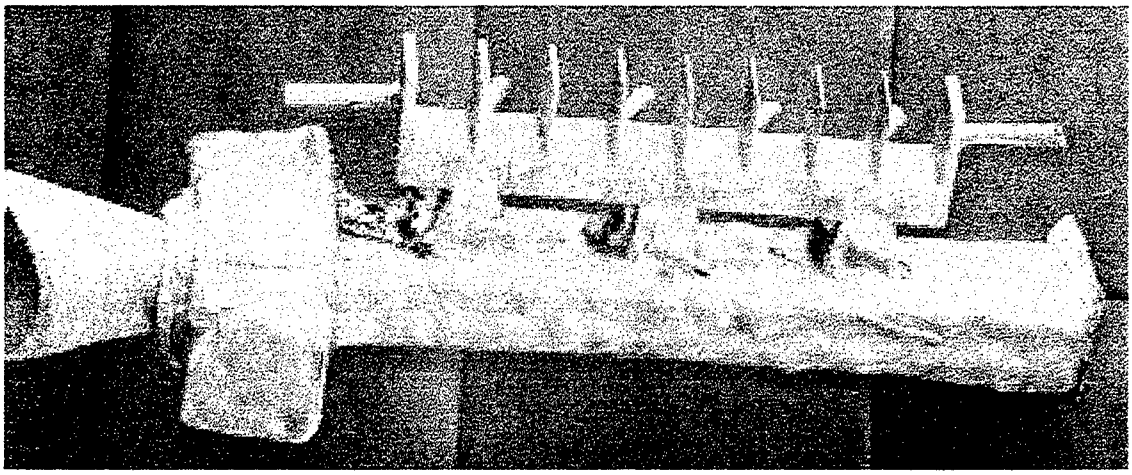


Figure 5 - As cast Nine-Wall prior to removal of excess material

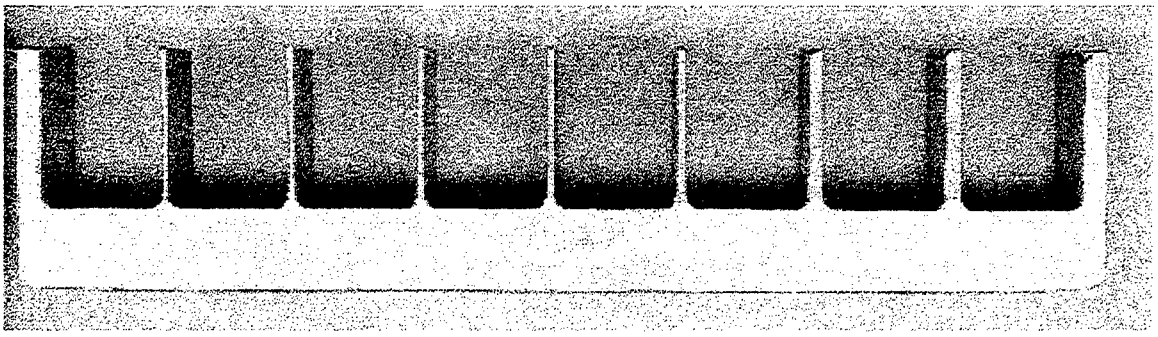


Figure 6 - Final Nine-Wall casting

8.2 Thermal Analysis

ABS Samples for thermal analysis were taken from a Nine-Wall pattern. The TGA test was then programmed to simulate the environment that the ABS would be exposed to, and react in, during the burn-out process. The ABS was subjected to a temperature range that started a 71.6 °F (22.0°C) and was raised to 1112°F (600°C). The gas environment used during the entire test period was air. At the completion of the test, the computer generated graphs showing the weight as a function of temperature, and the derivative of that function. This graph is illustrated in figure 7.

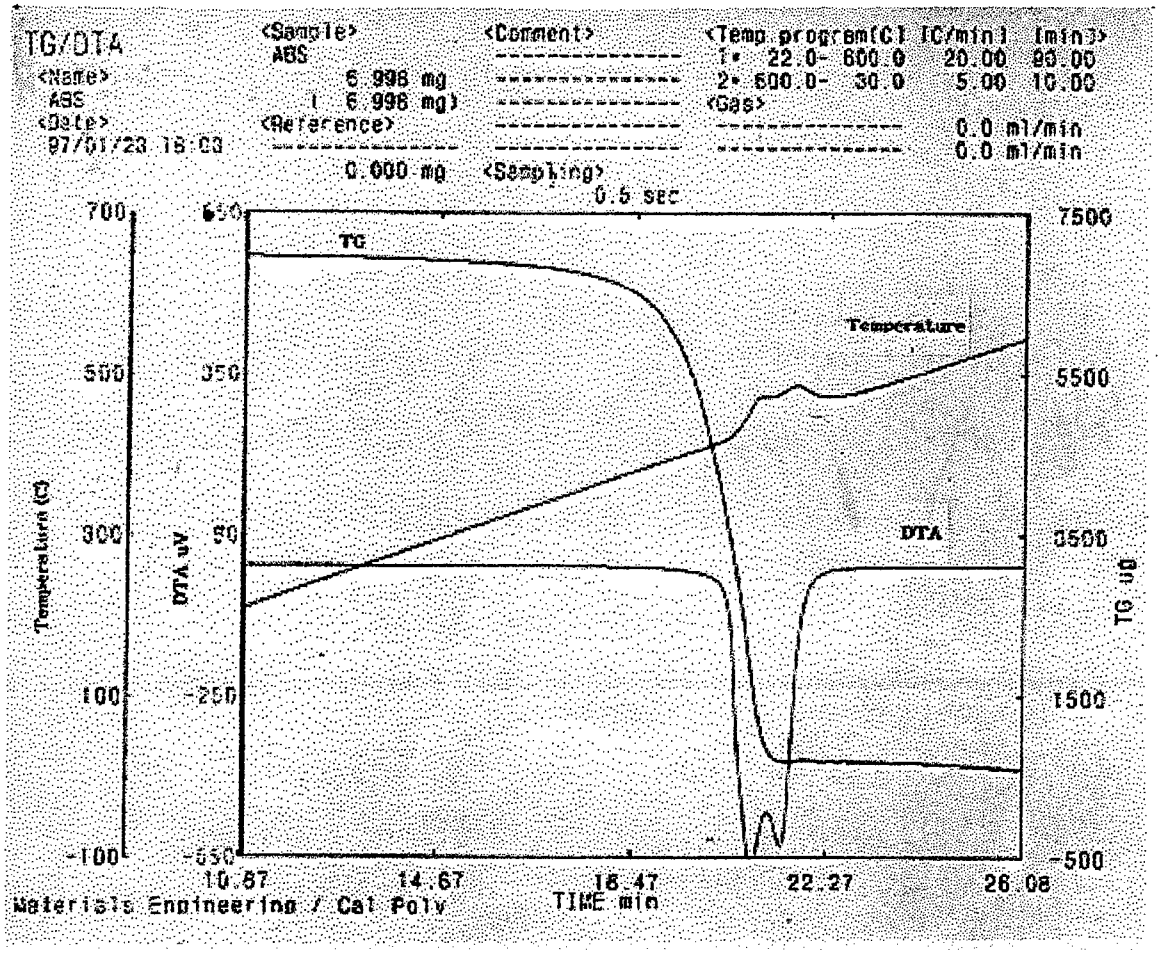


Figure 7 - TGA results showing degradation and exothermic peaks

9 RESULTS AND DISCUSSION

The FDM ABS builds all performed successfully as IC patterns. The ABS patterns, which were built at an academic institution, were transferred to industry and easily assimilated into the IC process.

Upon visual inspection of the final IC cast products, surface appearance was found to be acceptable, and an example of the surface is shown in figure 8. The surfaces in the cast products may be improved further, by increasing the time spent preparing the surfaces of the patterns. Fine, thin wall details, as in the fins on the Nine-Wall pattern and the Turbine pattern, as seen in figures 9 and 2 respectively, were accurately replicated. The only noticeable imperfection was found at the tip of one fin. This was most likely due to the fin cooling too quickly and the metal solidifying before it had completely filled this given area, a cold short.

The TGA confirmed that the ABS material burn-out process is above the required temperature for ABS to degrade. As was evident from figure 7, degradation of the plastic occurs at approximately 797°F (425°C). This is displayed by the exothermic reaction and is estimated from this figure.

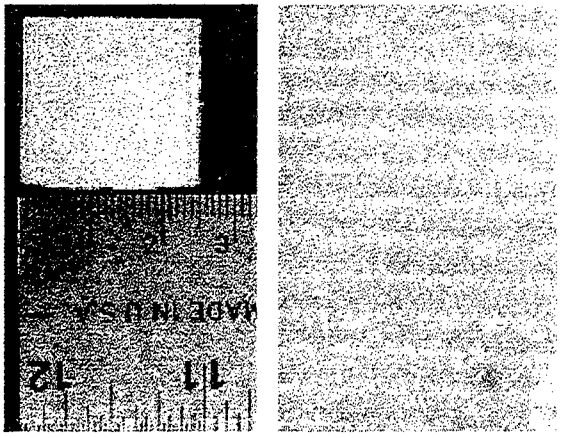


Figure 8 - Magnified view of the same as cast surface. The left picture was photographed with a light macroscope and the picture on the right with a SEM at 22.8X.

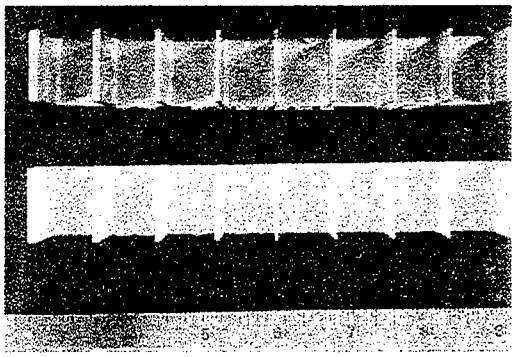


Figure 9 - As cast Nine-Wall on top and the ABS Nine-Wall pattern on the bottom.

10 CONCLUSION

This industrial/university joint project, addressed the IC requirements for FDM of ABS builds to be used as patterns in industry. It was determined that modifications would be necessary, but that these changes are easily adaptable with present IC techniques. Therefore, FDM ABS patterns are suitable for use in investment casting facilities.

11 REFERENCES

Jacobs, P. F. (1996) ***Stereolithography and other RP&M Technologies***, Society of Manufacturing Engineers, New York

Kelen, T. (1983) ***Polymer Degradation***, Van Nostrand Reinhold Company Inc., New York

Smith, W. F. (1990) ***Principals of Materials Science and Engineering***, McGraw-Hill, Inc., New York

Sharp, D. W. (1990) ***Dictionary of Chemistry***, Penguin Books, London

RAPID PROTOTYPING OF FUNCTIONAL METAL AND CERAMIC COMPONENTS BY THE MULTIPHASE JET SOLIDIFICATION (MJS) PROCESS

Donald Kupp and Harald Eifert
Fraunhofer Resource Center-Delaware
1 Innovation Way, Suite 301
Newark, DE 19711

Matthias Greul and Matthias Künstner
Fraunhofer-Institute for Applied Materials Research
Lesumer Heerstr. 36
28717 Bremen, Germany

Abstract

The need to generate high-quality conceptual models of manufacturing components and limited application functional components has driven the development of Rapid Prototyping (RP) in the last fifteen years. Recently, however, it has become increasingly obvious that an RP system that can produce fully functional components in materials other than polymers would be beneficial. In order to fulfill the requirements for the direct production of metallic and ceramic components for functional testing and application, the development of new processes and materials are key development areas at the Fraunhofer Institute for Applied Materials Research (IFAM) and the Fraunhofer Resource Center-Delaware (FRC-DE). For the free-form fabrication of ceramic and metal parts, the Multiphase Jet Solidification (MJS) process has been developed for producing metal and ceramic components. The MJS process extrudes metal and ceramic based binder systems (such as Al_2O_3, SiC, stainless steel, and Ti), forming the desired component layer by layer. As in powder injection molding, after a part is formed by MJS, the binder phase is removed chemically or thermally and the remaining powder compact is sintered to final density. This paper presents the MJS technique and outlines a variety of potential applications.

Introduction

Commercial rapid prototyping has matured tremendously in the last five years to include a wide range of process techniques and materials. Based on a 3D CAD description of the desired geometry, these advanced processes now represent rapid and economical methods for producing manufacturing models and prototypes. However, for the free-form fabrication of functional prototypes, only a few materials systems and deposition techniques currently exist. For example, for metallic prototypes, a second step of investment casting or infiltration of the rapid prototyped part is commonly needed to produce a dense, fully functional piece. This method presents limitations in terms of the compositions that can be produced and in the process time reductions that are normally achievable through rapid prototyping.

As the rapid prototyping technologies mature and materials availability broadens, the need to produce truly functional ceramic or metal components through rapid prototyping has become more apparent. In order to meet increasingly stringent requirements, several new approaches based on powder metallurgical techniques have evolved. One such process, Multiphase Jet Solidification (MJS), has been developed to produce free-form metallic or ceramic components from powder/binder mixtures.

Working Principles of the MJS Process

The working principle of the MJS system is shown in Figure 1. A mixture of metal or ceramic powder and a suitable polymer-based binder system (i.e. feedstock) is held for delivery in the heated chamber. The feedstock is heated to the desired temperature to achieve a suitable viscosity then extruded through the nozzle by a pumping system. As the feedstock is extruded, the extrusion nozzle is rastered in the x-y plane to deposit the molten feedstock. The feedstock solidifies as it contacts the substrate (first deposition layer) or previously deposited layers due to the temperature and pressure decrease and heat transfer to the part and surrounding environment. Since the extruded material is in the liquid state, it partially remelts the previously deposited layer, forming a well bonded, continuous structure. After each cross section or "slice" is completed, the extrusion head is incremented in the z direction in step sizes of 0.1 mm to 0.5 mm and the next layer is begun. This process is repeated until the part has been fabricated to its final extension.

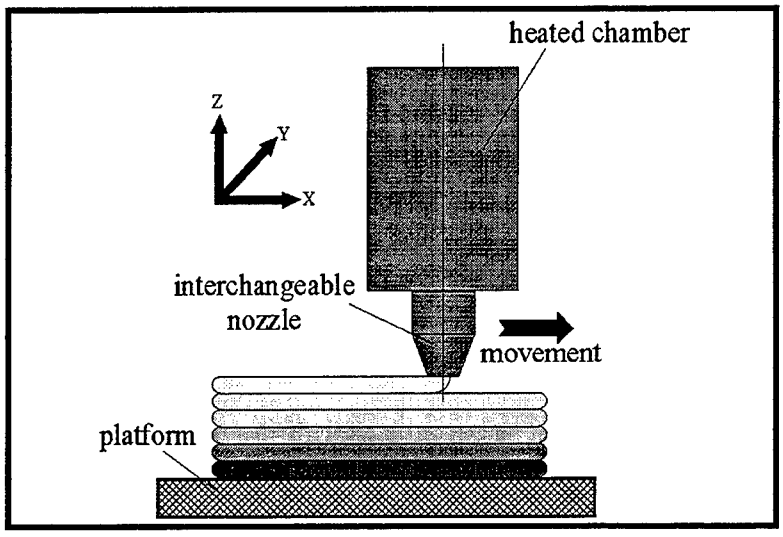


Figure 1. A schematic representation of the working principle of the Multiphase Jet Solidification System.

Components are fabricated on the basis of a 3D CAD model. From this description, STL files are generated to produce a numerical control code which drives the

extrusion head. Process parameters such as positioning speed and material extrusion rate are added and the control file for the machine is generated [1].

Based on the MJS technique, the RP Jet-200 System was developed and constructed in collaboration with the German manufacturer, Logeto GmbH. A heated extrusion chamber with a stability of ±1°C (up to 200°C) can accept feedstock in powder, granulate, bar or rod form. Various extrusion tip geometries from 0.02 in (0.5 mm) to 0.08 in (2.0 mm) have been successfully used. A computer is used to control the x-y-z positioning system with a precision of ± 0.0004 in (0.01 mm) and a total work volume of 10 x 10 x 7 in (250 x 250 x 175 mm). Figures 2 and 3 show the system installed at the FRC-DE.

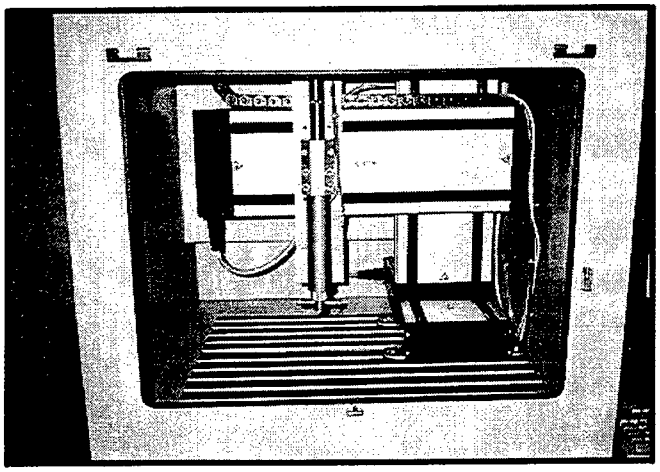


Figure 2. Extrusion head and translation system of the RP Jet-200 MJS machine.

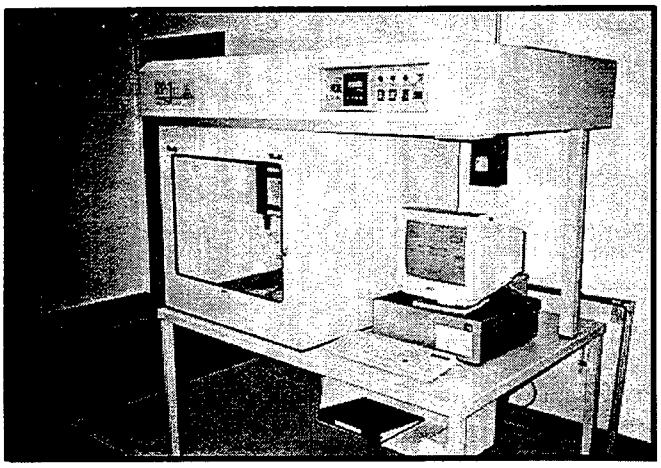


Figure 3. The RP Jet-200 MJS system from Logeto, GmbH. showing the deposition chamber and computer control station.

While the suitability of any feedstock system for use in the MJS process must be determined individually, the RP Jet-200 MJS system was developed specifically to accommodate the general rheological behavior and processability of PIM materials. Based on the use of such PIM feedstock materials, the fabrication of metal or ceramic components is carried out in three basic steps:

- The first step is to fabricate the component, comprised of metal or ceramic powder in a polymeric matrix. This "green" component is similar to that produced through powder injection molding except that the geometry has been developed without the use of any restrictive fixtures or molds. The feedstock and therefore, the "green " component is composed of up to 50-70 volume percent solid material (balance of polymer). This solids loading level can usually be modified somewhat depending upon the related processing criteria and ultimate performance characteristics of the finished part.
- After the part has been formed, the polymer matrix must be removed so that only metal or ceramic material remains prior to heat treatment to its final composition and microstructure. Depending on the type of polymer binder system used, different techniques for binder depletion can be implemented. Most commonly, a form of standard powder metallurgy or PIM methods involving chemical dissolution and/or thermal decomposition are used to produce a "brown" part (also known as debound or debindered part).
- This "brown" part, comprised of only metal or ceramic material, can now be heat treated or sintered to its final, desired density.

Figure 4 shows sample feedstock and prototype "green" and sintered components fabricated with the MJS process using an EVA copolymer/paraffin wax binder system.

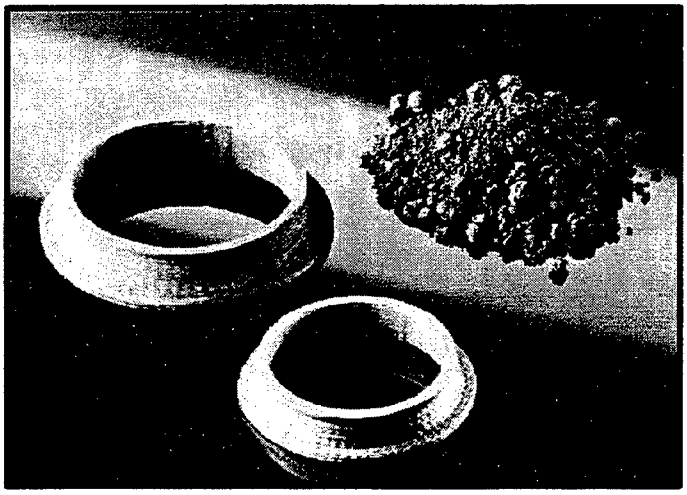


Figure 4. Feedstock for use in the MJS process (right) and "green" (left) and sintered (foreground) parts produced by Multiphase Jet Solidification.

Manufacturing Capabilities and Materials

A prime feature of the MJS technique is its ability to produce fully functional metal or ceramic components using commercially available feedstock material. Many types of feedstock systems are readily available for use in powder and polymer injection molding (PIM) and even low temperature alloys. The broad range of these systems allows the user to select the appropriate feedstock to meet specific criteria in component fabrication including such things as part complexity, binder removal technique, and most importantly, base material composition. Ceramic-based feedstock systems such as aluminum oxide, silicon nitride, silicon carbide, and zirconium oxide are currently available. Metal-based systems such as carbonyl iron, various stainless steels, magnetic materials and titanium are even more widely known and distributed.

MJS is closely related to the PIM process with the primary difference being that MJS enables fabrication of parts without the use of a mold. Table 1 shows some examples of typical PIM materials in different groups. Representative samples of each group have been successfully processed with the MJS system preparing tensile test bars and other testing shapes. Comparison of PIM and MJS processing is shown in Figure 5 [2].

Material Group	Examples for Typical MIM Materials in this Group	Successfully Tested with MJS
Stainless Steels	AISI 316L, 410, 430	316L
Heat Treatable Steels	17-4-PH, $Fe_2Ni0.5C$, Fe7Ni,0.9C	not tested
High Speed Steels	D2, CPM 9V/10V	M4T2
Magnetic Materials	FeNi, FeCo, FeSi, FeNdB, AlNiCo	FeNi
Lightweight Materials	Ti, TiAl6V4	Ti
Special alloys	WFeNi, WCu, NiAlCr, silicides, Stellites	Stellite (Co-Cr-Mo)
Ceramics and Carbides	Al_2O3, SiC, WC-Co, ZrO_2	SiC

Table 1. Examples of different material groups and typical MIM alloys.

The material most widely produced by PIM is 316L stainless steel. A comparison of typical MIM parts of 316L stainless steel to those fabricated using the MJS process can be seen in Table 2.

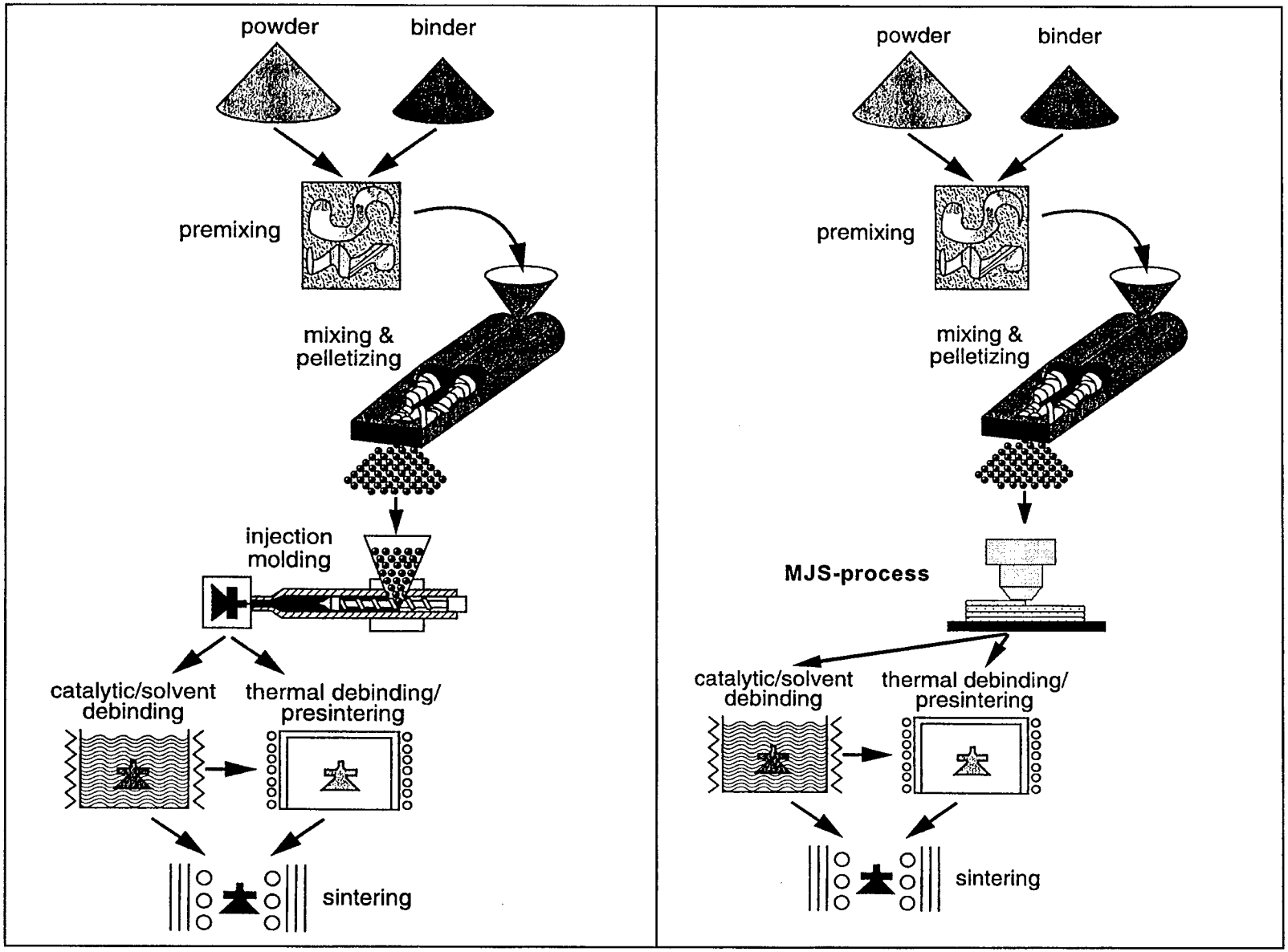


Figure 5. Comparison of PIM (left) and MJS (right) component fabrication routes [2].

Process and Material	Density (% of theoretical)	Ultimate Tensile Strength (MPa)
MIM 316L, typical values [2]	95-99.8	450-520
MJS 316L	97-99.3	480

Table 2. Mechanical properties of 316L stainless steel (Fe-17Cr-12Ni-2Mo-2Mn) prepared by metal injection molding and MJS.

Summary

Generally, the MJS technique can process any materials that can be processed via PIM. Currently, the only limitations are that the feedstock viscosity should be in the range of 10 to 200 Pa·s with a binder melting temperature below 200°C These process boundaries can likely be exceeded with minor hardware modifications. All material systems mentioned previously have been successfully processed via MJS with other materials such as tool steels, hard alloys, and ultrafine materials under development. Also, highly filled polymer systems such as carbon-black based feedstock for conductive polymers are suitable for MJS deposition.

Since the MJS process produces fully functional parts, it is useful not only as a rapid prototyping technique for producing demonstration and visualization components, but also as an agile manufacturing process which can produce limited production runs of specialty items for real applications and performance trials. Also, by using MJS in combination with PIM feedstocks, the materials development for injection molding (shrinkage, debinding, and sintering behavior) can be completed without using expensive tooling.

Rapid prototyping systems commercially available today do not satisfy the requirements of manufacturers in need of functional metallic or ceramic prototypes. Compared to Selective Laser Sintering [3] or 3D printing [4], the MJS process has the prime advantage of utilizing a broad range of materials in a process closely related to powder injection molding, an existing and already successful technology. Due to the variety of developed applications for PIM, many material systems or feedstocks suitable for MJS are already commercially available. The ability of MJS to form components using materials with high melting points combined with the relative simplicity of the deposition apparatus further enhances the usefulness of such a technique.

Common to all RP techniques, the development of new materials systems and optimization of the deposition technology in areas such as accuracy, surface finish and production times are on-going developmental issues. Further development in areas such as feedstock rheology, deposition mechanics, and hardware and software design will lead to the production of more complex geometries with improved accuracy and repeatability.

References

[1] M. Greulich, M.Greul and T. Pintat, "Fast Functional Prototypes via Multiphase Jet Solidification," Rapid Prototyping Journal No.1, S. 20-25, MCP University Press Ltd., West Yorkshire, 1995.

[2] German, R.M. and Bose, A., *Injection Molding of Metals and Ceramics,* Metal Powder Industries Federation, Princeton, NJ, 1997.

[3] T. Pintat, M. Sindel, M. Greul and O. Nyrhilä, "Direct Selective Laser Sintering of Metals and Metal Melt Infiltration for Near Net Shape Fabrication of Components," *Proceedings of the Solid Freeform Fabrication Symposium,* The University of Texas at Austin, Austin, TX, 1994, p. 175-180.

[4] E. Sachs, "3D Printing of Functional Parts and Tooling," *Proceedings of the International Conference on Rapid Product Development,* Stuttgart, Germany, 1994.

Bonding Methods for Laminated Tooling

by

Daniel F. Walczyk, Nathanael Y. Dolar
Department of Mechanical Engineering, Aeronautical Engineering and Mechanics
Rensselaer Polytechnic Institute
Troy, New York

Abstract

Laminated tooling consists of an array of stacked laminations that are mechanically clamped or bonded together, depending on the requirements of the manufacturing process. Various manufacturing processes that can benefit from tooling constructed of laminations include sheet metal forming, thermoforming, composites molding, metal extrusion, injection molding, resin transfer molding, and compression molding. When bonding of the laminations is required (e.g., incorporation of conformal cooling passages for injection molding temperature control) then laminations can be joined together by diffusion bonding, brazing and using adhesives. However, for a tooling engineer to effectively design a laminated tool, the physical and mechanical properties of these joints must be known. Consequently, a set of experiments is outlined for determining the tensile, shear, and peel strengths, tensile and shear elastic moduli, thermal contact resistance, and specific permeability (for gasses or liquids) of the aforementioned bonded joints for both steel and aluminum laminations. Some preliminary results with aluminum and future work are presented.

Introduction

The concept of making intricate parts (e.g. transformer core, door lock assembly, gear) by assembling profiled or contoured laminations is a well-established manufacturing technique [15]. Laminated constructions have also been investigated, and successfully implemented by a few U.S. and Japanese companies [1,2] as a direct rapid tooling technique because of demonstrable advantages over other more conventional methods like CNC-machining and EDM. These advantages include the elimination of tooling accessibility problems, reduced limitations on die geometry, faster fabrication, and easier incorporation of conformal cooling passages [1,3]. However, laminated tooling techniques have not yet seen widespread use in industry. One of the main reasons for industry's hesitance to adopt laminated tooling is the problem of having to make a rigid tool out of an array of laminations. As shown in Figure 1, the two methods for accomplishing this are by mechanical means (i.e., clamping laminations together) and by bonding methods (i.e., welding, brazing, soldering, diffusion bonding, and adhesives).

This paper focuses on the latter method (i.e., bonding), especially for laminations with beveled edges as shown in Figure 1. Furthermore, it will address the problem of bonding laminated tooling in a more comprehensive manner than has been done previously. Consequently, previous work in this area will first be discussed. A survey of manufacturing processes that can benefit from using laminated tooling will also be mentioned along with process requirements that are needed for tooling design. This will be followed by discussion of common bonding techniques available for laminations made out of the two most common tooling

materials used by industry, i.e., aluminum and steel. The complete experimental procedure of an ongoing research effort to characterize the mechanical and physical properties (i.e., tensile, shear and peel strengths, tensile and shear elastic moduli, thermal contact resistance, permeability, and dimensional changes) of bonded steel and aluminum laminations will be outlined. Finally, some preliminary results with aluminum will be presented.

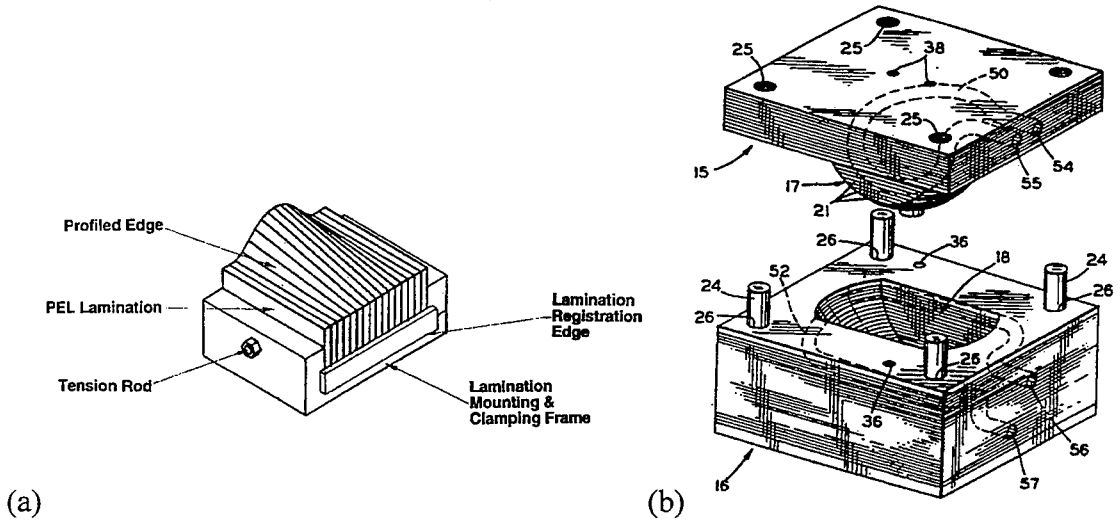


Figure 1 - Securing laminations together by (a) mechanical means and (b) with bonding methods.

Background

Several researchers have successfully used purely mechanical means to clamp die or mold laminations together for manufacturing production work. The manufacturing processes that tooling was created for include shoe making molds [4], sheet metal forming dies [1], polyurethane foam molds [5], and plastic injection molds [3,6].

Sometimes mechanical clamping of laminations is insufficient to meet the requirements of a particular manufacturing process. When this is the case, then the laminations will need to be bonded together into a solid die in order to meet these requirements (e.g., sealing required for conformal cooling passages, increased shear strength for sheet metal forming). Some preliminary work in lamination bonding includes laser welding lamination edges [7,8], brazing laminations together [9], bonding paper laminations together with a heated polymer layer [10], using adhesives for bonding plastic laminations [11], cementing steel laminations with a combination of adhesives and edge welding [12], diffusion and pressure bonding steel laminations together [13], and tack welding adjacent layers with an Nd:YAG laser [14]. Unfortunately, none of this previous work has investigated the specific mechanical and physical requirements (i.e., tensile, shear & peel strengths, tensile and shear elastic moduli, thermal contact resistance and permeability at various temperatures) for bonded joints that's required for a particular manufacturing process. Nor have any automated methods for bonding tool laminations (except for Ref. 10) been developed.

Candidate Manufacturing Processes for Bonded Laminated Tools

By virtue of previous research and a need for enhanced die or mold performance over that which is achievable using conventional fabrication means, the following manufacturing processes have been chosen as candidates for laminated tooling:

Sheet Metal Forming including cold and hot matched-die forming, drawing, and hydroforming. forming of sheet metal over a form die(s) of the desired shape. The metal is stretched to approximately 2% to 4% total strain, just beyond its yield point, to retain the contour of the die. High normal and shear forces on the die surface will tend to peel and shear bonds between laminations.

Thermoforming involves heating of a polymer sheet to its softening point, above the material's glass transition temperature (55-90°C), and drawing the pliable material against the contours (using vacuum or applied pressure) of the mold where it is held until cooled. Mild normal forces will tend to shear and pull bonds between laminations.

Composites molding involves curing of composite materials using a male or female mold at room temperature (25°C) and pressure or higher (autoclave curing). The pressures imposed by the autoclave is an overall external pressure, in essence, hydrostatic. Although in some cases, there is shrinkage involved with the heating of the composite. This can lead to some shearing loads on lamination bonds. Conformal cooling passages are sometimes used in composites molding.

Metal Extrusion involves forcing a billet of material (Aluminum, copper, magnesium, zinc, tin and their alloys) through a die opening, by way of a ram or a press, to produce a desired cross-sectional shape. Hot extrusion requires that the tool must be able to operate under severe conditions of temperature, pressure, and abrasive wear. Extrusion of metals creates very high shearing and normal forces on the inside surface of the billet container and die. Consequently, the lamination bonds will be subjected to tensile, shear and peel loads, regardless of lamination orientation. Cooling of the extrusion die with conformal cooling passages is not a common practice because of the difficulty of making these passages using conventional machining practices.

Injection molding involves melting and pressurizing granular or powdered thermoplastic polymer in a separate chamber and then forcing the molten polymer into a relatively cooler mold by way of a runner and injection system. It is in this "cooler" mold cavity that the part solidifies and forms. The high normal forces on the inside of the mold cavity (resulting from the high injection pressures) create very high tensile and peeling loads on the lamination bonds. Conformal cooling passages are commonly used in injection molding dies.

Resin transfer molding involves infusing liquid resin (i.e., thermosetting polymer) by vacuum, applied pressure or both into a pre-fabricated/assembled dry fiber preform contained by a mold. This molding process heats the granulated or powdered thermosetting polymers and while in the softened state, forced into the mold cavity through a runner system. The mild normal forces on the inside of the mold cavity create tensile and peeling loads on the lamination bonds. The mold is preheated to help in forming and curing thereby requiring conformal cooling passages.

Compression molding involves compressing a precise amount of thermosetting polymer or elastomer between heated mold halves and forcing the material to flow and conform to the shape of the mold cavity. Heating of the dies causes the thermoset to polymerize and cure into a solidified part. The normal forces on the inside of the mold cavity create tensile and peeling loads on the lamination bonds. Conformal cooling passages can be used to preheat the mold halves.

Important process information on these candidate processes for consideration with bonded joints include the maximum operating temperatures, internal or external pressures

involved, thermal conductivity requirements, permeability requirements, and typical die materials used. The data for each of the candidate manufacturing processes is listed in Table 1 and discussed in the following section.

Table 1 - Pertinent data on the candidate manufacturing processes.

Manufacturing Process	Maximum Operating Temp. (°C)	Typical Die or Mold Material	Maximum Operating Pressures (MPa)	Thermal Conductivity Requirements for tool.	Permeability Requirements	Applicable Bonding Methods	Worked Material
Sheet Metal forming	25	kirksite, Steel, Alum., Epoxy	7.0	low	none	diffusion, brazing or adhesives	sheet steel or aluminum
Thermoforming	55-90	Steel, Alum., Wood	0.8	low	vacuum, conformal cooling	diffusion, brazing, or adhesives ⊗⊗	plastics *
Metal extrusion	500	Tool Steel	60	high	cooling	diffusion, brazing	aluminum
Injection molding	100 to 150	Steel, Alum.	14 to 170 ⊗	high	selective heating & cooling	diffusion, brazing, or adhesives ⊗⊗	plastics **
Resin transfer molding	200	Steel, Alum.	0.3	high	vacuum, heating	diffusion, brazing, or adhesives ⊗⊗	plastics ***
Compression molding	200	Steel, Alum.	14 to 170 ⊗	high	cooling	diffusion, brazing, or adhesives ⊗⊗	plastics +
Composites molding	150	Steel, Alum.	1.4 ◊	medium to high	vacuum, heating	diffusion, brazing or adhesives	composites ++

* uses both thermosetting (T/S) and thermoplastic (T/P) polymers but generally T/P
** uses T/P only
*** uses T/S only
\+ uses both T/P and T/S with equal efficiency
++ as in fiberglass based composite polymers along with various graphite based epoxies and T/S
⊗ depending on the material
◊ under extreme conditions, though usually hydrostatic at 2.4 MPa
⊗⊗ adhesives to some extent depending on the pressures necessary to form the material properly

Lamination Bonding Methods

There are several methods suggested for bonding steel to steel, and aluminum to aluminum including diffusion bonding, brazing, and joining with adhesives [16]. Each of the aforementioned bonding methods is discussed below:

Diffusion bonding involves the filling of voids (asperities) at a bond interface by migration of molecules. Specifically, the diffusion kinetics at the bond are accelerated by applying the appropriate pressure and temperature to the lamination joint over a period of time. For example, Nakagawa et al. [13] diffusion bonded 55 sheets of cold-rolled steel by heating them together in a vacuum at a temperature 1100°C followed by the application of pressure of 5.9 MPa for one hour. Advantages of this process include no visible bond line, a clean fluxless process, strength of the bond up to 100% of the parent material strength, and no significant thermal contact resistance. Disadvantages include the limited application of this process to specific combinations of materials (e.g., aluminum to aluminum doesn't work), mild shrinkage (400 microinches at a joint), need for a hot press, need for a material that forms voids, low tolerance of poorly mating surfaces, and high processing temperatures (roughly $2/3^{rds}$ of the parent material's melting point). As a result, diffusion bonding is mainly limited to steel (and titanium) laminations [17].

Brazing involves introducing molten filler metal (e.g., copper, silver, nickel) between laminations to wet the mating surfaces of the joint and formation of a meturallurgical bond. Bonding is achieved by diffusion of

the filler material into the parent material and recrystallization of the filler material around the asperities thereby creating an enhanced surface area adhesion. Steel on steel requires a flux (i.e., non-metallic chemical compound) to clean the surface of oxides and other contaminants, facilitate easy wetting of the surface and then evaporates. Brazing is done at 450°C and above, and therefore is not recommended for relatively low melting point metals (e.g., aluminum). Advantages of brazing over other bonding methods include minimal effect on the base material composition, large bonding area for evenly distributing stresses, higher tolerance for mismatched surfaces than diffusion bonding because voids and gaps are filled. Disadvantages include the need for the joints to have controlled gaps or clearance, and fluxing. Brazing is mainly limited to steel.

Bonding with adhesives involves applying the adhesive material between the surfaces and letting it cure.

Soldering and edge welding are not being considered as suitable bonding methods for the following reasons:

Soldering is similar to brazing except that wetting of the filler material (e.g., tin, lead and their eutectic alloys) on the base material occurs at below 450°C. The measured strength is comparable to adhesive bonding but the processing is more difficult because gaps or clearance is needed between laminations. Initial experiments have shown that using soldering to bond the aluminum pieces together with minimal clearance led to poor bonding. Messler [16] suggests that adhesives would be a better choice than soldering because gaps won't need to be maintained with the former.

Welding of the lamination edges is not being considered because the piece-wise continuous surface afforded by the beveled edges would be significantly altered and secondary machining operations would be required as evidenced by Azuma [7], Pridham and Thomson [8] and Kunieda et al. [12].

Experimental Procedures

Various experiments being performed will establish the important mechanical and physical properties of various types of bonded lamination joints. Since the joints will add some degree of elasticity to the die, tensile and shear elastic moduli are important for the die designer to know. The types of laminated die failures that can occur due to the manufacturing processes listed in Table 1 are tensile (Fig. 2a), shear (Fig. 2b), and peeling (Fig. 2c), either separately or in some combination. For this reason, tensile, shear and peel strengths are also useful to know. Since the bonded interfaces provide a resistance to thermal conduction in the direction perpendicular to the bond plane, as shown in Figure 2d, the thermal contact resistance for a particular type of bond is also important. The degree of fluid (i.e., hydraulic oil or air) permeation in the lamination bonds is important to know when conformal cooling with pressurized fluid (e.g., injection molding), as shown in Figure 2e, or drawing of a vacuum (e.g., thermoforming) is being considered. For this reason, the specific permeability for various bonds is being determined. Finally, the minute separation of the bonded laminations is being measured to quantify the lateral expansion of a laminated die after bonding.

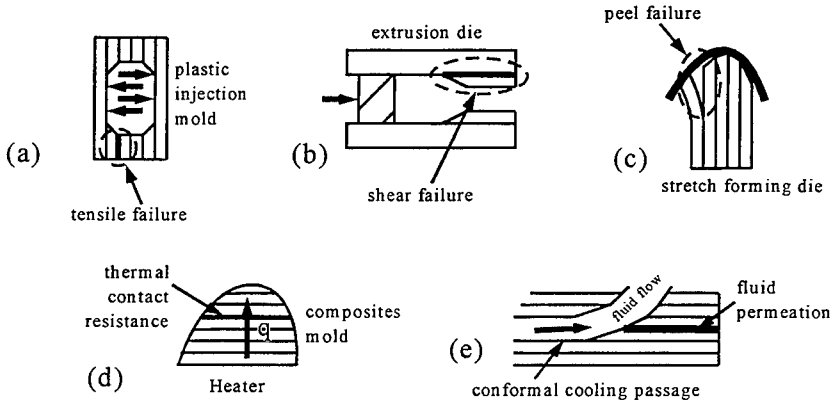


Figure 2 - Examples of (a) tensile (pull) failure, (b) shear failure and (c) peel failure (d) thermal contact resistance and (e) fluid permeation of various laminated dies and molds.

Tensile Strength (σ_t in MPa) and Tensile Elastic Modulus (E_t in MPa*)* - The tensile test is perhaps one of the most common of all strength tests. The basic premise of this test is to pull (using a Universal Testing Machine) a bonded specimen of area (A_{bond}) and thickness (t), as shown in Figure 3a, perpendicular the bonded surfaces and measure the elongation ($\delta_{failure}$) and force ($F_{failure}$) of the joint at failure with respect with its original position and unloaded state. The tensile forces applied must be uni-axial in order to achieve pure tension. This test is based on ASTM Designation: D 2095-72 standard test method. Assuming that the bond material obeys Hooke's law up to failure, then the tensile strength and elastic modulus are calculated using the following equations:

$$\sigma_t = \frac{F_{failure}}{A_{bond}} \text{ and } E_t = \frac{F_{failure} \cdot t}{\delta_{failure} \cdot A_{bond}} \qquad (1)$$

Shear Strength (τ_s in MPa) and Elastic Modulus (G_s in MPa*)* - The test being used to measure the shear strength and elastic tensile modulus of a lamination joint is a modification of ASTM Designation: D 2295 - 92 standard test method. The basic premise of this test is to pull a lapped joint of thickness (t), as shown in Figure 3b, parallel to the bonded surfaces and measure the elongation ($\delta_{failure,s}$) and force ($F_{failure,s}$) of the joint at failure with respect to its original position and unloaded state. Assuming that the bond material obeys Hooke's law up to failure, then the shear strength and elastic modulus are calculated using the following equations:

$$\tau_s = \frac{F_{failure,s}}{A_{bond}} \text{ and } G_s = \frac{F_{failure,s}}{A_{bond} \cdot \tan^{-1}\left(\frac{\delta_{failure,s}}{t}\right)} \qquad (2)$$

The small angle approximation for the shearing strain (i.e., $\gamma = \frac{\delta_{failure,s}}{t}$) is not used in determining G_s because $\delta_{failure,s}$ is typically much larger than t.

Peel Strength (α_p in $\frac{N}{m}$) - The T-peel test for determining the peel strength of a lamination joint of width (w) is based on ASTM Designation: D 1876-93 standard test method. Peel strength is a measure of a joints resistance to localized stresses and failure by progressively opening the adhesive face normal to its bond line. The basic premise of this test is to pull a T-

joint, as shown in Figure 3c, normal to and at one edge of the bonded surfaces and measure the average force, i.e., $F_{ave,p} = \frac{F_{max,p}+F_{min,p}}{2}$, of the joint at failure with respect to its unloaded state. Peel strength is calculated using the following equation:

$$\alpha_p = \frac{F_{failure,p}}{w} \qquad (3)$$

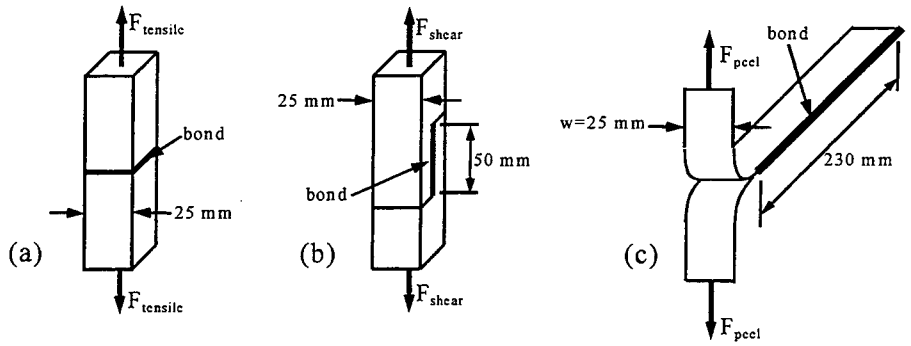


Figure 3 - Specimens for measuring joint strength and elastic modulus when subjected to (a) tensile, (b) shearing and (c) peeling loads.

To quantify the effect of elevated temperatures (particularly the maximum values listed in Table 1) on bond strengths and elastic modulus, the tests will be run at room temperature (i.e., 24°C), 100°C, and 200°C and 1000°C (diffusion-bonded steel only). As shown in Figure 4, uniform heating of the specimens is achieved by wrapping resistive-type heating tape around the bonded area. Using heating tape is an inexpensive means for heating the localized area up to 200°C without interfering with the failure mode of the specimen. The temperature of the bonded area is monitored by a digital thermometer using a K-type thermocouple in direct contact with the test specimen. This simple arrangement has been shown to maintain a uniform temperature to within ±3°C. These heated specimens were pulled apart on a Universal Testing Machine at a rate of 25 mm/min.

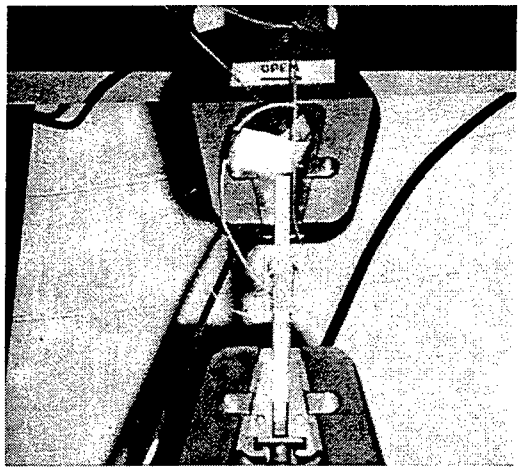


Figure 4 - Simple configuration for uniform heating of test specimens.

The *thermal contact (conductive) resistance per unit area* ($R''_{t,c}$) of the various joints will be measured using the apparatus shown in Figure 5a. Because of the symmetrical nature of the

heating element sandwiched between identical bonded metal laminations, the heat rate in the positive and negative x-directions is assumed to be the same (i.e., $\frac{q_x}{2}$). The equation for determining the value of this contact resistance is:

$$R''_{t,c} = 2\left[\frac{A(T_i - T_s)}{q_x} - \frac{L}{k_m}\right] \tag{4}$$

where:

A = cross sectional area of bonded joint
T_i = temperature at heating element
T_s = temperature at outside surface
q_x = total heat rate of heating element
L = thickness of single lamination
k_m = thermal conductivity of lamination material.

The *specific permeability* (k) of a bonded joint (i.e., how well it seals) will be measured using the experimental arrangement shown in Figure 5b. Assuming that the bond has some degree of permeability, the test fluid used is incompressible, and fluid flow through the bond is laminar, the specific permeability of the bond material is based on the Darcy's equation

$$k = \frac{-Q\mu h}{A_f(p_i - p_o)} \tag{5}$$

where:

Q = volumetric fluid flow rate (measured)
μ = viscocity of the fluid
h = width of the bond
$A_f = \pi(d_i + h)t =$ total cross-sectional area of bond perpendicular to the direction of flow
t = thickness of the bond
p_i = internal pressure of the bonded cylinder and
p_o = atmospheric pressure.

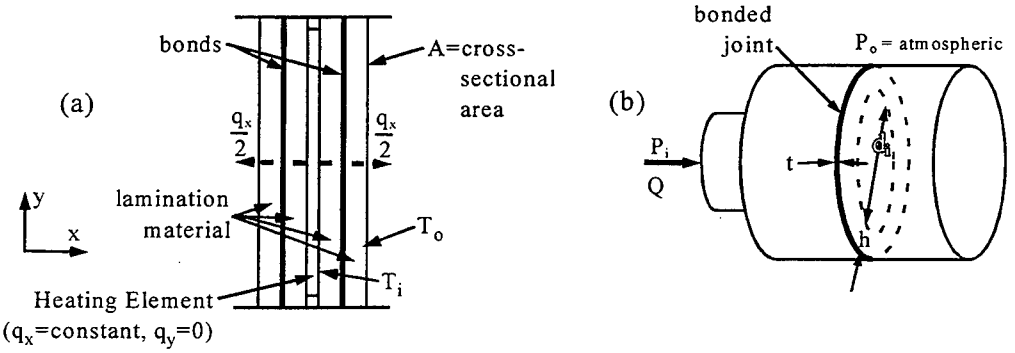


Figure 5 - Experimental set-ups for determined (a) thermal contact resistance and (b) specific permeability of a bonded lamination joint.

Preliminary Experimental Results

Some preliminary results are described for adhesive bonding of aluminum laminations. Four high strength, high-temperature adhesives (representative of the wide variety available) were tested including Devcon Plastic Steel® epoxy, Cotronics® Alumina-based Adhesive, Dymax 846® and 828® epoxy. Each adhesive consists of two parts, i.e., an activator (or hardener) and the base adhesive. The Devcon Plastic Steel adhesive is a metal-filled epoxy which cures to full strength at room temperatures in 24 hours, or at 120°C in 15 min and cooled back down to room temperature in 1 hour. The Cotronics adhesive system is a ceramic based adhesive that uses alumina oxide as a base adhesive. The alumina bonds to the oxidizing layer on the aluminum and creates the bond. The alumina based adhesive cures at room temperature for a 24 hour period or at 120°C for 2 hours. With the alumina based system, fast heating will create bubbles within the adhesive joint and must therefore be avoided. Dymax 828 and 846 adhesives are polyurethane oligomer-based mixtures that can cure at room temperature in 12 hours or at 100°C in 10 minutes. Devcon is widely-available and low cost, Cotronics gives a high temperature performance, and Dymax gives the lower viscosity and is the most elastic of the group, achieving elastic shear moduli of 9.1 and 7.5 MPa.

The tests show that there is a correlation between the distribution of the adhesive on the surface and the bond strength. A good distribution of an adhesive is when the adhesive has spread evenly and no voids are present. According to test data, the better and more even the distribution, the greater the failure strength. All samples broke in either a full cohesive failure (see Fig. 6a) or a partial cohesive failure (see Fig. 6b), suggesting strong bonds at the adhesive/adherend interface. Full cohesive failure mode suggests that the adhesive was used to the fullest, while partial cohesive failure suggests one of the following; sample surface was under-prepared (i.e., the surfaces were not completely free of contaminants), gap spacing between surfaces was uneven (attributing to thicker adhesive sections), or contaminants were introduced during processing (or heating).

The shearing experiments for every adhesive have shown that the slope of the shear force versus bond elongation curve is basically linear, i.e., obey Hooke's law, up until the point of failure. This implies that Equation 1 is valid for adhesive bonding. The shearing force and elastic moduli are calculated using Equ. 1 and listed in Table 2.

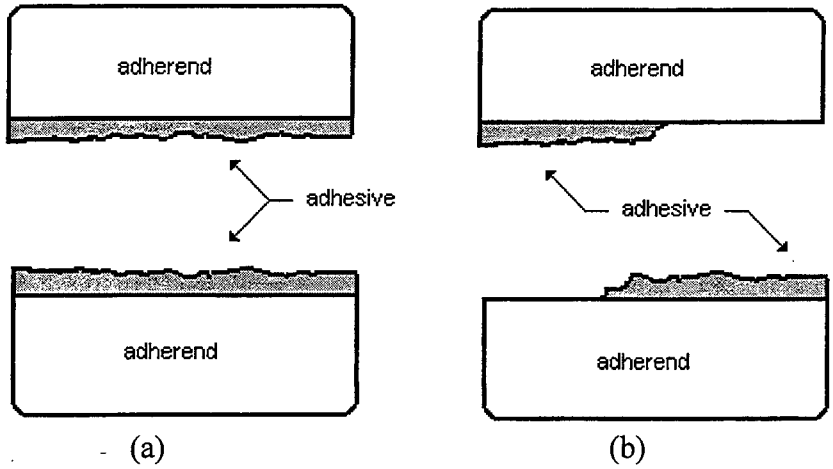


Figure 6 - Examples of (a) full cohesive and (b) partial cohesive failure for shear tests.

Table 2 - Shear test results for aluminum bonded with adhesives at room temperature and .

Adhesive used	Test temp. (°C)	Adhesive thickness (mm)	Failure Load (kN)	Shear Strength (MPa)	Elongation at Failure (mm)	Shear Modulus (MPa)	Cohesive Failure Mode
Devcon	24	0.19	13.0	10.1	2.1	6.8	Partial
Dymax 828	24	0.18	17.5	13.6	2.4	9.1	Full
Dymax 846	24	0.23	14.1	10.9	2.1	7.5	Full
Cotronics	24	0.47	2.47	1.91	0.38	2.8	Partial
Devcon	100	0.14	1.65	1.28	0.25	1.2	Partial
Dymax 828	100	0.24	10.4	8.06	1.9	5.6	Full
Dymax 846	100	0.21	9.61	7.45	1.8	5.1	Full
Cotronics	100	0.29	2.78	2.16	0.53	2.0	Partial

Future Work

The design and performance issues have been identified for laminated tooling and experimental set-ups have been devised for quantifying pertinent physical and mechanical properties. For the σ_t, E_t, τ_s, G_s, and α_p experiments, aluminum laminations will be tested at 25, 100 and 200°C. In addition to measurements at these temperatures, diffusion-bonded and brazed steel will be tested at 500°C which is the nominal operating temperature for metal extrusion. $R''_{t,c}$ and k will be measured at 25, 100 and 200°C for both steel and aluminum. As a comparison with bonded laminations, $R''_{t,c}$, and k will be measured for laminations that are clamped together under uniform pressure. Experimental results will be compared with theoretical models (e.g., Stefan's equation for predicting adhesive bond strength) whenever possible.

Following this experimental work, several examples of how the data can be used in designing laminated tooling for each of the aforementioned manufacturing processes will be developed. In addition, several techniques for automating the lamination bonding process (e.g., dip brazing, applying adhesive with a stationary roller) are being devised and will be demonstrated.

Acknowledgements

This work is being supported in part by the SME Education Foundation Grant #597-2423 and by Rensselaer Polytechnic Institute.

Bibliography

[1] Walczyk, D.F. and Hardt, D.E., "A New Rapid Tooling Method for Sheet Metal Forming Dies," *Proceedings of the Fifth International Conference on Rapid Prototyping*, Dayton, Ohio, June 12-15, 1994, pp. 275-289.

[2] Nakagawa, T., "Rapid Prototyping Techniques in Japan," *Proceedings of the 4th European Conference on Rapid Prototyping*, Paris, France, October 4-5, 1995.

[3] Soar, R.C., Authur, A. and Dickens, P.M., "Processing and application of rapid prototyped laminate production tooling," *Proceedings of the 2nd National Conference on Developments in RP&T*, Buckinghamshire College, England, Nov. 18-19, 1996, pp. 65-76.

[4] Hart, F.V., "Mold and Mold Making Method," *U.S. Patent #2274060*, Issued Oct. 31, 1938.

[5] Dickens, P., Simon, D. and Sketch, R., "Laminated Tooling for Moulding Polyurethane Parts," *Proceedings of the SME Conference on Rapid Prototyping and Manufacturing*, Dearborn, MI, April 22-25, 1996.

[6] Glozer, G.R., Brevick, J.R., "Laminate tooling for injection moulding," *Proceedings of the Institution of Mechanical Engineers, Part B: Journal of Engineering Manufacture*, Vol. 207, pp. 9-15.

[7] Azuma, K., "Manufacture of Press Die," *Japanese Patent #59-91123*, Issued December 8, 1984.

[8] Pridham. M.S. and Thomson, G., "Part Fabrication Using Laser Machining and Welding," *Proceedings of the Fourth Solid Freeform Fabrication Conference*, Austin, TX, August 1993, pp. 74-80.

[9] Weaver, W.R., "Process for the Manufacture of Laminated Tooling," *U.S. Patent #5031483*, Issued July 16, 1991.

[10] Feygin, M., "Apparatus and Method for Forming an Integral Object From Laminations," *U.S. Patent #5354414*, Issued October 11, 1994.

[11] Jahn, E.M., "Method of Manufacturing Laminated Plastic Tooling and Tooling Produced Thereby," *U.S. Patent #5247861*, Issued Sept. 28, 1993.

[12] Kunieda, M. and Nakagawa, T., "Manufacturing of Laminated Deep Drawing Dies by Laser Beam Cutting," *Proceedings of the 1st International Conference on Technology of Plasticity*, Vol. 1, Tokyo, Japan, 1984, pp. 520-524.

[13] Nakagawa, T., Kunieda, M. and Sheng-Dong L., "Laser Cut Sheet Laminated Forming Dies by Diffusion Bonding," *Proceedings of the 25th International Machine Tool Design and Research Conference*, Dept. of Mechanical Engineering, University of Birmingham, England, April 22-24, 1985, pp. 505-510.

[14] Engler, I., Schubert, E. and Sepold, G., "Direct Metal Prototyping with the LASP Technology," *Proceedings of the International Conference NNS (Near Net Shape) '97*, Bremen, Germany, April 14-16, 1997, pp. 335-341.

[15] Berry, H.D., "Intricate Shapes Built Up From Stacked Stampings," *Iron Age*, Vol. 198, No. 26, Dec. 29, 1966, pp. 44-45.

[16] Messler, R.W., *Joining of Advanced Materials*, Butterworth-Heinemann, Stoneham, Massachusetts, 1993.

[17] Hiatt, W.R., "Diffusion Bonding of AISI 4118 and 52100 Steels," *Masters Thesis*, Dept. of Materials Engineering, Rensselaer Polytechnic Institute, 1971.

High Speed UV Laser Beam Scanning by Polygon Mirror

Kenji Yamazawa , Toshiki Niino
The Institute of Physical and Chemical Research (RIKEN)
Seiji Hayano
ASPECT Co.
and
Takeo Nakagawa
University of Tokyo

1. Introduction

Since the stereolithograpy system appeared on the market, various rapid prototyping machines based on the layer laminated manufacturing process have emerged one after the other, the range of applications of which is classified according to their features. Of these, stereolithogrraphy methods which make use of photocurable resin as material and laser beam as processing tools are gradually being established. They are currently the most widespread with a rich variety of models available. The scanning device used in stereolithography serves as the key technology for this method but consists basically of only the galvanometer mirror known for outstanding high speed ability and the XY plotter known for outstanding scanning position accuracy[1),2)]. Lately, many models are seen to use the galvanometer mirror due to improved accuracy, but still this scanning device is used only when the fabrication size allows, etc. From such reasons, the authors have developed a laser stereolithograpy system capable of high speed high accuracy position scanning by the high speed raster scanning method using a polygon mirror as the scanning device[3)]. The polygon mirror, which has a higher scanning speed than the galvanometer mirror, is moved along the NC servo shaft and the raster scanning spacing is made considerably smaller than the laser beam spot diameter.

This paper describes this system and the results of fabrication experiments with this system.

2. Outline and Features of System

This system is composed of a laser optical device system made up of a laser oscillator, EOM laser modulator as laser shutter synchronizes with X axis and Y axis, beam expander, and reflection mirror, optical scanning device system made up of the polygon mirror , and f θ lens , recoating device, liquid resin supply unit, resin tank, and system controller. Its main features include a high speed scanning speed by the polygon mirror of 138.2m/s and 69.2m/s, high position accuracy scanning of below $\pm$0.05mm at the resin surface, use of highly viscous liquid resin of approximately 2200cP with a unique recoating method, and highly accurate fabrication with a layer thickness of 0.05 to 0.2 mm. The system has a simple and stable mechanism; the resin is drawn from the resin tank by the bucket, poured over the fabricated part and the liquid level is controlled by an overflow method. The 3D CAD data slice data generation software used is SOUPware by NTT DATA CMET INC. The slice data edited on the software is transferred to the controller of the unit from EWS by Ethernet and converted to raster scanning data. The photocurable resins used are mainly the ASAHI DENKA KOGYO 's epoxy resin HS series and versions of these resins with high viscosity.

Table 1 shows the specifications of the system, Fig. 1 shows the configuration of the system,

and Fig.2 shows the external view of the system and controller.

Table 1. Specifications of the system

Laser	He-Cd (325 nm, Multi-mode beam) ,100 mW
Laser penetration rate	65% (On liquid resin surface)
Laser beam spot diameter	ϕ 0.1mm (On liquid resin surface)
Laser shutter	EOM (Synchronizes with X axis and Y axis)
Laser scanning device	10 faces polygon mirror
Laser scanning speed (Y axis)	138.2 m/sec , 69.1 m/sec (Two steps)
Scanning position accuracy	$\pm$0.05 mm or less (On liquid resin surface.)
Recorter (X axis) speed (Simultaneous raster scan)	0.06 mm/sec ~ 6.67 mm/sec (Raster scanning line pitch 0.33~20 μ m)
Minimum layer thickness	About 0.05mm (Depends on the resin viscosity)
Work size	250 mm(X) x 250(Y) mm x 255(Z) mm
External dimensions	1950(W) mm x 1050(D) mm x 1400(H) mm

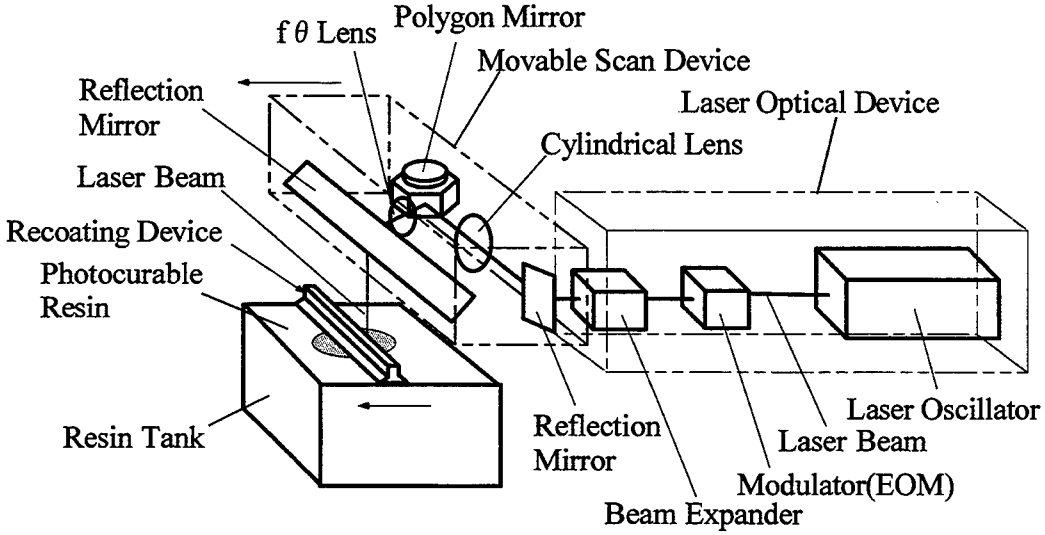


Figure 1. Configuration of the stereolithography system using by polygon mirror

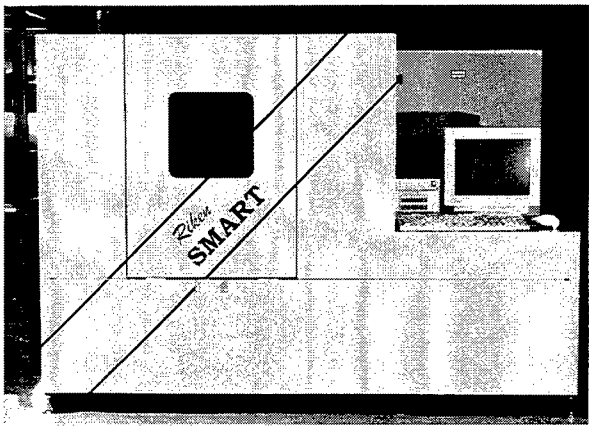


Figure 2. External view of the system and controller

3. Micro Spacing High Speed Raster Scanning

The polygon mirror is a laser beam deflection device currently used in scanning optical system such as the laser printer, etc. As shown in Fig.3 , a polyhedron mirror is rotated at a constant speed by a high speed motor to reflect the laser beam by each of its face so that scanning is performed linearly in one direction in one dimension[4]. Consequently, it is incapable of vector scanning which traces the contour of the slice data along one line during fabrication. Since the polygon mirror is rotated at an equiangular speed, the angular changes of the reflected laser beam are proportionate to time. A $f\theta$ lens is used to scan at a constant speed. For the polygon mirror to rotate stability, it cannot be rotated at low rotational speeds of less than about 1000 rpm. Scanning can therefore be performed only at high speeds, and the resin does not reach the critical exposure required for it to harden with only one scanning line at the resin surface. From such reasons, the scanning optical system incorporating the polygon mirror, etc. is moved by NC servo driving at very small spacing compared to the laser beam linewidth (spot diameter) as shown in Fig.4 while performing high speed raster scanning to form a consistent cured layer by drawing the desired photocurable liquid resin surface and average exposure.

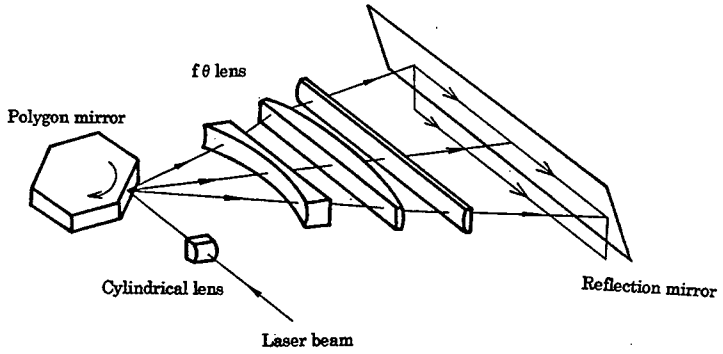


Figure 3. Optical scanning system

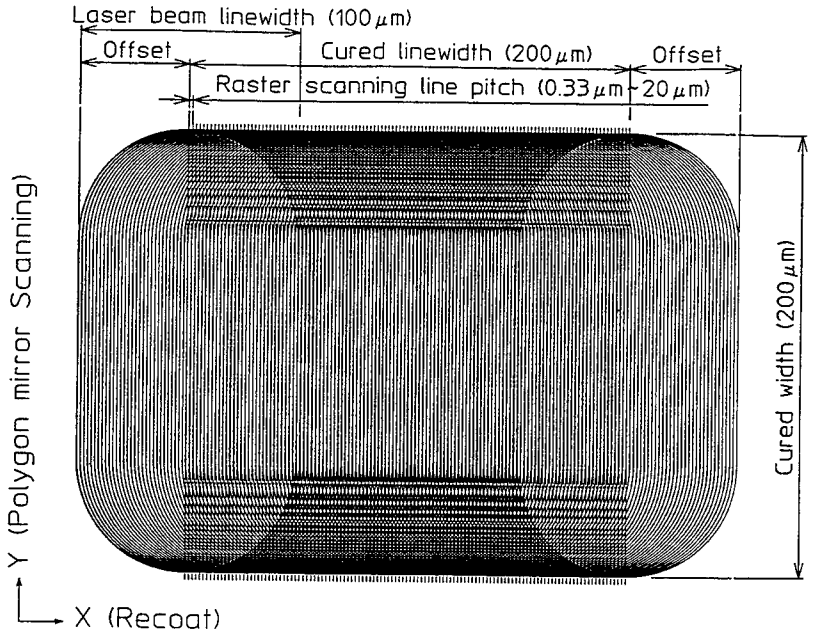


Figure 4. Drawing of micro spacing raster scanning locus

4. Recoating System

The scanning optical system comprised of the polygon mirror and the recoater which levels the unhardened resin liquid layer have been integrated and are moved together along the same axis to realize recoating of the liquid layer and raster scanning simultaneously. The liquid surface is controlled in a different way in this system. As shown in Fig.5 ,"the semi controlled liquid surface method" is used, in which laser beam is irradiated over the recoated layer, whose liquid surface has been semi controlled, immediately after the recoater blade passes through. This eliminates the need for waiting after recoating in order to remove the effects of the resin viscosity and trapped volumes of the fabricated product on the liquid level.

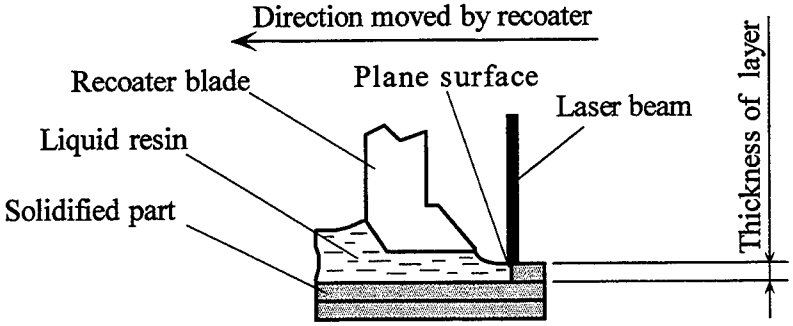


Figure 5. Semi controlled liquid surface method

5. Relation Between Laser Beam Raster Scanning Spacing (Raster Scanning Line Pitch), Recoating Speed, and Cure Depth

The cure depth required for the desired layer thickness can be calculated with the following equations from the laser beam scanning spacing, recoating speed, average exposure, and features of the resin used. The relation of these factors is shown in Fig. 6.

$$\text{Average exposure} \quad Eav\ [mJ/cm^2] = P_L / (Lp \cdot Vs \cdot 10) \quad 5)$$

where; P_L : Laser output on liquid resin surface[mW]

Vs : Laser scanning speed [m/s](set according to the rotation speed of the polygon mirror)

Lp : Raster scanning line pitch [mm] (set according to the recoater speed Vr)

$$\text{Cure depth} \quad Cd\ [mm] = Dp \cdot \ln (Eav / Ec) \quad 5)$$

where; The critical exposure is $Ec = 7.9[mJ/cm^2]$ and penetration depth is $Dp = 0.08[mm]$ based on "the Working curve" of the photocurable resin.

In this system, the raster scanning line pitch is made large and the recoating speed is raised as shown in Fig.7 in order to shorten the time required to laminate one layer. This however results in a shallow cure depth. Consequently, to shorten the fabrication time, it is necessary to project the average exposure over the liquid resin surface in such a way that the required cure depth can be obtained in respect to the layer thickness set, which means that the required cured depth can be achieved by using a high laser output and raising the photosensitivity.

6. Fabricating Process

As shown in Fig .8 , this unit completes the lamination of one layer by drawing the resin with the bucket, pouring it over the fabricated part, and performing recoating and laser scanning

simultaneously. After this, the Z table moves to the position of the next layer, and the same process is repeated. After completing the lamination of all layers, the table is raised up and pulled towards the front to remove the part built.

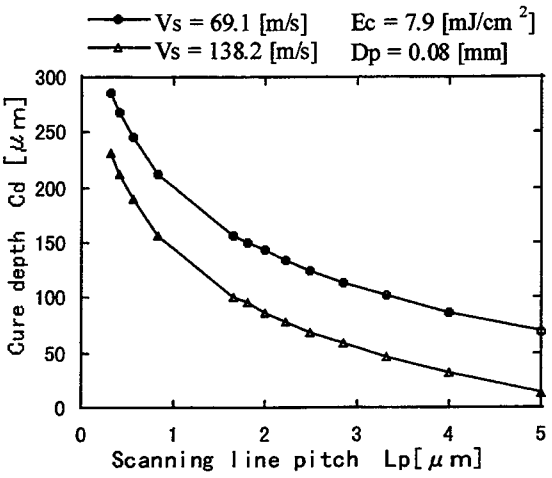


Figure 6 . Raster scanning line pitch versus cure depth for various raster scanning speed (P_L = 65 [mW])

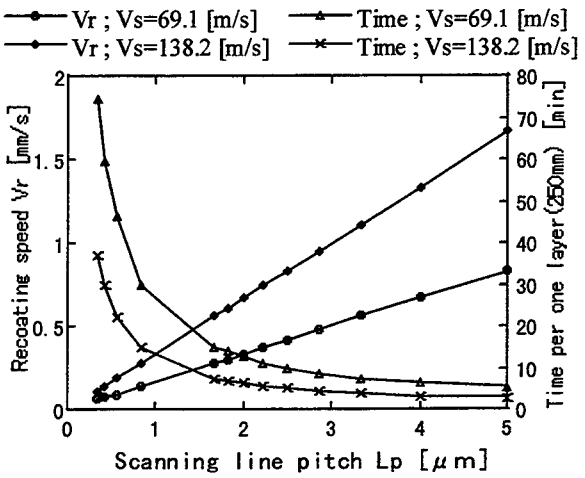


Figure 7 . Raster scanning line pitch versus recoating speed and time consumption par layer (X : 250[mm])

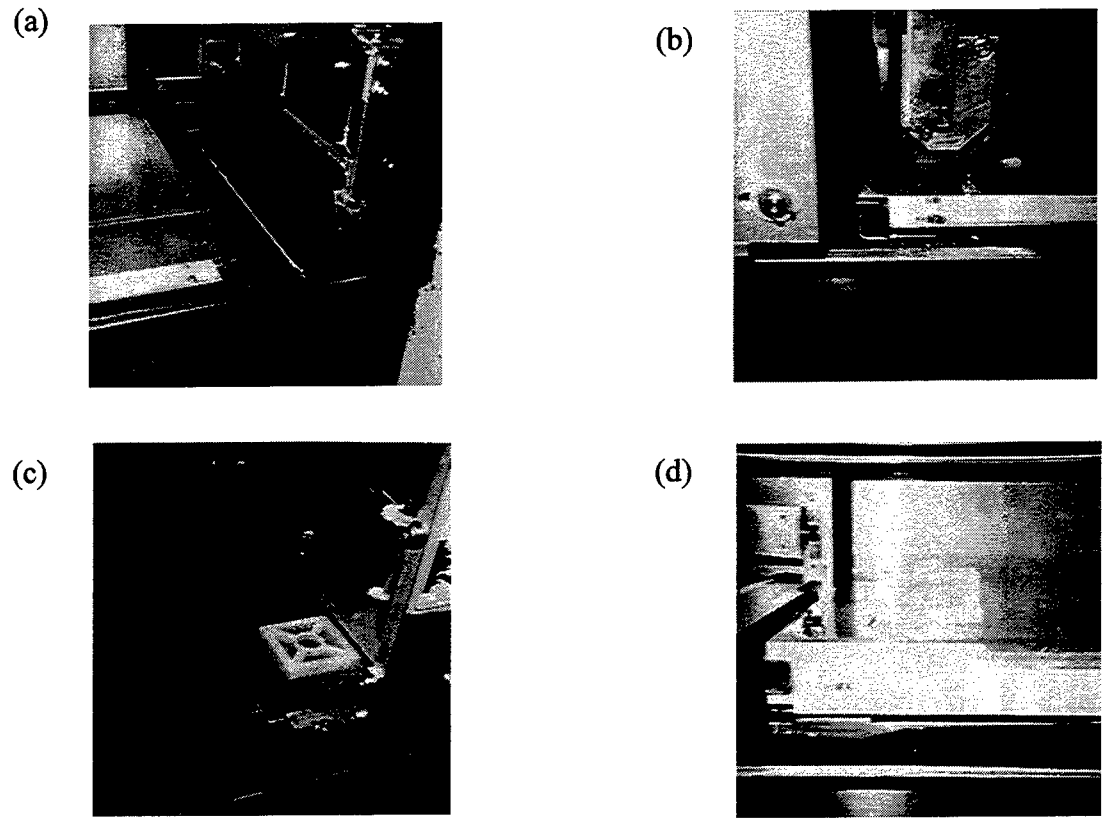


Figure 8 . Laminating process is shown as follows : (a) drawing of resin, (b) supply of resin over part built, (c) recoating and raster scanning, and (d) completion of lamination.

7. Results

Fabrication was carried out based on the conditions shown in Table 2 using the ASAHI DENKA KOGYO's epoxy photocurable resin. Fig. 9,10 and Table 3 show the fabricated sample part, the design contour of the fabricated product, and the position accuracy measurement results (height is the dimensions of the product). As seen in Fig. 11, the surface of the part fabricated by the micro spacing high speed raster scanning method and properties of the contour are good, indicating no need for contour scanning such as vector scanning. The minimum cured linewidth can be set on the control data up to 0.02 mm. As shown in Fig. 12, the linewidth could be calculated to the minimum of 0.1mm. This linewidth is the same as or smaller than that obtained by vector scanning using a galvanometer mirror. The cross-section of the part shown in Fig. 13 indicate that the part can be fabricated according to the thickness set. Lamination was also found to be good with the high viscosity resin (approx. 2200cP) and no effects of the change in the resin viscosity on the fabrication process were seen in particular. When the thickness of the uncured liquid is greater than the layer thickness set (cure depth), peeling occurs between the layers during fabrication. This requires the position of the recoater blade bottom to be set at an accuracy of ± 0.1mm in respect to the liquid resin level.

Table 2 . Example of laminating condition

Layer thickness	0.1 mm
Viscosity of resin	80~2200 cP
Beam scanning velocity	138.2 m/s
Raster scanning line pitch	0.83 μ m
Recoating velocity	0.28 mm/s
Average exposure	56.44 mJ/cm^2
Critical exposure	7.9 mJ/ cm^2
Penetration depth	0.08 mm
Cure depth	0.16 mm

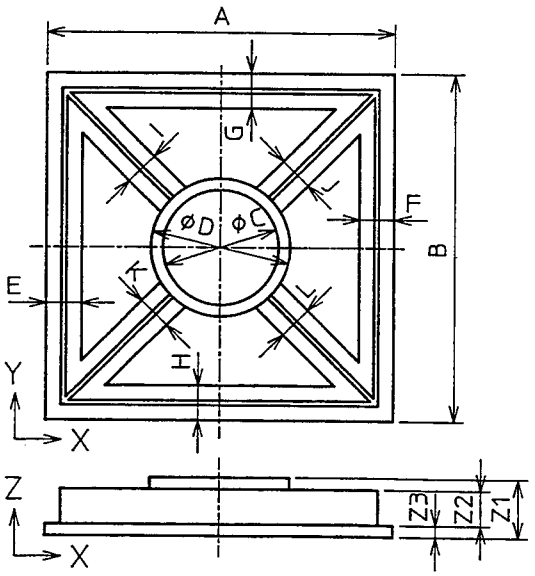


Figure 10. Drawing of sample part

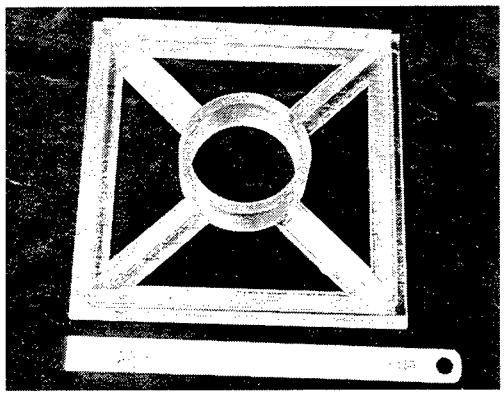


Figure 9. Photograph of the fabricated sample part

Table 3. Accuracy (Average of 10 samples : [mm])

Position	Dimension	Measurement	Error
A	150.00	150.01	+0.01
B	150.00	149.96	-0.04
C	50.00	49.96	-0.04
D	60.00	60.00	0
E	15.00	15.01	+0.01
F	15.00	15.04	+0.04
G	15.00	15.05	+0.05
H	15.00	15.05	+0.05
I	15.00	15.05	+0.05
J	15.00	15.03	+0.03
K	15.00	15.03	+0.03
L	15.00	15.05	+0.05
Z1	25.50	25.50	0
Z2	15.00	15.08	+0.08
Z3	5.00	5.04	+0.04

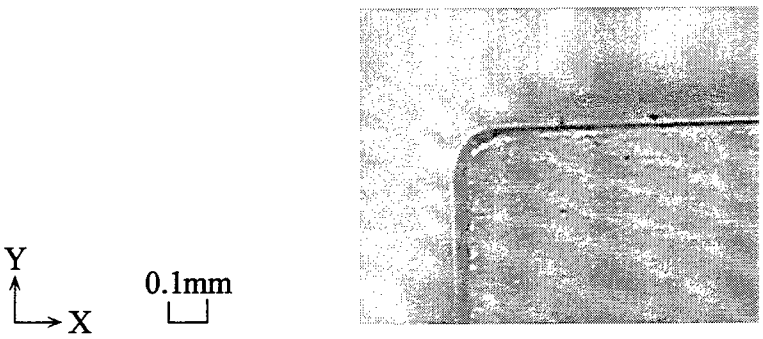


Figure 11. Photograph of surface and outline of part (Viscosity of resin 2200cP)

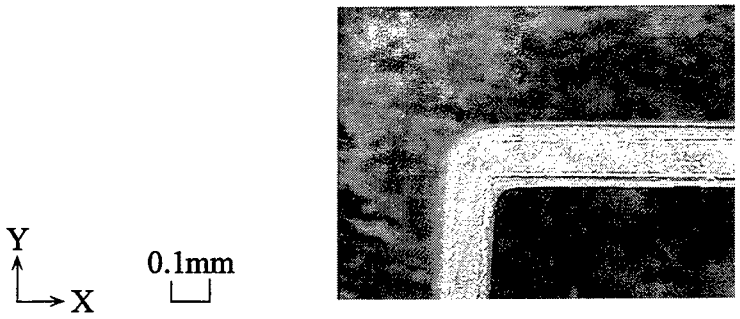


Figure 12 . Photograph of minimum cured linewidth of part (Viscosity of resin 2200cP)

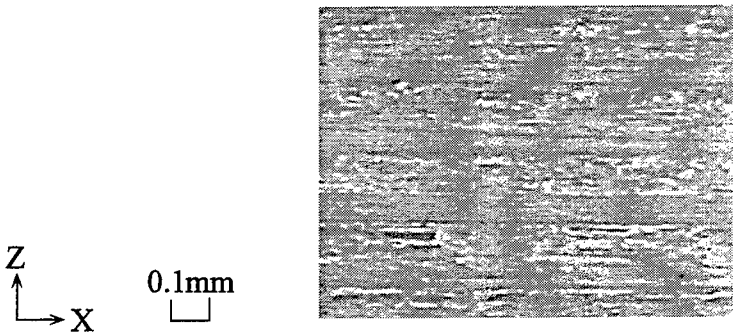


Figure 13 . Photograph of cross section of part (Viscosity of resin 2200cP)

8. Summary and Future Tasks

A new stereolithograpy system which employs a polygon mirror laser scanner and performs recoating and scanning simultaneously has been developed. The fabrication results show that layer manufacturing can be carried out for a broad range of resin viscosities using this high speed high accuracy scanning method. The fabrication process is also useful for reducing the waiting time after recoating in stereolithography process. In the future, efforts will be made to quantify the optimum fabrication parameters such a layer thickness, coefficient of resin viscosity, recoating speed, laser irradiation position, and cure shrinkage to raise the accuracy of the part built and put the method to practical application. Efforts will also be made to realize more accurate lamination of below 50 μ m.

Finally, the use of such laser beam deflecting devices capable of high speed scanning like the polygon mirror for stereolithography may shorten the fabrication time remarkably, given that lasers with higher outputs than current laser are available or photosensitivity of the photocurable resin is raised. Considered a promising stereolithography method, efforts will thus be made to further optimize the system as a productive and practical unit.

Acknowledgements

The authors would like to thank NTT DATA CMET INC. the co-developers of this device, as well as all those who gave their cooperation.

References

1) Y. Marutani, K. Ookawa, S. Hayano, N. Saito, and T. Nakai, "*Hikari-zokei-hou* (Laser Stereolithography - 3D-plotter using laser)", Nikkan Kogyo Shinbunsha , Japan, 1990, pp108-109 (in Japanese).
2) T. Nakagawa, Y. Marutani, "*Sekisou-zoukei sisutemu* (Layered Manufacturing System)", Kogyo Cyosakai, Japan, 1996, pp21-22 (in Japanese).
3) K. Yamazawa, T. Niino, T. Nakagawa, S. Hayano, *Development of Stereolithography uses polygon mirror*, Proc. of Autumn Conference of JSPE (1996), Japan, pp555-556 (in Japanese).
4) T. Kishikawa, "Kougaku-nyumon (An introduction to optics)", OPTRONICS-sya, Japan, 1990, pp306-307 (in Japanese).
5) P.F. Jacobs, *Rapid Prototyping & Manufacturing , Fundamentals of Stereolithography,* Society of Manufacturing Engineers, USA, 1992, pp263-277.

Layered Micro-Wall Structures from the Gas Phase

David Messia, Joseph Pegna, Woo Ho Lee

Department of Mechanical Engineering, Aeronautical Engineering and Mechanics
Rensselaer Polytechnic Institute
Troy, New York 12180-3590
U.S.A.
(518) 276-6030
Fax: (518) 276-2623
email: pegnaj@rpi.edu

Abstract: *The use of 3-D LCVD with volumetric rate feedback was investigated in the fabrication of micromechanical wall structures. These were constructed by recursive laser scanning and resulted in layered wall composed of recursive line deposition.*

Experiments were designed to uncover the relationship between scan rate, volumetric deposition rate, pressure and laser power for pyrolytic graphite from an ethylene precursor. Results point to a conduction dominated heat transfer which greatly limits the volumetric deposition rate at the wall. This also results in a highly unstable deposition process, since volumetric deposition increases by orders of magnitude as soon as rod growth is initiated.

An unexpected results of this work is the ability to grow rods at an angle to the laser axis, with good control of the linear growth rate. This is achieved by adaptive laser scanning during rod growth.

Keywords: *3-D LCVD, SALD, Process Control.*

1 INTRODUCTION

Our interest is to develop 3D-Laser Chemical Vapor Deposition (3-D LCVD) into a free-form fabrication tool from the micro-scale (0.1μm) to the macro-scale (cm). As such, 3-D LCVD offers a micromechanical complement to SALD and SALDVI [1], potentially allowing single stage mesoscale fabrication.

To test the adequacy of 3-D LCVD for the deposition of layered structures, we have performed a series of experiments to investigate the practicality of making upright panels by direct deposition. Both open and close loop deposition of layered walls will be described in this paper. To some degree, this work is reopening the research pioneered by Zong [2], in which a small layered cube structure was deposited using SALD. The main contribution over Zong's work is the evaluations of various strategies for closed-loop feedback control of the deposition process.

For close loop control, a new method that utilizes a previously developed feedback mechanism [3] has been enhanced. Various control methods were attempted and some exhibit promise in the field of manufacturing at the scale of micromachines and beyond. An unexpected result of this investigation is that the method allows one to achieve control over the type of structure deposited so that the user has the option of building either a wall or an angular rod.

© 1997 Joseph Pegna, Dave V. Messia and Woo-Ho Lee, printed with permission.

2 EXPERIMENTAL

2.1 Equipment

A schematic diagram of the Rensselaer 3D-LCVD system is shown in Figure 1 The 3D-LCVD reactor consists of a custom quartz tube with ports for viewing and laser input. The chamber is connected to a pumping station via a gate valve. The vacuum chamber and gas-delivery systems are enclosed within a ventilated hood for safety purposes. For the growth of pyrolytic graphite, 133 - 665 mbar (100-500 Torr) ranges of ethylene pressures were employed.

The beam source was a Coherent. model CR-18 argon ion laser with a maximum output of 12Watts (multi-mode) at the 488/514 nm primary lines. To vary the laser beam power, a liquid-crystal retarder and polarizing beam splitter were placed in series, allowing peak-to-peak power swings in under 200 ms. Incident powers reported herein represent total beam power at the deposit. Observation of the sample during growth and laser alignment is made with a custom-built short-focus telescope and CCD camera.

A photodetector, covered with narrow band filters, was mounted to one of the chamber windows, at a distance of roughly 200 mm from the sample. Using a two-decade pre-amplifier, the sensor could measure emissions as small as 0.25 mW at the substrate (at 656nm). The amplified signal was recorded by an Omega Nubus data acquisition system, with a typical sample period of 0.05-0.10 seconds, and was later time averaged as needed for real-time control.

At the core of the system is a precision five-degrees-of-freedom manipulator. This micromanipulator was designed to allow beam scanning not only in the plane of the substrate, but at any

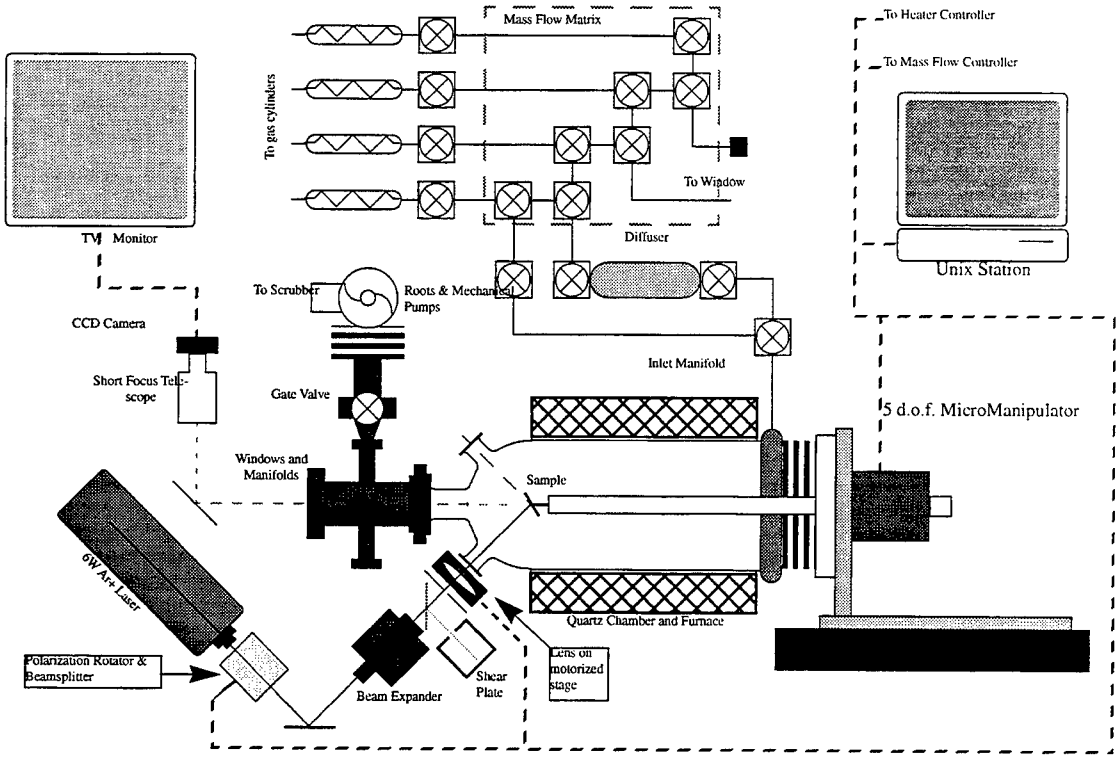


FIGURE 1. Schematic diagram of the 3-D LCVD reactor.

angle and orientation to the sample. This is effected through a computer-driven 5-axis micromanipulator. This tool allows sub-micron positioning with stepping motor control from outside the vacuum chamber. The translational and angular resolutions of this micro-manipulator are 1 μm and 0.005° at the full step control mode.

The manipulator arm holds the sample within the chamber. The manipulator attaches to the vacuum chamber via a flexible bellows to limit vibrations transmitted to the sample. Both the manipulator and the laser lie on a vibration-isolated table, their relative position is fixed.

2.2 Feedback Techniques

Various feedback techniques were attempted in order to determine the best approach:

1. The sum algorithm method: The volumetric reaction rate —as measured by the technique of Maxwell et al. [3]— is discretely integrated until it reaches a predetermined value. The sum is then reset and the appropriate stepper motor advances a given distance.
2. The threshold method: The reaction rate is monitored until it reaches a preset value. The appropriate stepper motor advances a given distance.
3. The volumetric deposition method: The feedback control unit attempts to maintain a reference emission value for constant scanning speed by adjusting the laser power with the LCD polarizer.

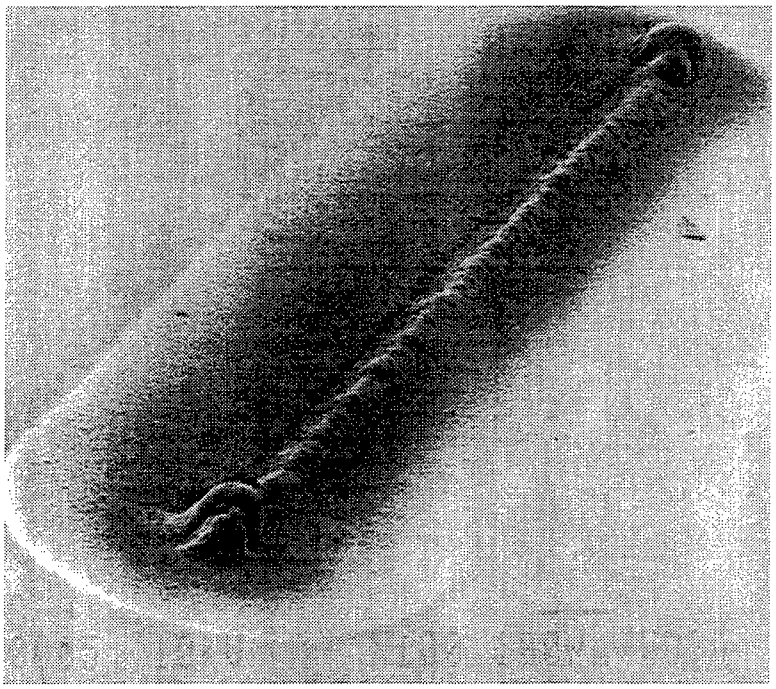


FIGURE 2. Sample linear scan results. Precursor: Ethylene at 200 Torr. Laser power: 5.6 Watts. Scanning Speed: 200μm/s.

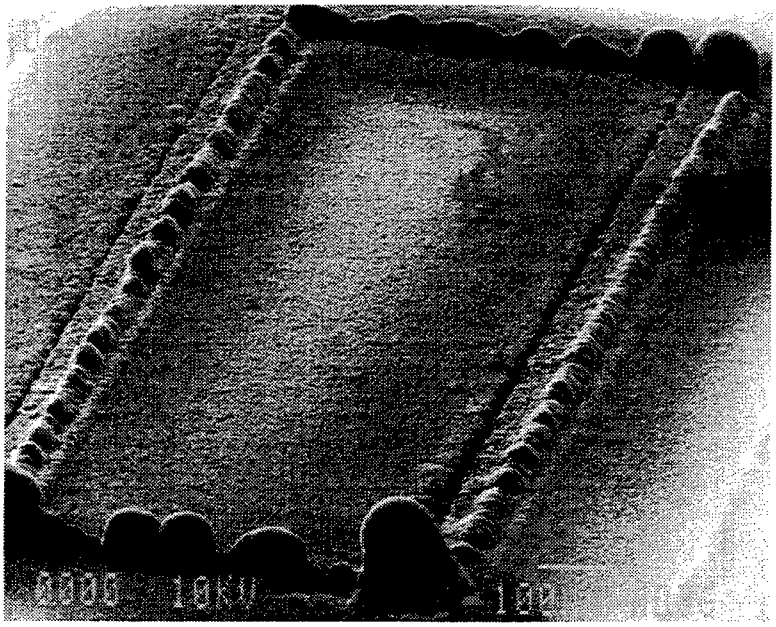


FIGURE 3. Sample scan results along a close contour. Precursor: Ethylene at 150 Torr. Laser power: 5.6 Watts. Scanning Speed: 200μm/s.

3 RESULTS AND DISCUSSION

3.1 Open-Loop Scanning

Figure 2 shows an attempt at building a 2mm long wall from ethylene without volumetric deposition control. The Ar+ CW laser was scanned at a constant speed of 200μm/s with

a constant power of 5.6 Watts. The total number of passes (i.e. layers) was 100, with a 15 second delay (0 Watts) at the end of each pass. The promontories at both ends of the ridge are a result of the increased loitering time due to the directional change of the laser. The pressure was 200 Torr. The substrate was Ti-coated quartz.

In an attempt to reduce the promontory effect at wall's end, attempts were made at building walls along a closed loop cross-section. Figure 3 shows a 2x1.5 mm rectangular wall structure built by repeated scanning of the laser around the closed contour, with no volumetric deposition control. Mark the beading throughout the upper layers especially on the shorter sides of the rectangle. These beading are characteristic or the Arrhenius relation controlling the deposition rate and are the cause of instabilities in the growth. As we shall see, volumetric control does provide a slightly better result. The total number of passes was 125. The laser power was 5.6 watts. The chamber pressure was 150 Torr. The scan rate was 200 mm /s.

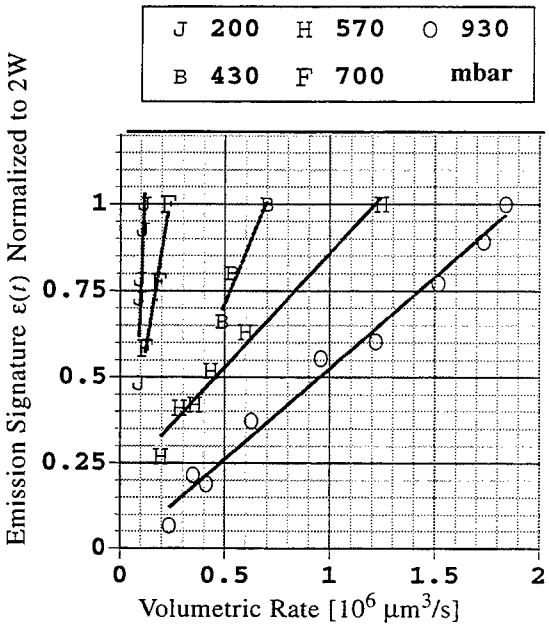


FIGURE 4. Correlation of steady state 656 nm emission intensity to volumetric deposition rate (from [3]).

The most noticeable result about open loop deposition is the poor quality of the deposit shape and the slow deposition rate associated with scanning speed 200μm/s. Open loop attempts performed at lower scanning speeds result in spurious local rod growth and an even more irregular deposit. In the next section, we shall monitor the volumetric deposition rate for various constant low scanning speeds.

3.2 Emission Calibration

One of the fundamental results obtained by Maxwell et al. [3] was the correlation of hydrogen by-product emission (at 656 nm) to the volumetric deposition rate. This linear relationship is captured in Figure 4, which provides us with emission (Volts) to volumetric rate ($\mu m^3/s$) conversion coefficients.

3.3 Volumetric deposition rates at low scanning speeds

In an effort to increase the volumetric deposition rate, the scanning speed must be significantly lower than the 200μm/s used in Section 3.1. The main problem with lower speeds, however is that the deposit growth tends to be extremely unstable. Experiments were conducted to monitor volumetric deposition rates at various scanning speeds ranging from 2 to 8 μm/s and pressures ranging from 100 to 440 Torrs.

Low pressure experiments, illustrated by Figure 5, were conducted with a constant laser power of 4.8 Watts for carbon deposit from ethylene onto a quartz substrate. We know from Maxwell et al. [3] that at the pressures of 100 and 150 Torrs, the axial growth rate of the deposit is below 2μm/s and reaches that bound for pressures of the order of 200 Torrs. It is interesting to note that at both 100 and 150 Torrs, the volumetric deposition rate remains relatively constant at scanning speeds over 2μm/s. In all instances, the deposit appears to be somewhat similar to a rod

laid flat on the substrate, as denoted by the noticeable speed transitions on the deposit. At the upper pressure of 150 Torr, as the scanning speed becomes of the same order as axial growth, note that explosive volumetric growth leads to rod growth. The combined increased axial growth and scanning speed in this instance lead to a rod growing at an incline.

A series of experiments were conducted to determine the transition between line deposition and rod growth. A series of scanning deposition at constant laser power was conducted, while the scanning rate was decreased from 8μm/s to 1μm/s every 2μm. These experiments were conducted for different pressures. The transition scanning rates for different pressures are summarized in Table 1.

Pressure (Torr)	Transition Scan Rate (μm/s)
500	10
400	8
350	8
300	6
250	6
200	4
150	2

TABLE 1. Line to rod growth transition scan rate for pressures ranging from 500 to 150 Torr.

3.4 Closed-Loop Scanning

Among the various feedback control methods experimented, both the threshold method and the volumetric feedback proved more useful at building rod structures.

For walls, it was found that the sum algorithm gave best results for building a wall structure. Figure 6 shows three views of a wall constructed using the sum algorithm. The reaction rate was integrated until it reached a set value (.05), which triggered a 10 μm step. Notice that using the feedback control, only 30 passes were needed to build a nearly 1mm high wall. This compares to 125 passes in Figure 2 to build a structure 20μm high, and already exhibiting instabilities. The structure exhibits a Pan flute formation but all of the members are fused together. This picture shows the potential of the sum algorithm method in obtaining an extended, relatively flat, and vertically developed structure. The pressure was 220 Torr. The laser power was 5.8 Watts. The length of the sample is 1 mm. This method appears to be the most promising for forming elevated panel structures. However, the structure still exhibits large irregularities in height and cross-section.

Emission measurements were recorded during wall growth and averaged for different height ranges. These measurement corroborate an average volumetric growth rate of the order $0.5\mu m^3/s$. The results are shown in Figure 7. Note that most irregularities in deposition rate occur at the substrate. Once wall growth has commenced, volumetric deposition rates seem to reach a steady state.

4 CONCLUSION

In this work we investigated the layered fabrication of micro-wall structures by direct deposition using 3-D LCVD. The feasibility of this construction was demonstrated by fabrication of sample vertical panel structures 1mm x 1mm. These panels were obtained using closed-loop feedback control of the reaction. By product emissions were used as direct measurement of the volumetric deposition rate and integrated until a set volume was reached, upon which the laser focus was stepped by 10μm.

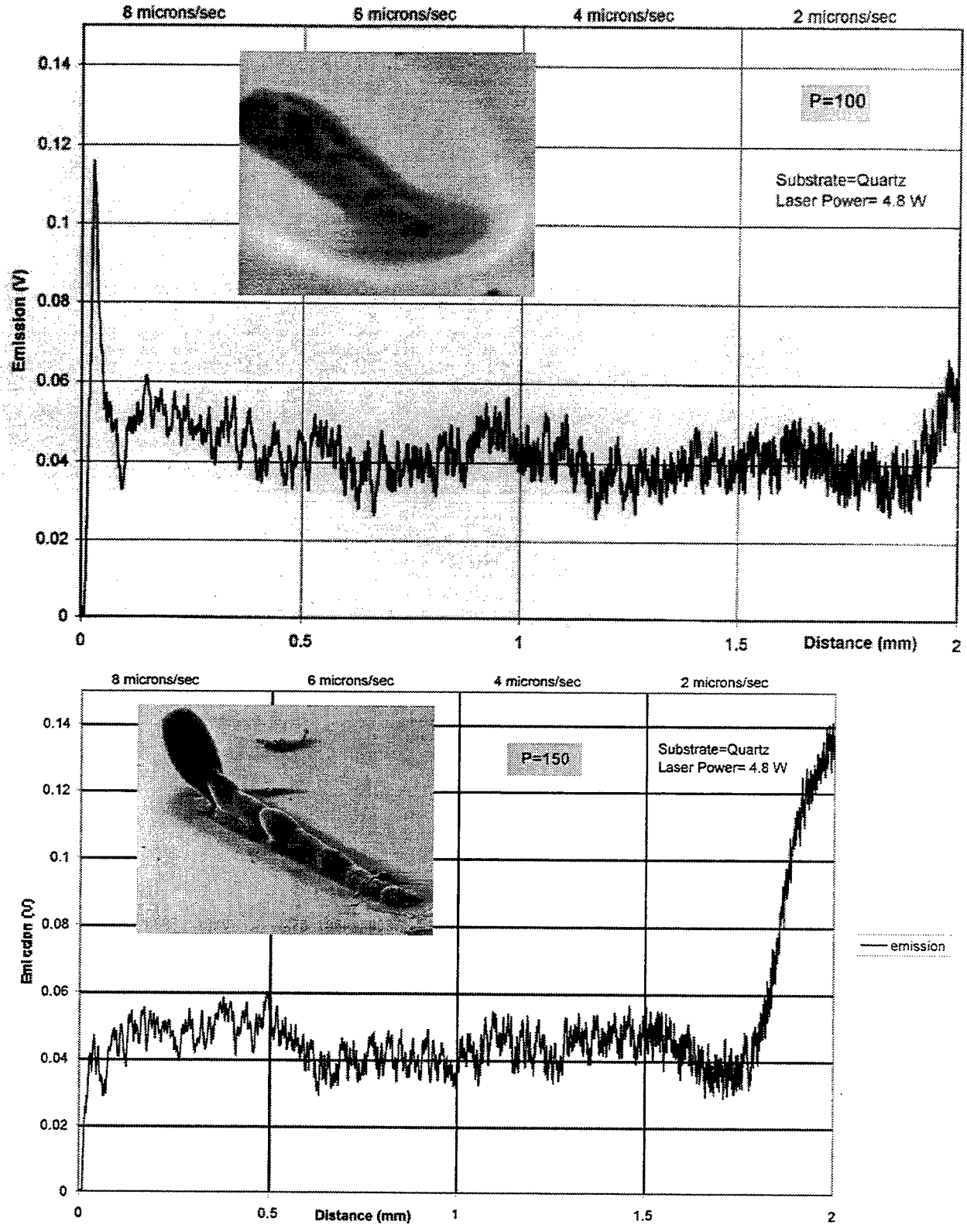


FIGURE 5. Low pressure emission / Volumetric deposition rate for scanning speeds ranging from 8 to 2 μm/s for carbon deposit from ethylene at 100 Torrs (top) and 150 Torrs (Bottom).

While closed loop control has proved vastly superior to open loop in these experiments, it remains that the structures fabricated exhibit large shape irregularities; mostly due to the instability of the deposition process. In addition deposition rates are hindered by the layered nature of the fabrication as opposed to rod growth, which exhibit volumetric rates an order of magnitude larger [6].

In the process of investigating the parameters and the conditions for wall growth it turned out that some rods were formed instead. As it turns out, scanning the laser focus during rod growth allows for a new method of forming angled rods similar to that demonstrated by Bauerle [4], and Lehmann and Stuke [5]. The results of this work are reported in a companion paper [6]. This process has the particular advantage that the laser remains perpendicular to the substrate at all times, simplifying the geometry of construction. It also features near optimal volumetric deposition rates as compared to layered growth.

It is therefore the conclusion of this research that 3-D LCVD is ill-suited for layered fabrication of volumes greater than $10^6 \mu m^3$. Alternative uses of the process however appear very promising in pursuit of tessellated (rod-based structures). This remark opens a new approach to freeform fabrication, away from layered manufacturing.

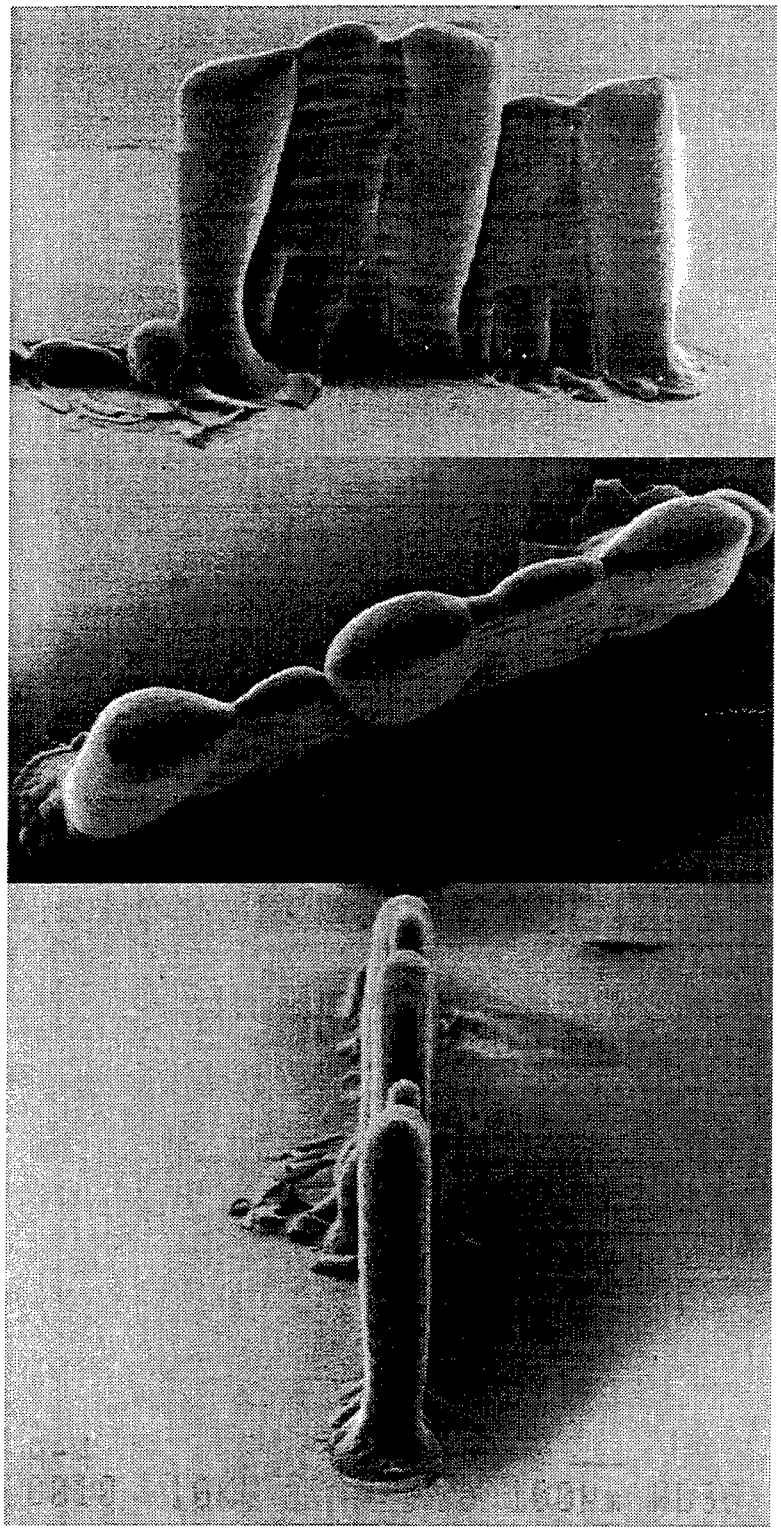


FIGURE 6. Side, Top and Edge views of a wall deposited by closed-loop scanning. Precursor: Ethylene at 220 Torr. Average laser power: 5.8 Watts, step size: 10μm, deposition rate per step: 0.05.

Support for this work was provided in part by the National Science Foundation under grants ECS-9314071 and DDM-9057059, and the Society of Manufacturing Engineers Education Foundation. Laboratory support was pro-

vided by Rensselaer's Center for Integrated Electronics and Electronics Manufacturing. All contributors to this project are gratefully acknowledged

5 REFERENCES

[1] Harrison, S., Crocker, J.E., Manzur, T., Marcus, H.L., "Solid Freeform Fabrication at The University of Connecticut", Proceedings of the Solid Freeform Fabrication Symposium, Ed. by D.L. Bourell, J.J. Beaman, H.L. Marcus, R.H. Crawford, and J. W. Barlow, The University of Texas at Austin, Texas, Aug. 12-14, 1996, pp. 345-348.

[2] Zong, G.-S., Ph.D. Thesis, Univ. of Texas at Austin, (1992).

[3] Maxwell, J.L., Pegna, J., and Messia, D.V., *"Real-time volumetric growth rate measurements and feedback control of three-dimensional laser chemical vapor deposition,"* To appear in Applied Physics A (1997)

[4] Bäuerle, D., *Laser Processing and Chemistry*, 2nd Ed., Springer-Verlag, pp. 317-346 (1996)

[5] Lehmann, O. and Stuke, M., *"Laser-Driven Movement of Three-Dimensional Microstructures Generated by Laser Rapid Prototyping,"* Science 270 (5242):1644 (8 Dec 1995)

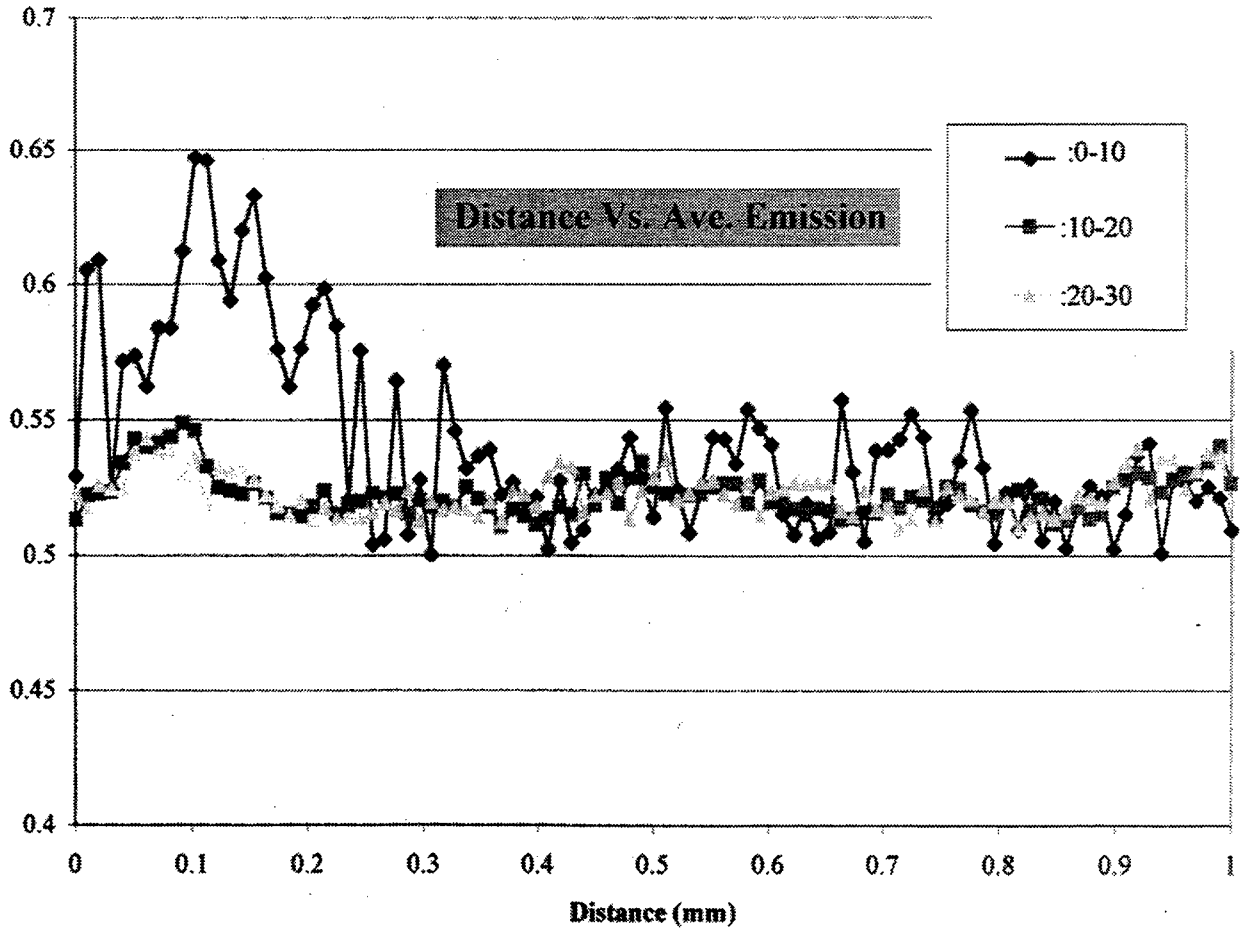


FIGURE 7. Averaged emission measurements for 3 height ranges during wall growth.

[6] Pegna, J., Messia, D.V., and Lee, W.-H., *"Trussed structures: Freeform Fabrication without the layers,"* Proceedings of the Solid Freeform Fabrication Symposium, University of Texas at Austin, August 9-14, 1997

Gas Phase SFF Control System for Silicon Nitride Deposition by SALD/SALDVI

by Shay Harrison, Chris F. Costa, Kevin J. Jakubenas, James E. Crocker, and Harris L. Marcus
Institute of Materials Science
University of Connecticut, U-Box 136
Storrs, CT 06269-3136

Abstract: A closed-loop laser scanning and temperature control system has been developed for SALD/SALDVI. Temperature control is especially important in SALD/SALDVI because temperature plays a defining role in both composition and deposition rate. The control system for SALD/SALDVI is presented which provides .STL file interpretation, real time temperature control, and laser response modeling, all on a PC. This control system was utilized with the SALD/SALDVI techniques for depositing silicon nitride. Characteristics of Si_3N_4 fabricated shapes are discussed, including composition, morphology, and electrical properties.

Introduction

Selective Area Laser Deposition(SALD)/SALD Vapor Infiltration(SALDVI) are gas-phase SFF approaches to forming a vast array of materials from a laser- induced, localized gas-phase reaction[1]. The deposition of ceramic shapes, such as silicon nitride, without post-processing presents one of the promising advantages of gas-phase SFF. Laser-CVD growth of silicon nitride fibers from silane(SiH_4) and ammonia(NH_3) gas mixtures has previously been shown[2]. Mixed gas environments of tetramethylsilane(TMS, $Si(CH_3)_4$) and ammonia have also experimentally produced silicon nitride deposits. A more thorough examination of the TMS and NH_3 deposition system, using thermodynamic modeling, was undertaken to understand the temperature and gas partial pressures necessary for formation of silicon nitride. With this knowledge, a gas-phase SFF computer control system, including closed-loop control of temperature, was implemented to verify the modeling predictions. These experiments were performed with a 150 watt cw Nd:YAG laser(λ=1.064 nm), an optical pryometer for temperature control, and an 8 inch diameter stainless steel vacuum chamber(the system is more thoroughly described in reference 3). In addition, the electrical and morphological nature of the formed silicon nitride shapes was examined.

Gas-phase SFF Computer Control System

Monitoring and control of both position and temperature are performed on a PC program written in-house in Visual Basic language[4]. This software is currently used on 2 gas-phase SFF systems at UCONN(references 5 to 10 detail the theory on which the control system is based).

The motion control can handle single two-dimensional layers or multiple 2D layers taken from a three-dimensional .STL or CAD models. The .STL/CAD capability requires that the 3D solid model be sectioned into 2D layers. Each layer must then be 'scanned' with the appropriate laser scan spacing to create a coordinate file for laser scan control. An in-house translation program takes the coordinate file for each layer and creates motion control code for scanning the laser. When creating a SALDVI structure, the control program also accesses a powder delivery program[11].

The original temperature control design utilized a proportional gain to vary the laser power and consequently adjust the reaction temperature to the desired target temperature, based on the following equation: $P_{laser}=P_{laser} + K * \Delta T$, where P_{laser} is the laser power, K is the gain,

and ΔT is the difference between the measured and target temperatures. This simplified control scheme was inadequate, leading to either large temperature overshoots or slow response times. As a result, a PID(Proportional Integral Derivative) filter was programmed into the control software. The PID filter functions according to the flowchart in Figure 1.

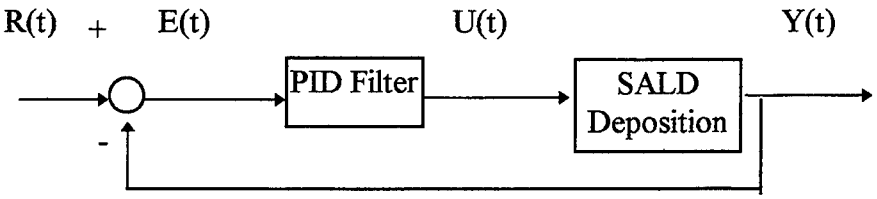


Figure 1 : PID Flowchart

R(t) is the desired target temperature, Y(t) is the measured target temperature by the optical pyrometer, E(t) is the error between measured and target temperatures, and U(t) is the PID adjustment signal to the laser controller. In a discrete time domain, where k represents a temperature measurement sampling, the PID signal is based on the equation: $U(k) = U(k-1) + K_p[E(k) - E(k-1)] + K_i E(k) + K_d[E(k) - 2E(k-1) + E(k-2)]$.

Due to the non-linearity of the laser power response to the analog control voltage from a Digital-to-Analog Card(DAC), a signal conditioner was employed to apply the PID output signal directly to the laser power. This conditioner is based on a laser calibration of the laser output power to the DAC input power, according to the equation: $V(t) = mU(t) + b$, where m is the slope and b is the y-intercept of the laser power versus DAC curve.

With the PID in place, the next step was to determine the appropriate PID parameters for small temperature overshoot and a quick response time. Experimentally, a trial and error approach could take a considerable amount of time. A first order estimation of the necessary PID values was obtained using a simple system model on a spreadsheet. The reaction zone temperature versus time response at constant laser power during deposition can be modeled using the following equation: $T(t) = P \times K(1 - e^{-\frac{t}{t_1}})$ where P is the laser power, $K = \frac{\Delta T(\infty)}{P}$, ΔT(∞) is the difference between the steady-state temperature and the initial temperature, and $t_1 = -\frac{t_{75\%}}{\ln\left(1 - \frac{T(t_{75\%})}{P \times K}\right)}$ ($t_{75\%}$ is the time to 75% of T(∞)). In order to use this modeling spreadsheet, a simple constant power, single line scan deposition experiment must be performed to obtain real values for T(∞), P, and $t_{75\%}$. After inputting these values into the worksheet, PID settings can be tested and a time-temperature response graph is generated, based on consecutive iterations of the following equation: $Y(k) + a_1 Y(k-1) = b_1 U(k-1)$, where $b_1 = K\left[1 - \exp\left(-\frac{t_0}{t_1}\right)\right]$, $a_1 = -\exp\left(-\frac{t_0}{t_1}\right)$, and t_0 is the sampling time. The graph details the expected system response of temperature overshoot and time to reach the steady-state temperature. This modeling program provided initial PID values of K_p=.01, K_i=.001, and K_d=.01

for the Nd:YAG laser. With further experimentation, the optimal temperature response and control for the YAG laser used PID parameters that are a factor of 10 less than the modeled values.

Thermodynamic Modeling of the TMS/NH3 Deposition System

A thermodynamic consideration of the tetramethylsilane and ammonia gas deposition system was performed using a modified version of software titled CET89[12]. CET89 is a Gibbs free energy minimization program for solids, liquids, and gases. The modifications made at UCONN to the routine involve the ability to calculate free energies over a specified temperature range. With this program, the deposition materials and phases of these products are projected based on what is favored by thermodynamics to be in equilibrium at selected temperatures, pressures, and molar ratios. Gas partial pressure were used as the independent variable. The effect of overall total pressure changes the temperature of transition from one region to another in the diagram below, but the net form of the map remains the same. Figure 2 shows a tetramethylsilane/ammonia gas mixture deposition map.

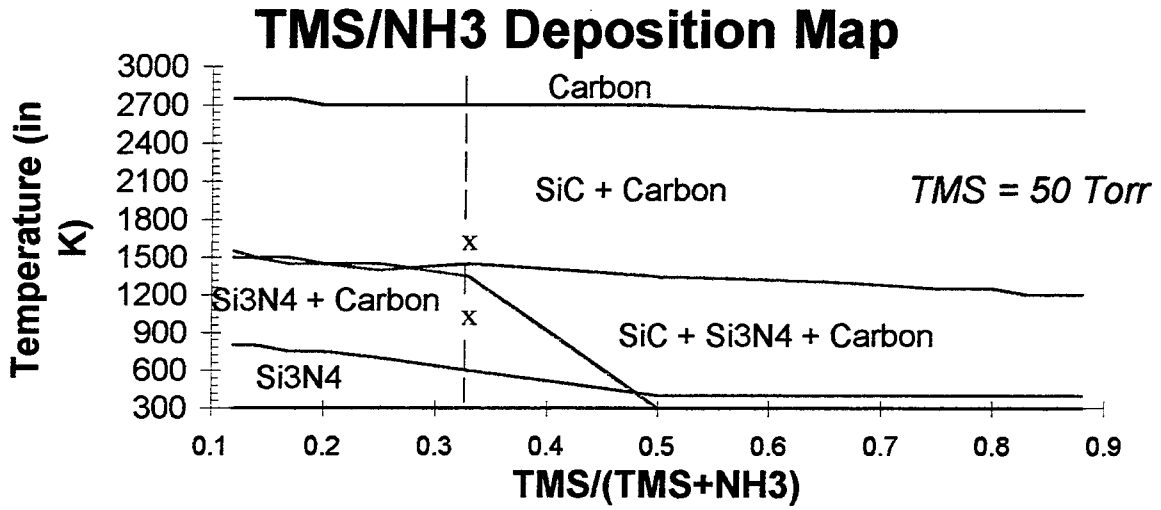


Figure 2 : TMS/NH_3 Deposition Map from CET89

Based on the deposition map, a partial pressure ratio of 1:2 for TMS:NH3 was chosen to demonstrate the ability to manipulate the product composition to form Si_3N_4.

Experimental

Selective Area Laser Deposition(SALD) of silicon nitride rods served as the initial focus of experiments to determine the composition of the formed material, utilizing x-ray diffraction spectroscopy(XRDS). Implementing the PID control computer program, deposition target temperatures from 1000^0 C to 1350^0 C were selected to achieve constant temperature growth conditions. These temperatures were based on the approximate region in the deposition map, at a 1:2 TMS/ NH_3 gas ratio, where silicon nitride would be expected to form(the experimental region can be seen on Figure 2, along the vertical line between the x's). The target temperature is actually a temperature parameter, with variations from the actual temperature due to differences in size between the heated reaction zone from the laser and the size of the sampling area of the

pyrometer. Some modeling of the relation between the actual and measured temperatures has been performed but a more complete analysis will be performed. A sample XRDS pattern in shown in Figure 3, where sample #37 was a rod grown at 1100^0 C target temperature.

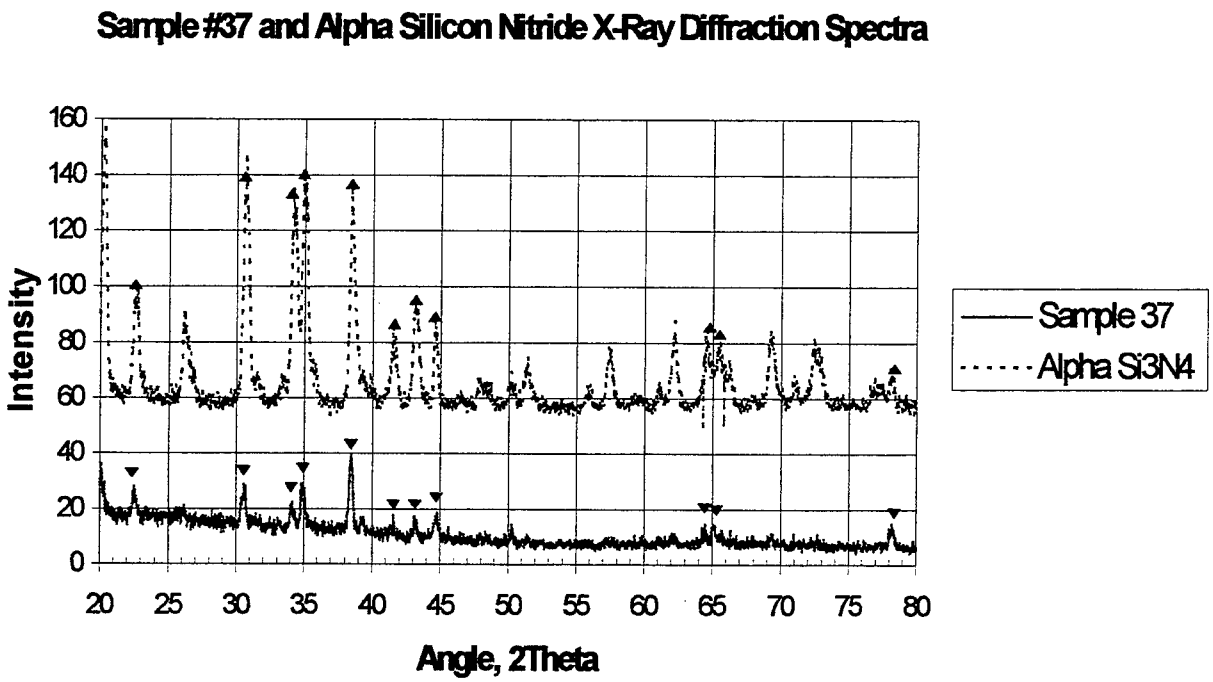


Figure 3 : X-ray Diffraction Spectra for a Si_3N_4 SALD Rod and an Alpha Si_3N_4 Standard (Note: A matched peak has an up and a down arrow associated with it)

The x-ray pattern shows a small texturing effect along the 211 plane, at $2\theta = 38.9^0$. Other rod experiments showed silicon nitride formation up to 1350^0 C deposition temperatures, which may imply a deviation from the thermodynamic modeling prediction for the transition temperature from silicon nitride to silicon carbide formation, depending on the accuracy of the temperature measurements.

The electrical resistivity of both SALD silicon nitride rods and SALDVI silicon nitride single layers was measured using a mega-ohm meter. Available literature report silicon nitride resistivity values greater than 10^{14} ohm-centimeters[12]. Resistivity(ρ) calculations are based on the following equation: $\rho = R*A/t$, where R is the resistance measured from an ohm-meter, A is the area of the sample, and t is the thickness of the sample. Both rod and layer samples exhibited resistances greater than 100 Mega-ohms, which was the maximum calibrated value of the ohm-meter used. Conservatively using this resistance, the SALD/SALDVI silicon nitride displayed resistivity of greater than 10^9 ohm-centimeters. An enhanced method for accurately determining the resistance is presently under consideration.

Infiltration of deposited silicon nitride into alpha-silicon nitride powder was performed at the 1:2 TMS/NH_3 gas ratio in a square raster scan pattern. Scan speeds ranged from 20 microns/second to 50 microns/second. A preponderance of dense SALD material, with very little

infiltration, resulted from the faster scan speed condition. At the slower, 20 microns/second scan speed, some infiltration could be seen, but there was still a great deal of SALD material growing off the powder surface. Figure 4 shows the powder/SALD growth interface of the 20 microns/second scan speed sample, with some deposited material(silver-white) infiltrated into the powder(black). A methodical assessment of the appropriate scan speed, deposition temperature parameter, and gas ratios will be undertaken to determine the best conditions for silicon nitride infiltration.

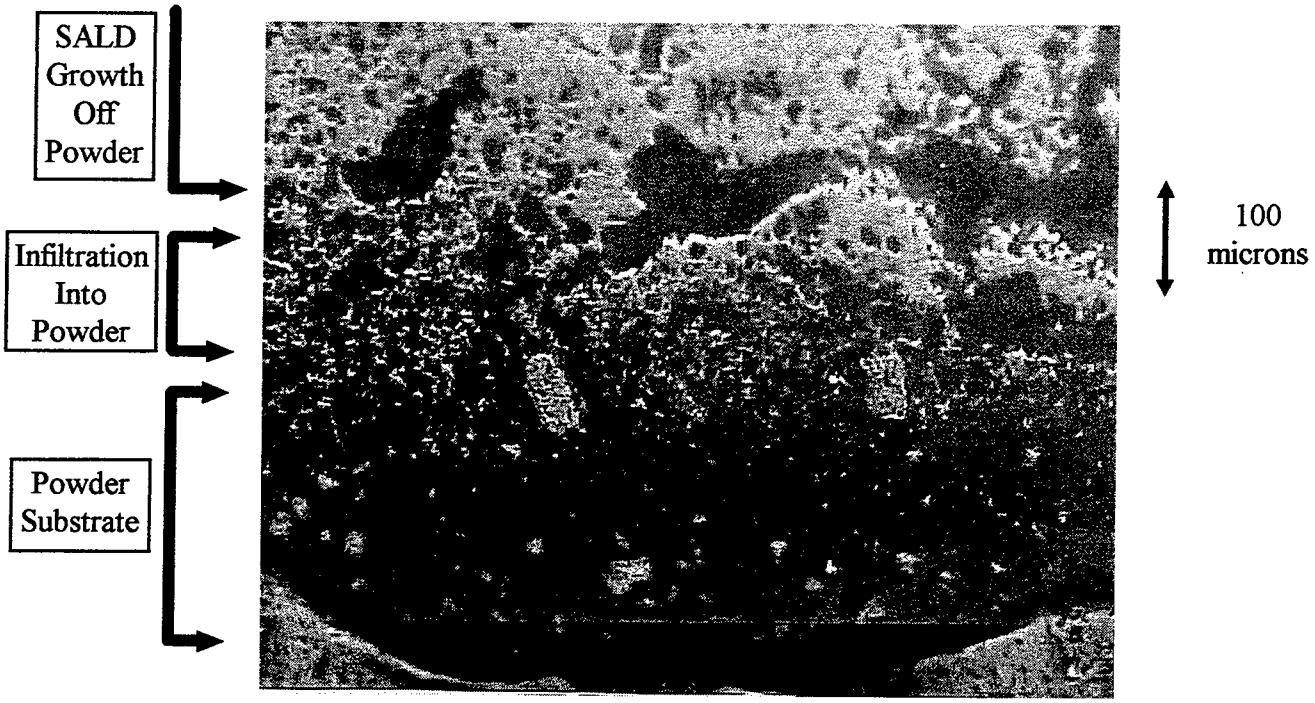


Figure 4 : SALDVI Si_3N_4 Cross-Section, Scan Speed 20 microns/second

Conclusions

A temperature and laser scanning closed-loop computer program was designed and implemented for use with the SALD/SALDVI processes. This program utilizes a PID filter to minimize the temperature overshoot and maximize the temperature response time, in an effort to create constant temperature deposition conditions. Thermodynamic modeling, using CET89 software, predicted regions where silicon nitride would be deposited in a tetremethylsilane and ammonia gas environment. Employing the closed-loop program, the deposition of silicon nitride was demonstrated, based on gas mixture pressures and deposition temperatures from the thermodynamics. Further experimental work will focus on the deposition transition temperature from silicon nitride to silicon carbide, with comparisons to the thermodynamic model. Multi-layer SALDVI silicon nitride shapes will be attempted, and the electrical characterization of Si_3N_4 will be improved to better judge the quality of the material being deposited.

Acknowledgments

The authors wish to acknowledge the support of DARPA/ONR, contract #N00014-96-1-1299, and ONR, contract #N00014-95-1-0978.

References

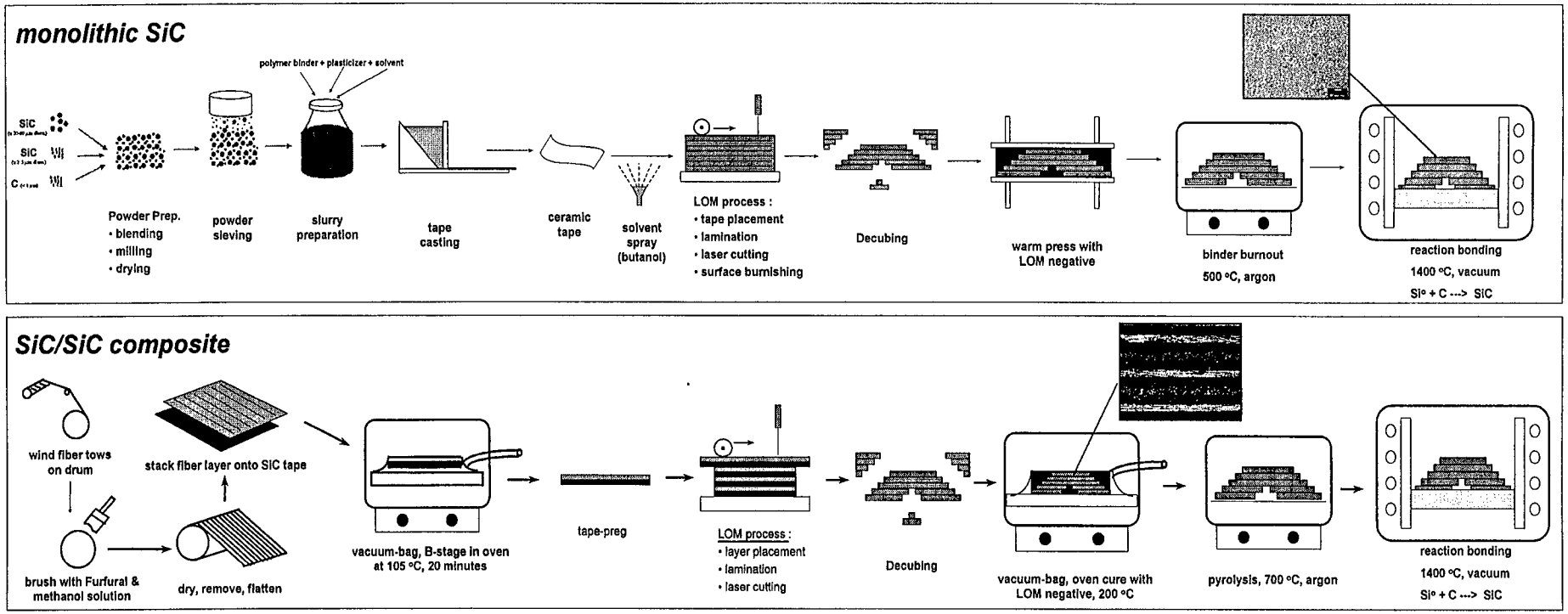
1. K.J. Jakubenas, B.R. Birmingham, S.Harrison, J.E. Crocker, M.S. Shaarawi, J.V. Tompkins, J. Sanchez, & H.L. Marcus, "Recent Advances in SALD and SALDVI", 7th International Conference on Rapid Prototyping, San Francisco, CA, April, 1997
2. F.T. Wallenberger, & P.C. Nordine, Journal of Materials Research, Volume 9, Number 3, March 1994, pgs. 527-530
3. S. Harrison, J.E. Crocker, T. Manzur, & H.L. Marcus, "Solid Freeform Fabrication at The University of Connecticut", Proceedings from the 7th Solid Freeform Fabrication Symposium, Austin, TX, August, 1996
4. Microsoft Visual Basic Version 4.0, Microsoft Corp., Redmond, WA
5. C.-T. Chen, Analog and Digital Control System Design, State University of New York at Stony Brook, Saunders College Publishing, New York
6. R. Iserman, Digital Control Systems: Vol 1, Springer-Verlag, New York, 1989
7. R.A. Serway, Physics: For Scientists and Engineers, Saunders College Publishing, New York, 1982
8. K.R. Pattipati, Notes for a Comprehensive Course on Feedback Control Systems, University of Connecticut, 1993
9. B.P. Lathi, Linear Systems and Signals, Berkeley-Cambridge Press, California, 1992
10. B.C. Kuo, Automatic Control Systems, Prentice Hall, New Jersey, 1991
11. S. Gordon & B.J. McBride, Computer Program for Calculation of Complex Chemical Equilibrium Compositions, Rocket Performance, Incident and Reflected Shocks, and Chapman-Jonguet Detonations, NASA Lewis Research Center, NASA SP-273, March, 1976
12. D. Richerson, Modern Ceramic Engineering, Marcel-Dekker, Inc., 1992, pg. 206

UDRI
UNIVERSITY of DAYTON RESEARCH INSTITUTE

Pre-LOM, LOM, and Post-LOM Processes for the Fabrication of SiC and SiC/SiC Components

Don Klosterman, Richard Chartoff, Nora Osborne, George Graves, Allan Lightman
University of Dayton, Ohio

RPDL
Rapid Prototype Development Laboratory



UDRI
UNIVERSITY of DAYTON RESEARCH INSTITUTE

Automated Fabrication of Nonresorbable Bone Implants Using Laminated Object Manufacturing (LOM)

Cheri Steidle[1], Don Klosterman, Nora Osborne, George Graves, Richard Chartoff

[1]Master's thesis, Chemical Engineering, University of Dayton, Manuscript Complete by October '97

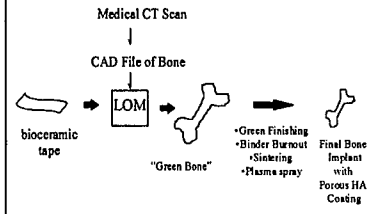
RPDL
Rapid Prototype Development Laboratory

Scope & Objectives

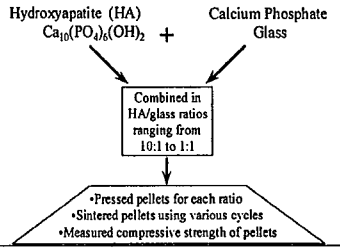
- Formulate and test[1] nonresorbable bioceramic material for use as bone implants
- Fabricate ceramic tapes from nonresorbable bioceramic powder
- Produce complex bone shapes using bioceramic tapes with Laminated Object Manufacturing (LOM)

[1]limited mechanical testing only, as this is only a feasibility study

Process Overview



Step 1 : Material Selection



Compression Test Results

	HA/glass ratio	Compressive Strength (MPa)
cycle 1 (1050°C, 5 min)[1]	10:1	81.6
	5:1	99.8
	3:1	104.8
cycle 2 (1050°C, 5 min)[1]	3:1	130.2
	1:1	73.2
cycle 3 (1050°C, 50 min)[1]	3:1	129.5
	1:1	83.3
cortical bone	--	100 - 230

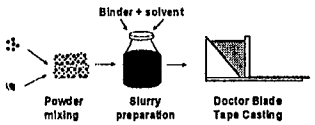
[1]rapid heat up cycle (sample placed in oven preheated at 1050 °C)

[2]heat up cycle = 5°C/min

Formulation Selection

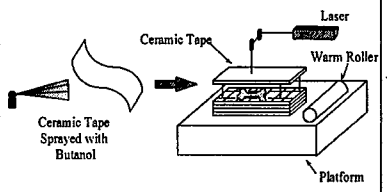
- 3:1 ratio was selected based on compressive strength
- However, FTIR analysis of sintered specimens revealed the presence of a reaction by-product, Tricalcium phosphate (TCP), at a level of 10%. Because TCP at this level is resorbed in the human body, the material system cannot be considered nonresorbable in a strict medical sense.
- Despite the presence of TCP, the current 3:1 HA/glass system was adopted to serve as a model system for use on the LOM

Step 2 : Tape Casting



Factors Involved in Tape Casting
- Binder Choice
- Slurry composition and viscosity
- Doctor blade setting
- Casting speed
- Drying conditions

Step 3 : LOM of Bioceramic Tapes



Factors Involved in Lamination

- Type and amount of binder present in the tape
- Type and amount of solvent used for lamination
- Roller temperature, speed, and pressure

LOM Results

- Conducted Lamination trials with a 2"x 4" rectangle divided into eight one-inch squares, 10 layers
- Adjusted tape binder formula to produce adequate lamination
- Reduced roller temperature to ambient to avoid sticking
- Determined speed, compression, and solvent parameters to achieve strong, reproducible adhesion
- Observed potential problem with burn zone around laser cut lines

Step 4 : Binder Burnout & Sintering

- Placed 1" squares in furnace, free-standing
- Binder burnout cycle : 25-500°C, ≅7°C/hr.
- Sintering @ 1050°C
- Samples looked good after sintering, no buckling or warping, ≅ 3% z-shrinkage

Conclusions

- HA/glass pellets in a 3:1 ratio demonstrated compressive strengths in the range of cortical bone.
- HA/glass formulation can be cast into useable tapes for lamination on the LOM.
- Early sintering trials of 1", 10-layer LOM squares appear promising.

Next Steps

- Finalize tape binder formulation
- Determine optimum binder burnout and sintering schedule
- Use CAD file of bone from CT scan
- Produce bone shape
- Determine mechanical properties of LOM bioceramic parts

Rapid Fabrication of Disposable Fixtures for Correct Assembly of Split Build Rapid Prototyped Parts

Samit R. Kadakia, Andrei S. Novac, Mark D. Van Roosendaal, Charles L. Thomas
Department of Mechanical Engineering
University of Utah
Salt Lake City, Utah 84112

Norman T. Smith, Matthew Balogh
Ford Motor Company

Abstract

The size of part that can be produced in a single build on any of the commercially available Rapid Prototyping systems is limited by the size of the particular machine's build envelope. Parts which exceed the dimensions of the build envelope are split into sections that fit the machine's envelope and these sections are fabricated separately. Assembly of the sections into an accurate three dimensional object often requires the creation of a fixture. This fixture ensures correct positional and angular orientation of the sections during assembly. This paper discusses the fabrication of such fixtures using Shapemaker II, a Solid Freeform Fabrication process developed at the University of Utah. Using Shapemaker II, large fixtures (4 ft. by 8 ft. or even larger) can be created in just a few hours. While the fixture is reusable, given the low cost of the fixture, it can be considered a throw away item.

Background

Application of rapid prototyping (RP) techniques during the development of a new product is often limited by the size restrictions imposed by the RP technique selected. The build volumes of the various commercial products vary from smaller than one cubic foot up to 32" by 32" by 20". (Thomas, 1996 and Burns, 1993) Even larger sizes are available through at least three different avenues: 1) using NC machining or traditional prototyping 2) large wax and sand prototypes (Berkstresser, 1997) 3) large prototypes from plastic foam (Lee et al., 1997).

It is often not possible to select an RP technique based only on the size of the fixture required. The different techniques produce fixtures with different material properties, with different accuracy, and with different costs. Often one of these factors will override part size as a selection criteria for the RP technique. Thus, it is often necessary to build a relatively large part on a machine with a small build envelope. As mentioned above, this is generally accomplished by splitting the part into multiple pieces that fit within the build envelope of the RP device, building the fixture in pieces, and manually assembling the pieces during post processing. This paper discusses two techniques for cutting an alignment fixture to support the splitbuild parts during assembly.

Fixture Design Specifications

Design specifications for the part fixture are as follows:

a) Construction of the fixture should be rapid and inexpensive.
b) The fixture should provide accurate alignment and positioning of split build parts over large distances.
c) It should orient and locate sections, but leave joints free of supports providing access for joining operations.

Fixture Construction Techniques

For either of the two fixture techniques proposed here, building the basic fixture starts with a solid model of the part. Using CAD software, a solid box surrounding the part is created. The part is then differenced from the box, resulting in a box having a cavity that matches the part geometry. Next, the top portion of the box is cut away to expose the cavity. This cut plane varies according to part height.

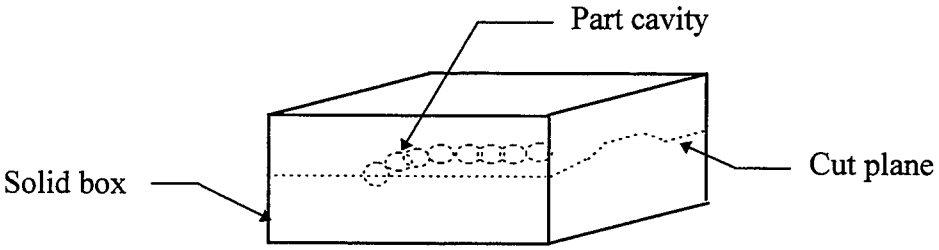


Figure 1. This figure shows how CAD software is used to enclose the part within a solid box. The box is then cut to expose the part geometry.

Once the basic fixture is designed, different techniques of fixture can be explored. These The Rectangular Grid fixture and the Multiple Tower fixture are discussed here.

A. Rectangular Grid fixture: The principle behind this fixture technique is to position the part using a rectangular grid of thin planar supports generated from the basic fixture described above. CAD files for each of the cardboard supports on which the part rests were cut on a plotter. A base was also constructed to allow correct registration of the supports.

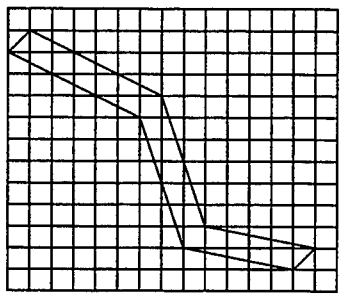


Figure 2. This figure shows the top view of the part enclosed within the rectangular grid.

The Rectangular Grid technique started with the base fixture discussed above. This fixture was divided into a rectangular grid of thin planar cross-sections separated at relatively large distances. Using CAD software, those sections of the grid which support the part were separated from the rest of the grid. Both the location (L) and the height (H) of each support were noted. Each support was then cut using a plotter. Two different kinds of cardboard sections were prepared. These are as follows: first, cardboard sections having a constant (L) and varying (H), and second, cardboard sections having a constant (H) and varying (L).

Each cardboard support was prepared as shown in Figures 3, 4 and 5. Parameters L and H have been marked on each support. Figure 3 shows a cardboard section with vertical slots cut in its lower half. This cardboard section has a constant H and a varying L. This section was mounted on another cardboard section perpendicular to it having slots cut in its upper half at constant L and a varying H parameters (see Figures 3 and 4). The base of the Rectangular Grid fixture consists of a plane board on which a 2 D drawing of the part's top view was printed (see Figure 5). To complete the fixture, the sections and the base were glued together. Figure 6 shows the final assembly of the fixture.

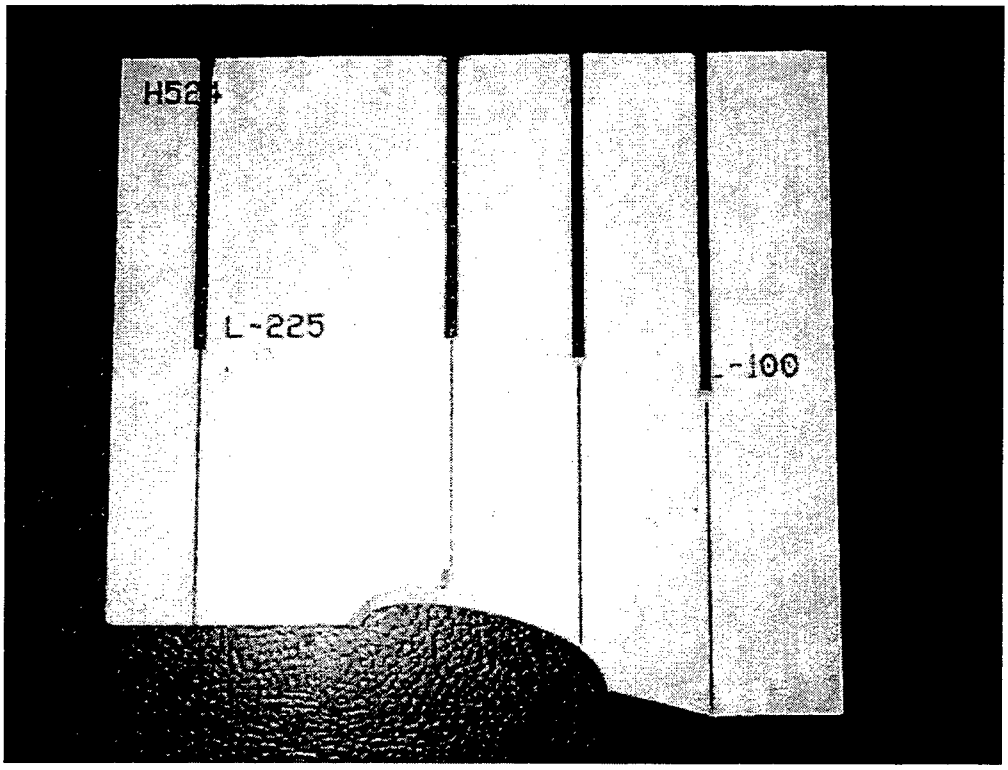


Figure 3. This figure shows the cardboard section at H=524 mm and L varying from 100 mm to 225 mm.

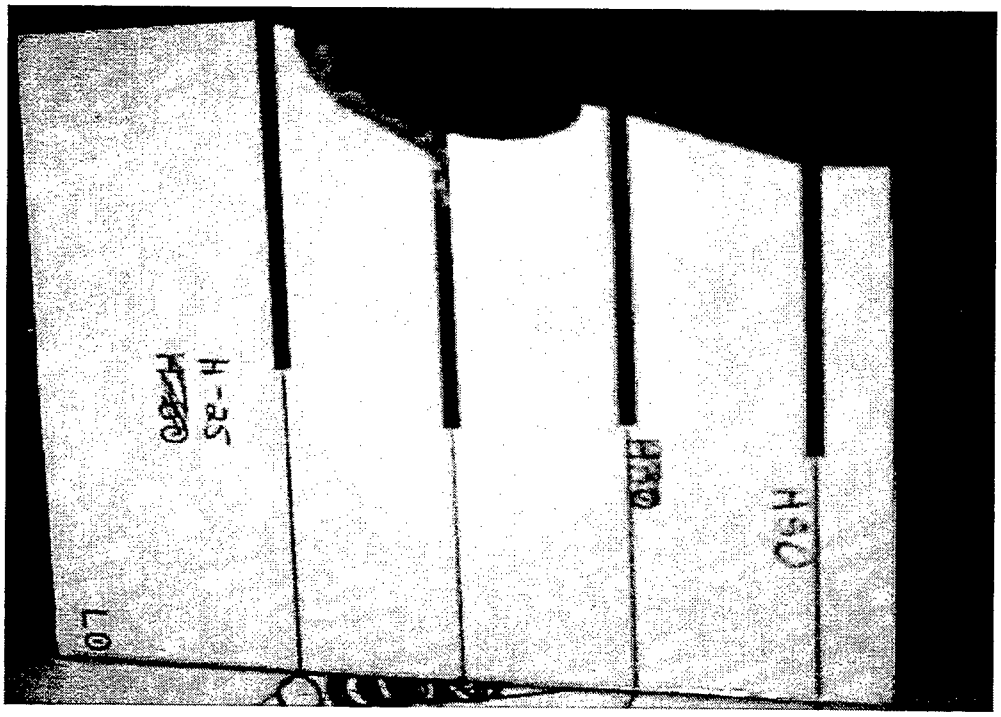


Figure 4. This figure shows the cardboard section at L=0 mm and H varying from 25 mm to 50 mm.

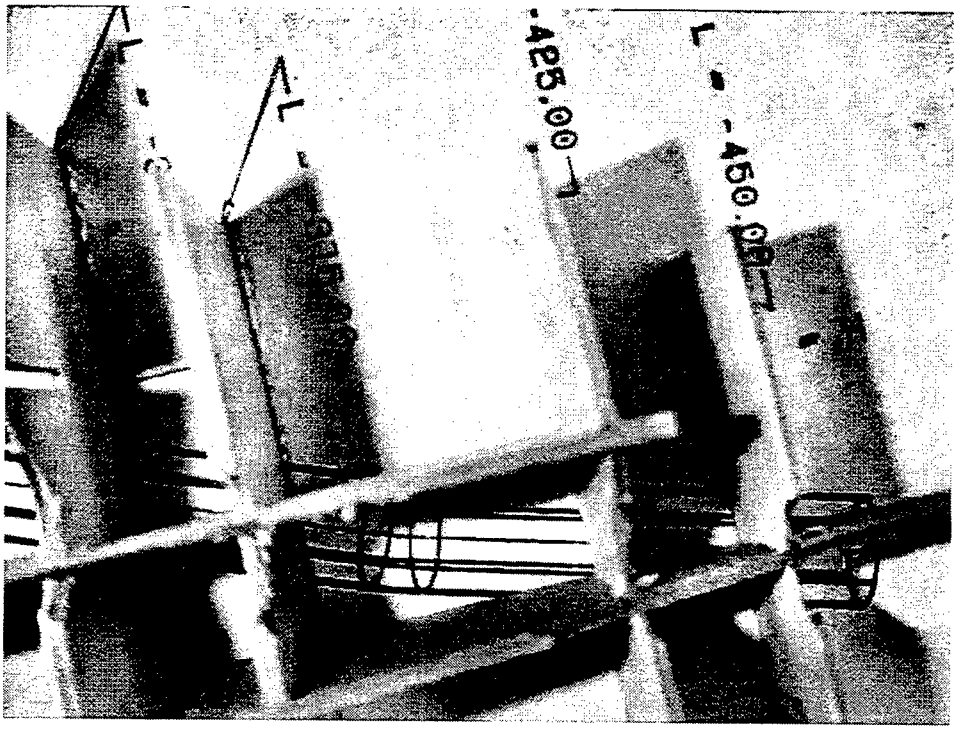


Figure 5. This figure shows the top view of the cardboard sections assembled together to form the grid. The part geometry is printed on the fixture base.

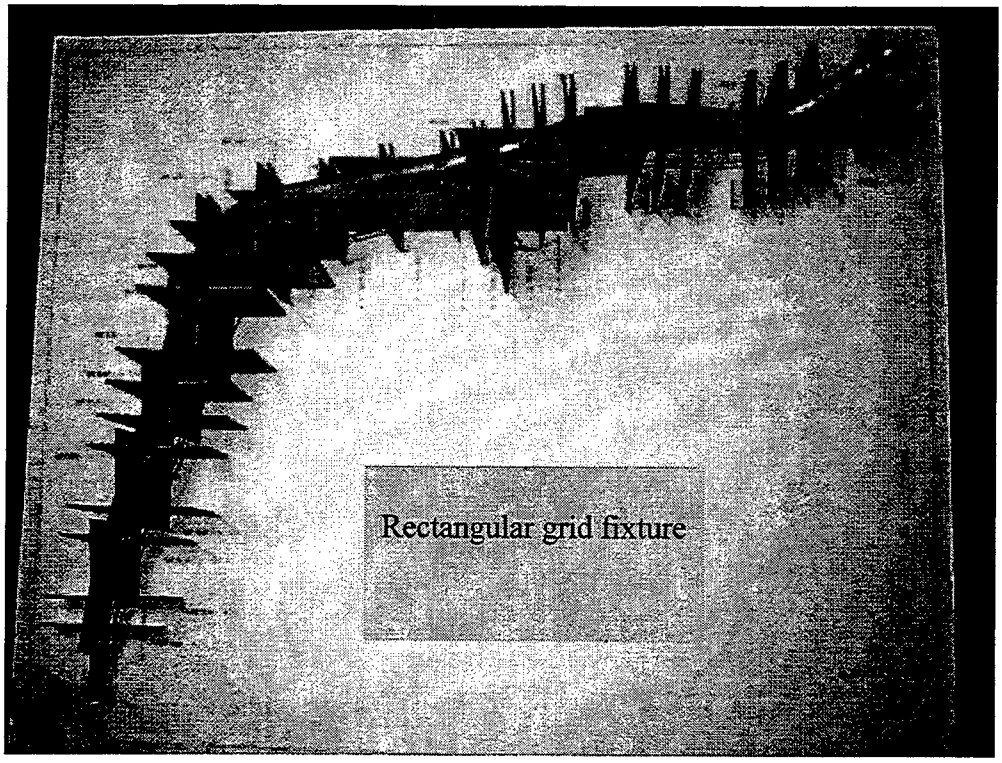


Figure 6. This figure shows the complete assembly of the Rectangular Grid fixture with the part mounted on it.

B. Multiple Towers: The principle behind this fixture technique is to position the part using Styrofoam towers. CAD files for each of the towers on which the part rested were cut using Shapemaker II. A base was also constructed to allow correct registration of the towers.

The Shapemaker II system utilizes *higher order construction algorithms* to cut build parts from thick Styrofoam layers with angled surface edges (Lee et al., 1997). In this manner, Shapemaker II allows rapid construction of large Styrofoam parts. Similar to the Rectangular Grid method, this technique started with the basic fixture discussed earlier. The part is supported at selected locations by means of Styrofoam towers. Using CAD software, decisions regarding tower locations were made based on the part's orientation. It was noted that a more accurate fixture results when the towers are oriented so that the slice direction is perpendicular to the part axis. This orientation also enables a good match between the tower and the part surface. Each tower was differenced from the basic fixture, sliced and built as a separate part using Shapemaker II. Once the layers were cut, they were bonded together. A base for the towers containing positioning holes that locate the towers was also cut on Shapemaker II (see Figure 7). The final assembly, including the towers, base and part is shown in figures 8 and 9.

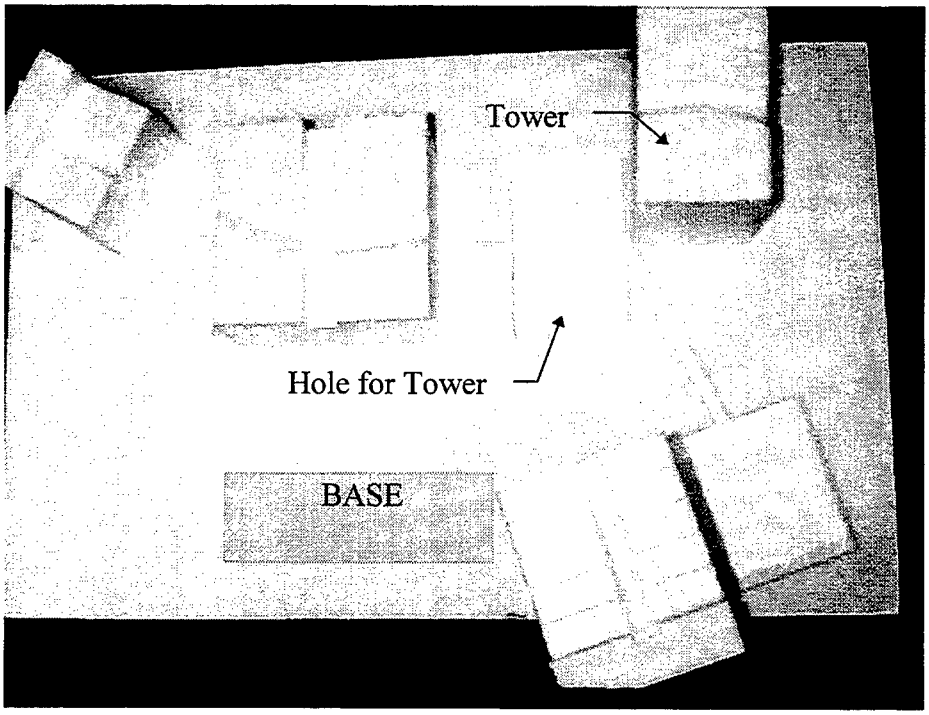


Figure 7. This figure shows the top view of the base of the Multiple Tower fixture. Two of the towers are placed beside the holes.

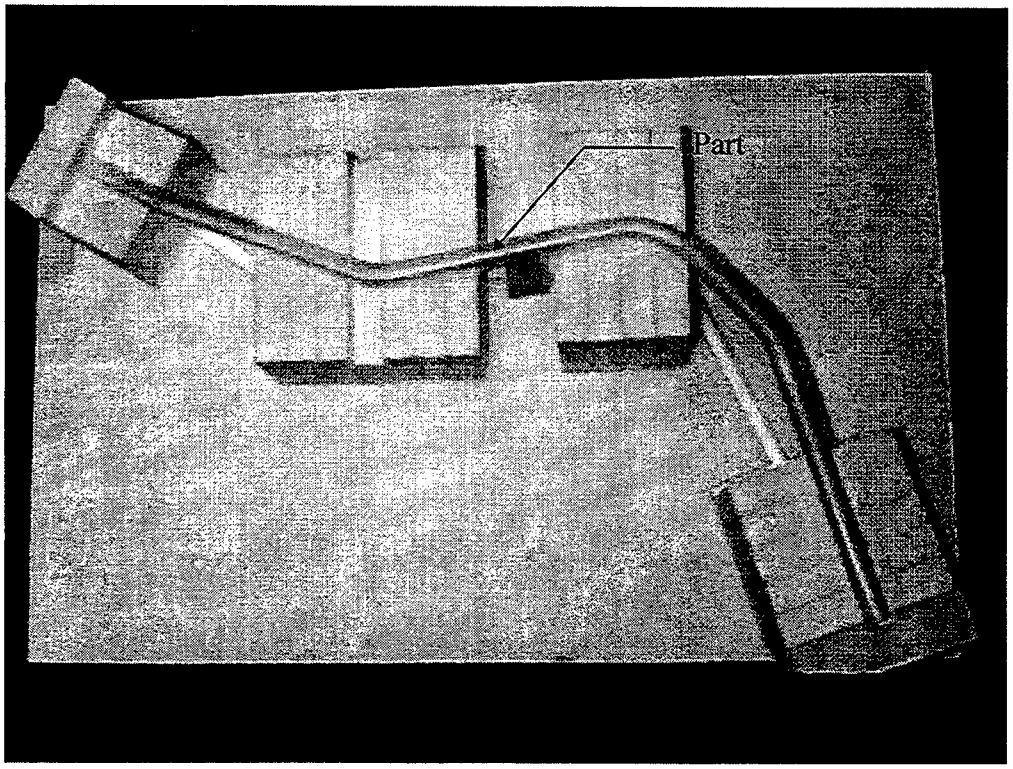


Figure 8. Top view showing the assembled Multiple Tower fixture. The part rests in the tower grooves.

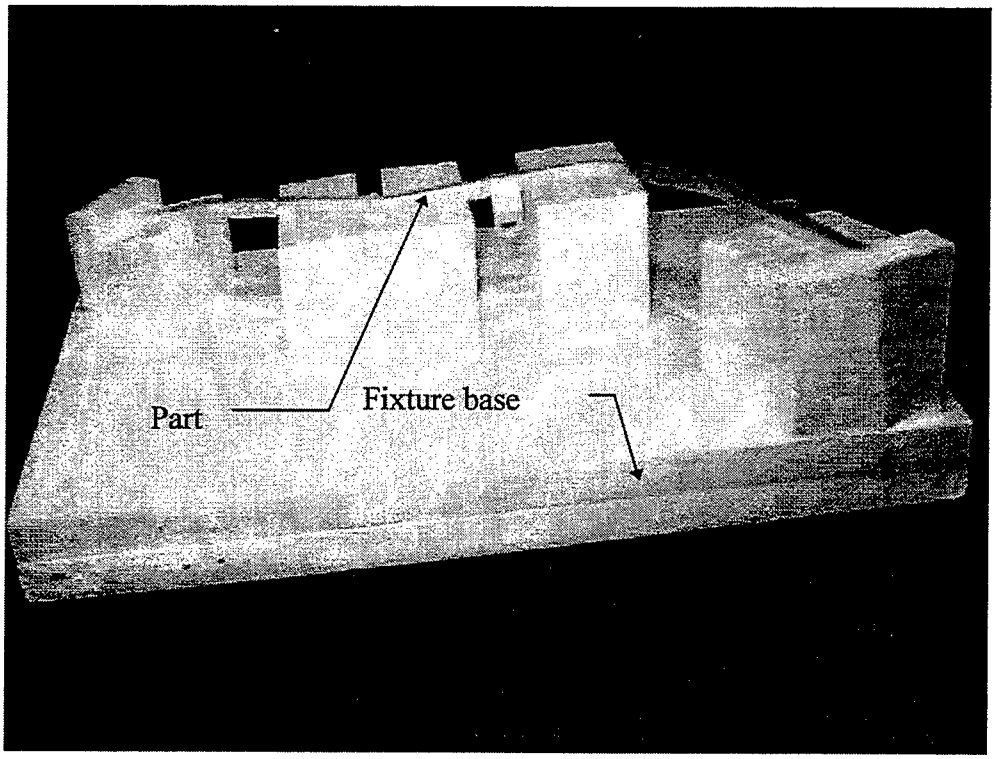


Figure 9. This figure shows the side view of the Multiple Tower fixture.

Results

Rectangular Grid Fixture

The Rectangular Grid fixture did provide accurate alignment and positioning of split build parts over large distances. In addition, it orients and locates sections, leaving joints free of supports providing access for joining operations, as long as the joint lies between the cardboard supports. The construction of the Rectangular Grid fixture however, did not prove to be rapid. The construction of the fixture base and the supports required extensive manual labor. The accuracy of the cardboard assembly is also limited by the operator's skill.

Multiple Tower Fixture

The Multiple Tower fixture did provide accurate alignment and positioning of split build parts over large distances. In addition, it orients and locates sections, leaving joints free of supports providing access for joining operations. The construction of the fixture was also rapid and inexpensive. The fixture was designed in five hours and built in two hours with a material cost of $5.00. The resulting fixture is quite stable for the weight of the part. One problem with the Shapemaker II system however, is its inability to cut angled edges greater than 50 degrees. This will limit the accuracy of the fixture.

Comparing The Fixtures

Because the Rectangular Grid supports are thin, they contact the part in 2D lines. This provides accurate support for any geometry. The Multiple Tower fixture however, supports the part with thick layers having ruled surface edges. If the fixture is designed such that a 3D curve part surface must lie against the ruled edge layers, positional error will result. This difference is shown in figure 10. In both cases, CAD files used for fixture design are limited by the accuracy of their stl file format (Novac 1997).

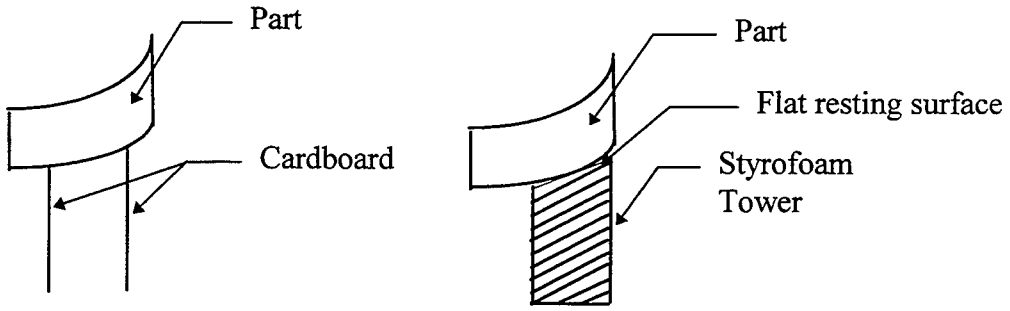


Figure 10. The cardboard supports support the part exactly, while the Styrofoam supports can potentially cause position error.

Conclusion

Parts which exceed the dimensions of the build envelope can be split into sections that fit the machine's envelope and fabricated separately. Assembly of the sections into an accurate three dimensional object often requires the creation of a fixture. This fixture ensures correct positional and angular orientation of the sections during assembly. In this paper, two fixture construction techniques were explored. These are the Rectangular Base fixture and the Multiple Tower technique utilizing the Shapemaker II system. It is concluded that both techniques have desirable features. It is also concluded that research in the rapid fabrication of disposable fixtures is promising and should be continued.

References

Berkstresser, D., Jansson, M., "Topographic Shell Fabrication (TSF) - RP for "the BIG stuff", *Proceedings of the International Conference on Rapid Prototyping*, San Francisco, CA, (1997).

Burns, Marshal, *Automatic Fabrication - Improving Productivity in Manufacturing,* PTR Prentice Hall, Englewood Cliffs, New Jersey (1993).

Lee, Cheol H., Thomas, Charles L., "Wavelet transform based analysis of object for layered manufacturing", *Proceedings of the International Conference on Rapid Prototyping*, San Francisco, CA, (1997).

Lee, Cheol H., Ph. D. Thesis, University of Utah, (1997).

Novac, Andrei S., M.S. Thesis, University of Utah, (1997).

Thomas, Charles. L. *An Introduction to Rapid Prototyping*, Schroff Development Corp., Mission Kansas, (1995).

Zirconium Diboride/Copper EDM Electrodes From Selective Laser Sintering

Brent Stucker*, Walter Bradley**, P.T. Eubank***, Somchintana Norasetthekul*** and Bedri Bozkurt***

The creation of electrical discharge machining (EDM) electrodes using freeform fabrication or rapid prototyping (RP) techniques has been the subject of numerous research initiatives around the world[1-6]. Most research projects have focused on finding ways to use RP to reduce the time necessary for producing traditional copper or graphite EDM electrodes. Although making copper or graphite electrodes using RP has potential benefits, those benefits are limited and it is unlikely that a large percentage of EDM users would use RP for producing EDM electrodes of copper or graphite.

If a material superior in EDM electrode performance to copper and graphite could be identified and this material could be made using RP, then users of EDM would be much more likely to use RP methods to make EDM electrodes. Such a material exists. It has been shown that a composite material made up of zirconium diboride (ZrB_2) and copper has an EDM electrode performance superior to any other EDM electrode material ever tested. In addition, a method for making ZrB_2/Cu electrodes using RP techniques has been developed.

Zyrkon™

Previous research at Texas A&M University by Gadalla & Cheng[7,8] had demonstrated that a composite material consisting of zirconium diboride particles surrounded by a copper matrix has superb EDM erosion resistance. That research showed the ZrB_2/Cu composite to be more resistant to wire EDM spark erosion than any other tested material conductive to heat and electricity[9].

Previously, the only published method for producing ZrB_2/Cu was to mix copper and ZrB_2 powders and hot-press them at temperatures in excess of the melting temperature of copper[10]. Hot-pressing, however, is not useful for creating geometrically complex parts. Therefore, a different method for fabricating ZrB_2/Cu electrodes, known as "Zyrkon™" electrodes, in geometrically complex shapes is necessary. Selective laser sintering of polymer coated ZrB_2 powders with post-processing will permit this fabrication[11]. The electrode production path is a four step process, and these steps are summarized in Table 1.

EDM Test Results

Electrodes of Zyrkon™, graphite, copper and W/Cu were tested against steel workpieces to compare their EDM performance characteristics. The graphite electrodes used were EDM-100 graphite electrodes from Poco Graphite. The copper electrodes used were alloy 110 copper bars purchased from McMaster-Carr, with a minimum purity of 99.9%.

---

* Department of Industrial and Manufacturing Engineering, University of Rhode Island
** Department of Mechanical Engineering, Texas A&M University
*** Department of Chemical Engineering, Texas A&M University

Zyrkon™ is a trademark of Materials and Manufacturing Technologies, Inc.

The W/Cu electrodes are the standard W/Cu EDM electrodes sold by Intech EDM. They are purported to have a composition of 70%W, 30%Cu by weight. The steel used as workpieces was a type 303 stainless steel purchased from McMaster-Carr.

Table 1 Zyrkon electrode production path

Step #1	Create a powder that contains ZrB_2 and a polymer binder that is compatible with SLS.
Step #2	Use SLS to process the powder from Step #1 into the desired shape.
Step #3	Place the SLS-produced part into a high-temperature, controlled-atmosphere furnace for debinding of the polymer binder and sintering of the ZrB_2 particles.
Step #4	Infiltrate the porous ZrB_2 structure with an appropriate copper alloy utilizing capillary action (minimizing the furnace oxygen content during Steps 3 and 4 is critical).

The Zyrkon electrodes used for the initial tests were produced by cold-pressing polymer-coated ZrB_2 powders instead of using SLS. The rest of the processing steps were identical to those described in Table 1--a sintering temperature of 1700°C and an infiltration temperature of 1200°C was used. (Cold-pressing was used during tests for optimization of the ZrB_2/Cu system because it was cheaper, faster and easier than using RP methods to make the 3/8" x 3/8" x 2" rectangular bars used in the tests.)

The results of EDM tests on these materials can be seen in Figures 3-6. For these tests, a constant off-time of 100μs was used and the on-times and amperages were varied from test to test. Although tests ranging from 8.3 amps to 37.1 amps were performed, only the tests at 14.8 amps are shown due to space limitations. The trends seen at this amperage are the same as the trends seen at other amperages.

A careful look at these graphs indicate that the Zyrkon electrode system is superior to any of the other electrode materials. Zyrkon wear ratios are comparable to W/Cu wear ratios and better than the other electrode wear ratios, but Zyrkon sink rates are much better than W/Cu sink rates. Zyrkon electrode sink rates are comparable to graphite sink rates at low on-times and better than graphite at higher on-times. In the places where graphite is comparable to Zyrkon in sink rate, the wear ratio of the graphite is very poor compared to Zyrkon. Zyrkon electrodes have a higher sink rate than the other electrodes at all conditions. Therefore, when both wear ratio and sink rate are considered, Zyrkon is the best electrode material at every on-time and current.

SLS

In order to make Zyrkon electrodes using SLS, an SLS-compatible polymer coated ZrB_2 powder needed to be created. DTM provided an SLS compatible thermoplastic binder, and it was applied to ZrB_2 powder purchased from Advanced Refractory Technologies, Inc.

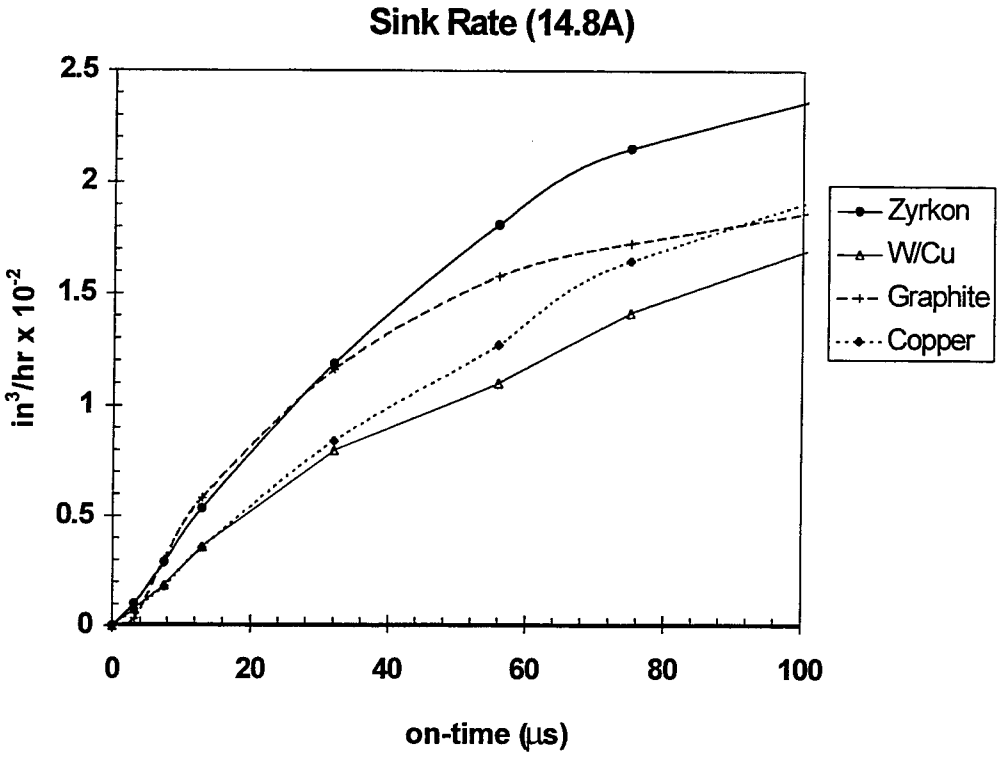


Fig. 3 Sink Rates for various electrodes, 14.8 Amps

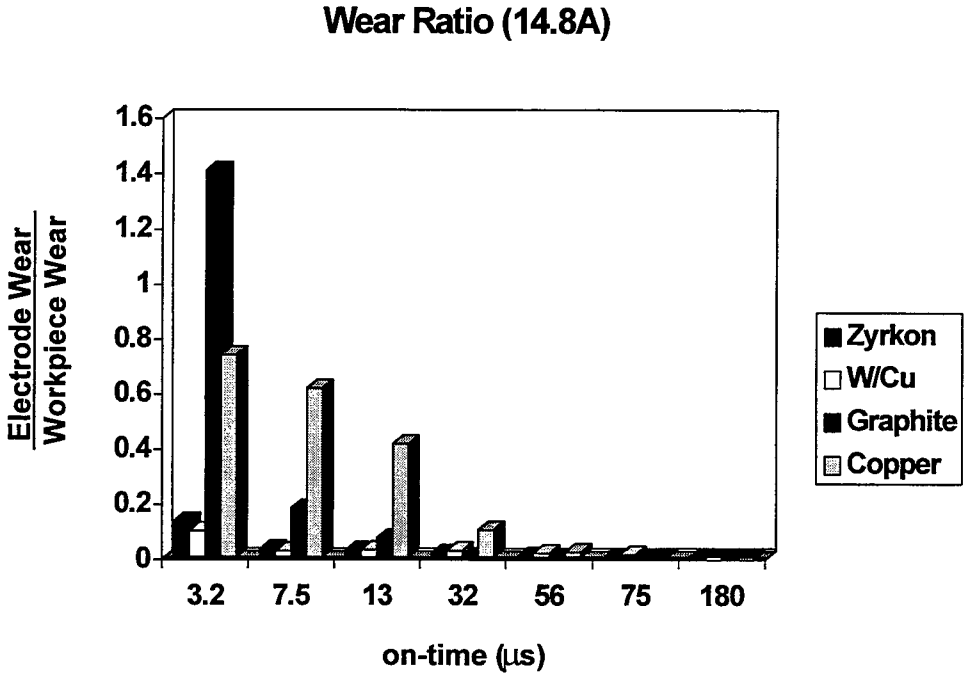


Fig. 4 Wear ratios for various electrodes at 14.8 Amps

using a combination of spray drying and fluidized bed treatment. This combination resulted in ZrB_2/polymer agglomerates that were not very dense. Thus, after SLS processing and binder removal, the resulting sintered parts were only 31% dense prior to infiltration. The cold-pressed parts, on the other hand, had ZrB_2 densities of 55-60% by volume.

The EDM test results using the SLS-produced parts in the electrode testing procedure can be seen in Figures 7 and 8. The on-times of 3.2μs, 7.5μs and 13μs were run at 14.8 amps. The on-times of 75μs and 180μs were run at 24.8 amps. These on-times and amperages were chosen to mimic finishing and roughing conditions respectively.

It can be seen from these results that the SLS-produced Zyrkon parts did not perform as well as the cold-pressed parts. This is due to the lower amount of ZrB_2 present in the parts. To verify that this was indeed the case, some of the powder used in the SLS machine was pressed to a higher density of 50%. This powder did perform similarly to the original pressed parts, confirming the hypothesis that it was the lower ZrB_2 amount that caused the reduced performance. However, even though the SLS-produced Zyrkon parts under-performed the pressed parts, they were still as good as or better than any of the other electrode materials.

In order to increase the ZrB_2 content in the SLS-produced parts a new approach to adding the binder must be used. Research is proceeding with the help of DTM to try new dry-mixable thermoset binders. If these binders prove effective, spray drying and fluidized bed treatment steps can be eliminated and the agglomeration density problem can be avoided.

In addition to these EDM tests, qualitative tests were performed on geometrically-complex parts created on the SLS machine and sent to Kodak and Steelcase. The electrode made for Kodak was a copy of a graphite electrode used to make a small spring. This electrode was small and thin, with an EDM electrode surface approximately 1.25" long (if uncoiled) and no greater than 0.0625" thick and 0.025" deep. Two different EDM tests were run using two different electrodes. One was run at 5 amps, 74μs on-time and 20μs off-time. This produced a semi-smooth surface, and the electrode ran with no problems. The other electrode was tested at an extreme current for an electrode this size. It was tested at 18 amps, 50μs on-time and 12-25μs off-time and the electrode and machined workpiece are shown in Figure 9. An identical graphite electrode was also run at the same conditions and is shown with its machined workpiece in Figure 10. Both electrodes produced equally poor surface finishes, but it was observed that the Zyrkon electrode cut faster than the graphite electrode. In addition, the graphite electrode exhibited short-circuiting, arcing, contamination and high electrode wear at these conditions--none of which was true for the Zyrkon electrode.

The electrode made for Steelcase was significantly larger, measuring approximately 1.25" long, 0.75" wide and 0.3" deep. This electrode was used at what they termed, "finishing" and "semi-finishing" EDM conditions. An aluminum block was cut at semi-finishing conditions and is shown with the Zyrkon electrode in Figure 11. A steel block was subsequently cut at finishing conditions and is shown in Figure 12. Several features on the electrode were measured to help determine wear on the Zyrkon electrode, and no measurable wear was found, even after both EDM operations.

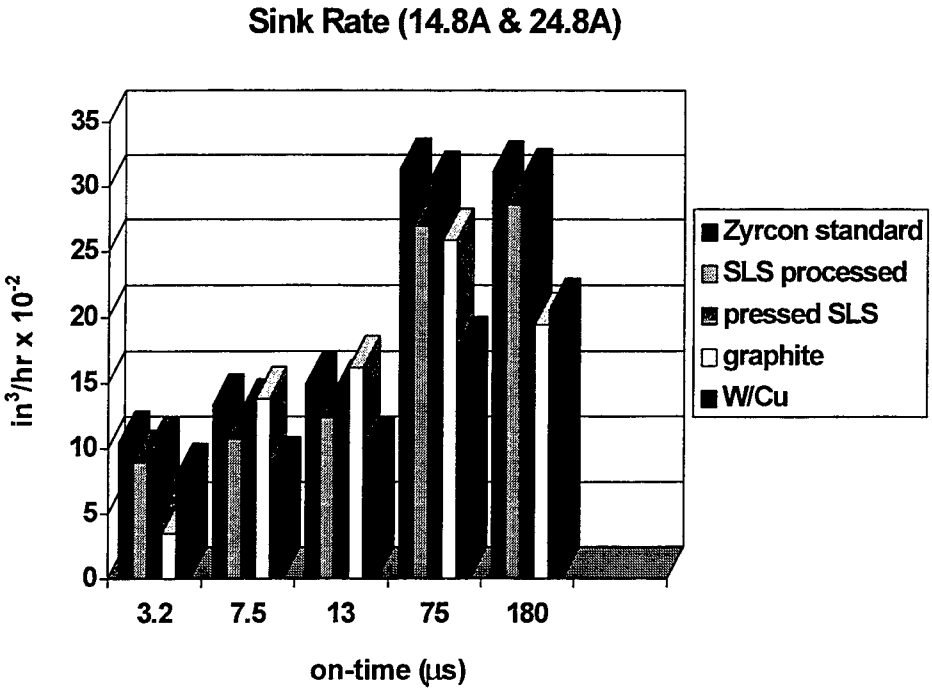


Fig. 7 Sink rates of various electrodes compared to SLS-made electrodes

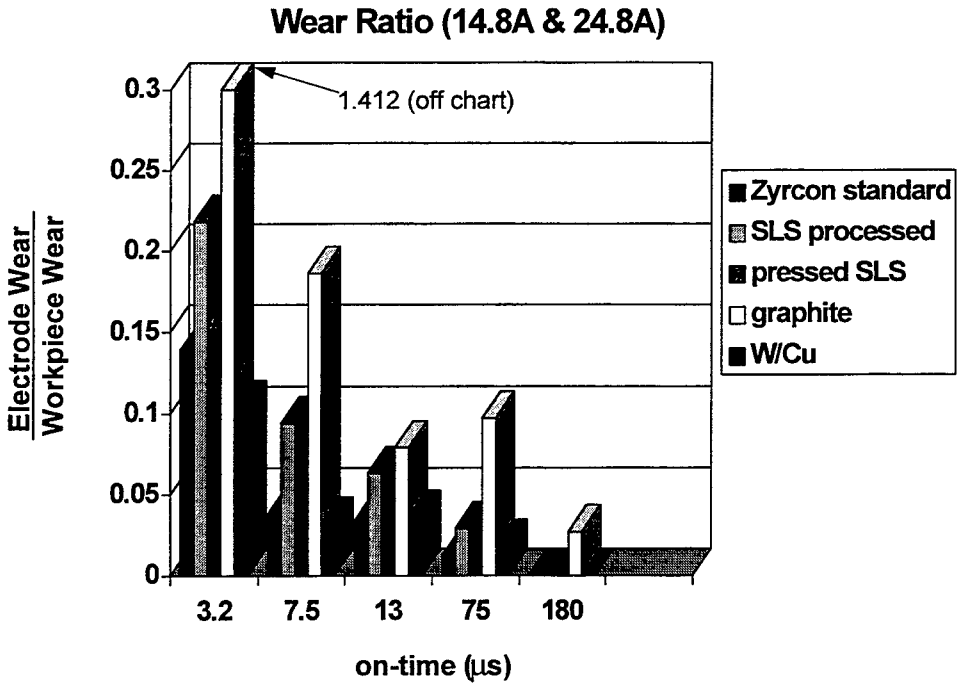


Fig. 8 Wear ratios of various electrodes compared to SLS-made electrodes

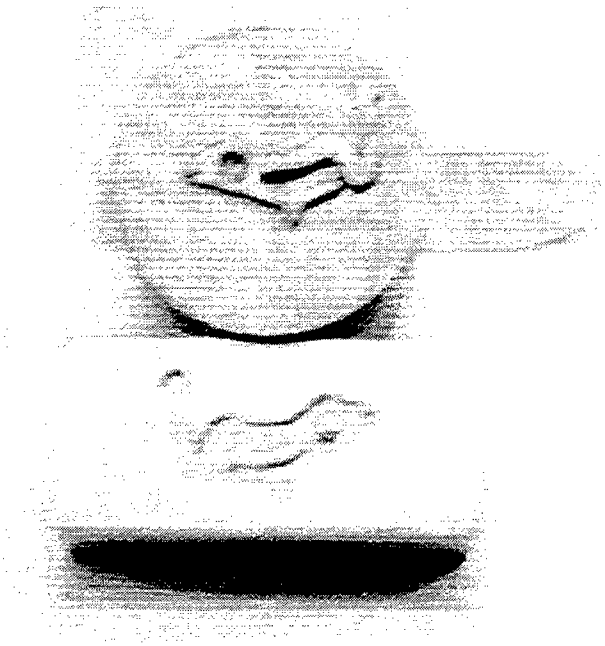


Fig. 9 Zyrkon electrode and steel workpiece after EDM at 18 Amps, 50μs on-time, 12-25 μs off-time (steel workpiece is 1.25" across its greatest dimension)

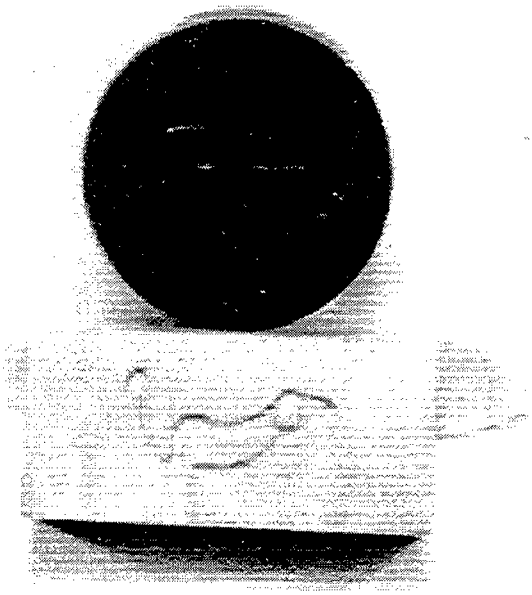


Fig. 10 Graphite electrode and steel workpiece after EDM at 18 Amps, 50μs on-time, 12-25 μs off-time (steel workpiece is 1.25" across its greatest dimension)

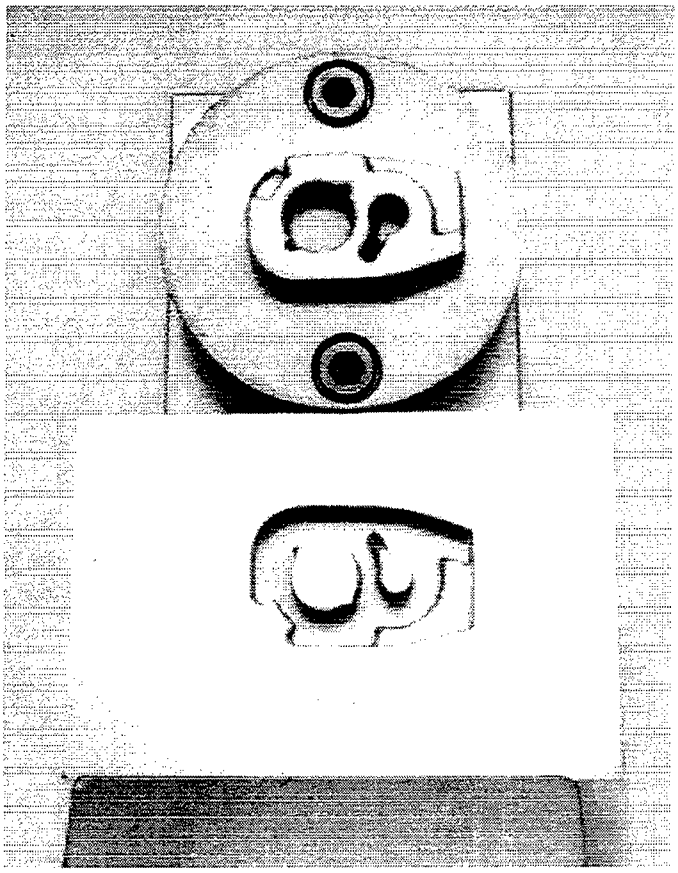


Fig. 11 Zyrkon electrode and aluminum workpiece after EDM at semi-finishing conditions

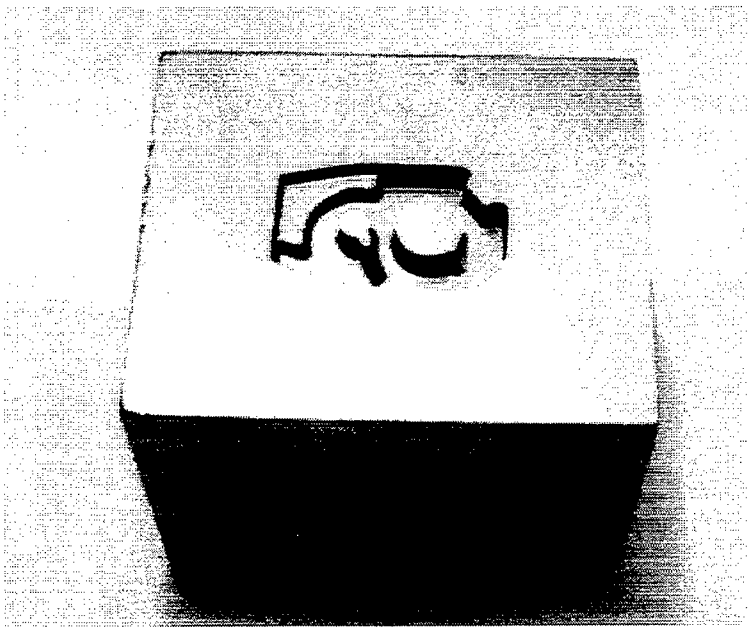


Fig. 12 Steel workpiece after EDM by Zyrkon at finishing conditions

In addition to good wear ratio and sink rate performance, the surface finishes of the cavities produced at Steelcase were very good. The EDM surfaces of both workpieces were surprisingly smooth after the EDM operation. This experiment confirmed the hypothesis that the degree of surface roughness present with current SLS technology is not highly detrimental to the fabrication and use of EDM electrodes.

SLS-produced electrodes, after debinding, sintering and infiltration, without performing any manual finishing except a light bead blasting, have a semi-rough feel, like 220 grit sand-paper. Following the use of these electrodes at semi-finishing and finishing conditions, these electrodes have the feel and look of polished metal. This is because the EDM process erodes the "high spots" on the Zyrkon electrode, giving a smoothing of the electrode with use, and thus, the surface finish it produces on the workpiece. This smoothing of the electrode surface, as observed at Steelcase, did not result in macroscopic dimensional changes.

Conclusions

The results of these studies on Zyrkon indicate several things:

(1) Because Zyrkon is an EDM electrode material that surpasses currently available electrode materials in its EDM performance characteristics, this material will become increasingly popular with EDM users.

(2) Zyrkon can be made using selective laser sintering and initial results indicate that electrodes made using SLS will perform better than traditional electrodes made using traditional techniques. As the binder problems are solved, the performance of SLS-produced Zyrkon electrodes will approach the performance of cold-pressed Zyrkon electrodes.

(3) The processing techniques developed for creating Zyrkon electrodes are compatible with a number of RP processes and molding techniques. Many other techniques for creating Zyrkon electrodes are being examined and a number of these techniques should be available to the public in the near future.

Acknowledgements

This research was made possible by generous funding from the National Science Foundation through grant DMR9420386 and through a National Science Foundation Graduate Research Fellowship, which paid for a significant portion of Brent Stucker's salary. The in-kind and financial support of DTM, Kodak, Advanced Refractory Technologies and Steelcase are gratefully appreciated.

REFERENCES

[1] Arthur, A., Dickens, P., Bocking, C. and Cobb, R., 1996, "Wear & Failure Mechanisms for SL EDM Electrodes," *Solid Freeform Fabrication Symposium Proceedings*, Bourell et al, eds., The University of Texas, Austin, TX, pp. 175-190.

[2] Bradley, W.L., and Stucker, B.E., 1995 "Producing EDM Electrodes with Rapid Prototyping Techniques," *EDM '95 Conference Proceedings*, Chicago, IL.

[3] Ippolito, R., Iuliano, L. and Gatto, A., "EDM Tooling by Solid Freeform Fabrication & Electroplating Techniques," *Solid Freeform Fabrication Symposium Proceedings*, Bourell et al, eds., The University of Texas, Austin, TX, pp. 199-206.

[4] Jensen, K.L. and Hovtun, R., 1992, "Making Electrodes for EDM with Rapid Prototyping." *Industriel Teknologi*, September.

[5] Killander, L.A. and Homer, B., 1996, "EDM Electrodes Made by RPT," *EARP European Action on Rapid Prototyping,* May, No.8.

[6] Stucker, B.E., Bradley, W.L., Norasetthekul, S., and Eubank, P.T., 1995, "The Production of Electrical Discharge Machining Electrodes Using SLS: Preliminary Results," *Solid Freeform Fabrication Symposium Proceedings*, Marcus et al, eds., The University of Texas, Austin, TX, pp. 278-286.

[7] Eubank, P.T., and Bozkurt, B., 1992, "Recent Developments in Understanding the Fundamentals of Spark Erosion for Composite Materials," *Machining of Composite Materials Symposium*, T.S. Srivatsan, D.M. Bowden, eds., Am. Soc. Materials, Materials Park, OH, pp. 159-166.

[8] Gadalla, M.A. and Cheng, Y.M., 1992 "Machining of Zirconium Diboride and Its Composites," *Machining of Composite Materials II Symposium* presented at ASM Materials Week Conference, October 18-21, Pittsburgh, PA.

[9] Cheng, Y.M., 1994, "Synthesis and Electrical Discharge Machining of Advanced Ceramics Containing Zirconium Diboride," *Doctoral Dissertation*, Texas A&M University, College Station, TX.

[10] Cheng, Y.M., and Gadalla, A.M., 1996, "Synthesis and Analysis of ZrB_2-Based Composites," *Materials and Manufacturing Processes*, Vol. 11, No. 4.

[11] Stucker, B.E., 1997, "Rapid Prototyping of Zirconium Diboride/Copper Electrical Discharge Machining Electrodes," *Doctoral Dissertation*, Texas A&M University, College Station, TX.

Thermal Effects on Accuracy in the 3DKeltool™ Process

Authors: Neil Hopkinson & Phill Dickens
Department of Manufacturing Engineering & Operations Management
University of Nottingham, UK

Abstract
The 3DKeltool™ process has been used to produce injection moulding inserts capable of producing millions of parts with quick cycle times (1). Short lead times are possible however accuracy is reduced for dimensions over 150mm.
The use of room temperature vulcanising (RTV) silicone rubber in the 3DKeltool™ process is a possible reason for the loss of accuracy in larger parts. Effects of temperature changes during the process are assessed both theoretically and experimentally.
The results show close agreement between theoretical predictions and experimental results for dimensional changes. Suggestions which could allow accurate manufacture of larger 3DKletool™ parts are presented.

Background
The 3DKeltool™ process uses a master, such as a stereolithography (SL) model, to make injection moulding inserts or electrode discharge machining (EDM) electrodes from powdered metal. The process uses intermediate steps which involve creating moulds from RTV silicone rubber (see Figure 1).

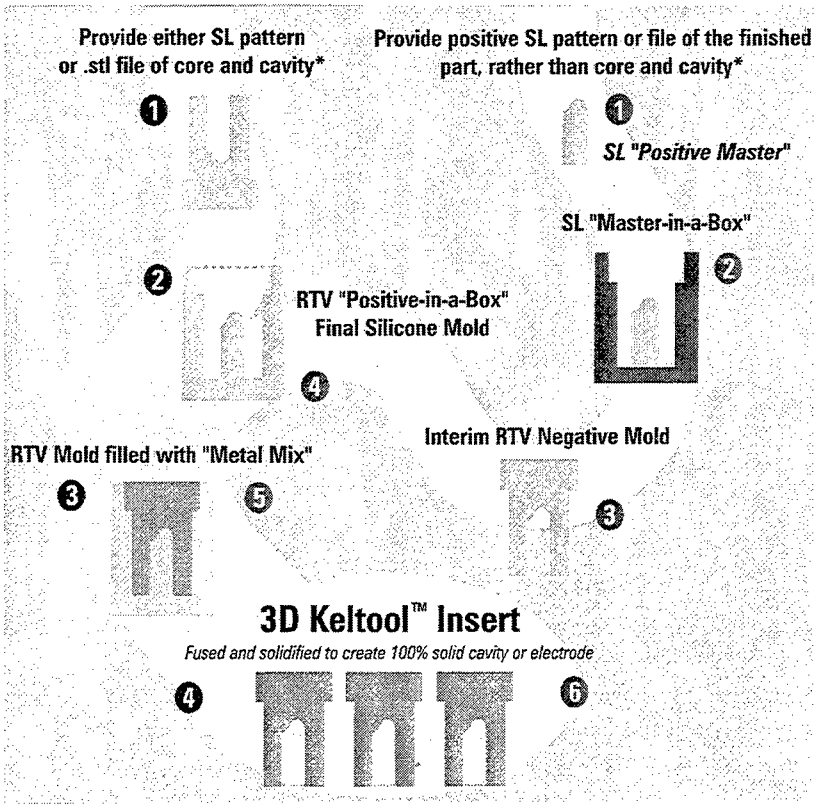


Figure 1: Outline of the 3DKeltool™ Process

The work covered in this paper is concerned with producing the RTV silicone rubber moulds and not with any of the later stages of the 3DKeltool™ process. This means that the work is also relevant to other processes such as vacuum casting with RTV silicone rubber moulds.
One of the major constraints with the current 3DKeltool™ process is that its use is limited to parts with dimensions under 150mm if high accuracies are to be achieved. The high coefficient of thermal expansion (CTE) of RTV silicone rubber is thought to be a possible cause for this limitation on part size when high tolerances are required. It is important to consider tolerances required in tooling when assessing the effects of any sources of loss of accuracy. For engineering parts tolerances of +/- 50 microns are usually specified although in some cases +/- 10 microns may be required (2).

Thermal Properties of materials used in the 3DKeltoolTM Process
When using the 3DKeltool™ process to create injection moulding tooling, the materials used are SL cured epoxy (as the master), cured RTV silicone rubber (for intermediate mould(s)) and tool steel (the final injection moulding insert). The linear CTEs for these materials at around room temperature are:

SL5170	8.8×10^{-5} mm/mm/°C
RTV Silicone Rubber	30×10^{-5} mm/mm/°C
Tool Steel	1×10^{-5} mm/mm/°C

How Thermal Properties Limit Accuracy
Figures 2 - 4 show how much expansion will be caused by temperature increases in parts made from the materials used in the 3DKeltoolTM process. Note that temperature decreases will result in similar contractions in dimensions.

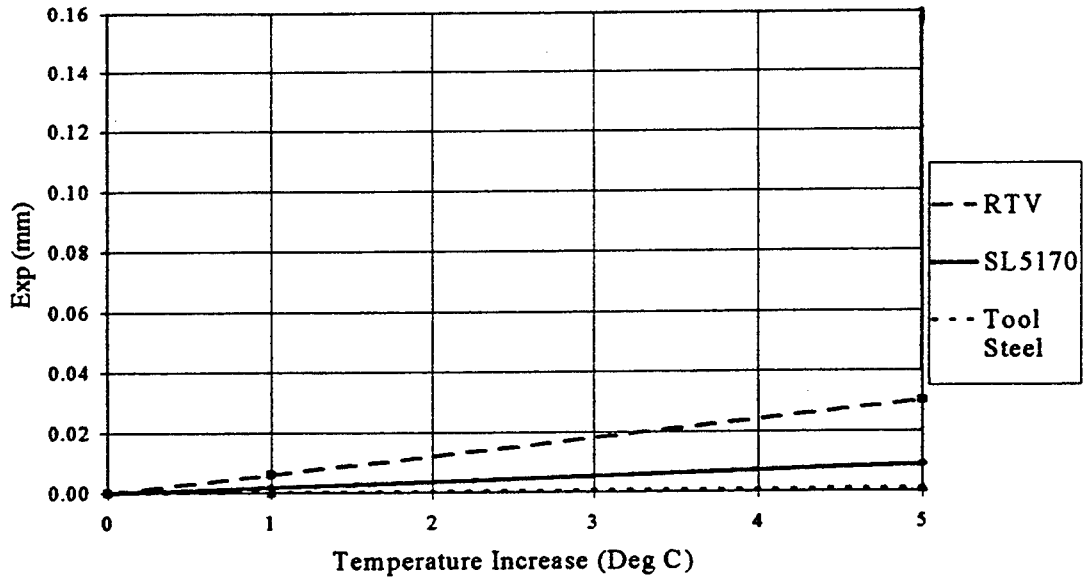


Figure 2: Effect of Increased Temperature on 20mm Dimensions

Figure 2 shows that for dimensions of 20mm or smaller, a change in temperature of up to 5°C (which is not unreasonable (3)) with either of the three materials shown should not be sufficient to cause expansion or contraction of over 50 microns through thermal expansion/contraction alone. The RTV silicone rubber is shown to change dimensions as a result of thermal expansion/contraction more than the other materials with an expansion of 30 microns caused by a temperature change of 5°C.

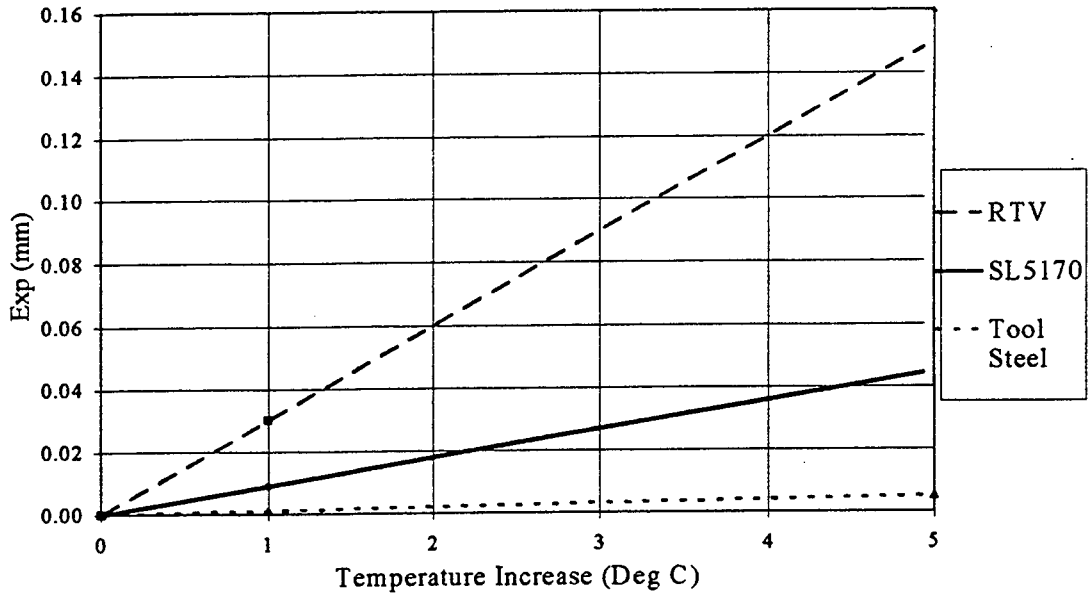


Figure 3: Effect of Increased Temperature on 100mm Dimensions

Figure 3 shows the amount of thermal expansion which may be expected in dimensions of 100mm which approaches the maximum size to which parts can be accurately made using the 3DKeltool™ process. The steep slope of the graph representing RTV silicone rubber thermal expansion indicates that a temperature change of only 2°C is sufficient to breach the 50 micron tolerance threshold with dimensions of 100mm. This suggests that the temperature control during the RTV silicone rubber stages of the3DKeltool™ process must be tight (around +/- 1.5°C) in order to produce parts with tolerances of +/- 50 microns. Such temperature control is unrealistic in most factory situations however under controlled conditions such as in a metrology laboratory tighter control (+/- 1°C) is possible. The graphs for SL resin and tool steel, however, indicate that thermal expansion alone will not cause 100mm dimensions to be outside a 50 micron tolerance if a +/- 5°C temperature can be maintained.

Figure 4 shows the thermal expansion caused in 200mm dimensions which is greater than the maximum size with which 3DKeltool™ parts can be produced to high tolerances. A temperature change of only 1°C will cause a dimensional change of 60 microns in RTV silicone rubber parts of this size. For SL parts, thermal expansion with a temperature change of 3°C will cause a dimension of 200mm to be outside a 50 micron tolerance, whereas the thermal expansion of tool steel remains negligible with regard to accuracy for parts of these sizes.

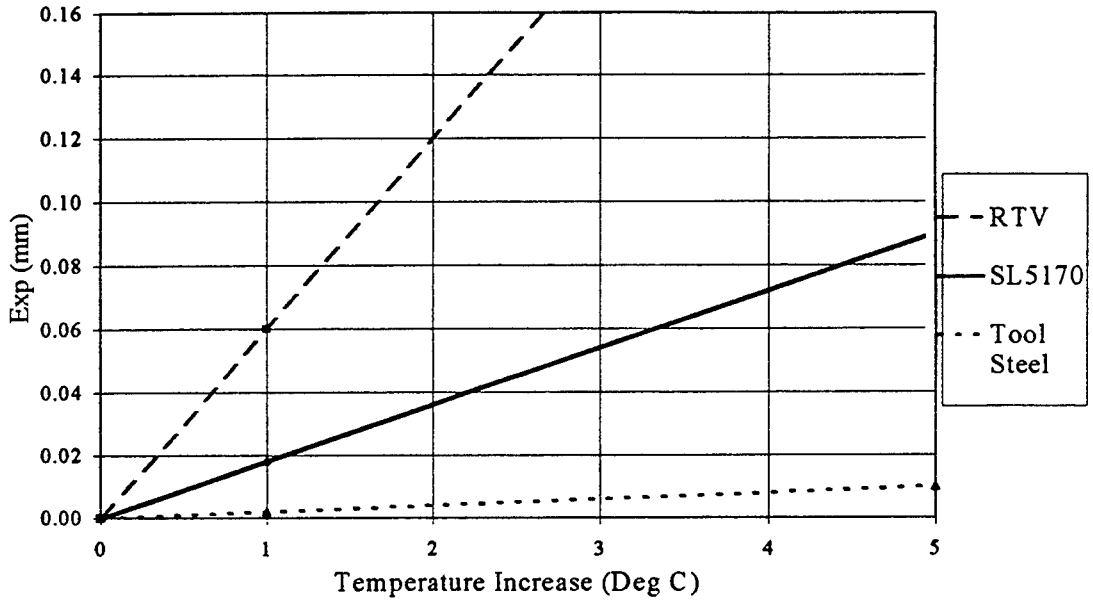


Figure 4: Effect of Increased Temperature on 250mm Dimensions

Practical Assessment of Effects of Heat on Accuracy

Method

The effects of heat on mould geometry were measured in a simple test using one SL mould built in the ACES build style and another mould made from RTV silicone rubber which had be cast around an SL master. The moulds used were based on a typewriter part with a largest dimension of 180mm (see Figure 5).

A thermocouple was inserted into the centre of each of the moulds which were then slowly heated on a lagged hot plate. When the mould temperature had risen to 45°C the mould was removed from the hot plate, placed on a co-ordinate measuring machine (CMM) and allowed to cool while measurements were taken. Ideally measurements would have been made using a non-contact method as softening of RTV silicone rubber during heating could affect the CMM results. It was assumed, however that such effects would be negligible.

Results

Figure 6 shows a clear shrinkage as the RTV silicone rubber mould was allowed to cool. The measured CTE for the RTV silicone rubber mould was 49 x 10^{-5} mm/mm/°C which is slightly higher than had been predicted. The reason for this being slightly higher than expected may be due to softening of the rubber at higher temperatures as mentioned above.

The slope of the graph in Figure 7 is less steep than that in Figure 6 indicating a lower CTE as expected. The CTE for the SL mould was calculated as 9.2 x 10^{-5} mm/mm/°C, which again is slightly higher than that which had been expected.

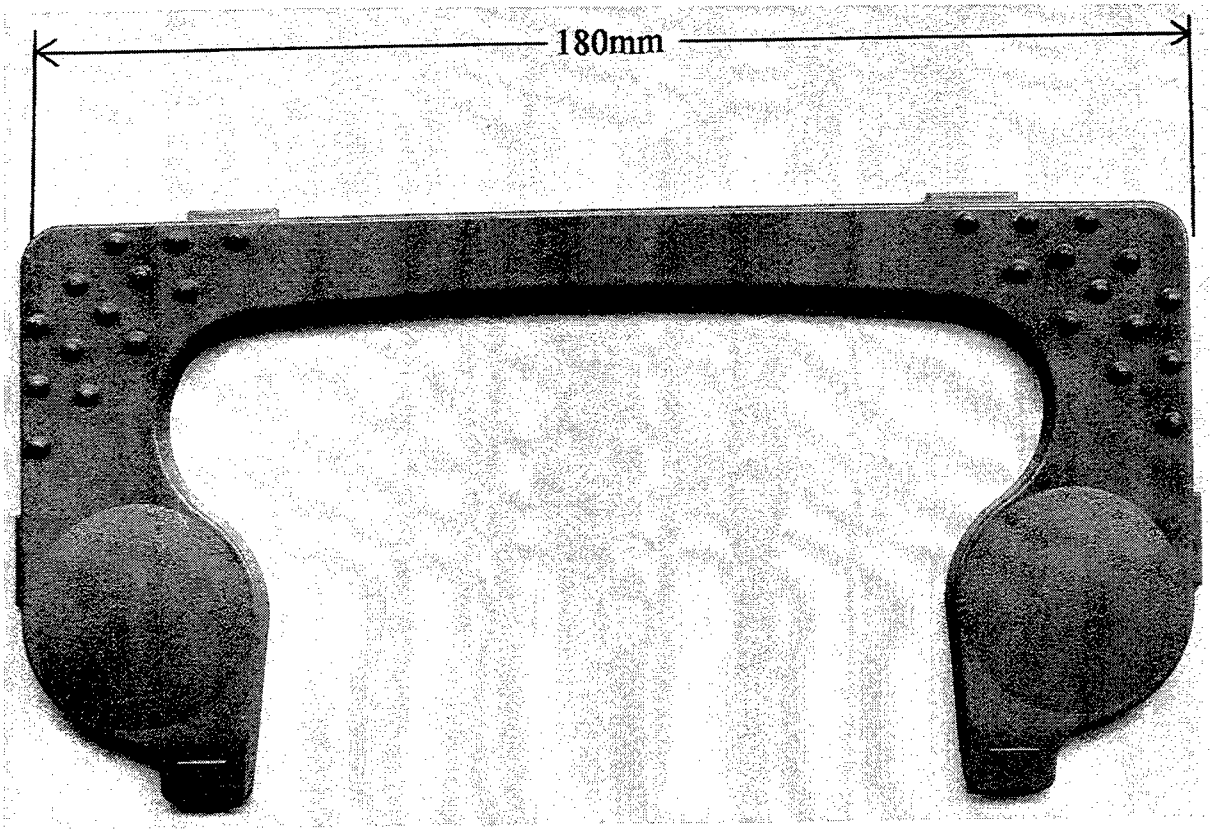


Figure 5: Typewriter part which mould shape was based on

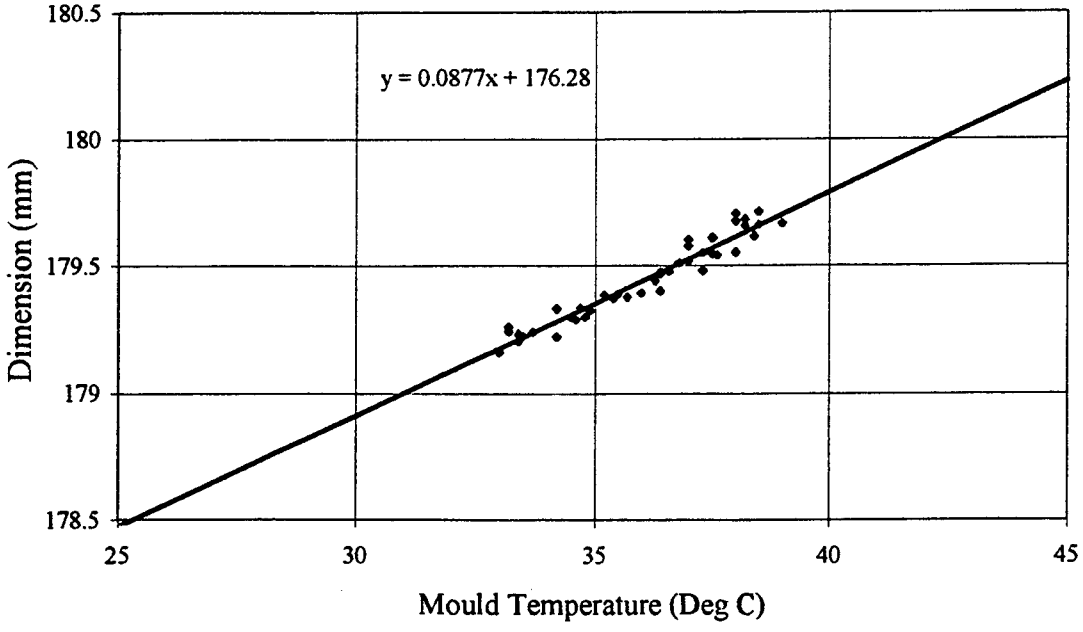


Figure 6: Graph showing relationship between RTV silicone rubber mould temperature and size

The measured CTEs for the RTV silicone rubber and SL moulds are similar to the expected values with the CTE of RTV silicone rubber being five times greater than that for SL5170. This would suggest that eliminating RTV silicone rubber from the 3DKeltool™ process could allow larger parts to be produced more accurately or with less temperature control.

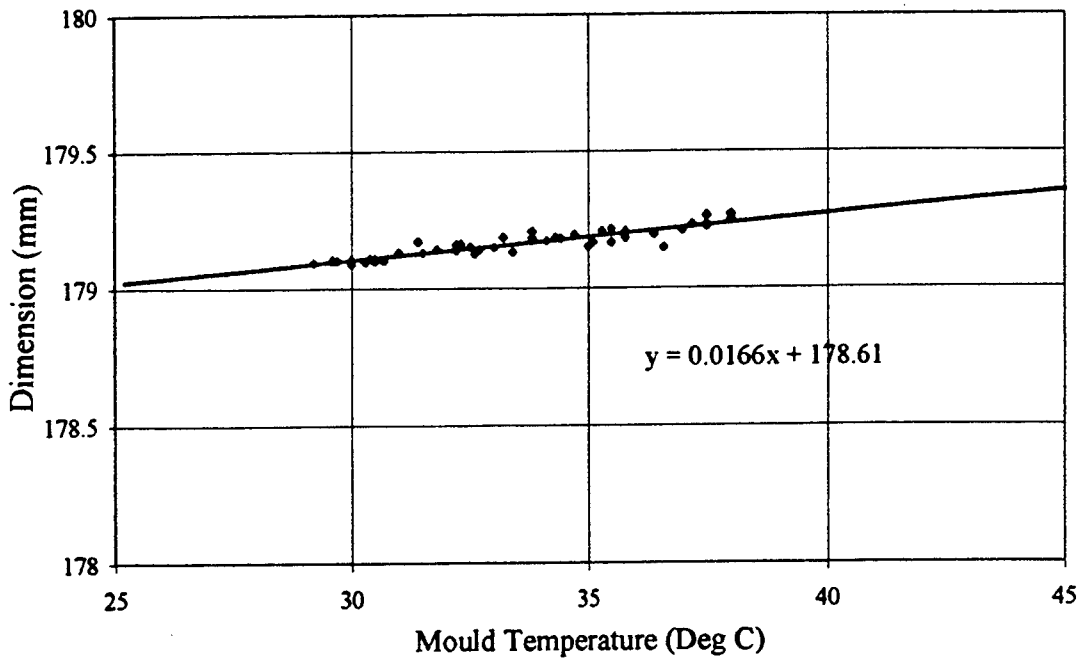


Figure 7: Graph showing relationship between SL mould temperature and size

Alternative Method

A number of possible alternatives to RTV silicone rubber have been considered by the authors including the use of low melt point alloys, wax, plaster of paris and direct SL use. However RTV silicone rubber has the advantages of good release, avoiding damage of the original SL model and green insert, and faithful reproduction of original features. For this reason, a composite mould consisting of an SL body with an RTV silicone rubber membrane was used. The idea behind the RTV silicone rubber membrane mould was to keep the advantages of good release and reproduction while minimising the effect of its high CTE.

Figure 8 shows how an RTV silicone rubber membrane mould is made, the injected RTV silicone rubber is allowed to cure at room temperature and then the core is removed. By allowing the RTV silicone rubber to key into the open Quickcast structure of the cavity part, the membrane remains fixed to the cavity with a surface that directly reflects the surface of the core part.

Practical Assessment of RTV Membrane Mould

An RTV silicone rubber membrane mould was made for the typewriter part mentioned above and this was subjected to the same test as the RTV and SL moulds had been in order to establish the effects of temperature on dimensions. Figure 9 shows the graph of temperature against mould dimensions. As expected the slope is between those for the solid RTV silicone rubber mould and the SL mould but much closer to the SL

mould. The equivalent CTE was calculated to be 12 x 10^{-5} mm/mm/°C which is under 25% of that for the solid RTV silicone rubber mould.
The effects of temperature on accuracy when using RTV silicone rubber moulds could be dramatically reduced allowing larger parts to be made with higher tolerances while still having the same variations in room temperature.

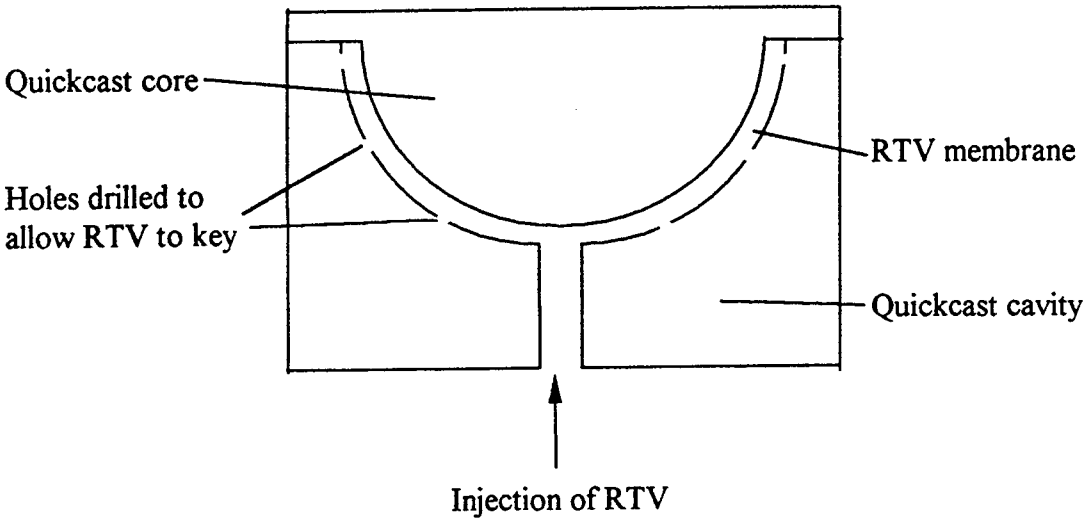


Figure 8: Cross section diagram showing how an RTV silicone rubber membrane mould is made

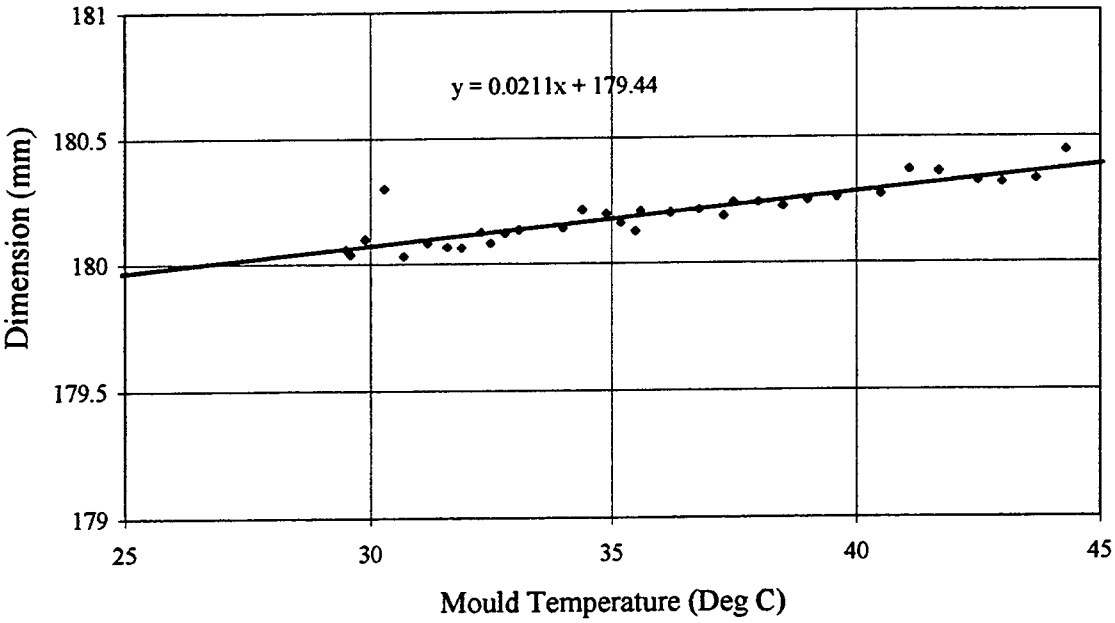


Figure 9: Graph showing relationship between RTV silicone rubber membrane mould temperature and size

Based on the measurements taken, assuming that a tolerance of +/- 50 um is required and temperature control of +/- 1°C can be maintained, the maximum part dimensions are :

RTV mould:	100mm
RTV membrane mould:	425mm

In fact for larger parts the effect of the CTE of the RTV silicone rubber membrane becomes less as a percentage of all thermal expansion and larger dimensions should be possible with the same temperature control.
Alternatively, using the RTV silicone membrane mould would allow production of a 100mm part with far looser temperature control. The temperature control required for such a part would only be +/- 4.25 °C as opposed to +/- 1°C.
The quality of the surface using an RTV silicone rubber membrane was as good as any conventional RTV silicone rubber mould.

Conclusions

The use of RTV silicone rubber in the 3DKeltool™ process has been shown as a possible reason for the limits on part sizes when producing high accuracy tooling. The alternative method of using an RTV silicone rubber membrane keyed into a QuickCast structure was successful in terms of its reduced thermal expansion and the quality of reproduction from the original SL model. This method should be particularly applicable to accurate vacuum casting of large parts.
The RTV silicone membrane method does, however involve extra time and cost especially due to the fact that an extra SL part is required. Alternatives methods to allow an RTV silicone rubber membrane to key into a base have been considered. The most promising of these is to used plaster of paris. By vibrating the SL model in curing plaster of paris with an amplitude equal to the required membrane thickness a sub mould is created. RTV silicone rubber is then poured into the plaster of paris sub mould, the SL model is pressed into the mould and the membrane is allowed to cure. The membrane which is achieved is not as uniform as that produced with a QuickCast sub mould however the cost will be less. Also, the CTE of plaster of paris is less than that of SL resin which suggests that even larger parts may be made to the same tolerances and with the same temperature control.

References

1. Jacobs, P.F. Recent Advances in Rapid Tooling from Stereolithography. Proceeding of the 2nd National Conference on Rapid Prototyping and Tooling Research. Buckinghamshire College 1996. ISBN: 085298 982 2

2. Killander, L.A. and Holmer, B. EDM Electrodes made by RP&T - A Study of Industrial Needs.
European Action on Rapid Prototyping Newsletter. Journal No. 8. May 1996 Danish Technological Institute

3. Jacobs, P.F. Stereolithography and other RP&M Technologies ASME Press, 1996 ISBN No. 0-87263-467-1

Stereolithographic Injection Molds for Direct Tooling

Suresh Jayanthi, Bronson Hokuf & Ronald McConnell
DuPont Somos®, Two Penn's Way, Suite 401, New Castle, DE 19720
and
Robert J. Speer & Paul S. Fussell
ALCOA, 100 Technical Drive, Alcoa Technical Center, PA 15069

Abstract:

The use of stereolithographic core and cavity sets in low volume injection molding is experiencing steady growth. The use of plastic instead of metal molds raises several issues in terms of mold handling, material injection and process cycle requirements. This study focuses on identifying and understanding these issues and optimizing them for low volume direct tooling applications. Some experimental observations are presented using DuPont Somos® epoxy photopolymers and representative mold geometries which identify the critical mold properties that influence mold life and the injection molded part quality.

Introduction:

Stereolithography (SL) is one of the rapid prototyping (RP) technologies that is a tool for reducing product development cycle times. Stereolithography creates physical models for visual inspection, form-fit studies and limited functional applications. With advances in accuracy, flatness capabilities and material properties, the push towards rapid creation of tooling using SL has become more pronounced. Newer generations of stereolithographic photopolymers like the DuPont Somos® 7100 family of materials, with their improved dimensional, mechanical and thermal properties are allowing the use of SL to directly create injection mold inserts for rapid tooling applications.

Rapid tooling approaches that use RP technologies like SL for tool fabrication are becoming an attractive alternative to traditional machining and casting techniques. The stereolithographic rapid tooling approaches essentially fall under two broad categories. The first category uses SL to make patterns and then creates conventional molds from these patterns. The second category, also called "direct tooling", uses SL to create the molds directly. The first approach is more time consuming because of the time required to convert a SL pattern into a conventional mold. It always leaves room for inaccuracies being induced into the process. By eliminating the step of making a mold from the SL part and using SL to directly create the mold, direct tooling holds the promise of further reducing the time and cost needed to create low volume quantities of parts in a production material. Though some direct tooling approaches may eventually be useful for high volume production, the limitations in speed and capability constrain their current applicability. There is no such thing as low volume tooling unless it produces quality parts. The immediate application for direct tooling is in the areas of prototype tooling for pre-production planning

and short run tooling for low volume production requirements. The following section will briefly highlight the current state of the art in low volume tooling. The remainder of this paper will primarily focus on the stereolithographic direct tooling.

Low Volume Tooling:

As a part progresses from concept to commercial reality, it is usually necessary to build prototypes for testing and modifications. For early functional part evaluation, the parts must be in the final design material. For pilot production of components, the parts must be dimensionally accurate and very similar to the production components. When manufacturing process development is needed, it is particularly useful to closely emulate the production process itself. Of all the plastics part production techniques, injection molding dominates with more than 92,000 machines operating in North America alone[1]. Prototype core and cavity sets placed in a production mold base enable process simulation in making a limited number of parts.

Tool development and fabrication using conventional techniques and materials can be time consuming and expensive, especially when the mold core and cavities have contours or other complex geometric features. In the initial stages of product development, when the final designs are still not proven, it is risky to commit to production tooling. Low volume prototype tooling is highly desirable if a limited number of parts can be produced in a fast and economical way are required. Rapid tooling is best positioned to meet the needs of such low volume tooling. By reducing the tooling costs, rapid tooling approaches enable traditional high volume processes, such as injection molding, to be competitive at lower production volumes[2].

Several low volume tooling options are currently used in the rapid tooling industry. These include castable steel alloy tools, milling aluminum tool inserts using a NC machine, use of reinforced composite tools, sprayed metal tools, epoxy tooling or silicone rubber molds from SL masters. These "soft tools" are later used in various techniques like reaction injection molding, thin walled reaction injection molding, simulated die casting, resin transfer molding and even on production injection molding machines. Most of these techniques enable the use of SL patterns as the starting point for rapid tooling. These approaches have been cited in the literature quite extensively and will not be described here[3,4,5]. While they are definitely a right step in the direction of rapid tooling, they still entail the need for several secondary processes.

Stereolithographic Direct Tooling:

The photopolymer materials that are currently preferred for rapid tooling applications are epoxies with improved physical properties. The SL process employs layers of low molecular weight multifunctional liquid photopolymers that are locally cross linked by the exposure to directed UV light to form polymeric systems with very high molecular weight. These are essentially amorphous in nature with a high degree of cross linking of their polymer chains. The latest generation of materials, like the DuPont Somos® 7100 series, provide both improved part quality features and the needed thermal and mechanical properties. These high temperature photopolymers may withstand continuous exposure in air to higher temperatures without significant loss of structural integrity.

Listed below are some of the chief physical properties of stereolithographic materials that may have an influence on the success of SL cores and cavities in injection molding.

- Compressive Strength
- Tensile Strength
- Flexural Strength
- Shear Strength
- Impact Strength
- Wear Resistance
- Surface Hardness
- Coefficient of thermal expansion
- Thermal Conductivity
- Specific Heat
- Thermal Diffusivity
- Heat Deflection Temperature & Glass Transition Temperature

A few other properties like the thermal fatigue characteristics and creep behavior under load for extended periods of time also influence the mold durability and the injection molded part quality. While the stress-strain data is normally used for metal tool design, the creep-rupture data is more suitable for composites and plastics. Because of viscoelasticity, the loading strength of plastics diminishes over time. Hence, the design strength of the mold is dependent upon both the magnitude of the applied load and the duration of its application. The strength required must be adequate to resist the compressive, bending and shearing stresses set up by the molding material under pressure as it moves into the mold cavity and hardens.

While many of the properties listed above are common to any tool material, heat deflection temperature is a characteristic unique to plastic molds. It is a measure of the temperature up to which the material can be used without significant degradation in strength. The heat deflection temperature of DuPont Somos® 7100 materials can be almost twice as high as most other commercial stereolithographic materials.

Stereolithographic tools for injection molding applications are primarily used in two forms.

a) Solid core and cavity inserts that are fully formed on the SL machine.

b) Shelled core and cavity inserts which are later back filled with reinforcing, thermally conductive materials like an aluminum filled epoxy or a low melt alloy.

Although creating the shelled core and cavity inserts reduces the SL fabrication time compared to solid inserts, it involves subsequent steps to fill the shells with reinforcing materials. The thermal conductivity of solid SL molds is around 0.2 W/m-K and that of the back filled SL molds is between 1 and 2 W/m-K[3]. Though the gains in thermal conductivity due to back filling are not substantial compared to steel molds (typically 50 W/m-K), back filled molds may be effective in reducing mold cycle times. Poor thermal conductivity of the tool material prevents the tool from allowing rapid cool down of the molding material which is needed to minimize cycle time.

There is a trend in the industry to complement the above two approaches with additional processing involving treatment of the tool face with surface coatings to improve the surface hardness and wear resistance. These treatments include electroless plating and vapor deposition techniques. While these additional treatments may improve the tool life, they require surface pre-treatments necessary to achieve good adhesion of the coatings to SL materials and entail additional time and resources in the rapid tooling process.

The heat transfer rate of the SL tool inserts may also be improved with the aid of internal cooling channels. To get optimal cooling it is necessary to create conformal cooling channels[6]. Cooling channels in close proximity to the core and cavity walls will improve heat removal and shorten cycle times. Since SL technology allows the fabrication of complex features without difficulty it is possible to create cooling channels which are not necessarily circular in cross section. At the present time several issues like the thermal behavior of the SL inserts, the thermal insulation characteristics of the SL material, the minimum distance from the mold surface to the cooling channels and the optimal positioning of the channels for specific tool geometries is not well understood. Initial studies have shown that cooling channels which are located without taking the above issues into consideration are not very effective[7]. It is more reasonable and effective to cool the mold surface with compressed air after each cycle. Care should be taken to avoid high thermal gradients which may result in excessive thermal stresses leading to mold failure. Thermal properties of the mold material including thermal conductivity and heat capacity will affect the part quality since both influence heat transfer out of the mold and the temperature. In general, slower heat transfer out of the mold results in greater shrinkage and poor part quality.

The emphasis of this paper is to report on studies using solid SL core and cavity inserts without involving major secondary operations. Several issues need to be properly addressed during the fabrication of SL core and cavity inserts to provide the properties necessary for successful molding. These are discussed below.

It is always desirable to fabricate the SL mold inserts with the thinnest layer thicknesses possible as this will lead to smoother side walls. Smooth side walls lead to better injection molded part quality. Moreover, smoother surfaces lead to easier part ejection from the cavities and extended tool life. While manual polishing methods may be used to reduce the surface roughness, it is not always possible to reach some of the intractable areas like deep recesses. Additional progress in thin layers requires advances in both SL mechanical and photopolymer systems.

The creation of trapped volume geometries, commonly encountered in the mold cavities, poses special challenges during the SL fabrication. The trapped volumes lead to liquid leveling problems and in some extreme cases to part failure due to layer delamination. A common practice to overcome this problem is to place holes in the trapped volumes to allow for better liquid leveling. These holes are later plugged during the post processing operations. However, it is not always desirable to create these holes since they tend to act as localized regions of high stress concentration which will compromise mold durability. Holes also lead to blemishes on the injection molded part. It is recommended that this problem be addressed by optimal orientation of the trapped volume regions in the build envelope during SL fabrication, modified recoating

cycles to achieve optimal leveling and the use of better recoating systems which minimize the impact of trapped volumes.

Thermal postcuring of the high temperature materials like Somos® 7100 series causes them to achieve better heat deflection temperature and improves other physical properties. Figure 1 shows the improvements in heat deflection temperature with different postcuring methods. Maintaining dimensional stability of the SL tool inserts is critical to producing accurate molded parts. During the thermal postcuring it is likely that the dimensional changes will occur in the SL tool inserts. The magnitude of the thermal shrinkage is necessarily dependent on the mold geometry. For Somos® 7100 the net shrinkage after UV and thermal postcure is likely to be around 0.1 to 0.15%. The specimens that are only UV postcured may show a shrinkage of around 0.05 to 0.1%.

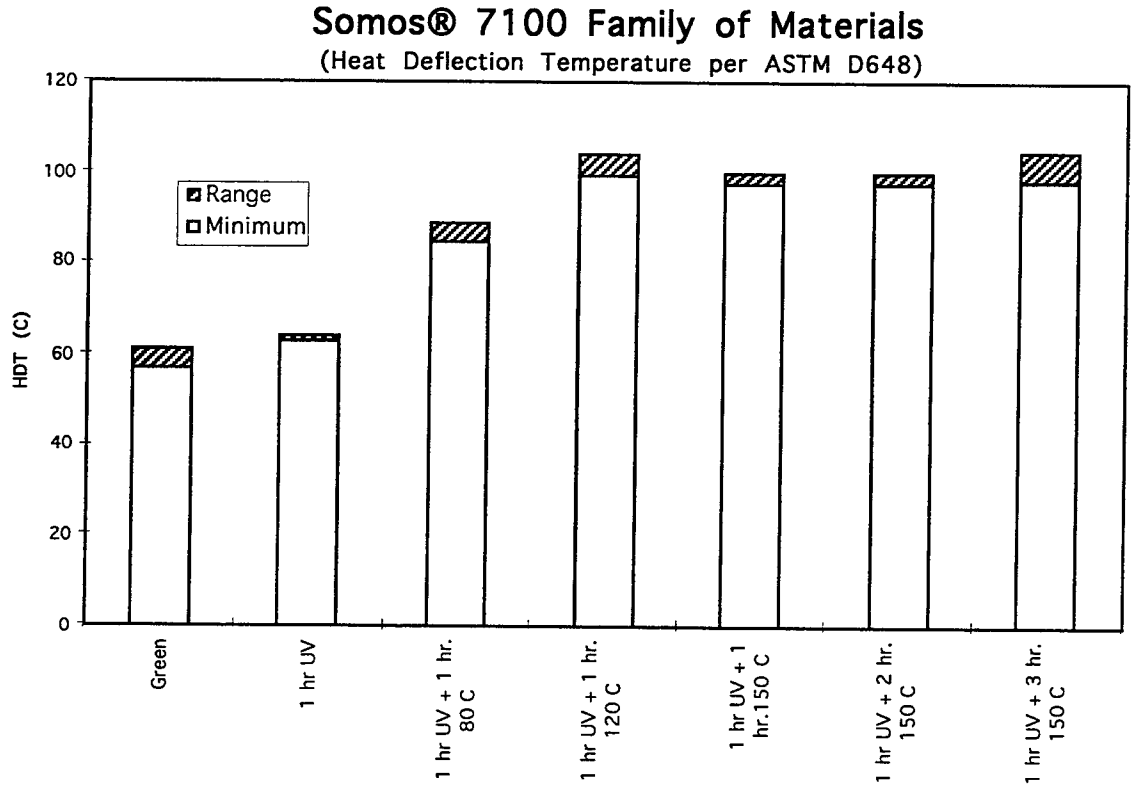


Figure 1: Heat Deflection Temperature Vs. Thermal Postcure Cycles

Care needs to be taken when using thermal postcuring cycles to avoid excessive build up of thermal stresses. It is recommended that steady, slow ramp up and ramp down cycles be used to thermally postcure mold inserts. For Somos® 7100 it is recommended that the maximum cure temperature be 120 °C with rate of heat build up between 0.5 and 1 °C/min. The heating rate and hold time at temperature are dependent on the geometry and the volume of the material. It is also possible to improve the physical properties of the SL inserts by fabricating them with a tighter hatching pattern during the UV laser scanning. Figure 2 below shows the influence of hatch spacing on the heat deflection temperature.

Processing Requirements:

An injection molding machine is characterized by its clamp size and its injection capacity. The clamp size refers to the force available to hold the mold closed during the high pressure injection of the plastic melt. The SL core and cavity inserts must be designed in such a way that they can conveniently fit into the mold base of a production injection molding machine. The success of SL tools in injection molding heavily depends on a full appreciation of the entire injection molding operation as well as on a thorough understanding of the recommended design practices for creating quality mold inserts. All standard mold design guidelines should be followed, paying special attention to the unique nature of the SL mold inserts[8].

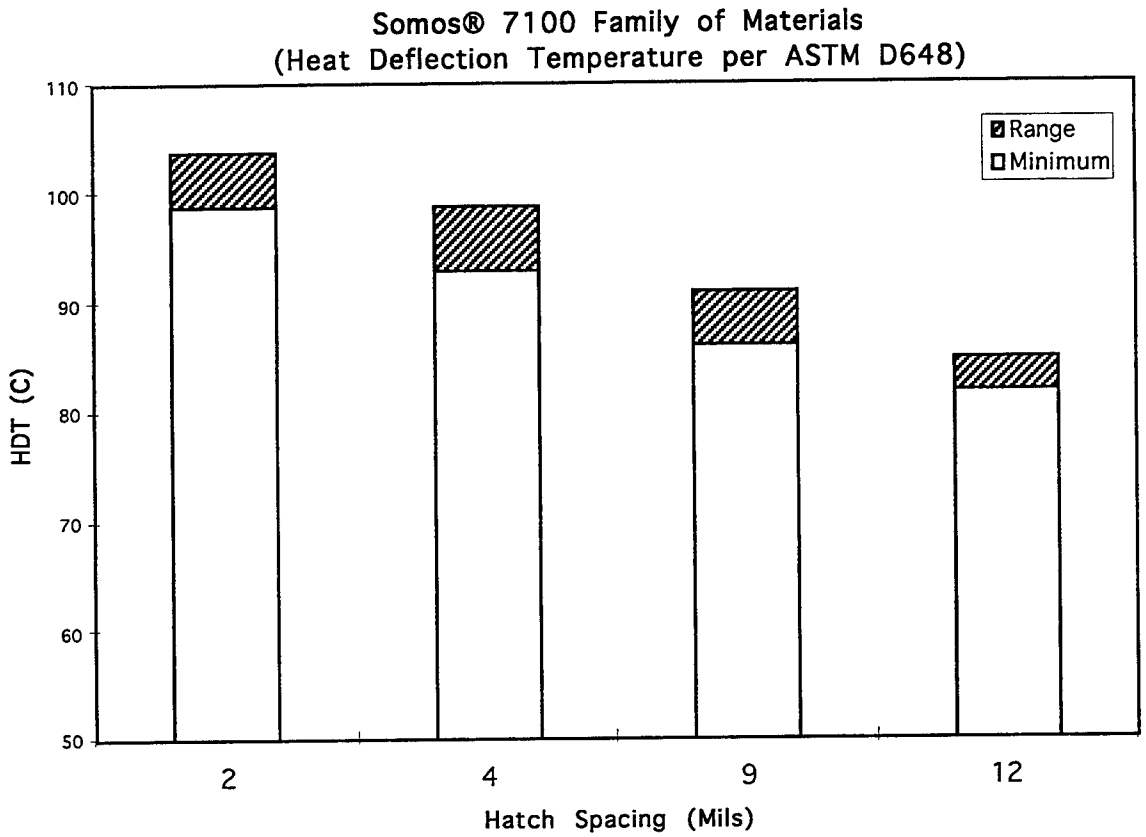


Figure 2: Influence of Hatch Spacing on Heat Deflection Temperature

Mold design features like the appropriate drafts, venting and cooling channels all play a crucial role in the quality of the molded part and the mold durability. It is important to design maximum allowable drafts into the core and cavity. The layer based SL fabrication by its very nature induces side wall surface imperfections due to the stair-stepping effects. This stair-stepping can act as localized undercuts in the cavities which can make ejection of the molded part difficult. To overcome this problem it is advisable to have sufficient draft angles (it is not uncommon to use values as high as 3 to 5 degrees). Poor venting leads to noticeable knit lines, poor surface cosmetics and burns. During the injection cycle, the thermoplastic material displaces the air in the mold cavity which gets trapped towards the end of the fill as knit lines or

air pockets unless sufficient venting is provided for the air to escape. Venting is especially important in the SL mold inserts because the trapped air may lead to excessive pressure buildup within the cavity which may lead to unusually high compressive stresses. Any moisture in the trapped air might also lead to generation of high pressure steam which might damage both the mold as well as the molded part. Poor venting also generally leads to slower injection speeds since it becomes necessary to allow more time for the trapped air to escape.

Thermoplastic materials perform better when they are injected quickly. By injecting quickly, the mold cavities can be filled and packed quickly without having to use higher temperatures to keep the material flowable. Higher injection speeds allow the use of lower injection temperatures and pressures, especially with the SL molds. The injection molding process is essentially a combination of three elements in varying proportions depending upon the processing characteristics of the material to be molded. These are temperature, pressure and time. Approximately 80% of any molding cycle time using steel molds involves heat exchange for either cooling or heating. For the SL molds this percentage should be even higher because of the poor heat transfer characteristics of the mold material. The use of SL inserts may lead to longer cycle times and differing properties of the injection molded parts. Longer cooling cycles lead to increased strength but reduced toughness[9]. As discussed in the previous section, the placement of optimized cooling paths greatly aids the injection molding cycle. The continous flow of the coolants such as water through the SL core and cavity cooling paths makes it imperative that the SL material withstand the water without structural degradation. Somos® 7100, for instance withstands the water and high humidity environments without a noticeable drop in strengthas illustrated in Figure 3 below.

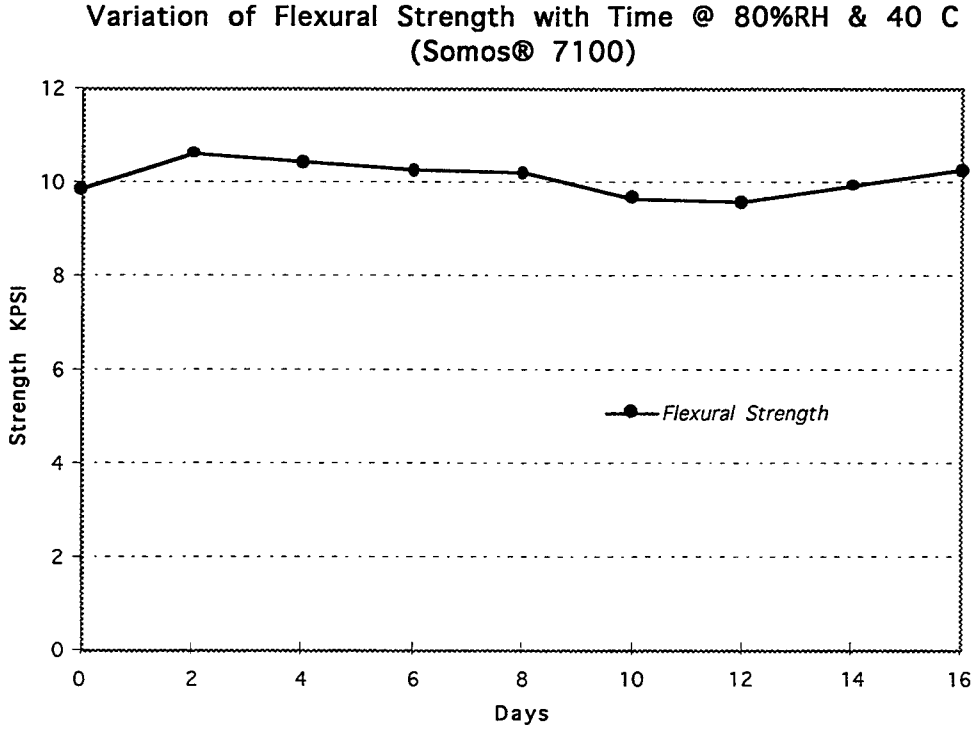


Figure 3: Influence of Humidity on Flexural Strength

Flashing is a common problem with the use of SL molds. If the mating surfaces of both the core and cavity are not in perfect alignment the tendency for the flash to occur is quite high. The core and cavity set should be loaded under sufficiently high clamping pressure to reduce flashing. The Somos® 7100 for instance has a compressive strength of around 15 Kpsi and can withstand sufficiently high clamping pressures. It is desirable to maximize the surface area of the core and cavity mating surfaces to enable them to withstand these high pressures.

Keeping the mold clamping surfaces clean during their use is absolutely critical for the survival of the SL molds. Any foreign objects, even if it is a plastic granule, concentrates the entire press clamp tonnage on this very small area - exceeding the elastic limit of any mold material regardless of their quality and hardness. In the case of non automated injection molding operations care should be taken while ejecting the molded parts from the cores. It is always desirable to have automated injection cycling operations as it would lead to better part quality and increased mold life.

Experimental Observations:

The viability of the stereolithographic injection molding has been established with many companies reporting their successes. Thermoplastic materials used included polypropylene, polyethelene, delrin, polystyrene, ABS, polycarbonate, glass filled nylon and glass filled PBT. It is not uncommon to achieve over 200 molded parts from some of these materials using the SL molds. With certain abrasive materials like the glass filled PBT or nylon fewer shots are achieved because of the high abrasive and ablative wear of the SL molds. While the general quality of the parts molded in SL molds is acceptable, no systematic effort has yet been made to compare dimensional chracterisitcs and physical properties of molded parts to those made using conventional molds. Some of the early reports show that the achievable dimensional consistency is acceptable[3]. However, no studies have been reported which show the shrinkage behavior of these thermoplastic materials under the modified injection molding environments created by SL molds.

The use of epoxy photopolymers like the DuPont Somos® 6100 and the Ciba SL 5170 to date have shown good results[10]. The heat deflection temperatures for these materials are in the 50 to 70 °C range. The recently introduced DuPont Somos® 7100 which can achieve a heat deflection temperature over 100 °C is very likely to produce better results. While thermal postcuring of the SL mold inserts improves the heat deflection temperature, care should be taken, both during the design of the insert geometries as well as during the thermal treatment, not to induce high thermal stresses which will lead to mold cracking. Geometric features which induce high stresses (like sharp corners, improper placement of holes etc.,) should be avoided. During the thermal treatment it is important to make sure that the mold is heated gradually and that the convective heat transfer within the thermal chamber is uniform. It may be desirable to heat treat the SL mold inserts in certain heat transfer mediums like silicone oils, to avoid mold cracking. In addition to the heat deflection temperature improvements several other mold properties play a role in successful injection molding.

In a study done at the Alcoa Technical Center using SL mold core and cavity inserts made in Somos® 6100 and 7100 materials, the following observations were made. The focus of this

work was to fabricate parts from the production material, in this case 30% glass filled Polybutylene Terepthalate (PBT).

•Tool life: With Somos® 6100 well over 80 parts were made before the SL tool set had to be discarded due to excessive wear. With Somos® 7100 around 23 parts were made before a catastrophic failure in the external ejection mechanism which was unrelated to the SL tool material. The parts made from the Somos® 7100 tool showed better feature definition. Given the agressive nature of the glass filled PBT, these results are quite satisfactory.

•Dimensional Stability: Though no detailed dimensional measurements were made, ad hoc measurements showed that the wall thicknesses were within +/- 50 microns on walls 4 mm thick. The feature to feature dimensional variations were within +/- 100 microns across spans of 100 mm.

•SL Mold Wear: The SL material wore in two modes during tool operation. First, in regions of medium flow stress, the material abraded. This was noticed particularly in regions were the flow was channeled around a sharp corner. Secondly, in regions of high flow induced stress, the SL material showed ablative wear: small chunks of the tool material were removed from the mold and retained in the injected polymer. The fractured surface showed small cracks which were apparently penetrated by the injected polymer. This ablative wear occured only in the region of the injection gate. The growth of the ablative wear increased with the use of the tool.

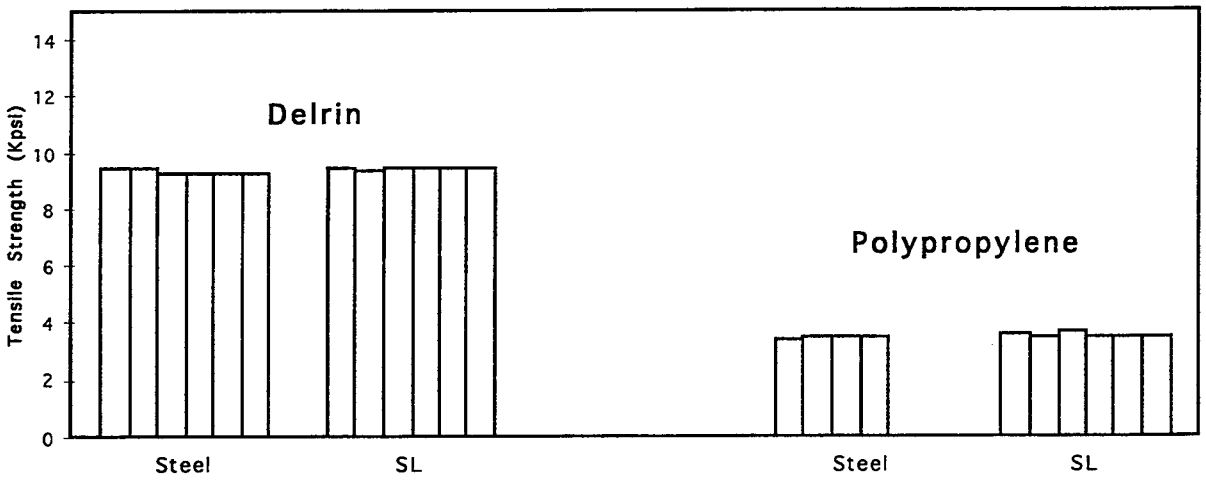


Figure 4: Strength of the Specimens Molded from Steel and SL Mold Inserts

•Holes with High Aspect Ratios: The Alcoa test part had several features that were designed to test the ability of the SL material to accept narrow, deep features. Generally these areas did not eject well (the SL tool side walls could not be adequately smoothed), although the mold filled reasonably well in these deep recesses with some mold tuning.

In an internal DuPont study using SL mold inserts, the need for proper drying of the injection material was shown. The use of SL materials (especially those with lower moisture resistance) as mold inserts would cause the mold surfaces to swell, as the moisture in the undryed injection material vaporizes inside the SL cavities during the molding operation.

In the same study a comparison of the mechanical properties of the molded material simultaneously injected in a SL mold and a steel mold was made. Two commonly available thermoplastic materials, polypropylene and delrin were used in this study. Figure 4 provides a comparison of the tensile strength of these two materials molded in SL and steel mold inserts. It is quite interesting to note that the tensile strength is essentially the same in parts made from both mold inserts. The values measured closely resemble those reported in the literature for these two materials. The following table lists the summary of the other tensile properties.

Table 1: Molded Part Properties from Steel and SL Molds

	DELRIN	Poly-propylene
Young's Modulus: Kpsi		
Steel Mold Inserts	335	-
SL Mold Inserts	288	-
Maximum Tensile Stress: Kpsi		
Steel Mold Inserts	9.38	3.53
SL Mold Inserts	9.55	3.62
% Elongation @ Break: %		
Steel Mold Inserts	12.4	>550
SL Mold Inserts	14.2	>550

In another joint study involving University of Delaware, several experiments were conducted using SL mold inserts under a variety of situations[10]. Here are a few of the important findings from that study.

• The use of cooling channels to help with heat removal will be ineffective unless they are placed with proper understanding of the heat transfer characteristics of the SL material and also the mold design. In the absence of effective cooling techniques, longer cooling times along with convective air cooling between cycles may be appropriate. Using polypropylene as the injection material in SL molds made from Somos® 7100, it was noted that the part quality and the ease of ejection of the molded parts was significantly improved as the cycle times were increased from 24 sec to 48 sec and later to 99 sec.

• It is not advisable to use different mold materials for the core and the cavity. In this particular study, the cavity was made from the Somos® 7100 material while the core was from steel. The consequence of this was excessive warpage in the molded part due to the vast differences in the thermal conductivities of the two materials.

Several other experiments are underway aimed at understanding the nature of the SL mold inserts. A more extensive study to look at all the mechanical properties, the dimensional properties and the quality attributes of the molded parts made from SL mold inserts is envisaged in the near future. Better appreciation of the nature of these SL materials will help define newer applications.

Future Trends:

As stereolithographic tooling evolves, the strengths and weaknesses of these plastic tools will be better characterized and understood. The properties of the commercial photopolymers are constantly improving and the next generations of materials will bring further improvements in both thermal and mechanical properties. Research is underway to develop reinforced and high performance unreinforced photopolymers which will overcome some of the limitations of the existing materials. Even as these property improvements are realized further experimental work needs to be done to determine the optimum properties suitable for injection molding. Coupled with the improvements in materials there is a need to better optimize the stereolithographic fabrication process for the direct tooling applications, as pointed out in some of the discussions above. The injection molding operation also needs to be closely examined to optimize the processing of molding materials using the SL molds. The strength and the thermal characteristics of the SL tools may eventually require special modifications to the typical injection molding machine. Thermal studies are required to improve the mold durability and to reduce cycle times with the optimal use of conformal cooling channels. Algorithms which automate the placement and geometry of these cooling channels will further reduce the time needed to accomplish rapid tooling. Studies need to be done to understand the variations in the final physical properties of the injection molded parts using the SL tools versus conventional hardened steel tools. Only when the stereolithographic direct tooling faithfully simulates the properties of the conventional injection molded parts will it fully qualify as a prototype tooling or a low volume tooling process. Moreover, as the SL tooling technology is better understood, it is likely that newer applications which will exploit the unique nature of these molds will be found.

References:

[1] Diane L. Hallum "**Fundamentals of Injection Molding**", *Manufacturing Engineering,* July 1997, pp68-72..

[2] Peter Hilton "**Making the Leap to Rapid Tool Making**", *Mechanical Engineering,* July 1995, pp75-76.

[3] Dr. Paul Jacobs "**Recent Advances in Rapid Tooling From Stereolithography**", *North American Stereolithography Users Group 1997 Conference and Annual Meeting.*

[4] Karsten Lumbye Jensen, "**Rapid Tooling: What, Why and How**", Prototyping Technology International '97, pp293-296. UK & International Press, ISSN: 1337-2436.

[5] David Babineau, **"Rapid Tooling - Options for Speed in Product Development"**, *Rapid News North America*, September 1996, pp-40-43.

[6] Emanuel Sachs et al., **"Injection Molding Tooling by Three Dimensional Printing"**, *Rapid Prototyping and Manufacturing 1996.*

[7] Yun Li, Michael Keefe, Ed Gargiulo, **"Studies in Direct Tooling by Stereolithography"**, *6th European Conference on Rapid Prototyping and Manufacturing 1997*, pp253-266.

[8] Paul Decelles and Michael Barritt, **"Direct AIM™ Prototype Tooling"**, *Procedural Guide 3D Systems Inc.,* P/N 70275/11-25-96.

[9] Karl Heinz Dusel, **"Materials for Rapid Tooling Techniques"**, *SME, RP&M 97 Conference.*

[10] Yun Li, **"Studies in Direct Tooling by Stereolithography"**, *Masters' Thesis* , Mechanical Engineering, University of Delware 1997

Acknowledgments:

This work has been made possible by the continued support and assistance from several members within the DuPont Somos® group, the RP group at the Alcoa technical center as well as from some of our valued customers.

Inquiries:

Inquiries regarding this study may be directed to Suresh Jayanthi at the address listed or by e-mail to jayantss@esvax.dnet.dupont.com.

Rapid Tooling by Powder Casting Transferred from R/P Model
-Manufacturing Conditions Pursuing Zero Shrinkage-

Hiroyuki NOGUCHI and Takeo NAKAGAWA
Institute of Industrial Science, University of Tokyo
7-22-1, Roppongi, Minato-ku, Tokyo JAPAN

SUMMARY

High accuracy is being sought in the rapid manufacturing of long life metal dies and molds by transferring from layer laminated models. Powder casting serves as a promising rapid tooling method as it enables high density filling and thus controls dimensional shrinkage to a considerable extent during sintering and infiltrating. This study aims to study the relation between the tooling conditions and dimensional changes of powder casting and find the conditions at which dimensional changes are minimum. In the experiments performed, a golf ball model was chosen as an example of a small mold and results show that dimensional changes can be controlled to below 0.1%, which will facilitate practical application. By subjecting the cast powder to vibrations after adding the binder to achieve higher density, and adding fine copper powder to a mixture of two different size stainless steel powders for dimensional adjustments, almost zero shrinkage control in rapid tool making was realized.

1. INTRODUCTION

In the recent years, small-lot production of different varieties of products is carried out widely in industry. As the life of products grow shorter and shorter, model changes are carried out in rapid succession, and therefore the reduction of the development time of new products has become a very important task to manufacturing industries. For this reason, the reduction of the production time of prototypes and forming die and mold is drawing widespread interests. With the emergence of the layer laminate manufacturing method which can produce prototypes directly from 3D CAD by the additive process, the production time of prototypes has shortened considerably. Also drawing strong hopes is "rapid tooling" which aims to make tools rapidly using this layer laminate R/P model. However, while the prototype tools made by soft tooling with silicon and metal-polymer composites have been widely received, metallic hard tooling which can be employed in mass production has not yet reached the practical application level. One of the main reasons for this is because it loses to milling methods in terms of accuracy, speed and cost. 3 to 4% shrinkage occurs in powder sintering

methods (SLS, 3D-Printing) and warp problems have yet to be resolved for the direct sintering of copper alloy powders.

In methods which transfer from a layer laminated model by the wet-type slurry casting method, mixing of fine cemented carbide powders has been said to successfully hold down shrinkage to 0.8%, although the additional finishing process like milling and drilling is said to be rather difficult.[1] The authors thus developed a method to hold down shrinkage by obtaining the highest possible density by applying the dry powder casting method using stainless steel powder, and demonstrated that shrinkage can be reduced to 0.4% and high density twice the current level can be realized.[2] This study aims to further develop this method and achieve higher density by refining the production conditions.

2. INCREASING DENSITY BY ADDING VIBRATIONS

2-1. Adding Vibrations After Binder Infiltration

In rapid tooling by sintering using metal powders as the tool material, the factor most closely related to dimensional accuracy is the powder density during powder molding. By obtaining the highest density possible, close contact between the powder particles can be achieved and shrinkage in post-processes can be controlled. For this, the authors developed a dry-type powder casting method expected to produce high densities than the wet-type slurry casting by mixing liquid binder. As shown in Fig. 1, the liquid binder is poured for infiltration in the post process after powder casting in this method.

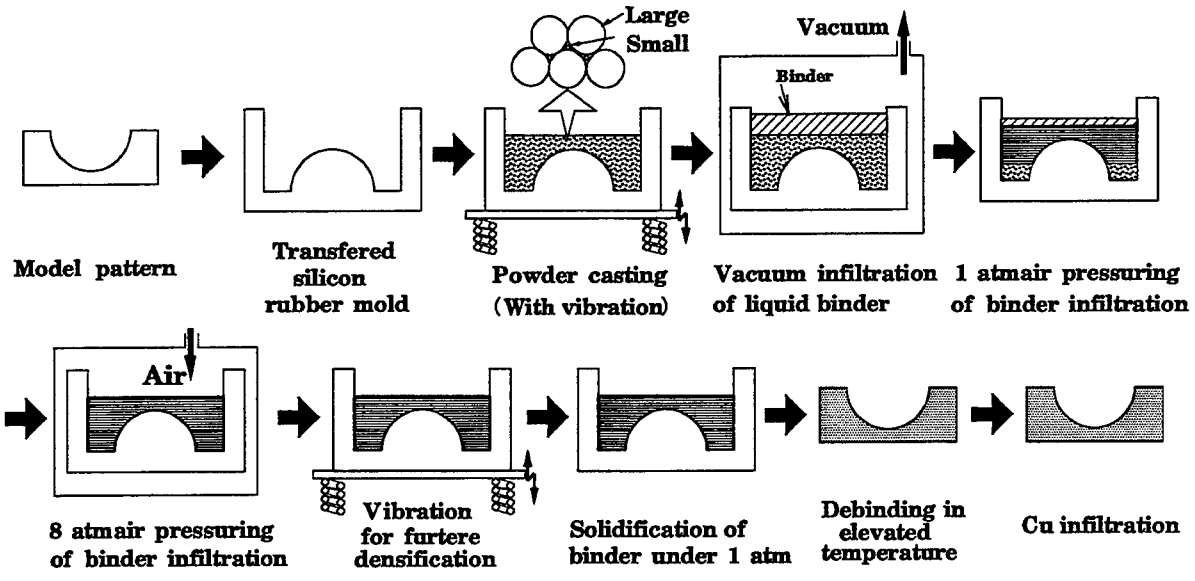


Fig. 1 Manufacturing process of powder casting for making rapid tool

The powders used are stainless steel atomized spherical powder and fine stainless steel powder. Table 1 shows the specifications of stainless steel powder used. Studies were then carried out to investigate if the density can be further increased in rapid tooling process using these powders. Although the powders are already vibrated during the powder dry casting , they were subject to vibration another time after infiltrating the liquid binder. As shown in Fig. 2, it was found that the density increases more than the current methods, because the powder show thixotropic behavior due to the vibration applied after infiltrating the binder. Such a high density of course cannot be obtained by the wet-type slurry method.

Table 1 Stainless steel powder used in experiments

a) Size distributions of nomal size powder

Mesh size	+145	145-200	200-250	250-350	−350
Volume ratio (%)	0.8	25.5	26	40.2	7.5

b) Tap density of powder

	Average diameter (μ m)	Tap density with vibration (vol%)
A: Large size	66	61
B:Small size	5	39
A(82.5%)+B(17.5%)	–	67

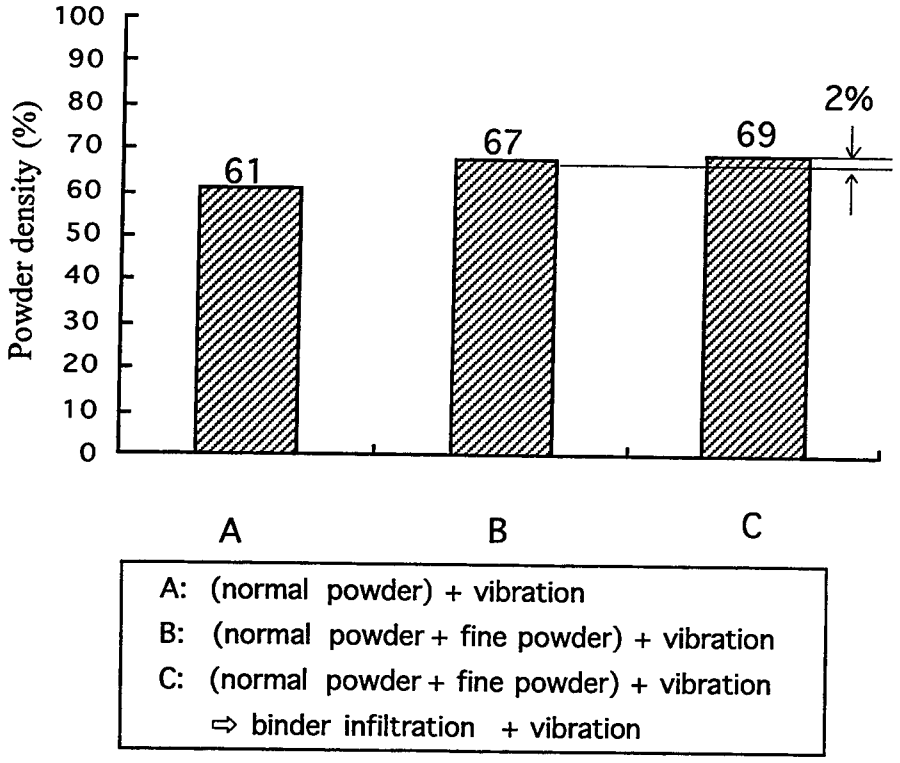


Fig. 2 Powder density by vibrating powder casting

2-2. Dimensional Change of Vibrated High Density Model

Next, effects of density increases by vibration on final dimensional changes were investigated. As shown in Fig. 3, by infiltrating copper in the dried and degreased tool model after vibration, the expansion on the contrary increased to 0.83% as compared to the 0.4% shrinkage when no vibration is applied after infiltrating the binder. The dimensional changes between each process were then measured, and as shown in Fig. 4, it was found that; the original dimensions of the product are maintained more or less in the drying and degreasing processes, and the expansion occurs considerably during the final copper infiltration process. It is assumed that this results because although close direct contact between the stainless powders is achieved during filling, the powders on the contrary tend to separate during copper infiltration through the surface traction phenomenon.

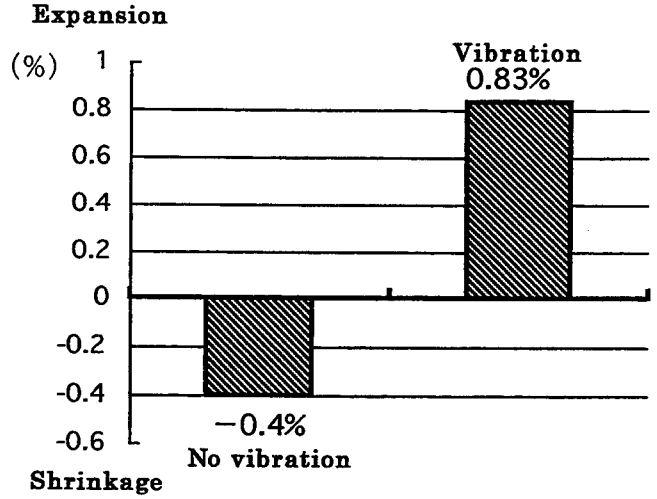


Fig. 3 Dimensional changes of vibrated high density product (after copper infiltration)

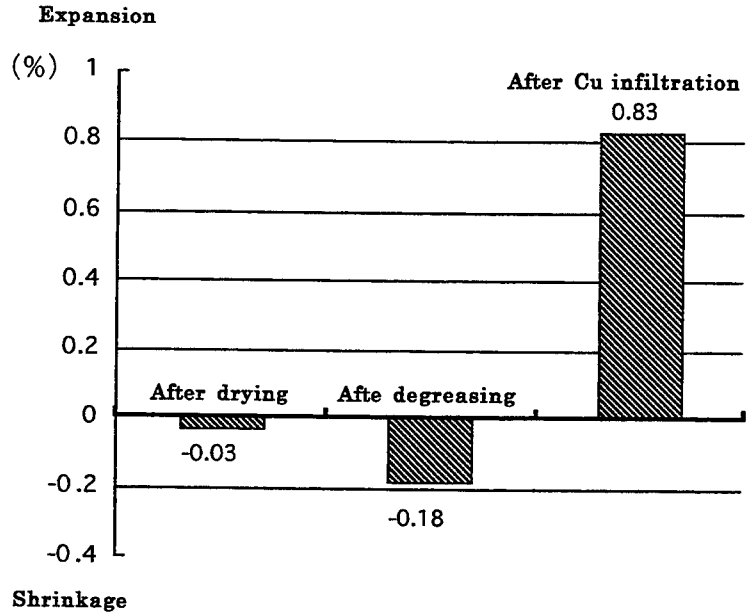


Fig. 4 Dimensional changes between each process of infiltrated high density product

3. CONTROL OF DIMENSIONAL CHANGES BY ADDITION OF COPPER POWDERS

As mentioned earlier, the fact that dimensions increase when copper infiltration is carried out raises the possibility that the overall final dimensional changes can be controlled by adjusting the material and process conditions. Attempts were therefore made to control the dimensional changes after copper infiltration to zero by controlling the powder density of the cast tool model. Various methods were considered for controlling the density of the product, such as adding powder which can be removed during degreasing. In this study, fine copper powders with an average diameter of 10 μ m were added. As for the amount added, half of the 17 vol% fine stainless steel powder proviously added was replaced with copper powder.

Fig. 5 shows the effects of adding copper powders. In this case, the drying and degreasing processes showed shrinkage of 0.22% and 0.53% respectively. In the liquid-phase sintering of the mixed stainless steel powders with copper and copper infiltration (copper powders for infiltration containing 2.7% cobalt) carried out next, 0.42% expansion and 0.26% expansion were recorded, and eventually shrinkage could be controlled to 0.07%. Fig. 6 shows the external view of the metallic rapid tool produced by this process and the cross-section of the tool material under these conditions. Fig. 7 shows the surface roughness of the flat surface which is relatively satisfactory.

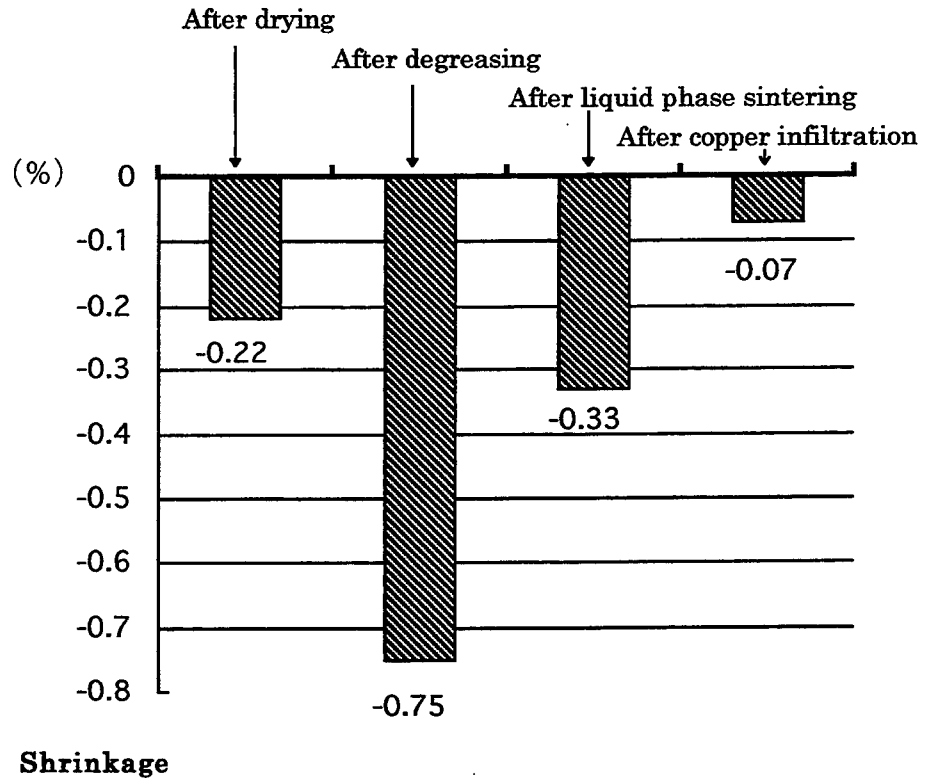
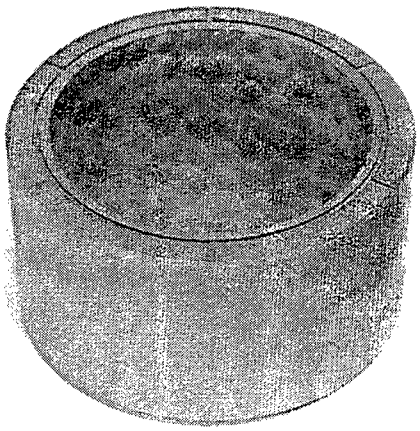
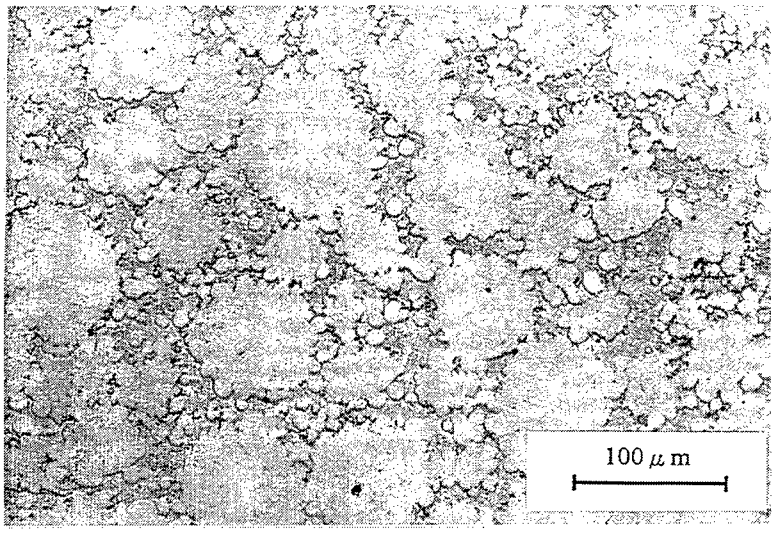


Fig. 5 Control of dimensional changes by adding copper powder



a) Tool made experimentally



b) Section of tool material

Fig. 6 Photograph of stainless steel rapid tool by powder casting

Nomal powder A	Rmax	13 (μ m)
	Rz	9
	Ra	2.2
Added fine powder B (8.5 vol%)	Rmax	6.5 (μ m)
	Rz	4
	Ra	0.9

Fig. 7 Surface roughness of golf ball mold after copper infiltration

4. CONCLUSION

Although much remains unknown on the reasons for the shrinkage in the drying and degreasing processes when copper powder is added, expanding mechanism during sintering and infiltration, and quantification of dimensional changes, the study clarified that the targeted dimensional changes below 0.1% can be achieved successfully. The dimensional accuracy of the layer laminated R/P model may not be high enough like machined one at the moment, and therefore if the accuracy of the transferred rapid tool can be controlled to 0.1%, the accuracy of the product produced by this rapid tool should at least be satisfactory for practical application. Fig. 8 shows an example of the metallic rapid tool for a cellular phone prototyped by this method. No problems were seen in the surface profile nor the post-polishing process. The tool strength, heat-transmission, cooling pipe

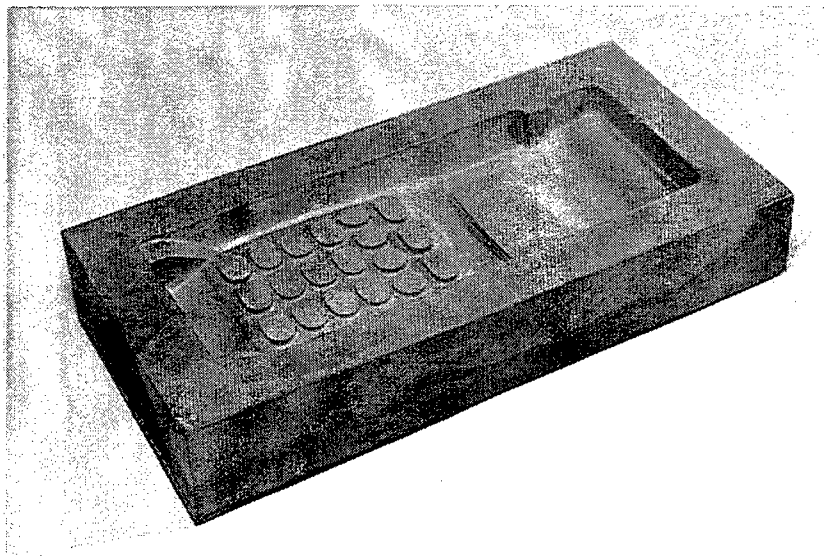


Fig. 8 Metallic rapid tool of cellular phone produced by this process

arrangement, machinability in post-processes, and durability as a tool for injection molding for mass production may be also satisfactory. As expansion characteristics were seen in the procedure of the whole powder casting process, it suggests the possibility of attaining more stable high accuracy through further studies. Next, attempts will therefore be made to manufacture different types of tools, establish the application range, standardize the manufacturing process, and consider the various dies and molds for spreading this method for rapid tooling. Since it requires no mention that this method can be also used to manufacture metallic rapid prototyping products, such applications should also be taken into consideration.

The authors would like to thank NTT CMET and Brother Industries for their cooperation in making the tool model and sintering for the cellular telephone.

References

1) Karsten Lumbye Jensen: Rapid Tooling What Why and How, Prototyping Technoloby International '97, pp293-296 (1997)

2) Hiroyuki Noguchi, Takeo Nakgawa: Manufacturing of High Precision Forming Tool Transferred from Laser Stereolithography Models by Powder Casting Method, Proceeding of 5th International User Congress, Intelligent Production Systems-Solod Freeform Manufacturing (September 1997, Dresden)

Stereolithography Injection Mould Tool Failure Analysis

Sadegh Rahmati & Philip Dickens

Department of Manufacturing Engineering & Operations Management
University of Nottingham
University Park, Nottingham
NG7 2RD
Email, EPXSR@epn1.nott.ac.uk

1.0 Abstract

Manufacturing technology does not always enjoy the traditional cost benefits of mass production because large quantities may not be required. Separating low cost from high volume requires new approaches to product and process design and technology. Stereolithography tooling supports this concept by providing tools quickly during the design process to prove out and select optimal new concepts. The SL tooling technique is a first step in realising the near-term objectives such as conceptual modelling and design verification, as well as the long-term objectives in production.

At the University of Nottingham development of the SL injection moulding tools has taken place along two fronts. The first to provide material data for tool design under extreme conditions of stress and temperature; and obtaining data from different tests carried out on simple tools which resemble real situations (Rahmati 1997). The second development is theoretical and analytical analysis of the simple tools during the injection process. Both of the above developments have ultimately been directed towards achieving the goal of successful SL injection mould tooling. The results of such developments may help the industry to reduce the lead time and provide a faster technique in a concurrent engineering environment.

The first experimental results proved the capabilities of the technique and demonstrated its advantages and weaknesses. In addition, the important parameters in SL injection moulding such as injection pressure, injection speed, injection temperature, freeze time, cycle time etc. were investigated. The results and derivations may be used either as an instruction guide for industry users to design SL injection tools, or to provide design information for particular conditions and to predict tool failure.

2.0 Introduction

Initially, because of the diversity of parameters, it was not clear how the tool was going to behave or which parameters were important. Therefore it was decided to design a SL injection tool and use it in a real situation. After each experiment new questions arose, and after four consecutive experiments, a better understanding of the technique was built up. Therefore, based on this experimental understanding and successful results, an analytical approach was essential to understand more fully the process. The tool design is based on a parametric feature approach, where different prismatic features are varied in the X, Y and Z-axis. The first moulding was a 2mm thickness part composed of eight hollow prismatic cubes of 10 x 10 x 10 mm, based on a circular plate where all cubes were located radially at a pitch radius of 28 mm (*Figure 1*). The core and cavity incorporats a 1.5^{o} draft angle to account for the injection moulding process (Menges 1986).

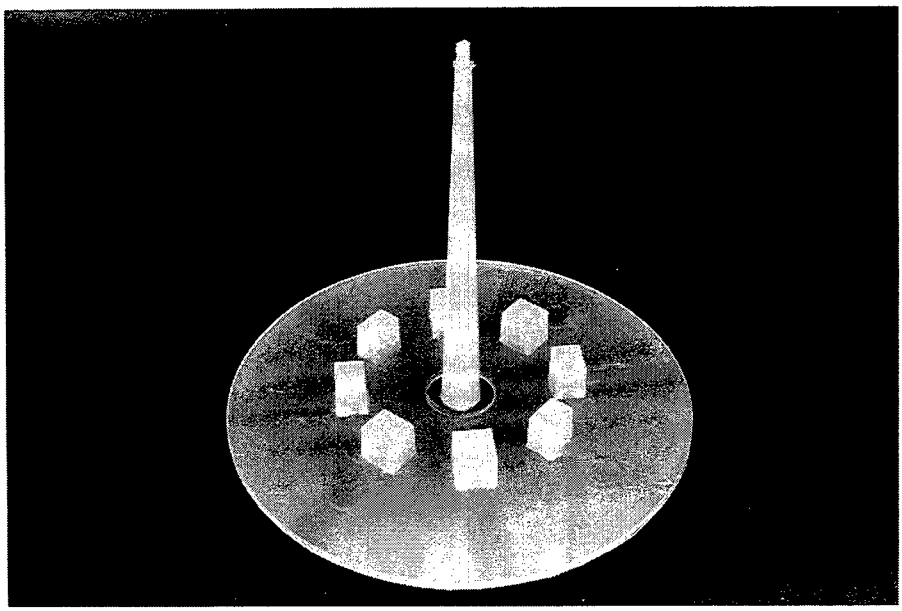


Figure 1. The moulding

A layer thickness 0.15-mm resulted in minimum stair stepping which was very helpful during moulding ejection. A sprue bush enters from the centre of cavity and fills the cubes uniformly. The large number of cubes may provide greater repeatability and better analysis of failure mechanisms. A total of 260 injections were made successfully without any tool failure. The plastic used was polypropylene (PP) which was injected at about 2000 psi. The next sets of tools were based on the same principle except the features changed in the radial width by increments of 1mm. Therefore the set would consist of two 10x10x10 cubes, two 10x9x10, two 10x8x10, and two 10x7x10 cubes. It was expected that this approach would indicate the limitations of the minimum web thickness or maximum web height.

SL moulds are placed in a steel sleeve and a steel plate behind the tool. The bolster assembly is set up (*Figure 2*) such that the actual tool is quickly interchangeable. This feature enables testing of different tools in minimum time. The SL mould is located into a 6mm thick steel sleeve and backed up by resin and aluminium chips to make it conductive and resistant to any compressive force during injection. Five pins of 8-mm diameter eject the part out of the mould. The ejector configuration will remain the

same throughout the coming moulds, because all different prismatic shapes are placed on the same round plate (*Figure 1*).

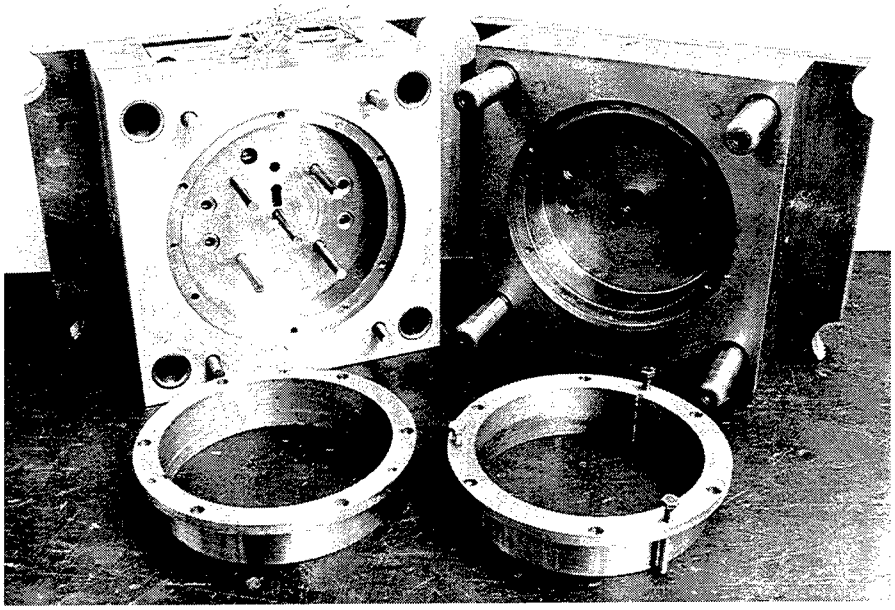


Figure 2. The complete bolster assembly

Following a large number of injections it was observed that when the flow hits one of the blocks it moves in three directions, upwards and around until the three flow fronts meet at the back symmetrically (*Figure 3*). The flow loses pressure as it moves away from the centre and in addition to this pressure loss the flow moving upwards faces additional loss due to the bends. There are two main forces acting on the block, one due to the shear stress acting on the base, the next is the bending stress trying to tip over the block. There is no clear indication of how the pressure profile is acting on the block as a function of time, so for the time being it is assumed that the resultant force is acting on the middle of block.

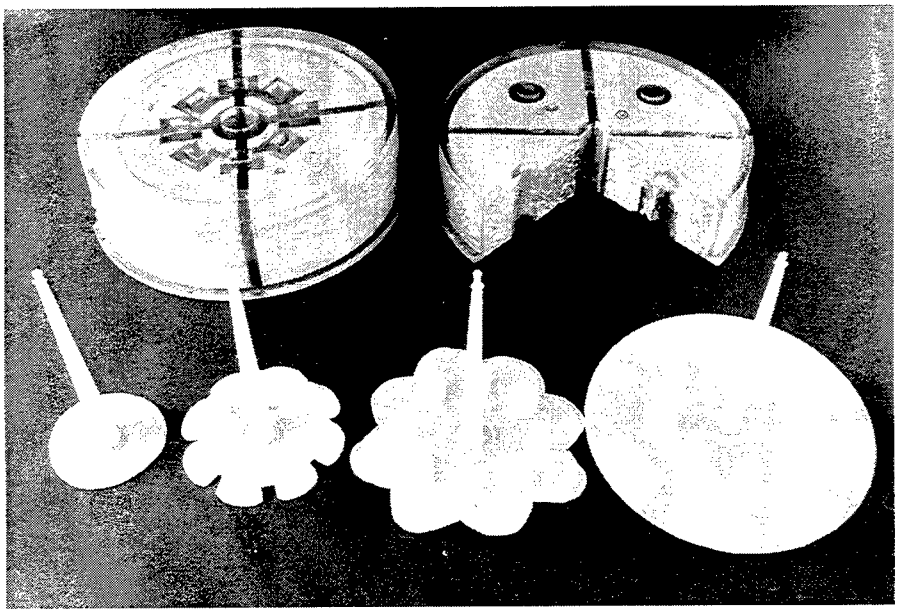


Figure 3. The flow progress sequence inside the cavity and a tool cross-section

3.0 Failure Mechanism Analysis

SL injection mould tooling has the potential of producing complex shapes at a rapid rate. SL tools have proved to be sufficiently strong when moulding PP plastics, for injections in excess of a few hundred parts (Rahmati 1997). Due to the lower thermal conductivity of SL tools, they must be treated slightly differently from metal moulds. The mould cannot be heated and cooled as quickly as with metals and hence a longer cycle time is inevitable. Using an air jet on the open tool has reduced a typical cycle time of 4-5 minutes to 1-2 minutes. However, the increased cycle time is not of prime concern in SL tooling in contrast to metal tooling where typically several thousands parts or more are required.

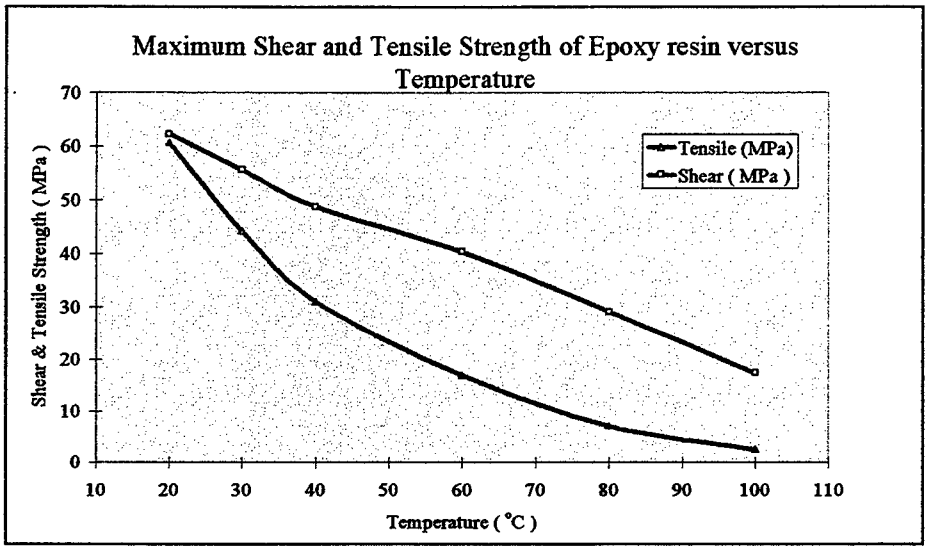


Figure 4. Maximum Tensile & Shear strength of epoxy SL5170 versus temperature

As tool temperature increases during injection, its strength continuously decreases (Ives 1971) until the maximum temperature is achieved (*figures 4 & 5*). This is the weakest situation of the tool, which may cause it to fail. The ejection time should be away from this weak point otherwise the core would be pulled off with the moulding during ejection. This is even more vital as materials with higher melting point and viscosity such as ABS, Nylon, or Polycarbonate are used.

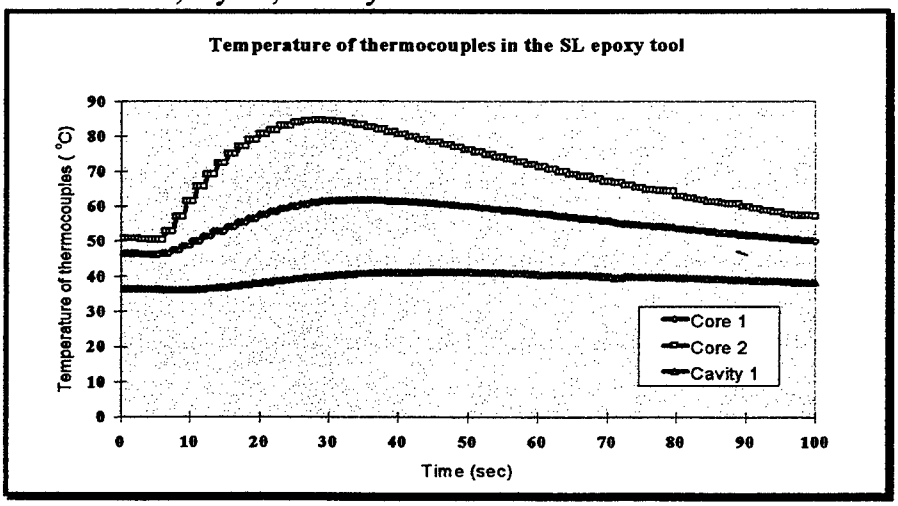


Figure 5. Temperature variation inside the epoxy tool during a cycle

It is important in SL tooling to remove the heat by all means. Three possible approaches are as follows which may be applied separately or as a combination of each. Cooling channels may add to the tool lead-time or cost. Therefore a more appropriate technique seems to be the first two by creating a conductive sink to absorb heat as much as possible and remove heat by air jet cooling.

- To backup the SL tool by conductive materials such as low melting alloy or aluminium chips or aluminium powder in conjunction with a resin. This will provide better conductivity as well as resistance against the injection pressure.

- To make the SL tool as thin as possible and apply the previous technique. This would provide even more conductivity and strength.

- To use cooling channels either in the traditional way or using conformal cooling channels. Regardless of increasing cost and overall lead-time, this may enable processing of thermoplastics such as Nylon or Polycarbonate.

SL tool failure falls into two main categories, first during initial injection, second during final part ejection from the SL tool. The first type of failure has occurred when the increase in temperature has weakened the material and the injection pressure is beyond the tool strength. Therefore when the molten plastic pushes through the cavity, if the instantaneous strength of the tool's particular feature is less than the injection pressure, it may cause that feature to break.

Secondary type of failures may happen during the final part ejection from the tool. When the part is ejected, the cube may be taken off the core and remain in the moulding. This type of failure is function of the following parameters:

- Stair stepping of the SL tool
- Draft angle on the tool
- Decrease in tool strength at increased temperatures

Stair stepping which is an inherent property of the SL process introduces more contact between the tool and moulding. This type of failure can be avoided by either delaying the ejection period or shortening it. However too early ejection cause the part to warp.

4.0 Pressure in SL Tooling

Pressure is acting instantaneously on the cube during injection. The pressure profile is derived from the strain gauges test mounted on the two ejectors (*figure 6*). As a matter of fact the peak pressure is higher than the average pressure (the integral of pressure over injection time), but the maximum pressure is acting on a limited area of the cube and only for a fraction of a second. Moreover the position of the peak pressure is continuously moving forward and therefore it is a fair assumption to apply the average pressure for the purpose of analytical calculations.

In general, at any instant where the injection pressure is higher than the tool strength, failure is feasible. To avoid this, care is taken to inject at a temperature where the tool material still has sufficient strength. This criteria has lead to a well defined cycle, where the new injection always takes place when the tool temperature has dropped to 45°C, where the material's strength is just enough to resist the injection pressure. Following this sequence regularly may help one to achieve a semi-automatic and consistent injection results.

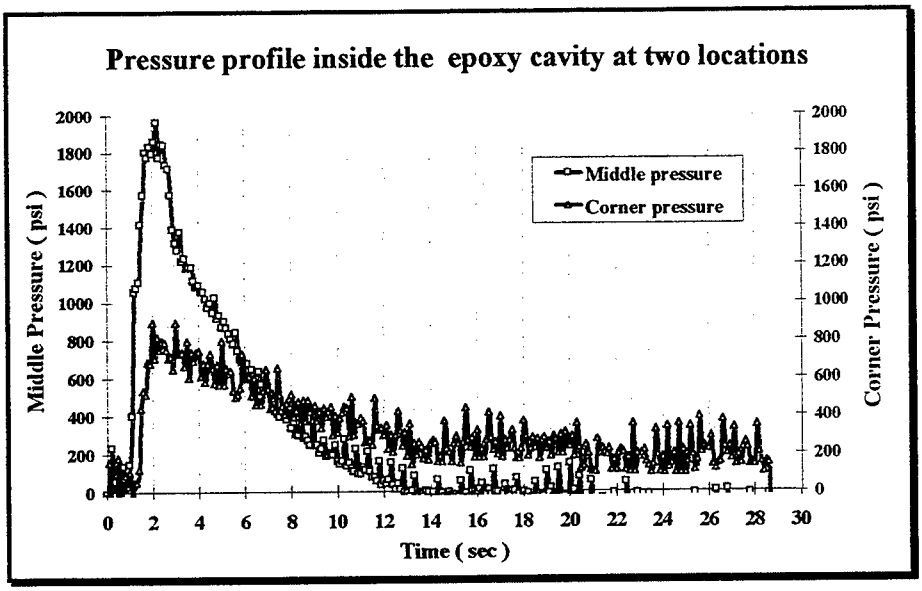


Figure 6. The pressure profile inside the cavity at the centre and after the cube

However, most of the failures observed were the result of not following this important guideline. Referring to *figure 4*, it is noticed that the tool's tensile strength has decreased to 25 MPa at 45°C which is enough for the tool to resist the injection pressure. Shear strength of the epoxy is investigated at different temperatures using British Standard 2782, method 341A, which is an approximation. This will determine the maximum possible temperature to begin the new injection in the cycle.

5.0 Flow Analysis

The molten plastic flow after impinging into the cavity, moves radially away from the centre where sprue bush is located. As the flow moves away from the centre it loses pressure, and in particular there is a sudden pressure drop as the flow gets to the blocks and moves upwards. Due to the fact the flow has high viscosity, low velocity, low density, and high pressure, the Reynolds number is not going to be very high which means that the flow within the cavity is *laminar*. Based on this fact it can be assumed that the flow within the cavity will create no *circulation* around the corners. This makes the flow analysis simpler.

6.0 SL Tool design Criteria

In general, to produce fracture, the ultimate shear and bending strength of the material must be exceeded. The assumption is that only *Shear and bending are the cause of failure* during injection. The base of the cube is the area which is resisting the melt flow during injection. Based on this assumption the important parameters affecting the tool failure would be the injection pressure, the moulding thickness, the cube height and the cube base area (shear area). Therefore the bending force and the shear force exerted to the cube as the result of the injection pressure are numerically calculated in the following section.

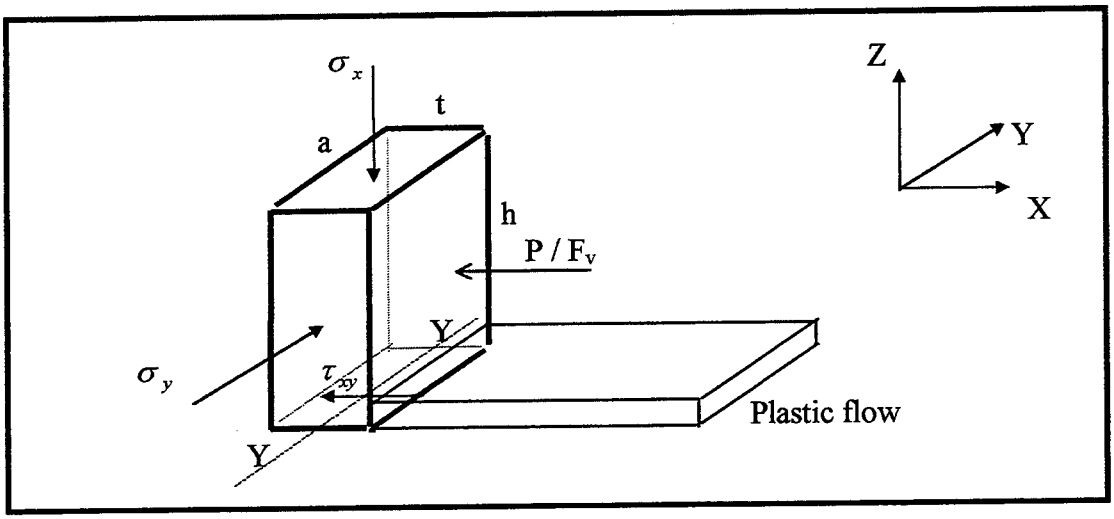


Figure 7. Schematic view of the flow and the block with parameters

Analytical Formulation of SL Tool Design

For design purposes, the largest stresses (both normal and shear stresses) are usually needed.

Ultimate shear strength of the Tool $> \tau_{design}$ (1)

Ultimate bending strength of the Tool $> \sigma_b$ (2)

where τ_{design} is the maximum shear stress applied to the tool during operation

σ_b is the maximum bending stress applied to the tool during operation

Since homogeneous, isotropic materials, when unrestrained expand uniformly in all directions when heated (and contract uniformly when cooled), neither the shape nor the shearing stresses and shearing strains are affected by temperature changes (Riley 1995).

$\mathbf{A_v = a * t}$ Cross-sectional area (3)

$\mathbf{F_V = P * (a * h)}$ Shear Force (4)

$\mathbf{M = \frac{(P * a)h^2}{2}}$ Bending Moment at root (5)

$$I = \frac{a * t^3}{12}$$ Second Moment of area of cross-section (about axis Y-Y) (6)

Where F_v is the shear force acting against the cube base
A_v is the effective sheared area (cube base)

Shear stress

$$\tau_{ave} = \frac{Fv}{Av} \quad (7)$$

$$\tau_{max} = \frac{F_v}{\mu A} \quad \text{where } \mu = \frac{2}{3} \text{ (Gere 1990)} \quad \text{for rectangle, } \therefore \tau_{max} = \frac{3}{2}\frac{F_v}{A_v} \quad (8)$$

Bending stress

$$\sigma_b = \frac{Mt/2}{I} \quad (9)$$

Maximum in-plain shearing stresses

Having known the maximum stresses (equations 7&9) acting on an element in plane stress, we next consider the determination of the maximum in-plain shear stresses (Gere 1990).

$$\tau_p = \sqrt{(\frac{\sigma_x - \sigma_y}{2})^2 + \tau_{xy}^2} \quad (10)$$

where $\sigma_x = \sigma_b$
$\sigma_y = 0$ (because the side pressures on the blocks are symmetrical)
$\tau_{xy} = \tau_{ave}$

$$\boxed{\tau_{design} = \text{Maximum of } \tau_p \text{ OR } \tau_{max}} \quad (11)$$

7.0 Analytical Calculations of SL Tool Design

Maximum pressure at the point of injection:
σ **= 2000 psi = 13.79 MPa**
Average pressure in front of the cubes:
σ **= 663.5 psi = 4.575 MPa**
$A_v = a * t = 6 * 3 = 18$ **mm²**

$$F_V = P * (a * h) = 4.575 * 10^6 \frac{N}{m^2} \text{ x } (6 * 8 * 10^{-6} \text{ m}^2) = 219.6 \text{ N}$$

$$M = \frac{(P * a)h^2}{2} = \frac{(4.575 * 10^6 * 6 * 10^{-3}) * (8 * 10^{-3})^2}{2} = 0.88 \text{ N.m}$$

$$I = \frac{a * t^3}{12} = \frac{6 * 10^{-3} * (3 * 10^{-3})^3}{12} = 13.5 * 10^{-12}\ m^4$$

Shear stress

$$\tau_{ave} = \frac{Fv}{Av} = \frac{219.6}{18 * 10^{-6}} = 12.2 * 10^6\ N/m^2 = 12.2\ MPa$$

$$\tau_{max} = \frac{F_v}{\mu A} \quad \text{where } \mu = \frac{2}{3} \text{ (Gere 1990)} \quad \text{for rectangle, } \therefore \tau_{max} = \frac{3}{2}\frac{F_v}{A_v} = 18.3\ MPa$$

Bending stress

$$\sigma_b = \frac{Mt/2}{I} = \frac{0.88 * 1.5 * 10^{-3}}{13.5 * 10^{-12}} = 97.8 * 10^6\ N/m^2 = 97.8\ MPa$$

Maximum in-plain shearing stresses

$$\tau_p = \sqrt{(\frac{\sigma_x - \sigma_y}{2})^2 + \tau_{xy}^{\ 2}} = \sqrt{(\frac{97.8 - 0}{2})^2 + 12.2^2} = 50.4\ MPa$$

$$\tau_{design} = 50.4\ MPa$$

According to the above calculations, τ_{design} is equal to the τ_p (i.e., τ_{design} = 50.4 MPa). This value must be compared to the Maximum in-plain shearing stress of the tool which is calculated as follows:

$$\tau_{tool} = \pm\sqrt{(\frac{31.05 - 0}{2})^2 + (48.81)^2} = 51.22\ MPa$$

where Max Tensile Strength at 40°C = 31.05 MPa
Max Shear Strength at 40°C = 48.81 MPa

Comparing τ_{tool} with τ_{design} one can conclude that tool must be able to resist the Maximum in-plain shear stress. The results shows a significant contribution of bending stress on the tool failure which means the height of the features play an important role in tool design.

8.0 Conclusions

Using a thermoplastic with a melting temperature of 200-300°C in epoxy SL tooling which has a Glass transition temperature of about 60-90°C, seems unrealistic or impossible. The key point to the success of this technique is the very low thermal conductivity of the SL tool and the short injection time (*figure 8*). These two factors are the key to the success of the SL injection mould tooling, which are overlooked by many.

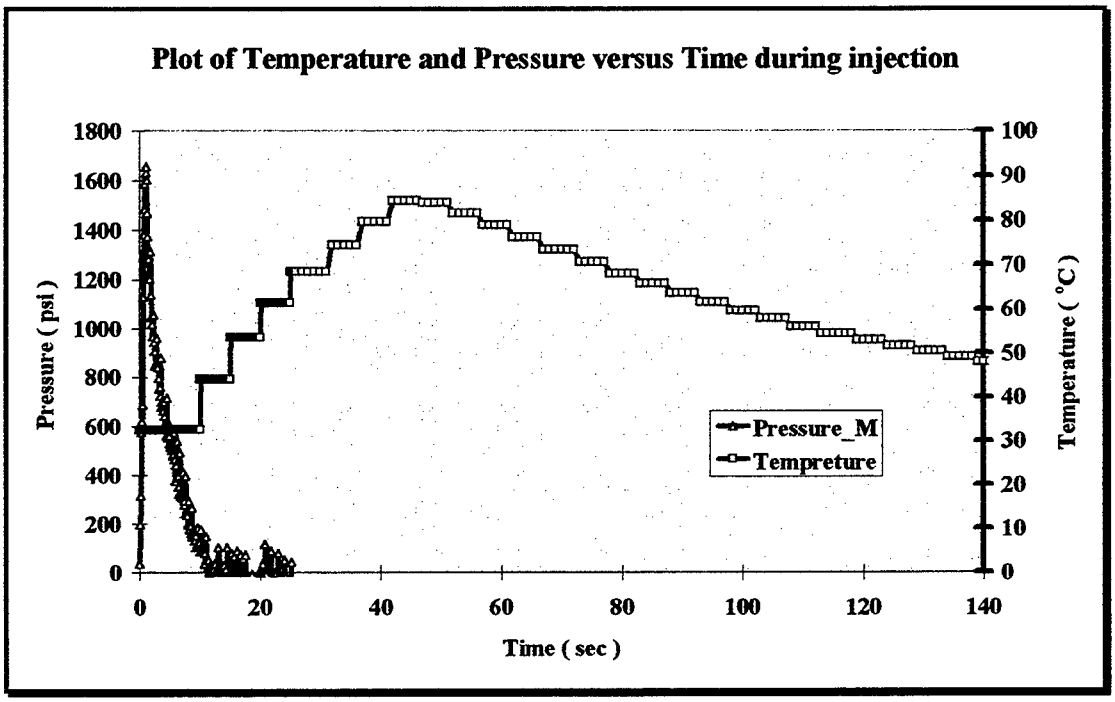


Figure 8. Plot of temperature and pressure versus time during injection

Although the epoxy has a very low tensile or shear strength at high temperatures, during the first few seconds, the maximum injection pressure is exerted on the tool, the heat has not been able to penetrate much (*figure 8*). Therefore the low conductivity of the epoxy works in favour of the process initially. It can be concluded that the tool must be cooled down to as low as 30-40°C before the next injection is made. This may increase the cycle time, but the tool success has the priority. At this point the tool temperature after new injection would not increase much and the tool failure could be avoided. This cooling can be achieved either through free convection which takes 4-5 minutes or through forced cooling by means of air jet which reduces the cycle time to 1-2 minutes.

9.0 References

Rahmati, S. and Dickens, P. M.,"Stereolithography Injection Moulding Tooling", Sixth European Conference on Rapid Prototyping and Manufacturing", Nottingham, UK, July 1-3rd 1997, ISBN 0 9519759 7 8, PP 213-224.

Menges, G. and Mohren, P., 1986,"How to Make Injection Molds", Hanser, Munich, ISBN 0-02-947570-8.

Gere, J. and Timoshenko, S., 1990, "Mechanics of Materials", PWS-KENT Publishing Company, Boston, ISBN 0-534-92174-4.

Ives, G. C., Mead, J. A. and Riley, M. M., 1971," Handbook of Plastics Test Methods", The Plastics Institute, London, ISBN 0 592 05449 7.

Riley, W. F., Sturges, L. D. and Morris, D. H., 1995 "Statics and Mechanics of Materials", John Wiley & Sons INC., New York, ISBN 0-471-01334-X.

Deflection and the Prevention of Ingress within Laminated Tooling for Pressure Die-Casting.

R.C.Soar & Dr P.M.Dickens.

The University of Nottingham, Centre for Rapid Prototyping,
Department of Manufacturing & Operations Management,
University Park, Nottingham, UK. NG7 2RD.

ABSTRACT

Within the context of rapid tooling, we are currently assessing the fundamental limitations of laminated tooling for pressure die-casting (PDC) applications. The use of individual laminates to form a die-cast tool presents it own problems, namely the prevention of excessive deflection that may lead to the ingress of pressurised molten aluminium between laminates. Ultimate solutions lie with bonding and clamping techniques of which work is already underway. This paper describes an initial study to establish the fundamental laminated die behaviour in extreme die-casting environments.

Keywords: Laminated Tooling, Rapid Prototyping, Freeform Fabrication, Rapid Tooling, Pressure Die-Casting, Deflection.

1. INTRODUCTION

Of all of the Rapid Tooling processes, Laminated Tooling is probably the simplest to conceptualise. The process uses the layered data from a 3D CAD model of a tool. Each slice is exported via DXF to a laser profiling machine. Each of the DXF files defines one laminate of the tool and all are nested to fit a pre-defined sheet of steel, aluminium, stainless steel, etc. After cutting they are de-burred and assembled into the finished tool. The benefits of laminated tooling[1] can be summarised as follows:-

- The production of large-scale tooling, as the size of each laminate is only restricted by the size of the laser profiling bed.
- The inclusion of conformal cooling channels for decreased cycle times.
- The replacement of damaged or worn laminates.
- The exchange of laminates for different profiles within a tool.
- Low cost and time of production, as there is little capital layout due to the abundance of laser sub-contractors.

Laminated tooling is becoming attractive to die-casters because of the huge expense of conventional die production. e.g. Dies commonly require modifications after manufacture; and there is the problem of reducing hot spots within a die. Conventional die manufacturing may only allows for one attempt to get the design correct, the die must also be dedicated to producing many

tens of thousands of parts to justify the cost. The rapid increase in the use of die-casting, particularly of aluminium to reduce fuel consumption and increase performance in cars, has resulted in larger dies, running faster. In addition, product lines can change annually requiring new tooling. Laminated tooling has the potential to offer low cost, large scale dies for limited runs. Even if they cannot perfectly match the performance of a conventional die they can allow the die-caster to produce prototype tools that can be run on the die-cast machines. This makes possible the following: the study of material flow throughout the die; the formation of hot spots and soldering (molten material bonds to the die); the effectiveness of cooling channels; ejector pin layouts; vortices; overflows; gating; etc. By exchanging laminates within the die many iterations can be carried out before the final die design is set.

Some of the groups involved in the development of Laminated tooling around the world include: Stratoconception®[2], CIRTES (France); Nottingham[3], Warwick, Leeds & Liverpool Universities (UK); MIT[4], Clemson[5] & Ohio State[6] Universities (USA); DTI[7] (Denmark); Tokyo University[8] (Japan); most are backed by major automotive and aerospace sponsors keen to see a viable process.

2. LAMINATED TOOLS FOR PRESSURE DIE-CASTING.

For the experimental work an EMB100 hot and cold chamber pressure die-casting machine was used. This is by no means the largest die-casting machine but it is fairly typical. Specifications in its cold chamber set up are: -

Die Locking Force	75 Tons (Imperial)	76 Tonnes(Metric)
Size of Moving Platen	16" by 16"	406 by 406 mm
Weight per Shot (Al)	.65 lbs	.29 kg
Volume per shot	6.5 ins^3	106 cm^3
Dia. Of Inj. Plunger	1.25"	31.8 mm
Total Force on Plunger	11,775 lbs	5,341 kg
Max. Pressure on Metal	9,600 lbs/in^2	674 MPa
Min. Cycle Time	4 secs	4 secs

The casting material chosen was Al-Si8-Cu3 or LM24 (BS1490)/A380 (ASTM). This alloy is globally used as one of the most applicable to pressure die-casting. Cast aluminium is by far the largest sector in the PDC field[2]. However, it readily oxidises and is aggressive to steel dies. It also has the highest melting point at 750^0C. If a laminated die can withstand the pressure die-casting of aluminium it will be suitable for zinc, magnesium as well as low pressure applications.

The research took four routes to achieve the aim of viable laminated tooling for pressure die-casting: -

1. Selection of suitable sheet material and thickness.
2. Testing laminate stacks against failure through thermal cycling/stress.

3. Assessing the fundamentals of laminated die behaviour to withstand deflection and ingress of molten aluminium.
4. The bonding of laminates for extreme environments.

The first two sections have been covered in previous papers in conjunction with United States Committee for Automotive Research (USCAR)[10]. A recent paper, in conjunction with GEC Marconi Hirst Division[11], covers the last section. This paper asks the more fundamental question of whether inter-laminar bonding is required at all. Also, what design constraints exist for laminated dies and over what aspect ratio will individual laminates fail or distort.

3. PROBLEMS OF LAMINATED DIES IN PDC ENVIRONMENTS

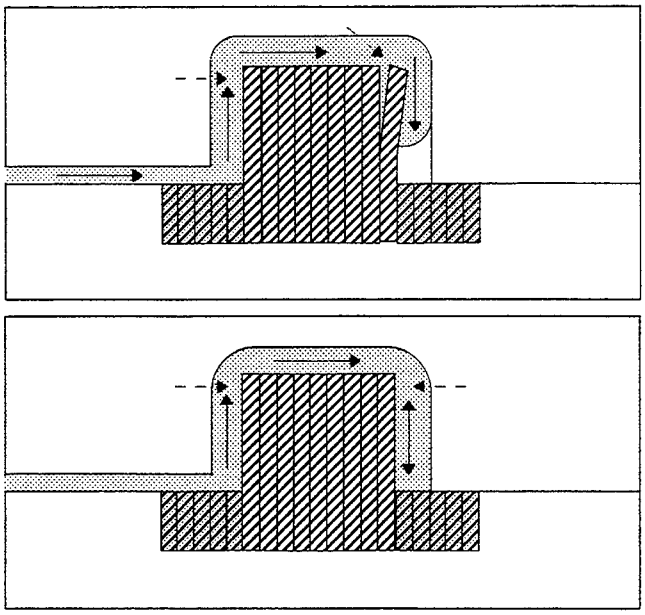
When using laminated tooling for pressure die-cast applications there is the possibility that molten material may force itself between the laminates of an up-stand feature within the die. If this occurs, then the subsequent casting may solidify onto a feature and be impossible to remove without damaging the tool.

For any laminate die design, the amount of deflection that occurs on an up-stand feature will be proportional to its height, area and geometry, as well as its orientation to the flow of the incoming material. Essentially, for any given sheet material there will be a design limit. The objective of this research is to find out, considering the unique conditions of die-casting, where this limit lies.

Due to the dynamic loading on the laminates, as molten material enters the die, the degree of deflection and the amount of ingress can only be established through direct observation of a laminated die in operation. What complicates matters further, is the nature of the molten material as it flows around an up-stand and fills the die. Depending on the influences of the various elements molten material will act as a dynamic load. It is not static, due to the brief time it takes to fill the cavity and the constantly changing pressure and velocity within the die. In effect, deflection will reach its maximum whilst material passes over the up-stand. However, it will cease as soon as the chamber is full producing an equal pressure on both sides of the up-stand.

Four things could happen at this point and are illustrated in the Figure 1, overleaf:

1. Molten material could flow over the up-stand and the pressure could equalise on both sides before any significant deflection or ingress of material occurs.
2. If ingress has occurred in the up-stand during material inlet, the chamber could remain hot enough to allow the equalising pressure to force that material out of the laminate up-stands.
3. Any material that forces its way between the laminates could chill so quickly that it will solidify before the back pressure can force it out and so cause the part to freeze onto the ejector side of the die set.
4. if the deflection is too great the laminate could deform plastically and could normalise into this new position



When molten material enters the chamber the end laminates will briefly deflect. Whether there is a permanent ingress of material depends on the equalising effect when the material fills the chamber.

As material fills the die chamber completely and the pressure equalises, the elasticity in the deflected laminate may allow it to spring back. If the material chills too fast whilst the laminate is deflected, the part will freeze onto the up-stand.

Figure 1. Effects of Material Flow within Die Cavity.

A final point to make about the possible outcomes relates to the viscosity/fluidity and wetability of the molten material. Even with a large deflection, ingress may not be possible due to the viscous nature of molten aluminium.

4. SELECTING SUITABLE SHEET MATERIAL.

There is generally considered to be only one type of steel that is suitable for aluminium pressure die-casting: This is H13 hot work tool steel (BH13 in the US).The selection and location of suitable sheet material for this experiment has been a central part of the work so far. One of the first decisions made was to establish a suitable thickness for the sheet material. The trade-off is between the degree of finish and detail required in the assembled laminate tool against the assembly time and availability of the material. The fastest way to build a laminated tool is to use very thick sheet material. But, as Figure 2 below shows, if the sheets are too large then all the detail is lost and secondary finishing becomes 90% of the job. The other extreme means the laminates would resemble a metal foil, as in Figure 3. The detail would almost be perfect but hard steels do not come this thin and the tool would be difficult to assemble.

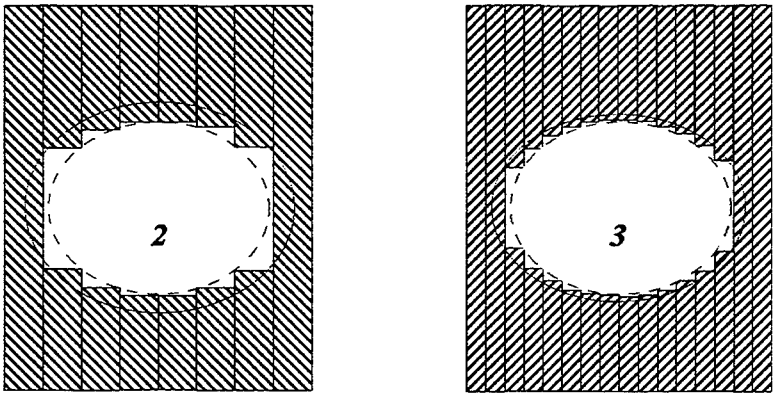


Figure 2 & 3. Effects of Laminate Thickness on Steeping

The most readily available sheet thickness for high strength and thermally resistant steels, giving adequate detail, is one millimetre. One millimetre is the thinnest that most sheet materials can be purchased for high performance steels such as H13. Rolling steel this thin can improve the grain structure and alloy distribution, but it does set up stresses that must be relieved later on (this is done during final hardening and tempering).

5. THE LAMINATED TEST DIE.

The ultimate test die design consists of a number of isolated laminate up-stands. Each up-stand has a different aspect, that will present one laminate in each group to receive the full force of the incoming, pressurised, molten aluminium. At a certain height there will be enough force to deflect this laminate to cause an ingress of molten material between itself and the laminate it abutts. Figure 4, below, shows a cross section of the two extremes of the up-stand arrays that will be created in the test die.

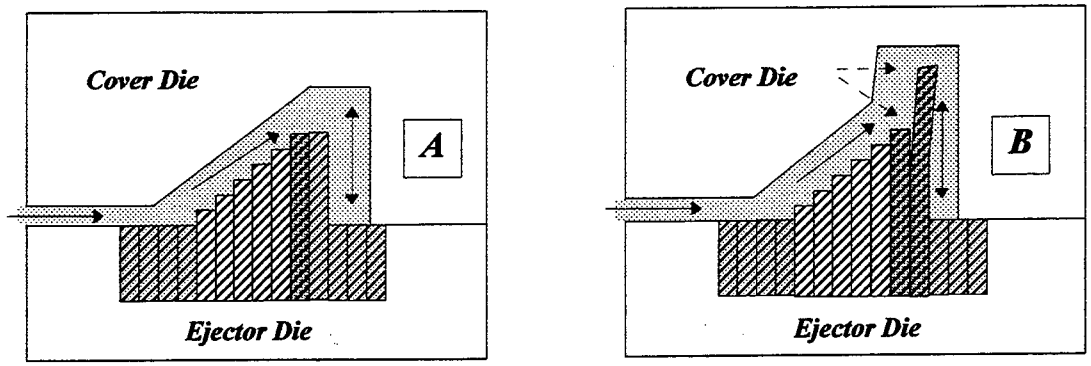


Figure 4. Effects of Deflection on Laminate Upstands.

The simplified illustration *(A)* shows molten material entering from the left and being forced upwards at 45^0 over a ramp formed by the laminates. Each laminate stands 1 mm higher than the laminate on the left. This design will not incur any deflection as the laminates in the up-stand support each other and the end laminate does not protrude into the flow of molten metal.

On illustration *(B)* material enters from the left and is directed up the laminate ramp where it will strike the last laminate before passing over and around it. This laminate will deflect but may move to the upright position again, due to its elasticity/rigidity, before the cast freezes. Trying to measure this deflection as it occurs in the die would be impossible, this measurement can only be taken by examining the casting after removal from the die. The answer to measuring deflection lies in the second laminate positioned next to the tallest up-stand. If the last laminate deflects enough then there will be an ingress of aluminium that will freeze between the laminates. When the cast is removed from the die a 'witness mark' will remain that can be measured as a direct indication of the amount of deflection that occurred in the last laminate, as shown in Figure 5.

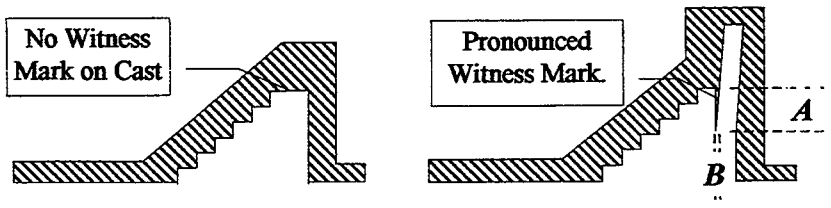


Figure 5. Measurable Witness Marks

Figures 6, 7 and 8 show the plan and cross-sectional view of the two halves of the laminated die. The laminated test die will be clamped into a bolster. The dimensions are shown below in Figure 9: -

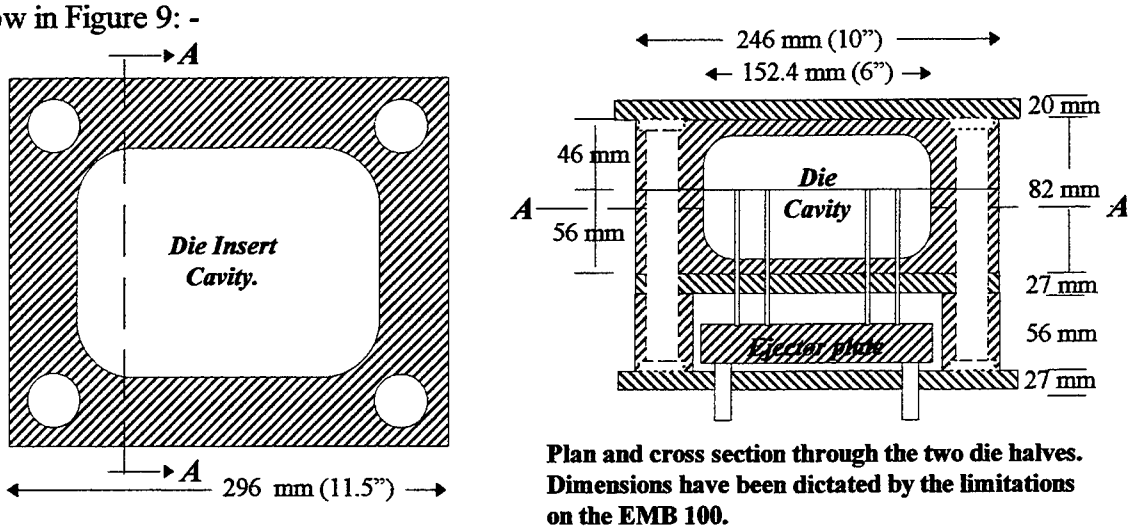


Figure 9. Complete Die Assembly.

The end-plates will be constructed in H13 to spread the clamping load on the individual laminates and prevent them from warping. Previous testing with GEC and USCAR has shown that a pressure of at least 10 MPa is necessary on each laminate to ensure rigidity and the elimination of any gaps between laminates this pressure will be provided by the eight M10 bolts.

The tool will run for around 500 shots as there is a time constraint on the use of the EMB100 die-casting machine. Over this time tool wear will be monitored as an indication of potential prototype life.

6. DISCUSSION.

This tool is now currently in testing and the results will be published early in 1998. The results from this work will dictate where the research will move next. If ingress occurs too readily then the next stage will be to investigate suitable bonding techniques to overcome ingress in these applications. If ingress does not occur readily, then un-bonded laminate dies will be explored further. To produce a laminated tool with no inter-laminar bonding for pressure die-casting would be a huge cost saving over having to use some bonding medium. Instead of looking into bonding techniques, the research would move onto look at clamping techniques.

The data collected from this experiment will then be used to formulate a model that will allow the designer of a laminated tool to know the limitations of this process when applied to pressure die-casting. The model will be able to compensate for different die-cast machines, different grades and thicknesses of sheet steel and different materials.

7. REFERENCES.

1 Soar, R.C. and Dickens, P.M. (1996) **Finishing Laminated Tooling with Stereolithography EDM Electrodes**, *Proc. from the 5th European Conference on Rapid Prototyping and Manufacture*, 4-6 June, 1996, Helsinki, Finland, Publ. by the University of Nottingham, Edited by Dr. P.M. Dickens, pp 87-106.

2 Lyett, D., Barlier, C., Weinstoerffer, M. and Delebecque, B. (1995) **Une Nouvelle Station de Prototypage Rapide par Stratoconception® et Microfraisage Rapide de Materiaux Legers**, *Proc. de 4emes Assises Europeennes du Prorotypage Rapide*, 4-5 October 1995, Paris, France, Publ. by Remark S.A., 2, rue des Garennes, 78570 Andersy, France, pp 1-11.

3 Dickens, P.M., Simon, D. and Sketch, R. (1996) **Laminated Tooling for Moulding Polyurethene Parts**, *Proc. from the Rapid Prototyping and Manufacture Conference*, Dearborn, Michigan, April 22-25, 1996.

4 Walczyk, D.F. and Hardt, D.E. (1994) **A New Rapid Tooling Method for Sheet Metal Forming Dies**, *5th Internationnal Conference on Rapid Prototyping*, June 12-15, 1994, Edited by R.P. Chartfoff et al., Sponsored by the Rapid Prototype Development Laboratory, The Management Development Centre, The University of Dayton, pp275-289.

5 Vouzelaud, F.A. and Bagchi, A., (1992) **Adaptive Laminated Machining for Prototyping of Dies and Molds**, *Proc. of Solid Freeform Fabrication Symposium,* Austin, Texas, 3-5 August 1993, Edited by Harris L Marcus et. al. University of Texas at Austin, Texas, USA, pp291-300.

6 Glozer, G.R and Brevick, J.R. (1992) **Laminate Tooling for Injection Moulding**, *Proc. from the Institute of Mechanical Engineers*, Part B: Journal of Engineering Manufacture, Vol. 207, July 1992, pp 9-15.

7 Schreiber, M.P. and Clyens, S. (1993) **Blanking Tools Manufactured by Laminated Laser Cut Steel Sheets**, *Proc. of the 2nd European Conference on Rapid Prototyping and Manufacture*, Nottingham, 15-16 July 1993, Edited by P.M. Dickens, Publ. by The University of Nottingham, ISBN 0-9519759-1-9, pp167-176.

8 Nakagawa, T. (1995) **Rapid Prototyping Technologies in Japan**, *Proc. de 4emes Assises Europeennes du Prorotypage Rapide*, 4-5 October 1995, Paris, France, Publ. by Remark S.A., 2, rue des Garennes, 78570 Andersy , France, pp 1-12.

9 Wall, A.J. and Birch, J.M., (1993) **Pressure Die Casting since 1970,** *Proc. from 14th International Pressure Die-Casting Conference.*, publ. by European Die-Casting Committee, London. UK.

10 Soar, R.C. and Dickens, P.M., **Design of Laminated Tooling for High Pressure Die-casting,** *Proc. of the 1996 Photonics East Conference,* 18-19 November 1996, Boston, Massachusetts, USA., publ by SPIE-The Int. Soc. For Optical Engineering, Ed. By Pierre Boulanger, Vol 2910, Rapid Product Developmnent Technologies, ISBN 0-8194-2312-2, pp 198-210.

11 Bocking, C., Jacobson, D.M., Sangha, S., Dickens, P.M. and Soar, R.C., (1997) **The Production of Large Scale Rapid Prototype Tools Using Layer Manufacturing Technology with Diffusion Soldering,** Publ. by GEC Journal of Technology, Vol 14, No.2.

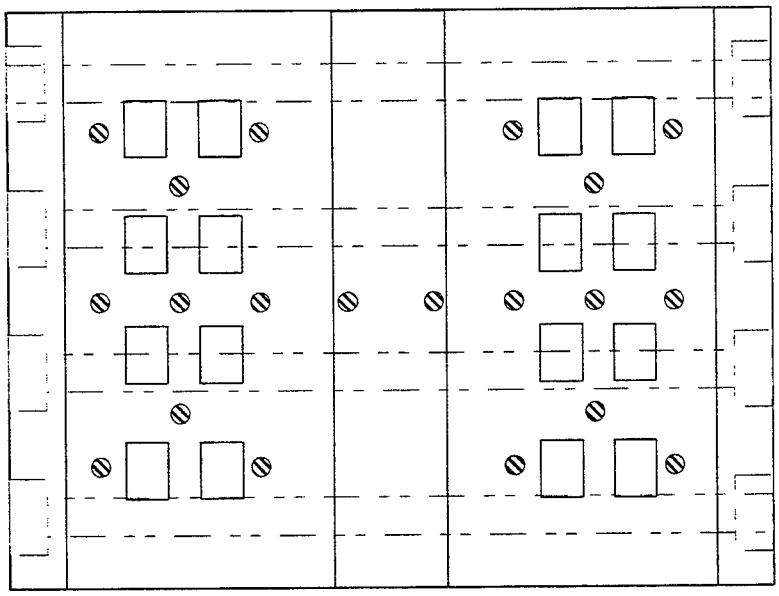


Figure 6.

Plan view of the ejector die, showing the laminate arrays. Phantom lines denote the M10 bolts used to clamp the laminates and prevent movement. End plates and a central clamping plate are shown to allow the interchange of laminates to change the profile.

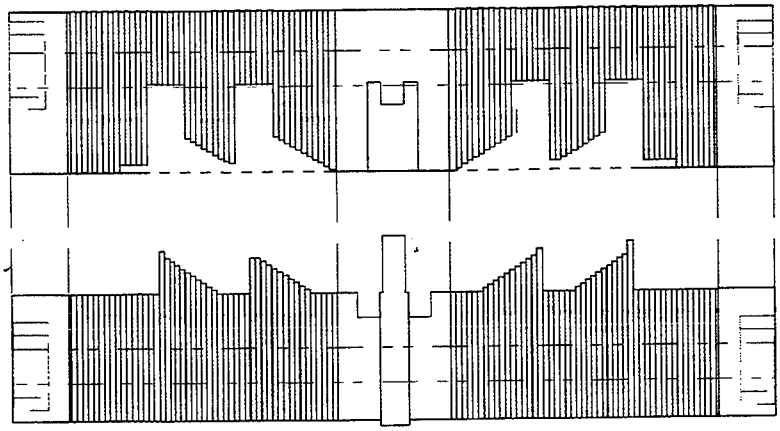


Figure 7.

Cross-sectional view of the cover & ejector die, showing the laminate arrays. Ejector pins are not shown but appear in Figure 8, below.

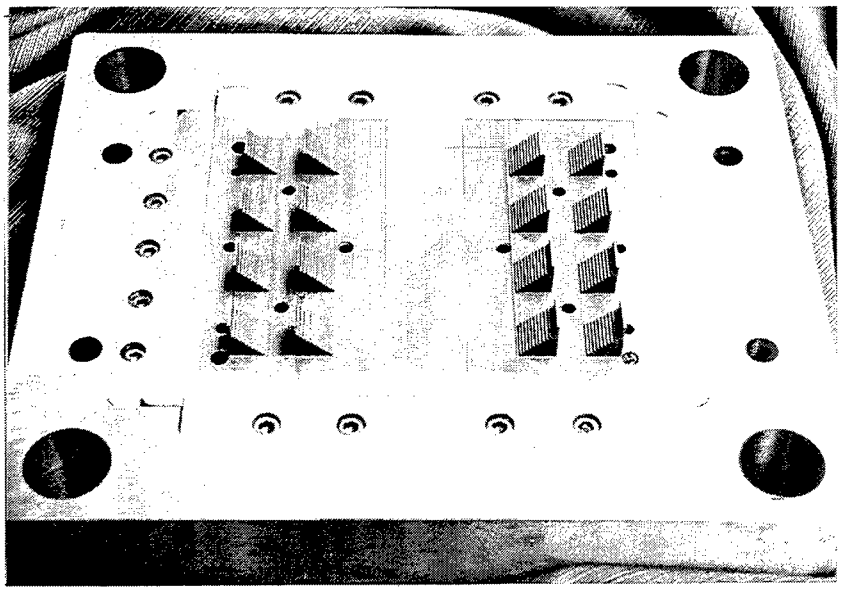


Figure 8.

Completed ejector die showing wedges used to hold the lasminated die in the bolster. Ejector pins have been removed.

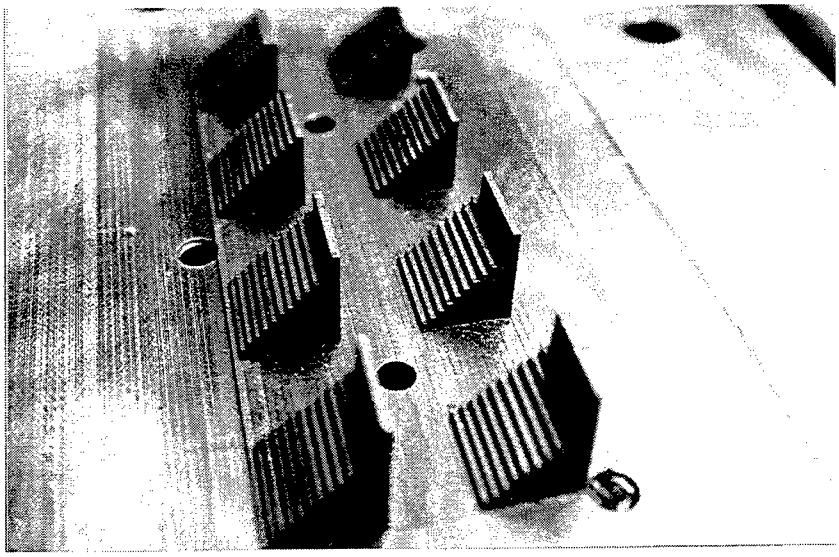


Figure 10

Two of the four rows of laminated arrays showing the laminate up-stand that will receive the full force of incoming molten aluminium to measure deflection.

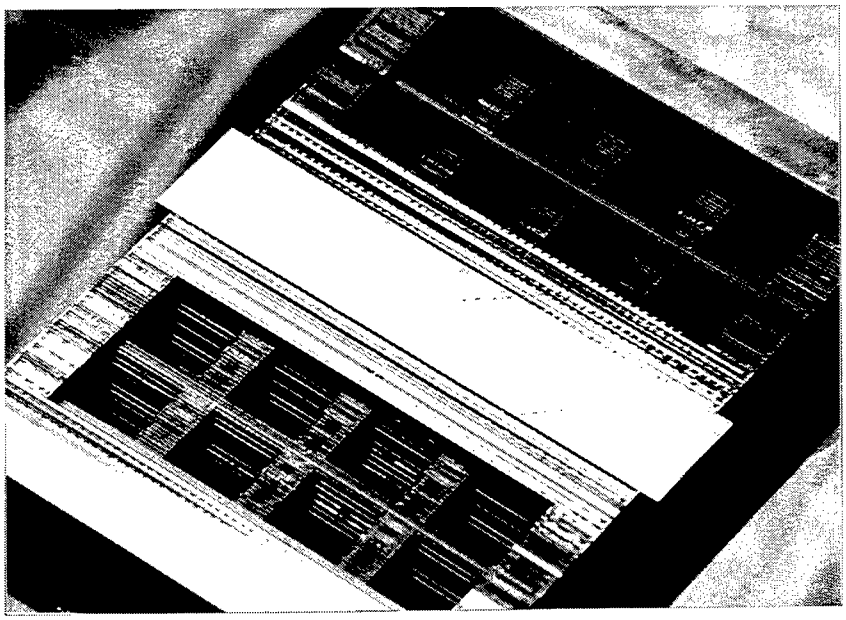


Figure 11

Laminates that make up the Cover Die assembled and clamped using solid end plates and a solid central core to facilitate disassembly.

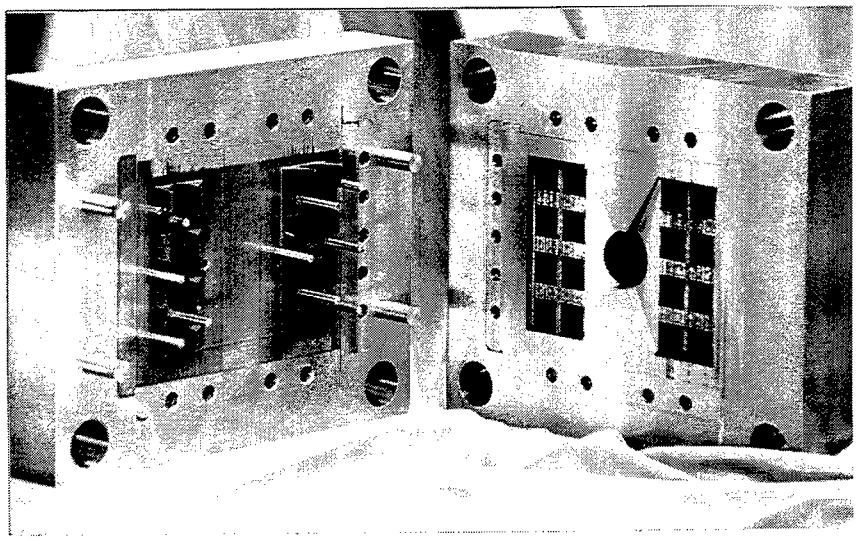


Figure 12

The completed laminated test die showing ejector pins and the fan gate in the cover die. The ground parting line makes the laminates hard to distinguish.

INJECTION MOLDS BEHAVIOR AND LIFETIME CHARACTERIZATION

Concept and design of a Standard Measurement Method

N. P. Karapatis, J.-P. S. van Griethuysen, R. Glardon

Department of Mechanical Engineering, Swiss Federal Institute of Technology, Lausanne

Abstract

This paper presents the concept of a standard method used to determine the durability of injection molds. In particular, some Rapid Tooling molds are less resistant to abrasive plastics than conventional steel molds. Some evidence of wear in a conventional mold is given, and a specific mold is designed for this test ; polymer materials are defined and the test methodology is outlined. Numerical simulation is utilized to show the areas of the mold subject to high shear stresses.

1. INTRODUCTION

Recent developments in Rapid Prototyping (RP) technology have brought new expectations for fundamental modifications of the development path of industrial products [1, 2, 3]. Time-to-market has been shortened, costs have been lowered, thanks to the reduced importance of prototyping time [4, 5]. RP has also supported the integration of Concurrent Engineering by providing tools and material required for rapid decision-making and fast reaction. However, tooling still had to be prepared by conventional methods.

Different Rapid Tooling approaches exist now, especially in the field of injection molding. Each process has inherent drawbacks, but each allows the fabrication of tools on the basis of a single CAD file, like in Rapid Prototyping, in very short times [6]. However, tool manufacturing is related to more specific requirements, and the mechanical specifications are much more severe than in RP. Rapid Tooling (RT) concerns various production fields, such as foundry casting, forging or injection molding. The latter is at the moment a rapidly growing market for RT vendors. This paper shall deal essentially with the characterization of tooling for injection molding.

Some of the available RT methods are based on the stereolithography (SLA) process ; according to 3D Systems' definition, these techniques can be divided into three classes : Soft, Bridge and Hard Tooling. SLA components are used as patterns for the preparation of rubber molds (silicone RTV), for investment casting (QuickCast™), as a prototype ACES epoxy mold (DirectAIM™), or for the manufacturing of the mold cavity and core (Keltool™) [5, 7]. Other commercial solutions directly generate the hard tool by "welding" metallic powders together, like 3D-printing [8] or Selective Laser Sintering [9]).

Generally, toolings made with rapid technologies have lower properties than those made conventionally, except for the Keltool™ and the RapidTool™ techniques. Especially in the case of the really Direct Rapid Tooling techniques (like SLS) [6], the raw tools surface quality is often poor, and requires time-consuming finishing. Besides, their accuracy is not sufficient and their surface is not hard enough to provide sufficient wear resistance for injection molding.

Many injection tests have been performed on Rapid Tooling molds [5, 8, 10] to assess the efficiency and the advantages of RT methods versus conventional machining, in industrial conditions. However, the test parts, the plastic materials and the injection parameters were always specific to a manufacturer or to a research institute. Little comparison can then be made between the processes, the materials and the improvements, as well as between conventional and Rapid technologies, because of the lack of common features. Furthermore, there is usually little or no information regarding the reasons why the tests were ended (insufficient precision or loss of surface quality).

2. PURPOSE

From the facts described above, it can be readily seen that performances and improvements of Rapid Tooling technologies are difficult to assess and to compare on a scientific and systematic basis, with each other and with conventional techniques. Time and cost comparisons may therefore not be valid, depending on the effective series size, tooling lead time, required surface quality and precision, cycle time, and so on. The purpose of this paper is to present the basic concept and definition of a standard test method for mold durability and quality measurement, as developed at the Swiss Federal Institute of Technology in Lausanne.

Similarly to the stereolithography users' group test part [11], the standard test method involves the design of a mold with specific wear features (describing surface roughness and tolerances requirements), the selection of processing parameters as well as the selection of abrasive plastic materials and the definition of a test methodology. In this paper, some evidence of wear on a conventional mold will first be given ; then, the mold, the material and the methodology selection will be presented, together with computer simulation to validate the choices. The first validation of the method has been made on a conventional mold made in aluminum, so that wear effects can be rapidly observed.

3. WEAR OBSERVATION

Traditionally, injection molds are manufactured by conventional methods, i. e. milling, drilling, EDM, etc., with steels such as *Werkstoff Nr.* 1.2343 or 1.2083. The properties of these molds are such that their durability should be longer than the expected life of the product on the market. However, these molds sometimes fail or present more wear than what is acceptable. For instance, figure 1 shows the worn surface of a steel mold at the injection point. About 20'000 parts in POM were injected in this tool, at an injection pressure of 900 bar and a polymer temperature of 215 °C. Figure 2 shows a surface map of the worn region, measured by laser profilometry. When the gate gets smaller, there is more wear at the runner walls because of increased polymer velocity and shear stress ; when the polymer enters the mold, its abrasive behavior erodes the steel surface. Though the wear effects are relatively small, there is a measurable difference of more than 4 μm between the nominal surface of the mold and the worn surface at the injection point.



Figure 1 : micrograph of the injection point (mag. 7.5 X)

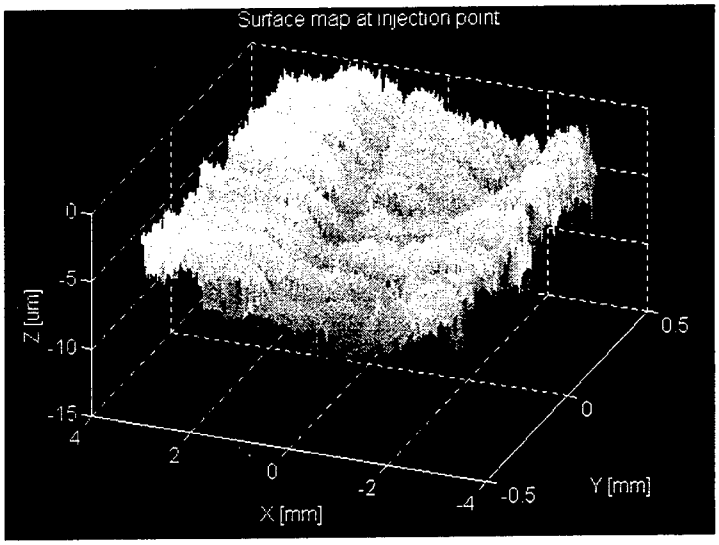


Figure 2 : laser profilometry map at the injection point.

4. STANDARD MOLD DESIGN

The design of the standard mold was made in collaboration with local moldmakers, on the basis of the following criteria : the mold has to be simple so that it can be manufactured easily, rapidly and at a low cost, either by conventional machining or by Rapid Tooling techniques. It must also comprehend typical wear features, and its size has to be compatible with generative manufacturing processes. Besides, the volume of the part has to be small enough to insure short cycle time for fast data acquisition.

Two important mold characteristics were chosen as test criteria : dimensional/angular accuracy and surface roughness. These issues are very important in plastic injection molding, since they influence the injected part functionality and esthetic aspect, as well as the ease of ejection from the mold. The mold was designed on the basis of a relatively simple part, conceived to take into account the desired wear features. The part integrates two plane areas, a slanted plane, two hollow cylinders, rectangular holes and bulges (figure 3). Two types of injection points have been chosen : a standard and a tunnel-type injection point, situated in the "fore" region of the part, so that wear can be observed on a wall directly opposite to it. In the first version of the mold, the standard injection type was chosen, as shown in figure 3. The slanted plane serves to quantify the surface roughness obtained by generative processes, and its modification during service. The holes and bulges give information on angular and dimensional accuracy in the mold.

For the first tests, a first version of the mold has been made in Fortal 60 aluminum (similar to AA7075), with an initial surface roughness CH20 (Charmilles Technologies roughness scale, $R_a \approx 2\ \mu m$).

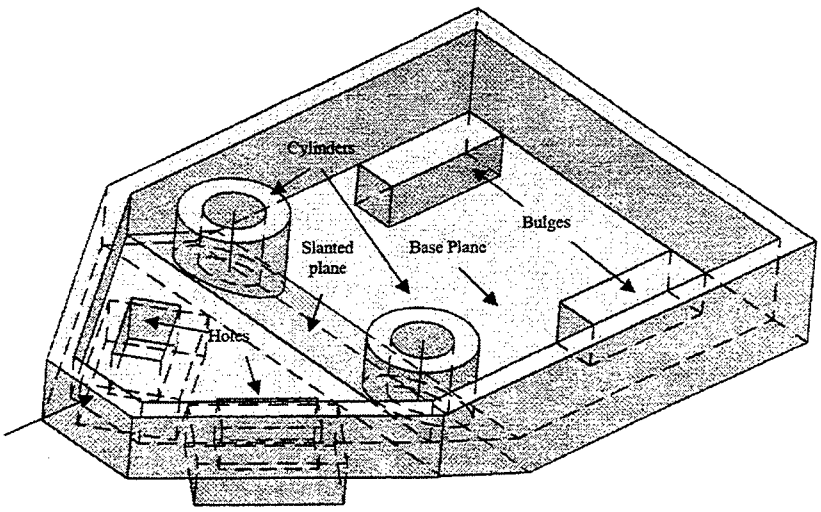


Figure 3 : preliminary version of the standard part. The arrow on the left side shows the location of the injection point.

5. PLASTIC MATERIALS

The purpose of this standard measurement method is to provide a means to view and quantify the wear of molds. Hence, in order to rapidly measure mold deterioration, several plastic materials were selected, according to their abrasive properties, and to their rate of use in industrial production, as well as availability and injection easiness. Glass fiber reinforced polyamide (PA), polypropylene (PP) and polyphenylene sulfide (PPS) comply with these requirements. The first tests were performed with glass fiber reinforced PP (Denilen M3010, similar to Hostacom G3 N01), which is easy to inject, does not require a tight mold temperature control, is readily available and can be recycled with little quality loss. The proposed processing parameters are the following : injection pressure, 900 bar ; polymer temperature, 250 °C ; mold temperature, 30 °C ; clamping force, 200'000 kN.

6. METHODOLOGY

The test methodology is simple, since data can be acquired fast and easily, with no specific equipment needed. Essentially two types of measurement are performed : first, the visual aspect of the plastic part is surveyed during production (by optical or electron microscopy), in order to determine possible mold degradation ; then, the mold is removed from the injection machine and dimensions and surface roughness are determined. A UBM laser light profilometry equipment provides surface roughness values, profiles and mapping, which are also used to determine dimensional variations.

Measurements are performed on explicit locations on the part and on the mold, particularly exposed to abrasive flow. The following measurements are specified :

- On the part : in-production changes of visual aspect, possible variation of wall thickness ;
- On the mold : surface maps and profiles of the plane in front of the injection point, surface map/profiles in the middle of the upper, lower and slanted planes, angles of the holes and bulges, inner diameter of the cylinders.

The mold will be considered "not suitable for production" if the dimensional or the average surface roughness exceed a certain value. If the visual aspect of the parts degrades too much beyond a given point (flashing, burning, etc), the production may also be ended.

Typically, the mold will have to be removed from the injection machine after each thousand to five thousand cycles ; if visual observation reveals sudden damage, measurements will also be immediately performed.

7. SIMULATION

Recent software packages such as SDRC's I-DEAS MasterSeries 4 include powerful finite-element simulation modules, including thermoplastic or thermoset injection molding. Although simulating the injection molding process is a rather complex task, it is relatively easy to obtain results showing, for instance, the shear stresses generated during the injection of the part, and therefore to visualize the zones that are particularly exposed to the abrasive flow.

As it can be seen in figure 4a, the flow on the plane situated in front of the injection point, as well as on the middle region of the part, is more rapid than in the other areas. The representation of the shear stress generated by the polymer flow substantiates this observation (figure 4b) : the shear is strongest in the plane opposed to the injection point, in the upper plane, in the slanted plane and in the region of the lower plane close to the slanted plane.

The simulation results shows in particular that some of the specific wear features may be purposeless, since they do not seem to be submitted to extreme wear. However, one should bear in mind that finite element simulation may not really provide shear stress values at bulges or holes angles, where the wear effects can be particularly important. Together with the wear evidence presented in section 3, these results served for the definition of the measurement areas.

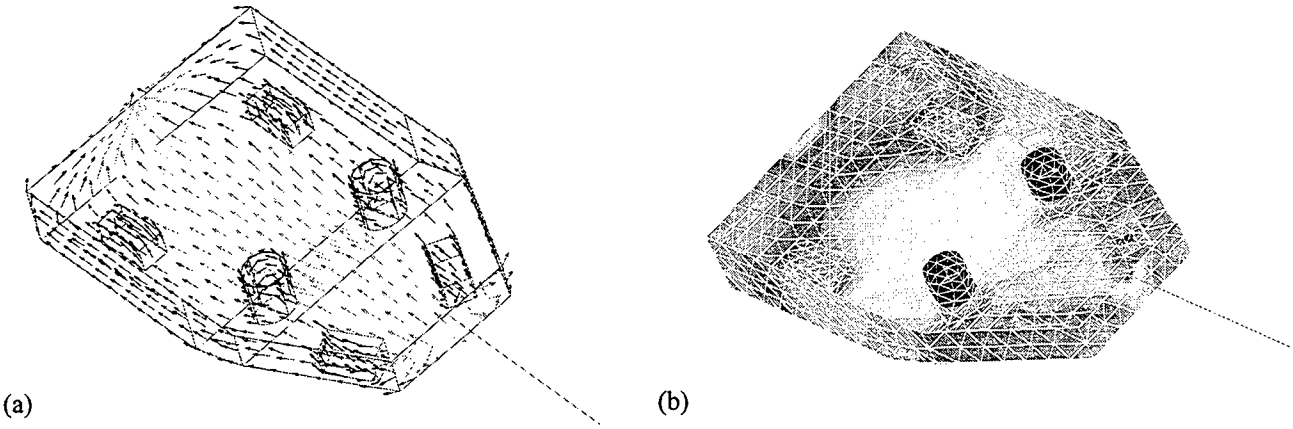


Figure 4 : numerical simulation results. (a) Bulk flow vectors ; (b) shear stress. The lighter shades indicate higher values. The light line on the right side represents the injection runner.

8. CONCLUSIONS

This paper has presented the concept of a standard measurement method for the evaluation of injection molds durability. The purpose of this method is to provide a scientific and systematic basis for the evaluation of the different Rapid Tooling methods with each other and with traditional machining.

The surface of a conventional steel mold has been investigated, demonstrating the existence of wear. A preliminary version of the standard mold has been presented, in which wear effects of the polymer flow on specific features can be easily measured. A commercial plastic has been chosen on the basis of its abrasive properties and its rate of industrial use ; indicative processing parameters have been proposed. Finite element simulation has been used to assess the specifically worn areas of the mold, according to velocity vectors and shear stress values. The results have also revealed that some of the wear features integrated in the mold were not necessarily subjected to excessive wear, compared with the high flow rate planes.

Future work will be oriented toward improved mold design for easy wear observation and toward a standardized test and evaluation methodology. More experimental results will allow a better understanding of wear phenomena in injection mold. Finally, the results given by this test method will provide information that will serve as a basis for the definition of the exact improvements required in Rapid Tooling.

9. ACKNOWLEDGMENTS

The work presented in this paper was made under Swiss Government CTI project 3409.1. The authors wish to thank R.-P. Gueissaz (A. Gueissaz & Cie SA) and X. Favre (Portescap Micromoteurs SA) for the worn mold and their very valuable assistance in mold design, J.-D. Wagnière and J.-D. Neuvecelle at the Department of Materials Science, Swiss Federal Institute of Technology in Lausanne, for the laser profilometry measurements and the optical micrographs, and the mechanics at the Department of mechanical engineering, Swiss Federal Institute of Technology, Lausanne.

10. REFERENCES

[1] S. ASHLEY, *Rapid Prototyping is coming of age*, Mechanical Engineering, July 1995, 63-68

[2] L. STYGER, *Firming designs*, IEE Review 41 1 (1995) 38-39

[3] L. STYGER, *Rapid prototyping & tooling : the enabling technology of the 90's*, IEE Manufacturing Division Colloquium on Rapid Prototyping in the UK, 1994

[4] M. GRIFFITHS, *Rapid prototyping options shrink development costs*, Modern Plastics 70 9 (1993) 24-27

[5] D. SMOCK, *New moldmaking systems slice art-to-part cycles*, Plastics World 53 7 (1995) 38-42

[6] N. P. KARAPATIS, J.-P. S. van GRIETHUYSEN, R. GLARDON, *Reducing time-to-market : the direct rapid tooling challenge*, to be published

[7] P. F. JACOBS, *Recent advances in Rapid Tooling from Stereolithography*, 3D Systems information booklet

[8] S. MICHAELS, E. M. SACHS, M. J. CIMA, *Metal parts generation by three dimensional printing*, Proceeding of the 4th International Conference on Rapid Prototyping and Manufacturing, Dayton, 1993

[9] D. L. BOURELL, R. H. CRAWFORD, H. L. MARCUS, J. J. BEAMAN, J. W. BARLOW, *Selective laser sintering of metals*, Manufacturing Science and Engineering ASME 68 2 (1994)

[10] A. LOHNER, *Laser sintering ushers in new route to PM parts*, MPR, February 1997, 24-30

[11] P. F. JACOBS, *Rapid prototyping and manufacturing : fundamentals of stereolithography*, SME 1992

Novel Liquid Crystal Resins for Stereolithography: Mechanical and Physical Properties

J. W. Schultz, J. S. Ullett, R. P. Chartoff, R.T. Pogue

Rapid Prototype Development Laboratory and
Ohio Rapid Prototype Process Development Consortium
The University of Dayton
Dayton, Ohio 45469-0130 USA

ABSTRACT

This paper considers photocurable liquid crystal (LC) monomers which are a new class of stereolithography resins. These resins form polymers with high upper-use temperatures. The rod-like molecules can be aligned by an external force. When cured in an aligned state, the aligned structure is "locked in" resulting in materials with anisotropic physical and mechanical properties. FTIR spectroscopy, thermo-mechanical analysis (TMA), dynamic mechanical analysis (DMA), and large strain mechanical tests were applied to liquid crystal photo-polymers, both in the green state and after postcure. These measurements showed that the photo-polymerization reaction locked in the molecular order. Elastic modulus in the glassy state, revealed approximately a factor of two difference between the directions parallel and perpendicular to the alignment. Thermal expansion measurements showed an anisotropic linear expansion that was very small, and sometimes negative in the alignment direction. Finally, these resins demonstrated high glass transition temperatures which could be advanced to as high as 150 °C by postcuring.

INTRODUCTION

To expand the applications of stereolithography, new resins must be developed that have better mechanical properties and higher use temperatures. Current stereolithography resins have softening temperatures well under 100 °C. As a result, they have limited usefulness in high temperature applications such as direct injection molding and under-the-hood automotive applications.

Liquid crystal (LC) monomers are a new class of stereolithography resins that can produce polymers with glass transition temperatures exceeding 100 °C and approaching 200 °C. These resins are typically made up of rigid, rod-shaped molecules. Unlike commercial resins, LC resins are often crystalline at room temperature and must be heated to exist in a liquid crystalline or isotropic liquid state. As a result, cure temperature becomes an important variable as it affects both processing parameters and green state properties. In addition, LC resins can be aligned unidirectionally using an external magnetic field. Curing the aligned monomer results in formation of an anisotropic network with a preferred direction, as shown in Figure 1. The resulting mechanical and physical properties of such a network are anisotropic. For example, the thermal expansion coefficient is much smaller in the direction parallel to alignment than perpendicular to the alignment. Thus parts can be directionally optimized for dimensional stability over broad temperature ranges. In addition, proper alignment allows optimization of

strength in a part. Finally, it may be possible to increase fracture toughness in these materials by varying the alignment from layer to layer.

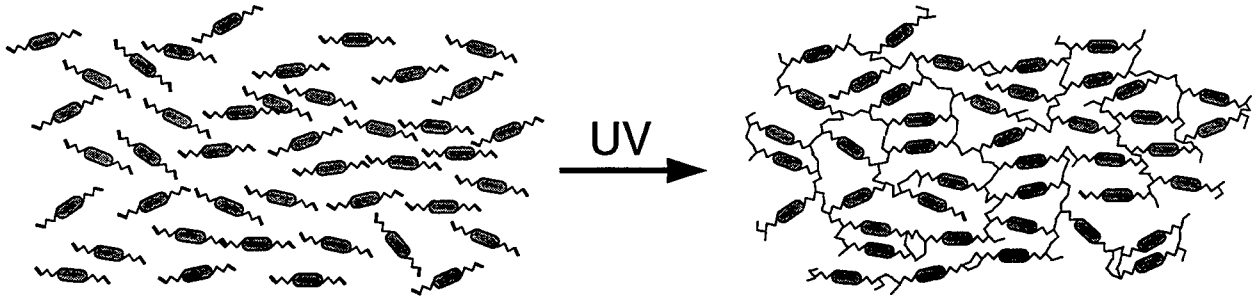


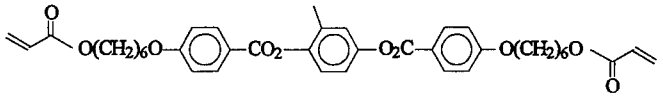
Figure 1. Schematic of aligned network of rigid rods formed by liquid crystal resins

In order to take advantage of these potentially useful properties, it is important to have a good understanding of the effects of polymerization conditions and postcure on the network formation and resulting anisotropic properties. A previous paper[1] considered some of the processing parameters of these resins, including orientation dynamics and working curve parameters. The present paper examines some of the anisotropic mechanical and physical properties of these new stereolithography resins. The focus of this paper is on the extent of anisotropy that can be achieved in the modulus and strength, and on the effect of different postcure conditions on the glass transition temperature. In addition, some linear thermal expansion data are also presented.

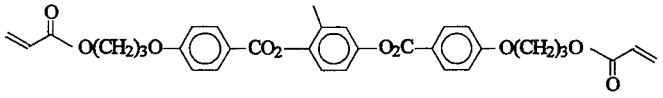
EXPERIMENT

Materials

The liquid crystal monomers used in this study, designated N1 and N2, are both diacrylate monomers with 'rigid rod' cores made of aromatic rings. The N1 monomer has 6-carbon aliphatic spacers on each side of the core while the N2 has shorter, 3-carbon spacers. N1 has been studied extensively by Broer et al.[2]. The molecular structures for the two monomers are,



(N1)



(N2)

The crystalline melting transitions for these monomers are 88 °C and 72 °C for N1 and N2 respectively. Above these temperatures, they are in a liquid crystalline phase. In the liquid crystal phase, the rigid cores of the molecules can be aligned towards a preferred direction. At higher temperatures (118 °C and 126 °C for N1 and N2 respectively) these resins undergo a second phase change into an isotropic liquid. In the isotropic phase, these resins loose their molecular order, so that their rigid cores are oriented randomly. For comparison purposes, commercially available resins also were considered. The commercial resins used were SL5149 and SL5170 (Ciba-Geigy).

Apparatus and Procedures

The samples were made in an experimental table-top stereolithography apparatus (TTSLA)[3]. The TTSLA includes a small heated aluminum vat and an external magnet with a field strength of approximately 0.32 Tesla. The magnet induces unidirectional alignment in the liquid crystal resin. The monomers were mixed with photoiniator and photopolymerized in the liquid crystalline phase. To reduce warpage during cure, single layer samples were sandwiched between glass slides. UV curing was accomplished with an argon ion laser delivering approximately 33 mW of power. Both single and multi-layer parts were made. The single layer parts were scanned multiple times with narrow line spacings to insure a uniform cure. The multi-layer parts were made using a typical stereolithography process using supports.

Infrared dichroism was measured using Fourier transform infrared (FTIR) spectroscopy measurements made on a Nicolet 20DXB spectrometer. The transmittance of various polymer samples was measured both parallel and perpendicular to the alignment direction by inserting an infrared polarizer at different orientations into the optical path. To ensure sufficient signal strength, the sample thickness was kept below 15 microns.

Dynamic mechanical measurements were conducted on a Rheometrics solids analyzer (RSA II), using a thin film fixture. The measurements were made in tension at a frequency of 1 Hz, and a strain of approximately 0.05 percent. Sample dimensions were typically 22 mm long, 3 mm wide, and 0.17 mm thick. To ensure a uniform thermal history, the samples were heated above their glass transition temperatures and quickly cooled before testing.

For large strain testing, a Rheometrics Minimat tester was used in conjuction with a high resolution digital camera for accurate strain measurement. Specimens were dogbone shaped with gauge dimensions of approximately 25 mm length, 5 mm width, and 1 mm thickness. The testing procedures were done in accordance with ASTM D638M.

Linear expansion as a function of temperature was measured on a TA instruments TMA 2940 thermomechanical analyzer using a thin film fixture. The measurements were made with a linear temperature ramp of 2 °C/minute and with a load of 0.5 grams. Sample dimensions were typically 13 mm long, 4 mm wide, and 0.22 mm thick.

RESULTS

Molecular Order

To better understand the origin of the anisotropy in the various physical properties of these polymers, FTIR analysis was used to measure the degree of molecular order. To describe the amount of molecular order in the liquid crystal state, a generally accepted quantity is the molecular order parameter, S. The order parameter is defined so that for a completely ordered material, $S = 1$, and for an isotropic material (completely disordered), $S = 0$. In the FTIR technique, an infrared polarizer is used to measure the sample's absorbance as a function of orientation angle. To obtain order parameter from the absorbance data, the dichroic ratio is calculated, which is the ratio of absorbances parallel and perpendicular to the alignment direction. The molecular order parameter is then calculated from the dichroic ratio.

Figure 2 shows the order parameter as a function of cure temperature for polymer N1. In this plot, the order parameter from two different absorbance bands are shown. The 1605 cm^{-1}

band arises from an aromatic stretch, and therefore corresponds to the stiff central core of the monomer. The 2940 cm^{-1} band is due to an aliphatic stretch and corresponds to the flexible spacer. The order parameter of the aliphatic spacer is considerably lower than that of the rigid rod core. This is expected because of the increased flexibility of the spacer and because it must stretch and contort to accommodate the crosslinked network. The data in Figure 2 also show that there is little variation in the order parameter as a function of cure temperature (except for very near the liquid crystal to isotropic temperature). Thus when optimum cure conditions are being determined for these resins, the order parameter is not an important consideration, since it is only weakly dependent on cure temperature.

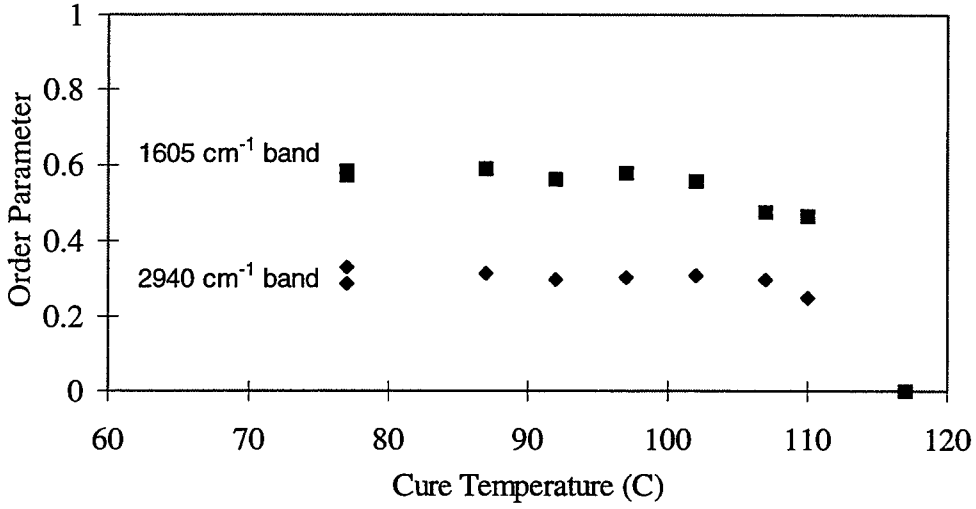


Figure 2. FTIR measured order parameter of N1 polymer as a function of cure temperature.

Mechanical Behavior

The DMA data show curves typical of network polymers with high crosslink densities. Because of the apparently high crosslink densities, the elastic modulus above T_g is too high to be called rubbery -- greater than 10^8 Pa. Figure 3 compares the elastic modulus of some commercial resins to the liquid crystal resins after they have been UV postcured. The LC resins show not only higher glass transition temperatures, but also the modulus above the glass transition is a factor of 5 to 15 higher than the commercial resins. Thus the usefulness of these liquid crystalline resins may extend well beyond their glass transition temperatures.

The data in Figure 3 also show that there is a significant difference in the modulus parallel and perpendicular to the alignment direction in these liquid crystal resins. This anisotropic modulus is shown in more detail in Figure 4. These data are for both single-layer and 2-layer parts made from resin N2. The modulus in the direction parallel to the alignment is 50 to 100% greater than in the perpendicular direction. In general the modulus of multi-layer parts is lower than that of the single layer films. This is expected, since multi-layer parts have a non-uniform cure. Other commercial resins have also shown similar differences in modulus when comparing multilayer parts to idealized single layer films[4].

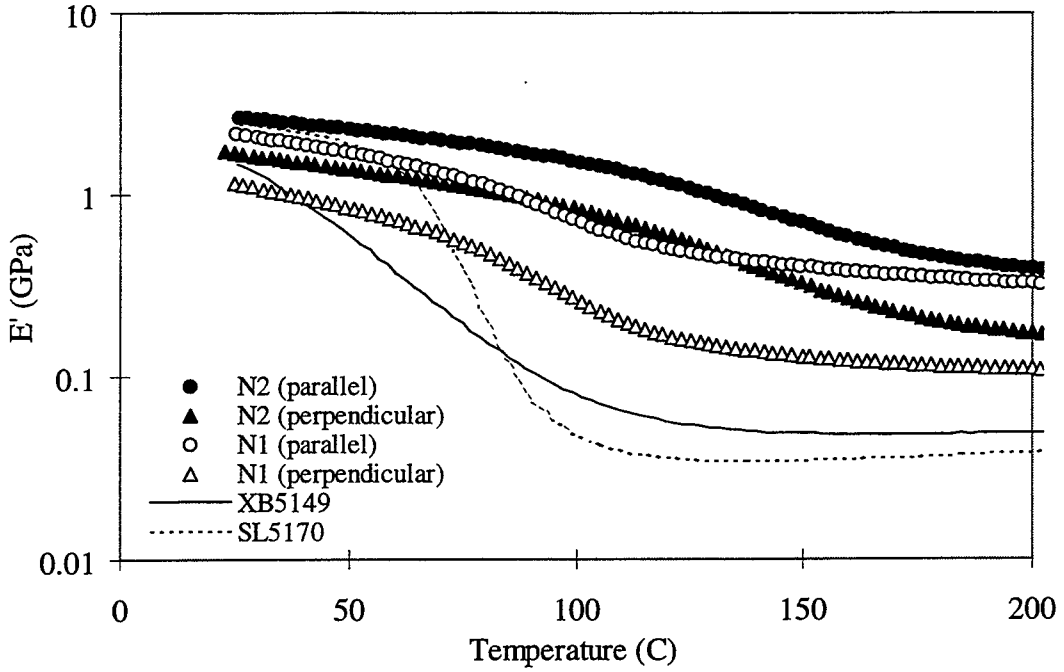


Figure 3. Comparison of elastic modulus of commercial resins and liquid crystal resins.

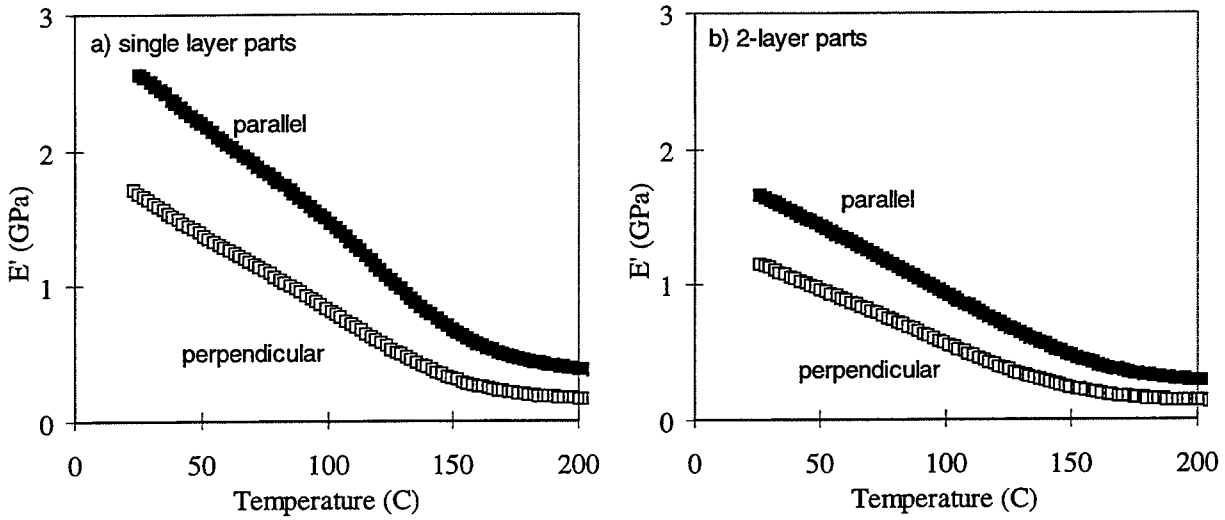


Figure 4. Anisotropic elastic modulus of N2 resins.

Since the linear elastic modulus is anisotropic, the tensile strength would be expected to behave similarly. This is indeed the case as shown for UV postcured samples of polymer N2 in Figure 5. While the strength is higher in the direction parallel to alignment, the strain at break is greater perpendicular to the alignment. N2 has tensile strengths of over 60 MPa parallel to alignment and 45 MPa perpendicular. Modulus values for N2 are about 3 GPa parallel to alignment and 2 GPa perpendicular. Because of the rotatable magnet, alignment can be varied on a layer to layer basis leading to composite-like structures. Thus mechanical modulus and strength can be directionally optimized in a part; though the amount of modulus anisotropy is still much less than in fiber reinforced composites.

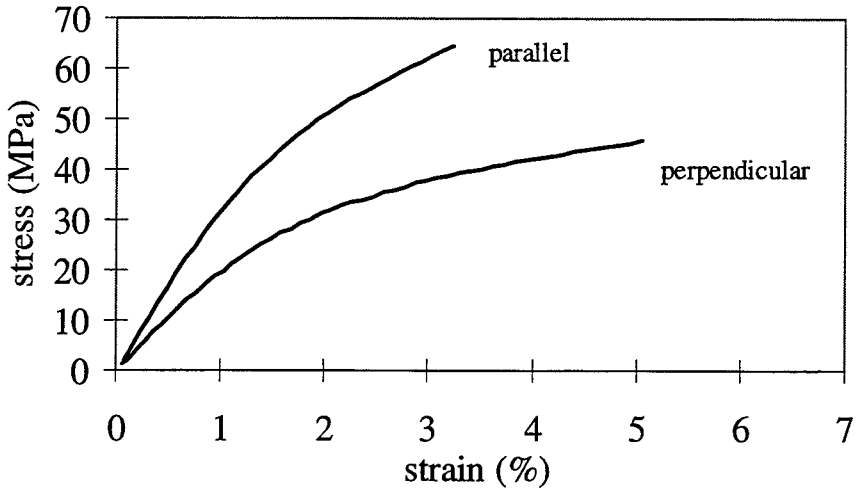


Figure 5. Typical tensile stress-strain curves for polymer N2 after UV postcure

Postcure Effects

While the glass transition temperature of the green polymer is already higher than current commercial resins, considerable advancement of the glass transition temperature is possible by postcuring. Two approaches to postcure have been studied: UV postcure at lower temperature and dark postcure at higher temperature. Figure 6a shows the effect of UV postcure on polymer N2. For these samples, a 100 W mercury vapor lamp was used to postcure with the temperature held at 150 °C. The data show that as postcure advances, the glass transition temperature shifts upward towards an ultimate T_g of approximately 120 °C as measured by the peak in the loss modulus at 1 Hz. In addition the intensity of the glass transition loss peak decreases as shown by the tan δ data. This decreasing intensity of the glass transition is an indication of the increasing crosslink density which results in an even stiffer network above the glass transition.

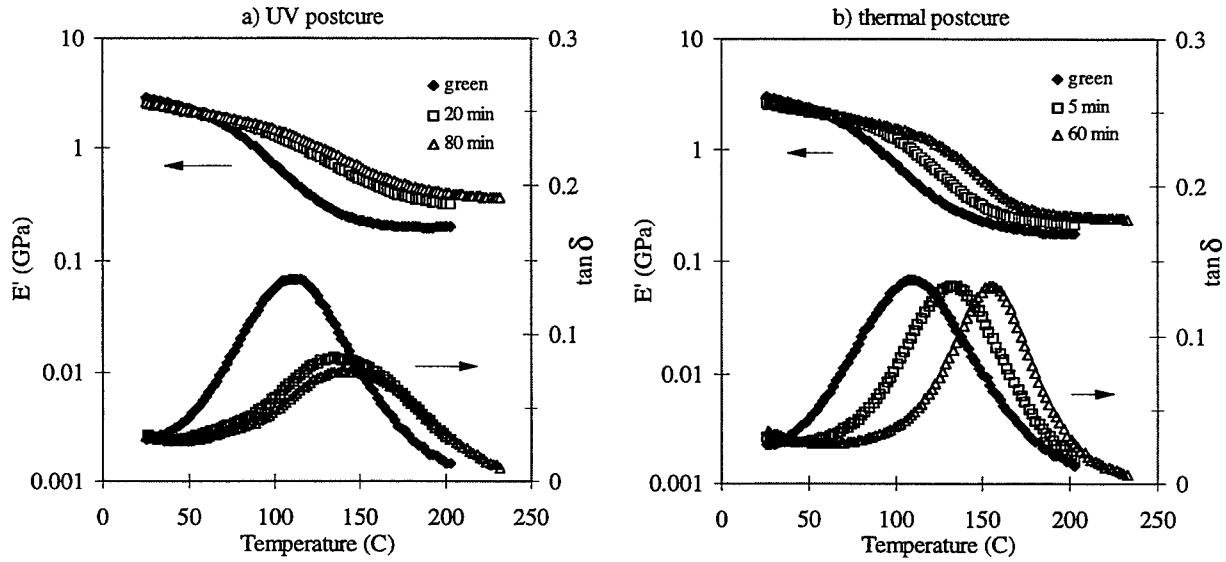


Figure 6. Postcure effects on N2 resin.

Figure 6b shows the effect of high temperature (250 °C), dark postcure on polymer N2 after various lengths of time. As in the UV postcure, the glass transition shifts upward, however the T_g's obtained from thermal postcure can be considerably higher. Instead of the 120 °C ultimate T_g from the UV postcure, thermal postcure can result in T_g's as high as 150 °C for polymer N2 and 105 °C for polymer N1. However, while the glass transition becomes weaker and broader during UV postcure (i.e. the tan δ peak), the thermal postcure results in glass transitions that are just as intense as in the green part. This indicates that with a high temperature thermal postcure, the increase in T_g may arise from a different chemical reaction than occurs in the UV postcure.

Linear Expansion

Just as the aligned polymer samples have anisotropic mechanical modulus and strength, they also have anisotropic thermal expansion. Figure 9 compares the linear expansion of polymer N2 with the commercial resin, SL5170. In the direction perpendicular to the alignment (i.e. in the y direction), the linear expansion of N2 looks much like the commercial polymer, with the linear thermal expansion coefficient going from approximately 110 mm/m°C below T_g to 220 mm/m°C above T_g . In the direction parallel to alignment, the liquid crystal polymer has a very small positive coefficient of expansion below T_g which changes to a negative coefficient of expansion above the glass transition region. This type of response has been cited in the literature for other LC thermosetting systems[5]. Thus, molecular alignment results in anisotropic thermal expansion, and by varying the layer to layer alignment, composite like structures can be manufactured to directionally optimize the linear expansion properties.

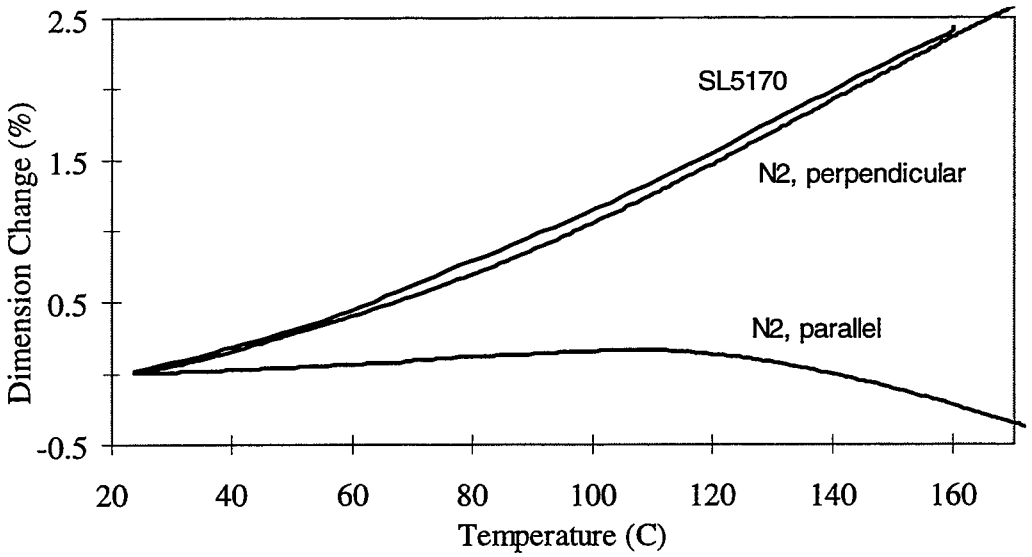


Figure 7. Linear expansion of N2 liquid crystal resin and XB5170 commercial resin.

CONCLUSIONS

Two liquid crystal monomers were processed in a table-top stereolithography apparatus. A magnet placed outside the vat aligned the monomer before photopolymerization. FTIR spectroscopy showed that the alignment was locked in by the photopolymerization, and that the amount of order in the polymer was relatively independent of polymerization temperature.

The aligned polymer specimens show anisotropic mechanical and physical properties. Glassy state elastic moduli of samples tested parallel and perpendicular to the alignment direction differ by a factor of two. The tensile strength shows a similar anisotropy. Linear expansion is similar to that of the commercial SLA resins in the direction perpendicular to alignment, while in the direction parallel to alignment, the expansion coefficient is very small and even becomes negative at temperatures above the glass transition.

In addition to the anisotropic properties, these new stereolithography resins show high glass transition temperatures. Green specimen T_gs ranged from 50 to 82 °C while postcured specimens had T_gs ranging up to 150 °C.

ACKNOWLEDGMENTS

The authors are pleased to acknowledge that this research was supported by the U.S. National Science Foundation through NSF Grant # DMR-9420357, from the Polymer Program, Division of Materials Research. Dr. Andrew Lovinger was program manager. From the University of Dayton, we also thank Mary Galaska and Katy Weaver for assistance in sample preparation and setting up experiments.

REFERENCES

1. Ullett, J.S., Schultz, J.W., Chartoff, R.P.. (1997) "Advanced High Temperature Resins for Stereolithography," ***Proceedings, 7th International Conference on Rapid Prototyping***.
2. Broer, D.J. , Mol, G.N., Challa, G. (1991) "In Situ Photopolymerization of an Oriented Liquid-Crystalline Acrylate, 5, Influence of the Alkylene Spacer on the Properties of the Mesogenic Monomers and the Formation and Properties of Oriented Polymer Networks," ***Makromol. Chem.***, 192, 59-74.
3. Ullett, J.S., Chartoff, R.P., Schultz, J.W., Bhatt, J.C., Dotrong, M., Pogue, R.T., (1996) "Low Shrinkage, High Tg Liquid Crystal Resins for Stereolithography," ***Solid Freeform Fabrication Proceedings***, Univ. Of Texas, Austin, TX September 1996, 471-479.
4. Herskowits, V., Meller, A. (1993) "Translation of the RP Process into Laboratory Characterization of RP Materials," *Proceedings, 4th International Conference on Rapid Prototyping,* Univ. of Dayton, Dayton, OH, 185-196.
5. Barclay, G.G., McNamee, S.G., Ober, C.K., Papathomas, K.I., Wang, D.W., (1992) "The Mechanical and Magnetic Alignment of Liquid Crystalline Epoxy Thermosets," *Journal of Polymer Science: Part A: Polymer Chemistry*, 30, 1845-1853.

Novel Liquid Crystal Monomers for Stereolithography: Reaction Rates and Photopolymerization Conversion

Robert T. Pogue and Richard P. Chartoff
The Center for Basic and Applied Polymer Research and
Rapid Prototype Development Laboratory
University of Dayton
Dayton, OH 45469-0130

ABSTRACT

Liquid crystal (LC) monomers are a novel type of resin for stereolithography that result in polymers having unique physical and mechanical properties. These monomers consist of rigid central cores connected to acrylate functional groups by short aliphatic chains. Because of the rigid-rod structure of the monomer the cross-linked polymer networks formed have high glass transition temperatures (T_g). The high T_g's result in particularly high upper-use temperatures for stereolithography parts.

This paper reports on photopolymerization reaction rates and monomer conversion for two acrylate monomers measured using reflectance real-time infra-red spectroscopy (RRTIR). The RRTIR method measures the disappearance of reactive acrylate groups in the monomer as a function of time while the monomers are being exposed to UV light. For the two new resins, UV irradiation using an argon ion laser gives rapid photopolymerization with acrylate conversion as high as 95 %. Conversion and polymerization rates in these monomers are dependent upon photo-initiator selection and concentration. In addition, the results indicate that conversion increases with increased laser intensity and elevated temperatures.

INTRODUCTION

Previously, researchers at the University of Dayton introduced the technique of reflectance real-time infra-red (RRTIR) spectroscopy for evaluating resins used in stereolithography [1]. This method is an extension of a technique originally described by Decker and co-workers [2,3] which allowed the elucidation of reaction rates and monomer conversions for photopolymerization reactions completed within seconds of the initial irradiation. The original method involved a transmission infra-red spectrometer held at the wavelength of interest throughout the measurement. The reflectance technique uses a similar detection scheme, but expands on these capabilities by allowing precise control of the photopolymerization temperature [1]. Using RRTIR, Chartoff and Du investigated the effects of irradiation time, laser power, and temperature on the monomer conversion and polymerization rates for two diacrylate stereolithography resins [1]. In the current paper, we discuss the application of this technique to two liquid crystalline (LC) diacrylate monomers which are being evaluated for use in stereolithography. The RRTIR technique is particularly useful for such experiments since it requires very small samples (a few mg). This is an advantage in developing experimental resins where only small amount of the monomer are available.

LC monomers are a new category of stereolithography resins [4, 5]. Chemically, they consist of rod-like cores which are attached to reactive end-groups by aliphatic spacers. These monomers are of considerable interest because the high T_g's of the resulting crosslinked

polymers allow high upper use temperatures for the build object. In addition, the ability to cure LC monomers in an aligned state allows the user to impart anisotropic mechanical properties to stereolithography parts [5]. In order to determine the operating conditions needed to optimize the properties of any new monomer system it is necessary to fully understand the polymerization rates and conversions which occur under high intensity illumination. However, unlike commercially available stereolithography resins, the LC resins are crystalline at room temperature. For this reason instrumentation used to probe the curing reactions must be able to operate at elevated temperatures. RRTIR is ideally suited for this application.

In this paper, the effects of several operating parameters on both reaction rates and conversion are discussed for laser irradiation of thin LC films. The data indicate that both rate and conversions are related to laser intensity and reaction temperature. Moreover, the results reveal that polymerization rates are affected by both photoinitiator type and concentration. The final monomer conversion, however, does not vary significantly when only photoinitiator parameters are taken into account.

EXPERIMENTAL

Materials: The two LC monomers of interest are shown in Figure 1 and were first reported by Broer et al. [6-8]. Recently, Ullett, et al. described the use of these materials in rapid prototyping and discussed some of the processing conditions which are necessary for their use [5]. In this study, monomers **1** and **2** were formulated with two photoinitiators (shown in Figure 2), **3**, (Irgacure-369, Ciba-Geigy Corp.) and ,**4**, (Darocur-4265, Ciba-Geigy Corp.). Photo-resins were prepared by mixing the appropriate amounts of both monomer and photoinitiator in a methylene chloride solution under low-light conditions. The solutions were then vacuum dried for several hours. Samples were refrigerated until use. RRTIR measurements were conducted by placing a small amount of resin onto a pre-heated sample holder. The samples were allowed to melt into the LC phase and then covered with a NaCl window. Sample thickness was less than 10 μ in all cases.

Instrumental: RRTIR is a dispersive IR method. The RRTIR assembly (Figure 3) consists of a Nernst Glower and controller designed at the University of Dayton to maintain a constant signal output in the range from 0.5 to 25 μm. After reflecting off the polished brass sample holder, the IR light is directed through a chopper operated at 1 kHz. The beam then passes through a monochromator and into a mercury cadmium telluride IR detector cooled by liquid nitrogen. Using this instrumentation, IR absorption data were collected at a wavelength of 810 cm^{-1} corresponding to the C=C bending vibration of the acrylate double bond. Data were collected at regular intervals beginning 0.5 ms after initial laser exposure. The samples were irradiated for the appropriate time by an argon-ion laser operating at 363.8 nm. The laser power was 0.05 W/cm^2 unless otherwise noted. Sample temperature was regulated by heating the brass sample block using a variable transformer attached to a strip heater.

RESULTS

Relationship between laser power and monomer conversion: The intensity of the incident radiation is an important factor in the initiation step of the free-radical crosslinking reaction. Changes in laser power can be related directly to the number of photoinitiator molecules which undergo dissociation during the first step of initiation. Since this step is the rate determining step in the initiation sequence, it must be considered in the determination of the overall rate of polymerization. It follows then, that the overall rate of polymerization is related to the intensity

of the radiation source. Figure 4 illustrates the change in monomer conversion for three different laser power settings. The lowest power employed (0.05 W/cm^2) is the lowest setting at which photopolymerization is observed for this resin system. The figure reveals that the major portion of the total reaction is completed within the first second of irradiation. It is also evident from the data that both reaction rate and conversion increase with increasing intensity at low powers (<10 mW). At higher powers both conversion and rate increase asymptotically until increasing the laser power no longer has a significant effect. This apparent deviation from the expected relationship may be caused by self-termination of photoinitiator radicals due to their increased population in the illuminated region.

For comparison, samples of SL5149 (Ciba-Geigy) were analyzed with RRTIR at room temperature using the 0.05 W/cm^2 setting. This resin cured much more slowly than the resin comprised of monomer **1** and 0.5 % of **3** under the same laser irradiation. Furthermore, the commercial resin still exhibited significant cure advancement after 10 s of irradiation, and the final conversion (after 100 s exposure) was less than 0.6.

Effects of photoinitiator type and concentration: Two commercial photoinitiators were tested in the development of the LC resins. In order for the resins to be applicable to stereolithography, it is necessary that they cure rapidly enough to permit acceptable scan speeds, that conversion is great enough to impart sufficient green strength to the part, and that swelling of the solid polymer is negligible. In addition to these requirements, the photoinitiator variables must be carefully selected so that appropriate penetration depths can be reached. Ullett and co-workers [5] previously reported that monomer **2** containing 2 % of **3** yields a penetration depth of less than 80 μ (2.7 mils). Under the same conditions a sample of **2** containing 0.5 % of **3** gave penetration depths greater than 190 μ (7.3 mils). The RRTIR results for these two resins are shown in Figure 5. From the slopes of these conversion curves it is evident that polymerization rate increases when the initiator concentration increases. The increased rate found in samples having greater photoinitiator concentrations leads to faster film formation and reduced laser penetration in these samples. This result is consistent with those observed by Ullett et al. [5] and helps to explain the relationship that was observed between photoinitiator concentration and penetration depth in their stereolithography working curves. It is important to note that this difference in rate causes the conversions at short exposure times (< 2 s) to be widely different between the two resin formulations. At extended irradiation times (up to 100 s) the difference in conversion between the two is less than 5%.

Examples of monomer 1 containing two different photoinitiators are shown in Figure 6. Here **3** is shown to give much faster polymerization rates than observed when **4** is used as the photoinitiator. Again, the RRTIR data are consistent with working curve data which reveal that samples containing **4** yield deeper penetration depths than those containing **3** [9]. Again, it is important to note that at longer irradiation times (up to 100s) the difference in monomer conversion between the resins containing different photoinitiators is less than 5%.

Effects of temperature on kinetic results: Comparison of conversion profiles for monomer **2** is given in Figure 7 at two temperatures. The final conversion (after 100 s irradiation) increases from approximately 84 % at 85 °C to greater than 95 % at 100 °C. Two factors may be contributing to the high conversions which are observed. First, it has been demonstrated with differential photo-calorimetry that in monomer **1** [10] and others [7, 11] both polymerization rate and conversion increase with polymerization temperature up to the point where the monomer undergoes a transition from a nematic liquid crystal to isotropic liquid. In addition, Ullett et al. have reported that the glass transition temperature (T_g) of the polymer resulting from the laser photopolymerization of **2** ranged from 75 to 94 °C following postcure [5]. During RRTIR

analysis of the reaction at 100 °C the reaction temperature is higher than the highest observed T_g. Therefore, the growing network remains in the rubbery state and the mobility of the chain radicals is not restricted by network vitrification.

Figure 8 reveals the relationship between temperature and polymerization rate for monomer **1** containing 2 % of **3** at six different fractional conversions. From this figure, several trends are evident. First, the polymerization rates increase with temperature up to 95 °C. Above this temperature the rates plateau at lower conversions and decrease slightly at higher conversions. Second, the polymerization rate is highest at a fractional conversion of 0.2 for all temperatures. Finally, the change in polymerization rate with temperature is much greater at higher conversions than at lower conversions. At 60 % conversion the rate undergoes a three order-of-magnitude change over the observed temperature range. In contrast, at 10 % conversion there is less than one order of magnitude change in the rate.

CONCLUSIONS

The effects of operating parameters on polymerization rates and monomer conversion for two experimental liquid crystalline monomers have been investigated using reflectance real-time infra-red spectroscopy. This technique is well suited for investigating monomers of this type since it ideal for documenting rapid reaction, uses only small samples, and operates conveniently at elevated temperatures. The results indicate that both conversion and rate increase asymptotically with temperature as well as laser power. Furthermore, changes in photoinitiator type and concentrations can alter the polymerization rates significantly. It is interesting to note that changing the photoinitiator type or concentration do not change the overall conversion. Using RRTIR it is possible to investigate the effects of operating parameters on small amounts of developmental resins prior to scale-up for testing in the stereolithography apparatus.

ACKNOWLEDGEMENTS

Financial support for this project was provided by the National Science Foundation (NSF Grant #DMR-9420357), Division of Mathematical and Physical Sciences, Polymer Program. Dr. Andrew Lovinger was NSF program manager. The authors would like to thank Jill Ullett for her helpful suggestions, John Murphy for help with the RRTIR experiments and Katy Weaver for her help in preparation of the LC resins.

REFERENCES

1. Chartoff, R. P., and J. Du, Proceedings of the 6th International Conference on Rapid Prototyping, Dayton, OH, 1995, pp. 103-111.

2. Decker, C. and K. Moussa, *Macromolecules*, **1989**, 22, 4455-4462.

3. Decker, C. and K. Moussa, *Makromol. Chem.*, **1988**, 189, 2381-2394.

4. Ullett, J. S., R. P. Chartoff, J. W. Schultz, J. C. Bhatt, M. Dotrong and R. T. Pogue, Solid Freeform Fabrication Proceedings, Austin, TX, 1996, pp. 471-479.

5. Ullett, J. S., J. W. Schultz and R. P. Chartoff, Proceedings of the 7th International Conference on Rapid Prototyping, San Francisco, Ca, 1997, pp. 203-211.

6. Broer, D. J., G. N. Mol, and G. Challa, *Makromol. Chem.*, **1989**, 190, 19-30.

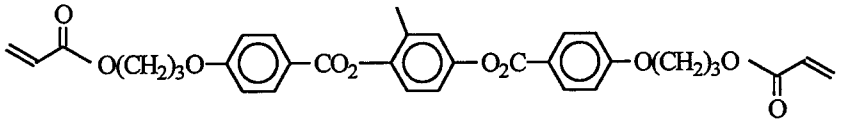
7. D. J. Broer, J. Boven and G. N. Mol, *Makromol. Chem.*, **1989**, 190, 2255-2268.

8. Broer, D. J., R. A. M. Hikmet and G. Challa, *Makromol. Chem.*, **1989**, 190, 3201-3215.

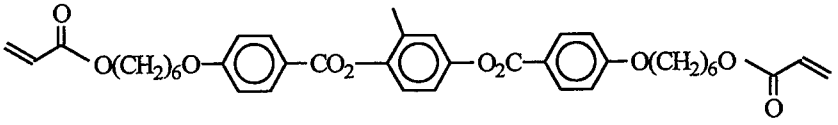
9. Ullett, J. S. and R. P. Chartoff, unpublished results.

10. Pogue, R. T. and R. P. Chartoff, unpublished results.

11. Broer, D. J., G. N. Mol, and G. Challa, Makromol. Chem. **1991**, 192, 59-74.

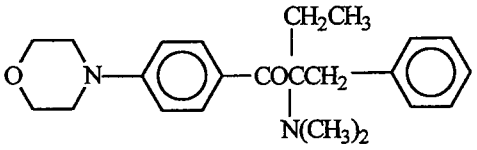


1

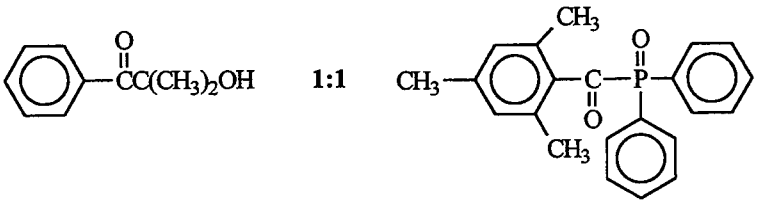


2

Figure 1. Chemical structures of the LC monomers



3



4

Figure 2. Chemical structures of the photoinitiators

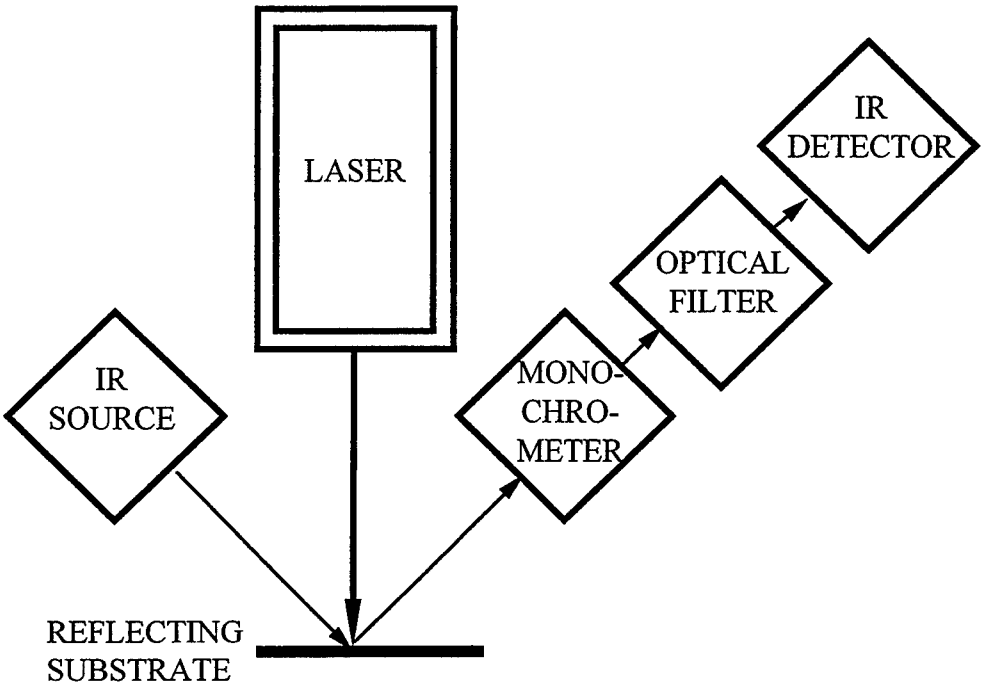


Figure 3. Block Diagram of RRTIR apparatus showing major components.

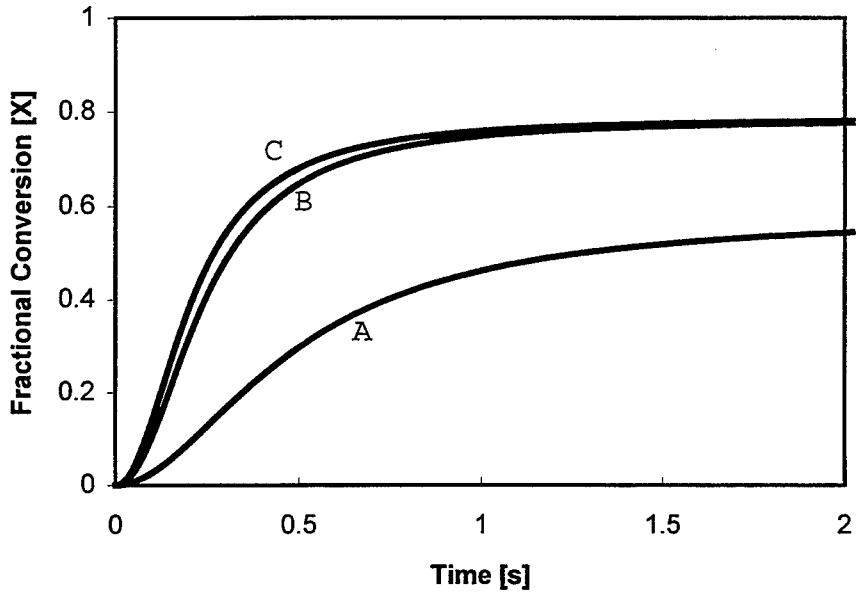


Figure 4. RRTIR Conversion profiles for monomer **1** containing 0.5 % **3** at (A) 0.05 W/cm^2, (B) 0.27 W/cm^2, and (C) 0.5 W/cm^2 laser power; 363.8 nm irradiation with argon-ion laser at 85 ^{o}C.

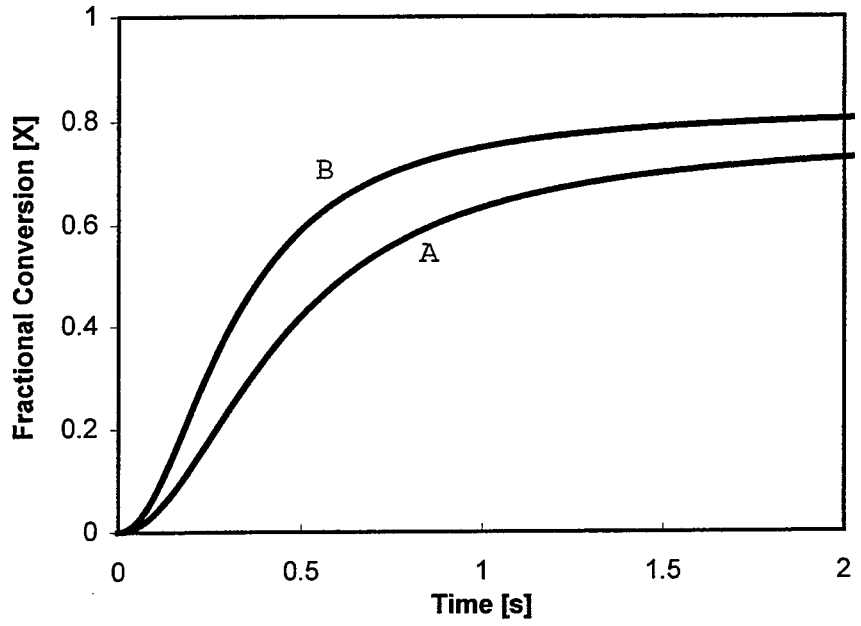


Figure 5. RRTIR conversion profiles for monomer **2** containing (A) 0.5 % and (B) 2 % of **3**; 363.8 nm irradiation at 85 °C, 0.05 W/cm^2.

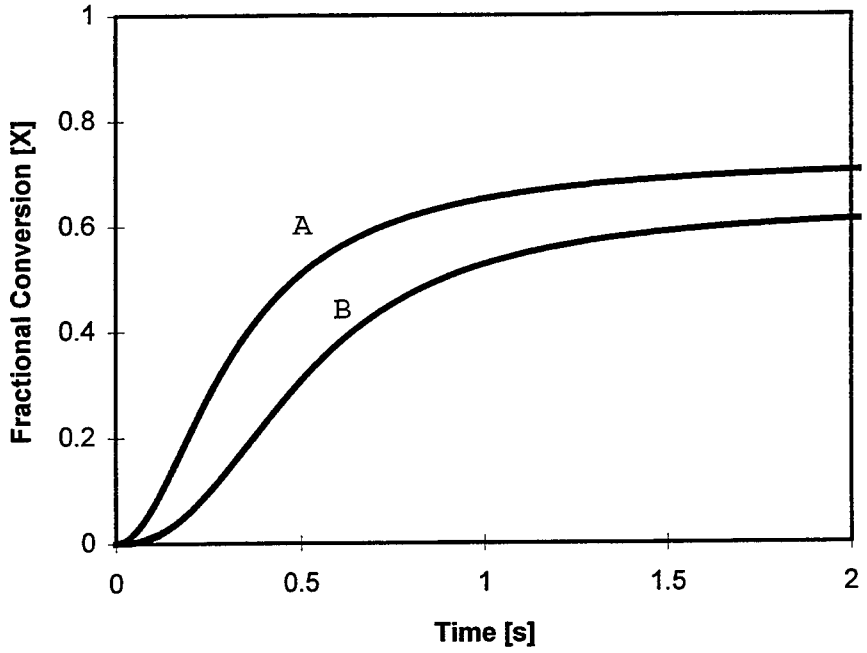


Figure 6. RRTIR conversion profiles for monomer **1** containing (A) 1 % of **3**, and (B) 1 % of **4**; 363.8 nm irradiation at 85 °C, 0.05 W/cm^2.

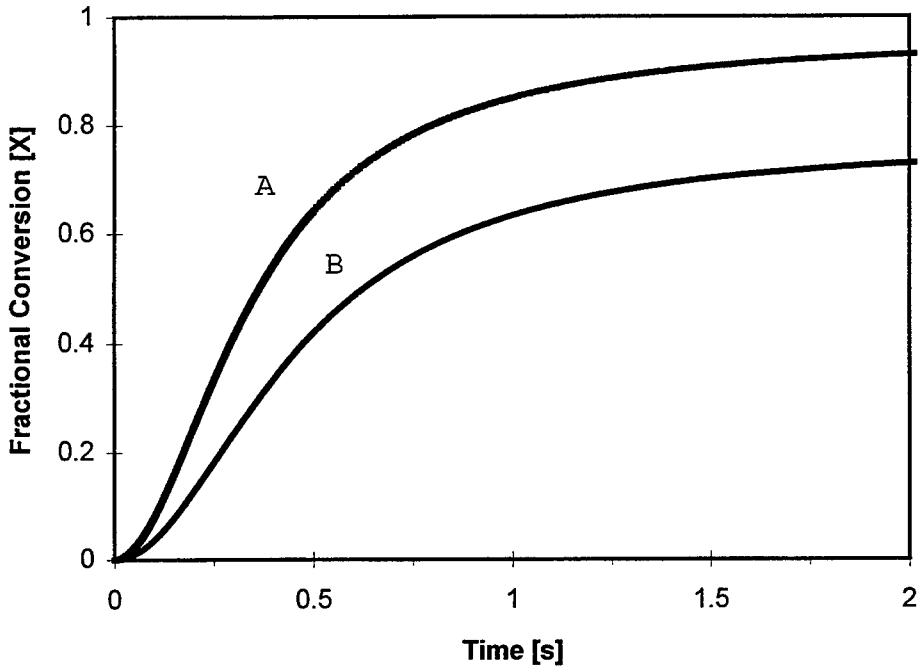


Figure 7. RRTIR conversion profiles for **2** containing 0.5 % of **3** at (A) 100 °C and (B) 85 °C; 363.8 nm irradiation with argon-ion laser at 0.05 W/cm^2.

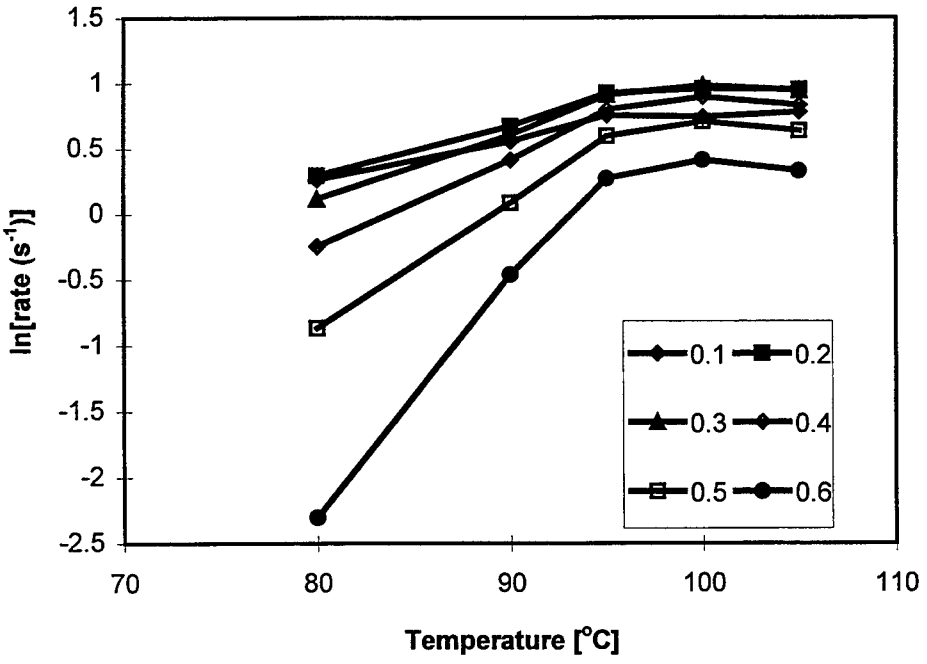


Figure 8. Relationship of reaction rate with temperature for six fractional conversion values for monomer **1** containing 2 % of **3** (wt/wt.); 363.8 nm irradiation with argon-ion laser at 0.05 W/cm^2.

Silica Filled Resins for Rapid SLA Tools

Douglas Taft Amod Ogale Frank Paul Elaine Hunt
Said Ahzi
Department of Chemical Engineering Department of Mechanical Engineering
Laboratory for the Advancement of Industrial Prototyping (LAIP)
Clemson University Clemson, SC 29631

Abstract

A stable silica /SL epoxy resin suspension has been developed at Clemson University. It has been processed to make parts in a commercial StereoLithography Apparatus (SLA). Results of testing show that the composite material has a higher modulus and increased abrasion resistance over the neat epoxy resin. An injection molding die has been made with the reinforced resin in the SLA and tested.

Introduction

StereoLithography (SL) has been used since its introduction in 1988 to build rapid prototypes of solid models out of photo polymers [1]. The solid models were a major development in product design, but not without limitations. Large flat parts would often build with a warp, due to shrinkage of each layer on top of the next. In 1993, 3D Systems released an epoxide based resin, SL-5170, with the intention to reduce curl and shrinkage in parts [2]. SL-5170 was an improvement over previous resins and is widely used in StereoLithography Apparatuses (SLAs) today. However, the mechanical properties of the crosslinked photo resins are different from the thermoplastics that many production parts are made of. Thus, performance tests are difficult to realize with direct rapid prototype (RP) parts.

The need for true prototypes prompted the idea of injecting thermoplastic into dies made in the SLA to produce an RP part made in the production material. In 1996, 3D Systems described the use of SL-5170 (and SL-5180) for building core and cavity inserts for injection molding of a limited quantity of high impact polystyrene parts [3]. Unfortunately, SL-5170 begins to soften at temperatures above 75°C, more than 100 °C below the normal injection temperature of some common thermoplastics, greatly limiting the number of parts (if any) that can be made in an SLA die [3]. However, previous research on particulate filled polymers has established the improvement in the resulting composite properties, including the thermal stability that is important in rapid tooling applications. The objective of this research was to develop a particulate reinforced resin suspension that is suitable for use in an SLA to make core and cavity dies.

Experimental

Materials

Powdered silica was used as a reinforcement in this study. It was added to Ciba Geigy SL-5170 to form a suspension. Viscosity measurements were conducted for the

particulate filled suspension samples at room temperature (73-75°F) using a Contraves Rheomat 15 concentric cylinder viscometer.

Processing

After compounding the suspension, it was introduced into a 3D Systems SLA-250/50 (equipped with a Zephyr recoater). The vat temperature was set to 28°C. Initially, the critical exposure (E_c) and depth of penetration (D_p) were not known for the suspension (the laser scan speed, V_s, was adjusted by varying E_c with D_p held constant in the resin file; V_s is inversely proportional to E_c on the SLA-250/50). Therefore, E_c was set to a high value of 150 mJ/cm^2 in the resin file and a single layer was drawn with success to verify that the resin would cure under laser power.

During subsequent processing trials, two build parameters were of primary concern. First, the scan time per layer, defines the amount of incident energy received by a layer, and is inversely proportional to E_c in the resin file. The second parameter was the time required for an uncured layer to level before being cured by the laser, Z-wait [1]. The first build was conducted using an E_c of 50 mJ/cm^2 and a Z-wait of 25 s. However, it was observed that the 25 s Z-wait did not allow the layers to level. Therefore, the next build was attempted with a longer Z-wait of 60 s, and was successful.

To characterize the composite material thus produced, four ASTM D638 Type I [4] dogbones and six ASTM D695 [5] compression samples were built using the same parameters as the first successful build. A block, 10 mm long, 10 mm wide, and 3 mm thick on a support structure of 0.25 in. was built repeatedly to refine the build parameters. It was observed that a Z-wait of 120 s and an E_c of 20 mJ/cm^2 in the resin file resulted in parts of satisfactory quality. An injection molding die with cavity dimensions specified according to ASTM D638 (Type I) was then processed in the SLA using the reinforced resin suspension with the refined processing parameters.

Characterization

Tensile properties of the particulate composite were investigated using ASTM D638 Type I dogbones. All tests were conducted in an Applied Test Systems (ATS) 900 universal testing machine. Load output was recorded using one channel of a Linseis L6012B 2 channel chart recorder. Three of the samples were tested for strength. The fourth sample was mounted with a Micro-Measurements type EA-50-125AC-350 strain gauge, wired to a Measurements Group P-3500 Strain Indicator. Output from the strain indicator was recorded simultaneously with load from the ATS on the chart recorder.

Injection Molding

Performance of the reinforced material was investigated by testing the ASTM D638 (dogbone) cavity made in the SLA-250/50 in an injection molding machine. An identical cavity was made in the same SLA from neat SL-5170 using standard build

parameters for neat SL-5170 as a control for testing. Both cavities were measured on a CMM coordinate machine (Brown and Sharpe) after postcure.

A standard procedure for finishing and mounting the dogbone die had been established with previous dies made in neat SL-5170. Approximately 20 mils of material was removed from the back of the SLA die for fitting into a Master Unit Die (MUD) frame using a belt sander. This proved ineffective for the reinforced resin die because of the high abrasion resistance. Consequently, a milling machine was used.

Injection molding was done in an Arburg 221-55-250 Allrounder 28 ton injection molding machine. Both dies were mounted in the Master Unit Die frame on the ejector side of the clamp. Because the "core" side of the dogbone was flat, a MUD insert made of tool steel was used. Six ejector pins were used in each die, two of which were fitted with thermocouples wired to a Linseis L6012B 2 channel chart recorder. Both MUD frames were cooled with city water (25°C). Manual cycle was used because flash caused parts for both dies to hang on an ejector pin during ejection. Cooling time was set at 30 seconds; actual cycle time was approximately 45 seconds which varied slightly because parts were removed by hand from the sticking ejector pin. General purpose polystyrene (GPPS) was injected at a temperature of 220°C and an injection pressure of 8000 psi.

Results and Discussion

Suspension Viscosity

Adding a solid reinforcement raises the viscosity of a liquid resin. Therefore, viscosity tests were first conducted to obtain an understanding of the flow characteristics of the suspension. *Figure 1* displays the viscosity of the suspension as a function of shear rate. The viscosity does not change significantly within the shear rate range of 2.5 s^{-1} to 25 s^{-1}. At a nominal shear rate of 15 s^{-1}, the viscosity of the suspension is 1500 cP. This

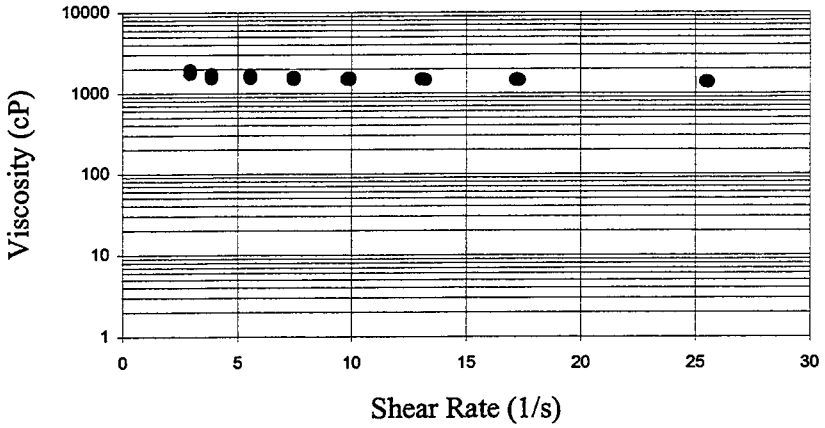


Figure 1. Viscosity Versus Shear Rate of a Sample of Reinforced Resin Suspension from the SLA-250/50 Vat.

value is about five-fold higher than that of 235 cP for the pure resin [6] and justifies the

longer Z-wait needed for the particulate suspension as compared with that for the pure resin.

Several equations have been proposed in the literature to predict the viscosity of suspensions [7]. *Figure 2* displays the predictions for the viscosity ratio (η/η_o) as a function of the weight fraction of the particulates using the Einstein, Mooney, and

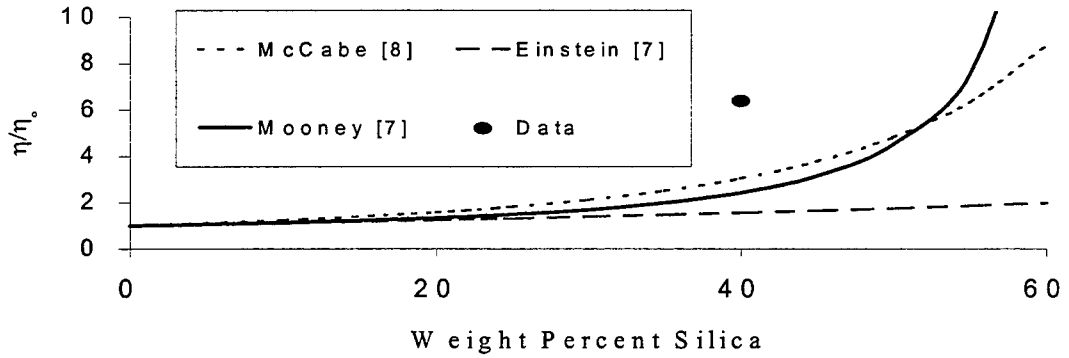


Figure 2. Comparison Between Empirical Equations for Estimating Viscosity of the Suspension and Experimental Data

McCabe [8] equations. The actual viscosity of the suspension is approximately twice that of the highest prediction. The most probable reason for the discrepancy is the agglomeration of the particles. It is known that agglomeration can lead to a viscosity ratio increase (at a fixed weight percent of particulates) of as large as 8 [7].

Stability of Suspension

Viscosity for samples from the SLA vat are shown over a 21 day period in *Figure 3*. Although the viscosity in the vat decreased slightly during the period, the actual change was less than 15% of the original value. A possible reason for the change in viscosity is the settling of particles during storage, a phenomenon that needs further investigation. However, the degree of settling was within useful limits.

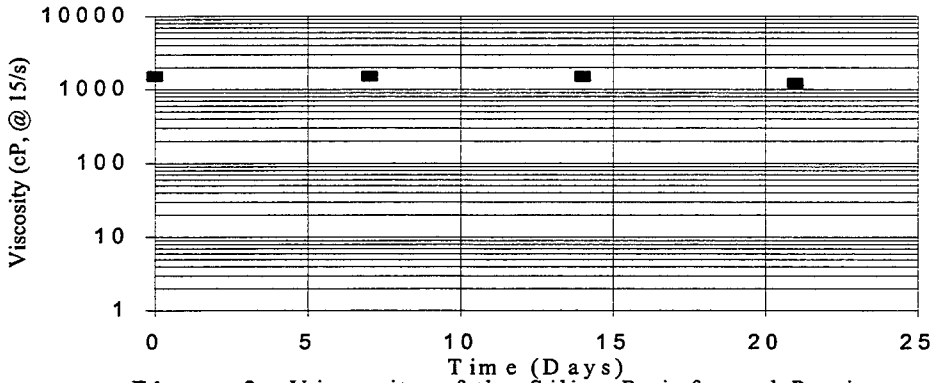


Figure 3. Viscosity of the Silica Reinforced Resin Over a 21 Day Period.

Processing in the SLA

Parts built with a Z-wait of 60 s in the reinforced resin exhibited a convex surface in the XY plane. This effect was a result of the laser scan commencing before the liquid resin had leveled off after recoating. As illustrated in *Figure 4*, a Z-Wait of 120 s eliminated the convex surface. However, because the convex layers of the part cured together properly even with a Z-Wait of 60 s, it is believed that the scan speed of the laser can be increased when building parts with a Z-Wait of 120 s due to the fact that there is less resin per layer to be cured.

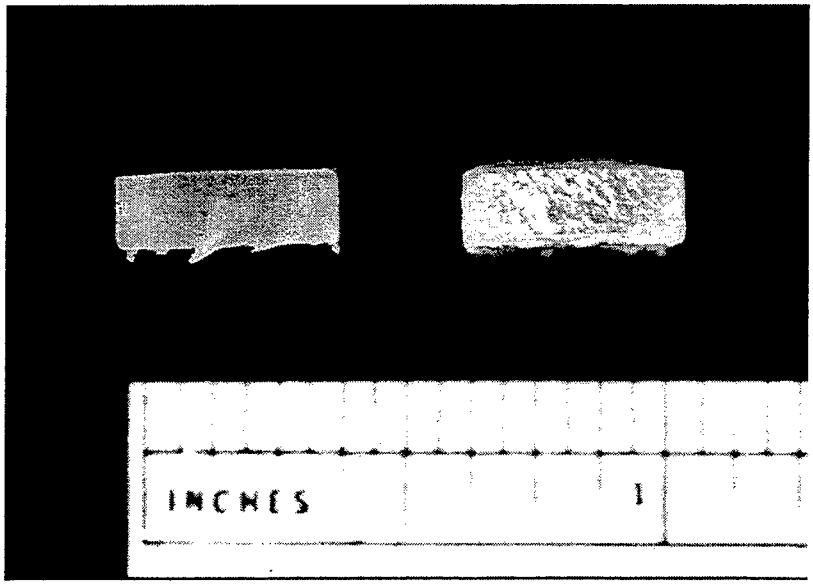


Figure 4. Sectional views of reinforced resin samples made at two different Z-waits – left: 120 s, and right: 60 s.

Dimensional Accuracy

Scattering of the laser beam by the reinforcement phase occurs because the refractive index of the silica is not identical to that of the resin [9]. This phenomenon is clearly seen with the naked eye during part building and was cause for some concern. If the beam scatters, a wider path is expected to be exposed to UV in the line drawn on the resin surface. The wider path drawn in the resin may affect part accuracy in the X and Y directions. The issue has not been fully investigated, but data for measurements on the cavity of the ASTM D638 Dogbone die are presented in *Table I.* Errors between the ASTM D638 CAD file specification and the actual SLA part were no larger for the reinforced resin than for the neat resin.

Table I. Dimensions of ASTM D638 Die Cavity

Dimension	Specification (in.)	Neat SL-5170 (in.)	Filled SL-5170 (in.)
Gauge Width 1	0.500	0.507	0.496
Gauge Width 2	0.500	0.507	0.496
Gauge Width 3	0.500	0.507	0.496

Injection Molding

The ASTM D638 Type I cavity die processed in the SLA using the reinforced resin was compared to an identical cavity die processed in the SLA using neat SL-5170. This test was performed to ensure that the composite material could, in fact, be used for rapid tools. Both the composite tool and the neat tool made 100 parts with no significant damage to the tool. The composite tool lost two small chips, one during ejection of part numbered 42 and the second during ejection of part numbered 49. The neat tool lost one chip during the ejection of part numbered 30. The temperature of both dies rose to 37°C after 10 molding cycles and remained steady thereafter.

The quality of parts leaving the mold did not appear to change (with the exception of the chips) during the test for both tools. *Figure 5* displays both the composite and the neat tools after testing along with parts numbered 12 and 100 from both tools. The parts injected in the composite tool appear opaque from the rough surface of the particulate reinforced resin.

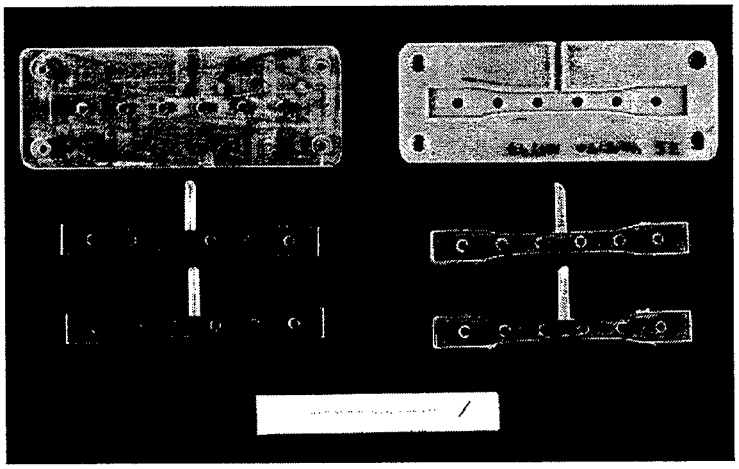


Figure 5. The neat SL-5170 ASTM D638 Die with 2 parts (left) and the reinforced SL-5170 Die with 2 parts (right).

Composite Material Characterization

The tensile strength of a particulate reinforced resin, σ, is expected to be less than the equivalent unreinforced resin tensile strength, σ_o, according to the equation

$$\sigma = \sigma_o(1 - (\frac{\phi_p}{\phi_m})^{\frac{2}{3}})$$

where ϕ_p is the volume fraction of the reinforcement and ϕ_m is the maximum packing content which can be assumed 0.6 for random loose packed spheres [10]. ϕ_p is 0.22 for 40 weight percent silica in SL-5170. According to the equation, it is expected that SL-5170 would lose 51% of its original strength after adding reinforcement. However, strength data, presented in *Table II*, indicated that the composite has a tensile strength of 48 MPa, a loss of only 20% as compared to that of neat SL-5170 [6]. A possible reason for the higher strength (than what is predicted) is the shape of the particles. Deviation from spherical shape toward an elongated shape will result in higher strength values.

Tensile modulus is expected to increase with the addition of particulate reinforcement. Quantitative estimates can be made using mechanical property data for the reinforcement phase and the resin phase (*Table III*). The estimated tensile modulus according to SMC, a program developed at the University of Delaware, is 4400 MPa compared to an experimental value of 2300 MPa for neat SL-5170 [6]. Experimental data indicated a tensile modulus of 4300 MPa for the reinforced photo polymer. It is expected that the more than 80% increase in the modulus (with the addition of particulates) will increase the creep resistance of the composite and will lead to an increase of the heat deflection temperature of the composite over that of the pure resin. These properties will be investigated in future work.

Table II. Properties of Composite

Property	Predicted	Experimental
Density (g/cm^3)	1.55	N/A
Tensile Modulus (GPa)	4.4	4.3
Tensile Strength (MPa)	30	48
Coefficient of Thermal Expansion (ppm/K)	55	N/A

Table III. Physical Properties of Silica and Ciba Geigy SL-5170

Property	Silica	Ciba Geigy SL-5170
Density	2.65 [11]	1.14 (uncured) 1.215 (cured) [6]
Refractive Index	1.55 [11]	1.49 (uncured) 1.53 (cured) [6]
Tensile Modulus (GPa)	73 [12]	2.3 [6]
Tensile Strength (MPa)	3400 [12]	60 [6]
Thermal Conductivity (W/m-K)	1 [12]	0.2002 [6]
Coefficient of Thermal Expansion (ppm/K)	5 [12]	90 [6]

Conclusions

The following conclusions are drawn from this study:

1. A silica/ epoxy suspension was used to make parts in a commercial StereoLithography Apparatus (SLA).
2. The composite material has an 80% higher modulus and increased abrasion resistance as compared to the base resin, and yet it retains about 80% of the strength of the base resin.

Acknowledgements

Financial assistance from the Industrial Consortium of the Laboratory to Advance Industrial Prototyping (LAIP) at Clemson University is gratefully acknowledged.

References

1. Paul F. Jacobs, "*Rapid Prototyping and Manufacturing: Fundamentals of Stereo Lithography*", Society of Manufacturing Engineers, Dearborn MI, 1992.
2. Thomas H. Pang, "*StereoLithography Epoxy Resins SL 5170 and SL 5180: Accuracy, Dimensional Stability, and Mechanical Properties*", p. 204, Proceedings of the Solid Freeform Fabrication Symposium, University of Texas, Austin, Austin Texas, August 8-10, 1994.
3. Paul F. Jacobs, "*Recent Advances in Rapid Tooling From StereoLithography*", product literature, 3D Systems, Valencia, CA, 1996.
4. Standard Test Method for Tensile Properties of Plastics (ASTM D638), Annual Book of ASTM Standards, American Society for Testing and Materials, Philadelphia, PA, 1995.
5. Standard Test Method for Compressive Properties of Rigid Plastics (ASTM D695), Annual Book of ASTM Standards, American Society for Testing and Materials, Philadelphia, PA, 1990.
6. 3D Cibatool® Resin Handbook, 3D Systems, Valencia, CA, 1994.
7. Lawrence E. Nielsen and Robert F. Landel, "*Mechanical Properties of Polymers and Composites*", 2nd edition, p. 378-382, Marcel Dekker, New York, 1994.
8. Warren L. McCabe, Julian C. Smith, and Peter Harriot, "*Unit Operations of Chemical Engineering*", fifth edition, p. 163, McGraw-Hill, New York, 1993.
9. Michelle L. Griffith and John W. Halloran, "*Ultraviolet Curing of Highly Loaded Ceramic Suspensions for StereoLithography of Ceramics*", p. 396, Proceedings of the Solid Freeform Fabrication Symposium, University of Texas, Austin, Austin Texas, August 8-10, 1994.
10. Thierry Renault, "*3-D PhotoLithography for Composites Development*", MS Thesis, Department of Chemical Engineering, Clemson University, May 1991.
11. "*Kirk-Othmer Encyclopedia of Chemical Technology*", 4th edition, vol. 10, p. 745-760, Wiley, New York, 1993.
12. Neil L. Hancox and Rayner M. Mayer, "*Design Data for Reinforced Plastics: A Guide for Engineers and Designers*", p. 97, Chapman and Hall, London, 1994.

SL 5410: High Humidity, Water, and Heat Resistant Resin for Stereolithography

Thomas Pang, Israel Figueroa, John Fong, Anastasios Melisaris, and Renyi Wang
Ciba Specialty Chemicals Corporation, Los Angeles, California

Stephen Hanna, Hop Nguyen, Michelle Guertin, and Cathy Phan
3D Systems Corporation, Valencia, California

(Presented at the Solid Freeform Fabrication Symposium, University of Texas at Austin, August, 1997)

Abstract

A new Stereolithography (SL) resin, CibaTool® SL 5410, which imparts good humidity and heat resistance, was released in July, 1997. This epoxy based resin for SLA-500 was developed mainly to eliminate the relatively weak resistance to high humidity and high heat that the first generation of resins suffered from. Namely, with this new resin, strength of QuickCast part and solid parts can now be maintained under high relative humidity. Even when immersed into water, part strength of SL 5410 is essentially preserved. Thermomechanical properties have also improved significantly relative to those of SL 5180. Heat deflection temperature and Tg values increased by +15°C to +40°C, to as high as 88 °C and 105°C, respectively, for SL 5410, when parts were additionally thermally postcured. Improvements in mechanical properties are also included in this paper. These property enhancements were achieved while further improving part accuracy, vertical surface finish, and productivity. Productivity may increase by as much as 2.5-fold over SL 5180. Also, SL 5410 requires no predip delay, hence cutting the overhead time. These newly achieved resin characteristics for SL 5410 are expected to improve the ease-of-use in today's applications, and open new fields of applications in the near future.

Introduction

Since the first commercialization in 1987, Stereolithography (SL) has established as one of the most accurate, efficient, reliable, versatile, and most widely used Solid Freeform Fabrication (SFF), or Rapid Prototyping and Manufacturing (RP&M) technologies available today, and continues to find worldwide acceptance. Among various elements that make SLA successful, resin technology is undoubtedly one of the key elements. Specifically, the upgrading of acrylate based to epoxy based SL resins in 1993 has shifted the paradigm of what can be achieved through SLA technology.

The first generation of epoxy based resins for 3D Systems Stereolithography Apparatus (SLA) were commercialized in 1993. The major advantages of these epoxy resins were their high accuracy, dimensional stability, mechanical properties, and numerous other positive characteristics that were not attained with the earlier acrylate based resins. However, one of the disadvantages of these first generation epoxy resins were their relatively poor humidity and water resistance. Also, their thermomechanical properties were often insufficient for thermally challenging applications[1] since they were not designed for that purpose.

SL 5410 was developed to combat these shortcomings, while maintaining almost all, or even improving some, of the positive traits generally associated with epoxy based SL resins. In the following sections, performance characteristics of SL 5410 will be presented, along with experimental data to support the claims. Improvements in high humidity and water resistance, heat resistance and other mechanical properties, as well as in part accuracy, surface finish, and productivity will be presented below. Other relevant material properties will also be included for purposes of reference.

Humidity Resistance

In order to measure humidity resistance, a small test part called "flexbar" having dimensions of 2.5 mm X 10 mm X 70 mm were built in the desired build style on an SLA. These parts were exposed to a designated relative humidity. Flexural modulus is then determined using a method similar to ASTM D790, as the samples were exposed over time to each environment. Both ACES solid and QuickCast quasi-hollow parts built in SL 5410 were tested in comparison with that of SL 5180.

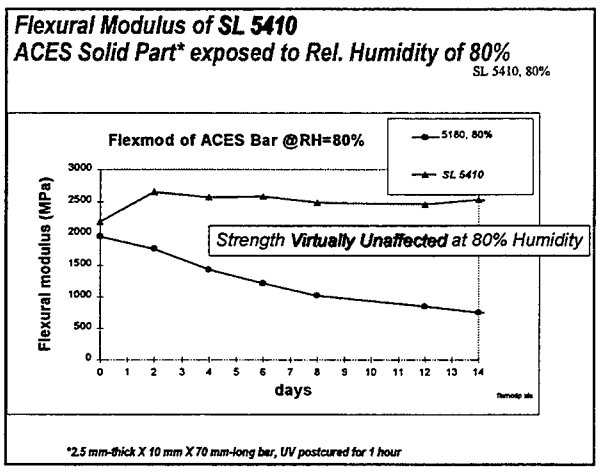


Figure 1

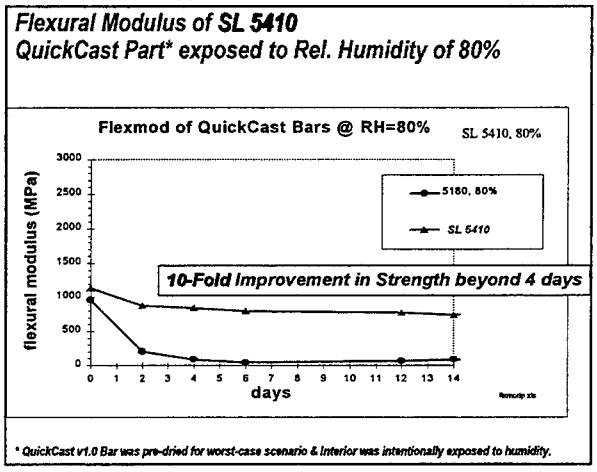


Figure 2

Flexural modulus of a solid test part built in SL 5410 is shown in **figure 1**. Notice that the flexural modulus of SL 5410 is almost invariable even when it is exposed to a relative humidity of 80%, while that of SL 5180 tends to decrease over time. In fact, the ultimate flexural modulus of SL 5410 is greater than at time = 0 since the resin undergoes continued epoxy crosslinking reaction. Hence, *flexural modulus of solid parts built in SL 5410 are virtually unaffected by humidity.* This property ensures that SL parts made in SL 5410 do not require special handling even under high humidities conditions. This should significantly prolong the useful life and increase the range of environments in which SLA parts can be used.

SL 5410 is also QuickCast capable. Based on one Beta test source, SL 5410 has not failed in the several months of testing, involving many different geometries. QuickCast parts for investment casting were built in the QuickCast 1.1 style. However, for purposes of comparing flexural modulus with data in the past, test parts were built using QuickCast version 1.0. Holes were drilled at the downfacing skins at the corners of the QuickCast flexbar test parts, and were left open to intentionally expose the internal sections to the surrounding humid air. This accelerates the water absorption and simulates the worstcase scenario of unsealed QuickCast parts.

The flexural modulus data of such a QuickCast test part built in SL 5410 is shown in **figure 2**. Here, there is an observable drop in modulus from about 1100 MPa to 800 MPa in about 2 days. Henceforth, the strength stays relatively constant. Notice that beyond about the 4-day mark, the *difference between the strengths of QuickCast parts built in SL 5410 and SL 5180 is more than ten-fold!*. This humidity resistance of SL 5410 is the key for potentially achieving much greater accuracy than SL 5180 for QuickCast casting process, since deformation is not expected to occur, and swelling due to humidity would be much reduced. Exposing SL 5410 QuickCast parts to atmosphere on or after a rainy day, or a humid day would not impair part strength.

Water Resistance

Water resistance has been measured with respect to part strength, shown in **figure 3**, and also with respect to photospeed variation, shown in **figure 4**. For the water resistance test, the flexbar part built in SL 5410 and SL 5180 were both completely immersed in water following the 1-1.5 hour of UV postcure. Notice that flexural modulus decreases for both resins during the first 7 days. However, the difference between SL 5180 to SL 5410 becomes very clear immediately.

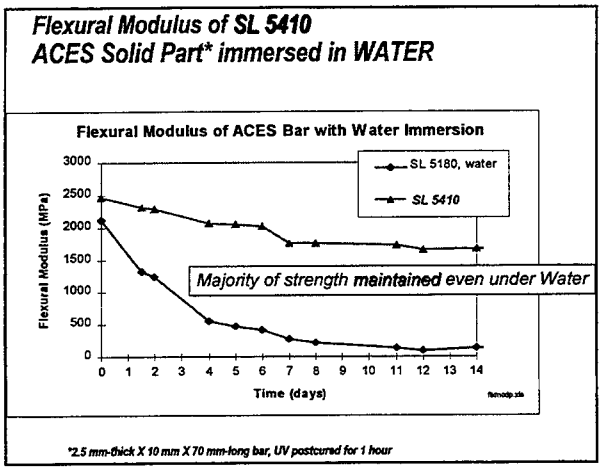


Figure 3

For example, let us define a 0.80-life to be the time that takes the modulus to drop by 20% of the initial value (e.g. down to 0.80 of initial), analogous to the concept of "half-life". Then, "0.80-life" of SL 5180 is one day. On the other hand, 0.80-life of SL 5410 is at least 5 days. By this measure, SL 5410 softens 5 times slower than SL 5180. An important point to make, however, is that after 7 days, SL 5410 stops becoming any softer. In comparison, modulus of SL 5180 continues to drop, and at 7 days it is only about 1/6 that of SL 5410. From this data, SL 5410 is expected to maintain flexural modulus of about 1700 MPa (~250 ksi) almost indefinitely in water, which should be sufficient for many applications.

This property shows that SL 5410 can be used in applications where the part may be constantly exposed to water. This is a new application area which could not have been easily carried out with, for example, SL 5180, unless surfaces were thoroughly coated with water repellent sealants beforehand. This was especially true to SL 5180 parts with very thin walls. However, now with SL 5410, even parts having thin walls have the potential to be used in under water applications.

To ensure that the photospeed of SL 5410 does not significantly change under high humidity environments, water was intentionally added to liquid resin, simulating water pick up by SL 5410. Standard WINDOWPANE working curves were constructed to measure the photospeed of the water-contaminated SL 5410. Water was added to the SL 5410 resin, up to a point (~ 2%) where the SLA laboratory environment corresponds to a relative humidity of 85%. Of course, if the SLA room is air-conditioned, such a high humidity is unattainable under normal circumstances. Therefore, this test simulates the worstcase that may more closely simulate an SLA that is placed in a non-air-conditioned room, and where the SLA may be exposed to the outdoor environment.

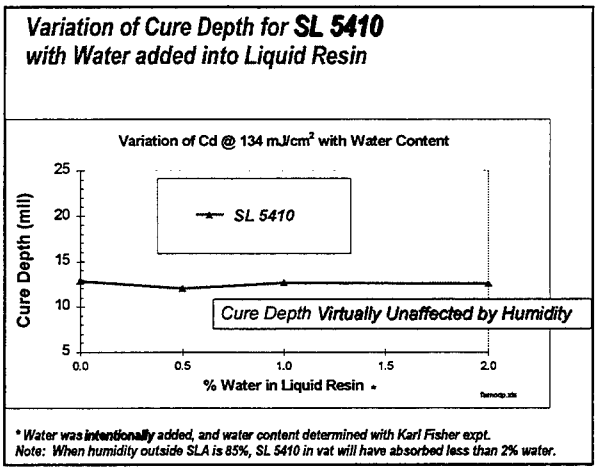


Figure 4.

In **figure 4**, cure depths at a constant laser exposure of 134 mJ/cm^2 are plotted as a function of the water concentration, as a measure of photospeed. Water concentration in the liquid resin was later confirmed by Karl Fisher titration. The data in this figure shows that the

change in photospeed of SL 5410 is negligible within the external relative humidity range of 0-85%. The cure depth variation for this test of ±0.3 - 0.4 mils, is actually well within the range of WINDOWPANE repeatability for the same resin. This test provides users the assurance that, not only do the cured parts perform, but liquid SL 5410 will build well on the SLA under high humidity conditions.

As an addendum, SL 5410 has also been confirmed to build well, while maintaining its photospeed, under extremely dry conditions. While no tests were run exclusively, SL 5410 continued to build good parts for several months in California, where the environmental humidity level at the time (inside the SLA lab), has been as low as 15-25% for a considerable period during the testing phase.

Mechanical Properties

Mechanical properties of SL 5410 are summarized in **Table 1**. Notice that both tensile and flexural strengths have increased by about 45-70% over SL 5180. Hence, SL 5410 would be able to take on higher loads than SL 5180 before part would give. Part rigidity, as measured by both tensile and flexural modulus, has also increased, making SL 5410 the most rigid SL resin for the SLA-500. This enhances the dimensional stability of parts made in SL 5410, especially under high humidity conditions, as discussed earlier. Elongation to break, however, decreased by about a factor of 2. Nevertheless, impact strength remains to be about the same as SL 5180, at a respectable 0.73 ft-LBS/inch, due to the increase in the ultimate strength compensating for the loss in elongation. These data show that SL 5410 has improved in many of the mechanical properties over SL 5180, in addition to the previously discussed improvements in humidity and water resistance. However, the most notable advances have been made in the thermomechanical properties, discussed in detail in the next section.

	SL 5410	SL 5180	Method
Tensile Strength	*10,450 psi*	6,150 psi	ASTM D638
Tensile Modulus	*449,000 psi*	391,000 psi	ASTM D638
Flexural Strength	*18,400 psi*	12,700 psi	ASTM D790
Flexural Modulus	*413,000 psi*	366,000 psi	ASTM D790
Elongation at Break	*4 - 7%*	6 - 16%	ASTM D638
Impact Strength, notched	*0.73 ft-lb/in*	0.6 - 0.8 ft-lb/in	ASTM D256
Hardness, ShoreD	*86*	84	ShoreD
Glass Transition Temp.	*105° C**	85°C	DMA tan delta @1Hz
	*88° C**	69°C	DMA E" peak @1Hz
Heat Deflection Temp.	*88° C**	49°C	ASTM D648 (@66psi)

** UV + thermally postcured @ 80°C for 2 hours.*
note: 145 psi = 1 MPa = 1 N/mm²

Table 1.

Thermomechanical Properties

Thermomechanical properties are not always as straight forward as one would like it to be. A simple statement of "a part having a Tg of 80°C cannot be used above 80°C" is not always true. This is because each testing method is performed in such a way as to address only one of many modes of application for the test material. For example, some SL parts are bent, while others are stretched. Others are exposed to hot air, and others are exposed to steam. The term "heat resistance" must be defined by special test methods.

Description of all of the test methods is beyond the scope of this paper, however, end-use application testing beyond the perceived thermomechanical values are highly recommended. Much of the recent, new applications of SL parts have emerged due to innovative pioneers pushing the envelope beyond the perceived limitations of the SL materials at the time.[2] These include such applications as direct tooling wherein engineering thermoplastics have been successfully injection molded into tools made of epoxy resins such as SL 5170, 5180, or 5190.[3, 4] It was, indeed, quite non-intuitive that SL 5180, having Tg_{DMA} of only 69°C, survived injection of thermoplastics at temperatures in excess of 200°C!

Three thermomechanical properties are presented here for both SL 5180 and SL 5410 resins, shown in **figures 5** and **6**. The first one is the heat deflection temperature (HDT), the second is the transition of coefficient of thermal expansion (CTE transition), and the third is the glass transition by dynamic mechanical analyzer (Tg_{DMA}).

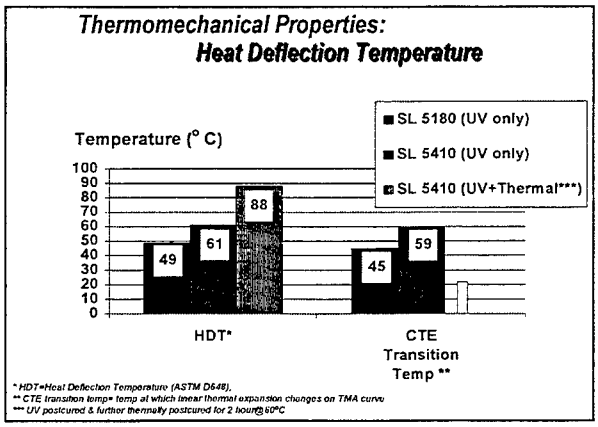


Figure 5

Heat Deflection Temperature

In short, HDT* shown in **figure 5**, is the temperature at which a beam (0.5 X 0.5 X 5 inch length) deflects by 10 mils at the midpoint when the midpoint is pressed at a fiber stress of 66 psi, when the surrounding temperature is constantly increased by 2°C/minute. *(Other variants are also allowed under ASTM D648.) In other words, this test measures how well a material can resist deformation under a load as the surrounding temperature is increased. The property may

be translated to be a measure of how well a material is able to maintain a given dimension when the part is placed under load. This is probably one of the most relevant properties for SL parts.

With UV postcuring alone, HDT of SL 5180 is 49°C and that of SL 5410 is 68°C. Interestingly, the HDT of SL 5180 does not significantly change upon further thermal postcuring. However, SL 5410 has shown a marked increase in HDT value when thermally postcured. Thermal postcure of 2 hours at 80°C was selected since higher postcuring temperatures increase the chance of significantly distorting SL parts. This defeats the whole purpose of maintaining high dimensional accuracy. With thermal postcuring, *HDT of SL 5410 increased to 88°C, which is nearly +40°C above that of SL 5180.* Coupled with the improved humidity resistance, dimensional stability under higher temperature conditions is expected to be much greater compared to SL 5180.

Transition of Coefficient of Thermal Expansion (CTE)

Another thermal property, the CTE (coefficient of thermal expansion) transition temperatures, are sometimes also referred to as the glass transition temperature. This property is measured with a thermomechanical analyzer, or TMA. In this test, a small sample is heated and its linear dimensional change (expansion) is measured as a function of the corresponding increase in temperature. The slope of the curve generated from measuring expansion versus temperature while the sample is a solid, represents the CTE of the solid. As the material becomes softer upon heating, it expands at a faster rate, and another CTE with a greater slope is eventually reached. This value is the liquidous CTE. The extrapolated intersection of these two nearly straight lines is the CTE transition temperature. Below the CTE transition temperature, the material expands like a solid, and above it, like a pseudo liquid. Of course, since SL resins are crosslinked, they do not flow like a liquid, as discussed elsewhere.[5] The CTE values for SL 5410 are tabulated in the last section, **Table 3**.

CTE transition temperature of SL 5410 is about 60°C, which is 15°C greater than that of SL 5180, which in turn is 45 °C. This means that the expansion upon heating up to 60°C is much smaller for SL 5410 than for SL 5180. SL 5410 may have significant advantage in having much smaller thermal expansion between the temperature range of 45-60°C. This expansion characteristic may be taken advantage of for secondary applications, especially where part must be heated.

For example, these applications may involve curing silicone rubber molds around an SL master pattern at a higher temperature, or directly pouring & heating castable urethane materials, or even injecting wax into SL toolings for eventual investment casting. All of these processes rely on the high dimensional tolerances of the SL master pattern.

Glass Transition Temperature, Tg

The last thermomechanical property is the glass transition temperature, Tg, as measured on a dynamic mechanical analyzer (DMA), shown in **figure 6**. DMA is a sophisticated thermomechanical analyzer that measures the change of dynamic mechanical properties as a function of temperature by deforming the sample dynamically at a given frequency, and is a very common mechanical means of measuring the Tg.

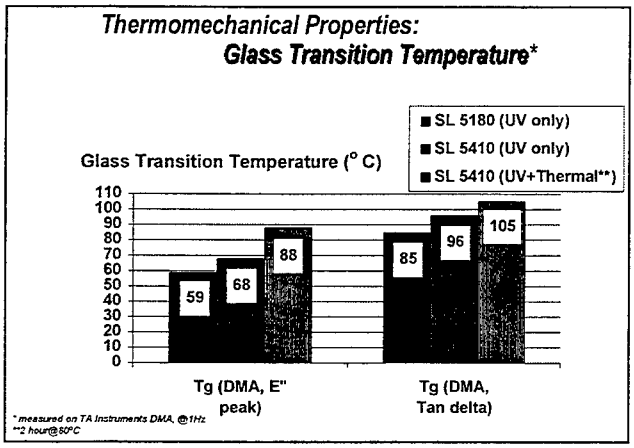


Figure 6

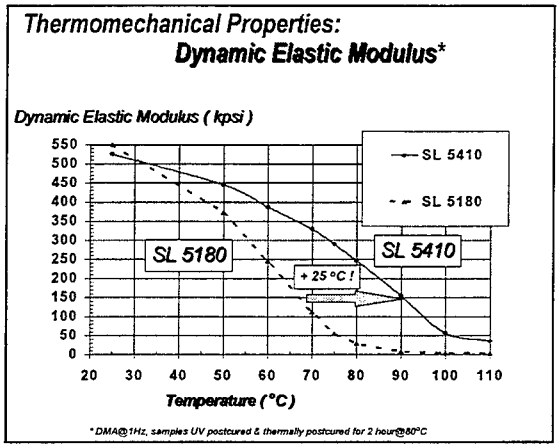


Figure 7

Instead of presenting one "Tg" value as is often the case, two "Tg" values will be given here. These two commonly quoted values arise from two different curves obtained from the same DMA test. These values are 1) Tg at dynamic *loss* modulus peak (Tg $_{E"peak}$), and 2) Tg at tangent delta (Tg $_{tan\ del}$). In many industries, Tg designations are not always clear, and often lead to skewed comparison of materials.

While not necessarily correct from theory, Tg $_{E"peak}$ for epoxy based SL resins tend to occur at approximately 1/3 of the dynamic elastic modulus, shown in **figure 7**, and Tg $_{tan\ del}$ occurs when the same becomes almost negligibly low. This may be a good rule of thumb to remember for similar epoxy based SL resins. In other words, at Tg $_{E"peak}$ SL parts have significant strength, but by the time temperature reaches Tg $_{tan\ del}$, most of the strength has been lost. Therefore, the Tg $_{E"peak}$ would be the relevant temperature for applications where SL parts are placed under some load, and Tg $_{tan\ del}$ would be relevant wherein SL parts are not stressed.

As shown in **figure 6**, ultimate Tg $_{E"peak}$ for SL 5410 is 88°C when thermally postcured. This *ultimate Tg $_{E"peak}$ of SL 5410 is almost +30°C greater than that of SL 5180.*

Similarly, Tg $_{tan\ del}$ of SL 5410 is 105°C, compared to that of SL 5180, which is 85°C. This is an increase of +20°C. The Tg $_{tan\ del}$ value suggests that SL 5410 may be used at temperatures as high as 105°C, when one only needs to maintain its original geometry.

It is important to remember that Tg is a term that indicates a change of property, and focuses on a contrast in the thermomechanical property as it traverses from the glassy to rubbery states. Therefore, it does not necessarily include the absolute strength of materials at a given temperature. Hence, knowing Tg does not necessarily give you the confidence that the material can be applied for your application where a finite resistance to stress is required. For this, one needs to know the residual strength of the material at each temperature.

The concept of dynamic elastic modulus provides this information, and may even be a little more intuitive parameter than Tg. Dynamic elastic modulus is a time-independent, residual modulus of a material, obtained from the same DMA test used to determine Tg. Theoretically, this is the part of the dynamic modulus that changes as a function of temperature, but essentially stays invariant even as the dynamic test frequency is reduced to zero. In SL applications, this modulus is simply a minimum measure of how strong the material is at each temperature. The Dynamic elastic modulus curves for SL 5180 and SL 5410 are shown in **figure 7**.

From **figure 7**, it is apparent that SL 5410 maintains dynamic elastic modulus at higher temperatures than SL 5180. In order to compare the heat resistance of each resin, let us consider the temperatures corresponding to modulus of 300 kpsi and 150 kpsi as an example. Assume here that application A requires 300 kpsi, and application B requires 150 kpsi, and one would like to know what temperature can each of the two applications in each of the two materials withstand.

SL 5180 maintains a modulus of 300 ksi at about 55°C, whereas SL 5410 does so at about 75 °C. This is a temperature resistance gain of about +20 °C. Similarly, SL 5180 preserves a modulus of 150 ksi at about 65 °C, compared to SL 5410, which does so at about 90 °C. This is a gain of +25 °C over SL 5180, designated by an arrow in **figure 7**. Hence, for application A, SL 5410 can be used at 75°C where SL 5180 may only be used up to 55°C. Similarly for application B where lesser strength is required, SL 5410 can be used at 90°C whereas SL 5180 can be used only up to 65°C. Depending on the needs of the application, a rough idea of the heat resistance can be obtained from the dynamic elastic modulus curve.

What would such increase in heat resistance offer to SL part users? In addition to numerous obvious uses of SL 5410, one useful application of this increase in temperature resistance may be the secondary process of curing silicone rubber mold at higher temperatures with SL 5410 as a master pattern. For example, if one has been successfully curing silicone rubber at 55 °C using SL 5180 as the master pattern, one should be able to do the same at 75 °C in SL 5410, based on the discussion above.

How would this increased curing temperature benefit the user for this application? Simple Arrhenius relationship tells us that the reaction rate would increase by a factor of four at 75 °C compared to 55 °C. Hence, a conventional (as an example) 24 hour silicone rubber mold curing time may be reduced by the same factor, down to 6 hours. This would be a substantial time savings for the users. As usual, actual cure times would vary based on the silicones used and part geometries.

Of course, other common applications of SL 5410 other than as master patterns may be for housings where higher heat resistance is required, or where water or high humidity environments exist such as in the design of air conditioners and refrigerators, or for any other general purpose applications. Here, the creative imagination of SLA users would be more appropriate.

Part Accuracy and Surface Finish

Part accuracy of SL 5410 was measured using the H-4 diagnostic test, which measures the SLA in-process build shrinkage. This shrinkage generates a distortion called either waist distortion, or bridge distortion.[6] This is a part that looks like a "letter-H", having the length of 4 inches. As the legs of the "H" builds and connects with the middle part of the "H" geometry, linear shrinkage of the downfacing and subsequent layer curing on top of each other pulls the two legs of the "H" shape closer with each other. The bridge distortion is the measure of the distance that these two legs are pulled in, as compared to a perfectly smooth-edged letter-H. Just as a reminder, this shrinkage is not necessarily related to the overall volume shrinkage, as discussed elsewhere.[7] Rather, this shrinkage is one that can not be removed by applying resin shrink factor, or even cured linewidth compensation on the SLA. Hence, H-4 bridge distortion is one of the most important distortion values that need to be minimized in order to build an accurate part in the SL process.

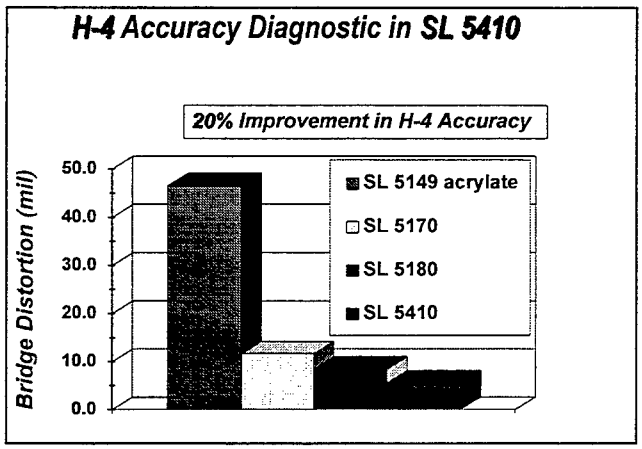


Figure 8

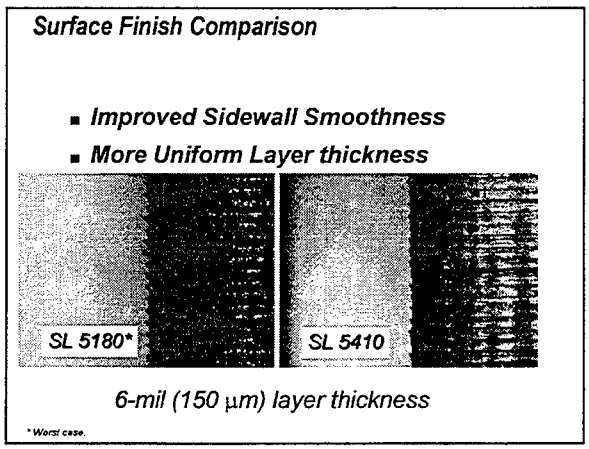


Figure 9

Bridge distortion values for SL 5149 urethane acrylate resin, and other epoxy based resins SL 5170 and SL 5180 are shown in **figure 8**, together with that of SL 5410. Based on the H-4 Bridge distortion values, SL 5410 is about 20% more accurate compared to other epoxy based resins that are considered very accurate already. SL 5410 should perform well where high accuracy is needed.

An additional advantage of parts built in SL 5410 is that it generates smoother vertical walls than SL 5180, as can be seen in **figure 9**. Note that the sidewall of SL 5180 in the **figure** is the worst case scenario. Of course, the degree of sidewall roughness depends on other factors such as the laser beam diameter and irradiation distribution, layer thickness, border overcure values used, and somewhat on the recoater blade speeds and predip delay. Also, by virtue of the chemical modification newly applied onto SL 5410, predip delay is no longer needed. Predip delay increases productivity by reducing the overhead time. This is discussed in the next section.

Productivity

Productivity is a measure of the overall build time using a particular resin, taking into consideration all of the overhead requirements, including the loss or gain due to photospeed, recoating, and other process activities. In other words, it is what is truly relevant for SLA users. Other factors affecting productivity are photospeed and predip delay, both of which are shown in **Table 2** for SL 5410, with respect to SL 5180.

One of the key advantages of *SL 5410 is that it does not require any predip delay*, which significantly contributes to increased productivity. Another advantage is the increased scanning speed. Using recommended build styles for both SL 5180 and SL 5410, ACES hatch are 24% faster, while Borders are 30% faster for SL 5410.

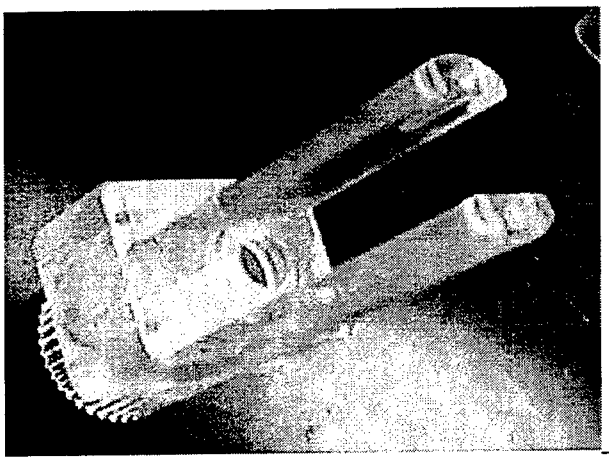


Figure 10: Hydraulic Wrench

Productivity of SL 5410

- *Faster Photospeed vs. SL 5180:*
  - *Dp = 4.8 mil Ec = 10.1 mJ/cm²*
  - *24 % faster for ACES hatch scan**
  - *30 % faster for Border scan**
- *Predip Delay :*
  - *PR = 0 sec (NO Predip delay Required)*

* Based on Recommended Build Parameters for 6-mil layer thickness, e.g. considering appropriate border & hatch overcure values for both resins.

Table 2.

Two geometries were selected to investigate the productivity of SL 5410. One was a part called the hydraulic wrench, shown in **figure 10**. This part is about 6 inches tall, and has a cylindrical bottom section, a rectangular and bulky middle section, and a pair of vertical sections on the top having pseudo crescent-shaped cross sections. This part was built in the upright configuration. Productivity for this part was calculated using the build estimator software, developed by 3D Systems. The second geometry, is a 12-inch long, 6-inch wide, and about 3-inch tall Racecar comprising of relatively thin walls. This part was built flat on the platform.

Productivity for this part was measured from actually building in SL 5180 & SL 5410 side by side on SLA-500 at 180 mW, using default build parameters for each resin.

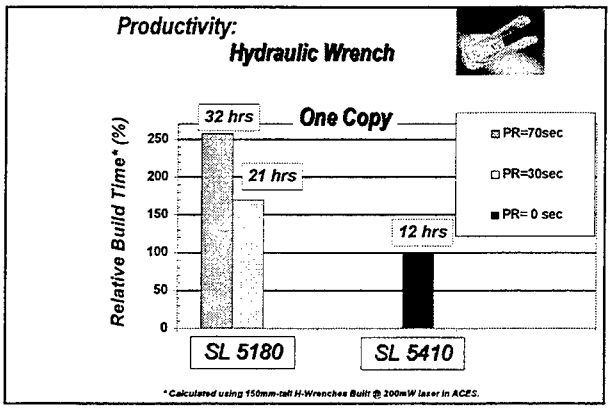


Figure 11

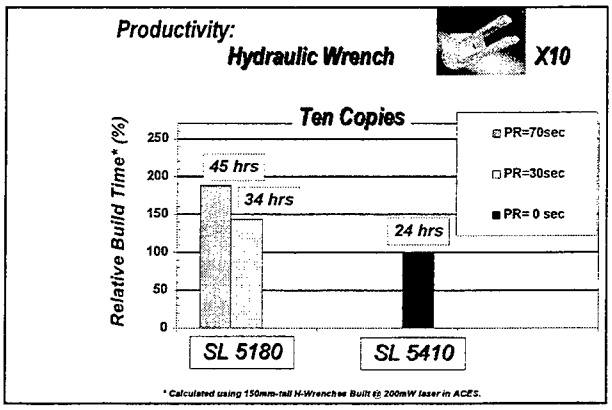


Figure 12

Since productivity is also a function of number of parts built on one platform, two scenarios were taken into account. The first case was that of building a *single* hydraulic wrench, shown in **figure 11**. The other case involved building *ten* of them, the result for which is shown in **figure 12**. Realistic situations for many SLA users may lie somewhere in between these two extreme cases. Also, comparisons have been made assuming a reduced, non-standard predip delay of 30 seconds for SL 5180, in addition to the standard 70 second predip delay.

Both **figures 11** and **12** show that SL 5410 has a significantly increased productivity compared to SL 5180. For example, as shown in **figure 11**, it takes about 32 hours to build one hydraulic wrench using SL 5180. SL 5410 would build the same part in only 12 hours, which corresponds to the productivity gain of about 2.5-fold. Even when predip delay for SL 5180 is reduced down to 30 second, SL 5410 is still faster by 1.7-fold.

Take the case of building ten copies of the wrench part, as shown in **figure 12**. The increase in number of parts places an emphasis on the difference in photospeed, and less on layer overhead parameters such as predip delay. Using SL 5180, about 45 hours is expended, whereas SL 5410 builds in 24 hours. This is an improvement of almost 1.9-fold. Similarly, even for the case of using the reduced 30 second predip delay for SL 5180, the advantage factor for SL 5410 of 1.4-fold is still achieved.

As a verification of these simulations above, a Racecar was built in SL 5180 and SL 5410. The Racecar took 27.5 hours in SL 5180, and 16.0 hours *in SL 5410, an advantage factor of 1.7-fold.* Depending on part geometry and the total, integrated suface scanning coverage, productivity gains in the range of 1.2 - 2.5-fold can be achieved with SL 5410.

An overall productivity comparison is the best way to compare one resin with another, instead of comparing each parameter piecemeal, since most often the effect on overall build speed is non-linear, and often non-intuitive. Using an overall productivity comparison, all of the relevant parameters have already been accounted for, and one can have high confidence at the results.

Other Properties of SL 5410

Other useful properties for SL 5410 are tabulated in Table 3 below for reference.

SL 5410 Resin
Other Properties

Coeff. Thermal Expansion (Cured)	
@ T < 50°C	82 ppm / °C
@ T > 75°C	190 ppm / °C
Refractive Index (liquid)	1.503
Liquid Density	1.164 (25 °C)
Cured Density	1.224 (25 °C)
Brookfield Viscosity	560 cps (25 °C)
	370 cps (30 °C)

Table 3.

Summary

A new Stereolithography resin, CibaTool® SL 5410 was recently released for SLA-500. This epoxy based resin virtually eliminated the negative effects of high humidity and water experienced by the first generation epoxy resins. QuickCast and solid parts built in SL 5410 can withstand high relative humidity without impairing part strengths. Significant strength is maintained even upon immersing SL 5410 into water. Photospeed has also been confirmed to be invariable under both dry and humid environments, thus ensuring consistent performance under adverse environments. With SL 5410, even underwater application can be realized.

The new resin also significantly improves heat resistance of SL parts. Thermomechanical properties of SL 5410 have improved significantly, ranging in temperature increases by +15°C, to as much as by +40°C, relative to those of SL 5180. Heat deflection temperature increased to 88 °C and Tg value as high as 105°C, when parts were additionally thermally postcured. These thermomechanical properties should open up new high temperature applications with SL 5410.

Additionally, part accuracy increased, and vertical surface finish and productivity also improved significantly. Productivity increase by as much as 2.5-fold can be realized with SL

5410, compared to SL 5180. Also, SL 5410 requires no predip delay, hence reducing the overhead time significantly. These newly achieved resin properties characteristics of SL 5410 are expected to improve the ease-of-use in today's applications, and open new fields of applications in the near future, where the combination of high humidity and water resistance, high temperature capabilty, and increased accuracy and dimensional stability is needed.

References

[1] Paul F. Jacobs, Chapter 2, p. 53, *Stereolithography and other RP&M Technologies: From Rapid Prototyping to Rapid Tooling*, published by the Society of Manufacturing Engineers, Dearborn, Michigan, January 1996.

[2] *ibid*, Chapter 12.

[3] Jeffrey Heath, "Direct Tooling for Injection Molding", Proceedings of the Rapid Prototyping and Manufacturing April 23-25, 1996, published by the Society of Manufacturing Engineers, Dearborn, Michigan, 1996.

[4] Adrian Schulthess, "Direct Injection of Thermoplastics into SL Tools", Proceedings of the North American SLA Users Group Annual Conference, March 11, 1996.

[5] *ibid*, Chapter 2, p. 31.

[6] Thomas Pang, "Accuracy of Stereolithography Parts: Mechanism and Modes of Distortion for a "Letter-H" Diagnostic Part", Proceedings of the Solid Freeform Fabrication Symposium, University of Texas at Austin, Austin, Texas, August, 1995.

[7] Paul Jacobs, Chapter 2, pp. 37-39, *Stereolithography and other RP&M Technologies: From Rapid Prototyping to Rapid Tooling*, published by the Society of Manufacturing Engineers, Dearborn, Michigan, January 1996.

STEREOLITHOGRAPHY OF CERAMICS

T. Himmer[(1)], T. Nakagawa[(1,2)], H. Noguchi[(2)]

[(1)] RIKEN-Instrumentation Center, Hirosawa 2-1, Wako-shi, Saitama, 351-01, Japan
[(2)] Institute of Industrial Science, University of Tokyo, 7-22-1 Roppongi, Minato-Ku, Tokyo 106, Japan

Abstract

For studies of Stereolithography of Ceramics (SOC), a composite has been produced by mixing ceramic powder with a photosensitive resin. To obtain high load of ceramics a lamination preprocess was used. Then, the produced ceramic-binder films have been laminated and selectively cured in a Stereolithography machine. After cleaning, the green bodies were fired to burn out the binder and afterwards sintered to achieve full strength.

1. Introduction

Special properties of Ceramics are for example hardness, heat-, and chemical-resistance. Furthermore, some ceramics provide piezoelectricity and superconductivity. A major problem is, that ceramics are brittle and difficult to machine, thus a layer additive process should be given preference rather than a subtractive technology like milling [1]. The task of this paper is to demonstrate that the generation of ceramic-binder models using common Stereolithography equipment is possible. Besides, parameters which have high importance for the SOC realization will be discussed.

2. Fundamentals

Firstly, it is necessary to find an appropriate method to fabricate thin ceramic-binder slices [2]. The problem is, a compound of ceramic powder and resin in the range of 55 vol.% - 65 vol.% ceramic component has very high viscosity. It is also essential that the slices stick perfectly to together (before scanning!), otherwise the effect of delamination will occur. Thus, usage of a doctor blade process or extruding of a thin film seems very difficult. Besides, if the material contains agglomeration, grooves on the uncured surface may appear as a result of "wiping". For these experiments rolling and pressing are chosen to manufacture the slices. It could be found that a proportion of 60 vol.% ceramic (Al_2O_3) and 40 vol.% resin (epoxy resin HS-660) is suitable for rolling and pressing. Some slices have been used to determine the cure depth and cure width of a single cured line. That was necessary to find out an appropriate scanning speed, to make sure that the cure depth exceeds the layer thickness. Figure 1 shows the measuring results after removing the slurry.

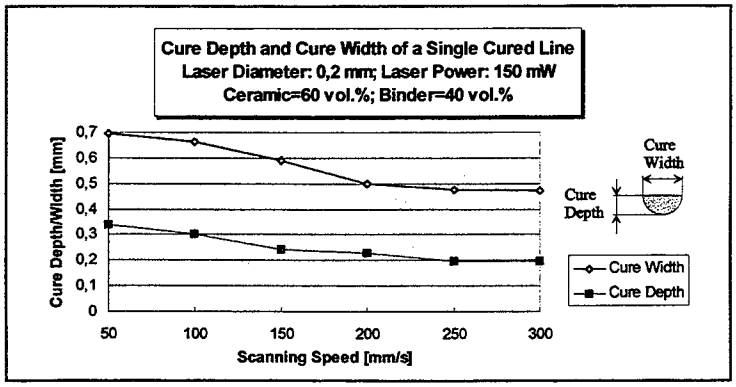


Figure 1: Cure depth and width.

These experiments have also been carried out for ceramic-binder combinations 55 vol.% ceramic - 45 vol.% resin and 65 vol.% ceramic - 35 vol.% resin. The results are similar to those given in figure 1. Obviously, the cure line is very wide for the applied laser diameter of 0,2 mm. The reason is to be found in a so called "scatter effect". If laser light irradiates the composite, it is reflected by the small powder particles (average 2 μm) and it solidifies not just the area below the beam and cures the surrounding area. Consequently, the cross section of a single cured line has not the typical parabolic profile, when resin is exposed by a Gaussian laser beam. Figure 2 illustrates this phenomenon. On the right, a microphotograph of a cross section at about 100× magnification is given (cure depth ~0,3 mm). The scatter effect is clearly visible.

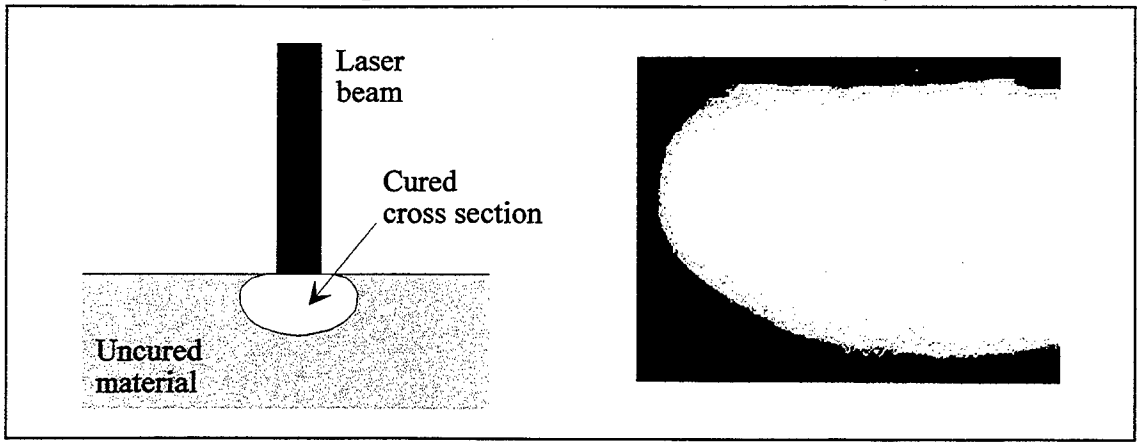


Figure 2: "Scatter effect"

According to figure 1, faster scanning speeds diminish the curing width. On the other hand, this error can be adjusted by correspondingly setting the beam compensation factor for the outline scan in the software. Moreover, figure 1 depicts that cure depth is low, since the powder particles reduce the penetration depth. It is also possible to use transparent ceramics like glass balls, but they are more expensive. Hence, the relatively cheap material Al_2O_3 was favored for the examination. The resin HS-660 possesses a high penetration depth, so it was selected to achieve good adhesion.

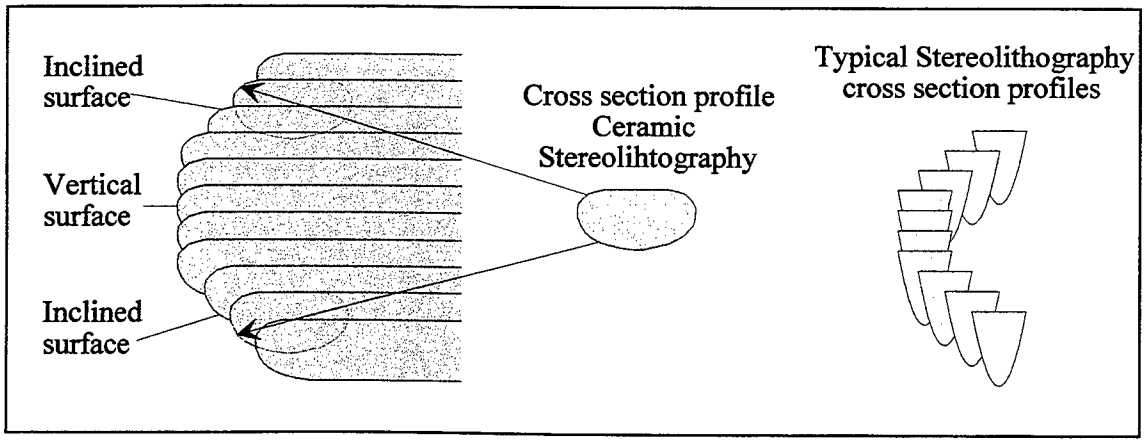


Figure 3: Stair stepping effect

The specific profile of the cross section leads to different results concerning surface roughness, compared with the conventional Stereolithography (figure 3).

If the layer thickness is for example 0,15 mm and the cure depth is about 0,3 mm (according to figure 1), the profile is advantageous, since the "round profile" improves the surface finish of sloping sections, especially upfacing surfaces. Vertical faces will have a similar appearance as STL-surfaces because of overcuring.

3. Experimental procedure

As mentioned in chapter 2, the quality of the lamination has crucial influence for the entire process chain. Therefore, different tests are executed to find out an appropriate method. This procedure has to fulfill the following requirements:

- quality; guarantee of an exact slice thickness,
- reliability and repeatability,
- swiftness, in view of an automation of the process,
- inexpensive solution.

At present, an automated technique is not available and a doctor blade type device was not considered. Therefore, rolling and pressing is done manually. As a result of the experiments, rolling can be recommended to form the slices. Figure 4 depicts the experimental setup.

Certainly, several stages are necessary to roll this viscous substance. But the major problem is: how to detach paper and plastic sheet from the mixture after rolling? If the slice thickness is very low (about 0,2 mm), the paper can hardly separated from the composite without destroying the ceramic film. For lamination, the plastic sheet must be removed from the plate and placed with the ceramic-resin layer in the Stereolithography machine. After that, it is essential to press the composite on the previously cured layer. The adhesive power between plastic sheet and compound should be less than the power between the ceramic layers, to secure easy removal of the plastic sheet. In case the mixture sticks to the covering, parts of the ceramic-binder layer will be pulled out with the effect that holes appear. Such cavities cannot be repaired during the building process, thus the reliability of rolling and pressing is most important. All problems that are just mentioned should be considered regarding automation.

With the described procedure it is possible to produce high viscous ceramic-binder slices in a relatively time and cost effective manner. After starting at 0,3 mm layer thickness, this "manual lamination method" could be improved and is now capable to make slices of 0,2 mm which is quasi standard in Stereolithography. Corresponding to figure 1, a scanning speed of 50 mm/s was used for the initial experiments to ensure sufficient adhesion.

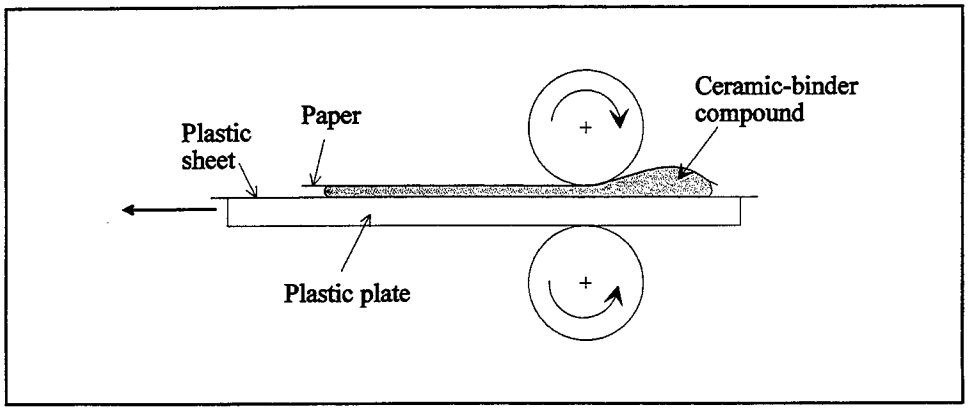


Figure 4: Lamination preprocess

The images in figure 5 represent discussed issues. For example, left, the scatter effect can be seen because the layer thickness is about 0,3 mm. The photograph in the middle depicts a block with some cavities due to imperfect lamination. The gap on the right photo arises from the same error, too.

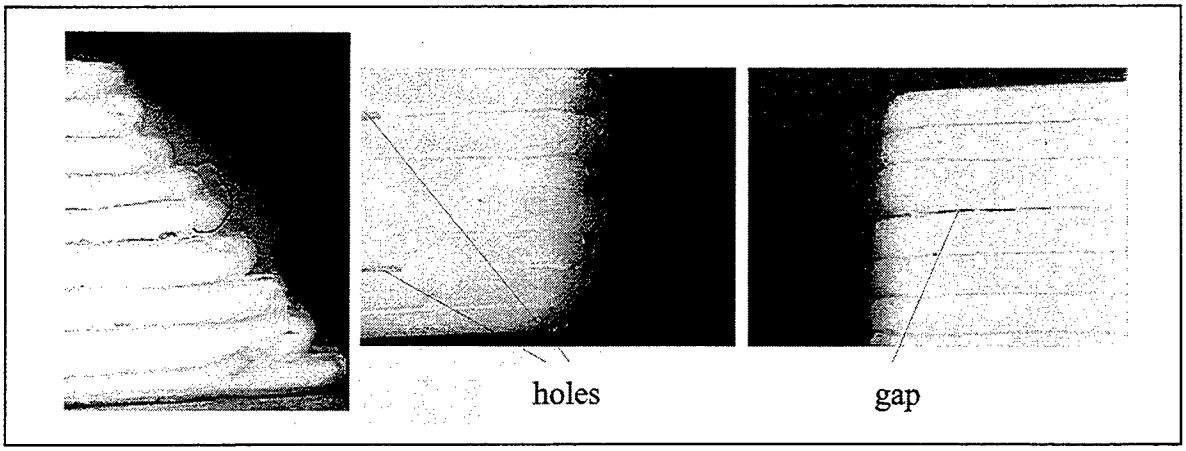


Figure 5: Magnified "layer views"

After building , the next step is support removal and cleaning respectively. Since the viscosity of the surrounding uncured material is high, this procedure can be very time consuming. Therefore, an automated cleaning unit should be developed to permit quick and unattended postprocessing. One well-known system is the automatic dewaxing machine of Cubital's Solider system. A similar device will shorten postprocessing time in Stereolithography of Ceramics. However, stiff support reduces curling and warpage. Moreover, the weight and the viscosity of the material reduce the tendency to curl.

Figure 6 shows various parts successfully built with SOC. The turbo impeller is not completed since only 20 layers were available for this experiment. The size of the part on the right is 20 mm in X- and Y-direction.

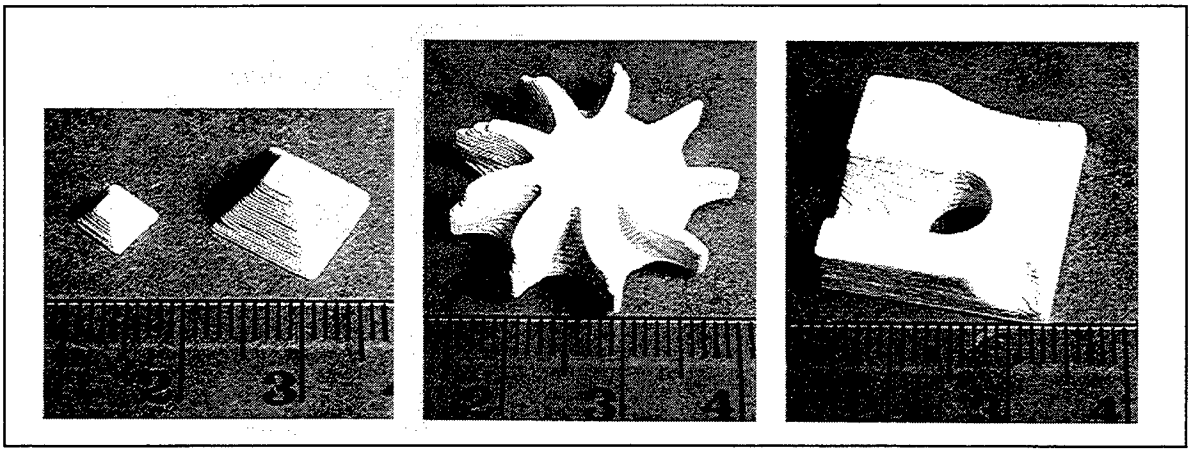


Figure 6: Fabricated composite models

To explain more by example, some close-up photographs are given. The right image is a magnification of one turbo impeller blade. About 20 layers were successfully laminated with a layer thickness of 0,25 mm. Of course, the lamination is not yet satisfactorily, but this is just the second building attempt.

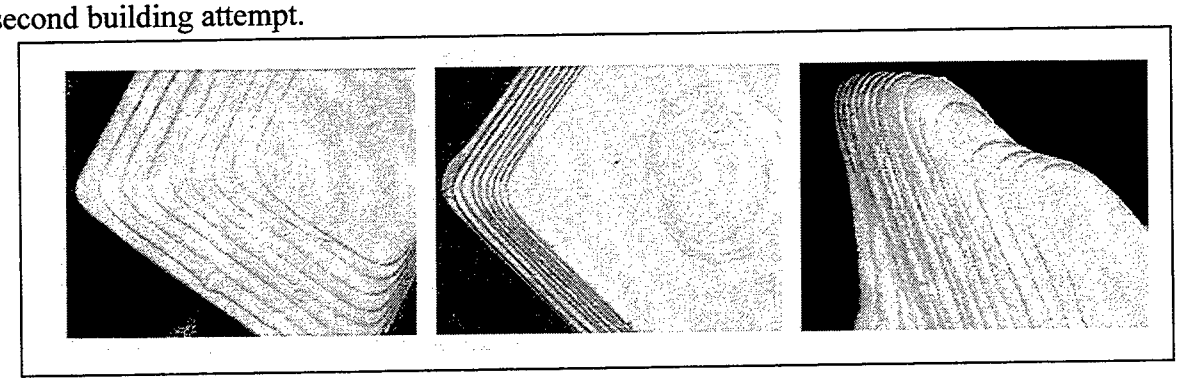


Figure 7: Magnified views of small samples

4. Debinding and sintering

As can be seen from figure 8, the debinding process is very time consuming. However, the main objective was not high speed, first it was necessary to show the possibility of debinding and presintering for laminated models with a high load of ceramic. After burning and presintering a so called "delamination effect" was not visible. Certainly it is possible to warm up faster, since the model size is relatively small. This should be a topic of further research.

The binder is now removed completely, that means the parts have a behavior like compressed powder. Therefore presintering is essential in order to obtain a strength which allows handling of the model.

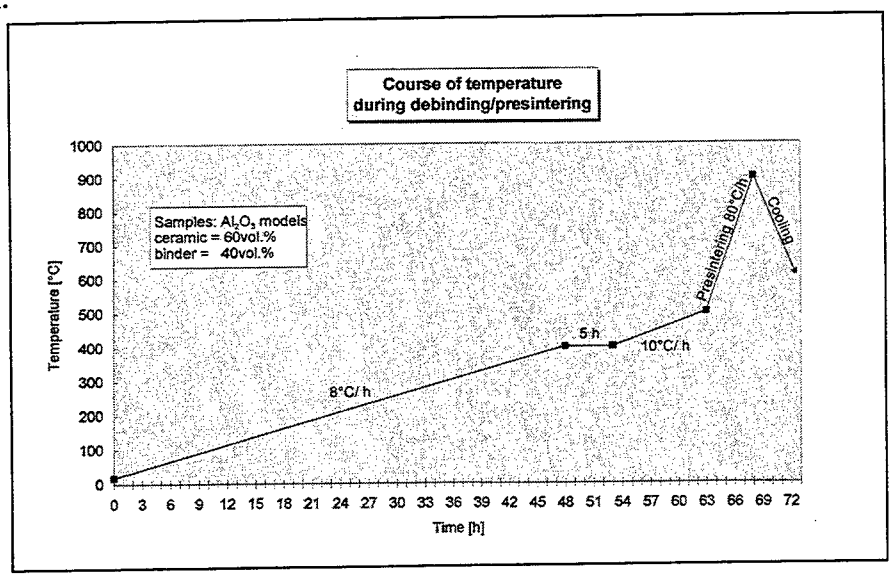


Figure 8: Debinding and presintering

Even after presintering the models are brittle, thus they should handled carefully. The structure of a sintered model has been checked with an electron microscope which shows, that they still contain 10-15 % air. The reason can be found in the grain size of the powder, that is given with an average of 2 µm. Actually the size varies from 0,2 µm up to 5 µm. If the diameter and the shape of the powder particles would be more uniform, the sintering effect is better.

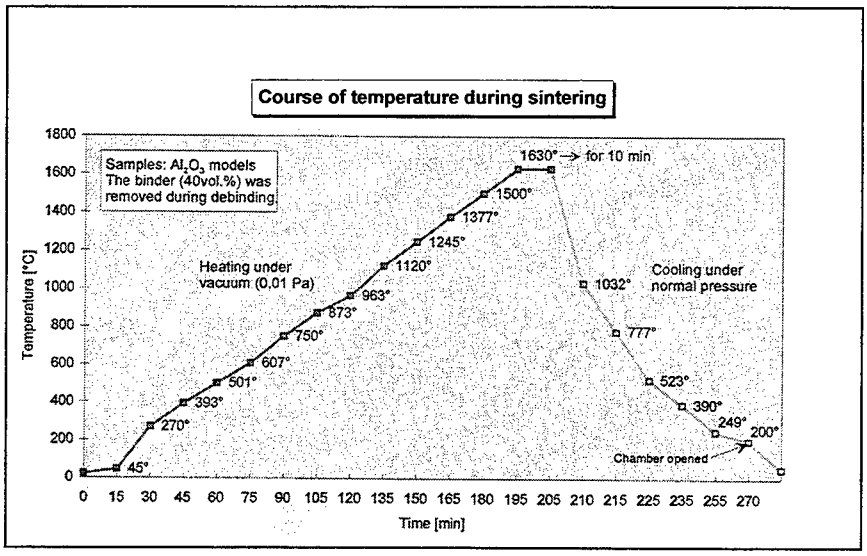


Figure 9: Sintering

5. Conclusion for Improvements

The experiments illustrate that problems occur with this technology. Main problem is the lamination, therefore improvements shall be is focused on the SOC preprocess. Furthermore this section will provide a proposal for automation. As already mentioned, only the optimal performance of rolling and pressing will lead to high part quality. A thinkable automation is described in figure 10.

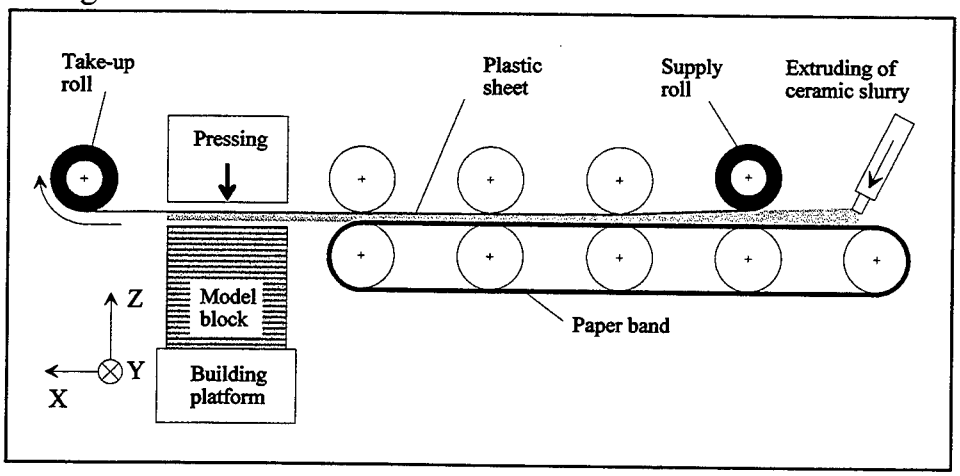


Figure 10: Automation of the preprocess

The composite is extruded on the lower paper band and will be formed between the two ribbons during rolling. The upper band (plastic sheet) has the additional function to transport the mixture under the pressing station. Now, the slice is ready to be pressed on top of the previous layer. For that, the building platform moves below the just prepared layer. The movement direction of the platform could be along the X- or Y-axis. After pressing, the building platform returns under the "scanning station". While the mixture is cured, the next slice can be prepared.

This allows a higher building speed compared to doctor blade type processes, since the non-scanning time is reduced. Pressing should be used to make the final Z-adjustment and pressing guarantees a sufficient adhesion between the ceramic-binder slices. In addition, rolling and then

slight pressing from the top will not destroy thin, delicate part sections as for example wiping could do. As band materials paper or plastic sheets may be considered to ensure easy separation (see figure 4). This "preprocessing" is similar to Laminated Object Manufacturing (LOM), however, LOM uses the ribbon as material. An advantage of such a preprocess is the flexibility, since the material can be exchanged by just replacing the extruding device.

To complete this discussion some remarks for further investigations are presented. For improvements of this technology following issues should be pointed out:

- Automation of the SOC process (lamination, building-, and postprocess),
- Part quality, especially sufficient accuracy: the entire process chain has to be examined; lamination, building, postprocessing, debinding, sintering,
- Tests for different materials e.g. ceramics, metals, resins [3],
- Analysis of debinding and sintering.

6. Summary

In order to fabricate a ceramic-binder composite, an Stereolithography epoxy resin and ceramic was mixed. The ratio of ceramic and resin was 60:40 vol.%. This slurry has been formed by rolling and pressing to produce thin slices. These layers were laminated and cured in a SOUP 600 Stereolithography system. Using this SOC process, several models with a slice thickness of about 0,25 mm were successfully built. After removing the binder by burning the parts were sintered to achieve full strength.

Based on the obtained results it can be concluded, that Stereolithography of Ceramics may be considered as one of the potential methods for the generation of three-dimensional ceramic models. However, only the reliable function of all system units, particularly the lamination unit, is necessary to achieve best results. This technology can help to generate ceramic models or shells for casting applications in a much shorter time and for lower costs. The technological realization of SOC could be an interchangeable module for an existing Stereolithography system.

7. Acknowledgments

The author would like to express his appreciation to Prof. T. Nakagawa, Mr. H. Noguchi, and Mr. Y. Xu for their advice and excellent assistance. CMET Inc. put both significant technical support and their assistance to our disposal.

8. References

1. "Rapid Prototyping Report", The newsletter of the desktop manufacturing industry, June 1995, September 1995; CAD/CAM Publishing Inc., USA
2. "Stereolithography of Ceramics and Metals", WWW-Information Technology Assessment & Transfer, Inc., USA
3. "Application of Laser Stereolithography to Forming Tool Manufacturing", M. Imamura, Y. Xu, H. Noguchi, T. Nakagawa, Sintokogio Ltd., Japan; Institute of Industrial Science, University of Tokyo, Japan

High green density ceramic components fabricated by the slurry-based 3DP process

Jason Grau[1], Jooho Moon[1], Scott Uhland[1], Michael Cima[1], Emanuel Sachs[2]
Department of Materials Science and Engineering[1]
Department of Mechanical Engineering[2]
Massachusetts Institute of Technology, Cambridge, MA 02139

Abstract

The 3DP process has been modified to directly fabricate high green density parts using submicron powder. The slurry-based 3DP process deposits the powder bed by spraying a dispersed slurry of the component material onto a piston. Alumina, silicon nitride, and lead zirconate titanate components with green densities as high as 67% have been fabricated by the slurry-based 3DP process. Solution phase binder systems have proven to be successful for the new process. Substantially improved surface finish over the conventional dry powder-based 3DP process has been demonstrated. Layer heights less than 50 μm can be prepared with this process. Thus, the stepped surface topography commonly observed in solid free form parts is substantially reduced.

Introduction

Structural ceramic components require fine-grained starting powders and high green density in order to achieve near theoretical density after firing. Wet processing techniques such as slip casting and injection molding are commonly used in ceramic forming processes to produce parts that meet these criteria. Structural ceramic components have been fabricated in the past with 3DP using spray-dried powders. These powders are ~50 μm agglomerates of submicron powder. Spray-dried powders were easily spread into uniform layers, but printed components had packing densities less than 35%. Post-processing was required to achieve sufficient density prior to firing.

The slurry-based 3DP process has been developed to overcome the difficulties of spreading fine submicron powder and also to enable layers as thin as 10 μm to be deposited. This paper discusses the slurry-based 3DP process and initial results with different ceramic materials systems. The process is sufficiently generic to be adapted to new materials systems. Our preliminary experiments have been performed on two types of ceramic materials, high purity alumina (several grades of Ceralox HPA) and sintered silicon nitride compositions (HC Stark M11, 6 wt. % Al_2O_3, 6 wt. % Y_2O_3). Firing conditions were 1650°C for 1 hr in air for the alumina samples and 1755°C for 1 hr under 2 psig N_2 for the silicon nitride.

The slurry-based 3DP process

The slurry-based 3DP process was developed to fabricate high green density components from submicron powders using wet processing techniques. Figure 1 shows a schematic of the slurry-based 3DP process. The primary difference from the standard 3DP process

is the manner in which the powder bed is deposited. The powder bed in the slurry-based 3DP process is deposited by spraying a dispersed slurry over the piston and drying. Typical slurry volume fractions are between 30 and 35 vol. %. Binder is then printed into the powder bed to define the shape of the component, and the process is repeated until the component is completed. The powder bed is cohesive, and the part is retrieved by redispersing the unprinted regions in an ultrasonic bath.

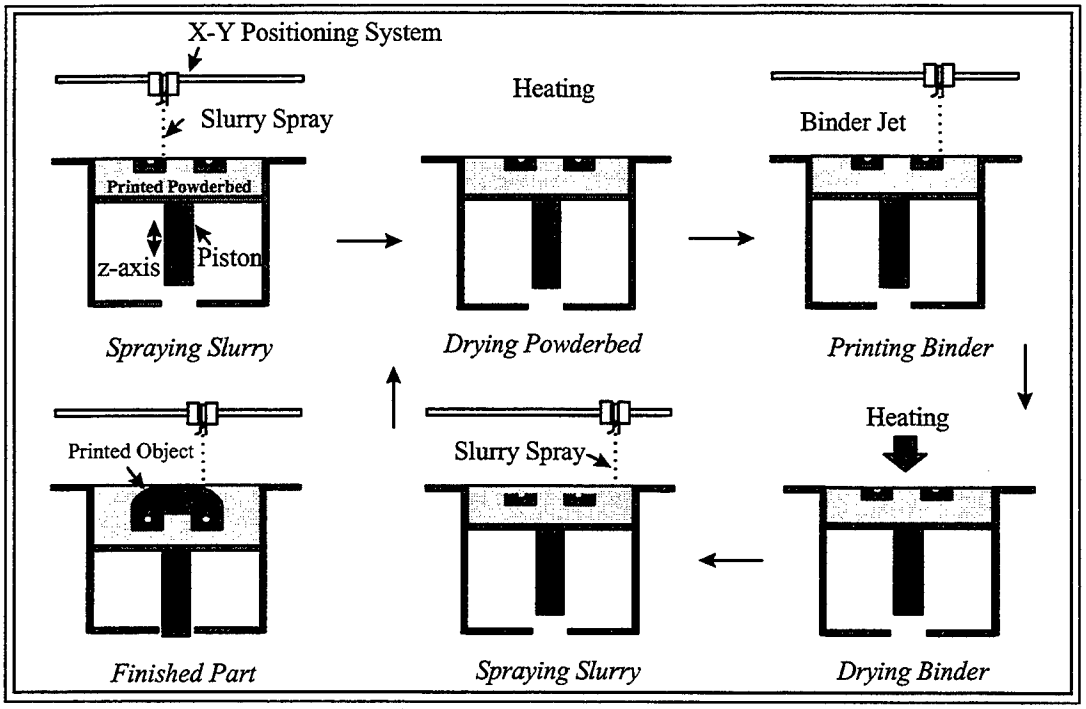


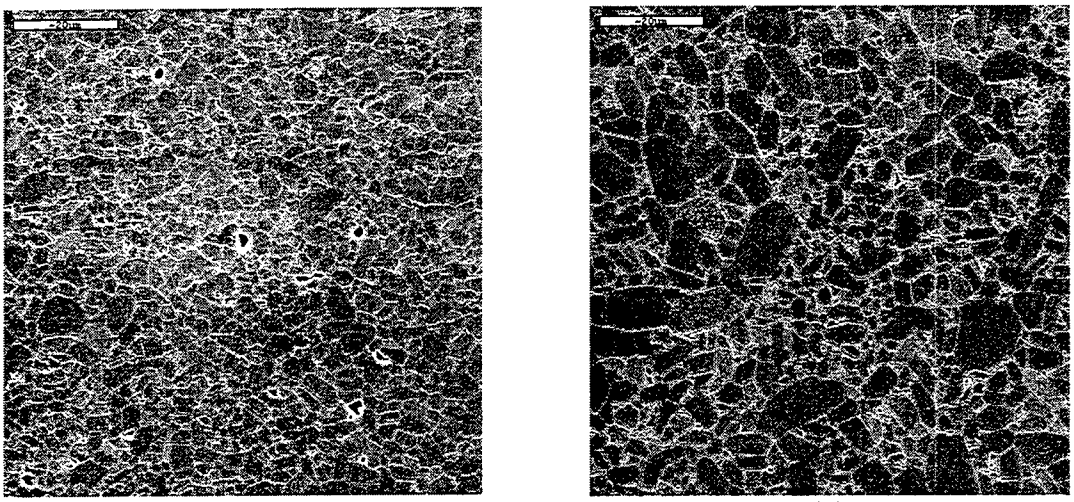
Figure 1. Schematic of the slurry-based 3DP process

Table 1. Densities of alumina powder beds sintered at 1650°C		
Formation Method	**Powder Size**	**Density**
Slurry-Based 3DP	0.5 μm	98.7%
Slurry-Based 3DP	1.0 μm	99.0%
Slip Cast	0.5 μm	99.0%
Slip Cast	1.0 μm	99.2%

Powder bed microstructure

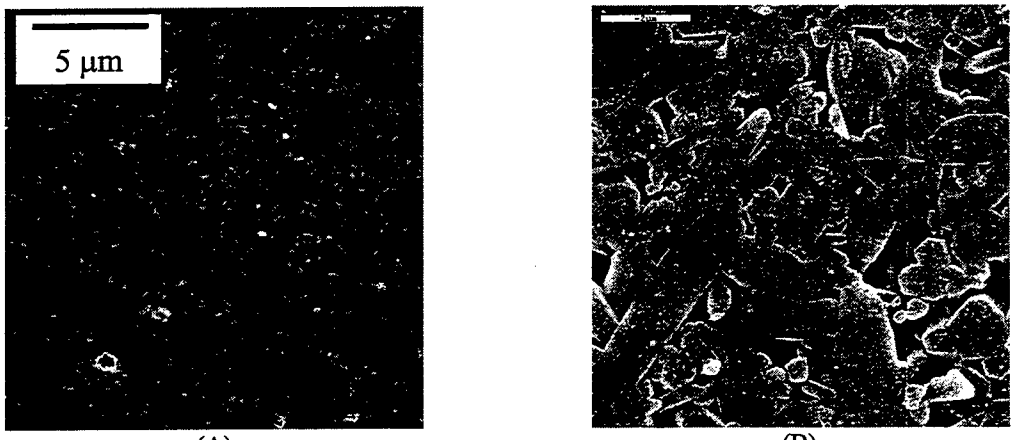
The microstructure of the powder bed is controlled by several variables including stability of the slurry, powder morphology, and the raster variables during the spraying process. Microstructure of powder beds was studied using mercury porosimetry and scanning electron microscopy (SEM). The green densities of powder beds was typically greater than 60% theoretical density and as high as 67%. Mercury porosimetry also indicated that the pore size distribution was uniform with a single population of fine pores. The densities and microstructure of Al_2O_3 powder beds prepared by the slurry-based 3DP process compare favorably with those prepared by slip casting. The densities of sintered

alumina powder beds are compared in Table 1. Polished cross-sections of sintered alumina and silicon nitride powder beds are shown in Figures 2 and 3, respectively.



(A) (B)

Figure 2. Polished cross-sections of samples sintered at 1650°C. Microstructure of slurry-based 3DP parts (A) are similar to powder beds prepared by slip casting (B). (Scale marker bar is 200 μm).



(A) (B)

Figure 3. Polished section of a sintered silicon nitride part made by 3DP (A). The section shown in (B) has been etched to reveal the structure of the silicon nitride grains.

Powder beds prepared by the slurry-based 3DP process do not contain lamination defects from the layered build process, but can occasionally contain a small number of pores in the 2 to 3 μm range, as shown in Figure 2A. The occurrence of these pores is related to improperly chosen parameters spraying of the powder bed. This dramatically illustrated by comparing surface profiles of sprayed lines separated by varying distance. Figure 4 shows such profiles for silicon nitride suspensions on a very flat slip cast support. The cross sections are perpendicular to the traversal of the spray head. The deposit from each individual line is trapezoidal in cross section and slightly less than approximately 300 μm wide at the top and has a base that is 400 to 500 μm wide. Two sprayed lines separated by less than this distance will overlap to produce a protuberance in the surface as observed in the surface profiles in Figures 4A and B. Larger sprayed line spacing leaves

a small gap as shown in Figure 4C. Also shown in Figure 4 are sections of sintered silicon nitride parts prepared with the corresponding sprayed line spacing. The occurrence of porosity seems to correlate with the production of gaps between individual sprayed lines. These small gaps between lines may not be filled when subsequent layers are deposited.

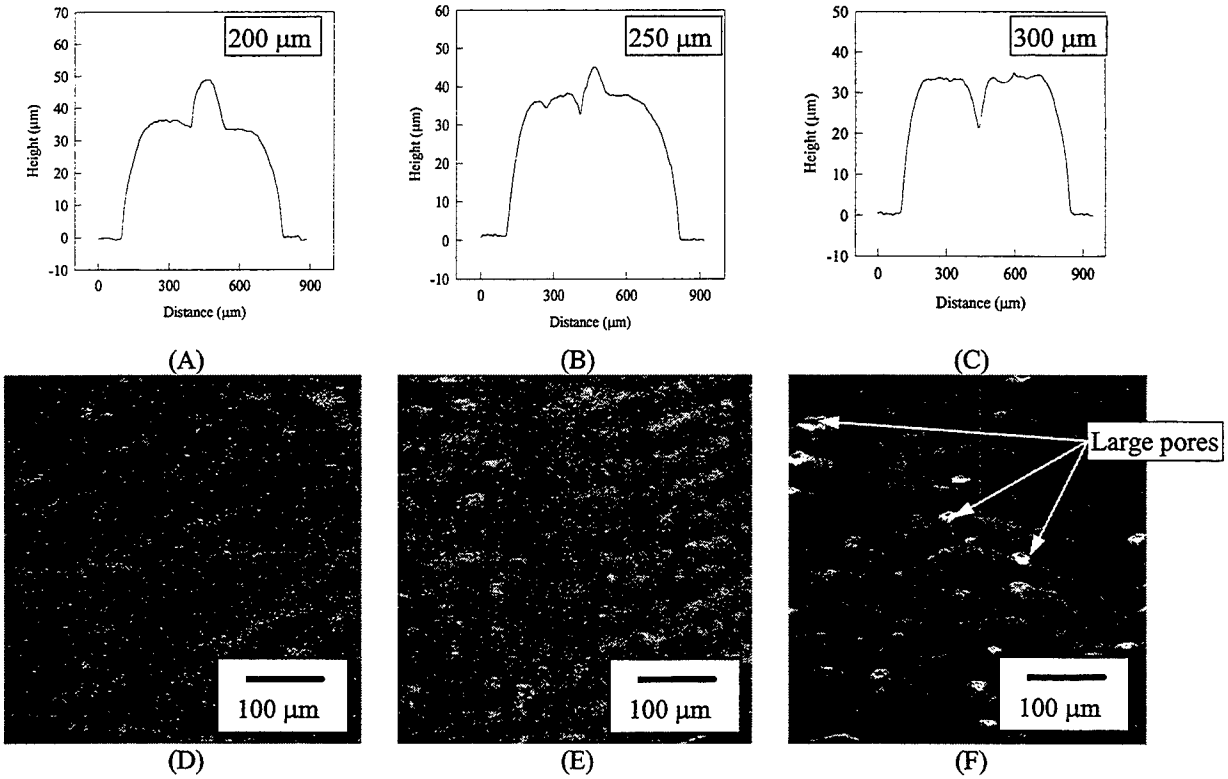


Figure 4. Figures A,B, and C are surface profiles of two sprayed silicon nitride lines spaced 200, 250, and 300 µm, respectively, apart on a slip cast bottom layer. Separation of sprayed lines by 300 µm or greater leads to a gap between the sprayed lines. Figures D, E, and F show the corresponding silicon nitride powder beds prepared with sprayed line spacing of 200, 250, and 300 µm, respectively, after sintering. The large pores in the microstructure coincide with conditions where the gap forms between two sprayed lines.

Binder selection and interactions

The binder systems used for the slurry-based 3DP process must meet several requirements. First of all, the binder needs to penetrate the powder bed and have sufficient strength to survive the part retrieval process. Secondly, the binder must be insoluble prior to redispersing the unprinted powder bed. The intrinsic properties of the binder are also critical to its performance in ink-jet printing and binder-powder interaction. Important intrinsic properties include surface tension, viscosity, conductivity, pH and chemical stability. Resolution of the printed part in the 3DP process mainly depends on binder-jet performance and binder-powder bed interaction. Low surface tension binder has high penetration rate and penetration depth, but it spreads more easily, reducing printing resolution as compared to high surface tension binder.

Three types of commercially available binder systems were examined- polymeric particle suspended binder (latex), wax emulsion binder, and homogenous solution phase binder systems. Latex binders do not infiltrate into the powder bed even if the individual polymer particles have smaller particle size than the mean pore size of the power bed. It is believed that the polymer particles tend to coalesce and form a surface film on the powder bed. The smallest particle size of polymeric particles examined was 14 nm in the Estek 1200 polyester latex as determined by dynamic light scattering technique. Even this latex forms a surface film. Wax emulsion binder also forms a surface film when it is printed onto the powder bed. However, during drying, the wax surface film easily melts and penetrates into the powder bed. Low melting point waxes such as carnauba wax and paraffin are preferred since they must melt to infiltrate the powder bed. Solution phase binders easily penetrate into the powder bed as long as the molecular weight of the binder is less than ~5,000. Solution phase binders must be cured at elevated temperature to strengthen the part and to make the binder insoluble in water.

Joncryl 52 is a water-based solution phase binder that has been used effectively. It is a styrene-acrylic copolymer with molecular weight 1800 and viscosity of 2.8 cps for a 10 volume % solution. Binder burn-out from the part is easily achieved during the firing cycle, and binder residue is not significant in the sintered component. Furfuryl alcohol resin has also been used as a solution phase binder. Furfuryl resin can be diluted in acetone to yield a low viscosity, low surface tension binder. These solution phase binders offer the ability to control both surface tension and viscosity. Penetration behavior of three different binder systems is summarized in Figure 5.

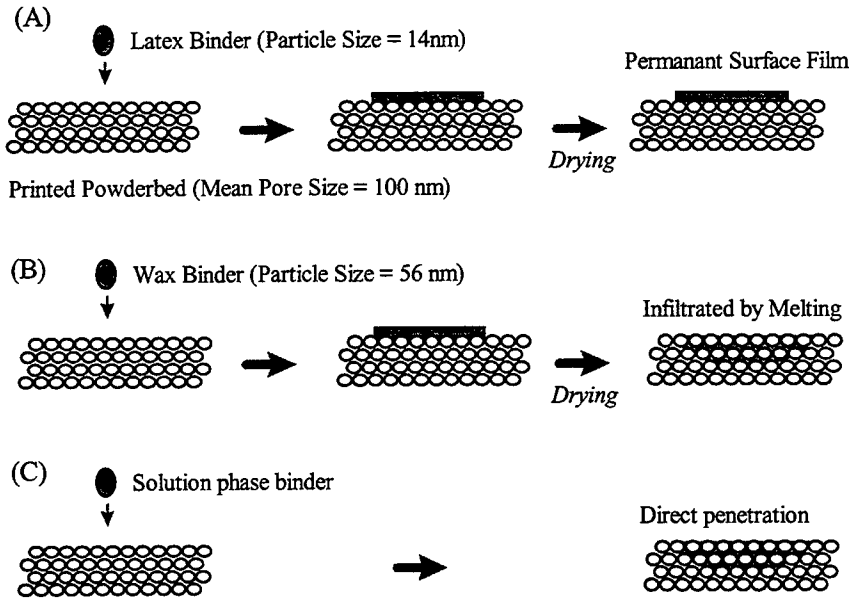


Figure 5. Schematic picture showing penetration behavior of three different binder systems.

Another important aspect of the binder system is the wetting behavior difference between the binder printed region and the unprinted region of the powder bed. Lamination defects

and surface roughness are observed when the wetting behavior differs substantially between the binder printed and unprinted regions. This wetting behavior difference depends on properties of binder materials. Aqueous slurries do not wet regions of the powder bed printed with wax emulsions due to the hydrophobic nature of the wax. Alcohol-based or aqueous-alcohol mixed slurries have a much lower contact angle and wet the binder printed regions more uniformly. Addition of a wetting agent into aqueous slurry also improves the wetting characteristics and consequently gives rise to better printed microstructure as shown in Figure 6. Triton X-100 surfactant decreases the contact angle of 35 v/o alumina slurry on paraffin substrate from 98° to 45° while maintaining a well-dispersed suspension state in the slurry.

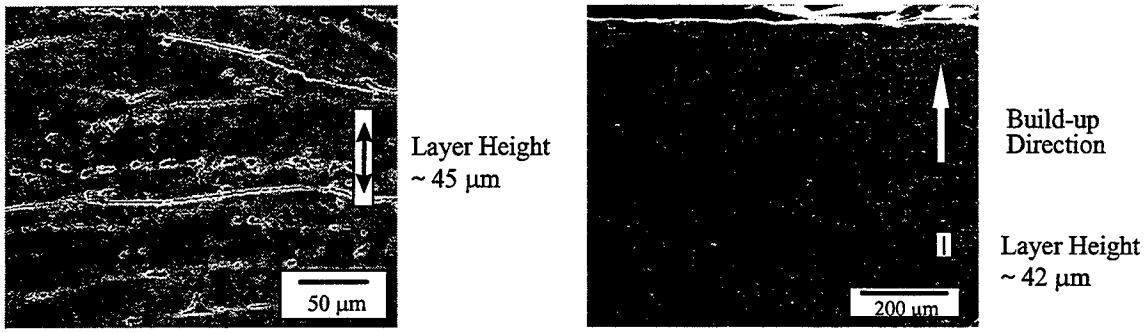


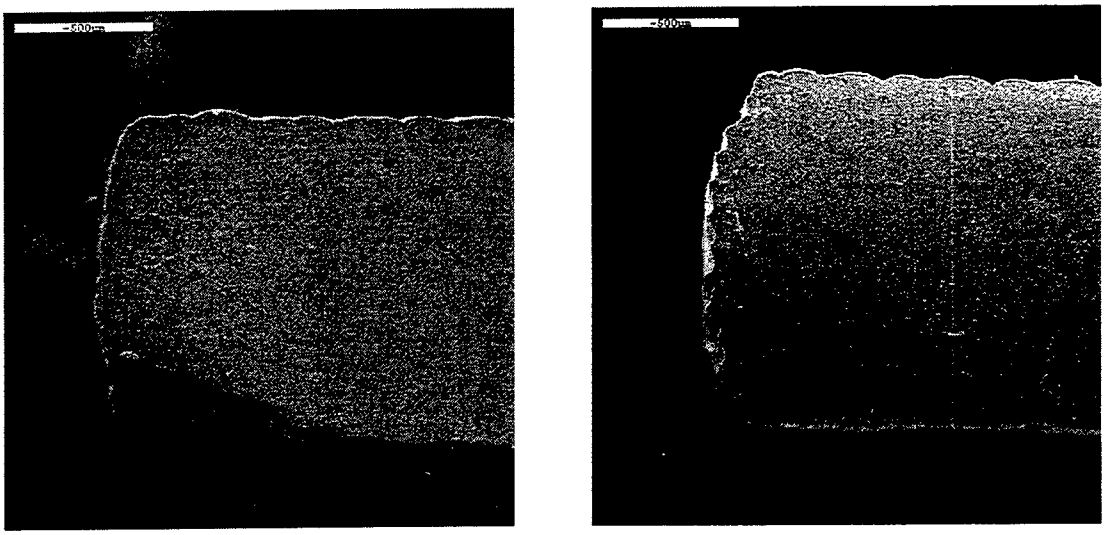
Figure 6. Cross sectional microstructures of sintered powder bed prepared with and without wetting agent in the slurry are shown in (A) and (B), respectively. Lamination defects are observed in (A) due to the wetting behavior of the slurry on binder printed regions.

Printed parts and surface finish

The effect of the amount of binder deposited on the microstructure of the printed part was studied in detail by varying binder flow rate, line spacing, print speed, and layer height. Single line primitives of binder printed into slurry-based 3DP powder beds have a semi-circular cross section compared to circular primitives that are observed for the standard 3DP process. The surface finish was found to be improved by printing with smaller layer heights. Figure 7 shows cross sections of alumina parts printed with 10 weight % Joncryl 52 solution. The edge of the part printed with 50 μm layers has a smoother surface finish compared to the part printed with 100 μm layers. Single line primitives with this binder are on the order of 150 μm thick. The surface finish begins to degrade and the edge of the part has a saw-toothed appearance as the layer thickness approaches the thickness of a single primitive.

Surface finish is also dependent upon the surface tension and viscosity of the binder system. Furfuryl resin binder has both low viscosity and surface tension (~23 dynes/cm) since it is diluted in acetone. Parts printed with furfuryl resin binder display the best surface finish among the binder systems. Figure 8 displays a cross section of an alumina part printed with furfuryl resin. The angled surface does not display stair-stepping that is

typical in most SFF processes, but printing resolution is substantially reduced due to significant spreading of the printed binder.



(A) (B)

Figure 7. Cross sections of alumina parts printed displaying the effect of layer height on the surface finish of the parts. Parts with 50 μm layer height (A) has smoother surface finish than parts printed with 100 μm layer height (B). Binder concentration is identical for both parts. (Scale marker bar is 500 μm)

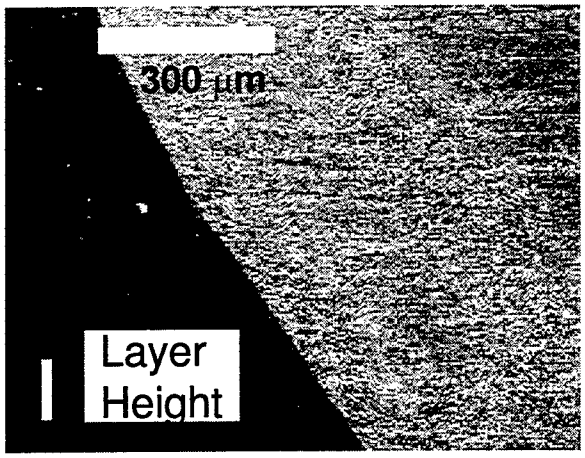


Figure 8. Cross section of alumina part printed with furfuryl resin binder. Angled surfaces do not display stair-stepping.

Parts have been printed with three ceramic materials systems to date: alumina, silicon nitride, and lead zirconate titanate (PZT). Two simple silicon nitride parts are shown in Figure 9 and a bisque fired cross section of one such silicon nitride part is shown in Figure 10. The sample remains porous upon bisque firing and does not shrink. The mounting material is observed to creep into the pores near the surface of the bisque fired sample and is the cause of the different contrast near the sample surface. The bisque fired

section is used to estimate the dimensional accuracy of the slurry based 3DP process. This is a fifty layer part which consists of a flat base with middle section of which rises above the base. The middle section is nine lines wide. A Joncryl 52 solution is used as the binder with a 300 μm line spacing. The binder flow rate is such that this spacing results in a part that is 3.4 wt. % binder. Also, the spcaing is such that the edge lines of the middle section are printed 2700 μm apart. Measurements of the binder spreading in silicon nitride powder beds reveals that individual lines of printed binder are on average 342 μm wide. The expected middle section width is, therefore, 2700 μm plus 342 μm or 3042 μm. The measured value is 3110 μm with an absolute error of 68 μm or 2%. More work is needed to refine the process planning rules to account for such systematic errors.

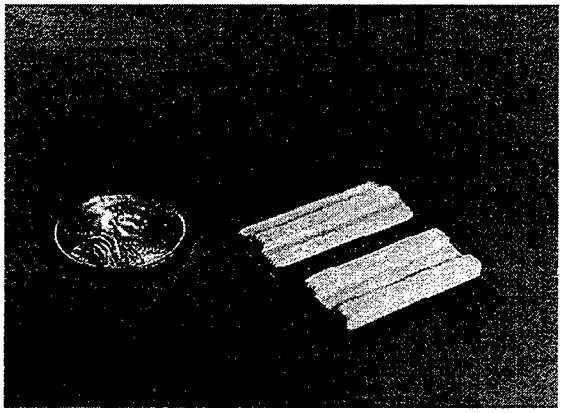


Figure 9. Two simple silicon nitride parts used for dimensional testing.

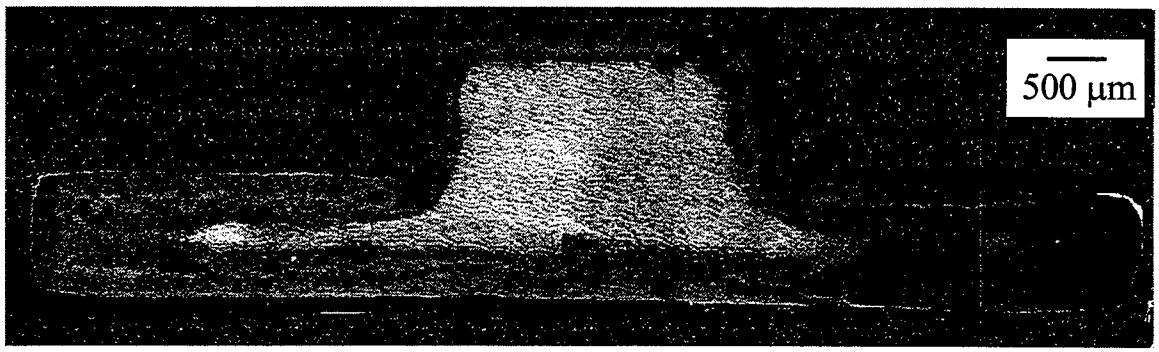


Figure 10. A cross section of a bisque fired silicon nitride part shown in Figure 9. The material with different contrast near the surface of the sample is the result of mounting material only partially permeating the porous sample.

Conclusions

The slurry-based 3DP process has been used successfully to prepare high green density components with fine-grained ceramics. Improved surface finish is possible by controlling the properties of the binder system and reducing the layer height. The process is generic and can be readily adapted for new materials systems by optimizing the stability of the slurry. Our future work will be to refine the process planning so as to more precisely control the final component dimensions.

CAM-LEM PROCESSING: MATERIALS FLEXIBILITY

Z. E. Liu, T. C. Ko, J. Best, J. D. Cawley, and A. H. Heuer
Department of Materials Science and Engineering
Case Western Reserve University
10900 Euclid Avenue
Cleveland OH 44106-7204

ABSTRACT

The cut-then-stack paradigm of computer-aided manufacturing of laminated engineering materials (CAM-LEM) offers choice of feedstock material, ease of handling finely divided (and therefore sinterable) powders, and the ability to mix materials. This combination of features was exploited to process fluidic devices. CAM-LEM processing was used to render the part in aluminum oxide, silicon nitride, and stainless steel.

INTRODUCTION

Computer-aided manufacturing of laminated engineering materials (CAM-LEM) has been developed as a solid freeform process to allow direct layered-manufacturing of components of complex geometry in any one of an array of engineering materials. To date, efforts has focussed on the use of powder-based processing of ceramics and metals.

When working in ceramics or metals using the CAM-LEM process, the method of part construction is robotic assembly of cut outlines followed by green-state lamination and conventional firing [1-4]. The feedstock for the process is a "green tape" that serves as a powder carrier. Separate preprocessing of the tape by methods such as tape casting [5] or compression molding [6] allows the process to employ finely divided powders (submicron, in the case of ceramics), creates uniform particle packing, and completely avoids problems associated with flow instabilities or segregation effects.

Powder-based tapes are widely used in industrial applications and a number of techniques have been developed for their production. Specific process selection is dependent on property requirements. For CAM-LEM processing, important tape characteristics include behavior during laser cutting and ease of lamination. It has been determined that some commercially available tape formulations are suitable for CAM-LEM processing, whereas others are not. In addition, tapes can be produced from either commercially compounded feedstocks or mixtures of raw materials.

Through the use of the cut-then-stack paradigm, CAM-LEM processing offers increased geometric flexibility relative to other forms of laminated object manufacturing. The ability to carry out "tangent cutting" yields improved surface finish and faithfulness in approximation of a CAD model [7-9]. Furthermore, the ready inclusion of a fugitive material during building allows parts to by built with highly complex interior surfaces [3,4].

DEFINITION OF TEST PART

One class of parts that are well suited to CAM-LEM processing are fluidics. These devices are used for a variety of purposes, but share a common operational characteristic; all operate by motion of a condensed fluid through a series of internal passages within the device under a pressure gradient. CAM-LEM processing is an appealing method for fabricating these parts because it allows integral fabrication (i.e., formation of a single monolithic piece with appropriate internal passages), thus mitigating the need separate processing of subcomponents and assembly, and increasing reliability. CAM-LEM also offers increased flexibility in material choice. The

material choice. The particular fluidic circuit selected for this study requires five layers, has a circular motif, and is disc-shaped with three fold rotational symmetry.

MATERIALS: SELECTION, PREPROCESSING, AND LAMINATION

Three materials were selected for construction: aluminum oxide, silicon nitride, and stainless steel. Silicon nitride powder (GS-44, AlliedSignal Ceramic Components, Torrance CA) was tape cast using a binder system based on polyvinyl butyral. Commercial (Coors Electronic Ceramics, Chattanooga) aluminum oxide tapes were used. These tapes were 96% alumina and fabricated by tape casting using a binder system also based on polyvinyl butyral. Stainless steel tapes were fabricated by compression molding using a developmental injection molding feedstock (Rohm and Haas, Springhouse PA). The steel powder was gas-atomized 316L and binder system in this case was determined to be based on polymethyl methacrylate. For working with both the silicon nitride and aluminum oxide tapes, a fugitive tape system based on graphite powder has been developed in-house. Characteristics for all tapes are given in Table 1.

Table 1. Green Tape Characteristics

Tape	Thickness	Solids Loading	Binder Content	Porosity
Aluminum Oxide	600 μm	56.6 vol. %	20.5 vol. %	22.9 %
Silicon Nitride	300	51.6	29.9	18.5
Stainless Steel	600	64.0	36.0	none
Graphite*	300 or 600	42.8	21.9	35.3

*Thicknesses were processed to match various feedstocks. For this system, all calculations assume a graphite density of 2.3 g/cc.

For all systems, lamination was achieved using a variant of the adhesive lamination process that has been reported elsewhere [10]. The specifics of the adhesive formulation were varied for each system in order to optimize lamination efficiency and to obtain process tolerance (e.g., allow good adhesion throughout a broader window in time after the adhesive formulation was applied). Both the nature of the organic "package" and the characteristics of the porosity influence the choice of adhesive.

CAM-LEM PROCESSED PARTS

Successful parts were produced from all three materials. Figure 1 shows the cut outlines for both the aluminum oxide and graphite fugitive. Figure 2a shows an assembled part made from aluminum oxide tape with a graphite fugitive. The fugitive plays two roles; it defines the internal passages and it serves as a pressure-transmitting medium during lamination. Figure 2b is an image of the same part after pyrolysis of the binder and removal of the fugitive have been effected. Note that the fugitive is always removed prior to the onset of macroscopic shrinkage. This is done to avoid the occurrence of backstresses or encapsulation of fugitive by a densifying matrix. Figure 2c is an image of the fully densified part, in which the nominally 17% linear shrinkage is observed.

Figure 3a and 3b are back lit images of the translucent aluminum oxide part from two sides, respectively. The interior passages are clearly imaged and these figures demonstrate that the details of the interior surface are well preserved during postprocessing, i.e., firing.

Similarly good results were obtained using silicon nitride. Figure 4 shows an image of one face of a completely processed part. The tearshaped contrast is produced by low-level carbon doping of the silicon nitride in the outer layer where it was in contact with the fugitive underneath. This has been shown not to affect the properties of the material [11]. As silicon nitride is opaque,

it was not possible to image the interior directly, but functionality was demonstrated by simple flow tests.

The stainless steel version of this part is shown in Figure 5a and 5b. A high quality part also was produced in this material.

High lamination efficiency was confirmed by sectioning and preparing the cut surfaces using standard metallographic techniques. External dimensions of aluminum oxide and silicon nitride were determined using a coordinate measuring machine. Line scans across the diameter of the face containing the larger oriface were collected from several aluminum oxide samples as well as one stainless steel, and a pseudo-2D map was generated of the same surface of a silicon nitride part. This surface was chosen, rather than the opposite, because the three teardrop-shaped voids in the second layer present a more critical test of the ability to process parts with interior channels.

The line scans from the alumina indicate that the inclusion of the fugitive does not significantly affect the tendency of the sample to slump during firing. Line scans revealed that a small amount of slumping, on the order of 150 μm over a 15 mm span, occurred over internal cavities in all cases. A typical result is shown in Fig. 6. Similarly, the surface relief map of the silicon nitride part shows modest relief, see Fig. 7. The line scans from stainless steel part also show evidence of relief, but it is considerably more modest. The difference is attributed to the fact that both of the ceramics form an appreciable amount of liquid during firing (due to the presence of silicate sintering aids) whereas under the conditions used to sinter the stainless steel, the system remains completely solid. The results are entirely consistent with the expectations associated with these materials; the deformation during firing is comparable to that observed in these materials when conventionally processed.

CONCLUSIONS

The use of CAM-LEM processing to directly produce a component in a variety of structural materials has been demonstrated. Thus, CAM-LEM processing is an attractive method for conducting small scale production in the context of materials substitution trials.

A fugitive has been developed that is compatible with both aluminum oxide and silicon nitride. The fugitive has been used to produce integral parts with highly complex internal geometrical features.

ACKNOWLEDGEMENTS

This research was supported by the CAMP, Inc. Applied Research Program and the Office of Naval Research (ONR Grant Number N00014-95-10107). Aluminum oxide tape was supplied by Dr. Debra Horn of Coors Electronic Ceramics. Dr. John Pollinger, AlliedSignal Ceramic Components, supplied the silicon nitride powder and fired the silicon nitride parts. The stainless steel feedstock was supplied by Dr. Len Bogan of Rohm and Haas. Firing of the stainless steel parts was carried out at BFGoodrich, Brecksville OH, by Tom Nixon. Dr. Ajit Sane granted access to compression molding facilities at BP America. Finally, CAM-LEM is a multidisciplinary activity at Case Western Reserve University, we gratefully recognize the contributions of our colleagues in the Electrical Engineering and Applied Physics Department; Prof. W. S. Newman, Dr. Y. Zheng, and S. Choi.

REFERENCES

1. J. D. Cawley, Z. Liu, W. S. Newman, B. B. Mathewson, and A. H. Heuer, "Alumina Ceramics Made by CAM-LEM (Computer-Aided Manufacturing of Laminated Engineering Materials) Technology," Proc. Solid Freeform Fabrication Symp., Univ. Texas Austin, pgs. 9-16, (1995).

2. B. B. Matthewson, W. S. Newman, A. H. Heuer, and J. D. Cawley, "Automated Fabrication of Ceramic Components from Tape-Cast Ceramic," Proc. Solid Freeform Fabrication Symp., Univ. Texas Austin, pgs. 253-260 (1995).
3. Z. Z. Liu, P. Wei, B. Kernan, A. H. Heuer, and J. D. Cawley, "Metal and Ceramic Components Made via CAM-LEM Technology," Proc. Solid Freeform Fabrication Symp., Univ. Texas Austin, pg. 377-384 (1996).
4. J. D. Cawley, A. H. Heuer, W. S. Newman, and B. B. Mathewson, "Computer-Aided Manufacturing of Laminated Engineering Materials," Am. Ceram. Soc. Bull., 75 [5] 75-79 (1996).
5. J. S. Reed, Principles of Ceramic Processing, pgs. 525-534, John Wiley and Sons, New York (1995).
6. H. F. Mark et al., Encyclopedia of Polymer Science and Engineering Vol. 4, John Wiley and Sons, New York, pgs. 79-108, 1985.
7. Y. Zheng, S. Choi, B. Mathewson, and W. Newman, "Progress in Computer-Aided Manufacturing of Laminated Engineering Materials Utilizing Thick, Tangent-Cut Layers," Proc. Solid Freeform Fabrication Symp., University of Texas at Austin, peform Fabrication Symp., University of Texas at Austin, pg. 9-16 (1995).
8. Y. Zheng, PhD Dissertation, Case Western Reserve University, 1997.
9. Y. Zheng and W. S. Newman, "Software Design Challenges for Computer-Aided Manufacturing of Laminated Engineering Materials, Proc. 6th Eur. Conf. on Rapid Prototyping and Manuf., Univ. Nottingham, UK, pgs. 21-30, (1997).
10. P. Wei, J. D. Cawley, and A. H. Heuer, "CAM-LEM Processing: Lamination Technology," Proc. 6th Eur. Conf. on Rapid Prototyping and Manuf., Univ. Nottngham, UK, pgs. 95-104 (1997).
11. Personal communication, J. Pollinger, AlliedSignal Ceramic Components.

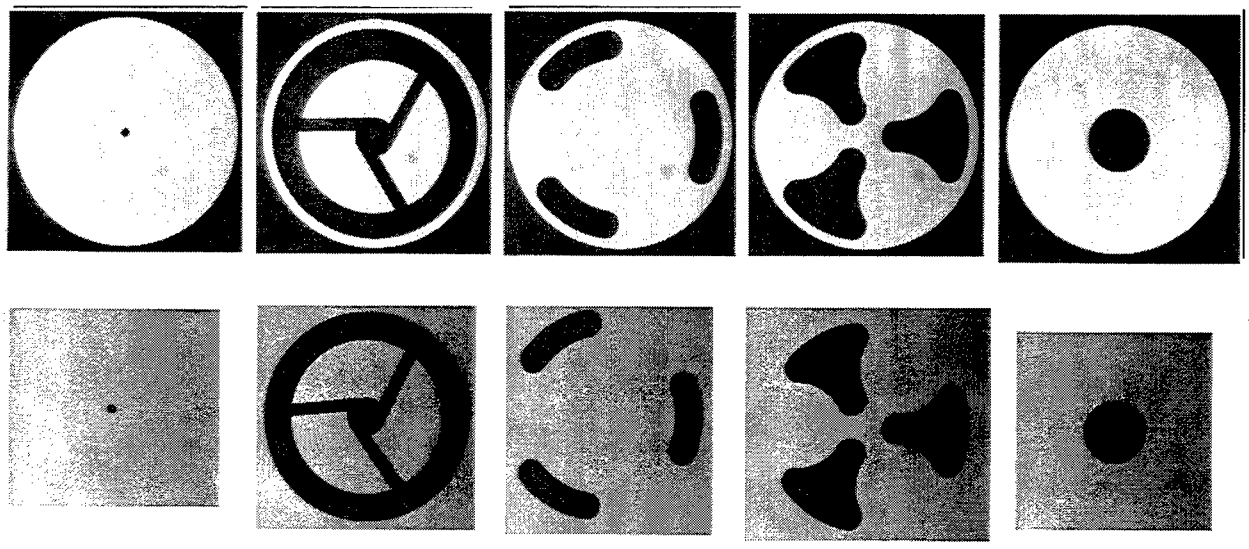


Figure 1 Digitial photographs of the cut outlines forming the positive space (from alumina, upper series) and the negative space (from fugitive, lower series) of the fluidic circuit selected for study.

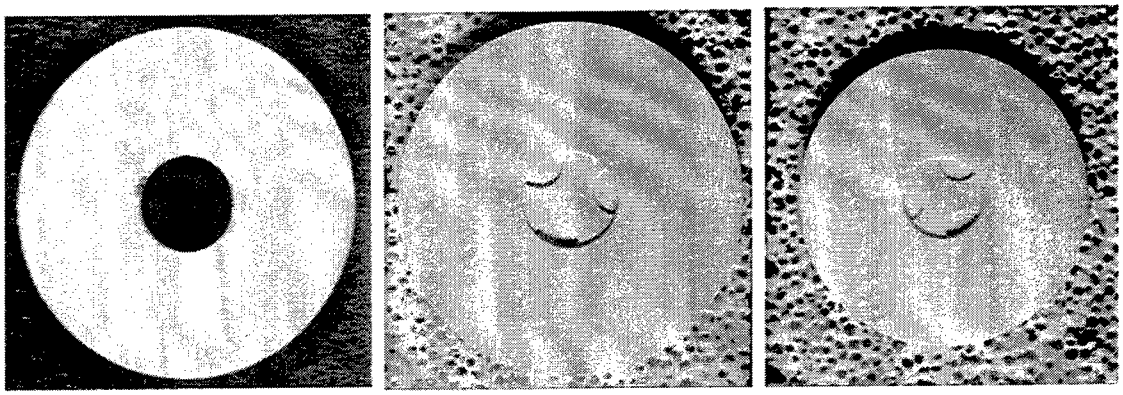


Figure 2 Aluminum oxide fluidic circuit after assembly. From left to right the images are: assembled with fugitive occupying the negative space, after heat treatment to remove binder and fugitive, and after complete densification.

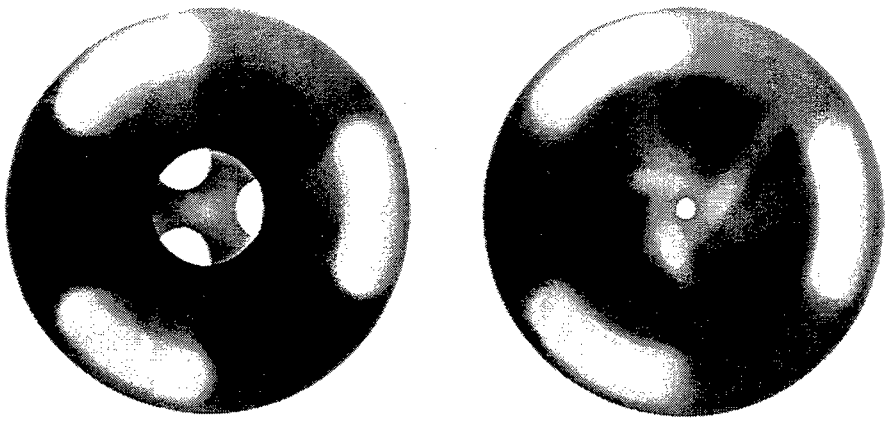


Figure 3 Back lit image of fired translucent aluminum oxide fluidic circuit allowing the well constructed interior channels to be observed.

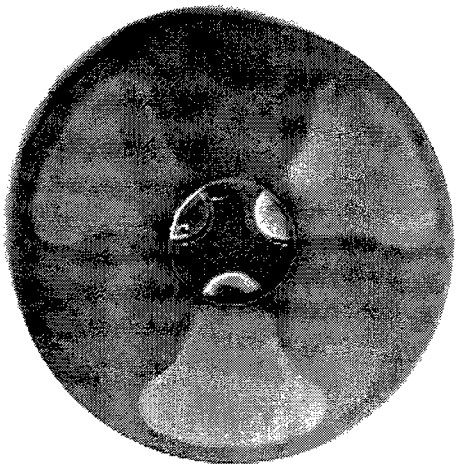


Figure 4 Fluidic circuit constructed in GS-44 silicon nitride.

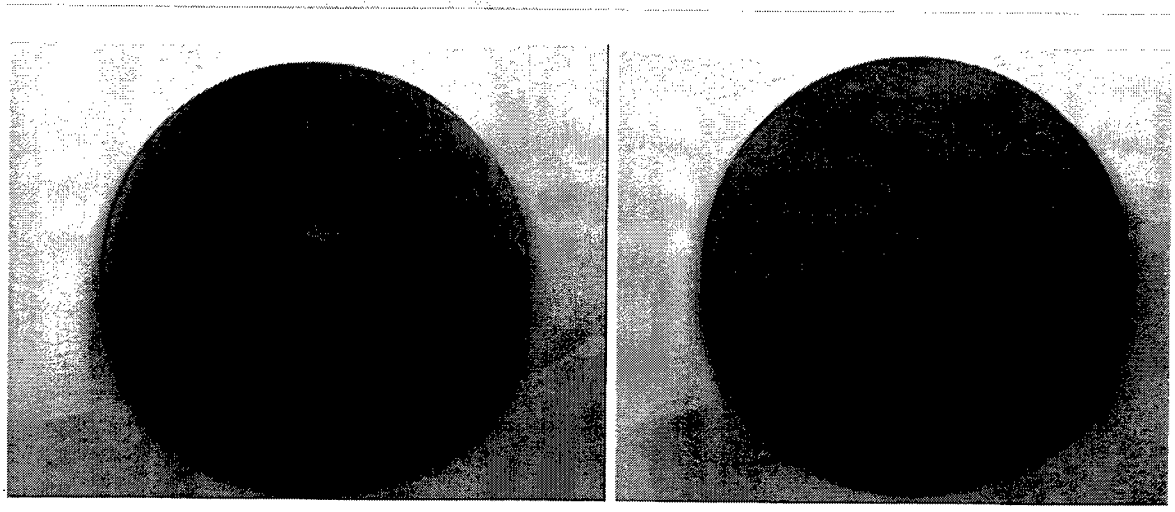


Figure 5 Fluidic circuit constructed in 316L stainless steel.

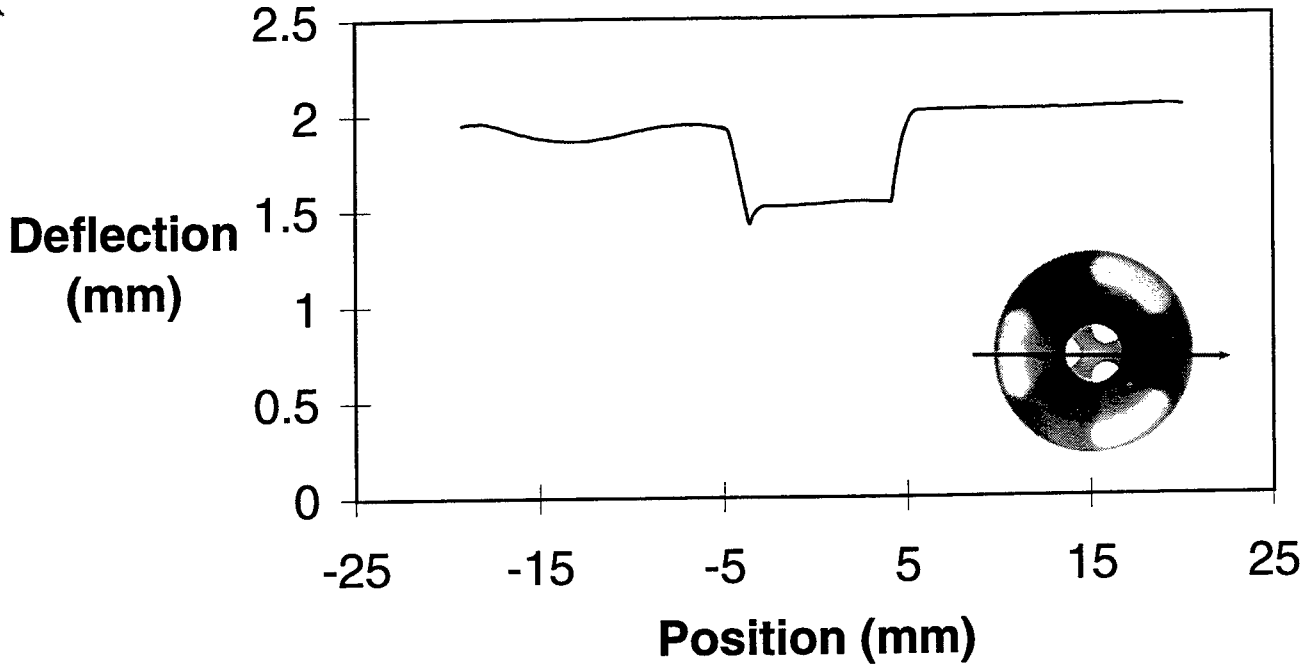


Figure 6 Images showing the direction of the coordinate measuring machine (CMM) line scan (inset) and typical results. The magnitude of the relief is unaffected by the presence or absence of the fugitive.

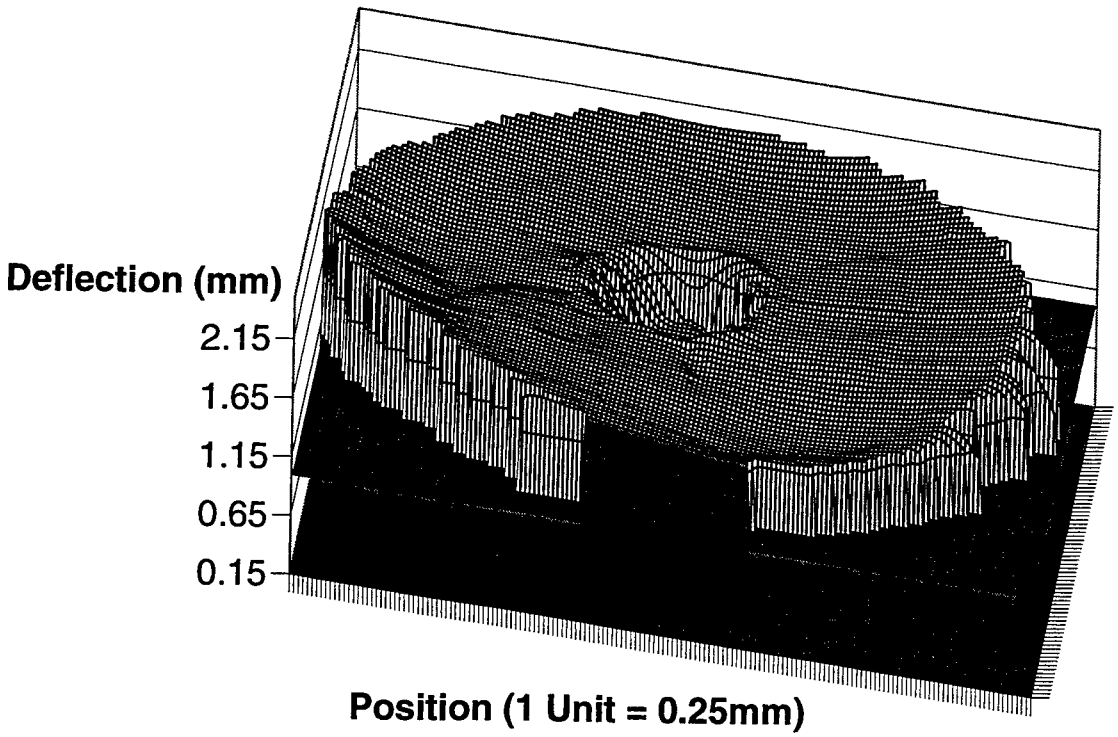


Figure 7 Relief map for the silicon nitride fluidic circuit generated using a series of parallel line scans on the CMM.

MULTI-MATERIAL PROCESSING BY LENS™

Michelle L. Griffith, Lane D. Harwell, J. Tony Romero,
Eric Schlienger, Clint L. Atwood, and John E. Smugeresky*

Sandia National Laboratories
Albuquerque, NM 87185, *Livermore, CA 94551

INTRODUCTION

During the past few years, solid freeform fabrication has evolved into direct fabrication of metallic components using computer aided design (CAD) solid models. [1-4] Laser Engineered Net Shaping (LENS™) is one such technique [5-7] being developed at Sandia to fabricate high strength, near net shape metallic components. In the past two years a variety of components have been fabricated using LENS™ for applications ranging from prototype parts to injection mold tooling. [8]

To advance direct fabrication capabilities, a process must be able to accommodate a wide range of materials, including alloys and composites. This is important for tailoring certain physical properties critical to component performance. Examples include graded deposition for matching coefficient of thermal expansion between dissimilar materials, layered fabrication for novel mechanical properties, and new alloy design where elemental constituents and/or alloys are blended to create new materials. In this paper, we will discuss the development of precise powder feeding capabilities for the LENS™ process to fabricate graded or layered material parts. We also present preliminary results from chemical and microstructural analysis.

EXPERIMENTAL

A. The LENS™ Process

The LENS™ system consists of a Nd:YAG laser, a controlled atmosphere glovebox, a 3-axis computer controlled positioning system, and multiple powder feed units. The positioning stages are mounted inside an argon-filled glove box (nominal oxygen level of 2-3 parts per million). The laser beam is brought into the glovebox through a window mounted on the top of the glovebox and directed to the deposition region using a focusing lens. The powder delivery nozzle is designed to inject the powder stream directly into the focused laser beam. The lens and powder nozzle move as an integral unit.

A CAD solid model is sliced into a sequence of cross sections and translated into a series of tool path patterns to build each layer. This file is used to drive the laser system to produce the desired component one layer at a time. A representation of the LENS™ fabrication process is shown in Figure 1. A solid substrate is used as a base for building the LENS™ object. The laser

beam is focused onto the substrate to create a weld pool in which powder is simultaneously injected to build up each layer. The substrate is rastered beneath the laser beam to deposit the desired geometry for each layer. After deposition of each layer, the powder delivery nozzle and focusing lens assembly is incremented in the positive Z-direction to build a three dimensional component, layer additively.

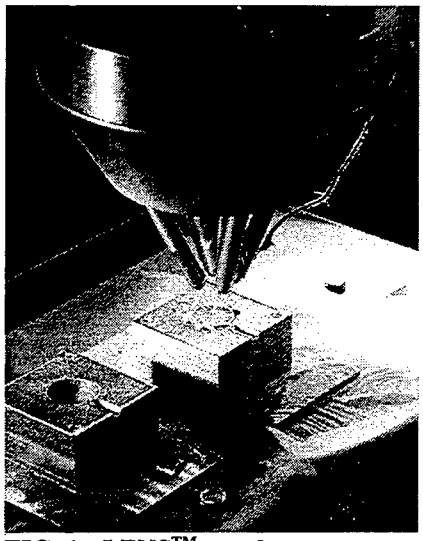


FIG. 1: LENS™ powder nozzle and fabricated parts.

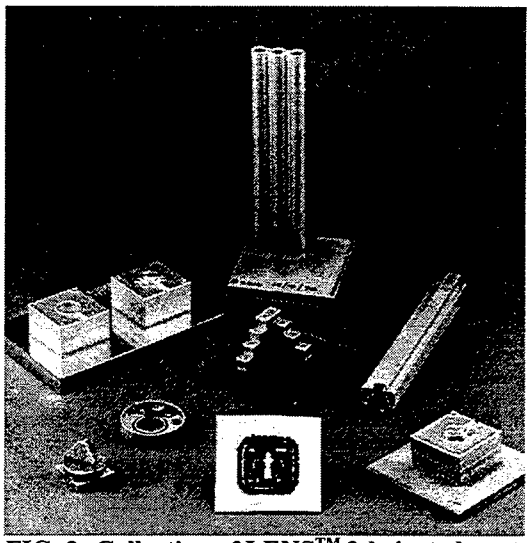


FIG. 2: Collection of LENS™ fabricated parts.

After determining the basic LENS™ parameters [laser power, powder feed rate, traverse velocity, layer thickness, hatch spacing] for a chosen material [5], extrusion or solid geometries are fabricated. Figure 2 shows a collection of components fabricated with LENS™. With an understanding of the LENS™ parameters, fully dense parts are repeatedly built with errors less than +0.005" in the X and Y dimensions and less than +0.015" in the Z dimension [1].

Near net shape components are fabricated with LENS™ having high strengths. Because of the rapid cooling of the weld pool, the as-processed material has a very fine grain structure (< 4 μm), which affects the mechanical properties. Results from room temperature tensile testing [1] of the as-deposited 316 stainless steel show high strength properties [σ_y = 90 ksi, σ_{ult} = 120 ksi] which significantly exceeds that for the reported value of annealed material [σ_y = 35 ksi, σ_{ult} = 85 ksi] [9]. Nevertheless, the ductility is retained in LENS™ fabricated parts, where elongation of 50% (in 1 inch gauge length) is typically achieved. Hardness testing of tool steel materials, such as H13, have values exceeding 59 R_c.

B. Multi-material Powder Feed

Development of accurate powder feeding capabilities was required for precise control of material placement. Previously, the LENS™ process fed powder into the molten pool for accurate control of line height over a narrow range of flow conditions. The powder feeder was redesigned for accurate flow conditions over a large range of flow rates. Moreover, computer control was integrated into the powder feed system for unattended operation during fabrication of parts. Diagnostic testing was used to test powder feeder designs and to study line heights to

determine flow over a variety of feed conditions. Figure 3 shows a comparison between two powder feeders versus flow rates for a chosen laser power and traverse speed. The powder feeders correspond reasonably well, where both feeders show a linear change in line height for increasing powder flow rate. This linear change is beneficial for controlling powder blending or grading in multi-material fabrication.

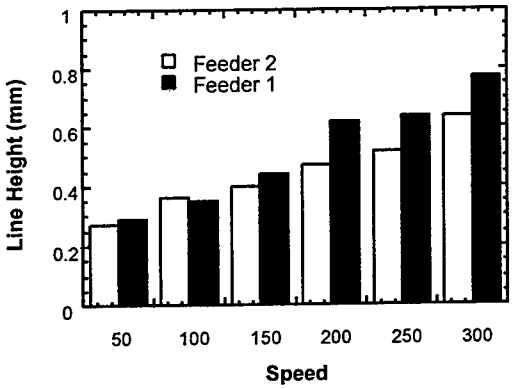


FIG. 3: Line build height versus powder flow rate for re-designed powder feeders 1 & 2.

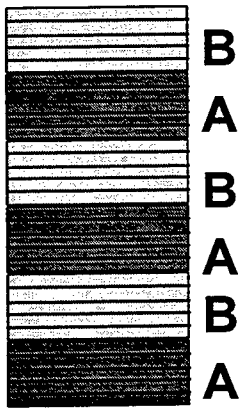


FIG. 4: Schematic of layered deposition. Each material region contains four layers of fabrication before alternating.

Two fabrication styles were used to test the powder feeders: (1) graded deposition and (2) layered deposition. Graded samples consisted of precise deposition where material A was homogeneously deposited, then material B was slowly blended into A from 0 to 100 volume percent (v/o), and lastly material B was fabricated on top. A schematic of layered deposition is shown in Figure 4. Layered samples consist of alternating regions of material, A and B, where each region is built with four layers of material. This paper will describe results for two material combinations: (1) stainless steel 316 (SS316) and Inconel 690 (In690), and (2) SS316 and a special tool steel grade Micromelt 10 (MM10) by Carpenter.

Samples were cross-sectioned, polished, and etched. Optical microscopy and scanning electron microscopy (SEM) were used to evaluate microstructure and porosity. Quantitative analysis of elemental constituents was determined with electron microprobe. Hardness was characterized by either Vickers or Rockwell techniques. Ferrite content in the microstructure was measured as Ferrite Number (FN) by a Magne gage and ferrrite scope.

RESULTS

A. Graded Structures

Figure 5 shows the quantitative elemental constituent results for blending In690 into SS316. As expected, the iron (Fe) content decreases as In690 is added, resulting in increasing nickel (Ni) content. The elemental constituents match with values calculated using a simple rule of mixtures model. Processing conditions were not optimized, but the density of the sample was greater than 98%.

Figure 6 shows the change in hardness over the graded sample. The hardness drops as small amounts of In690 are added to the SS316. At approximately 25 v/o In690, the hardness reaches a low value of 75 R_B. Beyond 25 v/o, the hardness increases until pure In690 is fabricated. This change in hardness at 25 v/o is due to a change in solidification mode. Pure SS316, as-processed by LENS^{TM}, begins solidifying as primary ferrite. Upon cooling, the primary ferrite undergoes a phase change to austenite with a small amount (< 5%) retained skeletal ferrite, referred to as the "ferritic-austenitic solidification mode". [10] In contrast, pure In690 solidifies by primary austenite solidification, with retained eutectic ferrite, otherwise known as the "austenitic-ferritic solidification mode". [10]

Figure 6 shows the change in the skeletal ferrite as measured by ferrite number (FN). In the pure SS316, the ferrite content is approximately 3 FN, and this decreases as In690 is graded into the mixture. In the range of 20-30 v/o In690, the skeletal ferrite disappears because of the changing solidification mode (ferritic-> austenitic) and FN = 0. Moreover, the decreasing iron content along with changes in the Cr/Ni equivalency ratio convert the solidification mode from the primary ferritic to the primary austenitic solidification mode. Beyond 25 v/o In690, the hardness increases linearly through solid solution of Ni and Cr additions.

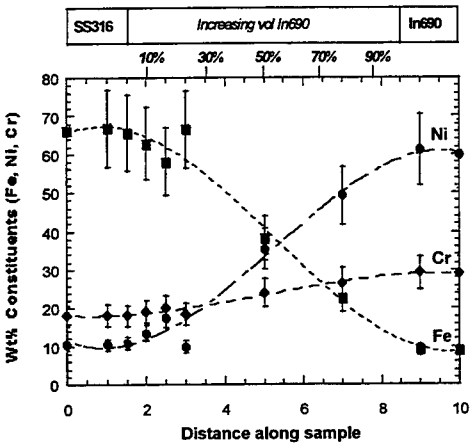


FIG. 5: Alloyed constituent results for blending In690 into SS316 from 0 -100 volume percent.

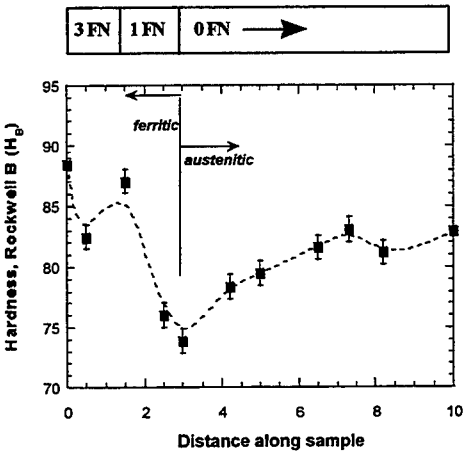


FIG. 6: Hardness values for graded structure from Fig. 5.

B. Layered Structures

(i) SS316/In690

Figure 7a is a SEM micrograph showing three layers in the alternating SS316/In690 part, where the darker shade material is SS316. During LENS™ fabrication of each layer, a small fraction of the previous layer is melted to create the weld pool into which the new material powder is injected. Interestingly, as the stainless steel is deposited onto the Inconel, the weld pool wicks the In690 into the solidification structure as shown in Figure 7b. However, the In690 retains a sharp interface when deposited onto the stainless steel. Further studies are required to understand this effect.

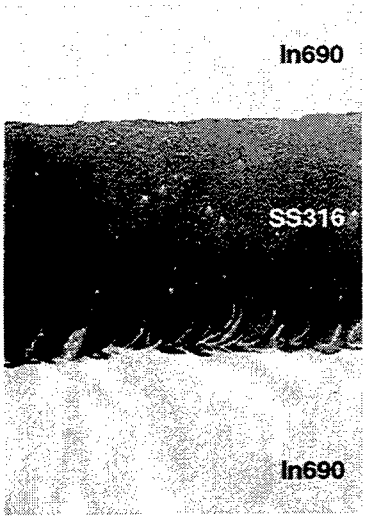


FIG. 7a: Layered structure of SS316 (Dark) and In690 (Light). Growth direction is vertical.



FIG. 7b: High magnification of interface region between SS316 and In690.

(i) SS316/MM10

Figures 8a and 8b show the layered structure for tool steel (MM10) and SS316. In contrast to the SS316/In690 layered sample, each interface is sharp. The fine precipitation of carbides in the tool steel results in high hardness, with a value of 62 R_c. The rapid solidification with fine grain size of the SS316 results in a hardness value of 22 R_c.

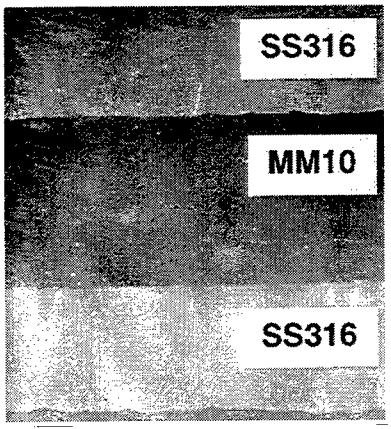


FIG. 8a: Layered structure of SS316 and MM10. Growth direction is vertical.

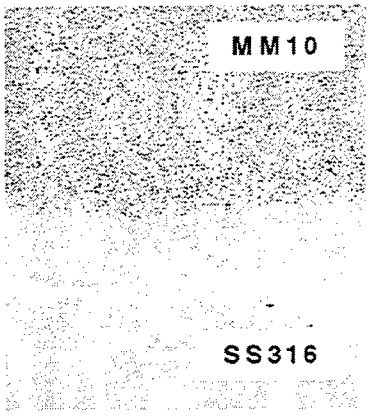


FIG. 8b: Interface between the tool steel MM10 and SS316.

CONCLUSIONS

In summary, a new powder feeder design allows for controlled flow, where dense parts were fabricated in either graded or layered structures. For graded structures, the microstructure and hardness could be tailored when blending In690 into stainless steel 316. Dense structures could be fabricated in a 4-layer composite for two materials, SS316 and In690, and SS316 and MM10.

With this initial work complete, studies of phase formation, microstructural development, and property tailoring have the potential for unique fabrication of components by LENS™ processing. Future work will require further software development to control material placement during part fabrication.

ACKNOWLEDGMENTS

This work supported by the U. S. Department of Energy under contract DE-AC04-94AL85000. Sandia is a multiprogram laboratory operated by Sandia Corporation, a Lockheed Martin Company, for the United States Department of Energy.

REFERENCES

[1] M. L. Griffith, D. M. Keicher, C. L. Atwood, J. A. Romero, J. E. Smugeresky, L. D. Harwell, D. L. Greene, *Free Form Fabrication of Metallic Components using Laser Engineered Net Shaping (LENS™)*, proceedings of the Solid Freeform Fabrication Symposium, August 12-14, 1996, Austin, TX, p.125.

[2] J. R. Fessler, R. Merz, A. H. Nickel, F. B. Prinz, L. E. Weiss, *Laser Deposition of Metals for Shape Deposition Manufacturing*, proceedings of the Solid Freeform Fabrication Symposium, August 12-14, 1996, Austin, TX, p. 117.

[3] F. Klocke, H. Wirtz, W. Meiners, *Direct Manufacturing of Metal Prototypes and Prototype Tools*, proceedings of the Solid Freeform Fabrication Symposium, August 12-14, 1996, Austin, TX, p.141.

[4] J. Mazumder, K. Nagarathnam, J. Choi, J. Koch, D. Hetzner, *The Direct Metal Deposition of H13 Tool Steel for 3-D Components*, Journal of Materials, Vol 49, Number 5, May 1997, p. 55.

[5] D. M Keicher, J. L. Jellison, L. P. Schanwald, J. A. Romero, D. H. Abbott, *Towards a Reliable Laser Powder Deposition System through Process Characterization*, 27th International SAMPE Technical Conference, Vol. 27, Diversity into the Next Century, proceedings of SAMPE '95, Albuquerque, NM, October 12-14, 1995, p. 1029.

[6] D. M. Keicher, J. A. Romero, M. L. Griffith, C. L. Atwood, *Laser Metal Deposition of Alloy 625 for Free Form Fabrication*, proceedings of the World Congress on Powder Metallurgy and Particulate Materials, June 16-21, 1996, Washington, D.C.

[7] J. E. Smugeresky, D. M. Keicher, J. A. Romero, M. L. Griffith, L. D. Harwell, *Laser Engineered Net Shaping (LENS^{TM}) Process: Optimization of Surface Finish and Microstructural Properties*, proceedings of the World Congress on Powder Metallurgy and Particulate Materials, June, 1997, Chicago, IL.

[8] M. L. Griffith, C. L. Atwood, J. E. Smugeresky, L. D. Harwell, D. L. Greene, E. Schlienger, *Using Laser Engineered Net Shaping (LENS^{TM}) to Fabricate Metal Components*, proceedings of the Rapid Prototyping and Manufacturing Conference, April 22-24, 1997, Dearborn, MI.

[9] Alloy Digest Typical Value (gauge length of 5.8 cm), ASM International p. ss-114.

[10] J. A. Brooks, J. C. Lippold, *Selection of Wrought Austenitic Stainless Steels*, ASM Handbook Volume 6: Welding, Brazing, and Soldering, published by the American Society of Metals, 1993, p. 456.

Shrinkage, Weight Loss and Crack Prevention During Binder Burn Out of Components Produced by Fused Deposition of Ceramics (FDC)

P. Bhargava, A. Bandyopadhyay, S. Rangarajan, G. Qi, C. Dai, S. Wu, S. Danforth and A. Safari
Department of Ceramic and Materials Engineering, Rutgers University, Piscataway, NJ 08855

ABSTRACT

In the present study the sequential stages of the previously established binder burn out (BBO) route were characterized by obtaining precise shrinkage and weight loss measurements from interrupted runs. A DoE (Design of Experiments) approach was adopted to systematically investigate the effect of process variables; such as the heating rates during critical segments, part dimensions and environment (flowing nitrogen vs vacuum) on the shrinkage, weight loss and cracking during binder burn out. A stepwise TGA was performed to study the effect of ramp rate and dwell time on the kinetics of binder burn out, and an experiment was conducted to determine optimum wicking conditions. The results from this study have been used to maximize the weight loss and minimize the cracking during binder burn out cycle for FDC parts with different sizes.

1. Introduction: Fused deposition of ceramics (FDC) is a very efficient near net shape processing technique to produce functional ceramic components with highly complex geometries without the use of any part specific tooling, dies or molds. The other key advantages of this process include rapid and cost effective iterative design optimization and small batch production of complex, high value parts. Among the different steps involved in FDC of functional ceramic components, binder removal is critical to producing defect free sintered parts with functional quality.

In the present study, binder removal is done by burning out the binder in two stages. In the first stage (Fig. 1), the majority of the binder is burned out in the presence of high purity flowing nitrogen. The residual binder after stage I is burned out in air during stage II of the process. The binder burn out (BBO) behavior is affected by a large number of variables including: (a) material specific variables such as - ceramic particle size distribution and surface area of the powder, ceramic volume fraction, ceramic powder agglomeration, binder composition, binder volume fraction, and the nature of powder bed, (b) process specific variables such as - binder distribution within the green part (as in extrusion or different FDC build patterns), heating rate, dwell temperature and times, furnace environmental conditions, the flow rate or partial pressure of gases (air, inert or vacuum), and (c) part specific variables such as - part size, geometry, surface area to volume ratio, FDC build orientation, preexisting porosity in the FDC part or other defects.

Previous work at Rutgers established a working heating schedule for BBO of FDC components up to 0.5" x 0.5" cross-sectional area (Fig. 1) [1]. In the first step of this BBO cycle, nearly 80 % of the binder is removed from the green body and the residual binder is removed using a static air cycle up to 450°C. The objectives of this study were: (a) to examine the sequential binder weight loss and the associated shrinkage at different temperatures of the BBO cycle, (b) to use a Design of Experiments (DoE) approach to identify the critical variables in the binder burn out process and their effects, (c) gain some insight into the mechanisms of BBO process that lead to shrinkage and cracking of parts, and (d) to optimize the existing BBO cycle to obtain defect free parts.

2. Experimental: Samples for this study were produced via FDC and single screw extrusion techniques with RU9 thermoplastic binder loaded with 55 volume % GS-44 silicon nitride powder [2]. Oleyl alcohol was used as a dispersant. The RU9 binder is composed of four components -a

polymer that acts as a backbone, an elastomer that imparts flexibility, a tackifier that promotes adhesion between roads during FDC, and a wax component that modulates the viscosity of the binder system.

Samples were ground in the green state using 120, 320, 600 grit SiC paper to obtain a smooth surface finish. Samples were weighed and the dimensions were carefully measured at the center of the opposing sample faces using a high precision micrometer. Interrupted binder burn out experiments were carried out with extruded samples with dimensions - 1.27cm x 1.27cm X 1.27cm. For the Design of Experiments (DoE) and other controlled studies, FDC samples with either - 1.6cm x 1.6cm or 2.5cm x 2.5cm cross-sectional area with 1.27cm along the thickness direction were used. The thickness dimension was also the build direction duirng FDC. The present study involved only the stage I of the BBO cycle since about 80 % of the binder removal occurs in this stage. Moreover, most of the cracking is most likely to occur during stage I of the BBO cycle [1]. For the interrupted runs, 3 extruded samples per temperature and time were used. For the DoE and other studies, 1 FDC sample per experiment was used. For at least one FDC sample per DoE condition, shrinkage along the build direction (z) was measured at the face center and also near the edges.

2.1 Interrupted binder burn out: The baseline BBO cycle, developed earlier for parts with 1.27cm x 1.27cm cross-section was used (Fig.1). Samples were heated up to selected temperatures, and after a 5 hour dwell time, the samples were furnace cooled to room temperature.

2.2 Design of Experiments (DoE): The DoE approach was initiated with the objectives of: (1) developing a model that can predict optimum BBO conditions, (2) identifying the most critical variable among the selected experimental variables and (3) determining if binder removal from larger cross-section parts can be carried out using the existing or modified cycle without generating any defects [3].

Based on historical data [1], the following factors were identified as the most critical experimental variables during BBO. For each of the variables the low and high values used in the DoE are also shown -

(1) Ramp rate ($\mathbf{r_1}$) for the segment 80°C to 150°C, with low and high values - 4 and 10°C/h.
(2) Ramp rate ($\mathbf{r_2}$) for the segment 150°C to 300°C, with low and high values - 2 and 10°C/h
(3) Cross-section (**x-sect**) of the samples, with low and high values - 2.56cm^2 and 6.25cm^2.
(4) Environment (**env**) following the 5hr hold at 200°C - flowing N_2 and vacuum.

The design matrix is shown in Table I. The low and high values for each of the factors were purposefully chosen such that significant changes in the measured response could be produced. Specifically, the lower values of the ramp rate were chosen based on the historical data for successful BBO runs. From the previously available data on Hg porosimetry, it was known that generation of interconnected porosity in the FDC samples starts around 200°C. Thus, in the DoE, condition involving the use of vacuum was implemented after a 5 hour hold at 200°C.

The following conditions were fixed during the DoE: heating rates except r_1 and r_2; dwell times for all the soak segments; peak temperature of each of the BBO segments; point of initiation of vacuum during BBO; placement of samples with respect to their build orientation during FDC; hand-tooling procedure; embedding of the part in the activated carbon setter powder.

The measures of response for the process were: (1) shrinkage along x, y and z (FDC build direction), (2) part cracking as determined by visual inspection, (3) binder weight loss, and (4) difference in z shrinkage from center to the edge of the sample on the x-y face. DoE KISS (Air Academy Associates, Colorado Springs, CO) software was used to analyze the experimental data.

TABLE I: DoE Design Matrix and the Corresponding Measures of Response:

Run #	r_1 (°C/hr)	r_2 (°C/hr)	x-sect (inch^2)	env$^+$	Δx (%)*	Δy (%)*	Δz (%)*	Crack/ Delamination	Gradient in Δz^{ϕ} (%/inch)	Δwt. (%)
1	4	2	0.4	1	-1.04	-0.99	-0.93	No		94.6
					-0.87	-0.89	-1.24	No	0.2	94
2	4	2	1	1	-0.31	-0.76	-0.81	No		96
					-0.72	-0.76	-0.60	No	-0.41	92
3	4	10	0.4	-1	-0.83	-0.86	-0.70	Yes		> 99
					-0.62	-0.62	-0.62	Yes	0.05	> 99
4	4	10	1	-1	-0.63	-0.80	0.78	Yes		> 99
					-0.67	-0.72	0.58	Yes	-1.16	> 99
5	10	2	0.4	-1	-0.73	-0.88	-0.64	No		> 99
					-0.79	-0.78	-0.9	No	0	> 99
6	10	2	1	-1	-0.65	-0.71	1.27	Yes		> 99
					-0.74	-0.44	0.44	Yes	-1.02	> 99
7	10	10	0.4	1	-0.85	-0.84	-0.32	Yes		> 99
					-0.58	-0.75	0.27	Yes	0.15	92
8	10	10	1	1	-0.41	-0.35	1.5	Yes		94.8
					-0.52	-0.56	1.8	Yes	-1.88	91

* negative values imply shrinkage and positive imply an expansion; + Here 1 represents N_2 and -1 represents vacuum; ϕ This is computed as the difference between measured shrinkage at the edge and center of the face divided by the half width of the sample, thus negative value implies greater shrinkage at the edge.

2.3 Thermomechanical (TMA) and thermogravimetric (TGA) analysis: A TMA (Perkin-Elmer) was used to measure the thermal expansion of the RU9 binder from room temperature to 70°C. The thermal expansion of RU9 was found to be $147x10^{-6}$ /°C, much larger than the $3.2X10^{-6}$ / °C for the Si_3N_4 used. A TGA was performed to determine the effects of heating rate and dwell time on the kinetics of weight loss in different temperature regimes. A RU955 sample fabricated by FDC was used for the TGA run. The results obtained are shown in Figure 2.

3. Results and Discussion

3.1 Interrupted binder burn out: The results from interrupted BBO tests are shown in Figure 3. The data obtained in these studies was compared to the previous data [1] on binder weight loss measured for samples air quenched from the temperatures considered. At 150°C, the binder weight loss increased from 4 % for quenched samples to 10 % for samples with a 5 hours hold. In contrast a 5 hour hold at 350°C did not lead to significant increase in the binder weight loss as compared to that obtained with no hold. Thus, at higher temperatures, the sample equilibrates with the surrounding environment in a much shorter time as compared to that at lower temperatures.

TGA analysis (Fig. 2) showed very little binder weight loss (≤ 2.5 %) until the temperature exceeded 190°C. Thus the weight loss at 150°C (~ 10 %) must have been due to the flow of liquid binder via capillarity into the surrounding bed of activated carbon powder [4]. This outward flow of binder enhanced by the presence of powder bed, in this case activated carbon, is termed wicking. The loss of binder by wicking induces particle rearrangement leading to particle compaction and thus

shrinkage in sample dimensions [5]. The largest shrinkage was obtained in the segment 80°C to 150°C (Fig. 3(b)). The measured shrinkage in part dimensions decreased with increase in temperature but this does not imply an increase in particle separation. The observed decrease in shrinkage is most likely due to the fact that when the part is cooled from higher temperatures it has lost more of the high thermal expansion phase, i.e. the binder [6].

3.2 Design of Experiments : A half factorial design matrix was used in this study. The design included 4 factors with 8 runs, and for each of the runs two iterations were performed. The design matrix and the corresponding results for the different measures of response are shown in Table 1. The run #1 represents the baseline BBO cycle that was previously developed at Rutgers for 0.5" x 0.5" cross-sectional parts. The complete baseline BBO cycle is shown in Fig.1. All the other conditions represent changes in the four variables incorporated into the baseline cycle.

The importance of the variables considered in this study can be understood by analyzing the step by step changes that occur during binder burn out of the FDC parts. As a part is heated, the binder begins to soften and expand causing the ceramic particles to move farther apart. With further increase in temperature, the viscosity of the binder system decreases allowing it to flow out of the part into the surrounding powder bed due to capillary forces. The capillary forces applied by the binder as it wicks out cause particle compaction that leads to shrinkage in part dimensions. As seen through weight loss and shrinkage (section 3.1) measurements, this mechanism is dominant at temperatures near 150°C . Since particle rearrangement occurs in this low temperature regime ($T < 150°C$), the heating rate r_1 can influence the final shrinkage percentage. During the low temperature regime, the two opposing processes in terms of particle packing that occur are the large thermal expansion of the binder that causes particles to move apart and the outward flow of binder at slightly higher temperature that cause particle compaction. When very high heating rates (r_1) are used, the particles that moved away due to expansion may not get compacted due to insufficient time for the binder to flow out especially in larger cross-section samples unless compensated for by longer hold times at appropriate temperature (see section 3.3). High values of r_1 can also cause cracking due to non-uniform heating of the sample cross-section. In the present DoE even though the sample size has been considered as a variable, the dwell time has not been considered as a variable.

Heating to higher temperatures ($T > 185°C$) initiates loss of binder by decomposition/evaporation mechanism (Fig.3). For 0.5" x 0.5" RU955 parts, porosity formation starts from 200°C [1]. Thus heating above 200°C will lead to a reduction in the diffusion path for escape of the binder from the dimensions of sample to the scale of the microstructure. It is notable that under the same environmental conditions as used for the 0.5" x 0.5" cross-sectional area parts, evolution of the pore structure in larger parts will require a different heating schedule due to the greater amount of binder that needs to be removed. For larger samples, heating at faster rates (r_2) for $T > 150°C$ will result in less time for formation of interconnected porosity, leading to a build up of vapor pressure within the sample due to rapid decomposition. The build up of vapor pressure within the sample can only be prevented if the removal rates match or exceed the vapor generation rate. Usually the high vapor pressure within the sample can cause formation of delamination/cracks. For the situation described above, if vacuum is used before the interconnected porosity has developed, the large gradient created between the inside of the sample (positive vapor pressure) and the vacuum (outside the sample) will promote the formation of delamination/cracks parallel to the build layers.

Analysis of the data presented in Table I indicates that the shrinkage along x and y direction was significantly affected by an increase in sample dimensions but was insensitive to changes in heating rates (Fig. 4(a)) or the environment. In contrast, the shrinkage along z (Fig.4 (b)) or the

build direction was significantly affected by all the variables - heating rates during low and high temperature regimes, part cross-section area and environment - but among them, the cross-section area exhibited the strongest influence. This difference is related to the binder distribution in the FDC samples. As shown by a previous study [1], a greater concentration of the binder exists in between the build layers (normal to the build direction). Thus, for the samples in this study (with z as the FDC build direction), the shrinkage after complete binder removal should be greater in z direction than in the x or y directions. For most of the DoE runs, measured shrinkage in the z direction was less than in x or y directions except for run #1 which is the cycle developed previously at Rutgers

The DoE analysis predicted that the part cracking tendency is most strongly influenced by changes in ramp rate during the high temperature regime specifically between 150 - 300°C . Most of the delamination cracks observed in this study were perpendicular to the FDC build direction. The use of vacuum had only a slight influence on the part cracking tendency.

The gradient in shrinkage along z (measured on the x-y face) from face center to the edge is a measure of the extent of porosity developed within the sample before significant weight loss begins to occur by decomposition/evaporation. Analysis of the measured data indicated that the gradient in shrinkage was most strongly influenced by the size of the samples. For smaller samples the shrinkage in z (build direction) was greater at the face center than at the edge, while for the larger samples (1" x 1" cross-sectional area) the measured shrinkage was always greater at the sample edges than at the face center, regardless of the environment used (N_2 or vacuum) (see Table 1). In general, the magnitude of this difference between shrinkage at the face center and the edge was greater for larger cross-section samples. This implies that for the larger samples, the binder could not be removed very uniformly from the whole volume of the sample possibly due to a lack of well-connected path for binder removal throughout the sample. The gradient in shrinkage along z from center to the edge of the sample was smallest for the condition with the lowest ramp rates (condition 2 in Table 1).

There are few studies [7] reported in the literature on the use of vacuum to enhance binder removal for larger size parts. In the present study, vacuum was used to investigate the removal of binder from large samples and to investigate the relationships between the use of vacuum and different heating rates. For the purpose of matching the rates of generation of vapors from the binder and their removal, vacuum should not be applied along with the use of high heating rates. Comparing conditions 3 and 5 (Table 1) it can be seen that the use of high ramp rate coupled with the use of vacuum (run # 3) leads to cracking, while a lower ramp rate (r_2 = 2°C/hr) with vacuum (run #5) did not lead to cracking. The use of vacuum with high heating rates can result in one or more of the following: (1) insufficient time to create adequate porosity leading to a pressure differential between the inside and outside of the sample, (2) binder removal preferentially from the surface causing a gradient in particle packing from outside to inside which leads to residual stresses, (3) excessive vapor generation due to both rapid heating and the driving force due to negative pressure (Le Chatelier's principle). The existence of large pressure differential or residual stresses can lead to defect formation inside or at the surface of the sample.

The initiation of vacuum at low temperatures can also lead to similar effects due to insufficient time for creation of well connected path for binder removal throughout the sample. This is illustrated by conditions 4 and 6 where the larger cross-section samples were used. For smaller samples, the time spent during heating to initiation of vacuum was sufficient as suggested by the uniform measured shrinkage and the absence of any cracks (condition 5). Notice that the heating rates (r_1 and r_2) were varied in the same range and dwell times were the same for both the small and large size samples used in this study. The former is a requirement to enable comparison among different DoE conditions. From the above discussion it can be concluded that the use of *low* vacuum

especially during dwell segments or accompanied by low heating rates may be favorable for enhanced binder removal rates. It is important to apply the vacuum only after generation of interconnected porosity in the sample.

3.3 Stepwise TGA and comparison of wicking at different temperatures: As shown in Fig. 3 it can be seen from the stepwise TGA that any significant weight loss by decomposition/vaporization does not start until about 185°C . The dwell segments at higher temperatures also show a higher weight loss rate than those at low temperatures. Thus larger samples should be subjected to longer dwell times (at higher temperatures) to achieve equilibrium weight loss before increasing the temperature further. The weight loss rate and thus the rate of vapor generation increased significantly above 300°C suggesting the use of lower ramp rates at high temperatures.

The previously established BBO cycle (Fig.1) included a dwell at 150°C to promote binder loss by wicking. A dwell at a temperature greater than 150°C but lower than the temperature at which significant weight loss by vaporization begins can enhance wicking due to lowering of binder viscosity. Since the TGA indicated that significant weight loss by vaporization begins around 185°C, an experiment was conducted to examine the effects due to wicking at higher temperature (T < 185°C). The following two conditions were chosen for comparison - 150°C and 175°C with 10 hour dwell times using the smaller size FDC samples (0.63" x 0.63" x 0.5"). The weight loss and the associated shrinkages obtained are shown in Table II. The z shrinkages from center to the edge of the sample were quite uniform. Similar experiments have to be performed to confirm if uniform shrinkage can be obtained at the higher wicking temperature for larger samples.

TABLE II. Comparison of Binder Wicking Conditions and Associated Shrinkage and Weight Loss.

Interrupted BBO condition	Δx (%)	Δy (%)	Δz (%)	binder weight loss (%)
150°C, 10 hours	-1.17	-1.15	-1.18	8.10
175°C, 10 hours	-1.44	-1.34	-1.97	11.19

From the data presented in Table II above, it can be seen that shrinkage caused by wicking along the z (FDC build direction) is a strong function of temperature, while shrinkage along x and y are somewhat less sensitive to the temperature at which wicking occurs.

Based on all the above results some of the changes to the BBO cycle (Fig.1) that have been/will be made include - direct ramp up to 80°C and a 2hours dwell; a higher temperature dwell at 175°C (5 hours) to promote wicking; increase dwell times with increases in sample size; increase the final temperature to 400°C (5 hours) to decrease the amount of residual binder/carbon to be burned off during the air cycle.

Summary and Conclusions: (1) Significant amount of the particle packing occurs in the low temperature regime when the dominant binder weight loss is due to wicking; (2) Binder removal by wicking at higher temperatures (low viscosity) can lead to greater weight loss and shrinkage; (3) Cracking of parts was found to be most significantly influenced by heating rates; (4) Cracks/delamination always occurred perpendicular to the z direction and not across the layer; (5) Changes in heating rates had a slight influence on shrinkage along x and y directions, but significant influence on shrinkage along z (build direction); (6) Shrinkage along x, y and z was strongly influenced by changes in the size of the sample; (7) Use of vacuum can prove to be very useful in accelerating binder removal when used at an appropriate stage i.e. when interconnected porosity has formed; (8) Vacuum should preferably be used during hold segments or with lower ramp rates.

Acknowledgments: The authors acknowledge the financial support from DARPA/ONR (contract no. N00014-94-0115). The authors also acknowledge the discussions and support provided by Mr.R. Clancy, Drs. P. Whalen and V. Jamalabad at Allied Signal, Research and Tech., Morristown, NJ.

References: 1. A. Bandyopadhyay et. al., unpublished research, Rutgers University, 1996.
2. "FDC, Rapid Fabrication of Structural Components," M.K. Agarwala, A. Bandyopadhyay, R. VanWeeren, A. Safari, S.C. Danforth, N.A. Langrana, V.R. Jamalabad, P.J. Whalen, Am. Ceram. Soc. Bull., November 1996, pp. 60-65.
3. Understanding Industrial Designed Experiments, S. R. Schmidt and R.G. Launsby, Ed. By M. J. Kimele, Air Academy Press, Colorado Springs, CO, 1994.
4. G. Bandyopadhyay and K.W. French, "Effects of Powder Characteristics on Injection Molding and Burnout Cracking," Bull. of the Am. Ceram. Soc., Vol. 73, no. 3, pp. 107-114, 1994.
5. "Observation of Poly(Vinyl Butryral)- Dibutyl Phthalate Binder Capillary Migration,"M.J. Cima, M. Dudziak and A.D. Devoe, J. Mater. Sci., 24 [6] 1087-90 (1989).
6. "Shrinkage and Particle Packing during Removal of Organic Vehicle from Ceramic Injection Mouldings," H. M. Shaw and M. J. Edirisinghe, J. Eur. Ceram. Soc., 13, 135-142, (1994).
7. "Binder Removal from Injection Moulded Ceramic Turbocharger Rotors," E. Carlstrom, M. Sjostedt, B. Mattsson and L. Hermansson, Sc. of Ceram., Ed. By Derek Taylor, 14, p.199, 1988.

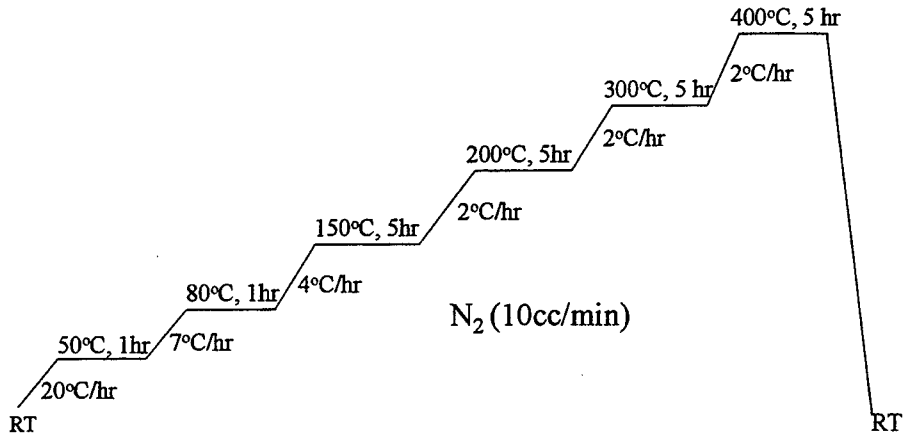
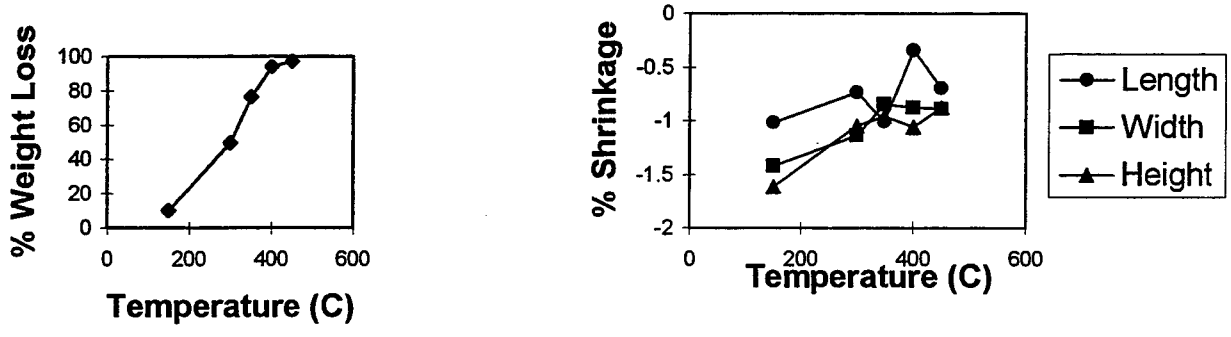


Fig.1 Previously developed binder burn out heating schedule for 1.27cm x 1.27cm cross-section area FDC parts.



(a) (b)

Fig.3 (a) Binder weight loss and (b) percentage shrinkage in green dimensions following a 5 hour hold at the temperatures of interrupted binder burn out.

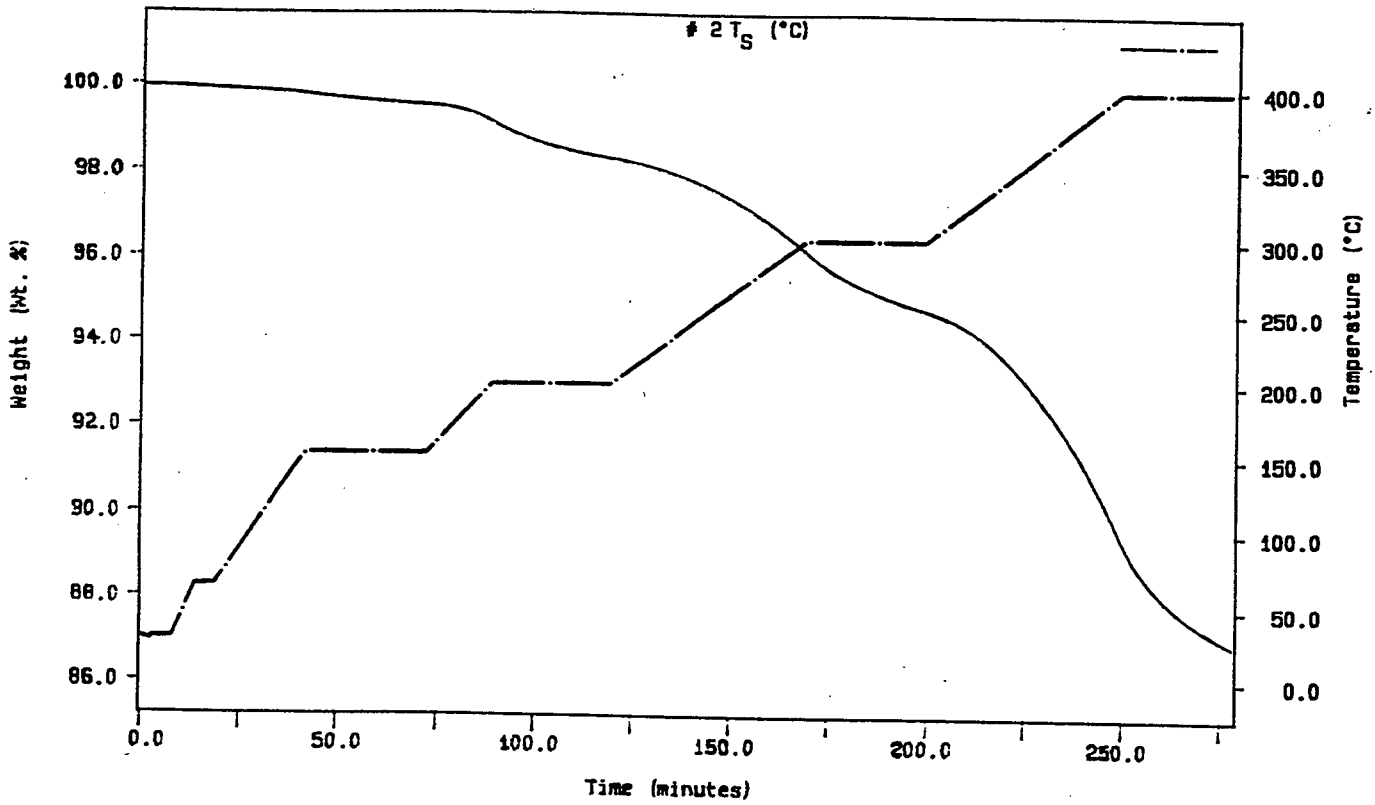
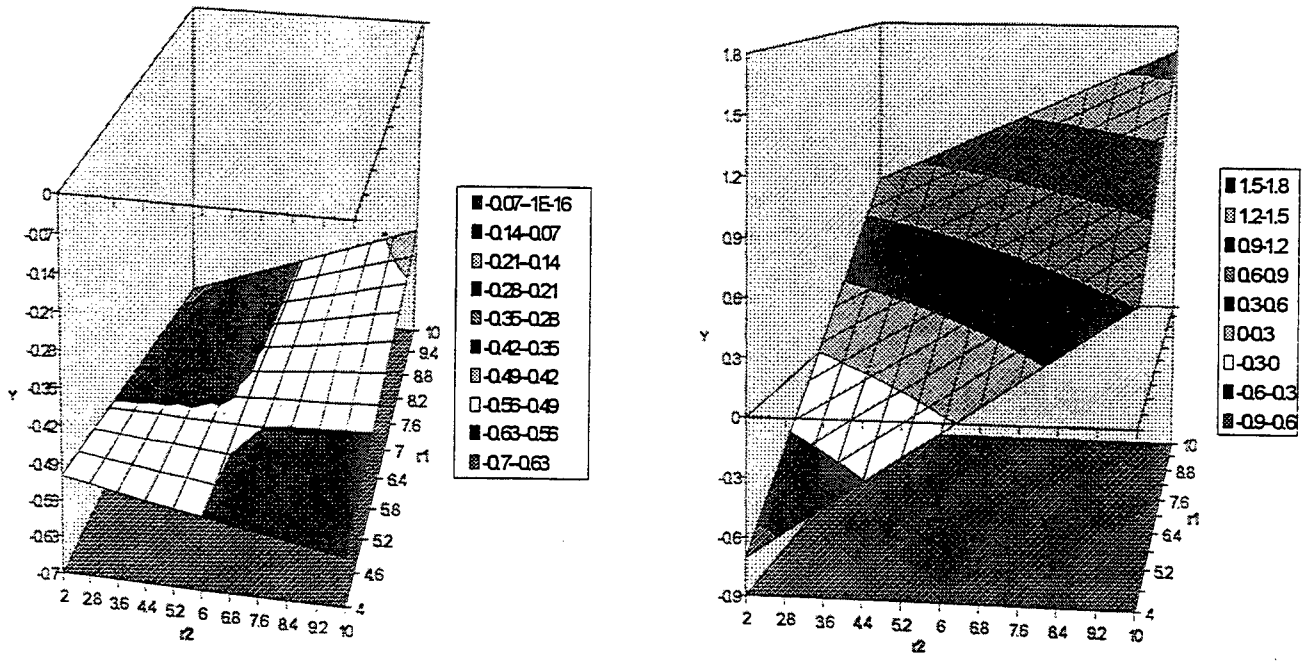


Fig. 2 TGA analysis of RU955 sample produced by FDC.



(a) (b)

Fig.4 Shrinkage along (a) x and (b) z as a function of the two heating rates r_1 and r_2.

PROCESSING OF NOVEL PIEZOELECTRIC TRANSDUCERS VIA SFF

A. Safari, S. C. Danforth, R. K. Panda, T. F. McNulty, F. Mohammadi and A. Bandyopadhyay
Department of Ceramic and Materials Engineering
Rutgers University, Piscataway, NJ 08855-0909

Abstract

Piezoelectric ceramics and ceramic/polymer composites exhibiting conventional and novel designs were fabricated using Solid Freeform Fabrication (SFF) techniques. SFF is used to develop and optimize numerous transducer designs with simple and complex shapes without using any part specific tools or dies. Fused Deposition of Ceramics (FDC), Fused Deposition Modeling (FDM™), and Sanders Prototyping (SPI) techniques were used to develop lead-zirconate-titanate (PZT) novel ceramic structures via: (1) direct fabrication and (2) indirect fabrication routes. For the direct fabrication route, green PZT ceramic preforms consisting of 50-55 volume fraction of powder with RU binders were prepared by FDC and used for piezocomposites. For the indirect route, SPI and FDM™ techniques were used build the polymer prototype or mold, and the ceramic parts were fabricated from the molds/prototypes using (a) lost mold and (b) soft tooling processes. Among the various ceramics and composites processed via the direct and indirect processes are dome shaped actuators, 3D honeycomb, ladder, annular, rods, tubes and various oriented PZT fiber structures. This presentation will review the processing routes for design, development and optimization of piezoelectric ceramics and ceramic/polymer composites for transducer applications.

Introduction

Piezoelectricity, discovered in Rochelle salt in 1880 by Jacques and Pierre Curie [1], is the term used to describe certain crystalline materials that have the ability to develop an electric charge that is proportional to an applied mechanical stress and vice versa. Piezoelectric materials show piezoelectric behavior due to their unique crystal structures. All natural crystals are grouped into 32 point groups which can be divided into two sub-groups: (1) crystals with a center of symmetry or centrosymmetric, and (2) crystals with no center of symmetry or non-centrosymmetric. Of the twenty-one non-centrosymmetric point groups, twenty of them show the piezoelectric behavior along unique directional axes. The piezoelectric effect is observed in a variety of materials including single crystals, ceramics, and polymers [2-4]. Among them, piezoelectric ceramics and ceramic polymer composites have found wide applications in consumer, automotive, medical and aerospace industries. The U.S. market for piezoelectric ceramic components was estimated to be ~$150 million in 1996 with a 10% growth rate per year, while the Japanese market for these components is > $500 million [5]. At Rutgers University, structural, piezoelectric, bio ceramics and composites have been processed using various SFF techniques [6-8]. Functional ceramic prototypes have been manufactured directly using the Fused Deposition of Ceramics (FDC) process. Ceramics and ceramic/polymer composites have also been manufactured via the indirect processing routes using either the lost mold or the soft tooling technique. In this work, novel piezoelectric ceramics and composites were developed and optimized via solid freeform fabrication techniques for improved electromechanical properties.

Processing

Indirect Process: The indirect fabrication route utilizes a lost mold technique. In this process, sacrificial molds having a negative of the desired structures were manufactured via Sanders Prototype MM6-PRO system (SPI Inc., Wilton, NH). The MM-6PRO is a liquid to solid inkjet plotter, which deposits the polymer onto a movable Z-platform. The main advantages of the SP technique include a very high resolution (a mold wall thickness of ~100 μm can be easily obtained) with a good surface finish due to finer Z-direction resolution. A high solids loading PZT ceramic slurry, with a solids loading of ~52 vol% was specially developed to infiltrate the polymer molds, thus avoiding cracking in the sample during drying and the subsequent binder burn out process.

Direct Process: In the direct technique, the piezoelectric ceramic structures were fabricated via Fused Deposition of Ceramics (FDC). Ceramic loaded filaments with a diameter of 1.75 mm were first extruded from a compounded mixture containing 52 volume % PZT-5H powder in a thermoplastic binder system. These filaments formed the input material for the Stratasys™ FDM™ 3D-Modeler (Stratasys Inc., Eden Prairie, MN). The ceramic loaded filaments were fed into a liquifier heated to a temperature between 170 to 210^{0}C. The liquifier extrudes a road of material through a 250 μm nozzle, depositing it onto a foam substrate attached to a fixtureless platform capable of moving in the Z direction. The liquifier moves in the X - Y plane based on the shape of the part to be built. After depositing the first layer, the fixtureless platform moves down the height of one layer, and the next layer is built on top of it. These steps are repeated until the whole structure is made. The final dimensions of the green ceramic part were about 25.4mm x 25.4mm x 10mm. The parts were then removed from the foam substrate for further processing.

Soft tooling: Soft tooling is a process in which flexible polymer molds are fabricated by encasing a prototype in a suitable polymer material. After the prototype is removed from the mold, the mold is then used to cast duplicates in a fashion similar to injection molding (IM), using IM ceramic / thermoplastic compounds. Although not a new process, it has yet to find usage in the transducer community because of the difficulty in producing suitable prototypes used for the creation of new molds. With the advent of SFF, a new technique has been created that will facilitate the quick and easy production of silicone molds. In this work, 1-3 composite designs were created using commercial CAD-based programs such as Auto-CAD™ and Pro-Engineer. These designs were used in conjunction with a Sanders Prototype rapid prototyping system to produce prototypes. The prototypes were then used to create molds by encasing them in silicone room temperature vulcanizing (RTV) rubber. Upon removal of the prototype, the molds were used to cast multiple duplicates with a custom designed PZT / thermoplastic compound. Several variables were explored for the fabrication of parts via soft tooling technique including:

1. optimization of the CAD designs,
2. testing of a variety of RTV rubbers to determine which materials are suitable for use in various part geometry, and
3. development of a thermoplastic binder with specific rheological, mechanical, and thermal properties.

Before any molds were made, suitable prototypes were designed. Key variables in the design of suitable prototypes are factors such as pole diameter and aspect ratio, pitch, base thickness, and pole taper. Designs were optimized to facilitate the flow of the materials inside the mold and for easy release after casting. Once the part design was complete, the .stl file was saved and transferred to the Sanders Prototype machine. Designs went through several iterations before good quality prototypes were made.

Various RTV silicone rubbers were tested in order to gain some insight into which material or materials work best for the production of flexible polymer molds. Two important material properties for mold-making are viscosity and flexibility. Several molds were fabricated using different RTV silicone rubbers with properties ranging from low viscosity and high flexibility to high viscosity and low flexibility.

Development of thermoplastic binder formulation was performed concurrently. Several important factors governed the material selection. It is important that the developmental PZT/thermoplastic compound exhibits a low viscosity at the operating temperatures of around 200^0C. The compound must also exhibit sufficient strength to allow for easy part removal once molded. The binder formulation should gradually decompose at temperatures up to about 500^0C to facilitate easy binder removal. Finally, the binder formulation should be hydrophobic to avoid complications in casting due to atmospheric humidity changes. A developmental binder was formulated which meets most of the existing criteria. The formulation consists of a major and minor binder, fluidizer, tackifier, and plasticizer in the appropriate proportions. For this work, PZT-5H powder was coated with a surfactant, and compounded with the binder formulation in a 60 volume % PZT5H solids loading. This formulation was used to cast multiple 12.5x12.5 mm green preforms using an RTV silicone rubber mold.

Post processing: The green parts, made either by indirect, direct or soft tooling techniques, were slowly heated to 550^0C and held for 1 hour to allow the organic components to evaporate. The temperature was then increased to 780^0C, with a dwell of 1 hour at that temperature, to provide enough bisque strength to the parts for mechanical handlability. The bisque fired samples were then placed in an alumina crucible with excess lead source, heated at 3.5^0C/minute to 1285^0C, and held at that temperature for 1.5 hours for sintering. The sintered samples were embedded in a standard Spurr Epoxy (Ernest F. Fullam Inc., Latham, NY) and cured in an oven at 70^0C for 12 hours.

The composites prepared with direct, indirect or soft tooling were cut, polished and electroded the top and the bottom surfaces with an air dried silver paint and poled in a corona poling apparatus using 25 kV at 65^0C for 15 minutes. Electromechanical properties of composites including dielectric constant (K), the charge coefficient (d_{33}), and the planar and thickness mode coupling coefficients (k_p and k_t) were measured. Scanning electron microscopy of the structures was carried out using an AMRAY 1400 SEM.

Results and Discussion

Indirect Process: Sacrificial polymer molds having a negative of the desired ceramic structure were made via the indirect technique, using the Sanders MM6-PRO equipment. Pro Engineer™ software was used to make a mold design that had 3-dimensional interconnected porosity. The ceramic structure obtained from these scarificial molds is shown in Figure 1. It shows uniform square PZT rods with ~ 600 μm sides separated by a spacing of ~600 μm. As shown in Table 1, 3-3 piezoelectric ceramic/polymer composites made from this structure gave good dielectric properties with a thickness coupling coefficient of 62%.

Direct Process: Using the direct technique, a variety of composites were made, where the ceramic rods were oriented at different angles to the poling direction. The specimens were fabricated to give a ladder type structure (*Type A*) as shown in Figure 2. This structure could be poled along many directions that will generate different electromechanical properties. The *type A* structure was poled along the Z-direction [001] perpendicular to the fiber direction. The ceramic connectivity was through the joints of the rods in the specimen. This structure can be poled in another way if it is rotated such that either the [100] or [010] direction of Figure 2 coincides with the poling axis. In *type B* composites, 50 % of the rods are continuous along the poling axis while the rest of the rods are continuous along the axes perpendicular to it. Yet another type of structure (*Type C*) can be obtained when the composite is poled along the [110] direction. In these structures, the rods are oriented at $\pm \theta^0$ to the poling direction. Figure 3 shows a SEM micrograph of an oriented fiber composite where the rods make an angle of $\pm$ 15 ° with the poling axis.

A comparison of the properties of *Type A*, *Type B* and *Type C* structures is shown in Table 1. The measured charge coefficient, d_{33}, of most of the oriented composites (*Type C*) is higher than the ladder structures (*Type A and Type B*). The d_{33} rises as the angle of orientation to the vertical poling axis increases. A maximum d_{33} of 510 pC/N is observed for an orientation angle of $\pm$ 30° to the poling axis. The d_{33} value decreases on further increasing the orientation angle. A value of 175 pC/N was obtained for a composite with fibers oriented at $\pm$ 75° to the poling axis. The thickness mode coupling coefficient, k_t, remain nearly constant for the samples with different orientations. The high values of d_{33} for these composites could be due to a contribution from the actual d_{33}, d_{31} and d_{15} components.

Monolithic dome shaped actuators has also been processed via FDC. The SFF approach is useful for a precise control on curvature, diameter and the size of these actuators compare to the conventionally processed curved shaped actuators such as Rainbow (**R**educed **a**nd **in**ternally **b**iased **o**xide **w**afer). The later was first produced with thin slices (0.5 mm) of lead lanthanum zirconate titanate (PLZT) ceramics by placing them between a carbon block and a zirconia plate in a preheated furnace at 975 °C for 45 minutes under reduced atmosphere. While still hot, the assembly is air quenched to room temperature. The reaction caused by the carbon block leaves a reduced surface layer with excess lead. The internal stress due to the reduced layer gives dome shape geometry to the original ceramic disk. Displacement and generative force in RAINBOW actuators are related to the thickness and the curvature of the disc that is difficult to control in conventional processing. Dome-shaped actuators with various sizes and curvature have been

produced by FDC. The green ceramic parts were fabricated via FDC using filaments loaded with 52 volume % of PZT-5H ceramic powders. Figure 4 shows the SEM micrograph of the sintered dome shaped actuator processed via FDC. Electromechanical properties of the sintered discs are currently being evaluated.

Soft Tooling: Figure 5 (a) and (b) shows the wax prototype, mold and four copies of the green ceramic structures processed via soft tooling technique. Sintered ceramic preforms fabricated via soft tooling technique consist of 25 poles of 800 μm diameter and a pole to pole pitch of 2 mm. For these structures, the volume fraction of PZT ceramics is approximately 15 % in the composite form, as shown in Figure 6. Figure 7 is an SEM micrograph of a single ceramic pole after sintering. The poles are very dense, and exhibit a 10:1 aspect ratio. Table 1 lists some of the average physical and electromechanical properties of composites fabricated via soft tooling. Although only conventional composite designs have been manufactured to this date, this technique has shown great potential for use in the production components with more complex architectures, such as random orientation, polar orientation, or volume fraction gradients.

Conclusions

In this work, Solid Freeform Fabrication (SFF) techniques such as Fused Deposition (FD) and Sanders Prototype (SP) were used to form a variety of novel piezoelectric ceramic/polymer composites. The indirect and the direct methods for the development of piezoelectric composites were discussed. The composites made via lost mold and direct FDC techniques gave excellent electromechanical properties. The properties of oriented fiber composites were found to greatly depend on the orientation of the rods with the poling axis. Theoretical modeling of the oriented structures is in progress to predict the structure with the best electromechanical properties.

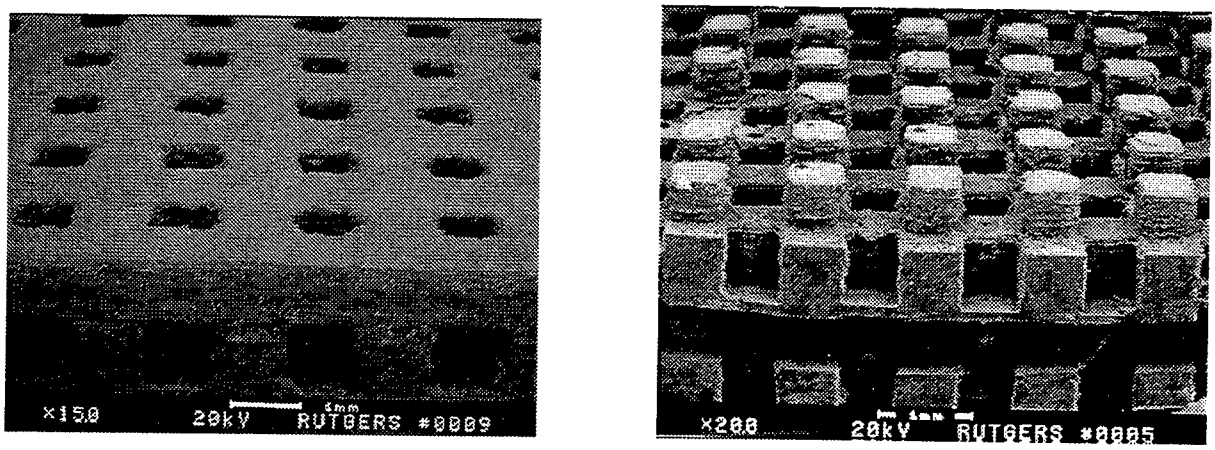
Acknowledgments

The authors would like to thank the Office of Naval Research for the financial support under the contract number N00014-94-1-0588 and N00014-96-1-1175.

References

1. W. G. Cady (1946), "Piezoelectricity", McGraw-Hill, New York.
2. S-E. Park and T. R. Shrout (1996), "Characteristics of Relaxor-Based Piezoelectric Single Crystals for Ultrasonic Transducers," IEEE Ultrasonics Symposium Proceedings, Edited by M. Levy, S. C. Schneider and B. R. McAvoy, San Antonio, TX, pp 935-42.
3. L. F. Brown (1992), " Ferroelectric Polymers: Current and Future Ultrasonic Applications"; pp. 539-550 in Proc. 1992 IEEE Ultrasonics Symposium. Institute of Electrical and Electronic Engineers, Piscataway, NJ.
4. V. F. Janas and A. Safari, " Overview of Fine-Scale Piezoelectric Ceramic/Polymer Composite Processing," J. Am. Ceramic Soc., 78 [11] 2945-55 (1995)
5. ---, "Ultrasonic Technology Provides Benefits," *Amer. Ceram. Soc. Bull.*, **74**[7], 25 (1995).

6. M. K. Agarwala, A. Bandyopadhyay, R. van Weeren, P. Whalen, A. Safari and S. C. Danforth (1996), "Fused Deposition of Ceramics: Rapid Fabrication of Structural Ceramic Components," *Ceramic Bulletin*, **11**, 60-65.
7. A. Bandyopadhyay, R. K. Panda, V. F. Janas, M. K. Agrawala, S. C. Danforth and A. Safari, "Processing of Piezocomposites by Fused Deposition Technique," *J. Am. Ceram. Soc.*, **80** [6] 1366-72 (1997)
8. A. Bandyopadhyay, R. K. Panda, V. F. Janas, M. K. Agarwala, R. van .Weeren, S. C. Danforth and A. Safari (1996), "Processing of Piezocomposites by Fused Deposition Technique," Proceedings of the 10th IEEE International Conference on Applications of Ferroelectrics, Edited by B. Kulwicki, A. Amin and A. Safari, E. Brunswick, NJ, pp 999-1003.



(a) (b)

Fig. 1 : Scanning Electron Micrograph (SEM) of (a) polymer mold and (b) 3-3 sintered PZT-5H ceramic structures obtained using the indirect technique.

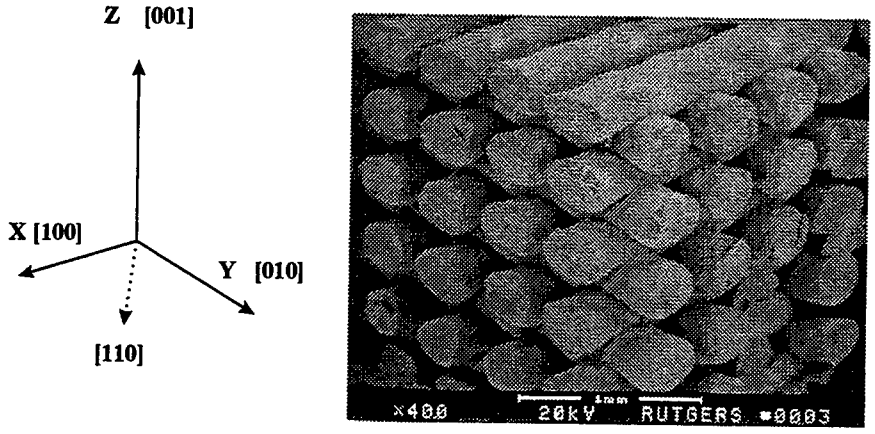


Fig 2 : SEM of sintered PZT-5H ladder type structure (*Type A*) obtained by direct deposition technique.

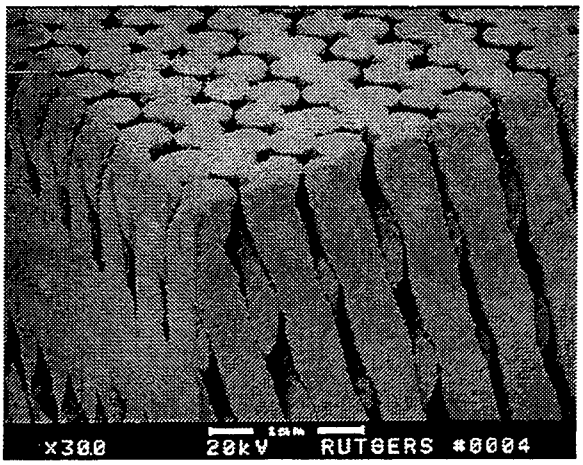


Figure 3 : SEM of the an oriented structure (*Type C*) where the PZT rods are aligned at $\pm 15^{\circ}$ to the poling axis.

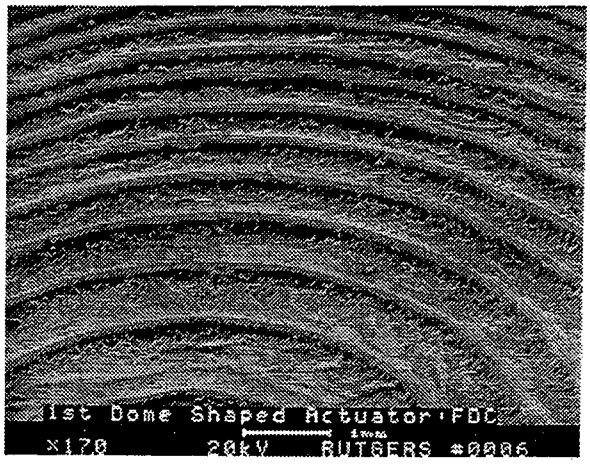
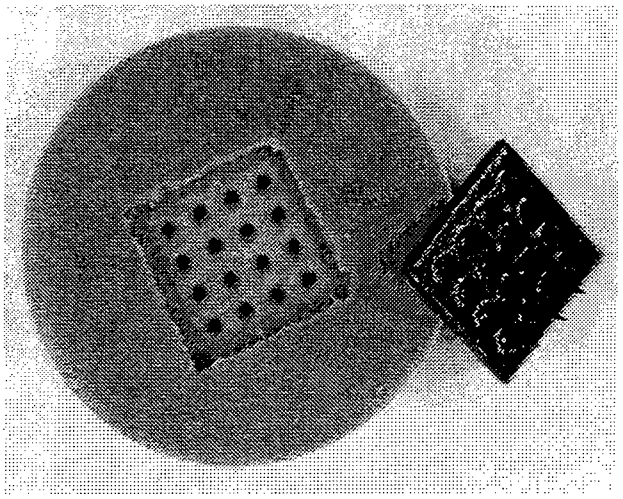
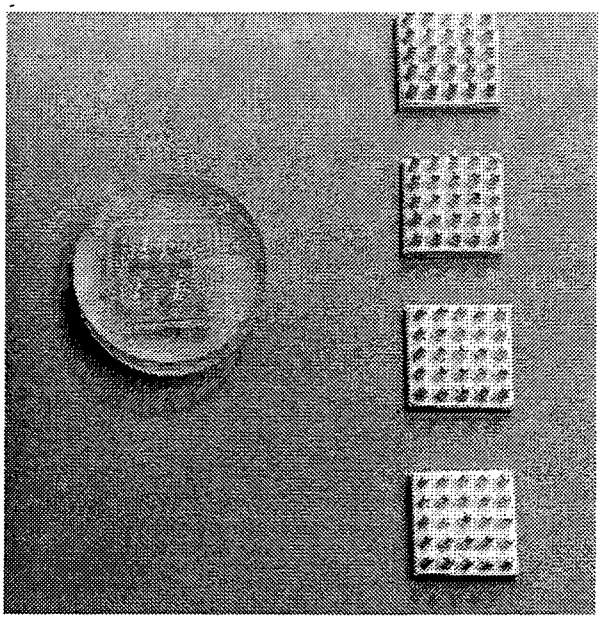


Figure 4: SEM micrograph of the interior of a dome shaped actuator, processed via FDC.



(a)



(b)

Figure 5: (a) Prototype with soft tooling mold and (b) green PZT ceramic preforms fabricated via soft tooling mold.

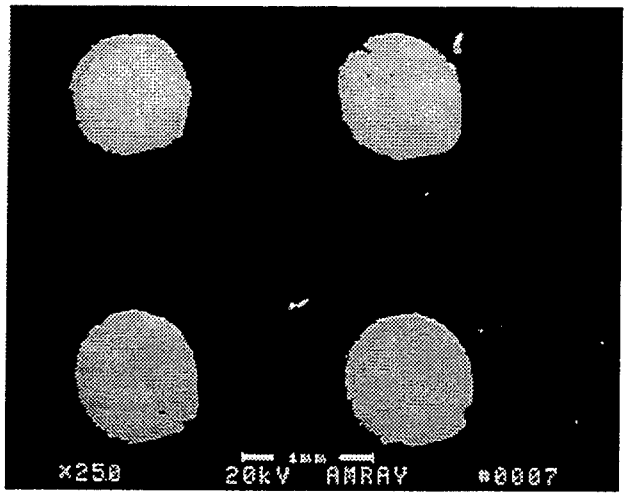


Figure 6: SEM of polished cross section

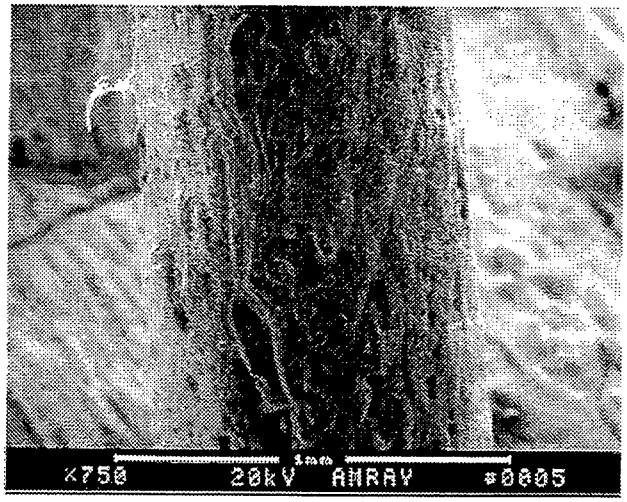


Figure 7: SEM of sintered ceramic pole

Table 1: ELECTROMECHANICAL PROPERTIES OF PIEZOELECTRIC COMPOSITES MADE BY INDIRECT, DIRECT AND SOFT TOOLING ROUTES

Technique	Composite Type	Vol % PZT-5H	Dielectric Const. K	d_{33} (pC/N)	k_t(%)
Indirect	3D Honeycomb	42	410	230	62
Direct	Ladder *(Type A)*	70	1300	290	50
	Oriented (0-90°) *(Type B)*	65	1545	300	51
	Oriented (±15°) *(Type C)*	60	1560	350	62
	Oriented (±30°) *(Type C)*	60	1580	510	59
	Oriented (±45°) *(Type C)*	65	1350	390	--
	Oriented (±60°) *(Type C)*	66	1200	225	--
	Oriented (±75°) *(Type C)*	58	620	175	--
Soft Tooling	1-3 composite	15	320	315	63

High Quality, Fully Dense Ceramic Components Manufactured Using Fused Deposition of Ceramics (FDC)

Cheng Dai, Gang Qi[+], Sriram Rangarajan[+], Suxing Wu[+]
Noshir A. Langrana, Ahmad Safari[+], Stephen C. Danforth[+]
Department of Mechanical and Aerospace Engineering
Center for Ceramic Research-Department of Ceramic and Materials Engineering[+]
Rutgers - The State University of New Jersey

Abstract
Solid Freeform Fabrication (SFF) is a technology that produces physical solid components or parts from computer design models. This technology has the potential of reducing functional ceramic product development cycle time in terms of reducing design iteration and production time, minimizing extra post processing, and therefore reducing cost. A commercially available Fused Deposition Modeling (FDM™) 3D Modeler was altered for use with ceramics. This newly developed method referred to as Fused Deposition of Ceramics (FDC) is capable of fabricating complex shape, functional ceramic components.

We have investigated issues related to hardware, software, feed material, and build strategy which are required to achieve high quality, fully dense green ceramic parts. In this paper, we report recent improvements made in the FDC process, including hardware modifications, software improvements, feed material standardization, as well as build strategy/condition control. We also report the current FDC status for making complex functional parts. Our goal is to optimize the FDC condition to ensure its robustness for producing defect free green ceramic parts consistently and without interruption.

1. Introduction:

Solid Freeform Fabrication (SFF) is a technology that produces real physical solid models from 3D computer-aided design (CAD) model data, electronic scan data and model data created from 3D digitizing systems for rapid prototyping applications such as testing of form/fit/function. Because SFF is able to quickly go from 3D electronic data to an arbitrarily complex shaped 3D part, it allows design engineers to make design corrections very early in the product development process, and reduces the number of design cycle iterations and cost dramatically. The solid freeform fabrication technologies also have an advantage for small quantity production. This is especially true for structural ceramic components, because the cost of manufacture of a structural ceramic component is a direct function of part complexity and production quantity.

Fused Deposition of Ceramics (FDC), developed at Rutgers University, is an SFF technique [1-6], based on the commercial Fused Deposition Modeling (FDM) process for fabrication of ceramic and metal (FDMet) objects. FDC uses a polymeric binder system to bond ceramic powders together in forming wire-like filaments which are melted in the liquefier delivery head which moves in the X and Y directions and is controlled by computer. The material is then

extruded from the heated head and deposited on a layer-by-layer basis. The extrusion process shears the material which quickly solidifies while reheating and bonding to the previous layers.

For plastic and wax parts manufactured by the FDM process, the primary concern is defects on the part's surface. Defects such as internal voids have not been a top priority for FDM, because plastic and wax parts do not necessarily require full density for their applications. For ceramic parts made by the FDC process, internal voids due to build defects are crucial because they will act as critical flows that lower the fracture strength (i.e. functionality) of the ceramic component.

Since our objective is to directly produce high quality functional ceramic parts, achieving full density in the FDC parts is the top priority in the building process. The production of fully dense ceramic parts using FDC requires a high quality and continuous feedstock filament of FDC'able material and a fully automated FDC process. Functional ceramic parts also require good FDC process control of deposition tool path, build parameters and build environment.

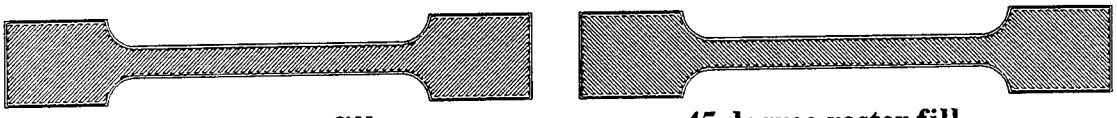
2. Build Strategy and Condition:

Green ceramic parts can be built by FDC in different orientations. The decision of which build orientation to use depends on the part's geometry and application. Parts can be made horizontally or vertically, with support or without support. Parts also can be made with different selections of perimeter/contour/raster combinations, and with different angles of raster fill. Build conditions, such as liquefier and envelope temperatures are also important and need to be considered before part production.

Producing high strength ceramic parts is a high priority in our FDC research. The strength of a green FDC part will be affected by the build orientation and the build conditions used. Control of the part's environment during the build process is also critical for ensuring a high quality part. If the build envelope temperature is too low or constant environment temperature is not maintained, previously deposited material will cool too much and imperfect adhesion to the next layer will result. Incomplete inter-road bonding also occurs when tool path vector lengths are too long.

Normally, a part with the largest cross section built in horizontal directions (X,Y) requires less build time compared with building the largest cross section in the vertical direction (Z). This is because of the Z-stage wait time of the 3D Modeler. When one layer is finished, the Z platform has to move down to open the space for brushing the nozzle tip, then move upward to the build position. This action normally takes about 4 seconds. For example the tensile bar shown in Figure 1 required 0.6 hour when built horizontally and 1.3 hour when built vertically with the same head speed.

Three RU955 GS-44 silicon niride tensile bars were made, all with 45, -45 degree raster fill shown in Figure 1. Two of them were made horizontally under different envelope temperatures, one with 45°C and one with 30°C. One of the bars was made vertically with a 30°C envelope temperature.



45 degree raster fill **-45 degree raster fill**

Figure 1: Green GS-44 silicon nitride tensile test sample with 45, -45 degrees raster fills.

According to the strength test results, Figure 2, the bar made in the horizontal direction with a 45°C envelope temperature had a higher strength (3.18 MPa) than the strength (2.84 MPa) of the identical bar made with a 30°C envelope temperature. However, the bar made in the vertical direction with a 30°C envelope temperature had the lowest strength (1.94 Mpa) of the three. The test data and stress vs. strain curves are shown in Table I and Figure 2. The results indicate that green FDC parts have a lower strength in the Z direction than in X-Y directions because of the nature of layer bonding in Z direction. This result suggests that in order to obtain a high strength green part, the largest or critical section of the part should be built in the X-Y plane.

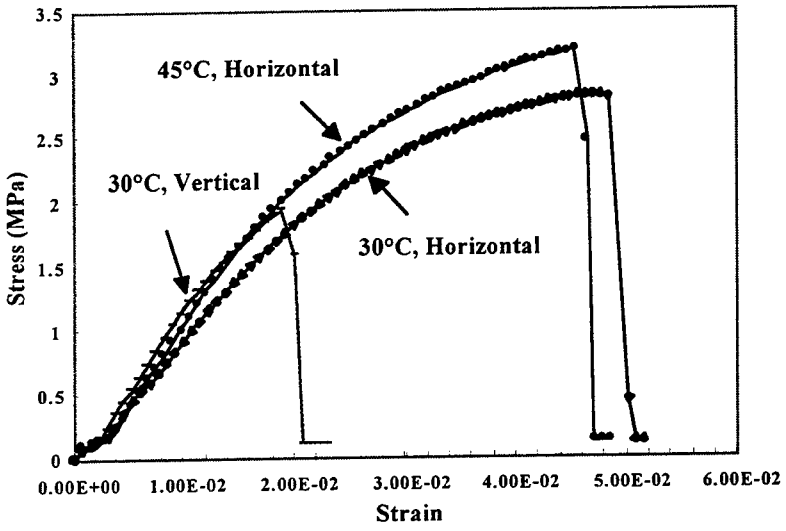


Figure 2: Tensile stress vs. strain curves of the green RU955 silicon nitride tensile bars made by FDC under different conditions.

The Fused Deposition build envelope temperature must be maintained at a sufficiently high temperature to provide for better material bonding [7]. The envelope temperature has an effect on material bonding between layers, and residual stresses in the green part. The temperature should be sufficiently high to ensure good bonding between layers. If the layers are cooled too rapidly (due to the surrounding temperature), then residual stress may develop and lead to cracking during BBO (Binder Burn Out). In addition, if the temperature is too high, the part may deform under its own weight.

Table I: Tensile Test Results for Green RU955 Silicon Nitride Bars.

			STRENGTH	STRENGTH
EnvTemp	Raster Angle	Road Width	Horizontal	Vertical
30°C	45, -45	0.015"	2.84 MPa	1.94 MPa
45°C	45, -45	0.015"	3.18 MPa	

3. Sub-Perimeter Void and Software:

The sub-perimeter void is a common defect for both FDM and FDC processes. The sub-perimeter void occurs in the conjunction areas of perimeter and rasters. Because of the linear approximation of tool path, sharp turns for rasters occur. As a result, empty spaces (voids) are left without being filled due to the curvature of the perimeter and sharp corners (angles) of rasters. These sub-perimeter voids in FDC parts are too large to be overcome in the sintering process, hence the strength of FDC ceramic parts is affected significantly.

Recently, we have been using a simple method to eliminate sub-perimeter voids in the FDC process. This method might not be the best solution for solving this problem, but it is an easy and effective way to get ride of the sub-perimeter voids.

Normally, when creating the tool path on each slice, the build parameters need to be specified in the software QuickSlice. The air gap between roads can be set with negative, zero, or positive offsets depending on the application. For example, if the offset is set to a positive offset, then there is a real gap between fill vectors. If the air gap is equal to zero, then there is no air gap, which in principle means perfect filling and that the roads are perfectly in contact with each other. If the air gap has a negative offset, there will be overlapped fill. In the past, we have used small negative offsetting of the air gap to ensure internally fully dense parts. In fact, the function of the offsetting technique can be used effectively for the elimination of sub-perimeter voids. This simple method works well in most cases especially for our RU955 silicon nitride parts.

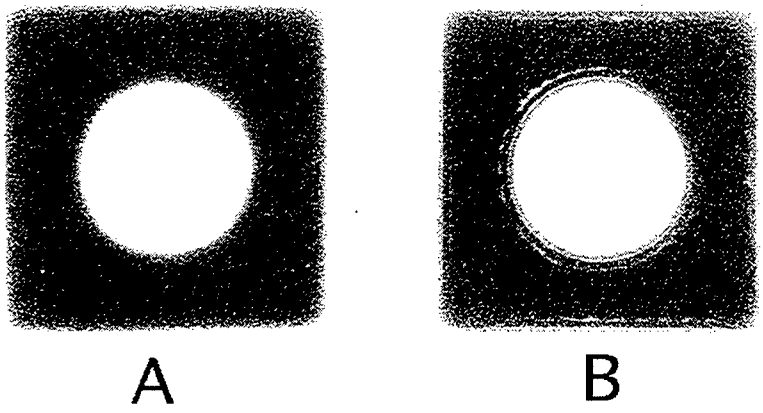


Figure 3 : X-ray radiographs of green GS-44 silicon nitride part made with a negative offsetting (A), and without negative offsetting (B).

Figure 3A shows an X-ray radiograph of a FDC green GS-44 silicon nitride part containing no sub-perimeter voids. This was accomplished by specifying an air gap with a negative offsetting in the build parameters. The negative offsetting allowed the raster fill to overlap with the contour fill, eliminating the possibility of voids. However, when an air gap with no offsetting was specified, sub-perimeter voids were created. Figure 3B shows an X-ray radiograph of a part, built without a negative offset, containing voids.

Overflow (too much material deposited on the part surface) created by using the negative offsetting is the disadvantage of this method. It sometimes causes dimensional changes in parts.

However, by carefully selecting the value of negative offsetting, the overflow problem can be minimized. We have been using negative offsetting from -1/4 to -1/3 of the raster width in most cases. The dimensional expansion of the part sometimes can be as large as 0.008", depending on the build condition and part geometry.

This negative offset technique works well for rasters with small road widths. This is because of the void created at the sharp turning corner for small road width rasters is smaller than the one created by large road width rasters. For parts which have an interior small boundary, e.g., a small hole, it is difficult to eliminate the sub-perimeter voids especially when the size of a small boundary or hole is not much greater than the road width of the raster fill.

4. Feed Material Standardization:

In the past, we had frequently experienced clogging of the nozzle in the FDC process especially for small size nozzles (0.020"D or less). The causes of nozzle clogging were foreign objects and agglomerates of ceramic particles. Recently, the FDC filament fabrication laboratory at Rutgers University has gone through a series of steps for improving the quality of the FDC filament [8, 9]. The main focus was to eliminate any foreign contamination, and to produce better mixing/deagglomeration and more uniform filament. A fine screen is used in filament extrusion to remove large particles or foreign objects. The Standard Operating Procedure (SOP) of filament fabrication has been implemented to ensure reproducibility and to minimize the chance of contamination and process variation.

Filament buckling is another critical problem in the FDC process. Buckling is caused by poor quality of filament and insufficient filament aging. Poor quality filament refers to filaments which either are not stiff enough, or have high viscosity, or is not uniform in diameter. Most buckling due to poor filament quality has been eliminated via improved ceramic processing. In most cases, we believe that the filament buckling is due to a material aging problem. In the recent past, we experienced some difficulties due to the inconsistency of FDC feedstock material. A large part of the problem was due to the effect of filament storage and due to the lack of understanding of the RU955 binder's aging. In order to produce the same condition of feed material which is feasible to FDC on a daily base, we performed a series of aging tests for the RU955 binder [8, 9].

According to the test results, moisture does affect the quality of RU955 filament. Too high a moisture content of the FDC filament results in a high drive motor current and bubbles on the extruded surface. However, the aging studies suggest that the moisture effect can be eliminated by a vacuum heat treatment as part of filament aging. A fixed and standardized filament aging process and storage procedure has been employed to ensure consistent FDC conditions [8, 9].

5. Hardware Improvements:

Since the filament used in the FDC process also acts as the piston for extrusion, the filament should have enough stiffness when entering the liquefier. It has been shown that the G' (storage modules of the filament) is a strong function of temperature between 0°C and 30°C. Therefore, cooling the filament near the top of the liquefier becomes critical. If the heat brought up from the

liquefier is not removed, then the heat will soften (lower the G' - stiffness) the filament and in turn cause buckling. Because the cool air (at R.T.) from the FDM cooling system at the top of the head is partially blocked by the wheels and motor block, the FDM cooling system is insufficient to maintain enough stiffness in the FDC filament. The cooling path shown in Figure 4 for FDC has been altered from the top to the right side to provide cooling directly in the region where the filament can buckle. In the new cooling system, the cooling path and the filament feeding path have been separated above the work platform. A temperature controlled cooler is attached to the air blower on the back of the machine, so that cool air (~15°C-18°C) is blown by the cooling fan into the liquefier head. The air then goes back to the cooler's thermostat chamber to make a closed-loop so that the temperature can be controlled. This modification has dramatically reduced the filament buckling problem, allowing better process control, and maintenance of more uniform FDC conditions.

Temperatures under three different conditions were measured for one FDC build condition (liquefier temperature=186°C; envelope temperature=44°C; envelope humidity=25% RH), they are with A/C (~18°C) cooling, without A/C but with room air (~25°C) cooling, and no cooling. Temperatures for each case were measured at two locations, at the location between filament rollers and at top of the liquefier (see Figure 4). The measured temperatures are listed in Table II.

Table II: Temperature Measurements With and Without Cooling.

	No Cooling	~25°C RT Cooling	~18°C A/C
Temp. Between Rollers (°C)	43-45	28-29	20-21
Temp. at Top of Liquefier (°C)	61-64	32-35	24-25

The thermostat on the A/C unit was set at 18°C, and it continuously pumped 18°C cool air into the liquefier head. The cool air then leaves the head from the electric wire conduit to the back of the 3D Modeler and back to the air conditioner. Since it is a closed-loop and the cooling system does not affect the build envelope environment, the envelope temperature can still be well controlled. The FDC build envelope temperature recently has been raised to 45°C from previous values used of 32°C-38°C. We believe that the relatively high FDC envelope temperature results in better material bonding in the FDC build process for RU955 binder, and therefore improved the green part quality.

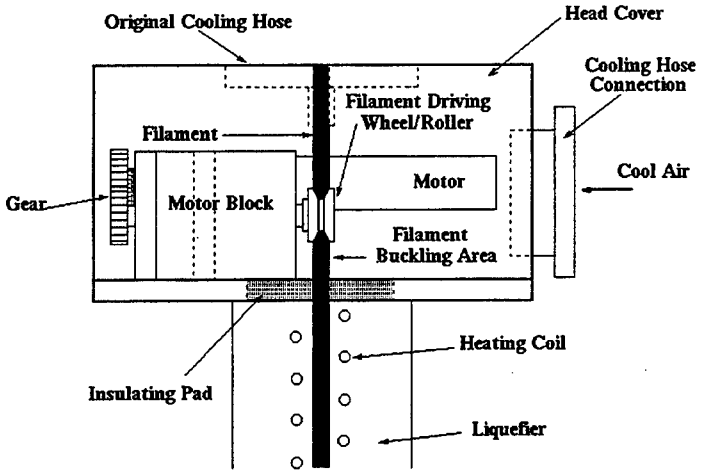


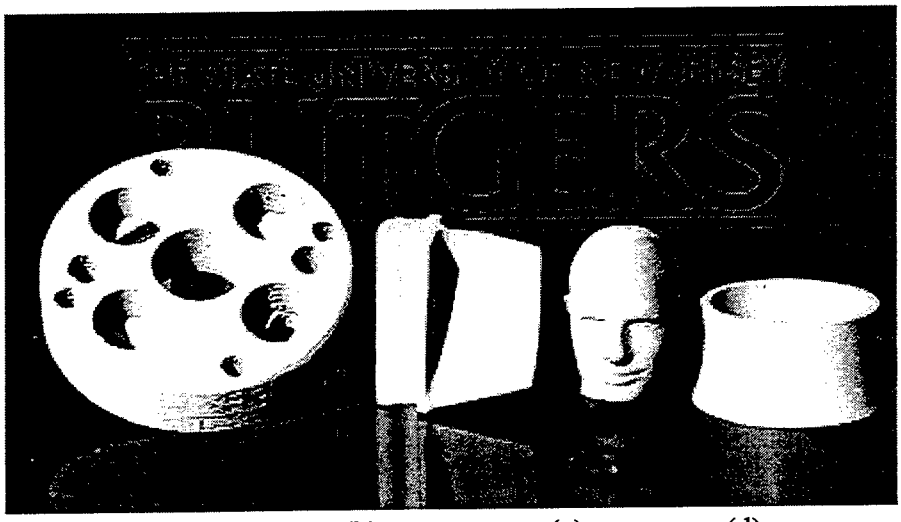
Figure 4: Schematic of FDC liquefier head with new cooling path.

6. FDC Issues and Components:

The selection of road width when creating build files is very important, especially for complex shaped parts. For example, the port plate shown in Figure 5(a) has several cavities. Improper selection of road width will cause internal fill air gaps most likely appearing in two regions. One is the area where the raster fill is parallel or near parallel to a curved boundary (sometimes, called high angles). The second is the area where two boundaries are separated from each other by a small distance. Improper selection of road width will cause voids in these two regions.

As an example, because of the complex geometry of the port plate shown in Figure 5(a), it is necessary to use more than one "set" of build parameters for creating internal roads. The advantage of using multiple sets for creating internal roads is that each set will match well with assigned slices which represent a particular geometry. The multiple assignments of sets will overcome the difficulty for handling a complex part by a single set, and will eliminate internal defects. However, complex objects normally require several iterations of internal road design. It is therefore important to investigate all different slices of internal roads created by QuickSlice before saving it into a build file or download it to the 3D Modeler.

The port plate shown in Figure 5(a) designed by AlliedSignal has a complicated geometry with different size holes and under cuts which is very difficult and expensive to make by normal manufacturing processes. A total of 3 port plates have been made by FDC recently. The turbine blade for an auxiliary power unit (APU) shown in Figure 5(b) is also a complex part because of the twisting curvature of the blade. Recently, we made several 1.5" tall turbine blades using the FDC process. The overall dimension, FDC build speed and time, and length of filament used for each port plate and turbine blade are listed in Table III.



(a) (b) (c) (d)

Figure 5: Demonstration of recent green FDC parts made out of silicon nitride.

The human head model and the curved cylindrical shell shown in Figure 5(c) and 5(d) respectively, were made by using a regular FDM 0.015"D nozzle. It took 4.6 hours build time to

make one human head model with 0.007" slice thickness at 0.5"/sec speed. During the FDC process of these parts, there was no human intervention and no process interruption. It has been shown that the current FDC process has great potential and the flexibility to use small size nozzles (0.015"D) and therefore improve the part surface quality. The surface quality of the parts made out of the 0.015"D nozzle are much better than using 0.025"D nozzle, and in some applications, may not require further machining.

Table III: Data Sheet for Each of the Port Plates, Turbine Blades, and the Radome and Cellular Filter Made Out of GS-44 Silicon Nitride.

FDC Part	FDC Part Dimension	FDC Build Speed (in/sec)	RU955 Si_3N_4 Filament (ft)	FDC Build Time (hour)
Port Plate	2.7"Dx0.6"tall	0.5	65	9.5
Turbine Blade	1.5" tall	0.5	24	4
Radome	4.5"Dx7.5"tall	0.5	117	16
Cellular Filter	3"Dx0.5"tall	0.5	41	4.3

Among all of the parts made recently, the largest part is the section of a missile radome shown in Figure 6 designed by Lockheed Martin. The radome section is 7.5" tall and the base section diameter is 4.5". This radome was made in 16 hours at 0.5"/sec speed and used approximately 117 ft of FDC filament. It was manufactured with total computer control in a fully automated process. There was not a single interruption during the 16 hour run. The RU955 GS-44 Si_3N_4 filament was used just like the ICW-05 wax filament, i.e. it was on a spool and automatically and continuously fed from the back of the 3D Modeler. During the entire process the Modeler's door was kept closed and the build envelope temperature was controlled at 40°C. A 0.015"D nozzle was used and there was no nozzle clogging. The surface quality of the radome is excellent even without green finishing. So far, this is the longest uninterrupted FDC build since the system has been modified.

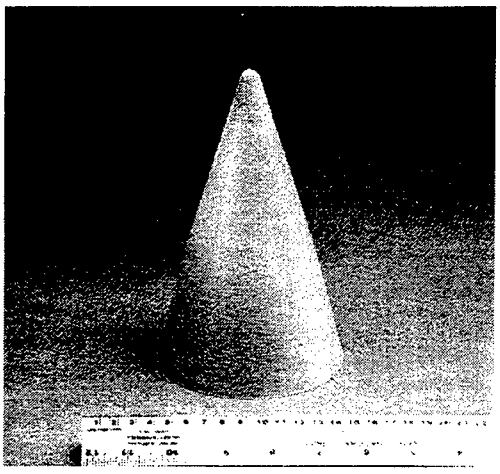


Figure 6: Green silicon nitride Lockheed Martin's radome made by FDC.

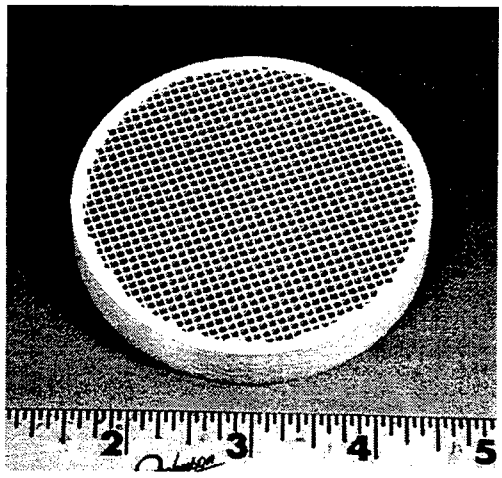


Figure 7: Green silicon nitride cellular filter substrate made by FDC.

Another complex part that has been made is the cellular filter substrate, which was designed and made for use as a sintering base as shown in Figure 7. This part is 3" in diameter and 0.5" thick. Because of its fine mesh structure, it is difficult and expensive to manufacture by the standard commercially available manufacturing processes. The filter was made in a 4.3 hour FDC build at 0.5"/sec speed with a 0.015"D nozzle, without interruption. The mesh structure was created by specifying a positive 0.040" offset between raster roads for the internal fill of the disk. The green cell wall thickness was 0.025", and the overall part quality was excellent.

7. Conclusion:

The success of the FDC manufacturing process demonstrated in this paper is mainly due to the recent efforts on improved filament fabrication, feedstock material standardization, new FDC build strategies, hardware modifications, and improved process control. The degree of automation for high quality FDC process has been increased dramatically. Now, the FDC process is capable of making complex, fully dense, and high quality ceramic parts using a fully automated FDC process. Since January, 1997, we have made approximately 100 parts using FDC without human intervention or interruption. This success has demonstrated the capabilities of the improved FDC process.

Further improvements in the areas of elimination of material flow variation, elimination of contamination, and good tolerance (shrinkage) control need to be made. Increasing the build speed along with using a fine sized liquefier nozzles need to be investigated further. Better process control and improved surface finishing are needed for commercialization [10].

Acknowledgments:

We gratefully acknowledge the support of this research by DARPA/ONR under contract #N00014-94-0115. This research has been conducted in the Laboratory for Solid Freeform Fabrication of Advanced Ceramics in the Center for Ceramic Research and the Department of Mechanical and Aerospace Engineering at Rutgers University, and the Research and Technology, AlliedSignal.

The authors wish to thank Dr. P. Whalen, Dr. V. Jamalabad, and Mr. R. Clancy of AlliedSignal for their valuable suggestions and contributions to this research. The authors also would like to thank Dr. P. Bhargava, Dr. A. Bandyopadhyay and Mr. R. C. McCuiston of Rutgers University, and Dr. G. Carrasquillo of Certech, Inc. for their help and contributions to this work.

Reference:

1. A. Bandyopadhyay, S. C. Danforth, A. Safari, C. Dai, G. Qi, S. Rangarajan and N. A. Langrana, "Structural Silicon Nitride Components via FDC", The American Ceramic Society's 99th Annual Meeting and Exposition, May 4-7, 1997.
2. M. K. Agarwala, R. van Weeren, A. Bandyopadhyay, A, Safari, S. C. Danforth, W. R. Priedeman, "Filament Feed Materials for Fused Deposition Processing of Ceramics," Proceeding of the Solid Freeform Fabrication Symposium 1996, pp. 451-458, Austin, Texas, August 12-14, 1996, University of Texas at Austin.

3 V. R. Jamalabad, N. A. Langrana, and S. C. Danforth, "Design Improvements in the Fused Deposition of Ceramics (FDC): Progress Towards Structurally Sound Components," Proceeding of ASME Design Automation Conference (Rapid Prototyping Session), La Jolla, CA, 1996.

4. M. K. Agarwala, A. Bandyopadhyay, R. van Weeren, N. A. Langrana, A. Safari, S. C. Danforth, R. Jamalabad, P. J. Whalen, R. Donaldson, J. Pollinger, "Fused Deposition of Ceramics for Structural Silicon Nitride Components," Proceeding of the Solid Freeform Fabrication Symposium 1996, pp. 335-343, Austin, Texas, August 12-14, 1996, University of Texas at Austin.

5. M. K. Agarwala, R. van Weeren, R. Vaidyanathan, A. Bandypadhyay, G. Carrasquillo, V. Jamalabad, N. A. Langrana, A. Safari, S. H. Garofalini, S. C. Danforth, J. Burlew, R. Donaldson, P. Whalen, C. P. Ballard, "Structural Ceramics by Fused Deposition of Ceramics," Proceeding of the Solid Freeform Fabrication Symposium 1995, pp.1-9, Austin, Texas, August 7-9, 1995, University of Texas at Austin.

6. R. van Weeren, M. K. Agarwala, V. Jamalabad, N. A. Langrana, P. Whalen, S. C. Danforth, C. P. Ballard, "Quality of Parts Processed by Fused Deposition", Proceeding of the Solid Freeform Fabrication Symposium 1995, pp.314-321, Austin, Texas, August 7-9, 1995, University of Texas at Austin.

7. M. A. Yardimci, S. I. Guceri, M. K. Agarwala, S. C. Danforth, "Part Quality Prediction Tools for FD Processing," Proceeding of the Solid Freeform Fabrication Symposium 1996, pp.539-548, Austin, Texas, August 7-9, 1996, University of Texas at Austin.

8. G. Qi, C. Dai, S. Rangarajan, S. Wu, S. C. Danforth, A. Safari, "Properties of RU955 Silicon Nitride Filament for Fused Deposition of Ceramics", submitted to The Solid Freeform Fabrication Symposium 1997, Austin, Texas, August 11-13, 1997, University of Texas at Austin.

9. S. Rangarajan, G. Qi, A. Bandyopadhyay, C. Dai, J. Han, P. Bhargava, S. Wu, A. Safari, and S. C. Danforth, "FDCability: The role of processing variables", Proceeding of the Solid Freeform Fabrication Symposium 1997, Austin, Texas, August 11-13, 1997, University of Texas at Austin.

10. R. Clancy, V. Jamalabad, P. Whalen, P. Bhargava, C. Dai, G. Qi, S. Rangarajan, S. Wu, S. C. Danforth, N. A.Langrana, A. Safari, "Fused Deposition of Ceramics: Progress towards a Robust and Controlled Process for Commercialization", Proceeding of the Solid Freeform Fabrication Symposium 1997, Austin, Texas, August 11-13, 1997, University of Texas at Austin.

Properties of RU955 Si_3N_4 Filament for Fused Deposition of Ceramics

Gang Qi, Cheng Dai, Sriram Rangarajan, Suxing Wu, Amit Bandyopadhyay, Noshir Langrana, Ahmad Safari, and Stephen C. Danforth, Center for Ceramic Research, Rutgers University, Piscataway, NJ 08855

Abstract

One of the key elements in the FDC process is the development of ceramic loaded fusible filament. The filament is not only material feed stock for deposition, but also serves as a piston to push the fused material through the FDC liquefier. Therefore, the FDC filament has to meet several requirements. It should have enough flexibility to satisfy the automatic feeding requirements, enough stiffness to carry the force for extrusion in the liquefier, and a low viscosity. A series of binders developed at Rutgers University show promising properties and meet these requirements. However, the change of filament properties with time and storage conditions was observed, and they dramatically influenced the FDC process. Systematic experiments were carried out in order to understand filament aging and establish proper storage conditions. The results indicate that moisture in the environment plays an important role in the filament aging. Vacuum treatment at 30°C apparently accelerates the aging process. The mechanisms of filament aging and the method of filament evaluation will be discussed.

I. Introduction

Solid freeform fabrication for ceramics has recently drawn much attention because of the high cost and difficulty of conventional ceramic component fabrication. Several solid freeform fabrication techniques have been developed for ceramic component fabrication, such as three dimensional printing[1], laminated object manufacture (LOM)[2] and fused deposition of ceramic (FDC)[3]. Among these SFF techniques, the FDC process provides a unique ability to form complicated shapes and dense ceramic components. One of the key elements in the FDC process is the development of ceramic loaded fusible filament. Because of the special feeding mechanism in the FDC 3D Modeler, the filament is not only the material feed stock for deposition, but also serves as a piston to push the fused materials through the FDC liquefier. Therefore, the FDC filament has to meet several requirements. The filament should have enough flexibility to satisfy the automatic feeding requirement, sufficient stiffness to carry the force for extrusion in the liquefier, and a low melt viscosity. A series of binders, designated as RU and developed at Rutgers University, show promising properties and meet these requirements. However, the newly fabricated (fresh) filament is sometimes too flexible to drive the extrusion in the liquefier. This filament has to undergo a post-extrusion treatment in order to meet the FDC requirements. Clearly, it is necessary and important to completely understand the change of filament properties with time and storage conditions in order to establish a reliable post-treatment of the filament.

In this work, systematic experiments were designed to investigate the change of filament properties with time and storage conditions. The mechanical tensile testing and viscosity measurements are major characterization methods in this study. A standard storage condition was proposed. Moreover, the mechanisms of filament aging and the method of filament evaluation will be discussion in this paper.

II. Experimental

In order to study the influence of environment, the freshly extruded RU955 filament was divided into four portions. RU955 refers to RU9 binder with 55 volume % GS-44 Si_3N_4 powder (plus 3 weight % oleyl alcohol added as a surfactant). The first portion of the

filament was stored in a glove box, which had almost zero relative humidity (<10 ppm H_2O) at a temperature of 15°C. The second portion of the filament was stored in a dry box, which had a 10% relative humidity and a 25°C. The third portion of the filament was placed in an environment, which was set at 55% relative humidity and 25°C. The last portion was stored in a vacuum oven with 30 mm mercury vacuum and 30°C. Filaments from the four primary conditions and their combinations were characterized by tensile testing and viscosity measurement.

Mechanic tensile testing

The mechanical testing was conducted on a miniature tester (Rheometric, Inc) using a 20N load cell. The cross head speed was set to 1 mm/min. The total filament length was 55mm and the gage length was 33 mm. The diameter of filament was 1.75mm. In order to increase accuracy of measurement, every test condition was repeated at least three times. The stress and strain were calculated from the data of load-displacement and elastic modulus was determined through linear regression of the first 30 data points in the stress-strain curve. In the most cases, the linear relevant factor (R) was greater than 0.996.

Viscosity Measurement

Capillary rheometry (Instron Co.) was chosen to measure the viscosity of the RU955 material because the viscous flow in the capillary was the same flow geometry as in the FDC liquefier. The rheometer had a barrel with a diameter of 9.528 mm and length of 388 mm. The capillary die used for most viscosity measurements had a diameter of 1.422 mm and the aspect ratio (L/D) was 20.29.

FDC trial

FDC trial of filament is the final test for FDC feasibility. The filament was fed into the 3D Modeler using the same conditions for part building. The 3D Modeler monitors the current of the motor that drives the RU955 filament delivery rollers. The value of this parameter, referred to as "torque (τ)", directly reflects the force on the filament during FDC. Filament diameter variation, motor fixture setting and alignment and other non-material parameters all influence the torque value. However, when all those parameters are fixed, the measured motor current directly relates to the force for the filament flow. Therefore, the variation in the motor torque reading can be viewed as resulting from changes in material properties.

III. Results

Mechanical Testing

Figure 1 summarizes the tensile strength of RU955 filament with different storage conditions. In the first two days of aging, the tensile strength of the filaments stored in the vacuum oven and glove box shows an increase with storage time. However, the

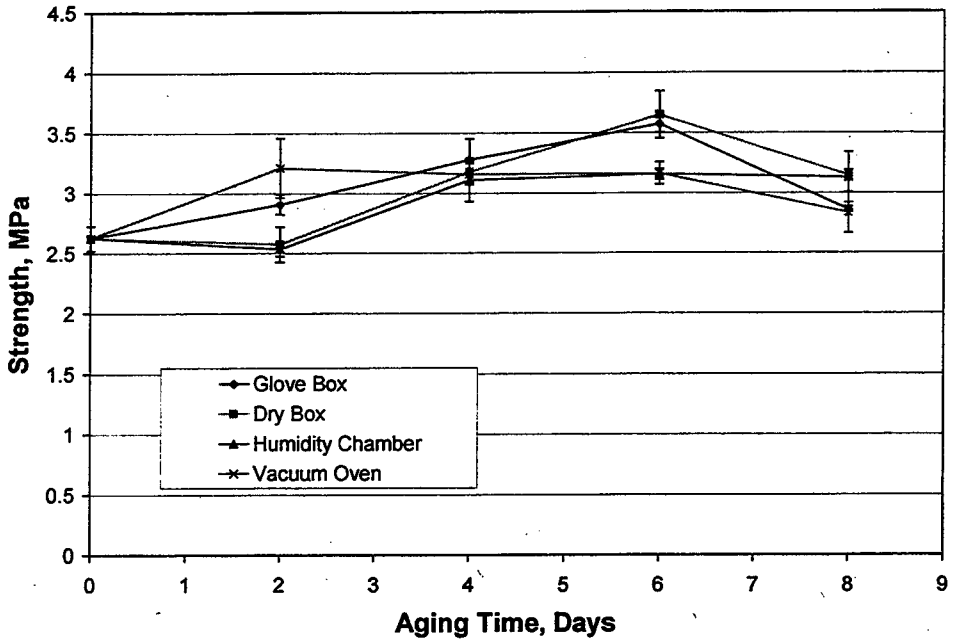


Figure 1. The tensile strength of RU955 filament stored under different conditions.

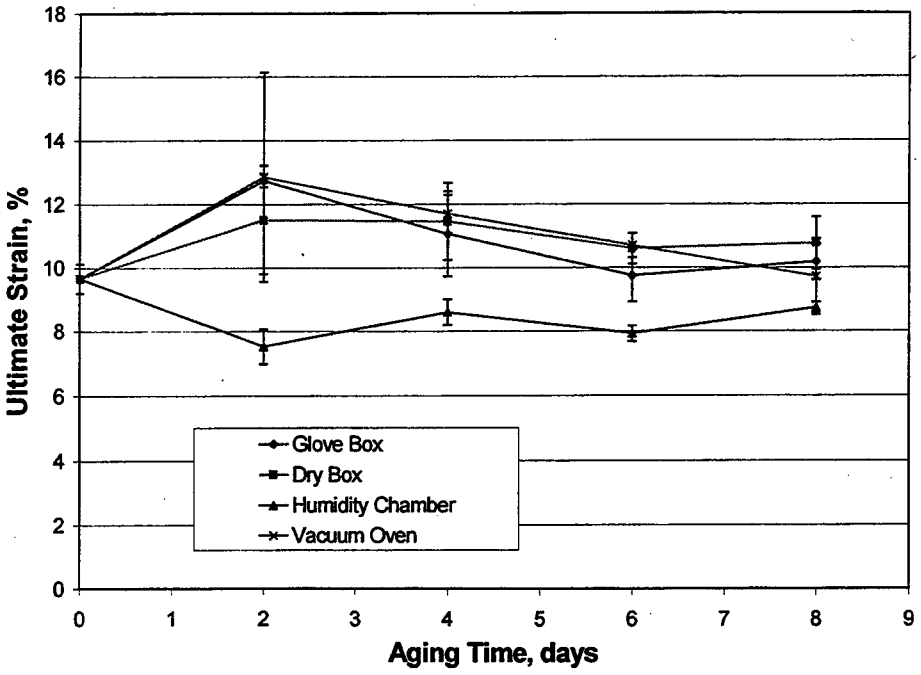


Figure 2. The tensile ultimate strain of RU955 filament stored under different conditions.

filaments in the dry box and humidity chamber showed no increase in the tensile strength for the first two days. The strength of filament stored in vacuum oven stopped increasing after two days of aging. The filaments stored in the other conditions reached the

maximum strength on the sixth day. On the eighth day, the differences among these different storage conditions were not significant. The measured ultimate strain of the RU955 filament showed little change with storage conditions and aging time, except for the storage conditions of the humidity chamber (Figure 2), where the ultimate strain was the lowest for all storage conditions for all aging times. The tensile elastic modulus of the RU955 for all storage conditions increased with storage time (Figure 3). The only exception was the filament stored in the vacuum oven, due to the fact that the elastic modulus of this filament remained almost unchanged with aging time. Generally, the strength and elastic modulus of the filament increased with storage time in the first six days. The ultimate strain of the filament stored in the environment chamber was lower than that for the other storage conditions.

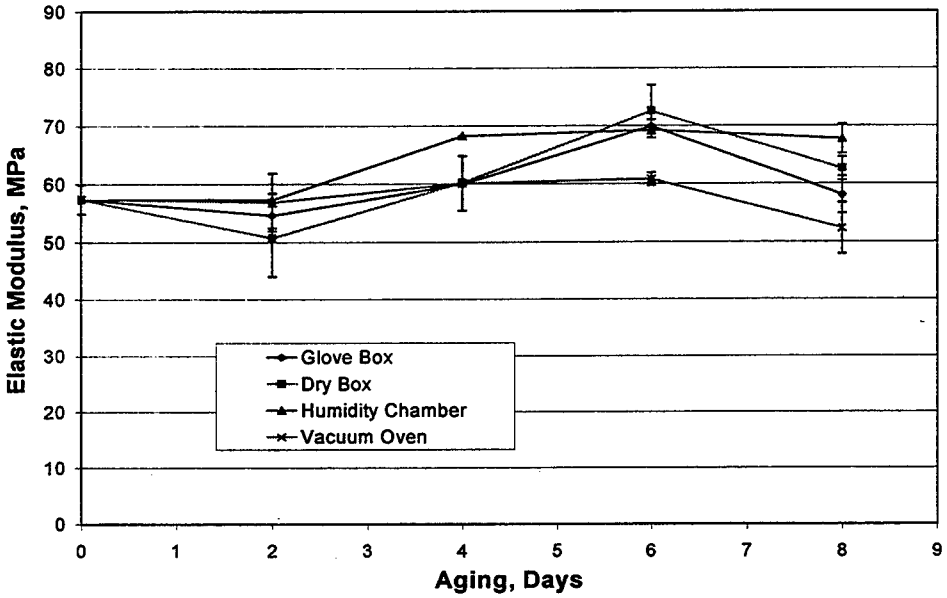


Figure 3. The tensile elastic modulus of RU955 filament stored under different conditions.

Viscosity of RU955 GS-44 filament and RU9 binder

The viscosity of the RU955 filament stored in the dry box (10% R.H.) was measured for three different aging times (Figure 4), 0, 7, and 15 days in the dry box. The plot of viscosity vs. shear rate shows no viscosity difference for storage times up to 15 days. In order to investigate the humidity impact on the viscosity of the RU9 binder, the binder was placed in a dry box with 10% relative humidity (R.H.) or 100% relative humidity environment for 7 days, respectively. The measurement results (Figure 5) show that moisture has a strong influence on the viscosity of the neat binder at 60C, but its influence is reduced as the temperature increases. However, Figure 6 indicates that the effect of high moisture (100% R.H.) on the viscosity of the filament melt persists to 175°C. This suggests that neat binder flow behavior is not sufficient enough to explain the filament melt viscous behavior. Meanwhile, viscosity measurements (Figure 6) also

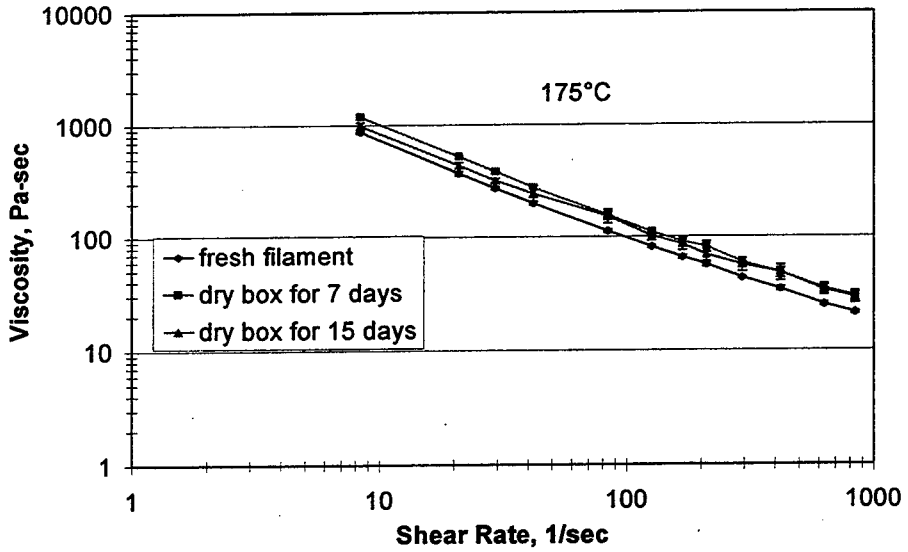


Figure 4. The viscosity vs. shear rate at 175C of RU955 filament stored in dry box for 0, 7, 15 days.

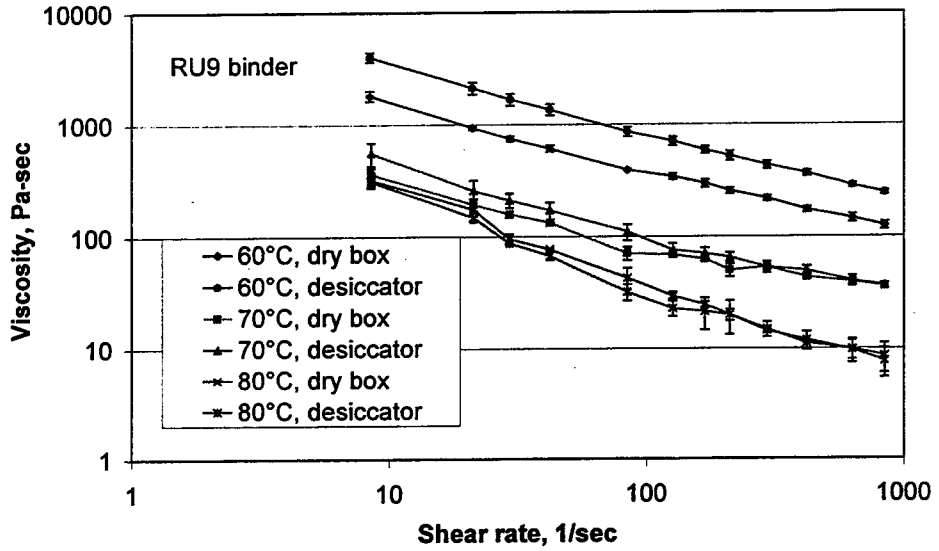


Figure 5. The viscosity vs. shear rate of RU9 binder stored in a dry box with 10% relative humidity and a desiccator with 100% relative humidity conditions, respectively, for 7 days.

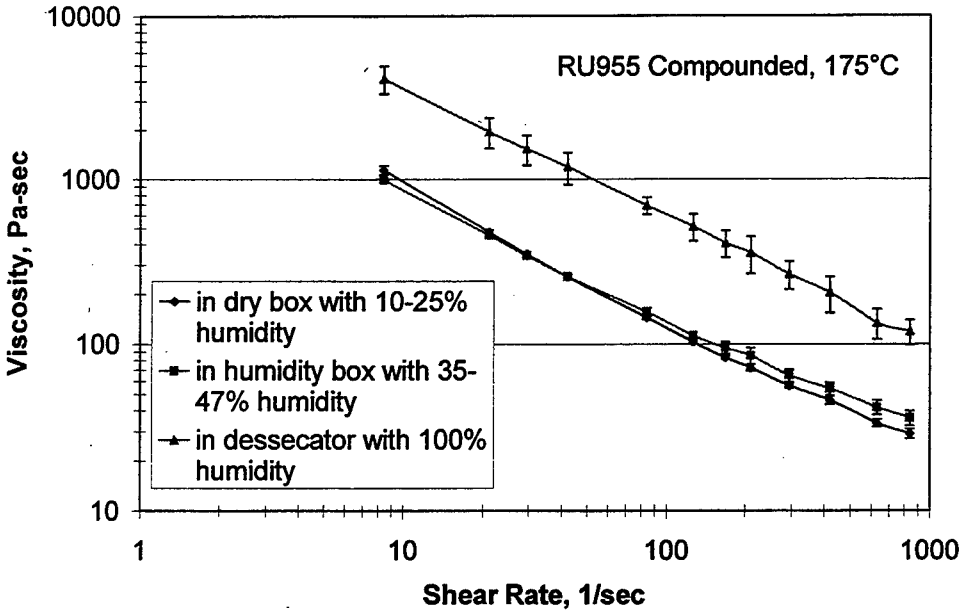


Figure 6. The viscosity vs. shear rate of RU955 compounded material stored in three different humidity conditions for 7 days.

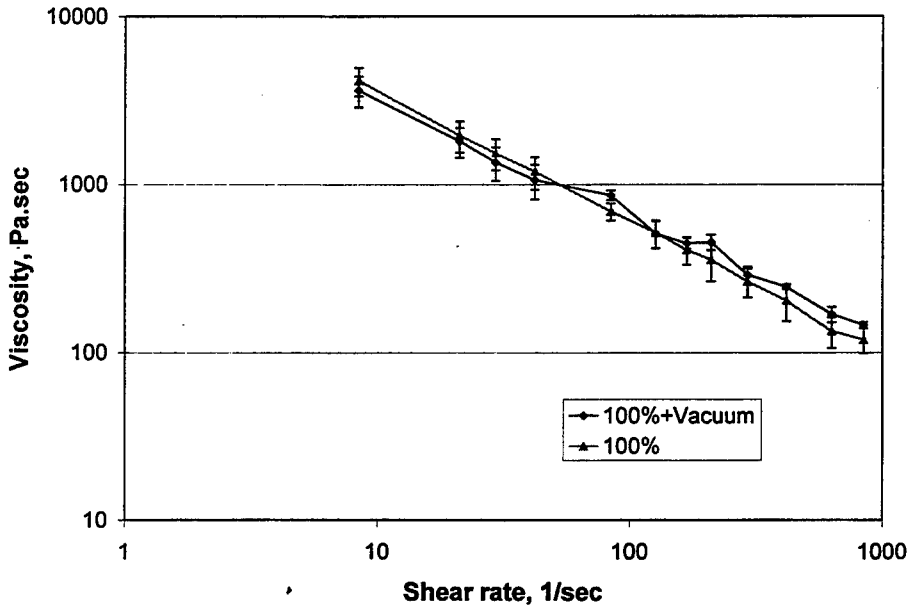


Figure 7. The viscosity vs. shear rate for RU955 compounded materials exposed to 100% relative humidity for 7 days and also followed by a vacuum treatment for 4 days.

show no difference for filament stored in a 10% and a 35% humidity environment. It seems that the filament is stable in low humidity conditions (<40% H.R.). In order to investigate the nature of high humidity influence and to control the humidity, vacuum treatment was applied to those filaments exposed to 100% relative humidity. The results

(Figure 7) show that the four days vacuum treatment has little impact on the viscosity of the RU955 filament exposed to 100% relative humidity for a week. This suggests that long time exposure to high humidity may cause a permanent increase on the viscosity of the filament melt. In summary, storage in high humidity has a strong impact on the RU9 binder and RU955 filament. The viscosity of RU9 binder clearly increases after exposure to 100% relative humidity. This increase, however, diminished as the measured temperature increases. In the case of the filament melt on exposure to a 100% relative humidity, the viscosity remains high up to 175°C. Low relative humidity storage (< 40% R.H.) seems to have little influence on the viscosity of the RU955 filament melt. The measurements also indicate that the filament may be permanently changed by exposure to 100% relative humidity and simple vacuum treatment may not be sufficient to eliminate the negative impact.

The Ratio of Filament Elastic Modulus (E) and drive Motor Current (T)

The FDC trials are performed with a 25 mil nozzle at 36% flow rate with the liquefier temperature at 175°C. In the FDC trials, the main focus is on two issues: filament buckling and the surface quality of the extruded road from the liquefier. Obviously, the smooth surface of the roads can reduce the defects and increase the density of the ceramic parts. Testing shows that the filament stored in with 55% relative humidity gives a very rough surface on the roads due to steam generation at 185°C. Without post-vacuum

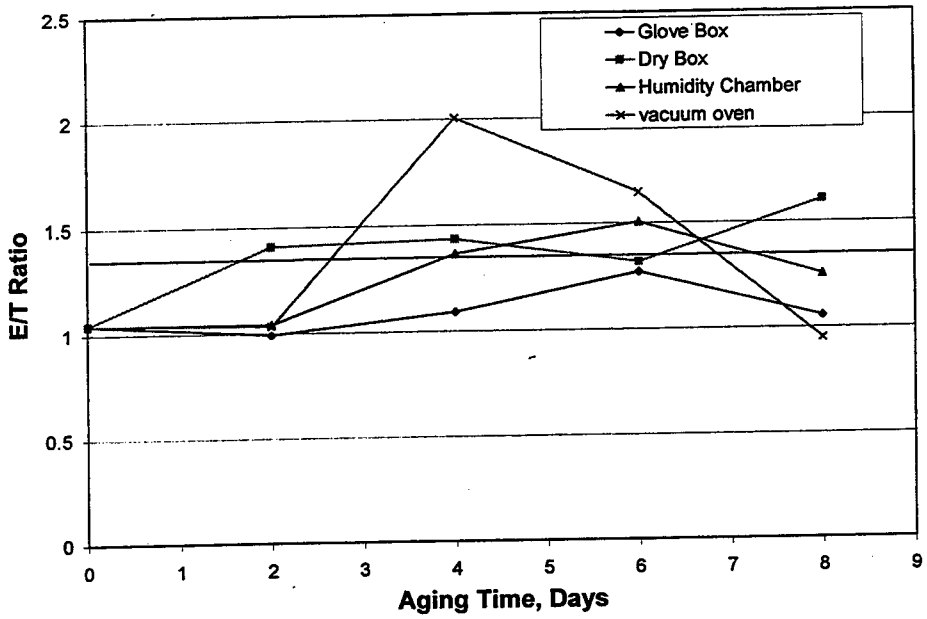


Figure 8. The ratio of elastic modulus (E) vs. motor current (torque τ) against storage time. Filaments, which have the ratio of E/τ of 1.4, show no buckling during FDC trials.

treatment, this filament stored in the humidity chamber cannot be used in FDC. In order to quantify the buckling behavior of the filament, the ratio of elastic modulus (E) over the motor current (torque, τ) is used. Figure 8 shows the E/τ ratio against aging time. When

the ratio is over the value of 1.4, no buckling occurred during FDC trials. Any point below this line resulted in filament buckling during FDC trials. By examination of this plot, one can find that all filament stored in a glove box buckled during FDC trials. Filament stored in humidity chambers showed no buckling after the sixth day. In most cases, no buckling was observed for filament stored in the dry box. However, the ratio is very close to the line. The filament placed in the vacuum oven for four days demonstrates the highest ratio of elastic modulus to motor current (torque). The filament showed no buckling during FDC trials and showed it can handle higher speeds of part building. Generally, like most figures of merit, the ratio of elastic modulus over the motor current (E/τ) is an empirical index. It does, however, give us an effective tool to evaluate the filament and to establish suitable filament storage conditions.

IV. Discussion

Mechanical testing and viscosity measurements both show that RU955 material experienced a change in properties with storage condition and time. The increase in the strength and elastic modulus with storage time results from a physical aging of the polymer binder[4,5]. Although crystallization of the wax occurs after RU9 binder melt and solidification, x-ray diffraction analysis shows that the binder in the GS-44 filled filament stored in the glove box remains in an amorphous state. This delay in crystallization may be due to high percent solids loading in the filament that may block the macromolecule movements needed for crystallization.

Viscosity measurements (Figure 5) indicate that water in the neat binder increases its viscosity. However, the influence becomes less pronounced when the temperature of the measurement increases. In FDC, the liquefier operation temperature is 185°C, much higher than the temperature in the measurement in figure 5. Based on the extrapolation from Figure 5, the influence of water on the neat binder viscosity is not expected to be large at the 185C liquefier temperature. However, Figure 6 shows that the viscosity of RU955 filament stored in the 100% relative humidity condition still remains 3 times higher at 175°C. These results suggest that the moisture on the surface of the Si_3N_4 particle and /or the hydrolysis may contribute to the increase of the viscosity. In contrast to the dramatic change of the viscosity in the high humidity, Fig. 6 also shows no difference in viscosity between 10% and 35% relative humidity. Fig. 4 provides evidence of the insensitivity of the viscosity of the filament melt to low humidity, even at a long aging time. Since the water molecules have to diffuse through the binder to attack the particles, the water concentration in the binder has to reach the water solubility of the binder to initialize the interaction between water and particles. This may be the reason that low humidity has no influence on the viscosity of filament melt. When the binder absorbs enough water, Si_3N_4 hydrolysis may occur. The hydrolyzed surface of particles may enhance the interaction between particles. In addition, the concentration of the dispersing oleyl alcohol at the surface of powder may also be reduced when water molecules occupy the surface sites of the particles. Consequently, the viscosity of the filament is expected to increase. When the hydrolysis does occur, the use of a vacuum treatment may be not sufficient to dissociate the hydrolysis produced. Based on this

reasoning, the viscosity of filament exposed to 100% humidity should remain unchanged followed by four days of vacuum treatment.

Although vacuum treatment seems to have no effect on the viscosity of the filament, especially in the 100% relative humidity condition, the mechanical testing results clearly indicate that vacuum treatment has a positive effect. After vacuum treatment, the filament stored in humidity chamber has an increase of almost 20% in elastic modulus, 34% in ultimate strain, and 28% in ultimate strength. It is interesting to point out that the vacuum treatment shows the positive influence only when the filament is freshly fabricated or stored in the humidity chamber.

V. Summary

FDC filaments stored under all conditions show some degree of aging. Water in the binder and on the surface of silicon nitride dictates the filament mechanical properties and viscosity. The current vacuum treatment accelerates the aging process, improves the mechanical properties, and reduces filament buckling. Based on this study, the suitable standard storage condition has been established. The freshly fabricated filament is stored in a vacuum oven at 30°C for four days and then, the treated filament is stored in the dry box at 30°C at <20% R.H. and is ready to be used in FDC 3D molder. Three consecutive batch filaments followed this standard storage procedure and the reproducible and stable process of FDC was achieved.

Acknowledgments

The authors gratefully acknowledge the support of this research by DARPA/ONR under contract #N00014-94-0115. The authors would like to thank Drs. P. Whalen, R. van Weeren, and V. Jamalabad, and Mr. R. Clancy of AlliedSignal for their valuable suggestions and contribution to this study. The authors would also like to extend the thanks to Dr. P. Bharagava, Mr. G. Zuo and Mrs. H. L. Wu of Rutgers University for their help during this research.

Reference

1. E. Sachs, M. Cima, and D. Brancazio, "Rapid Tooling and Prototyping by Three Dimensional Printing", 90 Trans., NAMRI/SME 41-45.
2. E. A. Griffin, D. R. Mumm and D. B. Marshall, "Rapid Prototyping of Functional Ceramic Composites", The Am. Ceram. Soc. Bull. 7[75] 65-68 (1996).
3. M. K. Agarwala, A. Bandypadhyay, R. van Weeren, A. Safari, S. C. Danforth, N A. Langrana, V. R. Jamalabad and P. J. Whalen, "FDC, Rapid Fabrication of Structural Components", Am. Ceram. Soc. Bull., 11[75] 60-65 (1996).
4. G. B. McKenna, Y. Leterrier, and C. R. Schultheisz, "The Evolution of Material Properties During Physical Aging", Polymer Eng. and Sci., 5[35] 403-410 (1995).
5. I. Spinu and G. B. McKenna, " Physical Aging of Nylon 66", Polymer Eng. & Sci., 24[34] 1808-1814 (1994).

The Role of Materials Processing Variables in the FDC Process

Sriram Rangarajan, Gang Qi, Amit Banyopadhyay, Cheng Dai, Joon W. Han,
Parag Bhargava, Suxing Wu, Ahmad Safari and Stephen. C. Danforth

Center for Ceramic Research - Department of Ceramics and Materials Engineering
Rutgers University, Piscataway, NJ 08855

The Fused Deposition of Ceramics (FDC) is based on the commercially available Fused Deposition Modeling (FDM™) technique developed by Stratasys Inc. The FDC process is being currently developed to make complex ceramic parts in an automated fashion. Although the current focus is on making Si_3N_4 parts, this technique has been successfully used to make electroceramic (such as PZT) and metallic (such as stainless steel) parts.

As feedstock for the FDC process, filaments loaded with 55 vol% GS-44 Si_3N_4 is being used. For the filament to be used in the FDC process, it must possess a unique combination of physical, rheological and mechanical properties. In this paper, we investigate the role played by some of the process variables on these properties. Our current processing sequence to make filaments is as follows - coating of powders with a surfactant, compounding the ceramic and binder, extrusion into filaments and finally treatment of filaments to achieve requisite properties. The study has resulted in improvements to the quality of the filament which can be used for automated FDC. The effect of moisture, agglomerates and filament aging on FDC will be discussed.

1.0 Introduction

One of the most promising ways to fabricate ceramic components to net or near net shape, is through solid freeform fabrication (SFF). Apart from being able to manufacture intricate shapes, this technique has the added advantages of flexibility of design, and is an inexpensive tool for prototyping. This technique is therefore suitable to make complex shapes and novel structures which are normally not feasible using conventional processing routes. Additionally, SFF has the advantage of being material insensitive and therefore finds a variety of applications ranging from macro scale aerospace components[1] to fine scale piezoelectric composites[2].

Many solid freeform fabrication (SFF) or layered manufacturing (LM) techniques are being actively researched and a few have found commercial success. Fused Deposition Modelling[3], Stereolithography[4], 3D Printing/Inkjet Deposition[5] and Laminated Object Manufacturing(LOM)[6] are a few major examples. Most of these techniques were initially developed to make polymeric or paper parts for design verification and form and fit, although recent research activities are directed towards manufacturing metallic and ceramic parts.

The fused deposition process, commercialized by Stratasys™ Inc. (Eden Praire, MN) as Fused Deposition Modeling (FDM™) [3] is one of the commercially available SFF techniques. In the FDM process, a thermoplastic polymer filament is unwound from a continuous spool and driven through a liquifier, which is heated to a temperature slightly above the melting point of the polymer. The liquifier extrudes a continuous bead, or road, of material through a nozzle (typically 10 - 25 mils) and deposits it onto a fixtureless platform. The liquifier movement is controlled along the X and Y directions by a computer, based on the build strategy of the object to be manufactured. When deposition of the first layer is completed, the fixtureless platform indexes down, and a second layer is built on top of the first layer. This process continues until the whole part is completed. The fused deposition modeling process, which until now has been used to make polymeric parts for

prototyping and investment casting, has been modified at Rutgers University to make ceramic parts directly through a process known as Fused Deposition of Ceramics (FDC). Towards this, ceramic powders are mixed with an appopriate binder to high volume fractions (typically from 50 to 60 volume%) and extruded into a filament which acts as the feed material for the fabrication process. Post processing involves binder burnout and sintering to obtain final parts.

Several important parameters determine the feasibility of manufacturing ceramic parts by FDC and can be broadly lumped into two categories: hardware/machine dependent and material dependent[7]. In this paper, the material dependent parameters specifically related to the processing of feedstock materials will be discussed. "FDCability" is defined as the ability to manufacture a green ceramic part in a continuously automated fashion by FDC. Although such a definition would suggest simplicity, the actual feedstock material, i.e., the filament, must possess a unique combination of physical and mechanical properties to achieve FDCability. The basic requirements for the filament to be FDCable are: (1) sufficiently low viscosity at high solids loading (in the range of 100 - 1000 Pa.s at the FDC extrusion temperatures), (2) filaments free of agglomerates that stop an automated FDC process through nozzle clogging, (3) sufficient filament stiffness to impart the ability to act as a piston to drive the extrusion, (4) sufficient tensile strength for continuous spooling and unspooling operations, (5) high filament dimensional tolerance of 70 ± 1 mil, (6) freedom from surface defects and kinks, (7) a binder with the ability to bond the layers during FDC building and (8) a binder which undergoes total decomposition during burnout.

Previous studies [8] have identified a binder material called RU9 for filament processing. RU9 is thermoplastic based binder with 4 components: i) a polymer which acts as a base, ii) an elastomer which lends flexibility to the binder, iii) a wax which lowers viscosity and increases the intrinsic stiffness of the binder, and iv) a tackifier which acts primarily to bond the layers. Also it has been demonstarted that the FDC process can fabricate Si_3N_4, PZT, Al_2O_3, hydroxy apatite and stainless steel parts. The skeletal framework for the process has been developed[8], however a better understanding has to be achieved to enable controlled processing and fabricating to high quality parts. This paper will focus on the processing of high quality Si_3N_4 filaments and process modifications made towards this goal. This paper will discuss the build up of requisite filament properties through improved particle dispersion, a more homogenous RU9-Si_3N_4 compounded mix (RU955) and the effect of better filament aging.

2.0 Experimental Procedure

2.1 Processing

The process of Si_3N_4 filament fabrication for FDC is schematically illustrated in the flow chart in Figure 1. Allied Signal's GS-44 Si_3N_4 powder is first coated with oleyl alcohol $\{CH_3 (CH_2)_7CH=CH(CH_2)_7CH_2OH\}$ as a dispersant in step I. In step II, the coated powders are compounded with the RU9 binder using a torque rheometer to 55 vol.%. The compounded mix is granulated and finally in step III, the granulated material is extruded into filaments using a single screw extruder. Each of the three steps is described below.

2.1.1 Dispersant Coating

The as recieved GS-44 Si_3N_4 powder was coated with oleyl alcohol by a solution ball milling procedure. 15 g (3 wt.%) of oleyl alcohol, 485 g Si_3N_4 powder and 1000 ml of ethanol as solvent, along with 1000 g of Si_3N_4 milling media are added to rubber lined ball mill. The mixture is ball milled for 14 hours and then sieved through a #120 mesh to separate the media from the mixture. A drying procedure is performed to remove the

solvent by heating a flask containing the mixture to the boiling point of ethanol (78°C). The evaporated solvent was condensed and removed through a distillation apparatus. After drying, the flask is placed in a vacuum oven for 12 hours to ensure a complete removal of the ethanol.

2.1.2 Compounding of Coated Powders with RU9 binder

The coated powder was compounded with the appropriate amount of binder using a Haake Rheocord torque rheometer. The rheometer has mixing bowls with a capacity of 250 cm^3 and Z blades to apply the shear. Efficient mixing was achieved through application of shear and heat. RU9 was first melted at 100°C and subsequently, the powder was added in four increments amounting to 40%, 30%, 20% and 10% by weight of the total powder. High torque results with each powder addition due to entrapment of the binder and the presence of agglomerates. The shear provided by the blades breaks down the agglomerates and lowers the torque. After all powder was added, the temperature was reduced to increase the shear to further breakdown agglomerates. When a stable final torque was reached, the compounded mix was removed and granulated for further processing.

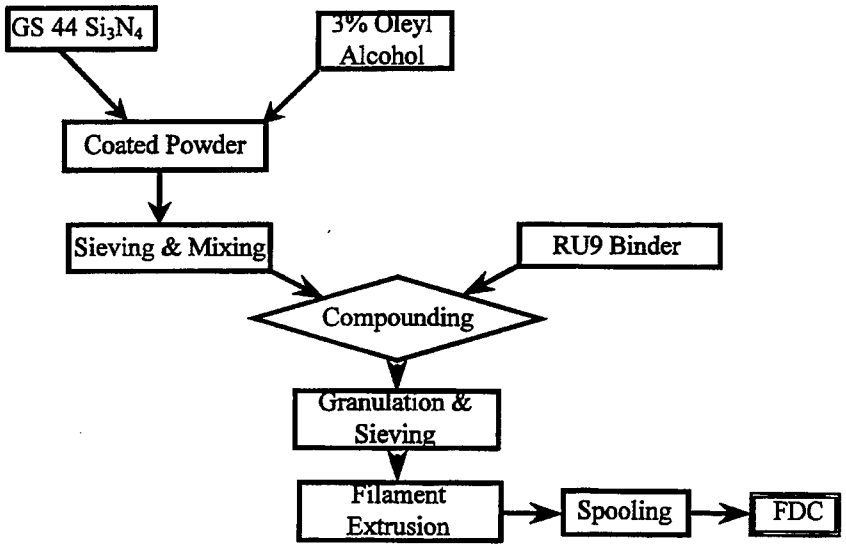


Figure 1. Process flow chart for FDC GS-44 Si_3N_4 filament processing.

2.1.3 Filament Extrusion

Extrusion of the compounded mix into filaments was performed using a single screw extrusion set up shown in Figure 2. The set up has a 70 mils cylindrical die. Granules of RU955 material were fed through a hopper and passed through four independently controlled heating zones. The screw had a uniform flight thereby transporting material through the barrel at a constant rate. The material was compressed by an increased pressure caused by the diameter constriction from barrel to die. Torque and pressure (see Figure 2 for placement of pressure transducers) were continuously monitored during extrusion. The rotational speed of the screw during extrusion was 5 rpm. Filament exiting the die was carried away by a conveyor belt whose speed was matched to the output flow rate. Two important modifications were made to the set up. First the screw design

was changed from simple constant flight to one with a shear tip (at the die end) to increase mixing efficiency. Second, a breaker plate and #120 mesh screen assembly were added for effective filtration of any debris and agglomerates.

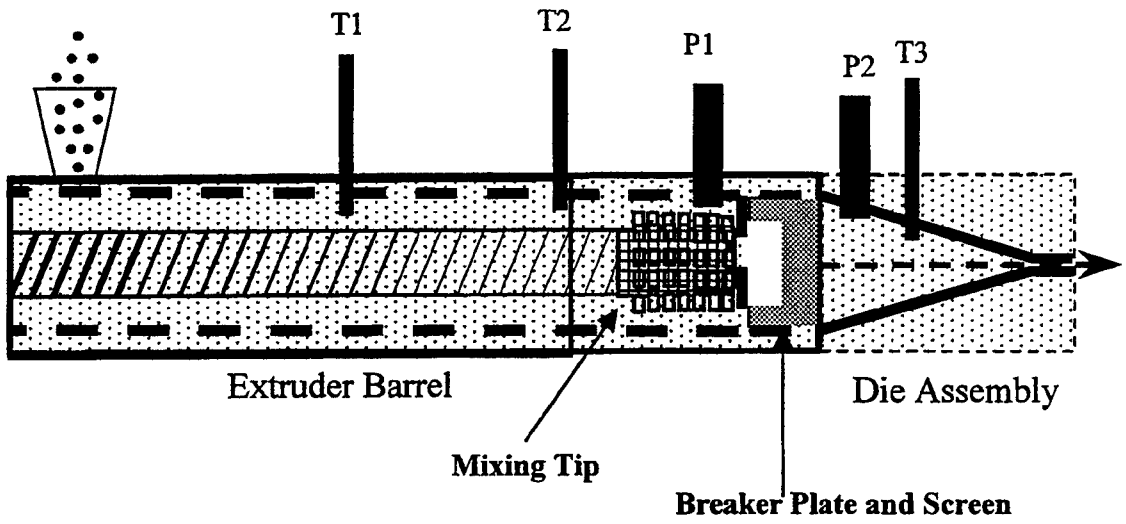


Figure 2. Extrusion set up with a single screw, breaker plate and screen assembly. Temperature and pressure in the melt is monitored at various points along the barrel.

2.2 Process Characterization

2.2.1 Loss on Ignition (LOI) Tests - LOI tests were performed on coated powders and RU955 compounded materials to determine the amount of coating and binder present respectively. LOI was simply performed by measuring weight loss in samples after exposure to temperature in air atmosphere. For coated samples, the temperature was 600°C while that for compounded samples was 700°C.

2.2.2 Particle Size Analysis - Particle size distribution is determine by light scattering method using a Microtrac FRA Particle Size Analyzer. Samples were prepared by mixing 0.5 g of powder and 50 ml of the ethanol and ultrasonicating for 5 minutes before testing.

2.2.3 Viscosity - Viscosity of RU955 materials was measured using an Instron Capillary Rheometer. Capillary nozzles for the measurements had an L/D ratio of 20.3. Measurements were performed at 120°C, 140°C and 185°C. Results from three tests were corrected for barrel drag and averaged, and viscosity vs. shear rate plots were obtained.

2.2.4 Instron QC Test - The Instron capillary rheometer was modified to test the RU955 compounded and filament materials for agglomeration. A 25 mils capillary die was attached and the extrusion was performed at 140°C and 1mm/min constant velocity for a period of 1 hour. The steady state load (P_{ave}) and deviation from steady state (ΔP) were measured. If all other variables remain the same, ΔP is a measure of the degree of agglomeration.

2.2.5 Tensile tests - Tensile tests on RU955 filament were performed to determine tensile strength, strain to failure and elastic modulus of the GS-44 Si_3N_4 filled FDC filament using a Minimat tester. Approximately, 10 cm long filaments were measured for diameter and tested to failure at a stroke rate of 1mm/min. Reported values represent an average of three measurements.

3.0 Results and Discussion

3.1 Powder Processing

The surfactant coating is a crucial step in the filament fabrication process. Earlier studies have shown a dramatic decrease in viscosity due to addition of oleyl alcohol as a surfactant[5]. However Loss on Ignition (LOI) results showed an uneven distribution of oleyl alcohol on the powder within each batch. Table I shows this variability to be ± 1.08% indicating that the dispersant coating procedure was not uniform. Indeed this is verified in Figure 3 which shows particle size analysis of the uncoated and coated GS-44 Si_3N_4 powders. The as received powder shows the presence of agglomerates with only 40% of the particles finer that 1μm, a result of the spray drying procedure used to prepare the GS-44 powder. After coating, this distribution improves only slightly to 50% < 1μm and coarser particles (agglomerates) still persist. As the sieving step before drying should remove agglomerates (> #120 mesh or 125 μm), the solvent drying step is responsible for reformation of soft agglomerates in the 10 -300 micron range. An additional sieving and mixing (S&M) step was therefore introduced to resolve this problem. Six batches of coated powders were sieved using a #60 mesh nylon sieve. The sieved powders were thoroughly mixed on a ball mill for two hours. The improvements made as a result of S&M step can be seen from Table I and Figure 3.

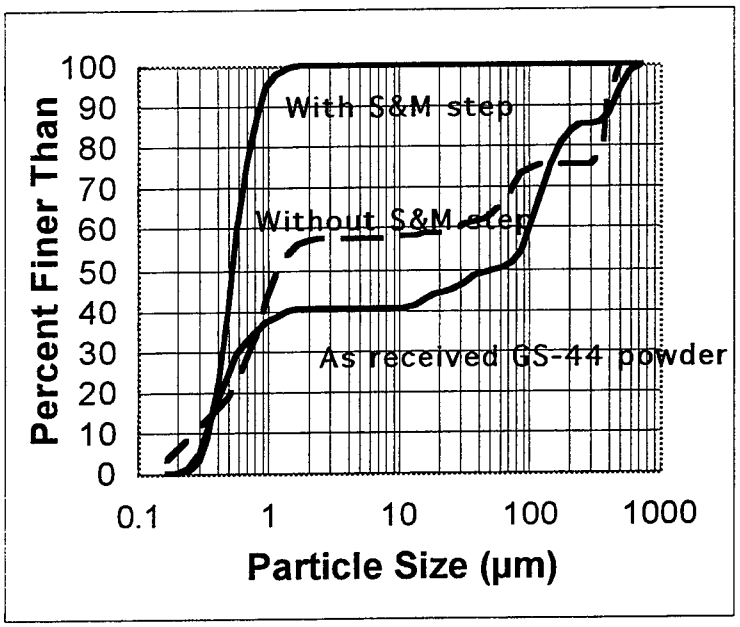


Figure 3. The results of particle size analysis on as received, spray dried, GS-44 Si_3N_4 powder, after coating with oleyl alcohol, and after coating with oleyl alcohol and also adding the sieving and mixing (S&M) step.

The data in Table I indicates that the homogeneity and distribution of oleyl alcohol on the powders is improved dramatically due to introduction of the S&M step. Also the distribution of particle size (see Figure 3) shifts to < 1μm with the median coinciding with the average particle size of 0.5μm. At this stage it is not known whether this additional S&M step has any effect on increasing the surface coverage of Si_3N_4 powders by oleyl alcohol although the particle size analysis results indicate that agglomerates have been eliminated.

Although the effectiveness of oleyl alcohol as a dispersant up to 62 vol% solids loading for injection molding compounds has been demonstrated[9], the adsorption mechanism remains largely unclear. More importantly, the effect of moisture on the adsortion is unknown. As a preliminary experiment, weight change of samples of coated powder exposed to 100% RH was monitored periodically for 21 days. Results showed a 1.1% and 1.7% weight gain after 2 days and 21 days respectively. This moisture uptake may affect the particle dispersion and consequently increase the viscosity in loaded systems. Indeed, such increase in viscosity has been observed and will be discussed in the next section. Moisture acts to disrupt the surfactant coating possibly by displacing oleyl

alcohol on the powder surface. From a processing standpoint, the coated powders should be free from moisture and are therefore stored under dry conditions to maintain a good dispersion.

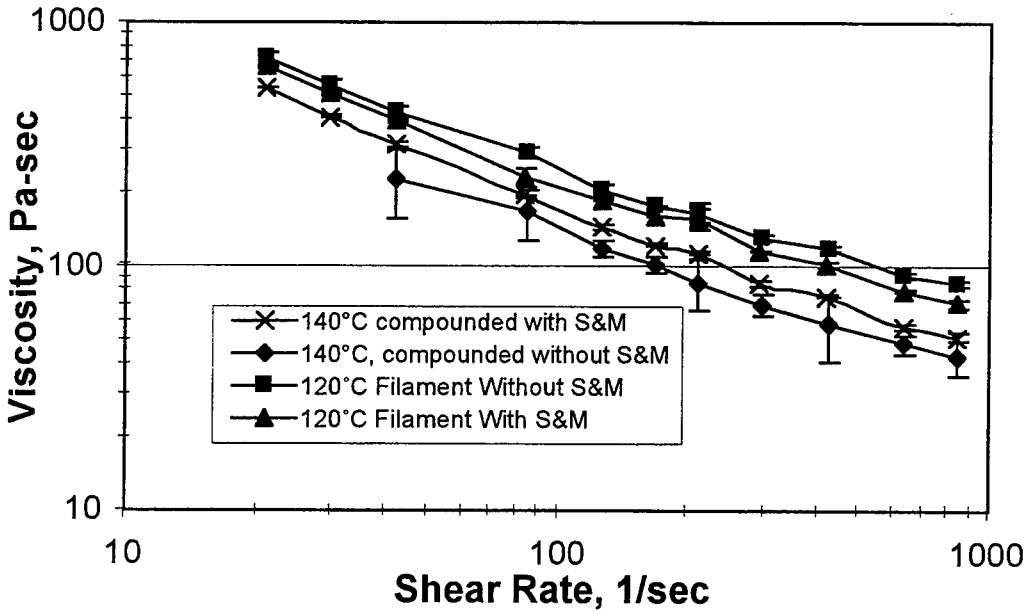


Figure 4. Graph showing the effect of Sieving & Mixing (S&M) on viscosity of compounded (at 140°C) and filament materials (at 120°C).

3.2 RU955 Compounded Materials

RU9 binder and coated GS44 powder were compounded to a 55 vol% solids loading using the procedure described earlier. The addition of the sieving and mixing step had a positive influence on the properties of the compounded materials. Table I shows the load variations during the Instron QC test for the compounded materials with and without the S&M step. Comparison of the results show a 62% decrease in variability of the materials by addition of the S&M step due to agglomerate breakdown.

Table I. Process Characterization Tests Results Showing the Effect of Sieving and Mixing on Coated and Compounded Materials

	LOI on Coated Powders (% Wt. Loss)	Load Variation ΔP in Instron QC Test (N)
Without S&M step	2.93 ± 1.08	61
With S&M step	2.86 ± 0.18	23

Figure 4 shows results from viscosity measurements made on RU955 compounded and filament materials with and without the S&M step. It is seen from Figure 4 that the sieving and mixing step may have a small effect on the viscosity of the compounded and filament materials. The significant result is that the viscosity measurements show a marked decrease in the variability in the viscosity due to S&M as indicated by comparisions of the ± σ standard deviations shown in Figure 4.

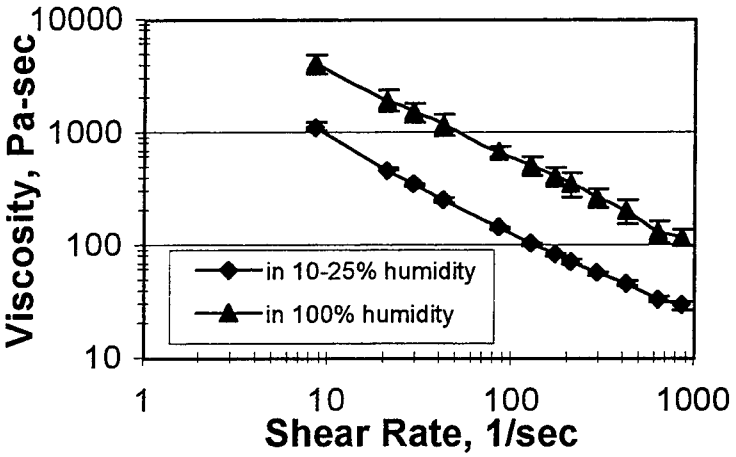


Figure 5. Data showing the increase in viscosity at 175°C of RU955 compounded materials due to exposure to high humidity for 7 days.

Figure 5 shows the effect of moisture on the viscosity of RU955 compounded materials. The viscosity of the compounded material exposed to ~100% RH for a period of 7 days increased by nearly an order of magnitude. This is clearly undesirable for the FDC process and therefore moisture intake into the feedstock materials needs to be carefully controlled. The viscosity of pure RU9 binder (at T > 100°C) is not significantly affected by humidity, implying that the primary effect of humidity is to increase inter particle interactions.

3.3 Extrusion of Reproducible High Quality Filaments

3.3.1 Homogeneity, Deagglomeration and Dimensional Tolerance of Filaments

The important extrusion variables are temperature profile, shear rate (determined by rpm, temperature profile and die and screw design) and feed rate[10]. The output from a single screw extruder (Q) can be derived as

$$Q = Q_d - Q_p = \alpha N - \beta P/\eta \qquad (1)$$

where, Q_d = drag flow transportation of material caused by rotation of the screw, Q_p = pressure flow counteracting the drag flow and arising due to restrictions imposed by the die, N= rotational speed of the screw, α, β = constants depending on screw and die design, P = pressure before die entrance and, η = viscosity of the melt.

Several process improvements were enacted to improve the quality of the GS-44 filled filaments for FDC. A breaker plate and screen assembly was added to the extrusion set up, just upstream of the die entrance. The screen size used was #120 corresponding to 125μm mesh size opening. The screen therefore acts as an effective filtration agent. Also a new screw design with a mixing tip was introduced. This, in conjunction with the breaker plate assembly, was desired to increase the shear of the material before the die entrance, leading to better mixing efficiency and increased homogeneity in the filament and a further decrease in agglomerate size. Although quantitative estimates of the effect of breaker plate and screen assembly on modulus and viscosity is not available, the combined effect along with the sieving and mixing step is to decrease the agglomeration and variation in viscosity of the filament as seen in Figure 4. An important consequence of these process improvements on FDCability is that nozzle clogging during FDC part building has been eliminated and finer nozzle sizes of 15 mils (compared to 25 mils before) are being utilized, thereby increasing part surface quality and fine feature capability.

Torque and pressure profiles (at the extrusion die entrance) recorded during an extrusion run showed a large fluctuation. The maximum change in pressure was 800 psi (approx. 53%). The existence of variation in pressure leads to variations in the output Q of

the extruder as given by Equation 1. This is significant from the perspective of high filament dimensional tolerance. Deviations from steady flow cause the filament to be extended or compressed at the die exit, which changes the diameter of the filament. Maintaining steady pressure is therefore essential as this will also eliminate kink formation. Although this has not been resolved yet, several factors can minimize the pressure fluctuations. (1) Hardware modifications such as automatic feeding will maintain a constant feed rate and improved screw design should maintain a steady volumetric flow rate of materials through the barrel. (2) By increasing the rotational speed of the screw during extrusion, an increased contribution from drag flow Q_d with respect to pressure flow Q_p will arise, and the overall flow rate fluctuations will decrease. (3) By further increasing homogeneity and particle dispersion, load fluctuations caused by agglomerate break down will be reduced.

3.3.2 Filament Aging to Achieve Necessary Mechanical and Rheological Properties

The freshly extruded GS-44 filed RU955 filament has to be aged prior to FDC. Preliminary studies indicate that the aging phenomenon is a time, temperature, humidity phenomenon involving 2 or more processes. Experiments were conducted to study this aging phenomenon and are detailed elsewhere[11]. In this paper, the effects of vacuum aging treatment are discussed.

Table II. Process Characterization Tests Results Showing the Effect of Vacuum Aging RU955 Filament Materials

	Elastic Modulus, E (MPa)	Tensile Strength, σ (MPa)	FDC Motor Current, τ Torque (mA)
Before Aging	57.4	2.65	75
After Aging for 4 days	60.4	3.15	50

Table II shows the properties of the RU955 filament before and after aging. After four days in vacuum, the filament elastic modulus (E) is increased by 5.2 %, the filament tensile strength by 18.7% whereas the FDC motor current (τ) is lowered by 33.3%. The FDC motor current τ is a measure of the resistance experienced by the FDC rollers to push down the filament through the liquifier [12]. If all machine parameters are kept constant, then τ is a measure of the viscosity of the filament. Figure 6 shows the effect of vacuum aging time on the E/τ ratio. The horizontal line at $E/\tau = 1.3$ is the critical E/τ ratio below which filaments buckle during the FDC process[11]. From Figure 6 it can be seen that a 3 day vacuum treatment at 30°C and <0.1"Hg increased the E/τ to above 1.3. Several factors can contribute to aging and can be related to mechanical properties and/or viscosity of the filament:

(1) Viscosity of "wet RU955 materials" was higher (cf. Figure 4) as seen earlier indicating that H_2O has a significant effect on the filament properties. Vacuum drying may therefore decrease the viscosity by lowering the water content in the filament.

(2) XRD analysis shows that two of the binder components, the wax and the polymer, crystallize over time. This crystallization process would increase the stiffness of the filament thereby increasing FDCability through reduced filament buckling. The kinetics of the crystallization process for the filled binder is seen to be retarded when compared to pure binder and/or its pure constituents. Crystallization in pure components and binder occur within 24 hours at room temperature, but in the case of RU955, there is no evidence of crystallization after a 5 day exposure at room temperature. However, at increased

temperatures of 30°C in the vacuum oven, a crystalline polymer peak in RU955 was observed after 5 days.

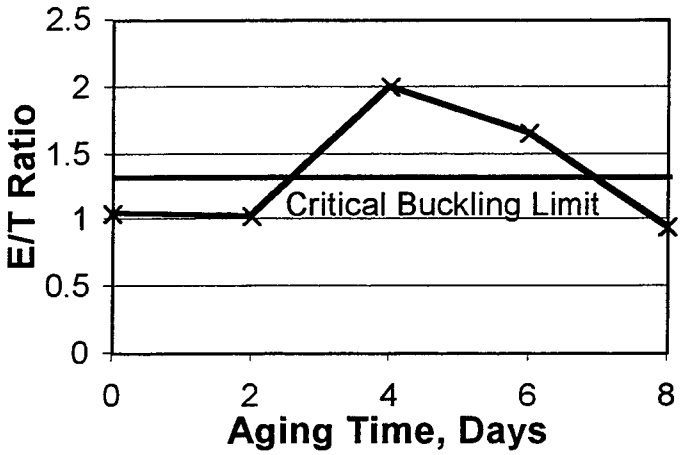


Figure 6. Effect of aging time on E/τ ratio showing that a four to six day vacuum treatment at 30°C increases the filament E/τ ratio to above critical buckling limit (1.3).

At this time, research efforts are currently directed towards understanding the relative significance of various phenomenon on the filament aging. From an FDCability standpoint a suitable filament aging condition has been identified which increases the E/τ ratio to beyond critical buckling limit.

4.0 Summary and Conclusions

Several process modfications have contributed towards the build up of requisite filament properties for continuous FDC. The quality and homogeneity of filament fabrication has been improved considerably due to the introduction of sieving and mixing step and the breaker plate and screen assembly. Specifically, the filament is more homogenous with lower ± σ (standard deviations) in viscosity, lower agglomeration and high dimensional tolerance of 70 ± 1 mils. It is now possible to extrude over 1200 ft of continuous spoolable and FDCable filament. The resulting filament, after adequate aging, has been qualified by continuous and automated FDC. The filament was continuously FDCed for 16 hours using a 15 mils nozzle[11]. There was no nozzle clogging (due to agglomeration) or filament buckling (due to either agglomeration or high viscosity/low stiffness).

Acknowledgements

The authors would like to thank the Office of Naval Research (ONR) and the Defense Advanced Research Projects Agency (DARPA) for their financial support under contract # N0014-94-0115. The authors would also like to thank R. Clancy and Dr. P. J. Whalen at AlliedSignal Research and Development for their valuable discussions and contributions. Laboratory assistance from G. Zuo, L. Ordonez, G. Walker, R. Jaico and M. Miller is greatly appeciated.

References.

1. M. K. Agawala, A. Bandyopadhyay, R. van Weeren, A. Safari and S. C. Danforth, *Ceramic Bulletin*, 75 [11], 1996, pp. 60-65.

2. A. Bandyopadhyay, R. K. Panda, V. F. Janas, S. C. Danforth and A. Safari, *J. Am. Cer. Soc.*, 80, [6], 1997 pp. 1366 - 1372.

3. W. Walters, *Solid Freeform Fabrication Proceedings*, 3, Ed. H. L. Marcus, J. J. Beamen, J. W. Barlow, D. L. Bourell and R. H. Crawford, University of Texas, Austin, TX, 1992, pp 301-308.

4. P. F. Jacobs, *Rapid Prototyping & Manufacturing: Fundamentals of Stereolithography*, Chapters 4 & 8, Society of Manufacturing Engineers, Dearborn, MI, July 1992.

5. E. Sachs, M. J. Cima, and J. Cornie, *Solid Freeform Fabrication Proceedings*, 1, Eds. J. J. Beamen, H. L. Marcus, D. L. Bourell, R. H. Crawford, and J. W. Barlow, University of Texas, Austin TX, 1990, pp 24-47.

6. M. Feygin and B. Hsieh, *Solid Freeform Fabrication Proceedings*, 2, Eds. H. L. Marcus, J. J. Beamen, J. W. Barlow, D. L. Bourell, and R. H. Crawford, University of Texas, Austin TX, 1991, pp 123-130.

7. M. K. Agawala, A. Bandyopadhyay, R. van Weeren, N. A. Langrana, A. Safari, S. C. Danforth, V. R. Jamalabad, P. J. Whalen, R. Donaldson and J. Pollinger, *Solid Freeform Fabrication Proceedings*, 7, Ed. D. L. Bourell, J. J. Beamen, H. L. Marcus, R. H. Crawford, and J. W. Barlow, University of Texas, Austin TX, 1996, pp 335-343.

8. M. K. Agawala, R. van Weeren, A. Bandyopadhyay, A. Safari, S. C. Danforth, and W. L. Priedeman, , *Solid Freeform Fabrication Proceedings*, 7, Ed. D. L. Bourell, J. J. Beamen, H. L. Marcus, R. H. Crawford, and J. W. Barlow, University of Texas, Austin TX, 1996, pp 451-458.

9. D. J. Shanefield, Organic Additives and Ceramic Processing, Kulwer Academic Publishers, 1st edition, 1995, pp 251-254.

10. G. Challa, *Polymer Chemistry An Introduction*, Ellis Horwood, West Sussex, Great Britain, 1993, pp 172-182.

11. G. Qi, C. Dai, S. Rangarajan, S. Wu, A. Safari and S. C. Danforth, to be published in *Solid Freeform Fabrication Proceedings*, 8, Ed. D. L. Bourell, J. J. Beamen, H. L. Marcus, R. H. Crawford, and J. W. Barlow, University of Texas, Austin TX, 1997.

12. C. Dai, G. Qi, S. Rangarajan, S. Wu, A. Safari, N. Langrana and S. C. Danforth, to be published in *Solid Freeform Fabrication Proceedings*, 8, Ed. D. L. Bourell, J. J. Beamen, H. L. Marcus, R. H. Crawford, and J. W. Barlow, University of Texas, Austin TX, 1997.

Soft Elastomers for Fused Deposition Modeling

Kurt Elkins[1], Howard Nordby[2], Christopher Janak[3], Robert W. Gray IV[4],
Jan Helge Bøhn[3], and Donald G. Baird[4]

Department of Aerospace and Ocean Engineering[1]
Department of Materials Science and Engineering[2]
Department of Mechanical Engineering[3]
Department of Chemical Engineering[4]

Virginia Polytechnic Institute and State University

This paper describes an ongoing effort towards extending the capabilities of the fused deposition modeling (FDM) process to soft thermoplastic elastomers (STPEs). Two thermoplastic elastomers with hardness of 72 and 78 Shore A, respectively, have been processed into 0.070" (1.78 mm) filament stock for use in the FDM 1600 rapid prototyping system. The FDM 1600 liquifier subsystem has been modified to accommodate the reduced column strength of the STPE filament stock. Sample STPE parts have been fabricated with ABS material support structures.

1.0 Introduction

There are a number of applications for layered manufacturing with soft elastomeric materials, however few layered manufacturing systems offer this fabrication capability. The work reported herein arose from the U.S. Air Force need to fabricate custom fit aircrew oxygen masks (CFAOMs). These masks would need to have a stiff and strong member to provide a fixed and firm interface to hardware, and a soft member to provide a seal against the unique geometry of each person's face. One potential solution towards this end would therefore be to fabricate these soft members using existing FDM rapid prototyping systems loaded with 65-85 Shore A thermoplastic elastomer filament materials.

A theoretical feasibility study by the University of Texas at Austin [1] concluded that the weak column strength and high melt viscosity of STPE filament materials relative to other FDM filament materials would be the major obstacles to using STPEs with existing FDM ram extruder systems (Figure 1). The higher melt viscosity increases the force required to ram the filament through the liquifier, while the weaker column strength reduces the available ramming force provided by the filament. A number of recommendation were made to overcome these problems. First, it was recommended that sleeve be extended to prevent filament buckling between the drive wheels and the liquifier. Second, it was recommended that the drive wheels be modified to increase their friction with the filament, thereby maximizing the force transferred to the material in the liquifier. Finally, it was recommended that the filament be cooled to make it

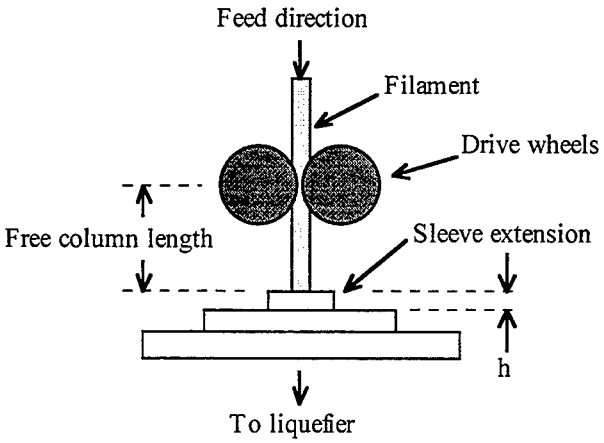


Figure 1 : Diagram of filament loading

stiffer, thereby both preventing it from buckling and enabling it to exert more force into the liquifier.

This paper describes the subsequent effort at Virginia Tech to implement these recommendations on an existing FDM 1600 rapid prototyping system. The following sections discuss the materials selection, the hardware modifications, and the fabrication results.

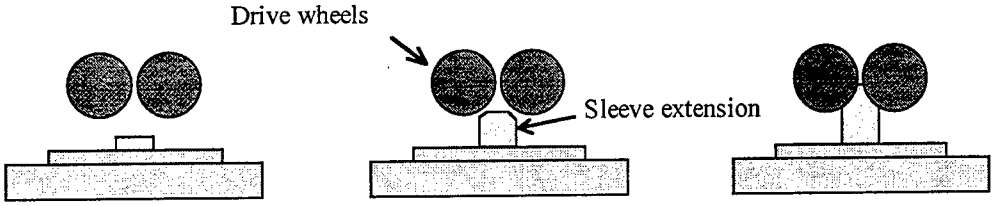
2.0 Materials Selection

The FDM 1600 ram extruder places a number of restrictions on candidate materials with respect to melt processibility and compressive strength. For instance, while most commercial thermoplastics are processed by mechanically inducing shear to help, or make, the thermoplastic flow, the FDM 1600 ram extruder generates minimal or no shear. Candidate materials must therefore be melt processible; that is, they must have the ability to flow with only the addition of heat. Furthermore, since unmelted filament is used as the ramming piston in the FDM 1600 liquifier, it is essential that candidate filament materials have enough compressive strength to push the molten thermoplastic through the liquefier. Specifically, sufficient compressive strength is required for the filament to retain its shape after being forced through the drive wheels so it can transfer the force provided by these wheels forward into the liquifier.

Two soft thermoplastic elastomers that satisfy these requirements and that can be processes by the FDM 1600 ram extruder, have been identified. These two STPEs, which have a respective hardness of approximately 78 and 72 Shore A, will be referred to in this paper as "STPE-1" and "STPE-2".

3.0 Hardware Modifications

In order for material to be extruded by the FDM 1600, the force that is generated by the motors must be transferred to the filament via the wheels and then into the liquifier (Figure 1). This transfer of force can be inhibited by a number of factors. First, the motors must generate



(a) Original sleeve (b) First sleeve redesign (c) Final sleeve redesign; contoured to the wheels

Figure 2 : Sleeve modifications

sufficient force. Next, the wheels must have enough friction with the filament to transfer the force from the wheels to the filament. At the same time, the filament must be strong enough to avoid shearing due to the friction from the wheels. Finally, the filament must not buckle between the drive wheels and the entrance to the liquifier. That is, the force transferred from the drive wheels to the filament should be efficiently transferred into the center of the liquifier in the direction of the melt flow, with minimal loss to filament buckling and compression.

The following sections will discuss the hardware modifications that were made to the existing FDM 1600 ram extruder system to facilitate this efficient transfer of force. They include extending the liquifier sleeve, increasing the friction between the drive wheels and the filament, and the use of air cooling to prevent softening the filament.

3.1 Sleeve Extension

One of the main challanges to extruding a soft filament through the FDM 1600 ram extruder system is its low column strength. The driving force supplied by the motors is greater than these soft materials can support. Consequently, these soft filaments buckle across the free column length in the FDM 1600 system; that is, between the drive wheels and the filament sleeve extension shown in Figure 1.

Since the maximum force that can be transferred by a filament without bucking is inversely proportional to the square of the free column length, an obvious solution to this buckling problem is to reduce the free column length by extending the sleeve up towards the drive wheels (Figure 2). In our first redesign iteration, the sleeve extension height was increased from 0.050" (1.27 mm) to 0.237" (6.02 mm), illustrated in Figures 2(a) and 2(b), respectively. This modification prevented the soft filaments from buckling. However, now the filament material squeezed out through the small triangle formed by the two drive wheels and the flat tipped sleeve. To prevent this leakage, the sleeve was extended further upwards and was contoured to the drive wheels as shown in Figure 2(c), for a maximum sleeve extension height of 0.350" (8.89 mm). This effectively closed the entire gap between the drive wheels and the sleeve extension, leaving only an approximately 0.030" (0.76 mm) gap between the wheels and the curved sides of the sleeve, in addition to the small space provided by the narrow filament guiding

Table 1 : Candidate drive wheel descriptions

Wheel Type	Description
Hard	A pair of hard epoxy wheels, typically used with the ABS filaments
Soft	A pair soft rubbery wheels, also available on the FDM1600
Coarse Gear	Two gears : 32 Pitch, 3/16" Face, 1/4" Bore, 15 teeth, Pitch Dia. = 0.469", Outer Dia = 0.531"
Fine Gear	Two gears : 72 Pitch, 3/16" Face, 1/4" Bore, 36 Teeth, Pitch Dia. = 0.500", Outer Dia. = 0.528"
Sandpaper	One 'soft' wheel and one wheel covered with a coarse grit sandpaper

groove which is carved into the drive wheels. Indeed, this latter redesign has proved itself sufficient for FDM fabrication with our two target STPEs.

3.2 Drive Wheels

The force required to extrude the filament through the liquifier is supplied by two counter-rotating drive wheels as shown in Figure 1. The drive wheels are circumferentially grooved to fit around the filament diameter, in order to properly guide the filament towards the liquifier. The filament is fed through the wheels which contact the filament on both sides. All of the driving force is transferred by the frictional force along the filament as it comes into contact with the wheels. The driving force transferred to the filament is dependent on the coefficient of friction between the wheels and the filament, and on the normal force exerted by the wheels on the filament. It is important that the wheels are positioned close enough together to provide sufficient normal force on the filament, and that a suitable drive wheel surface is selected to maximize the coefficient of friction between the wheels and the filament.

A number of different drive wheels surfaces (Table 1) were tested experimentally with several different STPE filament materials. For this a special purpose test apparatus was built that measured the force exerted by the filament on the liquifier, as the filament is driven forward by the FDM drive motors and wheels. The apparatus consists of a 10 lbs maximum load cell, a bridge amplifier, a voltage meter, and a test rig holding the FDM drive motors and wheels and the load cell (Figure 3). The entire system is rated to 13.3 lbs (52.2 N) of force with better than 0.001 lbs (0.044 N) accuracy, though only 0.05 lbs (0.22 N) accuracy is required. The base plate and motor block assembly were mounted such that the SM-10 Interface load cell could be located at the point equivalent to just inside the liquifier. Its precise location could be adjusted with a bolt mounted in the load cell arm, and which would be raised until it almost touched the exit hole

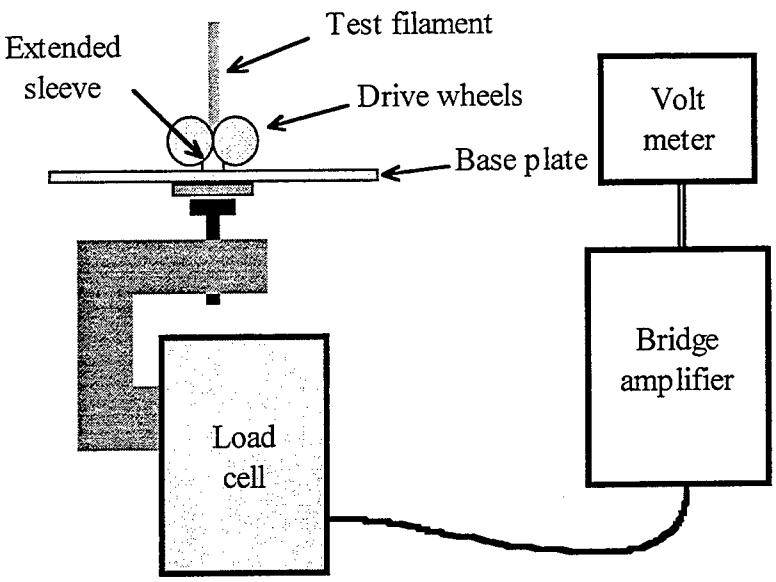


Figure 3 : Force test apparatus

that would mate with the entry hole of the liquifier. This setup would allow the filament to fed through the wheels and the sleeve, and dead end onto the load cell in place of the liquifier. The load cell was then attached to a Gould Brush bridge amplifier. The output from the load cell was calibrated to 0.001 lbs (0.044 N) accuracy, using the bridge amplifier and a set of 1 and 2 lbs (0.4536 and 0.9072 kg) weights. The output from the bridge amplifier was read using a Sperry DM-2A voltmeter.

Each of the five wheel types were tested on the force test apparatus with six different filaments (Table 2). Five measurements were taken for each wheel/filament combination. The forces recorded were the maximum axial forces measured by the load cell. These forces represent an upper limit on the available force for extrusion through the liquifier.

The results listed in Table 2 confirm that decreasing material hardness reduces the force exerted into the liquifier. It also shows that for these particular drive wheel surfaces, the rubber wheels produced in general the greatest amount of driving force for the soft filament materials.

3.3 Cooling

It had been suggested [1] that the filament be cooled using a thermoelectric cooler (TEC) to significantly increase the filament column strength, thereby both preventing filament buckling and increasing the force exerted by the filament into the liquifier. However, for most STPEs, a TEC system would be insufficient since their T_g's are in the proximity of, or below, what can be achieved with liquid nitrogen -77°C (-107 °F). Cooling a STPE filament to above T_g will only marginally increase its column strength. We verified this by bathing a STPE filament in liquid nitrogen; it displayed only a slight increase in stiffness compared to that at room temperature.

Table 2 : Force measurements for wheels and filaments
Values given as : Average maximum force in pound (standard deviation in pounds)

Wheel Type	Santoprene 80 Shore A	Sarlink 69 Shore A	Multibase 57 Shore A	"STPE-1" 78 Shore A	"STPE-2" 72 Shore A	ABS
Epoxy Wheels	1.32 (0.356)	1.04 (0.055)	0.52 (0.045)	1.84 (0.297)	0.98 (0.045)	12.92 (0.531)
Rubber Wheels	1.64 (0.055)	1.1 (0.071)	0.46 (0.055)	2.08 (0.303)	1.22 (0.130)	2.35 (0.147)
Fine Gears	1.04 (0.055)	1.04 (0.055)	0.44 (0.055)	1.2 (0.200)	1.22 (0.259)	TL
Coarse Gears	1.3 (0.071)	1 (0.071)	0.38 (0.045)	1.64 (0.114)	1.1 (0.000)	TL
Sandpaper Wheel	1.34 (0.055)	0.94 (0.055)	0.42 (0.045)	1.66 (0.055)	0.94 (0.089)	13.22 (0.179)

Note: TL -- Torque Limit. In these two cases the ABS filament was crushed between the two gears until the motors were stopped by the torque limit function of the FDM 1600. A larger gap between the gears would be required in order to use them for the ABS filaments.

Limited cooling, however, does help the filament maintain its room temperature column strength as it approaches the liquifier. For instance, "STPE-2" has a softening point of 41 °C (106 °F) while the liquifier has a processing temperature of 230 °C (446 °F). As the filament approaches the liquifier, it heats up and quickly becomes too soft to act as a ram piston. The solution to this problem is to use the air conditioner attached to the standard FDM 1600. With it we have been able to cool the area around the motor blocks and drive wheels sufficiently to keep the filament from loosing its column strength as it approaches the extruder inlet.

4.0 FDM with Soft Elastomers

The FDM 1600 ram extruder system requires only a few minor modifications for it to fabricate with filament stock made from our two target STPEs. These modifications include extending the sleeve, contoured around the drive wheels; utilizing rubber drive wheels; and, in the case of "STPE-1", widening the die diameter to a 0.037" (0.94 mm).

The low force exerted by the "STPE-1" filament into the liquifier and the relative high viscosity of its elastomers necessitated widening of the die. The standard 0.025" (0.64 mm) die provided too much resistance. However, widening this die to 0.037" (0.94 mm) reduced the pressure drop sufficiently to enable extrusion. It is estimated that the minimum die diameter for "STPE-1" and the current wheel-sleeve-material combination is in the range of 0.032" to 0.035" (0.81 mm to 0.89 mm). This is still relatively wide compared to other FDM materials and would inhibit fabrication of smooth, non-horizontal surfaces and delicate part features. "STPE-1" is therefore ill suited for use in small-volume FDM systems. On the other hand, it might be acceptable for use in large-volume systems; in these systems, its limited deposition resolution might be of less consequence, and thus it be considered adequate.

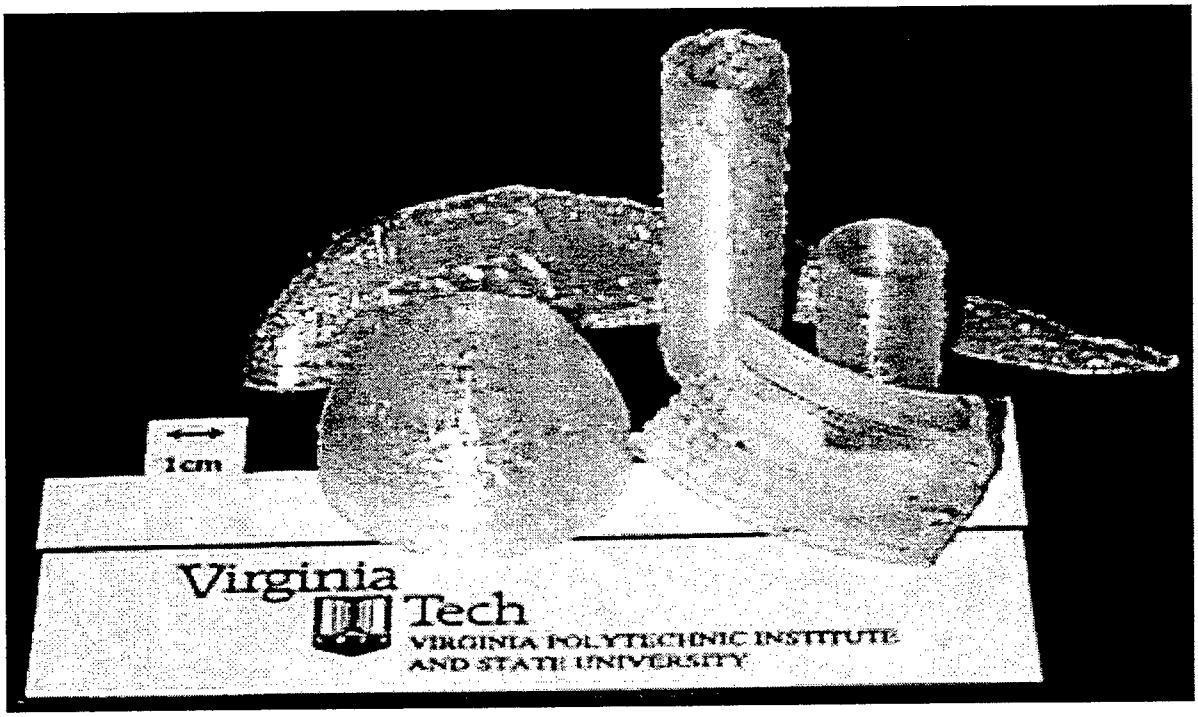


Figure 4 : Very first batch of sample parts fabricated with "STPE-2" on a modified FDM 1600 rapid prototyping system (0.010" layers, 0.030" roads, 0.037" die, 0.8"/sec head-speed) (0.25 mm layers, 0.76 mm roads, 0.94 mm die, 20 mm/sec head-speed)

Extrusion with the "STPE-2" filaments was actually less problematic, even though it is softer than "STPE-1" and has an order of magnitude lower melt flow index. For "STPE-2", the filaments extruded through the standard 0.012" (0.31 mm) die This enabled fabrication with 0.010" (0.25 mm) layer thicknesses, 0.012" (0.30 mm) road widths, and 0.8"/sec (20 mm/sec) head motion in the XY-plane. These are values are comparable to those of the ABS modeling material that is available for the FDM 1600.

The relatively high processing-temperature of "STPE-2", about 230 °C (446 °F), made it temperature-compatible with the standard FDM ABS support material. These two materials also bond reasonably well together, which enables the use of this ABS material for fabricating support structures. Several sample parts have been fabricated with this material combination, using both the 0.037" (0.94 mm) die (Figure 4) and the 0.012" (0.30 mm) die (Figure 5). The removal of these support structures appeared to be quicker, cleaner and easier than for those of other FDM build materials, in part because the elastomeric model material can flex while being peeled off the stiffer ABS plastic support structures.

The "STPE-1" model material did not bond well to the standard FDM ABS support material. Therefore, until a better support material is formulated, it will not be possible to fabricate parts with "STPE-1" that require secondary material support structures.

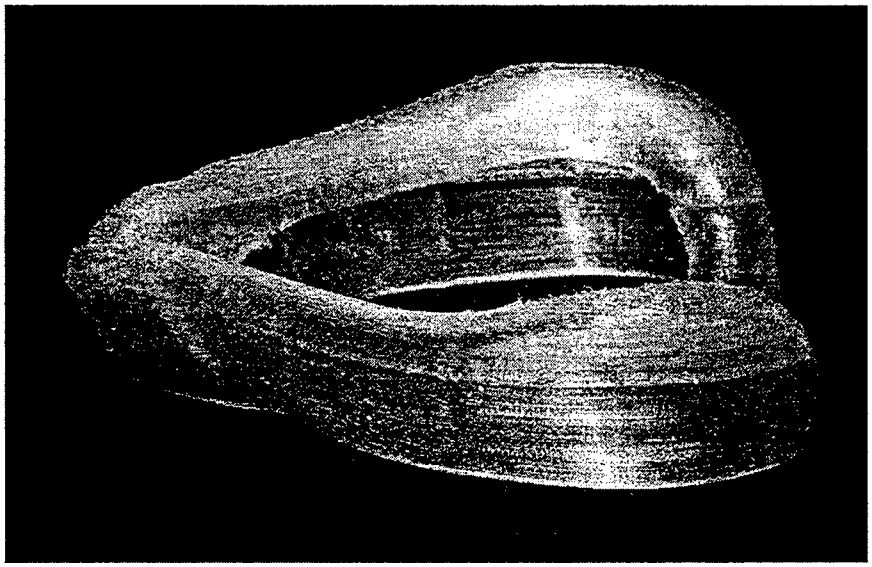


Figure 5 : The seal of custom fit aircrew oxygen mask, fabricated directly with FDM 1600 using "STPE-2"

5.0 Conclusions

The FDM 1600 rapid prototyping system has sucessfully been modified to facilitate direct fabrication of soft thermoplastic elastomer parts. The materials have hardnesses of approximately 72 and 78 Shore A, respectively. The hardware modifications that were necessary include (1) extending the liquifier sleeve up to and around the drive wheels; (2) using rubber coated drive wheels; and (3) widening the standard die to 0.037" (0.94 mm) in the case of the "STPE-1" material. "STPE-2" was the easier of the two materials to work with. Several sample parts were fabricated, using the standard FDM ABS support material for support structures. The support structures were quicker, cleaner and easier to remove than those for other FDM build materials.

Acknowledgments

This research was supported by Armstrong Laboratory, Brooks AFB and the Naval Surface Warfare Center, Dahlgren Division under contract N60921-89-D-A239, Order 0059. Any opinions, findings, conclusions, or recommendations expressed in this paper are those of the authors and do not necessarily reflect the views of Armstrong Laboratory, Brooks AFB or the Naval Surface Warfare Center, Dahlgren Division. The authors would also like to thank Mr. Larson of Stratasys; Maj. Diesel and Mr. White of Armstrong Laboratory; and Drs. Kander, Furey, Eiss, Hendricks, Clark, and Davis of Virginia Tech, for their technical assistance.

References

[1] D. Cidon, J. Bohling, and J. Brostrom, "Fused Deposition Modeling using Soft Elastomeric Materials," Department of Mechanical Engineering, The University of Texas at Austin, Summer 1996.

Effects of Processing Conditions on Prototypes Reinforced with TLCPs for Fused Deposition Modeling

R. W. Gray IV, D. G. Baird, and J. H. Bøhn

Department of Chemical Engineering,

Department of Mechanical Engineering,

Rapid Prototyping Laboratory, and

Polymer Materials and Interfaces Laboratory

Virginia Polytechnic Institute and State University

Polypropylene (PP) composite strands, reinforced with thermotropic liquid crystalline polymers (TLCPs), were generated using a novel dual extrusion process which allowed for the use of a TLCP with a significantly higher melting temperature than that of the PP. Pregenerated TLCP/PP microcomposite strands were reprocessed using a second novel process to produce a well-controlled monofilament composite for use in a FDM 1600 rapid prototyping system in order to build complex geometries. Uniaxial parts were built to determine the effect of differing material compositions and processing temperatures, in order to develop an operating window for the optimal mechanical properties. By adjusting the lay down pattern of orientable materials, the final mechanical properties of the part could be engineered independent of the material. To understand the effect of the reprocessing steps on the pregenerated microcomposites, the final mechanical properties of the monofilament composite were compared with those of the pregenerated strands.

1.0 Introduction

At present, only a few polymeric materials with limited mechanical properties are used in fused deposition modeling (FDM) rapid prototyping systems. Many of the prototypes fabricated can only serve as geometric replicas of the proposed production part because of the inherently poor mechanical properties. The materials that are commercially available for the FDM 1600 rapid prototyping system are acrylonitrile butadiene styrene copolymer (ABS), a nylon copolymer, and investment casting wax. Of the three commercially available materials, ABS has the highest tensile modulus and strength, and the properties of prototypes fabricated using ABS have been determined to be 1.5 GPa and 22 MPa, respectively [1]. Therefore, there is interest in developing materials that can be used to fabricate prototypes with higher mechanical properties which give the parts greater functionality.

Thermotropic liquid crystalline polymers (TLCPs) are a novel class of materials that have potential for use in FDM applications for several reasons. First, it has been shown that TLCPs have excellent tensile properties with moduli ranging from 50 GPa to 100 GPa for neat fibers. It has also been shown that due to their excellent tensile

properties and due to their fibril forming nature, TLCPs have been used to reinforce thermoplastics [2 - 4]. The diameter of the reinforcing TLCP fibrils are typically one order of magnitude smaller compared to typical glass and carbon fiber. However, it may be not possible to extrude glass and carbon fibers through the die head and still maintain high aspect ratio fiber (i. e. L/D > 100) due to the small diameter capillary die used in order to fabricate dimensionally precise prototypes.

The final mechanical properties of TLCP based composites, where the reinforcing fibrilar morphology is developed during the processing step on an in situ basis, are directly dependent upon the processing conditions [4 - 7]. Shear and extensional flow fields during processing serve to deform dispersed TLCP droplets into reinforcing fibrils and impart molecular orientation to the fibril, which results in increased tensile properties in the direction of the flow field. This preferred orientation, of both the molecules and the fibrils, results in anisotropic mechanical properties. It is generally known that extensional flow fields develop higher aspect ratio fibrils and greater molecular orientation, and hence extensional flow yields higher tensile properties than strong shear flow. For example, 20 wt% Vectra A, a commercial TLCP marketed and sold by Hoechst Celanese, was used to reinforce polypropylene (PP), and composites that were generated via fiber spinning and injection molding had tensile moduli of 9.6 GPa and 2.6 GPa, respectively [5, 8, 9]. Therefore, in order to obtain the optimal reinforcement, strong extensional forces, such as those present in fiber spinning, are necessary. The purpose of this work is to fabricate TLCP reinforced composite prototypes in such a fashion as to capitalize on the full potential of the reinforcement.

2.0 Experimental

2.1 Materials

The TLCP used was Vectra A950 (Hoechst Celanese). It is a random copolyester based on hydrobenzoic acid (73% mole) and 2-hydroxy-6-napthoic acid (27% mole). It has a glass transition temperature of 108°C and a melting point of 283°C [10]. However, Vectra A needs to be heated to 320°C to melt out all of the residual crystallites [11]. The matrix material used was the 4018 grade of Amoco polypropylene (PP). It has a melting point of 160°C and a melt flow index (MF) of 13.5 [12].

2.2 Spinning of TLCP/PP Composite Strands

A novel dual extrusion process was used to blend the TLCP and PP forming a self reinforced composite fiber in order to obtain optimal mechanical properties in the composite [13 - 15]. In this extrusion process, the thermoplastic and TLCP are plasticated in separate extruders so that independent thermal histories are imposed to the two materials. TLCP is heated to sufficiently high temperatures to fully melt all of the crystallites. For example, the melting point of Vectra A is 283°C, but it needs to be heated to 320°C in order to fully melt all the residual crystallites [11]. Vectra A is then supercooled to the temperature at which the matrix is processed, and using a multiple-port injection nozzle is then injected into the matrix stream which results in continuous TLCP

streams encapsulated within the matrix. The melt is passed through a series of static mixers which serve to divide the TLCP streams, before being extruded through a capillary die and drawn in the spinline to high draw ratios in order to achieve high levels of molecular orientation in the TLCP fibrils.

There are several advantages of the dual extrusion process over generating TLCP fibrils in situ during FDM. Processing the TLCP in a separate extruder minimizes degradation of the matrix because the matrix is not exposed to the high temperatures that are necessary to fully melt the TLCP. The TLCP is supercooled before being injected into the matrix minimizing the degradation of the matrix. The dual extrusion process does not rely on droplet deformation because the multiple-port injection nozzle introduces continuous TLCP streams into the matrix, resulting in high aspect ratio fibrils. Finally, the composite strands can be post-processed above the melting point of the matrix and below the melting point of the TLCP using a variety of conventional processing techniques (e. g. FDM) which allow for the retention of the TLCP reinforcing fibrils generated during the dual extrusion process in the final part [1, 8, 9, 14 - 23].

3.0 Discussion and Results

3.1 Novel Process for Generation of Composite Feed Stock for FDM

In order to develop new materials for use in the FDM 1600 rapid prototyping system that could be used to fabricate prototypes with greater mechanical properties and greater functionality than those presently available, self-reinforced thermoplastic composite strands were generated using a novel dual extrusion process. Vectra A, a TLCP know for its exceptional mechanical properties, was used as the reinforcing phase, and PP served as the matrix. Vectra A/PP strands were spun with 20 wt% and 40 wt% TLCP concentrations, and the moduli of the strands were 9.55 GPa and 22.8 GPa, respectively. Further results concerning the properties of these strands are given elsewhere [8, 9].

Strands from the dual extrusion process were then post-processed to form monofilaments with a well controlled diameter for use in the FDM 1600 rapid prototyping system. In this process, the continuous TLCP reinforcement was granulated into short TLCP fibrils having lengths less than 6 mm and diameters ranging from 1 to 5 μm. The tensile moduli of the 20 wt% and 40 wt% monofilaments were 1.9 GPa and 2.2 GPa, respectively, and the strengths were 25.6 MPa and 21.1 MPa, respectively. The properties compare favorable to those of pure PP where the tensile modulus and strength are 0.98 GPa and 23.2 MPa, respectively [15]. The Vectra A reinforcement resulted in an increase in modulus of approximately 100% over those neat PP, while having similar strengths. The tensile properties of the monofilaments were significantly lower than those of the strands from the dual extrusion process. Previous work has shown that these lower properties were probably due to a reduction in aspect ratio, poor fibril distribution, and poor fibril alignment [20 - 22].

3.2 Plaque Fabrication via FDM

Vectra A/PP monofilaments were used as feed stock to fabricate plaques via FDM, and the effects of fabrication temperature on the tensile properties of the final part were examined. Monofilaments with 20 wt% and 40 wt% Vectra A were used to build parts with a lay-down pattern aligned uniaxially in the machine direction. In Figure 1, the tensile modulus is shown as a function of fabrication temperature for both the 20 wt% and 40 wt% Vectra A composite parts. Plaques with 20 wt% Vectra A reinforcement were fabricated at processing temperatures of 190°C, 240°C, and 290°C. The moduli of these plaques were essentially independent of processing temperatures and were approximately 1.6 GPa, even above the melting point of the reinforcement. The 40 wt% Vectra A monofilaments were processed at 240°C and 290°C, and the moduli of the plaques were 2.7 GPa and 2.4 GPa, respectively. Thus, the moduli of the fabricated plaques decreased somewhat when processed above the melting point of the reinforcement. Parts were not fabricated at 190°C because the FDM 1600 rapid prototyping system was unable to generate the pressure required to extrude the composite.

In Figure 2, the tensile strength is shown as a function of fabrication temperature. The strengths of both the 20 wt% and 40 wt% Vectra A reinforced plaques decreased by approximately one third when processed at 290°C as compared to the strengths of the plaques when processed below the melting point of Vectra A. The strength of the 20 wt% Vectra A plaques decreased from approximately 33 MPa when fabricated below the melting point of the Vectra A to 21 MPa when fabricated above the melting point. Similarly, the strength of the 40 wt% Vectra A plaques decreased from 37 MPa when post-processed at 240°C to 25 MPa when extruded above the melting point of the TLCP. When processed below the melting point of Vectra A, the composite relies on the reinforcement generated in the dual extrusion process. However, when Vectra A/PP composites are processed above the melting point of the TLCP, the reinforcing fibrils are melted and orientation is lost within the TLCP phase. In the melt state, the fibrils form into droplets, and there are minimal extensional forces present in the FDM 1600 rapid prototyping system to develop the fibrilar morphology required for the optimal tensile properties. Thus, tensile properties of Vectra/PP prototypes, where reinforcement was generated in the dual extrusion process, were somewhat better than those where the reinforcement was generated during prototype fabrication.

The mechanical properties of the Vectra A/PP monofilament feed stock were compared to those of the plaques fabricated via the FDM 1600 rapid prototyping system. The modulus of the 40 wt% Vectra A monofilament was measured to be 2.2 GPa. Plaques fabricated uniaxially in the machine direction at 240°C had a modulus of 2.7 GPa. Similarly, the strength of the composite increased from 21 MPa to 37 MPa in the fabricated plaque. The modulus of the 20 wt% Vectra A monofilaments and plaques was similar before and after fabrication and was approximately 1.8 GPa. The strength of the 20 wt% Vectra A monofilaments increased from 26 MPa to 33 MPa after being fabricated into a plaque. The increase in mechanical properties of the 40 wt% Vectra A composite was probably due to a change in alignment of the reinforcing fibrils as a result of the flow

kinematics of the FDM 1600 extruder. It has been shown elsewhere that the tensile properties of post-processed long fiber composite strands are very sensitive to the flow kinematics of the die [8, 9]. It was shown that a critical L/D was necessary in order to obtain the optimal mechanical properties and that the extrusion rate, and die diameter can effect the tensile properties of the extrudate. Vectra A/PP (28/72 wt%) composite strands from the dual extrusion process were post-processed into monofilaments, and the maximum tensile modulus and strength were 4.0 GPa and 45 MPa. Thus, higher properties can be obtained with lower Vectra A concentrations under the proper post-processing conditions [8, 9].

Plaques were fabricated from composite monofilaments using three different lay-down patterns: uniaxial in the machine direction, uniaxial in the transverse direction, and a 0-90 lay-down pattern. The plaques were fabricated from the Vectra A/PP (40/60 wt%) composite monofilaments at 240°C which was the processing temperature that resulted in the greatest tensile properties for plaques fabricated uniaxially in the machine direction. In Figure 3, the mechanical properties are shown as a function of lay-down pattern. The abscissa is defined as the volume percent of material laid in the machine direction. Thus, plaques fabricated entirely in the transverse direction had 0 vol% laid in the machine direction, and parts with 0-90 lay-down patterns had 50 vol% laid in the machine direction, and parts built uniaxially in the machine direction had 100 vol% of the material laid in the machine direction. It is shown that both the tensile modulus and strength increased monotonically with the volume percent laid-down in the machine direction. For parts fabricated uniaxially in the transverse direction and parts fabricated uniaxially in the machine direction, the modulus increased from 1.3 GPa to 2.7 GPa, and the strength increased from 10 MPa to 37 MPa. This dependence of mechanical properties on the lay-down pattern was due to anisotropic reinforcement of the matrix by the TLCP fibrils as was observed in Figure 4, and this reinforcement was aligned in the direction in which the roads were laid. This was why the greatest mechanical properties were observed in the plaques fabricated uniaxially in the machine direction. Plaques fabricated uniaxially in the transverse direction had the lowest properties because the reinforcement was aligned orthogonal to the machine direction. Thus, the bulk properties of these plaques were highly dependent on the tensile properties of the matrix. Also, the mechanical properties of a part built in the transverse direction were probably somewhat lower due to weld lines perpendicular to the machine direction. As predicted by composite theory, there was a monotonic increase in mechanical properties with increasing volume fraction laid-down in the machine direction [24]. Therefore, using composite theory, the mechanical properties of the final part can be engineered to match the requirements of the proposed prototype by adjusting the lay-down pattern.

4.0 Conclusions

Plaques were fabricated from Vectra A/PP composites and neat Vectra A monofilaments via FDM. The tensile modulus of Vectra A/PP (40/60 wt%) composite plaques were approximately 100% greater than those of ABS prototypes and

approximately 150% greater than those of pure PP, and these properties could probably be increased if long fiber reinforced composite monofilaments were used as feed stock.

Due to the anisotropic mechanical properties present in TLCPs and TLCP composites, the lay-down pattern affected the properties of the final part. It was found that the tensile properties of Vectra A/PP composites increased monotonically with roads laid in the machine direction. Thus, the final mechanical properties of a prototype can be tailored to a specific application by adjusting the lay-down pattern, increasing the functionality of the prototype.

5.0 Acknowledgments

The authors would like to gratefully recognize the support from the Army Research Office (Grant No. DAAH04-94-G-0282), the Naval Surface Warfare Center, Dahlgren Division and Armstrong Laboratory, Brooks AFB under contract N60921-89-DA239, Order 0059, and Stratasys, Inc. Also, the authors would like to thank Prof. G. L. Wilkes for the use of the SEM and M. A. McLeod for operating it.

1 R. W. Gray IV, D. G. Baird, J. H. Bøhn, *Rap. Proto. J.*, in preparation (1997).
2 A. I. Isayev, in Liquid-Crystalline Polymer Systems Technological Advances, ed. A. I. Isayev, T. Kyu, and S. Z. D. Cheng, American Chemical Society, Washington D. C. 1996.
3 D. G. Baird, in Polymeric Materials Encyclopedia, ed. J. C. Salamone, CRC Press, Boca Raton 1996.
4 A. A. Handlos and D. G. Baird, *J. Macromol. Sci.-Rev. in Macromol. Chem. and Phy.*, C35, 183 (1995).
5 K. G. Blizard and D. G. Baird, *Polym. Eng. and Sci.*, 27, 653 (1987).
6 G. G. Viola, D. G. Baird, and G. L. Wilkes, *Polym. Eng. and Sci.*, 25, 888 (1985).
7 A. Kohli, N. Chung, and R. A. Weiss, *Polym. Eng. and Sci.*, 29, 573 (1985).
8 R. W. Gray IV, M. S. Thesis, Virginia Polytechnic Institute and State University (1997).
9 R. W. Gray IV, D. G. Baird, and J. H. Bøhn, *Polym. Comp.*, in preparation (1997).
10 M. Y. Cao and B. Wunderlich, *J. Polym. Sci.: Polym. Phy. Ed.*, 23, 521 (1985).
11 S. M. Guskey and H. H. Winter, *J. Rheol.*, 35, 1191 (1991).
12 Amoco Polypropylene Homopolymers Bulletin PP-8n, Amoco Polymers, Inc. (1996).
13 D. G. Baird and A. Sukhadia, U.S. Patent 5,225,488 (1993).
14 E. A. Sabol, M. S. Thesis, Virginia Polytechnic Institute and State University (1994).
15 E. A. Sabol, A. A. Handlos, and D. G. Baird, *Polym. Comp.*, 16, 330 (1995).
16 C. R. Robertson, M. S. Thesis, Virginia Polytechnic Institute and State University (1995).
17 C. G. Robertson and D. G. Baird, *Intern. Polym. Proc.*, in press (1996).
18 R. K. Krishnaswamy and D.G. Baird, *Polym. Comp.*, in press (1997).
19 C. G. Robertson, J. P. de Souza, and D. G. Baird, Recent Advances in Liquid Crystalline Polymers, A. I. Isayev, T. Kyu, and S. Z. D. Cheng eds., ACS Books, Washington D. C. (1996).
20 A. A. Handlos and D. G. Baird, *Intern. Polym. Proc.*, XI, 82 (1996).
21 A. A. Handlos and D. G. Baird, *Polym. Comp.*, 17, 73 (1996).
22 A. A. Handlos and D. G. Baird, *Polym. Eng. and Sci.*, 36, 378 (1996).
23 R. K. Krishnaswamy, J. Xue, and D. G. Baird, *SAMPE J.*, in preparation (1997).
24 J. C. Halpin, *Polym. Eng. and Sci.*, 16, 344 (1976).

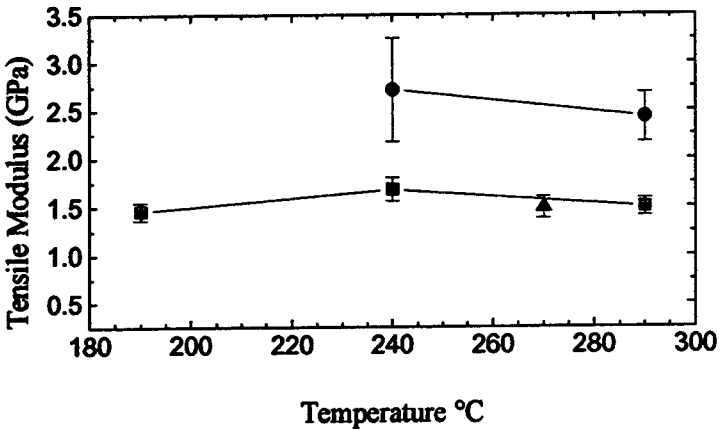


Figure 1 : Tensile modulus of Vectra A/PP (20/80 wt%) (—●—) and (40/60 wt%) (—■—) and ABS (—▲—) plaques built uniaxially in the machine direction as a function fabrication temperature.

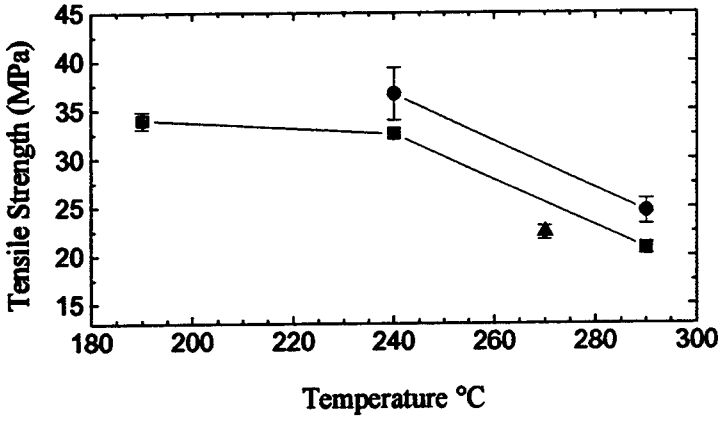


Figure 2 : Tensile strength of Vectra A/PP (20/80 wt%) (—●—) and (40/60 wt%) (—■—) and ABS (—▲—) plaques built uniaxially in the machine direction as a function fabrication temperature.

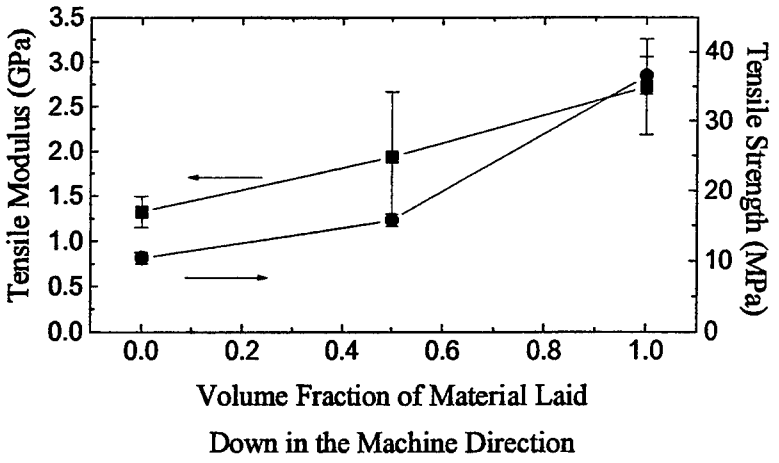


Figure 3: Tensile modulus (—■—) and strength (—●—) of Vectra A/PP (40/60 wt %) composite plaques fabricated via FDM as a function of volume fraction laid in the machine direction processed at 240°C.



Figure 4 : Micrographs of the cross-section of Vectra A/PP (40/60 wt%) composite prototypes fabricated via FDM at 240°C.

Issues Associated with EFF & FDM Ceramic Filled Feedstock Formulation

John L. Lombardi, Robert A. Hoffman, Jason A. Waters, Dragan Popovich
Advanced Ceramics Research, Inc., Tucson, AZ 85713
Chad Souvignier, Sajiv Boggavarapu University of Arizona, Arizona Materials Laboratories, Tucson, AZ 85712

INTRODUCTION

Fused deposition modeling (FDM) and Extrusion Freeforming (EFF) of ceramics has recently been the subject of much research and discussion (1) . These techniques have been used to fabricate green ceramic prototype components "from the ground up" by the precise deposition and solidification of successive molten ceramic filled thermoplastic layers upon one another until the final part is completed. Both EFF and FDC methods were variants of the Stratasys Fused Deposition Modeling (FDM) technique but differed from each other in that the latter fabricated parts using flexible, continuous green ceramic filament feedstock extruded by a conventional Stratasys Modeler while the former produced parts from green ceramic feedrods using a Stratasys Modeler retrofitted with a high pressure extrusion head (2,3).

The quality of the FDC and EFF green ceramic feedstocks has a strong influence upon the robustness of these processes and their ability to reproducibly fabricate high strength, dimensionally accurate ceramic components. Some of these qualities include high degree of compositional homogeneity, reproducible rheology, facile binder removability, and capacity to be sintered to a dense ceramic body after debinderization. A high degree of homogeneity is desirable in order to minimize density gradients between the binder and ceramic powders present in the feedstock which could ultimately lead to nonuniform firing shrinkage and defect formation within the freeformed ceramic bodies (4). The feedstock should also possess a reproducible rheology so that it can be accurately freeformed into the desired green ceramic component. Further requirements for the rheology of EFF and FDC compatible feedstock are a low melt viscosity (extrudable at low pressures) as well as the ability to undergo rapid solidification upon deposition (enabling more rapid part build rates). The binder should be easily removable from the freeformed green bodies under controlled conditions and leave minimal pyrolysis residue. Finally, the resulting bodies should be readily sinterable to dense ceramic materials.

These feedstocks have many of the qualities commonly desired in raw materials for ceramic injection molding (5). Consequently, FDC and EFF feedstocks were developed which had formulations similar to those employed by conventional ceramic forming processes. These formulations essentially consisted of high loadings (> 50 volume percent solids) of silicon nitride powder dispersed in an organic binder. The binder was a mixture of polymer, waxes, and plasticizer and served as a vehicle for the freeformed silicon nitride ceramic powder. The wax was an important component in the binder since it lowered the melt viscosity of the binder polymer at elevated temperatures (ca. > 100° C) while simultaneously enabling the green body to rapidly solidify while maintaining its dimensional accuracy after freeforming. A liquid

plasticizer was believed to be an important binder constituent since it lowered the binder melt viscosity. Its lower volatility compared to the wax and polymer enabled a gradual, more controllable removal of binder components prior to sintering the freeformed ceramic bodies (6). The suitability of this binder composition in EFF feedstocks was demonstrated after successfully extrusion freeforming and subsequently pressureless sintering >97% dense, crack free silicon nitride bladed disks ("blisks") using this type of formulation. Figure 1 below depicts both green and pressureless sintered silicon nitride blisks which were fabricated using extrusion freeforming techniques.

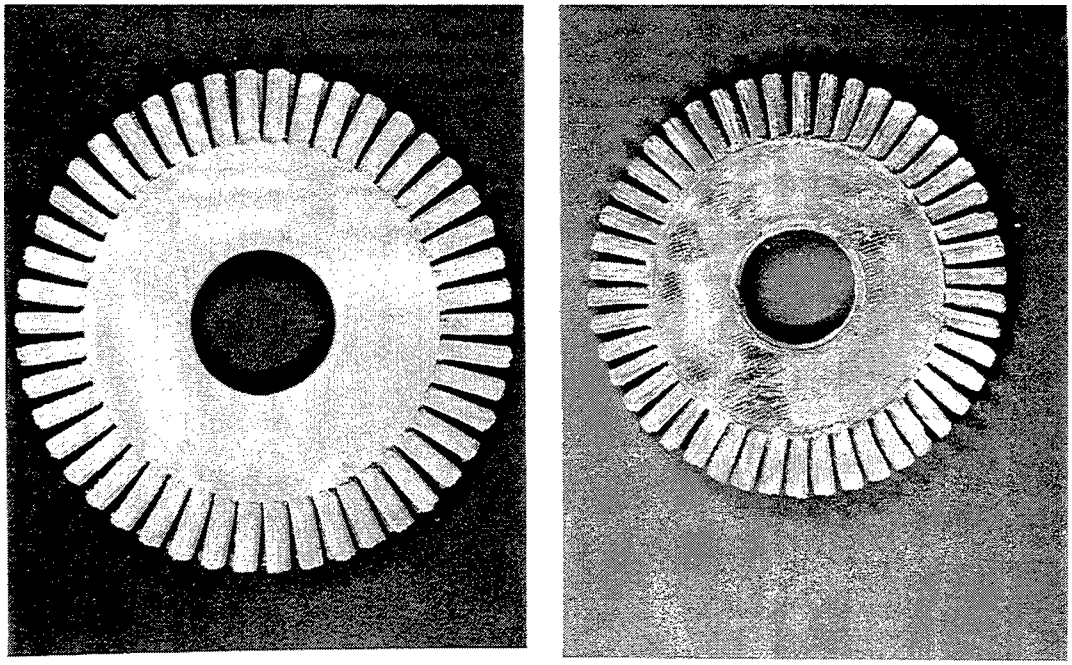


Figure 1. Photograph of green (5.1") and sintered (3.5") silicon nitride bladed disk fabricated using EFF techniques.

Some additional requirements must be met in order to adapt the above EFF silicon nitride feedstock formulation for use in FDC processing. In particular, FDC compatible filaments should also possess sufficient strength and flexibility such that they can be continuously extruded through a conventional Stratasys Modeler without fracturing. Significant FDC filament breakage could lead to dimensional inaccuracies and flaws within the FDC parts. Consequently, the utilization of filament feedstocks possessing reproducible mechanical properties is a key issue in successful FDC part fabrication. Experiments were subsequently conducted in an attempt to identify some of the processing issues associated with adapting the EFF feedstock formulation for use in FDC fabrication techniques.

EXPERIMENTAL

Green ceramic feedstock having a composition similar to that employed during extrusion freeforming of the aforementioned bladed disk (listed in Table I below) was batched using a Brabender Shear Mixer. A separate batch of the feedstock binder was also prepared separately.

TABLE I Green Ceramic Feedstock Composition

Component	Concentration (Volume %)
Silicon Nitride	56.6
Saturated Elastomer	25.4
Paraffin Wax	8.3
Fatty Acid Ester Plasticizer	9.35

All raw materials present in the green ceramic feedstock listed in the above table were obtained from commercial sources. The silicon nitride powder was a pressurelessly sinterable composition containing yttrium and aluminum oxide sintering aids in a 9:3 weight ratio. The saturated elastomer in the binder was an amorphous, noncrystallizable copolymer. Gel permeation chromatography characterization of the paraffin wax binder component was reported to exhibit a weight average molecular weight of 3779 g/mole and a polydispersity index value of 2.5. The fatty acid plasticizer was a liquid under ambient conditions.

After shear mixing, the green ceramic material was extruded into four, two ft. long lengths of ceramic filament measuring 0.070 inches in diameter. EFF feedrods measuring 5/8" in diameter by 6 " in length were pressed from the remainder of the green ceramic material. Filaments were also extruded from the ceramic binder composition and had dimensions similar to those prepared from the green ceramic material. All filaments were aged after extrusion at room temperature in a desiccator for time periods ranging from 15 hours to 86 days.

The degree of crystallinity and maximum melting point of the binder present in both the unfilled and ceramic filled filaments at various stages of filament aging was determined using a DuPont Instruments Model 2100 differential scanning calorimeter (DSC). Differences in the mechanical properties of the binder filament at various stages of aging were also determined using a method proposed by Siemers which measured the minimum radius that the filament could be uniformly bent prior to its fracture (7).

RESULTS

As can be seen from the results presented in Table below, the minimum radius at which the silicon nitride filled filaments were bendable without fracturing increased upon aging. This indicated that the filaments became increasingly brittle upon aging. Even though the moduli (E) of these filaments were not directly measured, trends in filament bending strengths were semiquantitatively compared to each other using a relation expressing bend strength (σ) in terms of filament diameter (z) and minimum bend radius (ρ) (9):

$$\sigma = (E\ z) / \rho$$

In this case the bend strength for a brittle filament is directly proportional to its elastic modulus and inversely proportional to the minimum filament bending radius. These bend strength values are also given in Table II below.

Table II Flexure Properties of Green Ceramic Filament as a Function of Aging

Filament Aging Time After Extrusion	Minimum Filament Bend Radius (in.)	Bend Strength (σ)
1 hr.	1.80	0.039E
15 hr.	1.75	0.04E
20 days	2.50	0.028E
50 days	2.92	0.024E

These results suggested that a change in filament morphology was occurring upon aging. A possible explanation for this could entail recrystallization of the wax present within the filament binder upon standing at room temperature. Attempts were made to measure changes in the crystallinity of various aged silicon nitride filaments using DSC. Unfortunately, this proved difficult since the wax component was present in low concentration within these filaments making an accurate determination of its crystallinity by DSC difficult. Consequently, a separate set of filaments, composed of pure binder, was extruded and characterized at various stages of aging using DSC. The DSC characterization results for these binders is provided in Table III below.

TABLE III DSC Characterization of the Aged Binder

Aging Time	Binder Melting Point (°C)	Sample Crystallinity (%)
15 hr.	91.9	2.5
6 days	92.3	2.7
17 days	101.5	3.0
50 days	101.4	3.8
86 days	101.14	5.8

As can be seen from the above results, both the melting point and crystallinity of the wax component in the binder increased during aging where the former increased to a much more significant extent than the latter. This indicated that the wax present in the filaments was recrystallizing. Large wax crystallites were growing at the expense of the small crystallites which initially formed upon solidification of the extruded filament fabrication. The DSC output presented in Figures 2 & 3 for samples aged for 1 day and 86 days respectively, revealed that the melting endotherm in the latter was sharper than the former. In particular the endotherm for the sample aged for 86 days appeared to be composed of two peaks with one peak having its maximum at 101°C while the other was near 87 °C. This suggested that the wax in the binder was phase separating with time into separate crystals composed of high molecular weight and low molecular weight waxes (10). Since the melting point of a wax crystal varies directly with the molecular weight of its constituents, the presence of the two high and low melting endotherm peaks in the aged sample is readily explicable. Further attempts to resolve these two peaks by annealing the sample at 88 °C for 3 hours proved successful as evidenced from the DSC plot in Figure 4 . These results are not entirely surprising since the wax has a reasonably high polydispersity (PDI) index value of 2.5. Most common paraffin waxes have similar PDI values (some waxes have PDI < 4). Furthermore, segregation of different molecular weight polymer species during solidification of samples having broad molecular weight distributions is well documented in the literature (11, 12).

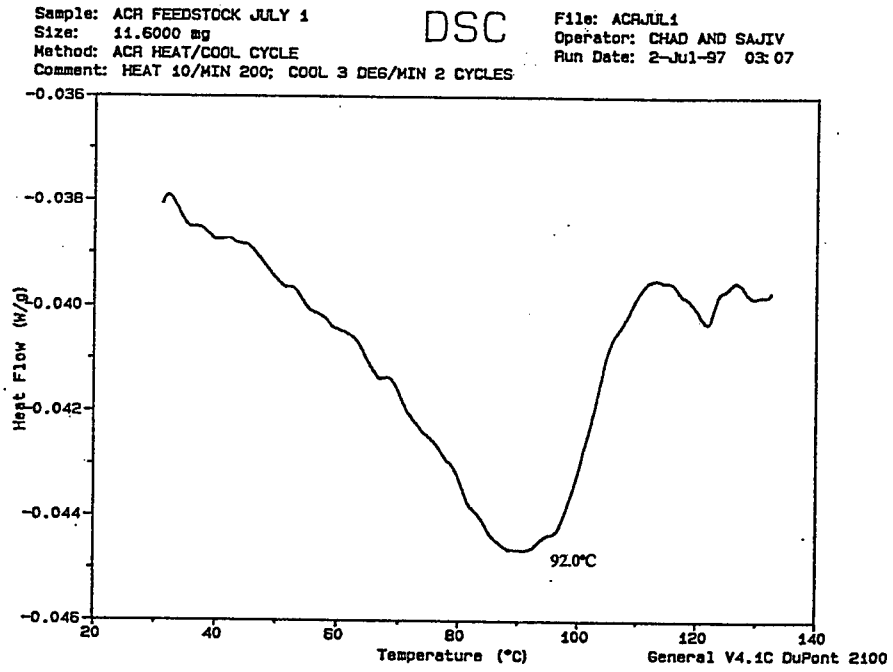


Figure 2. DSC plot for wax based binder filament aged for 1 day.

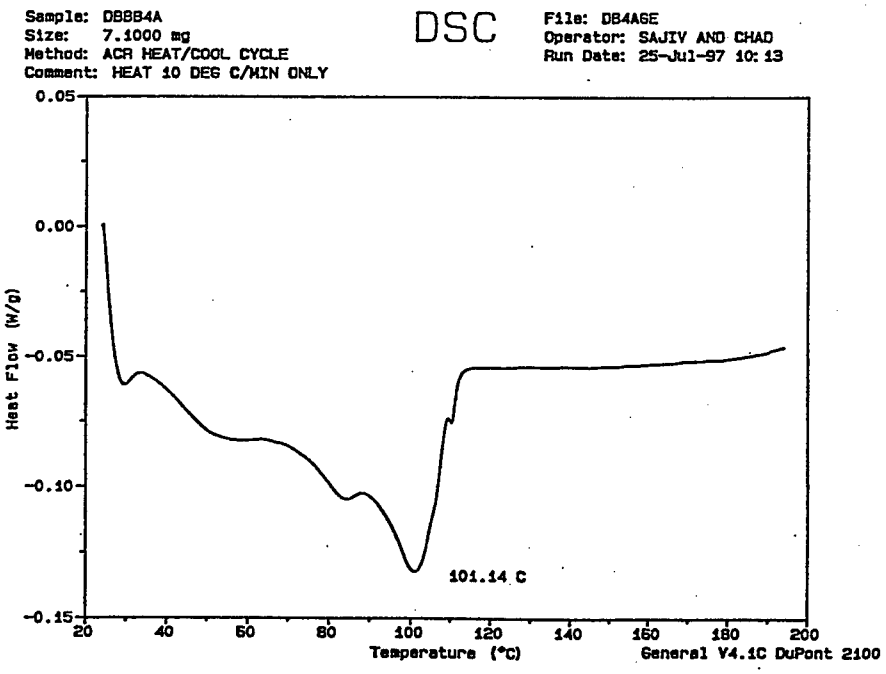


Figure 3. DSC plot for wax based binder filament aged for 86 days.

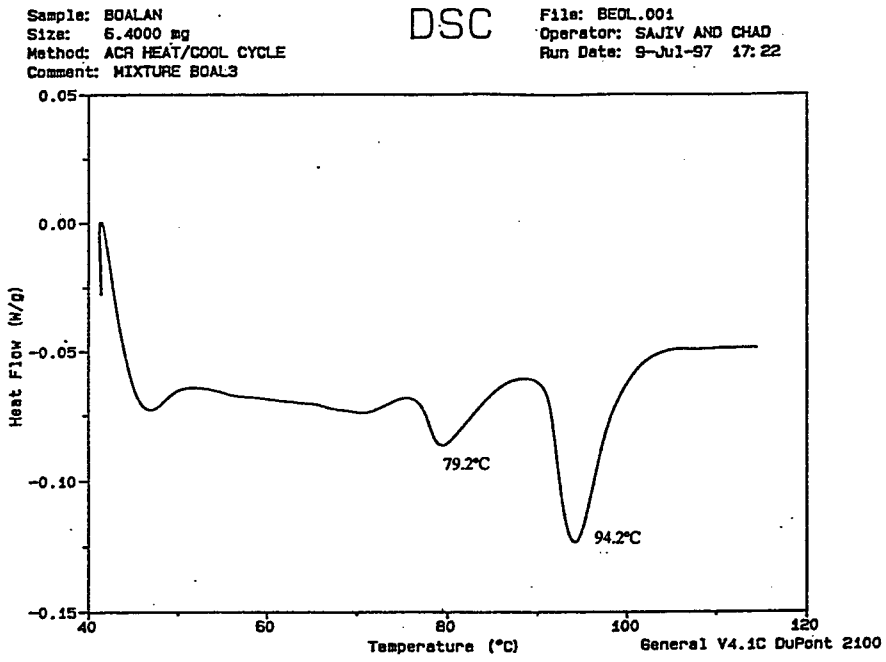


Figure 4. DSC results for wax based binder filament annealed at 88 °C for 3 hours.

CONCLUSION

In this study it can be concluded that the mechanical properties of wax based EFF compatible ceramic feedstocks changed with time at room temperature. The DSC results obtained during this study also suggest that the binder, which contained wax with a broad molecular weight distribution, may have underwent a segregation effects during aging. This aging increased the brittleness of the green ceramic feedstock investigated. In order for the green ceramic material to be utilized as FDC feedstock in conventional Stratasys Modelers, its composition should be modified such that the material is less brittle and possesses greater bend strength. Some modifications to the formulation could include replacement of the existing wax with a microcrystalline wax that is highly branched and crystallizes to a lesser extent upon solidification. It may also be possible to replace the current wax with wax that has a narrower molecular weight distribution than the former and would be less likely to segregate upon solidification.

ACKNOWLEDGMENTS

This work was supported under NASA Marshall Spaceflight Center STTR Research Program and was a joint research effort between Advanced Ceramics Research, Inc. and the Materials Science and Engineering Department at the University of Arizona. Additional support for the FDM green ceramic filament research was provided by Dr. W. S. Coblenz from DARPA and Dr. P. Whalen from Allied Signal, Morristown Tech. Center. The authors would also like to thank Dr. Paul Calvert, Dr. Greg Hilmas, Ronald Cipriani, Kevin Johnston, William Priedeman, and Marcus Short for their assistance.

REFERENCES

[1] M.K Agarwala, A. Bandyopadhyaya, R. van Weeren, N.A. Langrana, A. Safari, S.C. Danforth, V.R. Jamalabad, P.J. Whalen, R. Donaldson, and J. Pollinger: *Proceedings of the 1996 Solid Freeform Fabrication Symposium,* The University of Texas at Austin, August 1996, pp.335-344.

[2] M.K Agarwala, R. van Weeren, R. Vaidyanathan, A. Bandyopadhyay, G. Carrasquillo, V. Jamalabad, N. Langrana, A. Safari, S.H. Garofalini, S.C. Danforth, J. Burlew, R. Donaldson, P. Whalen, and C. Ballard: *Proceedings of the 1995 Solid Freeform Fabrication Symposium,* The University of Texas at Austin, August 1995, pp. 1-8.

[3] P. Calvert, R. Crockett, J. Lombardi, and J. O'Kelly: *Proceedings of the 1994 Solid freeform Fabrication Symposium,* The University of Texas at Austin, August 1994, pp. 50-55.

[4] R.M German and A. Bose: *Injection Molding of Metals and Ceramics,* Metal Powder Industries Federation, Princeton, New Jersey, 1997, pp. 23

[5] M.J. Edirisinghe and J.R.G. Evans: *Materials and Design,* vol. 8, 1987, pp. 284-8

[6] M.J. Edirisinghe and J.R.G. Evans: *Journal of Materials Science,* vol. 22, 1987, pp. 269-277

[7] Reference 4, pp. 89

[8] P.A. Siemers, R.L. Mehan, and H. Moran: *Journal of Materials Science,* vol. 23, 1988, pp. 1329-33

[9] B.H. King and J.W. Halloran: *Journal of the American Ceramics Society,* vol. 78, 1995, pp. 2141-2148

[10] A. Mehta and B. Wunderlich: *Colloid and Polymer Science,* vol. 253, 1974, pp. 193

[11] B. Wunderlich: *Macromolecular Physics Vol. 2 Crystal Nucleation, Growth, Annealing,* Academic Press, New York, 1976, pp. 94-98

[12] M.I. Bank and S. Krimm: *Journal of Polymer Science Part B,* vol. 8, 1970, pp. 1785

Selective Laser Sintering of Quartz Powder

Hongyun Wang, David L. Bourell, Joseph J. Beaman Jr.
Laboratory for Freedom Fabrication and Center for Materials Science and Engineering
University of Texas at Austin

Abstract

This research describes the feasibility of fusing quartz powder by Selective Laser Sintering (SLS). SLS is a method of rapid prototyping three-dimensional objects from a computer-aided design database. The effects of different processing parameters, including powder size, laser power and scan rate were explored. Single and multiple layer specimens have been made. The resulting structures were evaluated using SEM and the density of the multiple-layer structure was detected by a geometrical mass/volume technique. It was determined that particle size was the dominant variable affecting part quality. Smaller and spherical uniform particles are preferred. Future work will concentrate on optimizing powder size and shape and higher laser power.

Introduction

Preliminary experiments on SLS of quartz

Selective Laser Sintering (SLS) is a process in which a three-dimensional object is constructed directly from a computer-aided design (CAD) database without part-specific tooling or human intervention [1]. Conceived and designed at the University of Texas at Austin (UT), the process not only produces parts from polymers successfully, but is also capable of producing parts from high-temperature materials like metals and ceramics directly, without the aid of low -temperature binders. Polymers have relatively low melting temperature. They can be sintered with low laser power at relatively low operating temperatures. Ceramics melt at much higher temperatures. For example, crystalline quartz melts at 2000 K [2], making it difficult to process. Preliminary work at UT has indicated that ceramic with a polymer coating can be processed by using SLS to make turbine blade cores [3]. This present work is to test the feasibility of fusing quartz powder in an SLS apparatus and to find the optimum processing parameters for silica.

Experimental Aspects

Powder Supply

Two different kinds of powders were used. Powder A was supplied by Cyrco Quartz, Inc. Powder B was provided by the University of Texas at Austin to compare the research results.

Powder Physical Properties

Before using Powders A and B to make single or multiple layers, physical properties such as particle shape and size, surface area and crystallinity were characterized.

Particle size and shape were studied using a JSM-35C model scanning electron microscope. A Quantachrome Corporation Autosorb surface analyzer was used to measure the specific surface area of different powders, adopting the BET method. A Philips Automated Diffractometer was used to study the crystallinity and phase content of these powders.

SLS apparatus

The SLS apparatus is depicted in Figure 1.

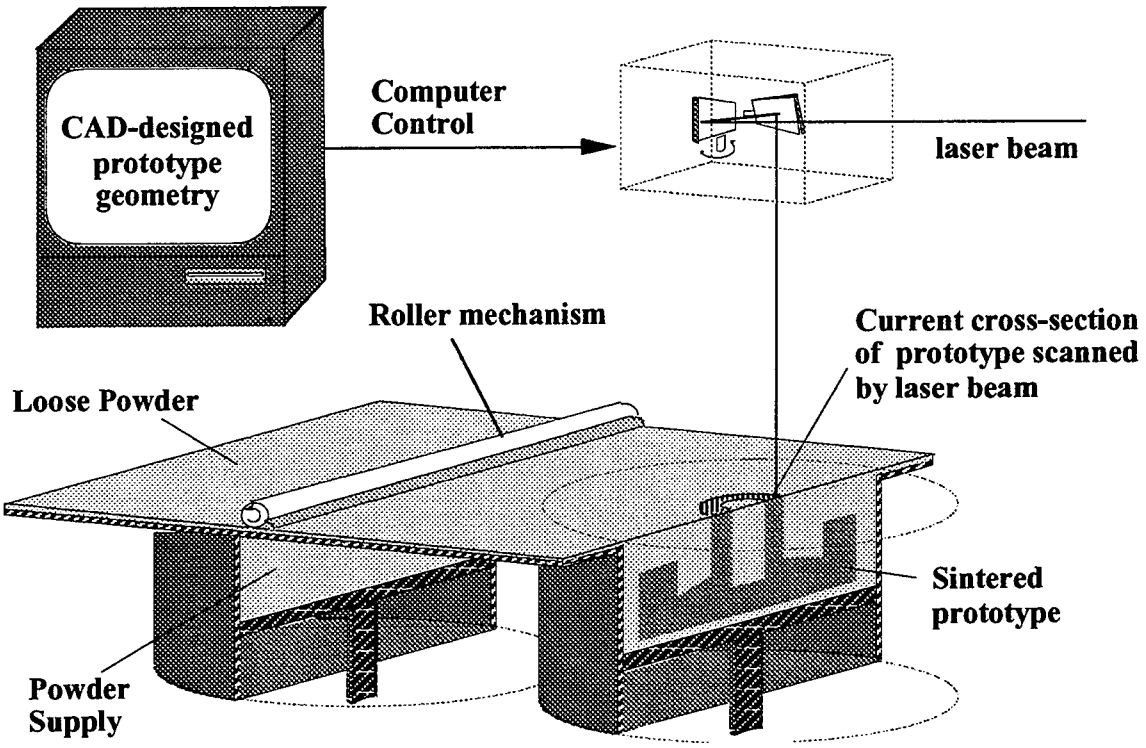


Fig. 1 A schematic drawing of an SLS process

This research was mainly performed on a UT prototype SLS machine. It has a maximum 25 watts CO_2 (wavelength = 10.6 μm) laser power. The characteristic radius of the laser spot is approximately 622 μm. The scanner was supplied by General Scanning Inc. Single layer structures of these powders were made. Multi-layer structures were made on a DTM beta SLS machine. For this research work, a 50 watt CO_2 laser was installed.

The microstructure, porosity and density of the specimens were studied using techniques discussed earlier for the powder.

Results and Discussion

Particle size and shape

Figure 2 shows an SEM photo of Powder A. The shape of the particle is angular and irregular. The particle size for A varied between 100 μm and 300 μm. Powder B is also angular, and the particle size varied between 0.5 μm and 3 μm.

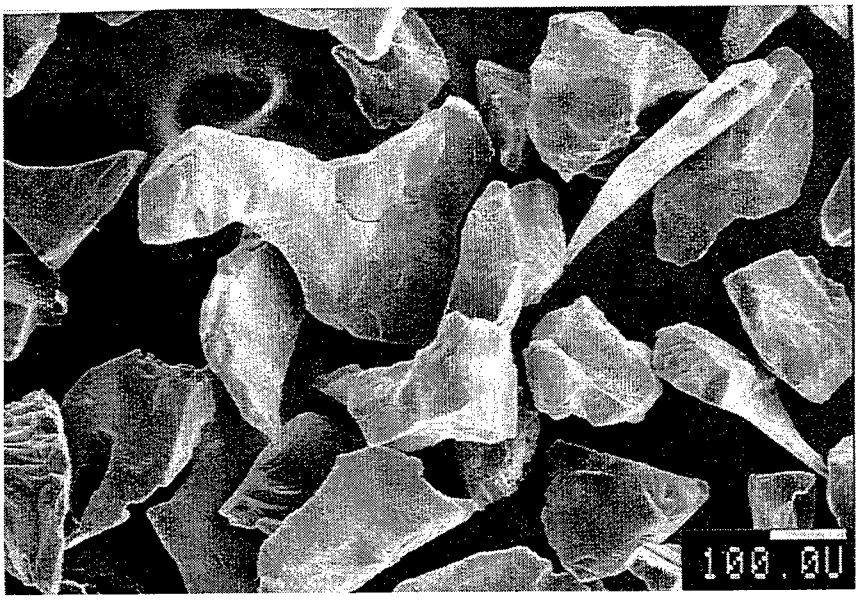


Fig. 2 SEM Photo of Powder A

X-ray analysis

From the x-ray analysis of these powders before and after laser sintering, it can be seen in Figure 3 that all powders were crystalline quartz before sintering and in Figure 4 they became amorphous silica after sintering.

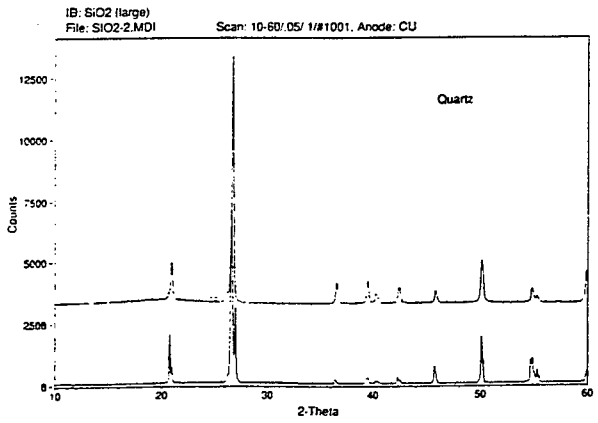


Fig. 3 XRD Pattern of Powder A and B
upper : A, lower: B; before sintering

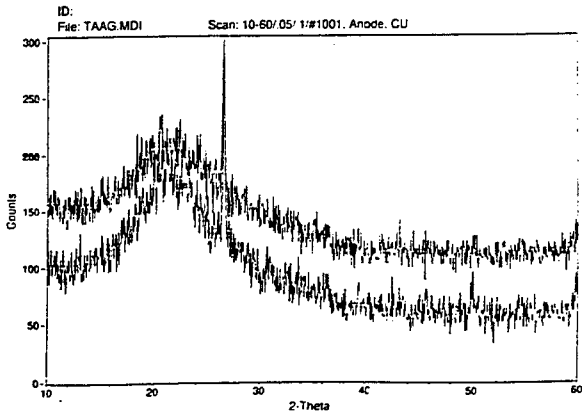
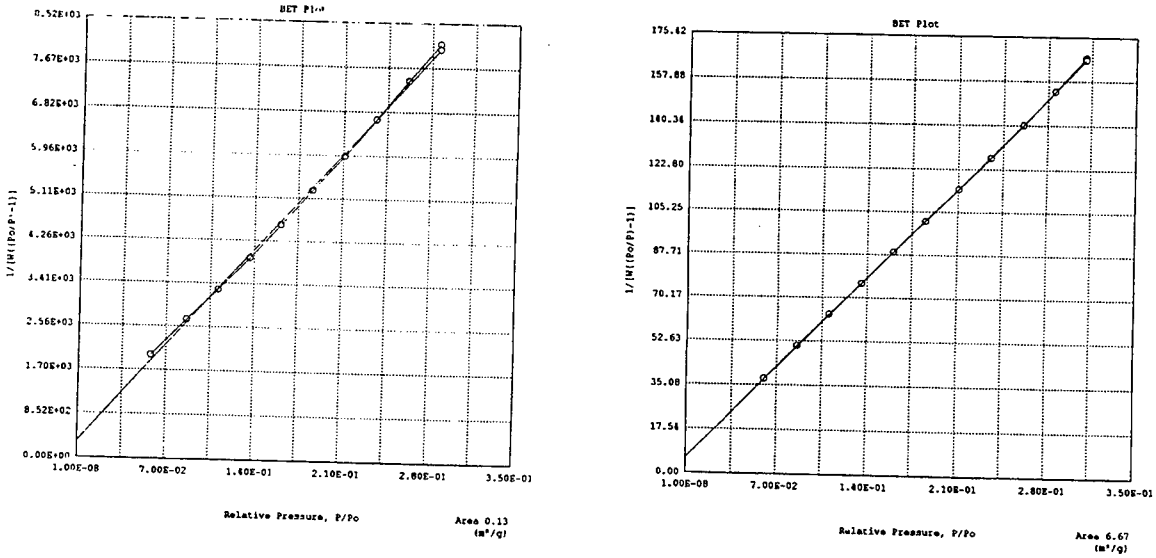


Fig. 4 XRD Pattern of Powder A and B
upper: A, lower: B; after sintering

BET results

Specific surface area plots of Powder A and B, Figure 5, confirm that smaller particles have larger surface area. The surface area of Powder A and B were 0.13 m^2/g and 6.67 m^2/g respectively .

Single layer runs were made on the prototype SLS machine to optimize the laser power and machine parameters, and multi-layer parts were produced on the beta SLS machine.



(a) (b)

Fig. 5 BET Plots of Powder A (a) and B (b)

Single layer SLS

SLS is a process that uses a rastering laser to sinter powder particles. The laser is typically rastered at speeds from 1 to 10 cm per second. For this research, the sintering speed was about 1 to 2 cm per second. In such a short time without chemical reaction, this sintering process must involve melting to form particle necks [4]. By using identical processing parameters, single layer samples using Powders A and B were made.

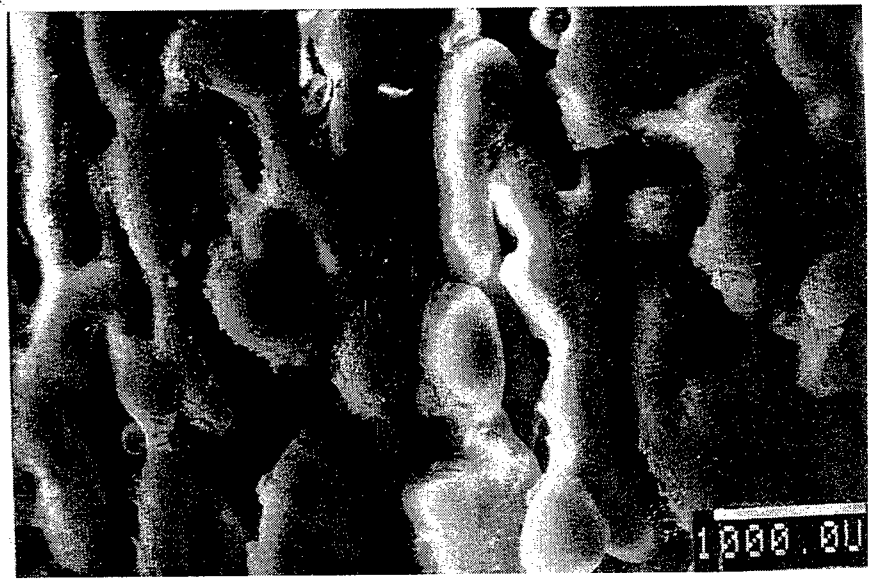
Under the same magnification, it can be seen that the lines in the SEM photo, Fig. 6a, are discontinuous, but in Fig. 6b are continuous. The characteristic radius of the laser spot is about 622 μm. Because the particle shape is angular, it is difficult to compare the laser spot and particle size. This notwithstanding, the laser spot is comparable to the coarse particle size. But it is much larger than the powder particle size of Powder B. The heat conductivity of quartz powder is 0.49w/m·K for the temperature range from 370K to 585K [5]. It is therefore difficult to conduct heat to adjacent powder particles. As a result, the volume of material in the powder bed reaching the melting point of quartz is limited to several particles directly under the moving laser beam. These areas will only experience a molten phase for a short period of time, of the order of one second. So the melting area is discontinuous for Powder A. On the other hand, the laser spot can melt a lot of Powder B at one time to form enough liquid to wet the adjacent powders and help to form continuous melting areas.

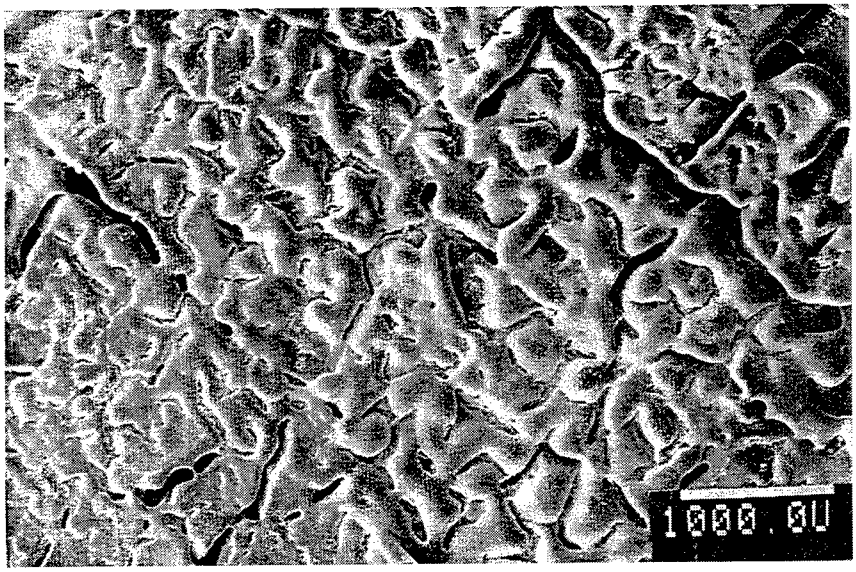
Before and after laser sintering, Powder A and B had different crystalline phases shown in Figs. 3 and 4. This is due to the rapid cooling rate associated with SLS without powder-bed heating.

The driving force for liquid phase sintering is the surface energy. The effect of surface energy is to drive the microstructure towards a minimum energy configuration by reducing the amount of free surface. Surface energy is proportional to surface area [6]. Because Powder B has larger surface area than Powder A, the driving force for Powder B is greater than Powder A. So for Powder B, the laser power is enough for liquid sintering to continue, producing the continuous lines in Fig. 6b. For the larger powder, the driving force is relatively small and the sintering

process is difficult to proceed. Additionally, laser coupling to the fine powder is better than for the coarse powder, resulting in higher local sintering temperature. To compensate for this small driving force, more laser power is needed. The limited laser power combined with the discontinuous nature of the scanning raster and low thermal conductivity is responsible for the discontinuous structure illustrated in Fig. 6a.

Particle shape also has an effect on sintering. Angular particles tend to bridge each other and cause low green packing density [7]. The low density of the powder bed is detrimental to later densification. As for the spacing between lines in Figure 6, we believe it can be eliminated by choosing appropriate sintering atmosphere and processing parameters. To get a homogeneous and continuous structure which will give high specimen density and strength, smaller and more spherical, uniform particle morphology is needed.

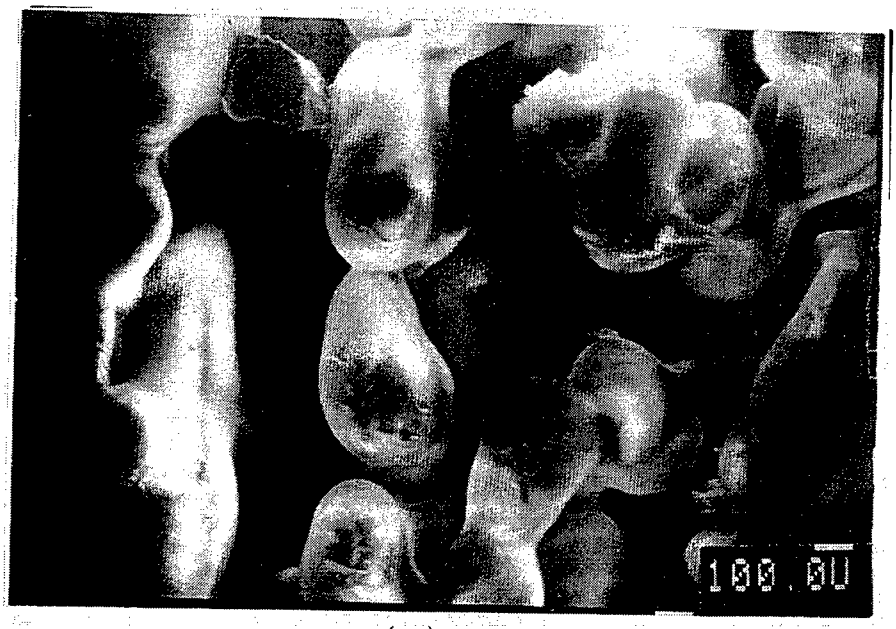




(b)

Fig. 6 SEM photos of single layer specimens made from (a) Powder A and (b) Powder B, laser power: 25 watts

Fig. 7 shows SEM photos made of Powder A by using 25 watts and 45 watts laser power, respectively. It can be seen that at 25 watts, Powder A particles only form point contacts in Fig. 7a, which means that sintering is in the initial stage of liquid sintering -- necking. Intermediate neck growth occurs at 45 watts as shown in Fig. 7b. The point contacts formed at 25 watts laser power have formed into continuous lines at 45 watts. Higher laser power increases the degree of sintering.



(a)



(b)

Fig. 7 SEM photos of specimens made from Powder A at laser power of (a) 25 watts and (b) 45 watts

Multiple layer SLS

After the single layer tests for Powder A and B, multi-layer tests were performed. Although Powder B performed well in the single layer tests, it has higher specific surface area (Figure 5), making it difficult to spread automatically and evenly over previous layers. For optimum SLS processing, particle size should larger than 3 μm. Powder A had no problem spreading. But because of its large particle, the thickness between each layer was too thick (about 3 times of the particle size which is 0.025 inch) for the laser to induce melting. By using up to 45 watts of laser power, we made several "boxes" (Figure 8) using Powder A. The laser power was still not high enough for strong interlayer bonding. By approximation, the density of these boxes is about 44% of theoretical density (for quartz, the theoretical density is 2.65 g/cm^3). By using colloidal silica to infiltrate it, the parts density was increased to around 70% of theoretical density.

By using proper processing parameters and small particle size, dense structure of quartz can be made by SLS. Figure 9 shows some promising dense structures made from Powder B.

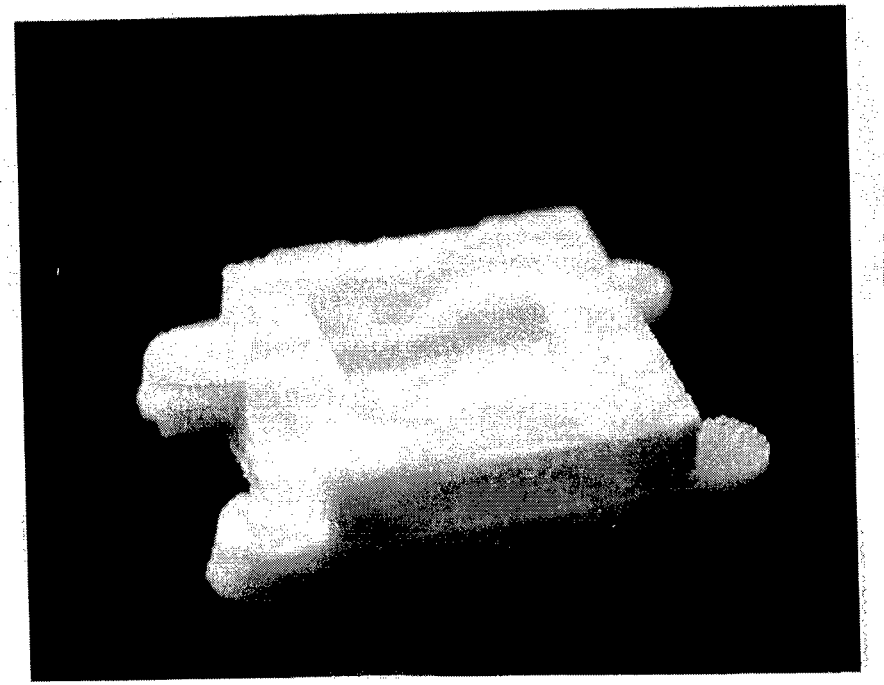
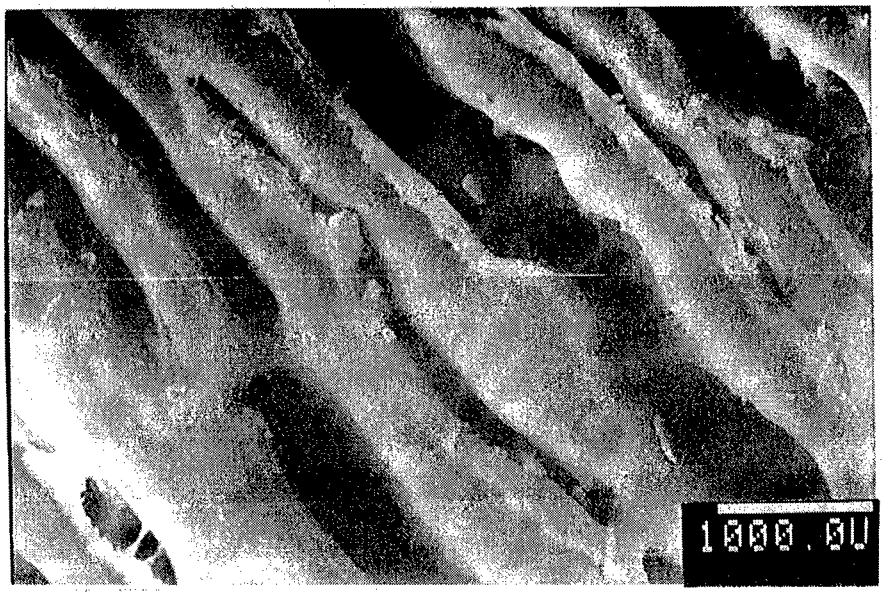


Fig. 8 Photo of multilayer box, the overall box length: 1.75 in; width: 1.25 in; height: 0.5 in.



(a)



(b)

Fig. 9 SEM photos of specimens made from Powder B, laser power 20 watts, (a) continuous scanning, (b) discontinuous scanning.

For quartz, the thermal expansion coefficients are very small, which is $14\times10^{-6}/^{\circ}C$ normal to the c axis and $9.0\times10^{-6}/^{\circ}C$ parallel to the c axis [2]. There is no significant volume change during laser sintering. This is beneficial for specimen shape design and net-shape laser fabrication processing.

Conclusions

From above work, it can be concluded that direct SLS of quartz is feasible.

Particle size and shape are very important parameter for laser sintering. The powder provided by the Cryco Inc. was too coarse and angular for optimum SLS processing. Particle size and shape not only affects the density and strength of the products, but also the appearance. Smaller spherical particles will give a smooth product surface. Powder B is too fine, an intermediate particle size is needed. From UT former work on SLS [8], typical layer thickness is controlled to lie in the 75-125 μm range. As mentioned before, layer thickness is about 3 to 4 times the particle size, so particle size around 30 to 60 μm is preferred.

Large powder sintering requires high laser power and/or slow scanning speed. Processing time is also a function of powder size and laser power. Using the same particle size, high laser power can reduce the processing time. For the multi-layer box, Fig. 8, it took approximately two hours to make at 45 watts. For higher laser power or smaller particle size, a faster scanning speed may be chosen to significantly reduce the processing time.

These initial results are very promising. Even better parts should be produceable using fine particulate and higher laser power.

Acknowledgments

The authors would like to thank Britton Birmingham, Kenwei Chen, Suman Das and Martin Wohlert for their help in this research work. The authors also acknowledge the research grants form Cryco Quartz Inc., Austin, TX.

References

1. D. L. Bourell, H. L. Marcus, J. W. Barlow, and J. J. Beaman, "Selective Laser Sintering of Metals and Ceramics", Int. J. Powder Met., 28 (4), 1992
2. David W. Richerson, Modern Ceramic Engineering, Marcel Dekker, Inc. New York, 1992
3. James C. Nelson, Dissertation, Selective Laser Sintering: A Definition of the Process and an Empirical Sintering Model, The University of Texas at Austin, May 1993
4. Randall M. German, Liquid Phase Sintering, Plenum Press, New York, 1985
5. Y. S. Touloukian, Thermophysical properties of Matter, vol. 2, Plenum Press, New York, 1972
6. Randall M. German, Sintering Theory and Practice, New York, 1996
7. Randall M. German, Powder Metallurgy Science, Princeton, N. J. 1984
8. Kamatchi Subramanian, Neal Vail, Joel Barlow and Harris Marcus, "Selective Laser Sintering of Alumina with Polymer Binders", Rapid Prototyping Journal, vol. 1-2, 1995

Extrusion Freeforming of Nylon 6 Materials

John L. Lombardi *, Paul D. Calvert** Advanced Ceramics Research, Inc. Tucson, AZ 85713 *
University of Arizona - Arizona Materials Laboratories Tucson, AZ 85712 **

INTRODUCTION

Numerous commercial rapid prototyping (RP) processes are capable of fabricating complex shaped components. These processes build prototypes "from the ground up" by first reducing a CAD design of the desired prototype to a series of geometrical slices followed by the precise sequential deposition of raw material layers upon one another. Unfortunately, these RP processes are limited to producing prototypes from polymers that exhibit inferior mechanical properties compared to commercial engineering thermoplastics. Consequently, there are significant advantages in extending the materials processing capabilities of RP technology into the realm of producing tough, high strength functional prototypes from engineering polymers.

BACKGROUND

A possible method of fabricating high strength polymer prototypes utilizes extrusion freeforming techniques (EFF) where parts are built from a series of precisely deposited liquid monomer layers that are subsequently thermally polymerized to form the desired thermoplastic component (1). EFF monomer deposition is typically performed using a syringe pump fitted with a fine bore nozzle that is interfaced to a CAD based motion control hardware. A major advantage of freeforming liquid monomer compared to molten engineering thermoplastic feedstock is that the former have lower viscosity (which facilitates accurate dispensing) and do not exhibit many of the viscoelastic rheological problems encountered during extrusion of the latter (i.e. die swell) (2). It is necessary that the EFF resin used to fabricate these parts rapidly polymerizes to a high molecular weight thermoplastic in high yield. It is also necessary that the resin polymerizes with minimal shrinkage and reaction exotherm otherwise there may be significant stresses or poor adhesion present between the freeformed part layers.

A review of the literature reveals that caprolactam monomer satisfies the above EFF resin requirements since it is a low viscosity liquid when molten (86° C melting point) and readily undergoes ring opening polymerization to yield Nylon 6 polymer. This polymer is a thermoplastic that is used in a wide variety of structural applications including gears and pump impellers and bearing housings (3,4). In comparison to monomers used in other RP techniques (i.e. stereolithography acrylates) caprolactam also exhibits a lower polymerization exotherm. (- ΔH nylon = 10 kcal/mol - ΔH acrylate = 18-25 kcal/mol) (5,6).

Rapidly polymerizable caprolactam resin is commercially available in bulk quantities (typically used in nylon casting & reaction injection molding (RIM) processes) and is primarily composed of molten monomer containing small amounts of sodium caprolactamate base and an N-Carbamoyl Caprolactam activator compound (7). Polymerization proceeds via an anionic ring opening mechanism presented below, whereby sodium caprolactamate base initially opens the lactam ring portion of the activator compound which in turn initiates caprolactam polymerization (8). (See Fig. 1 below for reaction mechanism depiction.)

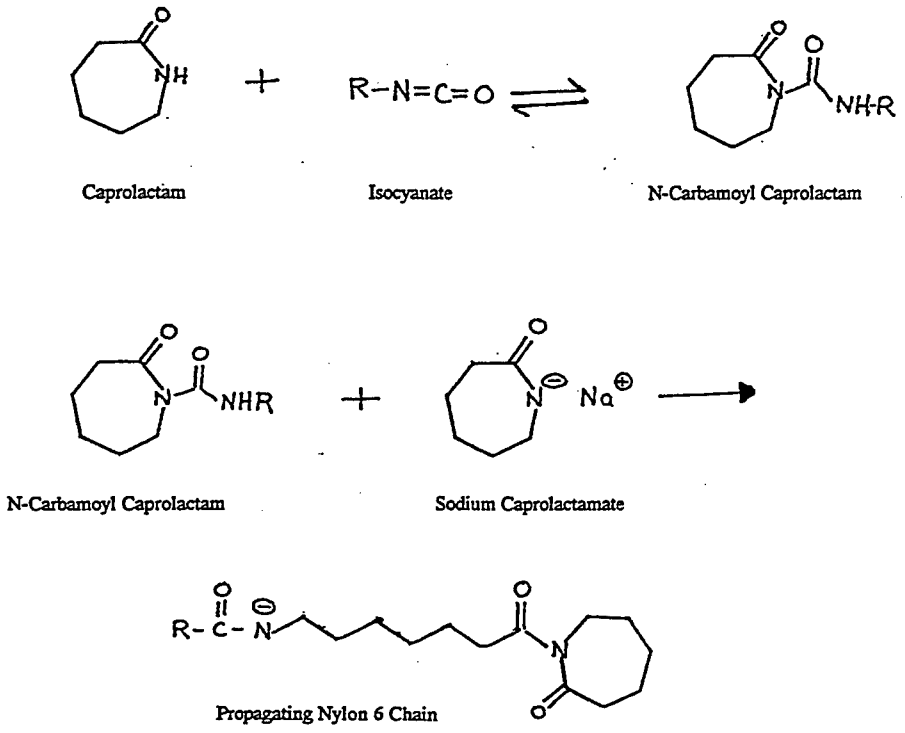


Figure 1. Anionic caprolactam ring opening polymerization reaction mechanism

N-Carbamoyl Caprolactam activators are a key component in the caprolactam resin since these compounds lower the activation energy and reaction temperature for Nylon 6 polymerization. Most commercial activators are multifunctional isocyanates which produce Nylon 6 polymer in > 96 % yield within a few minutes after heating the resin above 150° C (9).

EFF Compatible Nylon 6 Resin Development

Despite its numerous advantages, the high reactivity and low shelf life of commercial caprolactam resins precluded their use in EFF processing due to their propensity to gel and clog the EFF apparatus syringe pump dispensing system. The resin had to be reformulated with an activator that was stable at the EFF pump reservoir temperatures (70° C) while simultaneously having the ability to polymerize the resin shortly after dispensing onto a resin curing platen heated at 165° C. Experiments were conducted with various isocyanate compounds to obtain a latent activator. Tetramethylxylxylene diisocyanate (TMXDI) and dimethylbenzyl meta-isopropenyl benzene (TMI) were two compounds found to be suitable EFF compatible latent polymerization activators. The cure properties of these two activators are summarized in Table I below.

TABLE I TMXDI & TMI NYLON ACTIVATOR CURING CHARACTERISTICS

ACTIVATOR	ISOCYANATE FUNCTIONALITY	TIME (MIN) REQ'D TO GEL RESIN @ 165° C	TIME (MIN) REQ'D TO GEL RESIN @ 70° C
TMXDI	2	10	35
TMI	1	20	45

* Nylon resin composition: 30g caprolactam, 1 mol.% activator, 2 mol. % Na Caprolactamate

After determining EFF compatible latent activators, optimal curing conditions for the reformulated resins were determined by measuring the percent crystallinity and crystallization undercooling on cast Nylon 6 specimens using differential scanning calorimetry (DSC). The percent crystallinity within a cast sample varied directly with its modulus and strength while melt undercooling also varied directly with the melt viscosity and molecular weight of the Nylon 6 polymer present in each sample (10,11). The results from the DSC characterization of samples cast with TMXDI activator at 165° C for time periods ranging from 15 minutes to 4 hours are presented in Table II below. DSC results for a sample cast with half the amount of sodium caprolactamate base and TMXDI activator are also presented in Table II.

TABLE II DSC RESULTS FOR TMXDI CAST NYLON 6

Sample (Polym Temp-Time)	% Crystallinity	Undercooling Temp. T
165-15	40	41
165-30	41.6	43
165-45	42.7	44
165-4hr.	50.4	44.4
165-15 ½ TMXDI, Base	48.5	47

* Nylon resin composition was similar to that given in Table I above

From the above results it can be seen that sample crystallinity and melt undercooling increased with reaction time indicating that the nylon polymer increases in molecular weight and crystallinity upon prolonged reaction. The molecular weight of the final nylon polymer was found to level off after a four hour reaction period. Decreasing the amount of sodium caprolactamate base and activator in the resin yielded a polymer product having both higher molecular weight and crystallinity. This too is expected since the anionic polymerization of caprolactam is believed to be a quasiliving process where polymer product molecular weight is inversely proportional to activator concentration (12). The mechanical properties of these samples were also determined using an Instron Model 1011 tensile testing apparatus. The tensile testing results are provided in Table III below.

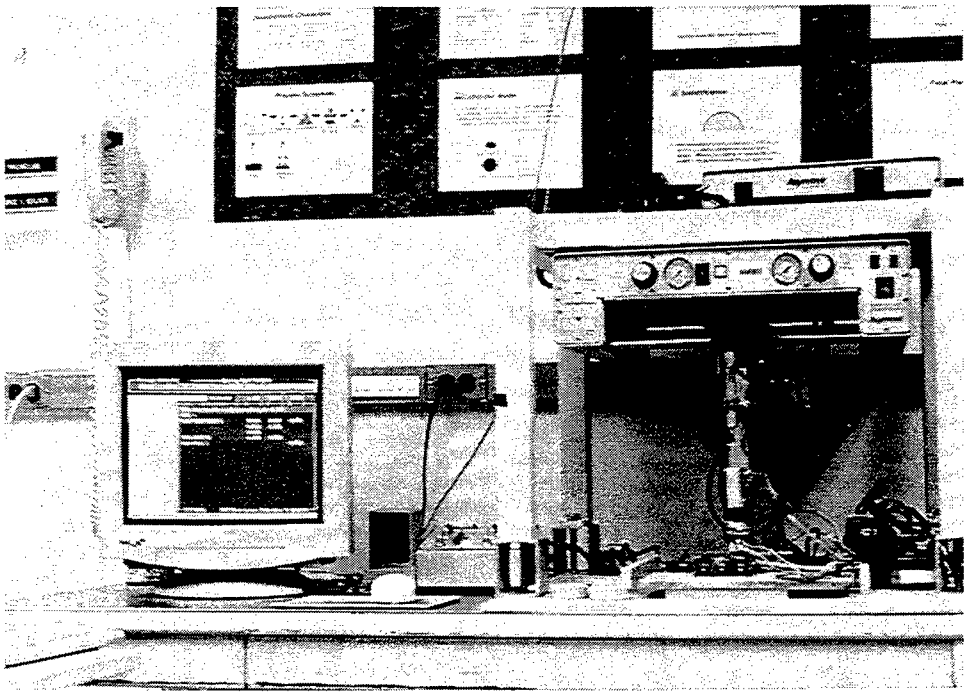


Figure 2. Photograph of Asymtek Fluid Dispenser used for nylon resin extrusion freeforming.

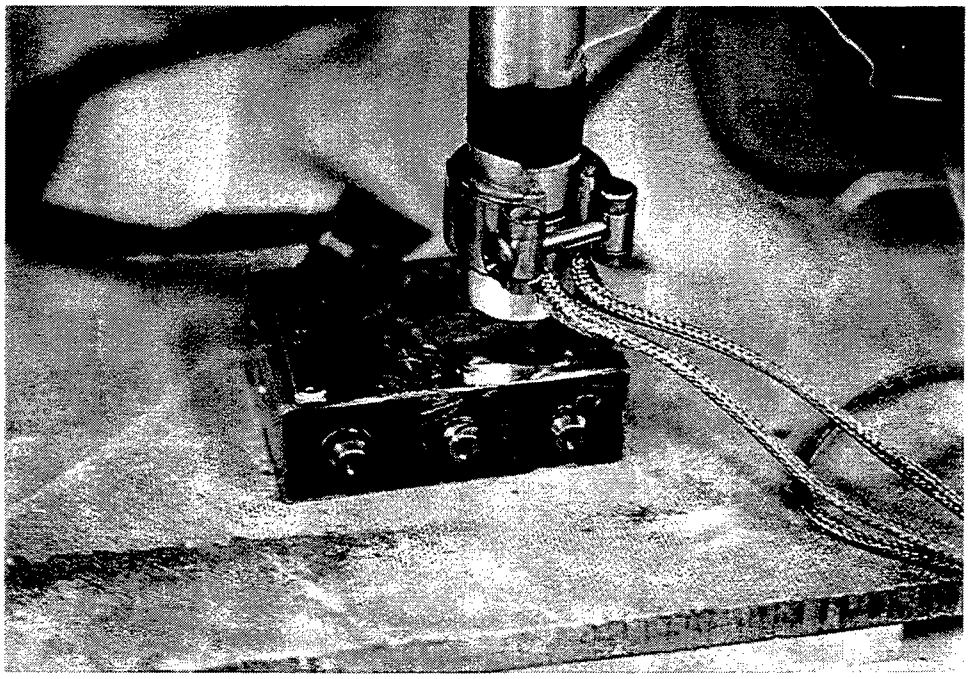


Figure 3. Photograph of Asymtek EFF apparatus syringe pump nozzle freeforming nylon resin onto a heated aluminum platen.

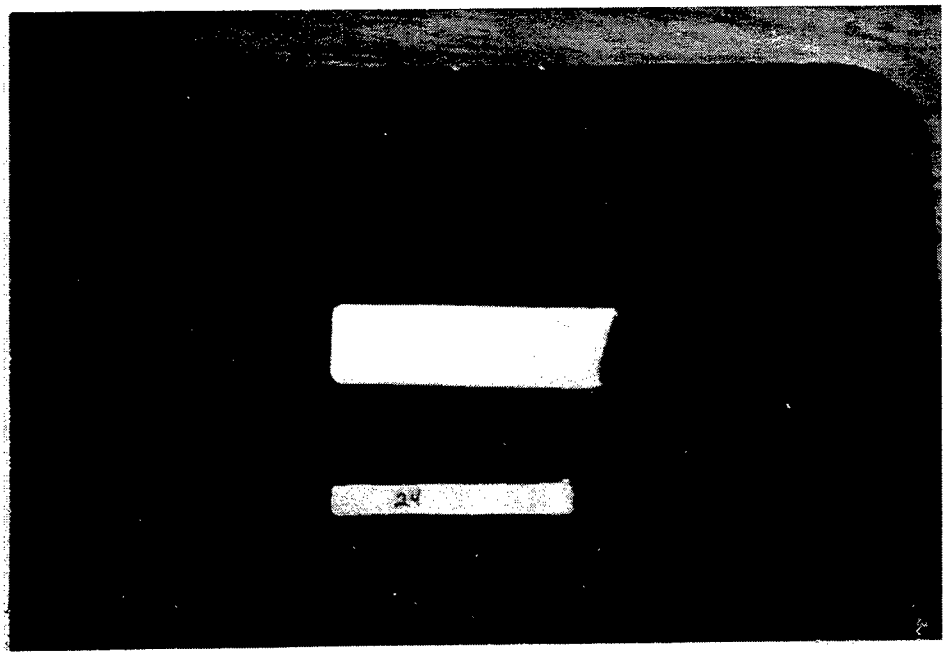


Figure 4. Freeformed (bottom) and a cast (top) Nylon 6 bar specimen . Scale 0.3"=1.0"

TABLE IV TENSILE TEST DATA FOR EFF/CAST NYLON 6 SPECIMENS

Specimen	Yield Stress (MPa)	Young's Modulus (MPa)	% Elongation at Break
Control TMI Cast	83.02	2248	3.51
EFF TMI	74.52	2257	3.10
Control TMXDI Cast	74.59	2257	4.31
Commercial Cast Nylon 6 (Unfilled)	80	3280	3.5

* Resin compostion 30g caprolactam, 8 wt. % fume silica, 1 mol. % TMI, 2 mol. % Na Caprolactamate

From the results above it can be seen that the extrusion freeformed bars had lower strengths and elongation to break values than those cast under identical conditions. This suggested that the nylon in the extrusion freeformed bars may have a lower molecular weight than that present in the cast bars. It is possible that exposure of nylon resin to the atmosphere during extrusion may have an inhibitory effect upon its polymerization (13). The difference in mechanical properties between the extrusion freeformed bar and both the cast control and commercial specimens was not significant, however.

TABLE III CAST NYLON 6 TENSILE TESTING RESULTS

Sample	Yield Stress (MPa)	Young's Modulus (MPa)	% Elongation @ Break
165-15	45.29	1856	3.5
165-30	43.05	1821	2.4
165-45	54.08	2148	2.0
165-4	55.6	2340	1.5
165-15 ½ TMXDI, Base	67.4	1866	16.0

The results from the tensile testing indicated that both yield strength and sample modulus increased with reaction time. A concomitant decreasing trend in elongation to break values was also observed. This data was supported by the DSC results which showed an increasing degree of crystallinity for samples with heated for long time periods. Furthermore, the increase in sample elongation to break observed in the sample polymerized with reduced amounts of activator and base suggests that the Nylon present in this sample has a higher molecular weight than that present in the other samples. This too is supported by the DSC results. These results demonstrated that curing the caprolactam resin for four hours at 165° C produced high strength nylon 6 parts.

Extrusion Freeforming of Nylon 6 Resin

Extrusion freeforming of the resin was accomplished using an Asymtek Automove Model 402 Fluid Dispenser which had a syringe pump attached to the machine dispensing head. In particular, nylon resin was pumped through at 25 gauge needle heated at 70° C onto an aluminum platen heated at 165° C. Photographs of the Asymtek Fluid Dispenser and its syringe pump nozzle in the process of freeforming nylon resin are presented in Figure 2 and 3 respectively.

Preliminary attempts to accurately freeform the nylon resin onto a platen heated at 165° C were met with some difficulty because the resin was much too fluid at these temperatures and completely wetted the platen surface. Consequently, eight weight percent of hydrophobic, trimethylsilylated fumed silica thickening agent was added to the resin to increase its thixotropy. The resin was also reformulated with TMI rather than TMXDI activator in order to further increase its pot life. Test bars specimens were then extrusion freeformed using the reformulated resin. Shortly after extrusion freeforming, the test bar specimens were cured for an additional four hours in a mineral oil bath heated at 165° C. After curing , the bars were tensile tested and a comparison was made between these specimens and bars cast under identical conditions. A photograph depicting both a freeformed and a cast Nylon 6 bar specimen is shown below. The tensile testing results are depicted in Table IV below.

Conclusions

In this study, it has been demonstrated that a high molecular weight structural thermoplastic can be freeformed from a reactive monomer. Consequently, the materials processing capability of the extrusion freeforming technique can be extended into the realm of processing high strength engineering nylon 6 thermoplastic. Furthermore, the freeformed materials possess mechanical properties comparable to nylon 6 produced using conventional processing techniques. This demonstrates that freeforming technology has the potential to produce functional prototype parts.

References

1. K. Stuffle, A. Mulligan, J. Lombardi: *Materials Research Society Proceedings*, vol. 346, 1994, pp. 1027-31
2. H.A. Barnes: *An Introduction to Rheology*, Elsevier Publishers, Amsterdam, 1989
3. H. Klare: *Synthetic Fibers from Polyamides*, Akademie Verlag, Berlin, 1963
4. F. Wiloth: Die Makromolekulare Chemie, vol. 27, 1958, pp.37
5. C.W. Macosko: Plastics Engineering, April 1983, pp.36
6. F.R. Wight, Polymer Engineering & Science, vol. 18, 1978, pp. 378-81
7. R.M. Hedrick and J.D. Gabbert: *Reaction Injection Molding*, ACS Symposia Series #270, 1985, pp. 135
8. H.K. Hall, Jr.: Journal of the American Chemical Society, vol. 80, 1958, p.6404
9. O. Wichterle: Die Makromolekulare Chemie, vol. 35, 1960, pp. 174-83
10. L. Mandelkern, F.A. Quinn, P.J. Flory: Journal of Applied Physics, vol. 25, 1954, pp. 830
11. E. Turska and S. Gogolewski: Polymer, vol. 12, 1971, pp. 629-41
12. J. Sebenda and V. Kouril: European Polymer Journal, vol. 8, 1972, pp. 437-47
13. B. Sedlacek, *Polymer Composites*, Walter de Gruyter & Co., New York, 1986, pp. 283-296

Fabrication of In-situ SiC/C Thermocouples by Selective Area Laser Deposition

Lianchao Sun, Kevin J. Jakubenas, James E. Crocker, Shay Harrison, Leon L. Shaw, Harris L. Marcus

Institute of Materials Science
The University of Connecticut, U-136
97 North Eagleville Road
Storrs, Connecticut 06269-3136

Abstract

With the intrinsic nature to process relatively small features, selective area laser deposition (SALD) is a potential technique to fabricate complex shaped macro-components with in-situ high-resolution micro-devices. In this study, SALD was used to deposit in-situ silicon carbide/carbon (SiC/C) thermocouples on alumina and silicon carbide substrates with a CO_2 laser. Tetramethylsilane (TMS) and acetylene (C_2H_2) were chosen as precursors for deposition of the silicon carbide and carbon lines respectively. The electromotive force (emf) of the deposited thermocouple was measured and found to respond sensitively to temperature variations from room temperature to 800^{0}C. The effect of the deposition parameters on the product morphology was also investigated.

1 Introduction

Among the many advantages of Solid Freeform Fabrication (SFF) technology is the possibility of building geometrically complex shapes, tailoring functionally graded materials or composites spatially, and embedding electromechanical devices in situ within parts during the fabrication process. An approach to these goals is to combine two SFF methods, Selective Area Laser Deposition (SALD) and the closely related SALD-Vapor Infiltration (SALDVI)[1-5]. SALDVI is used to build the bulk structure of the part while SALD is used to embed the sensors. Many kinds of sensors, such as thermistors, thermocouples, strain gauges, etc., could be formed based on this approach. Since SALD and SALDVI are completely compatible gas phase approaches, whole parts can be fabricated in a single integrated SALD/SALDVI process system. As a first attempt using the SALD/SALDVI technique, thermocouples have been embedded within a silicon carbide substrate. This paper discusses the SALD formation of the thermocouple; the SALDVI substrate is described elsewhere in these proceedings [6].

Forming a good thermocouple requires consideration of several factors including compatibility with the substrate, formation of a strongly bonded hot end junction, connections from the cold end to readouts, and the physical stability. To avoid thermal residual stresses, differences in the thermal expansion coefficient between the substrate, insulation, and thermocouple lines must be as small as possible. Obviously, embedding SiC/C thermocouples into a SiC substrate has the advantage of the low thermal expansion mismatch, which will help to maintain continuity of the thermocouple lines during heat/cool cycles.

The first SiC/C thermocouple was developed to measure the temperatures of molten steel by Fitterer in 1933[7]. This thermocouple was formed through simply putting SiC and graphite rods together. An extremely high electromotive force constant, up to 300μV/^{0}C, was reported. But, this thermocouple is not stable in both liquid metals and gas environment. This greatly hindered the further application of SiC/C thermocouple. With the SALD technique, these problems could be avoided by enclosing SiC/C thermocouples within a SiC substrate.

2 Experimental procedures

2.1 Procedures of the device fabrication

An overall process schematic to make the embedded thermocouple device is shown in Figure 1. The substrate is first built layer by layer with SALDVI. An electrically insulating layer is then put on this substrate. With different gas precursors, the thermocouple lines are deposited on the insulation layer by SALD. The final steps of building device are repeating the electrically insulating layers and continuing to build the remainder of the substrate with SALDVI. Single-point or multiple-point thermocouples could be made in one layer through this process. In addition, multiple thermocouples could also be built within different layers. This will be useful when the multi-point temperature control is needed.

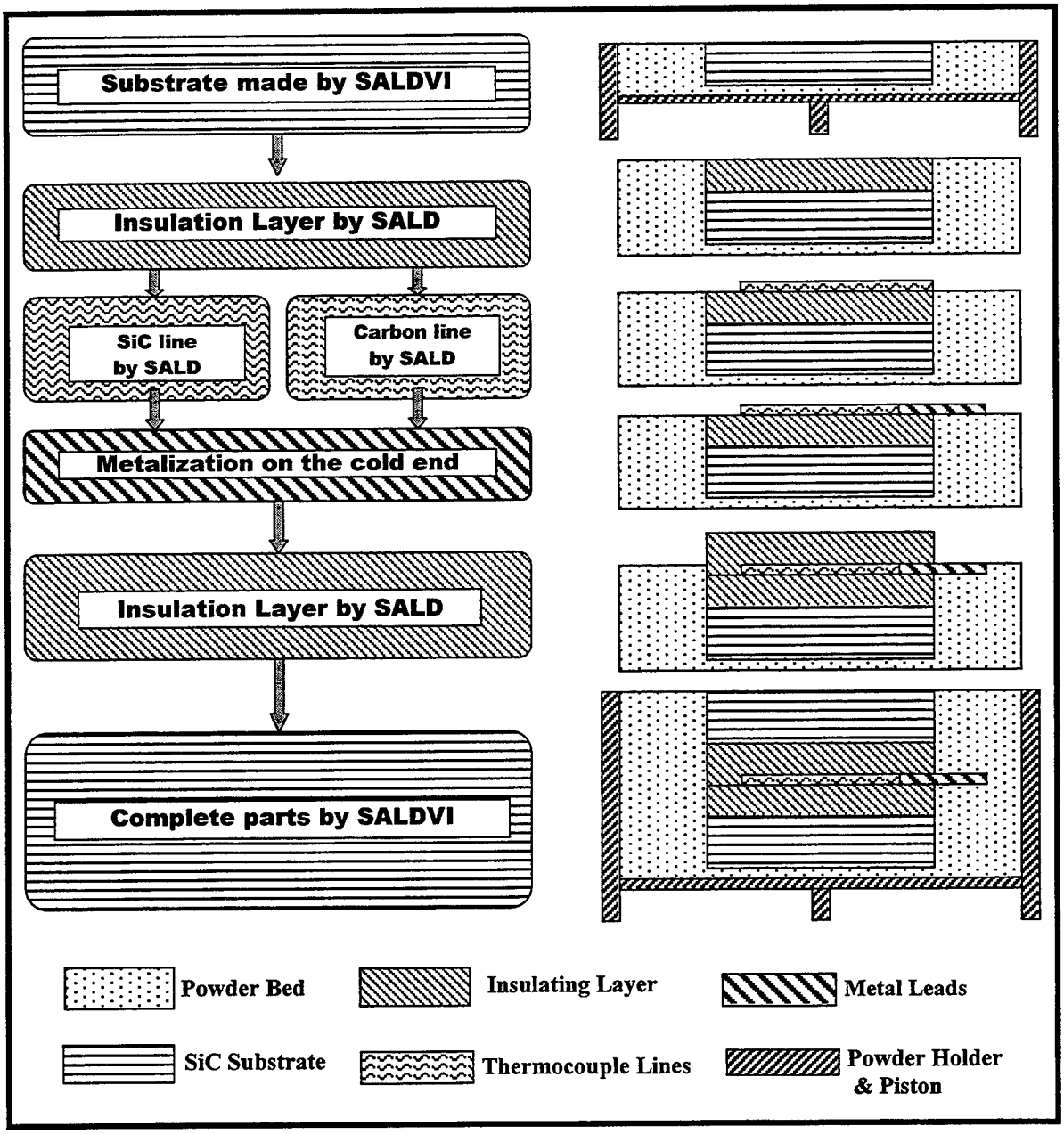


Figure 1 Flowchart of fabricating in-situ device embedded in macro-component

2.2 Deposition of silicon carbide line, carbon line and insulation layer

SALD was carried out using a SFF system which is comprised of a reaction chamber, powder delivery system, 2-D laser beam scanning control stage, gas precursor supply system, observation and recording system, closed-loop temperature control system, and a CO_2 laser with a maximum output of 50W in cw mode and a wavelength of 10.64μm. To get a theoretical spot size of about 500μm, a 254mm focal lens was used. Maximum power density is about 255W/mm^2.

Tetramethylsilane $Si(CH_3)_4$ (TMS) was chosen as the precursor for deposition of SiC because it produces silicon carbide free from halogens and the by-products of pyrolysis reaction are neither corrosive nor contaminant.

For carbon deposition, several precursors, acetylene, ethylene, and methane, were evaluated. The overall reactions are as followings:

$$C_2H_{2(g)} \Leftrightarrow 2C_{(s)} + H_{2(g)}$$
$$C_2H_{4(g)} \Leftrightarrow 2C_{(s)} + 2H_{2(g)}$$
$$CH_{4(g)} \Leftrightarrow C_{(s)} + 2H_{2(g)}$$

Insulation layers were deposited with a gas mixture of TMS and NH_3. Preliminary thermocouple depositions were carried out on alumina and silicon carbide substrates, which were made with conventional sintering method. Additional experiments were conducted on SALDVI silicon carbide substrates.

2.3 Measurement of electromotive force (emf)

The emf of the thermocouple was measured by connecting the cold end directly to the measurement unit through copper wires. Strawberry tree software was applied to collect the emf signals. The laser beam was used to heat the hot end of the thermocouple. A standard K type thermocouple was also put on the hot end as an independent temperature sensor to monitor the temperature change of the hot end. The measurement setup is shown in Figure 2.

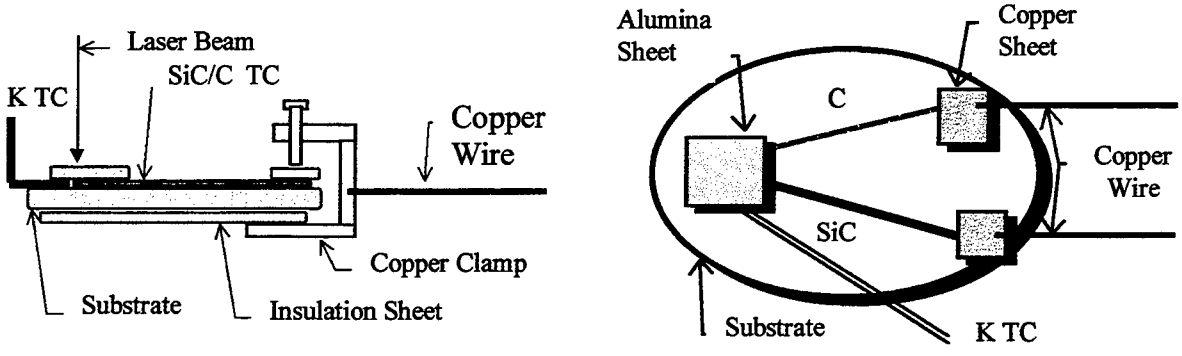


Figure 2 Setup for measuring emf of the SiC/C thermocouple

2.4 Characteristics of the deposited product

SALD thermocouple line morphologies were analyzed with scanning electron microscopy (SEM). The thickness profile of the lines perpendicular to the scan direction was examined with a contact profilometer.

3 Results and discussion

3.1 Silicon carbide lines

A series of SiC lines were deposited on the sintered alumina, the sintered SiC substrates and SALDVI SiC substrates. It was found that line profiles were affected by the deposition conditions of temperature and gas pressure. Generally, with the increase of temperature and TMS gas pressure, the line shape changes from a sharp peak to a flat top to a coarse, rough top surface. In addition, both width and thickness increase with temperature and gas pressure at the range of the present research. These results are listed in Table 1; the typical profiles of deposited lines are shown in Figure 3.

Table 1 Width and thickness of deposited silicon carbide lines on the alumina substrate (scanning speed: 0.5mm/sec; 8 passes)

TMS gas pressure	Line width And Thickness (μm)	SALD Temperature (^{0}C)				
		700	900	1000	1100	1250
20 Torr	Width	/	510	620	750	1040
	Thickness	/	13.9	28.8	42.1	58.3
40 Torr	Width	/	390	570	810	1195
	Thickness	/	31.9	114.1	142.9	143.8
60 Torr	Width	375	410	/	830	/
	Thickness	16.5	68.8	/	147.8	/

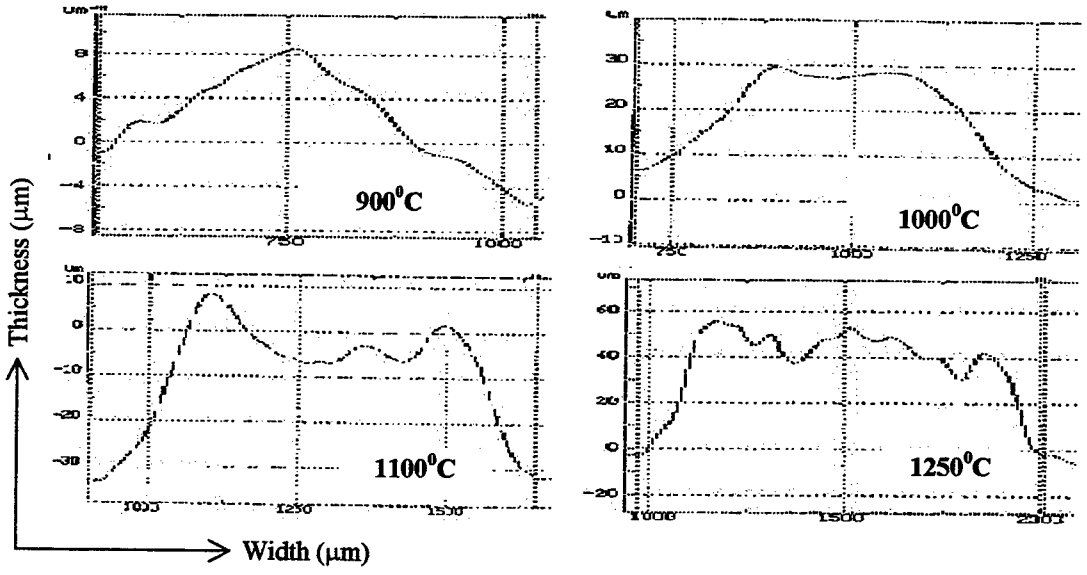


Figure 3 Typical profile changes of the deposited SiC lines (P_{TMS}=20 Torr; Scanning speed: 0.5mm/sec; CO_2 laser; Alumina substrate; 8 passes)

3.2 Carbon deposition

The deposition rate of carbon is relatively slow compared to that of silicon carbide especially when methane or ethylene was used. This is consistent with other research results [8]. After the preliminary experiments, acetylene was chosen for deposition of carbon lines. Three kinds of morphologies, cotton-like shape(Fig 4a), disc shape(Fig 4d), and nodular shape(Fig 4b&c), are observed. The cotton-like shape was observed usually at a low deposition temperature, while nodular morphology was obtained at relatively high temperatures. The disc shape was only observed on the SiC substrate. When the deposition temperature exceeds 1250°C on the both alumina substrate and SiC substrate, carbon growth becomes unstable. The similar phenomenon was also observed on the effect of the gas pressure. It was found that the deposition process could be easily controlled if the C_2H_2 pressure is lower than 200Torr. The surface quality of the deposited carbon lines depends on the surface finish of the substrate. In addition, depositing carbon on the alumina substrate is easier than depositing on the SiC substrate under the same deposition conditions when the CO_2 laser was used. These results showed that the processing conditions obviously affect the deposition of the carbon.

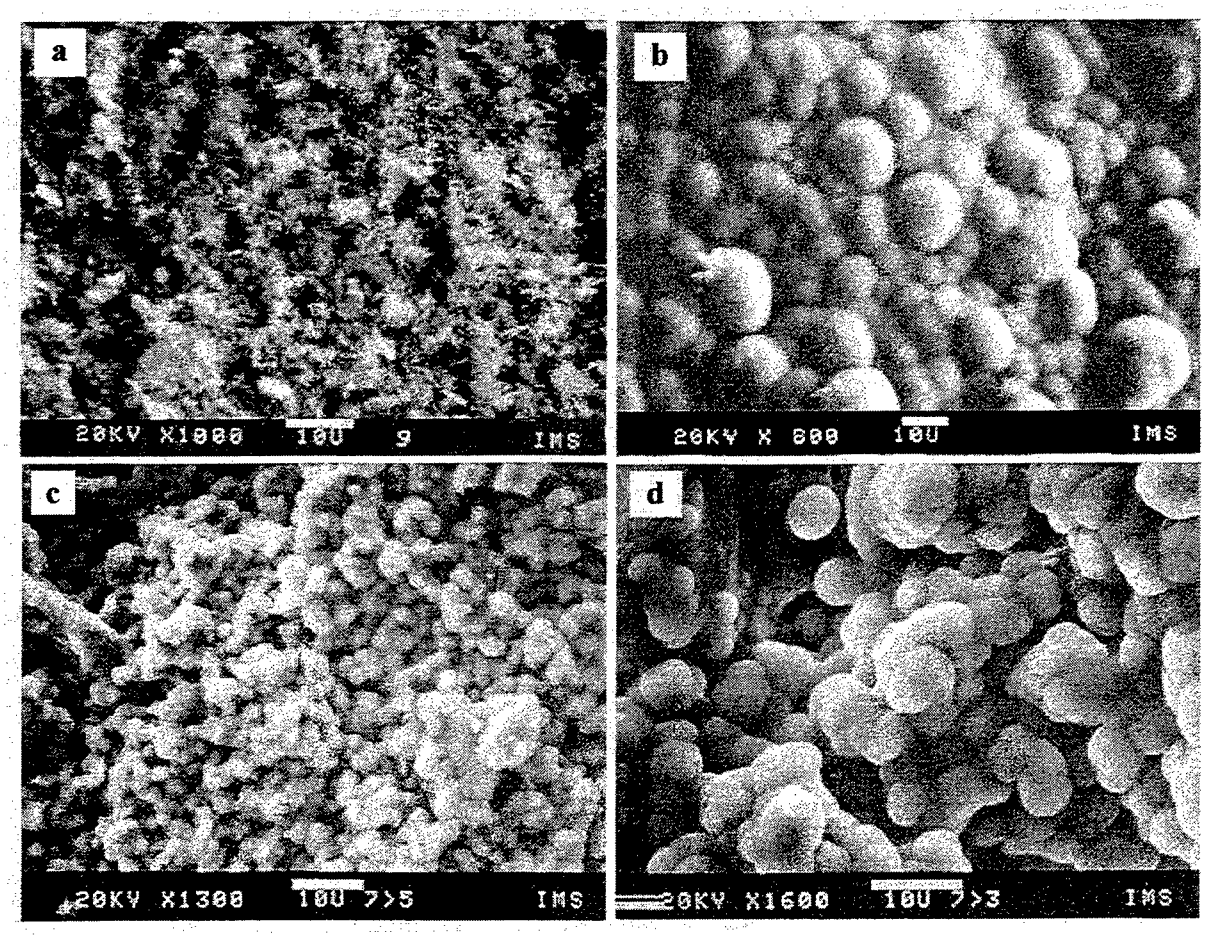


Figure 4 Surface Morphologies of the deposited carbon lines using CO_2 laser on
(a) P_{C2H2} = 200 Torr; Temperature: 800°C; Scanning Speed: 0.06mm/sec; Alumina substrate; 20 passes.
(b) P_{C2H2} = 100 Torr; Temperature: 1250°C; Scanning Speed: 0.76mm/sec; Alumina substrate; 20 passes.
(c) P_{C2H2} = 100 Torr; Temperature: 1000°C; Scanning Speed: 0.38mm/sec; SiC substrate; 20 passes.
(d) P_{C2H2} =200 Torr; Temperature: 900°C; Scanning Speed: 0.13mm/sec; SiC substrate; 20 passes.

3.3 Deposition of insulation layers

Since the thermocouple must be electrically insulated from the substrate, an insulating layer is deposited from the gas mixture of TMS and NH_3. It is found that the surface quality of the insulating layer depends on the scan speed and the surface finish of the substrate. For a substrate with poor surface finish, a very low scanning speed is required to get a uniform insulating layer. Under a condition of a 15Torr TMS plus 15Torr NH_3 and constant temperature (900^0C), a continuous layer with a thickness of about 30μm is obtained. Electrical measurement showed that it is an insulator.

3.4 Electromotive force from SiC/C thermocouples

Some physical parts with the SiC/C thermocouples are shown in Figure 5. The electrical

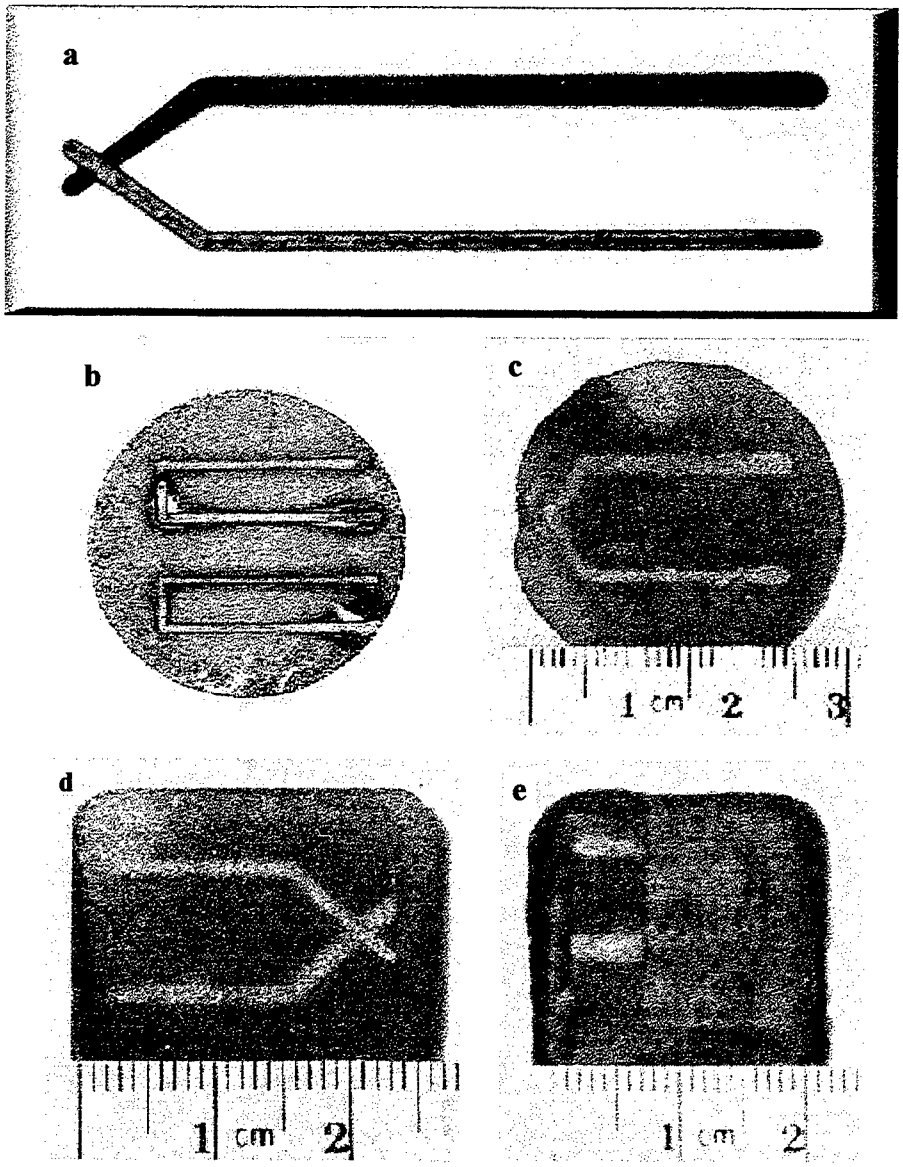


Figure 5 Physical parts with the thermocouples on (a) alumina substrate; (b) the sintered SiC substrate; (c) the single layer SALDVI SiC substrate; (d) multiple-layer SALDVI SiC substrate; (e) multiple-layer SALDVI SiC substrate with the insulating layers at the bottom and top of the thermocouple.

measurements showed that the SALD SiC/C thermocouples, which were deposited on both sintered alumina substrates and SALDVI SiC substrates, exhibited sensitive response to temperature variation. Two typical temperature-emf curves from the SiC/C thermocouples on alumina and SiC substrates are given in Figure 6.

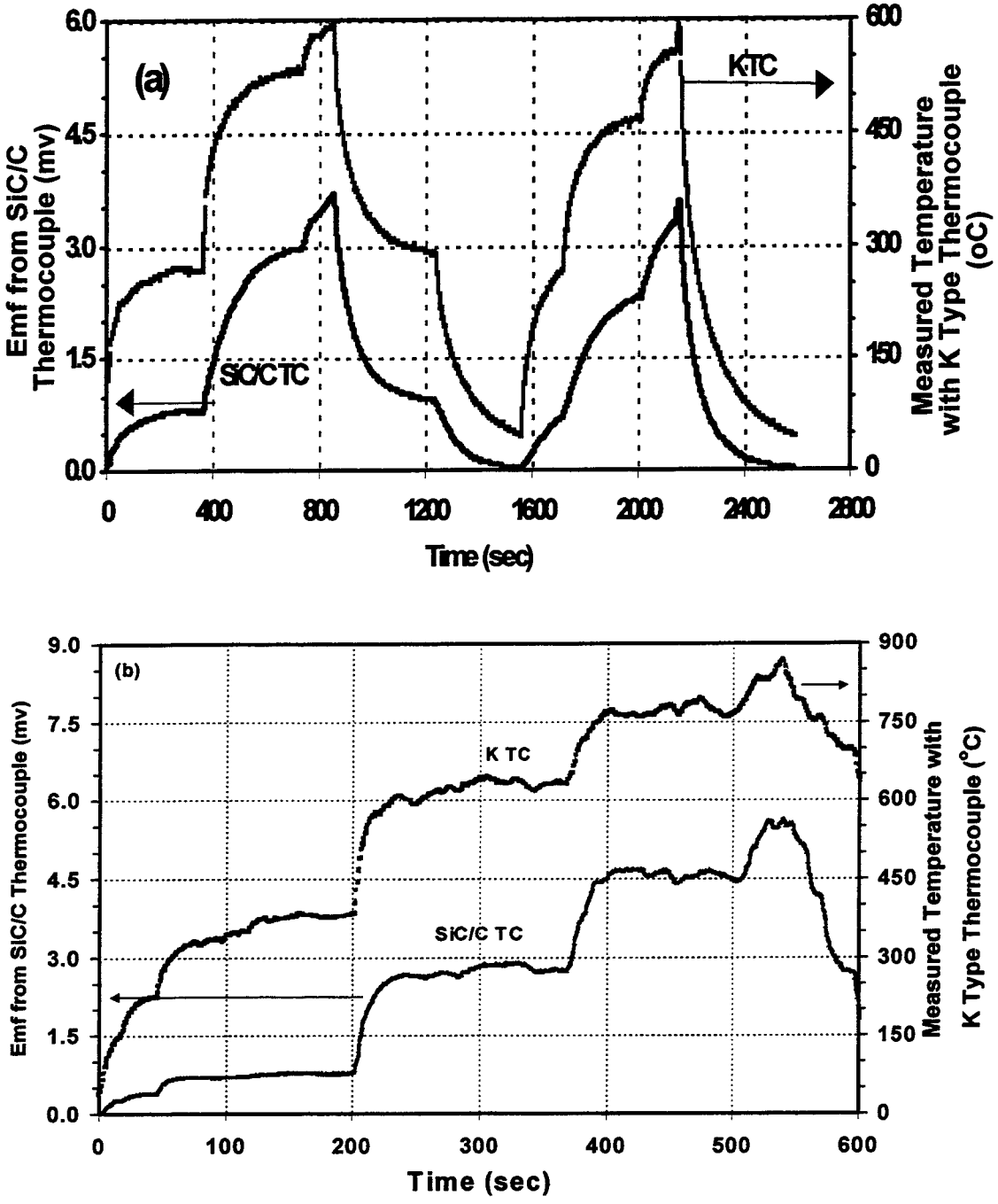


Figure 6 Emf from SiC/C thermocouples as a function of temperature: (a) Thermocouple deposited on sintered alumina substrate; (b) Thermocouple deposited on SALDVI substrates.

It was found that the electromotive force constants are almost same for both thermocouples on the alumina and SiC substrates, which is around 6.7μV/°C. This value is much lower than Fitterer's results [7]. This difference probably comes from a difference in material structures. First, the SALD carbon line may not be in fully graphite form. In addition, the electrical conductivity of silicon carbide may also be too low. The experiments have shown that SiC obtained is amorphous and non-conductive when it is deposited at low temperature and with an unfocused beam, while the SiC substrates made with the conventional sintering method showed a fully conductive behavior. These indicated that the low emf constant could be increased through optimization of SALD process to obtain better structural characteristics of the deposits.

4 Summary

The preliminary experiments have shown that it is feasible to make a structure containing in-situ thermocouples by a combined SALDVI and SALD approach.

Silicon carbide lines, carbon lines and insulating layers have been deposited from the precursors TMS, acetylene, and a gas mixture of TMS and ammonia respectively. The line profile of silicon carbide changes with temperature and gas pressure. Three type of carbon morphologies, cotton-like shape, disc shape and nodular shape, are identified.

It was found that the SALD SiC/C thermocouples respond to temperature variation sensitively. The emf constant of SALD thermocouple is much lower than that obtained with the SiC/C thermocouple made of SiC/C rods. Optimization of SALD process is needed to improve the emf constant of the in-situ SiC/C thermocouple.

Acknowledgement

The authors acknowledge the support of ARPA/ONR Grant N00014-96-1-1299 and ONR Grant N00014-95-1-0978 in funding this research.

Reference:

1. J. L. Maxwell, J. Pegna, D. Messia, and D. DeAngelis, "Direct Feedback Control of Gas-Phase Laser-Induced Deposition," *Solid Freeform Fabrication Proceedings*, The University of Texas at Austin, 1996, pp227-237

2. O. Lehmann and M. Stuke, "Laser-Driven Movement of Three-Dimensional Microstructures Generated by Laser Rapid Prototyping," *Science*, Vol. 270, pp1644-1646

3. F.T Wallenberger, "Rapid Prototyping Directly from the Vapor Phase," *Science*, Vol. 267, pp1274-5

4. G. Zong, R. Carnes, H. G. Wheat and H. L. Marcus, "Solid Freeform Fabrication by Selective Area Laser Deposition," *Solid Freeform Fabrication Proceedings*, The University of Texas at Austin, 1990, pp83-90

5. B. R. Birmingham, J. V. Tompkins and H. L. Marcus, "Silicon Carbide Shapes by Selective Area Laser Deposition Vapor Infiltration," *Solid Freeform Fabrication Proceedings*, The University of Texas at Austin, 1994, pp348-355

6. J. E. Crocker, K. J. Jakubenas, S. Harrion and H. L. Marcus, "SALDVI Optimization for the Tetramethylsilane – Silicon Carbide System," *Solid Freeform Fabrication Proceedings*, The University of Texas at Austin, 1997, To be published

7. G. R. Fitterer, "A New Thermocouple for the Determination of Temperatures up to at least 1800°C," *AIMME Transaction*, V105, 1933, pp290-301

8. Helena Westberg, Mats Boman, Ann-Sofie Norekrans and Jan-otto Carlsson, "Carbon Growth by Thermal Laser-assisted Chemical Vapor Deposition," *Thin Solid Films*, V215, 1992, pp126-133

9. H. O. Pierson, "Handbook of Carbon, Graphite, Diamond and Fullerenes: Properties, Processing and Applications," Noyes Publications, New Jersey, 1993

SALDVI Optimization for the Tetramethylsilane - Silicon Carbide System

James E. Crocker, Kevin J. Jakubenas, Shay Harrison, Leon L. Shaw, and Harris L. Marcus
Institute of Materials Science
University of Connecticut
Storrs, CT

Selective Area Laser Deposition Vapor Infiltration (SALDVI) of silicon carbide powder infiltrated with silicon carbide deposited from tetramethylsilane (TMS) was studied. The effects of deposition time, temperature, and gas precursor pressure are discussed. The discussion centers on the efforts to properly balance these parameters to produce multi-layered shapes with structural integrity, particularly for use as the matrix material for shapes containing embedded devices. This includes optimizing scan speed, deposition temperature, and gas pressure to maximize infiltration to increase density and layer to layer bonding, and minimize excessive deposition to maintain critical dimensions. Initial powder properties are also optimized to minimize bulk motion in the powder bed during deposition, which was observed and identified as a mechanism that reduces inter-layer bonding.

Introduction

The ability to fabricate structurally sound complex shapes quickly and directly in the desired final material without post processing is the ultimate goal of Solid Freeform Fabrication. One possible route toward direct single step fabrication of a variety of metals, ceramics, and composites is the Selective Area Laser Deposition Vapor Infiltration (SALDVI) process[1]. SALDVI builds shapes by selectively infiltrating layers of powder with material thermally decomposed from a reactive gas. The hot spot generated by directing a laser beam onto a powder bed defines both the selective nature and spatial resolution of the process. Scanning the beam across the powder bed defines each two dimensional layer. Each additional layer is produced by spreading a measured layer of powder on the previous layer and scanning the beam in the desired 2-D pattern. Under the proper process conditions, the layer is simultaneously infiltrated and bonded to the previous layer. In this manner a 3-D shape is built consisting of powder particles bonded within a matrix of material deposited from the reactive gas or gas mixture. Because material is added from the gas phase to the powder during the SALDVI process, high densities are possible without post processing or shrinkage considerations.

The infiltration of powder by laser-induced gas decomposition distinguishes SALDVI from other gas phase SFF approaches. For example, Selective Area Laser Deposition (SALD) builds shapes entirely from thermally decomposed gases. Such SALD processes have been used for fabricating rods and fibers of constant diameter[2] and varying diameters[3], springs and helixes[4], in complex micro devices composed of rods of various orientations[5], and in the joining of ceramics[6]. The advantage of SALDVI in producing 3-D bulk shapes from sliced CAD models is that the uninfiltrated powder provides a support structure for producing overhangs. Also, confining the deposition to thin powder layers provides dimensional control in the third dimension, which can be a difficulty in SALD due to unstable growth kinetics[7]. Furthermore, SALDVI provides additional opportunities over SALD to tailor the local chemistry and microstructure.

The SALDVI process as a SFF method was introduced with the infiltration of SiC powder with SiC deposited from the thermal decomposition of tetramethylsilane (TMS, SiC_4H_{12}) gas[1]. This initial effort investigated the effect of some important process parameters involved in SALDVI: gas pressure, powder size, and heating time. The necessary interactions between the laser, reactive gas, and powder bed such as reflectivity, absorptivity, and transmissivity relevant for the SALDVI process were discussed. Multiple layer bulk shapes of SiC were fabricated; however, poor mechanical bonding between adjacent layers was identified as a key factor limiting structural integrity. This paper builds on that initial research in the development of the SALDVI SiC system. Process improvements are discussed including the use of feedback from an optical pyrometer to control the laser power and video monitoring of the powder bed during the deposition process. The focus is the effect of processing conditions on the bonding of adjacent layers. Adequate bonding between adjacent layers is required for structural integrity of the bulk shape and in using the SALDVI shapes in the fabrication of embedded devices[8]. Single and multiple layer samples were fabricated using a scanned laser beam. Characterization includes microscopic observations of the infiltration density and the layer-to-layer bonding. The SALDVI system used in these experiments[9] consists of a 50 watt CO_2 laser and a fully automated powder delivery, closed loop temperature control, and laser scanning system.

Closed Loop Temperature Control

One of the most important processing parameters in the densification of a powder bed by vapor infiltration is thermal history. For a given laser beam power profile, the distribution of temperature in the powder bed initially depends on the optical properties (reflectivity and absorptivity) and thermal properties (thermal conductivity) of the powder. As the infiltration of the powder proceeds, the optical characteristics and the thermal conductivity of the substrate change with time. As the SALDVI process proceeds, the part becomes larger, denser and a better heat sink, especially when depositing a good thermal conductor like SiC. Thus, more laser power is required to maintain a given temperature. To smooth out these temperature fluctuations throughout the infiltration process, feedback from an optical pryometer is used to continually adjust the input voltage to the laser. The pyrometer output is compared to a target temperature parameter set by the operator at the beginning of an infiltration experiment. Any difference in temperature between the pyrometer reading and this target temperature parameter is used to modulate the laser power. Using this closed loop control system, infiltration experiments have been performed at a constant pyrometer value. It is important to note that the temperature profile in the substrate due to laser beam heating is not uniform. Rather, it follows the gaussian-shaped profile of the incident laser beam. So while the pyrometer reading gives an indication of the temperature of the powder bed, it is misleading to describe a temperature distribution with a single number. Hence we use the term target temperature parameter rather than referring to the pyrometer reading as the absolute deposition temperature.

Effect of the Target Temperature Parameter on Infiltration of Single Layers

The sensitivity of the infiltration to the target temperature parameter is illustrated in Figure 1. The cross-sections reveal the single layer deposition and infiltration into a thick

powder layer at target temperature parameter values of 975, 1000, and 1050°C. Infiltration density increases significantly when the target temperature parameter increases from 975 to 1000°C. Further increase to 1050°C does not improve the infiltration into the powder bed. Rather, gas phase material deposits primarily at the top surface of the powder layer in a SALD mode, sealing off the powder bed and preventing further infiltration. This effect is due to the strong dependence of the decomposition rate on temperature coupled with the existence of higher temperatures at the powder surface due to laser surface heating. The result is a thick layer of SALD material deposited on a poorly infiltrated powder layer, obviously an undesirable result for SALDVI. Thus, a target temperature parameter value of 1000°C gives the optimum infiltration for SALDVI.

Effect of Scan Speed on Infiltration of Single Layers

Heating time is a critical parameter in SALDVI. For a scanned beam, the time duration that a given area remains heated depends on the beam diameter and the speed at which it is scanned across the powder bed. Figure 2 shows infiltration cross-sections for a 3.5-mm diameter beam scanned at three scan speeds. The infiltration density increases as the scan speed decreases. At a scan speed of 5 μm/s, significant infiltration occurs to depths greater than 400 μm into the thick powder layer.

Effect of Gas Precursor Pressure on Infiltration of Multiple Layers

In order for SALDVI to be useful in fabricating 3-D shapes, processing conditions that simultaneously densify a particular layer as well as bond it to the previous layer must be identified. Figure 3 shows the effect of varying the tetramethlysilane precursor gas pressure on infiltration and bonding of adjacent layers. Each sample consists of two 250 μm thick layers on a thick base layer. The infiltration density is low at a TMS pressure of 5 torr, increases at 10 torr, and increases further at 20 torr. At 20 torr there is significant infiltration and bonding between adjacent layers, although some isolated porosity remains.

Effect of Scan Geometry on Interlayer Bonding of Multiple Layers

The scan geometry used in the target temperature parameter, scan speed, and gas pressure experiments discussed above consisted of simple straight line scans in which the laser was turned on, scanned at a given speed for 10 mm, and then turned off. Using the best combination of these parameters, we obtain cross-sections showing good infiltration and bonding between adjacent layers as in Figure 3c. Larger and more complex shapes, such as squares, rectangles, and disks, are fabricated by scanning a series of lines separated by a given scan spacing. Figure 4 shows a cross-section of a multiple layer rectangle scanned at a beam spacing of 3 mm. The infiltration density within individual layers is high (Figure 4a), however, a significant separation is apparent between adjacent layers (Figure 4b). Video observations of the powder bed during the SALDVI process reveal a powder bubbling effect occurring in the powder bed. Gas appears to be bubbling up through the surface powder layer from near the submerged previous layers. Although not yet completely understood, possible explanations of this flow may be volume expansion of the gas in the powder bed due to decomposition of the TMS molecules or natural convection effects due to the large temperature gradients. The powder bubbling has been

minimized by using larger SiC particles in the powder bed, and by adjusting the composition of the gases in the reactive gas mixture. It is possible that this powder levitation phenomenon is the cause of the separation between layers observed in some multiple layer shapes.

Conclusions

SALDVI of SiC has been shown to depend strongly on three parameters: temperature, heating time, and gas pressure. Multiple layer deposits of low porosity have been built by optimizing these parameters. The primary challenge in building SiC shapes without post processing is the gap between layers, believed to be caused by bulk motion of powder during infiltration. Several approaches are under consideration to overcome this challenge, including closer examination of the effects of gas mixture, and powder size.

Acknowledgements

The authors gratefully acknowledge the generous support of the Office of Naval Research (grant #N00014-95-1-0978) and ARPA/ONR (#N00014-96-1-1299).

References

1. B.R. Birmingham and H.L. Marcus, "Silicon Carbide Shapes by Selective Area Laser Deposition Vapor Infiltration," Proceedings of the Solid Freeform Fabrication Symposium, The University of Texas at Austin, 1994, pp. 348-355.
2. F.T. Wallenberger and P.C. Nordine, "Amorphous Silicon Nitride Fibers Grown From the Vapor Phase," *J. Mater. Res.*, vol. 9, No. 3, March 1994.
3. J.L. Maxwell, J. Pegna, and D.V. Messia, "Real-time Volumetric Growth Rate Measurements and Feedback Control of Three-dimensional Laser Chemical Vapor Deposition," to appear in *Applied Physics A*, 1996.
4. H. Westberg, M. Boman, S. Johansson, and J-A. Schweitz, "Free-standing Silicon Microstructures Fabricated by Laser Chemical Processing," *J. Appl. Phys.* 73 (11), 1 June 1993.
5. M. Wanke, O. Lehmann, K. Muller, Q. Wen, and M. Stuke, "Laser Rapid Prototyping of Photonic Band-Gap Microstructures," *Science*, vol. 275, 28 February 1997.
6. J.V. Tompkins, B.R. Birmingham, and H.L. Marcus, "Ceramic Joining by Selective Beam Deposition," Proceedings of the Solid Freeform Fabrication Symposium, The University of Texas at Austin, 1995, pp. 409-416.
7. G.S. Zong, R. Carnes, H.G. Wheat, and H.L. Marcus, "Solid Freeform Fabrication by Selective Area Laser Deposition," Proceedings of the Solid Freeform Fabrication Symposium, The University of Texas at Austin, 1990, pp. 83-90.
8. L. Sun, K.J. Jakubenas, J.E. Crocker, S. Harrison, L. Shaw, and H.L. Marcus, "Fabrication of In-Situ Silicon Carbide/Carbon Thermocouples by SALD," Proceedings of the Solid Freeform Fabrication Symposium, The University of Texas at Austin, 1997.
9. S. Harrison, J.E. Crocker, T. Manzur, and H.L. Marcus, "Solid Freeform Fabrication at The University of Connecticut," Proceedings of the Solid Freeform Fabrication Symposium, The University of Texas at Austin, 1996, pp. 345-348.

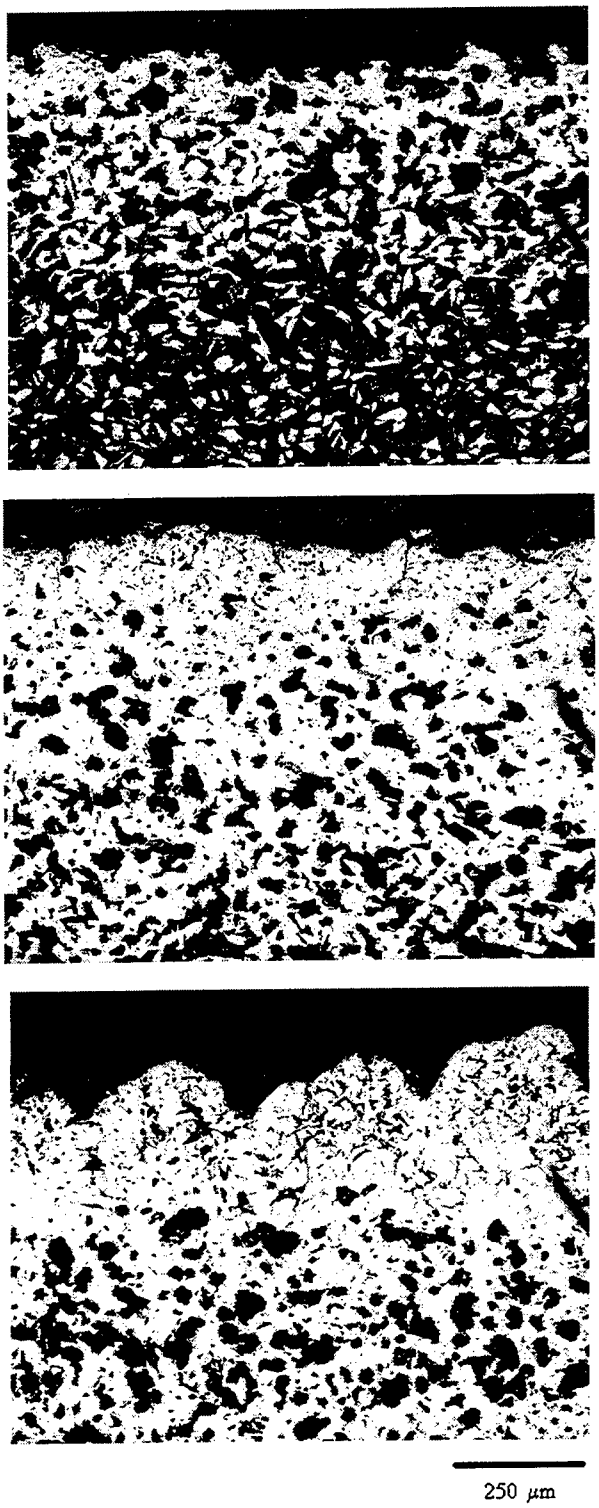


Figure 1. Effect of Target Temperature Parameter
(a) 975 °C (b) 1000 °C (c) 1050 °C
10-20 μm SiC powder, 25 torr TMS + 25 torr H_2, 5 μm/s scan speed, single layer into thick powder

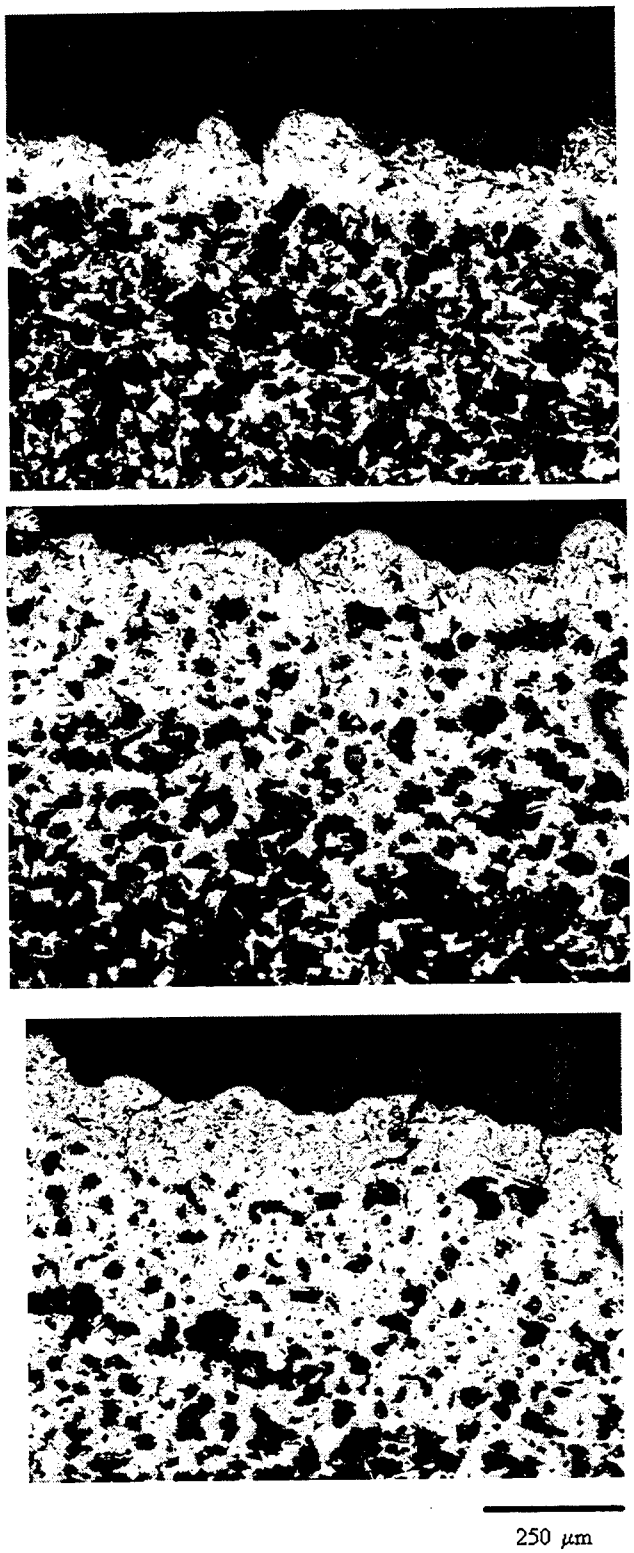


Figure 2. Effect of Scan Speed
(a) 20 μm/s (b) 10 μm/s (c) 5 μm/s
10-20 μm SiC powder, 1100 °C target temperature parameter,
25 torr TMS + 25 H_2, single layer into thick powder

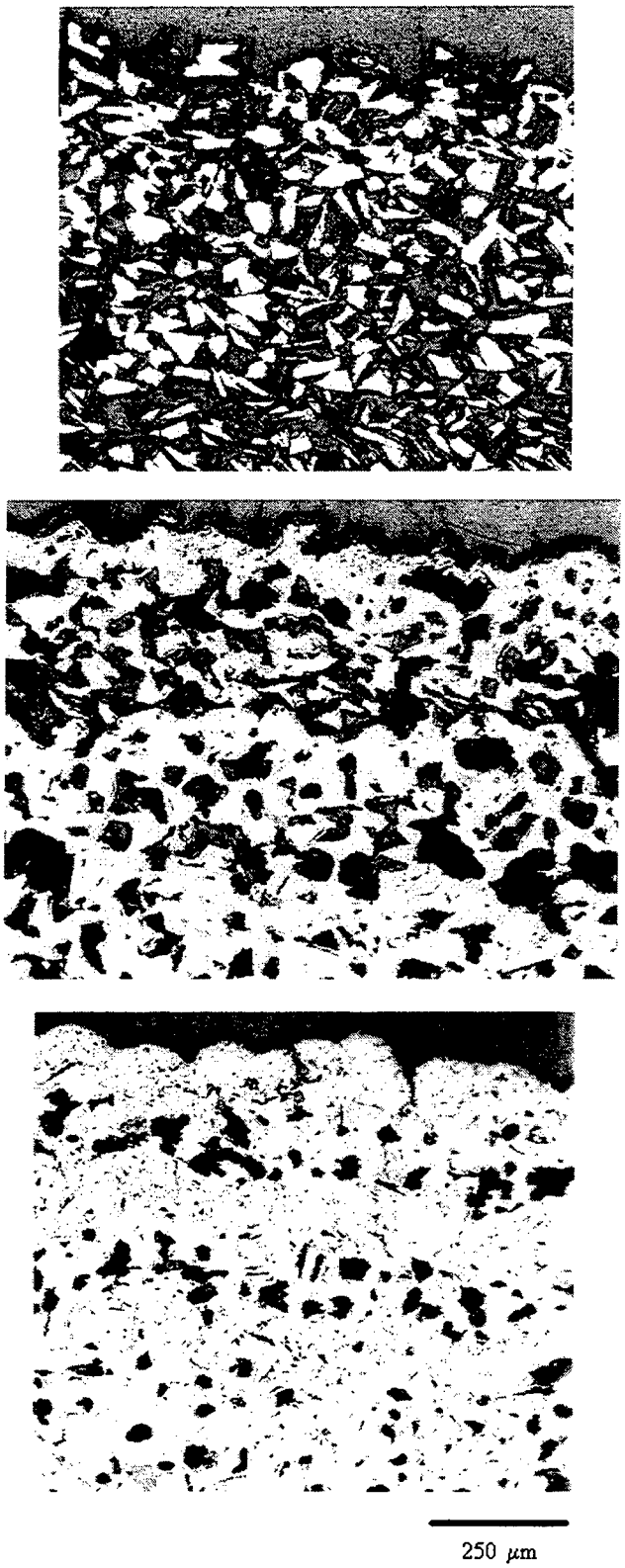
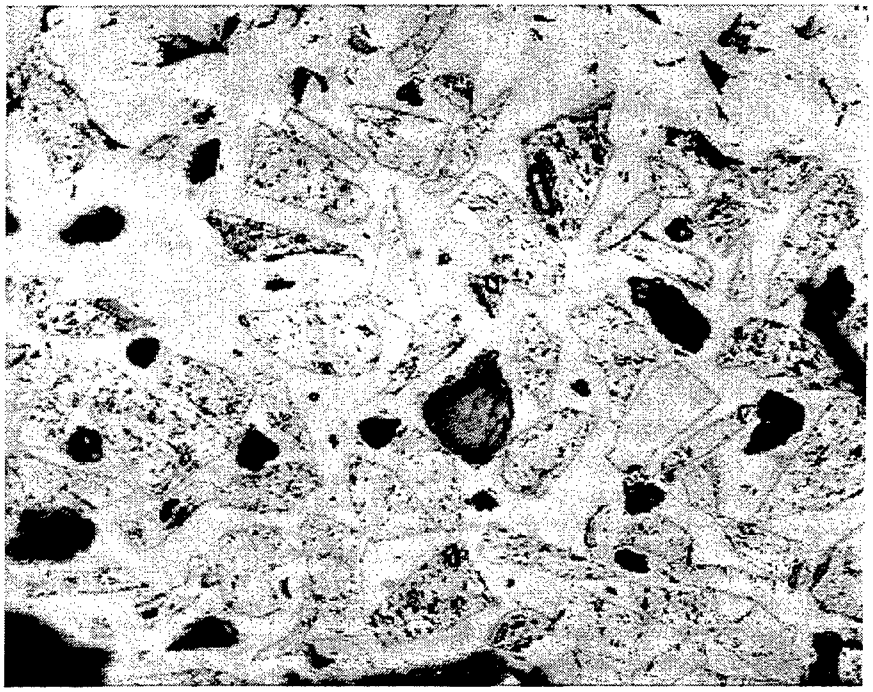


Figure 3. Effect of Tetramethylsilane Gas Pressure
(a) 5 torr (b) 10 torr (c) 20 torr
60-80 μm SiC powder, 1000 °C target temperature parameter,
5 μm/s scan speed, two 250 μm layers on a thick base layer



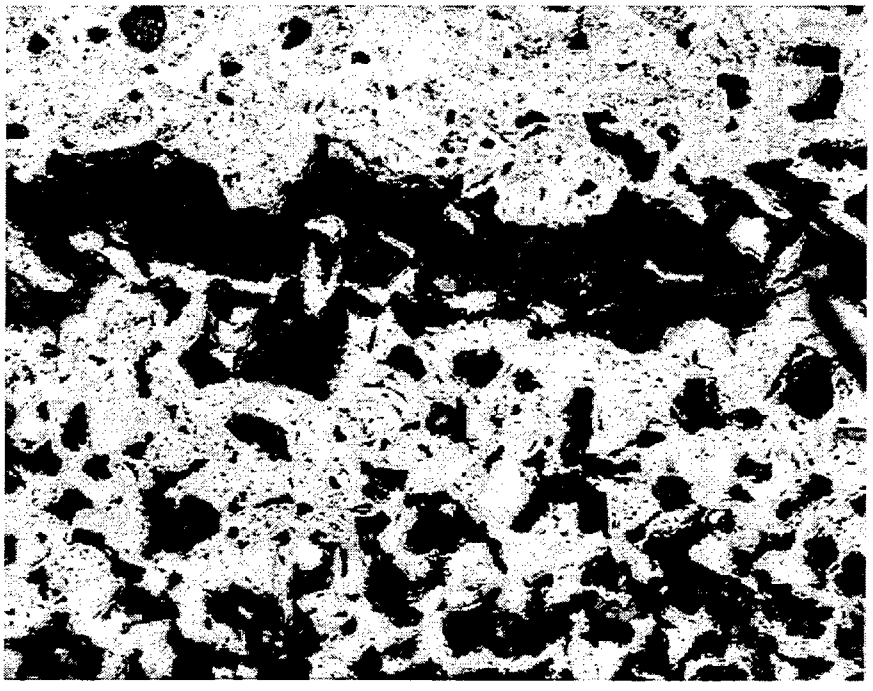


Figure 4. Multiple layer rectangular shape
(a) Infiltration within a layer (b) Gap between adjacent layers
10-20 μm SiC powder, 1000 °C target temperature parameter,
25 torr TMS + 25 torr H_2, 5 μm/s scan speed, 3 mm scan spacing

High Pressure, Convectively-Enhanced Laser Chemical Vapor Deposition of Titanium

James Maxwell
Ramnath Krishnan
Suresh Haridas
Institute for Micromanufacturing
Louisiana Tech University

Laser chemical vapor deposition is a freeform technique that can generate three-dimensional structures from organometallic or metal halide precursors. To obtain enhanced growth rates, a novel high pressure reactor has been constructed where impinging jets of volatile fluids are heated and pyrolyzed to create parts. Argon Ion and Nd:YAG lasers have been used to selectively generate three-dimensional titanium shapes from titanium tetrachloride, titanium tetrabromide, and titanium tetraiodide, at pressures up to 3.0 atmospheres. Emission lines characteristic of the reaction rate have been identified which will allow feedback control of the reaction rate. The process is being optimized to obtain high deposition rates, energy efficiency, and desirable material morphologies. A feedback control system is required to generate 3-D structures with dimensional accuracy and predictable deposition rates.

I. Introduction

This paper reports the development of a new process which holds promise for the desktop manufacture of metal and ceramic parts at the centimeter scale or larger. Termed high-pressure, convectively-enhanced, laser chemical vapor deposition (HPCE-LCVD), the process employs convective flows of precursor gases to enhance the growth rate of vapor-phase solid freeform fabrication (SFF). Preliminary results in the growth of titanium from the titanium halides at moderate pressures and flowrates (up to 3 atmospheres) are presented herein. These early results will be used to evaluate the utility of each precursor for future use in the HPCE-LCVD apparatus.

A) Three-Dimensional LCVD

Derived from chemical vapor deposition (CVD), *pyrolytic* laser chemical vapor deposition (LCVD) employs a scanning laser beam to selectively *heat* portions of a substrate, and in this way induce a localized CVD reaction.[1] If the growth is not self-limiting either due to the deposit material being highly-conductive,[2] being highly-reflective of the laser light,[3,4] or having a low melting point,[5] then high-aspect ratio microstructures may be grown, such as those shown in Fig. 5. Careful adjustment of the laser power may be required during the transient growth[6] of metals to obtain continuous, uniform dimensions--as will be seen in this paper, where the growth of titanium is thermally-self-limiting at low pressures (see Fig. 3).

Several authors have explored the possibilities of three-dimensional growth using LCVD, prototyping rods,[7] fibers,[8] coils,[9] blocks,[10] and more complex structures.[11] Rods have been grown of aluminum,[12] alumina,[13] gold,[14] nickel,[15] tungsten,[16] silicon,[17] chromium-oxide,[18] iron,[19] steel,[20] and boron.[21] It is noteworthy, however, that the materials with the greatest thermal conductivities, e.g. aluminum, gold, and tungsten, are highly irregular in shape, whilst

continuous, steady-state rod growth was readily demonstrated with the other materials. Materials with high thermal conductivity also tend to grow more broadly, or in the extreme case, only as hemispheres.[22] Thus, controlled growth of highly-conductive metals is a needed goal.

One method for increasing the aspect ratio of a metal deposit is to use a pulsed-laser or a chopped beam.[23] This method was employed throughout the Ti growth experiments. Another method for obtaining controlled freeform growth was previously demonstrated by the author;[24] where spectral emissions generated during an LCVD reaction were measured to determine the volumetric growth rate. This measure was then used to automatically compensate for errors in the growth, adjusting the incident laser power and other process inputs in real-time. This technique will be required for controlled growth of titanium, whose bulk thermal conductivity is 21.9 W/m-K at 300K.

B) Mass Transport Effects and the Growth Rate

While low-pressure LCVD processes are much too slow for macro-scale prototyping, the volumetric deposition rate rises with pressure. At pressures above 1 atmosphere, Wallenberger *et al.* recently reported volumetric growth rates of nearly 0.1 mm^3/s.[25] This rate increase occurs from greater adsorption of the precursor onto the reaction surface, as well as from enhanced natural convection--which permits more rapid transport to (and from) the surface. The growth rate continues to rise with pressure until the fluid reaches a critical pressure;[26] for the metal halides, this critical pressure typically lies in the range of 25-100 atmospheres. Thus, by directing a forced flow of precursor fluids onto a heated reaction zone, an enhanced deposition rate is obtained, allowing parts to be grown quickly. This is the principle behind the HPCE-LCVD process. An added benefit is that the use of high pressures favors the growth of amorphous or fine-grained polycrystalline materials--which possess greater strength than cast, extruded, or sintered materials. These effects will be demonstrated later in this paper, where fine-grained, titanium rods were grown at enhanced rates.

C) Chemical Vapor Deposition of Titanium

The titanium halides are commonly employed for the chemical vapor deposition of titanium. These are pyrolyzed either directly, or by hydrogen reduction at temperatures above 1500 K.[27] The overall reactions are:

$$TiX_{4(g)} \rightarrow Ti_{(s)} + 2X_{2(g)}, \qquad (1)$$

where X=Cl, Br, or I, respectively. Titanium thin films have been deposited from $TiCl_4$,[28,29] as well as from $TiBr_4$.[30] TiO_2 films have also been deposited[31] from a mixture of $TiCl_4$, H_2, and CO_2--while titanium dioxide rods have been grown from $TiCl_4$, H_2, and atmospheric oxygen.[32]

II. Experimental

A) Moderate Pressure Experiments (to 1.5 bar)

The titanium growth experiments were carried out in a heated stainless steel reactor as shown in Fig. 1. The reactor (A) consisted of a six-way cross, with windows on two sides, one for laser input (B) and another for cross-illumination of the sample (not shown). A UV-grade fused-silica window was located for observation at right angles to the laser input and opposite the illumination source. A microscope and CCD camera were used to monitor the growth.

Throughout the experiment, a 90 mm focal-length, gradient-index lens (C) was used to focus the gaussian input beam to a $1/e^2$ spot size of approximately 50 microns. A Coherent Innova 70 argon-ion laser with output power to 2.2 W TEM_{oo} (8 Watts Multimode) was used at

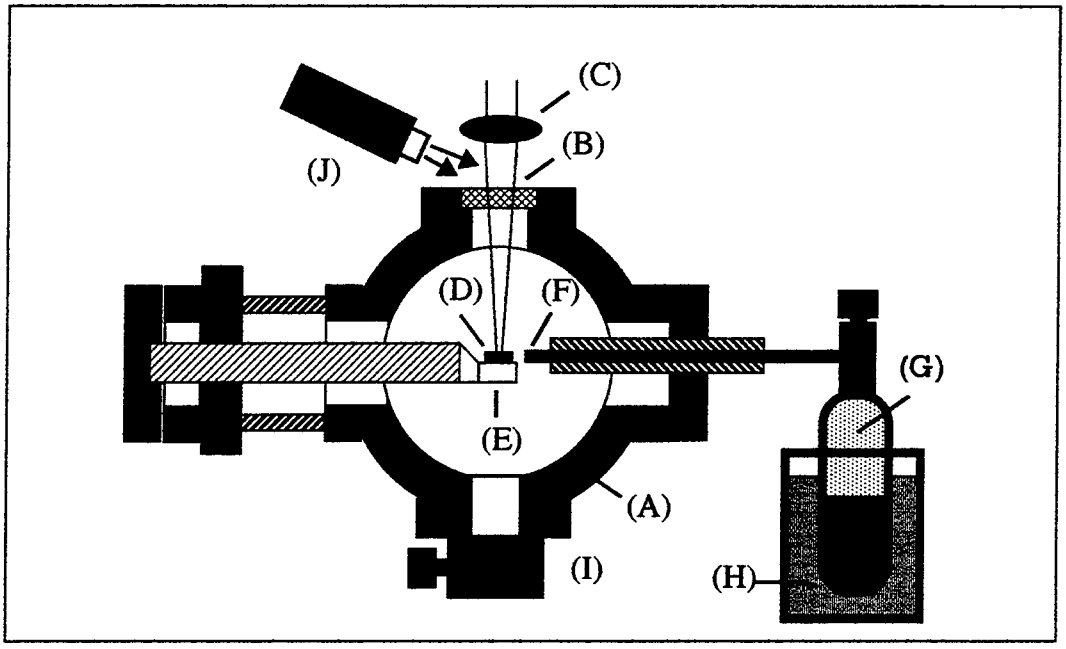


Fig. 1: Apparatus for Moderate Pressure Experiments

the primary 488/514 nm lines; this laser was readily interchanged with a Lee Laser 40 W (10 W TEM_{oo}) Nd:YAG laser. This was operated in cw mode at 1064 nm.

A variety of substrates (D) were employed to initiate sample growth. Experiments were performed using bare titanium, glassy carbon, and graphite disks. The latter two were chosen for their low spectral reflectances and high melting points. All substrates were mounted on a sample holder (E), attached to a micromanipulator, allowing the substrate to be scanned relative to the beam focus.

Reactants were introduced into the reactor via a 1/16" stainless steel entrance tube (F), which could be independently heated at the nozzle exit to temperatures up to 2400 K. Since titanium tetrachloride is a liquid at room temperature with a boiling point of 137 C, and titanium tetrabromide and tetraiodide boil at 230 C and 377 C respectively, each precursor was first heated in a sample cylinder (G) to obtain a sufficient vapor pressure for growth. The sample cylinders were heated in a beaker of water or ethylene glycol (H). During the static growth experiments, the precursor vapor pressure was prescribed by the temperature of this heated sample cylinder (G), while for the convective experiments, the roughing valve (I) was opened, allowing the overall chamber pressure to drop to less than 50 mbar; in this way, a constant flow was obtained down the 1/16" stainless steel entrance tube (F), which could be preheated and directed toward the sample (D). The entire assembly was wrapped with heater tape and insulation, except for the windows, to maintain a constant chamber temperature above that of the sample cylinder. To eliminate condensation of the precursor on the laser window, a hot air gun (J) was directed at the window, at a temperature equal to or greater than that of the chamber.

B) Design of the High-Pressure Experimental Apparatus (to 300 bar)

In parallel with the apparatus described above, a high-pressure vessel has been constructed which will allow further investigation of metal deposition at much greater growth rates. The high-pressure chamber has been designed for operation up to 300 atmospheres, and has three fused-silica, Poulter-sealed windows, as shown in Fig. 2, allowing up to three orthogonal laser beams to be focused simultaneously to a common point (A). The high pressure reactor (B) is enclosed inside a heavy steel dome (C), which acts both as furnace and fume hood. Two

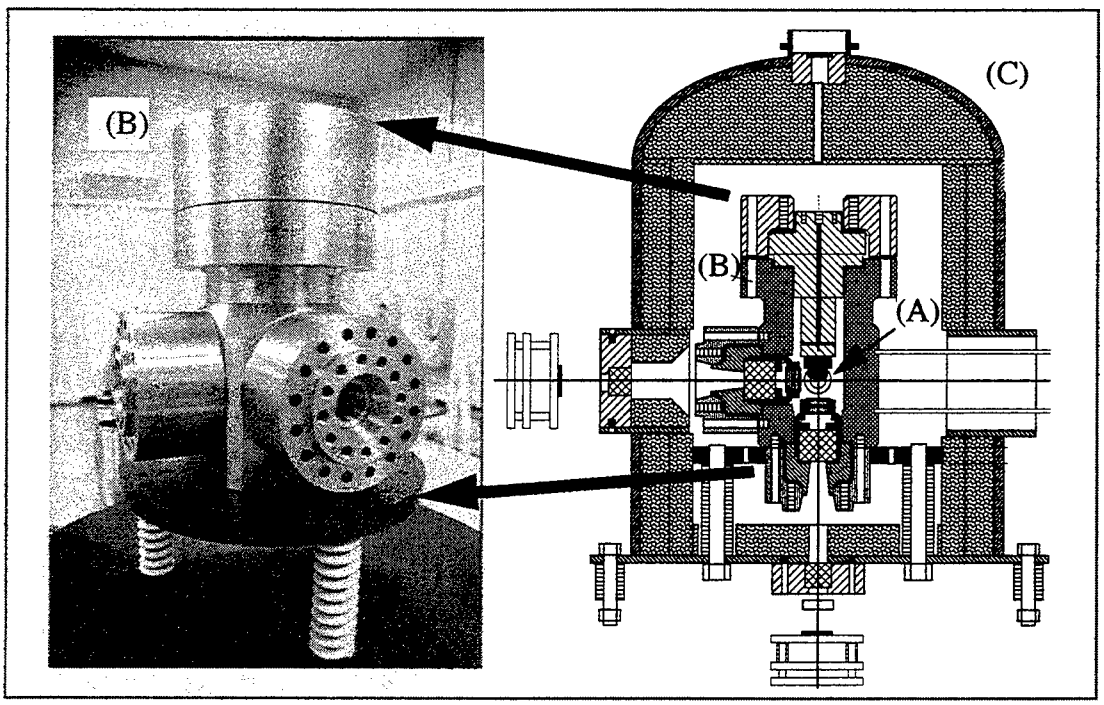


Fig. 2: High Pressure Assembly and Reactor

3000 W heaters circulate hot air around the reactor, allowing the windows to be warmed to the same temperature as the chamber. Laminated graphite and stainless steel gaskets are being employed to seal the windows and reactor cap, allowing chamber temperatures of up to 500 C. Precursor gases are supplied from a high-pressure evaporator (not shown), and are directed toward the laser focus (A) through a small nozzle. The chamber is evacuated using a simple Venturi pump, and reaction by-products are passed through a burn box to the clean room scrubber.

To scan the laser focus inside the chamber, four high-pressure motion feedthroughs are being installed in the lower portion of the reactor; these are attached to internal stages which position the sample and allow for three linear and one rotational degree of freedom. In addition, two orthogonal beams will be modulated at the common focus, providing one more degree of freedom (tilt). In this way, completely arbitrary structures may be fabricated.

III. Results

Experiments with the titanium halides at *low pressures* were unimpressive. At the room-temperature vapor pressure of $TiCl_4$ (i.e. at abt. 13 mbar), no growth was observed on the glassy carbon substrates up to their softening temperature (abt. 1500 K). At higher pressures, the *transient* growth rate of each precursor improved steadily on the graphite and titanium substrates. Samples (A), (B), and (C) in Fig. 3, were successfully grown at $TiCl_4$, $TiBr_4$ and TiI_4 vapor pressures of 330, 8.5, and 180 mbar, respectively, and at transient rates of up to 0.37 μm/s. Titanium tetrachloride, with its greater vapor pressure, exhibited the highest growth rates, but only at temperatures approaching the melting point of Ti (1953 K). To initiate growth with this precursor, we first ablated a portion of the titanium substrate, then lowered the average power (or defocused the beam) until the substrate could no longer be melted (10 W, 60 μm spot size). Growth could then be initiated at incident powers as low as 4.3 W. Using the well-known expression for the peak temperature rise of a Gaussian beam on a semi-infinite solid (1):

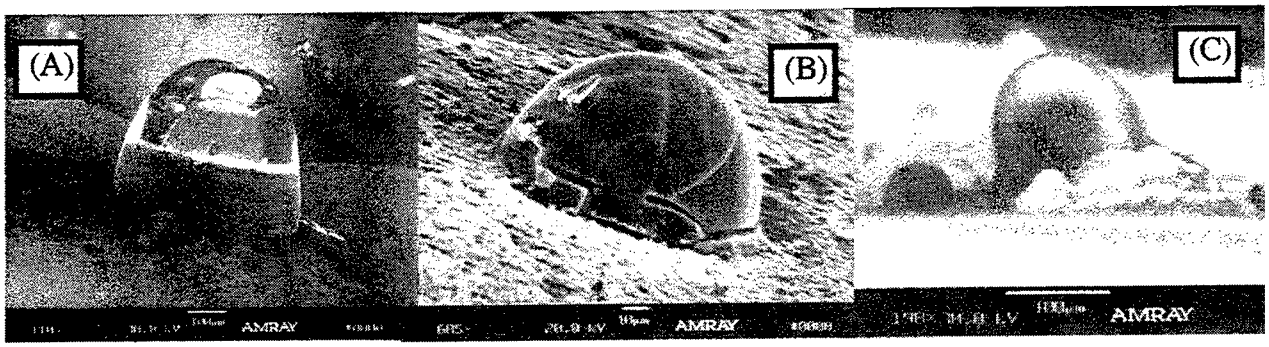


Fig. 3: Titanium Shapes from the Ti Halides

$$T_p = \frac{P(1-R)}{\sqrt{\pi\kappa\omega_o}}, \qquad (1)$$

this initial power indicates a $TiCl_4$ threshold deposition temperature of approximately 1130 K. Below this temperature no thick Ti films or rods were formed.

At similar incident powers, titanium iodide yielded growth rates nearly commensurate with that of $TiCl_4$, although at a fraction of the vapor pressure. It also exhibited a lower threshold deposition temperature of abt. 870 K (3 W incident power), which is consistent with reports that it possesses an activation energy lower than that of $TiCl_4$.[33] The growth rate from $TiBr_4$ was less impressive, giving rates of at most 0.04 μm/s, at pressures up to 8.5 mbar. Thermodynamic calculations, minimizing the Gibb's free energy, confirmed that little deposition is likely to occur from pure $TiBr_4$ at temperatures up to the melting point of titanium.[34] However, further experimentation at higher vapor pressures will be necessary to determine the potential of this precursor for HPCE-LCVD.

Overall, titanium growth tended to be thermally self-limiting. This is illustrated in Fig. 4, where rods were grown for 30 minutes each from TiI_4 at a variety of vapor pressures. Note that

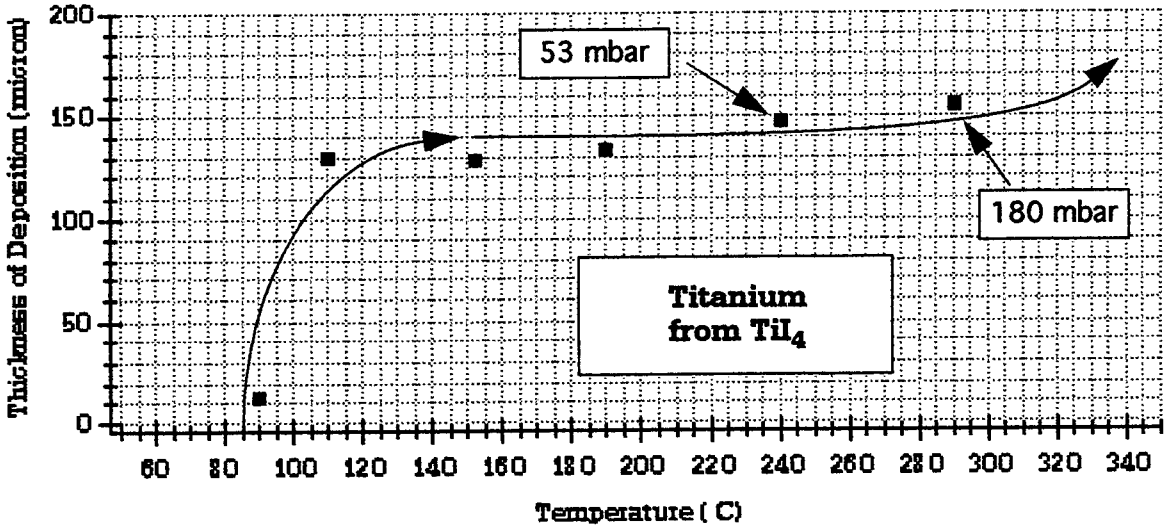


Fig. 4: Low-Pressure Transient Titanium Growth vs. Evaporator Temp.

after initial rapid transient growth, each rod approaches a limiting height. This can be explained either by rapid cooling as the deposit grows (and losses increase to its surroundings), or by overheating and melting as the rod grows away from the substrate (which acts diminishingly as a heat sink). To explore this self-limiting effect, the laser power was ramped up slowly, from an initial power of 6 W to over 10 W; surprisingly, this did not yield tall deposits as well as the opposite approach, i.e. lowering the power from an initially high temperature. Thus, since insufficient convection occurs, the temperature increases[6] as the rod lengthens, and the rod subsequently overheats and melts. Evidence of melting can also be seen in Fig. 3 (A), where the self-limiting rod height was attained. Clearly, steady-state[6] rod growth cannot be obtained at low gas pressures unless the temperature of the deposit is lowered continuously in a controlled manner--and with the titanium halides little latitude exists between the temperature at which growth initiates and the melting point of Ti--making the reaction especially difficult to control.

At *higher* vapor pressures, however, gas convection begins to contribute significantly to the heat losses, giving rise to a steady-state temperature distribution at the rod tip--and allowing continuous 3-dimensional growth without temperature control. For titanium tetrachloride, this was realized at pressures above 2000 mbar, as can be seen in Fig. 5. At 3000 mbar, Ti rods over 1 mm long were grown without changing the laser focus or the average power. By gradually increasing the laser power as the rod grew (to compensate for the stationary laser focus and diminishing beam intensity), rods up to 4 mm long could be grown at axial rates up to 1.4 μm/s. In addition, rods grown at the highest pressures exhibited no apparent grain structure, down to 100 nm or less. This confirms the results of Wallenberger,[25] who also obtained fine-grained

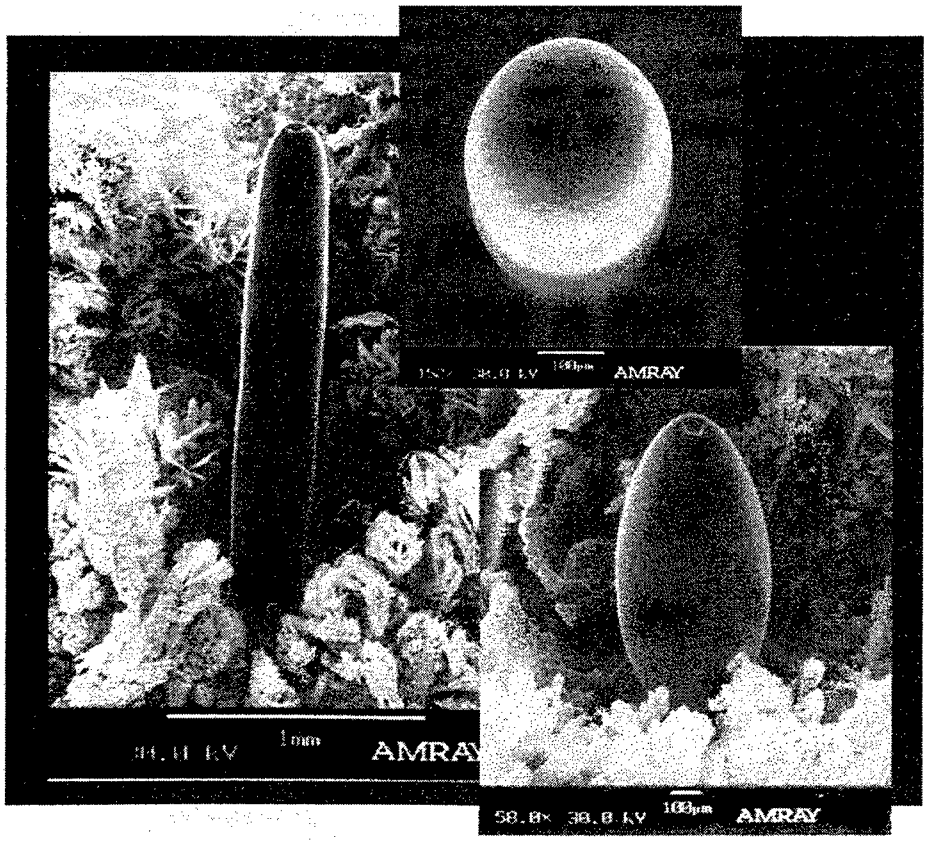


Fig. 5: Titanium Rods Grown at High Pressure

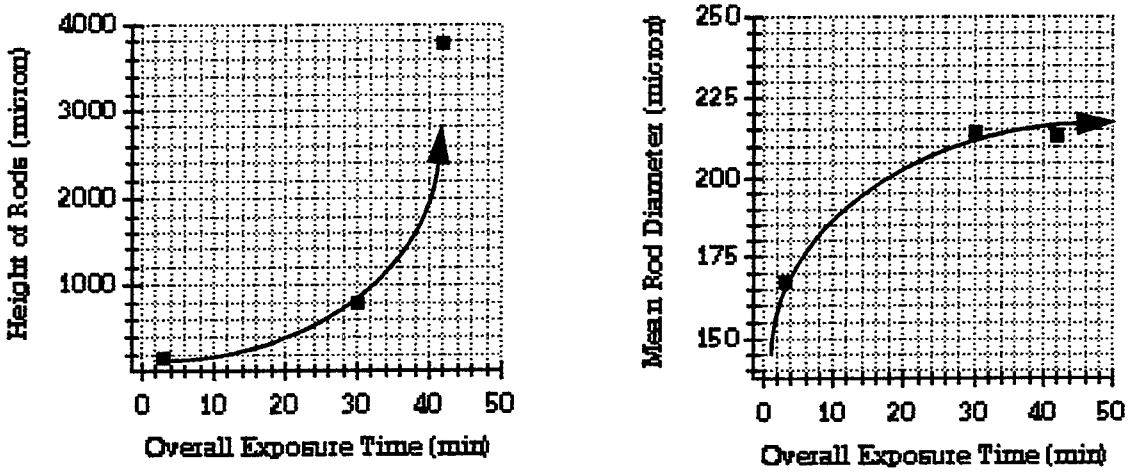


Fig. 6: Rod Height and Diameter vs. Laser Power

and amorphous rods at high vapor pressures. In Fig. 6, the height and diameter of the Ti rods are also plotted vs. exposure time. As expected for steady-state growth, the rod height increases without bound, and the rod diameter approaches a constant (steady-state) radius.

During the high-pressure reaction, a broad band of blue-violet emission lines were also observed, well below the blackbody emissions--which appeared to peak in the yellow portion of the spectrum. These have been identified as the strong 455-468 nm emission lines of the singly ionized Cl_2^+ molecule, a by-product of the $TiCl_4$ reaction.

Analysis of the Ti rod composition was carried out with an X-ray diffractometer. Combined results from several samples indicated that the rods were primarily pure Ti, with small quantities of TiO_2. No $TiCl_3$ was found to be present in the rods, although this solid by-product formed readily in a ring around the Ti rods. The titanium rods were exposed to atmospheric oxygen prior to the X-ray analysis. Further measurements will be conducted using a scanning Auger microprobe to determine the extent of oxide contamination within the rods.

IV. Conclusions

To obtain continuous Ti growth, sufficient precursor pressure must be present for natural convection to establish a constant temperature distribution over the reaction zone. Without this convective heat loss, it is difficult to sustain growth; the temperature must be monitored continuously to avoid melting the deposit. In addition, gas convection enhances transport of the precursor to the reaction, raising the volumetric growth rate by more than an order of magnitude.

While steady-state growth may be obtained using $TiCl_4$ at high pressures, the greatest promise for HPCE-LCVD may be TiI_4, which exhibits the largest latitude between its threshold temperature and the melting point of titanium, facilitating growth control. Further work will study the deposit composition and growth rates of these precursors at significantly higher pressures--up to their critical points. In addition, the emission spectra discovered at 455-468 nm will be used to control the growth of the $TiCl_4$ reaction using the emissions feedback technique.

V. Acknowledgments

Our appreciation goes to the Louisiana Education Quality Support Fund (LEQSF) and the College of Engineering and Science at Louisiana Tech for their support of this work.

VI. Bibliography

1. Bäuerle, D., Springer Series in Chemical Physics 39, (1984), pp. 166-182.
2. Allen, S. D., Jan, R. Y., Edwards, R. H., Mazuk, S. M., Vernon, S. D., Proc. of SPIE, Laser Assisted Deposition, Etching, and Doping, Vol 459, (1984), pp. 42-48.
3. Meunier, M., Izquierdo, R., Desjardins, Thin Solid Films, Vol. 218, (1992), pp. 137-143.
4. Allen, S. D., Jan, R. Y., Mazuk, S. M., Vernon, S. D., J. Appl. Phys., Vol. 58, No. 1, (1 Jul. 1985), pp. 327-331. [344]
5. Westberg, H., Boman, M., Norekrans, A.-S., Carlsson, J.-O., Thin Solid Films, Vol. 215, (1992), pp. 126-133.
6. Maxwell, J. L., Ph.D. Thesis, Rensselaer Polytechnic Institute, (1996).
7. Bäuerle, D., Leyendecker, G., Wagner, D., Applied Physics A, Vol. 30, (1983), pp. 147-149.
8. Leyendecker, G., Bäuerle, D., J. Electrochem. Soc., Vol. 130, No. 1, (1983), pp. 157-160.
9. Westberg, H., Boman, M., IEEE MEMS Conference Proc., (Feb. 1992), p. 172.
10. Zong, G.-S., Ph.D. Thesis, University of Texas at Austin, (1992).
11. Wanke, M.C., Lehmann, O., Muller, K., Wen, Q, Stuke, M., Science, Vol. 275, (28 Feb. 1997), pp.1284-1286.
12. Rytz-Froidevaux, Y., Salathé, R. P., Gilgen, H. H., Physics Letters, Vol. 84A, No. 4, (27 Jul. 1981), pp. 216-218.
13. Lehmann, O., Stuke, M., Materials Letters, Vol. 21, (Oct. 1994), pp. 131-136.
14. Comita, P. B., Kodas, T. T., J. Appl. Phys., Vol. 62, No. 6, (15 Sep. 1987), pp. 2280-2285.
15. Kräuter, W., Bäuerle, D., Fimberger, F., Appl. Phys. A, Vol. 31, (1983), pp. 13-18.
16. Allen, S. D., Tringubo, A. B., J. Appl. Phys., Vol. 54, No. 3, (Mar. 1983), pp. 1641-1643.
17. Westberg, H., Boman, M., Johansson, S., Schweitz, J.-A., J. Appl. Phys., Vol. 73, No. 11, (1 Jun. 1993), pp. 7864-7871.
18. Arnone, C., Rothschild, M., Black, J. G., Ehrlich, D. J., Appl. Phys. Lett., Vol. 48, No. 15, (14 Apr. 1986), pp. 1018-1020.
19. Maxwell, J., Pegna, J., DeAngelis, D., Messia, D., Material Research Society Symposium Proceedings, v. 397 (B3.30): Fall 1995 Meeting, Boston, MA (Nov. 27--Dec.1, 1995).
20. Ibid.
21. Wallenberger, F. T., Nordine, P. C., Materials Letters, Vol. 14, No. 4, (1992), pp. 198-202.
22. Baum, T. H., Larson, C. E., High Temperature Science, Vol. 27, (1990), pp. 237-249.
23. Morishige, Y., Kishida, S., Appl. Phys. A, Vol. 59, (1994), pp. 395-399.
24. Maxwell, J., Pegna, J., DeAngelis, D., (Accepted for Publ.: Applied Physics A, Aug. 1996)
25. F.T. Wallenberger, P.C. Nordine, Science, 260, 66-68 (1993)
26. Bradley, R. S., High Pressure Chemistry, Pergamon Press, Oxford, NY (1965), p. 101.
27. Pierson, H. O., Handbook of Chemical Vapor Deposition, Noyes Publications, Westwood, NJ, (1992), pp. 146-148.
28. Izquierdo, R., Lavoie, C, Meunier, M., MRS Symposium, Vol. 158, (1993), pp. 141-146.
29. Alexandrescu, R., Cireasa, R., Dragnea, B., Morjan, I., Voicu, I., Andrei, A., Vasiliu, F., Popescu, C., Advanced Materials for Optics and Electronics, Vol. 5, (1995), pp. 19-30.
30. Chou, W. B., Azer, M. N., Mazumder, J., J. Appl. Phys., Vol. 66, No. 1, (1989), pp. 191-195.
31. Allen, S. D., J. Appl. Phys., Vol. 52, No. 11, (Nov. 1981), pp. 6501-6505.
32. Jakubenas, K., Marcus, H.L., Solid Freeform Fabrication Symposium, (1995), pp. 381-388.
33. Eizenberg, M., Materials Research Society Bulletin, Vol. 20, No. 11, (Nov. 1995), p.38.
34. Boman, M., Personal Communication, Univ. of Uppsala, Sweden (1997).

The LMP Process: Layered Metal Prototyping of Titanium from Condensed Thin-Films for Microelectromechanical Devices

James Maxwell
Sandesh Borse
Institute for Micromanufacturing
Louisiana Tech University

Layered prototyping of three-dimensional titanium micromechanical components was demonstrated using selected area laser photolysis of liquid-phase organo-metallic and metal halide thin films. Scanning KrF and XeF excimer lasers were employed at 248 and 351 nm, respectively, generating solid titanium traces from condensed precursor films. Multiple layers were patterned to produce high-aspect ratio titanium lines. Laser pulse repetition rate, scan rate, pulse energy, and layer thickness were related to the resulting layer topography. This process is a first step toward layered metal rapid prototyping of electronic packaging microstructures and microelectromechanical systems.

I. Introduction

Surface micromachining has been the primary means of fabricating microelectromechanical systems (MEMS) for over 15 years.[1] this process employs photolithography and selective chemical etching to obtain desired micromechanical forms from thin films. The purpose of this work was to demonstrate a method of selective deposition which performs the function of surface micromachining, but which also possesses all the advantages of a solid freeform fabrication tool. A process was desired which would allow electronic materials to be deposited, both metals and dielectrics, with a single instrument. In this way, rapid prototyping and complete integration of MEMS and supporting electronic packaging would be possible.

II. Background

Several alternatives to lithographic methods have been developed in the literature, which employ laser-induced deposition, and thus do not require a mask to obtain selective growth. Three-dimensional microstereolithography of photosensitive resins has been demonstrated by several authors.[2] Techniques which can be used to deposit metals were developed for the custom metallization and soldering of interconnects in microelectronics. Laser-induced electroplating,[3] for example, may be used to selectively plate metal onto a semi-conductive surface from a liquid electrolyte. Laser-induced electroless plating has also been demonstrated on metals and insulators.[4] Finally, lasers have been used to heat and decompose a variety of spun-on inks and liquid films.[5]

In this paper we will demonstrate the prototyping of titanium from thin liquid films of titanium tetrachloride. Since the bond energies of the $TiCl_4$ molecule correspond closely with the wavelength of the KrF laser (248 nm),[6] titanium tetrachloride can be dissociated directly by the laser light; this is termed photolysis. $TiCl_4$ can also be thermally decomposed, yielding solid titanium, according to the overall reaction:

$$TiCl_{4(l)} \rightarrow Ti_{(s)} + 2Cl_{2(g)}. \quad (1)$$

$TiCl_4$ has been explored previously as a gas-phase precursor for excimer laser-induced chemical vapor deposition (LCVD); Alexandrescu *et al.* recently demonstrated that the mechanism through which vapor phase Ti growth occurs,[7] is: first, *adsorption* of the vapor-phase $TiCl_4$ onto the growth surface; second, photolysis of the $TiCl_4$ to nuclei of Ti and adsorbed $TiCl_3$; and third, the thermal decomposition of additional $TiCl_4$ and $TiCl_3$ adsorbate by heating of the Ti nuclei. Thus, *gas-phase* photolysis of $TiCl_4$ contributes little to deposition of Ti during excimer-laser induced vapor deposition. This is borne out by other authors.[8,9] However, Meunier *et al.* proposed that photolysis of *adsorbed* $TiCl_4$ was the dominant growth mechanism for Ti films[10] during the initial stages of growth; while for Ti deposit thicknesses greater than 3 nm, laser heating became the dominant mechanism, yielding much greater growth rates (on the order of 2-7 nm/s). Mochizuki *et al.* additionally reported that the rate limiting step in the LCVD of Ti is not the adsorption of the $TiCl_4$, but the desorption of Cl_2.[11] For this reason, it is common practice to use hydrogen reduction of $TiCl_4$ to eliminate build-up of Cl_2 at the growth surface. Kubat *et al.* also showed that high UV laser fluences and the use of hydrogen reduction, favored the growth of pure Ti from $TiCl_4$ --again implying a pyrolytic growth mechanism.[12]

Since the adsorbed layer was shown to be the dominant source of reactants during LCVD, and the normal spectral reflectance of $TiCl_4$ at 248 nm is only 0.05, thick condensed films of $TiCl_4$ should be readily pyrolyzed--and should exhibit Ti growth rates greater than those obtained from vapor-phase diffusion during LCVD. In addition, the use of a KrF excimer laser at 248 nm, should provide the best means of initiating the reaction, and may also enhance the growth rate through photolytic decomposition of $TiCl_4$ into $TiCl_3$ --and subsequently to Ti.

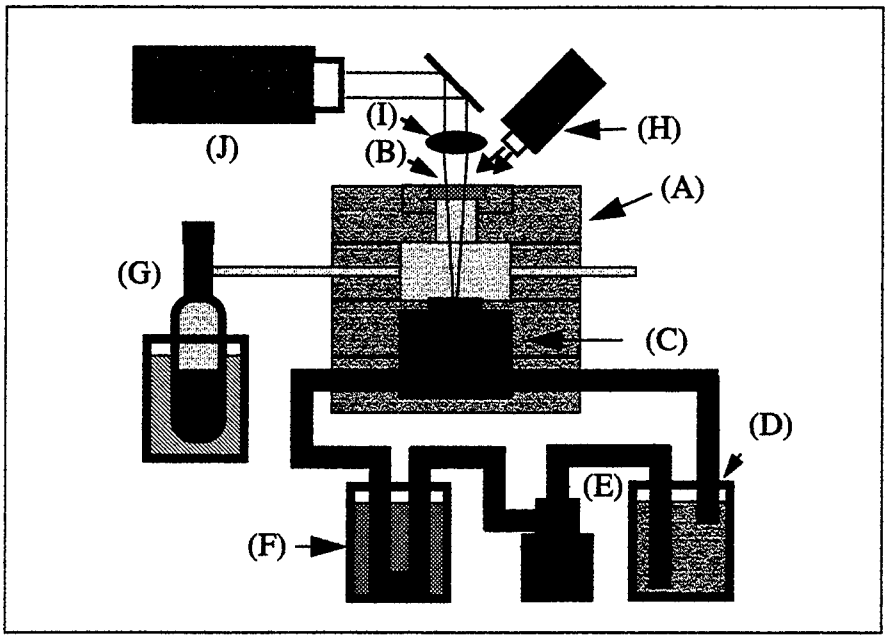


Fig. 1: Apparatus for Moderate Pressure Experiments

III. Experimental

While several methods were devised to disperse the $TiCl_4$ as a thin liquid film, practical difficulties in handling the chemical, e.g. its reactivity with atmospheric water vapor, high room-temperature vapor pressure, etc., required a closed delivery system. $TiCl_4$ also readily adsorbs and decomposes on quartz and glass windows, making it necessary to remove the windows from the vicinity of the laser focus. This also eliminated the possibility of merely sandwiching the liquid between the window and the sample. For simplicity the titanium tetrachloride was merely evaporated from a source container, and allowed to recondense as a liquid coating on the target substrate. In this way, a highly-uniform film of sub-micron thickness could be obtained, and the liquid film could be grown continuously--even while it is being patterned by the laser.

For the LMP experiments, a simple apparatus was constructed, consisting of a reaction chamber, cooling apparatus, and precursor source, as shown in Fig. 1. The reactor (A) was made from two 1-1/3" Conflat flanges, sealed by a viton gasket. The upper flange had a 0.75" diameter sapphire window attached (B), while the lower flange had two machined recesses, one to hold the target substrate, and the another behind the substrate which acted as a cooling reservoir (C). The gap between the substrate and this reservoir was minimized to obtain effective cooling. A recessed aluminum base plate with two 1/8" outlets formed the other half of the cooling reservoir. In this way, a high vacuum could be maintained in the chamber, while chilling the sample from outside the chamber.

Two methods were used to cool the substrate. In the first case, liquid nitrogen was passed directly through the cooling reservoir; this yielded high cooling rates, but was difficult to maintain over long periods due to moisture freezing in the cooling line. The second, more flexible method employed a closed-loop system which recirculated ethylene glycol from a large heated storage reservoir (D), through pump (E), past a liquid-nitrogen cooled copper coil (F), and finally through the cooling reservoir (C). The advantage of this method is that the temperature could be maintained precisely within 1-2 degrees, and varied according to the pumping rate.

Precursor gases were released into the reactor from a heated sample cylinder (G), and thereafter condensed on the cooled substrate. The sapphire window was heated by

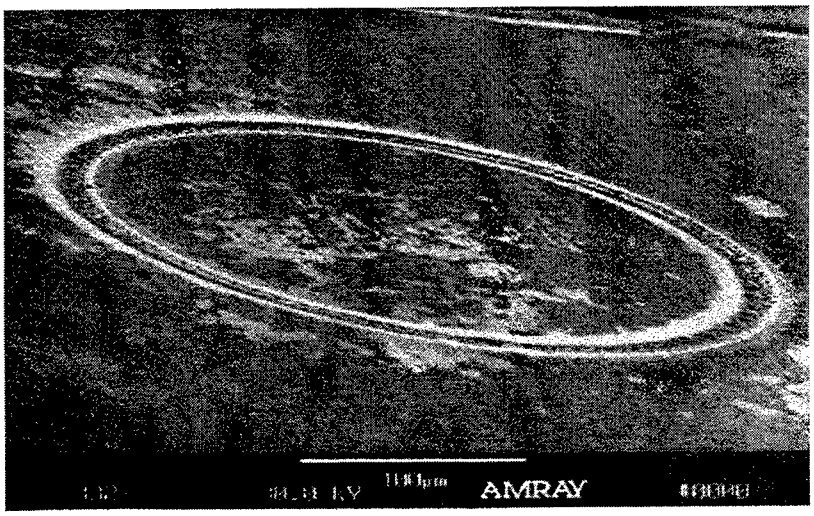


Fig. 2: Titanium Circular Line Traces

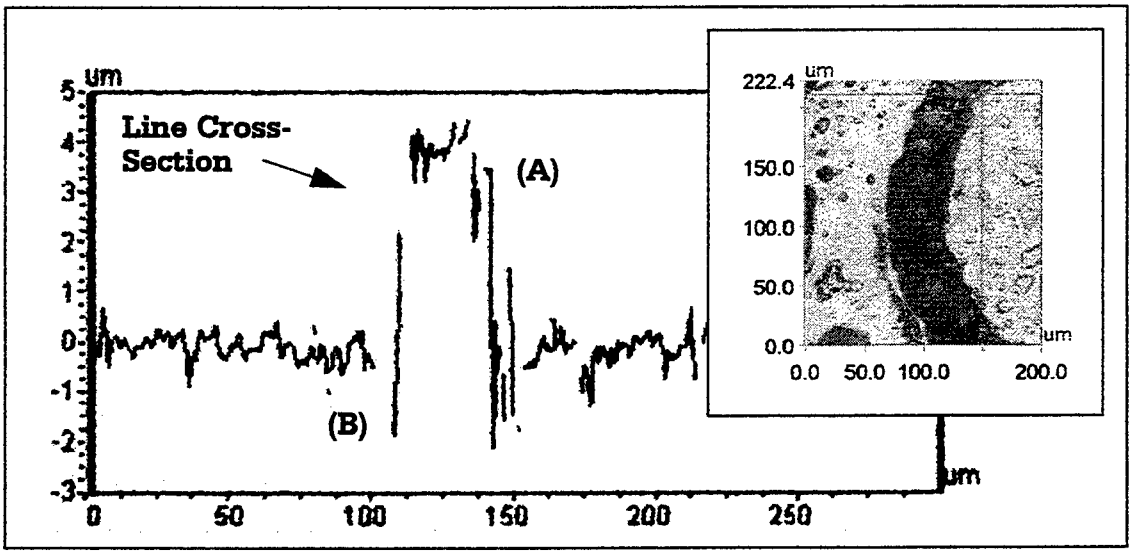


Fig. 3: RST Profile of a Titanium Line

a hot air gun (H) to prevent condensation inside (or outside) the window, and a heater tape was placed around the upper flange to maximize condensation on the substrate. Temperatures from -55°C to 0°C were readily attained at the substrate, while the upper portion of the chamber was maintained at 50-90°C.

A 25 mm f.l. plano-convex, fused-silica lens (I) was used to focus the incident beam on the substrate, yielding spot sizes of roughly 30 microns. A KrF or XeF excimer laser (J) could be interchanged at will, yielding 60-70 ns pulses of 87 μJ at 248 nm or 20 μJ at 351 nm, respectively.

IV. Results

To deposit titanium films, the chamber (A) in Fig. 1 was first evacuated using a roughing and turbomolecular pump, then the substrate was cooled as described previously. When a stable temperature of approximately -4 to -12°C was attained, the valve on the source chamber (G) was opened, releasing $TiCl_4$ vapor into the reactor, and the roughing valve was closed. The precursor was allowed to condense for a prescribed amount of time (with the source valve continually open), and then the laser was scanned once over a prescribed pattern. This procedure was then repeated for a designated number of times, allowing the precursor to condense for a given interval prior to each laser scan. For all experiments, the laser scan speed was a constant 167 μm/s.

Preliminary results in the deposition of Ti from condensed $TiCl_4$ thin films were encouraging. High-aspect ratio lines were patterned with thickness up to 15 microns. A typical pattern is shown in Fig. 2. Note the raised titanium circular film, straddled on either side by thinly-ablated rings on the Ti substrate. Excellent film uniformity was obtained at thicknesses up to 5 microns, with grain structure and surface roughness on the order of 1 micron or smaller. This is illustrated in Fig. 3, where a profile of a 4 μm-thick Ti line was scanned using a Wyko phase-shifting interferometer. Note that the upper surface of the film is relatively flat and exhibits a roughness similar to that of the substrate--which was not polished. Also, note the ablation trenches to either side of the deposited line, which sharply define the deposited region. While the focused beam

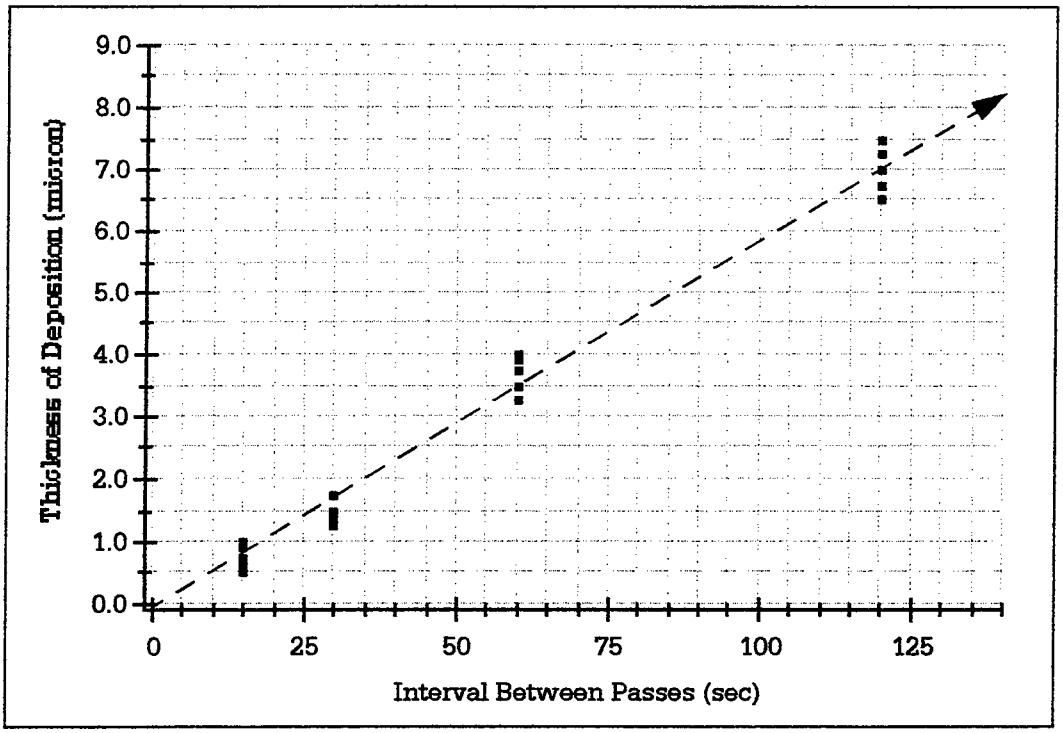


Fig. 4: Deposit Thickness [μm] vs. Condensation Interval [s]

was approximately Gaussian in profile, the Ti film exhibits nearly vertical side-walls and a flat top--clear advantages for continued high-aspect ratio growth.

To optimize the LMP process, a series of experiments were carried out, varying the condensation time, beam pulse repetition rate, exposure time, and focal position. Fig. 4 shows the thickness of the deposited Ti films for varying intervals between scans. The purpose of this experiment was to see if the $TiCl_4$ condensed layer would increase without bound, or if an optimal adsorbed layer thickness exists. During the experiment, the pulse repetition rate was held constant at 200 Hz, and each pattern was scanned a total of 40 times, with the given interval between passes. The substrate was held at a constant temperature of -4°C, while the source chamber was maintained at a moderate temperature of 28°C, providing a $TiCl_4$ vapor pressure of about 13 mbar. Note that there appears to be no limit to the condensed layer which can be converted to Ti--up to a nominal $TiCl_4$ thickness of at least 175 nm/scan.

The slope of the line in Fig. 4 provides a measure of the Ti film growth rate, which was approximately 1.4 nm/s. However, this rate was set by the $TiCl_4$ condensation rate, which was by no means optimal; if the source temperature were instead 145°C, and the vapor pressure within the source cylinder 1300 mbar, then $TiCl_4$ transport to the substrate could be increased by nearly two orders of magnitude. The substrate could also be cooled to lower temperatures and the conductance of the flow path from source to sample improved. Thus, the ultimate limit of this process will not be the rate of $TiCl_4$ transport, but rather the pulse repetition rate of the excimer laser!

To observe the effects of varying exposure, the pulse repetition rate was varied between 150-225 Hz, while the interval between scans was held constant (at 30 s/scan). As can be seen in Fig. 5., two competing processes were found to occur; first, at low repetition rates, the adsorbed layer is incompletely converted to Ti, and the growth rate

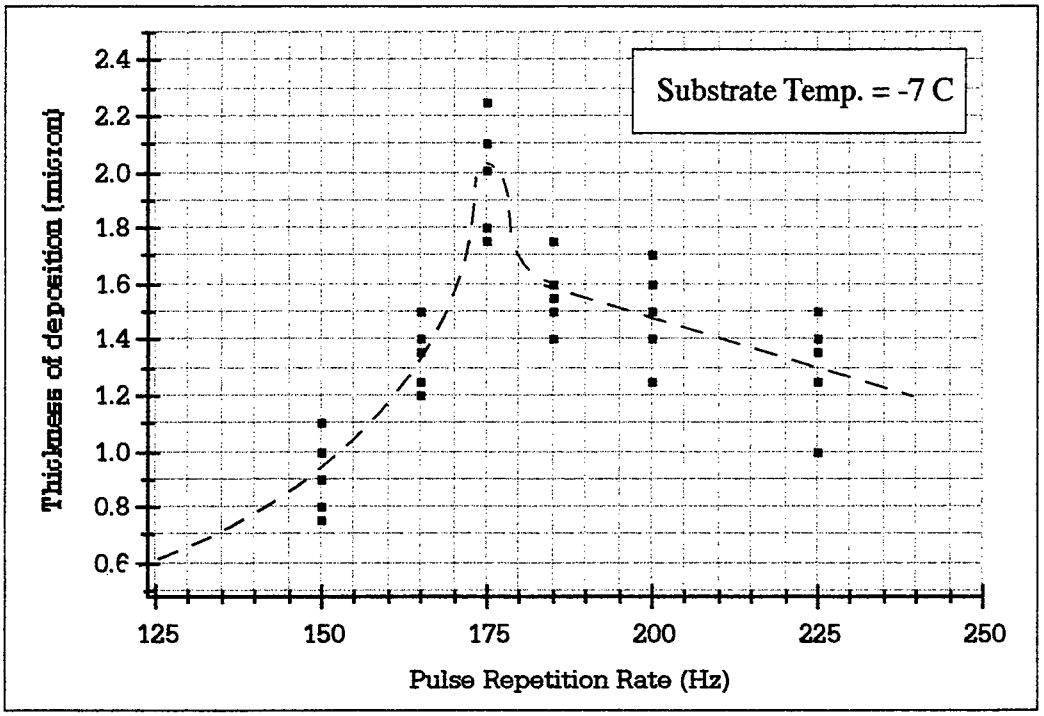


Fig. 5: Deposit Thickness [μm] vs. Laser Pulse Repetition Rate

increases steadily with exposure; second, following the optimal exposure, the Ti thickness drops linearly due to evaporation of the condensed layer and/or ablation of the titanium deposit. Desorption of an adsorbed precursor film due to excessive exposure has been noted by other authors.[13] At this time, however, it is not known whether it is the adsorbed $TiCl_4$ layer or the titanium itself which is removed.

Fig. 6 shows the Ti deposit thickness vs. the cumulative number of laser scans, for a constant scan interval of 8 s. The pulse repetition rate was maintained at 200 Hz throughout the experiment. Observe the similarity of this plot to Fig. 5; however, in this case, the cumulative effects of continuous scanning at constant repeated exposures are represented--rather than the effects of varying exposure (e.g. in Fig. 5). Since the time between scans is large, while the time for the titanium film to cool after exposure is short (generally less than 1 ms), no cumulative heating of the Ti film should occur *between* scans; the deposit height should rise linearly, since each scan adds to the preceding deposit. As expected, linear growth is observed up to 60 cumulative scans, with a growth slope of abt. 11 nm/pass. Surprisingly, the deposit height drops dramatically above a peak at 70 passes--at a rate of 30 nm/pass! The mechanism for this *continual etching* is unknown. If a self-limiting deposit height were reached, the growth would merely cease--leaving a constant film thickness above 70 scans.

Several possible explanations have been proposed to explain this phenomenon. The most likely is that chlorine in the reaction chamber builds up during the processing of each pattern, and that once a sufficient concentration is present, laser-induced etching of the freshly deposited titanium occurs. If so, the effect is merely an artifact of processing in a small, static reactor. Another possible explanation is that the $TiCl_4$ can no longer condense or migrate to the Ti film after an excessive number of scans--hence deposition slows or ceases, and ablation of the film becomes dominant. However, further investigations will be required to determine a precise cause.

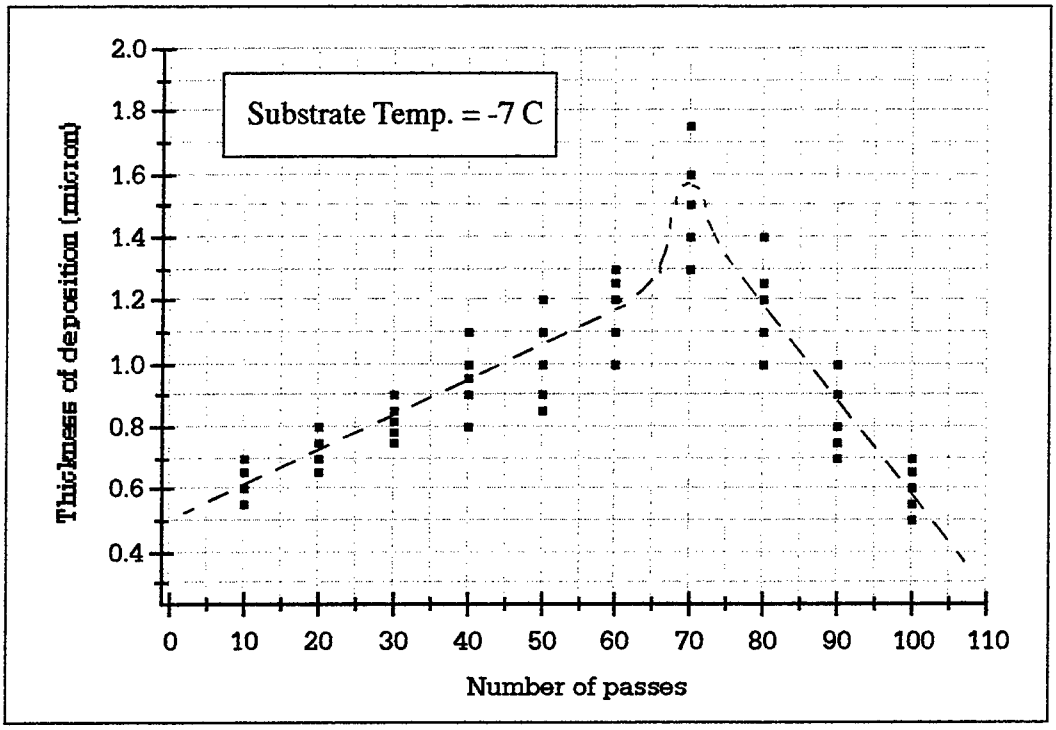


Fig. 6: Deposit Thickness [μm] vs. Number of Laser Scans

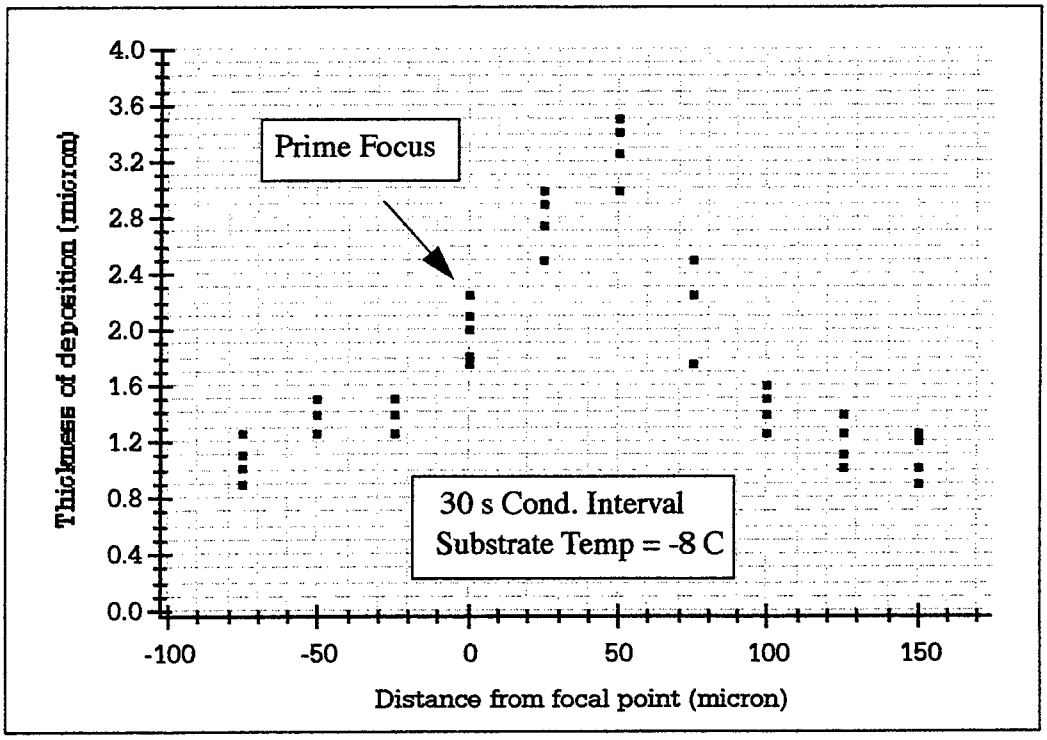


Fig. 7: Deposit Thickness [μm] vs. Focal Position [μm]

To investigate the effects of beam intensity on the growth, it was not possible to vary the power per pulse of the excimer lasers. However, the position of the laser focus could be varied axially relative to the target substrate, lowering pulse intensities by up to two orders of magnitude above and below the prime focus. If the $TiCl_4$ were underexposed or at precisely the optimal exposure, one would expect the growth rate to drop symmetrically to either side of the prime focus. However, if the films were overexposed, ablation or etching would result, and the optimal growth would appear at some extra-focal location, where the pulse intensity is less. From Fig. 7 it is clear that the film is, in fact, over-exposed, confirming that ablation of the Ti and/or condensed $TiCl_4$ film is occurring. The optimal intensity is found approximately 50 microns below the prime focus, implying an optimal power/pulse as low as 0.27 μJ/pulse with a repetition rate of 175 Hz and scan rate of 10 μm/s.

V. Conclusions

The LMP process is a viable method for prototyping thin titanium films without the use of lithography. High-aspect ratio films may be grown with vertical sidewalls and flat-topped cross-sections. Two competing processes were observed during growth: (1) photolytically-enhanced pyrolysis of the condensed film, and (2) ablation of the Ti deposit or $TiCl_4$ adsorbed film. The process may be optimized for high speed growth by lowering the intensity per pulse of the excimer laser so that ablation of the Ti deposit or condensed film is minimized--and by heating the source vessel. Further studies will concentrate on optimizing the deposition speed and surface morphology of the Ti films, allowing the microfabrication of freestanding microstructures.

VI. Bibliography

1. Petersen, K., Proc. of the IEEE, Vol. 70, No. 5, (May 1982), Repinted in Microsensors, pp. 39-77.
2. Ikuta, K., Hirowatari, K., IEEE Micro Electro Mechanical Systems Proceedings, (1993), pp. 42-47.
3. Von Gutfeld, R. J., Gelchinski, M. H., Vigliotti, D. R., Romankiw, L. T., MRS Symp. Proc., Vol. 29, Laser-Controlled Chem. Processing of Surfaces, (1984), pp. 325-332.
4. Bali, K., Geretovszky, Zs., Tóth, A. L., Szörényi, T., Appl. Surf. Sci., Vol. 69, (1993), pp. 326-329.
5. Gupta, A., Jagannathan, R., MRS Symp. Proc., Vol. 101, (1988), pp.95-100.
6. Decleva, P., Fronzoni, G., Stener, M., Chem. Phys., Vol. 186, (1994), pp. 1-16.
7. Alexandrescu, R., Cireasa, R., Dragnea, B., Morjan, I., Voicu, I., Andrei, A., Vasiliu, F., Popescu, C., Adv. Materials for Optics and Electronics, Vol. 5, (1995), pp. 19-30.
8. Izquierdo, R., Lavoie, C, Meunier, M., MRS Symp., Vol. 158, (1993), pp. 141-146.
9. Lavoie, C., Meunier, M., Izquierdo, R., Boivin, S., Desjardins, P., Applied Physics A, Vol. A53, No. 5, (Oct. 1991), pp. 339-342.
10. Meunier, M., Lavoie, C., Boivin, S., Izquierdo, R, Desjardins, P., Applied Surface Science, Vol. 54, (1992), pp. 52-55.
11. Mochizuki, Y., Odamoto, Y., Ishitani, A., Hirose, K., Takada, T., Jpn. J. Appl. Phys., Vol. 34, (1995), pp. L326-L329.
12. Kubat, P., Engst, P., J. Photochem. Photobiol. A: Chem, Vol. 63, (1992), pp. 257-263.
13. Braichotte, D., Van Den Bergh, H., Appl. Phys. A., Vol. A49, (1989), p.189.

Properties of Near-Net Shape Metallic Components Made by the Directed Light Fabrication Process

Gary K. Lewis
John O. Milewski
Dan B. Thoma

Materials Science and Technology Division
Los Alamos National Laboratory
Los Alamos, New Mexico

Ron B. Nemec
SyntheMet Corporation
Los Alamos, New Mexico

The DLF Process

Directed Light Fabrication (DLF) [1-8] is a process invented at Los Alamos National Laboratory that can be used to fuse any metal powder directly to a fully dense, near-net shape component with full structural integrity. A solid model design of a desired component is first developed on a computer work station. A motion path, produced from the solid model definition, is translated to actual machine commands through a post-processor, specific to the deposition equipment. Shown schematically in Figure 1, the DLF process uses a multi-axis positioning system, (3 and 5 axes are used) to move the laser focal zone over the part cross-

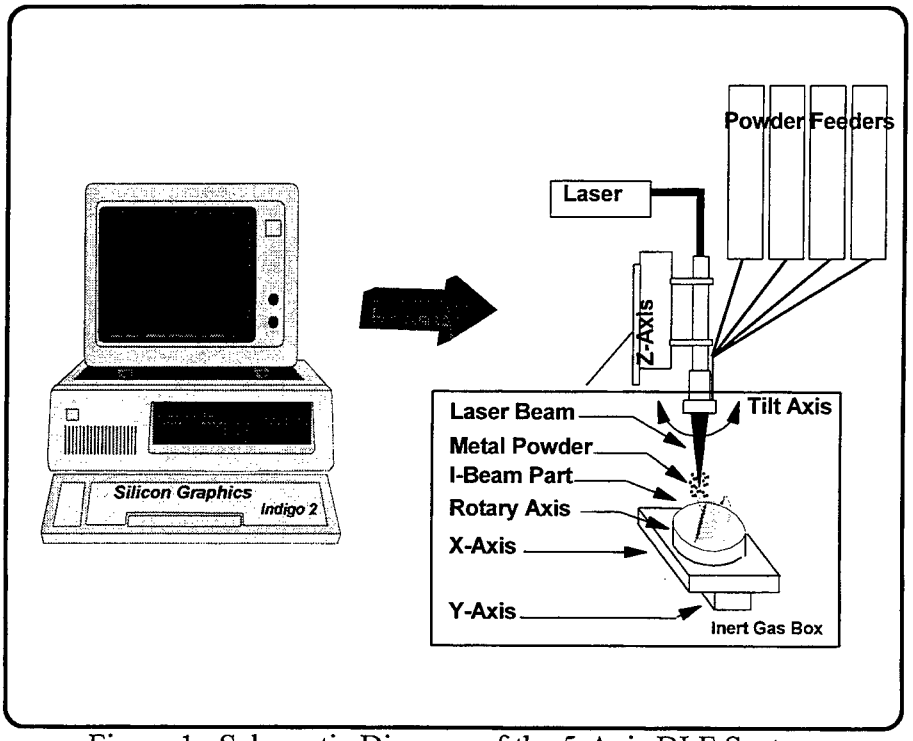


Figure 1. Schematic Diagram of the 5-Axis DLF System

section defined by the part boundaries and desired layer thickness. Metal powders, delivered in an argon stream, enter the focal zone where they melt and continuously form a molten pool of material that moves with the laser focal spot. Position and movement of the spot is commanded through the post-processor. Successive cross-sectional layers are added by advancing the spot one layer thickness beyond the previous layer until the entire part is deposited. The system has 4 powder feeders attached for co-deposition of multiple materials to create alloys at the focal zone or form dissimilar metal joint combinations by changing powder composition from one material to another.

Parts produced by the DLF process vary in complexity from simple bulk solid forms to detailed components fabricated from difficult to process metals and alloys. Deposition of complex 3D parts such as the hemisphere in Figure 2 require more degrees of freedom in the motion path and additional axes of motion (4) than 2.5D bulk solids or hollow parts that are simple "extrusions" of part cross section in a single direction. Figure 3 shows representative parts

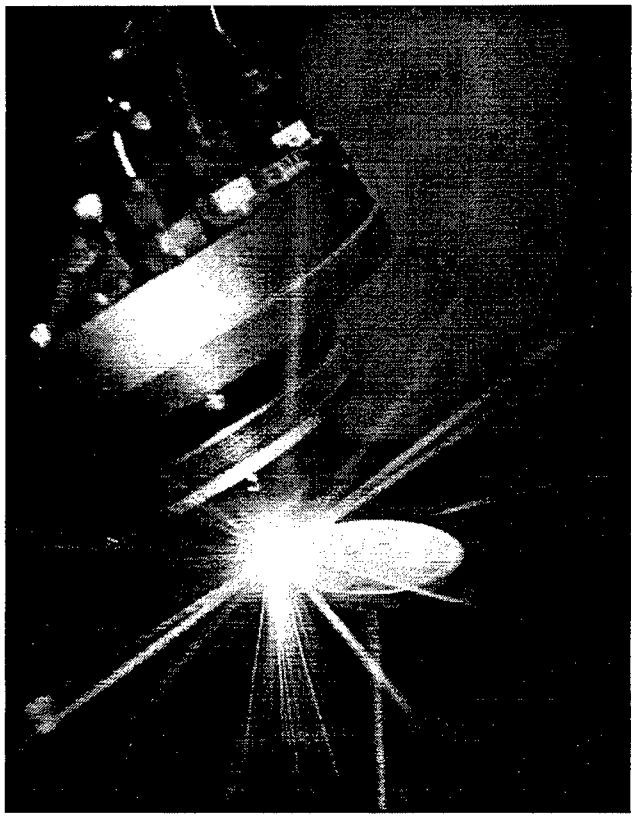


Figure 2. DLF deposition of a hemisphere on a tubular stem demonstrates 4-axes of motion to produce an over-hanging part.

produced by the DLF process. Assemblies of components can be built as one DLF deposited component, such as the multi-tube assembly and housing, which would have to be welded or brazed if processed conventionally. Components 355mm tall and 200mm x 200mm in the horizontal plane requiring build times of over 120 hours continuous operation have been

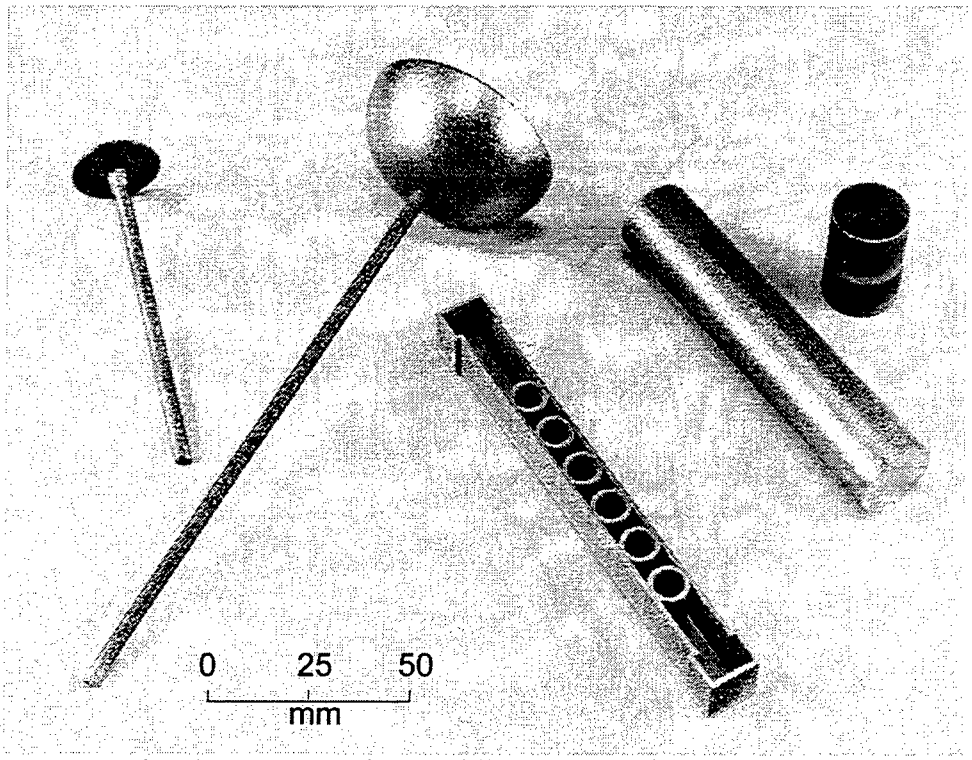


Figure 3. Representative DLF parts and assemblies. From left to right, tantalum stem and disc, 316 stainless steel stem and hemisphere, 316 stainless steel tube assembly and housing, and Inconel 690 solid cylinders.

fabricated with capability to build larger with the present system. Parts have been deposited at rates up to 33 cm^3/hr with 12 cm^3/hr more typical. Feasibility of processing any metal ranging in melting point from aluminum to tungsten has been demonstrated.

Control over process parameters provides optimization of deposit density and deposition rate. Laser power, velocity, powder feed, layer thickness (step-up), and overlap (step-over) are controlled. All but powder feed rate can be controlled within the post-processor code in the DLF process. Parameter optimization depends on the thermal balance for any specified component and material.

DLF Deposit Properties and Characteristics

Metallurgical characterization of DLF metal deposits reported in previous DLF studies has shown that fully dense deposits can be formed at high solidification rates and velocities. Cooling rates of 10,000 k/s [2] have been observed by measurement of secondary dendrite arm spacing [9] on plate structures. Solidification velocities [2] have been measured by eutectic spacing measurements [9] and are shown to be scaleable to the beam velocity during processing. Knowledge of the microstructural development during the DLF process is necessary both to understand the resultant mechanical properties and to improve the characteristics of the deposits.

Mechanical properties of bulk deposits in this study were measured for three alloy

powders using DLF. Ti-6Al-4V and 316 stainless steel powders were fabricated into rectangular bar, and Inconel 690 powder was fabricated into a solid cylinder. Flat tensile bars were machined from the Ti-6Al-4V and 316ss material and round tensile bars were machined from the solid Inconel 690 cylinders. All tests reported were run in the longitudinal direction, which is parallel to the laser beam axis.

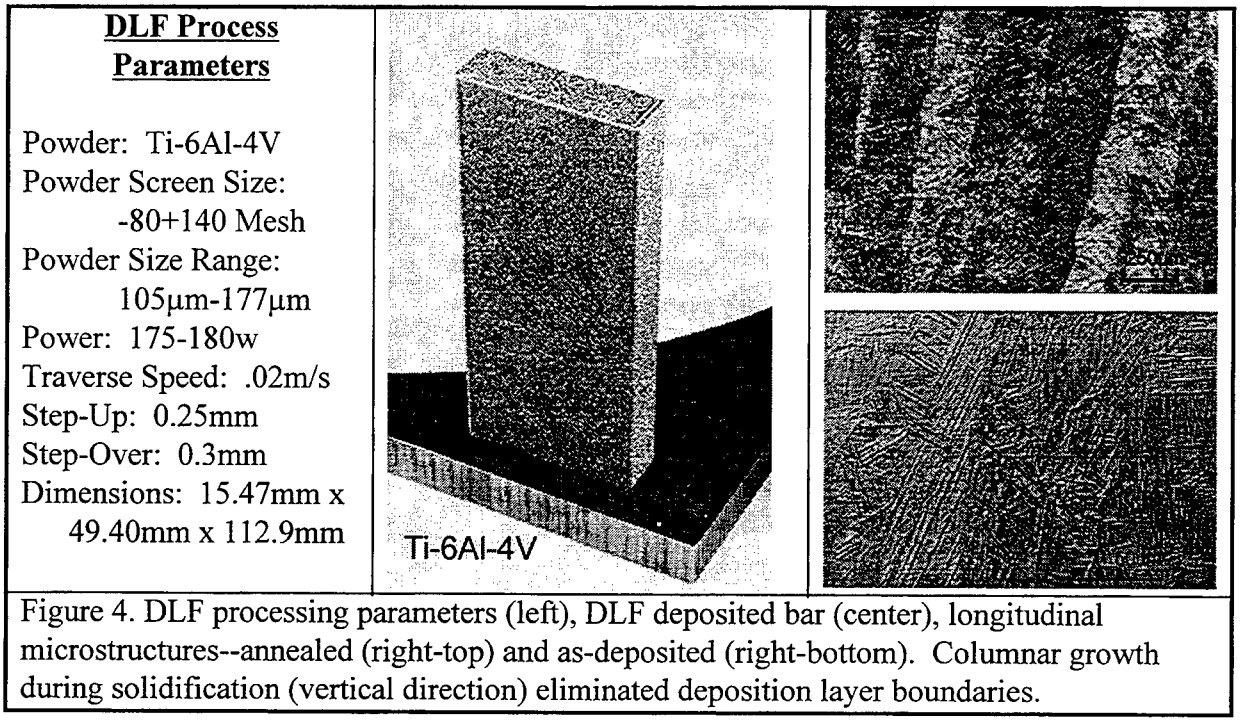


Figure 4. DLF processing parameters (left), DLF deposited bar (center), longitudinal microstructures--annealed (right-top) and as-deposited (right-bottom). Columnar growth during solidification (vertical direction) eliminated deposition layer boundaries.

Figure 4 shows the DLF processing parameters for the bar (center) and the as-deposited and annealed microstructures (right). The deposited microstructure is comparable to Ti-6Al-4V weld microstructures [16] showing acicular alpha with some beta phase. No voids due to lack of powder fusion or cracks were observed on the surface or interior of the bar, however some small pores due to gas evolution during solidification were observed in the Ti-6Al-4V microstructure. Columnar growth in the longitudinal direction of the plate, which is perpendicular to the deposited layers, is in the as-deposited structure and the boundaries remained after the annealing cycle.

DLF material, in the mill annealed condition (730C/4 hr/furnace cool), was tested in the longitudinal direction. Tensile test results are shown in Table 1 with comparison to wrought, cast and powder met forged Ti-6Al-4V bar in the annealed condition. Yield and tensile strength properties of the DLF deposited Ti-6Al-4V exceeds or is equivalent to wrought bar, cast and powder metallurgy forging material in the annealed condition. However, elongation was 6.2% compared to AMS specified 10%. Gas analysis of powder and deposit, additional heat treating and testing are being conducted to explain the low ductility or how to improve it.

Bars of 316 stainless steel were deposited and milled into flat tensile bars. Processing conditions and the deposit microstructure are shown in Figure 5. No porosity was observed and

Table 1 Tensile Properties of Annealed Ti-6Al-4V Bar Produced From Powder by DLF Compared to Conventionally Processed			
Heat Treatment	**0.2% YS (ksi)**	**UTS (ksi)**	**%El**
DLF--Mill Anneal -- 730C/4 hrs/furnace cool Average of 4 Tests	139	149	6.2
Conventional Processed Wrought Bar –Annealed (Spread for 36 tests) [11]	120-145	135-155	15-20
Cast + Anneal [12]	129	147	10
Powder Met Annealed and Forged	134	122	12

a fully fused and resolidified cellular microstructure is shown. The deposition layers are defined because of the melt back depth into each previous layer. Tensile test results in Table 2 for 316 stainless steel in the as-deposited and annealed condition are compared to conventionally processed wrought material and investment cast 316 stainless steel. Yield strength is 11% higher for the DLF material but elongation is 47% compared to 63% for wrought material, however the DLF material exceeds investment cast 316ss in strength and ductility.

Inconel 690 round bars were deposited and shown with the deposition process parameters used in Figure 6. Deposited bars were fully dense and crack free. Microstructures for the as deposited bars and material heat treated at 1700F and 2000F are shown in Figure 7 and resultant tensile properties in Table 3.

DLF Process Parameters

Powder: 316 stainless steel
Powder Screen Size: 140+325 Mesh
Powder Size Range: 44μm-105μm
Power: 175-180w
Traverse Speed: .015m/s
Step-Up: 0.25mm
Step-Over: 0.3mm
Dimensions: 4.06mm x 14.22mm x 114.3mm

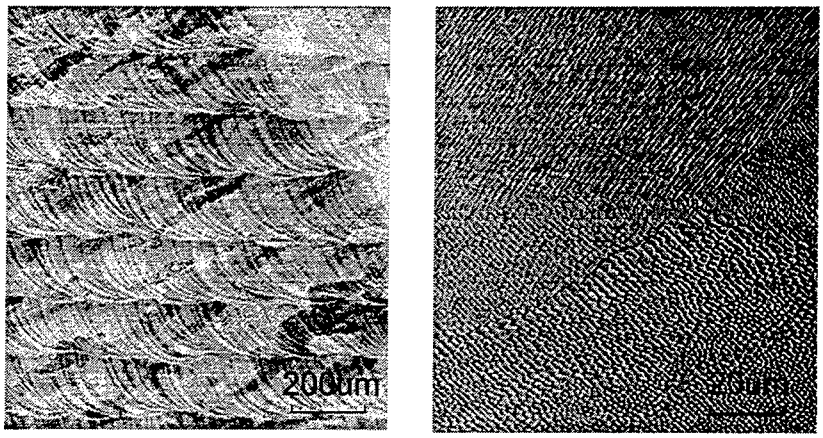


Figure 5. Process parameters for deposition of 316 stainless steel bars (left), microstructure showing the deposited layer structure (center) and cellular microstructure within the layers (right).

Table 2
Tensile Properties of As-Deposited and Annealed 316 Bar Produced From Powder by DLF Compared to Conventionally Processed

Heat Treatment/Condition	0.2% YS (ksi)	UTS (ksi)	%El
DLF—As deposited Average of 3 tests	43	84	41
DLF-- Annealed 1050C/0.5 hr/water quench Average of 2 Tests	43	76	47
Wrought annealed 316 [Ref. 13]	38	83	63
Type 316 (CF8M) Investment Cast (Nominal 316 cast composition) [Ref. 14]	39	75	39

DLF Process Parameters

Powder: Inconel 690
Powder Screen Size:
100+325 Mesh
Powder Size Range:
44μm-149μm
Power: 330w
Traverse Speed: .025m/s
Step-Up: 0.381mm
Step-Over: 0.305mm
Dimensions: 21.0mm dia.
x 356mm

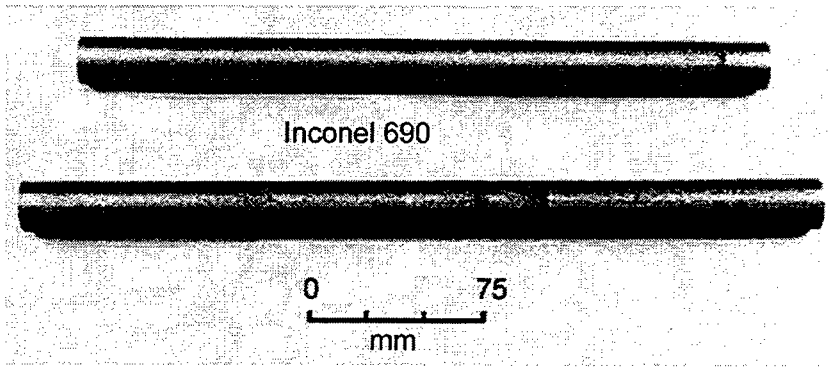


Figure 6. Inconel 690 process parameters (left) and bars (right).

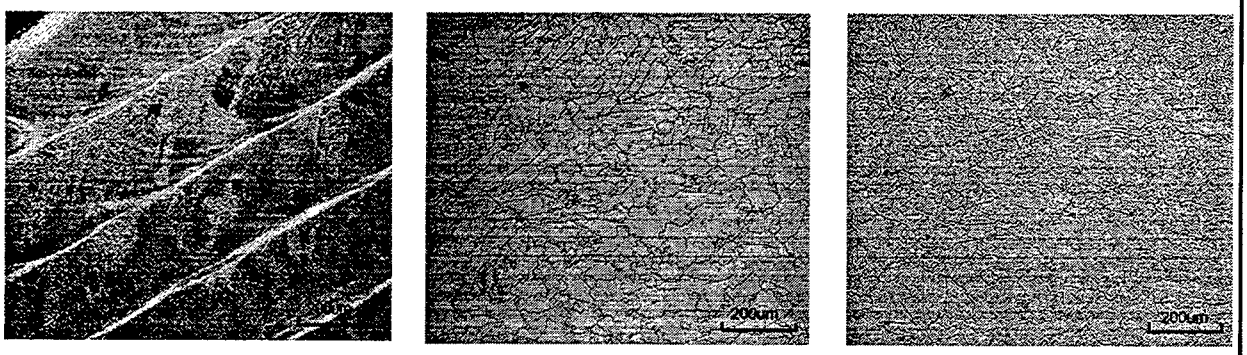


Figure 7. Inconel 690 microstructures are shown as deposited (left), 1700F/1 hr (center) and 2000F/1hr (right). The layered cellular microstructure in the deposit was transformed to equiaxed grains with 26.5μm grain size at 1700F and 37μm grain size at 2000F.

Inconel 690 tensile properties are shown in Table 3 for the as-deposited and heat treated conditions. Properties for conventionally processed hot rolled rod of similar diameter are shown for comparison. Yield strengths for the DLF material exceeded conventional in all cases. Ultimate strengths were lower by about 10% and elongation's were similar.

Table 3
Tensile Properties of As-Deposited and Heat Treated Inconel 690 Bar Produced From Powder by DLF Compared to Conventionally Processed

Heat Treatment/Condition	0.2% YS (ksi)	UTS (ksi)	%El
DLF—As deposited	65.2	96.6	48.8
DLF—1700F/1 hr.	70.7	99.7	46.0
DLF—1800F/1 hr.	69.0	99.3	46.0
DLF—1900F/1 hr.	65.0	97.0	47.0
DLF—2000F/1 hr.	55.6	94.4	52.0
Conventionally Processed 16mm hot rolled rod [15]	54	107	50

Conclusions

Yield strength for the DLF processed Ti-6AL-4V, 316ss and Inconel exceed wrought, cast and powder metallurgy yield strengths for conventionally processed material. Elongation's are less than wrought, powder and cast Ti-6AL-4V and 316ss material, but equivalent for wrought Inconel 690. The importance of the data is that it shows that strengths equivalent or higher than conventionally processed material can be achieved in a single step with the DLF process. Conventional wrought and powder metallurgy processing require mold or die design and manufacture followed by many thermomechanical processing steps in series to refine grain structure, achieve chemical homogeneity, and desired properties. DLF requires no molds or dies and offers potential for controlling solidification microstructures, which determine resultant mechanical properties so that desired properties may be achieved in a single step.

Acknowledgments

Work by Los Alamos National Laboratory was performed under contract W-7405-ENG-36. Inconel 690 investigations were performed under DOE contract DE-AC12-76SN00052 and Ti-6Al-4V deposition tests were performed by SyntheMet Corporation. The authors wish to thank Patrick Dickerson, Ann Kelley, and Joe Fonseca for the deposition processing and metallography performed on the test samples.

References

1. G.K. Lewis, R.B. Nemec, J.O. Milewski, D.J. Thoma, M.R. Barbe, and D.A. Cremers, "Directed Light Fabrication", *Proc. ICALEO '94*, Laser Institute of America, Orlando, Florida, 1994, p. 17.
2. D.J. Thoma, G.K. Lewis, R.B. Nemec, "Solidification Behavior During Directed Light Fabrication", To appear in *Beam Processing of Advanced Materials"*, J.Singh, ed., ASM, Cleveland, OH, 1995.
3. D.J. Thoma, C. Charbon, G.K. Lewis, and R.B. Nemec, "Directed Light Fabrication of Iron-Based Materials", To appear in *Advanced Laser Processing of Materials-Fundamentals and Applications,* MRS, Pittsburgh, 1996.
4. G.K. Lewis and D.J. Thoma, "Free Form Metal Deposition to Near-Net Shape", ASM-TMS, Cincinatti, Ohio, October 6-10, 1996.
5. G.K. Lewis, and D.J. Thoma, J.O. Milewski, J.O., and R.B. Nemec, "Directed Light Fabrication of Near-Net Shape Metal Components", World Congress on Powder Metallurgy and Particulate Materials, Washington, D.C., June 16-21, 1996.
6. D.J. Thoma, G.K. Lewis, E.M. Schwartz, and R.B. Nemec, "Near Net Shape Processing of Metal Powders Using Directed Light Fabrication", Advanced Materials and Technology for the 21st Century, Journal of the Institute of Metals, 1995 Fall Annual Meeting (117th) Hawaii, Dec. 13-15, 1995.
7. G.K. Lewis, and D.J. Thoma, J.O. Milewski, J.O., and R.B. Nemec, "Directed Light Fabrication of Refractory Metals", 1997 International Conference on Powder Metallurgy and Particulate Materials, Chicago, Illinois, June 29-July 2, 1997.
8. D.J. Thoma, G.K. Lewis, J.O. Milewski, R.B. Nemec "Rapid Processing of Materials Using Directed Light Fabrication, Thermec '97, University of Wollongong, Australia.
9. W. Kurz and D.J. Fisher, "*Fundamentals of Solidification*", 3rd. ed., Trans Tech Publications, VT, (1989).
10. American Society for Metals, *Metals Handbook, Ninth Edition, Vol. 7, Powder Metallurgy*, Metals Park, Ohio, 44073, 1980, p. 295-492.
11. *Aerospace Structural Metals Handbook, Vol. 4, 1995 Edition*, Code 3707 Pg. 15, Fig. 3.0312, Purdue University, West Lafayette, IN 47907-1293.
12. American Society for Metals, *Metals Handbook, Ninth Edition, Vol. 3, Properties and Selection: Stainless Steels, Tool Materials and Special Purpose Metals*, Metals Park, Ohio, 44073, 1980,p. 370.
13. *Aerospace Structural Metals Handbook, Vol. 2, 1995 Edition*, Code 13307 Pg. 32, Fig. 3.03113, Purdue University, West Lafayette, IN 47907-1293.
14. *Aerospace Structural Metals Handbook, Vol. 2, 1995 Edition*, Code 1307 Pg. 35, Fig. 3.03120, Purdue University, West Lafayette, IN 47907-1293.
15. Huntington Alloys, Inc., "Inconel 690", Product Literature, Huntington Alloys, Inc., Huntington, WV.
16. American Society for Metals, *Metals Handbook, Eighth Edition, Vol. 7, Atlas of Microstructures of Industrial Alloys*, Metals Park, Ohio, 44073, 1972, p. 330.

Functional Gradient Metallic Prototypes through Shape Deposition Manufacturing

J. Fessler, A. Nickel, G. Link, F. Prinz
Stanford University

P. Fussell
ALCOA

Abstract

Stanford's SDM laser deposition system has been recently improved to enable the deposition of functionally graded metals through the use of powder mixing. While Shape Deposition Manufacturing has always had the capability to produce multimaterial artifacts, powder mixing enables the deposition of single layers in which material properties can be smoothly varied without discrete interfaces between dissimilar materials. It has been shown that certain materials will completely mix during deposition and form alloys which exhibit material properties intermediate to those of the constituent feed powders. To date, oxidation and hardness have been effectively controlled through appropriate mixing of powders. Functional gradient material deposition has been exploited to construct an advanced injection molding tool which transitions from Invar in the center to stainless steel on the outside. The resulting tool exhibited minimal distortion from thermal stress and excellent exterior corrosion resistance.

Introduction

A functional gradient material is a single, solid piece of material which exhibits spatially varying material properties. By creating such materials, one can tailor the composition of an artifact such that material properties are locally optimized. For example, for optimal tool life it is desirable to have a hard outside shell for wear resistance and a ductile core to resist brittle fracture. Traditionally, such benefits have been achieved through the coating or cladding of existing artifacts with shells of different physical characteristics. While these techniques have been used extensively with great success, problems can result from sharp interfaces between dissimilar materials. Internal stresses and coefficient of thermal expansion mismatches can result in delamination, and the sharp interface can act as an initiation site for fracture. A monolithic structure with smoothly varying composition could alleviate some of these problems. Objects with extremely complex geometry can also be difficult to coat or clad effectively. If these complex parts were built in a layered fashion, any surface could be effectively coated regardless of the geometric complexity.

Shape Deposition Manufacturing (SDM) [1, 2] presents the possibility to create metallic artifacts with functional gradient materials. SDM uses laser deposition to fuse metallic powders onto a substrate and these powders can be mixed to create a range of alloys. For example, one can a produce a solid sample of stainless steel with a smooth variation in hardness from 20 and 45 Rockwell C (R_C) simply by mixing hard and soft powders in the proper ratio. By depositing these materials in layers, SDM enables the production of objects in which functional gradient materials are used throughout the volume of the object. For example, artifacts with alternating layers of soft and hard materials are expected to be much less susceptible to failure through fatigue. As shown in bimaterial structures [3], much of the crack energy is dissipated in the soft layer, preventing the penetration of cracks into the harder layer. By using SDM, one could realize the benefits of these layered materials in objects of arbitrarily complex geometry. This paper will examine some of the benefits and properties of the functional gradient materials produced with SDM. In particular it will examine the homogeneity of the deposits and the resulting material properties. Finally, it will present an example artifact which benefits from the use of functional gradient materials.

Laser Deposition System

The laser deposition system for producing functional gradient materials is essentially the same system described in Reference [2]. A 2400 W, continuous wave Neodymium:YAG laser is used to fuse metallic powders onto a substrate. The laser is focused onto the substrate where the transferred energy creates a melt pool. Metallic powders from three different powder feeders are fed from a single powder feed nozzle into the melt pool and subsequently melted. Mixing of the powders occurs in an input funnel and along the length of a 1.5m feed tube. The feed rate of each of the powders and laser power are controlled automatically and the deposition apparatus is moved across the surface of the part using a four degree-of-freedom robotic manipulator. By using this system, the composition of the metal deposit at any point on the surface can be accurately controlled.

Alloying of Metal Powders

The first issue regarding the mixing of metallic powders for laser deposition is whether a homogeneous material is formed during solidification. Because of inadequate mixing or melting, the resulting material could possibly be comprised of isolated islands of one material in a matrix of the second material. Such behavior would result in material properties significantly different than expected for a full alloy.

To investigate the degree of alloying, electron backscatter microscopy was performed on samples of 50% Invar and 50% 316L stainless steel. Such a material combination is of interest for SDM because Invar exhibits a very small coefficient of thermal expansion and stainless steel has high corrosion resistance. A combination of the two results in a part which has minimal distortion due to thermal stresses and can withstand the acid etch required to remove the copper support structure. Figures 1 and 2 show the composition of chrome and nickel for samples A and B versus location. In sample A, a sharp interface between the two materials was achieved by depositing stainless steel next to an already existing deposit of Invar. The transition from one material to the other occurs over the length of 1.5mm, which is approximately the overlap of one laser pass on another. Sample B was deposited in a continuous fashion where the composition was varied between 100% Invar and 100% stainless steel in 10 discrete increments over 50mm. Electron backscatter images at the midpoint of each sample are shown in Figures 3 and 4 for samples A and B respectively. In electron backscatter images, elements with high average atomic number appear lighter than those with low average atomic number. Figure 3 shows a distinctly lighter region of high atomic number material (Invar) separated from the darker, lower atomic number region (stainless steel) by a jagged interface. Figure 4 shows an image from sample B where the composition is 50% Invar and 50% stainless steel. This image has essentially uniform intensity, indicating a homogeneous composition. If the powders were not fully melting and mixing, one would expect to see pockets of light and dark on the order of the particle diameter (100 μm). Separate X-ray diffraction analysis shows that only a single phase is present in the material. This indicates that the constituents have formed a single-phase, solid-solution and are fully alloyed.

The alloying properties of Invar and stainless steel should be contrasted with those of Aluminum-bronze and 316L stainless steel. Deposits which transition from 100% bronze to 100% stainless steel show visible segregation of the two materials into distinct bands and significant cracking. Figure 5 shows an electron backscatter image of such a composition where there are dark regions of stainless steel surrounded by the lighter bronze. X-ray diffraction analysis of this sample shows multiple phases present in the material. Such segregation is not surprising considering that copper and iron have very low solubility below 1400°C at any concentration [4].

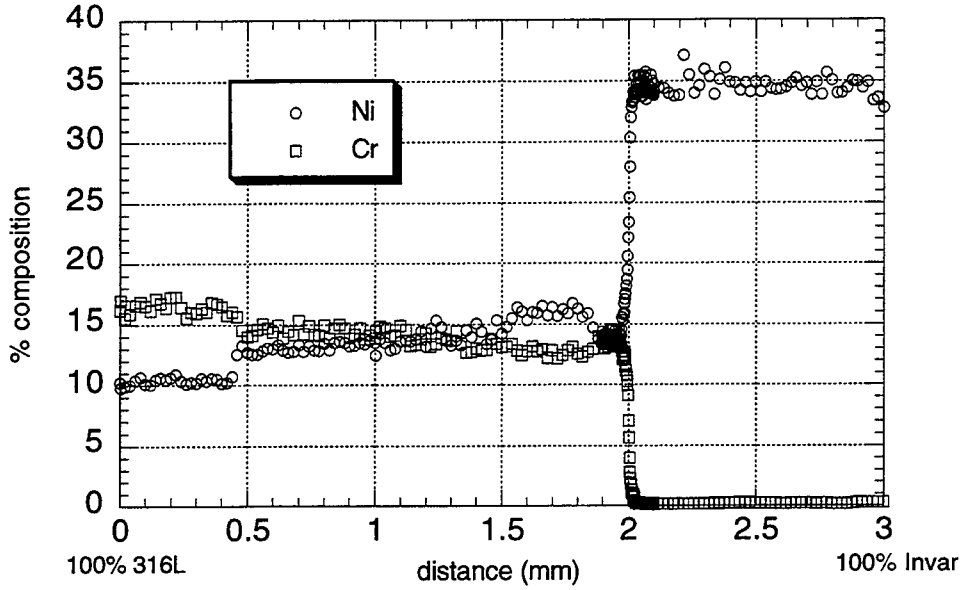


Figure 1: Composition of Chrome and Nickel versus location for a sharp interface between Invar and 316L stainless steel. (Sample A)

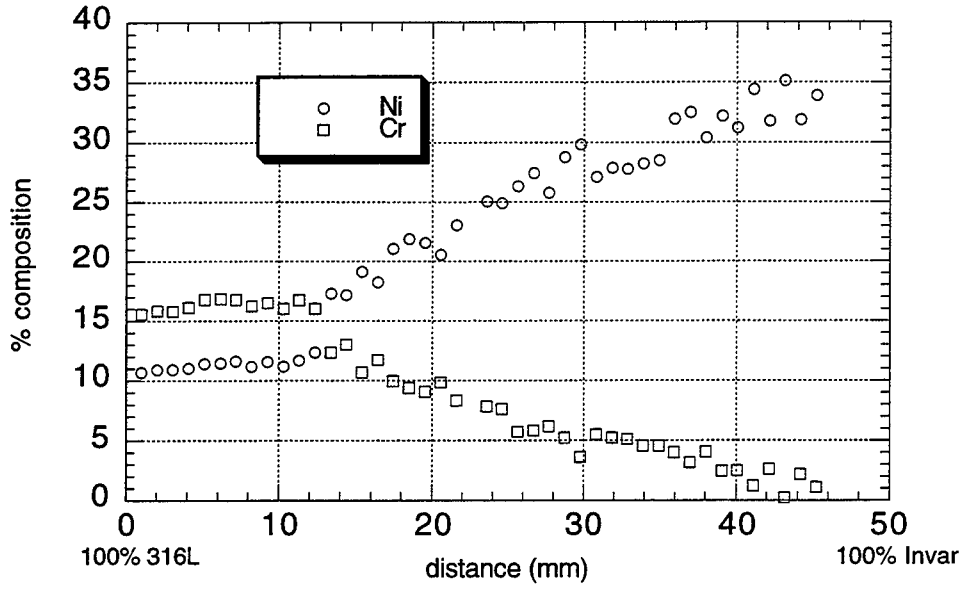


Figure 2: Composition of Chrome and Nickel versus location for a graded interface between Invar and 316L stainless steel. (Sample B)

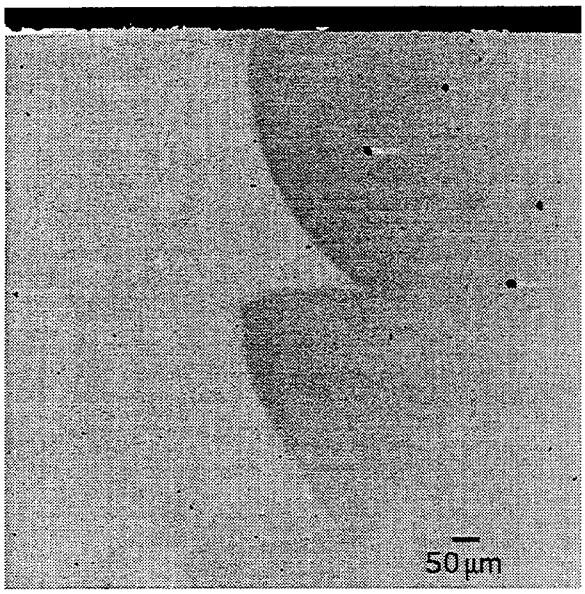


Figure 3: Electron backscatter image for Sample A at location of 2mm. Lighter shades indicate higher atomic number of Invar.

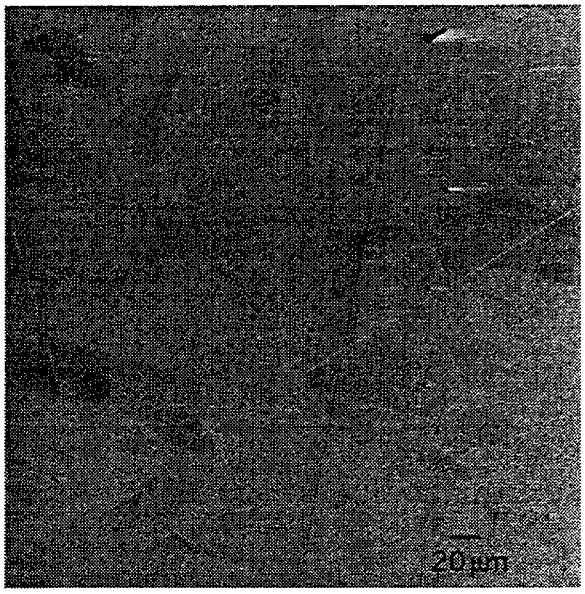


Figure 4: Electron backscatter image of Sample B at midpoint. Uniform shade indicates complete alloying of 50% Invar and 50% stainless steel.

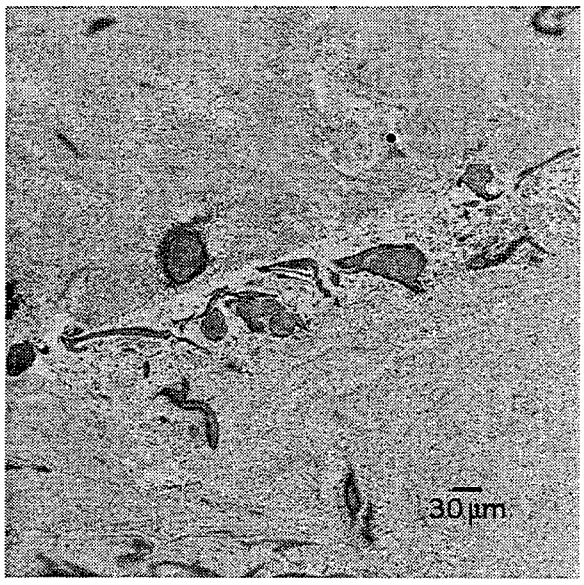


Figure 5: Electron backscatter image of aluminum-bronze and 316L stainless steel mixture. Note the distinct islands of stainless steel (dark) within the largely bronze matrix.

Properties of Graded Materials

Given that certain materials will fully alloy during the deposition process, one would expect the material properties in the graded sections to transition smoothly between the two extremes. This is indeed what occurs. For instance, in the Invar to stainless steel graded material illustrated in Figure 2, there is a continuous distribution of oxidation resistance which scales with the level of chrome. Invar, which has no chromium will oxidize to dark blue at elevated temperatures while stainless steel will remain silver. Figure 6 shows images of both the graded sample (Sample B) and the sharp transition samples (Sample A) after oxidation in a 400°C furnace for 25 minutes. Note the continuous distribution of oxidation in the graded sample.

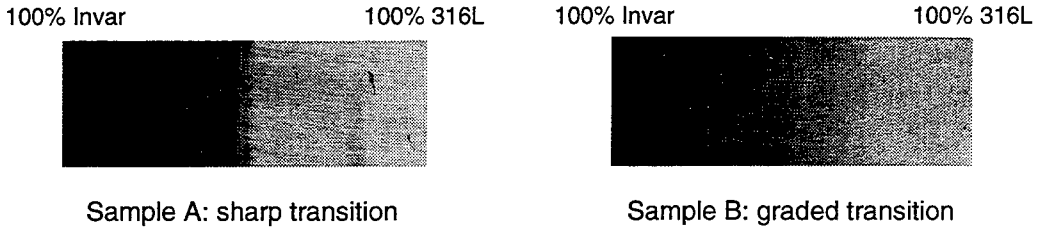


Figure 6: Oxidation of sharp (Sample A) and graded transitions (Sample B) from Invar to stainless steel.

Invar-stainless steel transitions are especially important for the SDM process because the presence of Invar has been found to drastically reduce the amount of deformation resulting from residual thermal stresses. Pure Invar deposits show approximately 1/2 the deflection of pure stainless steel deposits of the same geometry [2]. Laser-deposited Invar, however, cannot withstand the long-term immersion in nitric acid that is required to remove the copper support material used in the fabrication of metal parts. A thin layer of stainless steel is sufficient to protect the part in the acid bath, and beams made with a core of Invar and a thin shell of stainless steel have been found to have only 2/3 the deflection of pure stainless steel beams.

As stated in the introduction, one of the most useful functional gradient materials involves a hard outer shell for wear resistance surrounding a more ductile core. The laser deposition system has been used to produce samples which continuously transition from 316L stainless steel ($R_c < 20$) to a harder, corrosion resistant alloy ($R_c = 43$) similar to 414 stainless steel. Figures 7 and 8 show the distribution of hardness and iron content versus location for a sample of this graded material which transitions from 100% hard alloy to 100% 316L stainless steel over 50mm. Note that while there is essentially a linear distribution of the iron content, the hardness distribution is distinctly non-linear. Most of the hardness variation occurs between 20 and 30mm which corresponds to concentrations of 40 to 60%. The plateaus on either side of this transition region correspond closely to the hardness of the major constituent. It should be noted, however, that hardness on the Rockwell C scale does not scale linearly with carbon in stainless steels and the nonlinearity can be qualitatively explained by the variation of carbon content. While the hardness variation is not linear, it is a continuous, smooth variation so any desired hardness between 20 and 45 R_c can be obtained through the proper mixing of these two powders.

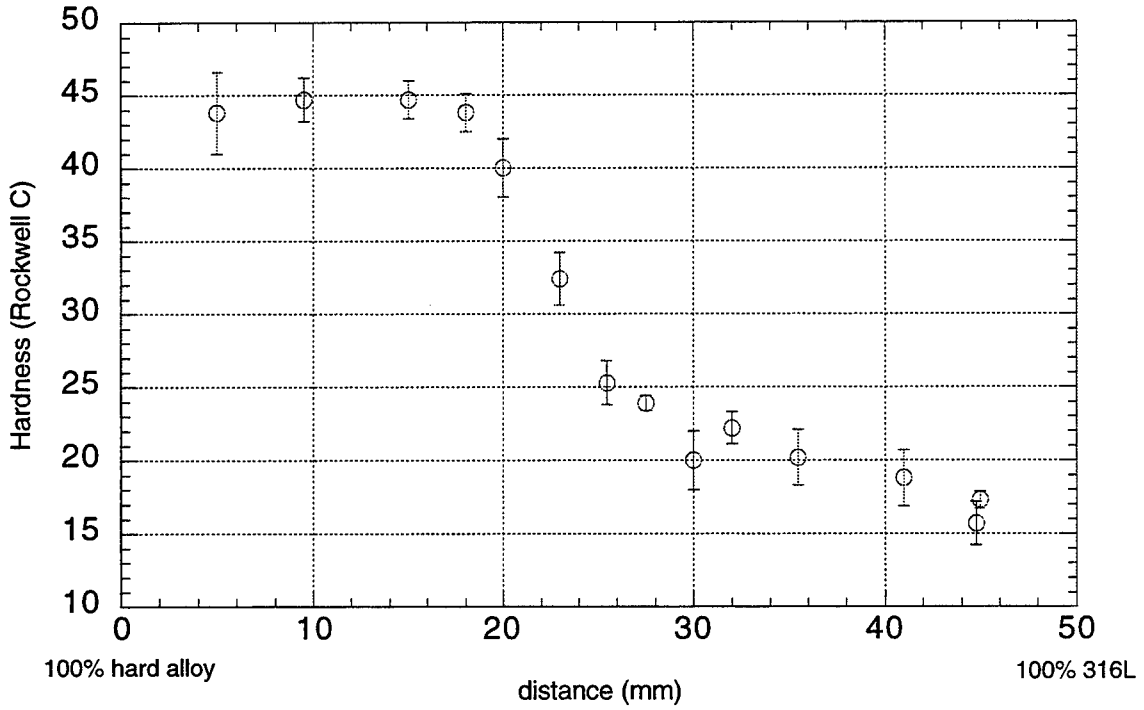


Figure 7: Hardness distribution for a hard alloy to 316L stainless steel graded material.

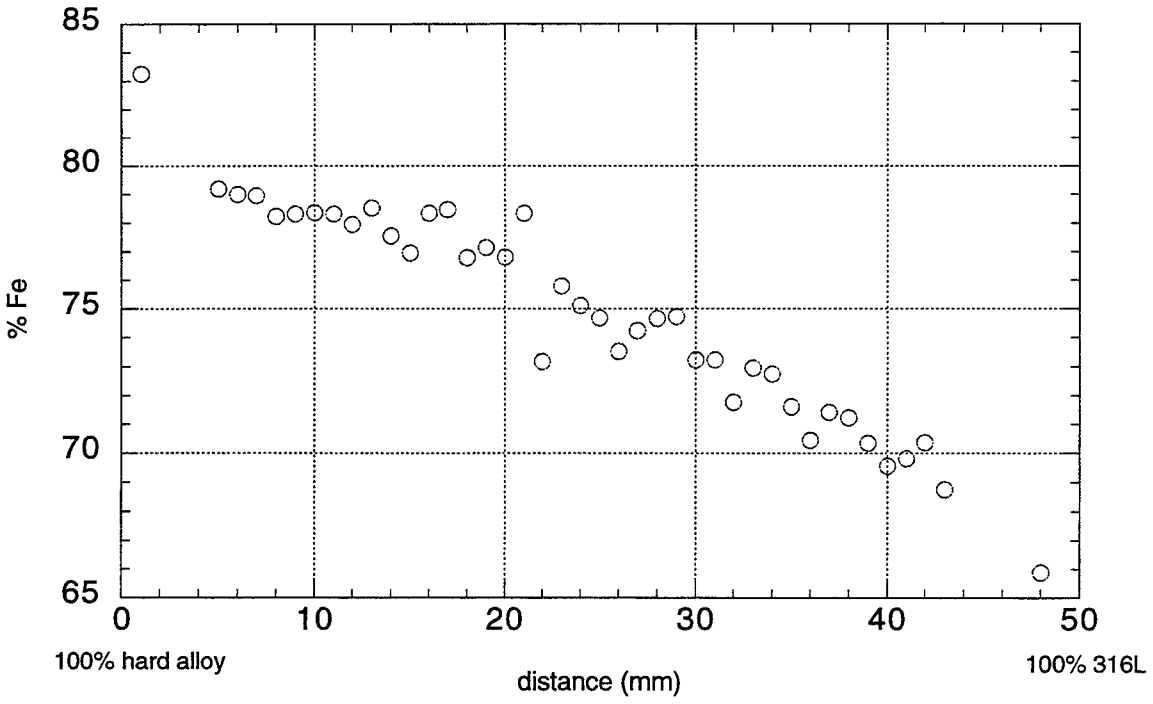


Figure 8: Iron concentration distribution for a hard alloy to 316L stainless steel graded material.

Functional Gradient Metallic Prototypes

The first application of functional gradient materials to SDM artifacts is an advanced injection molding tool designed by ALCOA. This tool, which is shown schematically in Figure 9, is comprised of three materials: Invar, stainless steel and copper. The bulk of the tool is made from Invar to reduce deformation due to residual thermal stresses. A thin shell of stainless steel surrounds the part to protect it during the acid etch process. To minimize cycle time, cooling channels would ideally be placed directly under the mold section of the tool; this, however, would not allow for ejector pins for part removal. As a compromise, solid deposits of copper have been located 2mm below the mold surface to facilitate heat removal form the part during production. Conformal cooling channels are located 2mm on either side of the copper to facilitate heat removal from the copper. The proximity of the copper to both the cooling channels and the plastic part should significantly decrease the cycle time for each part by reducing the time necessary for temperature stabilization.

Near net shape deposition of each layer began with Invar at the center of the part and spiraling outward following the geometry of that layer. In the outer few passes, a continuous transition was made from Invar to stainless steel to assure all outside surfaces were corrosion resistant. Internal features such as the cooling channels and the pocket for the copper deposit, were machined layer-by-layer as the part was deposited, while outside features were machined and electro discharge machined (EDM) after the entire part was deposited. Figure 10 shows a cross section of the part which shows the relative locations of Invar, stainless steel and copper. Construction of this part illustrated that continuous transitions between materials could be made within a single deposited layer. Future work will include tools with very hard outside shells to decrease tool wear and Invar cores to reduce thermal distortion.

Conclusions

The ability to specify material properties at any location within an artifact presents numerous benefits to designers in terms of choosing the optimal material for each application. Recently, the laser deposition system within SDM has been modified to enable the continuous deposition of graded metals from up to three constituent feed powders. This, coupled with the inherent flexibility of SDM, now enables the production of complex three dimensional artifacts with continuously varying material properties throughout the volume of the artifact. Materials which traditionally alloy also alloy with this system to form homogeneous, single phase deposited material. In general these graded materials exhibit varying material properties with varying composition but the property variations are not necessarily linear with concentration. The new system has been used to produce samples with continuously variable oxidation resistance and hardness. Future work on the material properties of these graded materials will focus on their fracture and fatigue properties as compared to sharp material interfaces.

The system has also been utilized to fabricate an advanced, multimaterial injection molding tool. The tool has copper deposits and cooling channels to minimize cycle time and Invar core to reduce distortion due to residual thermal stresses. The outside of the tool is stainless steel to prevent corrosion while in the acid bath used to remove the copper used as a sacrificial support material. The Invar and stainless steel were deposited in a continuous, outward spiral, where the transition to stainless steel was made within the outer few passes along the contour. The same technique could be also used to produce long-life, wear-resistant tools with a hard, corrosion-resistant outer shell. This technique can be extended to any multimaterial application where stress concentrations due to sharp material interfaces may limit performance.

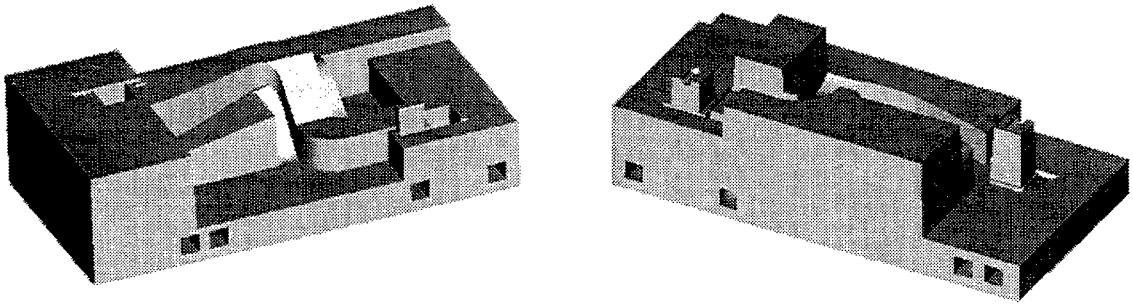


Figure 9: Model of advanced ALCOA injection molding tool. Tool is made of Invar, stainless steel and copper and has two conformal cooling channels in each half to remove heat quickly from the part.

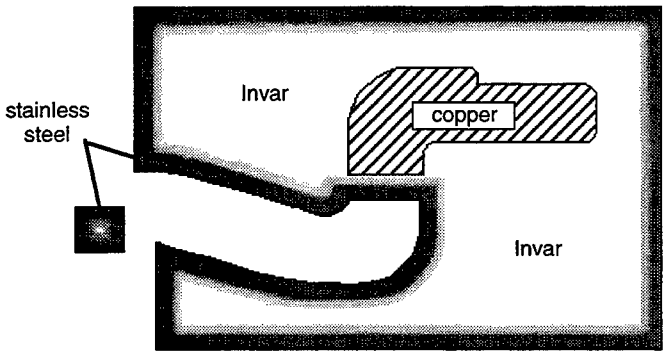


Figure 10: Horizontal cross-section of one half of advanced injection molding tool illustrating gradient from Invar to stainless steel on surface of part.

Acknowledgments

The authors gratefully acknowledge the Defense Advance Research Projects Agency (#F33615-94-C-4450 and #F33615-95-C-5560), the Office of Naval Research (#N00014-96-1-0354), the National Science Foundation (#MIP-9618050) and ALCOA for their support of this research.

References

[1] Merz, R., Prinz, F., Ramaswami, K., Terk, M., and Weiss, L. (1994) "Shape Deposition Manufacturing," Proceedings of Solid Freeform Fabrication Symposium, The University of Texas at Austin, pp. 1–8.

[2] Fessler, J., Merz, R., Nickel, A., Prinz, F., and Weiss, L. (1996) "Laser Deposition of Metals for Shape Deposition Manufacturing," Proceedings of Solid Freeform Fabrication Symposium, The University of Texas at Austin, pp. 117–124.

[3] Suresh, S., Sugimura, Y., and Tschegg, E.K. (1992) "The growth of a fatigue crack approaching a perpendicularly-oriented, bimaterial interface," Scripta Metallurgica et Materialia, Vol. 27, pp. 1189 – 1194.

[4] Hansen, M., Constitution of Binary Alloys, 2nd ed., McGraw Hill, New York, 1958.

LAMINATED OBJECT MANUFACTURING OF Si_3N_4 WITH ENHANCED PROPERTIES

Matthew J. Pope, Mark C.L. Patterson, Walter Zimbeck and Mark Fehrenbacher
Ceramic Composites Inc., 1110 Benfield Boulevard, Millersville, MD 21108

ABSTRACT

The potential to fabricate near net-shape ceramic components of intricate shape is attractive and offers considerable savings in cost and time. The laminated architecture inherent in many Rapid Prototyping techniques can be utilized to enhance material properties by providing weak interfaces at regular intervals, oriented microstructures, and functionally graded compositions. By design and control of these variables it is possible to enhance the strength, toughness and performance of components fabricated from structural ceramics. A range of oriented microstructural features have been investigated in Laminated Object Manufacturing of Si_3N_4 materials. Changes in the mechanical properties can be related to specific architectures and microstructural developments which took place during sintering.

INTRODUCTION

The damage-critical material properties of ceramics can be significantly improved through lamination of the structure prior to densification. Building ceramics in this way has been shown to reduce the primary flaw size and introduce a number of interfaces, which if carefully designed can influence the microstructural development and material properties, resulting in materials which exhibit damage tolerance and non-catastrophic failure modes, especially in bending. Lamination is an inherent signature of many Rapid Prototyping techniques and it is a powerful and flexible approach to materials design that can be used to produce a wide range of material structures. In this study, three approaches have been investigated in an attempt to improve the mechanical properties of Si_3N_4 laminates for Laminated Object Manufacturing (LOM). The composition of the individual layers was gradually changed to produce functionally graded materials (FGMs),[1,2] primary seed crystals were aligned within each of the layers to achieve a microstructure with a preferred orientation,[3] and the interlaminar composition and microstructure has been changed through the addition of a second phase to introduce non-linear fracture behavior and thereby overcome the inherent brittleness of the materials within the individual layers.[4]

Although several techniques are available from which to fabricate laminated or graded architectures, tape casting followed by lamination has demonstrated excellent control over laminate thickness, scale, and uniformity of properties.[5,6,7,8] In order to obtain optimal properties with the manual lamination of ceramic tapes it is necessary to "heal" the interfaces between the individual tapes via thermocompression, which normally takes place at the softening temperature of the plasticizer (50°C to 100°C), for 10 minutes under a pressure of 30 - 70MPa.[8,9] Thermocompression is essential in manually laminated ceramics where strong interfacial forces are required (i.e., Al_2O_3/Al_2O_3 and Al_2O_3/ZrO_2). Although ceramic tapes can be used for Rapid Prototyping through the LOM process, the thermocompression stage is difficult to reproduce. The equivalent, but less effective stage in the LOM process utilizes a hot roller or plate[10] which traverses or rests on the tape, thereby applying a small load (~0.7Mpa) for a much shorter period of time. Additionally, post pressing of the laminated block[11] has been investigated prior to decubing. Although higher loads, temperatures and longer periods of time would be beneficial in promoting bonding between the tapes, increasing these parameters could distort the tapes, leading to shape dependent dimensional changes that are incompatible with the net-shape LOM process. It has therefore been necessary to investigate alternate methods to achieve interlayer adhesion during LOM fabrication of ceramics. Applying a solvent-based solution between layers has demonstrated sufficient adhesion to successfully complete the LOM fabrication process, following which, laminate healing without anisotropic dimensional distortion of the net-shape component can be achieved by isopressing.[12]

Since it is apparent that an interlayer adhesion processing stage is necessary during LOM fabrication of ceramics, this stage has been investigated further to introduce different laminate interface material systems, thereby changing the overall material properties. Selection of the appropriate material systems, layer thickness and interlayer coating (if any), should enable LOM fabrication of components which exhibit damage tolerance and graceful failure similar to that which has been described in the literature for manually laminated systems. The nature of the designed interface between subsequent layers can be broadly classified as weak bonding, strong bonding, or a combination (hybrid bonding) of both of these mechanisms.[4] Typically, weak interfaces have given rise to flaw-tolerant behavior[13,14] through the deflection of cracks and the dissipation of energy along the interface normal to the load. Flaw-tolerance has also been demonstrated in strong interface systems containing two brittle materials,[15] in transformation toughened systems,[6,16] and in systems based on alternating layers of metals, intermetallics or ceramics.[17,18,19] Unless considerable care is taken to ensure otherwise, most components fabricated via the LOM process will exhibit weak interfaces due to uncontrolled interfacial mating of the layers, and residual oriented porosity. Many of the weak interface composites fabricated from Si_3N_4/BN,[20,21] Al_2O_3/phosphate,[22,23] and SiC/C[13,14] could be applied to components laminated by LOM with resulting improvements to the damage tolerance and component performance.

This paper reports on a materials study in which the compatibility of Si_3N_4 tapes with the LOM process was investigated, and three "easy to apply" microstructural variants were evaluated to enhance the properties of multilayer Si_3N_4 structures. Specifically, second phase interface compositions, FGMs, and oriented microstructures were studied. Differences in mechanical properties are related to the specific architectures and the microstructures which evolved during sintering. A gas pressure sintering technique, which unlike hot pressing does not create anisotropic dimensional changes that significantly distort the net-shape component, has been investigated and is of particular relevance to the LOM process because it provides controlled or uniform shrinkage during densification.

EXPERIMENTAL APPROACH AND RESULTS

I. Materials Study: Designed Architectures in Si_3N_4 Laminates

Three different laminated architectures were fabricated in an attempt to tailor the microstructure and properties of Si_3N_4. Although the materials were manually laminated, the architectures can all be easily applied to the automated LOM process. The source of the Si_3N_4 powder and Y_2O_3, Al_2O_3, and ZrO_2 sintering aids is given in Table I. The fabrication process for the laminated Si_3N_4 ceramics is illustrated schematically in Figure 1. Powders were ball milled in toluene and ethanol for 24 hours, followed by a further 24 hours with the plasticizer and binders in a proprietary composition. Following blending, the ceramic slips were degassed for two minutes and cast at a speed of 4 cm/sec onto mylar using a 6" blade caster. Casting and drying were carried out at a temperature of between 21°C and 23°C. For all materials, the tapes were cut, stacked, and thermocompressed at a temperature of 70°C and pressure of 14MPa for 10 minutes.

Table I. Powder source and composition

Material	Source	Size (μm)	Purity%
Si_3N_4	UBE SNE10	~0.3	98.5
Al_2O_3	Baikowski CR125	<0.2	>99.99
Y_2O_3	F.J. Brodmann	~1.0	>99.99
ZrO_2	Tosoh TZ-3Y	~0.03	~94.8

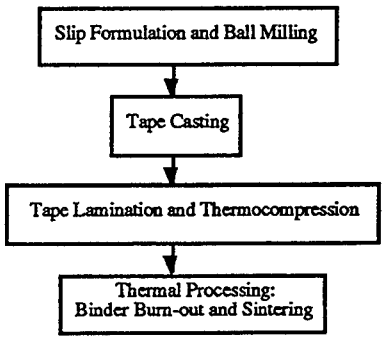


Figure 1. Lamination of Si_3N_4

Functionally Graded Materials (FGMs)

Functionally graded Si_3N_4/SiC laminated structures were fabricated in an attempt to introduce surface compressive stresses resulting from the difference in thermal expansion coefficients between SiC and Si_3N_4. For armor applications, the graded architecture allows for the development of a back surface compressive stress that can increase the time to failure of ceramic armor plates while minimizing the impedance mismatch that has caused poor ballistic behavior in non-graded bi-material laminated armor.[24] The Si_3N_4/SiC powder mixtures were blended with 5wt% of both Al_2O_3 and Y_2O_3 as sintering aids, and the process shown in Figure 1 was used to fabricate laminated structures that graded from 50wt% Si_3N_4/50wt% SiC in the middle of the structure to 100% Si_3N_4 on both surfaces. Grading took place in increments of 10wt% as shown in Figure 2. These materials were hot pressed in a Si_3N_4/BN powder bed at 1780°C and 25MPa for two hours. Figure 3 is an optical micrograph of the densified Si_3N_4/SiC FGM and Figure 4 is a schematic diagram of the estimated surface compressive forces that are balanced by an internal tensile force. Si_3N_4/SiC FGMs containing SiC (Nicalon) continuous fiber reinforcement were also fabricated, but it was observed that even when hot-pressed the introduction of fibers led to poor densification and porosity around the fibers that weakened the structure, resulting in a lower strength and inferior ballistic performance.

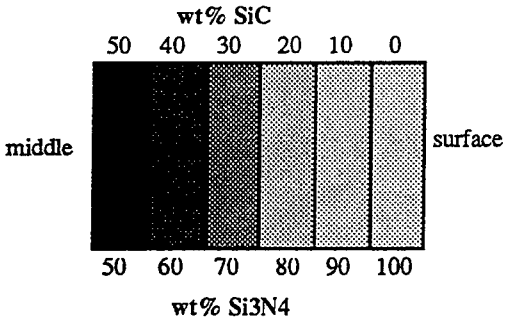


Figure 2. Graded Si_3N_4/SiC Structure

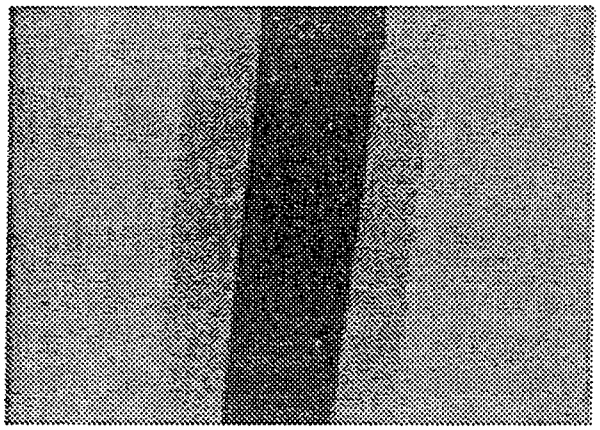


Figure 3. Micrograph of Graded Si_3N_4/SiC

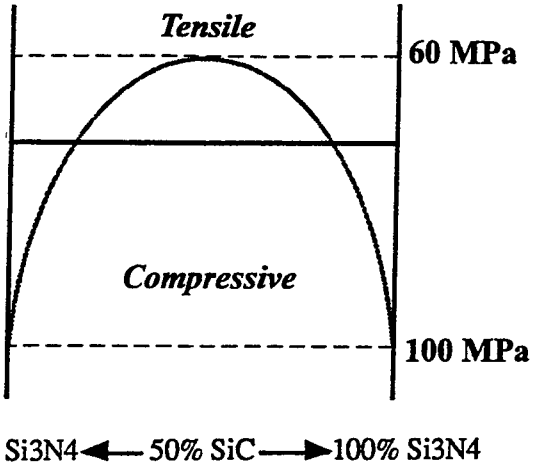


Figure 4. Stresses in Graded Si_3N_4/SiC

Second Phase Interfacial Design

Investigation of four different laminate interfaces was carried out using Si_3N_4 tapes with 5wt% of both Al_2O_3 and Y_2O_3 as sintering aids. A thin coating of a second phase interface material was applied as a 5wt% solution/suspension in ethanol, by a simple spray technique prior to lamination. The interface materials evaluated were BN, SiO_2, TiO_2/SiO_2, and SiC (formed in-situ from SiO_2 and sugar[25]). These materials, designated as SN-BN, SN-SiO_2, SN-TiO_2/SiO_2, and SN-SiC, respectively, were hot pressed in a Si_3N_4/BN powder bed at 1780°C and 25MPa for two hours.

This study was undertaken to determine if the laminate interface could be tailored to control the fracture behavior of laminated Si_3N_4 structures. The BN and TiO_2/SiO_2 materials were intended to provide weak interfaces due to the low strength and lubricious characteristics of BN and TiO_2, while the SiC and SiO_2 materials were intended to provide strong interfaces through efficient load transfer across the interfaces of the laminated Si_3N_4 structure. Four-point flexural strength was measured on five specimens of each interfacial architecture. The results given in Table II show that SiC acted as a strong interface (730MPa) relative to the other materials, but we were unable to demonstrate significant work of fracture for any of the laminated structures, possibly due to the fact that the interface layers were too thin (<1μm). It was expected that all second phase interface materials, especially the weak interfaces, would act to increase damage tolerance by mimicking the type of fracture pattern pictured in Figure 5, which shows the fracture surface of a scallop shell consisting of calcite laminates with weak protein interfaces that yielded a 30x increase in the work of fracture[13] compared to monolithic calcite. Figure 6, which shows the fracture surface of a Si_3N_4-TiO_2/SiO_2 specimen, indicates brittle fracture without significant delamination that would yield the type of textured fracture pattern consistent with a high work of fracture resulting from interfacial energy dissipation.

Table II. Strength of Si_3N_4 with Designed Interface

Material	Average Flexural Strength (MPa)
SN-BN	369
SN-TiO2/SiO2	371
SN-SiC	730
SN-SiO2	312

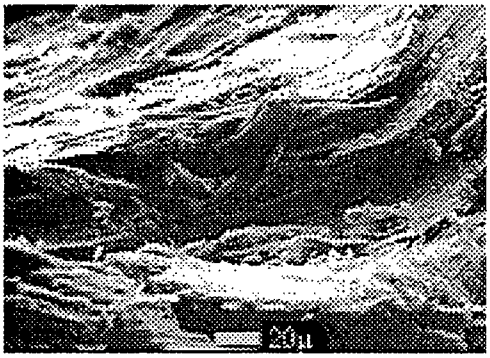


Figure 5. Scallop Shell Fracture Surface Indicating High Work of Fracture

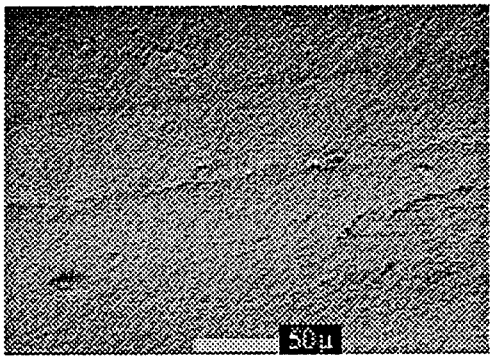


Figure 6. Si_3N_4-TiO_2/SiO_2 Fracture Surface

Microstructural Orientation

By incorporating β-Si_3N_4 seed crystals in the tape casting slip, Si_3N_4 microstructures were produced with elongated acicular grains oriented in the tape casting direction. Hiroa et al.[3] have demonstrated increased strength, toughness, and Weibull modulus via this process. In the current study, Si_3N_4 tapes with 2wt% β seed crystals (~3-5μm in length) and 7.25wt% Al_2O_3, 2.5wt% Y_2O_3 and 0.25wt% ZrO_2 as sintering aids were used to fabricate laminated specimens. Also, Si_3N_4 laminates containing no β seed crystals, as well as dry pressed Si_3N_4 specimens were fabricated for comparison. These materials were gas pressure sintered at

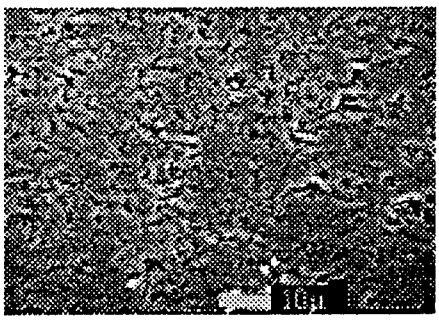


Figure 7. Oriented Si_3N_4 Microstructure

1810°C under a nitrogen gas pressure of 0.7MPa for three hours, followed by a further hour at 10MPa. Figure 7 shows a microstructural image of the top of a laminated specimen containing 2wt% β seed crystals. The casting direction in this photo was from left to right. The elongated β grains have grown during sintering to a length of ~10μm and it is apparent that acicular alignment has occurred in the casting direction.

Room temperature four-point flexural tests were conducted on eight specimens of each material, and chevron notch toughness measurements were conducted on five specimens for two of the laminated materials as indicated in Table III. The results in Table III indicate that laminated Si_3N_4 materials exhibit significantly higher strengths as compared to dry pressed Si_3N_4, due in part to the fact that the flaw size within the laminated structures is limited to the thickness of the individual tape layers. It appears that microstructural orientation in the casting direction leads to greater breaking consistency, as indicated by the reduction in flexural strength standard deviation. However, microstructural orientation did not yield a significant increase in the strength or toughness of the laminated Si_3N_4. Further microstructural development and greater acicular grain growth may be necessary in order to achieve higher strengths with toughnesses in excess of 10MPam$^{1/2}$ as described in the literature.[3] It is interesting to note that when the 2wt% β tapes were stacked such that the oriented acicular grains were aligned perpendicular to the length of the flexure specimen, a 200MPa reduction in strength was observed. This strength reduction confirms the anisotropic nature of the oriented microstructures.

Table III. Mechanical Property Results for Oriented Microstructure Study

Material Architecture	Ave. Flexural Strength and St. Dev. (MPa)	K_{1C} (MPam $^{1/2}$)
Dry Pressed Si_3N_4	715 (80)	---
Laminated Si_3N_4	924 (101)	5.76
Laminated Si_3N_4 - 2% β	920 (59)	5.81
Laminated Si_3N_4 - 2% β (β aligned perpendicular to specimen length)	711 (92)	---

II. LOM Processing of Si_3N_4 Aerofoils

LOM processing was performed to determine the compatibility of CCI's proprietary Si_3N_4 tape composition with the LOM fabrication process. Since the thermocompression stage used for manually laminated multilayer ceramics is not applicable for the LOM process, tape bonding experiments were conducted to determine an effective spray solution that would provide sufficient interlayer adhesion to allow for the fabrication of 3-dimensional Si_3N_4 components by LOM. Initial experiments evaluated ethyl alcohol, toluene, hexane, and isopropyl alcohol by spraying a thin layer of each onto a piece of Si_3N_4 tape, then laminating a second piece of tape and applying a 0.7MPa load for 10 seconds to mimic the load applied by the LOM roller. Although ethanol yielded the best results, there were pockets of non-bonded areas within the laminates which had occurred due to the rapid evaporation of the solvent prior to lamination. Further experiments demonstrated that the addition of either binder or plasticizer to the solvent spray would suppress the evaporation of the solvent and allow for more uniform bonding. Similar results have been reported previously.[12] Following the evaluation of various amounts of binder and/or plasticizer addition to the ethanol, a 10wt% polyvinyl butyral (PVB) in ethanol solution was selected for LOM processing because it demonstrated uniform bonding with relatively low organic content (10wt%).

LOM processing of Si_3N_4 components was performed using a LOM 2030 machine. The system is not configured for automated processing of green ceramic tapes and therefore it was necessary to manually laminate through the application of the bond solution followed by manually rolling each layer of tape prior to laser cutting. Three-dimensional aerofoils were fabricated using CCI's Si_3N_4 tapes and the 10wt% PVB in ethanol interlayer bond solution. The laser power was

constant at 67% with a beam radius of 0.005" and speed of 10"/sec. Tile size of the cross-hatched excess tape was 0.25". The aerofoils were decubed, subjected to a binder burnout cycle and densified via the gas pressure sintering process described previously. The green-state aerofoils (prior to sintering) are pictured in Figure 8. During sintering, delaminations occurred, which indicates that although the bond solution provided sufficient interlaminar tape adhesion to complete the LOM process, it did not provide the intimate bonding that is necessary for strong interfaces and structural integrity in a dense component. This indicates that an additional processing stage, such as dry bag isopressing, should provide stronger interlaminar bonding during sintering. In order to remove all traces of the laminate architecture however, it may be necessary to introduce a warm bag isopressing process.

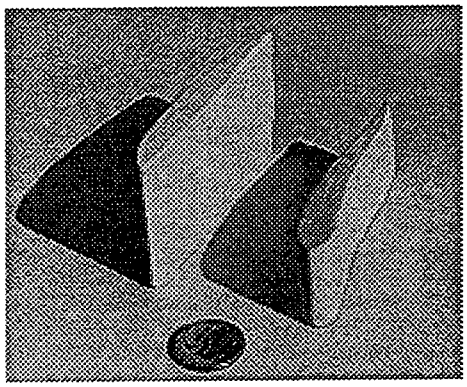


Figure 8. Green-state Si_3N_4 Aerofoils

DISCUSSION AND CONCLUSIONS

This study on the lamination of Si_3N_4 ceramic tapes suitable for LOM fabrication investigated three different design approaches in an attempt to enhance the mechanical properties. While it has been found that the sintered properties of laminated Si_3N_4 are superior to those of non-laminated Si_3N_4 (924MPa versus 715MPa, respectively), this is only true if intimate interlaminate bonding has been achieved prior to sintering.

To facilitate the use of Si_3N_4 tapes in the LOM process it was necessary to "stick" the individual tape layers together so that they could be stacked and laser cut without curling. A number of adhesives in the form of solvent sprays were investigated and it was concluded that a 10wt% PVB in ethanol solution was the most effective for this purpose. Unfortunately, delamination occurred during the binder burn-out cycle, and without post processing (such as isopressing) of the LOM shape prior to binder burn-out and sintering it was not possible to obtain a sintered component with structural integrity and good mechanical properties.

Three approaches for enhancing the properties of manually laminated tapes were investigated in an effort to identify material designs which can be incorporated into the LOM fabrication process. The first approach involved the fabrication of a plate that was functionally graded from a 50wt% Si_3N_4/50wt% SiC interior to a 100% Si_3N_4 exterior. The resulting FGM exhibited an estimated surface compressive stress of 100MPa, which should improve the damage tolerance, thereby extending its performance in wear and structural applications. Compressive surface stresses have been investigated in the past[24] in order to improve the ballistic performance by extending the time to failure of the back surface of the ceramic armor tile. If there is a large impedance mismatch in the bi-material system (in this case, Si_3N_4 and SiC) then the armor will prematurely fail at the laminate interfaces rather than at the back surface of the tile. It is proposed that functionally grading the composition will minimize the impedance mismatch and thereby allow the back surface compressive stress to extend the time to failure. To date, these graded armor plates have not been ballistically tested.

The second approach involved the application of a second phase material between each of the laminates. The composition of this second phase can be designed to bond the layers together during LOM fabrication as well as to provide a strengthening and/or toughening mechanism in a sintered component. Of the four different laminate coatings investigated, SiO_2, TiO_2/SiO_2, and BN significantly reduced the strength to approximately 350MPa without improving the damage

tolerance. The coating of SiC (which resulted from the in-situ reaction between SiO_2 and sugar) resulted in a strength of 730MPa but with very little increase in the work of fracture. No energy absorbing delamination was observed and only brittle fracture resulted. Electron microscopy revealed that these interfacial layers were <1μm and were discontinuous in nature. Further work is required to optimize the layer thickness in order to achieve enhanced damage tolerance.

The third approach involved the fabrication of specimens which contained an oriented microstructure obtained from the alignment of acicular β-Si_3N_4 grains during tape casting. Although laminated Si_3N_4 specimens with oriented microstructures did not exhibit improved strengths and toughnesses compared to non-oriented laminated Si_3N_4 (approximately 920MPa and 5.8MPam$^{1/2}$), they showed considerably better reproducibility. When the flexural strength was evaluated perpendicular to the alignment of the acicular grains, the strength dropped to 711 MPa, thereby indicating the anisotropic nature of the aligned microstructure.

In summary, this work has shown that the nature of LOM fabrication can be used to create materials which possess designed architectures based on the merits of lamination. Laminated Si_3N_4 structures are superior in strength to dry pressed Si_3N_4, provided that intimate bonding is achieved between each of the layers. This evaluation confirmed the potential to fabricate functionally graded laminates with designed properties and it also demonstrated the ability to produce oriented β-Si_3N_4 microstructures with high strength and good reproducibility. The most versatile laminated architectural design approach may be interfacial design. The introduction of an interfacial second phase material (such as BN or SiC) within the bond solution used to stick the tapes during LOM processing should be explored further for the production of materials with designed fracture behavior.

ACKNOWLEDGMENT

CCI would like to thank Mr. Steve Brown at the Naval Air Warfare Center - Aircraft Division for his support and assistance in using the LOM 2030 machine.

---

[1] W. Kowbel, "The Mechanism of Oxidation Protection of C/C Composites Coated with Graded, Codeposited Carbides and Nitrides," Ceram. Trans., Vol.34, *Functionally Gradient Materials*, Ed. J.Birch Holt. Amer. Ceram. Soc., 1993, p. 237.
[2] P. Sarkar, X. Huang and P.S. Nicholson, "Zirconia/Alumina Functionally Gradient Composites by Electrophoretic Deposition," *J.Amer. Cer. Soc.*, vol.76, 1993, pp 1055-1056.
[3] K. Hiroa, M. Ohashi, M.E. Brito and S. Kanzaki, "Processing strategy for Producing Highly Anisotropic Silicon Nitride," *J.Am. Cer. Soc.*, Vol.87, 1995, pp. 1687-90.
[4] D.B. Marshall, "Design and Properties of Multilayered Ceramic Composite," Mat. Res. Soc. Symp. Proc., Vol. 434, *Layered Materials for Structural Applications*, Ed. J.J. Lewandowski, C.H. Ward, M.R. Jackson and W.H. Hunt Jr., MRS 1996, pp.195-203.
[5] T. Chartiful, J.L. Besson and P. Boch, "Mechanical Properties of Al_2O_3/ZrO_2 Laminated Composites," Adv. in Ceramics, Vol 24B, *Science and Technology of Zirconia III*, Ed. S. Somiya, N. Yamamoto and H. Yanagida, Am. Ceram. Soc. Inc., 1988, p1131.
[6] P. Boch, T. Chartier and M. Huttepain, "Tape Casting of Al_2O_3/ZrO_2 Laminated Composites," *J.Am.Cer.Soc.*, 69[8], 1986, pp.191-2.
[7] J.L. Besson, P. Boch and T. Chartier, " Al_2O_3/ZrO_2 Layer Composites," in *High Tech Ceramics*, Ed. P. Vincenzini, Elsevier Science Pub.,1987, pp 633-642.
[8] G. Burger, R. Lemay, D. Lloyd, T. Shaw and P.S. Apte, "Microstructure-Mechanical Property Relations in Al_2O_3 Laminates," Proc. 11th Riso Int. Symp. Met. Mat. Sci., *Structural Ceramics - Processing, Microstructure and Properties*, Ed. J.J. Bentzen et. al. Roskilde, Denmark, 1990, pp. 217-224.
[9] R. Ham-Su and D.S. Wilkinson, "Strength of Tape Cast and Laminated Ceramics," *J.Am. Cer. Soc.*, 78[6], 1995, pp. 1580-84.
[10] C. Griffin, J. Daufenbach and S. McMillin, "Desktop Manufacturing: LOM vs Pressing", *Am. Cer. Soc. Bull.*, 73[8], pp. 109-113.
[11] D. Klosterman, R. Chartoff, N. Osborne, G. Graves, A. Lightman and G. Han, "Laminated Object Manufacturing of Advanced Ceramic Composites," *Proc. Int. Conf. Rapid Prototyping*, San Francisco, CA. March 31st - April 3rd, 1997, pp. 43-50.
[12] Z.E. Liu, P. Wei, B. Kernan, A.H. Heuer and J.D. Cawley, "Metal and Ceramic Components Made via CAM-LEM Technology," *Proc. 1996 SFF Symp*, Austin, TX, Aug. 12th - 14th, 1996, pp. 377-384
[13] W.J. Clegg, K. Kendall, N.M. Alford, T.W. Button and J.D. Birchall,"A Simple Way to Make Tough Ceramics", *Nature*, 347, 1990, pp. 455-457.
[14] A.J. Phillipps, W.J. Clegg and T.W. Clyne, "Correlation of Interfacial and Macroscopic Toughness in SiC Laminates," *Composites*, 24[2], 1993, pp. 166-176
[15] W.C. Tu, F.F. Lange and A.G. Evans, "Concept for a Damage Tolerant Ceramic Composite with Strong" Interfaces," *J. Am. Cer. Soc.*, 79[2], 1996, pp. 417-424.

[16] D.B. Marshall, J.J. Ratto and F.F. Lange, "Enhanced Fracture Toughness in Layered Composites of Ce-ZrO2 and Al2O3," *J. Am. Cer. Soc.*, 74[12], 1991, pp. 2979-2987.
[17] M.C. Shaw, D.B. Marshall, M.S. Dadkhah and A.G. Evans, "Cracking and Damage Mechanisms in Ceramic/Metal Multilayers," *Acte Met.*, 41[11], 1993, pp. 3311-3322.
[18] D.R. Lesuer, J. Wadsworth, R.A. Riddle, C.K. Syn, J.J. Lewandowski and W.H. Hunt, "Toughening Mechanisms in Al/Al-SiC Laminated Metal Composites," Mat. Res. Soc. Symp. Proc., Vol. 434, *Layered Materials for Structural Applications*, Ed. J.J. Lewandowski, C.H. Ward, M.R. Jackson and W.H. Hunt Jr., MRS 1996, pp.205-211.
[19] J. Heathcote, G.R. Odette, G.E. Lucas and R.G. Rowe, "Mechanical Properties of Metal-Intermetallic Microlaminate Composites," Mat. Res. Soc. Symp. Proc., Vol. 434, *Layered Materials for Structural Applications*, Ed. J.J. Lewandowski, C.H. Ward, M.R. Jackson and W.H. Hunt Jr., MRS 1996, pp.101-112.
[20] H. Liu, B.R. Lawn and S.M. Hsu, "Hertzian Contact Response of Tailored Silicon Nitride Multilayers," *J. Am. Cer. Soc..*, 79[4], 1996, pp. 1009-1014.
[21] H. Liu and S.M. Hsu, "Fracture Behavior of Multilayer Silicon Nitride/Boron Nitride Ceramics," *J. Am. Cer. Soc..*, 79[9], 1996, pp. 2452-2457.
[22] P.E.D. Morgan and D.B. Marshall, "Ceramic Composites of Monazite and Alumina," *J. Am. Cer. Soc..*, 78[6], 1995, pp. 1553-1563.
[23] P.E.D. Morgan, D.B. Marshall and R.M. Housley, "High temperature Stability of Monazite-Alumina Composites," *J. Mat. Sci. Eng.*, A195, 1995, pp. 215-222.
[24] DARPA "Advanced Survivability Technology" Contract #DAAL04-92-C-0029, Final Report, Nov., 1995.
[25] H.P. Martin, E. Muller, Y. Knoll, R. Strienitz and G. Schuster, "Silicon Carbide Derived From Silica Sol and Sugar," *J. Mater. Sci. Let.*, vol.14, 1995, pp. 620-622.

Automated Fabrication of Monolithic and Ceramic Matrix Composites via Laminated Object Manufacturing (LOM)

Don Klosterman, Richard Chartoff
Nora Osborne, George Graves
Rapid Prototype Development Laboratory and
Ohio Rapid Prototype Process Development Consortium
University of Dayton
300 College Park
Dayton, OH 45469-0130

Abstract

This report summarizes recent developments in a research program for fabricating advanced monolithic and ceramic matrix composite parts using Laminated Object Manufacturing (LOM). Both silicon carbide (SiC) and SiC/SiC composites are discussed. The LOM process is used to produce green forms that are then densified using various post processing operations. The monolithic ceramic LOM process was advanced through the implementation of an automated solvent spray bonding step, significant improvement in decubing with new software, and an intensive round of mechanical characterization. The LOM process for making CMC green forms is fully developed. This entailed implementing a process for making suitable SiC fiber preforms, a laser cutting capability, a decubing strategy, and a binder resin cure procedure. Further research is ongoing for the post processing pyrolysis and reaction bonding steps as discussed herein.

Introduction

The rapid prototyping and manufacturing of monolithic ceramics and ceramic matrix composites (CMCs) is being studied by a university/industry collaborative team lead by the University of Dayton and Helisys, Inc. This technology, based on Laminated Object Manufacturing (LOM), will be capable of producing high performance, near-net-shape structural ceramic parts. The standard LOM process [1] is illustrated in Figure 1. The technical objectives of the program are: 1) to produce CMC parts with structural integrity similar to CMC parts made by current fabrication techniques, and 2) to develop a commercially viable machine capable of automated fabrication. The rationale for using this process for composite fabrication is LOM's inherent capacity to handle flat sheet materials, to produce geometrically complex objects, and to operate with a high degree of automation, all without special tooling or fixturing.

The program involves a multidisciplinary effort that can be decomposed into the following interrelated sub activities:

- Machine design and control
- Software modifications and enhancements
- Ceramic preform formulation and manufacture
- Ceramic LOM process development
- Laser cutting
- Binder burnout
- Ceramic precursor pyrolysis
- Ceramic densification via reaction bonding
- Mechanical testing and characterization
- Part building and demonstration

Past efforts in all of these areas have been summarized in previous articles [2-6]. In this paper, recent progress in the areas of ceramic preform formulation and manufacture, ceramic LOM process development, ceramic precursor pyrolysis, and mechanical testing and characterization will be presented.

Monolithic Ceramics

Automation of Solvent Spray

The LOM process for monolithic ceramics is being developed using SiC as a focus material system. Ceramic tapes of 250 μm thickness comprised of a bimodal SiC powder (3 μm and 60 μm), carbon and graphite powders, and a polymeric binder system are fabricated with a standard doctor blade tape casting process. As described in previous reports [3], the tapes are laminated on a standard LOM2030 using a solvent assist spray technique. A hobby/artist's airbrush is used to apply a fine spray of butanol to the resin rich side (bottom) of the ceramic tape. The solvent acts as a tackifier to enhance the strength of the lamination, lower the required lamination temperature, and drastically increase the reliability of repetitive layer lamination, all compared to lamination without using a solvent. Butanol as a solvent has several advantages: low vapor pressure so that it doesn't evaporate during the spraying operation, reduced toxicity compared to aromatic solvents, and reduced flammability compared to lighter solvents.

A semi-automatic spraying process was developed to facilitate efficient, reliable, and reproducible part building (see Figure 2). The airbrush nozzle was mounted to the laser gantry of a LOM1015 machine. Solvent was fed to the nozzle through a flexible tube connected to a reservoir. The spray stream, directed normal toward the platform, was manually turned on and off with a solenoid switch regulating the gas pressure. A standard LOM software routine (i.e., "Cut Tiles") was used to move the nozzle in a raster pattern while the solvent spray was activated. Tapes were placed and removed manually from the platform. The sprayed tapes were placed solvent side down on the part being built on an adjacent LOM2030.

The following parameters affect the solvent spray process: internal nozzle adjustments, gas pressure, gantry speed, platform to nozzle distance, raster spacing, overall area sprayed. All these were determined by trial and error within a day's time, and they remain the same for all parts with the exception of the overall sprayed area. This procedure has proven itself effective: parts of up to 50 layers have been built in an efficient, methodical, and reliable manner without any lamination flaws. Although this process is only semi-automatic, personnel with minimal training can easily handle it. Only one person is required to run the process.

Decubing

The application of solvent to improve layer adhesion has important implications on the decubing step. The solvent assists in partially fusing the layers together, thus blurring the boundary. In general, the ease of decubing relies on the existence of an interface which, regardless of whether it is strong or weak, *must be distinct*. After building several different ceramic parts with various geometries, it became apparent that the decubing step was difficult and tedious at best, and in many cases ceramic parts could not be decubed without severe damage. To address the problems of decubing ease and damage, two strategies were investigated: adaptive crosshatching and adaptive surface burnishing. Both these strategies are similar and required additional software to be developed. These strategies, illustrated in Figure 3, involve selectively modifying the region of overlap between cube area and part area in successive layers. In the case of adaptive crosshatching, the area is cut with a fine (0.5 mm) crosshatch. With adaptive surface burnishing, the surface of the overlap zone is burnished with the laser, removing the binder from the surface while leaving the powder. The thin layers of loose powder serve as a release mechanism during decubing.

Software developed by Helisys, Inc. for adaptive crosshatching was tested on three parts shown in Figure 4. This strategy was largely successful. Each part was decubed with relative ease in ten or twenty minutes. More importantly, there were no flaws introduced from cubes sticking to the part or layers delaminating. Some of the success is directly attributable to the strength of the layer-to-layer bond as a result of the solvent lamination process. Upon closer examination of the surface with a microscope, it is evident that the pattern of fine crosshatches remains on the stair steps (see Figure 5). Thus, removal of this pattern and surface finish become issues to consider. Depending on the intended use of the part, it may not be necessary to improve the surface finish. However, if finishing is necessary, it is expected that normal grinding and polishing can be used to smooth the surface with no more difficulty than for parts made with other rapid prototype techniques. Therefore, the existence of the fine crosshatch pattern is not expected to pose any serious disadvantages.

A preliminary analysis of adaptive surface burnishing using simple geometries has revealed that surface burnishing is at least as effective as adaptive crosshatching. The advantages of surface burnishing compared to adaptive crosshatching are 1) burnishing the overlap zone generates less dust compared to cutting; and 2) the part surface is not left with a fine crosshatch pattern.

Mechanical Properties

An intensive characterization of the mechanical behavior of LOM SiC parts was made. MOR bars (4mm x 3 mm x 50 mm) were fabricated using the latest version ceramic LOM process and densified via reaction bonding. Over 50 bars were made in each of 6 different LOM runs. The results of the 4-point flexure tests are summarized in Table 1. It is important to note here that these specimens were tested as-received without any polishing.

Table 1 : four-point flexure test results for as-received (unpolished), reaction bonded, monolithic SiC specimens made with LOM.

LOM Run #	# specimens	Displace-ment rate (cm/min)	Flexure Strength (MPa)	σ (MPa)	Weibull Modulus
1, 2, & 3	10 each run	0.5	158	34	5.2
4, 5, & 6	10 each run	0.5	152	25	5.7
1	23	0.5	157	22	10.4
2	22	0.5	151	22	8.3
3	24	0.5	158	18	9.0
4	25	0.05	142	23	6.6
5	7	0.05	142	20	8.2
6	8	0.05	154	10	17.5
5	22	0.005	152	21	8.7
6	21	0.005	165	23	7.6

The 4-point bend strength of the unpolished SiC specimens is about 150 MPa. It is not valid to compare this strength to that of commercially available SiC because of the effect of polishing and chamfering in the case of the latter. In general, the strength of reaction bonded SiC is not expected to be as high as sintered SiC, which is approximately 400 MPa [7]. With proper preparation, the bend strength of LOM SiC is expected to significantly increase from 150 MPa, most likely by a factor of two. If this is found to be the case, then the bend strength of reaction bonded SiC will compare favorably with that of similar commercially available material made with conventional techniques.

The consistency of the bend strength from LOM run to run and within each LOM run is noteworthy. This consistency is characteristic of SiC as a material in general. The fact that the bend strength does not change with strain rate indicates that this material does not exhibit slow crack growth, another characteristic of SiC in general. Thus, in two more instances, LOM SiC compares favorably with commercially available material.

A photomicrograph of reaction bonded SiC (Figure 6) illustrates little evidence of a layering effect. In addition, low porosity indicates effective infiltration during reaction bonding.

Ceramic Matrix Composites (CMCs)

The fabrication of continuous fiber CMCs with LOM is another objective of this program. SiC/SiC is being used as a focus material system. From the onset, the two most critical issues were considered to be 1) the availability of preforms, suitable for LOM, which incorporate a high volume fraction of continuous SiC fibers; and 2) near-net-shape densification of the CMCs. Described in this section is the development of a suitable SiC/SiC preform for LOM and the various stages of the LOM process that dictated the preform's design. Issue 2 is being addressed through application of the reaction bonding process, as demonstrated with monolithic SiC, although detailed results are not yet available.

The approach to fabricating CMCs with LOM involves the layup of separate, alternating monolithic ceramic tape layers and fiber/resin prepreg layers. The development of a SiC fiber (Nicalon^{TM}, Dow Corning) and furfural resin (FurCarb^{R} UP-440, QO Chemicals) prepreg was described in a previous report [3]. The furfural is a thermoset resin that serves a dual role: as a binder during LOM fabrication and as carbon source for the reaction bonding process. Layers are bonded through heat and pressure applied by a flat heating plate or iron; no solvent is necessary. The fiber/tape layup is subsequently post-cured and pyrolyzed, followed by reaction bonding.

Early attempts to fabricate CMCs with separate layers of tape and fiber were limited by two practical problems, illustrated in Figure 7. First, the required laser power to cut through a fiber layer is much higher than for a monolithic tape layer. Although the laser power can be adjusted accordingly, it is not possible to handle the problems associated with random variations in the layer thickness or fiber content. Specifically, if the laser does not cut completely through a fiber layer, it will not be possible to simply "snap off" the adjacent waste cube during decubing due to the connected fibers. On the other hand, it the laser over compensates and delivers more power than is required to a fiber layer, the monolithic tape layer below will be severely damaged.

The second problem associated with the use of separate layers is that the adhesion of a fiber layer to the top of a tape layer is significantly weaker than to the bottom of a tape layer. This effect is caused by the ceramic tape which contains a resin-rich side on the bottom. The decubing is impractical because it is difficult to separate layers at the strong interface without delaminating the adjacent weak interface in the process. Thus, the problems can be generalized as an inherent difficulty of working with two separate layers that have significantly different bonding and cutting characteristics.

The situation is resolved by combining the separate tape and fiber preforms into one preform during the prepreg B-staging cycle, as illustrated in Figure 8. This new preform, the "tape-preg", is a simple fiber-on-tape laminate that solves both the laser cutting and laminating problems by eliminating the weak interface so that each layer contains both fibers and monolithic tape. The laser cutting is improved because the fiber component is the first to be cut. Therefore, if insufficient power is delivered to cut the

entire tape-preg layer, the remaining material will be ceramic tape which is easily "snapped-off" during decubing. If too much laser power is delivered accidentally, the tape-preg layer immediately below will be minimally damaged, since its surface is comprised of fibers. The decubing is also improved because all the layer interfaces are of the same strength. The only practical complication is that the part layer thickness is necessarily doubled, unless thinner monolithic tapes and fiber prepregs are used. In this study, the tape-preg thickness was 0.5 mm (0.25 mm ceramic tape and 0.25 mm fiber prepreg).

To test the effectiveness of the SiC tape-preg, a small scale turbine engine seal (Figure 9) was fabricated with the "Table-Top LOM" (TTLOM) system at University of Dayton [4]. This experimental system was assembled to study laser cutting of high performance fibers and build CMC parts throughout the research program. The apparatus combines a copper vapor laser with a computer controlled XY gantry, manually adjustable z-platform, and manual layer lamination via hot iron. With this apparatus, one is able to obtain high quality laser cuts, illustrated in Figure 10, as defined by steep cut channels, no fiber end damage, and a minimal resin burn-back zone. The turbine engine part was built with seven layers of SiC tape-preg alternating in a $0/90^{\circ}$ arrangement. It was built and decubed without any problems. The decubing process was more similar to that for LOM paper parts rather than that for LOM monolithic ceramics. The reason for this is that the tape-preg layers maintain a distinct interface, i.e. the monolithic layers do not migrate into the fiber layers and vice-versa. For this reason, the use of adaptive crosshatching was not required.

After decubing, SiC/SiC parts must undergo a resin cure cycle to complete the cure of the furfural resin and to provide additional consolidation. The turbine engine seal was fit with a negative made from LOM paper, placed in a vacuum bag set-up, and cured in an oven using the following cycle: 25-200°C for 7 hrs; 200°C for 1 hr. After this cycle, the part was physically robust. The microstructure is given in Figure 11. Notice that the layers are well compacted with little or no porosity present.

The next step in the post-processing cycle was simultaneous resin pyrolysis and binder burnout. This step was evaluated by pyrolysis of free-standing, 6-layer, 1-inch SiC/SiC squares in flowing argon. Early studies revealed that the laminates were prone to delamination during the pyrolysis cycle. A variety of cycle conditions were tested under the initial suspicion that the problem was related to inability of the pyrolysis products to successfully diffuse out. However, two general observations were made: the delaminations always occurred within the tape-preg layers, not between the tape-preg layers; and the layers tended to curl perpendicular to the fiber direction. Thus, it is more likely that the problem is caused by the shrinkage of the furfural resin and the differential bond strength throughout the CMC. Although the bond within the tape preg layers is relatively strong during the LOM layup process, it becomes a relatively weak bond during the subsequent cure and pyrolysis cycle as the furfural resin cures evenly throughout the bulk.

The delamination problem worsens with increasing mass loss during the pyrolysis cycle. When the cycle is stopped at 250°C, there is 6% mass loss in the composite and it is possible to obtain an undamaged laminate using a slow heating cycle (2.5–5°C/hr). However, when the cycle is advanced to 300°C, there is 9.5% mass loss and the sample is delaminated. Based on thermogravimetric analysis, the laminates are expected to lose 20% mass through 700°C. It appears that to solve this problem a strategy involving only adjusting the heating rate will be unsuccessful. Alternative solutions are suggested. The first involves applying pressure to tape-preg laminates during pyrolysis. In an initial test, a sample that was placed under 15 psi pressure still delaminated during the pyrolysis cycle carried out to 300°C. Higher pressures will be investigated. A second strategy involves lamination of fiber layers only, omitting the tape layers. This strategy was successful in an initial study when a 10-layer laminate made of fiber layers survived the pyrolysis cycle through 550°C without delaminating. A third approach is to reconsider bonding separate layers of tapes and prepregs. The most appropriate strategy of these three is now under evaluation.

Conclusions

The monolithic LOM process was made more reliable and less labor intensive through recent hardware and software improvements. Monolithic SiC parts can now be fabricated with ease via LOM and post processed to dense ceramic through reaction bonding. These parts exhibit comparable mechanical behavior to commercially available SiC specimens fabricated with traditional processes. The LOM process for making flat layer, continuous fiber SiC/SiC composites has been demonstrated to the point of making fully cured green parts. Additional work is needed to develop a fully effective pyrolysis cycle. Once achieved, reaction bonding of SiC/SiC is expected to be feasible using monolithic SiC technology.

References

1. Helisys, Inc., 24015 Garnier St., Torrance, CA, 90505, USA.

2. Klosterman, D., R. Chartoff, N. Osborne, G. Graves, A. Lightman, and G. Han, "Laminated Object Manufacturing (LOM) of Advanced Ceramics and Composites," *Proceedings of the 7th International Conference on Rapid Prototyping*, University of Dayton and Stanford University, San Francisco, CA, April 1997.

3. Klosterman, D., R. Chartoff, N. Osborne, G. Graves, "Laminated Object Manufacturing, A New Process for the Direct Manufacture of Monolithic Ceramics and Continuous Fiber CMCs," *Proceedings of the 21st Annual Cocoa Beach Conference & Exposition,* Cocoa Beach, Florida, January 12-16, 1997.

4. Klosterman, D, R. Chartoff, B. Priore, N. Osborne, G. Graves, A. Lightman, G. Han, S. Pak, J. Weaver, "Structural Composites via Laminated Object Manufacturing

(LOM)," *Solid Freeform Fabrication Proceedings,* University of Texas at Austin, August, 1996.

5. Kalmanovich, G., L. Dodin, S. Tu, "Curved-Layer Laminated Object Manufacturing," *Proceedings of the 7th International Conference on Rapid Prototyping*, University of Dayton and Stanford University, San Francisco, CA, April 1997.

6. Kalmanovich,G., "Curved-Layer Laminated Object Manufacturing," *Solid Freeform Fabrication Proceedings,* University of Texas at Austin, August, 1996.

7. *Effects of Environment on the Mechanical Behavior of High-Performance Ceramics, A Compendium of Data Prepared for Oak Ridge National Laboratory*, University of Dayton Research Institute, Dayton, OH, July 1997.

Acknowledgments

The work reported here was performed under a grant from the United States Defense Advanced Projects Agency (DARPA) and the Office of Naval Research (ONR). Dr. William Coblenz and Dr. Steven Fishman are the program officers.

Illustrations

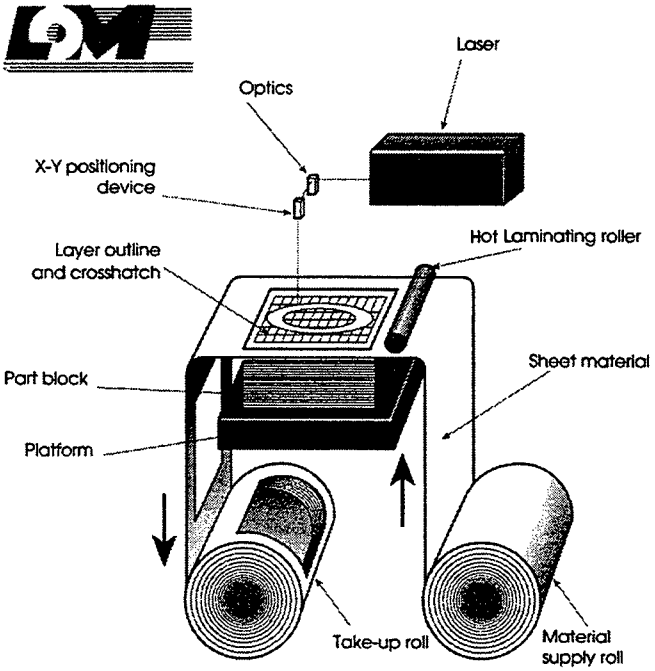


Figure 1 : Schematic of the LOM process (courtesy Helisys, Inc. [1]).

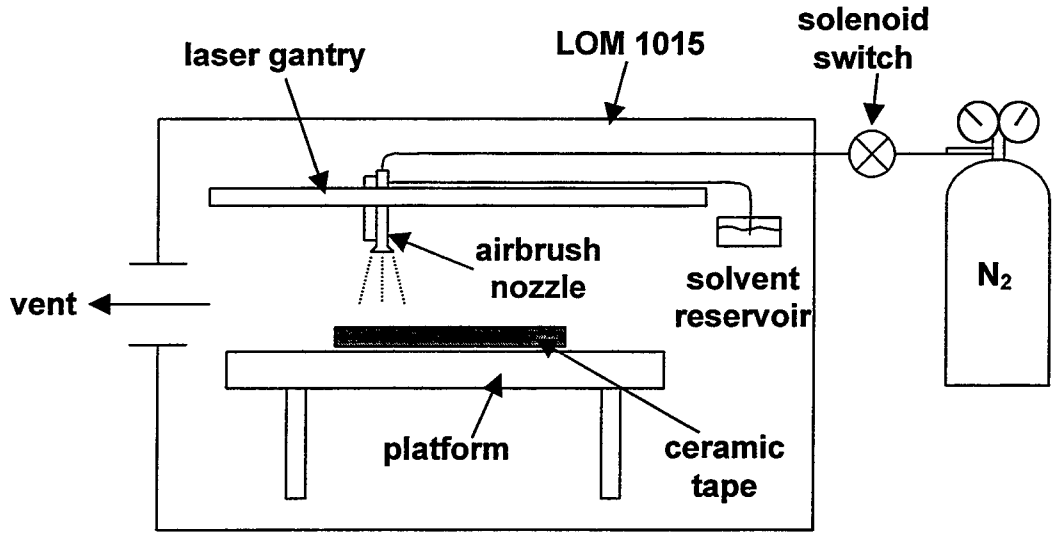


Figure 2 : Semi-automatic system for applying solvent to monolithic ceramic tapes.

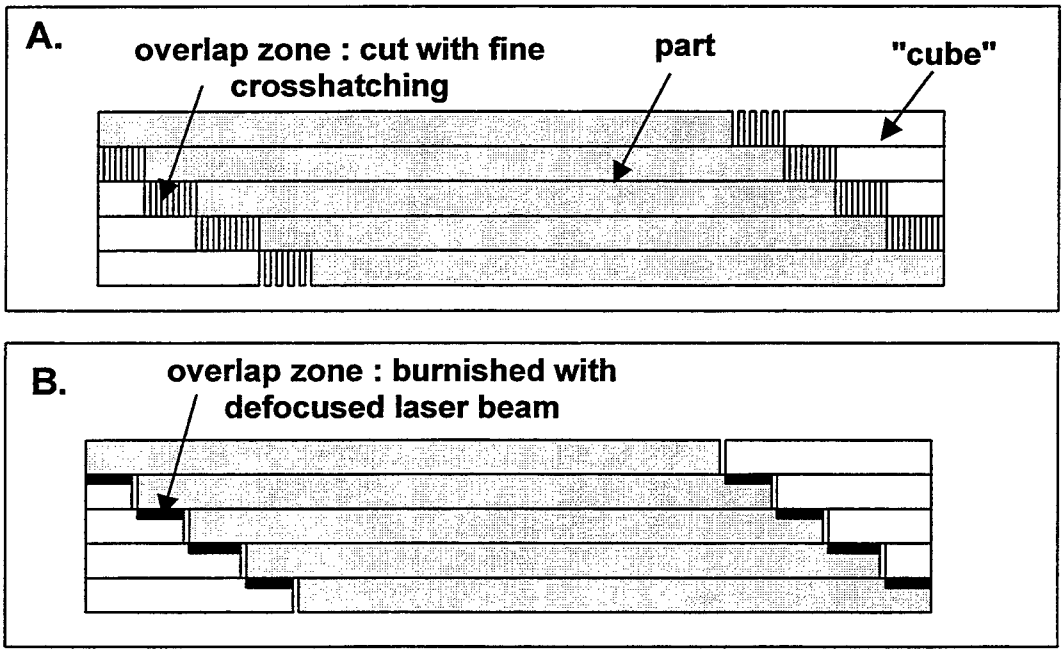


Figure 3 : Two strategies aimed at improving decubing by affecting the overlap zone between the waste cubes and the actual part : **a) adaptive crosshatching** and **b) adaptive surface burnishing**. This diagram is not drawn to scale; with the materials used in this study, the layer thickness was the same as the cut width (0.25 mm).

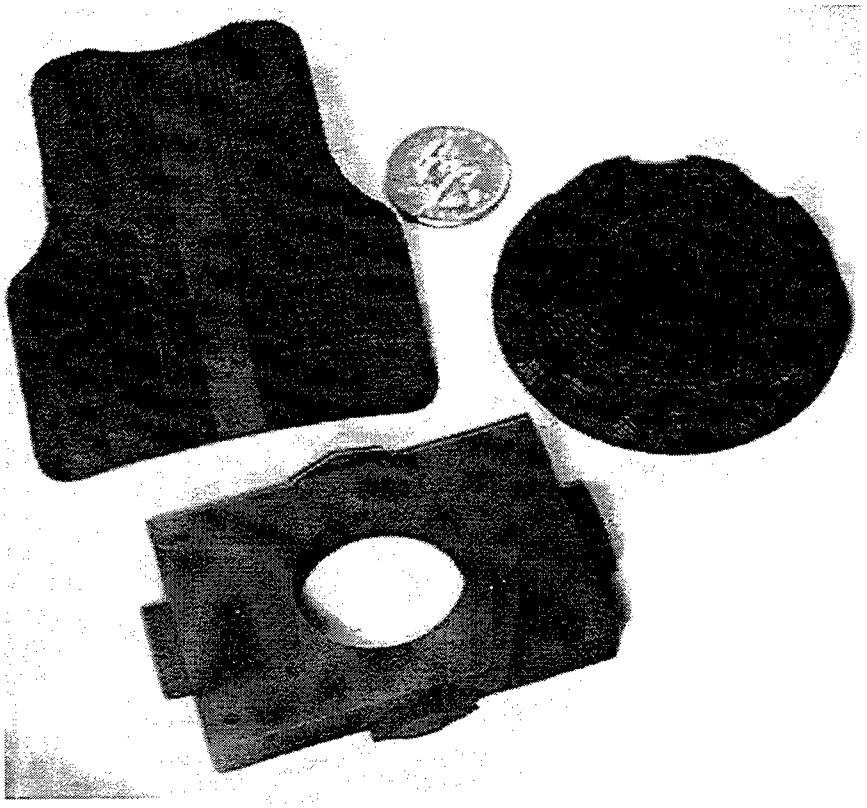


Figure 4 : Monolithic SiC parts made on a LOM2030 using the adaptive crosshatching software.

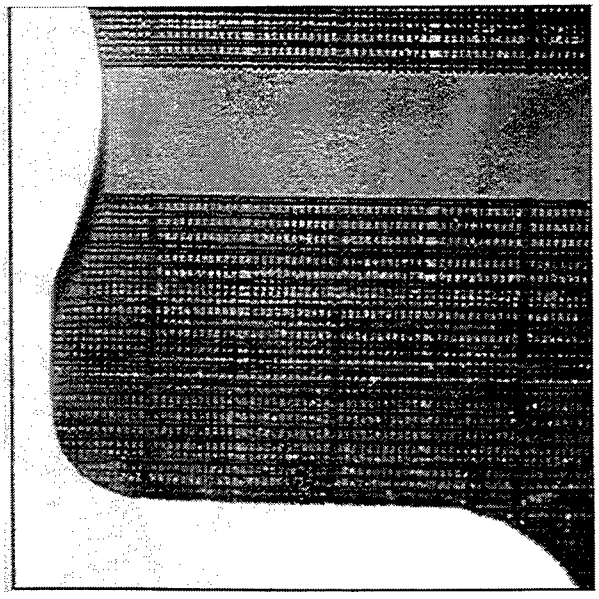


Figure 5 : Close-up of surface of body armor piece made with adaptive crosshatching.

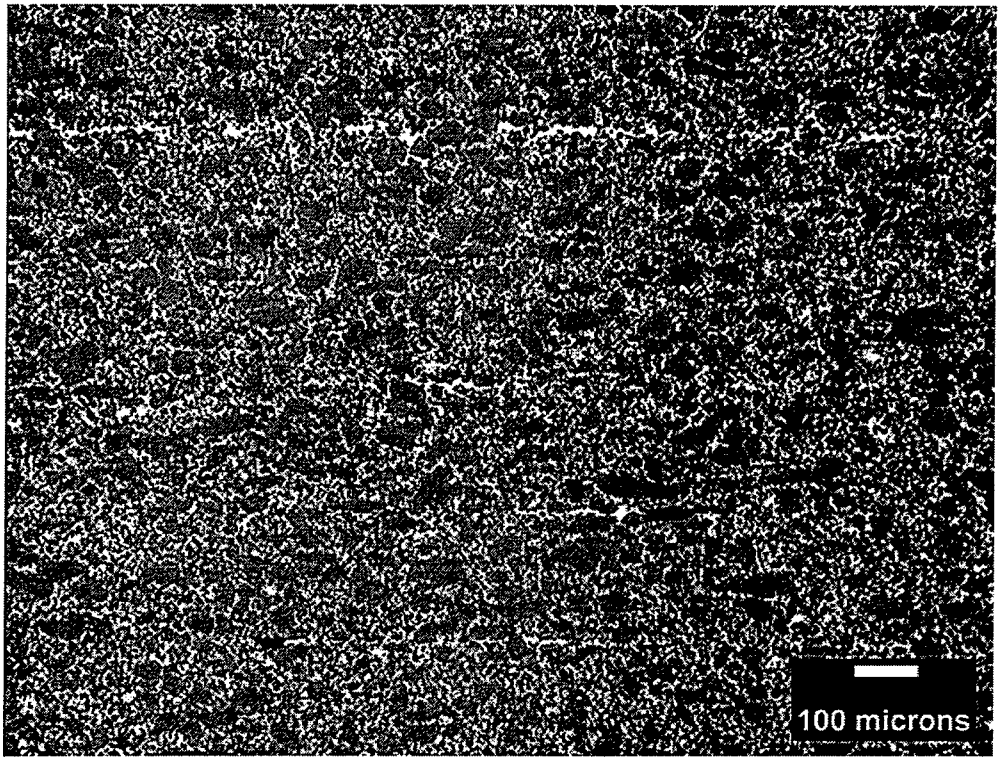


Figure 6 : Cross section of reaction bonded, monolithic SiC bar made with the ceramic LOM process.

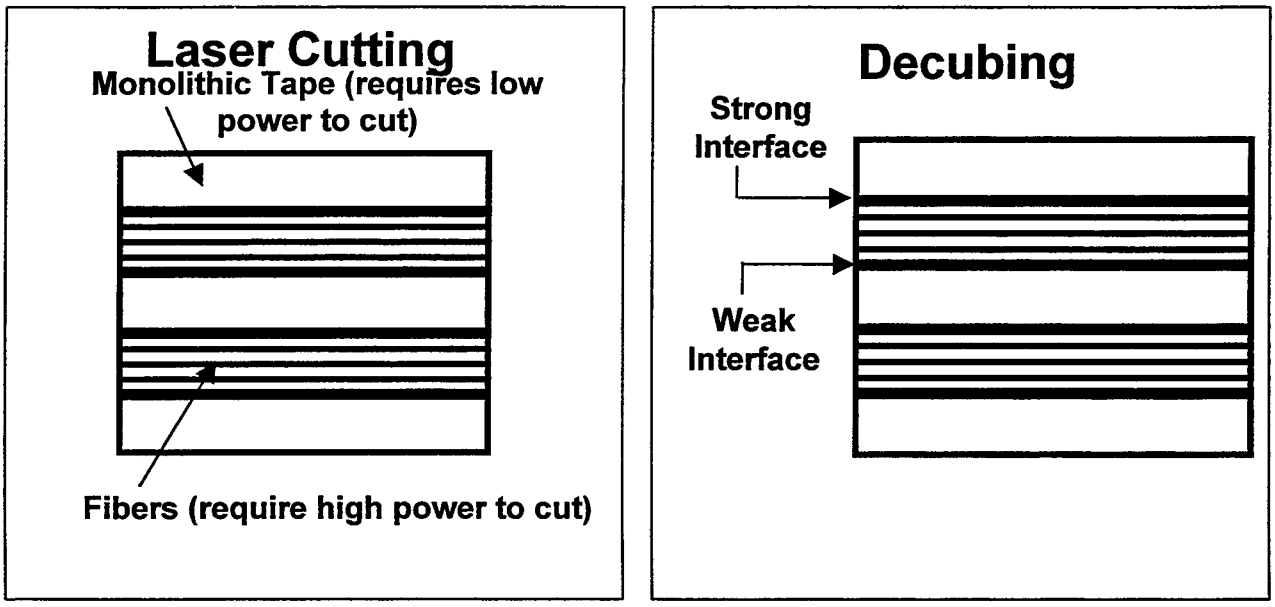


Figure 7: Illustration of origin of LOM processing difficulties for separate layers of fibers and monolithic ceramic tapes.

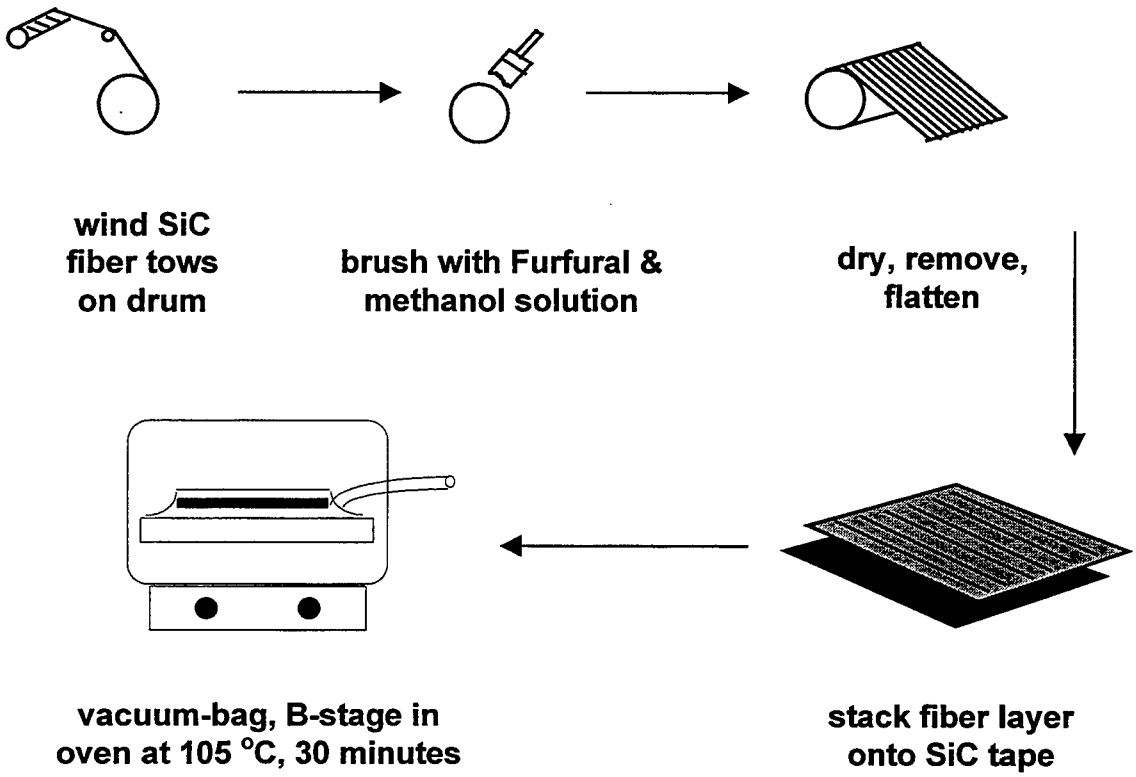


Figure 8 : SiC tape-preg fabrication process.



Figure 9 : 1/5 scale, turbine engine seal built from 7 layers of SiC tape-preg. As it appears, this part is fully cured but has not been pyrolyzed or reaction bonded yet.

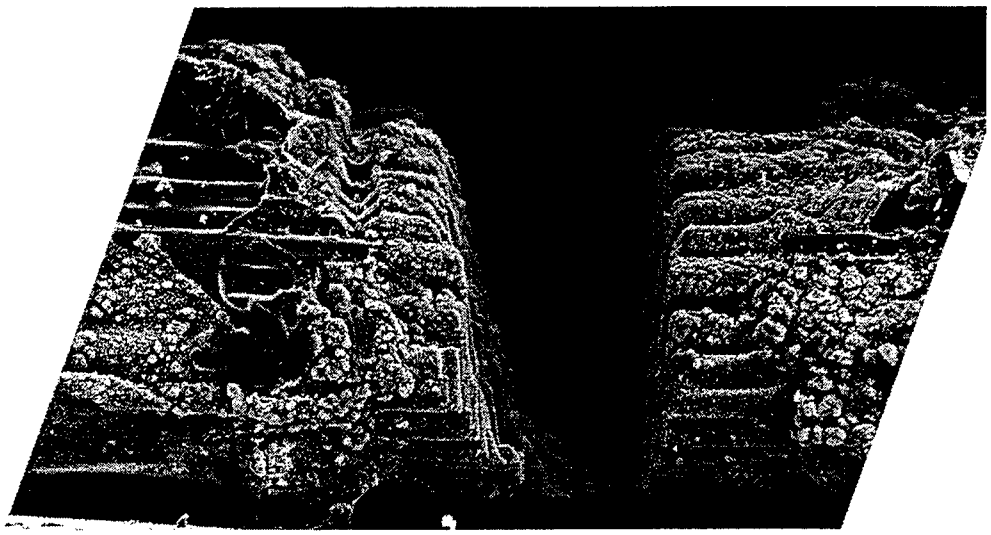


Figure 10 : SiC fiber/furfural prepreg cut with a copper vapor laser. The fiber diameter is approximately 15 μm and the cut channel is approximately 80 μm in width. High quality laser cutting is characterized by the vertical walls, clean fiber ends, and minimal burn back zone.

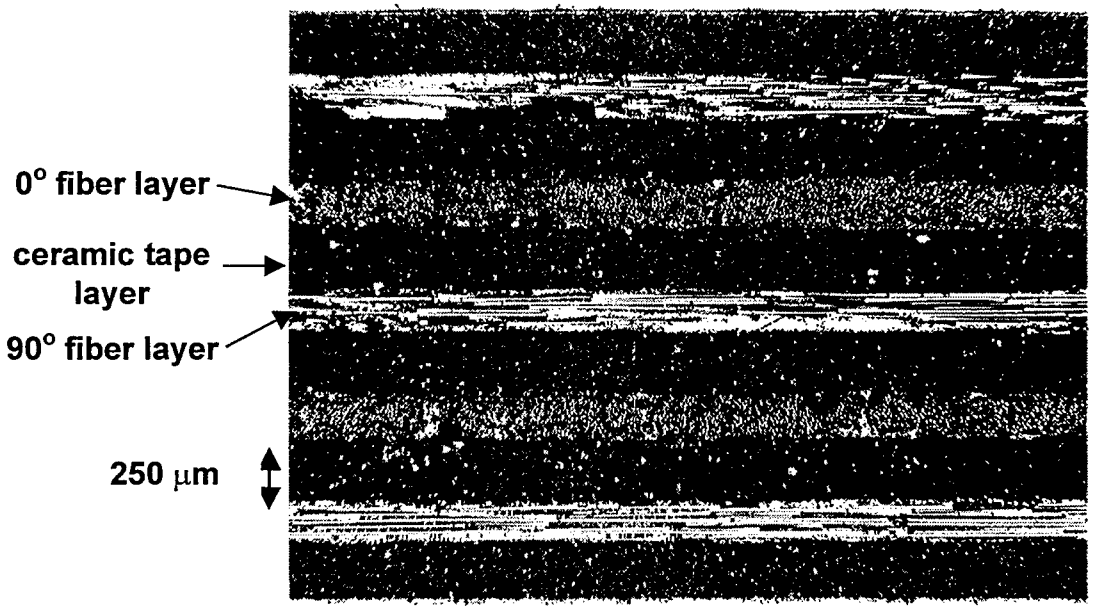


Figure 11 : Photomicrograph of green SiC/SiC composite made with "TTLOM" test bed. The sample has been fully cured, but not fully pryrolyzed.

RAPID PROTOTYPING DECISION SUPPORT SYSTEM

K. G. Jones and R. I. Campbell
Department of Manufacturing Engineering and Operations Management
University of Nottingham
Nottingham, UK

Abstract

An application has been produced to rate Rapid Prototyping system suitability based on designer requirements. The software is part of a project to produce a comprehensive Design For Rapid Prototyping (DFRP) methodology. Using a combination of database searches and user-defined weighted rating, the system uses various design requirements to make qualitative suitability decisions. MS Visual Basic has been used to implement a user-interface to manipulate an MS Access database. Proposed features include system validation achieved by designers' feedback on prototype performance. This will help to remove the false expectations sometimes associated with RP and will ultimately promote its wider usage.

Introduction

Rapid Prototyping (RP) is a revolution in manufacturing technology. The use of RP can significantly reduce manufacturing lead-time, lower product development costs and produce better quality products. It is not surprising that the RP industry continues to grow rapidly[1]. To fully maximise the benefits of RP, there are several factors which require consideration. These include firstly the decision of whether the use of RP is appropriate. If this is confirmed, the designer is faced with an array of RP processes and materials from which to select.

Currently, the decisions regarding which RP process, machine and material are dependant on the company's in-house facilities or made by the Service Bureaux (SB). A tool which aids this decision making process offers designers a wider choice when selecting an SB. If the designer is able to determine the most appropriate RP combination, then the constraints of a certain SB do not apply and the prototype is likely to satisfy its requirements more closely. In order to make such a decision, designers require access to data relating to all prospective alternatives which optimises the effective use of RP. With the continual introduction of improved RP technologies and systems, current performance levels are very difficult to assess. Consequently, there is a requirement for an expandable system capable of accommodating the advances made within the field of RP. It would inform designers of the different RP systems available and the typical results to expect.

The ultimate goal of producing a Rapid Prototyping Decision Support System (RPDSS) is to enable RP to be used to its full potential throughout a project's duration, maximising all the associated time-to-market, cost reductions and quality benefits. A fully functional RPDSS would be able to accept CAD data and through its analysis, determine firstly whether the use of RP is appropriate, and subsequently to decide which process, machine, material and RP specific parameters (such as part orientation) to use. The long-term project aim is for the software to apply analysis directly to the CAD data to determine RP suitability, with little or no designer interaction. Achieving this goal is dependant on many factors; one such factor is that the design requirements such as tolerances and surface finishes be represented by the CAD model, achievable by using

feature based design[2]. A complete RPDSS capable of achieving the proposed functions will only be achieved through development of a standard format for representing such design requirements.

Software Requirements

The ultimate project aim was therefore to design and produce a design tool which would suggest the optimal RP system and material for a variety of processes using desired or inherent prototype attributes. The core software function is to suggest the optimal RP system and material for a variety of RP processes based on prototype attributes and designer requirements. The software was developed to operate through a user-friendly interface requiring little or no prior RP knowledge. To enable the expansion into a complete RPDSS, the software produced includes a universal shell and database structure into which the other RPDSS modules may be placed. The software also requires the ability to learn via designer feedback of prototype satisfaction enabling the continual improvement of output.

The core prototype attributes (1-3) and requirements (4-9) specified by the designer and used to determine the suitability were selected to be:

1. Quantity
2. Timescale
3. Budget
4. Dimensions
5. Function
6. Features
7. Accuracy
8. Strength
9. Surface Finish
10. Machinability

Computer-aided RP selection systems are not a completely new concept but have tended to focus on one specific RP process [3-7]. With the numerous RP alternatives now offered by SBs it was considered much more useful to model several of the available RP processes. Based on their degree of industrial presence and availability of data, the RP processes selected for comparison were:

- Fused Deposition Modelling
- Laminated Object Manufacture
- Selective Laser Sintering
- Solid Ground Curing
- Stereolithography

An important consideration in selecting the suitability evaluation method was to be aware of possible system improvements, potential data structural changes and the modelling of subjective data. The advantages of relational databases lie in the high degree of flexibility regarding subsequent modifications of the data structure. The use of weighted rating in conjunction with a database offers the advantage of combining subjective measure modelling with real data and was therefore chosen as the processing method to determine system suitability.

This project concerns the pairing of design requirements and RP machine capabilities and the subsequent quantification of suitability. Calculating the degree of coalescence is highly dependant on the data concerned. The data used by the software can be categorised into design requirements (specified by the designer) or RP capabilities (determined by benchmarks/manufacturer specifications). With respect to suitability evaluation, each data item can be further classified as either static or dynamic. Part size is one such example of a static data item and is of no relevance unless it exceeds the capacity of the RP machine. There exists no conformance measure that can be made as to how well a machine can accommodate a prototype of a certain size; it either can or cannot.

Using static data alone will only provide Boolean constraints upon suitability without indicating its degree. Nevertheless, static data must be modelled into the system since it will be meaningless to provide a solution which fails to meet the constraining factors, regardless of how well it may meet the more dynamic requirements. Dynamic data items are therefore of much greater interest since they can be used to represent measures of system suitability, i.e. how well a system is suited to a particular application when compared to another.

Suitability Calculation

Suitability is the ratio between design requirement and machine capability. For a prototype budget requirement of £2,000, a certain machine is 100% suitable with respect to budget satisfaction if the prototype it produces costs £2,000; following this, the suitability is then 50% if costing £4,000. The percentage suitability for a specific requirement can be formulated as shown in Equation 1:

$$\text{Percentage Suitability} = \frac{\text{Design Requirement}}{\text{Capability}} \times 100 \qquad (1)$$

There are some constraints over the use of Equation 1. Using the above example, if the prototype price (Capability) is £1,000 it cannot be said that the suitability is 200%. This formula also only applies when a low level of capability is superior. This is true for accuracy, surface finish, build-time and cost. For strength and machinability the formula requires inversion.

Weighted rating states the suitability rating be multiplied by the importance value of that attribute. However, in doing so the problem arises that a high specification prototype with corresponding importance values will perform disproportionately when compared to a less important prototype. To remedy these discrepancies, before weighting the individual suitability ratings, the importance values must be levelled. This can be formulated by Equation 2:

$$\text{Levelled Importance} = \frac{\text{Importance Value}}{\sum \text{Importance Values}} \qquad (2)$$

The possible numeric values associated with the importance specified by the designer were given consideration and the most logical system was found to be a five level system. The lowest level of importance, 'Irrelevant' implies that the design requirement is not considered by the designer to bare any relevance to the prototype's conformance to specification. The suitability for

a requirement determined irrelevant automatically receives a suitability rating of 100% although this score is not used in the aggregation of the overall suitability.

At the other extreme, it was considered necessary to provide the option for 'knock-out' importance criteria to be specified. Selecting the importance level, 'Mandatory' for any factor will ignore any system which fails to satisfy the specific design requirement irrespective of other suitability rating, and thus immediately giving the system a suitability rating of 0%. Clearly, this importance level should be used with care or very few systems will be considered, however, having the option to place a very demanding requirement upon it was considered appropriate as the situation may arise in industrial situations. For example, if the part is to be stressed to at least 20MPa, a system offering an RP solution incapable of satisfying this constraint will render the system invalid for such occurrences.

Intermediate levels of importance 'Unimportant', 'Desirable' and 'Important' were chosen to provide the weighting schema each with increasing associated importance values. Naturally, for multiplication purposes these levels require quantification. The importance values using the scale; Important: 3, Desirable: 2 and Unimportant: 1 have been totalled, and each value divided by this total, giving a levelled importance for each factor. The overall system suitability can therefore be formulated by Equation 3:

$$\text{Total Suitability} = \sum \left(\frac{\text{Design requirement}}{\text{Capability}} \times \left(\frac{\text{Importance Value}}{\sum \text{Importance Values}} \right) \right) \qquad (3)$$

Software Implementation

The design requirements are input via a form-filling method programmed using MS Visual Basic 4.0. indicated in Figure 1.

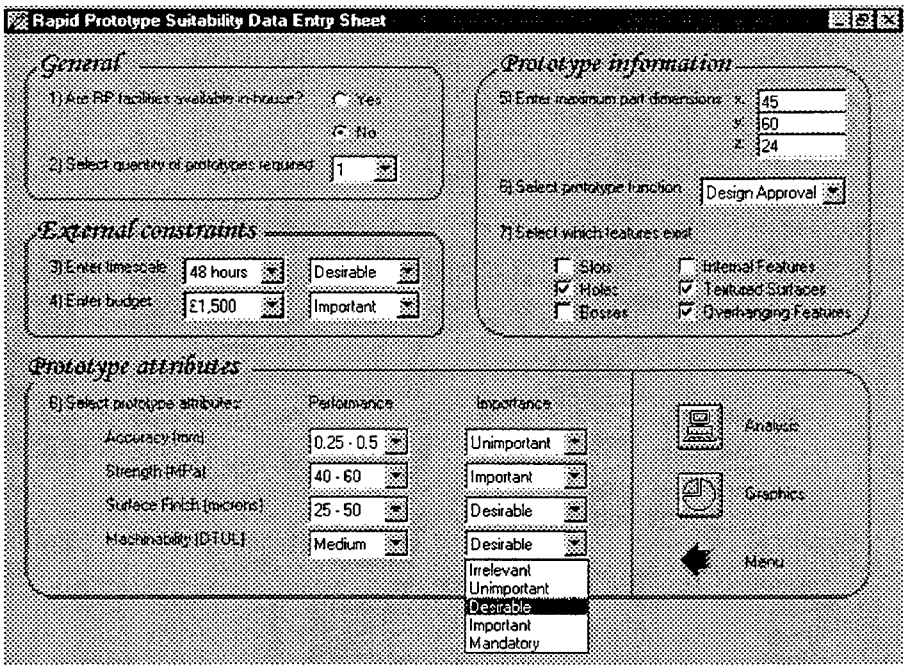


Figure 1: RPDSS suitability requirements entry screen

The form uses a series of drop-down boxes giving a selection of pre-defined options. Once the requirements have been entered, the analysis is performed following Figure 2. The boxes to left of the diagram indicate table names within the database where the relevant data is stored and the labelled lines indicate the data flow.

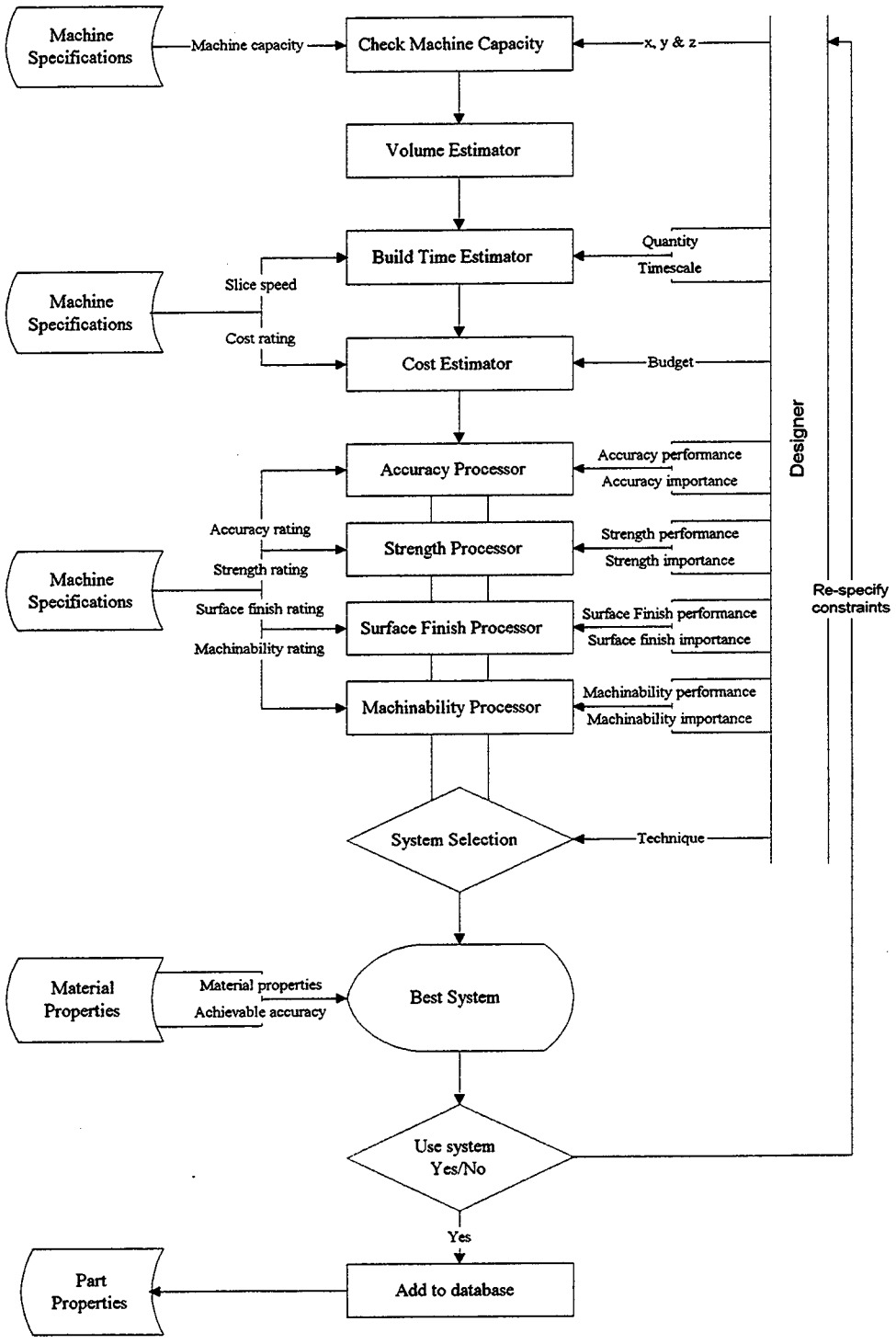


Figure 2: Flowchart for suitability procedure

The subsequent analysis is presented to the designer with a list of suitability percentages, highlighting the most superior process (see Figure 3). For the suggested process, the most suitable machine and material is detailed. Specific material properties may then be viewed, as can the best machine and material for other processes. The RP data stored within the database has been collected via an extensive literature search and manufacturers' specifications.

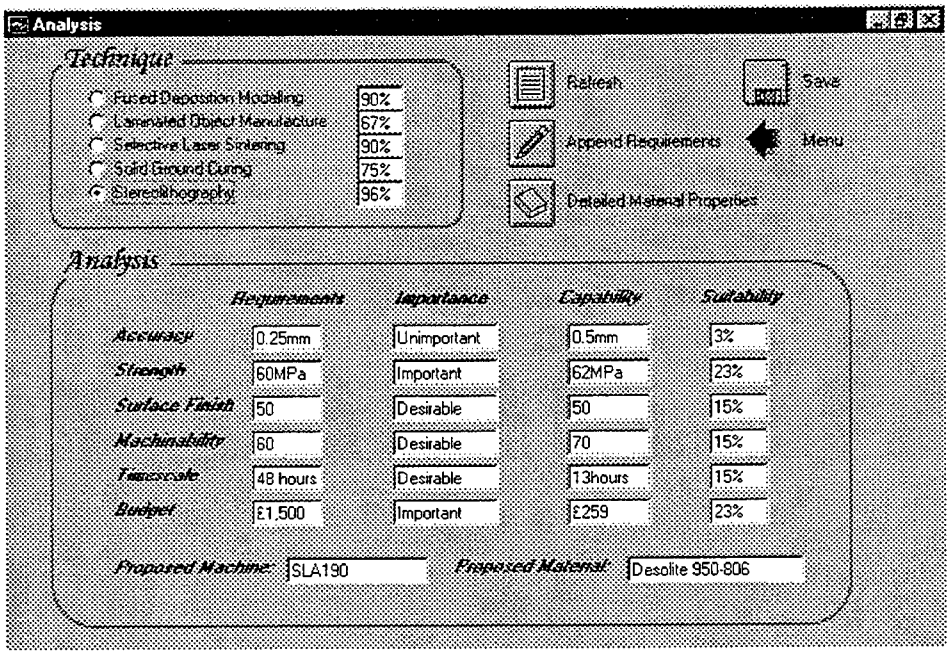


Figure 3: RPDSS analysis screen

Validation Case Study - Fan Development Scenario

The prototype attributes and requirements were selected based on the requirements of a industrial fan. Since the case study selected for implementation did not include all the data required, it was necessary to make occasional assumptions (see Table 1).

Characteristic	Value	Characteristic	Value
In-house facilities	No	Accuracy required	0.5mm*
Quantity	12	Accuracy importance	Important*
Length	150mm	Strength required	30MPa
Function	Functional testing	Strength importance	Desirable
Timescale	< 5 weeks	Surface finish required	20 microns*
Timescale importance	Important	Surface finish importance	Desirable
Budget	£2,000*	Machinability required	N/A
Budget importance	Important	Machinability importance	Irrelevant
Accuracy required	0.5mm*		

* indicates assumed data

Table 1: Fan design requirements

After data entry, the software performed the analysis. The suggestions produced by the software are summarised in Table 2, listed in order of suitability. This was a highly successful test of the software since LOM was highlighted as the most appropriate method, the same process used by ABB Fläkt Industri AB, Sweden[8]. The software also gives a relatively high level of suitability which is agreement with the satisfaction expressed. The analysis showed not only consistency between software recommendations and real-life applications but also indicated areas where different RP solutions may have provided more satisfactory results[9].

Process	System	Material	Suitability
Laminated Object Manufacture	LOM 2030	Bleached kraft paper	94%
Fused Deposition Modelling	FDM 1500	Plastic P301	92%
Stereolithography	SLA 500	EXactomer 5201 AR	90%
Selective Laser Sintering	Sinterstation 2000	LN 4010	87%
Solid Ground Curing	3D Modeler	Solimer G-5601	86%

Table 2: Summary of software results

Future Work

Several areas have been identified for further work which include improved build-time and cost estimation modules. Research at the University of Nottingham is examining the use of neural networks in conjunction with an RP model database to enhance these such modules. There is also the possibility for the development of an RPDSS internet web-site. This would enable world-wide usage of the software, access to the RP capability database and provide the means for user feedback.

More design scenarios should be applied to test the software validity and identify its weaknesses. These weaknesses exist largely due to lack of RP database entries. Software development is to continue with the integration between the RPDSS and CAD. This is intended to enable direct analysis of the CAD model to determine RP suitability with less designer interaction. This is only possible through the use of feature-based design and a CAD model format capable of representing all prototype requirements[10].

Conclusions

This project has established a framework for an RPDSS and produced a user interface for its implementation. The RPDSS module relating to evaluating the suitability of different RP machines has been the main area of development. This has been conceived, designed and implemented to evaluate the suitability percentages for several combinations of RP machine and material and to display the suitability ratings for five major RP processes. There are several potential benefits of using such a system:

- Higher level of designer productivity
- Improved access to RP data
- Promotion of RP

It is hoped that this development work will be furthered by future projects and that the goal of producing a fully functional RPDSS is achieved.

References

1. Wohlers, T., *Rapid Prototyping Journal Vol. 2, No. 1.*, pp 42-43.
2. Campbell, R.I., "Using feature-based design to optimize rapid prototyping", *Journal of Engineering Design, Vol. 7, No. 1*, 1996, pp. 95-103.
3. Müller, H., Jurgen, B., Kingenburg, H.H., "Computer based RP system selection and support", *Time-Compression Technologies 96 Conference,* 1996, pp. 242-248.
4. Masood, S. H., "Intelligent rapid prototyping with fused deposition modelling", *Rapid Prototyping Journal* , Vol. 2, No. 1, 1996, pp. 24-33.
5. Kirschman, C.F., Gara-Almonte, C.C., Bagachi, A., Dooley, R.L., Ogale, A.A., "The Clemson intelligent design environment for stereolithography", *2nd International Conference on Rapid Prototyping*, Dayton, OH, June 1991.
6. Mieritz, B., "A methodology for introducing RPT in product development", *Nordic Industrial Experience, 5th European Conference on Rapid Prototyping and Manufacturing*, Helsinki, Finland, June 1996.
7. Phillipson, D.K., "Rapid Prototyping Machine Selection Programme", *6th European Conference on Rapid Prototyping and Manufacturing*, Nottingham, UK, July 1997, pp. 291-303.
8. ABB Fläkt Industri AB, "Fan development using rapid prototyping", *Nordic Industrial Experience, 5th European Conference on Rapid Prototyping and Manufacturing*, Helsinki, Finland, June 1996.
9. Jones, K.G., "Rapid Prototyping Decision Support System", *BEng Thesis*, University of Nottingam, *UK.* 1997.
10. Campbell, R.I., Chrisp, A.G. & Geldart, M., "Using features to integrate design and rapid prototyping", *Proceedings of 13th International Conference on Production Research,* Addendum, Jerusalem, Israel, 1995, pp. 1-3.

Empirical Similitude Method for the Functional Test with Rapid Prototypes

Uichung Cho
Graduate Student

Kristin Wood
Associate Professor

Mechanical Engineering Department
The University of Texas at Austin

ABSTRACT

Rapid prototyping has the potential to improve the performance of the design process both in cycle time and resources. Such improvements may be realized through the timely visual, ergonomic, and functional information provided by solid freeform fabrication (SFF) parts. Of these information classes, functional information is perhaps the least realized with current technology. A number of technical issues have limited functional testing of SFF parts, including sensor fusion, range of prototyping materials, part size etc. Our focus here concerns the material issues of functional testing, especially the potential differences in prototyping material choices to actual production materials. For example, to derive accurate functional information of non-polymeric products from polymeric rapid prototypes, an improved similitude method that can overcome the distortion of material characteristics is necessary. In this paper, a new similitude method that utilizes specimen test data is introduced. This method develops a mathematical transformation between prototype and product behavior through specimen testing. This transformation replaces the role of the scale factor of the traditional similitude method, and provides a basis for relating prototypes to proposed production parts, even under dependent loading and material conditions. Computational and experimental results of a structural design provide verification of the new method.

1 INTRODUCTION

Design is an iterative process that recursively transforms customer needs into the appropriate set(s) of design parameters within various constraints, and the decision on design parameters are made from virtual and physical models. In order to maintain competitiveness, companies need to provide high-quality products at demanded time within allowable financial resources. Rapid prototypes provide effective visual, ergonomic, and functional information that is similar to the future product in a single physical entity, so it has the potential to accelerate the design process by providing required information with minimal time delay. The derived information is used to verify virtual models or to correct design faults. Among the various information classes, perhaps the functional information is the least realized.

The required effort to build testable models is critical when the geometry of the target system is complex. Fortunately, a new technology, called rapid prototyping (RP) or solid freeform fabrication (SFF), enables effective fabrication of geometrically complex parts. Traditionally, a scaled physical model that can show similar behavior is designed on the basis of the Buckingham Π theorem, and the behavior is correlated to the target system behavior through the derived scaling laws [Kline 75, Baker 91].

It is natural to expect various similitude studies with rapid prototypes, but very little literature exists on that subject [Dornfeld 95, Steinchen 95]. Some of the factors, that are limiting the utilization of rapid prototypes for the functional testing, are: (1) non-similar material characteristics of the rapid prototyping and production materials (e.g., nonlinear material properties); (2) distinct material structure (e.g., non-homogeneous and anisotropic material properties of rapid prototypes); (3) limited material choices; and (4) restrictions on loading conditions (e.g., burning of polymer under combustion). Due to these problems, the

testing models fabricated from various rapid prototyping processes may not be suitable to make a precise prediction with traditional similitude methods.

In order to extend the utilization of rapid prototypes for the reliable prediction of the functional behavior of future products, a new similitude method is developed and tested. In comparison to traditional methods, where only the restricted information (the dimension of parameters and variables) is utilized, our new similitude method attempts to derive a local state transformation from the specimen pair(s) whose geometry is simple to fabricate. This novel specimen-based *empirical similitude method* is experimentally and computationally evaluated with three example problems. The new similitude method predicts the functional information well with one or two specimen pairs.

2 Problems in Deriving Functional Information from Rapid Prototypes

There exist two main obstacles that lies in wide utilization of rapid prototypes for functional tests. One originates from the characteristics of rapid prototypes, and another comes from the restrictions on the traditional similitude methods.

2.1 Current Status of Rapid Prototyping Techniques

The last decade has seen the emergence and continuous advancement of various rapid prototyping techniques, and at least 20 companies commercialized diverse rapid prototyping systems in Europe, Japan, and USA. Most of the systems can fabricate geometrically complex prototypes within 50 hours, where polymers are the most popular base material [Aubin 94]. As rapid prototyping emphasizes the dramatically reduced fabrication cost and time, the loss or distortion of some information classes is inevitable. The limited capacity (fabricable prototype size) and material choices of the rapid prototyping system are main factors that prevents full scale tests in various situations.

2.2 Limitations of Traditional Similitude Methods

Traditional similitude methods, which are based on the Buckingham Π theorem, have been widely used in order to transform the behavior of physical prototypes to that of target systems [Kline 75, Baker 91]. The methods simply correlate (by multiplying scale factors) the corresponding behavior through a dimensionless parameter group. However, these methods have following limitations to make precise prediction of product behavior through rapid prototypes.

(i) When two systems are governed by equations with different configurations, the prediction is erroneous. The prediction of the deformation of a structure with small deflection from a structure with large deformation is the typical example of this type.

(ii) The system parameters, that are related to the system behavior of interest, should be constant. However, the dependency of material parameters (e.g., thermal conductivity) on the system behavior (e.g., temperature) may not be negligible. In addition, the spatial distribution of material properties of the prototype and product are expected to be distinct, due to the unique fabrication schemes.

(iii) All corresponding dimensionless parameters of two systems should be identical in the traditional methods. Due to the limited material choices and difficulties in generating exact boundary conditions, the corresponding dimensionless parameters cannot always made to be identical.

3 New Specimen-Based Empirical Similitude Method

The above mentioned limitations of traditional similitude methods seem to come from the utilization of restricted information, i.e., the dimensions of parameters and variables. In comparison, our new similitude

method attempts to derive extended information from the geometrically simple specimen pair(s) (one from the rapid prototyping and another from the production process) that can be easily fabricated.

The new specimen-based empirical similitude method, that may overcome the limitations of traditional similitude methods, assumes that there exists a consistent local transformation between the corresponding *n*-dimensional sub-state vectors[1] of two systems *only if* the geometry is similar. Based on this concept, the new similitude method derives a local state transformation matrix from the measured states of specimen pairs, and the derived state transformation matrix replaces the role of the scale factor in traditional methods. Then, the unknown states of the future-product are estimated from this derived state transformation matrix and the measured states of the rapid prototype. In Figure 1, the overall concept of the new similitude method is described, the state vectors are defined, and two plausible methods that realizes the concept are introduced in following subsections.

The state transition due to the material change is abstracted from the specimen pair. As the state variation due to the geometrical variation is represented with the measured state vector of the target model, one can estimate the state vector of the target product.

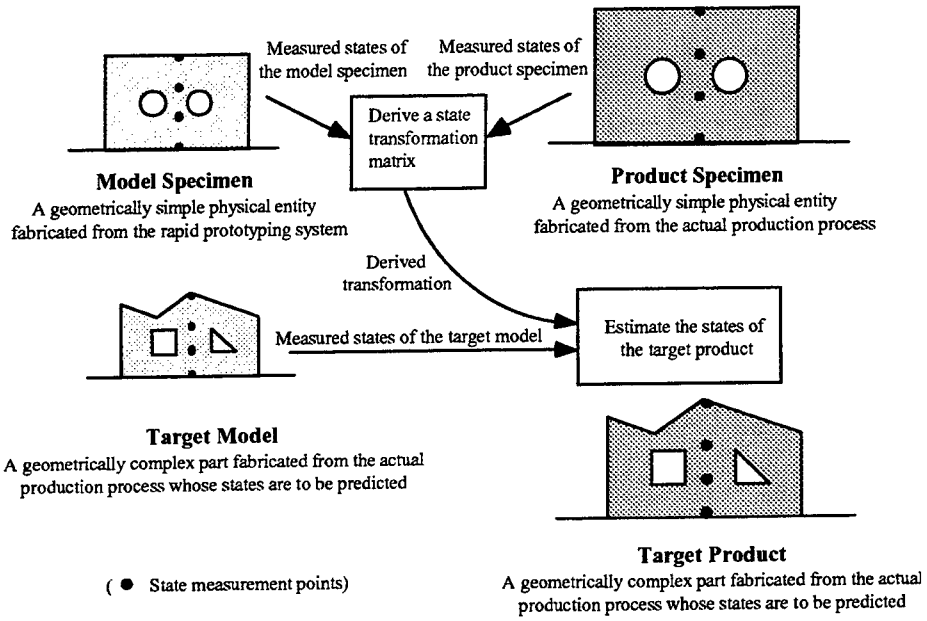


Figure 1: Overall Concept of the New Similitude Method.

Definition of State Vectors

- *Sub-state vector of the target product*, $\mathbf{x}^{tp} = (x^{tp}{}_1 \; x^{tp}{}_2 \cdots x^{tp}{}_k)^T$: *k by 1* vector that is composed of unknown physical values of interest (e.g., temperature) on at *k* local points of target product
- *Sub-state vector of the target model*, $\mathbf{x}^{tm} = (x^{tm}{}_1 \; x^{tm}{}_2 \cdots x^{tm}{}_k)^T$: *k by 1* vector that is composed of measured physical values of interest at *k* corresponding local points of the target model
- *Sub-state vector of the i-th product specimen*, $\mathbf{x}^{psi} = (x^{psi}{}_1 \; x^{psi}{}_2 \cdots x^{psi}{}_k)^T$): *k by 1* vector that is composed of measured physical values of interest at *k* corresponding local points of the product specimen
- *Sub-state vector of the i-th model specimen*, $\mathbf{x}^{msi} = (x^{msi}{}_1 \; x^{msi}{}_2 \cdots x^{msi}{}_k)^T$: *k by 1* vector that is composed of measured physical values of interest at *k* corresponding local points of the model specimen

[1] The sub-state vector is defined as n by 1 vector whose components are composed of measurable quantities to be predicted, on a sub-domain D_s in local coordinate space, where $D_s \subset D$ and D is entire domain of the interest.

3.1 Similitude with Absolute Linear Transformation

The unknown relationship between $\mathbf{x}^{tp}$ and $\mathbf{x}^{tm}$ is approximated from the relation(s) of $\mathbf{x}^{psi}$ and $\mathbf{x}^{msi}$. As an initial attempt, the relationship is assumed as a discrete linear transformation.

Let's consider a linear transformation matrix **T** that satisfies following equation

$$\mathbf{x}^{ps1} = \mathbf{T} \cdot \mathbf{x}^{ms1} \tag{1}$$

where **T** is a *k by k* matrix.

In traditional similitude methods, the **T** is a diagonal matrix whose diagonal terms have identical state scale factor s. The scalar scale s is a real constant, and it is a function of N design parameters, DP_i (e.g., characteristic length, material constants), and M loading parameters, F_j, as shown below.

$$\begin{aligned} s &= \frac{x_i^{\,p}}{x_i^{\,m}} \\ &= \left[\left(\frac{DP_1^{\,p}}{DP_1^{\,m}} \right)^{R_1} \cdot \left(\frac{DP_2^{\,p}}{DP_2^{\,m}} \right)^{R_2} \cdots \left(\frac{DP_N^{\,p}}{DP_N^{\,m}} \right)^{R_N} \cdot \left(\frac{F_1^{\,p}}{F_1^{\,m}} \right)^{R_{N+1}} \cdot \left(\frac{F_2^{\,p}}{F_2^{\,m}} \right)^{R_{N+2}} \cdots \left(\frac{F_M^{\,p}}{F_M^{\,m}} \right)^{R_{N+M}} \right]^{R_{N+M+1}} \end{aligned} \tag{2}$$

where R_i is a real number, and superscript p and m denote the product and model respectively. Once all the DP_i's and F_j's are decided, s becomes a constant real value, and the ratio of corresponding states of the product to model is same to the state scale factor s, at any point.

In comparison, the new similitude method expects improved similitude results by empirically deriving the matrix **T** that satisfies equation (1). The empirically derived transformation matrix T is generally not a diagonal matrix, and the elements, t_{ij}'s, of the matrix **T** can be interpreted as the weighting factor on the *j-th* state of $\mathbf{x}^{ms1}$ to predict the *i-th* state of $\mathbf{x}^{ps1}$. So, the state of the product specimen is not a scaling of only corresponding state of the model specimen but a balance of the considered neighboring states.

If states of n specimen pairs are measured, then the transformation matrix **T** should satisfy the following equation,

$$\left[\mathbf{x}^{ps1}\ \mathbf{x}^{ps2}\ \cdots \mathbf{x}^{psn}\right] = \mathbf{T} \cdot \left[\mathbf{x}^{ms1}\ \mathbf{x}^{ms2}\ \cdots \mathbf{x}^{msn}\right]. \tag{3}$$

It is desired to minimize the number of specimens n, so the number of columns is usually lesser than that of rows, i.e., the size of the considered states. So, the number of unknowns are lesser than that of given equations. When the $\left[\mathbf{x}^{ms1}\ \mathbf{x}^{ms2}\ \cdots \mathbf{x}^{msn}\right]^{-1}$ does not exist, one way to find the **T** that satisfies equation (3) is to use the pseudo-inverse matrix [Strang 1988] as follows.

$$\mathbf{T} = \left[\mathbf{x}^{ps1}\ \mathbf{x}^{ps2}\ \cdots \mathbf{x}^{psn}\right] \cdot \left[\mathbf{x}^{ms1}\ \mathbf{x}^{ms2}\ \cdots \mathbf{x}^{msn}\right]^{+} \tag{4}$$

where A^+ is the pseudo-inverse matrix of A.

Once the transformation matrix **T** is obtained, the state vector of the target product $\mathbf{x}^{tp}$ is derived from the following equation,

$$\mathbf{x}^{tp} \cong \mathbf{T} \cdot \mathbf{x}^{tm}. \tag{5}$$

As the transformation matrix **T** characterizes the state transition due to the material variation, the matrix for both specimen and target pair may be identical if the corresponding points' location in specimens and targets are well decided. If not specially stated, this approach is used as the new similitude method in Section 4.

3.2 Relative Linear Transformation

The previous method assumes that the derived state transformation matrix **T** is independent of the geometry. However, the transformation may be dependent on the geometry. So, a method, that involves an alternative linear transformation $\delta\mathbf{T}$ that relates the deviation of states with respect to the reference specimen, is introduced as an adherent of the first method.

In this method, the state vectors of the first specimen pair, $\mathbf{x}^{ps1}$ and $\mathbf{x}^{ms1}$, are considered as reference vectors. The variation of the state vectors of the second specimens are defined as

$$\begin{aligned} \Delta\mathbf{x}^{ps} &= \mathbf{x}^{ps2} - \mathbf{x}^{ps1} \\ \Delta\mathbf{x}^{ms} &= \mathbf{x}^{ms2} - \mathbf{x}^{ms1} \end{aligned} \tag{6}$$

where $\mathbf{x}^{ps2}$ and $\mathbf{x}^{ms2}$ are state vectors of the second specimen pair. Similar to the previous method, the linear transformation $\delta\mathbf{T}$ that maps the state variation instead of the state itself, is derived from the following equation.

$$\delta\mathbf{T} = \Delta\mathbf{x}^{ps} \cdot (\Delta\mathbf{x}^{ms})^{+} \tag{7}$$

Assuming that $\delta\mathbf{T}$ is constant (instead of **T**), i.e., the following equation is satisfied

$$(\mathbf{x}^{tp} - \mathbf{x}^{ps1}) = \delta\mathbf{T} \cdot (\mathbf{x}^{tm} - \mathbf{x}^{ms1}), \tag{8}$$

$\mathbf{x}^{tp}$ can be determined from

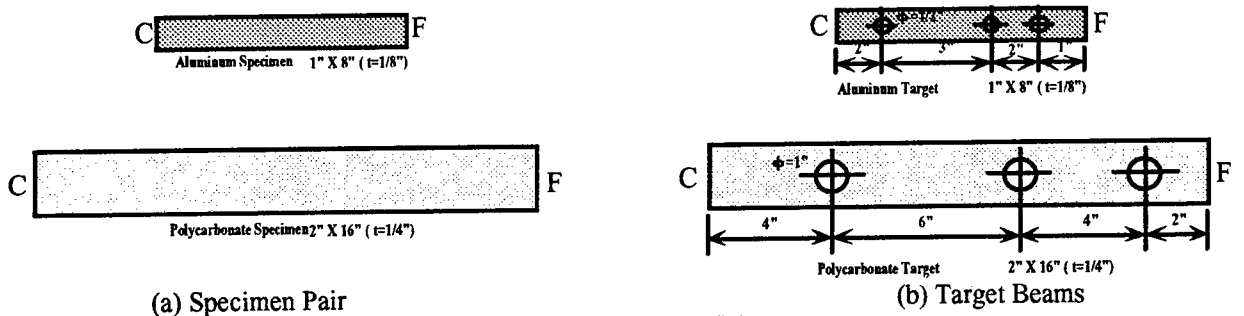
$$\mathbf{x}^{tp} = \mathbf{x}^{ps1} + \delta\mathbf{T} \cdot (\mathbf{x}^{tm} - \mathbf{x}^{ms1}) \tag{9}$$

as $\mathbf{x}^{ps1}$, $\mathbf{x}^{tm}$ and $\mathbf{x}^{ms1}$ are to be measured.

4 EVALUATION of the NEW SIMILITUDE METHOD

Several experimental and numerical tests are carried out to test the validity of the new specimen based empirical similitude method.

4.1 Beam Experimentation



(a) Specimen Pair (b) Target Beams

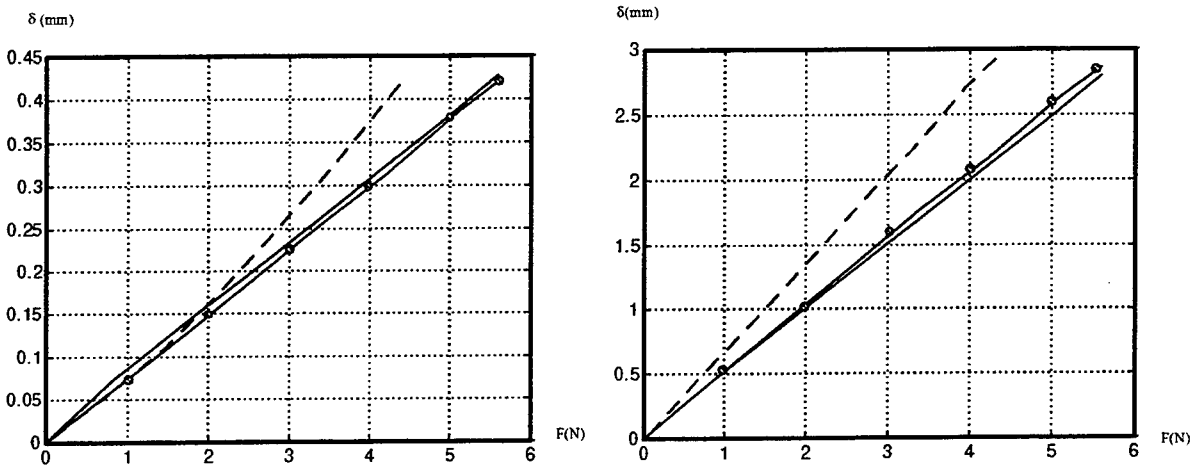
C: Clamping Point, F: Loading Point

Figure 2: Aluminum and Polycarbonate Specimens and Targets

In the beam experimentation, the deflection of the aluminum target beam at 1" (25.4 mm) and 7" (177.8 mm) from the clamping point is predicted. In **Figure 2,** the geometry of the specimens and target

beams are shown (excluding the clamping and loading zone). The force on the polycarbonate specimen and target is scaled down to half of that applied to aluminum specimen and target, in order to emphasize the geometrical non-linearity due to the large deflection. For the convenience of the measurement, the LVDT is fixed to the same location without following the point of the beam when the large deflection is measured.

Two possible sources of dissimilarity, that obstruct the reliable prediction of the deflection of the aluminum target with traditional similitude methods, are: (1) the nonlinear stress-strain characteristics of the polycarbonate; and (2) the geometrical non-linearity due to the large deflection.



(a) Vertical deflection at the near-clamping point (b) Vertical deflection at the far-clamping point

Solid line: Measured deflection, Dashed line: With the traditional method, Circle line: With the new method

Figure 3: The Vertical Deflection of the Aluminum Target

The vertical deflection of the aluminum target beam is predicted at two points (near-clamping point: 1" (25.4 mm) from the clamping point, far-clamping point: 7" (177.8 mm) from the clamping point) with the traditional and new similitude method. As shown in **Figure 3**, the similitude result with the new method shows remarkable matching with the actually measured deflection of the aluminum target beam in comparison to the traditional similitude method.

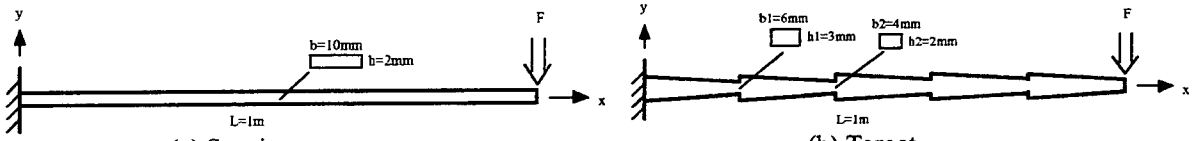
4.2 Computational Evaluation

Two finite element (FE) simulations were performed with ANSYS to test the validity of the new similarity method in various situations. The assumed material properties for the FE simulations are as follows.

Material	Young's modulus E (GN/m^2)	Density (kg/m^3)	Thermal conductivity k (W/m K)	Thermal expansion coefficient α (/K)
Aluminum	69.0	2720.0	170.0	0.23E-4
Polycarbonate	4.0 ~ 7.0	1000.0	0.193	0.7E-4

Table 1: Material Properties for the FE Models

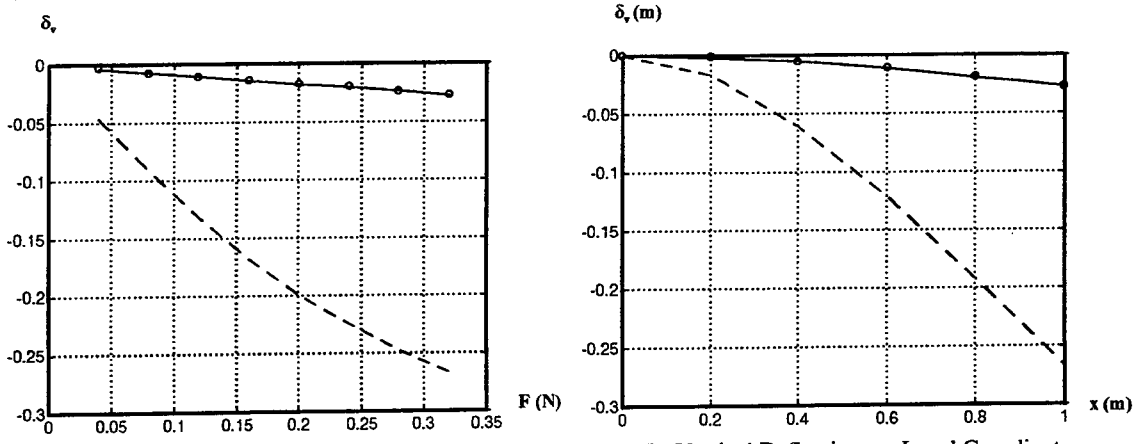
4.2.1 Static Structural Problem



(a) Specimen (b) Target

Figure 4: Specimen and Target Beam

The problem is to predict the deflection of the aluminum target on the basis of the specimen testing results and the deflection of the polymer target. The geometry and force scale factor is set to one, and the specimen and target geometry is shown in **Figure 4**. The Young's modulus of aluminum is assumed as a constant, and the polycarbonate is modeled as stress softening material whose Young modulus varies from 7 to 4 GN/m^2. In addition, the aluminum beams are assumed to show small deflection (geometrically linear), and deflection of the polycarbonate beam is large (geometrically nonlinear)



(a) Vertical Deflection vs. Applied Force (at x=1m)

(b) Vertical Deflection vs. Local Coordinate x (when F=0.32N)

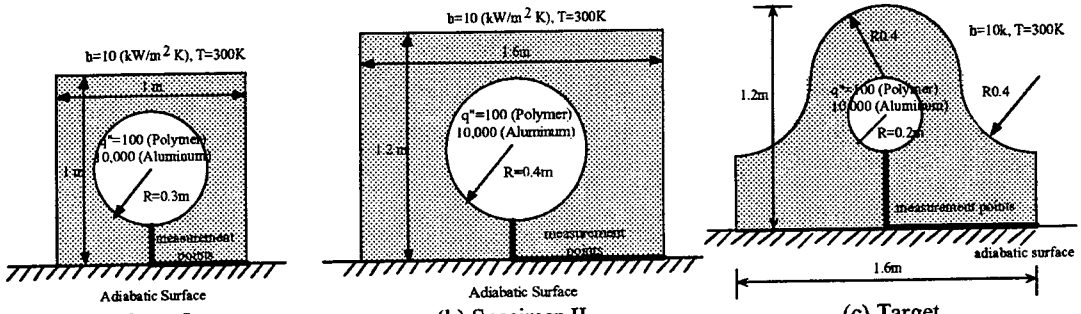
(Solid line: Aluminum target, Dashed line: Polycarbonate target, Circle: Similitude Results)

Figure 5: Similitude Results of the Beam Deflection

As shown in **Figure 5**, the new method predicts the deflection of the aluminum target beam within 1% error. The results on the angular displacement shows the similar results, even though it is not shown here due to the space limitation. In this simulation, the new method demonstrated its ability to map the behavior of two systems whose governing equations take different forms. Besides, the new similitude method successfully predicts the behavior of the target beam when the Young's modulus is not constant.

4.2.2 Steady State Temperature and Thermal Stress

The thermo-structural problem is introduced as an example to demonstrate the feasibility of the new similitude method when some of the dimensionless parameters are not kept to be identical. The geometry and boundary conditions of the considered specimen pairs and the target system are shown in **Figure 6**. The boundary condition at the outer surface of the polymer and aluminum specimens and targets are set to be same, assuming that one cannot easily control them (e.g., natural convection). The difficulty in using polymeric rapid prototypes for the thermal similitude lies in the small thermal conductivity constant, and the low sintering temperature. Considering these material characteristics, the boundary conditions at the inner surface is determined as shown in **Figure 6**.



(a) Specimen I (b) Specimen II (c) Target

Figure 6: Thermal Specimens and Targets

In the two dimensional problems, the difficulty lies in deciding corresponding measurement points. In this example problem, characteristic points are defined as the point on the boundary surface with same boundary conditions, and the characteristic lines are defined as the line that connects two characteristic points. Once the characteristic lines are determined, the lines are linearly divided to find out the corresponding measurement points. The steady state temperature are measured along the two characteristic lines as shown in **Figure 6.**

As shown in **Figure 7**, the accuracy of the predicted temperature increases as the number of considered specimens increases. Even though the improved prediction accuracy is expected by considering more specimens, alternative method that utilizes the relative state transformation (see Subsection 3.2) has been applied and tested. In **Figure 8**, the alternative method shows noticeable improvement of the prediction accuracy with the same number of specimens.

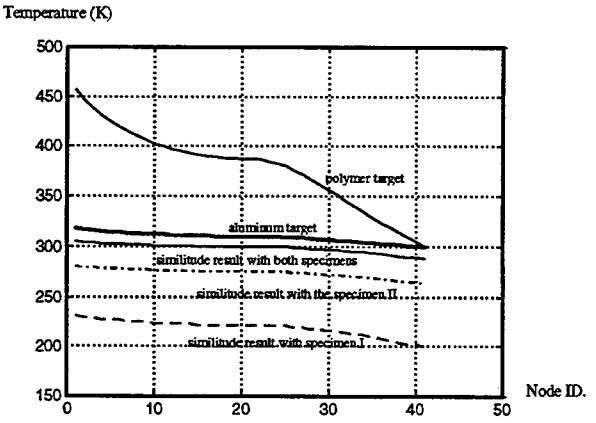


Figure 7: Similitude Results with the Absolute Transformation

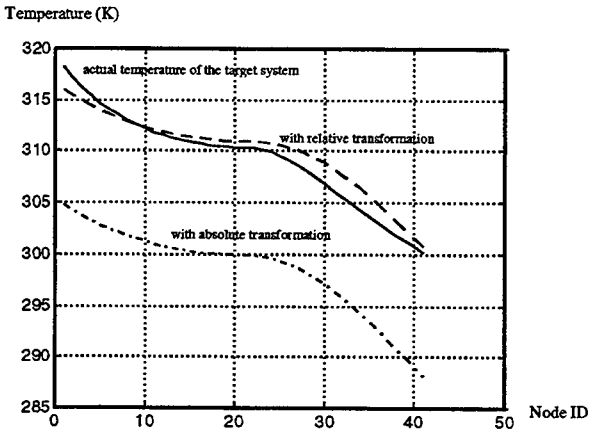
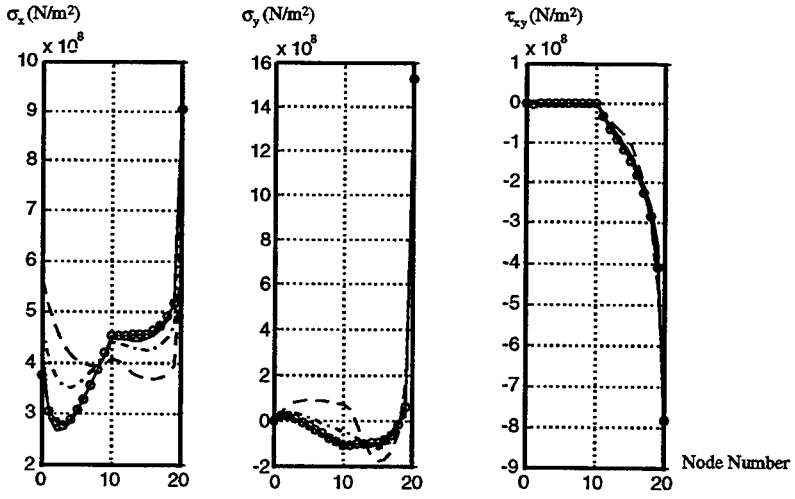


Figure 8: Similitude Result with the Absolute and Relative Transformation

In comparison to the similitude error in the temperature, the accuracy of the predicted thermal stresses (normal and shear) is remarkable as shown in **Figure 9.**



Solid line: Aluminum Target, Circle: Similitude results with 2 specimens
Dashed line: Similitude Results with Specimen 1, Dashdot line: Similitude Results with Specimen 2

Figure 9: Thermal Stress Similitude Results

5 Conclusions

The new specimen-based empirical similitude method predicts the various functional behavior (deformation, pure stress, temperature, and thermal stresses) of all considered example problems that cannot be accurately predicted with traditional similitude methods. The new similitude methods with absolute and relative transformation have pros and cons their own, and a better transformation may be derived under the same concept of this paper – utilization of specimens to derive a consistent state transformation.

Other problem domains (e.g., structural dynamics) will be tested to define the feasible application areas. For the more realistic evaluation of the new similitude method, experimentation with SLS prototypes will be carried out in the near future.

6 Acknowledgments

The research reported in this document was made possible, in part, by a Young Investigator Award from the National Science Foundation. The authors also wish to acknowledge the support of Ford Motor Company, Texas Instruments, Desktop Manufacturing Corporation, and the UT June and Gene Gillis Endowed Faculty Fellow. Any opinions, findings, conclusions, or recommendations are those of the authors and do not necessarily reflect the views of the sponsors.

References

[Aubin 94] Aubin, R.F., "A World Wide Assessment of Rapid Prototyping Technologies," *Solid Freeform Fabrication Symposium Proceedings*, Austin TX, August, 1994, pp.118-145

[Baker 92] Baker, W.E., Westine, P.S., Dodge, F.T., Similarity Methods and Engineering Dynamics: Theory and Practice of Scale Modeling, Elsvier, 1992

[Baker 67] Baker, W.E. and Westine, P.S., "Model Tests for Structural Response of Apollo Command Module to Water Impact," *Journal of Spacecraft*, vol.4, n2, February 1967, pp.201-208

[Dornfield 95] Dornfield W.H., "Direct Dynamic Testing of Scaled Stereolithographic Models," *Sound and Vibration*, August 1995, pp. 12-17

[Elliott 69] Elliott, W., "Plastic Models for Structural Analysis," U S Naval Research Lab., *Shock and Vibration Bulletin* n40 pt 4, Dec. 1969, pp. 89-96

[Fay 93] Fay, R.J., "Scale Model Tests of Vehicle Motions," *Vehicle and Occupant Kinematics: Simulation and Modeling SAE Special Publication* n 975, SAE, pp51-54, 1993

[Jacobs 92] Jacobs, P. F., Rapid Prototyping and Manufacturing: Fundamentals of StereoLithography, Society of Manufacturing Engineers, McGraw-Hill Inc., 1992

[Kline 72] Kline, S.J., Similitude and Approximation Theory, McGraw-Hill Co., New York, 1975

[Steinchen 95] Steinchen, W., Kramer, B., Kupfer, G., "Photoelastic Investigation Using New STL-Resins," *Solid Freeform Fabrication Symposium Proceedings*, Austin TX, August, 1995, pp.204-212

[Strang 88] Strang, G, Linear Algebra and Its Applications, Harcourt Brace Jovanovich, Inc., 1988

THE CLEMSON INTELLIGENT DESIGN ENVIRONMENT FOR STEREOLITHOGRAPHY – CIDES 2.0

Jill S. Kirschman
Industrial Engineering Department
jkirsch@ces.clemson.edu

Charles F. Kirschman
BPM Technology Inc.

Georges M. Fadel
Mechanical Engineering Department
gfadel@ces.clemson.edu

Joel S. Greenstein
Industrial Engineering Department
jsg@ces.clemson.edu

Laboratory to Advance Industrial Prototyping
Center for Advanced Manufacturing
Clemson University
Clemson, SC 29634 USA

ABSTRACT

There are a large number of commercial Rapid Prototyping (RP) devices available today. All of these machines begin with a Computer-Aided Design (CAD) model, which is tessellated, sliced and then built layer-by-layer on the RP device. All of these operations, except the actual building of the part, are completed on a computer. Therefore, many improvements to the RP processes can be achieved through software, without affecting the RP devices or the warranties on them. This has led to the development of a front-end software product to support the task of preparing the part to be built. The Clemson Intelligent Design Environment for Stereolithography (CIDES) is a user-centered interface between the CAD system and RP systems, primarily the Stereolithography Apparatus (SLA).

CIDES 2.0 is designed to provide a variety of tools which are valuable to the users of RP systems, including the ability to view and modify tessellated (STL) files, generate supports, and slice STL files into layer (SLI) files for use on an SLA. It also provides the ability to view SLI and merged (V) files. Furthermore, CIDES offers additional translation capabilities that make it valuable for other RP processes. The package has proven useful in the Laboratory to Advance Industrial Prototyping (LAIP) at Clemson University. CIDES 2.0 is a new X Windows-based release based on the original version of CIDES with many additional features. A new Human-Computer Interface is the major improvement to this release.

INTRODUCTION

Rapid Prototyping (RP) is the name for a number of processes that generate three-dimensional objects directly from a Computer-Aided Design (CAD) solid model. Regardless of which process is used, the procedure to create these objects is to generate the CAD model, tessellate it, slice it, and finally build it on the RP device. All of these steps, except the actual building of the part, are completed on a computer. This was the motivation for the development

of a front-end software package to support the task of preparing a part to be built (Kirschman et al., 1991A). The Clemson Intelligent Design Environment for Stereolithography (CIDES) is fundamentally a user-centered interface between a CAD system and the Stereolithography Apparatus (SLA).

Rapid Prototyping is an active research area. Many researchers have custom-designed devices to conduct their experiments; however, much research is done using commercially available machines. Researchers can achieve significant changes to the parts produced on these machines without voiding the manufacturer's warranty by making changes to input files, or by interacting with the layer files that will be used to build a part. CIDES was developed for this purpose; it includes a number of features that have enabled Clemson University to enhance the capabilities of the RP systems that it has. CIDES provides input, output, and viewing capabilities for several common file formats. It also enables input file modification, support generation, slicing, and file format translation. A number of research activities have been based on the CIDES platform, including support structure generation (Kirschman et al., 1991B), optimal orientation (Frank and Fadel, 1994), NURBS-based slicing (Vuyyuru et al., 1994), adaptive slicing (Tata, 1995), and optimal placement of parts (Wodziak et al., 1994). Currently CIDES is closely coupled with an SLA because that was the first available RP device, and the only one at Clemson University for several years. However, the code is being expanded to work with other RP systems, including the selective laser sintering testbed at Clemson University (Terala, 1996).

The original version of CIDES (version 1.0) was written in 1991. CIDES 1.0 runs on SunOS 4.3 or earlier. However, Clemson University has nearly completed the process of upgrading from this operating system to Solaris on all Sun workstations. Although the kernel of functionality is very portable, the CIDES 1.0 graphical user interface (GUI) and graphics engine were developed using the Hierarchical Objected Oriented Programming System (HOOPS) from Ithaca Software. HOOPS was an excellent choice for a graphics system in 1991, when there were few GUI standards for workstations. It is highly portable with versions for many platforms, and very powerful for display. However, HOOPS has two shortcomings. First, HOOPS is designed for graphics and object display; it does not offer the GUI-building capabilities of a typical fourth generation language or a GUI builder. Second, Ithaca Software imposes royalties for the distribution of HOOPS-based software. As a result, CIDES 1.0 can not be freely distributed. This is the primary reason that CIDES has not found its way outside Clemson University, despite heavy use in the Laboratory to Advance Industrial Prototyping (LAIP).

Another problem with the original version of CIDES is that it was designed for research purposes rather than general use. Very little attention was devoted to the user interface during the development of the product. Gould (1988) proposes that four principles of system of design be followed if one is to design a usable computer system. First, there should be an early and continual focus on the users. There should be direct contact with the users so as to understand their job and what they need to do their work better. Second, there should be integrated design. All aspects of usability should develop in parallel and under one focus or one person. Third, there should be early and continual user testing. To ensure that a design usable by and useful to its users, the system must be tested by its intended users. Finally, the design process must be

iterative. The system should be modified based on the results of user testing. Once the modifications are complete, user testing should be repeated. This refine-and-test cycle is repeated until testing demonstrates that the product satisfies its usability specifications. The methodology used to redesign the CIDES interface applied these four principles.

CIDES 2.0 was developed to achieve greater product accessibility. A new development platform, SGI workstation, was chosen and a new GUI was designed for the system. Several of the underlying data structures were revamped, and code was modularized to separate the functional kernel from the interface. This paper describes the redesign of the software from the top down and discusses the capabilities that are now available in the product.

METHODOLOGY

A four phase structured methodology was used to redesign the CIDES interface (Ulrich and Eppinger, 1995). This methodology was chosen because it involves users in the design process, is user-centered and is self documenting. The first phase of the process begins with the development of a mission statement. For the CIDES redesign project, the mission statement was:

> *Redesign the CIDES interface to make it more usable in and beyond the Laboratory to Advance Industrial Prototyping (LAIP) at Clemson University.*

Once the scope of the project was defined, representative users were identified based on several different criteria, including familiarity with CIDES, exposure to CIDES and similar packages, and frequency of use. A thirty minute semi-structured interview was conducted with five of the nine users. The remaining four users were interviewed via email because of their geographical location or scheduling difficulties. Upon completion of theses interviews, each user statement was translated into a user need statement. To determine the relative importance of each need, the users were then asked to rate each need statement using a five point scale.

The second phase of the design process translated the list of user needs into performance measures which were both testable and measurable. Some needs were not easily translated into quantifiable metrics. In such instances, metrics were created based on the user's subjective evaluations of the interactive system. Next, products similar to CIDES were identified and used as competitive benchmarks. The three products benchmarked were: the original version of CIDES, Partman (3D Systems) and Surfacer (Imageware). These products were benchmarked in terms of all the product performance metrics. The information obtained from the interviews with users and the benchmarking process was used to establish a set of product specifications.

Phase three consisted of concept generation and concept selection. It began with each design team member individually generating ideas. Then the design team brainstormed together to create additional concepts and refine the initial ones. This process was repeated several times. The concept selection process was also iterative. First, the team selected the user needs and product specifications most able to differentiate among the concepts and prepared a selection matrix. The selection criteria were then placed in the rows of the matrix in descending order of importance. Next, the team chose one concept as a reference, and all other concepts were rated

on a +, 0, - scale against this reference on each criteria. When there was no difference, or if doubt existed as to whether a concept was better or worse than the reference, a score of "0" was given. The concepts were ranked based on the number of +'s, 0's and -'s assigned to them. The decision to carry a concept forward was based upon team consensus, taking into consideration the rank, strengths and weaknesses of the concept. As a result, the team decided that a concept employing a Toolbar, Menu and Hot Keys would be carried on to the detail design and development phase.

In the final phase, the selected concept was developed and tested. Employing a process similar to that used by IBM to develop the 1984 Olympic Message System (Gould et al., 1987), the team obtained feedback regarding the effectiveness of the interactive system being developed early and repeatedly. Initially the team used paper-and-pencil prototypes to test user reactions to the proposed design. Once the organization of tasks within the interface was completed the team began developing focused software prototypes. When the majority of the tasks were coded, the team moved to a comprehensive prototype so that users could identify any remaining design flaws before the overall design concept was frozen for detail design. Once detail design was complete, the interface was tested and refined using real tasks. Testing and refinement was an iterative process that began with the prototype developed in the detail design phase. Initial testing focused primarily on the layout of the interface as well as the labels used. This was followed by four iterations of additional testing and refinement. During each of the four iterations, as many of the users as practical were included in the product testing. After the four iterations of testing and refinement, the interface appeared to be ready for final evaluation against the product specifications. The final version of the interface met or exceeded every product specification when it was tested in the Laboratory to Advance Industrial Prototyping (LAIP).

STRUCTURE

CIDES 2.0 was redesigned to enhance portability and simplify improvements to the user interface. All of the core functionality of CIDES, including input/output, part manipulation, slicing, and supporting has been combined into a set of library routines that are called from the GUI (Figure 1). This separation enables the kernel, which is written in ANSI C, to be ported to different platforms more easily. Once the kernel is running, any interface from a simple text menu to a full graphical display or even a virtual reality helmet can be used on top of the kernel to provide access to the routines. The library contains routines to carry out all of the non-graphic functions capabilities discussed in the next section.

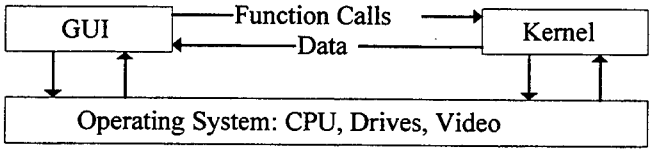


Figure 1. Kernel Structure of CIDES.

This library approach enhances the utility of the software for research. While changes to the kernel must be more stringently tested, researchers can use the basic capabilities of input/output

and slicing without the risk of damaging the base code. Thus, additional user functionality can be added through software modules by anyone with a working knowledge of C.

CAPABILITIES

Since CIDES is a research testbed, its capabilities may change rapidly. Its current capabilities can be broken into three categories: Display, Modification and manipulation, and Utilities. Each of these categories will be discussed in detail.

The first function of CIDES is to display files of various formats. Included in this must be the ability to read these files; currently STL, SLI and V files are supported. STL files are industry standard tessellated files used as input to all RP processes. CIDES supports reading and writing both ASCII and binary files that follow the STL file specification. Because some CAD packages generate non-standard STL files, CIDES is capable of handling several common anomalies, including non-standard headers or lines, incorrect case or number format, and bad concatenation. STL files can be viewed from any of the standard views (Figure 2) or the user can pan, rotate, and zoom via mouse commands.

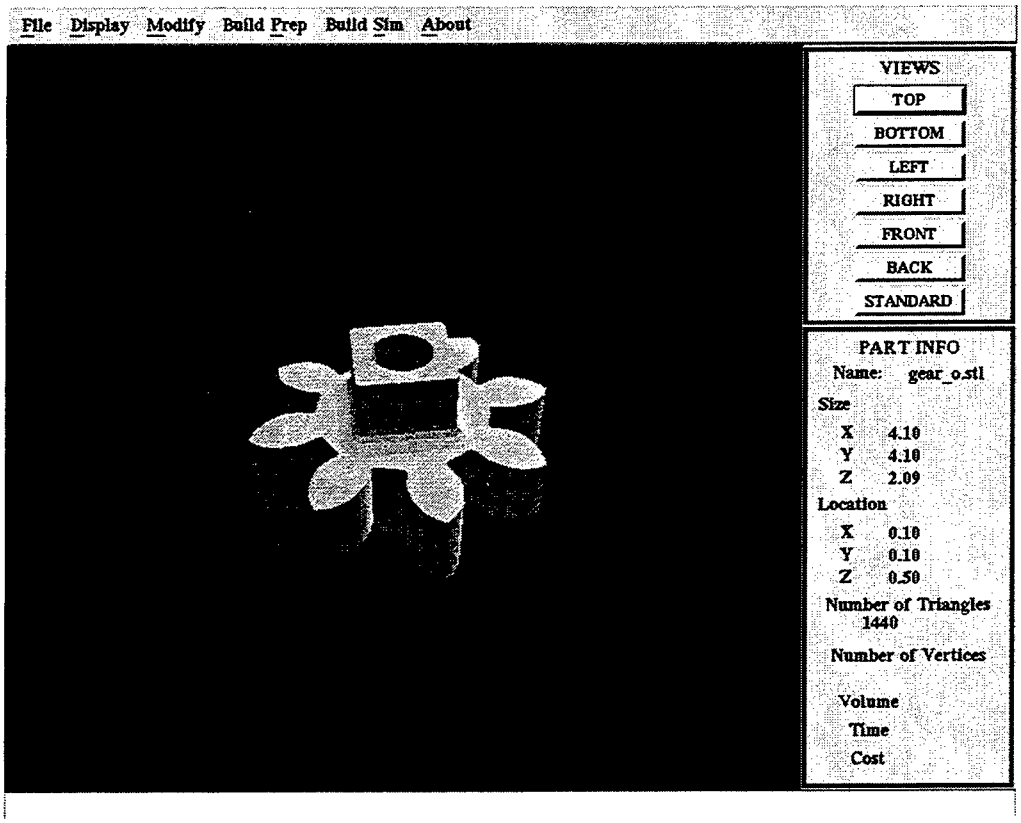


Figure 2. STL Viewing Screen.

Currently CIDES supports only flat shading of the image. Flat shading helps the user to detect errors in the STL file, especially when combined with what is called "disco lighting" by the users. This type of lighting is simulated by placing four different color light sources at the corners of a cube surrounding the part to give the part a multicolored appearance. Since the color

of a facet is dependent on its normal, any errors in the normal of a facet are quickly evidenced by a triangle of one color in the midst of a face that is a different color.

The second type of file read and written by CIDES is the SLI file, which is a 3D Systems Inc. slice or layer file. The dialog which allows the user to interact with these files is shown in Figure 3. SLI files are displayed layer-by-layer, allowing the user to turn on and off various vector types. For more rapid viewing, the user can choose to run up or down through the files, selecting the delay before each layer is replaced on the screen via the slider; delays range from no delay to half of a second. As with the STL file, the user can pan, zoom, and rotate with the mouse. The third type of viewable file is the V file, which are 3D Systems Inc. "merged" file used to build a part. These are also layer files, and are viewed using the same tools as the SLI files.

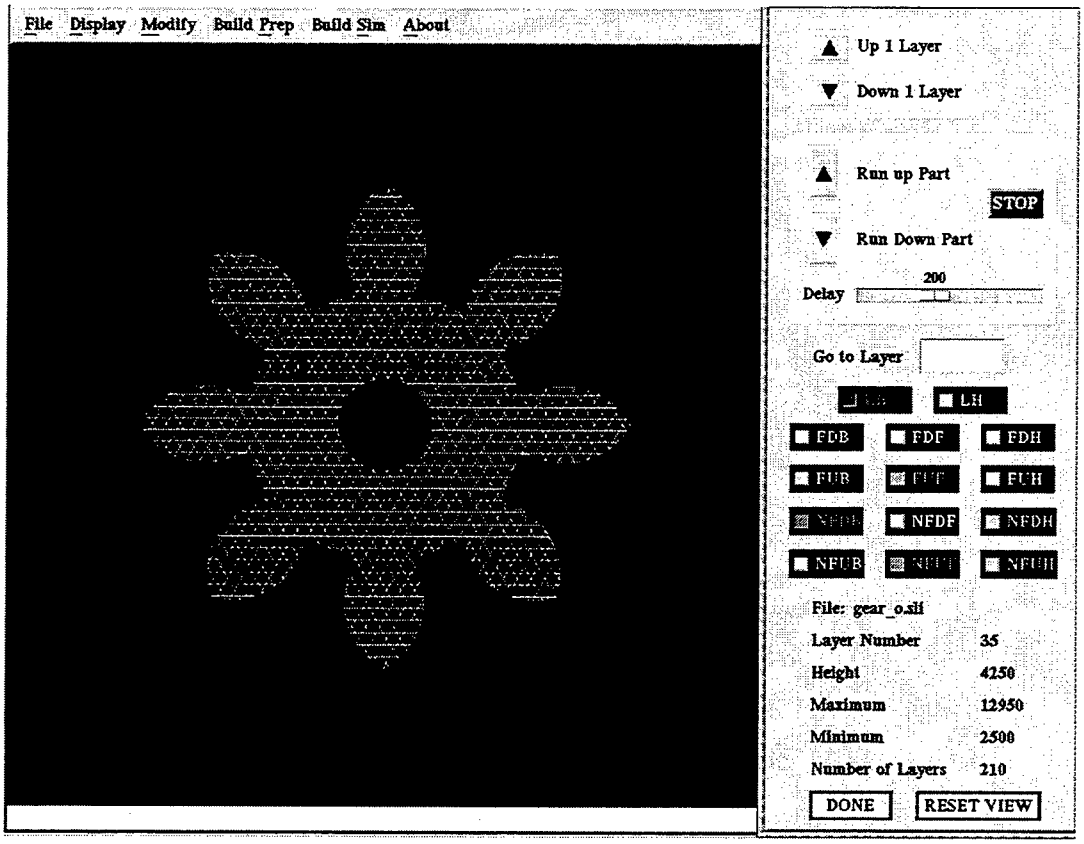


Figure 3. Layer Viewing.

CIDES also has several capabilities that help the user modify and manipulate files. Objects can be moved, rotated, and scaled in order to achieve the best build. The move feature includes both *Move*, which translates the part a relative distance along any of the coordinate directions, and a *Move To*, which sets the part minimum to a specified location. The latter is useful in order to assure that the part is in the positive octant. Another modification function sorts the facets of the STL file based on height for faster slicing.

The utility functions provide the user with capabilities to improve the SLA output or input new files. Verification routines check for and fix inverted normals and provide information on

missing facets. The support algorithm (Kirschman et al., 1991B) allows the user to customize a support structure and view it on the screen. The slicing routines are not as robust as their commercial variants, but the support can be sliced when generated, and a variety of hatch and fill capabilities are available. Volume information is provided for cost estimation. Algorithms are also included to translate from AutoCad neutral (DXF) files to STL files. CIDES offers sufficient capability to help the user of an RP system get more out of the system. The results of current research at Clemson University will be incorporated into future releases of CIDES to increase the utility of the software.

CONCLUSIONS

Rapid prototyping technologies are used to produce parts quickly directly from their CAD representations. However, many areas of the technology have not been made accessible to researchers wishing to "extend the envelope" of RP technology. CIDES includes a number of important features that have enabled Clemson University to increase the capabilities of the Rapid Prototyping (RP) systems that it has through software. CIDES provides input, output, and viewing capabilities for several common formats. It also provides facilities for STL file modification, support generation, slicing, and file translation. This has made CIDES a research testbed for a number of different projects at Clemson University. Currently CIDES is closely coupled with the SLA because that was the first available device, and the only one at Clemson University for several years. However, the code is being expanded to work with other RP systems, including the selective laser sintering testbed at Clemson University. CIDES 2.0 incorporates a new GUI which was created using sound GUI design principles.

ACKNOWLEDGMENTS

The authors thank NASA for its support of this research through NASA grant NAG3-2046. The authors also wish to acknowledge the contributions of Oliver Heim, Shannon Hughes, and Vishal Jadhav to the development of the CIDES 2.0 interface. Finally, the authors would like to thank all the users who were involved in the development and use of CIDES; their insights, comments and suggestions were the driving force of this project.

REFERENCES

Frank, D., and Fadel, G. (1994). "Preferred Direction of Build for Rapid Prototyping Processes." *Proceedings of the Fifth International Conference on Rapid Prototyping* Dayton, OH.

Gould, J. D. (1988). How to Design Usable Systems. In M. Helander (Ed.), *Handbook of Human-Computer Interaction.* (pp 757-789) Amsterdam: Elsevier Science Publishers.

Gould, J. D., Boies, S. J., Levy, S., Richards, J. T., and Schoonard, J. (1987). "The 1984 Olympic Message System: A Test Of Behavioral Principles Of System Design." *Communications of the ACM*, Volume 30, Number 9, September 1987, pp. 758-769.

Kirschman, C. F., Bagchi, A., Jara-Almonte, C. C., Dooley, R. L., and Ogale, A. A. (1991A). "Stereolithographic Support Structure Design for Rapid Prototyping." In *Proceedings of the Second International Conference on Rapid Prototyping* Dayton, OH.

Kirschman, C. F., Jara-Almonte, C. C., Bagchi, A., Dooley, R. L., and Ogale, A. A. (1991B). "The Clemson Intelligent Design Environment for Stereolithography." In *Proceedings of Second the International Conference on Rapid Prototyping* Dayton, OH.

Tata, K. (1995). "Efficient Slicing and and Realization of Tesselated Objects for Layered Manufacturing." Masters Thesis, Clemson University, Clemson, South Carolina.

Terala, K. (1996). "Feed Forward Geometric Compensation for Selective Laser Sintering." Masters Thesis, Clemson University, Clemson, South Carolina.

Ulrich, K. T. and Eppinger, S. D. (1995). *Product Design and Development*. New York: McGraw-Hill.

Vuyyuru, P., Kirschman, C., Fadel, G., Bagchi, A., and Jara-Almonte, C. C. (1994). "A NURBS-Based Approach for Rapid Product Realization." *Proceedings of the Fifth International Conference on Rapid Prototyping* Dayton, OH.

Wodziak, J, Fadel, G., and Kirschman, C. (1994). "A Genetic Algorithm For Optimizing Multiple Part Placement To Reduce Build Time." *Proceedings of the Fifth International Conference on Rapid Prototyping* Dayton, OH.

The Clemson University Laboratory to Advance Industrial Prototyping (LAIP) can be reached through: Elaine Hunt, Director (elaine.hunt@ces.clemson.edu) by phone at (864) 656-4435 or via the World Wide Web at http://design.ces.clemson.edu/rp/.

An Analysis Technique for Layered Manufacturing Based on Quasi-Wavelet Transforms

Cheol H. Lee and Charles L. Thomas
Department of Mechanical Engineering
University of Utah
Salt Lake City, Utah 84112

SUMMARY

An analysis technique based on the Wavelet transform (WT) has been recently introduced that allows the spatial frequency content of objects produced by layered manufacturing (LM) techniques to be interpreted in terms of manufacturable features. (Lee and Thomas, 1997) Using Haar's wavelet as a basis function, layers with vertical edges are modeled exactly. Using analysis, a 3D model can be transformed, filtered, and inverse transformed resulting in an image of the part as it would look if constructed from layers of a specific thickness. In order to extend this analysis to construction techniques using higher order edges (ruled surface edges or curved edges), the quasi-wavelet transform (QWT) is introduced. QWT analysis is conceptually the same as WT analysis, except that the basis function can be selected by the user, allowing exact analysis of layered manufacturing techniques using higher order construction algorithms. This work is supported by a grant from the University of Utah Research Foundation.

INTRODUCTION

When a solid model of an object is reproduced physically using a layered manufacturing technique, the result is a double approximation of the electronic model. The first level of approximation occurs when the model is converted to the *.stl format. This triangular tessellation of the part surface clearly results in error between the CAD model and the triangular mesh. The second level of approximation occurs when the part is constructed from layers. Using finite thickness layers, any surface that is not either parallel or perpendicular to the slicing plane has a ridged, stepped appearance. Researchers are attempting to address the stepped edge problem by cutting ruled surface edges on the layers (Lee et al, 1995), but the result is still an approximation to the designed surface.

In order to minimize the error caused by these approximations and maximize the construction speed by increasing the layer thickness, it would be useful to have analysis tools that would assess the manufacturability of a given model using LM. Desirable features of these techniques might include: The ability to compare the geometric complexity of a specific part to a specific devices' ability to create complex geometry. The ability to predict the output of a specific device. The ability to identify the preferred slicing direction for a specific part.

A previous paper addresses these issues and suggests that objects be decomposed in terms of spatial frequency. (Lee, 1997) Fourier analysis was shown to be of little use since it does not identify the location on the part of the high or low frequency information. Wavelet analysis was shown to be quite useful since the frequency information is spatially localized and Haar's wavelet provides an exact match to the stepped edge layers produced by existing LM devices.

This paper provides a brief discussion of Fourier and Wavelet Transform Analysis (FTA and WTA) applied to 3D objects and introduces Quasi-Wavelet Transform Analysis (QWA).

Fourier Analysis

The Fourier transform is currently used in applications such as signal analysis and image processing. It allows frequency analysis and filtering, of an analog signal by decomposing a time domain signal in terms of it's frequency content. A wave form can be filtered and inverse transformed to predict the form of the time domain signal if certain frequencies were missing. Using a 2D FT, images can be analyzed or compressed by deleting the information for frequencies that make little contribution to the image features. (Proakis, 1992)

A 1D FT is often used to examine a time domain signal (amplitude as a function of time). We can examine a slice of an object in terms of spatial frequency by replacing amplitude and time with the two coordinate axes of the slice. Since LM devices in general can create quite complex geometry in the plane of the slice, but are limited by the layer thickness in the slicing direction, one might say these devices are low pass filters in the slicing direction and that they pass all frequencies in the slicing plane. If basis functions can be selected that represent the cutter shape, then Fourier analysis will produce meaningful results for LM.

The limitation of the Fourier transform that lead to the investigation of wavelet transforms is the inability to spatially localize the frequency information. Fourier analysis averages the frequency content over the entire shape under analysis. The transform cannot identify that certain parts of the object are simple and other parts are complex.

Wavelet Analysis

The Wavelet transform decomposes a signal in terms of both frequency and position. While it has similar applications to the FT, it not only identifies the frequency content of a signal, but also keeps track of where in the signal the frequencies occurred. The WT decomposes a signal using basis functions called wavelets. A wavelet is a family of functions derived from a single function, called mother wavelet expressed as:

$$W_{(a,b)}(x)=\frac{1}{\sqrt{|a|}}W\left(\frac{x-b}{a}\right) \tag{1}$$

where 'a' and 'b' adjust the frequency and position of the wavelet. Using the WT, a signal, f(x) can be expressed as: (Newland, 1993, and Tewfik, 1992)

$$f(x)=a_0u(x)+a_1W(x)+\begin{bmatrix}a_2 & a_3\end{bmatrix}\begin{bmatrix}W(2x)\\W(2x-1)\end{bmatrix}+\begin{bmatrix}a_4 & a_5 & a_6 & a_7\end{bmatrix}\begin{bmatrix}W(4x)\\W(4x-1)\\W(4x-2)\\W(4x-3)\end{bmatrix}+\ldots$$

$$+\ldots+a_{2^j+k}W(2^jx-k)+\ldots. \tag{2}$$

and

$$u(x)=\begin{cases}1 & for\ 0\le x<1\\ 0 & otherwise\end{cases}$$

where a_{2^j+k} is a contribution of a wavelet at frequency 2^j with a shift k. At a frequency 2^j, there are 2^j wavelets with independent amplitudes. Fig. 1 shows four levels of wavelet components for a typical transform. The wavelet used here is Haar's D2 wavelet which consists of a step to amplitude a_i followed by a step down to $-a_i$. Thus the WT to spatially localizes the frequency information.

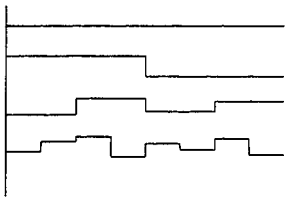


Fig. 1: Wavelet components for a typical transform.

Although wavelets must meet criteria similar to the orthogonality constraints required for basis functions for FT, one wavelet, Haar's D2 wavelet function, consists of steps. Thus, it is perfect for representing the stepped edges of LM. Using Haar's D2 wavelet, the levels of the WT correspond to layer thickness'. The summation of several wavelets of different frequencies results in a stepped surface that can always be reproduced using layers corresponding to the highest of the summed frequencies. Using WT it is possible to transform a 3D object, filter the object, and inverse transform the object producing a prediction of the geometry realized from layers of a selected thickness. (See Fig. 2) (Lee, 1997) Note that the object is first mapped into cylindrical coordinates to get a single valued function.

There are limitations to the wavelet transform: The wavelets double in frequency at each level. Thus, only certain layer thickness' are actually considered in the analysis. If a LM device were capable of varying the layer thickness in an analog fashion, the technique as described would not be able to properly analyze the problem. A second limitation is that there are no known wavelets that match the cutter shapes used by the new higher order construction algorithm LM devices that are currently under development.

QUASI-WAVELET ANALYSIS

The Quasi-Wavelet Transform follows the spirit of the WT, but relaxes the constraints on the basis functions. As a result the QWT can use any function as a basis function. The QWT decomposes a function in terms of quasi-wavelets that are scaled and shifted in a similar fashion to wavelets. The requirement for QWT is that, at the lowest frequency, a single quasi-wavelet is scaled such that the squared error between the quasi-wavelet and the function is minimized. The next level has two quasi-wavelets and each is scaled independently to minimize the squared error between the function and the sum of the two quasi-wavelet levels. At the third level there are four wavelets and each is scaled to minimize the error between the function and the sum of the three levels of wavelets. This process continues until the highest frequency of interest is reached.

A function W(x), made up of a linear combination of general functions g(x), is defined as a quasi-wavelet function, within the interval 0<=x<=1, and is set to zero outside the interval. Thus, an n term quasi-wavelet function can be expressed as:

$$W_n(x)=\sum_{i=1}^{n} g_i(x) \qquad (3)$$

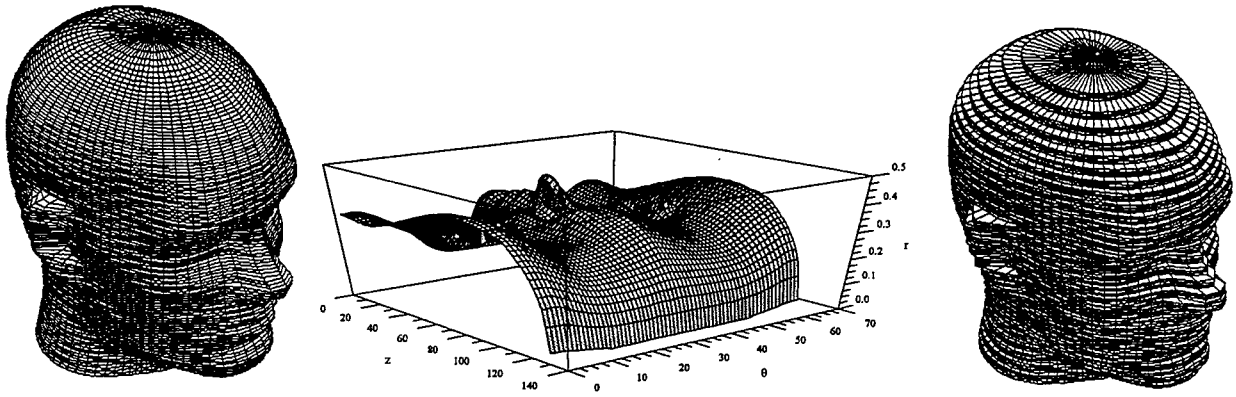


Fig. 2: CAD file, cylindrical coordinate mapping, and filtered inverse transform.

The actual signal, f(x), is:

$$f(x)=\sum_{i=-1}^{m} f_i(x) \tag{4}$$

where each $f_i(x)$ is one level of the transform and is composed of 'r' independent wavelets each with a vector amplitude $\vec{\alpha}_k$:

$$f_i(x)=\sum_{k=1}^{r} \vec{\alpha}_k \cdot \vec{W}_n(rx-k+1)\,, \qquad r=2^i \qquad =\sum_{k=1}^{r}\sum_{j=1}^{n} \alpha_{kj} g_j(rx-k+1) \tag{5}$$

and

$$f_{-1}(x)=\alpha_{-1}u(x)$$

where $\vec{W}_n$ is a quasi-wavelet function expressed as a vector, and $f_{-1}(x)$ is the DC level of f(x).

We define $F_i(x)$ as the sum of levels from level -1 to level i:

$$F_i(x)=\sum_{k=-1}^{i} f_k(x) \tag{6}$$

As a result, $F_i(x)$ is the output of a low pass filter within QWT. The error of $F_i(x)$ is defined as:

$$\varepsilon_i(x)=f(x)-F_i(x) \tag{7}$$

Calculating the QWT involves finding the appropriate coefficient vectors $\vec{\alpha}_k$ in order to minimize this error. Details of this calculation can be found in (Lee, 1997).

Using the quasi-wavelet function $W_n(x)$, the function f(x) should be discretized into $2^\mu n$ points, where μ is a positive integer. Here the highest level is μ and there are 2^μ layers (or cycles of the basis function) at this level. Therefore, there must be 'n' points for each layer. Since $W_n(x)$ has n coefficients, n points per layer results in a unique set of coefficients without error. Thus, QWT is capable of perfectly reconstructing data points using the highest level.

QWT for Object Analysis

In this analysis the object is first mapped into cylindrical coordinates and unwrapped to produce a single valued function. Complex objects with multiple surfaces must be analyzed one

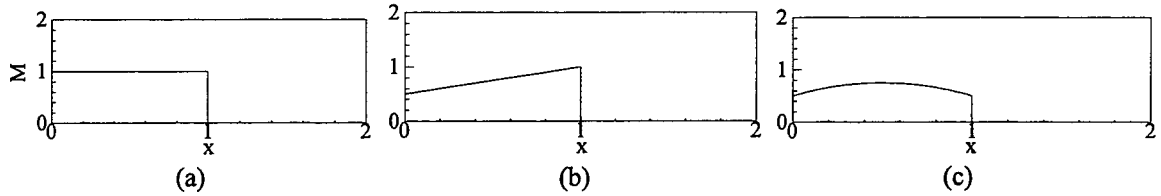


Fig. 3: This shows three quasi-wavelet basis functions. a) Step - This is equivalent to Haar's D2 wavelet. b) Angle - This quasi-wavelet models the ruled cut algorithm for layered manufacturing. c) Curve - This quasi-wavelet models the curved cut algorithm for layered manufacturing.

surface at a time. The z axis of the cylindrical coordinate system is assumed perpendicular to the slicing plane. When applying QWT, the quasi-wavelet function should be carefully chosen so the basis function can properly represent the LM machine. Quasi-wavelet functions for stepped edges (Stepped Cut Algorithm, SCA), ruled edges (Ruled Cut Algorithm, RCA), and curved edges (Curved Cut Algorithm, CCA), were selected as follows:

$$W_{SCA}(z)=W_1(z)=a_1\,u(z) \tag{8a}$$

$$W_{RCA}(z)=W_2(z)=a_1\,u(z)+a_2\,z \tag{8b}$$

$$W_{CCA}(z)=W_3(z)=a_1\,u(z)+a_2\,z+a_3\,z^2 \tag{8c}$$

where a_i are the coefficients that define the shape of each quasi-wavelet. An example of each is shown in Fig. 3. The QWT coefficients, a_i's, of $W_n(z)$ for SCA, RCA, and CCA for all levels, make up $\{a_i\}$ as follows:

$$QWT_{SCA} : \{a_{-11}, a_{01}, a_{11}, a_{12}, \ldots, a_{ij}, \ldots, a_{m2^m}\}$$

$$QWT_{RCA} : \{a_{-111}, a_{-112}, a_{011}, a_{012}, \ldots, a_{ij1}, a_{ij2}, \ldots, a_{m2^{m}1}, a_{m2^{m}2}\}$$

$$QWT_{CCA} : \{a_{-111}, a_{-112}, a_{-113}, a_{011}, a_{012}, a_{013}, \ldots, a_{ij1}, a_{ij2}, a_{ij3}, \ldots, a_{m2^{m}1}, a_{m2^{m}2}, a_{m2^{m}3}\}$$

where the first subscript identifies the level (frequency), the second subscript identifies the position of the wavelet, and the third subscript identifies the function within the wavelet. Fig. 4 is a pictorial example of the coefficients for QWT_{RCA} at level 1 and 2. In QWT_{SCA}, if there are 2^{m+1} coefficients, then a_{-11} is the average value for all data, and a_{ij} is the coefficient of $u(2^i z-j+1)$. If there are 2^{m+2} coefficients in the QWT_{RCA}, a_{111} is the data average, and a_{-112} is usually zero, where a_{ij1} is the coefficient of $u(2^i z-j+1)$ and a_{ij2} is the coefficient of $(2^i z-j+1)$. In a QWT_{CCA}, if there are $3\times 2^{m+1}$ coefficients, a_{-111} is the data average, and a_{-112} and a_{-113} are usually

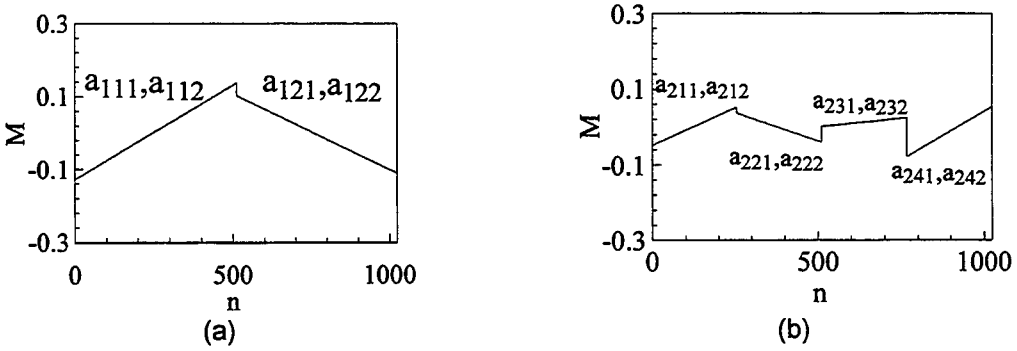


Figure 4: This shows two levels of a transform using the Angle quasi-wavelet. each sloped quasi-wavelet has its own independent coefficients.

zero, where a_{ij1} is the coefficient of $u(2^i z - j + 1)$, a_{ij2} is the coefficient of $(2^i z - j + 1)$, and a_{ij3} is the coefficient of $(2^i z - j + 1)^2$.

APPLICATIONS

Frequency Analysis

In LM, expressing objects in the frequency domain is very meaningful because frequency can be related to the number of layers. The contributions of individual frequencies to the geometry of a part can be found using frequency analysis. At certain cut off frequencies, the loss of geometric information is easily visualized through frequency component charts.

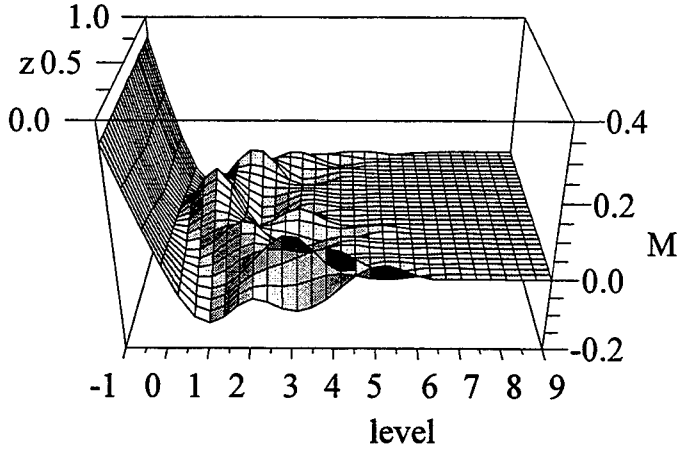


Figure 5: This is the Quasi-Wavelet Transform of a slice of a vase using Angle quasi-wavelets.

Fig. 5 shows the QWT_{RCA}. of a cross section of a vase shown in Fig. 6. The vase has been scaled to unit height with height shown as the z axis. The level axis corresponds to frequency or number of layers with 2^n layers at level 'n'. The magnitude is simply the quasi-wavelet components drawn on the M, z axis in this figure. The figure shows higher frequency components near the bottom and top of the vase. The center of the vase has higher amplitude components at low frequency and little contribution from higher frequencies. This suggests that the base can be constructed from 128 layers corresponding to level 7.

Output Prediction

The output of a SFM device can be predicted by applying a low pass filter to the data from Fig. 5. This is done by setting the magnitudes of all wavelets at levels above the filter cut off to zero. Next, an inverse transform is performed and an image of the object is produced as it would look if constructed using the selected algorithm at the selected layer thickness. Fig. 6 shows examples of output prediction for SCA, RCA, and CCA. As would be expected, the RCA and CCA produce an accurate representation using thicker layers than required for SCA.

Advanced Filtering

Using QWT it is not only possible to filter frequencies, it is possible to create filters that match machine constraints. If an RCA device can cut angled edges on the layers, but the angle is limited, this can be accounted for in the transform. A CCA device might be able to produce curved surfaces as long as the radius of curvature is greater than some minimum.

For Shapemaker II, a LM machine that implements RCA, hardware limitations constrain the maximum angle of cut. The design of Shapemaker II allows for a maximum cut angle of 45 degrees. For some layer thickness', the maximum angle may be reduced from this value. In QWT_{RCA}, cut angles are specified by the coefficient of the z term. By setting a limiting value on the z terms, it is possible to limit the angle of cut. (Lee, 1997)

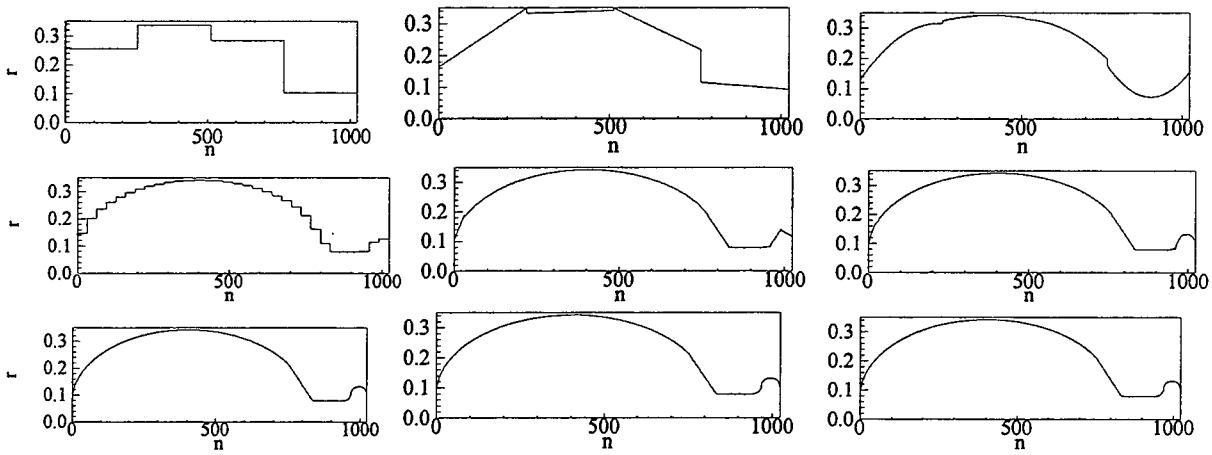


Figure 6: The vase shape has been transformed using Step, Angle, and Curve quasi-wavelets. Then it was filtered at different frequencies and inverse transformed.

Demonstration

The head shown in Fig. 2 was constructed using Shape Maker II. The model, in STL format was sliced in 1.8 mm thick slices. The slices were cut from commercially available 1.22 m by 2.44 m, white polystyrene foam, with an average thickness of approximately 1.8 cm. The size of the 47 layer head is 57 cm by 74 cm by 83 cm.

Using QWT_{RCA}, the shape of the head was predicted for 47 layers with a maximum cutter angle constraint of 45 degrees. Fig. 7(a) shows the inverse QWT_{RCA} of a three dimensional head with 47 layers and a 45 degree constraint on the cut angle. Fig. 7(b) shows a completed head made by SM2. As demonstrated by the predicted head, because of machine constraints, there is obvious error due to the constrained angle near the top of the completed head.

Advantages and Limitations

The QWT uses any linear combination of functions as a basis function. Frequency localization identifies where on an object the frequency components exist. As a result, QWT should be capable of analyzing any LM technique. Using the QWT, the output of LM systems can be predicted and reconstruction errors can be evaluated mathematically. Since the quasi-wavelet transform decomposes a three dimensional surface geometry into frequency components, a frequency analysis can be performed by inspecting the transform coefficients. Optimal construction directions can be found through coordinate rotation and frequency analysis.

Limitations for the application of three dimensional object analysis mainly arise from limitations of the three dimensional surface representation. Currently, the cylindrical representation method is used, which maps the three dimensional surface of an object onto a cylinder. This is done to produce a single valued function for the analysis. However, this method may still produce a multiple valued function for certain types of geometry's.

By nature of the analysis, frequencies analyzed by the QWT are integer powers of two. As a result, building an object from 3 layers or 115 layers is not considered. Most current SFM devices build parts from layers of fixed thickness and, as a result, seldom build parts from layers

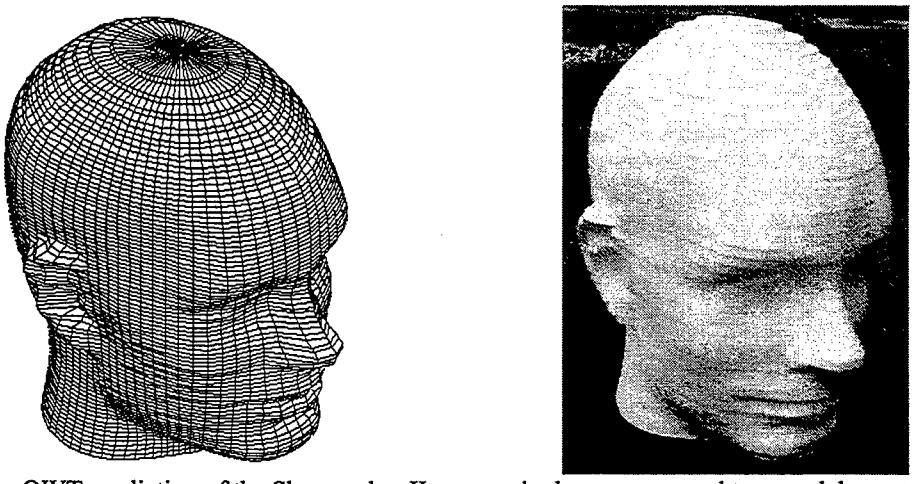


Figure 7: The QWT prediction of the Shapemaker II process is shown compared to a model constructed using Shapemaker II.

that are an integer power of two. This problem can be handled by zero padding. Essentially the model is placed in build volume that is an integer power of two layers thick at the desired layer thickness, and the analysis is done on the entire volume.

CONCLUSIONS

The quasi-wavelet transform is a method for mathematically analyzing the spatial frequency content of three dimensional objects. This technique allows the complexity and manufacturability of a part to be analyzed. Using an inverse transform it is possible to reconstruct the part as it would look if it were manufactured by a specific process. The quasi-wavelet transform is a generalization of the wavelet transform technique that allows any function to be used as a wavelet. This allows any manufacturing process to be modeled by this technique.

REFERENCES

Lee, C. H., Gaffney, T. M., and Thomas, C. L. (1995) Paradigms for Rapid Prototyping, *Proceedings of the Sixth International Conference on Rapid Prototyping*, pp. 131-143.

Lee, C. H., Gaffney, T. M., and Thomas, C. L. (1996) Soft Tooling for Low Production Manufacturing of Large Structures, *Proceedings of the 1996 Solid Freeform Fabrication Symposium*, pp. 207-214.

Lee, C. H. and Thomas, C. L. (1997) Wavelet Transform Based Analysis of Objects for Layered Manufacturing, *Proceedings of the Seventh International Conference on Rapid Prototyping*,.

Lee, C. H. (1997) *New Analysis Methods for Three Dimensional Objects in Solid Freeform Manufacturing*, Ph.D. Thesis. University of Utah.

Newland, D. E. (1993) *An Introduction to Random Vibration, Spectral and Wavelet Analysis*, Longman Scientific & Technical, England.

Proakis, J. G., and Manolakis, D. G. (1992) *Digital Signal Processing*, 2nd ed., Macmillan, New York.

Tewfik, A., Sinha, D., and Jorgensen, P. (1992) On the Optimal Choice of a Wavelet for Signal Representation, *IEEE Transactions on Information Theory*, Vol. 38, No. 2, pp. 747-765.

Thomas, C. L., Gaffney, T. M., Kaza, S., and Lee, C. H. (1996) Rapid Prototyping of Large Scale Aerospace Structures, *Proceedings of the 1996 IEEE Aerospace Applications Conference*, Vol. 4 of 4, pp. 219-230.

Using adaptive ruled layers for Rapid Prototyping: principles and first results

P.J. de Jager, J.J. Broek and J.S.M. Vergeest
Faculty of Industrial Design Engineering,
Delft University of Technology,
Jaffalaan 9, NL-2628 BX Delft, The Netherlands,
email p.j.dejager@io.tudelft.nl

ABSTRACT

Current 2.5D layered rapid prototyping has as disadvantage the staircase effect, requiring thin layers to be used to achieve a reasonable accuracy. Slices with inclined outer surfaces can be constructed using linear interpolation between adjacent contours, resulting in ruled slices. A methodology to approximate a given model geometry within a specified accuracy using ruled slices and an adaptive layer thickness is described. This involves matching successive contours and analysing the geometry for curvature and inclination to calculate allowed layerthicknesses. First results show a significant reduction in the number of layers when compared to adaptive slicing using 2.5D layers. A proof-of-concept software, the Delft University of Technology Improved Slicer (DUTIS) has been developed to perform the adaptive slicing using either 2.5D or ruled layers allowing a comparison between the two alternative methods.

Keywords zero order approximation, first order approximation, comparison, direct adaptive slicing, matching contours, ruled slices

1. INTRODUCTION

In the commonly used 2.5D Layered Manufacturing Techniques (LMT), which in effect use a zero-order approximation of the original geometry, a relatively small layer thickness d must be used to constrain the errors that are introduced by this approximation (the stair-case effect). The layer thickness d can be increased when a first-order approximation is used in which the side surfaces of the slices can be inclined. A possible solution to accomplish this is by using ruled slices, interpolating between two adjacent planar contours. Moreover, when also an adaptive layer thickness is used, the number of layers required for a user defined error δ can be further reduced. In this paper the zero and first order approximation algorithms, combined with direct adaptive slicing of BREP CAD model geometry will be compared.

An advantage of this so-called ruled slicing is that, because the edges of the adjacent slices meet, C^0 continuity in the slicing direction (z-direction) is guaranteed, eliminating the staircase effect as present in the 2.5D approach. An improved surface finish is the result. Another advantage is the reduction in the number of layers, resulting in faster manufacturing. A disadvantage is that manufacturing of the ruled slices requires a process with 4 degrees of freedom, which is generally more expensive than a process with 2 degrees of freedom.

The Delft University of Technology Improved Slicer (DUTIS) software has been developed using the ACIS® geometric modelling kernel (ACIS, 1996) and C++ on an SGI platform to

approximate a given BREP CAD model geometry using either a zero or a first order approximation within the specified δ. The paper is divided into the following sections. Section 2 describes the related research. In section 3 the general procedure will be introduced. In section 4 the calculation of an adaptive layer thickness will be explained and the method of matching arbitrary contours from adjacent slices will be discussed. In section 5 the results for some examples will be shown. Finally in section 6 the results will be discussed and conclusions will be given.

2. RELATED RESEARCH

A lot of work is carried out by other researchers in the area of adaptive slicing and first order approximation of model geometry.

In our software the algorithms for the zero order approximation are based on the work of (Suh and Wozny, 1994) and (Kulkarni and Dutta, 1995 and 1996). A horizontal layer (in the xy-plane) with a vertical outer surface can be regarded as a zero order approximation in the vertical slicing direction (z) of a part of the original model geometry. The usual procedure to reconstruct such a layer is to slice the model and to extrude the slice into the slicing direction to give the slice a certain thickness. Each contour is independently used for this reconstruction. The reconstruction error depends on the local curvature and the z component of the surface normals of the model geometry. The basic idea behind the calculation of an adaptive layer thickness is that a surface can be locally approximated in a certain plane by a circle with radius R equal to the local curvature in the plane. The approximation error can be calculated and from this an expression for the allowed layer thickness for a convex surface can be derived as shown in (Suh and Wozny, 1994) and (Kulkarni and Dutta, 1995 and 1996)

$$d = -R\sin\theta + \sqrt{R^2\sin^2\theta + 2R\delta + \delta^2} \qquad (1)$$

in which R radius of curvature in vertical direction, δ the user-defined error and θ in [0..π] the angle between the surface normal and the horizontal plane at the bottom of the slice. Using the same approach it is also possible to derive expressions for convex surfaces and for θ in [-π..0].

Other researchers have been working on the subject of manufacturing layers with inclined side surfaces. The term *twisted profile layers* is used in (Barlier et al.1995) to describe ruled slices as a means to improve layered manufacturing. Layers with inclined side surfaces are also used by (Hope, 1996) for the manufacturing of large objects. Ruled slices are also used for the CAM-LEM process (Newman et al.1995) and the Shapemaker II process (Thomas et al.,1996). These processes are capable of producing ruled slices by using either a 5-axis laser cutting system or a 4-axis hot-wire cutter (for foam material). In general, because ruled slices are described by means of a set of non-intersecting straight line segments connecting the upper and lower contours of the slice, ruled slices can be produced from sheet material by processes that employ line visibility (Woo, 1994) and have at least 4 degrees of freedom (translation in the x,y plane and additional rotations ϕ, θ). Among these processes are wire EDM, hot-wire cutting, laser cutting, water-jet cutting, CNC side milling and more.

3. GENERAL PROCEDURE IN DUTIS

DUTIS is an interactive program that allows the user to load a CAD model, and manipulate this CAD model by rotation, translation and scaling options if desired. Also boolean operations are implemented, allowing for a project to be assembled from multiple CAD models that must be sliced as a whole. When the CAD model has the desired orientation, such that the z-axis of the CAD model coincides with the required approximation direction, a number of steps have to be taken in sequential order to complete the process for a non-equidistant layered approximation of a given BREP CAD model within a user-defined δ. These steps are

1. User input: The approximation method must be chosen, either zero- or first order
2. User input: The required accuracy must be specified
3. Automated procedure:
    - The CAD model is analysed for important features that must be preserved, such as horizontal areas and sharp edges
    - The z-heights of the found features are used to divide the CAD model into segments
    - The CAD model segments are sliced with an adaptive layer thickness according to δ using the equations for either 2.5D or ruled slices
    - Either 2.5D or ruled slices are reconstructed

The resulting layered approximation can be interactively viewed on screen and, if accepted, the data can be used for manufacturing.

The segmentation procedure samples the curves between adjacent surfaces as well as the surfaces to find segment borders, based on the extrema of the curves and horizontal areas of the surfaces.

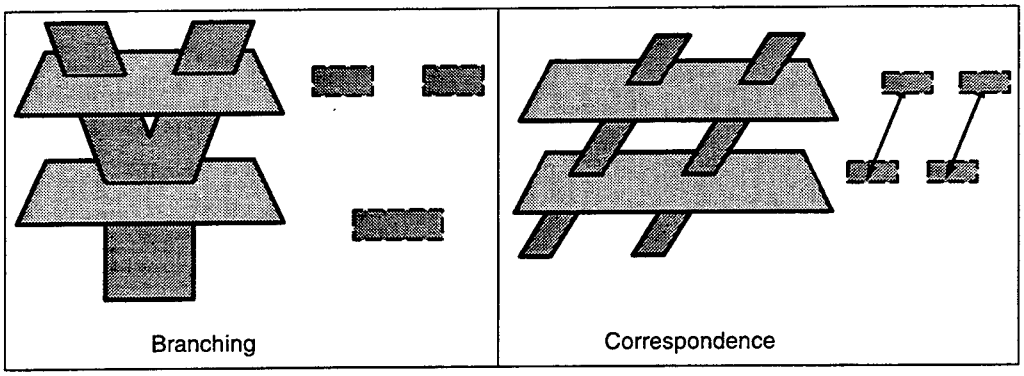


Figure 1. Problems with reconstructing a surface between 2 contours: the branching and correspondence problems

The differences between the zero and first-order approximation approaches are the calculation of an allowed layer thickness and the reconstruction of the slice. The CAD model segmentation is a necessary step in this procedure for the reconstruction of ruled slices, because the reconstruction of a three-dimensional shape from 2 successive contours is a complex problem. A surface connecting the contours must be found. This is difficult because of two problems, (a) branching

and (b) correspondence as shown in figure 1. The branching problem indicates that the number of contours is different between two successive slices. The correspondence problem indicates that the number of contours per slice is the same but larger than one for two successive slices. In both cases it is unknown how the contours should be connected from one slice to the other. The branching problem is eliminated when the model is first segmented as explained above. We will discuss the correspondence problem further in section 4.4.

4. ADAPTIVE SLICING OF SEGMENTS

In this section it is assumed that the CAD model is divided into a set of segments. These segments are processed individually. The subdivision of the segments into a set of slices with an adaptive layer thickness must take account of the curvature, slope of the CAD model surface and the user-specified δ.

4.1. First order approximation

The first order approximation is based on linear interpolation between successive contours using geometrical and topological information from the original geometry. In effect a ruled surface (Farin, 1990) between 2 adjacent contours is constructed. For ruled slicing an expression for the error and thus for the allowed layer thickness can be derived as

$$d = \cos\alpha\cos\theta\sqrt{2R\delta - \delta^2} \qquad (2)$$

in which R radius of curvature in the plane of interest, δ the user-defined error, θ in $[-\pi..\pi]$ the angle between the surface normal and the horizontal plane at the half height of the slice and α in $[-\pi/2..\pi/2]$ the angle between the vertical direction and the line connecting the points on the upper and lower contour of the ruled surface.

4.3. Implementation of the slicing algorithm

The algorithms that are implemented in DUTIS to slice a segment in the z-direction uses as input a CAD model segment and the user-specified δ. DUTIS also takes explicitly into account the limitations of the manufacturing process. Depending on the type of process used to manufacture the ruled slices and the available sheet materials either a set of n allowed layer thicknesses $th_{1..n}$ or the fact that an arbitrary layer thickness is possible can be indicated. The general procedure can be described as

1. Define the extent of the segment in z-direction: z_{min}, z_{max}
2. Approximate the segment using a stepwise approach:
   - Calculate the intersection at $z = z_i$ (starting at z_{min}), resulting in a set of contours C_i
   - Sample C_i and calculate the maximum allowed layer thickness d_i according to either eq. (1) or eq. (2) for zero- or first-order approximation respectively.
   - If only a limited set of layer thicknesses is available, select the nearest smaller layer thickness $d_i := d'_i \leq d_i$ from the available set of thicknesses
   - Check if new sample height is not exceeding the segment dimensions: $(z_i + d_i \leq z_i)$
   - Check at suggested new sample height $z_i + 1$ if the assumptions used in the calculation for the layer thickness are still correct (see below)

- if correct, continue
- if not correct, repeat with layer thickness $d_i = \alpha\, d_i$ with $0 < \alpha < 1$

In this algorithm a two-way approach is used to ensure that regions of higher curvature are not missed. First in the upward direction a new layer thickness is calculated. Secondly in the downward direction at the new proposed slice height a check-calculation is made. This check-calculation is made to ensure that the proposed layer thickness does not result in exceeding the user-specified δ in the approximation. This check is necessary because of a possible changing curvature in the upward direction of the CAD model. Furthermore the third point in step 2 of the described algorithm selects the appropriate sheet thickness from the available set of thicknesses for the manufacturing process. This set is user-specified and can thus be adapted to local circumstances.

4.4 Constructing the slices and solving the correspondence problem

After all segments are processed, a list of contours must be processed to generate the slices. For a zero-order approximation, this is a simple procedure that exists of an extrusion in the positive z-direction to give the slice the desired thickness. For a first-order approximation, two successive contours must be matched using a more difficult procedure. This matching can be accomplished using either matching in parameter space (see (de Jager, 1996A) and (de Jager et al., 1996B)) or matching in geometric space such that the correct starting points on the successive contours can be found.

A calculated intersection of the CAD model and a plane consists of a set of planar contours. A contour consists of a closed and ordered set of connected curves which are originating from slicing the BREP geometry. In the slicing procedure we keep track of the original surfaces in order to evaluate the geometry around the contours. We can use the topological information from the original CAD model to match corresponding curves. All contour curves from one contour have a corresponding curve in the adjacent contour, because as a result of the segmentation procedure they are originating from the same surfaces. Therefore we can always find a correspondence between adjacent contours.

5. Results

The results for a simple test object (a sphere with radius 25mm) show clearly that depending on the ratio between the curvature of a model and the allowed error, the ratio between the number of layers for a zero-order approximation and a first-order approximation varies between approx. 4 and 14 times as shown in table 1.

In figure 2 the result of the first order approximation using ruled slices for a non-rotational symmetric shape (a perfume bottle) is shown. You can see the original model and the approximation with 29 ruled slices. For the same accuracy 134 2.5D slices were needed, which is a factor 4.6. In table 2 the results for different δ's are summarised.

δ	*number of 2.5D slices*	*number of ruled slices*	*ratio 2.5D/ruled*
1.0	26	6	4.3
0.5	54	8	6.8
0.1	253	18	14.1

Table 1 Layered approximation of a sphere with radius R = 25.0mm

δ	*number of 2.5D slices*	*number of ruled slices*	*ratio 2.5D/ruled*
30.0	69	10	6.9
10.0	134	29	4.6
1.0	288	60	4.8

Table 2 Layered approximation of the model 'bottle' with size 454x104x300mm

In figure 3 the results for a more complex geometry are shown. This example consists of a more difficult geometry with different features: straight faces, a hole, a cylinder and different radii. The dimensions of this model are 200x100x50mm and the allowed δ is 1.0mm. The zero order approximation requires 23 layers, while the first order approximation requires 11 layers, a reduction of 2 times the number of layers. It can be noted that the correspondence between the adjacent contours is solved correctly.

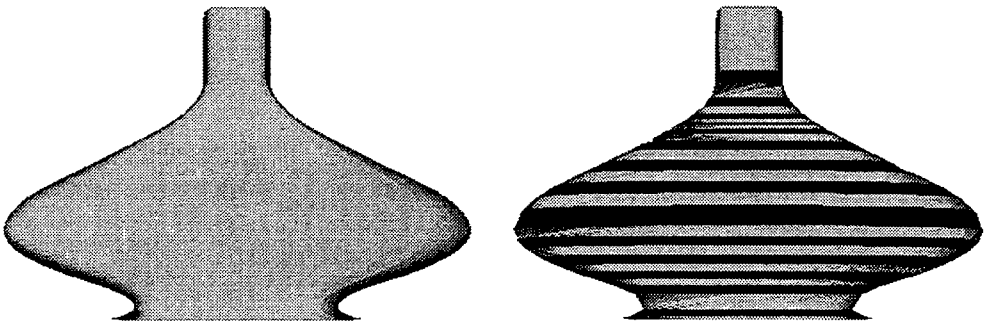


Figure 2. Object "Bottle" and the approximation with 43 ruled slices. The size of the object is 454x104x300mm, and the δ is 10mm.

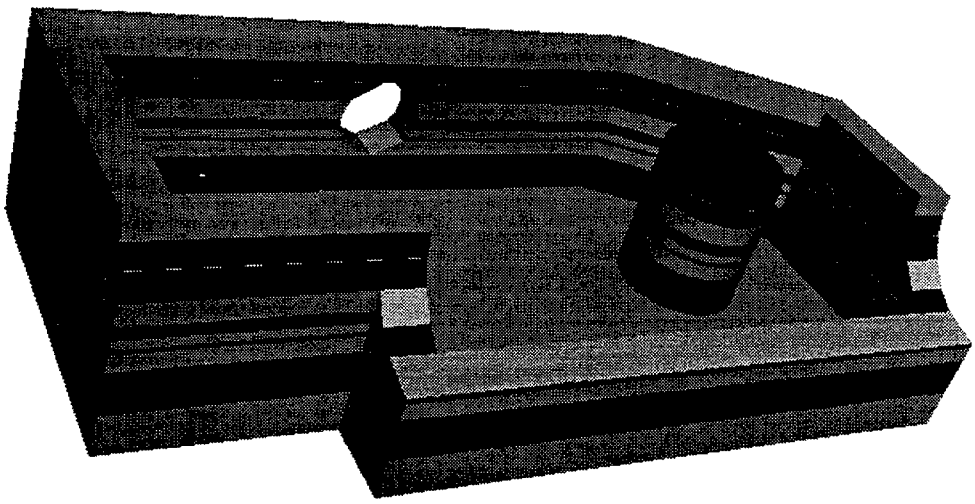


Figure 3. The approximation of a more difficult geometry with 11 ruled slices. The size of the object is 200x100x50mm, and the δ is 1mm.

The figures in this section are screenshots of the geometry before and after the approximation procedure. The user of DUTIS can interactively manipulate the view of the geometry to evaluate the result before taking a decision whether or not to manufacture the model.

For demonstration purposes, we have experimented with a 6-axis robot milling workcell (Vergeest and Tangelder, 1996) using side milling, simulating a 4-axis NC milling machine and have managed to use the robot set-up for 4-axis machining. Some models have been manufactured using the robot to manufacture individual slices and by manually assembling these slices.

6. Discussion and conclusions

We have shown in this paper that it is possible to get a significant reduction in the required number of layers for a user-specified δ when adaptive ruled layers are used. The theoretical results in this paper are valid for a range of processes that employ line-visibility. Although this type of equipment to manufacture a ruled slice is more expensive than the equipment necessary to manufacture a 2.5D slice, we are confident that for large smooth shapes (with not too many surface details) it is very profitable to use ruled slices. Depending on the model geometry and the user-defined δ, the actual reduction in number of layers for the examples shown varies between 2 and 14 times, based on the use of a continuously varying layer thickness. However, DUTIS is also capable of taking into account user-defined discrete sets of thicknesses. The reduction in the number of layers improves the time and costs to manufacture and assemble the model. The interactive viewing of the result gives an opportunity to evaluate the approximation before the actual manufacturing.

We are aware that the overall improvement depends also on several other factors. For a more thorough analysis the time and costs to produce one layer, the costs of material and the time and

costs of assembly should also be taken into account. Therefore both the 2.5D as well as the ruled slicing methods have been implemented in DUTIS to give the user the opportunity to evaluate the results for both methods and make a proper choice of an appropriate manufacturing method.

References

[1] ACIS® Geometrical Modeler Application Guide (1996), Version 2.0 Issue 1 3/96, © Spatial Technology Inc., Boulder, Colorado

[2] Barlier, C., Gasser, D., Muller, F. and Feltes, U.(1995), "Stratoconception-Rapid Prototyping for Die-Forging Tooling", in J.I. Solliman and D. Roller, eds., *Proceedings of the 28th ISATA Conference, dedicated on rapid prototyping in the automotive industries*, pp. 51-57

[3] Farin, G.(1990), *Curves and Surfaces for Computer Aided Geometric Design*, Academic press Inc.

[4] Hope, R.L., Riek, A.T. and Roth, R.N. (1996) "Layer building with sloped edges for rapid prototyping of large objects", in P. Dickens (ed), *Proceedings of the 5th European conference on Rapid Prototyping and Manufacturing*, Helsinki, ISBN 0 9519759 5 1, pp. 47-58

[5] Jager, P.J. de (1996) "Using slanted and ruled layers for rapid prototyping", in P. Dickens (ed), *Proceedings. of the 5th European conference on Rapid Prototyping and Manufacturing*, Helsinki, ISBN 0 9519759 5 1, pp. 15-30

[6] Jager, P.J. de, Broek, J.J. and Vergeest, J.S.M. (1996) "Rapid prototyping: extending the layer concept", *Proceedings of the 2nd International Conference on Rapid Product Development*, Stuttgart, pp. 325-334

[7] Kulkarni, P. and Dutta, D.(1995), "Adaptive slicing of parametrizable algebraic surfaces for layered manufacturing", *Proceedings DE-Vol. 82, Design Engineering Technical Conferences*, Volume 1, ASME, pp. 211-217

[8] Kulkarni, P. and Dutta, D.(1996), "An accurate slicing procedure for layered manufacturing", *Computer Aided Design*, Vol. 28(9), pp. 683-697

[9] Newman, M., Zheng, Y. And Fong, C.C (1995) "Trajectory generation from CAD Models for Computer-Aided Manufacturing of laminated Engineering Materials", *Proceedings of the 26th International Symposium on Industrial Robots,* pp. 153-158

[10] Suh, Y. And Wozny, M.J. (1994) "Adaptive slicing of solid freeform fabrication processes", *Proceedings of the Solid Freeform Fabrication Symposium, University of Texas at Austin, Austin, Texas,* pp. 404-411

[11] Thomas, C.L., Gaffney, T.M., Kaza, S. and Lee, C.H. (1996) "Rapid prototyping of Large Scale Aerospace Structures", *Proceedings of the 1996 IEEE.Aerospace Applications Conference*

[12] Vergeest, J.S.M.and Tangelder, J.W.H.(1996) "Robot machines rapid prototype", *Industrial Robot*, 23(5), pp. 17-20

[13] Woo, T.C. (1994), "Visibility maps and spherical algorithms", Computer Aided Design, Vol. 26(1), pp. 6-16

Reverse Engineering: Algebraic Boundary Representations to Constructive Solid Geometry*

by

S. F. Buchele** and W. A. Ellingson

** Argonne National Laboratory Lab-Grad Student
Computer Sciences Department
The University of Texas at Austin
Austin, TX 78712

Energy Technology Division
Argonne National Laboratory
Argonne, IL 60439

Abstract

Recent advances in reverse engineering have focused on recovering a boundary representation (b-rep) of an object, often for integration with rapid prototyping. This boundary representation may be a 3-D point cloud, a triangulation of points, or piecewise algebraic or parametric surfaces. This paper presents work in progress to develop an algorithm to extend the current state of the art in reverse engineering of mechanical parts. This algorithm will take algebraic surface representations as input and will produce a constructive solid geometry (CSG) description that uses solid primitives such as rectangular block, pyramid, sphere, cylinder, and cone. The proposed algorithm will automatically generate a CSG solid model of a part given its algebraic b-rep, thus allowing direct input into a CAD system and subsequent CSG model generation.

1. Introduction

1.1 Solid Modeling

Solid modeling is the process of defining and manipulating unambiguous computer representations of physical solid objects that are specified using normalized or specific dimensions. Computer systems designed for this purpose are called solid modeling or CAD (Computer Aided Design) systems. A fundamental use of these systems is designing or engineering mechanical parts, although their use in other application areas, such as free-form sculpting and automated mesh generation, is currently growing.

Two basic types of CAD system architectures are in use today: (a) boundary representation (b-rep) modelers, which store objects' boundaries and other neighborhood and orientation information; and (b) constructive solid geometry (CSG) modelers, which construct objects from solid primitives by using the Boolean operations union, intersect, and difference; store CSG trees; and compute boundary representations when needed [3]. In practice, few CAD systems can be classified strictly as one type or the other, however. Sweep representations, in which a 2-D or 3-D object is swept along a 3-D trajectory, and spatial partitioning representations, in which a solid is decomposed into collections of adjoining cells or solids, are often included in CAD modelers as well [1,2]. Hybrid CAD systems, in which some combination of the above representations are used in tandem or conjunction with each other in a single CAD system, are the norm for current modeling systems. In particular, CAD systems for the design of mechanical objects provide a CSG interface, regardless of the underlying architecture(s) of the CAD system itself. For example, a CAD system with a Non-Uniform Rational B-Spline (NURBS) b-rep representation as its base architecture may provide a CSG-type input interface for the engineer. In this case, a part definition is entered as the union, intersection, and difference of instances of (properly parameterized) solid primitives. The boundary of the resulting CSG-specified solid object is then evaluated and represented internally in b-rep fashion. The initial CSG representation of the object may be stored internally as well. User interfaces that allow sweeps to be entered are also common in conjunction with CSG user interfaces, regardless of the underlying CAD architecture.

1.2 Reverse Engineering

Reverse engineering (or geometry recovery) of a part (mechanical, biomedical, etc.) is the general process of recovering a model of a physical object from information obtained by some type of sensing technique. These sensing techniques include, but are not limited to, computed tomographic imaging (CAT scans), nuclear magnetic resonance imaging (MRI scans), laser rangefinder scans, stereoscopic sensing, and coordinate measuring machine (CMM) sensing. In some cases, the process of recovering a model of the part is enhanced by using an existing model of an as-designed part and altering the existing model on the basis of information from the sensing device. In many other cases, however, an original model of the part does not exist. Many currently manufactured parts predate the existence or prevalence of CAD systems, which are a relatively new development. In addition, many parts have been modified in use and no record exists of these modifications. In these cases, it is advantageous to derive a CAD model of an existing part.

Most current advances in reverse engineering of mechanical parts have focused on recovering a b-rep of the part under study. Recovered boundary representations of the

surfaces of the part can vary from a triangulation of points to piecewise parametric surfaces (common representations include parametric spline surfaces and NURBS surfaces) to piecewise algebraic surfaces. For reverse engineering, a triangulation (or tesselation) of points is often not sufficiently detailed to fully recover the original geometry of an object. Piecewise parametric surfaces, while providing a high level of detail, can fail to recover the original geometry of the object due to inherent limitations of parametric representations. Consider for example a circular cylinder. A typical b-rep of a cylinder describes the surfaces on the boundary of the cylinder; two planar surfaces at the top and bottom, and a parametric surface wrapped around the cylinder. Anyone who wishes to recover specific quantitative information from this object desires information such as the height and diameter of the cylinder. Such parameters are not readily available from a parametric boundary representation of the cylinder [3].

Most mechanical objects are composed of well-defined primitives, and mechanical designers often think in terms of primitives when describing an object. Recovering a bounded solid CSG representation of an object does provide information about the object that is directly applicable to the way an engineer would model the object in the usual forward engineering sense. Figure 1 is a diagram of a CSG tree of a mechanical part (a portion of an injection mold), indicating the constructive process inherent in the engineering process. For the purpose of reverse engineering, a CSG representation of a solid is a "user friendly" form for the geometric data, because it is easier than a boundary representation for an engineer to visualize and manipulate and could be entered into CSG, b-rep, and hybrid modeling CAD systems through a CSG user interface. The Initial Graphics Exchange Specification (IGES), a standard representation for interchange of CAD data, includes a specification for CSG trees as an exchange data format. This is important for portability of any CSG file.

1.3 Previous Work

Extensive research has already been conducted in computing a b-rep of a solid from sensed data, but that work is not discussed here because of space limitations. The work described in this paper focuses on the development of a CSG-type solid model. The importance of CSG in rapid prototyping, an area related to reverse engineering, has been discussed by Crawford [4].

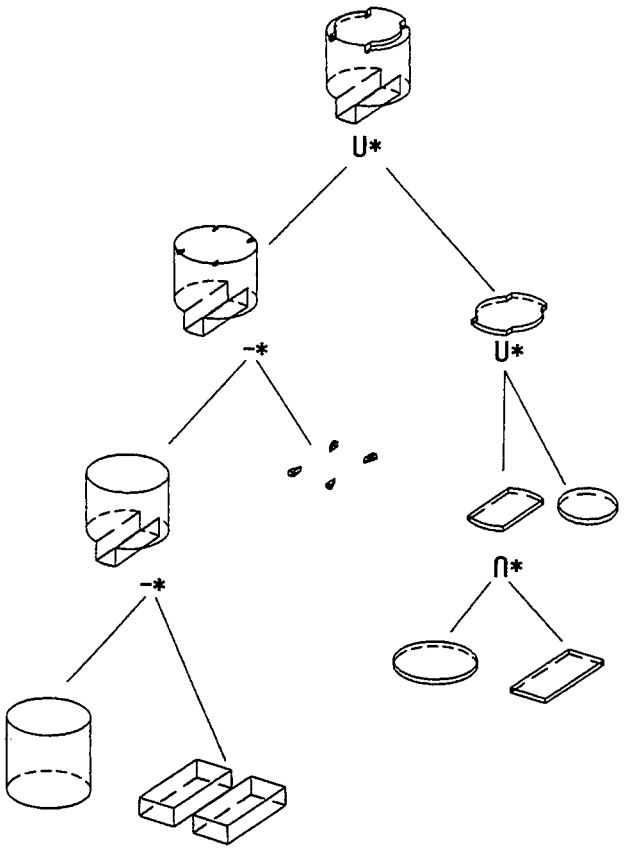


Fig. 1. Diagram of a CSG tree of a mechanical object.

At the advent of modern CAD systems, a duality developed between CSG and b-rep representations. Algorithms were quickly developed and optimized for the CSG-to-b-rep conversion process. The problem of b-rep-to-CSG was considered too difficult and unnecessary for general-purpose implementation. In recent years, however, progress has been made in the b-rep-to-CSG conversion process.

In 2-D, Peterson [5] presented a solution to the problem of finding a halfspace CSG representation for the interior of a closed curve. Peterson approached the problem from a reverse engineering viewpoint, recognizing that many 3-D mechanical objects are sweeps of a closed 2-D curve along an orthogonal axis. Also in 2-D, Vossler [6] presented a solution to finding a CSG representation for the interior of a closed curve using bounded primitives, such as rectangle, circle, chorded circle, and right triangle. In 2-D, therefore, the problem is considered solved for cases with modest (and realistic) limitations, for both halfspace and bounded solid CSG.

Limited attempts have been made to date to construct a solid-primitive 3-D CSG representation from a point cloud or a b-rep of an object [7-10]. These works do not extend to general 3-D objects. For example, in Lin and Chen's work [7], all planar

surfaces are assumed to be part of a cube. A further assumption of Lin and Chen is that each primitive can act as a subtractor no more than once, which in general prohibits objects that contain more than one subtraction operator on any path from the root to a leaf in the CSG tree representing the object. The work of Woo [8] and Tang and Woo [9,10] does not scale to nonpolyhedral objects due to the use of the convex hull operator.

The general 3-D b-rep-to-CSG conversion has only recently been tackled [11-13]; these pioneering works deal only with halfspace CSG representations, however. A halfspace CSG tree is a CSG tree in which the leaves of the tree are halfspaces. In the present work, a CSG tree is used in which the leaves of the tree are bounded solid primitives (the typical case in CAD systems with a CSG interface) and such a CSG tree is defined as a bounded solid CSG tree (e.g., that shown in Fig. 1).

Shapiro and Vossler [11] first presented a solution to recovering a halfspace CSG tree for 2-D objects. They also presented a solution to recovering a halfspace CSG tree of polyhedral solids [12]. Shapiro and Vossler followed up this work with steps to extend the work to include solids bounded by quadric surfaces [13]. The solution technique employed by Shapiro and Vossler is cumbersome and necessitates extensive CSG tree simplification. However, their method [13] of adding separating halfspaces to a solid object to make the object describable is of significant importance.

2. Problem Description

2.1 Background

CAD systems typically use regularized sets and regularized set operations. This avoids problems with manipulating regions of space with empty interiors that are not meaningful in a solid modeling context. The regularization of a set X, reg (X), is the closure of the interior of the set X. Thus, the regularization of a set with empty interior, such as a line in 2-D or a surface in 3-D, is the empty set. The regularized set operations $\cup^*$ (union), $\cap^*$ (intersection), $-^*$ (difference), and $^{-*}$ (complement) produce a regularized set as the result of the operation on the regularized set operands and are defined as follows:

$$a \cup^* b = reg(a \cup b), \tag{1}$$

$$a \cap^* b = reg(a \cap b), \tag{2}$$

$$a -^* b = reg(a - b), \tag{3}$$

$$\bar{a}^* = reg(\bar{a}), \tag{4}$$

A halfspace ψ of R^3 is a set of the form $\psi = \{(x,y,z): g(x,y,z) \geq 0\}$ for some function $g: R^3 \rightarrow R$. The work herein utilizes quadric functions, that is, polynomial functions of degree 2. The zeros of the function map a surface in 3-D. A surface, $S_\psi = \{(x,y,z): g(x,y,z) = 0\}$, *induces* the two halfspaces $\psi = \{(x,y,z): g(x,y,z) \geq 0\}$ and $\overline{\psi} = \{(x,y,z): g(x,y,z) \leq 0\}$. It can be shown that for the surfaces under consideration in this work, namely planar, spherical, cylindrical, and conical surfaces, the halfspaces induced by these surfaces are regularized sets. A solid will be defined as a non-empty regularized subset of R^3. A natural halfspace of a solid is defined to be a halfspace induced by a surface in the b-rep of the solid.

A solid Γ is said to be *describable* by halfspaces $\Psi = \{\psi_1, ..., \psi_N\}$ if there exists a (halfspace) CSG tree representing the solid, such that each leaf of the tree is an element of the set $\{\psi_1, \overline{\psi_1}^*, ..., \psi_N, \overline{\psi_N}^*\}$ [11,12].

2.2 Approach

In our approach, a mechanical object is represented as a bounded solid, a regularized, non-empty, bounded subset of R^3. The subset of quadric surfaces that is allowable to bound the solid contains the surfaces of the bounded solid CSG primitives to be used as primitives in the CSG representation. Primitives to be used consist of a rectangular solid, a pyramid, a sphere, a cylinder, and a cone. Therefore, the allowable surfaces in the boundary representation of the solid are planes, spherical surfaces, cylindrical surfaces, and conical surfaces (surfaces bounding cones), although other nondegenerate quadric surfaces of a single sheet could be used as well. It is assumed that the input bounding surfaces are piecewise algebraic surfaces in implicit form (e.g., a spherical surface in the form $x^2 + y^2 + z^2 - r^2 = 0$), with an additional representation of the boundary of each surface patch. Our approach seeks to produce a bounded solid CSG tree of Γ consisting of the operations union, intersection, and difference operating on the canonical primitives rectangular solid, pyramid, sphere, cylinder, and cone, if the solid Γ is describable by its natural halfspaces. If the solid Γ is not describable by its natural halfspaces, this condition will be detected and the attempt will be terminated.*

*An extension would be to use the work of Shapiro and Vossler [13] to add separating half-spaces to make the solid describable.

This approach is shown schematically in Fig. 2. A quadric binary space partitioning tree (BSP tree) is used as an intermediate representation, which facilitates the process. A (typical) BSP tree is a binary tree used to represent arbitrary polyhedra, in which internal nodes are planes and leaf nodes represent homogeneous regions of space called "in" cells and "out" cells [1]. The definition of a BSP tree is extended to a *quadric BSP tree*, in which internal nodes are no longer limited to be planes, but can also be quadric surfaces such as the spherical, cylindrical, and conical surfaces we will use. Thus, in a quadric BSP tree, each internal node is a quadric surface with two child pointers, one for each side of the halfspace induced by the surface. Just as in a typical BSP tree, if either child halfspace is subdivided further, then it is the root of a subtree; if the halfspace is homogeneous with respect to the solid, then it is a leaf node, classified as either an "in" cell or an "out" cell. Figure 3 shows an example of a 2-D solid and a BSP tree representation of the solid.

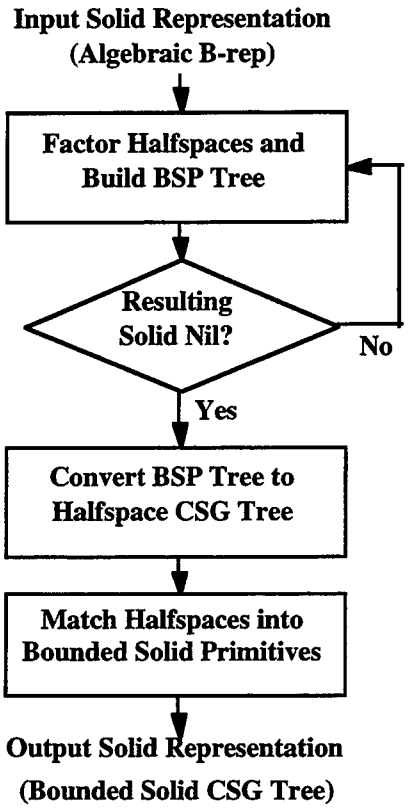
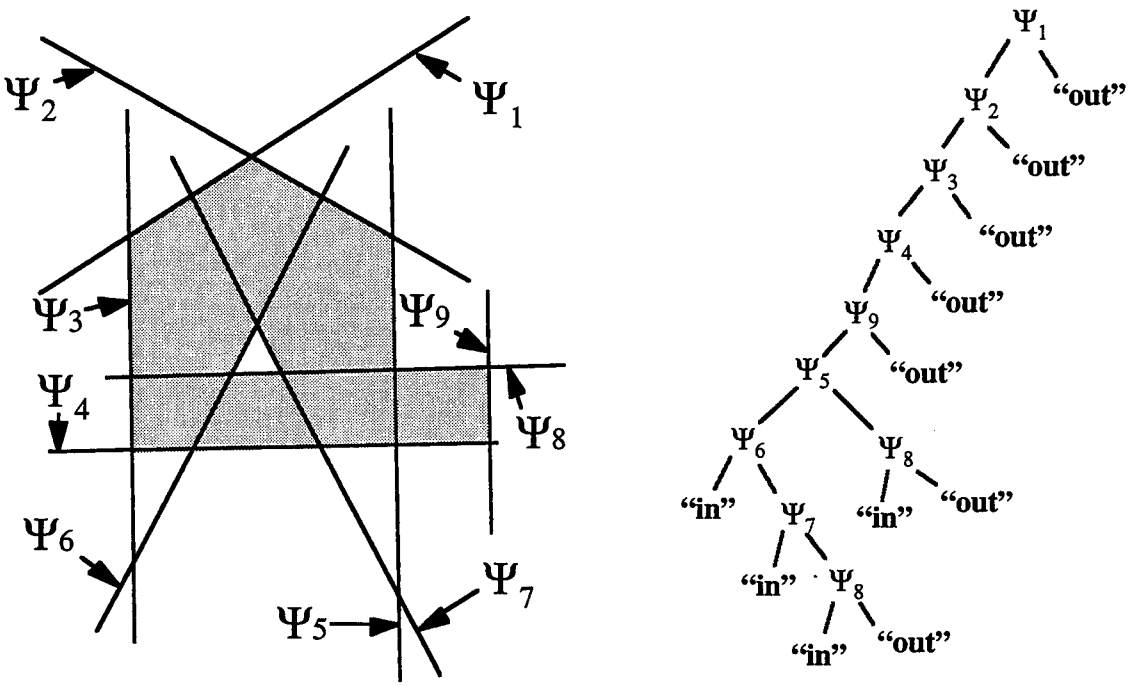


Fig. 2. Flow chart of approach.

In our approach, the input is currently an algebraic b-rep of the solid Γ and a null BSP tree. Surfaces are systematically factored from the b-rep of the object, and once factored, the surfaces and their induced halfspaces are added to the BSP tree representation. As the surfaces are factored, additional information in the form of *special faces* is added to the data structure representing the solid Γ (partially factored), to facilitate the building of a valid BSP tree representation.



a) A 2-D solid

b) Its associated BSP tree

Fig. 3. BSP Example: a) Diagram of a 2-D bounded solid (shaded region is interior of bounded solid); b) BSP tree representation of solid shown in a).

When there are no more unfactored surfaces in the b-rep of the solid, the BSP tree representation is complete. The BSP tree is converted to a halfspace CSG tree, performing some simplification techniques as a part of this process. Further simplification may be performed after this operation to the halfspace CSG tree itself, if desired. The last step is to match the halfspaces into solid primitives and construct the bounded solid CSG tree.

3. Conclusions

A new approach that uses 3-D CSG has been described to allow an advancement in reverse engineering. In particular, this method will allow algebraic surface representations (that can be obtained from a 3-D point cloud data set) to be used as input

to the 3-D CSG algorithm, which can be used to provide direct input into any CAD package. This research is an extension of the work of Shapiro and Vossler to allow for bounded solid CSG conversion from a b-rep of an object. The approach is expected to be more intuitive and computationally efficient.

Theoretical and algorithmic development of this process is continuing. In particular, computational analysis theory, halfspace CSG tree simplification, and heuristics needed to construct the bounded solid CSG tree have yet to be fully investigated. Implementation, beginning with the b-rep to BSP procedure, is commencing.

Possible extensions to this work may facilitate its usefulness in the areas of reverse engineering and solid modeling. First, the possibility of including sweep representations as primitives in the bounded solid CSG tree would increase the applicability of the process, because sweep representations are often combined with CSG interfaces in mechanical CAD systems. It is currently unknown if parametric rather than algebraic representations of the quadric surfaces (or sweeps) may be used in practice; this would also increase the applicability of the procedure because most commercially available point-cloud-to-b-rep software outputs parametric surface representations. Converting parametric to algebraic representations has been discussed [14], but there may exist fundamental problems of numerically unstable computations.

The work described here is part of a contribution to the early stages of general-purpose 3-D b-rep-to-CSG conversion. The advantages of the proposed algorithm in the area of reverse engineering are in providing a more intuitive model representation of a mechanical part than that provided by existing b-rep recovery methods.

References

[1] J. D. Foley, A. van Dam, S. F. Feiner, and J. F. Hughes. Computer Graphics: Principle and Practice. Addison-Wesley, 1990.

[2] M. E. Mortenson. Geometric Modeling. John Wiley & Sons, 1985.

[3] A. A. G. Requicha and J. R. Rossignac. *Solid Modeling and Beyond*, IEEE Computer Graphics and Applications, Sept. 1992, pp. 31-44.

[4] R. H. Crawford. *Computer Aspects of Solid Freeform Fabrication: Geometry, Process Control, and Design*, Proceedings of the 1993 Solid Freeform Fabrication Symposium, Aug. 1993, pp. 102-112.

[5] D. P. Peterson. *Boundary to Constructive Solid Geometry Mappings: A Focus on 2D Issues*, Computer Aided Design, Vol. 18, No. 1, Jan./Feb. 1986, pp. 3-14.

[6] D. L. Vossler, *Sweep-to-CSG Conversion Using Pattern Recognition Techniques*, IEEE Computer Graphics and Applications, Vol. 5, No. 8, Aug. 1985, pp. 61-68.

[7] W. Lin and T. Chen, *CSG-Based Object Recognition Using Range Images*, Proceedings of the 9th International Conference on Pattern Recognition, Rome, Italy, Nov. 1988, pp. 99-103.

[8] T. C. Woo, *Feature Extraction by Volume Decomposition*, Proceedings on CAD/CAM Technology in Mechanical Engineering, Cambridge, MA, 1982, pp. 76-94.

[9] K. Tang and T. Woo, *Algorithmic Aspects of Alternating Sum of Volumes: Part 1: Data Structure and Difference Operation*, Computer Aided Design, Vol. 23, No. 5, June 1991, pp. 357-366.

[10] K. Tang and T. Woo, *Algorithmic Aspects of Alternating Sum of Volumes: Part 2: Nonconvergence and its Remedy*, Computer Aided Design, Vol. 23, No. 6, July 1991, pp. 435-443.

[11] V. Shapiro and D. L. Vossler, *Efficient CSG Representations of Two-Dimensional Solids*, Transactions of the ASME, Vol. 113, Sept. 1991, pp. 292-305.

[12] V. Shapiro and D. L. Vossler, *Construction and Optimization of CSG Representations*, Computer Aided Design, Vol. 23, No. 1, 1991, pp. 4-20.

[13] V. Shapiro and D. L. Vossler, *Separation for Boundary to CSG Conversion*, ACM Transactions on Graphics, Vol. 12, No. 1, Jan. 1993, pp. 25-55.

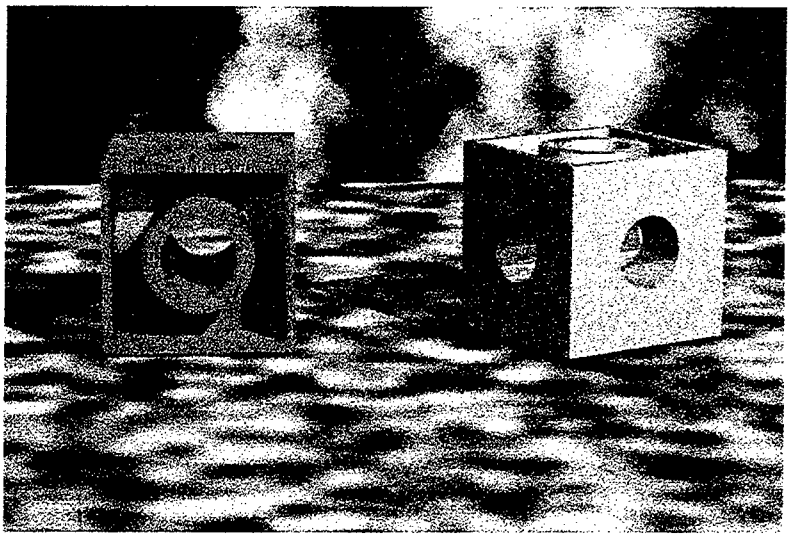
[14] D. Manocha and J. F. Canny, *The Implicit Representation of Rational Parametric Surfaces*, Journal of Scientific Computation, Vol. 15, No. 2, 1992, pp. 485-510.

Reverse Engineering: Practical Considerations for Rapid Prototyping

Alair Griffin[1], Scott McMillin[1], Curtis Griffin[1], Dr. Charles Knox[2]
[1]Lone Peak Engineering, Inc.
[2]Image3, LLC

Abstract

It is now possible to generate three-dimensional (3D) solid models of extremely complicated systems from which full plastic replicas can be generated using a variety of rapid prototyping technologies. The cycle time has been reduced to several hours, where it previously took months to produce a comparable prototype. The process of taking a design into the 3D environment, whether UNIX- or PC-based, is getting easier and fairly straightforward.



3D Models Presented in a 3D Environment

The design engineer interested in producing a 3D model from unique data sets such as computer tomography (CT) or magnetic resonance (MR) image data is particularly concerned with time, cost, accuracy, and conversion problems. This paper presents an approach that Lone Peak Engineering, Inc. (LPE) has used that allows them to successfully handle CT and MR data for reverse engineering (RE).

Introduction

Flexibility and "time-to-market" are key factors for any company to remain competitive in either the defense or commercial marketplace. The ability to rapidly prototype products has to be an integral part of any agile manufacturing scenario in order for a company to remain competitive. Rapid prototyping refers to the practical ability to build high-quality physical prototypes as an engineering aid. With rapid prototyping, full-scale models can be built in a variety of materials using a large number of commercial systems. With the advent of rapid tooling techniques, RP has started to transition into a rapid manufacturing technology. Responding to pressure for shorter time-to-market cycles, industry has been pushing for functional parts fabricated with engineering materials, not prototypes made of non-structural materials. Driven by the high cost and long lead time required to make tooling, and threatened by the growing shortage of skilled tool and die makers, rapid prototyping may offer ways of producing tooling quicker and more affordably.

Most reverse engineering approaches involve imaging or digitizing an object and then creating a computerized reconstruction that can be integrated, in 3D, into the particular design environment. Relying on volume visualization technology, a fundamental technique for interpreting and interacting with large, 3D data sets,

Lone Peak investigated the potential of reverse engineering as an integrated step in rapid production and agile manufacturing. Over the past four years, LPE has evaluated the potential of integrating CT-based reverse engineering with the following rapid prototyping systems (RP): Laminated Object Manufacturing (LOM)™, Fused Deposition Modeling (FDM)™, Stereolithography (SLA)™ and Selective Laser Sintering (SLS)™. During this time, they demonstrated that it is possible to reconstruct objects from CT data and to produce prototypes using virtually any commercial RP system. This paper presents a summary of practical considerations for the designer or engineer considering implementing such CT-based reverse engineering into their operations.

First Step: Reconstruction Software

Literally thousands of image reconstruction software packages are available. Most target the medical market and few support the file formats recognized by rapid prototyping systems or other equipment, such as numerically controlled machines. Without software specifically designed to address conversion of volumetric data to complex design and rendering, the majority of image reconstruction packages are not be able to deliver what is needed for a true reverse engineering application. Lone Peak currently uses a state-of-the art imaging software package, (*Velocity2™)*[1] to create computer reconstructions of 3D objects taken directly from volumetric data sets. This package directly supports a rapid prototyping interface. The software package consists of several programs:



Image. An image processor and high resolution surface reconstructor, featuring several classes of functions, including radiometric, filtering, morphological and geometric operations. Sequences of image processing operations can be recorded, saved to script files and used later to process the same or different image sets. Up to eight region-of-interest masks can be defined for each image and subsequently used to define objects to be reconstructed. **Image** can read data in a number of different image formats, including formats used on the more common CT and MR scanners.

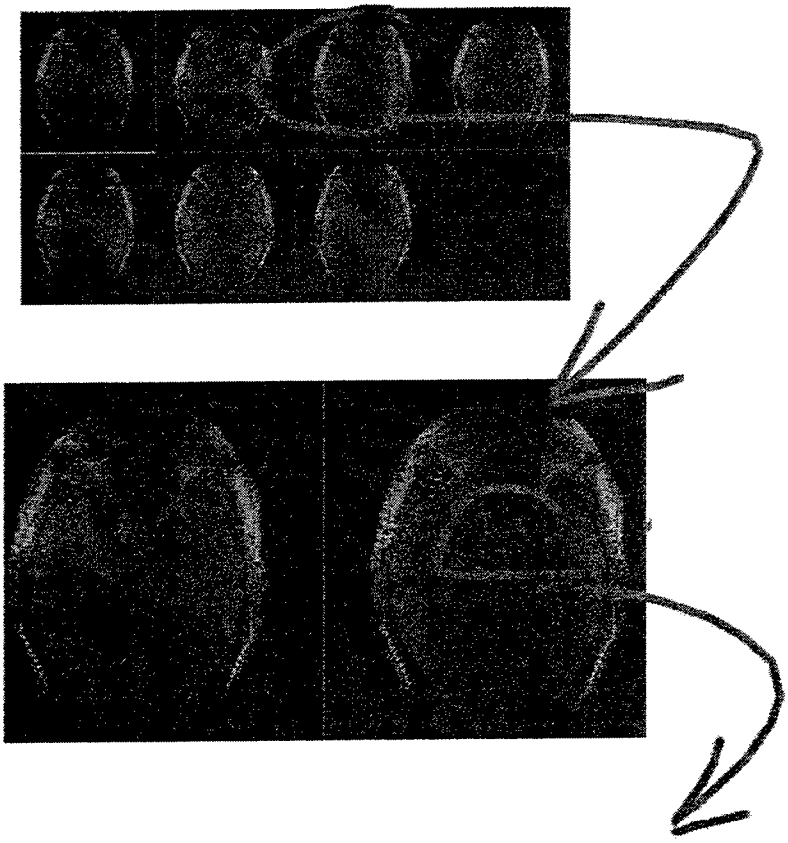
Surfer. A high resolution surface generator that processes the volumetric image data sets and stores a geometry file containing a winged-edge, linked list of surface polygons that describes the 3D model. **Surfer** can extract surfaces using gray value isosurface definitions, region-of-interest masks as defined in **Image** or combinations of both.

Display. A visualization program that displays and animates the 3D models using sophisticated graphics techniques, including: interactive viewpoint control, multiple light sources, user-defined surface material properties (ambient, diffuse, specular, transparency, emissivity), surface smoothing, and stereoscopic viewing.

PolyMerge. Reduces polygon count and file size of a 3D model by merging small surface polygons into larger ones in regions of relatively flat surface as determined using local surface curvature criteria. Local surface smoothing can also be applied prior to polygon merging, resulting in significant improvements in count reduction.

[TM]LOM is a registered trademark of Helisys, Inc. Torrance, CA. FDM is a registered trademark of Stratasys, Inc., Eden Praire, MN, SLA is a registered trademark of 3D Systems, Valencia, CA. SLS is a registered trademark of DTM, Inc, Austin, TX [1]Velocity2 is a trademark of Image3, LLC, Draper, UT

Velocity/STL. Creates STL files from the 3D model geometry data. Fault-free surfaces with all the benefits of surface smoothing and polygon merge as performed by **Display** and **PolyMerge**.



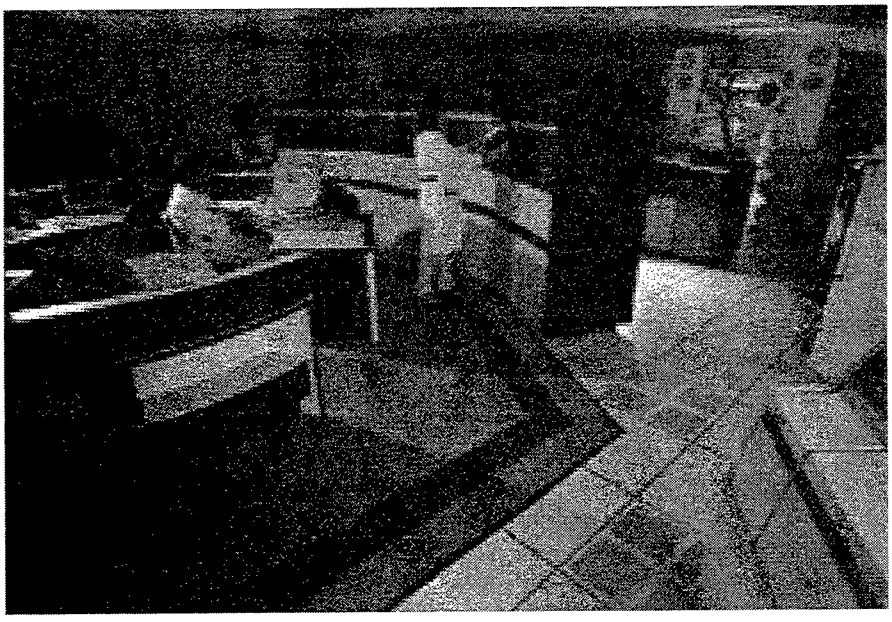
Scanning and Reconstruction

Reconstruction is the "rebuilding" of something that has been taken apart. In medical imaging the process involves rebuilding an internal view of the body from a series of images, or "slices", taken along parallel planes through the body. Each pixel in a slice represents an intensity value, the absorption of X-rays in CT imaging or the strength of the magnetic signal induced in the oscillations of hydrogen atoms in MR imaging. Once an object has been reconstructed, 3D computer visualization techniques are used to view the data.

Object slice data can be obtained in a variety of ways. Three methods: serial-section reconstruction, computed tomography and magnetic resonance imaging, are discussed in more detail below.

Although Lone Peak has worked with a variety of scan data, due to the availability of medical and industrial scanners, they consider CT scanning as the best option for reverse engineering applications

Serial-Sectioning - In traditional serial-section light microscopy, the tissue being studied is sliced on a microtome into a number of thin sections which are then prepared on glass slides and viewed in a microscope. Then digitized images are captured of each section. To recreate the sectioned object, all of the images must be put back together again in the right sequence and with the correct geometric alignment. The technique has the advantage of being able to create extremely thin sections, but the drawbacks are the large expenditure of time, destruction of the specimen, and serious problems with tissue distortion and realignment of sections for 3D reconstruction.



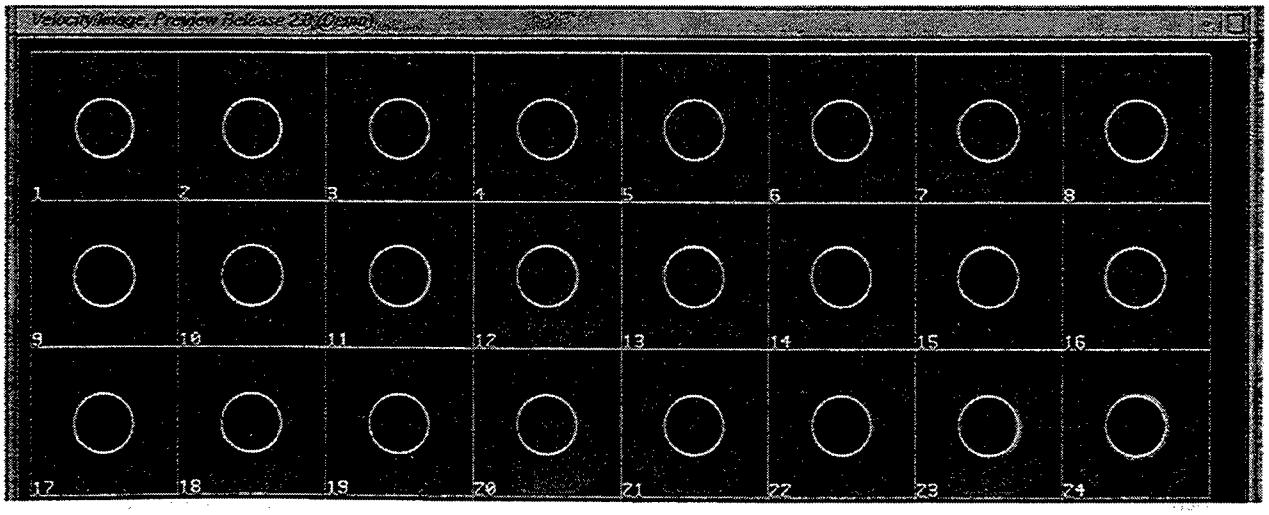
Problems with section distortion and realignment for 3D reconstruction can be reduced, if not eliminated, by forming digitized images of the cut surface of an object as thin layers are successively removed. This method has been used to create an anatomical atlas of serial-sections of the human body (Visible Human Project), and is also the basis of some industrial machines for reverse enginering (CGI). However, the methods are still time-consuming and destroy the specimen, making them of limited application for reverse engineering.

Computed Tomography - In CT imaging, a 3D image of an X-ray absorbing object is reconstructed from a series of 2D cross-sectional images. An X-ray beam penetrates the object, and transmitted beam intensity is measured by an array of detectors. Each such "projection" is obtained at a slightly different angle as the scanner rotates about the object. The 2D image is computed from the projected images using the approximate method of "back projection" or the more accurate method of inverse Fourier transformation. CT was introduced in the early 1970's as a neurological examination technique and later extended to industrial applications. It is a radiographic examination technique used whenever the primary goal is to locate and size planar and volumetric detail in three dimensions.

Current industrial CT systems can provide dimensional measurements at an accuracy competitive with coordinate measuring machines (CMMs). Of the existing methods for generating a CAD model of a physical part, only CT can nondestructively dimension internal, as well as external, surfaces. CT does not require elaborate fixturing, positioning or part-specific programming and CT has the unique ability to detect and quantify defects—a key consideration if the performance of as-built parts must be predicted via engineering models. Additionally, CT is indifferent to surface finish, composition and material; and it can measure part coordinates as fast as laser scanners—and orders of magnitude faster than CMMs [1].

Because of the relatively good penetrability of X rays, as well as the sensitivity of absorption cross sections to density and atomic number of matter, CT permits the nondestructive evaluation (NDE) and, to a limited extent, chemical characterization of the internal structure of materials [1]. Also, since the method is X-ray based, it applies equally well to metallic and non-metallic specimens, solid and fibrous materials, smooth and irregularly surfaced objects.

Magnetic Resonance Imaging - In MR imaging, the device acquires a number of cross-sectional planes of data through the tissue being studied. MR imaging technology is most commonly associated with mapping of the human anatomy and is based on the oscillation of hydrogen nuclei contained in soft body parts, such as in muscles, blood and brain tissue. However, industrial uses of MR imaging exist. These include studies of mobility and diffusion of water in hydrogels used for contact lens manufacture and imaging of the flow of feedstock in membrane filtration modules [2]. In some cases, a part can be submersed in water, and the inverse of the object can be created. Reverse engineering can be accomplished by simply reconstructing the inverse of the images.



MR imaging also requires reconstruction and visualization., since all of these planes must be stacked back together to obtain a complete picture of what the original object was like.

Information Required and General Parameters Recommended

It is relatively easy to create RE digital models of a part using CT. First, the object of interest is fastened to the platen of a suitable CT system and is scanned. Generally, standard machine tool hardware is available for clamping the part to the platen. Occasionally, a special fixture may be necessary to keep it from shifting during a scan. No special pre-programming or positioning is required, and scanning can begin as soon as the part has been secured to the platen. The scan data may consist of a few slices, a stack of planes, or a full volumetric image.

The following list presents information and/or parameters that you will have to determine before you scan an object.

1. Type of scanner: You will need to determine the model and make of the CT scan machine. Then check to make sure that your image reconstruction software can translate the data.

2. Kind of scan: Axial or helical

3. Slice Thickness: 1.0 mm recommended

4. Scan spacing: 0.5 mm or at least one-half the smallest dimension of interest

5. X-ray strength

6. Resolution: Options include image dimensions of 256 x 256, 512 x 512, and 1024 x 1024 pixel and 8, 16 or (on some machines) 32 bits/pixel.

7. Field of View (FOV): Object imaged should fill the field of view without extending beyond it.

8. Position: Long axis of the object should be parallel to the bore of the scanner. Generally, scans should start just off the object and finish off the other side of the object (so that the entire object is imaged). Objects to be scanned should not be taped down or placed on similarly dense objects, that will show up in the scan.

9. Artifacts: If significant variations in material densities exist within the object to be scanned, distortion can be experienced. In the case of metal artifacts, the distortion can be severe. The scan protocol can and should be adjusted to take into account the presence of artifacts.

10. Slice Time: 2 second/slice is recommended

Images reconstructed at 512 x 512 pixels with a 16 bits/pixel resolution should require about 0.5 Mbytes of memory per slice. Average data sets can be expected to range from 25 to 100 Mbytes [3]. From the image data, the reconstruction software is then used to extract part contours and/or surfaces, as the case may be. Many thousands of internal and external measurements are quickly generated from the data. Depending on the amount of data and performance of the software, processing takes from seconds to minutes on a UNIX-based workstation. Since penetrating radiation is used, there is no inherent difference between inside and outside, hidden or visible. All features in the object are present in the image data and can therefore be extracted by the software with no penalty in scan time. Moreover, defects are captured as well. If they are important, they can also be extracted and characterized. If only an ideal description of the part is important, defect information can be discarded. The end result is a 3D model that should be exportable, in different file formats, to allow interfacing with other design environments.

Medical and Industrial CT Scanning

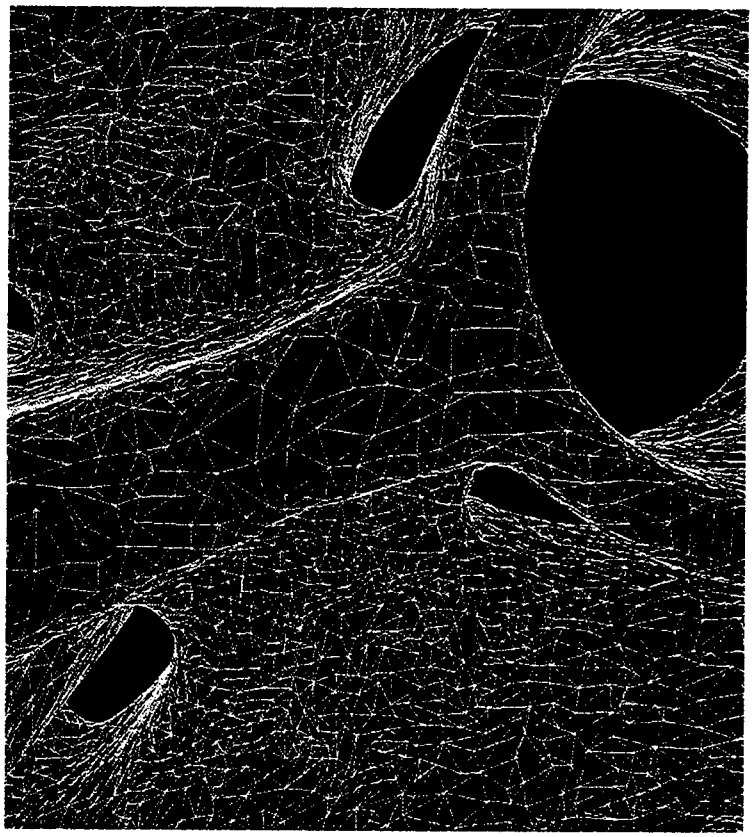
Lone Peak has found that scan time on hospital scanners is lower cost than the industrial scanners and much lower cost than laser scan systems. However, there are issues that should be considered before using hospital-based CT systems.

A major consideration, when using hospital scanners, is that your part might get bumped due to patient load requirements. Medical technicians may also insist that you provide specific scanning protocols written for your RE components. Medical scanners may not be able to get the resolution that you want. With hospital CT scanning systems you can typically expect the largest matrix to be 512 x 512 pixels versus 1024 x 1024 for an industrial CT system. The lowest FOV would be 9.6 cm which would result in an X-Y pixel dimension of 0.19 mm x 0.19 mm (where Z resolution is 0.5mm) [4].

Industrial scan costs may be higher than a local hospital and they may not be located close by. The industrial CT systems are well suited for large parts or thick-walled metal parts that would require high-intensity scanning. Aracor, an industrial CT system manufacturer, reports maximum part weight of 1000 lbs and maximum working volume of 20" x 20" x 24" for one of their systems [5].

Dealing with Artifacts

When there is a severe artifact present in the area of interest, such as a metal pin in a jaw bone, the X-ray strength and intensity must be maximized in order to reduce the effect of the artifact [6]. Slice thickness is important when a metal artifact is present. The slice thickness will depend on the amount of signal noise in the slice as opposed to spatial accuracy. To allow for the distortion, the slice thickness may vary from 3 mm to 4 mm depending on the spacing. Although not always practical, the simplest solution is to remove the artifact.



Accuracy Issues

With good technique and data, CT scan accuracy generally falls within ± 20% of the slice data. For a 1 mm slice this would equal ± 0.2mm [6]. Accuracy of the reconstruction can be influenced by the skill of the image reconstruction operator and the strength of the mathematical algorithms within the reconstruction software. Accuracy of the re-engineered components will also be influenced by the rapid prototyping or tooling technique used to produce the physical representations.

Slice or scan spacing is critical for 3D model reconstructions, and should not be confused with slice thickness. Anything over 3mm is not acceptable for complex structures. Slice spacing determines spatial accuracy. The accuracy in the Z-axis is determined by the spacing.

ARACOR's CTM 500 industrial scan system reports an accuracy of ±0.001 in. With a resolution of ± 0.007 inch and a tracking speed of 100-300 slice/hour [1]. The Aracor-built ICT-1500 CT system at Hill AFB, UT employs a 9- MeV linear accelerator and achieves a maximum resolution of 1 mm and a minimum scan time of 1 minute per slice[7].

Using their scanning system, Aracor has compared the measurement reliability of CT vs. UT and UT vs. Calipers. They found that the least reliable measurement method is UT, with a calculated standard deviation of 5.5 mils. The most reliable turned out to be CT, with a calculated standard deviation of 2.4 mils. The caliper results were in between, a calculated standard deviation of 4.4 mils. From an industry perspective, caliper measurements are generally regarded as the "gold standard," and that they provide the most reliable measurement method. Instead, ARACOR's results suggest that calipers are only marginally better than UT. Additionally, the absolute magnitude of the uncertainties were much higher than expected. Caliper measurements, for example, are assumed to be good to sub-mil accuracy, maybe a mil or two under shop conditions, certainly not 4.5 mils [7].

Model Surfaces

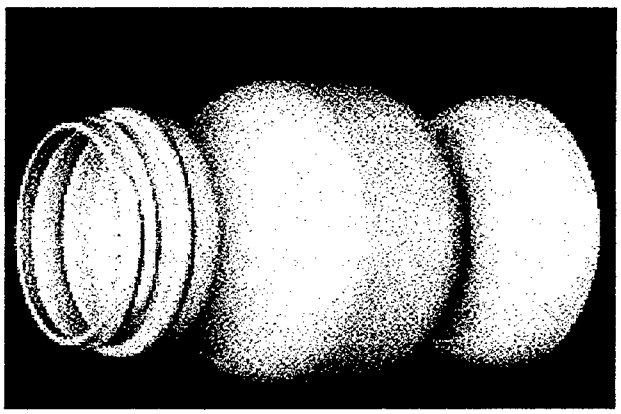
When working with scan data, LPE found that it is fairly common to produce models that have large numbers of surface polygons. Very large files can be difficult to export to rapid prototyping systems. When this occurred, *Velocity's* polygon reduction program, **PolyMerge**, was used to selectively reduce the numbers of surface polygons by collecting small triangles into larger ones in regions of the surface that are relatively flat. With **PolyMerge,** you specify this "surface flatness" as the deviation in the local surface normal vector, the "delta value", in units of angular degrees. For example, a perfectly flat surface i.e. one with a delta value of zero, will have no variation of the surface normal vectors from one triangle to the next; whereas, in regions of high surface curvature the delta value will be large. Typically, delta values of 20-30 degrees provide reductions in numbers of triangles of 30% or more in flat areas of the model without significantly affecting surface detail.

File Size Reduction

In many cases, LPE found that the original reconstruction may have surface irregularities simply due to noise, etc. in the image set. In these cases, it is advantageous to smooth the surface prior to polygon reduction to remove local surface roughness. The smoothing algorithm used in *Velocity's* **PolyMerge** (and in **Display** as well) recalculates the locations of triangle vertices as the average of a given vertex and its immediate neighbors. Significant file size reduction can be achieved, which greatly improved the ability to export reconstruction files (in the rapid prototyping STL file format) to RP systems.

CAD Interface

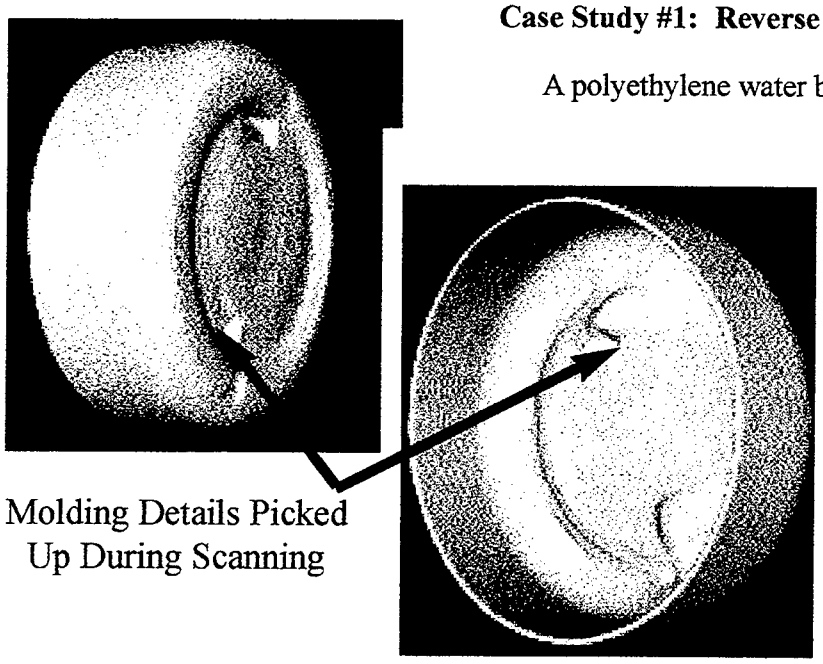
While reverse engineering from CT scans to rapid prototyping systems has been streamlined, the ability to interface universally with high-end CAD software is still problematic. Additional development is required to go beyond IGES and DXF formats so that solid models, rather than surface models can be imported into a range of CAD packages.



Case Studies

The following section summarize three case studies conducted during Lone Peak's evaluation of reverse engineering for rapid prototyping and rapid tooling.

Case Study #1: Reverse Engineering a Polyethylene Bottle



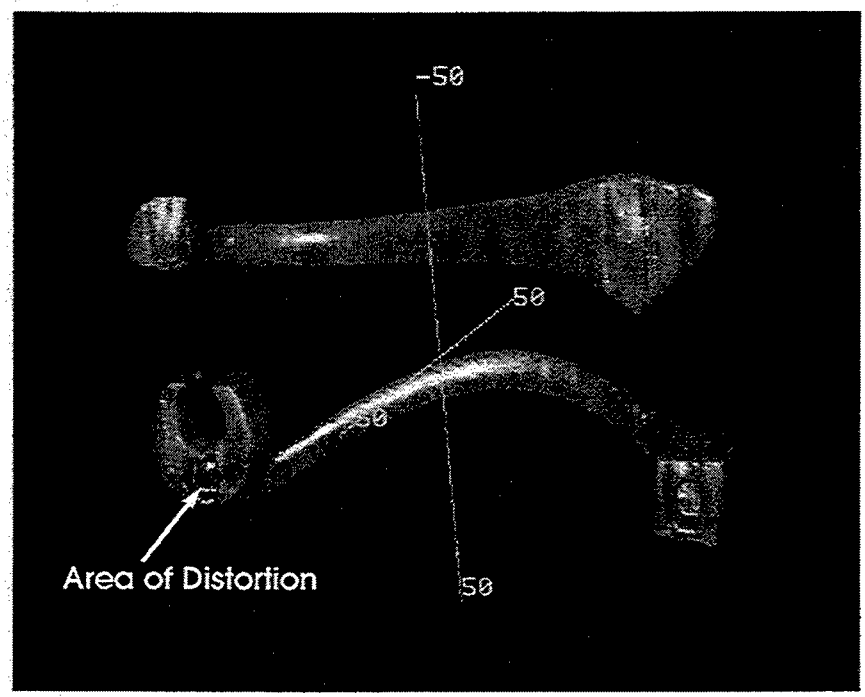
Molding Details Picked Up During Scanning

A polyethylene water bottle was chosen by Lone Peak Engineering to demonstrate reverse engineering of a thin-wall part. Lone Peak had a CT scan of the water bottle conducted. The first set of scans turned out to be unusable because, prior to scanning, a technician placed the water bottle on top of a plastic sheet. The sheet material was identical to that of the water bottle. It was not possible to easily remove the scanned image of the plastic sheet from the water bottle and it was necessary to rescan the bottle. During the second scan, another error occurred. This time the scanning technician taped down the water bottle to the foam support that had been provided by Lone Peak. Fortunately, the tape was only present in a few of the CT images and could easily be edited out.

The slice data underwent a conversion and reconstruction using the *Velocity* reconstruction software. The binary file that was produced was large; 30 Mbytes. The file was sent to a Fused Deposition Modeling system and the part was built in ABS plastic.

The reversed engineered part satisfactorily duplicated the original bottle. It was possible to screw the bottle lid from the original onto the threads of the reverse engineered prototype. The detail was sufficient that it picked up molding marks created during molding of the original bottle.

Case Study #2: Reverse Engineered Hand-Crafted Wax Handles



Hand-crafted cabinet handles were sent to Lone Peak Engineering for a reverse engineering evaluation. The handles were crafted by an artist in wax. The artist wanted to obtain a computer model of the mirror image of the handles made with a 15% enlargement. She wanted to have both the STL file and the prototypes to use as patterns for soft tooling.

Lone Peak had a CT scan of the handles conducted. The first set of scans exhibited severe distortion in certain sets of slices. This was due to metal inserts that the artist had pressed into the wax handles that allowed her to screw them onto an actual cabinet. It was necessary to remove these inserts and rescan the handles.

The CT slice data underwent conversion and reconstruction using the *Velocity* software. The STL file was produced of the mirror image the client requested. Using the file, an ABS plastic part was built using the FDM system. Overall, the scanning, reconstruction, and rapid prototyping accurately reproduced the original parts to within the limits of the FDM process, but the client felt that they still lacked some detail. She felt that she was unable to use the file. In order to achieve a more detailed prototype, Lone Peak offered to produce the prototype on an SLA system which can achieve tolerances of +/- 0.002" and/or subject the part to scanning in an industrial scanner which would have produced higher resolution scans. The client did not want an SLA prototype because she felt that the build material was artistically unacceptable. She did not wish to pursue the industrial scan options for cost reasons.

Case Study #3: Reverse Engineering a Turbine

A hand-crafted metal turbine with multiple blades was sent to Lone Peak Engineering for reverse engineering. The turbine had been used for many years as a pattern. Over time, the blades had been damaged and repaired. Since CAD data did not exist for the geometry and the pattern is still used, the client wished to have the turbine scanned, an .STL file made, and a prototype produced.

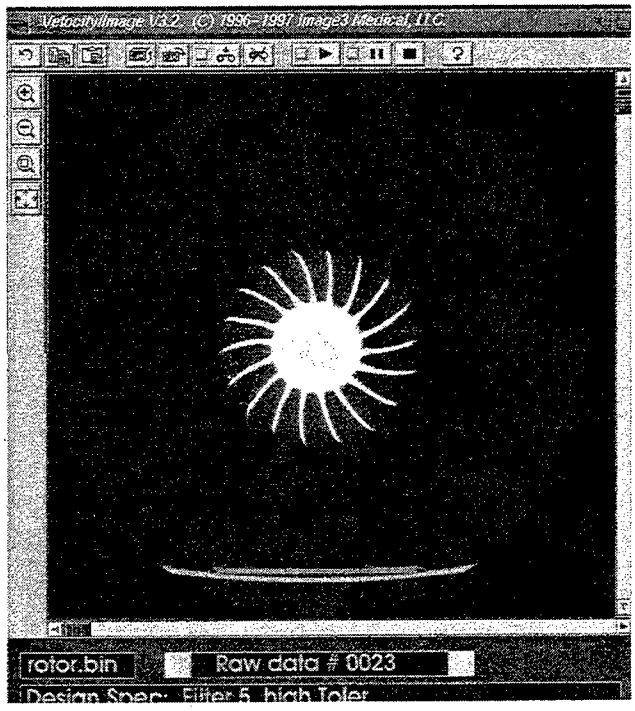
The client wanted to use the STL file in a rapid prototyping process that can rapidly produce investment castings from STL files. In this manner, they would be able to produce multiple metal parts, rapidly, and using the original turbine as the source for the castings.

Lone Peak had a CT scan of the turbine conducted. It was necessary to prototype a special support for the turbines so that it could be scanned in the proper orientation. Lone Peak has found that improper orientation of the part during scanning will result in poor data that is unsuitable for reconstruction. The scanning was conducted at a local hospital.

Once downloaded, the data underwent conversion and reconstruction. An error-free STL file was produced from the CT data. The .STL file was used to build the part using Fused Deposition Modeling out of ABS plastic. The overall tolerance achieved was +/- 0.060". The information was sent to the client. Unfortunately, the client did not understand the size of files that are generated during reverse engineering, and was unable to handle a 35 Mbytes STL file, even though LPE could handle this large file size.

Summary

Computed tomography-based reverse engineering and rapid prototyping methods are now being considered for applications in rapid tooling and manufacturing. If successful, manufacturing methods will dramatically change, which will pave the way for flexible, rapid manufacturing of a variety of components.



Acknowledgements

Lone Peak Engineering wishes to thank the Small Business Innovative Research Program for its support under contracts: U.S. Army Missile Command DAAH01-97-C-R142, technical monitor Dr. Bill Coblenz, NASA NAS8-97028, technical monitor Floyd Roberts, and U. S. Navy N00014-97-C-0070, technical monitor, Dr. Steve Fishman. Lone Peak also wishes to thank Craig Goodrich, LDS Hospital, Salt Lake City, Utah and Dr. Robert Yancey,

Advanced Research and Applications Corp., Dayton, Ohio for their input and guidance during the reverse engineering activities presented in this paper.

References

1. Yancey, R. et. Al. 1996."Integration of Reverse Engineering, Solidification Modeling, and Rapid Prototyping Technologies for the Production of Net-Shape Investment Cast Tooling" Advanced Research and Applications Corporation (ARACOR) Dayton, OH 45431

2. Pope, J. 1996. "QUT Magnetic Resonance NMR MRI Web Site". j.pope@qut.edu.au

3. Haystead, J. 1997. "Computed-Tomography-Based Medical Imaging", in *Visions Systems*. July 1997. pp. 14-19. Volume 2, No. 7. July, 1997.

4. Private communication. 1997. Craig Goodrich. LDS Hospital. Salt Lake City, Utah.

5. Waterman, P. 1997. "3D Digitizing". In *Desktop Engineering*. pp. 51-57. Volume 2, Issue 12. August, 1997.

6. Cyberform International, Inc. Richardson Texas. 1996 Marketing Literature.W. Towson and T.R. Hill Howmet Corporation, Hampton, Virginia

7. J. Stanley, R. Savage ARACOR, and G. Strabel Howmet Corporation. 1996. CT-Assisted Manufacturing Process Demonstration.

Solid Model Creation for Materially Graded Objects*

Vinod Kumar
vinodk@engin.umich.edu

Debasish Dutta
dutta@engin.umich.edu

Department of Mechanical Engineering and Applied Mechanics
University of Michigan, Ann Arbor, MI 48109-2125

1.0 Introduction

Materially graded objects are objects composed of different constituent materials and could exhibit continuously varying composition and/or microstructure [1][2]. Such continuous changes results in gradation in their properties and distinguish them from objects made of conventional composites. They are also known as heterogeneous objects, functionally graded/gradient materials (FGM) and multi-material objects/structures [1]. In this paper, we use the terms "materially graded objects" and "heterogeneous objects" interchangeably. Recently, heterogeneous objects have found use in several engineering applications. The fabrication process that has shown potential to manufacture heterogeneous objects is called Solid Freeform Fabrication (SFF), also known as Layered Manufacturing (LM) [3][4]. SFF is a material deposition process in which the material deposition can be controlled to vary the material composition throughout an object, thus fabricating a materially graded object.

All SFF technologies are computer-based and require the CAD model of the object to be manufactured. However, current CAD systems are capable of representing only the geometry/topology information. Therefore, heterogeneous objects are fabricated using SFF by manually feeding the material information along with the geometry data. This is a cumbersome process and leads to the under-utilization of the SFF process. An assessment of existing representations for SFF is presented in [5] highlighting the need for CAD models which represent material information along with the geometry data of the object.

2.0 Previous Work

Traditional geometric/solid modeling has focussed on modeling objects based on their geometry and topology [6][7][8]. There is no additional information in the solid model regarding the material of the object. The geometry of the object is modeled by considering the mathematical space $\mathbf{T} = \mathbf{R}^3$. Certain subsets of this space called r-sets and manifold solids are widely accepted as valid mathematical models of physical objects [7][8]. The most commonly used representation schemes for this model are the Constructive Solid Geometry (CSG), Boundary Representation (B-Rep) or a hybrid [6][7][8].

In our earlier work [9], we proposed an approach to model objects composed of finite number of domains with each domain made of a single material or the domain being a single embedded component. Examples of these multiple material objects are shown below in Figure 1.

* Financial support for this work was received from Office of Naval Research grants N00014-95-1-0767 and N00014-97-1-0245 and is gratefully acknowledged.

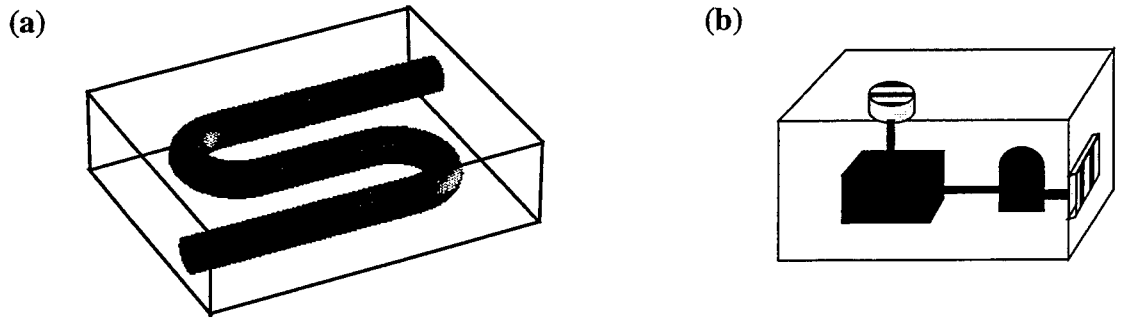


FIGURE 1. Objects with distinct material domains (a) Two material object: copper cooling channel in steel block (b) Object with embedded electromechanical systems

In order to represent these objects, the mathematical space **T** was expanded to include a material space (**M**) along with the spatial dimensions $\mathbf{R}^3$. The choice $\mathbf{M} = \mathbf{Z}$, the set of integers, was sufficient to model objects made of a finite number of unique materials. Thus, the product space $\mathbf{T} = \mathbf{R}^3 \times \mathbf{Z}$ with the product topology formed the new modeling space for representing these objects. Subsets of this space **T** called r_m-sets were proposed to model a single material domain of a multiple material object. In r_m-sets, the geometry was still modeled by the traditional r-sets and the additional integer identifies the material of the domain. A set of r_m-sets called r_m-classes was then defined to model objects made of these material domains. Boolean operations were defined to create and manipulate these models. Computer representation to implement this model was developed by including additional data structure on the B-Rep scheme. The main advantage of this approach is that the geometry is still modeled using traditional solid modeling methods and hence, the internal structure of the representation is unaffected. Additional structure has to be included to implement the material dimension of the proposed model.

3.0 Modeling of Materially Graded Objects

In this paper, we propose a method to model heterogeneous objects which have continuous variation in material composition. Refer Figure 2 for examples. The material composition of a heterogeneous object can be fully specified by specifying the volume fractions of all its constituent materials. From the volume fraction information, the density of the object at any point can be calculated.

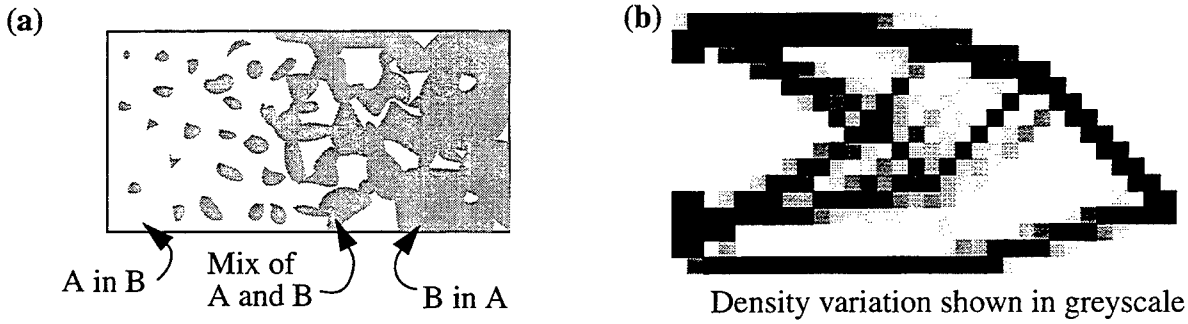


FIGURE 2. Materially Graded Objects (a) Two material object with varying composition (b) Object made of single material with varying density [13]

Modeling: To model objects with continuous material variation, the material space (**Z** in Section 2.0) must be expanded. A suitable choice for the new mathematical space is $\mathbf{T} = \mathbf{R}^3 \times \mathbf{R}^n$, n being the number of constituent materials (also referred to as primary materials). $\mathbf{R}^3$ is the geometry space, the space where the geometry and topology of the object is defined. $\mathbf{R}^n$ is the material space with each dimension representing a primary material. Each point in the object can be composed of either a single primary material or a combination of several. Thus, the material at any point can be identified by volume fractions of each of the primary materials. Noting that these volume fractions must sum to 1, we can precisely define the space of volume fractions **V** as:

$$\mathbf{V} = \left\{ \underline{v} \in \mathbf{R}^n \,\middle|\, \|\underline{v}\|_1 \equiv \sum_{i=1}^{n} v_i = 1 \text{ and } v_i \geq 0 \right\} \qquad \text{(EQ 1)}$$

where v_i (i-th component of $\underline{v}$) represents the volume fraction of material i. An underline is used to denote a vector in the corresponding space, such as $\underline{v}$. Note that porosity of a local region can also be modeled by including void as one of the primary materials. A set of n points ($\underline{m}^1$, $\underline{m}^2$,..., $\underline{m}^n$) called the primary points can be defined in **V** to represent the n primary materials. The coordinates of these primary points in **V** are defined as $v_i(\underline{m}^j) = \delta_{ij}$.

Each point in an object S can now be characterized in product space **T** as ($\underline{x}$, $\underline{v}(\underline{x})$) where $\underline{x} \in$ S is a point in the object and $\underline{v}(\underline{x})$ represents the material at that point such that $\underline{v}(\underline{x}) \in \mathbf{V}$. The material $\underline{v}(\underline{x})$ of any point $\underline{x}$ in S can be considered as a mapping **F** from the geometric points $\underline{x}$ to the material space **V**. The geometry of the object S can be modeled as an r-set P and the material distribution for the r-set P can be represented by the set B in **V** which is defined by function **F**. Thus, an object having varying material distribution can then be modeled as an r_m-*object*:

$$S = (P \in \mathbf{A}, B \subseteq \mathbf{V}) \text{ where } B = \{\underline{v}(\underline{x}) \equiv \mathbf{F}(\underline{x}) \in \mathbf{V}, \forall \underline{x} \in P\} \qquad \text{(EQ 2)}$$

Here, **A** denotes the class of r-sets. It might not always be possible to define the mapping **F** (i.e., $\underline{v}(\underline{x})$) using a single function for each $v_i(\underline{x})$ to characterize the material distribution for the entire object. Instead, **F** can be composed of a finite number of piecewise C^∞ functions:

$$\underline{v}(\underline{x}) \equiv \mathbf{F}(\underline{x}) = \{v_i^j(\underline{x}),\ j = 1 \ldots k \text{ (finite)}\},\ \forall i = 1 \ldots n \qquad \text{(EQ 3)}$$

In this case, the geometric domain of each function $\underline{v}^j(\underline{x})$ has to be prescribed separately and explicitly which is equivalent to specifying C^0 and C^1 discontinuities of **F**. The r_m-*object* can then be defined as:

$$S = (P_j \in \mathbf{A}, B_j \subseteq \mathbf{V}),\ j = 1 \ldots k \text{ (finite)}$$
$$\bigcup_{j=1}^{k} P_j = P,\ \bigcup_{j=1}^{k} B_j = B \text{ where } B_j = \{\underline{v}^j(\underline{x} \in P_j)\} \equiv (v_1^j(\underline{x}), \ldots, v_n^j(\underline{x})) \qquad \text{(EQ 4)}$$

The material distribution B_j for each r-set P_j can be defined with respect to a local coordinate system L_j attached to P_j. This would make the definition of the functions $\underline{v}^j(\underline{x})$ simple. A point $\underline{x}$ that does not belong to the object is assigned $\underline{v}(\underline{x}) = \underline{0}$.

Boolean Operations: In order to create and manipulate these models, boolean operations are necessary. Consider two r_m-objects $D = \{D_t\} = \{(P_t, B_t), t= 1...k\}$ and $G = \{G_w\} = \{(P_w, B_w), w=1...m\}$. The boolean operations on any two regions D_t and G_w can be defined as:

$$D_t \square^*_m G_w = \left\{ P_t \square^* P_w, B \right\}, B = \left\{ \underline{w}(\underline{x}) \in \mathbf{V}, \forall \underline{x} \in P_t \square^* P_w \right\} \qquad \text{(EQ 5)}$$

$$\underline{w}(\underline{x}) = \text{normalize}(\underline{c}_u(\underline{x})(\underline{u}(\underline{x}) \in B_t) + \underline{c}_v(\underline{x})(\underline{v}(\underline{x}) \in B_w))$$

where $\square$ represents the three boolean operations /, $\cap$ and $\cup$. The "normalize" is the normalization operation with respect to the L_1 norm as in (EQ-1) and is performed only if the norm of $\underline{w}(\underline{x})$ exceeds one. The weight functions $\underline{c}_u(\underline{x})$ and $\underline{c}_v(\underline{x})$ can be used to manipulate $\underline{w}(\underline{x})$. Alternate functions can also be used to define the material in the intersecting region as long as $\underline{w}(\underline{x})$ lies in **V**. Now the difference operation on the two r_m-objects D and G is defined as:

$$D /^*_m G = \left\{ \cap^*_m{}_{\forall(G_w \in G)} (D_t /^*_m G_w) \,\middle|\, \forall D_t \in D \right\} \qquad \text{(EQ 6)}$$

where the difference operation between each D_t and G_w is now defined using (EQ-5). Similarly, the intersection operation can be defined as:

$$D \cap^*_m G = \bigvee \left\{ D_t \cap^*_m G_w \,\middle|\, \forall D_t \in D, G_w \in G \right\} \qquad \text{(EQ 7)}$$

where the intersection between D_t and G_w is now defined using (EQ-5). The join operator ($\vee$) is defined as the union of two r-sets if their corresponding material distribution is constant and equal. Finally, the union operation is defined as:

$$D \cup^*_m G = \bigvee \{(D \cap^*_m G), (D /^*_m G), (G /^*_m D)\} \qquad \text{(EQ 8)}$$

with the union between D_t and G_w defined using (EQ-5).

Representation: The computer representation of the r_m-object model can be implemented as shown in Figure 3.

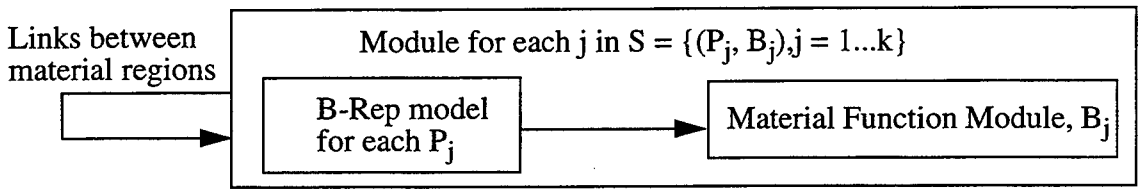


FIGURE 3. Computer representation of r_m-object

4.0 Example

We will illustrate the proposed modeling strategy through an example shown in Figure 4. The example object is a simplified model of a valve seat and is made of three regions. The outer shape (L) is made of one material (Al33) and the inner deposit (M) is made of another material (brass). The interfacial region (N) between the two is a mixture of two materials with the composition gradually changing from one material to another.

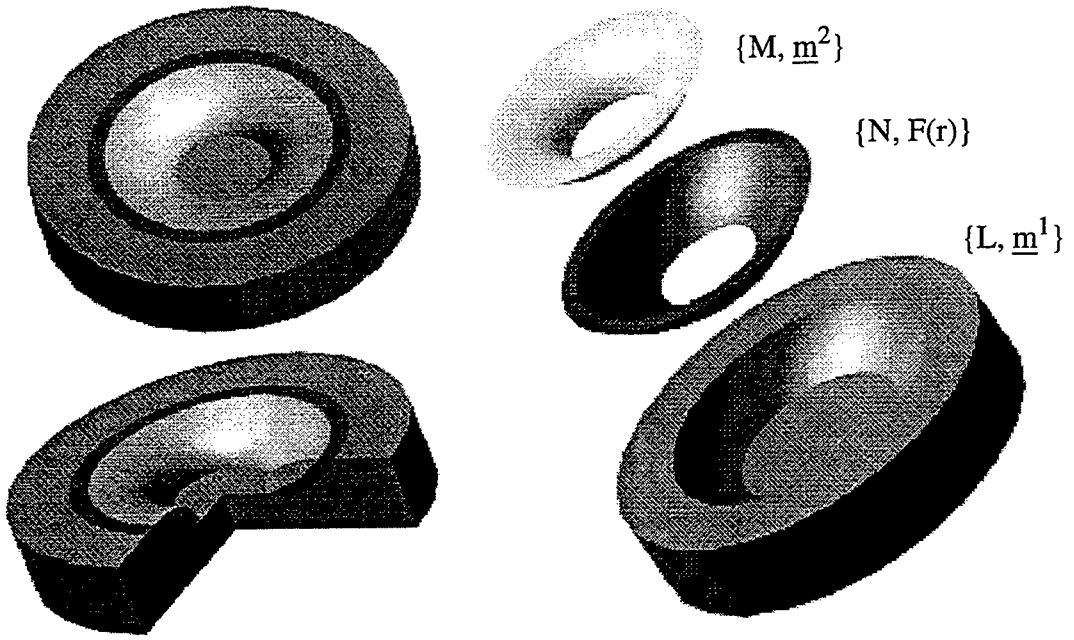


FIGURE 4. Sample Heterogeneous Object

We model this object in $\mathbf{R^3} \times \mathbf{R^3}$ with both the geometry space and the material space being $\mathbf{R^3}$. The space of volume fractions $\mathbf{V}$ is a plane in the first quadrant of the $\mathbf{R^3}$ joining the three material points $\underline{m}^1 = (1, 0, 0)$ and $\underline{m}^2 = (0, 1, 0)$ and $\underline{m}^3 = (0, 0, 1)$. The point $\underline{m}^3$ is the void space which is used for constructing objects as shown in this example. The region L is modeled as a cylinder, the region M as a elliptical torus and the region N as a spherical shell.

The sequence of operation we used to model this object is shown in Figure 5. The primitives used are cylinder (C, $\underline{m}^1$), spheres (S1, $\underline{m}^3$) and S2, and an elliptical torus (T, $\underline{m}^2$). The material distribution of each primitive is defined with respect to its local coordinate system. Note that S2 is not assigned any material because it is used only for the difference operation. When two regions are united, the material for the intersecting region is chosen using the "matl" function (as shown in the figure). The spheres are split by two planes P1 and P2 to obtain (S1c, $\underline{m}^3$) and S2c. The object (S1c, $\underline{m}^3$) is then united with the cylinder C by choosing the material for the intersecting region as $\underline{m}^3$. From the resulting object, S2c is subtracted followed by the union of object (T, $\underline{m}^2$). Finally, the material distribution for N is changed to $F(r) = \underline{m}^1 + t(\underline{m}^2 - \underline{m}^1)$ where t is the thickness of N and r is the radius in the local co-ordinate system of N. Although the final model does not contain any region made of material $\underline{m}^3$, the sphere S1 is assigned that material in order to construct the model. The final object contains three regions and is represented by an r_m-object as $\{(L, \underline{m}^1), (N, F(r)), (M, \underline{m}^2)\}$.

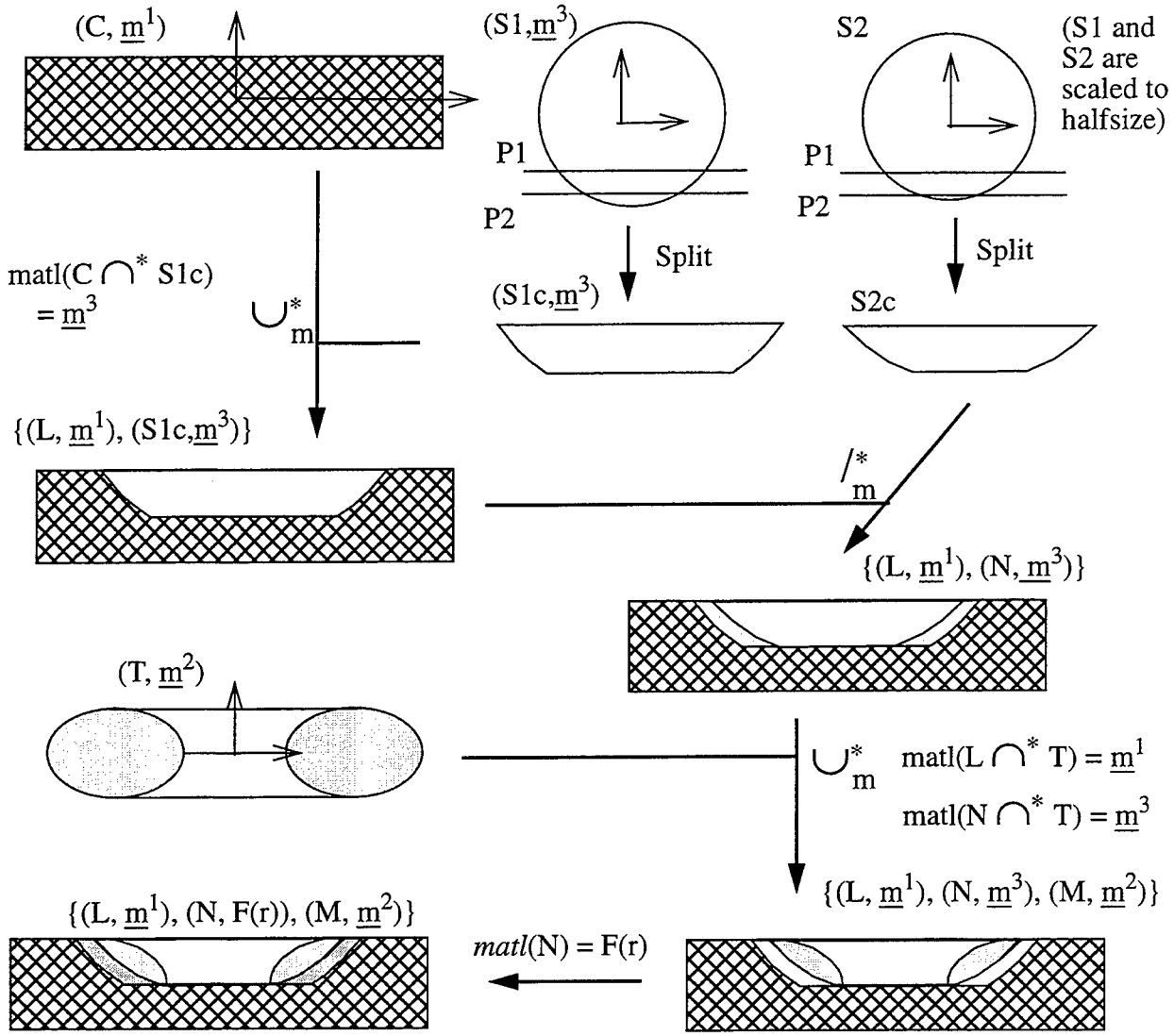


FIGURE 5. Steps in the creation of the valve model

5.0 Fabrication

Fabrication of materially graded objects by SFF involves additional processing compared to fabrication of homogeneous objects. These are identification of material distribution in each layer after performing the slicing procedure and material based tool path generation for deposition in each layer. To illustrate the steps involved, consider an r_m-object $S = \{(P_i, F_i), i=1...k\}$ (equivalent definition of $S= \{(P_i, B_i), i=1...k\}$ where F_i is the material distribution defined in the local coordinate system of P_i. The r_m-object $S = \{(P_i, B_i), i= 1...k\}$ is processed by performing the operations on (P_i, F_i).

Orientation: Denoting the transformation by OT, the oriented r_m-object can be defined as:

$$S_z = OT(S) = \{(OT(P_i), F_i), \forall i = 1...k\} \quad \text{(EQ 9)}$$

Slicing: The oriented r_m-object S_z is sliced by the slice planes SP(z) to obtain the layers L(z):

$$L(z) = S_z \cap SP(z) = \{(OT(P_i) \cap SP(z), F_i \cap OT^{-1}(SP(z))), \forall i = 1 \ldots k\} \quad \text{(EQ 10)}$$

The material distribution function for each layer obtained in (EQ-10) (denoted by $F_z(x,y)$) has to be approximated depending on the resolution of the fabricating process. An example of a 1D single material distribution $F_z(x)$ and its approximation is shown in Figure 6.

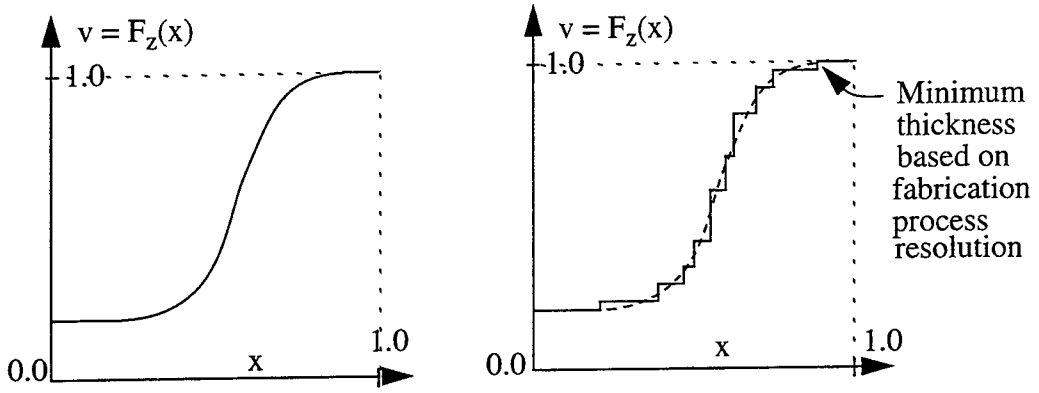


FIGURE 6. Approximation of a distribution function by series of step functions

Toolpath Generation: Once the material distribution for each layer is obtained, the tool paths for material deposition have to be generated. Currently, there does not exist any automated way of generating optimal tool paths for a given material distribution in a layer and this issue has to be addressed. Figure 4 illustrates these steps for the example discussed in Section 4.0.

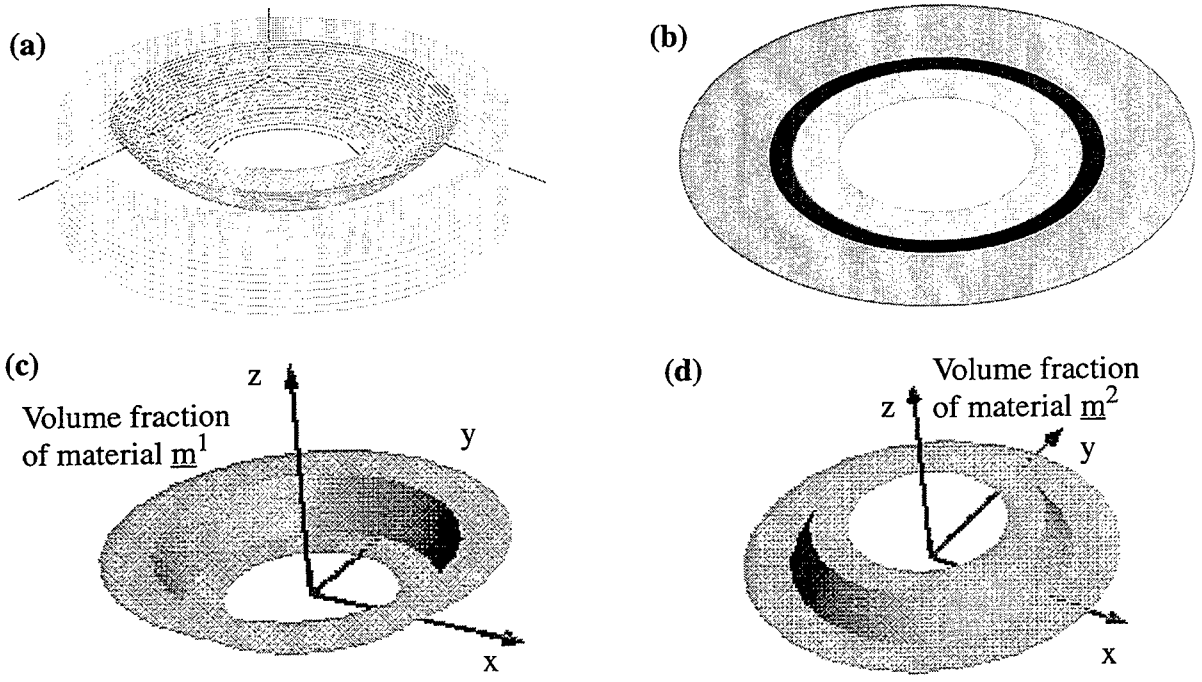


FIGURE 7. (a) Adaptive slicing (b) Material Distribution at slice z=0.8 (c) Variation of volume fraction of material-1 in slice z=0.8 (d) Variation of volume fraction of material-2 in slice z=0.8

Figure 7(a) shows the adaptive slicing [10] of the object and Figure 7(b) shows the material regions of a slice at z=0.8. The variation of volume fraction of material $\underline{m}^1$ and material $\underline{m}^2$ are shown in Figure 7(c) and Figure 7(d) respectively. The slice geometry is in the x-y plane and the variation of volume fraction of each material is shown along the z-axis.

6.0 Summary

In this paper, we proposed a solid modeling scheme for materially graded objects by extending beyond geometry/topology representation (based on r-sets) to include the material variation of the object. For a more detailed treatment of this problem, refer to [12]. The r_m-object model enhances the theory of r-sets and is compatible with traditional solid models. The computer representation of this model was built on existing B-Rep scheme and hence, can easily be adapted into existing solid modeling systems. Finally, fabrication of objects modeled as r_m-objects using SFF was also discussed.

7.0 References

1. Special Issue on Functionally Gradient Materials, MRS Bulletin, January 1995.
2. Functionally Gradient Materials, Ceramic Transactions, Editors: J. Birch Holt, Mitsue Koizumi, Toshio Hirai, Zuhair A. Munir, Vol. 34, 1993.
3. J. Mazumder, J. Koch, K. Nagarathnam and J. Choi, *Rapid Manufacturing by Laser Aided Direct Deposition of Metals*, preprint, Dept. of Mechanical Engineering, University of Michigan, Ann Arbor, 1996.
4. R. Merz, Shape Deposition Manufacturing, Dissertation, Technical University of Vienna, Austria, 1994.
5. V. Kumar and D. Dutta, *An Assessment of Data Formats for Layered Manufacturing*, Advances in Engineering Software, Vol. 28, No. 3, pp. 151-164, April 1997.
6. C. M. Hoffmann, Geometric & Solid Modeling, Morgan Kaufmann Publishers, 1989.
7. M. Mäntylä, An Introduction to Solid Modeling, Computer Science Press, 1988.
8. A. Requicha, *Representations for Rigid Solids: Theory, Methods and Systems*, Computing Surveys, Vol. 12, No. 4, 1980.
9. V. Kumar and D. Dutta, *An Approach to Modeling Multiple Material Objects*, Proceedings of 4th ACM Solid Modeling Symposium, Atlanta, May 1997.
10. P. Kulkarni and D. Dutta, *An Accurate Slicing Procedure for Layered Manufacturing*, Computer Aided Design, Vol. 28, No. 9, pp. 683-697, 1996.
11. J. R. Zuiker, F*unctionally Graded Materials: Choice of Micromechanics Model and Limitations in Property Variation*, Composites Engineering, Vol. 5, No. 7, pp. 807-819, 1995.
12. V. Kumar and D. Dutta, *An Approach to Modeling & Representation of Heterogeneous Objects*, ACM Transactions on Graphics, in review, available as technical report UM-MEAM-97-05, Department of Mechanical Engineering, University of Michigan, Ann Arbor, 1997.
13. M. P. Bendsoe and N. Kikuchi, *Generating Optimal Topologies in Structural Design using a Homogenization Method*, Computer Methods in Applied Mechanics and Engineering, Vol. 71, pp. 197-224, 1988.

A data format providing side wall orientation and adaptive slicing for use in stepless rapid prototyping

Wei Fang, Chan Siang Ngooi, and Haiqing Gong*
School of Mechanical and Production Engineering
Nanyang Technological University
Nanyang Avenue
Singapore 639798
Email : mhqgong@ntu.edu.sg

Abstract

Current Rapid Prototyping systems mainly use 2D layers building techniques that result in the 'staircase' effect on slanted surface. A new method has been developed to eliminate the 'staircase' effect and to improve the surface quality by extending the 2D layers to 3D layers building. In this approach, a new data format, Layer Transfer Interface (LTI), is introduced to generate layers having slanted side wall. It provides a faster slicing algorithm and accurate reconstruction of 3D objects. This format is independent of any particular RP machines. Furthermore, adaptive slicing has been achieved using this format and implemented on a five-axis milling RP system.

1. Introduction

Research in rapid prototyping places a constant emphasis on the need for improvement of accuracy and surface smoothness. From the CAD model point of view, the three main ways of slicing are:

- Fixed slicing where peaks or flat areas (areas parallel to the slicing planes) are ignored [1,2,3,4].
- Adaptive slicing where the slice thickness varies in response to the surface curvature [2,3,4].
- Direct slicing from CAD original models as opposed to tessellated models [5,6].

Presently, Common Layer Interface (CLI) [7] and 3D system's format SLC [8] are the universal slice formats that are simple, efficient and unambiguous. However, the staircase effect cannot be totally eliminated using these formats. Also, there are redundant data between slices due to 2D slice contours in these formats, which result large data file being produced.

The use of slanted and ruled slices can remove the staircase effect. Slanted slices can be generated using these approaches [9]. However, it requires a minimum of 4-axis control to make the slanted edges of the RP part. In order to have a slanted slice, a data format must be able to be read by the RP machines.

* To whom the correspondence should be addressed

2. Layer Transfer Interface (LTI) Format

A new data format is proposed to use in new RP machines with at least 4-axis control. Figure 1 shows the slope information of a point of a slice. These additional information of the roll and pitch angles enable slanted slices to be represented.

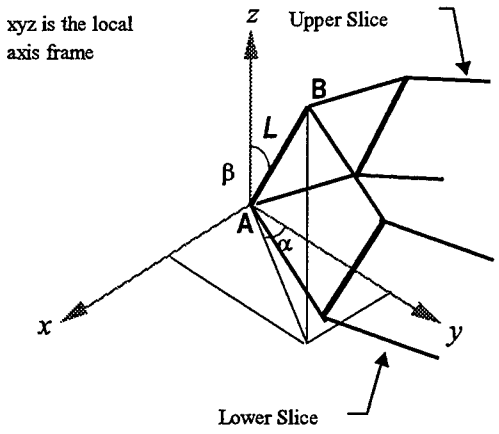


Figure 1 – Slope information of a point

The LTI data format consists of a collection of segments as shown below.

```
// LTI format
Parts_Begin
        Head
                Number_of_Layer: [number]
                Part_size: [x1, y1, z1, x2, y2, z2]
                units: [mm or inch]
        End Head
        Layer_Begin
                Index: [number]
                Thickness: [z]
                Number_of_Contour: [number]
                Contour_Beign:
                        Number_of_Hole: [number]
                        Begin_Tool:
                                Number_of_Point: [number]
                                        x, y, z, α, β,
                                        ......
                        End_Tool
                        Hole_Contour_Begin:
                                Begin_Tool:
                                        Number_of_Point: [number]
                                                x, y, z, α, β,
                                                ......
                                End_Tool
                        Hole_Contour_End
                Contour_End
Layer_End
Part_End
```

The first segment is the header segment that contains the global information of solid model such as layer number, size etc. The second segment contains the layer contour data. Inside this segment, the layer structure is sectioned into many parts that consists of contour, hole and hatching data for each slice.

With the slope information of the LTI, data transfer to other slice data format can be done readily. In the generation of the sliced contour data for a user defined layer thickness, the interpolation from the upper and lower contours can be carried out. This technique is fast and easy and also adaptive slicing can be implemented.

3. Method

A new slicing method is developed to provide the roll and pitch angle information. Currently, only faceted model is used. The slicing starts with the determination of the topological information of the input model. This topological information consists of the vertex and face lists. The vertex and face lists are linked using a circular link list. The vertex list is later sorted along the direction of build direction. Using the vertex information, the flat areas are determined.

Next, an advanced marching algorithm is carried out using two parallel planes to obtain the slope information. With this information, the Layer Transfer Interface (LTI) data file is then generated. This data format is independent of any RP machines. A five-axis milling machine has been developed to use this data format to build parts using layering techniques. This data format is further preprocessed to create each layer with variable layer thickness. The system parameters that affect the slice thickness are the tool diameter and tool length. Figure 2 shows the faceted .STL model. The slicing algorithm is developed using C++ with OpenGL working in Windows NT platform. Figure 3 shows the sliced part with slope information for slanted side wall using LTI data format.

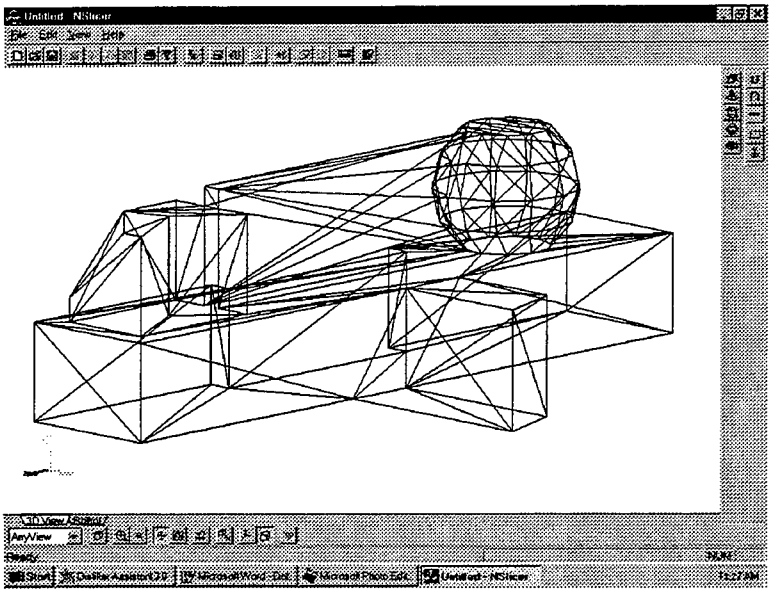


Figure 2 - A .STL facet model

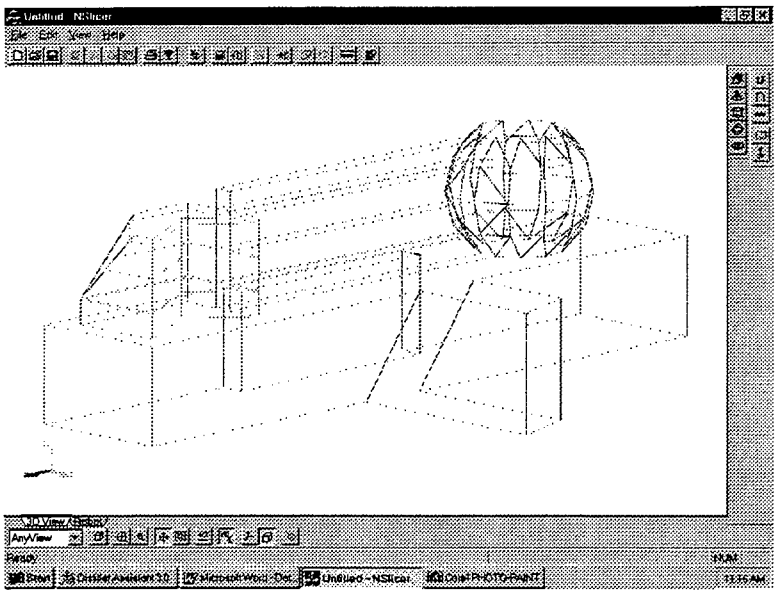


Figure 3 – A sliced part with slope information for slanted side wall using LTI format

4. Implementation

A five-axis milling machine was developed to build layers with slanted side wall. Figure 4 shows a part built using this machine. The slope information obtained from the LTI format was used to machine the slanted side wall. With this slanted building technique, part accuracy and speed are greatly improved. The offset and tool path calculation are performed using this new LTI format.

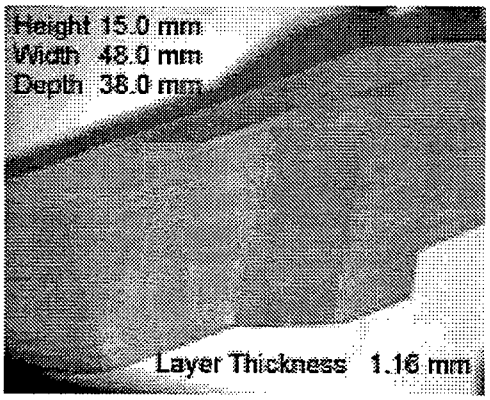


Figure 4 – A part with layer having slanted side wall fabricated using a five-axis milling machine

5. Conclusion

The new data format (LTI) was proposed for producing stepless RP parts. This format increases the part accuracy and it is easy to perform adaptive slicing. With the capability of the RP machines keeps on improving, the use of more than 3-axis control to built layers will be seen in the near future.

6. References

[1] Wozny, M.J. 1992. Systems issues in solid freeform fabrication. Technical Report 92023, Rensselaer Polytechnic Institute, Troy, NY12180.

[2] Suh, Y., and Wozny, M.J. 1994. Adaptive slicing of solid freeform fabrication processes. *Solid Freeform Fabrication Symposium Proceedings.* University of Texas at Austin, Austin, Texas. pp. 404-411.

[3] Dolenc, A., and Mäkelä, I.. 1994. Slicing procedure for layered manufacturing techniques. *Computer-Aided Design.* Vol. 26:2, pp. 119-126.

[4] Kulkarni, P., and Dutta, D. 1995. Adaptive slicing for parametrizable surfaces for layered manufacturing. *Design Automation Conference Proceedings.* Boston, Massachusetts. pp. 211-217.

[5] Guduri, S., Crawford, R.H., and Beaman, J.J. 1992. A method to generate exact contour files for Solid Freeform fabrication. *Solid Freeform Fabrication Symposium Proceedings.* University of Texas at Austin, Austin, Texas. pp. 95-101.

[6] Jamieson, R. and Hacker, H. 1995. Direct Slicing of CAD models for Rapid Prototyping. *Rapid Prototyping Journal.*MCB Press.Vol. 1:2, pp 1-6.

[7] Common Layer Interface (CLI) VERSION 2.0. http://www.cranfield.ac.uk/aero/rapid/CLI/cli_v20.html.

[8] .SLC file format. http://cadserv.cadlab.vt.edu/bohn/rp/SLC.html.

[9] Jager, P. J. 1996. Using slanted and ruled layers for Rapid Prototyping. *Proceedings of the 5th European Conference on Rapid Prototyping and Manufacturing.* Helsinki, Finland. pp. 15-29.

Build Style Decision Support for Stereolithography

Joel E. McClurkin and David W. Rosen
Rapid Prototyping and Manufacturing Institute
Georgia Institute of Technology
Atlanta, GA 30332-0405
(404) 894-9668 http://rpmi.marc.gatech.edu

ABSTRACT

When building parts in a stereolithography apparatus (SLA), the user is faced with many decisions regarding how the part will be built. The quality of the build can be controlled by the user via changing one of several build style variables, including part orientation, cross sectional layer thickness, and laser hatch density. A user will probably have preferences for the part build (i.e., accuracy or speed), but may not understand how to vary the build style variables to produce the desired results. A method based on response surface methodology and multi-objective decision support is described in this paper for relating build goals to three build style variables, and the use of these relationships in providing decision support for building a part on a SLA. The method is applied to the build style of a circuit breaker handle.

1. INTRODUCTION

Stereolithography (SLA) machines have dozens of processing variables that can be controlled by experienced operators to meet exacting build requirements of accuracy, surface finish, and build time. Experienced operators know qualitatively how process variables are related to build goals and can quantify some of their knowledge. Although SLA machine operation is predictable, the quality of resulting parts is not always obvious, particularly when trade-offs must be made among accuracy, surface finish, and build time.

A decision support method is presented in this paper to aid SLA operators in selecting appropriate values of process variables in order to achieve build goals as closely as possible. The goals can have importances specified in order to reflect preferences of the operator or part designer. The method is adapted from multiobjective optimization and utilizes response surface modeling to quantitatively relate variables to goals. Since our study was limited, we looked at only three process variables: part orientation, layer thickness, and hatch spacing, and three goals: accuracy, surface finish, and build time. Designer/operator preferences among the goals are also modeled using two different methods: weightings and priorities. Our objective is to render decision support by handling trade-offs among conflicting objectives quantitatively. Our method is demonstrated on a part with non-trivial geometries, a circuit breaker handle. Results reflect our intuition.

2. PREVIOUS RESEARCH

2.1 SLA Build Style Optimization

There have been several approaches to optimizing the build performance of SLA machines. These approaches vary from finding an optimal build layout to reduce build time to adaptively slicing a part to improve surface finish and reduce build time. One approach for optimizing build layout has been to use an expert system for determining preferred build direction as shown by Frank and Fadel [1]. Expert systems are heuristic in nature because most of the rule systems and knowledge used to create them are based on the experience of an expert. For example, an expert knows that thin layered parts build slower on the SLA, but are more accurate. This expert system uses information on geometric feature orientations to determine the preferred build style.

Another method for automating build layout addresses the problem of laying out a build with multiple parts to minimize build time. A problem arises when the parts need to be packed as closely as possible to maximize the utilization of space in the build vat and also reduce build time.

A genetic algorithm was developed by Wodziak et al. [2] to automatically place multiple parts to reduce build time. The parts may be translated or rotated +/- 90 degrees about the z-axis to aid in part packing. The creators of the genetic algorithms for part packing reported it to be a successful method for optimizing multiple part layout to reduce build time.

Build style optimization research has also been done with regards to build time and surface finish of curved surfaces. A technique, called adaptive slicing, involves slicing the part thinner in areas of high curvature and thicker throughout flat areas [3]. The main idea is to estimate the surface finish for a particular curved surface by determining how much stair stepping is present. First, the part is sliced using the maximum allowable layer thickness. If the amount of stair stepping creates a surface that is rougher than a pre-determined limit, the part is sliced thinner in that region. This work was done in the context of a fused deposition modeler (FDM).

A build style issue that is not dealt with in this paper, but is very important, is support structure generation. A method has been developed by Hur and Lee [4] to automatically generate support structures in SLA build styles. Not only does their method generate support structures, but it determines the best build orientation to minimize the amount of support structures required. Hur and Lee determine which facets of the STL file need to be supported based on the following criteria: orientation of the facet, area of the facet, part instability, and base support.

The build optimization research discussed in the previous paragraphs is based primarily on single objective optimization. For instance, the genetic algorithms for part packing utilized the single objective of reducing build time. The research in this paper deals with multiobjective decision support, where several objectives such as build time and accuracy are considered. A companion study was performed, based on selection among alternatives rather than multiobjective optimization, and was reported in [5].

2.2 The Compromise DSP

The method of rendering build style decision support described in this paper is based on solving a compromise Decision Support Problem (DSP) [6]. The compromise DSP is a type of multiobjective optimization method and is used to model decisions that consist of decision variables, constraints, and multiple goals. The goals are often in conflict with one another (i.e., accuracy and build time). The compromise DSP is an extension of Goal Programming and Sequential Linear Programming [7]. Solution of compromise DSPs is typically performed using the Adaptive Linear Programming (ALP) algorithm. The structure of the compromise DSP is shown below.

Given:	A feasible alternative, assumptions, parameter values.
Find:	Values of design and deviation variables.
Satisfy:	System Constraints, System Goals, and Bounds on variables.
Minimize:	Deviation Function that measures distance between goal targets and design point.

To use the compromise DSP, a part is presented in a "default" build style to serve the purpose of the existing alternative to be improved. This build style is then improved by changing the build style variables. The goals are build speed, part surface finish, and part accuracy. More accurate builds usually take longer to build. The alternative (in this case a build style) is improved by finding a combination of system variables such that all the system constraints are satisfied while the deviation function is minimized. The deviation function is solely a function of the deviation variables, which in turn are a measure of how well the system goals are met.

3. BUILD STYLE DECISION SUPPORT METHOD

Now that some of the background pertaining to build style decision support has been presented, the methods for solving the build style decision support problem are presented. This includes a brief discussion of the important build style variables and goals and how they are applied in the formulation of a compromise Decision Support Problem.

3.1 Build Style Variables, Parameters, and Goals

The build style variables, parameters, and goals are those quantities which drive the solution of the compromise DSP. Build style variables are those quantities which describe the attributes of the build style. These variables are directly affected by user input. Throughout the remainder of this paper, the build style variables will also be referred to as system variables. The system variables chosen for this project are the most common variables the user can change when setting up a build style. They are: Build Orientation (Surface Angle and Z-Height), Layer Thickness, and Hatch Spacing.

Build Orientation The build orientation variable is important because it can have an effect on every measure of build performance. The important aspects of the build orientation are the z-height of the part, and the various angles the surfaces of the part create with respect to the x-y plane. The part z-height can be controlled by the user by changing the orientation of the part. The bounds for this variable are 0.0025" and 10", which are limited by the smallest layer thickness and the size of the vat, respectively. However, the bounds of this variable can be narrowed significantly by dimensional information contained in the STL file that represents the part. Z-height can affect build speed dramatically. Builds with larger z-heights take longer to build because there are more build layers to build, causing more elevator movement and delay times.

Z-height also affects accuracy because the SLA is generally not as accurate in the z-direction due to overcure, print through, and build quantization errors [8]. Orientation also affects the locations of support structures which affect accuracy and surface finish. However, support structure generation and location is another issue too big to be dealt with in this paper. Technically build orientation can be considered a continuous variable due to the infinite number of orientations in which a part can be placed.

Layer Thickness When the STL file is sliced by the Maestro™ [9] processing software, it is sliced into many cross-sectional layers of finite thickness. The layer thickness variable refers to the thickness of these layers. The user has the ability to specify the thickness of the layers that represent the sliced part. The bounds for this variable are 0.0025" to 0.02". These bounds were determined from the Maestro™ build software version 1.8.

Layer thickness has a great effect on surface finish and accuracy, and to some extent build time. The accuracy and surface finish of curved surfaces will be better when thinner layers are used. However, parts usually build faster using thicker layers because recoat time will be greatly reduced. The phenomenon of build quantization plays a major role in accuracy and surface finish. If the top of a part falls on a half layer thickness, the SLA builds the extra layer which adds an extra half layer thickness to the top of the part. The scan speed of the laser, coupled with the pre-dip delay, affects down facing z-errors [8]. It is for the reasons above it is often necessary to select the *correct* value for layer thickness to increase build performance.

Hatch Spacing Hatch spacing is important because it affects build time, part accuracy, and surface finish. Hatch spacing refers to the density of the hatching pattern the SLA uses when "filling in" each cross section of the build. When the hatch vectors are closer together, the laser must scan more vectors per unit of cross sectional area, and the part will take longer to build. The fewer vectors the laser has to trace, the quicker the build will be completed. However, increased hatch vector density results in more resin being cured during the build and less during the post-cure process. This reduces part shrinkage, therefore increasing part accuracy. Also, as the hatch spacing on the up-facing surfaces (called fill vectors) increases, the quality of the surface finish decreases. If the hatch spacing is too wide, the build will most likely crash, which was experimentally observed. The bounds for hatch spacing were 0.004" to 0.020".

Build Style Parameters The build style parameters are quantities which describe properties inherent to the part being built. The build style parameters will also be referred to as system parameters throughout the rest of the paper. The user cannot change these properties because they

are determined from the part's STL file or other uncontrollable parameters such as resin properties or laser power.

3.2 Modeling Of Build Goals

The build goals considered for this paper are: (1) Low Build Time, (2) High Accuracy, (3) Smooth Surface Finish. In order for the build style to be improved, it is necessary to be able to predict how the measures of build performance (the system goals) will change as the build style variables are altered. Response Surface Modeling is used to model the behavior of two goals, build time and accuracy, as a function of the build variables and parameters. An analytical equation is used to predict the behavior of the other goal, surface finish.

A response surface model is a means for expressing the build goal (the response) as a function of several build style variables. This is done by running several experiments and fitting a polynomial equation, called the response surface, to the resulting data. In support of this research, a series of experiments were conducted to generate data for the build time and accuracy response surfaces [10]. Four experimental factors were selected. A face-centered, central composite experiment design was used to create quadratic response surfaces. Block-shaped and cylindrical parts were built in various sizes and orientations to correspond to the experimental factors and their settings, shown in Table 1. Minitab™ is the statistical analysis software package that was used to define the experiments and fit the response surfaces.

Table 1 - Experiment Settings for each of the Build Style Variables

Build Style Variable	Low Value (-1)	Middle Value (0)	High Value (+1)
Layer Thickness (in.)	0.004"	0.006"	0.008"
Hatch Spacing (in.)	0.004"	0.012"	0.020"
Z-Height (in.)	0.5"	1.0"	1.5"
Part Volume	0.75 in^3	1.5 in^3	2.25 in^3

Accuracy Prediction The factors used to formulate the accuracy response surface are: part height, layer thickness, and hatch spacing. Part height was chosen as a factor because the SLA is less accurate in the z-dimension than in the x and y-dimensions. Layer thickness affects build quantization errors, which detract from accuracy. Hatch spacing has a dramatic affect on post cure shrinkage which in turn greatly affects accuracy. When the hatch spacing is less dense more resin is cured after the build process and this causes shrinkage.

The unrefined response surface for accuracy is shown in Eqn. 1. The fit parameters are: S = 380.0 and R-Sq = 92.1%.

$$Accuracy = -12.6E6(H)(LT) + 11125(Z)(LT) + 48344(Z)(H) + 96.2E6(LT)^2 + 3470000(H)^2 + 577(Z)^2 - 703617(LT) - 41629(H) - 321(Z) + 2665 \quad (1)$$

Build Time Prediction The Build Time Estimator (BTE) program [11] was used to obtain data for the build time response surface, rather than building each parts individually. All four experimental factors from Table 1 were used. The BTE program is usually accurate within 3 percent.

The unrefined build time response equation is shown in Eqn. 2. The statistical fit parameters are: S = 48.61, R-Sq = 95.4%.

$$Build\ Time = 117(V)(Z) - 203(H)(Z) - 5135(H)(V) - 33813(LT)(Z) + 1125(LT)(V) - 1910000(LT)(H) + 95(Z)^2 + 42(V)^2 + 693238(H)^2 + 9470000(LT)^2 + 33(Z) - 81(V) - 4479(H) - 70138(LT) + 301 \quad (2)$$

where: V = part volume (in^3), Z = part height (in), H = hatch spacing (in), and LT = layer thickness (in).

The resulting equations (Eqns. 1 and 2) are used to define the build style aspiration space which determines the performance of a particular combination of build style variables. These equations can be refined to eliminate some statistically insignificant variables, however this could reduce the accuracy of the equation with minimal benefit to computational time.

Surface Finish Prediction The theoretical method for determining surface finish uses equations based on layer thickness and the surface angle. The surface angles can be determined from the STL file that describes the part. In order to predict the surface finish for a given STL file, a computer routine to estimate surface finish is used. This routine takes uses the STL file as the input. From this information, the routine can predict the *relative* surface finish of several different build orientations. The equation used to predict surface finish for one facet is shown in Eqn. 3 and was calibrated using experimental data.

$$PRC = (2 * \cos(\Theta) * \sin(\Theta) * 937) + 3.5*\Theta + 48 \quad (3)$$

The predicted surface finish will be weighted by facet area, then normalized for use in the compromise DSP formulation.

3.3 Compromise DSP Formulation

As mentioned in Section 2, the compromise DSP is a design decision making formulation. Values for a set of design variables are chosen to meet a set of goals as well as possible, subject to constraints. For our problem, the design variables are the build style variables, part orientation, layer thickness, and hatch spacing. Goals include build time, accuracy, and surface finish. The constraints for build style decision making apply to all builds; they arise due to the SLA machine limitations and manifest themselves as bounds on the design variables.

For a compromise DSP, goals are formulated using Eqn. 4. In this formulation, the objective is to bring each of the goals to the minimum achievable value for that goal. That is, it is desirable to have the numbers quantifying build time, accuracy, and surface finish as close to the minimum as possible. This requires estimating the minimum (best) and the maximum (worst) possible values for each of the system goals. This normalizes the goals to ensure that no single goal dominates the solution process. The closer the goal value is to 0, the smaller the deviation variable will be. For this formulation the deviation variable d_i^- will always be zero because it is impossible to underachieve a minimum. Thus, the only deviation variable under consideration is d_i^+.

$$\frac{A_i(X) - A_{i,\min}(X)}{A_{i\max}(X) - A_{i,\min}(X)} + d_i^- - d_i^+ = 0 \quad (4)$$

where: $A_i(X)$ = The achievement function, $A_{i,\min}(X)$ = the minimum (best) possible achievement, $A_{i,\max}(X)$ = the maximum (worst) possible achievement. The minimum and maximum values are dependent on the part being built. The equations for $A_i(X)$ were given as Eqns. 1, 2, 3 in the previous subsection. X represents the vector of build variables.

A deviation function measures the distance from a point in the feasible design space to the goals. Deviation functions can be formulated in two ways: the preemptive formulation which uses goal priorities, and the Archimedian formulation which uses goal weights (importance values). Using the compromise DSP, the mathematical formulation of the build style decision problem for the circuit breaker handle in Section 4 is shown in Figure 1.

Solving compromise DSP problems is usually accomplished using a multiobjective optimization code such as DSIDES [6]. However, since the build style design space is relatively small, an exhaustive search (i.e., every possible combination of build style variables) can be performed to yield a solution fairly quickly. With this method, the true minimum value of the deviation is found in about two seconds. The ranges and number of values for each design variable are listed here along with the number of points in parentheses: Layer Thickness 0.002" - 0.010" (17), Hatch Spacing 0.004" - 0.020" (17), and Part Height 0" - 10" (3). Height is

dependent on three different build orientations, defined by the dimensions of a bounding box, but could be increased to many more orientations to account for support structures or other build goals not considered in this paper. Thus, the number of possible points to evaluate for any part is 17 x 17 x 3 = 867.

Given: STL file of circuit breaker handle. Goal importances.

Find: Values of system variables: X_1 = layer thickness, X_2 = hatch spacing, X_3 = part orientation
Values of the deviation variables associated with the goals:
d_1^+ - build time, d_2^+ - accuracy, d_3^+ - surface finish

Satisfy: System goals:

$$\frac{A_1(X)-116.8}{1006.6-116.8}-d_1^+=0 \qquad \text{Build Time}$$

$$\frac{A_2(X)-2088}{8725-2088}-d_2^+=0 \qquad \text{Accuracy}$$

$$\frac{A_3(X)-251.3}{523.2-251.3}-d_3^+=0 \qquad \text{Surface Finish}$$

Bounds: Layer Thickness 0.002" <= X_1 <= 0.010"
Hatch Spacing 0.004" <= X_2 <= 0.020"
Build Height 0" <= X_3 <= 10"

Minimize: the Deviation Function:
$Z = [d_3^+, 0.5(d_1^+ + d_2^+)]$ (Scenario 1), $Z = \Sigma W_i d_i^+$ (Scenarios 2, 3)

Figure 1 - Compromise DSP Build Style Problem Formulation.

The exhaustive search method has been embodied in a software tool called CABSS (Computer-Aided Build Style Support) and has been validated using several examples, one of which is included in the next section.

4. A TEST CASE: CIRCUIT BREAKER HANDLE

This section shows some results of applying the compromise DSP to generate build styles for different solution scenarios. The part considered is a circuit breaker handle manufactured by the Siemens corporation. This part was chosen for its geometric complexity. The breaker handle was scaled to twice its normal size so that it would lie within the bounds of the experimental design space that was used to create the response surface models. When using empirically derived equations, it is important to only interpolate within the bounds of the experiment space, and not extrapolate beyond these boundaries. The wireframe and STL models of the handle are shown in Figure 2. Its overall dimensions are 1.45" x 1.62" x 2.86" (X x Y x Z).

4.1 Solution Scenarios

The problem of determining the build style will be solved using three different scenarios for prioritizing and weighting the build goals. Scenario 1 emphasizes surface finish using a preemptive formulation of the deviation function. Scenario 2 places a high importance on accuracy. Scenario 3 places a medium emphasis on build time, followed by accuracy. Numerical weighting values for these scenarios are shown below. These scenarios will be used to determine how the build style variables change with respect to changing build goals.

Goal	Scenario 1	Scenario 2	Scenario 3
Surface Finish	Level 1, Weight 1.0	0.1	0.2
Build Time	Level 2, Weight 0.5	0.2	0.5
Accuracy	Level 2, Weight 0.5	0.7	0.3

4.2 Results

The STL file of the handle was entered into CABSS where volume, surface area, and theoretical surface finish for three orientations were calculated. After entering the build scenarios (above), CABSS exhaustively searches the design space defined by goal equations presented in Section 3. The results of this search are presented in Table 2.

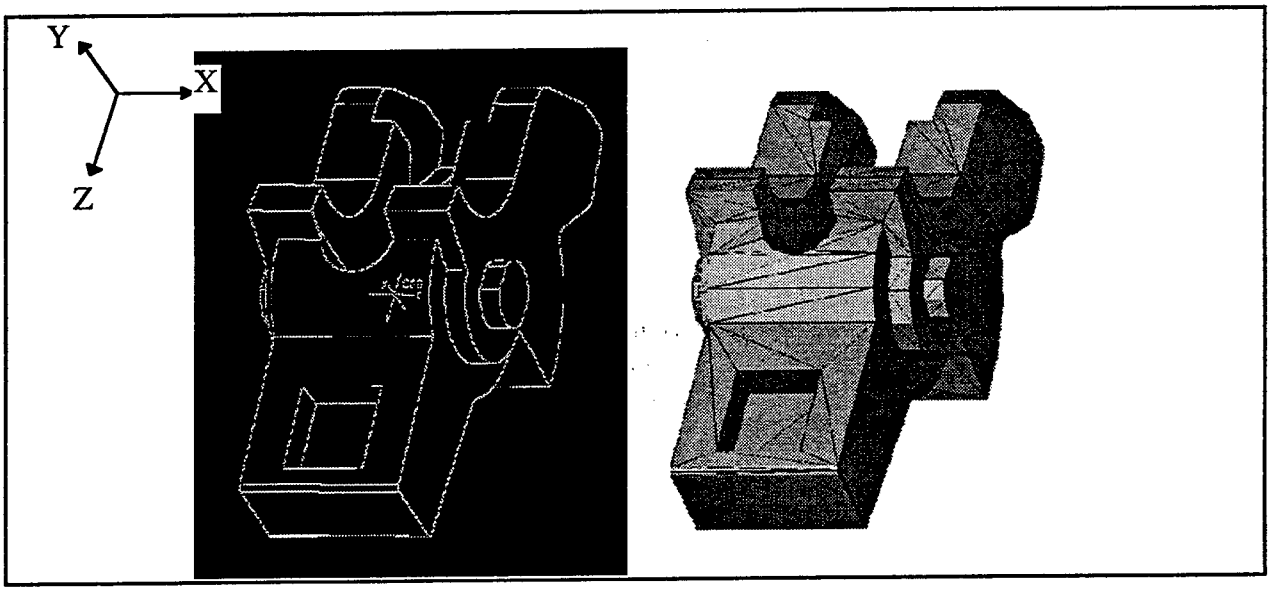


Figure 2 - Siemens circuit breaker handle. Wire frame and STL renderings

Table 2 - Results from Exhaustive Search for Circuit Breaker Example

Scenario	Build Style Variables	Build Goals	Deviation Function
#1	Layer Thickness = 0.0055" Hatch Spacing = 0.013" Height = 1.45"	Build Time = 301.28 Average Inaccuracy = 2597.21 Surface Finish = 251.77	level 1 = 0.0 level 2 = 0.061
#2	Layer Thickness = 0.0045" Hatch Spacing = 0.007" Height = 1.45"	Build Time = 403.7 Average Inaccuracy = 2239.48 Surface Finish = 251.77	level 1 = 0.036
#3	Layer Thickness = 0.006" Hatch Spacing =0.015" Height = 1.45"	Build Time = 271.74 Average Inaccuracy = 2824.78 Surface Finish = 251.77	level 1 = 0.046

From knowledge of SLA operation, build time decreases as layer thickness and hatch spacing increase. However, part inaccuracy increases as layer thickness and hatch spacing increase. Therefore, it is reasonable to assume that as the importance of accuracy increases, layer thickness and hatch spacing should decrease. Increasing the importance of build time should have the opposite effect on these values. As can be seen from Table 2, layer thickness and hatch spacing attain their largest values in Scenario 3, when build time is most important. In Scenario 2, when accuracy is most important, layer thickness and hatch spacing take on their smallest values.

In order to validate the results obtained, the handle should be built with the "best" build style variable values. At present, only the build time goal has been tested. The BTE program provided the baseline build time measurements. Comparison of BTE and CABSS build times shows an error of less than 2 percent for Scenarios 1 and 3 and an error of 5 percent for Scenario 2.

5. CONCLUSIONS

Several conclusions can be drawn from this research. The main conclusion is that it is indeed possible to provide decision support for stereolithography build styles using the compromise DSP. This is done by formulating and solving a DSP with a computer tool. Several specific conclusions are used to support this main conclusion.

- The selected build style variables have a significant impact on SLA build performance: build orientation (part height and surface angles), cross sectional layer thickness, and laser hatch density. This research verified the expected behavior of these variables.

- Build performance can be predicted by constructing response surface models of the build goals as functions of the relevant build style variables and parameters. These response surface models apply to parts of a wide range of geometric complexities and sizes. This conclusion is based on observing the test case results and comparing them with expected SLA build behaviors. However, the response surface models should only be applied to parts whose parameters fit within the experimental design space on which the response surface is based.

Even though this method for decision support is viable, more work needs to be done to improve the results. This includes creating more accurate response surface models that encompass a wider range of part parameters (volume and height).

ACKNOWLEDGEMENTS

We gratefully acknowledge the support from ARPA TRP grant #2187 and from the RPMI member companies.

REFERENCES

1 Frank, D and Fadel, G, "Expert System Based Selection of the Preferred Direction of Build for Rapid Prototyping Processes," Clemson University report, 1993.

2 Wodziak, J R, Fadel, G M, Kirschman, C, "A Genetic Algorithm for Optimizing Multiple Part Placement to Reduce Build Time," Clemson Intelligent Design Systems Laboratory, Clemson University, 1994.

3 Sabourin, E, Houser, S A, Bøhn, J H, "Adaptive Slicing using Stepwise Uniform Refinement," *Rapid Prototyping Journal*, 2(4):20-26, 1996.

4 Hur, J and Lee, K, "Efficient Algorithms for Automatic Support Structure Generation in Layered Manufacturing," Proceedings ASME Computers in Engineering Conference, paper #96-DETC/CIE-1324, 1996.

5 McClurkin, J E and Rosen, D W, "A Build Style Selection Method for Stereolithography," Proceedings 1997 NASUG Conference, Orlando, February 16-20, 1997.

6 Mistree, F, Hughes, O F, Bras, B A, "The Compromise Decision Support Problem and Adaptive Linear Programming Algorithm," *Structural Optimization: Status and Promise*, AIAA, Washington, DC, pp. 247-289, 1993.

7 Mistree, F, Hughes, O F, Phuoc, H B, "An Optimization Method for the Design of Large, Highly Constrained Complex Systems," *Engineering Optimization*, 5(3):141-144, 1981.

8 Tata, K and Flynn, D, "Quantification of Down Facing Z Error and Associated Problems," Proceedings 1996 NASUG Conference, San Diego, March 11-13, 1996.

9 Maestro 1.8 Users Manual, 3D Systems Inc., Valencia, CA, 1996.

10 McClurkin, J E, "A Computer-Aided Build Style Decision Support Method for Stereolithography," Masters Thesis, Georgia Institute of Technology, June 1997.

11 McClurkin, J E, Build Time Estimation via the World Wide Web, available at: http://rpmi.marc.gatech.edu/BTE.html.

Validation of Rapid Prototyping Material for Rapid Experimental Stress Analysis

by **C. Schley, G.F. Smith,** Warwick Manufacturing Group, Advanced Technology Centre, University of Warwick *
G.C. Calvert, Advanced Power Train Technology, Rover Group *

ABSTRACT
The paper will detail the validation work carried out on various Rapid Prototyping (RP) materials to determine their suitability for the application of Thermoelastic Stress Analysis. The overall objective is to drastically reduce the product design cycle, by providing "real experimental data" for correlation with Finite Element Analysis (FEA), prior to any expensive manufacturing process. In order to achieve this the homogeneity of the Rapid Prototyping material has to be established to ensure a valid transfer of results from model to actual part.

ACKNOWLEDGEMENTS
Rover's Rapid Prototyping and Tooling Department
University of Warwick Manufacturing Group
University of Warwick Mechanical Engineering Department
Rover's Experimental Analysis Department
Universität Stuttgart, Institut für Kunststoffkunde und Kunststoffprüfung (IKP)

1. INTRODUCTION AND THEORY

Especially in the automotive industry, there is a requirement to fully optimise the design in order to produce a lightweight but durable product. The work described here, is to determine the feasibility of using models produced by Rapid Prototyping machines for experimental stress analysis techniques (Calvert, 1994), in this case Thermoelastic Stress Analysis. Using this method, the FEA can be checked at the concept stage and the design validated early reducing the need for actual testing and subsequent design changes ,i.e. producing a high integrity product at reduced cost and time.
Thermoelastic Stress Analysis is a non-destructive technique which can be used to obtain a stress field over the whole surface of a component or structure. Its use on metallic parts is well established and proven (Stanley and Chan, 1988), but its effectiveness on RP materials is unknown. The stress measurement is based on the sensitive detection of the part surface temperature change induced in materials under dynamic stress conditions. Under adiabatic conditions there is the following linear relationship (Thomson, 1855)

$$\Delta T = -K_m \cdot T \cdot \Delta\sigma \qquad (1)$$

where ΔT is the peak to peak temperature change [K], K_m is the thermoelastic material constant [mm^2/N], T is the absolute surface temperature of the solid part [K] and $\Delta\sigma = \sigma_1 + \sigma_2$ is the peak to peak change in the sum of principal stresses [N/mm^2].

This relationship is only valid for homogeneous and isotropic material in the linear elastic region. The thermoelastic constant K_m is expressed

$$K_m = \alpha / \rho \cdot c_p \qquad (2)$$

where α is the heat coefficient of linear thermal expansion [1/K], ρ is the density [g/cm^3] and c_p is the specific heat capacity at constant pressure (under constant stress) [J/g·K].

* University of Warwick, Coventry CV4 7AL, United Kingdom

For the detection of this cyclic temperature change any kind of infrared camera system can be used, but SPATE is especially designed to make stress measurements. The SPATE system equation to make a theoretical calibration (Ometron, 1996) is

$$\Delta\sigma = F_{th} \cdot S = \frac{D \cdot G \cdot R}{T \cdot e \cdot 2048 \cdot K_m} \cdot S \qquad (3)$$

where F_{th} is a theoretical calibration factor [N/mm^2], S is the measured signal [-], D is the temperature response [K/volt], G is the Correlator sensitivity [volt], R is a temperature correction factor [-] and e is the emissivity of the paint. This relation is dependant on equation (1) and the measurement equipment. The parts are normally painted to get a high and consistent emission.

2. SUITABILITY CRITERIA

The following criteria can be defined for the suitability of a Rapid Prototyping material for Thermoelastic Stress Analysis.

2.1 Homogeneous and isotropic behaviour

Equation (1) is only valid for an homogeneous and isotropic material. Because of the manufacturing process (the test part is created by building one layer on top of another) the material may show different strength behaviour in different directions, also there could be defects in the form of voids inside the material.

2.2 Linear elastic deformation and adiabatic conditions

Only the linear elastic temperature change is proportional to the sum of principle stresses. But in reality there will also be other reasons which may cause a temperature change

$$\Delta T = \Delta T_{le} + \Delta T_{ve} + \Delta T_{pl} + \Delta T_{flow} \qquad (4)$$

where ΔT_{le} is due to linear elastic effect, ΔT_{ve} is due to visco-elastic behaviour, ΔT_{pl} is due to plastic deformation and ΔT_{flow} is the heat flow due to temperature gradient. A correlator can be used to filter all the changes that are not periodic with dynamic load, but some of the terms may still have some influence:

ΔT_{ve} increases with the differential of strain after time $d\varepsilon/dt$. This differential $d\varepsilon/dt$ is periodical to the test frequency (f). Therefore a low f would be positive. ΔT_{pl} is low, if there is less plastic deformation. Therefore the offset yield stress should be small. ΔT_{flow} is proportional to the thermal conductivity k. Under adiabatic conditions a part under stress will have infinitesimal low heat flow between areas of different stress and temperature. Therefore, there is a need for a high f, especially if k is high. But on the other side, the paint is like a thermal resistor. For a good heat flow from the stress area through the paint, a low f would be an advantage, especially if the paint thickness is thick.

It should therefore be possible to find a test frequency, where the last 3 terms are low and the signal due to the linear elastic effect is high. Additionally it is necessary to define a linear elastic limit stress σ_θ.

2.3 Repeatability and calibration

It should be possible to calibrate the test equipment for a specific material enabling every test to give directly, good stress values. Therefore the material itself should always have the same mechanical properties throughout. If the environmental conditions or the load test procedure are different, the influence of those differences will need to be established. Otherwise the test conditions must remain the same and not vary from test to test. Especially, it should be ensured that the following should not change: material, surface finish, test frequency, load waveform and test surface temperature.

2.4 Correlation with theoretical solution in a wide region of stress

In the case of a known stress calibration the thermoelastic signal can be multiplied by a constant calibration factor F_{known}. Therefore the stress value will be exact for a certain signal. It is necessary to investigate the effect of signal variation on stress values.

2.5 Accuracy and correlation with theoretical calibration

For the SPATE system a theoretical calibration after the equation (3) is possible. The variation between the theoretical and the known stress calibration should be investigated. The size of the thermal emission from a material has an influence on the minimum measurable stress value $\Delta\sigma_{min}$. To obtain a high degree of accuracy the quotient of $\sigma_\theta/\Delta\sigma_{min}$ should be as high as possible

$$\frac{\sigma_\theta}{\Delta\sigma_{min}} = \frac{\sigma_\theta}{\frac{\Delta T_{min}}{K_m \cdot T}} = \frac{\sigma_\theta \cdot K_m \cdot T}{\Delta T_{min}} = \frac{\sigma_\theta \cdot \alpha \cdot T}{\rho \cdot c_p \cdot \Delta T_{min}} \qquad (5)$$

where ΔT_{min} is the minimum measurable temperature change of the camera system.

2.6 Transferability

The RP model will be of a different material to the real component, but its elastic stress distribution (or stress field) should be similar to that of the metal prototype for similar loading conditions. In simple cases, the stress field is only dependant on the geometry. But for isotropic materials there can also be an influence due to material constants:

a) different Poisson's Ratio ν: can cause different stress distribution, if the lateral deformations are suppressed (examples: rigid boundaries, friction in contact surfaces)
b) different density ρ: can cause different stress distribution, because centrifugal body forces are dependant on density and the self-weight of a model will cause body forces as well
c) different Young's modulus E: will cause different deformation under similar load condition (examples: distortions become appreciable and therefore the deformation is not linear any more, with instability problems.the different distortion may drastically change the magnitude of forces).

3. INVESTIGATIONS AND EXPERIMENTS

To prove the suitability of a Rapid Prototyping material, the following experiments were carried out. At the IKP in Stuttgart experiments were conducted to determine the material constants $\alpha = \alpha(T)$ and $c_p = c_p(T)$. Tensile tests were conducted with a horizontal and a vertical extensiometer. Brazilian Disc tests were conducted to establish the materials thermoelastic performance.

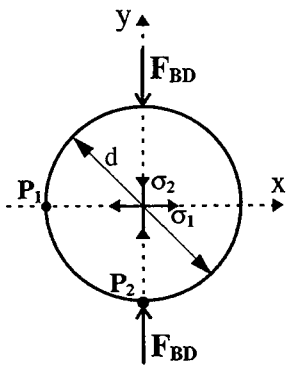


Figure 1 Brazilian Disc Test

The disc under compression (see figure 1) has a well known stress field (Timoshenko, 1951 and J.M. Dulieu-Smith,1995). At the point P_1 for example the sum of principal stresses is zero while at the point P_2 it is unlimited.
Test specimens were manufactured using SLA technology (Stereolithography): lying (layers parallel to the load direction) and standing (layers vertical to the load direction) for the tensile tests, lying discs for the Brazilian Disc test. For nylon (SLS technology, Selective Laser Sintering) material details were taken from reference books.
In the following the RP material will be evaluated due to the criteria in section 2. The criterion is identified in brackets { } before each evaluation.

3.1 Evaluation of Basic material and tensile test results

{ 2.1 }
Results for lying and standing dogbones:

E_S/E_L [-]	D_E [%]	$\sigma_{maxS}/\sigma_{maxL}$ [-]	$D_{\sigma max}$ [%]	ν_S/ν_L [-]	D_ν [%]
1.028	2.8	0.976	-2.4	0.966	-3.4

Notation: D_E is the Deviation of Young's modulus, $D_{\sigma max}$ is the Deviation of maximum stress and D_ν is the Deviation of Poisson's ratio.
Notation of the indices: L for lying and S for standing

{ 2.2 }
The material had in all directions a region with very low plastic strain. So it was possible to determine σ_θ.

{ 2.3 }
The following table presents the standard deviation in % for each series of specimens:

SD_{E_L}	SD_{E_S}	$SD_{\sigma max_L}$	$SD_{\sigma max_S}$	$SD_{\sigma 0.2_L}$	$SD_{\sigma 02_S}$
2.2	1.2	1.0	1.1	3.4	2.8

Notation: SD_E is the Standard Deviation of Young's modulus, $SD_{\sigma max}$ is the Standard Deviation of maximum stress and $SD_{\sigma 0.2}$ is the Standard Deviation of offset yield stress at offset strain 0.002 mm/mm.
Notation of the indices: L for lying and S for standing
All results are less than 5%, hence the mechanical repeatability of part manufacturing is good.

For the repeatability of Thermoelastic Stress Analysis it is important, that the calibration of the camera signal is only constant, if the part surface temperature doesn't change. But in reality it is very difficult and expensive to test always at the same temperature. Therefore it would be useful to know the influence of the temperature on the calibration factor. A temperature influence is given due to the measurement system and equation (1), but in this particular case it is also due to the thermoelastic constant K_m.
By using equation (3) the calibration factor can be described as below

$$F_{th}(T) = A \cdot \frac{R(T)}{T \cdot e(T) \cdot K_m(T)} = A \cdot \frac{R(T) \cdot \rho(T) \cdot c_p(T)}{T \cdot e(T) \cdot \alpha(T)} \qquad (6)$$

where A is a constant factor. The temperature influence of e and ρ is very low, while the investigations have shown, that the influence of $\alpha(T)$ and $c_p(T)$ are quite considerable. The glass temperature of the RP material is quite low and near to room temperature and therefore α for example will increase, if temperature is increasing.

The whole influence of temperature to the calibration factor can then be described as

$$Q_{F20}(T) = \frac{F_{th}(T)}{F_{th}(20°C)} = Q_{MC}(T) \cdot Q_{Km}(T) \qquad (7)$$

where $Q_{MC}(T)$ is the influence of measurement conditions and $Q_{Km}(T)$ is the influence of the thermoelastic material constant. The figure 2 below presents the results of equation (7).

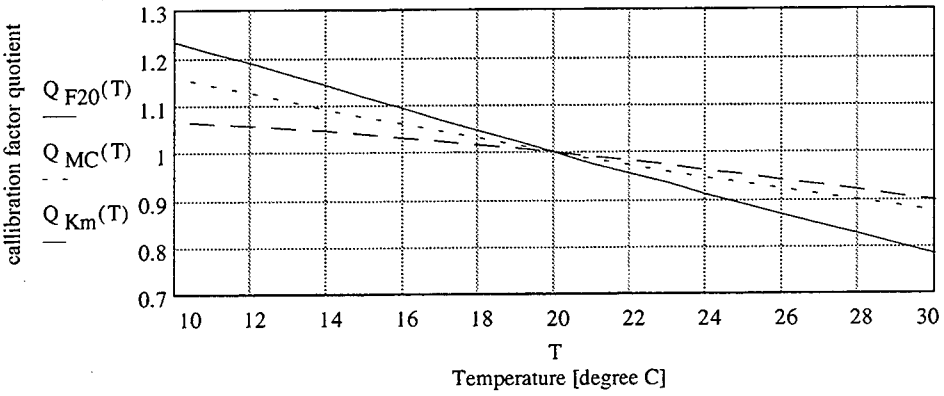


Figure 2 Influence of temperature to the calibration factor

{ 2.5 }

With the help of the material constants it is possible to calculate K_m, $\Delta\sigma_{min}$ and $\sigma_\theta/\Delta\sigma_{min}$. The table below for $\sigma_\theta/\Delta\sigma_{min}$ compares two Rapid Prototyping materials with a steel plate at 20 degree Celsius.

Material	$\sigma_\theta/\Delta\sigma_{min}$ [-]
Rapid Prototyping material 1 (SLA)	351
Rapid Prototyping material 2 (Nylon, SLS)	44
steel plate material 3	198

{ 2.6 }

The table below shows a comparison of ρ, E and ν with a common steel material ($\rho_{steel}\approx 7.8$ g/cm^3, $\nu_{steel}\approx 0.3$, $E_{steel}\approx 200000$ N/mm^2).

Material	ρ/ρ_{steel} [-]	ν/ν_{steel} [-]	E_{steel}/E [-]
Rapid Prototyping material 1 (SLA)	0.16	1.37	66
Rapid Prototyping material 2 (Nylon, SLS)	0.15	(?)	157

3.2 Evaluation of Brazilian Disc test results

{ 2.2 }

Figure 3 below presents the measured signal over a range of test frequencies.

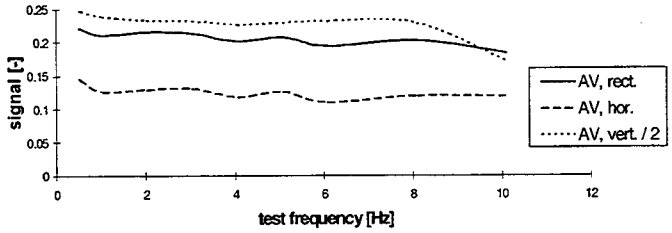


Figure 3 Measured signal over different test frequencies

In figure 3 the Brazilian Disc test results have been averaged. Notation of the legend: AV, rect. is the averaged signal in an rectangle area near the centre, AV, hor. over the horizontal diameter and AV, vert. over the vertical diameter of the disc.
The signal was high and quite constant at a low frequency comparing well with the necessary frequency of steel for example. This is reasonable, because the thermal conductivity k of the RP material is much lower than k of steel.

{ 2.3 }
A calibration factor can now be defined by making a known stress calibration.

$$F_{known}(T_{disc}) = \frac{\sigma_{sum_C}}{signal_{centre}(T_{disc})} \qquad (8)$$

where σ_{sum_C} is the theoretical sum of principle stresses in the centre of the disc (known stress), $signal_{centre}$ is the measured signal in the centre of the disc and T_{disc} is the surface temperature of the test specimen used for determining F_{known}.
Because the signal was a little noisy, a filter was used to obtain the signal for calibration. For tests with another test body temperature, this calibration factor can be corrected with the help of figure 2.

{ 2.4 }
After calibration it is possible to compare the whole measured stress field with the theoretical solution.

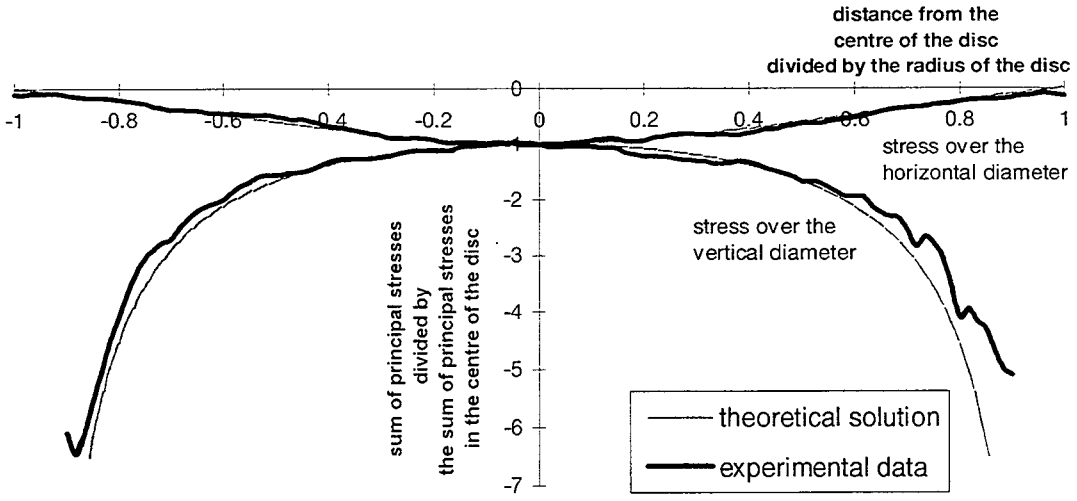


Figure 4 Comparison of experimental data with the theoretical solution for a machined disc

Scan image:



FE image:

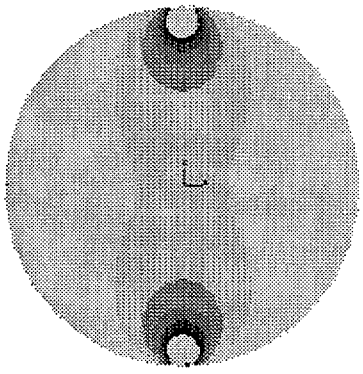


Figure 5 Comparison of the measured stress field with theoretical FE solution of $\Delta\sigma$.

In figure 4 the upper curves are the stresses over the vertical disc diameter and the lower curves are the stresses over the horizontal diameter. Figure 4 and 5 show a very good correlation below and over the calibration point. The deviation outside the vertical diameter can be explained by the method of clamping. First of all the theoretical solution goes to infinity. This is not reasonable, because in reality there is an area pressing instead of a point load. Therefore it is correct, that the measured results are below the theoretical solution.

{ 2.5 }
Using the SPATE system the following quotient should be near to one:

$$\frac{F_{th}(T_{disc})}{F_{known}(T_{disc})} \approx 1$$

The table below shows the results for the RP material and a steel plate.

Material	$\frac{F_{th}(T_{disc})}{F_{known}(T_{disc})}$ [-]
Rapid Prototyping material 1 (SLA)	0.68
steel plate material 3	0.61

The signal for the RP materials is about 30% and for steel about 40% lower as expected, but the results are in the right region. The potential for errors in equation (3) should be noted.
The deviation of the experimental results with the theoretical solution can be calculated as shown in figure 6.

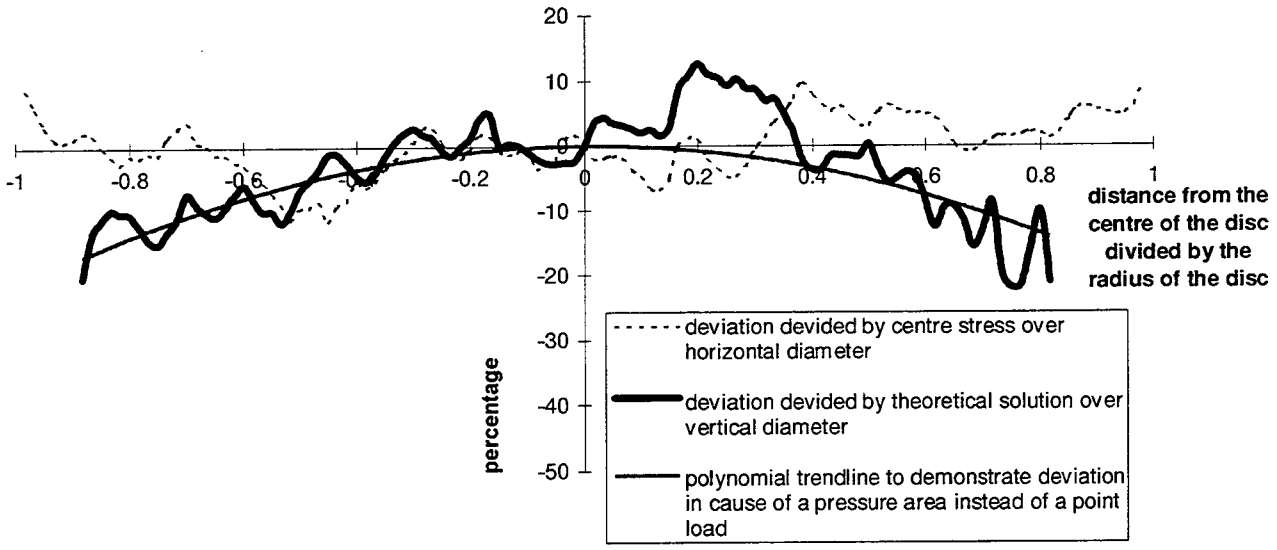


Figure 6 Deviation of experimental data from theoretical solution

Except near the load input the deviation is below or about 20%.

3.3 Summary

The results for the criteria {2.1} to {2.5} show good results and the RP material can be validated for Thermoelastic Stress Analysis, while the following facts should be highlighted:

- The theoretical accuracy $\sigma_\theta/\Delta\sigma_{min}$ of the measurement is about 2 times higher than for the steel plate material, which is a common metallic material in the automotive industry.
- The test can be conducted at about 10 times lower test load and about 10 times lower frequency. That means the test can be conducted on cheaper testing machines and probably under office conditions.

- The low necessary test frequency reduces the influence of the paint thickness and the losses of the emission are lower.
- The finishing and preparation of the disc specimens hasn't been costly. Any other test prototype could be built within hours from the CAD-file.

Because E, ρ and ν are different from a metallic material, the transferability (criterion {2.6}) depends on the geometry and on the loading of the part. Curiously enough, if no elastic deformation is suppressed, the load is much higher than body force due to self weight and the deformations are small, then practical examples have shown, that the stress fields of two different materials are very similar. But also the absolute value of σ_1 (positive) + σ_2 (negative) has been smaller than the von Mises stress σ_{Mises}, which is often used as a comparison stress with the unidirectional limit stress σ_{max}.

4. CASE STUDY AS FUTURE WORK

The transferability and the interpretation of the results could be investigated theoretically by FEA within a case study by defining the following two criteria.

4.1 Similar stress distribution

The influence of ρ, E and ν can be checked and estimated theoretically by a comparison of the von Mises stress fields as follows:

σ_{Mises} of FEA(ρ, E, ν of RP material; testload)

$\Updownarrow$

σ_{Mises} of FEA(ρ_C, E_C, ν_C of the case study material, critical load).

If the two calculations produce a similar stress field for a linear static problem, the influences of ρ and ν can be ignored. The influence of E can be estimated with the theoretical deformation.
It is then possible to convert the results (measured stresses) directly to the sum of principal stresses in the metal part by simply scaling the loads from RP model to series part.

4.2 Interpretation of measuring results

The interpretation could be done by a comparison of the measured results with $\Delta\sigma$ of an FEA postprocessing as follows:

Dynamic Test and Measurement(RP material, testload)

$\Updownarrow$

$\Delta\sigma$ of FEA(ρ_C, E_C, ν_C of the case study material, critical load)

and by calculating the following stress quotient: $\left|\frac{\Delta\sigma}{\sigma_{Mises}}\right|$.

REFERENCES

Calvert, G. (March 1994) **Rapid Prototyping for Experimental Analysis**, Proc. of colloquium on "Rapid Prototyping in the UK", IEE Manufacturing Division, Digest No. 1994/077 Paper 7

Dulieu-Smith, J.M. (February 1995) **Alternative calibration techniques for quantitative thermoelastic stress analysis**, Journal of Strain Analysis

Ometron (February 1996) **Operators Manual**, The OMETRON 4000 Series,

Stanley, P. and Chan, W. (1988) **Quantitative stress analysis by means of thermoelastic effect** Journal of Strain Analysis, Vol23 No.3 1988 pp177-186

Thomson, W. (Lord Kelvin,1855), **J Maths**, reprinted in Phil Mag 5, 4-27 (1878)

Timoshenko, S.P. (1951) **Theory of elasticity** (2nd Edition), Mc Graw Hill, New York

CAD and Control Technologies for Computer-Aided Manufacturing of Laminated Engineering Materials

Sangeun Choi [1], Ravi Hebbar [2], Yong Zheng [3] and Wyatt S. Newman [4]

Abstract

This paper presents recent progress in software, material handling and tangent-cutting control in support of Computer-Aided Manufacturing of Laminated Engineering Materials(CAM-LEM). Progress in CAD focuses on the definition of a new layered file format for describing 3-D solids in terms of thick slabs with ruled-surface edges. For material handling, we present new algorithms for automatic generation of mask hole patterns used in selective-area vacuum gripping, which is required for our laminated assembly process. Finally, we present recent results of object fabrication using thick-slab, tangent-cut layers

1. Introduction

Computer-Aided Manufacturing of Laminated Engineering Materials (CAM-LEM) is a sheet-based approach to Solid Freeform Fabrication being developed at Case Western Reserve University [7, 8, 10, 11]. In this process, layers computed from cross sections of an object's CAD description are laser-cut from sheet material and subsequently stacked and laminated to assemble a part. Such stacks are post-processed to densify the material, fusing it into a monolithic solid. With this approach, we not only realize the original CAD description, but we also satisfy functional engineering properties (e.g. rigidity, strength, thermal expansion, surface finish, etc).

One of the most important characteristics of a part fabricated from a successful SFF system is acceptable surface finish. With few exceptions [e.g., ShapemakerII [1], SDM [2], Stratoconception [3]], current SFF processes build parts from thin, vertically-extruded layers resulting in "staircasing" of the resulting surface. Commonly, one reduces the magnitude of the staircase roughness by reducing the thickness of each layer, but at the cost the fabrication speed.

For our CAM-LEM system, a 5-axis laser cutting platform was built to translate and rotate sheet material under a stationary laser. By cutting contours at the appropriate tangent angles with this platform, it is possible to better approximate an object's surface and/or improve the build rate. However, our process of tangent-cutting and assembling layers presents multiple significant technical challenges. Progress in three of our challenge areas is presented here. First, we describe how to represent the original CAD model in terms of an approximation using relatively thick slabs with ruled-surface edges. Second, we introduce improvements on our technique for extracting desired regions from the cutting table and precisely stacking them on the part assembly. Finally, we illustrate and discuss recent progress in building 3-D objects with our 5-axis CAM-LEM system.

[1] Department of Mechanical Engineering , Case Western Reserve University.
[2] Department of Electrical Engineering , Case Western Reserve University.
[3] Department of Electrical Engineering , Case Western Reserve University.
[4] Associate Professor , Department of Electrical Engineering and Applied Physics , Case Western Reserve University, Cleveland, Ohio 44106 .

2. Layered File Format (LFF) Representation of Solids

To exploit the potential advantages of building objects with thick, tangent-cut layers, we must first derive an approximation of our original CAD model in terms of layers that can be fabricated with a practical system. Laser cutting is used in our system, but the same constraints apply to 5-axis CNC machining, 4-axis wire-EDM or hot-wire cutting and 4-axis water-jet cutting of sheet materials. For this geometric processing task, we preferably perform computations directly on the native CAD file, although our approach is applicable to STL format files as well.

In our process, we distinguish "slices" from "layers." We define a "slice" as the 2-D cross section of our model at a given z-height. A slice can be represented in terms of closed contours—"outer" contours enclosing regions of material, and "inner" contours describing punctures within the enclosed regions. Such contour information can be used in an alternative model representation, such as in the contour file formats SLC[4] and CLI[5]. A representation in terms of slices alone is adequate for systems that build with thin, vertical extrusions of layers. For thick, tangent-cut slabs, however, such representation is inadequate; it is also necessary to specify the shape of the edge surfaces of thick slabs. We thus define a "layer" as a 3-D body with planar upper and lower surfaces (slices) connected by edge surfaces. Objects can be defined in terms of stacks of such layers. Technically, such a layered representation can identically redescribe any CAD model. However, the class of layers that can be fabricated by a line-of-sight cutting process is restricted to those with edge surfaces defined in terms of *ruled surfaces* [6]. Layer bodies with ruled-surface edges are simply described by one-to-one mappings of each contour on the upper surface to a corresponding contour on the lower surface. The mapping includes a functional specification of the path of a span—connecting upper and lower contours—swept along the perimeters. The swept path corresponds identically to the cutting-tool path for fabricating the layer, thus guaranteeing feasibility of fabrication.

Since a ruled surface cannot identically match an arbitrary surface, our thick-layer representation with ruled edge surfaces can only approximate an exact CAD model. Since a ruled-surface description joining two contours is not unique, the space of alternative ruled surfaces should be explored to identify the best fit to the original model. An algorithm for performing this computation based on an energy-relaxation technique was introduced in [7] and is further detailed in [8]. Having computed an optimal reconstruction that can be fabricated by a line-of-sight cutting process, the result should be stored in a format that is compact, precise, and efficient to interpret on-line during fabrication. For this purpose, we define a layered file format (LFF), as illustrated in Fig 1.

In an LFF file, a part is represented by successive parallel *layer*s in ascending order in the vertical direction. Each layer is defined by a *bottom slice*, *top slice*, and ruled layer *edge-surface*s between the two slices. Slices are described by the boundary contours, which can be composed of polylines as well as higher-order curves. An LFF file can be generated by slicing CAD models and stitching upper and lower cross-sectional contours with ruled surfaces, or by interpreting reverse engineering data collected by surface digitizing or from Computed Tomography (CT) imaging.

Since our layers describe true 3-D bodies, we can also associate material descriptors with layer bodies. To represent mixed material composition within a layer, we define a layer in terms of a number of regions. Each region is a 3-D body described in terms of a closed (possibly punctured)

surface description, and each closed surface contains a labeled material. The regions can be adjacent to each other or disjointed.

Fig. 1 illustrates the format. Layer i is bounded by lower slice-plane "slice i-1" and upper slice plane "slice i." Each slice is defined in terms of closed contours, identified as outer (enclosing material) or inner (defining a puncture). Pairs of contours, upper and lower, are associated through a functional ruled-surface description, specifying the edge surface connecting them. We describe this mapping in terms of a tabulated function of arc-length along the top contour vs. arc length along the bottom contour, specifying endpoints of connecting spans. Edge surfaces that connect upper and lower outer contours occur once for each region within a layer, and we thus associate with this mapping a material tag identifying the material enclosed within the region.

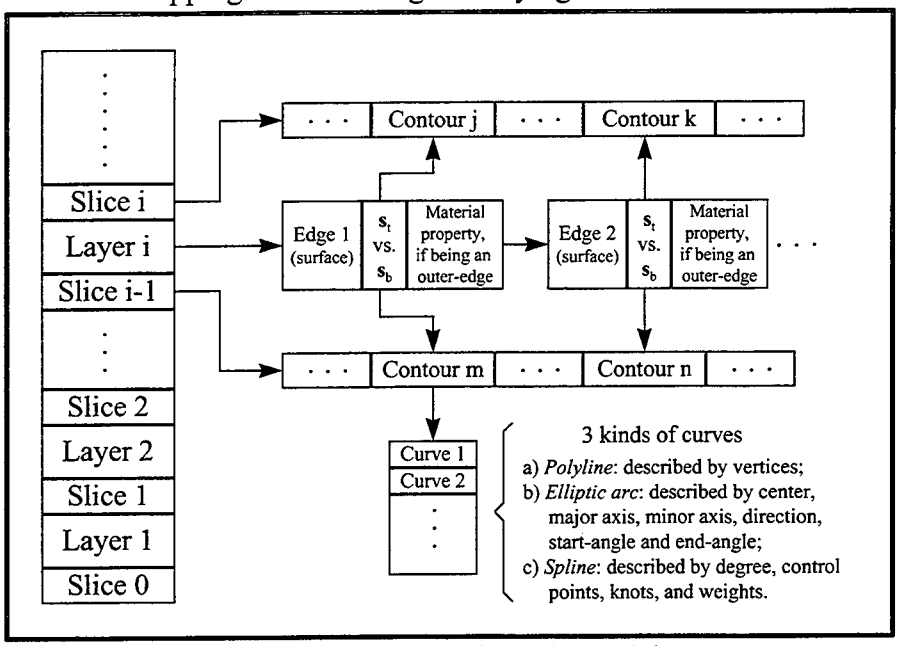


Figure 1 : LFF representation of a solid model

Finally, we encode contour descriptions in terms of "curves." Three types of curve entities have been defined in the current version of the LFF file format. They are the polyline, the elliptic arc, and the spline curve, including Non-Uniform Rational B-Splines (NURBS). Since all contours in our description lie in parallel planes, only 2-D curve descriptors are needed .

A *polyline* is a series of connected straight line segments. A polyline with n segments is defined by its n+1 2D vertices given in x-y coordinates.

An *elliptic arc* is part of an ellipse. It is defined by a center point, a major axis vector, a length-ratio of the minor axis to the major axis, a direction flag, a start-parameter, and an end-parameter (analogous to start and end angles). A circular arc is a special case of elliptic arc when the length-ratio equals 1.0. The elliptic arc is parameterized. Given the center $\boldsymbol{C}$, major axis $\boldsymbol{M}$ and minor axis $\boldsymbol{N}$, a point $\boldsymbol{P}$ on the ellipse can be located by parameter u as $\boldsymbol{P}(u) = \boldsymbol{C} + \boldsymbol{M}\cos(u) + \boldsymbol{N}\sin(u)$.

Spline curves, rational and non-rational, are also parameterized. A spline is defined in terms of a specified degree, control points, knots, and (for rational splines) a set of weights. (see [9] for details).

Our LFF file format achieves our stated objectives. It can represent contour descriptions within a slice plane precisely and compactly through the use of higher-order functions. It can also encode material information throughout the volume of a body. It represents tangent information for edge

surfaces in terms of a compact representation (scalar functions defining ruled surfaces) that encodes the full precision achievable by a line-of-sight cutting process. Finally, and most importantly, the format guarantees that each layer can be fabricated using a line-of-sight cutting means, and the specification decomposes efficiently for real-time interpretation for machine control. We consider this format to be ideal for sheet-based processes, including our CAM-LEM system.

3. Selective-Area Material Handling of Layers.

A second technical challenge of the CAM-LEM approach is material handling. Since we cut each layer individually, the desired regions must be extracted from the cutting table and assembled precisely to form the desired part. For this task, we utilize a novel masked vacuum gripper technique (see [10] for details). In previous work, we demonstrated that it is feasible to extract selective regions using a vacuum gripper masked by a selectively-punctured, non-porous material. In recent progress, we have improved and automated the mask-hole pattern definition, we have extended the mask design to automated computation of multi-purpose masks, and we have proposed a means to extract tangent-cut regions from waste material.

Our procedure for automated mask generation is described here. Consistent with our LFF layer descriptions, we refer to the closed contours defined on the upper slice plane of each layer. (Only the upper slice plane will come in contact with the vacuum gripper). This slice consists of one or more *outer* contours, each possibly enclosing one or more *inner* contours. In our mask generation process, simply stated, each outer contour is successively eroded, each inner contour is successively dilated, and mask holes are defined at fixed intervals along the resulting contours. Ideally, this results in a sequence of closed, non-intersecting contours describing a uniform distribution of mask holes that can be punched along efficient trajectories.

While conceptually simple, complications occur with this approach. For a non-convex contour, erosion eventually leads to self-intersecting contours, as illustrated in Fig 2. (A similar problem can occur with dilation of inner contours). To resolve this problem, we analyze each eroded contour to test for self intersections. Self intersections define multiple closed loops. Each such closed loop is tested for its direction of rotation. If the direction of rotation is consistent with the direction of rotation of the original contour, then the resulting loop is retained. Reversed circulations indicate contours to be deleted. In a similar manner, the problem of intersections among multiple eroded/dilated contours is solved by locating the points of intersection of one contour with another and then retaining those inner/outer contours consistent in direction , as illustrated in Fig 3. Incorporating these considerations, our algorithm is capable of generating correct mask-hole distributions for arbitrarily complex regions, resulting in fill patterns along concentric, closed contours. The corresponding mask production time is faster and more precise than a raster scan, analogous to the comparison between vector graphics and raster graphics. (This same algorithm may be applicable to efficient scan patterns for point-wise SFF building techniques as well.)

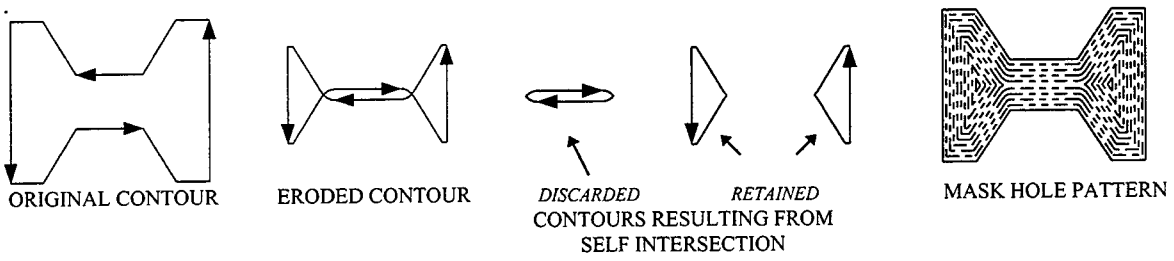


Figure 2

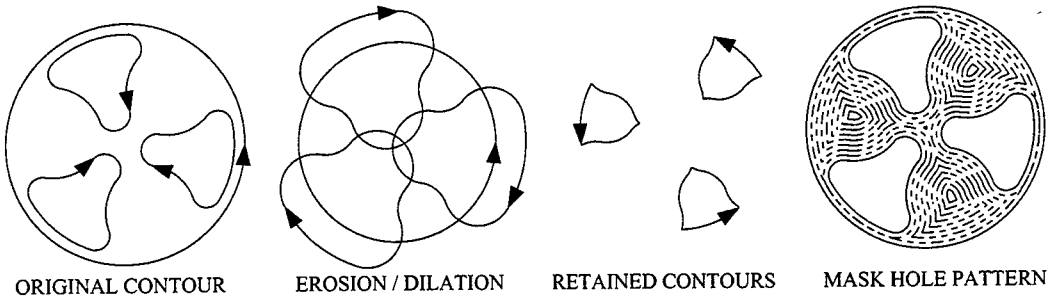


Figure 3

A limitation of our masked vacuum gripper technique is that production of masks can be too time consuming if a separate mask is required for each layer. In a recent extension, we automatically generate masks applicable to multiple layers. The motivation is obvious for gradually changing layers, since the corresponding masks would also be similar. However, multi-use masks can also be employed for surprisingly dissimilar layers. The procedure for generating multi-use masks is illustrated in Fig 4. The first two shaded regions are the desired areas to be grasped. The third image shows the Boolean intersection of the two desired regions. The mask pattern applicable for grasping both regions, the fourth image, is generated by our generic technique, but based on the contours of the intersection of regions.

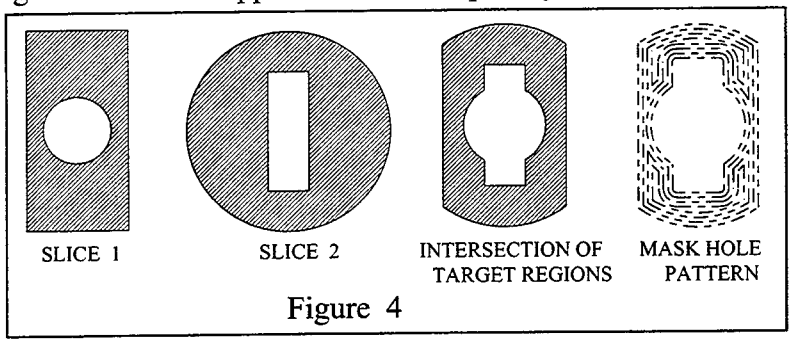
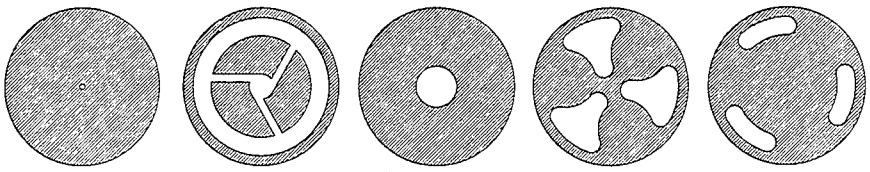


Figure 4

A multiusable mask once generated should be checked for feasibility. An analysis of the force exerted by the gripper on the part is done by solving for Newton's force balance and Euler's moment balance equations . The analysis requires the gravity force on the slice, the centroid, suction force per mask hole, the location of the mask holes and the number of mask holes, which are all known. The only unknown is the reaction pressure distribution between the grasped part and the mask . The space of the possible reaction pressure distributions is approximated by a finite number of hypothetical concentrated reaction forces distributed over the interior of the target region . In proposing reaction force coordinates, there is no penalty for including an excess number of locations. To assure a complete flooding of candidate reaction force locations the same mask generating algorithm is employed. The result is used as input to a linear programming equation solver, which solves for force/moment equilibrium feasibility.



FIVE SLICES OF A FLUIDIC DEVICE

Figure 5



INTERSECTION OF TARGET REGIONS

MASK HOLE PATTERN

Figure 6

The above method was employed to test the feasibility of a multiusable mask for five slices of a fluidic device, shown in Fig 5. The multiusable mask for the five slices, shown in figure 6, was fabricated and tested, and it successfully picked up each of the five layers while leaving the waste material behind in all cases.

A third recent advance in our material-handling challenge is the extension of our masked-gripper technique to manipulating tangent-cut sections. Figure 7 illustrates the potential problem of extracting a desired section of material when tangential cutting is employed. The figure represents a side view of a layer of a tilted cylinder cut from sheet stock, still surrounded by waste material. It is not possible to extract the desired section vertically without interfering with the waste material, nor is it possible to first extract the waste material vertically without interfering with the desired region. To solve this problem, we propose a second pass cutting trajectory in which the laser cuts the waste material as shown in the top view of Fig 7. The second-pass cut is oriented vertically, and it follows the upper contour of the desired region over those path segments bounding "overcut" regions (sections for which the surface normal of the layer's tangent-cut edge surface has a downward-facing component, thus blocking waste material from vertical extraction). The second pass cuts only through waste material. The result is that the waste material exposed to the top surface is then extractable vertically without interfering with the desired region. After the waste is extracted and discarded, the desired region is removable by vertical extraction without interference. The target slice can then be easily extracted, and what remains on the cutting table is discarded. This technique is still under development and testing, but it appears to be general enough to handle arbitrarily complex cases.

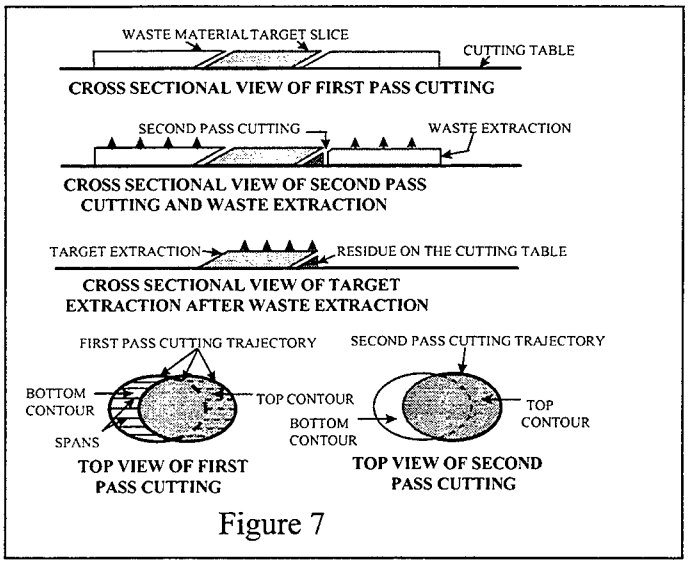


Figure 7

4. Tangent-cut Parts Fabrication

Our CAM-LEM tangential cutting system is comprised of 3 parts: a cutting tool, a cutting platform and a material handling module. Our cutting tool is a 50W CO_2 laser mounted vertically above the cutting table. The cutting platform consists of 3 translational axes (x,y,z) and two rotational axes (roll and pitch). This mobility enables the mechanism to position an arbitrary point on its cutting surface at an arbitrary orientation (within joint constraints) at the laser focal point. Our 5-axis mechanism carries a cutting table that clamps sheet feedstock to an aluminum honeycomb cutting surface by drawing a vacuum beneath the cutting surface. Material handling (loading, picking-up and stacking) is executed by 3-axis motion of a Cartesian robot with our selective-area vacuum gripper design as its end-effector.

Recent results of tangential cutting performance based on thick-slab, ruled-surface layered approximations of solid objects are presented here. Figure 8 shows the fabrication of a geometric test object consisting of the union of a 60mm-high cone with a 30mm-high rectangular prism. The object was defined in a CAD modeller, sliced at 11 slice planes, and redefined in terms of 10 layers with ruled-surface edges. The functional relationship defining the ruled-surface edges was used to define the path of the cutting tool. Motion of the cutting platform was derived from this tool path through inverse kinematics, as described in [11]. The ten layers were cut from 6mm sheets of polystyrene foam. (Our models were assembled by hand, since our automated material-handling concept for tangent-cut layers has not yet been implemented in our system).

Since each layer of the test object was defined in terms of ruled edges, a feasible tool path was guaranteed. Each ruled surface was approximated in terms of interpolation between more than 500 tabulated spans. Although this data constituted a feasible and accurate model, some trajectory modifications were required at run time. In particular, some of the spans near complicated regions required high joint velocities and accelerations to maintain a constant material removal rate. To avoid dynamically-undesirable or infeasible joint commands, the prescribed paths were preprocessed before execution to identify problem conditions. Cutting speeds were scaled down linearly (preserving the same path shape) in such regions to satisfy dynamic constraints. A consequence of this time scaling is that it was not possible to maintain a constant material removal rate, yet the laser power remained fixed. As a result, some overcutting (excessive erosion) occurred in regions where the trajectory speed was reduced. This problem should be relieved by coordinating laser-power modulation with cutting speed.

A second test part, a 22-layer reconstruction of a head, is shown in Fig 9. The tangent-cut layered head is compared to the corresponding 22-layer reconstruction using vertically-cut layers.

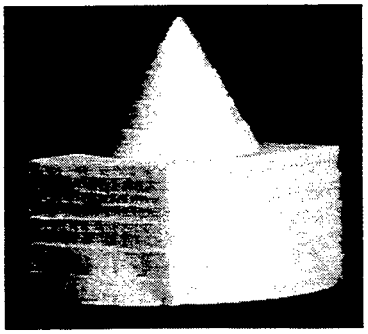


Figure 8: Simple, 10-layer geometric test part

The fabrication parameters for both of the tangent-cut test parts shown are summarized in Table 4.1. The present examples deliberately illustrate exaggerated cases of the advantages of tangent cutting. All 22 layers of the more complex test part (the head) could be cut in under 15 minutes using the quoted parameters (but ignoring material-handling time). In practice, thinner layers would be used to achieve greater precision, with corresponding increases in build time. Nonetheless, significant advantages in build speed can be expected relative to SFF systems

employing point-wise build techniques. More importantly, the CAM-LEM tangent-cutting process is applicable to a wide variety of materials in sheet form. We are currently working with tape-cast advanced ceramics (alumina and silicon nitride) and sheet-based powdered metals.

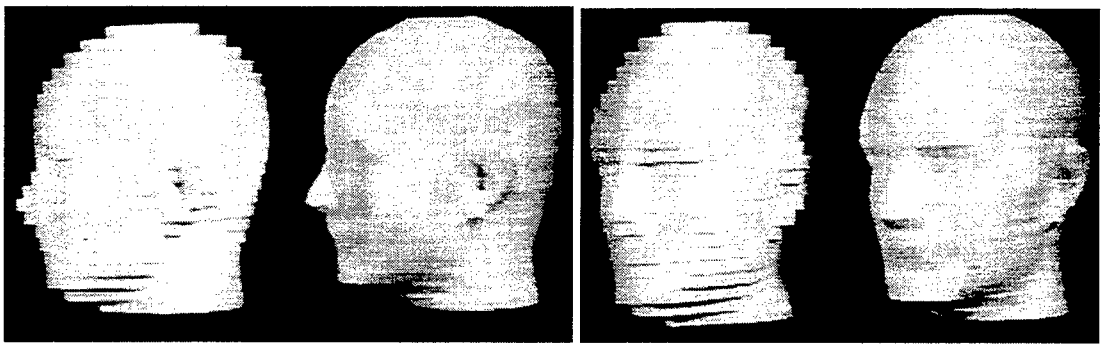


Figure 9: A 22-layer Model of a Head; vertical-cut layers vs tangent-cut layers

	part 1(Fig 8)	part 2(Fig 9)
max. cutting speed (mm/sec)	10.0	10.0
min. cutting speed (mm/sec)	2.5	1.8
max. tangent angle (degree)	34.280 (from vertical : in 1st slice)	71.562 (from vertical : in 1st slice)
part size (mm × mm × mm)	57.05 × 57.05 × 60.10	117.83 × 89.77 × 132.22
material (thickness : mm)	polystyrene foam (6.01)	polystyrene foam (6.01)
# of layers	10	22
# of spans at each layer	600	800
laser power (W)	36	30

Table 4.1 : Cutting Parameters and Part Specifications

5. Summary and Conclusions

This paper has presented our recent progress in CAM-LEM. We have emphasized the value of approximating solids in terms of relatively thick layers with ruled-surface edges, as such a description compactly captures the full model resolution achievable by line-of-sight type sheet cutters. At the same time, such a description guarantees the feasibility of fabrication of each layer using a line-of-sight cutter. This realization leads to a natural file format, which we have described as our "Layered File Format" (LFF). We argue that an LFF representation is optimal for sheet-cutting processes in terms of compactness, precision and ease of conversion to machine control.

We have also described our advances in automated mask generation for our masked vacuum gripper material-handling technique. Our new algorithm for mask design results in concentric, closed contours, leading to a uniform distribution of mask holes as well as an efficient trajectory for punching mask holes. The gripper technique is further extended to multi-use masks. Experiments verified the value of the approach using significantly dissimilar layers.

Finally, we have shown recent results from our 5-axis laser-cutting CAM-LEM system. Examples illustrate the value of tangent cutting, either in terms of surface finish or in build speed. Although the examples shown were fabricated from styrofoam, the process is applicable to engineering

materials. In ongoing work, we are developing procedures for fabricating tangent-cut, laminated objects from advanced ceramics and powdered metals.

Acknowledgments

This work was supported by the National Science Foundation under NSF grant DMI-94-20373, and by the Cleveland Advanced Manufacturing Program and industrial sponsors. This support is gratefully acknowledged. The work reported here is part of a multi-disciplinary program, and the authors recognize the contributions of team members professor James Cawley, professor Arthur Heuer, and Der-Lin Chow.

References

1. Lee, C. H., T. M. Gaffney, and C. L. Thomas, "Soft Tooling for Low Production Manufacturing of Large Structures," *in Solid Freeform Symposium Proceedings*, University of Texas at Austin, Austin, Texas, pp. 207-214, Aug. 1996.
2. Weiss, L., Prinz, F., Neplotnik, G., Padmanabhan, K., Schultz, L. And Merz, R., "Shape Deposition Manufacturing of Wearable Computers," *in Solid Freeform Symposium Proceedings*, University of Texas at Austin, Austin, Texas, pp. 31-38 , Aug. 1996.
3. Philippe Bonaldi and Claude Barlier , "Examination of Various Stochastic Algorithms . Research on Placement Methods Dedicated to the Rapid Prototyping Process : Stratoconception ," *Proceedings of the 6th European Conference on Rapid Prototyping and Manufacturing* , Nottingham , UK, July 1997 .
4. 3D Systems, Inc. *SLC File Specification*. Nov. 1994.
5. Brite-EuRam Projects. "Common Layer Interface (CLI) Version 2.0" available at internet web addreaa "http://222.cranfiled.ac.uk" and "http://www.cs.hut.fi~ado/rp/rp.html".
6. National Institute of Technology of Standards and Technology , Department of Commerce , USA (1991) , *The Initial Graphic Exchange Specification* (IGES) Version 5.1 .
7. Zheng, Y. And W. S. Newman, "Software Design Challenges for Computer-Aided Manufacturing of Laminated Engineering Materials," *the Sixth European Conference on Rapid Prototyping and Manufacturing*, Nottingham, UK, July 1997.
8. Zheng, Y., "Enabling Computational Techniques for Tangential-Building Solid Freeform Fabrication ," Ph.D Thesis , Aug. 1997 , Department of Electrical Engineering and Applied Physics, Case Western Reserve University .
9. DeBoor, C. *A Practical Guide to Splines*. Springer-Verlag, New York, 1978.
10. Newman, W. S., B. B. Mathewson, Y. Zheng and S. Choi, "A Novel Selective-Area Gripper for Layered Assembly of Laminated Objects," *Robotics and Computer-Integrated Manufacturing*, Vol.12, No.4, pp. 293-302, 1996.
11. Newman, W.S., Zheng, Y., and Fong, C. C., "Trajectory Generation from CAD Models for Computer-Aided Manufacturing of Laminated Engineering Materials," *in the proceedings of the 26th International Symposium on Industrial Robots*, Singapore, pp. 153-158, Oct. 1995 .

Optimising Build Parameters and Hatch Style for Part Accuracy in Stereolithography

S.O. ONUH and K.K.B. HON
Rapid Prototyping Centre
Department of Industrial Studies
The University of Liverpool, UK.

Abstract: A detailed study of the effects of layer thickness, hatch spacing, hatch overcure depth, and hatch fill cure depth on the quality of the StereoLithography (SL) product was carried out using acrylic based resin. Taguchi Method was used for analysing all experimental results. The ANOVA and the Signal-to-noise ratio (S/N) results were used to select the optimum parameters and the appropriate factor levels for further experiments. A new hatch style with an optimum layer thickness is proposed for the build process with minimum geometrical distortion.

1.0 INTRODUCTION

The activity of manufacturing has been practiced by mankind for thousands of years with a ceaseless drive towards improvement and innovation. Manufacturing industries are one of the key makers of a successful economy. All nations in the world are striving towards a strong manufacturing base capable of changing to the needs of fluctuating markets. Manufacturing creates wealth and opportunity bringing with it an increased quality of life which can be a direct result of the consumption of goods or the production of goods. A strong manufacturing base is the key to economic success which is achieved with increased efficiency and productivity. Very few technologies have offered as much as rapid prototyping technologies (RPT) have in the last few years. One of such important new tool in RPT is Stereolithography (SL), a technology that let us transform digital designs into 3-dimensional solid objects for production of machine parts, models, prototypes, and moulds Components can now be produced in a fraction of the time that was required previously with the added benefits of reduced costs and more design iterations. Designers have been released from old constraints with new tools from the array of RPT. Managers must take on new business practices, designers must understand the power at their fingertips , process engineers need know of the new process routes and marketing personnel must be aware of their new found ability to react quickly to market changes. Without doubts, products with outstanding quality, satisfying a market niche, are pre-requisites for a successful company.

The main process stages involved in fabricating parts are common to most systems, but the mechanisms by which the individual layers are created obviously depends on the particular system. A schematic for SL is as shown in **figure 1.**

2.0 RESEARCH RATIONALE

One of the most challenging goals of Rapid Prototyping is the generation of accurate and dimensionally stable parts. The ultimate dimensions of a part built on a layer by layer basis depend on many factors that must be carefully balanced to produce accurate parts . **Laslie et al (1991)** concluded that the inability to understand and control these parameters has leads to many problems including post-cure shrinkage, swelling, cantilever curl distortion, vertical wall post-cure distortion and horizontal slab distortion. In their work, **Murphy et al,. (1988),** concluded that an unfortunate fact of acrylate polymerisation is shrinkage and the attendant residual stresses which reside in the cured parts. This stresses often result in the distortion of the work piece.

The problem of dimensional and form accuracy, and surface finish has been discussed by several authors and a number of ways to minimise it have been proposed. What is required for industrial applications are functional metal prototypes. These components are often needed early in a project to determine not only form and fit but function as well.

Despite significant advancement in build styles and material properties, there has been no such perfect part. **Dickens (1995),** commented that all the commercial Rapid Prototyping Systems can only produce for now in materials that are not suitable for production tooling. But he agrees that the emphasis has changed over the year from Rapid Prototyping to Rapid Tooling.

Previous investigations **(Gargiulo, 1992)** have shown that it is not only important to observe the overall shrinkage (liquid to solid transition) to achieve good part accuracy but also the polymerisation dynamics which influence both the mechanical properties and the shrinkage are significant. In some related works, **(Wiedemann et al 1995; Konig et al 1994)** the use of hatch strategies has been proposed. Hatch strategies are understood to mean the specific configuration in terms of duration and location of individually polymerised lines to describe the respective cross-sectional area on the resin surface. So the use of hatch strategies is intended to reduce or compensate the accumulation of internal stress resulting from polymerisation shrinkage.

Konig et al. concluded that when layers are scanned in only one direction, shrinkage forces occur mainly in the scanning direction which results in one-sided curling of the parts. An alternating exposure of the layers resulting in a more homogeneous structure of residual stress in the part and to a higher part stability was therefore proposed. Based on this proposal, the *Divergent STAR-WEAVE* (DSW), shown in **figure 2** was developed. This development is based on the hypothesis that if alternating the exposure of the layer will homogenised the residual stress structures, starting the hatching from the middle of the part and alternating it will normalise the residual stress to give a more uniform distribution of the stress. This will result in a more accurate and dimensionally stable parts.

In this research work, the effects of the parameters shown in **table 1** on the product quality will be experimentally determined. The definition of these factors are as follows:

1. ***Layer thickness:*** The three-dimensional objects are sliced into series of constant thickness, two-dimensional layers to be solidified by the UV laser. Each two-dimensional layer is solidified on the photopolymer surface with a specific hatch style selected by the user.

2. ***Hatch style***: Hatching or printing is the process of solidifying the cross section of a layer of the model to be built.
3. ***Hatch spacing***: Hatch spacing is the distance between parallel vectors used to hatch the interior of the part. If the hatch spacing is very small, the solidifying vectors will overlap causing a completely solid layer. Large hatch spacing allow liquid polymer to be trapped in the part to be solidified in the postcuring operation.
4. ***Hatch overcure***: Hatch overcure is the depth that one cured vector string pierces into the lower adjacent layer. This is what keeps the individual layers connected together to form a complete part.
5. ***Hatch fill cure depth***: Fill cure depth is the depth of the solid layers formed on the upper and lower faces of the solid. This holds the remaining liquid inside the part for subsequent post-curing.

In this type of experiment, the Taguchi method for full and fractional factorial is most suitable according to **Box, et al (1978).** Hence, the Taguchi method was used for the selection of the experimental parameters. By using Taguchi method therefore, a full factorial experiment with an L8 array is required (i.e. 2^3) giving a total of eight experimental runs. However, an L4 array - fractional factorial as shown in **table 1** and **table 2** which satisfies the conditions proposed by Taguchi in **Box, (1978)**, were used.

In this work, the hatch style chosen is the STAR-Weave™. This is because as stated above it is the most advanced build style by the systems' vendor which gives the best dimensional accuracy and surface finish with the acrylic resin. Apart from the STAR-Weave™ the other hatch style developed for this study is the DSW and the scanning technique is done as shown in **figure 2.** In this technique, the scanning is commenced from the middle of the part in such a way that half of the part is first scanned from the middle to one end and the other half is then scanned from the middle to the other end. This process is repeated in either x or y-direction as done in STARWEAVE™.

3. EXPERIMENTAL METHODS

The following equipment were used in this investigation: Sun Sparc 10 and Silicon Graphics Indigo Workstations, 3D Systems StereoLithography Apparatus SLA - 250 series 40, and Post Curing Unit (PCU). The entire investigation was conducted in the Rapid Prototyping Centre and all dimensional measurements were taken from a Mitutoyo BHN-706 CNC Co-ordinate Measuring Machine (CMM) with an accuracy of ±5μm. As for the surface finish measurements, a Taylor-Hobson Talysurf model surtronic-3 was used with a wavelength cut-off of 2.5 mm. The experimental part as shown in **figure 3,** was designed in DUCT5.

4.0 RESULTS AND DISCUSSIONS

Figure 4 shows the flatness of the experimental models for the two hatch styles and the experimental runs for the 0.125 mm layer thickness. The flatness is calculated from the measurement taken at different points on the surface of the models. This is the XY-plane ABCD shown in **figure 3.** The SW hatch style gives the least average values of 0.388 mm for the flatness. This is the third experimental run (R_3). The smaller the flatness the better for a flat part. From ANOVA, R_3 consistently gives the highest S/N values for all the four runs

and also the least sensitive values. This implies that for a flat part, the SW hatch style is more robust than DSW hatch style. The three factors are also consistently statistically significant in all the states of the model (i.e. green, cured or detached).

As for the DSW hatch style in the green state, all the three factors are statistically significant while factor C is not statistically significant in the cured and detached state. In addition, the percentage contribution of factor B is significantly higher than the percentage contributions of the other two factors in either green, cured or detached state of the part. This suggests that for the DSW hatch style, controlling factor B will significantly affect the flatness of the part. The significant effect of factor B may be due to the mechanics of curing which is dependent on the hatch style. It was discovered that R_1 which has a higher value of overcure depth, consistently gives higher S/N values than all the other runs. Hence factor B can be said to significantly affect the quality of a flat SLA model. In the confirmation experiment, R_2 of DSW or R_1 of SW may be used for the confirmation experiment.

For the layer thickness of 0.190 mm, the average flatness value does not follows a similar pattern as observed in the results for the 0.125 mm layer thickness where the SW hatch style gives the minimum average flatness. From **figure 5** which is a plot of the flatness for the 0.190 mm layer thickness and the two hatch styles, the DSW hatch style gives the minimum average flatness value. This suggests that hatch method and the layer thickness do significantly affect the flatness of a part. From ANOVA data, R_4 gives the combination for the optimum condition for the DSW hatch style while in SW hatch style is R_3. Factors A and B are consistently significant for all the hatch styles in all the runs. Where factor C is significant it is at level 1 and its percentage contribution is least and this seems to suggest that for DSW hatch style, the flatness is determined by the effect of factors A and B. In DSW hatch style the percentage contribution of factor B is the second highest but it is least sensitive to variability. For further experiments as to confirm which combination of factors and at what level will give the optimum value, DSW hatch style will be used with R_4 or R_3 combination. This is because R_4 and R_3 with DSW hatch style gives the minimum value of flatness and this is more robust.

For the layer thickness of 0.250 mm, there seems not to be a similar pattern to what was observed in the flatness results for the 0.190 mm layer thickness. However, it is similar to what was observed in the results of the 0.125 mm layer thickness where SW hatch style gives the least value of flatness as shown in **figure 6** for 0.250 mm layer thickness. This suggests that both the hatch style and the layer thickness affect the flatness of the model.[ref] From the ANOVA data, R_4 gives the optimum combination for SW hatch style while for DSW hatch style it is R_1 hatch style. Factor C is consistently significant for SW hatch style in all the stages while factor A is only significant in the cured state. As for DSW hatch style all the three factors are significant but the percentage contribution of factor A is higher than the other two factors while the percentage contribution of factor C is the least. Since factor C deals with the surface, it should be better to contribute more and this may explained why the flatness is least is SW hatch style where factor C is not only statistically significant but also the percentage contribution is the highest of the three factors. As for the DSW hatch style it is more robust with factor A at level 2, factor B at level 2 and factor C at level 1. Hence changing the factors A and B levels may give a very robust design. It will therefore be a good idea to carry out further experiment with R_2 of SW hatch style or R_2 of DSW hatch style to confirm these findings.

5.0 CONFIRMATION EXPERIMENT

For the confirmation experiment, R_3 with DSW was used after considering other factors and their effect on the process mean. **Figure 7** shows the flatness of the part for the three different layer thicknesses. The chart shows that there is a significant improvement in the flatness as a result of the optimum factor combination which has been used. There is about 15% improvement in the flatness of the part for the 0.125 mm, 64% for the 0.190 mm and 80% for the 0.250 mm layer thickness. These low values of the flatness confirms that the optimum combination is in line with Taguchi philosophy of the smaller-the-best.

	Level 1 (mm)	Level 2 (mm)	Level 3 (mm)
Layer thickness	0.125	0.190	0.250
Hatch spacing (A)	0.210	0.200	
Hatch overcure (B)	-0.04	-0.035	
Hatch fill cure depth (C)	0.250	0.200	

Table 1 List of experimental parameters and their factor levels.

		FACTOR/LEVEL		
		A	B	C
No.1	R_1	1	1	1
No.2	R_2	1	2	2
No.3	R_3	2	1	2
No.4	R_4	2	2	1

Table 2 Experimental Runs and Level Combination.

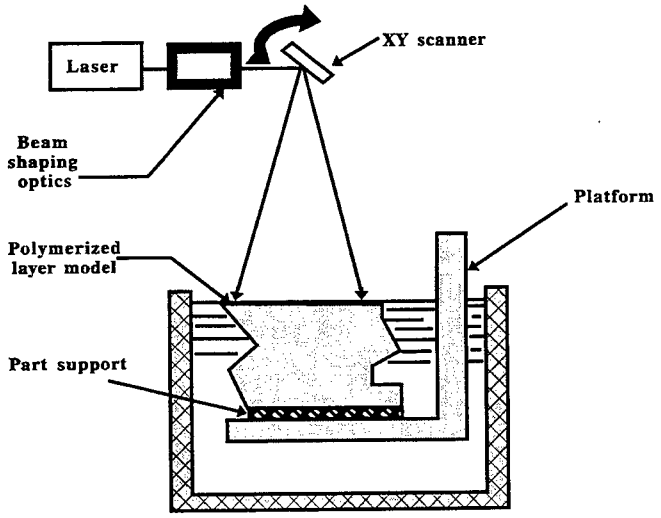


Figure 1 Schematics of Stereolithography.

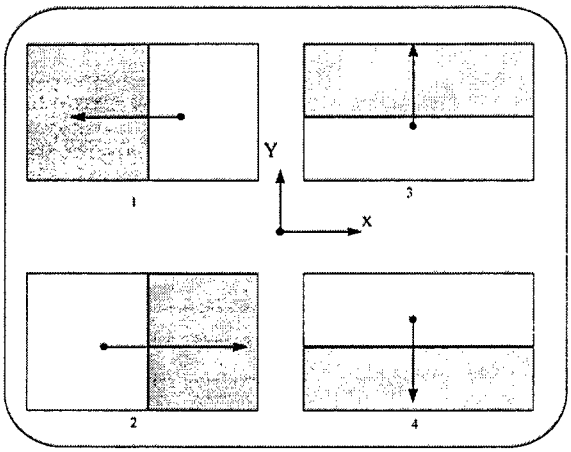


Figure 2 Schematic of DSW hatch style.

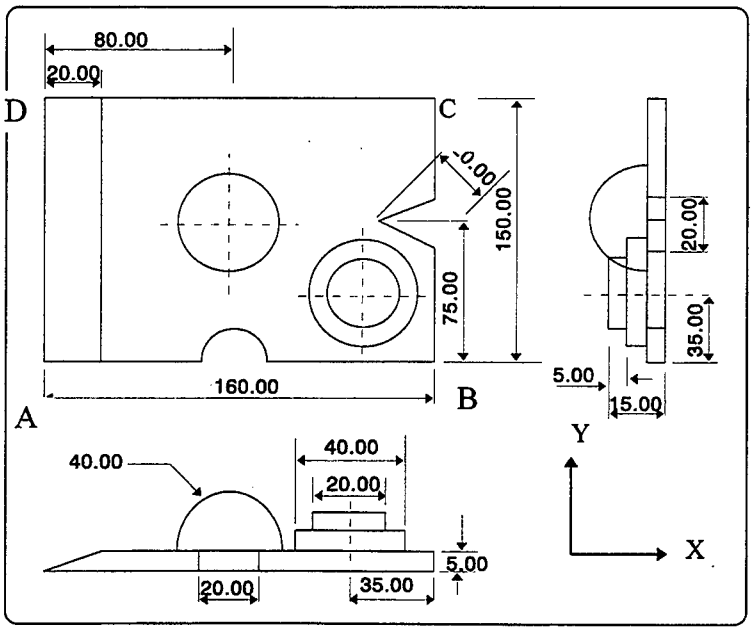


Figure 3 The Experimental Model.

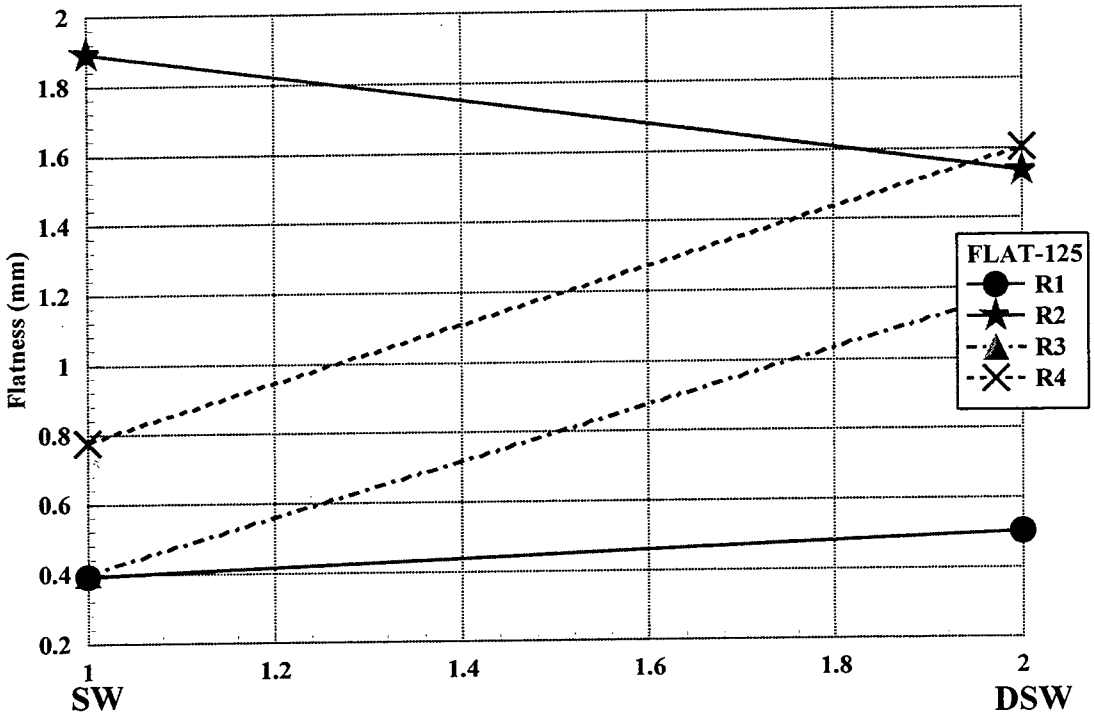


Figure 4 Average flatness values for the 0.125 mm layer thickness.

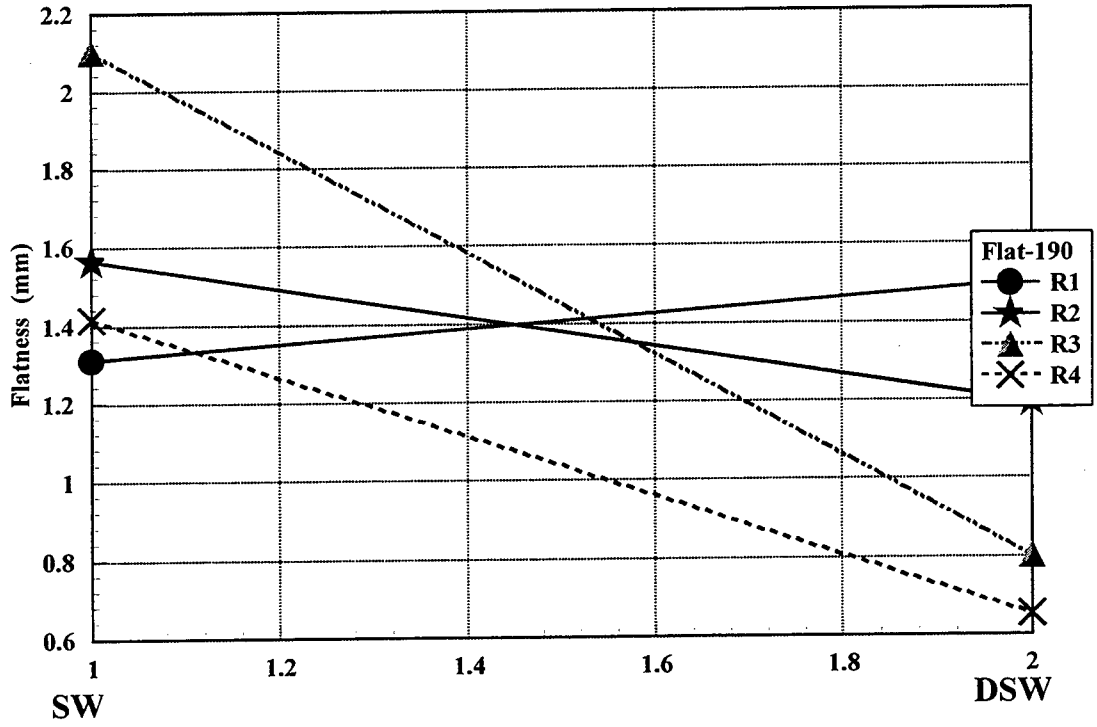


Figure 5 Average flatness values for the 0.190 mm layer thickness.

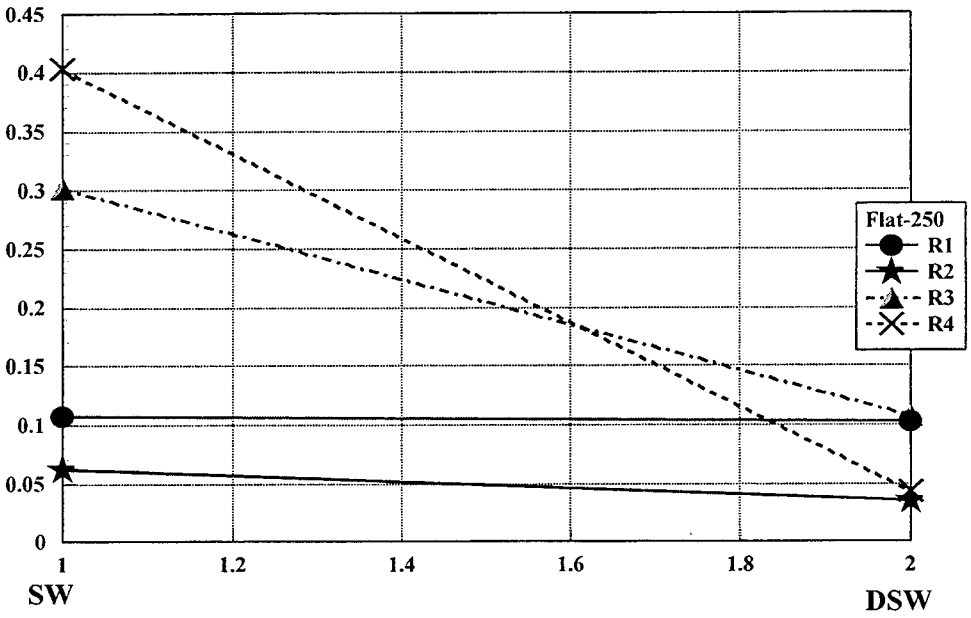


Figure 6 Average flatness values for the 0.250 mm layer thickness.

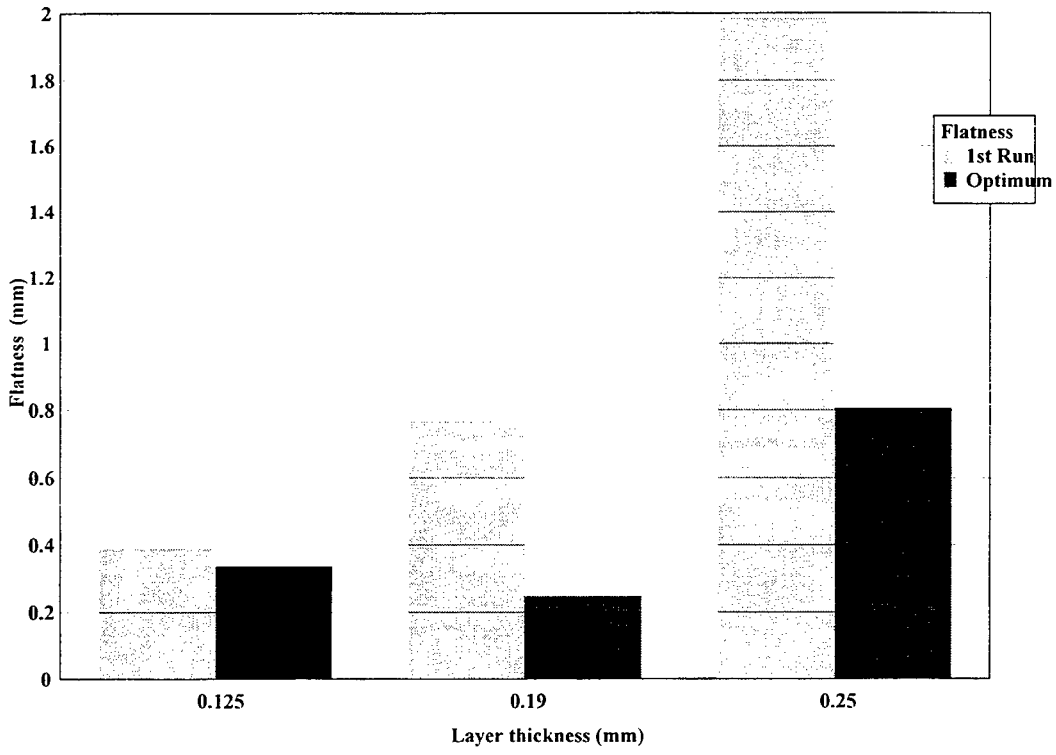


Figure 7 First run and confirmation experiment values for the flatness.

An Integrated Software System for Process Planning for Layered Manufacturing

Anne L. Marsan, Seth Allen, Prashant Kulkarni, and Deba Dutta
CAD/CAM Group
Department of Mechanical Engineering and Applied Mechanics
The University of Michigan, Ann Arbor
http://www.engin.umich.edu/dept/meam/deslab/cadcam

Abstract

An integrated process planning system for layered manufacturing (LM) reduces the time between design and part fabrication and improves the quality of the final part. Process planning for most LM processes includes part orientation, support structure generation, slicing, and path planning. In this paper we describe an integrated process planning system we are developing. Our software accommodates both novel and traditional design models as input, and supports a variety of LM processes. The modules described in this paper include Solid Builder Module, which generates a solid model from design data such as medical images, surface functions, or digital elevation models; Orientation Module, which determines the optimal build orientation of a part and automatically generates the support structures required; and Adaptive Slicing Module, which adaptively slices the part.

Introduction

Process planning for layered manufacturing (LM) is performed to generate the tool paths and process parameters for an object that is to be built by a particular LM process. The steps required are: part orientation, support structure generation, slicing, and path planning. The orientation of a part as it is built will affect the time to build the part, mechanical properties, surface quality and the need for support structures. Thus the first task is to determine an optimal orientation based on those criteria which are most important to the designer. With certain LM processes, layers which form overhangs or enclose voids must have a sacrificial support structure beneath them to support build material as it is added. Supports are built along with the part, possibly by a different material. Once an orientation for the part has been selected, support structures are designed. Then the part and its supports are sliced into manufacturing layers and finally tool paths are generated.

A process planning system is under development by the CAD/CAM Group at the University of Michigan Department of Mechanical Engineering and Applied Mechanics which is the synthesis of several software modules. The software accommodates both novel and traditional design models as input, and supports a variety of LM processes. The system currently has three component modules. The first, Solid Builder Module (SBM), receives design data in the form of planar images and assembles from them a B-rep solid model of an object. This solid model then becomes input to the other two modules in the system. The Orientation Module (ORM) finds the optimal build orientation for an object and generates support structures for it. The Adaptive Slicing Module (ASM) slices the solid model of the object and generates the necessary command files for driving a particular LM process. The final process planning step, path planning, is not treated

in this paper because we currently use commercial software for this step. A schematic of the software system is shown in Figure 1. Each highlighted module is described in greater detail in the following sections.

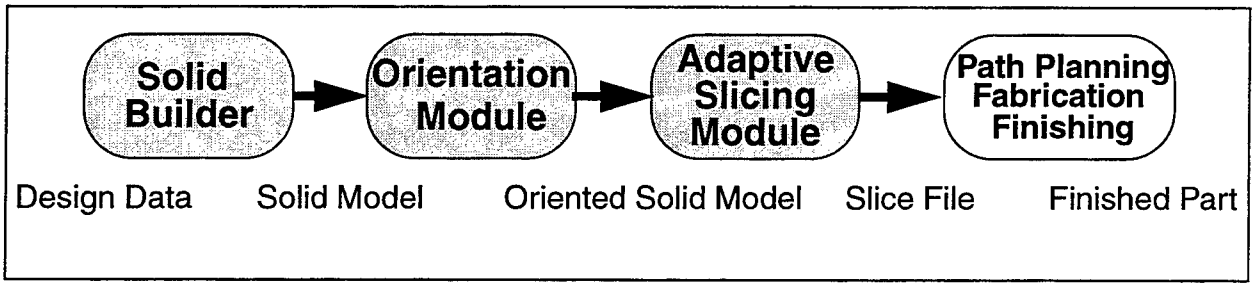


Figure 1. The structure of our software system

Our process planning system has the advantage that it accommodates both traditional and novel design inputs. The engineer can begin process planning with either a solid model of an object (in which case the SBM is bypassed) or image data. A second advantage is that the design model does not need to be converted into an .STL file in order to be read into the system. This increases the potential accuracy of the fabricated part and eliminates the need for .STL correction and repair. Finally, our system automates the process planning tasks resulting in high quality parts in lesser time.

Solid Builder Module

Inputs

The Solid Builder Module takes as input design data and generates a solid model which is then used to prepare for part manufacture. Currently this module accepts implicit (algebraic) surfaces and stacks of planar images (derived from or representing an object). Images can come from a variety of sources including CT and MRI scans (medical images), DEMs (Digital Elevation Models - images representing the elevation of the earth in a certain location), and finite element models from topology design software.

While the sources that produce CT, MRI, and DEM images are not traditionally considered design tools, they can be used as a first step in the design or redesign of, for example, a prosthetic device or physical model of a particular geographic terrain. Finite element models can be treated as a stack of images as long as the structure is modeled with regular brick elements. Each layer of brick elements can be treated as a planar image, each brick translating into a single pixel. Novel structural design software, such as OptiStruct, which is based on a homogenization method developed by Bendsøe and Kikuchi [1], takes a design envelope which has been discretized into brick finite elements and determines the density of material that should be present in each of the elements to form the stiffest structure possible. Thus we can treat the output of this software as a stack of planar images representing a structure and use it as input to the SBM. An example of image data is shown in Figure 2.

Algebraic surfaces that are input to the SBM are converted to a stack of planar, binary images. A z-value is associated with each image, and the pixels within each image represent an x, y cartesian coordinate. A 1-pixel represents a point on or below the surface and a 0-pixel indicates a point above the surface.

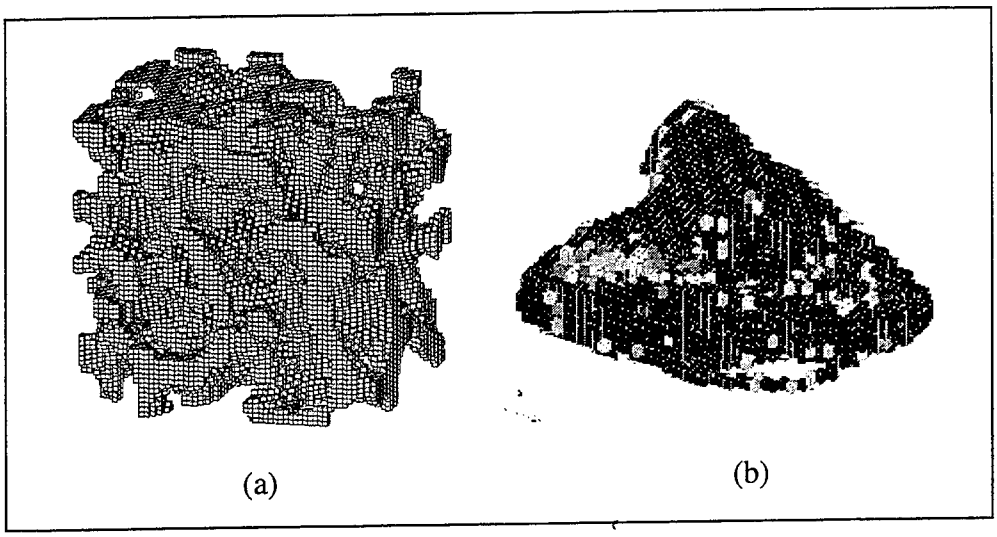


Figure 2. Examples of image data that can be input to the Solid Builder module (a) segmented CT data of bone microstructure (b) finite element model of a suspension arm

Images representing an object composed of a single material will be binary. In other words, the pixels in the images will have a value of 1 if the pixel represents material and 0 if it represents void. However, in the engineering world objects are often composed of more than one material, or material properties can vary throughout an object. In this case, the object will be represented by gray scale images, where a particular gray value is assigned to each individual material or it indicates some material property such as density. This material information that is present in the image model of the object should be passed along to the solid model which is generated. Work is being done to develop enhanced solid models which can represent material in addition to geometry/topology. See for example [2] and [3].

Model creation

Given a stack of planar images, the SBM begins constructing a solid model of the object by extracting points from the boundary of each material region in each image. These become control points for contours which are formed by B-spline curves. Often objects are multi-branched and require several surfaces to completely describe them. For this reason, the contours are then grouped into individual branches of the object and separate B-spline skinning surfaces are fit to each contour group. The surfaces are modified at their ends so that where they touch adjacent surfaces, they join smoothly. In addition, if the contours in a group are non-convex, care is taken in choosing knot values for the surface so that it is continuous and non-twisted. Planar surfaces are fit to the end contours in each group and stitched to the skinning surfaces to form a B-rep solid model of each branch of the object. The union of all branch solids forms the complete solid model of the structure. We use the ACIS geometric modeling functions and data structures for storing and working with our solid models. For complete details on the algorithms used in this module, see [4].

Often a design represented by a stack of planar images can be built in the orientation indicated by the stack direction. In this case, generating a solid model for input into the ORM and the ASM is not necessary. If the images are spaced close together, simply extracting the boundaries of each material region within each image and storing them in a slice file is sufficient. For images

spaced farther apart than the maximum resolution of the desired LM process, two approaches can be taken. First, we can interpolate intermediate images between two given images and then extract the boundaries of each material region in this augmented stack of images. This can be expensive if the images are large and quadratic, cubic or higher order interpolation is used. The other approach is to extract the boundaries of each material region from the given images, form contours from the boundaries, group the contours, and interpolate between contours. All of these slicing techniques have been implemented in the SBM module and yield uniformly spaced slices. If support structures are required for fabrication, they must be generated by a separate software module.

Implementation

The SBM has been implemented in the C programming language on the Sun, HP, and SGI platforms and is currently being used by the CADCAM Group to prepare objects represented by images for LM. The user supplies the image data (DICOM version 3.0 Implicit VR Little Endian format, United States Geological Survey 1 degree Digital Elevation Model format, or OptiStruct .fem and .sh files) which is read in and displayed on the screen. The images must be segmented (several image processing operations are provided) and thresholded if they are not already binary. To generate the solid model, the user must indicate the maximum degree of surfaces desired in the u and v directions, the number of filtering passes desired for the control points (to reduce wiggle in the skinning surfaces), and the minimum area of overlap for two contours to be placed in the same group. The software then groups the contours, modifies the end contours of each group, fits skinning surfaces, caps the ends of each group, and performs a Boolean intersection of each group to get the final B-rep solid model of the object. It is saved in an ACIS .SAT file.

The purpose of the Solid Builder module is to take non-traditional design information for an object and build a B-rep solid model. However, quite often a part is designed using a CAD package such as Unigraphics or AutoCAD, so a solid model of the object is available upon completion of the design process. In this case the Solid Builder module is not required and the engineer can directly employ the ORM and/or the ASM.

Orientation Module

Orientation Determination

The Orientation Module determines the optimal build orientation based on one of the following criteria: minimum build height, minimum support contact area, maximum area of base, minimum volume of supports, or minimum average surface roughness. Minimum build height corresponds to less build time. Minimum support contact area and minimum average surface roughness improve the surface accuracy of the final part. Maximum area of base improves the stability of the part as it is being built and often corresponds to less build time. Minimum volume of supports decreases the amount of wasted material.

Orientations are determined by first faceting the solid model, which results in a list of points lying on the part's surface. The convex hull of these surface points is then found. Each face of the convex hull becomes a potential base for the object, thus indicating a possible part orientation. For each possible orientation, the objective function is evaluated and the orientation which minimizes (or maximizes) it is selected.

The build height of the object is measured by finding the bounding box of the object in the candidate orientation and measuring the height of the box in the z-direction. The base area of the

object is found by projecting the part onto the x-y plane and measuring the resulting area. For each facet in the object, the surface normal indicates the angle the facet makes with the build direction. Facets whose normal is not perpendicular to the build direction will suffer from the stairstep effect. The distance from the manufactured surface to the desired surface is called the cusp height (see Figure 3). This can be computed for each facet based on the angle its normal makes with the build direction. The average surface roughness R for a particular orientation is

$$R = \frac{\sum_{i=1}^{nfacets} d_i A_i}{\sum_{i=1}^{nfacets} A_i} \quad (1)$$

where A is the area of a facet and d is its cusp height.

Measuring the support contact area and volume of supports requires that the support structures for the object in the candidate orientation first be found. First the surface normal is computed at each point sampled in the orientation step. If the surface normal at a point has a negative z component, the point is Type-s and may require supports. For each Type-s point, we determine if adding support structure at it will prevent the part from toppling over, support a floating component, or support an overhang. If this is the case, the point is tagged as requiring support structure. Now the object is projected onto the x-y plane to form an extended base. The base is divided into a dense, regular grid. If the projection of a Type-s point requiring supports falls into a grid rectangle, a ray is fired from the center of that rectangle up in the build direction. Thin, columnar support structures are constructed up from the base to where the ray intersects the part. Once those facets requiring supports have been determined, their area is summed to determine the support contact area. Volume of supports is found by measuring the area of the facets requiring supports and the height of each facet.

After the optimal orientation has been found, the original solid model of the part is transformed to this orientation and written out to a file. This transformed object becomes input to the ASM. See [5] for more details on the ORM.

Implementation

The ORM has been implemented in C++ and makes use of the ACIS geometric modeling kernel. It runs on the Sun and HP platforms. This module accepts both ASCII .STL and ACIS .SAT files (representing either a surface or solid model of a part) as input, and produces .STL or .SAT output depending on the type of input. The user indicates how many possible orientations should be displayed (these correspond to the largest faces of the convex hull in descending order) and the maximum angle a surface can make with the build direction without requiring supports. The module saves a file of the object in its optimal orientation as output.

Adaptive Slicing Module

Slicing procedure

The ASM takes the solid model of the object and adaptively slices it to minimize the error in the final manufactured part due to the stairstep effect. Thus where the curvature of the part is

greater, the slices will be thinner. The slice thickness of a part at a particular z-level is determined such that the cusp height - the distance between the 2.5D manufactured slice and the original object surface - is equal to or below a user specified maximum distance. Figure 3 illustrates the cusp height for a layer of a curved surface. By adaptively slicing a part, surface accuracy can be improved without a large increase in the time required to build the part.

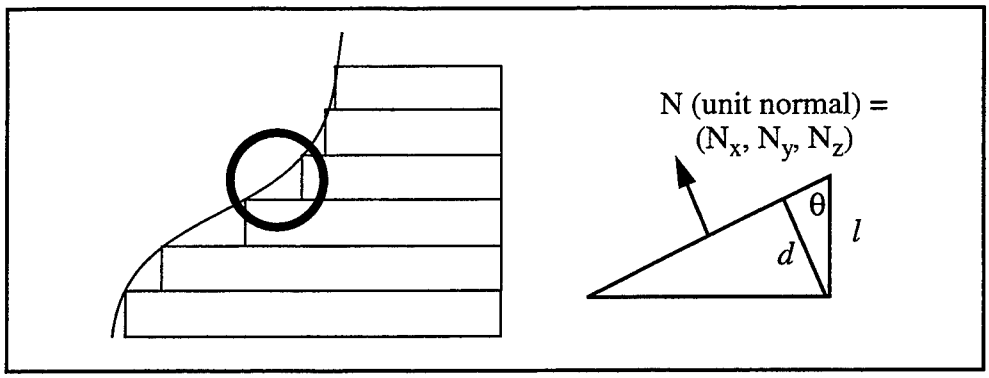


Figure 3. Illustration of cusp height (*d* is cusp height, *l* is layer thickness)

The software begins by determining the base slice for the part. Then given a point on a contour in the current slice, the normal curvature κ_n of the surface in the slicing direction is calculated. We can approximate the normal section of the surface at the considered point with a circle of radius $\rho = 1/\kappa_n$. Depending on whether the manufactured layers should be completely contained within the solid model of the part or vice versa (we refer to this as deposition strategy), the maximum allowable layer thickness *l* at the considered point on the surface is calculated using the allowable cusp height *d*, ρ, and the angle the surface normal makes with the build direction θ. As we move around the contour, *l* varies with ρ and θ. An SQP algorithm is used to find the minimum value for *l*. See [6] for more details.

Implementation

The ASM has been implemented in C++ using the ACIS geometric modeling kernel. It runs on the Sun platform. The module accepts ACIS solid models as input (.SAT files) and requires the user to supply the maximum allowable cusp height, the deposition strategy (manufactured part contained within the envelope of the solid model of the part or vice versa), and the minimum and maximum allowable slice thicknesses (dictated by the chosen LM process). Slices are generated and are written to a slice file. Currently both the 3D Systems and Stratasys .SLC files are supported.

Example

In Figure 4 we show an example structural part that begins its life as a collection of planar images and results in a model fabricated by a LM technique. The part was designed using a structural topology optimization software and subsequently the SBM was used to generate a B-rep solid model. This solid model then became the input to the ORM module, which determined the optimal orientation of the part and generated the necessary support structure. The part was then sliced using the ASM and finally built by the Stratasys FDM process.

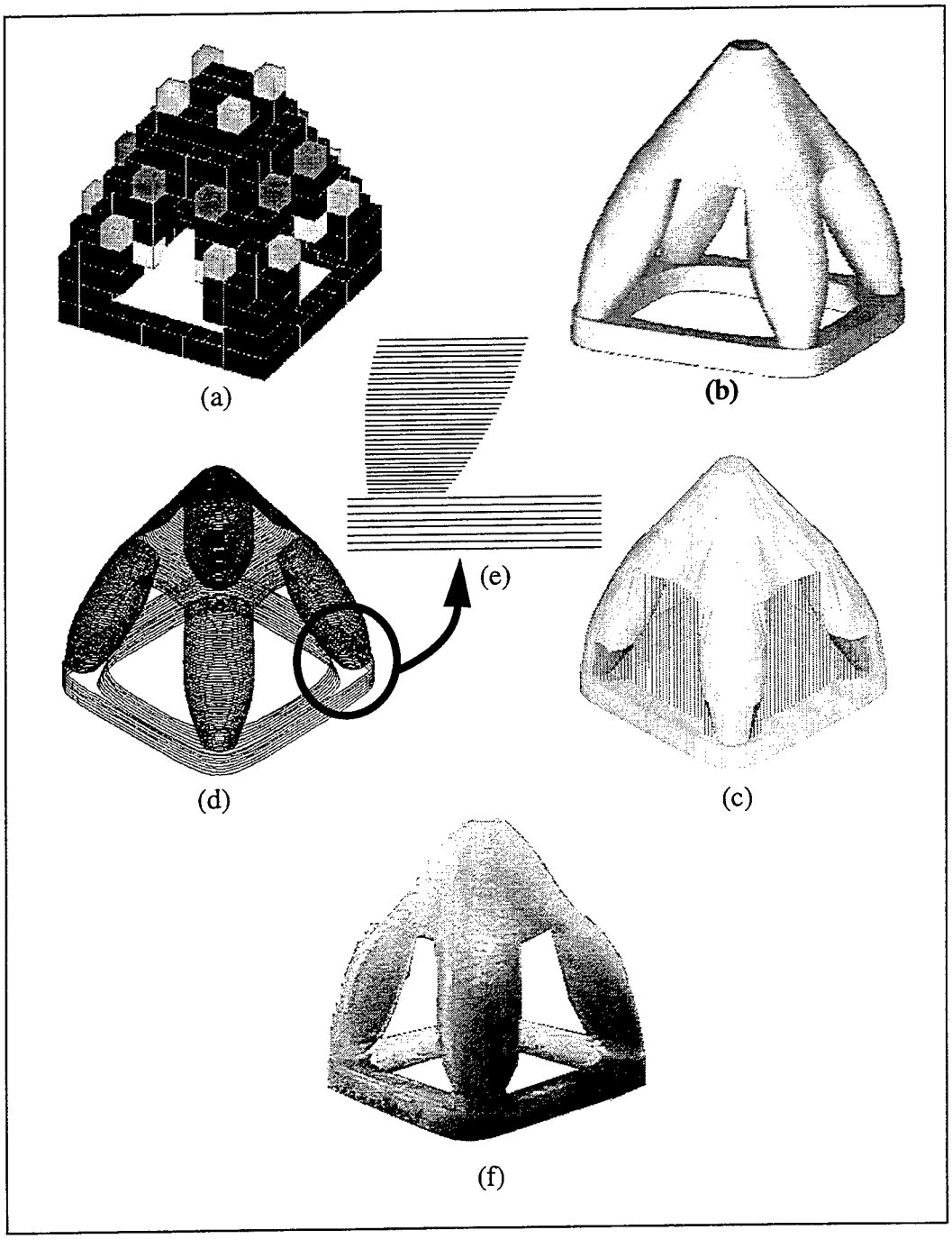


Figure 4. Structural example: (a) Image data (b) Generated B-rep solid (c) Optimal orientation and generated support structures (d) Slices (e) Close-up of slices (e) Fabricated structure

Future Work

The three modules which make up our LM process planning system thus far are currently in the final stages of development. Further enhancements and improvements will allow the engineer more flexibility in using them. In addition, new modules can be added to the software system

as changes in the design and manufacturing processes continue. For instance, a technique for selectively thickening the walls of thin-walled objects so that they can be built without supports is being investigated and a module to be added to our system is under development [7]. We have thus far used commercially available software for path planning after contours are generated. However, we are now developing tools to aid the engineer in choosing a deposition strategy to decrease the time to build a part and increase its stiffness and strength [8]. Finally, we are investigating different file formats for the transfer of design data to process planning software, process planning data between different process planning tools, and process planning data to the various LM hardware tools in an effort to develop appropriate neutral file formats [9]. (Readers may check our website given on the title page for software developments and usability status.)

Acknowledgments

The support of grants ONR N00014-94-1-0022, ONR N00014-95-1-0767 and NSF DDM-9300326 during the development of this software system is gratefully acknowledged.

References

1. M. Bendsøe and N. Kikuchi, "Generating Optimal Topologies in Structural Design Using a Homogenization Method," *Computer Methods in Applied Mechanics and Engineering*, vol. 71, 1988, pp. 197-224.
2. V. Kumar and D. Dutta, "An Approach to Modeling Multi-Material Objects", *Proceedings of the 4th Symposium on Solid Modeling and Applications*, Atlanta, GA, May 14-16, 1997 pp. 346-355.
3. V. Kumar and D. Dutta, "An Approach to Modeling Heterogeneous Objects", *Proceedings of the 1997 Solid Freeform Fabrication Symposium*, Austin, TX, August 1997.
4. A. Marsan and D. Dutta, "Construction of a Surface Model and Layered Manufacturing Data From 3D Homogenization Output". *Journal of Mechanical Design*. vol. 118, no. 3, 1996, pp. 412-418.
5. S. Allen and D. Dutta, "Determination and evaluation of support structures in layered manufacturing". *Journal of Design and Manufacturing*, vol. 5, 1995, pp. 153-162.
6. P. Kulkarni and D. Dutta, "An Accurate Slicing Procedure for Layered Manufacturing", *Computer Aided Design*, vol. 28, no. 9, 1996, pp. 683-697.
7. S. Allen and D. Dutta, "Wall Thickness Control in Layered Manufacturing," *Proceedings of the 13th ACM Symposium on Computational Geometry*, Nice, France, June 4-6, 1997, pp. 240-247.
8. P. Kulkarni and D. Dutta, "Deposition Strategies and Resulting Part Stiffness in Layered Manufacturing," *ASME Journal of Manufacturing Science and Engineering*, in review, 1996. Currently available as Technical Report UM-MEAM-96-17, Dept. of Mechanical Engineering, The University of Michigan, Ann Arbor, MI, 48109.
9. V. Kumar and D. Dutta, "An Assessment of Data Formats for Layered Manufacturing", *Advances in Engineering Software*, vol. 28, no. 3, April 1997, pp. 151-164.

The Use of VRML to Integrate Design and Solid Freeform Fabrication

Yanshuo Wang Jian Dong * Harris L. Marcus
Solid Freeform Fabrication Laboratory
University of Connecticut
Storrs, CT 06269

ABSTRACT

The Virtual Reality Modeling Language (VRML) was created to put interconnected 3D worlds onto every desktop. The 3D VRML format has the potential for 3D fax and Tele-Manufacture. An architecture and methodology of using VRML format to integrate a 3D model and Solid Freeform Fabrication system are described in this paper. The prototype software discussed in this paper demonstrates the use of VRML for Solid Freeform Fabrication process planning. The path used from design to part will be described.

1. INTRODUCTION

The STL or Stereolithography format, established by 3D System, is an ASCII or binary file used in Solid Freeform Fabrication (SFF). It is a list of the triangular surfaces that approximate a computer generated solid model. This file format has become the *de facto* standard for rapid prototyping industries. But STL format has the limitation of visualization, communication and sharing information among different places. In the recent years, Tele-Manufacture has become a new area in the design and manufacture research. Researchers try to create an automated rapid prototyping capability on the Internet (Bailey, 1995). In order to improve the communication and information exchange through Internet, a new data format is needed for SFF. Bauer and Joppe (1996) suggested to use Virtual Reality Modeling Language (VRML) data format as standard for rapid prototyping. VRML was created to put interconnected 3D worlds onto every desktop and it has become the standard language for 3D World Wide Web. VRML is also a rapidly emerging industry standard for exchanging three-dimensional data over Internet, and has the potential for 3D fax and Tele-Manufacture. This paper describes the use VRML as 3D model description for the SFF process planning. The path used from CAD system to SFF part is described.

2. SFF PART DATA EXCHANGE FORMATS

Several intermediate data formats have been developed to transfer the 3D geometry information to the process planning for SFF.

The STL file is the most widely used standard for SFF processes. This format represents a solid object by approximating the object surface with a collection of triangular facets. The STL file format allows for the representation of triangles and their normal vectors. Several limitations of the STL format have been recognized. Those include: redundant data representation, large file size, lack of the topological information between triangles, a non-robust and imprecise geometric representation, lack of tolerance information and extendibility

*Current address: Boeing North American Inc., Space Systems Division, Downey, CA 90242

(Gilman and Rock, 1995). Rock and Wonzy (1991) proposed a flexible and extensible RPI format, which focuses on facet models with support for additional manufacturing information. The RPI format provides the topological information and eliminates the redundant information found in a comparable STL files. Gilman and Rock (1995) presented the use of STEP (the Standard for the Exchange of Product Model Data) to integrate design and SFF. Cubital introduced CFL (Cubital Facet List) format which uses an approximate n-side polygon representation. This format maintains topological information and does not redundantly represents vertex information which happens in STL format. SLC, introduced by 3D System, represents a 3D model using two and a-half-dimensional contour data. It can be generated from solid or surface modeling software or CT scan data. CLI (Common Layer Interface) originated in the Brite-EuRam Project and is supported by the EARP (European Action on Rapid Prototyping). It is the format for the input of 2D geometric information to layer-wise SFF processes, and would support medical scan data. IGES (International Graphics Exchange Standard) is an international standard used by most CAD vendors. It represents the solid model with CSG primitives and boundary representation support. The size of this format is very large and difficult to handle.

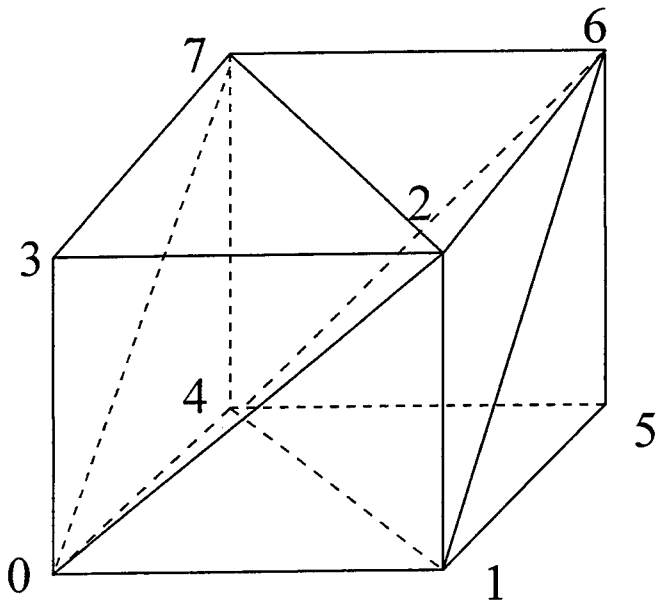
3. VRML

3.1 Overview of VRML

The origin of VRML dates back to the middle of 1994, to a European Web conference in which Tim Berners-Lee talked about for a 3D Web standard. Then the group of people picked up on this idea and joined the VRML mail list and started to produce the VRML specification. VRML is a subset of the Silicon Graphics OpenInventor file format for use in Internet application. It is a platform-independent language for virtual reality scene. This particular format has become the standard Internet Modeling Language format for the 3D World Wide Web. VRML is also a rapidly emerging industry standard for exchanging three-dimensional data over Internet.

The VRML 97 specification (ISO/IEC DIS 14772-1, 1997) states: "*The Virtual Reality Modeling Language (VRML) is a file format for describing interactive 3D objects and worlds. VRML is designed to be used on Internet, intranets, and local client systems. VRML is also intended to be a universal interchange format for integrated 3D graphics and multimedia. VRML may be used in a variety of application areas such as engineering and scientific visualization, multimedia presentation, entertainment and educational titles, web pages, and shared virtual worlds.*". San Diego Supercomputer Center (SDSC) announced the availability of a repository on the World Wide Web for exchanging information, software, and utilities related to the VRML. The repository, located at *http://www.sdsc.edu/vrml/*, provides the Internet community with information about VRML, hyperlinks to VRML documents, and access to VRML-related software.

3.2 An Example of VRML Format




```
#VRML V2.0 utf8
Transform {
    Children [
        Shape {
            appearance Appearance {
                material Material {
                    diffuse Color 1 0 0
                        }
                    }
            geometry IndexedFaceSet {
                coord DEF C Coordinate {
                    point [ -1.000000  -1.000000  1.000000,
                             1.000000  -1.000000  1.000000,
                             1.000000   1.000000  1.000000,
                            -1.000000   1.000000  1.000000,
                            -1.000000  -1.000000  -1.000000,
                             1.000000  -1.000000  -1.000000,
                             1.000000   1.000000  -1.000000,
                            -1.000000   1.000000  -1.000000 ]
                        }
                coordIndex [    0, 1, 2, -1,
                                0, 2, 3, -1,
                                1, 6, 2, -1,
                                1, 5, 6, -1,
                                2, 7, 3, -1,
                                2, 6, 7, -1,
                                4, 6, 5, -1,
```

```
                4, 7, 6, -1,
                0, 7, 4, -1,
                0, 3, 7, -1,
                0, 4, 1, -1,
                1, 4, 5, -1 ]

                    }
                }
            ]
        }
```

Figure 1 An Example of VRML Format

Figure 1 shows an example of VRML format for a cube. In that file, the *Transform* node has a *Children* field that can hold a *Shape* node. Inside the *Shape* node, there is an *Appearance* node that holds the *Material* field. The *diffuse color* is defined in the *Material* field. Following the Material field, the *IndexedFaceSet* is used to describe the geometry of the shape. It contains the *coord DEF C Coordinate* node and the *coordIndex* multiple value field. The *point* field which lists the coordinates of the points is under the *coord DEF C Coordinate* node. The polygon is defined in the *coordIndex* by a list of indices into the *point* list. In the VRML file, polygons are still used to approximate the 3D surfaces.

Unlike STL file, the VRML format does not redundantly represent the vertex information, and reuses the points in the file. The reusability of points can save a lot of space in the file. Also VRML maintains the topological information among polygons.

3.3 Use of VRML for SFF Part Data Exchange

Several researchers have suggested applying VRML as 3D-SFF data exchange format (Bauer and Joppe 1996, Fadel 1996). However, few VRML - SFF implementations exist. Fadel and his student (1996) have done some work from STL to VRML translator. This translator allows you to view STL files on a VRML viewer.

At the University of Connecticut, the SFF process planning and virtual prototyping (using OpenGL) system have been developed directly to read VRML subset "*Material and Geomertry IndexedFaceSet*". The laser path-planning data generated by the process planning are transferred to a virtual prototyping system to check the design and process planning correctness, and then transferred to the close-loop laser scanning and temperature control system for SALD (Selective Area Laser Deposition) and SALDVI (Selective Area Laser Deposition Vapor Infiltration) for physical prototyping. The architecture of this system is shown in Figure 2.

In the system listed in Figure 2, the 3D model is built using specific CAD packages (ex,. I-DEAS , CADKey). Then it can be translated to VRML format. The new versions of CAD package (I-DEAS MS 5 and CADKey 97) contain the VRML translator. Because VRML is the standard for 3D World Wide Web, it is convenient to show 3D shapes in any platform in Netscape. This is beneficial for the remote communication between designer and manufacturer.

4. RESULTS

The production of SFF is directly from a CAD model. An I-DEAS CAD model of a bracket is shown in Figure 3. Using the VRML translator of I-DEAS MS 5, a VRML file is created for the bracket. Figure 4 shows the VRML model of the bracket displayed in Netscape. The VRML file is used as input to the process planning system - Geometric Slicing and Path Planning. Then the path planning data are transferred to the virtual prototyping system. Figure 5 shows the 3D shape of the bracket after the virtual prototyping. The coarse features are due to the scan line which is used for the virtual model building.

There are several advantages of using VRML instead of STL as 3D format for SFF. (1) VRML file has better structure and it is smaller than the comparable STL file. (2) VRML is the 3D extension of World Wide Web. (3) VRML maintains the topological information among polygons. (4) VRML can do everything that STL can do. But VRML still uses the polygons to approximate the 3D surface. So it can not improve the geometry accuracy in SFF.

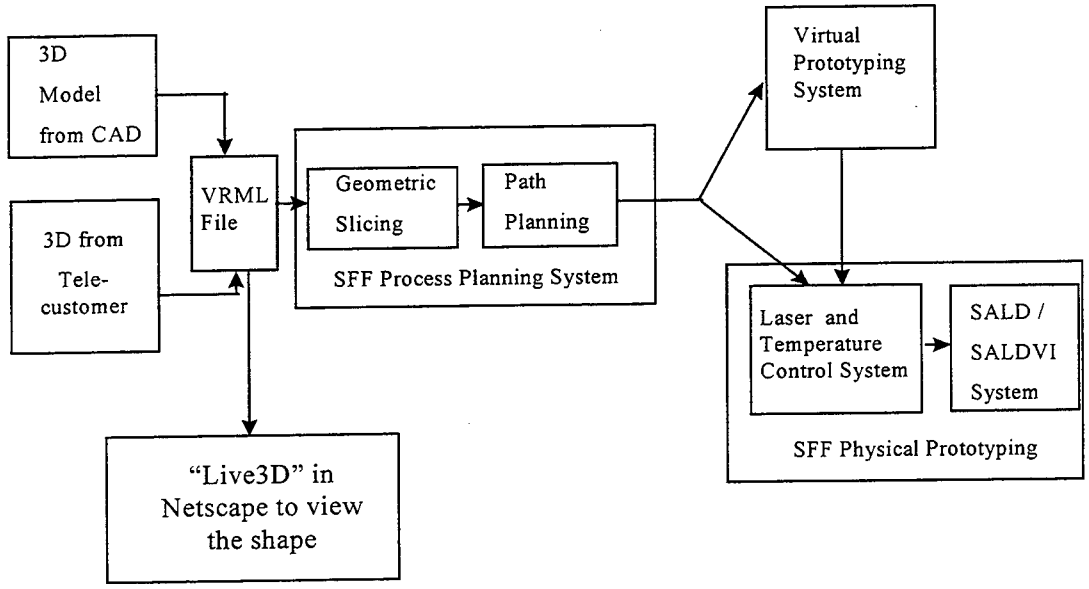


Figure 2 System Architecture

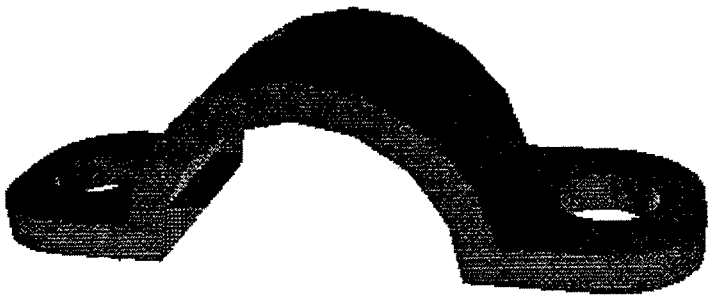


Figure 3 A CAD Model from I-DEAS Package

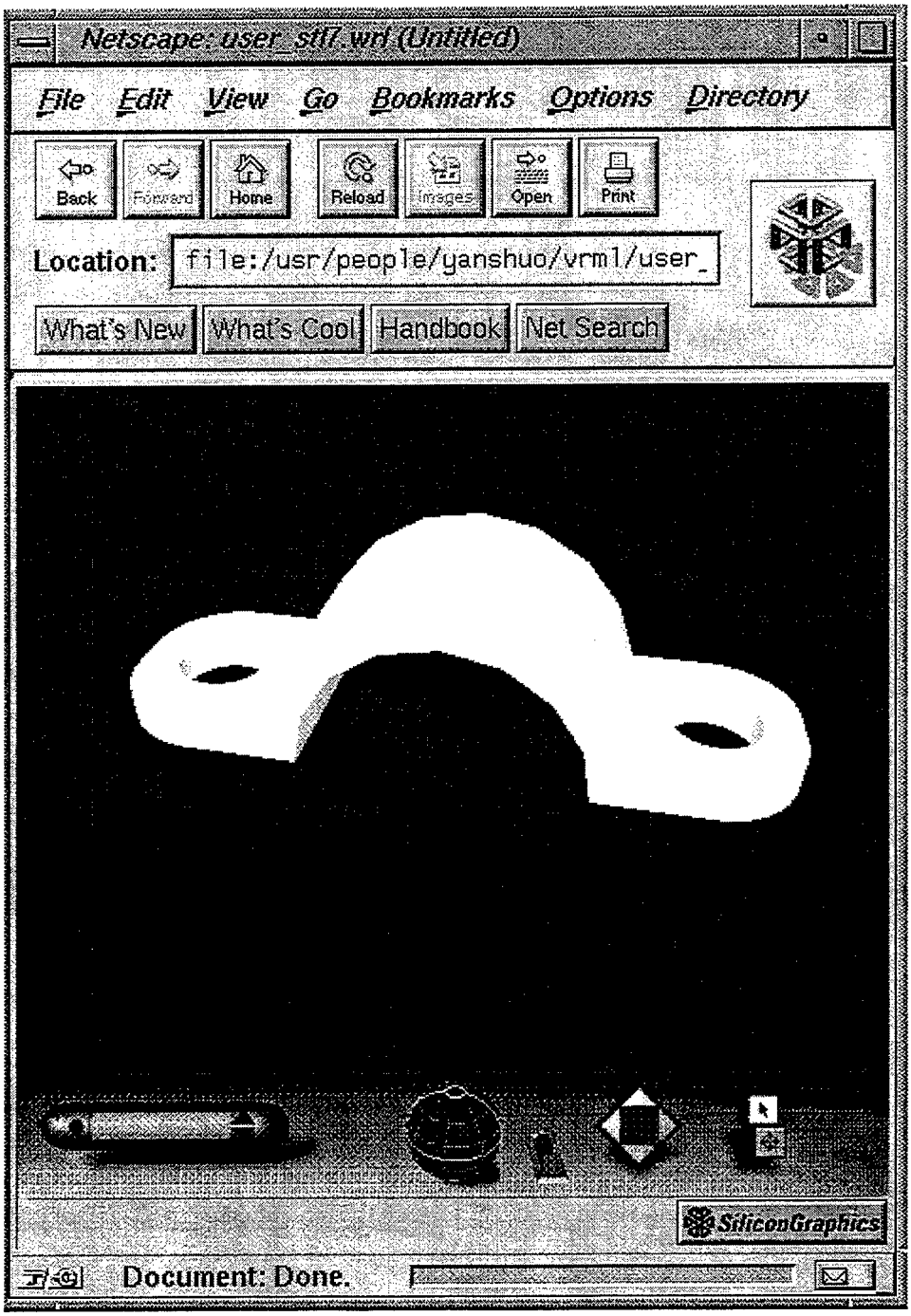


Figure 4 Bracket VRML Model Displayed in Netscape

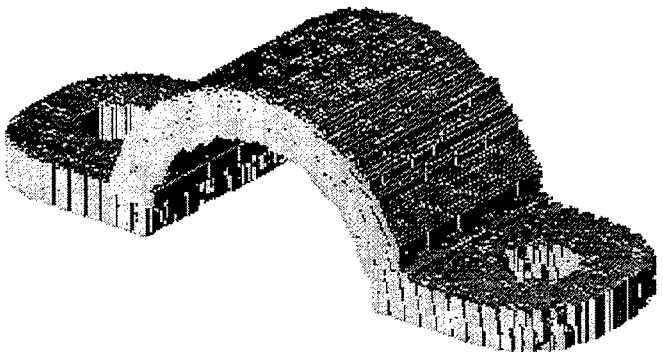


Figure 5 The Virtual Prototyping of the Bracket

5. CONCLUSIONS

VRML is a Standard for the exchange of 3D data in Internet. VRML format can do everything that STL can do. It doesn't redundantly represent vertex information, and contains the topological information among polygons. It is also independent of the platform and has become the standard 3D format for World Wide Web. So using VRML as 3D format for SFF can improve the communication between designer and the manufacturer.

The SFF process planning and virtual prototyping system that described in this paper is an example of VRML as 3D data format for SFF.

6. ACKNOWLEDGMENTS

This work is supported under the grants DARPA/ONR N00014-96-1-1299 and ONR N00014-95-1-0978. Also acknowledge to Dr. Bzymek in Mechanical Engineering at UCONN for his assistance.

7. REFERENCES

Bailey, M. J., 1995, "Tele-Manufacturing: Rapid Prototyping on the Internet", IEEE Computer Graphics and Applications, November, 1995.

Bailey, M. J., "Tele-Manufacturing: Rapid Prototyping on the Internet with Automatic Consistency-Checking", http://www.sdsc.edu/tmf/Whitepaper/ whitepaper.html, University of California at San Diego and San Diego Supercomputer Center.

Bauer, Jurgen and Joppe, Marcus, 1996, "Use VRML as Standard for Rapid Prototyping". http://www.biba.uni-bremen.de:80/docs/users/bau/s2v.html, BIBA, Germany.

Dolenc, A and Makela, I., 1996, "Rapid Prototyping from a Computer Scientist's Point of View", Rapid Prototyping Journal, Vol. 2, No. 2, 1996, pp. 18-25.

Dong, J., 1996, "The Issues in Computer Modeling and Interfaces to Solid Freeform Fabrication", 1996 ASME Winter Congress and Exposition, Atlanta ,GA.

Dong, J., 1997, " New Challenges in Computer Aided Solid Model Design for Rapid Prototyping of Vehicle Components", International Journal of Vehicle Design, Vol-18, No.5 pp548-557.

Fadel, G. and Krischman, C., 1996, "Accuracy issues in CAD to RP translations", Rapid Prototyping Journal, Volume 2- Number 2, 1996, pp. 4-17.

Graphics 3D Object File Formats, " 3D Object File Formats", http://www.cee.indiana.edu/~brian/graphics/3D.formats.html

Harrison, S., Crocker, J. E., Manzur, T. and Marcus, H. L., 1996, " Solid Freeform Fabrication at the University of Connecticut", Solid Freeform Fabrication Symposium, University of Texas at Austin, Austin, TX, August 1996, pp. 345-348.

ISO/IEC DIS 14772-1, 1997, " The Virtual Reality Modeling Language", http://vrml.sgi.com/moving-worlds/spec.DIS/index.html.

Lehner, V. D. and DeFanti, T. A, 1997, "Distributed Virtual Reality: Supporting Remote Collaboration in Vehicle Design", IEEE Computer Graphics and Applications. March-April, 1997, pp13-16.

Marrin, C. and Campbell, B., 1997, "Teach Yourself VRML 2 in 21 Days", Sams.net Publishing.

Martin, J., 1997, "Part Design Comes Together on the Net", Mechanical Engineering, June 1997. pp76-78.

Rock, S. J. and Gilman, C. R., 1995, "The Use of STEP to Integrate Design and Solid Freeform Fabrication", Solid Freeform Fabrication Symposium, University of Texas at Austin, Austin, TX, August 1995.

Rock, S. J. and Wozny, M. J., 1991, " A Flexible File Format for Solid Freeform Fabrication", Solid Freeform Fabrication Symposium, University of Texas at Austin, Austin, TX, August 1991, pp. 1-12.

SDSC Announces the VRML Repository: "A World Wide Web Resources for the Virtual Reality Modeling Language",http://www.sdsc. edu/vrml_repository/Press/repository_press.html

Whitehouse, K., 1996, "VRML Adds a New Dimension to Web Browsing", IEEE Computer Graphics and Applications, July 1996, pp7-9.

A THERMAL MODEL FOR LAMINATED OBJECT MANUFACTURING (LOM)

Lawrance Flach
Department of Chemical Engineering

Donald A. Klosterman and Richard P. Chartoff
Rapid Prototype Development Laboratory
and
Ohio Rapid Prototype Process Development Consortium

University of Dayton
300 College Park Avenue
Dayton, OH 45469
U.S.A.

ABSTRACT

A thermal model for Laminated Object Manufacturing (LOM) has been developed. The model is based on 3-dimensional transient heat conduction in a rectangular geometry LOM part. Heat transfer from the heated roller to the laminated part as well as heat loss to the surroundings and the base plate are considered. It allows calculation of the transient temperature distribution within the part during the application of a new layer as well as during other periods of the LOM build cycle. To verify the model performance, thermocouples were embedded every 4^{th} layer in a 20-layer ceramic part while it was being built on a standard LOM-2030. The model predictions are in excellent agreement with the measured temperature profiles. In addition to explaining the observed thermal behavior of LOM parts, model predictions also have direct application to on-line control of the part temperature during the build process, to be discussed herein.

INTRODUCTION

The LOM process, illustrated in Figure 1, is described as follows. First, a fresh layer of material is placed on top of the stack. (The first layer is bonded to the platform via double sided carpet tape.) In the case of the standard paper process, this step is automated via a paper roll feeding mechanism; in the case of experimental materials such as ceramic tapes, this step is accomplished by hand. Next, the heated roller makes a forward and backward pass to laminate the layer to the stack. The roller height relative to the stack is maintained such that the roller compresses the top layer by approximately 0.5 mm, thus enabling lamination via pressure. After the roller is retracted, a CO_2 laser cuts the part cross sectional area, the cross hatching, and the boundary box. Any excess material outside the boundary box is removed and a new layer is placed. The process repeats until all layers have been added. Thus, a part is built from the platform up one cross section at a time.

The temperature distribution that develops in a part during LOM fabrication has a

significant influence on a number of aspects of the build process. Low temperatures in the upper layers may result in poor adhesion of the individual layers causing delamination of the completed part. On the other hand, excessive buildup of heat in the body of the part may result in a general loss of structural rigidity during the build leading to excessive compression or shearing during application of pressure by the roller. Thus, a knowledge of the transient thermal behavior of the part is essential to successful building and to a more comprehensive understanding of all aspects of the LOM process.

Mathematical models for heat transfer in general tape laying processes have been developed [1, 2, 3, 4], but the majority of these are formulated for pseudo-steady-state situations. As a result, existing models can not accommodate the transient behavior that is observed during the different phases of the LOM build cycle. The mathematical model presented here has been developed to overcome this difficulty. We present the basic model structure, its capability, and some results obtained from the simulation of the build process for a simple ceramic LOM part built from layers of ceramic tape. Ceramic tapes are thin (0.25 mm), flexible sheets of ceramic powder bound together with a thermoplastic binder. The simulation of the building cycle for this ceramic part is compared to actual experimental measurements in an attempt to verify model predictions. Possible applications of model predictions for on-line control of the process are also discussed.

LOM users are fast becoming aware that an understanding of the thermal behavior of the part during the build process is crucial for the fabrication of parts with good lamination characteristics. While this is important for prototype parts made from the standard LOM paper and plastic materials, it has become extremely significant now that the fabrication of high performance, functional ceramic and composite parts is being considered [5, 6, 7, 8]. To address this concern techniques are being developed where the surface temperature of the part is measured (referred to as the part body temperature or PBT) and used in some form of feedback control to adjust roller speed and/or roller temperature [9]. The objective of the control is to obtain a PBT within a certain desirable range. The use of mathematical models with such feedback control would constitute intelligent, adaptive, on-line control which will be discussed later.

MODEL DEVELOPMENT

The thermal behavior of a LOM part is primarily determined by the following:

- heat transfer from the heated roller to the surface of the partially completed part,
- heat conduction within the part itself, typically away from the heated surface,
- heat loss from the bottom of the part to the metal base-plate on which the part is being fabricated, and
- heat loss from the various exposed surfaces of the part to the surroundings via free or forced convection.

These heat transfer mechanisms determine the temperature profiles that develop in the LOM part

during the various phases of the build cycle, thus the mathematical model developed must describe them as accurately as possible.

A mathematical model for a simple rectangular geometry LOM part was developed. Figure 2 indicates the geometry of the part as well as the coordinate system used for development of the mathematical model. Since all LOM parts are built as rectangular blocks, the model geometry is universally applicable to all LOM parts. At any instant during lamination, the heated roller contacts the surface only through a narrow strip in the x direction, and moves in the y-direction, applying both heat and pressure to the surface. Although the contact surface is three dimensional in nature, it is approximated by a rectangular zone, the "contact strip", that moves along the top surface on the part.

Heat conduction within the rectangular region of material is described by the following equation:

$$\rho C_p \frac{\partial T}{\partial t} = \nabla \bullet (k \nabla T) \tag{1}$$

It should be noted that no energy source term is included in the equation since no heat is generated or consumed within the ceramic part itself. The binder is a highly plasticized thermoplastic resin, therefore, it will not undergo a chemical reaction or melting transition. Thus, energy addition or loss from the region is handled through the boundary conditions.

Boundary conditions for the part are specified using general heat transfer coefficient (convection-type) boundary conditions. For surfaces of the part other than that in contact with the roller or the bottom in contact with the base-plate, the following expression is adopted:

$$k_i \frac{\partial T}{\partial x_i} = h_{air}(T_{surface} - T_{air}) \tag{2}$$

where the subscript i indicates that the variable may take on values appropriate for any of the three major coordinate directions. The value of the heat transfer coefficient selected should be appropriate for the air flow regime around the part being fabricated.

The region of the surface in contact with the roller is handled in much the same way. An expression of the following form is used:

$$k_z \frac{\partial T}{\partial z} = h_{roll}(T_{surface} - T_{roller}) \tag{3}$$

An appropriately high value for this heat transfer coefficient is used. This has the effect of forcing the surface temperature to be close to that of the roller only in the region of contact. Movement of the roller across the surface is accomplished simply by moving the position of the "contact strip" or region with high heat transfer coefficient. The position of the contact strip is calculated as a function of time from the roller speed. The width of the contact strip can be calculated from the roller diameter and the amount of surface indentation that occurs on roller contact, or measured directly.

The bottom of the fabricated part is typically attached to the LOM base plate using a layer of double-sided adhesive foam tape. This boundary is also accommodated using a heat transfer coefficient boundary condition as follows:

$$k_z \frac{\partial T}{\partial z} = h_{tape}(T_{bottom} - T_{base}) \quad (4)$$

The heat transfer coefficient for the tape is an effective value that can be estimated or experimentally measured. The base plate temperature was treated as a lumped parameter that could be held constant or computed as a function of the heat flux through the bottom of the laminated part.

The heat conduction equation (Eqn. 1) together with the boundary conditions described above were solved numerically using a 3-dimensional alternating direction implicit method. This technique involves discretizing the solution region, and then solving sets of simultaneous linear equations to compute the temperature distribution after a specified time increment. The nature of the LOM build process with its relatively short period for lamination followed by longer periods of "inactivity" required that the time increment used for numerical solution be varied depending on what part of the build cycle was being simulated. A very short time increment is required during the actual lamination process because rapid temperature transients occur in the part while in contact with the moving roller. During other periods of the build cycle which involve less activity, a much larger time increment was used.

Addition of a new layer of material is accomplished by expanding the solution region in the appropriate direction, i.e. adding additional nodes to the existing mesh structure. It is assumed that the new layer of material is at ambient temperature and that the temperature distribution of the old upper surface is as calculated by the model for that time of the build cycle. The temperature discontinuity at the instant of new layer application is handled by simply adjusting the temperature of the interfacial nodes to the average of the computed old surface temperature and the temperature of the new layer.

The model developed thus has the ability to simulate the entire build process including all phases of the build cycle. Rapid temperature transients during periods of roller activity are handled by decreasing the solution time increment, and periods of relative inactivity handled by increasing the time increment. This decreases the computation time required and also the amount of temperature data that has to be interpreted or graphically presented.

MODEL PREDICTIONS AND VERIFICATION

In order to perform a build simulation, a number of parameters must be specified and input to the mathematical model. These parameters relate to the physical and thermodynamic properties of the material being used to construct the part, the LOM machine parameters (roller temperature, speed, compression, cycle times), physical dimensions of the part, and estimates of heat transfer coefficients to the surrounding air and base plate. The parameters used for the simulation results presented are summarized in Table 1. All parameters were experimentally measured [10] except

the roller-to-part heat transfer coefficient which was used as a tuning parameter.

TABLE 1. Data for LOM build simulation

Material	Silicon carbide ceramic tapes
Thermal Conductivity	1.25 $Wm^{-1}K^{-1}$
Density	1.98 g cm^{-3}
Heat Capacity	1.05 $Jg^{-1}K^{-1}$
Part dimensions	121.9 mm x 53.3 mm
Layer thickness	0.25 mm
Number of layers	20
Heat trans coeff (part to air)	18 $Wm^{-2}K^{-1}$
Heat trans coeff (part to base)	14 $Wm^{-2}K^{-1}$
Air temperature	22°C
Base plate temperature	22°C
Initial temperature of material	22°C
Roller velocity	25.4 mm sec^{-1}
Roller contact strip width	9 mm
Roller temperature	91°C
Heat trans coeff (roller to part)	3300 $Wm^{-2}K^{-1}$
Build cycle time	120 seconds

A simple experiment was conducted to verify the model performance. A twenty-layer rectangular parrt was built using a standard LOM-2030 machine and the ceramic LOM process [5]. A thermocouple was placed in the center of the top surface of every fourth layer beginning with layer 0 (the double-side tape layer). Temperature from each thermocouple was recorded every 0.5 seconds through the entire 40 minute build.

Figures 3 and 4 show the transient temperature behavior for thermocouples below the 1st, 5th, 9th, 13th, and 17th layers. Figure 3 depicts experimentally measured data, whereas Figure 4 represents model predictions for a simulation of an identical LOM part build. Before being embedded, the thermocouples were held in reserve at ambient temperature as indicated by the base lines. The random instances of noise in the base line might be explained by accidental bumping of the thermocouples during layer placement. Each temperature peak represents the cycle for one layer and is comprised of several events annotated in Figure 3. The first spike is the temperature rise upon the forward roller pass. The second spike, higher than the first, is for the reverse roller pass, where the temperature is expected to be higher. The third peak can be explained by local heating from the laser cutting. The fourth feature is the abrupt drop in temperature as a new layer is added.

From these figures it can be seen that the layer temperature varies widely when it is near the top of the stack. However, apart from short term transients of near-surface layers, the temperature of the part body through the thickness is fairly uniform with only minor gradients in the z-direction.

Also of interest is the "long term" temperature of the part (in this case fluctuating between 35 and 40°C) since it can be used as a good indicator of the overall part body temperature. It is this temperature that will determine the behavior of the part during lamination.

Figure 5 shows the transient temperature behavior for the thermocouple between the foam and 1st layer of the part. Both experimental results and model predictions are shown. As can be seen there is a excellent correspondence between simulation predictions and actual experimental measurements. As the part increases in size and more layers are added between the bottom of the part and the roller, the influence of roller passes on the temperature at that location decreases.

APPLICATION TO PROCESS CONTROL

As described above, the mathematical model has the ability to predict transient temperature distributions in a part being fabricated. Of interest is the temperature distribution in the z- or depth-direction. This information gives an indication of the overall average temperature of the part body. Experimental measurements and simulations have revealed the existence of only minor z-direction gradients for the ceramic material under investigation.

Excessive buildup of heat within the body of the part can result in a loss of structural rigidity, possible compression or shearing during application of pressure by the roller, and/or binder degradation. The part body temperature is determined by the roller temperature, the roller speed, heat transfer to and from the part, and time between roller passes. This last factor may vary widely from layer to layer as a direct function of the laser cutting time.

It is desirable to maintain the part body temperature within a certain range to ensure good lamination and also to prevent loss of structural rigidity. Helysis has suggested a method to control the surface temperature of the part during certain phases of the build cycle using the roller temperature and roller speed [9]. The mathematical model described here and the depth profiles calculated can be used to relate the surface temperature to the overall part body temperature. Model predictions could thus be used to indicate how well the surface temperature represents the part body temperature and could be used to investigate alternate control strategy.

If control of the process temperature is a critical issue for the fabrication of structurally sound laminated parts, then these modeling studies suggest an alternative method to control this parameter. Roller temperature and speed are the obvious variables to manipulate to control the part body temperature, but these may be constrained by other issues, e.g. good layer adhesion, low overall build time, etc. Simulations have been conducted where the base plate temperature was modified in order to examine the effect on the part body temperature. As can be seen in Figure 6, modifying the base plate temperature seems to provide a means to control the overall part body temperature without changing roller parameters. The efficiency of this control strategy will depend on the thermal conductivity of the double sided adhesive foam tape between the bottom of the laminated part and the base plate. In order for this strategy to be feasible, heat loss to the base plate needs to be at least of the same order of magnitude as convection heat loss to the surrounding air. This is the case with the current parameters although heat loss to the air is certainly higher than heat

loss through the plate. This observation was made by noting the overall part temperature which rose only about 15°C although the roller temperature was incrased 40°C. Another method for controlling part temperature is through radiative heating via heat lamps. The model described here could be used to simulate this scenario by including radiative heating boundary conditions although no attempt has been made to do so at this time.

CONCLUSIONS

A mathematical model has been developed that describes the heat transfer occurring during building of LOM parts. The model is based on 3-dimensional transient heat conduction within the solid part body together with appropriate boundary conditions. It is capable of accurate predictions of both short term transient temperatures in the part as well as overall part body temperatures. The model also has direct applicability in the area of on-line process control and will be used as the basis for the future development of temperature control strategies for LOM processing.

NOMENCLATURE

C_p	heat capacity of build material (J/g K)
h_{air}	heat transfer coefficient, part to air (W/m^2 K)
h_{roll}	heat transfer coefficient, part to roller (W/m^2 K)
h_{tape}	heat transfer coefficient, part to base plate (W/m^2 K)
k	thermal conductivity of build material (W/ m K)
k_i	thermal conductivity in any of the 3 principal coordinate directions (W/ m K)
k_z	thermal conductivity in z-direction (W/ m K)
t	time (sec)
T	temperature (°C or K)
T_{air}	temperature of air surrounding part (°C or K)
T_{bottom}	temperature of part bottom surface (°C or K)
T_{roller}	temperature of heated roller (°C or K)
$T_{surface}$	temperature of part surface (°C or K)
x	spatial coordinate

x_i	any of the 3 principal spatial coordinates
y	spatial coordinate
z	spatial coordinate
ρ	density of build material (g/cm^3)

REFERENCES

1. Sarrazin, H. and G.S. Springer, "Thermochemical and Mechanical Aspects of Composite Tape Laying", *J. Comp. Mat.*, Vol. 29, No. 14, 1995, pp. 1908-1943.

2. Sonmez, F.O., *Modeling of the Thermoplastic Composite Tape Placement Process*, Ph.D. Dissertation, Univ. of California, Los Angeles, 1995.

3. Sonmez, F.O. and H.T. Hahn, "Thermomechanical Analysis of the Laminated Object Manufacture (LOM) Process", obtained from Helisys, Inc., January, 1996.

4. Pak, S. and G. Nisnevich, "Interlaminate Strength and Processing Efficiency Improvements in Laminated Object Manufacturing," *Proceedings of the 5th International Conference on Rapid Prototyping*, University of Dayton, June 1994, pp. 171-180.

5. Klosterman, D., R. Chartoff, et al., "Laminated Object Manufacturing (LOM) of Advanced Ceramics and Composites," *Proceedings of the 7th International Conference on Rapid Prototyping*, University of Dayton and Stanford University, March 31-April 3, 1997, San Francisco, CA, pp. 43-50.

6. Klosterman, D., B. Priore, R. Chartoff, "Laminated Object Manufacturing of Polymer Matrix Composites," *Proceedings of the 7th International Conference on Rapid Prototyping*, University of Dayton and Stanford University, March 31-April 3, 1997, San Francisco, CA, pp. 283-292.

7. Chi, C., L. Dodin, S. Pak, "Development and Fabrication of Metallic LOM Objects," *Proceedings of the 7th International Conference on Rapid Prototyping*, University of Dayton and Stanford University, March 31-April 3, 1997, San Francisco, CA, pp. 293-299.

8. Griffin, A., et al., "Bioceramic RP Materials for Medical Models," *Proceedings of the 7th International Conference on Rapid Prototyping*, University of Dayton and Stanford University, March 31-April 3, 1997, San Francisco, CA, pp. 355-359.

9. "Measure Part Block Temperature", *LOM Insight*, Helisys, Inc., Vol. 1, Issue 4, May 1996.

10. Janz, B., "Development of Predictive Models and Adaptive Control of the LOM Process,"

manuscript in development, M.S. thesis, University of Dayton, Dayton, OH, July, 1997.

ACKNOWLEDGMENTS

This work was made possible by a grant from the Ohio Board of Reagents, Research Challenge Program through the University of Dayton. Use of the LOM equipment was made possible through a grant from DARPA/ONR, N00014-95-1-0059.

ILLUSTRATIONS

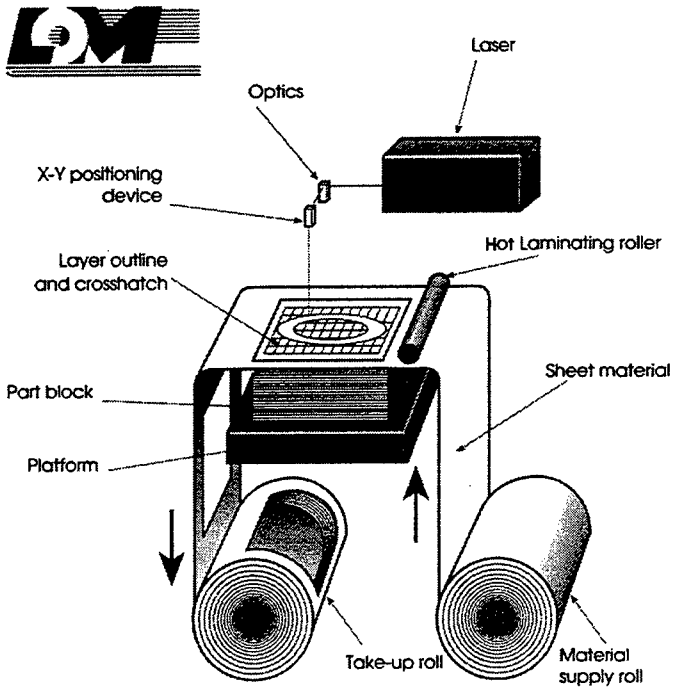


Figure 1 : schematic of the LOM process.

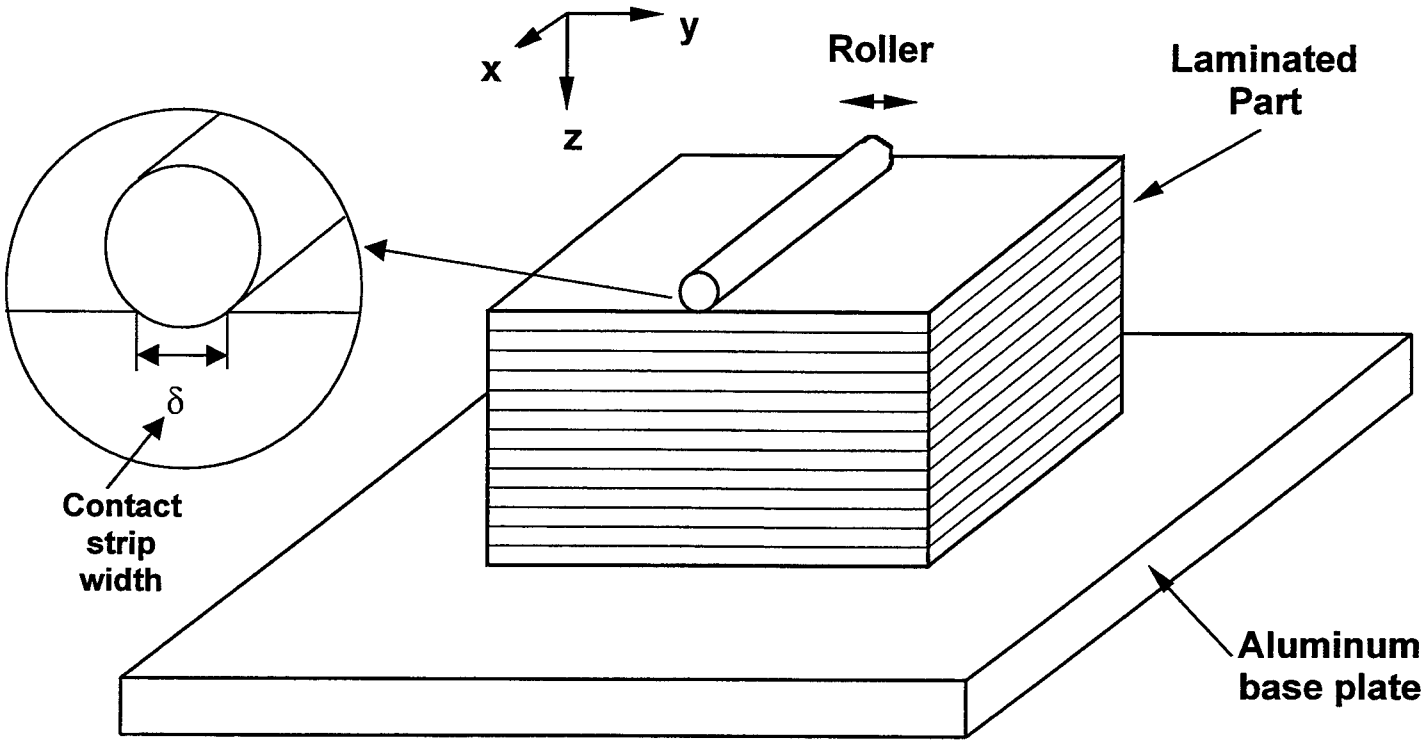


Figure 2 : geometry and coordinate system for model.

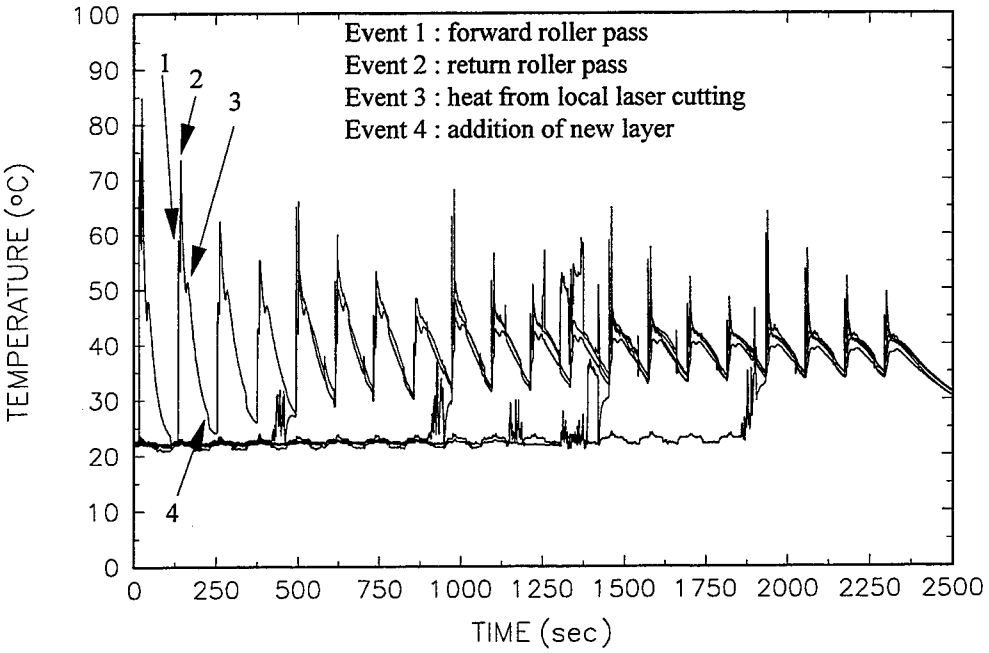


Figure 3 : measured temperature profiles from embedded thermocouples above the 0^{th}, 4^{th}, 8^{th}, 12^{th}, and 16^{th} layers in a 20 layer ceramic part built on a LOM2030.

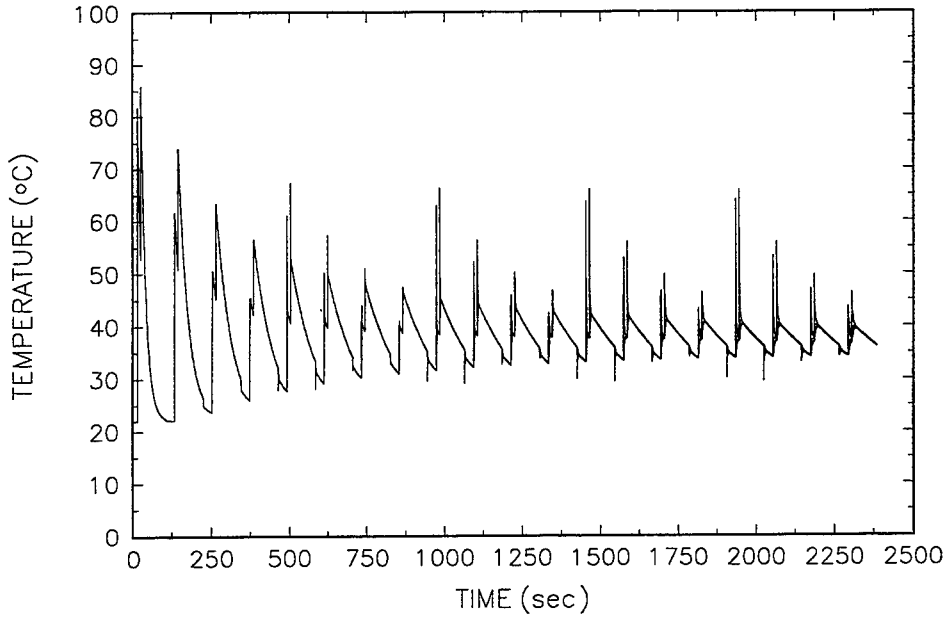


Figure 4 : predicted temperature profiles for nodes above the 0^{th}, 4^{th}, 8^{th}, 12^{th}, and 16^{th} layers in a 20 layer ceramic part.

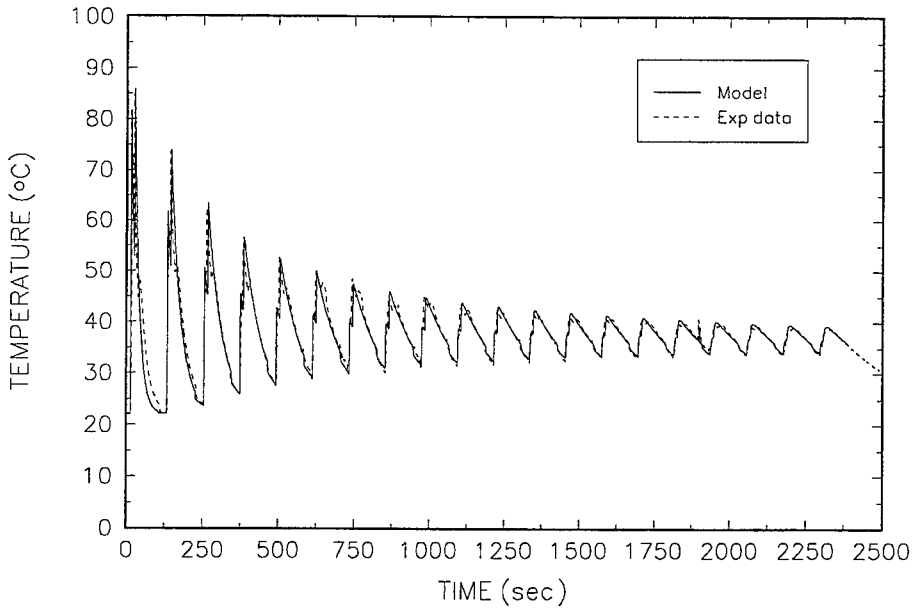


Figure 5 : measured and predicted temperature profile for thermocouple just above the 0th layer (foam tape base).

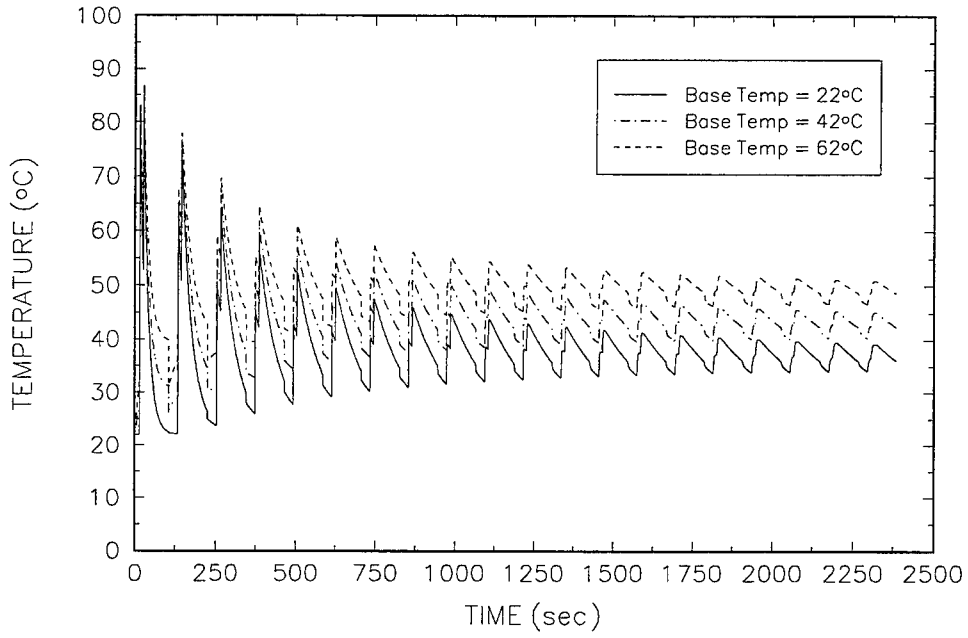


Figure 6 : predicted temperature profiles, analyzing effect of varying base plate temperature on overall part temperature.

THERMAL ANALYSIS OF FUSED DEPOSITION

M. Atif Yardimci, Takeshi Hattori, Selcuk I. Guceri
University of Illinois at Chicago,
Chicago, Illinois USA

Stephen C. Danforth
Rutgers University
Piscataway, New Jersey USA

ABSTRACT
Fused Deposition processes involve successive melting, extrusion and solidification of thermoplastic polymer melts. Fluid mechanics and heat transfer of neat or particle-filled polymeric melts, viscoelastic deformation and solidification of the roads that are being produced, and repetitive thermal loading of the growing part are important physical processes that control the final quality of the part. Previous computational process models investigated deposition and cooling processes for single and multiple filaments. In the current study, complimentary computational models are presented for the extrusion phase of the process. Impact of liquefier and nozzle design on thermal hardware behavior and operational stability has been quantified. Also a detailed study of temperature field near the vicinity of deposition point is presented with particular emphasis on dimensional analysis and deposition of multiple material systems.

BACKGROUND

Fused Deposition process involves deposition of thermoplastic melts by a computer controlled minirobot to produce arbitrary geometry three dimensional objects (Crump, 1992.) Fabricated objects possess a two level hierarchical meso-structure, which consists of curvilinear roads packed into discrete layers. The thermal energy stored in the molten material is redistributed into the part through conduction, and is consumed by lateral convection cooling. The redistribution of thermal energy ensures bonding at the interfaces of deposited roads, and generates the structural integrity of the part. Material delivery into the workvolume can be achieved by a liquefier which employs a self-extruding filament (Comb et.al, 1994), a fluid metering rotary pump (Batchelder et.al, 1994) or through a high-pressure plunger system (Hilmas, 1996). The road cross-sections are shaped through fountain flow of polymer melt between the previously deposited material and nozzle tip, resulting in flattened ellipsoids. These ellipsoid shapes are basically rectangles with two semi-circles attached at each lateral side of the road, which have the layer thickness as their diameter Recently computer controlled surface forming mechanisms, trowels, have been proposed to shape the road cross-sectional geometries (Khoshnevis, 1997). The available material set for filament deposition techniques has been increased through introduction of particles into the feed-stock, which enabled the production of intermediate powder processing products, particulate polymeric composites or *green* bodies, that can be processed further to obtain porous and/or fully dense metallic and ceramic articles (Geiger, 1994), (Agarwala et.al, 1995).

Previous process modeling effort for Fused Deposition was concentrated on the cooling behavior of single and multiple filaments (Yardimci et.al, 1995), (Yardimci and Guceri, 1996),

and development of build file, *SML* file, interpretation and analysis tools for heuristic simulation of part building with FD (Yardimci et.al, 1996). In the current work four critical aspects of extrusion process are addressed: thermal design of liquefier entrance, analysis of melt front location in the liquefier, degree of cooling in the nozzle and the impact of nozzle design on operational stability of the hardware. Also a deposition level thermal model is presented to investigate the effects of relevant non-dimensional numbers, Peclet and Biot numbers, on temperature distribution across multiple filament configurations.

LIQUEFIER DESIGN

The operation of the liquefier is controlled through two different channels: whereas flow control is facilitated through servo controllers that command the motion of the traction rollers; temperature regulators adjust heater power to keep liquefier temperature at the constant pre-set value. The decoupled nature of the temperature regulation from motion or flow control generates unique challenges for liquefier design, e.g. the temperature at the liquefier entrance shall not exceed a critical value even though the liquefier temperature is constant at pre-set temperature, the liquefier length should be long enough to achieve the desired temperature at its end for all flowrate conditions.

Entrance Insulation

In the current section the conduction heat transfer phenomena at liquefier entrance, Figure 1, is analyzed. A thermal model is presented for the prediction of entrance temperatures with different liquefier designs (geometry of filament / liquefier / seperator plate), material properties (thermal conductivity of filament and plate) and processing conditions (degree of convective cooling at the entrance). The axisymmetric conduction equation can be written for a heterogeneous domain as:

$$\frac{1}{r}\frac{\partial}{\partial r}\left(k\,r\,\frac{\partial T}{\partial r}\right)+\frac{\partial}{\partial z}\left(k\,\frac{\partial T}{\partial z}\right)=0$$

$$-k\frac{\partial T}{\partial n}=h_1\left(T-T_1\right)@\,\vec{r}\in\Gamma_1\quad;\quad -k\frac{\partial T}{\partial n}=h_2\left(T-T_2\right)@\,\vec{r}\in\Gamma_2 \tag{1}$$

$$T=T_0\;@\,\vec{r}\in\Gamma_3\,,\;\frac{\partial T}{\partial n}=0\;@\,\vec{r}\in\Gamma_4$$

, where r and z are radial and axial coordinates, k is spatially distributed thermal conductivity, T_0 is liquefier temperature, h_1 and T_1 are liquefier side convective cooling coefficient and temperature and h_2 and T_2 are entrance side convective cooling coefficient and temperature respectively. Finite volume method is employed in the numerical discretization of the governing equations on a triple block grid. The resulting set of equations are solved using a pseudo-transient scheme, Alternating Direction Implicit (ADI). A sample solution for k_f = 0.2 W/(m K), k_p = 3.0 W/(m K), k_l = 400.0 W/(m K), h_1 = 100 W/(m^2 K), h_2 = 10 W/(m^2 K), T_0= 270°C, T_1= 20°C, T_2= 70°C, w_p= 2mm, l_1= 10 mm, l_2= 20 mm, r_f= 0.914 mm, r_{liq}= 10 mm, is presented in Figure 2.a. The sharp drop in temperature through the seperator plate is remarkable, hence the width of the seperator plate can be effectively utilized as a design variable. The dimensional

analysis of governing equation and boundary conditions reveals that plate and filament Biot numbers can consolidate the number of process variables.

$$\theta = \frac{T_e - T_2}{T_0 - T_2} \quad , \quad Bi_p = \frac{h_2\, w_p}{k_p} \quad , \quad Bi_f = \frac{h_2\, 2r_f}{k_f} \tag{2}$$

Furthermore, through definition of non-dimensional entrance temperature the operation map of the liquefier has been estimated with ten numerical experiments documented in Figure 2.b. Entrance temperature decrease with increasing plate and filament Biot numbers and safe liquefier designs can be predicted using the generated map for different filament materials.

Location of Melt Front

The heating of the filament inside the liquefier is governed by the two-dimensional axissymetric steady-state advection-conduction equation (Burmeister, 1983). A resistive heater is wrapped around the aluminum liquefier. Due to high thermal conductivity of this material, temperature is more or less homogeneous along the tube. Hence it becomes appropriate to replace constant heat flux wall boundary condition with constant wall temperature. Furthermore since the filament remains solid upto the point of melting, the flow may be approximated with plug flow, i.e. constant flow across the cross-section. The solution of this Graetz problem in non-dimensional form is:

$$\theta = 2\sum_{n=1}^{\infty} e^{\left(-\lambda_n^2 z'\right)} \frac{J_0\left(\lambda_n r'\right)}{\lambda_n J_1\left(\lambda_n\right)} \quad , \quad J_0\left(\lambda_n\right) = 0 \quad , \quad \theta = \frac{T - T_0}{T_2 - T_0}$$
$$r' = \frac{r}{r_f} \quad , \quad z' = \frac{\alpha}{V r_f} \frac{z}{r_f} \tag{3}$$

, where r' and z' are non-dimensional coordinates, V is filament velocity, α is thermal diffusivity, λ_n are roots of zero order Bessel function of first kind, J_0, and J_1 is first order Bessel function of first kind. If a melting temperature, T_m, is defined for the material; the melt front location, z'_m i.e. the axial location at which the temperature at the center of the filament reaches T_m, can be calculated from:

$$\theta_m = 2\sum_{n=1}^{\infty} \frac{e^{\left(-\lambda_n^2 z'_m\right)}}{\lambda_n J_1\left(\lambda_n\right)} \tag{4}$$

Examination of definition of z' reveals that the actual melt front distance is linearly proportional to filament speed and square of filament diameter and inversely proportional to material diffusivity.

Degree of Cooling in the Tip

The liquefier temperatures set on the front panel of Fused Deposition equipment may not reflect the correct deposition temperature, since the deposition tip itself is not heated and insulated. Axissymmetric heat conduction equation has been solved for nozzle geometry presented in Figure 3.a (representing a T16 nozzle), using linear triangular ring finite elements,

to investigate the degree of cooling in the nozzle. The base of the nozzle is kept at liquefier temperature, 270 °C for the cases presented in the report; external surface of the nozzle is insulated half way down, which represents the band heater around the threaded section in Fused Deposition hardware, and the rest of the external surface is open to convective cooling, with a convection coefficient of h = 100 W/(m^2 K) and an envelope temperature of 70 °C. The internal surface of the nozzle which interfaces the filament has been simulated using an adiabatic boundary condition. This boundary condition represents the worst case scenario, minimum tip temperature, since during deposition there will be net heat transfer from filament to the nozzle. A sparse linear solver has been utilized for the solution of resulting set of equations. Two materials were considered aluminum (k = 400 W/(m K)), and stainless steel (k = 100 W/(m K)). The resulting temperature distributions are shown in Figures 3.a and 3.b. Higher thermal conductivity material resulted in higher tip temperatures, although total heat loss was higher. Both materials resulted in tip to base temperature differentials which were within %6 of the base to envelope temperature differential. A new tip design with a metal core and insulating coating may be the best choice to keep liquefier to tip temperature differential at a minimum.

Impact of Nozzle Design on Liquefier Requirements

The internal transition angle of the nozzle from the filament diameter to extrusion tip diameter is generally 120°, the tip angle of the drill Such large contraction angles combined with large contraction ratios of 6:1 may result in the formation of corner vortices (also named dead zones in extrusion practice) (Liang et.al, 1996). The presence of these vortical regions is especially critical for particle loaded materials, since the regions may create flow instabilities and eventual clogging of the nozzle. One remedy is to decrease the transition angle below the Natural Convergence Angle (NCA) below which vortical regions disappear. However lower transition angles result higher cumulative shear stresses and pressure drops, since the effective Reynolds number of the flow is much less than one for polymer melts through capillaries. Higher pressure drops in turn may impede the operational stability of the hardware causing filament buckling.

The pressure drop of neat or particulate loaded thermoplastic melts, described with shear thinning power law fluid behavior, across circular straight channels may be found in literature (Michaeli, 1992). The pressure loss in a conical convergent tube may be represented as the sum of discrete pressure losses of equivalent infinitesimal tubes connected in series and contract in diameter as:

$$\tau = \left(\frac{\dot{\gamma}}{\phi}\right)^{1/m} \quad , \quad \Delta p = \left[\frac{(m+3)(2L)^m \dot{Q}}{\pi R^{m+3} \phi}\right] \quad \textit{Tubes}$$

$$\Delta p = \frac{mL}{3(R_0 - R_1)}\left[\frac{(m+3)2^m \dot{Q}}{\pi \phi}\left(\left(\frac{1}{R_1}\right)^3 - \left(\frac{1}{R_0}\right)^3\right)\right]^{1/m} \quad \textit{Cone Sections} \qquad (5)$$

The Euler buckling analysis of the filaments results in the following expression for critical pressure drop:

$$P_{cr} = \frac{\pi^2 \, E \, d_f^2}{16 \, L_f^2} \tag{6}$$

Combining equations 5 and 6 with the empirical data on NCA for RU955 material, the operation windows have been predicted for T15 and T25 tips under different internal cone angles, as shown in Figure 4 a. & b. The filament elastic modulus was selected as E = 15MPa, and filament buckling length as 7.62 mm (0.3"). It is apparent that there is a upper limit on flow rates for given filament and tip diameters, and material properties.

DETAILED DEPOSITION MODEL

The temperature field near the vicinity of deposition region can be analyzed in detail, if one would assume: a. the previously deposited material had ample time to cool down an equilibrium temperature, b. temperature field can be averaged across the thickness reducing the dimensionality of the problem by one, c. the heat transfer to ambient and previous layer can be modeled effectively with heat sink terms. The resulting quasi-steady state, two dimensional modified advection conduction equation in the reference frame of the moving deposition head may be written as:

$$\rho \, c_p \, V \frac{\partial T}{\partial x} = \frac{\partial}{\partial x}\left(k \frac{\partial T}{\partial x}\right) + \frac{\partial}{\partial y}\left(k \frac{\partial T}{\partial y}\right) - \frac{h_\infty}{th}\left(T - T_\infty\right) - U\left(T - T_{sub}\right)$$

$$T = T_0 \, , @ \, \vec{r} \in \Gamma_1 \quad , \quad T = T_{sub} \, , @ \, \vec{r} \in \Gamma_2 \tag{7}$$

$$-k \frac{\partial T}{\partial n} = \frac{h_\infty}{th}\left(T - T_\infty\right) , @ \, \vec{r} \in \Gamma_3 \quad , \quad \frac{\partial T}{\partial n} = 0 \, , @ \, \vec{r} \in \Gamma_4$$

, where h_∞ is envelope convective cooling coefficient, T_∞ is envelope temperature, T_{sub} is equilibrium temperature of previously deposited material, U is a general heat transfer coefficient which may be defined as the ratio of effective interface thermal conductivity to a characteristic depth at which equilibrium temperature is reached in previous layer, and th is road thickness. It should be noted the conservative definition of diffusive heat flux terms enables the equation to be applicable to heterogeneous material systems.

The governing equation is discretized with finite volume method on multiple-block grids, Figure 5. ADI method is utilized for the solution of discrete equations utilizing a pseudo time integration scheme.

Dimensional Analysis

The governing equation may be non-dimensionalized as:

$$x' = \frac{x}{w} \quad , \quad y' = \frac{y}{w} \quad , \quad \theta = \frac{T - T_\infty}{T_0 - T_\infty}$$

$$Pe_w \frac{\partial \theta}{\partial x'} = \frac{\partial}{\partial x'}\left(\frac{\partial \theta}{\partial x'}\right) + \frac{\partial}{\partial y'}\left(\frac{\partial \theta}{\partial y'}\right) - Bi_w \frac{w}{th}\theta - Uw^2\left(\theta - \theta_{sub}\right) \tag{8}$$

$$\theta = 1 \,, @\vec{r} \in \Gamma_1 \quad ; \quad \theta = \theta_{sub} \,, @\vec{r} \in \Gamma_2$$

$$-\frac{\partial \theta}{\partial n} = Bi_w \frac{w}{th}\theta, @\vec{r} \in \Gamma_3 \quad , \quad \frac{\partial \theta}{\partial n} = 0 \, @\vec{r} \in \Gamma_4$$

,where

$$Pe_w = \frac{\rho c_p V w}{k} \quad , \quad Bi_w = \frac{h_\infty w}{k} \tag{9}$$

Six numerical experiments have been conducted to investigate effect of Peclet and Biot numbers on temperature distributions, by assuming θ_{sub}=0 and U = 0. The results are shown in Figures 6 and 7. Peclet number variations mainly effected the axial, along deposition direction, temperature distributions. Higher Peclet configurations result in longer 'active interface lengths', and hence better interface bonding for the production of same geometrical features. However the cooling time of road-substrate interface has been found to be weakly dependent on Peclet number due to linear inter dependence of Pe, V and time. Biot number variations on the other hand produced a more isotropic effect on the temperature distributions, with high Biot numbers resulting in shorter 'active interface lengths' and shallower extent of the heat affected zone in lateral direction. Since deposition velocity does not appear in Biot number definition, the reductions in active lengths also corresponded to reductions in residence times.

Multiple Materials

Fabrication of spatially distributed materials, embedded structures and topologically optimized composite articles require sequential deposition of neat and particle filled materials in Fused Deposition. Thermal behavior of parts composed of multiple materials may be different during production, due to differences in their thermal properties. Additional parameters that would characterize the deposition sequence are needed to investigate different thermal behavior patterns during deposition. As an example the sequential production of a three road part made out of two different material systems is considered. Thermal conductivities of 'plastic'(P) and 'metal filled'(M) phase are k = 0.2 W/(m K) and 3.0 W/(m K) respectively. Following parameters were considered for both of the materials in the current study: ρ=1200 kg/m^3, c_p=1500 J/(kg K), V = 20 mm/s, th = 0.25 mm, w = 0.5 mm, T_0 = 270°C, h_∞=100 W/(m K), T_∞=70°C. Two stacking sequences were considered, P/M/M and M/M/P. The results are depicted in Figure 8 a & b. For first stacking sequence the lateral penetration of heat effected zone is limited compared to the second sequence, however the active interface length is longer due to smaller road 1 Peclet number.

CONCLUSIONS

A set of computational tools has been presented for the analysis of extrusion phase in Fused Deposition. Design methodologies have been developed for liquefier entrance, liquefier length, unheated tip and internal duct design through employment of analytical and

computational thermal design tools. Particular emphasis has been placed on identification of non-dimensional groups to consolidate number of variables in the analysis.

Also a detailed description of quasi-steady state, two dimensional deposition thermal model is presented. Finite volume method on non-uniform multi-block grids has been utilized in the formulation. Peclet and Biot numbers based on road width were identified as important parameters from dimensional analysis, and their effect on temperature distributions is demonstrated through computational experiments. Peclet number has been found to modify the temperature field anisotropically (dominantly in axial direction) whereas Biot number changed temperature distributions isotropically. Also building scenario effects have been investigated for a two material, three road configuration. Significant penetration depth were observed.

REFERENCES

1. Agarwala M. K., van Weeren R., Vaidyanathan R., Bandyopadhyay A., Carrasquillo G., Jamalabad V., Langrana N., Safari A., Garofalini S. H., Danforth S. C., Burlew J., Donaldson R., Whalen P., Ballard C., "Structural Ceramics by Fused Deposition of Ceramics," *Proceedings of SFF Symposium 1995*, pp. 42-49, 1995.
2. Batchelder J. S., Curtis H. W., Goodman D. S., Gracer F., Jackson; R. R., Koppelman G. M., Mackay J. D., *Model generation system having closed-loop extrusion nozzle positioning*, US Patent #5,303,141; April 12 1994.
3. Burmeister, L. C., *Convective Heat Transfer*, pp. 218, John Wiley & Sons, 1983
4. Crump S., *Apparatus and method for creating three-dimensional objects,* US Patent #5,121,329, June 9, 1992.
5. Comb J. W., Priedeman W. R., Turley P. W., "FDM technology process improvements," *Proceedings of SFF Symposium 1994*, pp. 42-49, 1994.
6. Geiger M., Steger W., Greul M., Sindel M., "Multiphase Jet Solidification - a new process towards metal prototypes and a new data interface," *Proceedings of SFF Symposium 1994*, pp. 9-16, 1994.
7. Hilmas G. E., Lombardi J.L., Stuffle K., "Recent developments in extrusion freeform fabrication (EFF) utilizing non-aqueous gel casting formulation," *Proceedings of SFF Symposium 1996*, pp. 432-439, 1996.
8. Khoshnevis B., "Contour Crafting: A new Rapid Prototyping process," *Proceedings of The Seventh International Conference on Rapid Prototyping*, March 31-April 3 1997, pp. 13-22, 1997.
9. Liang J.Z., Ling Y. Z., Li. R.K.Y., Tjong S.C., "Quantitative description of vortical region length of non-newtonian fluids through an abrupt contraction," *ASME - AMD vol.217*, pp. 105-107, 1996.
10. Michaeli W., *Extrusion Dies for Plastics and Rubber: Design and Engineering Computations*, 2nd Edition, Hanser Publishers, 1992.
11. Yardimci M. A., Guceri S.I., Danforth S. C, Safari A., "Numerical modeling of Fused Deposition processing", *Proceedings of The ASME Materials Division, MD-Vol. 69-2*, pp. 1225-1236, 1995
12. Yardimci M. A., Guceri S. I., "Conceptual framework for the thermal process modeling of Fused Deposition", *Rapid Prototyping Journal*, vol.2, no.2, pp. 26-31, 1996

13. Yardimci M. A., Guceri S. I., Agarwala M., Danforth S. C., "Part quality prediction tools for Fused Deposition processing," *Proceedings of SFF Symposium 1996*, pp. 539-548, 1996.

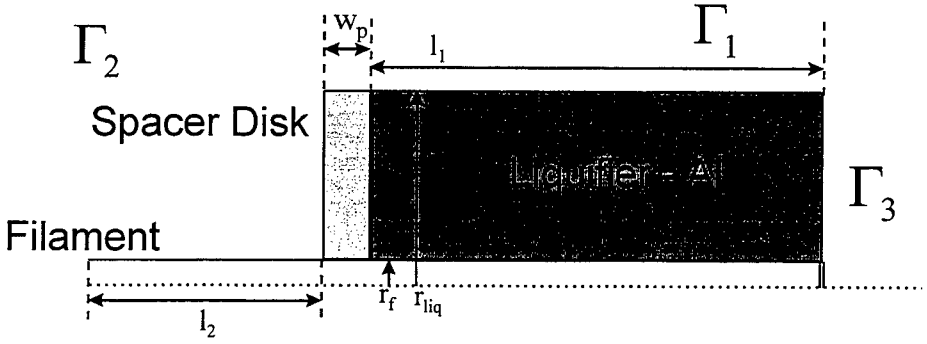
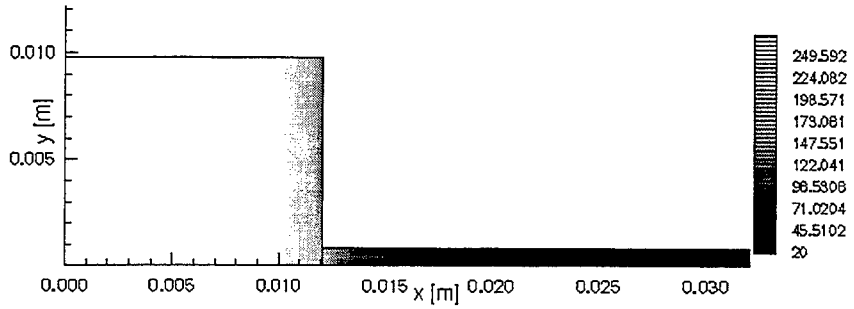
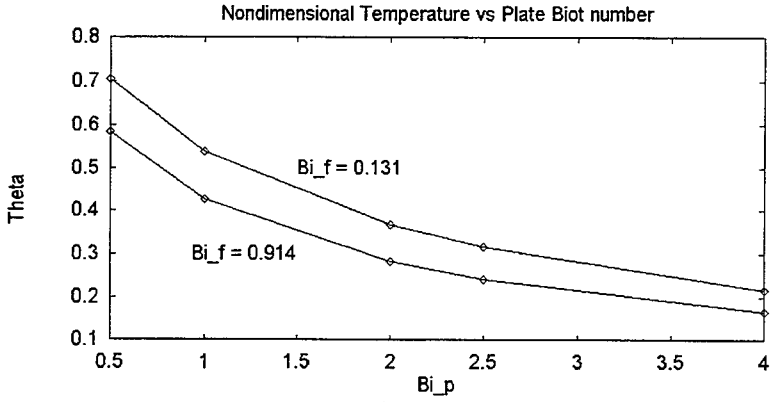


Figure 1. Liquefier Entrance

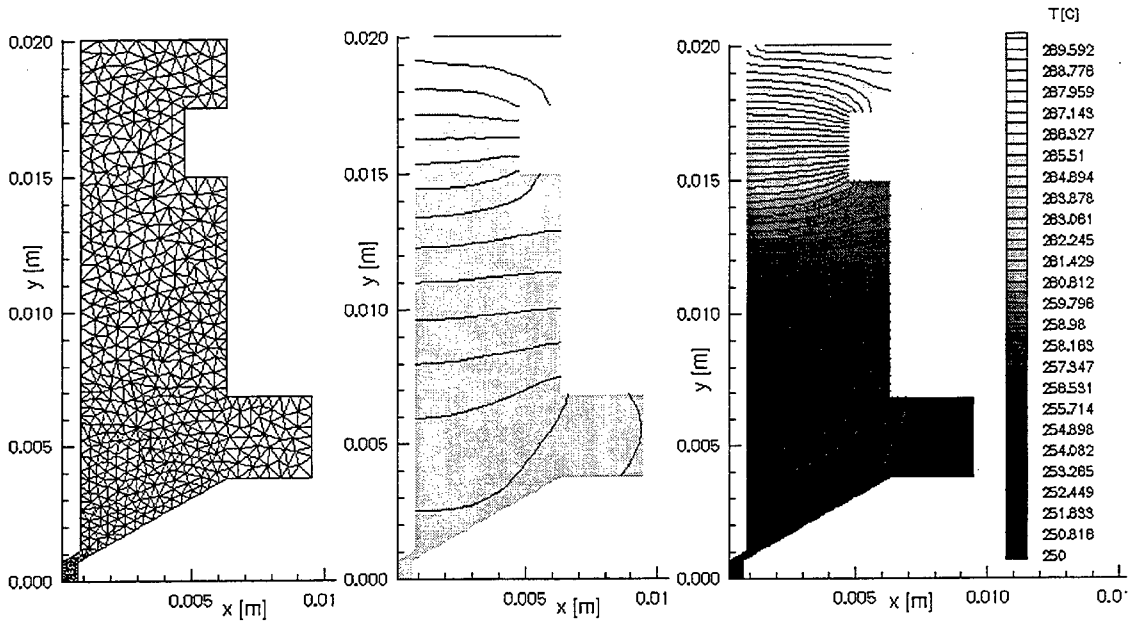


a.



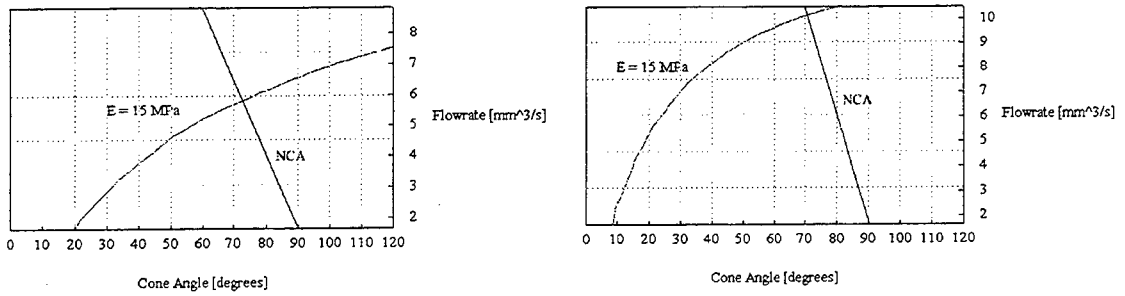
b.

Figure 2. a. Temperature distribution at liquefier entrance for example case, b. Dependence of entrance temperature on plate and filament Biot numbers



a. b. c.

Figure 3. FE Mesh (a) and Temperature distributions for Aluminum (b) and Steel (c) T16 (0.0016" diameter) nozzles



a. b

Figure 4. Operation windows of RU955 with T15 (a) and T25 (b) nozzles

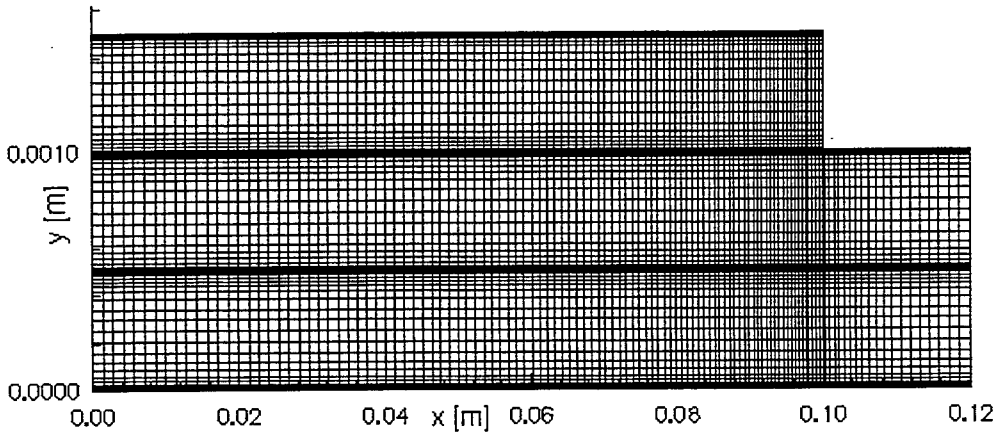


Figure 5. Employed multi-block grid for quasi steady state deposition model

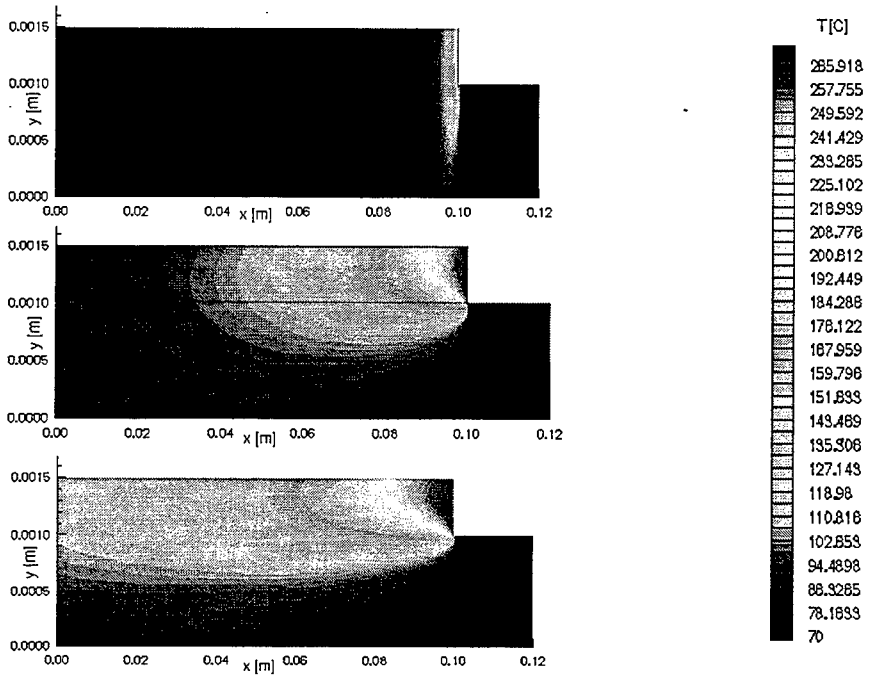
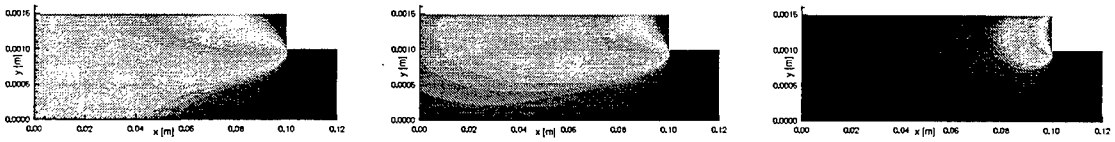
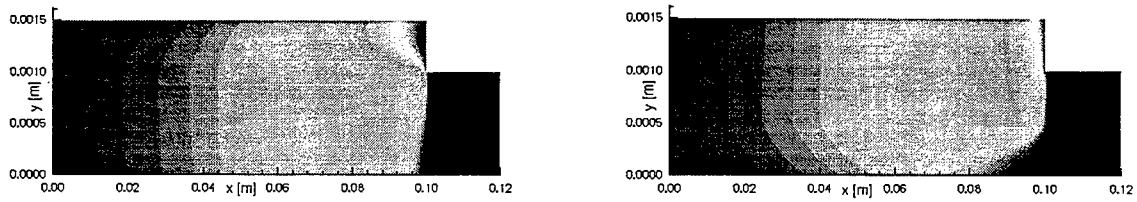


Figure 6. Effect of Peclet number variations on temperature distributions, Bi_w w/th = 0.5; a. Pe_w = 5.0, b. Pe_w = 90.0, c. Pe_w = 180.0



a. b .c.

Figure 7. Effect of Biot number variations on temperature distributions, Pe_w = 90.0, w/th=2.0; a. Bi_w = 0.0125, b. Bi_w = 0.125, c. Bi_w = 1.0



a. b.

Figure 8. Multiple Material Fused Deposition, a. Plastic/Metal/Metal, b. Metal/Metal/Plastic

SIMULATION OF COARSENING DURING LASER ENGINEERED NET_SHAPING

by
Veena Tikare, Michelle Griffith
Eric Schlienger, John Smugeresky*
Sandia National Laboratories
Albuquerque, NM
*Livermore, CA

Abstract

Laser Engineered Net_Shaping, otherwise known as LENS™, is an advanced manufacturing technique used to fabricate complex near net shaped components directly from engineering solid models without the use of dies or machining . The ultimate objective of this project is to develop predictive simulation capability which will allow the LENS™ processors to determine fabrication conditions given the material, shape, and application of the final part. In this paper, we will present an incremental achievement to meeting the ultimate goal, a model capable of simulating the coarsening of microstructural features under the unique thermal history to which a LENS™ part is subjected during processing. The simulation results show how grains of very different shapes and sizes form within the same deposition line. They also show that relatively minor changes in the dynamic temperature profile results in microstructures with vastly different characteristics. The implications of this work for LENS™ fabrication is that controlling the temperature profile is essential to tailoring the microstructure of a component to its application.

Introduction

In the past, the development cost of a product was amortized over a large number of manufactured units. Current markets often demand small quantities of many different components with highly specialized performance requirements. Thus, development cost of each component cannot be amortized over large numbers and becomes prohibitively expensive. To reduce development cost, a number of solid free-form fabrication techniques are being developed. One such free-form technique, Laser Engineered Net_Shaping, LENS™, is being developed at Sandia for rapid forming of complex shaped engineering components made from a variety of metals[1]. LENS™ parts are made by depositing metal particles directly into a weld pool formed by an Nd:YAG laser; the particles are melted and the weld pool is rastered under the laser beam to build each cross section or layer of a component. Subsequent layers are additively fabricated to form the part.

This fabrication process results in microstructures which are unique. Each deposited line has features which are inherent to it. Some features extend into the neighboring lines and into the adjoining layers as shown in figure 1, an SEM micrograph of a tool steel component fabricated by the LENS™ process. These features such as grain size and shape have a large effect on materials

properties and performance. Therefore, it is essential that microstructural evolution during LENS™ fabrication be controlled. To this end, we are developing a model which will predict microstructural evolution during fabrication. In this paper, we will present a model which is capable of simulating coarsening in a single-phase system under an assumed temperature profile of a LENS™ fabrication technique.

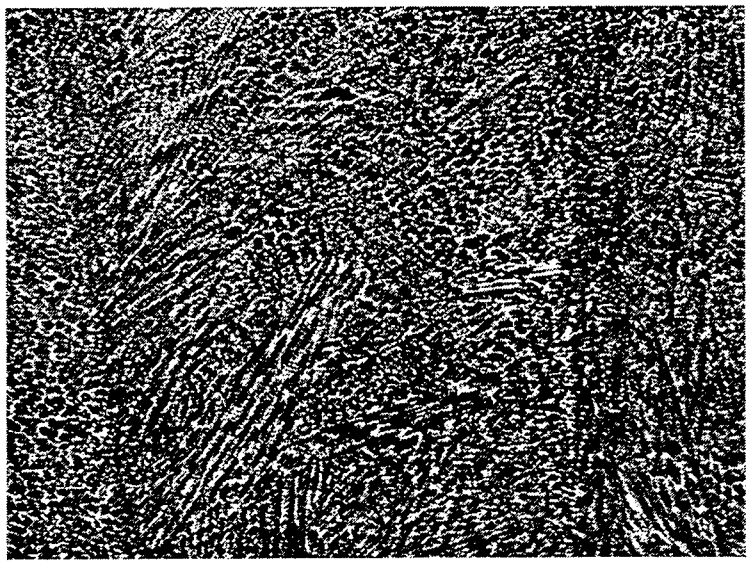


Figure 1. Optical micrograph of a LENS™ component showing microstructure within a deposition line. The direction of raster is to the top. (250 x)

LENS™ Process Description

In the LENS™ process, a metal part is formed by depositing lines with widths and heights of approximately 300 μm to form a layer with the topographical features of the part at the height of that layer. Once that layer is deposited, the next layer is deposited above it, again in a line by line sequence. The actual deposition process is accomplished by melting a pool at the part surface using a laser beam. Next, material in the form of particles is fed into the molten pool. The laser beam and feed material are rastered across the part surface to form deposition lines. As the laser beam moves away, the material cools and solidifies incorporating the added material. The previously formed layer will be heated as the laser beam rasters across. At higher temperatures, microstructural evolution will occur in this layer. The process which will be simulated in this work is the coarsening of grains driven by capillarity in the layer under the current deposition layer.

Model Description

The Potts model, a statistical-mechanical model[2], was used to simulate microstructural evolution during the LENS™ process. It has been used to simulate a number of microstructural evolution processes, including grain growth, recrystallization, Ostwald ripening, and phase-

transformations. In this study, we have modified the Potts model to simulate two-dimensional coarsening in the dynamic temperature profile of the rastering laser used by the LENS™ process.

Microstructural representation in the Potts model is done by populating a lattice with a canonical ensemble. We use a square lattice and each lattice site is assigned a "spin"*. Contiguous sites of the same spin form a grain with a sharp grain boundary between adjacent grains. The number of different, degenerate spins that the lattice sites can assume is Q. The individual state is designated by the symbol q and the total number of states in the system is Q, $q_{grain} = [1, 2, \ldots Q]$. All the simulations in this work used $Q = 100$. The equation of state for these simulation is the sum of all the neighbor interaction energies in the system given by

$$E = \frac{1}{2}\sum_{i=1}^{N}\sum_{j=1}^{8}\left(1-\delta\left(q_i, q_j\right)\right) \qquad \textit{eq. 1}$$

where N is the total number of sites, δ is the Kronecker delta with $\delta(q_i = q_j) = 1$ and $\delta(q_i \neq q_j) = 0$, q_i is the state of the grain at site i and q_j is the state of the nearest neighbor at site j. Thus, the only energy considered in the simulation is the interfacial energy and all unlike neighbors contribute one arbitrary unit of energy to the system. This yields a single-component, single-phase system with uniform, isotropic[3] interfacial energies between grains.

Now that the microstructural representation and system energies are defined in the simulation, we turn to the grain growth mechanism and kinetics. Grain growth is simulated using the method developed in previous works[4,5]. First, a grain site is chosen at random from the simulation space. Then a new state q is chosen at random from the Q possible states in the system. The grain site is temporarily assigned the new state and the change in energy is evaluated using eq. 1. Next the standard Metropolis algorithm is used to perform the grain growth step based on Boltzmann statistics. A random number, R, between 0 and 1 is generated. Next, the transition probability, P, is calculated using

$$P = \begin{cases} \exp\left(\dfrac{-\Delta E}{k_B T}\right) & \textit{for} \quad \Delta E > 0 \\ 1 & \textit{for} \quad \Delta E \leq 0 \end{cases} \qquad \textit{eq. 2}$$

where k_B is the Boltzmann constant and T is absolute temperature. If the $R \leq P$, then the grain growth step is accepted, if not, the original state is restored. The simulation temperature used for grain growth was $k_B T = 0$ which has been shown to simulate grain growth well. Time in the Potts

*The term spin originates from the original application of the Potts model which was used to study domain growth in magnetic materials.

model is measured in units of Monte Carlo step; 1MCS corresponds to N attempted changes where N is the total number of sites in the system.

In order to simulate the LENS™ process, the Potts model was modified to include a dynamic temperature profile. This was done by considering the grain boundaries to have a velocity, V_{gb}, which is proportional to grain boundary mobility, M_{gb}, and to the driving force, μ, as

$$V_{gb} = M_{gb}\mu \qquad \textit{eq. 3}$$

Assuming that the mobility of the grain boundaries is a function of temperature, one can simulate coarsening in a dynamic temperature environment by using a temperature dependent mobility term, $M_{gb}(T)$. At high temperatures, the mobility term is large and at lower temperatures it is small. Since we are simulating a laser beam rastering across a part, the mobility term becomes a function of position, x, and of time, t, $M_{gb}(x,t)$. The transition probability given in *eq. 2* is modified to include temperature dependence by multiplying by the mobility term as

$$P = M_{gb}(x,t)\begin{cases} \exp\left(\dfrac{-\Delta E}{k_B T}\right) & \textit{for} \quad \Delta E > 0 \\ 1 & \textit{for} \quad \Delta E \le 0 \end{cases} \qquad \textit{eq. 4}$$

The temperature profile assumed for the LENS™ process is a laser beam with a Gaussian temperature distribution. Preliminary characterization of the laser beam indicated that the beam was elliptically shaped; thus, a Gaussian distribution as shown in figure 2 was used for the simulation. Grain growth in a single line width and of an arbitrary length was simulated in this work with a temperature profile, as shown in figure 2, rastered across the length of the line.

Simulation Results

Simulation of normal grain growth of an isotropic, single phase system under isothermal conditions has been studied and reported in previous works[3,6]. The microstructures from the isothermal grain growth simulations are shown in figure 3. The resulting microstructures are characterized by grain growth exponent, n=2, as predicted by theory[7]. After an initial transition period, the microstructures exhibit self-scaling behavior, so that the grain size distributions normalized by the average grain size and topology are independent of grain size. Thus, it has been shown that the Potts model can accurately simulate isothermal normal grain growth when grain boundary mobility is constant with temperature.

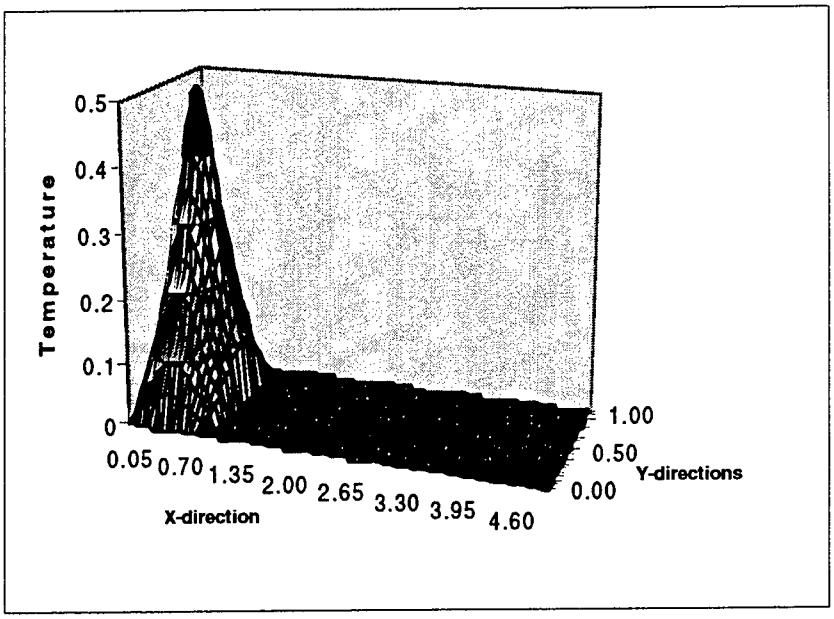


Figure 2. The temperature profile with Gaussian distribution in the X- and Y- directions was used to simulate coarsening.

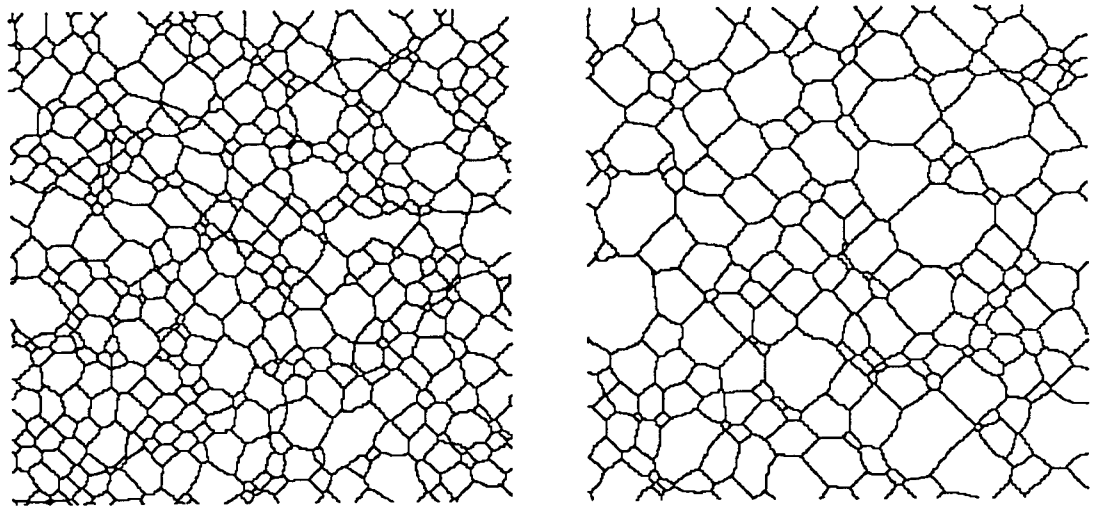


Figure 3. Simulation of isothermal grain growth using the Potts model at 40,000 and 90,000 MCS.

Next, we turn our attention to the simulation of grain growth under a rastering temperature profile of a laser beam. As shown in figure 2, a Gaussian temperature profile with a hot center and progressively cooler edges was rastered with a speed of V_{lb}= 0.05 sites/MCS. The resulting microstructures at mid- and full-raster are shown in figure 4. At the higher temperatures in the center of the line, grains have grown larger. They are also slightly elongated in the center. Another simulation under the same conditions was run with the same temperature profile, but

with a laser raster speed of half the previous simulation speed, V_{lb} = 0.001 sites/MCS. The resulting microstructures is shown in figure 5. This microstructure is dramatically different from the one at the faster raster rate, shown in figure 4. At the slower raster speed, the grain in the higher temperature region are highly elongated in the direction of laser raster. The grains in the cooler region are progressively less elongated and become equiaxed at the coolest region.

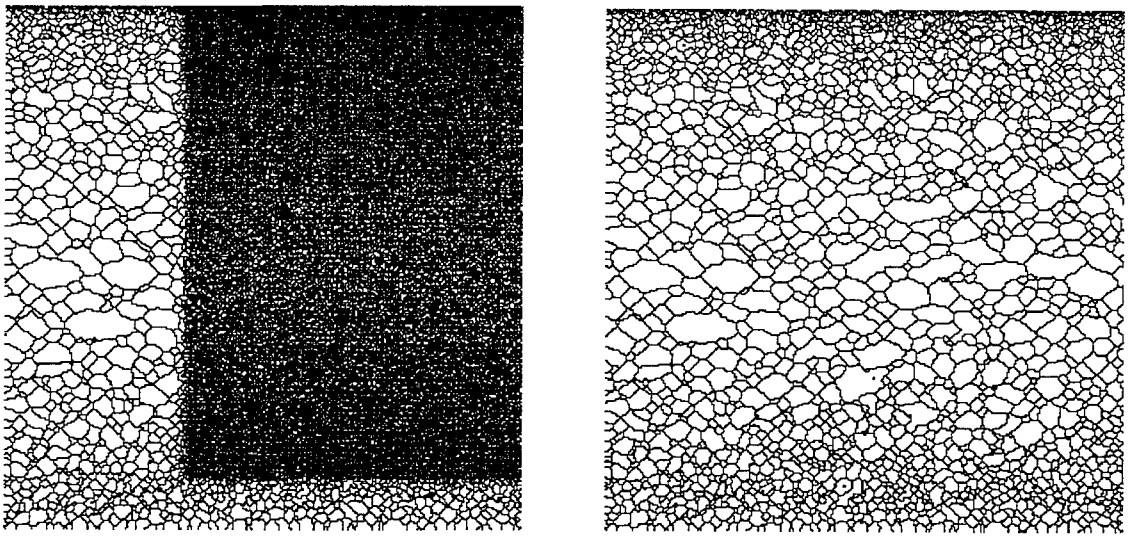


Figure 4. Coarsening in a deposition layer at mid- and full-raster of a laser beam. The raster velocity, V_{lb} = 0.05 sites/MCS. The laser raster direction is to the right. The strip at the bottom of the figure is the previously deposited line.

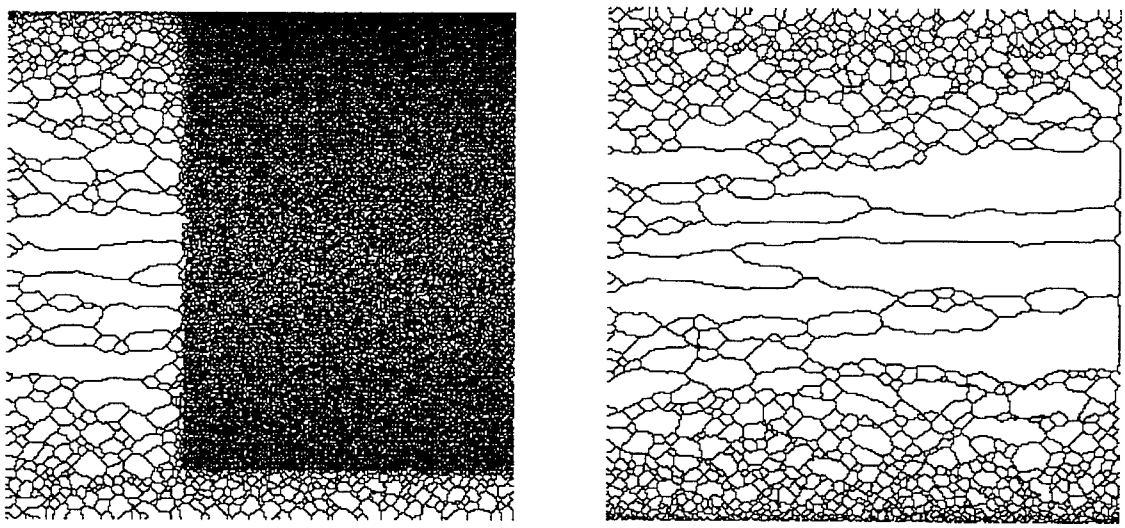


Figure 5. Coarsening in a deposition layer at raster velocity, V_{lb} = 0.001 sites/MCS. The raster direction is to the right and strip is previously deposited line.

Preliminary characterization of the laser beam revealed that the elliptical Gaussian shape of the laser beam was not perpendicular to the laser raster direction, but tilted as shown in figure 6. To understand the effect of such a laser beam, we ran simulations with a tilted beam. The simulation parameters were the same as the previous simulation whose results are shown in figure 5, except

that a tilted temperature profile is used. As shown in figure 7 the grains are highly elongated which was expected as the slower raster speed of $V_{lb} = 1x10^{-3}$ sites/MCS was used. However, unlike the previous simulation, the elongation is tilted like the laser beam. The abrupt change in microstructure at the left end is due to the use of periodic boundary conditions. At the beginning of the simulation, the bottom of the laser beam is at bottom, left corner of the simulation space and the top is wrapped around to the right of the line at the left end of the simulation space. At the end of the raster, the laser beam is positioned at the line. This leads to the abrupt discontinuity in the microstructure seen in figure 7.

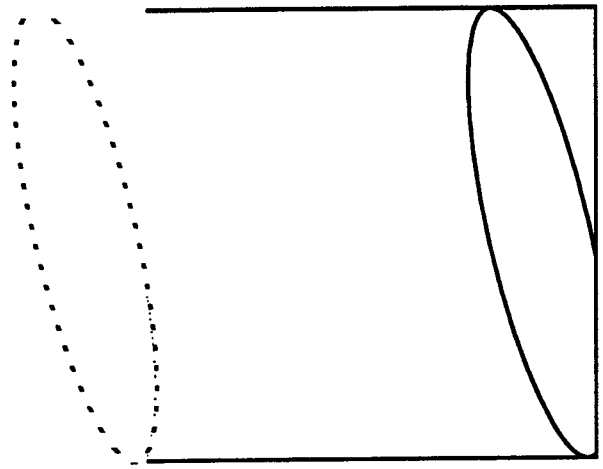


Figure 6. The temperature distribution across the simulation space with periodic boudary conditions at time t = 0. Light areas are at higher temperature than dark areas

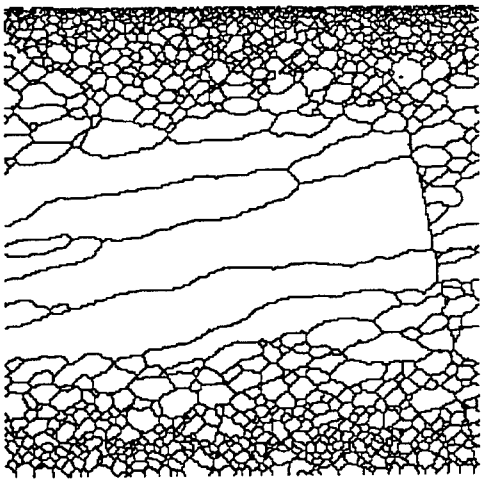


Figure 7. Grain growth with a tilted temperature distribution.

Discussion

The Potts model has been used extensively to study many different coarsening phenomena, however incorporating a dynamic, non-linear temperature in the Potts model to simulate coarsening in a ™ part during fabrication is a unique application of this model. In this work, simulation of coarsening in a dynamic temperature environment was achieved by varying the mobility of the grain boundaries with temperature. This is an accurate modeling method as long as the grain growth mechanism and driving force for grain growth are temperature independent and only grain boundary mobility changes with temperature. This is a valid assumption as the growth mechanism and driving force for a number of thermally activated processes is temperature independent over fairly large temperature ranges. Furthermore, in the current study, we were not interested in the effects of multiple grain growth mechanisms or temperature dependent driving force on coarsening. The objective here was to understand coarsening in single-phase, isotropic, material subject to an unusual thermal history.

The simulations presented in this paper show that the raster speed of the laser beam and the temperature distribution around it has a large effect on the grain size and shape. At the faster

laser beam raster speed of $V_{lb} = 0.05$ sites/MCS, the grains were slightly elongated in the hot section. At this speed, the grain boundary velocity was too slow to grow with the laser beam. When the laser raster speed was slowed to 0.001 sites/MCS, the grain boundary velocity was able to move with the laser. In the cooler regions, on the top and bottom of the simulations, the grain boundary velocity was slower; thus, unable to move with the laser beam. This resulted in progressively smaller, more equi-axed grains away from the center line of the simulation.

The tilted grains seen in figure 7 were unexpected. While the laser beam is tilted, the hot-zone still rasters in the same position, the center of the deposition line. It is only the distribution around the hot-zone that changes slightly. This result demonstrates that grain growth is highly sensitive to any asymmetry in the temperature profile of the system.

The microstructure within a deposition line of the a LENS™ component is shown in figure 1. One can see the highly elongated features and as well as the equiaxed features in the microstructure. From our simulation results, we know that the elongated features are forming in the regions where the grain boundary velocity is sufficiently large to move with the moving high temperature of the laser. The equiaxed features are forming in the lower temperature region of the deposition line where the grain boundary velocity is slower and cannot keep pace with the rastering laser beam.

The elongated features are not in the direction of laser raster, rather they are at angle to the raster direction. The results of the simulation suggest that the temperature profile in the LENS™ part during fabrication is far more complex than was assumed for the purposes of this investigation. We assumed a Gaussian temperature distribution centered in the middle of the deposition line with symmetric distribution around it and moving at a constant rate in the direction of raster. Clearly, the LENS™ part experienced a temperature profile which is does not have these characteristics. The direction of elongation is not is the direction of laser raster. This suggests that the direction of temperature profile movement is not in the direction of laser raster. The part of the LENS™ component which has already been formed will act as a heat sink and draw heat away in the direction of previous deposition lines yielding asymmetry in the temperature profile of the part. Furthermore, the asymmetric cooling will move the high-temperature zone away from previously deposited lines. There are also abrupt changes in the microstructural features within a deposition line like the one seen in figure 7. This suggests that the temperature profile in a deposition line is not a continuous smooth raster, but has some discontinuities yielding the abrupt microstructural changes.

The simulations in this work demonstrate the importance of knowing and controlling the temperature distribution during fabrication of a LENS™ part. The temperature distribution influences microstructural evolution and therefore must be controlled to tailor the microstructure for optimal performance. Conversely, if certain microstructural features are desirable, this simulation capability can be used to determined the temperature profile necessary for their formation.

Conclusions

The Potts Model can predict the coarsening of grains during LENS™ fabrication. It can simulate grain growth driven by capillarity in a non-linear, dynamic temperature profile of a rastering laser beam. The simulated microstructures had many of the features seen in the actual LENS™ parts, in particular they had elongated grains in the direction of a moving temperature profile, equiaxed grains at the cooler regions of the same moving temperature profile and abrupt change in size and shape of grains where there was a discontinuity in moving temperature profile. Thus, the grain size and shape were shown to vary within a deposition line depending on the thermal history of that particular region.

References

[1]M. L. Griffith, D. M. Keicher, C. L. Atwood, J. A. Romero, J. E. Smugeresky, L. D. Harwell, D. L. Greene, *Free Form Fabrication of Metallic Components using Laser Engineered Net Shaping (LENS™)*, proceedings of the Solid Freeform Fabrication Symposium, August 12-14, 1996, Austin, TX, p.125.

[2] F. Y. Wu "The Potts Model," Rev. Modern Phys., 54 [1] 235-268 (1982).

[3] E.A. Holm, James A. Glazier, D.J. Srolovitz, G.S. Grest, "Effects of Lattice Anisotropy and Temperature on Domain Growth in the Two-Dimensional Potts Model," Phys. Rev. A, 43 [6] 2662-2668 (1991).

[4] D.J. Srolovitz, G.S. Grest, M.P. Anderson, and A.D. Rollett, "Computer Simulation of Recrystallization II. Heterogeneous Nucleation and Growth," Acta Metall., 36 [8] 2115-2128 91988).

[5] J. Wejchert, D. Weaire, J.P. Kermode, "Monte Carlo Simulation of the Evolution of a Two-Dimensional Soap Froth," Phil. Mag. B53 15-24 (1986).

[6] M.P. Anderson, D.J. Srolovitz, G.S. Grest, and P.S. Sahni, "Computer Simulation of Grain Growth I. Kinetics," Acta Metall. 32 [5] 783-791 (1984).

[7] M. Hillert, "On the Theory of Normal and Abnormal Grain Growth," Acta Metall., 13 227-231 (1965).

On dimensional stabilities : Modeling of the Bonus-Z during the SLS Process

Alexandre L. Papadatos, Said Ahzi, Carl R. Deckard and Frank W. Paul

Laboratory to Advance Industrial Prototyping
Department of Mechanical Engineering, Clemson University, Clemson, SC 29634

Abstract

This work is a first step towards the prediction of the dimensions and thermo-mechanical properties of parts made with the Selective Laser Sintering (SLS) technology. An important variation of the dimensions is found in the Z-direction of the build. This phenomenon is known as the "Bonus-Z" where material properties differ from those in the rest of the part due to a non-homogeneous sintering. The focus of this work is the characterization and the modeling of the bonus-Z phenomenon, by relating it to the energy input. The polymer powder used in this study is polycarbonate.

1. Introduction

In a recent tensile experiment we have dealt with problems of dimensional stabilities of the tensile samples using polycarbonate powder. The results we got are biased by the failure to obtain the same dimensions on parts built with different process parameters. The most important variation was found in the Z-direction of the build, a phenomenon known as "Bonus-Z". Bonus-Z counts for the extra sintering of powder that occurs under the first layer built. This extra sintering is due to laser energy that is in excess from the ideal laser energy that would be enough to sinter the particular layer.

Due to the phenomena of growth, shrinkage and curling, we also get different dimensions in the X-Y directions when building a specific part with different process parameters, but the highest difference is found in the Z-direction. As a result, the tolerances in the Z-direction are far away from the wanted ones.

Rapid prototyping part accuracy has been documented in a number of studies [1-4]. In most of these studies accuracy is reported as the deviation of measured dimensions from the desired ones. The basic remedy to the bonus-Z phenomenon is the sintering of the first layers with less laser power, implying less energy delivered to the powder bed. Due to the complexity of the part's geometry, a dynamic variation of the laser power during the build is a very complex task. In this study, the accuracy of SLS parts in the Z-direction of the build will be discussed. We will focus on the energy delivery into the powder bed.

To fabricate a part, powder is first spread in a thin, uniform layer over the part bed surface, and a typical layer thickness is 0.12 mm. The laser beam is raster scanned over the part bed surface with the scanning mirrors and the laser energy modulated so that only the area which corresponds to the cross section of the object is fused. The two

dimensional cross sections are defined by software that "slices" the three dimensional CAD model into layers. Once the first layer is built, a new layer of power is spread. This new layer is then scanned with the laser and this process is repeated until the part is completely built. Sufficient laser energy is used so that each new layer is bounded to the previous layer and as the part is fabricated, the unsintered powder beneath the scanned layers provides support for features as overhangs.

The part bed temperature is typically held just below the glass-transition temperature of the polymer, so that little laser energy is enough to sinter the desired areas. This method also prevents high thermogradients within the powder bed. However, controlling the amount of energy that penetrates into the powder bed within and beneath the scanned layer is a very complex task mainly due to the following reasons :

i) when about to build a layer that is scanned on unsintered powder (in contrast with a layer built on previous layers), we need to know the exact amount of energy to deliver in order to sinter only the powder that corresponds to the thickness of one layer. Otherwise, powder beneath this layer will also be sintered resulting in bonus Z.

ii) the properties that dictate the behavior of the sintering (such as powder density, thermal conductivity, temperature) change with the degree of sintering, and are function of the time and the geometry of the build (such as scan direction, scan pattern, scan spacing, scan speed etc.).

iii) a certain amount of energy penetrating beneath the scanned layer is needed in order to bound the currently scanned layer with the previous one.

2. Experiments

At Clemson University, we are working on the SLS with the objective of developing process understanding that will lead to system performance improvements. Previous studies from our team [5-6] have dealt with the control of thermal gradients within (and beneath) the layer being sintered (or melted) that has been identified as a key process issue. Large thermal gradients are a significant feature of the SLS process using polycarbonate, the material we used in our studies.

We are interested in finding the contribution of each layer of a build to the final bonus Z of the part. The experimental approach uses square parts of one inch side, fabricated on a research SLS workstation. In the same run, eight squares are being built, all with the same process parameters. The process parameters are kept constant for all the layers and the most important parameters are :

Bed Temperature : 120°C
Laser Power : 7.5 Watts

Beam Speed : 5.70 in/s
Glass Transition Temperature : 150°C

The first square is one layer thick, the second square two layers thick and so on. Then we measured their thickness, compared it to the expected thickness and we derived the bonus-Z. Table 1 shows that, out of 19 mils (482 μm) of bonus-Z after 8 layers, 12 mils (305 μm) of the bonus-Z are obtained during the building of the very first layer. 3 more mils of bonus-Z are related to the third layer. One more mil of bonus-Z comes with the building of the fifth, and with the seventh layer. Finally two more mils of bonus-Z result from the eighth (the last) layer. These results were obtained by using the above process parameters. When the laser power was increased to 12.5 Watts, a bonus-Z of 18 mils (457 μm) was obtained for the first layer. Our objective was to build these squares with the less bonus-Z possible. For laser power values less than 7.5 Watts, sintering in our SLS station was not enough to sinter a first layer.

Table 1 : Evolution of Bonus-Z during the built of 1 in. side squares

Layer Number	Measured Thickness (mils)	Expected Thickness (mils)	Bonus Z
# 1	0.017	0.005	0.012
# 2	0.022	0.010	0.012
# 3	0.030	0.015	0.015
# 4	0.035	0.020	0.015
# 5	0.041	0.025	0.016
# 6	0.046	0.030	0.016
# 7	0.052	0.035	0.017
# 8	0.059	0.040	0.019

3. Simulations

In order to reduce bonus-Z, DTM Corporation advises to reduce the laser power while building the first layers. However, bonus-Z is not only a function of laser power : It also depends on the geometry of the part to build, and manual control of the energy delivery becomes impossible due to the high speed of the build. In order to control automatically the delivery of the laser energy, both a hardware and a software have been developed at Clemson University. The hardware part is described in full details in [7]. It is now possible to include in the scan file (file that describes the part to build in scanning commands) a new command that controls the laser power. Based on the remarkable work of Sun and Beaman [8-9] a building simulator has been developed. We have implemented the model of Sun and Beaman to simulate the building of a part using the same scan file that is sent to the General Scanning Inc. (GSI) scanners. As an output we get predictions of the time of the build, temperature, density and energy in the powder bed. In their physical modeling of the SLS process, Sun and Beaman have used three sub-models : a optical sub-model that predicts the energy input from the laser, a thermal sub-model

solving the heat transfer model, using finite differences method and a sintering model that predicts the change of the material properties.

We have implemented these three sub-models as in the work of Sun [8]. We added to this implementation the simulation of the operations the GSI scanners. According to the GSI scanner user manual, we have implemented all the operations performed by the CPU controlling the scanners. Each of these operations last usually 270 microseconds, which is a common value for the Step Period parameter. By simulating all the operations done by GSI processor, we are able to predict the time needed for the building of a layer. These predictions are shown in Table 2 and compared to the real time to build one layer of different objects. The "Real Time" was obtained by measuring the difference of the starting time and the ending time of the build, given by the SLS building software.

Table 2 : predicted built time versus real build time

File Number	Real Time	Predicted Time
File #1	0:38.69 s	0:39.04 s
File #2	0:20.44 s	0:20.50 s
File #3	0:03.84 s	0:03.78 s
File #4	0:13.82 s	0:13.24 s
File #5	1:16.62 s	1:16.03 s
File #6	0:38.84 s	0:38.65 s
File #7	0:34.18 s	0:33.93 s
File #8	1:05.50 s	1:05.58 s

In order to validate the time prediction, we have used different scanning files, Table 2, representing different patterns to be scanned. File #1 represents a tiger paw in which, each of the vectors to be scanned is of a different length. File #2 represents three tensile dogbones built simultaneously. Files #3, 4 and 5 represents squares of different sizes. Finally, files #5, 7 and 8 were randomly chosen from the wide collection of scan files we have.

The Optical Model :

The models dealing with the energy delivery and the heat transfer that we are using in the simulator can be found in the literature [8-9-10]. The intensity of the laser beam within the powder bed as a function of depth is :

$$I(z)=(1-R)*I0*\exp(-b*z)$$

where

R = surface reflectivity (assumed constant over time)
I0 = laser light intensity at the surface (value derived from the process parameters given by the user)
b = extinction coefficient (assumed constant over time)

z = the depth into the powder bed.

The Thermal model :

The absorption of the beam by the powder creates a three dimensional heating of the powder. The energy input at a point is time varying due to the motion of the beam. From [8-9], the heat source function is :

$$g(x,y,z)=(1-R)*b*I0*\exp(-((\Delta X)^2+ (\Delta Y)^2)/w^2-b*z)$$

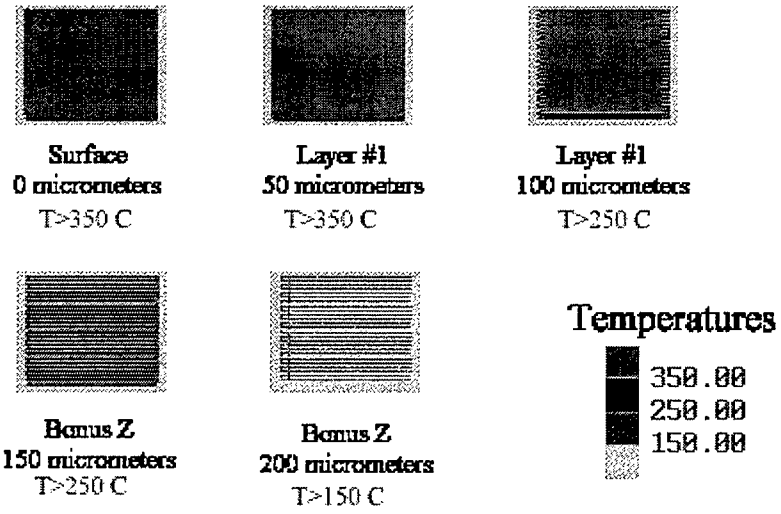
where

x,y,z = coordinates of the point we want to consider of the powder bed

ΔX,
ΔY = difference between the current position of the laser beam and the point of the powder bed we consider in the X-Y plane.
w = radius of the Gaussian laser beam.

When the energy input is calculated using the optical model, the resulting temperature distribution becomes the initial condition for a three dimensional transient heat transfer problem with variable coefficients [9]. Based on the work of Sun [8], this problem is solved using a finite difference method. The computer implementation of this method constitutes the basis for the development of the simulator. For the simulations, we have used a powerful PC compatible computer.

Results of Temperature Distribution : We simulated the temperature distribution in the first layer of a one inch (25.4 mm) square build. As it can be seen in the following figure, underneath the imposed thickness of 5 mils (127 μm), the temperature is still higher than the glass transition temperature of polycarbonate. At this range of temperatures, sintering is likely to occur. This is an indication of growth in the Z-direction (bonus-Z). This observation correlates qualitatively well with the experimentally observed bonus-Z.



Status and further work : The simulations we have conducted so far give us very encouraging results. Based on these results, the next steps are :

(i) Validate the temperature and density simulation results using the adequate equipment.

(ii) Use the hardware and software we already have to create an advanced laser power management that will allow us to vary dynamically the laser power.

(iii) Use the results given by our simulator to design a building script that would minimize the bonus-Z.

4. Conclusion

Key issues which define the requirements for an improvement in the vertical accuracy of parts in the SLS process and preliminary experimental and simulation results are presented. These are the issues that are driving the SLS process research at Clemson University. This work is a first step that should lead to an improvement of the accuracy in the SLS process.

5. Acknowledgments

The authors wish to thank the Office of Naval Research, grant #N00014-94-1-0489, and the Center for Advanced Manufacturing of Clemson University for their financial assistance and DTM Corporation for advice and for the donation of equipment and material.

6. References

1. N.P. Juster and T.H.C. Childs, "A Comparison of Rapid Prototyping Processes", Proceedings of the 3rd European Conference on Rapid Prototyping and Manufacturing, University of Nottingham, Nottingham, United Kingdom, 1994

2. D. Jayaram, Benchmarking of Rapid Prototyping Systems - Beginning to Set Standards, Master's Thesis, Clemson University, 1994

3. L.D. Schmidt , "Process Performance Study of Comercially Produced Rapid Prototyping Systems", Proceedings of the Rapid Prototyping & Manufacturing '95 Conference, Dearborn, Michigan, May 1995

4. Christian Nelson, Kevin McAlea,Damien Gray,"Improvements in SLS Part Accuracy", Proceedings of the Solid Freeform Fabrication Symposium pp. 159-169 , DTM Corporation, Austin, Texas, 1995

5. David McKinley Miller, "Design and Evaluation of a Selective Laser Sintering Process for Enhanced Speed trough Variable Laser Beam Spot Size", Master's Thesis, Clemson University, Dec. 1995

6. John D. Williams Jr., "Numerical Modeling and Experimental Analysis of Selected Parameter Effects on the Selective Laser Sintering Process Response", Master's Thesis, Clemson University, May 1997

7. Kenneth R. Stanley Jr., "Using Closed Loop Digital Control to Enhance Selective Laser Sintering", Master's Thesis, Clemson University, August 1997

8. Sun Ming-shen Martin, "Physical modeling of the selective laser sintering process", Ph.D. Thesis, The University of Texas at Austin, 1991

9. Ming-shen M. Sun, Joseph J. Beaman, "A Three Dimensional Model for Selective Laser Sintering", Proceedings of the Solid Freeform Fabrication Symposium pp. 102-109, The University of Texas at Austin, 1991

10. J. Christian Nelson, Samuel Xue, Joel W. Barlow, Joseph J. Beaman, Harris L. Marcus, and David L. Bourell, "Model of the Selective Laser Sintering of Bisphenol-A Polycarbonate", Ind. Eng. Chem. Res., vol. 32, pp 2305-2317, 1993

RHEOLOGY AND SOLID FREEFORM FABRICATION: MODELING MATERIAL FLOW IN DEPOSITION TECHNIQUES

R.S. Crockett
Milwaukee School of Engineering, Milwaukee, WI

P.D. Calvert
University of Arizona, Tucson, AZ

Introduction

Deposition is the broad category of Solid Freeform Fabrication techniques that accomplish the layerwise buildup of an object through direct placement of a fluid material in the form of droplets or thin beads. Solidification of a bulk material or binder for ceramic / metal particles is achieved by cooling from a melt (Fused Deposition Modeling[1], Fused Deposition of Ceramics[2], Extrusion Freeform Fabrication[3]) or by polymerization combined with rheology changes which occur as solvent rapidly evaporates during the dispensing process (Extrusion Freeform Fabrication, Reactive Stereodeposition[4]). Post-processing can later be performed on the object as a whole to achieve final properties, such as completion of polymerization or burnout of binder and sintering of ceramic particles.

Objects have been produced from a spectrum of materials, including waxes[1] and thermoplastics such as acrylonitrile-butadiene-styrene (ABS) and medical grade methyl-methacrylate-acrylonitrile-butadiene-styrene (MABS),[5] polyetheretherketone (PEEK), and polymethyl-methacrylate (PMMA).[4] By adding ceramic or metal particles to a thermoplastic binder, silicon nitride,[2] alumina,[4] and stainless steel[6] parts have been produced. Bulk materials and binders that solidify by chemical means have also been successfully demonstrated. Examples include nylon,[7] alumina and silicon carbide particles bound with acrylics,[8] and silica and borosilicate glass objects produced using sol-gel solutions as a binder.[4]

Key to this material flexibility is the ability to operate under a wide range of liquid-to-solid transformation rates; the only requirement in a deposition technique is that a material be dispensed as a fluid and then undergo sufficient solidification to support the next cross-sectional layer. The amount of material flow which occurs during the liquid-to-solid transition is critical, however, as it ultimately impacts the precision and quality of the final object.[9]

The consequences of too rapid a solidification relative to the melt viscosity are increased porosity and poor inter-layer bonding[9] (Figure 1). Additionally, the large contact angles associated with low material flow produces low resolution and noticeable surface roughness. On the other hand, in systems characterized by low viscosity and low solidification rates, avoiding object slump becomes a challenge; this is generally controlled by adjusting the time between placement of adjacent beads (t_1) and layers (t_2) to prevent further shape changes. In certain extremely fluid systems, "balling" of the deposited liquid or "castling" (gaps in the deposited bead) can occur, driven by the surface tension of the liquid.[8] Understanding and controlling the material parameters involved in the initial flow during solidification is thus a requirement for developing new material systems for deposition techniques.

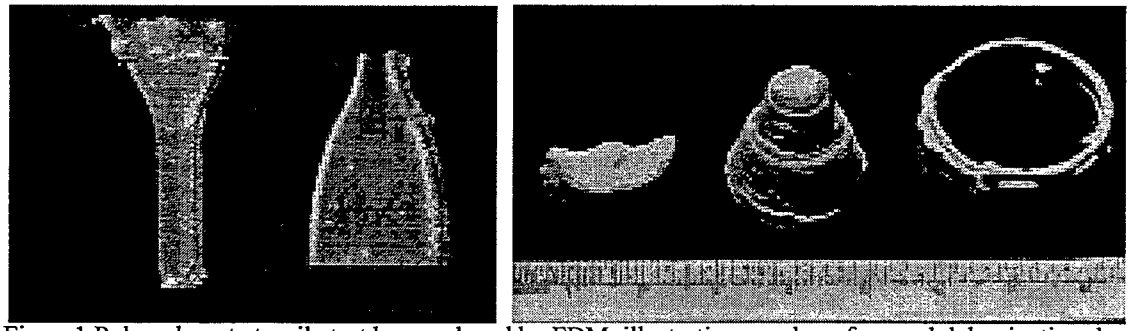


Figure1 Polycarbonate tensile test bar produced by FDM, illustrating rough surface and delamination due to insufficient material flow. Slumping of objects produced by reactive stereodeposition of a silica slurry

Bead Spreading Model

The foundation for a model of a spreading bead of deposited liquid was presented at last year's symposium.[9] The derivation will be published elsewhere.[10] In the model, a bead spreads on the curved surface of the previously deposited layer and is followed as a series of state "snapshots"; surface forces produce an incremental bead deformation in an increment of time. This approach allows flexibility in the time and geometry dependence of the forces associated with a spreading liquid. If the deposited bead conforms to a Bingham-type rheology with a time-dependent yield strength (due to cooling, solvent removal, polymerization) and/or viscosity (due to cooling, changes in the liquid shear rate), it is possible to derive a differential equation for the change in angle over which the bead has spread in an increment of time:

$$\left(\frac{\Delta\phi}{\Delta t}\right)_{x=R\phi} = \frac{1}{32\phi}\frac{\lambda}{\beta}\left[\frac{\cos\phi - \cos(\theta+\phi)}{\phi} - 2\alpha\left(1+\frac{\delta t^{\frac{1}{2}}}{\phi}\right)\right] \tag{1}$$

The above equation is combined with the geometrical relationship between bead spreading angle (ϕ) and bead contact angle (θ) to provide the full solution for bead spreading (see Figure 2):

$$\left(\frac{\sin\theta}{\tan\phi}+\cos\theta\right)^2(\lambda+\phi-\sin\phi\cos\phi) = \theta+\phi-\sin(\theta+\phi)\cos(\theta+\phi) \tag{2}$$

Equation (1) contains a number of parameter groups. In the absence of time-dependent property changes, the final contact angle of a deposited bead is controlled by the dimensionless *strength parameter*, α:

$$\alpha = \frac{\tau_y R}{\gamma_{LV}} \tag{3}$$

Where τ_y is the yield strength of the liquid, R is the radius of the surface onto which the bead is deposited, and γ_{LV} is the surface tension of the liquid. The rate of bead spreading is controlled by the *time parameter*, β, which has units of (s):

$$\beta = \frac{\eta R}{\gamma_{LV}} \tag{4}$$

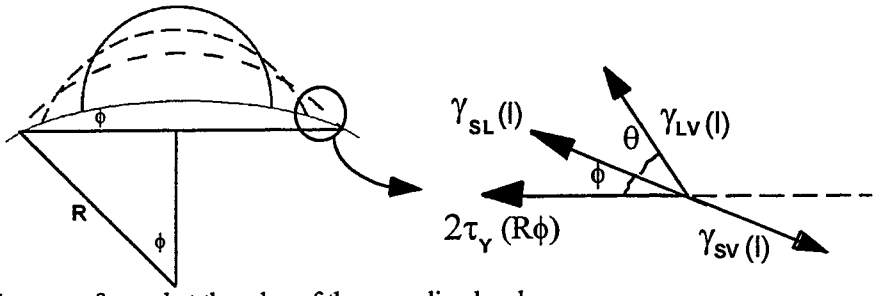


Figure 2 Force balance performed at the edge of the spreading bead.

The time parameter contains the viscosity of the liquid, η. This parameter grouping is the same as that which controls the rate of amorphous material sintering, capillary penetration of liquids, and the dynamic wetting of drops.[11] Note that in deposition techniques, viscosity is rarely a true constant. In the cooling of an amorphous material, it will be a function of bead temperature (thus a function of spreading time). Slurries used in the author's experiments were shear thinning, where viscosity was highly dependent on the shear rate of the liquid (and thus a function of contact angle). The viscosity value in the model is adjusted as required to reflect an average value over the applicable range of temperature or shear rates associated with spreading.

The parameter which controls the diffusion-related property changes of a liquid during solidification is the *strength diffusion coefficient*, δ, which introduces the permeability of the solidifying fluid (P) and the driving force for diffusion (ΔC). δ has units of $s^{-1/2}$:

$$\delta = \frac{(2P\Delta C)^{\frac{1}{2}}}{R}\left(\frac{\tau_{Y,solid}}{\tau_Y} - 1\right) \tag{5}$$

The strength diffusion coefficient represents an increase in the yield strength of the liquid resulting from a surface shell that increases in thickness by diffusion of solvent from the surface or crystallization of a surface layer due to cooling. Finally, bead spreading is dependent on the bead cross-sectional area (A) and substrate radius, represented by the dimensionless *bead geometry parameter*, λ:

$$\lambda = \frac{A}{R^2} \tag{6}$$

Experimental Procedure

To validate the model, dynamic measurements were performed on the spreading of slurries of silica particles in various liquids (ethyl silicate, ethanol, and glycerol). Slurries with a range of α, β, and δ values were prepared by varying slurry surface tension (through liquid selection), viscosity and yield strength (through particle loading and milling time), and amount of volatile ethanol. Two values of λ were obtained by performing all tests on beads with two different cross sectional areas (0.08 mm^2 and 0.32 mm^2). The slurry formulations used in the experiments are presented in Table 1.

Slurry viscosity was determined from the slope of a plot of shear stress measured at various shear rates. Because slurries of silica in ethyl silicate and ethanol are highly shear thinning, single viscosity values were insufficient to describe their behavior over the full spreading process. Average viscosity values were thus determined over the high shear rate range associated with

Table 1 Experimental slurry matrix.

Slurry	Liquid	Loading (vol. %)	Viscosity, initial spreading ($N.s/m^2$) (shear rate = 3.48 - 17.4 s^{-1})	Viscosity, final spreading ($N.s/m^2$) (shear rate = 0.09 - 0.17 s^{-1})	Yield (N/m^2)	Surface Energy (N/m)
A	Ethyl Silicate	35	0.24	12.5	2.4	.023
B	Ethyl Silicate	37	0.3	13.5	2.5	.023
C	Ethyl Silicate	39	0.47	13.5	4.7	.023
D	50:50 ETS:EtOH	35.5	0.52	7.0	3.9	.023
E	Ethanol	35	0.15	4.3	5.6	.023
F	Glycerol	0	1.6	1.6	0	.06
G	Glycerol	19	3.18	3.5	0.9	.06

dispensing, 3.5 - 17 s^{-1}, and the low shear rate range typical of continued bead spreading, 0.09 - 0.17 s^{-1}. The data in Table 1 illustrates the nearly two orders of magnitude increase in the values of viscosity for slurries A-E between these shear rate ranges. The glycerol slurries (F&G) were not highly shear thinning, and a single viscosity value was sufficient for the model. Slurry yield strength was calculated from the shear stress vs. shear rate plot as the 0-shear rate extension of a linear curve fit through the lowest measured shear rate.

Slurries were dispensed onto a borosilicate glass rod, with bead width observed as a function of time by a video camera viewing from the underside of the rod. The output of the camera was recorded on S-VHS tape. After the beads were dispensed, the video was reviewed frame-by-frame, with bead width measured by a video measuring system at 0.033 s intervals, as tracked by an onscreen timer (Figure 3).

Results

Full results are available elsewhere;[10] a representative set of experimental results is presented here for illustration. Bead contact angle (θ) as a function of time is plotted as Figure 4 for a bead cross sectional area = 0.08 mm^2. For comparison, time = 0 is taken as when the contact angle reaches 45 degrees. The values of contact angle stop changing at approximately 3 s for ethyl silicate slurries A, B, C. Slurry E (which contained ethanol) reaches a final contact angle much more rapidly, at 0.2 s. The glycerol slurries, F & G, continue to spread and did not reach a final contact angle within the time period of the measurements. The final contact angle increases with

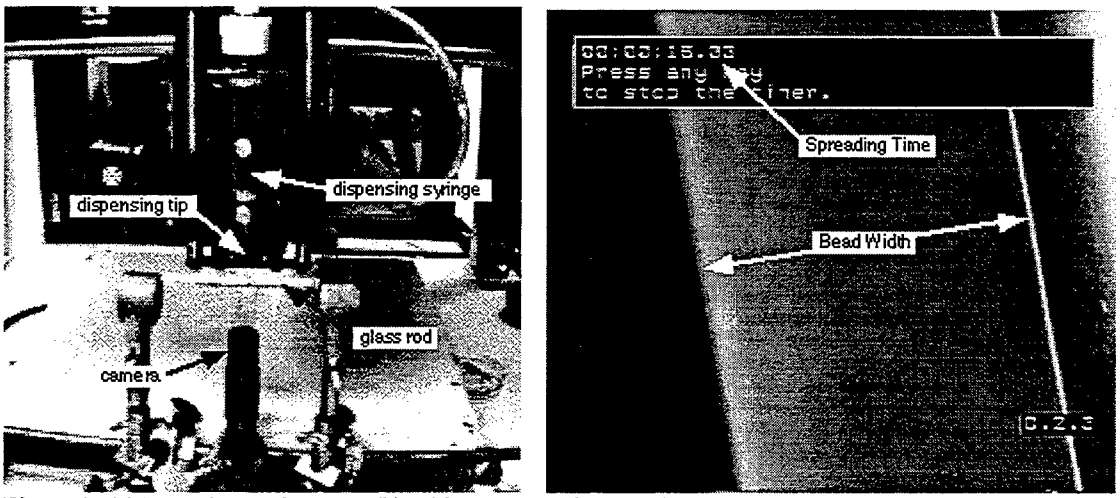


Figure 3 (a) Experimental set-up. (b) Video output of bead width and time.

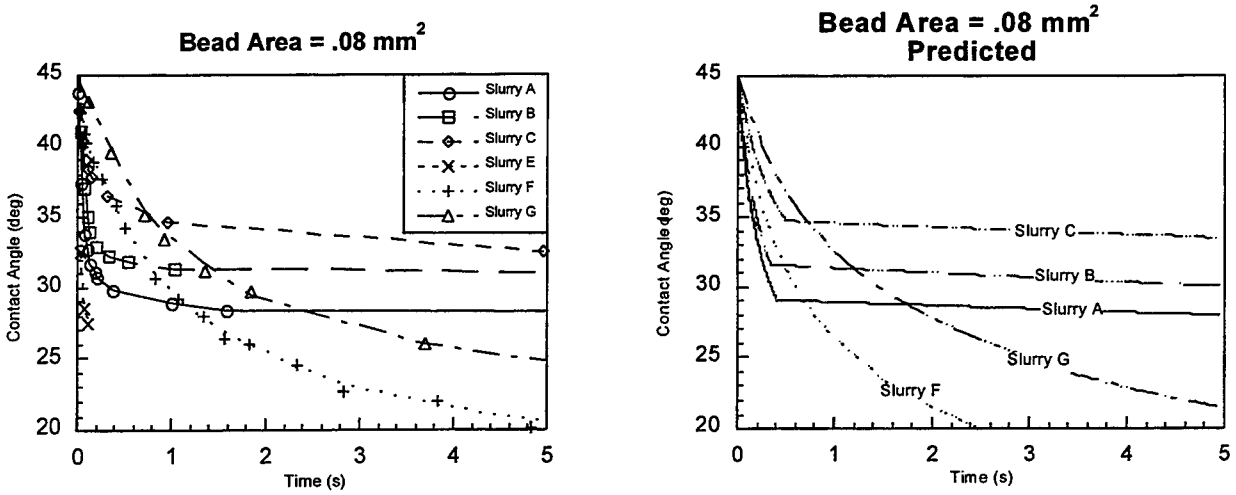


Figure 4 Measured (left) and predicted (right) spreading data.

increasing slurry yield strength, as would be expected. The shape of the curves is dramatically different between the shear-thinning slurries A-E and the non-shear-thinning slurries F & G, although within a given set, the shape of the spreading curve is consistent with decreasing slope with increasing slurry viscosity. Similar curve shape and trends were obtained for bead cross sectional area = 0.32 mm^2, but with higher contact angles and longer spreading times.

Contact angle as a function of time as predicted by the spreading model, using the rheological values of the experimental slurries and A = 0.08 mm^2, is plotted in Figure 4 (right) for the slurries which do not contain solvent. The shear-thinning slurries (A-C) are a composite curve, representing the two viscosity values listed in Table 1. Two predicted values are quantitatively compared in Table 2. These values are: 1) the averaged slope of bead contact angle over time, as represented by the value for the change in contact angle over 5 s, and 2) the final bead contact angle at a small, finite shear rate ($\dot{\varepsilon} = 0.005\ s^{-1}$).

The shape and trends of the model predictions in the early stage of spreading are reasonable when compared to experimental values for slurries which do not involve mass transfer during spreading. Taken over the first 5 s of spreading, the model predicts contact angle changes that vary from experimental results by 6-7%, with a maximum error of less than 17%. The predictions for the final contact angle of shear-thinning slurries, which is expected to be predictable based on a simple equilibrium force balance and independent of slurry viscosity or the selected boundary conditions, are quantitatively poor, however, differing from experimental

Table 2 Change in bead contact angle over 5 s, final contact angle: model predictions vs. actual.

Slurry	Bead Area (mm)	Change in Contact Angle over 5 s (deg, spreading data)	Change in Contact Angle over 5 s (deg, predicted)	% Diff.	Final Angle (deg, calculated)	Final Angle (deg, predicted $\dot{\varepsilon} = 0.005\ s^{-1}$)	% Diff.
A	0.080	16.9	17.0	0.6	28.2	28.8	-2.1
A	0.319	21.0	22.3	6.2	38.2	33.5	12.3
B	0.081	14.0	15.0	7.1	30.6	29.6	3.3
B	0.318	21.0	22.3	6.2	38.9	34.4	11.6
C	0.083	12.5	11.7	-6.4	32.6	34.4	-5.5
C	0.304	13.8	15.6	13.0	46.5	40.9	12.0
F	0.088	25.0	29.0	16.0			
F	0.312	N/A	42.2	N/A			
G	0.081	20.1	23.5	16.9			
G	0.336	32.2	35.0	8.7			

data by as much as 37%. An explanation was developed based on the difficulty of defining a single solidification point for a highly viscous material.[10] An operational definition of solidification as the shear rate beyond which further motion is unlikely, $\dot{\varepsilon} = 0.005\ s^{-1}$, produced predictions for bead final contact angle which were within nominally ± 12% of experimental data. With the model evaluated and shown to provide a reasonable description of the spreading process, the next step is to apply the model to actual deposition systems.

System Contact Angle and Deposition Parameter Space

In an operational deposition system, an object is built up layer-by-layer, not simply by stacking individual beads. Because the outside of a layer is generally deposited first and then the interior filled, however, the surface properties of the object ultimately depend on the single-bead problem developed by the model. After the first few deposited layers, the system will achieve a "system contact angle", where the newly deposited bead spreads until it's final radius equals the radius of the bead onto which it was deposited[9] (Figure 5). Under these equilibrium conditions, the bead geometry parameter, λ, is fixed by the other parameters α, β, and δ. This greatly simplifies analysis by eliminating one system variable and allows the liquid to be plotted on a graphical representation of the α, β, and δ parameter space (Figure 5). The system contact angle in this chart is directly related to the bead contact angle predicted by the spreading model, with large system contact angles producing low part resolution and high surface roughness. System contact angle, θ_{eq}, is determined by the *total* bead strength at equilibrium, which is a function of not only α but also δ, and thus of total spreading time, t:

$$\text{Total Bead Strength} = \alpha\left[1+\delta t^{\frac{1}{2}}\frac{\left(\sin\theta_{eq}+\theta_{eq}\right)^{\frac{1}{2}}}{\frac{\pi}{2}+\frac{\theta_{eq}}{2}}\right] \tag{7}$$

Thus the left axis in Figure 5 contains the parameters α and δ, while the horizontal axis contains β; bead spreading time is read off the chart, and final system contact angle is found on the left axis. This figure may be used in place of a numerical solution to quantify the combined effect of

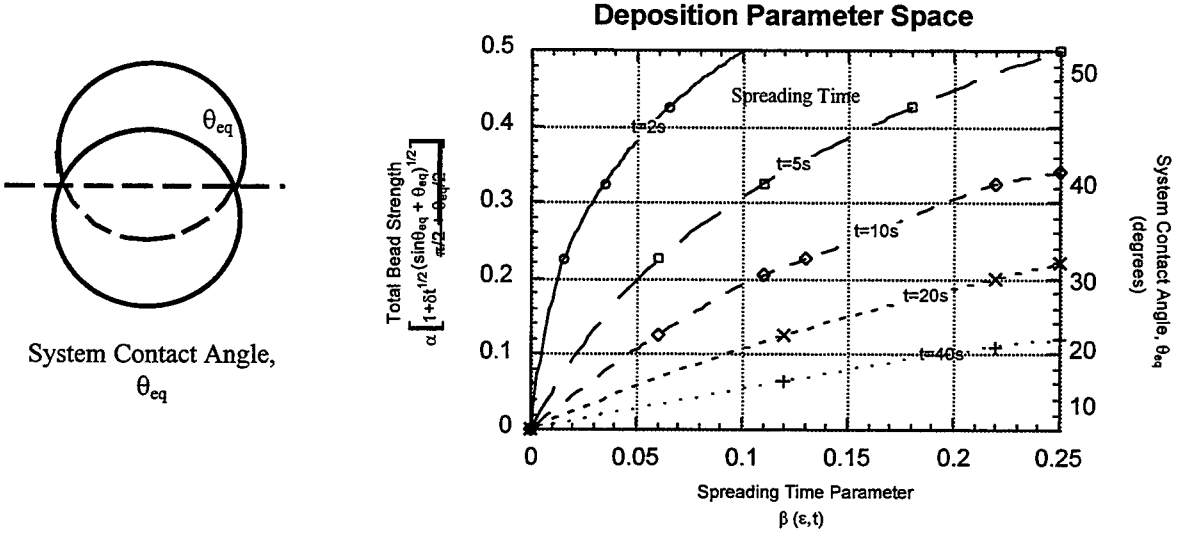


Figure 5 System Contact Angle. Deposition Parameter Space.

all three parameter groupings on bead spreading time and final contact angle. Because of the dependence of system contact angle on spreading time, the spreading time and system contact angle achieved for a given set of α, β, and δ values must be found by iterative use of the chart. Using as an example a deposition liquid with $\alpha = 0.2$, $\beta = 0.1$, and $\delta = 0.1$, the iteration would begin by finding the bead strength / spreading time parameter intersect at $\alpha = 0.2$, $\beta = 0.1$, and $t = 0$ in the total bead strength equation (Equation (7)). These values result a spreading time of approximately 10 s at a system contact angle of 30 degrees. Substituting $\alpha = 0.2$, $\delta = 0.1$, $t = 10$ s, and $\theta_{eq} = 30$ degrees back into Equation (7), the modified value for total bead strength becomes 0.25, corresponding to a spreading time of 7.5 s and a system contact angle of 34 degrees. This process of iteration is repeated until a single value is found for spreading time and system contact angle consistent with the values of α, β, and δ. For the above example, this value is a system contact angle of 31.5 degrees and a spreading time of 8.5 s.

It is also possible to perform a second iteration on this chart for a variable β, to achieve approximate results for cases in which viscosity is not constant throughout the spreading process. For shear thinning slurries, β is a function of shear rate (as represented by θ), and for amorphous thermoplastics, β is a function of t. The iteration would be performed similar to the iteration for bead strength, whereby spreading rate is modified to a new value of β at each new contact angle value or time until a single value is narrowed in on for system contact angle and spreading time.

This chart can be used to provide insight as to how the initial liquid conditions, modified by solidification strategies, will impact the ultimate freeforming characteristics such as object resolution, flaws, and gaps. The bead strength parameter, α, indicates a liquid's resistance to motion. It is in effect a ratio of the restraining force to the driving force for spreading, thus a large α represents a system similar to extrusion, where flow is limited. This is indicated in the schematic of Figure 6 as the region at the top of the chart. Typical systems in this region include the extrusion of engineering thermoplastics; these are characterized by high deposition pressure requirements, high contact angles leading to low object resolution and high roughness, and the possibility for poor interlayer bonding. The time parameter, β, determines the system's spreading rate and response time, with a large β (high viscosity) indicating a slow-moving or "sluggish" system. This is seen in Figure 6 as the region to the extreme right of the chart.

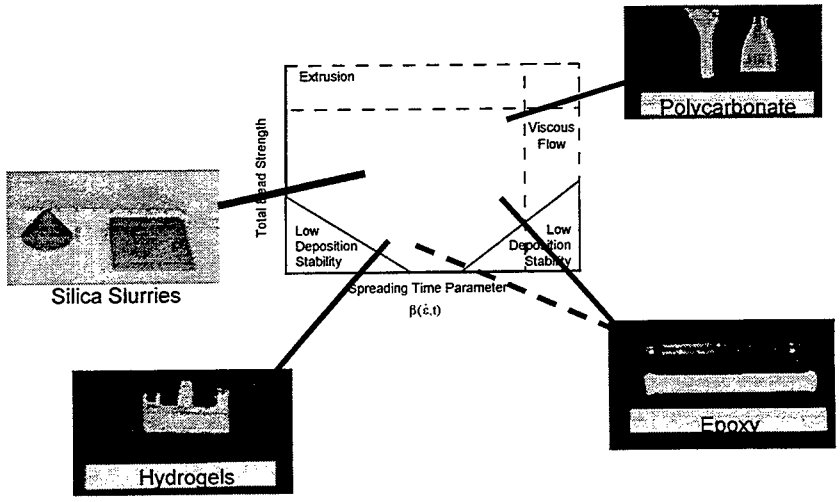


Figure 6 Effect of spreading on object characteristics.

The shaded regions at the bottom of the chart indicate conditions where the liquid may be susceptible to instabilities in the deposition process. One example is the phenomenon of castling, wherein irregularities in deposited lines grow into large peaks and troughs in the course of forming multiple layers. This occurs under conditions of low viscosity and yield strength relative to the liquid surface tension (low $\alpha + \beta$). If the time required for a dispensed bead to reach the surface is greater than some critical value, surface forces will break it into smaller sections. Thus dispensing height becomes an important control parameter to avoid flaws for liquids in this regime. For liquids with low bead strength, α, plus high β, control of dispensing *speed* becomes critical. At large viscosities, a bead will not be able to rapidly "neck down" from a large dispensing orifice; this, combined with low bead strength, will create periodic tears in a deposited bead. This is indicated in Figure 6 by the diagonal shaded region at the bottom right.

An important result from this chart is that proper use of the solidification method can create a workable deposition system from a liquid with "difficult" initial properties. As discussed previously, the time-dependent modifications which can occur during spreading are: 1) viscosity as a function of shear rate (through producing a shear-thinning rheology), 2) viscosity as a function of time (through cooling from a low-viscosity melt), and 3) yield strength as a function of time (through diffusion of mass or thermal energy to the surface). Rheology control, by establishing a shear-thinning slurry such that the viscosity increases during deposition, moves the liquid from its initial placement on the chart horizontally to the right towards longer spreading times. Mass transport, by increasing the yield strength of the fluid in a surface shell, moves it vertically upward in Figure 6 during deposition to higher contact angles. Thermal transport, by modifying the bulk properties of the liquid, generally moves the liquid toward the upper right. Thus initial liquid property characterization and modification, combined with proper selection and control of solidification method, can result in a successful deposition system.

REFERENCES

[1] J.W. Comb, W.R. Priedeman, and P.W. Turley, "FDM Technology Process Improvements," in *1994 Solid Freeform Fabrication Symposium Proceedings*. Austin, TX: University of Texas at Austin (1994) 42-49.

[2] M.K. Agarwala, *et. al.*, "Structural Ceramics by Fused Deposition of Ceramics", in *1995 Solid Freeform Fabrication Symposium Proceedings*. Austin, TX: University of Texas at Austin (1995) 1-8.

[3] P. Calvert R. Crockett, J. Lombardi, J. O'Kelly, and K. Stuffle, "Extrusion Methods for Solid Freeform Fabrication", in *1994 Solid Freeform Fabrication Symposium Proceedings*. Austin, TX: University of Texas at Austin (1994) 50-55.

[4] R.S. Crockett, J. O'Kelly, P.D. Calvert, B.D. Fabes, K. Stuffle, P. Creegan, and R. Hoffman, "Predicting and Controlling Resolution and Surface Finish of Ceramic Objects Produced by Stereodeposition Processes", in *1995 Solid Freeform Fabrication Symposium Proceedings*. Austin, TX: University of Texas at Austin (1995) 17-24.

[5] W. Priedeman, "Thermoplastics for Fused Deposition Modeling (FDM)", in *1996 Solid Freeform Fabrication Symposium Proceedings*. Austin, TX: University of Texas at Austin (1996).

[6] M.K. Agarwala, *et. al.*, "Fused Deposition of Ceramics and Metals: An Overview", Poster presented at *1996 Solid Freeform Fabrication Symposium Proceedings*. Austin, TX: University of Texas at Austin (1996).

[7] J. Lombardi, G. George, L. Rintoul, and P. Calvert, *Polymer Preprints*, **37** [1] (1996) 221-222.

[8] P. Calvert and R. Crockett, "Chemical Solid Free-Form Fabrication: Making Shapes without Molds" *Chem Mater.* **1997** [9] 650-663.

[9] R.S. Crockett and P.D. Calvert, "The Liquid-to-Solid Transition in Stereodeposition Techniques", in *1996 Solid Freeform Fabrication Symposium Proceedings*. Austin, TX: University of Texas at Austin (1996) 257-264.

[10] R.S. Crockett and P.D. Calvert, submitted to Journal of Materials Research, September 1997.

[11] See, for example, J.S. Reed, "Introduction to the Principles of Ceramic Processing," John Wiley and Sons, New York, 1988.

Modeling of Mechanical Behavior of SLA Parts

Zhanping Wu, Said Ahzi, Frank W. Paul, Elaine Hunt
Department of Mechanical Engineering
and Amod A. Ogale
Department of Chemical Engineering
Laboratory to Advance Industrial Prototyping (LAIP)
Clemson University, Clemson, SC 29634

ABSTRACT

In recent years, important efforts have been focused on producing functional parts using Stereolithography Apparatus (SLA). One of the applications is the development of rapid polymer tooling such as dies for injection molding. For these applications, optimal thermal as well as mechanical properties are of significance. In this paper, the mechanical behavior of the cured resin SL5170 is discussed by use of an elastic-viscoplastic material model. Uniaxial compression tests at different deformation rates are conducted. The stress-strain curves of these tests are predicted by the model, and comparisons of these results with experiments show good agreement.

1. Introduction

Recently, rapid prototypes made from polymers, ceramics and metals have lead to interest and research focus in the possibility of fabricating functional and semi-functional parts. Rapid prototyping and manufacturing (RP&M) techniques, having various building materials, can basically be classified into two fields: one is mainly aimed at directly making final parts and the second is concerned with building semi-functional parts or models. StereoLithography Apparatus (SLA) is used to produce parts by photopolymerization. This process is one of the main RP&M processes that were initially aimed at producing models. However, SLA has recently shown its great potential for rapid polymer tooling. One example in the development of rapid polymer tooling using SLA is the fabrication of dies for injection molding. It is commonly known that materials, building styles, environments and postcuring process all together account for parts' size limitation, accuracy and behavior. Compared to the earlier SL acrylate photopolymer systems, parts built in photopolymer SL5170 have significantly enhanced mechanical properties, that is, a high level of overall accuracy, negligible curl, improved flatness, minimal green creep distortions, better tensile modulus and flexural modulus [1]. The fabrication of polymer matrix composite dies for injection molding, using filed SL5170, is of current interest [2].

To characterize the mechanical behavior of the SLA die, it is necessary to understand the mechanical response of the cured resin. In this paper the mechanical response of the epoxy resin SL5170 is investigated. Our goal is to develop a model that will be used to simulate complex thermo-mechanical loading for the analysis of the die behavior during injection molding. In the current study, we considered homogeneous deformation such as uniaxial compression and implemented a three-dimensional model to simulate the elastic-viscoplastic response of SLA built samples using epoxy resin SL5170. Since the current effort of development of polymer

tooling is focused on composite dies, our current study is concerned only with the behavior of the matrix.

Postcured SL5170 parts have high degree of polymerization and cross-linking density. The cross-linking is formed by strong covalent bonds that connect the polymer chains to each other. Since the chemical forces must be overcome before molecular flow can be realized, solidified SL5170 part can not melt upon heating. Therefore, cured SL5170 is classified as a cross-linked thermoset polymer. However, the elastic-viscoplastic response of this resin under compression is similar to that of glassy thermoplastics such as polycarbonate. Note the glassy temperature of SL5170 is about 80°C.

In the past decades, various models have been developed to explain the mechanical response of different polymers including rubbers and glassy polymers. Treloar [3] reviewed physically-based models for rubber elasticity. For the plastic deformation of glassy polymers, Argon [4] proposed a model for local shear transformations in these materials. Boyce et al. [5] used Argon's model and developed a three-dimensional constitutive model for large elastic-viscoplastic deformation of glassy polymers. This model encompasses factors affecting the stress-strain curves, such as strain rate, temperature and pressure, and accounts for strain softening and hardening after yield. The strain hardening in these materials is due to molecular orientation and is modeled using a back stress as a measure of orientation hardening. In our work, we use the model of Boyce et al. (1988) [5] with the strain hardening model of Arruda and Boyce [6] to simulate uniaxial compression of postcured epoxy resin SL5170.

2. Experiments

Two kind of samples are used: the first one (designated as type I) is 50.8mm in height and 25.4mm in diameter, i.e., 2inch x 1inch (Fig.1.a); the second one (designated as type II) is 8mm in height and 8mm in diameter (Fig.1.b). All parts are built along the Z-direction at 28°C and under ACES part building style. The machine is a 3D Systems SLA 250/50. The samples were postcured.

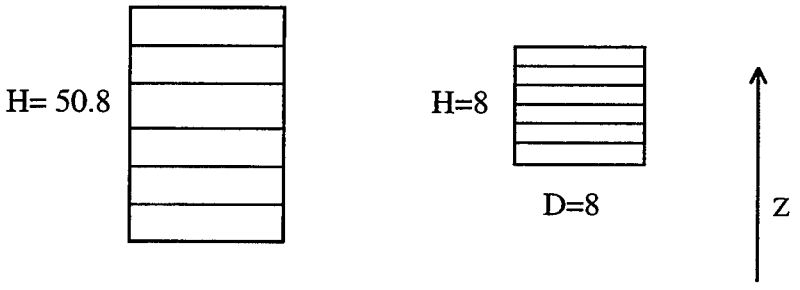
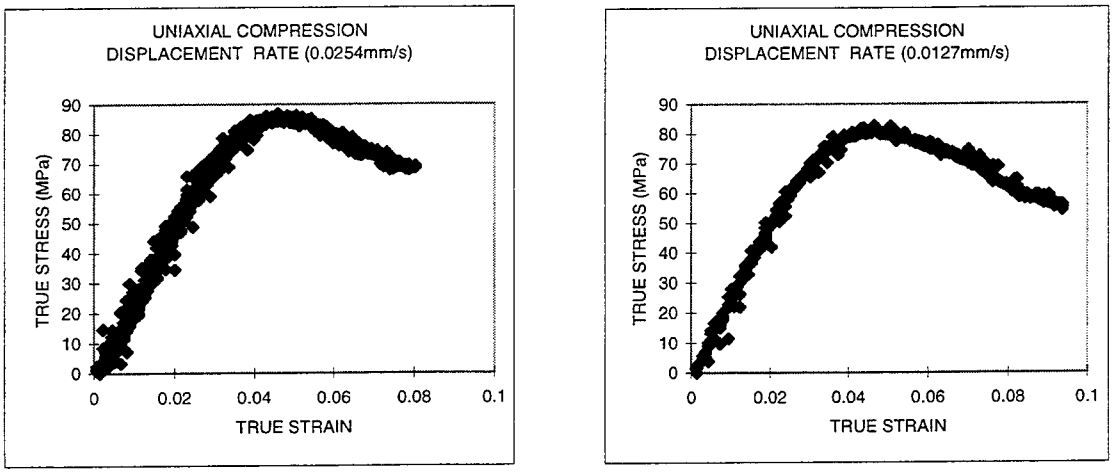


Fig.1

Uniaxial compression tests at constant displacement rates of deformation are imposed on Instron machine. Thin teflon films are used as lubricant to reduce friction between the platens and the sample. Compression direction is parallel to the Z-direction. Series of tests are carried out to get stress-strain response and material parameters necessary to the mathematical model. Results are listed as follows:

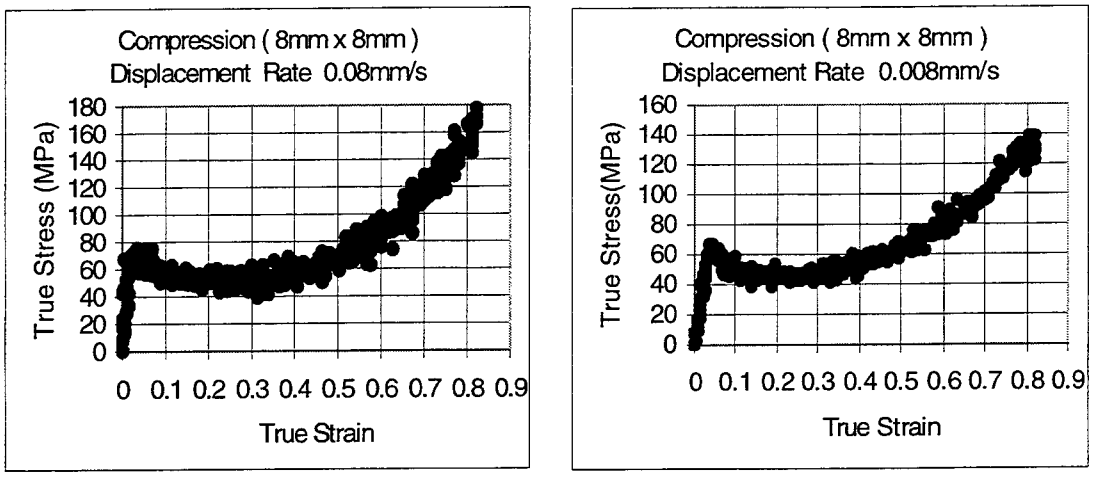
(1) Rate dependent yield: As shown in Fig.2, at different displacement rates, stresses at yield point are significantly different. A yield stress of 85MPa is observed for displacement rate of 0.0254mm/s, and 80MPa for displacement rate of 0.0127mm/s. Samples of type I are uniaxially compressed in this case. The strain rate at small deformation is approximately the same as the ratio of the displacement rate to the initial sample height, thus, strain rate dependent yield is concluded.



(a) (b)

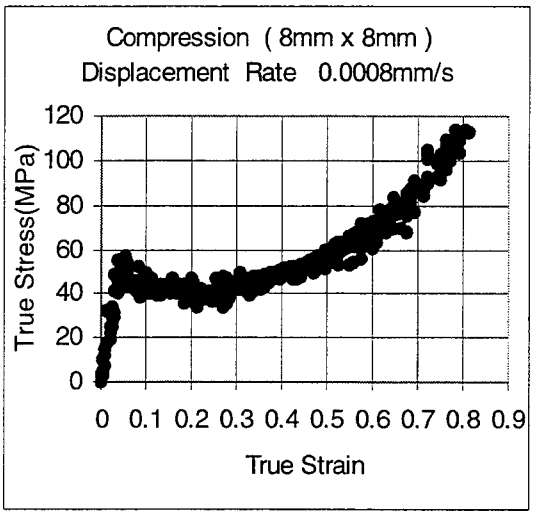
Fig.2

(2) Large deformation behavior: In addition to linear elastic and nonlinear part before the yield point (Fig.2), the stress-strain curves in Fig.3 are the response at large strain. These figures display strain softening after yield followed with a steady state and strain hardening. The compression tests in Fig.3 are conducted using type II samples. Here again, strain rate effects on the yield are observed.



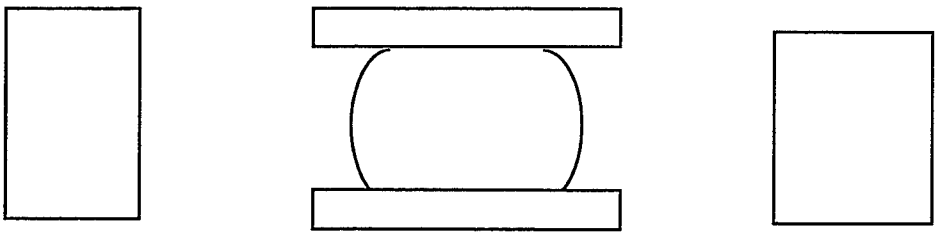
(a) (b)

Fig.3



(c)
Fig.3

(3) Recovery test (Fig.4) : After uniaxial compression in the Z-direction, a type I sample is compressed to 1.44 inch in height and 1.23 inch in diameter, which exhibits a true strain of about 32%. The compressed sample was then put in an oven at 90°C for four hours. Note that postcured SL5170 sample has a glass transition temperature at about 80°C. When the sample was taken out of the oven, its original size was almost totally recovered. This is a well known phenomenon in glassy polymers that are plastically deformed then heated above their glass transition temperature.



(a) (b) (c)

Fig. 4

3. Model Description

Several models have been developed for rubbers and glassy polymers. The proposed constitutive model for the simulation of the stress-strain behavior is briefly summarized below. Details are given in the work of Boyce et al. [5].

The deformation gradient tensor **F** is multiplicatively decomposed as elastic part $\mathbf{F}^e$ and plastic part $\mathbf{F}^p$:

$$F = F^e F^p \tag{1}$$

The plastic part $\mathbf{F}^p$ designates the deformation gradient from the undeformed configuration to the relaxed one. The relaxed configuration is obtained by elastic unloading. The elastic deformation gradient is assumed symmetric and represents elastic stretching of the material. The plastic velocity gradient $\mathbf{L}^p$ is defined in terms of $\mathbf{F}^p$ as:

$$L^p = \dot{F}^p F^{p-1} = D^p \tag{2}$$

Note that $\mathbf{L}^p = \mathbf{D}^p + \mathbf{W}^p$ where the plastic spin is assumed null and the plastic strain rate $\mathbf{D}^p$ is given by the flow rule:

$$D^p = \dot{Y}^p N \tag{3}$$

with,

$$N = \frac{1}{\sqrt{2}\tau} T^{*'} \tag{4}$$

Here, $\dot{Y}^p$ is the plastic shear rate, τ is the equivalent shear stress, $\mathbf{T}^{*'}$ is the deviatoric part of driving stress $\mathbf{T}^*$ given by:

$$T^* = T - \frac{1}{J} F^e B F^{eT} \tag{5}$$

In relation (5), $\mathbf{T}$ is Cauchy stress tensor and $\mathbf{B}$ is the back stress tensor representing a measure of the orientational hardening. The elasticity relation gives:

$$T = \frac{1}{J} C^e [\ln F^e] \tag{6}$$

where $\mathbf{C}^e$ is the elastic stiffness tensor of the material, J is the volume change, and $\ln\mathbf{F}^e$ represents the logarithmic strain. In the applications, isotropic elasticity is assumed.

Now, we consider the Argon's model for the shear rate $\dot{Y}^p$. This model was modified by Boyce et al. [5] and Hasan et al. [7] to include pressure and rate sensitivity and it is expressed as:

$$\dot{Y}^p = \dot{Y}_0 \exp[-\frac{AS}{\theta}(1-\frac{\tau}{S})] \tag{7}$$

with,

$$\dot{S} = h \cdot (1 - \frac{S}{S_{ss}}) \cdot \dot{Y}^p \tag{8}$$

Here, $\dot{Y}_0$, pre-exponential factor; A, a constant dependent on rate and temperature; θ, absolute temperature. Eqn.(8) is the evolution of athermal deformation resistance S, h is the slope of yield drop with respect to plastic strain and Sss is the steady state resistance.

For an initially undeformed glassy polymer, the principal components of the of the back stress $\mathbf{B}$ evolve with straining and can be expressed as [5] [6] [7]:

$$B_i = \frac{C^R}{3}\sqrt{N} L^{-1}(\frac{\lambda_{chain}}{\sqrt{N}}) \frac{\lambda_i^2 - \frac{1}{3} I_1}{\lambda_{chain}} \tag{9}$$

In Eqn.(9), L^{-1} is the inverse Langevin function; $\sqrt{N}$ is equal to the locking stretch; C^R is rubbery modulus; λ_{chain}, stretch experienced by each network chain; I_1, first invariant of plastic stretch.

The material parameters used in the model are obtained from the experimental results in Fig.2 and Fig.3. Material constants such as Young' modulus, locking stretch, coefficients for rate dependent yield are measured directly from the experimental stress-strain curves. The other parameters, such as rubbery modulus, are selected to fit the compression stress-strain curves to the experimental ones. The Poisson ration is estimated based on results in literature to be 0.45. The following is a list of factors put in the mathematical model.

Shear modulus:	$\mu = 900$ MPa
Poison's ratio:	$\nu = 0.45$
Pre-exponential constant:	$\dot{Y}_0 = 3.65 \times 10^{12}$
Constant A:	A = 118.85 K/MPa
Temperature of test:	Tem = 298 K
Initial athermal shear resistance:	$S_0 \cong 0.077*\mu/(1-\nu) \cong 126$ MPa
Steady stress:	$S_{ss} = 0.71*S_0 = 90$ MPa
Slope of yield drop:	h = 400 MPa
Rubbery Modulus:	$C^R = 20$ MPa
Locking Stretch:	$\sqrt{N} = \lambda_L = 3$

4. Simulations and Comparisons

After all required material constants have been identified as listed above, computer simulations

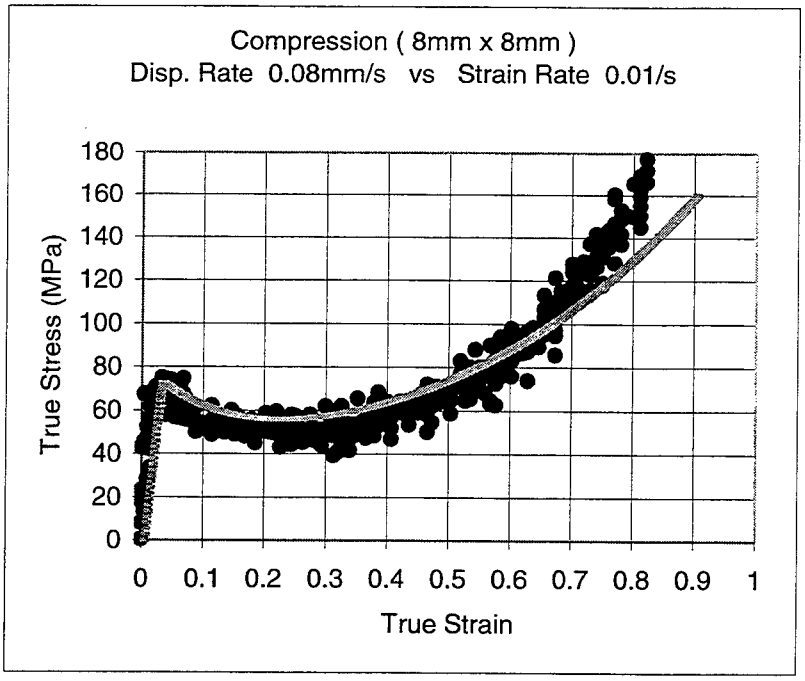


Fig.5

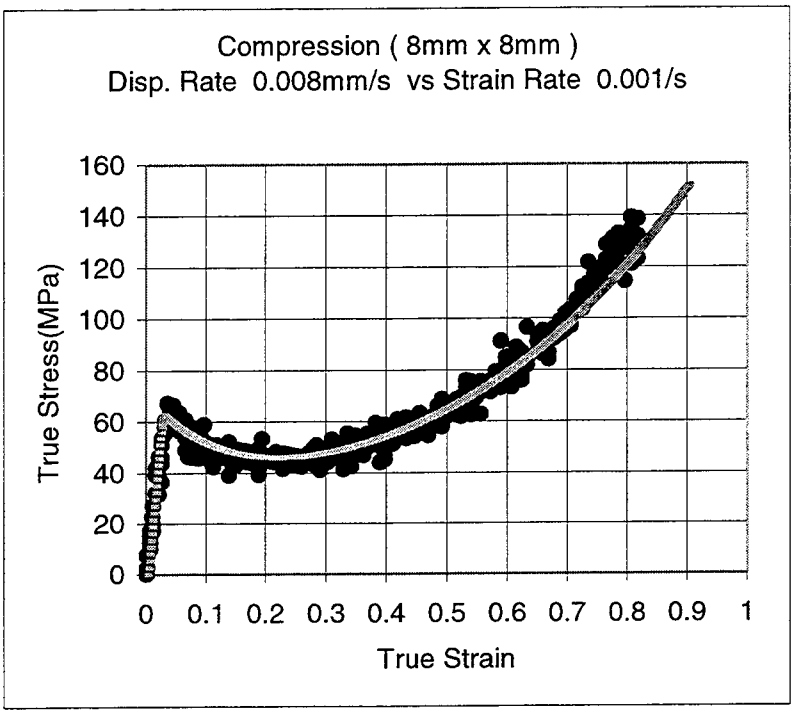


Fig.6

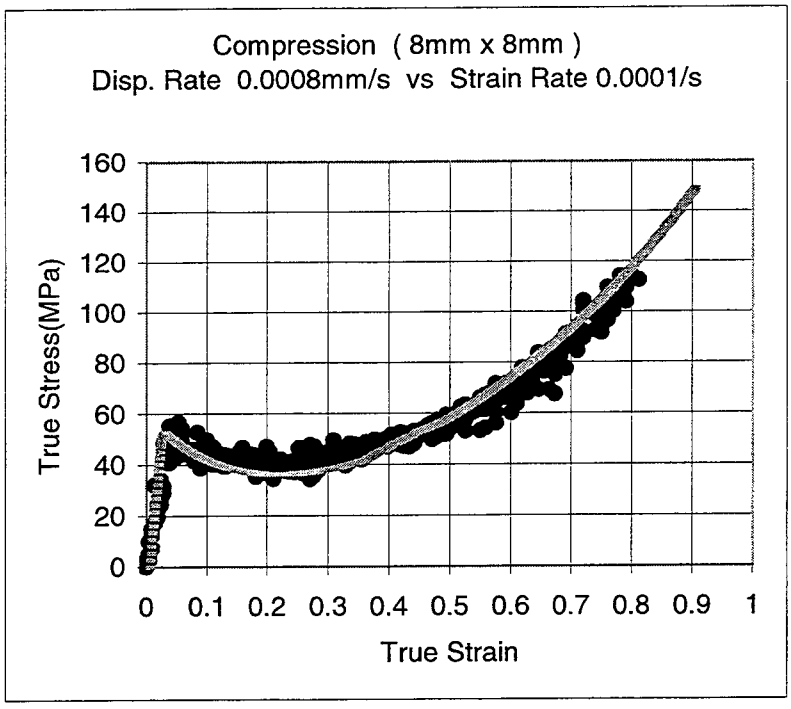


Fig.7

of uniaxial compression tests are accomplished for different strain rates: 0.01/s, 0.001/s and 0.0001/s. The comparison with the computed stress-strain curves with experimental ones in Figures 5-7 show a good agreement for different strain rates. Note that the rate dependent yield is well predicted as well as the softening after yield and orientational hardening. Since the

simulations are conducted based on constant strain rate rather that displacement rate, this leads to some discrepancies especially at large strains. At small strains, the ratio of displacement rate to initial sample height and the strain rate are almost identical.

5. Conclusions

The mechanical behavior of postcured SL5170 layered parts, deformed in uniaxial compression perpendicular to the layers, exhibits elastic and inelastic response. These show a rate dependent yield and high ductility when deformed in compression at room temperature. The rate dependent yield and large deformation properties of the photopolymerized and postcured SL5170 are thus characterized using uniaxial compression tests. The mechanical response of these SLA parts is simulated by use of an elastic-viscoplastic material model. We are currently implementing the model in a finite element code to simulate non-homogeneous deformations. The proposed work finds its application in the simulation of complex loading conditions of SLA parts made from the photopolymer SL5170. We are also conducting other tests to identify temperature effects and to investigate the response under compression at directions other than the Z-direction.

Acknowledgement

The authors gratefully acknowledge the financial assistance from the Industrial Consortium Laboratory to Advance Industrial Prototyping (LAIP) at Clemson University. We would like to thank Prof. J. M. Kennedy for his help with the experiments.

References

1. Jacobs, P.F., *"Stereolithography and Other RP&M Technologies"*, SME, New York, New York, 1996.
2. Douglas Taft, A. Ogale, Elaine Hunt, Said Ahzi, Frank Paul, *"Particulate Filled Resins for Rapid SLA Injection Tools"*, SFFS, Austin, Texas, 1997.
3. Treloar, L.R.G., *"The elasticity and related properties of rubbers"*, Rep. Prog.Phys., 1973, Vol. 36, pp.755-826.
4. Argon, A.S., *"A theory for the low-temperature plastic deformation of glassy polymers"*, Phil. Mag. 28, Vol. 39, 1973.
5. Boyce, M.C., Parks, D.M. and Argon, A.S., *"Large inelastic deformation of glassy polymers"*, Mechanics of Materials, 7.(1988).15-33.
6. Arruda, E.M. and Boyce, M.C., *"A 3-dimensional constitutive model for the large stretch behavior of rubber elastic materials"*, J. Mech. Phys. of Solids, Vol. 41, 1993, pp. 389-412.
7. Hasan, O.A. and Boyce, M.C., *"A constitutive model for the nonlinear viscoelastic viscoplastic behavior of glassy polymers"*, Polymer Engineering and Science, 1995, Vol. 35, N0. 4, pp.331-344.

REACTION HEAT EFFECT ON INITIAL LINEAR SHRINKAGE OF STEREOLITHOGRAPHY RESINS

Hiroyuki NARAHARA*, Fumiki TANAKA**, Takeshi KISHINAMI**,
Satoru IGARASHI** and Katsumasa SAITO***

* Department of Mechanical Systems Engineering,
Kyushu Institute of Technology,
680-4 Kawazu, Iizuka City, Fukuoka 820, JAPAN.
** Hokkaido University, 060 kita-13, Nishi-8, Kita-ku, Sapporo 060.
***Gunma Polytechnic college, 918 Yamana, Takasaki city, Gunma 370-12.

ABSTRACT

In the industrial use of the Stereolithography, the precision is always a problem. Basic phenomenon of the solidification shrink has not sufficiently investigated. This study aims at clarifying the initial linear shrinkage of cured resin in a minute volume. Experimental equipment has been developed which measures the time history of the single strand in situ in a stereolithography machine. Analysis model about the time history of a minute volume linear shrinkage has been shown using with the measured shrinkage of a cured line segment. The relation between the time history of the linear shrinkage and the temperature was measured and the shrinkage in the minute volume after irradiation has been caused by the temperature variation.

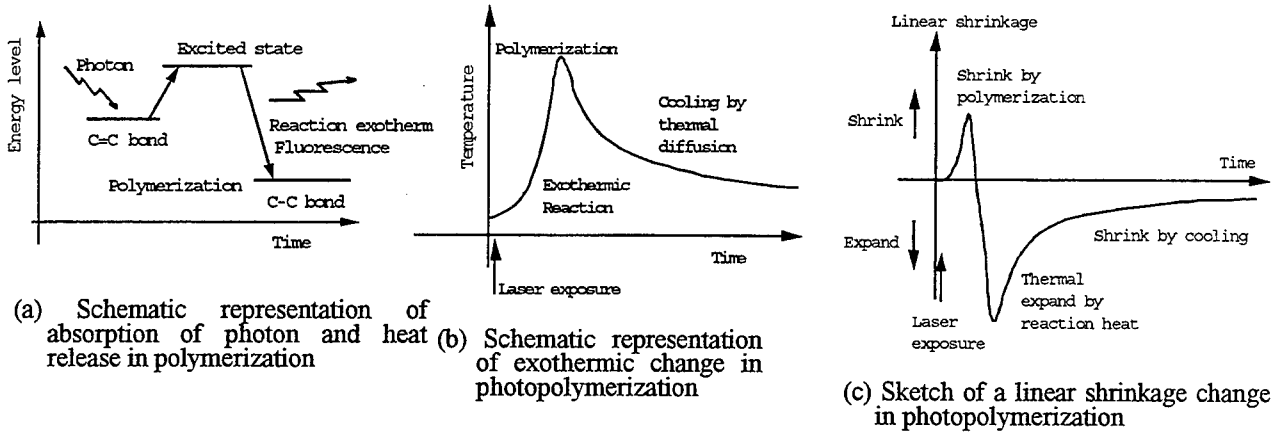
1. INTRODUCTION

Stereolithography is a method to make use of phase change of material from liquid phase monomer to solid phase polymer. This phase change is the result of the polymerization by irradiation of UV-laser beam. As laser beam can select infinitesimal volume to solidify, details of solid shape can be expressed.

On the other hand, it is pointed out that the problem is its worse shape stability and surface roughness than the removal processing, or machining, for example, since it uses additive method based on the material phase change in a free space [1]. Especially deformation of stereolithography part is the significant problem to improve accuracy [2]. Researches have not been studied sufficiently to establish the basic theory of solid forming [3][4]. It is not known well how physical properties interact each other within a minute volume during scanned laser beam solidifies photopolymer. For finding a guide of material design and an optimum fabrication method with computer simulation [5][6], it is important to clarify a mechanism of resin dynamics at the initial exposure hardening.

In order to observe this material change continuously, development of the equipment to measure linear shrinkage and shrinkage force at hardening by laser scanning has been reported [7][8]. Several kinds of resins for stereolithography have been measured.

In this paper, a basic solidification model about mechanical property is shown. Procedure to extract a minute volume linear shrinkage from measured data is explained and experimental setup is also shown. Finally, appropriateness of the basic model is described by



(a) Schematic representation of absorption of photon and heat release in polymerization

(b) Schematic representation of exothermic change in photopolymerization

(c) Sketch of a linear shrinkage change in photopolymerization

Figure 1. Sketch of the time history of linear shrinkage in a minute volume for explanation

comparing with experimental results.

2. BASIC MODEL OF LINEAR SHRINKAGE AT INITIAL STAGE

The problem dealt here is hardening reaction of green material of photopolymer just after the moment of laser beam irradiation. A problem of the extra hardened shrinkage induced by additional exposure, for example, the exposure at a time of lamination or the one at a post curing, and so on, will not be discussed in this paper.

When photopolymer absorbs ultraviolet ray, it is activated and the potential energy becomes high. After resin is polymerized, it transits to stable basic state. The energetic difference of excess energy to shift to stable state is released as polymerization heat (Figure 1).

It is illustrated as a time history of temperature before and after photopolymerization. After polymerization starts with laser exposure, polymerization shrinkage occurs as proportion to the reaction extent of functional groups. Temperature rises with heat release of polymerization. At the same time, resin swells by the thermal expand. As the functional group decreases with the progress of reaction, or as the irradiation is reduced, the flux of heat decreases. Slow variation of shrinkage caused by the thermal shrink, or cooling result by heat diffusion, must be observed.

For the reason mentioned above, when light passes by a minute volume of resin, the phenomenon described below will occur.

Schematically indicated by Figure 2, when UV light is irradiated to minute volume of resin, shrink starts with polymerization reaction, and resin is supplied from environs at the same time. However, during light is in passing, this supplied resin also hardens. Volume increases as the heat expansion with a temperature rise that is generated by the polymerization reaction heat. When a heat release ends, resin is cooled by the heat diffusion, and a shrink occurs by the thermal shrink. Such polymerization shrink → heat expansion → shrink by cooling, the repetition of expansion and shrink will occur in an every part of a hardening green parts. It is anticipated that this heating and cooling variation will influence on the time history of shrinkage.

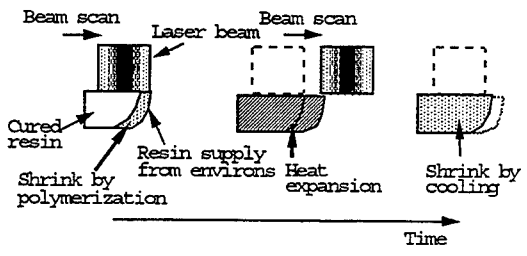


Figure 2. Sketch of a single strand formation irradiated by laser scanning

3. EXPERIMENTAL SETUP OF LINEAR SHRINKAGE AND SHRINKAGE FORCE MEASUREMENTS OF SINGLE STRANDS

Principle of the experimental equipment is indicated on Figure 3. After laser beam starts from a fixed end, it reaches a free end and the single strand of cured resin combines the fixed end and the free one. A non-contact eddy current sensor is used to measure a displacement of a ferromagnetic needle that connects the free end of a single strand. For tracing the beam position and the measuring time, a photo sensor is used to detect the laser traverse during laser scanning. The time lags exist between the time history origins of sensors, because sensors have different spatial positions. For the time correspondence, origins of time histories, temperature and linear shrinkage histories, for example, are compensated with laser scanning speed. Shrinkage force is obtained by force sensor from a single strand with both restricted ends.

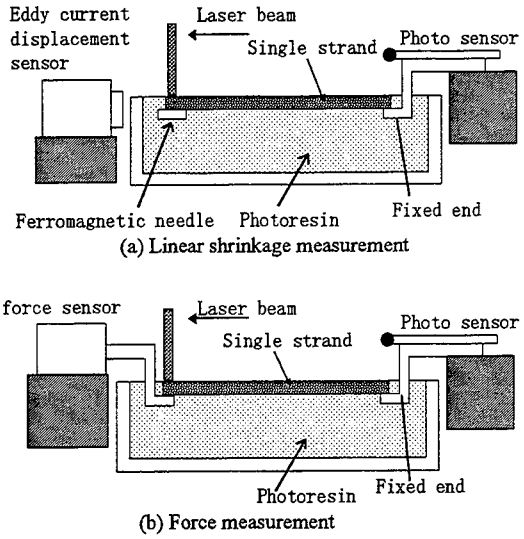


Figure 3. Experimental arrangements for single strand measurements

Linear shrinkage value is obtained to divide a displacement by the set distance, which is defined as a distance between fixed end and free end. Sectional area of a single strand is measured after experiment. The stress value is calculated from the shrinkage force divided by the sectional area.

4. MEASURING METHOD AND EXPERIMENTAL CONDITION

4.1. MEASUREMENT OF LINEAR SHRINKAGE AND REACTION HEAT OF SINGLE STRANDS

Analytic method about a time history of the minute volume in a single strand is described.

Now, the length l of a single strand is drawn from a fixed end to a free end by laser scanning (Figure 4). Time history of the strain $\varepsilon_S(t)$ is measured by sensor. The time when the laser beam reaches the free end is defined as 0. Strain of minute volume is defined as $\varepsilon_P(t)$.

Consider the laser beam scans at speed V. In any part of a single strand, the minute

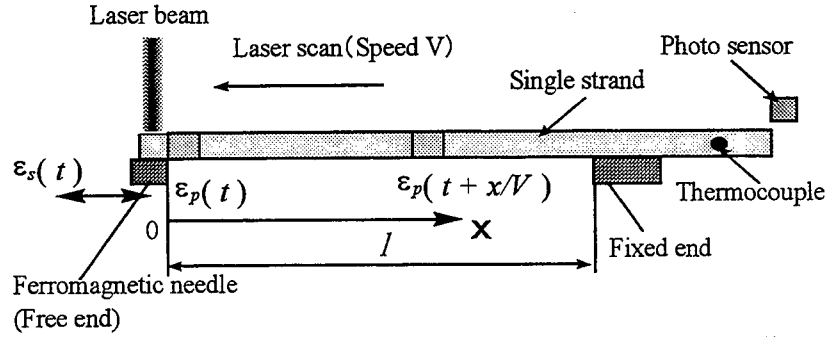


Figure 4. Definition of measured linear shrinkage and minute volume linear shrinkage

volume linear shrinkage $\varepsilon_P(t)$ should be the same but have the different irradiation start time. Therefore, the time history of a measured linear shrinkage $\varepsilon_S(t)$ of a single strand is equal to the integration of the minute volume linear shrinkage $\varepsilon_P(t)$ with the time delay that corresponds to the scan speed V.

$$\varepsilon_s(t) = \frac{1}{l}\int_0^l \varepsilon_p(t + x/V)dx = \frac{V}{l}\int_t^{t+\frac{l}{V}} \varepsilon_p(u)du \tag{1}$$

The minute volume linear shrinkage $\varepsilon_P(t)$ is derived as following equation:

$$\varepsilon_p(t) = -\frac{l}{V}\frac{\partial \varepsilon_s(t)}{\partial t} + \varepsilon_p(t + l/V) \tag{2}$$

If the time has passed sufficiently, linear shrinkage will be uniform in a length direction. Thus, linear shrinkage value of a single strand coincides with linear shrinkage value of its minute volume:

$$\varepsilon_s(\infty) = \varepsilon_p(\infty) \tag{3}$$

Therefore, $\varepsilon_P(t)$ is obtained by backward substitution of strain $\varepsilon_S(t)$, which is a time history of linear shrinkage measured by displacement sensor from initial exposure to steady state.

An experimental condition is indicated on Table 1. Relation between the time histories of linear shrinkage and temperature of a single strand has experimented.

4.2. MEASUREMENTS OF THE EFFECTS OF SCAN ORDERS

By the difference of scan order, an influence over the shrinkage and the stress of a single strand is measured. When three lines are drawn, the case to scan a line from side by side continuously is defined as the continuous scan. The case to scan the middle line after scanning two sides lines is defined as the skip scan. A scan order and the difference of the three lines irradiation experiments are shown in Figure 5. In the case of skip scan, the second line is drawn immediately after the first scan. But the third line is scanned for about tens or twenties seconds later of the second scan which corresponds to the time lag of the case of parts building.

The measurements of model deformation are also tested with the different scan types mentioned above. The size of the sample shape used for the experiments is shown in Figure 6. The plate with several support pillars is used. The curvature ρ, which is the reciprocal 1/r of the curvature radius r, of the plate is defined as the evaluation value of the deformation. It is measured immediately after fabrication and is calculated by the minimum square method from

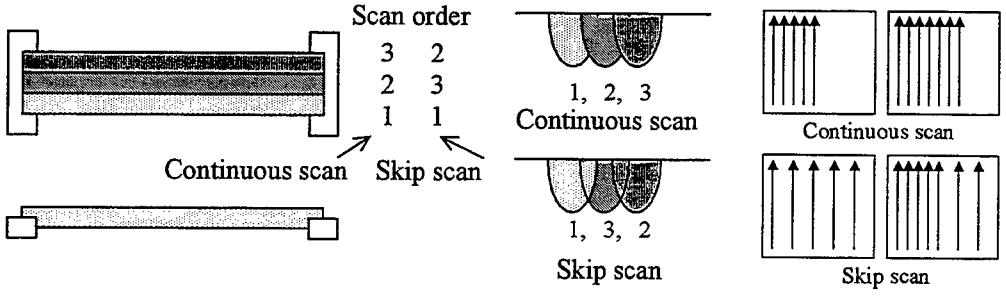


Figure 5. Scan orders of continuous scan and skip scan

the measured points. In the calculation of the curvature, the positive value is defined as the case where the circular center exists in the upper part of the model. Also, the negative value is defined as the case to exist in the lower part of the model. The reference points of the model are also shown in Figure 6.

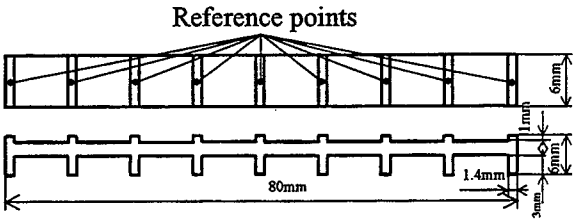


Figure 6. Sample Shape for scan orders experiment

5. EXPERIMENTAL RESULTS

Different laser powers and scanning speeds conditions are experimented, and the relation between linear shrinkage and stress after the largest expand of a single strand is drawn. As shown in Figure 7, it is understood that they move on almost the same curve. This result means that the relation is not influenced by fabrication conditions with this experimental arrangement. In other words, a characteristic of each resin is observed with this experiment.

Time history of the minute volume linear shrinkage calculated from the measured linear shrinkage is indicated on Figure 8. A vertical axis defines positive value as a shrink and negative one as an expansion. The value 0 of the horizontal axis is the origin about the time history of linear shrinkage, which is calculated from the detection time of the light sensor near the fixed end side. The representative curve of a minute volume linear shrinkage in a single strand changes to grow just after the irradiation and then to shrink afterward.

A measured result of a time history of linear shrinkage and temperature is indicated on Figure 9. Followed by the temperature fall after the rise of temperature, the single strand shrinks linearly. It is understood that the variation of the time history of the linear shrinkage after exposure is caused by heat.

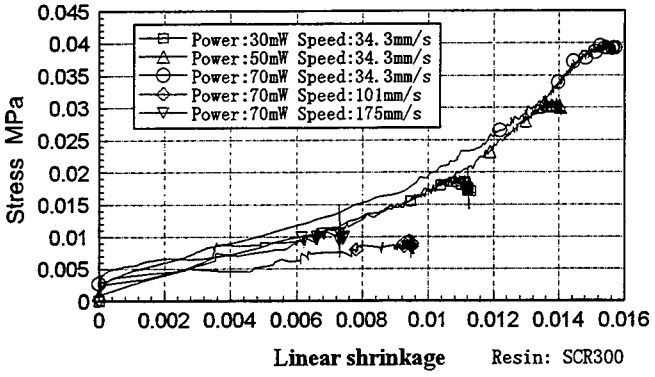


Figure 7. Relation of linear shrinkage-stress curves with different irradiation conditions.

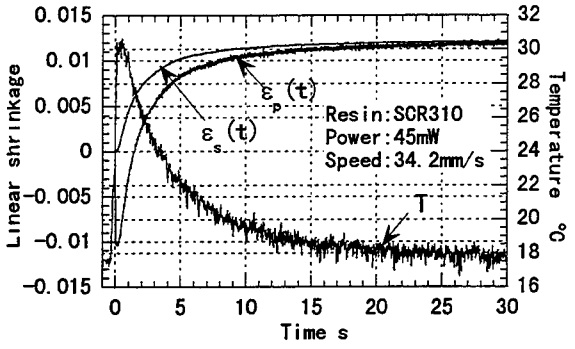


Figure 8. Time history of linear shrinkage and temperature.

Table 1 Experimental condition

Machine	Sony Co. JSC2000
Laser source	Coherent Inc. INNOVA 90-6
Wave length	UV-Ar (363.8,351.1nm)
Sampling time	0.01s
Resin (radical polymerization)	SCR300, SCR310, SCR600 (JSR Co.): All resins are urethane acrylate resin
Thermocouple	Chromel-Alumel thermocouple (K-type) ϕ 0.127mm
Set length of single strand	25mm

In the three lines scanning experiment, a smaller shrinkage and a stress have been observed when the skip scan is applied (Figure 10). It has been shown by the experiment that the skip scan has an effect of the linear shrinkage reduction in case of a layer forming.

In the case of model deformation experiment, the skip scan showed the tendency of the

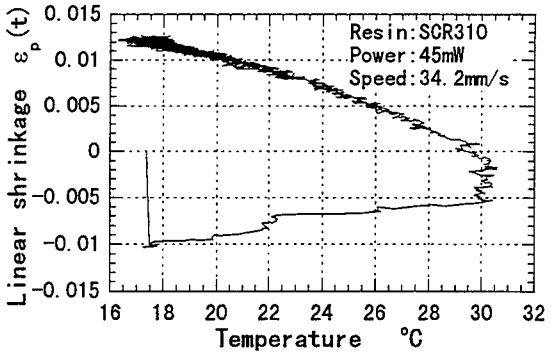


Figure 9. Relation of temperature and linear shrinkage $\varepsilon_P(t)$

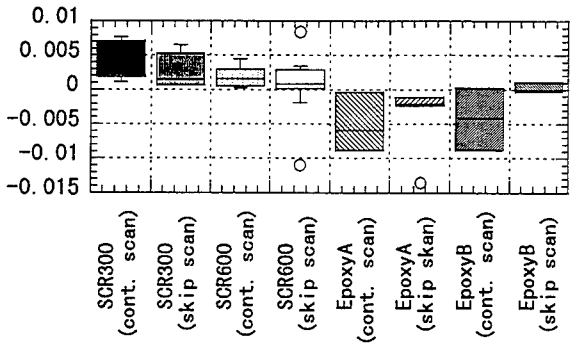
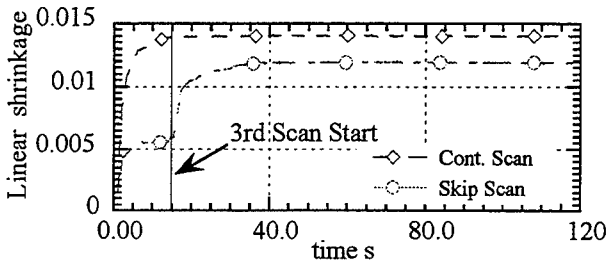
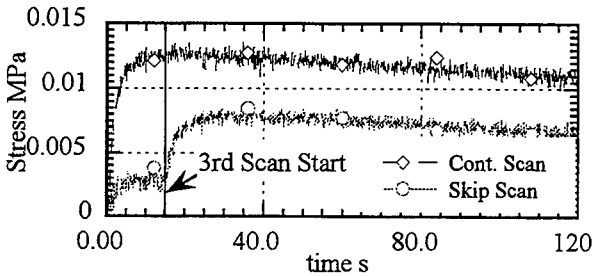


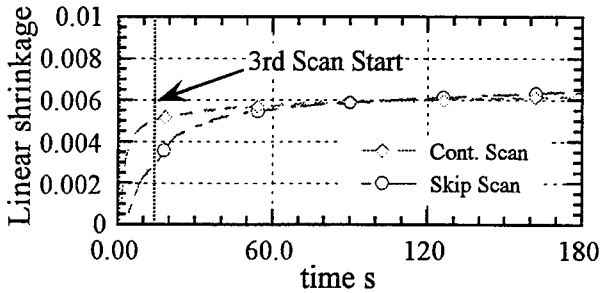
Figure 11. Deformation results of three lines scan experiment.



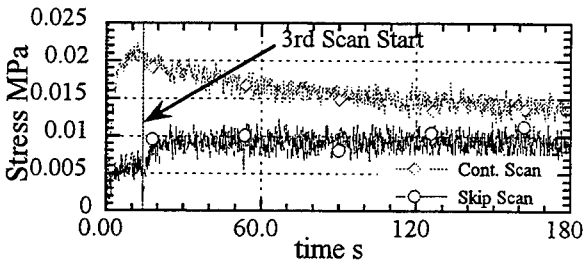
Resin:SCR300, Power:50mW
ScanSpeed:686mm/s, Length of Cured Resin:15mm



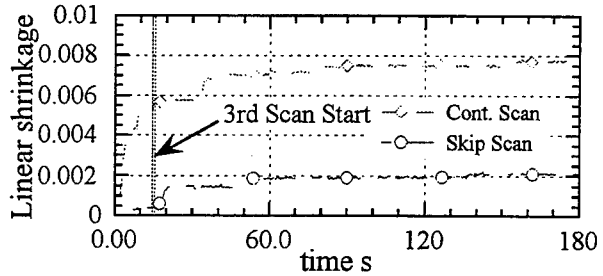
Resin:SCR300, Power:50mW
ScanSpeed:686mm/s, Length of Cured Resin:15mm



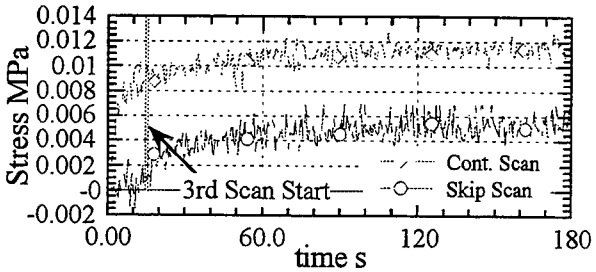
Resin:SCR600,Power:50mW
ScanSpeed:686mm/s, Length of Cured Resin:15mm



Resin:SCR600, Power:50mW
ScanSpeed:686mm/s, Length of Cured Resin:15mm

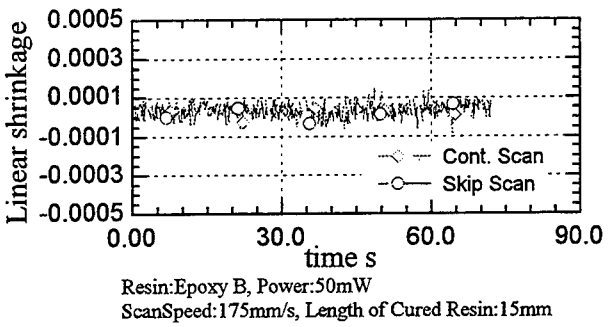


Resin:Epoxy A, Power:50mW
ScanSpeed:175mm/s, Length of Cured Resin:15mm



Resin:Epoxy A, Power:50mW
ScanSpeed:175mm/s, Length of Cured Resin:15mm

Figure 10-1. Time histories of linear shrinkage of three lines scan experiment.



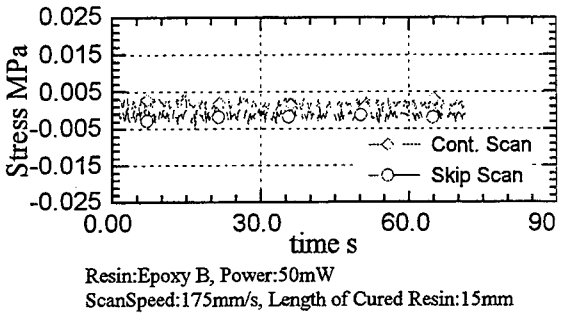


Figure 10-2. Time histories of linear shrinkage of three lines scan experiment.

smaller deformation (Figure 11).

6. DISCUSSIONS

With the single strand experiment, it has been clarified that time history of the shrinkage after irradiation is caused by the temperature change. The result that the skip scan shows the smaller shrinkage and the smaller deformation is obtained by the scan order experiments.

The experimental results that the skip scan showed the smaller value can be explained as follows: Consider the time history of the linear shrinkage when a new layer is formed as shown in Figure 12.

In case of continuous scan, because the time difference between each scan is short, there are few differences between the hardening temperature patterns around. Therefore, the shrinkage pattern of a strand resembles the ones around and little restriction from the surrounding occurs.

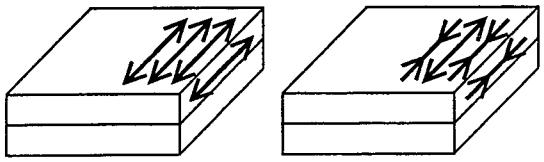


Figure 12. Sketch of strain distributions at building a new layer.

On the other hand, in the case of the skip scan, because the time difference to harden the middle among the single strands is long, the cooling progresses during the period and the single strand shrinks more. Then, the surrounding restricts the thermal expansion of the middle strand. Therefore, the linear shrinkage will be observed smaller.

In the case of the urethane system resin, whose basic reaction is radical polymerization, reaction does not progress if light is not irradiated. Method of this experiment is nothing but to observe the variation of the linear shrinkage and the stress that are caused by heating and by cooling. In the case of the epoxy resin whose basic reaction is cationic polymerization, this supposition will not be the case, since reaction does not stop after irradiation. This phenomenon in detail should be examined further.

The skip scan showed the tendency of the smaller deformation in the case of model deformation experiment. However, depending on the kind of the resin, a different result was observed in some case. As for this point, it is suggested that further analysis and experiment of the interaction among layers is necessary. It concludes that the more detailed future analysis is necessary.

7. CONCLUSIONS

This study aims at clarifying the initial linear shrinkage of cured resin in a minute volume. Experimental equipment has been developed which measures the time history of the single strand in situ in a stereolithography machine. The following results are obtained from this study:

1. The analysis method of an initial linear shrinkage of minute volume in a single strand is proposed.
2. It has been observed that a change of linear shrinkage after irradiation has been caused by the heat change, that is the results of the heating by exothermal and the cooling by heat diffusion, when the relation of the linear shrinkage and the temperature has been examined based on this method.
3. It is indicated that temperature distribution of layer surfaces that is the result of reaction heat by laser beam scanning can be one cause of shape deformation. By skip scanning, changes of shrink of adjacent lines restrict the heat expansion of middle line at initial stage of exposure. As a result, lower linear shrinkage has been observed to a single strand and model deformation has been also indicated to be small.

REFERENCES

1) H. Narahara, S. Igarashi and K. Saito: A New Stereolithography Process for Improved Performance and Surface Roughness, Proc. of the 8th International Conference on Production Engineering -Rapid Product Development- (held on August 18-20, Sapporo Japan), Chapman & Hall, UK, (1997) (in printing).
2) J. S. Ullett, R. P. Chartoff, A. J. Lightman, J. P. Murphy and J. Li: Reducing Warpage in Stereolithography Through Novel Draw Styles, Proc. of the Fifth International Conference on Rapid Prototyping, Dayton, Ohio, (1994) 109-125.
3) H. Narahara and K. Saito: Shape Analysis of Solidified Photopolymer for the Three Dimensional Photofabrication, International Journal of JSPE, 30, 4, (1996) 311-316.
4) H. Narahara and K. Saito: Characterization of Solidified Resin Created by Three Dimensional Photofabrication, Proc. of the Fourth International Conference on Rapid Prototyping, Dayton, Ohio, (1993) 271-281.
5) L. Flach and R. P. Chartoff: Stereolithography Process Modeling: Shrinkage Prediction, Proc. of the Fifth International Conference on Rapid Prototyping, Dayton, Ohio, (1994) 181-189.
6) T. Kishinami, F. Tanaka and H. Narahara: Distortion Mechanism of Stereolithography Parts, Proc. of the 8th International Conference on Production Engineering -Rapid Product Development- (held on August 18-20, Sapporo Japan), Chapman & Hall, UK, (1997) (in printing).
7) R. P. Chartoff and J. Du: Photopolymerization Reaction Rates by Reflectance Real Time Infrared Spectroscopy: Application to Stereolithography Resins, Proceedings of the Solid Freeform Fabrication Symposium, University of Texas at Austin, Texas, Austin, (1995) 298-304.
8) T. R. Guess and R. S. Chambers: In-Situ Property Measurement on Laser-Drawn Strands of SL 5170 Epoxy and SL 5149 Acrylate, Proceedings of the Solid Freeform Fabrication Symposium, University of Texas at Austin, Texas, Austin, (1997) 134-141.

Keyword Index

3-D LCVD 49, 231
3D Data Format 669
3D Printing 115, 371
Accuracy 267, 653, 709
Acrylonitrile Butadiene Styrene Patterns 195
Adaptive Control 677
Adaptive Slicing 621, 661
Adhesive Bonding 211
Alumina 133, 363
Aluminum Oxide 379
Anionic Caprolactam Polymerization 11
Ash Handling 195
Average Exposure 223
Benchmark 551
Binder 421
Binder burn out (BBO) 395
Bone 473
Bonus-Z 709
Boundary Representations 593
Brazilian Disc Test 635
Brazing 211
Build Style 627
Build Time 627
CAM-LEM 643, 379
Carbon 481
Ceramics 25, 133, 159, 185, 203, 247, 248, 363, 371, 537, 677
Chemical Vapor Deposition 497
CibaTool SL5410 349
Coefficient of Thermal Expansion 267
Comparison 585
Composites 149, 247, 341, 449, 537
Compression Stress-Strain 725
Computer Tomography 167
Conformal Cooling 115
Constructive Solid Geometry 593
Containerless HIP 81
Control Chart 141
Control Exothermic Reaction Of Combustion 91
Correlation 635
Cracking 395
Crystalline Polymers 449
CSG 593
Cure Depth 223
Curvature Measurements 125
Custom Manufacturing 149
Data Handling 603
Debinding 363
Decosopm Support 627
Deflection 307
Deformation 159, 733
Density Distribution 177
Deposition 125, 717
Design for Rapid Prototyping (DFRP) 551
Design Hierarchy 41
Design Rules 41
Device 481
Diffusion Bonding 211
Dilatant 25
Dimension 709
Dimensional Control 115
Direct Adaptive Slicing 585
Direct Metal Fabrication 81
Direct SLS 91
Direct Tooling 275
Direct-Write Fabrication 33
Disposable Fixture 249
Distorted Model 559
DOE 395
Drying 25
EDM 257
Elastic-Viscoplastic 725
Elastomer 441
Electrical Discharge Machining 257
Electrodes 257
Electromotive Force 481
Endoscopic Ultrasound (EUS) 167
Epoxy 341
Epoxy Tooling 295
Eutectic Powder Compositions 91
EWMA 141
Experientially Weighted Moving Average 141
Experimental Design 185
Extrusion 25, 689
Extrusion Freeform Fabrication 457
Extrusion Freeforming 11
Failure Analysis 295
FDC 411, 421
FDM 441, 449, 717
FDM of ABS Patterns For Investment Casting 195
FEA 635
Feedstock 203
Fiber-Coupled Cw Diode Laser 99
Fiber-Reinforced Composites 17
Filament Aging 421, 431
Filament Properties 421
First Order Approximation 585
Flatness 653
Free Space Diode Lasers 99
Free-Form Fabrication 203, 307, 387, 513
Functional Components 203

Functionally Graded Materials (FGMs) 67, 521, 529
Functional Test 559
Fused Deposition 689
Fused Deposition Modeling 195, 403, 411, 441, 449, 457
Fused Deposition Of Ceramics 159, 185, 395, 403, 431
Gas Phase Deposition 241, 481
Gastrointestinal Tract 167
Gelcasting 133
Gels 473
Glass Transition Temperatures 325
Graded Materials 203, 307, 387, 513
Grain Growth 699
Graphical User Interface (GUI) 569
Green Ceramic Feedstock 457
Green Parts 733
Hatch Fill Cure Depth 653
Hatch Overcure Depth 653
Hatch Spacing 653
Heat Resistant Resin 349
Heterogeneous/Materially Graded Objects 613
High Density 363
High Pressure CVD 497
Hot Isostatic Pressing (HIP) 81
Human-Computer Interface 569
Humidity Resistant Resin 349
Hydrogels 473
Inconel 625 81
Industrial Design Process 559
Infra-Red Spectroscopy (RRTIR) 333
Injection Mold Lifetime 317
Injection Molding 275, 295
Injection Molding Tooling 295, 521
Insulation 481
Investment Casting 195
Isotropic 149
Keltool 267
L-Block 141
LADRP (Laser Aided Direct Rapid Prototyping) 41
Laminated Bonding 211
Laminated Object Manufacturing 247, 248, 529, 537, 677, 643
Laminated Tooling 211, 307
Large Prototypes 249
Laser Beam 223
Laser Deposition 521
Laser Exposure 177
Laser Processing 387, 513
Laser-Driven Gas-Phase Deposition 489
Layer Thickness 653
Layered Fabrication 41
Layered Manufacturing 17, 577, 643
Layered Materials 387
Layered Metal Prototyping 505
Lead-Zirconate-Titanate 403
LENS 387, 699
Line Width Compensation 141
Linear Shrinkage 733
Liquid Crystal (LC) Monomers 325, 333
Liquid Photopolymer 177
LOM 247, 248, 529, 537, 677, 643
Low Volume Tooling 275
Machine Vision 59
Magnetic Resonance Imaging 167
Matching Contours 585
Material Selection 133
Materials 363
Mechanical Properties 11
Medical Modeling 248
Metal 203, 521
Metal Deposition 387
Metal Fabrication 387
Metal Jetting 1
Microcasting 125
Microelectromechanical Devices 505
Microscopic Flow 177
Microstructural Coarsening 699
Mineralization 473
Modeling 677, 717, 725
Moisture Effects 431
Mold SDM 133
Multilayer Ceramic 33
Multimaterial 521
Multiobjective Optimization 627
Multiphase Jet Solidification 203
Muscle 473
Near-Net-Shape Processing 1, 149, 513
Net Shape Functional Parts 99
Novel Isocyanate Activator 11
Numerical Modeling 689
Nylon 6 11
Orientation 661
Oriented Microstructures 529
Photocuring Resin 733
Photopolymer 733
PID Temperature Control 241
Piezoelectric Transducers 403
Plastic Molds 275
Polycarbonate 709
Polygon Mirror 223

Polymer 449
Polyurethane 133
Position Accuracy 223
Powder Casting 287
Powder Injection Molding 203
Preheating 125
Presintering 363
Pressure Die-Casting 307
Process Control 49, 59, 231
Process Modeling 677
Process Monitoring 141
Process Planning 669
Prototype Accuracy 577
Prototyping 569
Prototyping Material 559
Pseudoplastic 25
Quality 141, 653
Quartz 465
R/P Model 287
Rapid Composite Process 149
Rapid Manufacturing 513
Rapid Prototype 559
Rapid Prototyping 1, 141, 149, 257, 307, 411, 513, 551, 569, 621, 635, 643
Rapid Prototyping Decision Support System (RPDSS) 551
Rapid Tooling 211, 267, 275, 287, 307, 317
Raster Scanning 223
RCP 149
Reaction Heat 733
Recoating 223
Reinforcement 149
Residual Stress 125
Resin 725
Response Surface Methodology 627
Reverse Engineering 593, 661
Reverse Engineering: Practical Considerations 603
Rheology 25, 717
Robocasting 25
Rod Growth 49
RP 643
RTV Silicone Rubber 267
RU955 Si_3N_4 421
Ruled Slices 585
SALD 49, 231, 481
SALDVI 481, 489
Sanders Prototyping 403
Scale Factor 559
Scanning Device 223
Scanning Speed 223
Selected Area Laser Photolysis 505
Selective Area Vapor Phase Deposition 99
Selective Laser Sintering 59, 67, 81, 91, 99, 257, 465, 709
Self-Propagating High-Temperature Synthesis (SHS) 91
Semiconductor Diode Lasers 99
SFF 1, 41, 149, 411, 613, 643
Shape Deposition Manufacturing 125, 133, 521
Shrinkage 159, 395
Shrinkage Compensation 141
Si_3N_4 411
Silica 341
Silicon Carbide 481, 489
Silicon Nitride 159, 241, 379, 395, 431, 529
Silicon Nitride Blisk 457
Similitude Method 559
Simulation 699, 709
Sintering 287, 363
Sintering Behavior 33
SKINFLEX 167
SL5170 725
SLA 17, 141, 177, 223, 267, 275, 295, 325, 333, 341, 349, 363, 569, 627, 653
Slanted Layers 621
Slicer 41
SLS 91, 99, 59, 67, 81, 257, 465, 709
Slurry 25
Soft 441
Software 551, 569
Soldering 99
Solid Freeform Fabrication 1, 41, 149, 411, 613, 643
Solid Interchange Format 41
Solid/Geometric Modeling 613
Solidification 717
Spatial Frequency 577
SPC 141
Split Prototypes 249
Spray Deposition 1
Spreading 717
Stainless Steel 379, 387
State Transformation 559
Statistical Process Control 141, 185
Stepped Surface 371
Stereolithography 17, 141, 177, 223, 267, 275, 295, 325, 333. 341, 349, 363, 569, 627, 653

Strong Interfaces 529
Structural Ceramics 411
Support Structure 133, 661
Surface Finish 115, 371
Surface Roughness 317
Tangent Cut 249, 577
Tele-Manufacture 669
Temperature Distribution 177
Temperature Sensor 481
Tessellation 49
Testing 635
Tetracast 149
Tetramethylsilane Gas Environment 489
Tetramethylsilane/Ammonia Gas Mixture 241
Theoretical Solution 635
Thermal Analysis 689
Thermal Stress 125
Thermocouple 481
Thermodynamic Modeling 241
Thermoelastic Stress Analysis 635
Thermoplastic 133
Thermoplastic Elastomer 441
Thermoset 133
Thermotropic Liquid 449
Titanium 497, 505
Titanium Halides 497
TLCP 449
Tolerance Loss 125
Tooling 115, 341
Transferability 635
Vacuum Casting 267
Vapor Infiltration 489
Virtual Prototyping 669
Viscosity 25, 717
VRML (Virtual Reality Modeling Language) 669
Warpage 159, 125
Water Resistant Resin 349
Wavelet 577
Wax Segregation And Recrystallization 457
Weak Interfaces 529
Wear, Injection Molds 317
Weighted Comparison 551
Wicking 395
X-Ray Diffraction 125
Zero Order Approximation 585
Zero Shrinkage 287
Zirconium Diboride (ZrB_2) 257
Zirconium Diboride And Copper 257
Zyrkon 257

Solid Freeform Fabrication Symposium - 1997
Author/Attendee List

Said Ahzi (341, 709, 725)
Clemson University
Department of Mechanical Engineering
Clemson, SC 29634
Phone: (864)656-7190
Fax: (505)656-4435
Email: sahzi@ces.clemson.edu

Pedro Alaniz
The Boeing Company
3855 Lakewood Blvd.
Long Beach, CA 90845
Phone: (562)982-6919
Fax: (562)593-2678
Email: sla@hc1882.mdc.com

David Alexander
Pratt & Whitney
P.O. Box 109600
West Palm Beach, FL 33410-9600
Phone: (561)796-6149
Fax: (561)796-7454
Email: alexnder@pwfl.com

Anthony Anderson
Ford Motor Company
P.O. Box 2053 MD3135 - SRL
20000 Rotunda Dr.
Dearborn, MI 48121-2053
Phone: (313)845-8226
Fax: (313)323-1129
Email: aanders4@ford.com

Clint Atwood (387)
Sandia National Labs
P. O. Box 5800
MS 0958
Albuquerque, NM 87185-5800
Phone: (505)844-0816
Fax: (505)844-5589
Email: clatwoo@sandia.gov

Donald Baird (441, 449)
Virginia Polytechnic Institute and State University
Department of Chemical Engineering
Blacksburg, VA 24061-0211
Phone: (540)231-5998
Fax: (540)231-2732
Email: dbaird@vt.edu

Amit Bandyopadhyay (395, 403, 421, 431)
Rutgers University
Center for Ceramic Research
Brett and Bowser Rds
P.O. Box 909
Piscataway, NJ 08855
Phone: (908)445-5617
Fax: (908)445-3258
Email: amitband@rci.rutgers.edu

Joseph Beaman (67, 81, 465)
University of Texas at Austin
Mechanical Engineering
C2200
Austin, TX 78712
Phone: (512)471-3058
Fax: (512)471-8727
Email: jbeaman@mail.utexas.edu

Jack Beuth (125)
Carnegie Mellon University
Department of Mechanical Engineering
5000 Forbes Ave.
Pittsburgh, PA 15213
Phone: (412)268-3873
Fax: (412)268-3348
Email: beuth@andrew.cmu.edu

Jan Helge Bøhn (441, 449)
Virginia Polytechnic Institute and State University
Department of Mechanical Engineering
Blacksburg, VA 24061-0238
Phone: (540)231-3276
Fax: (540)231-9100
Email: bohn@vt.edu

Sandesh C Borse (505)
Louisiana Tech University
Institute for Micromanufacturing
606 Bond St.
Ruston, La 71270
Phone: (318)255-0093
Fax: (318)257-5104
Email: scb008@engr.latech.edu

Dave Bourell (67, 81, 465)
University of Texas at Austin
Mechanical Engineering
C2200
Austin, TX 78712
Phone: (512)471-3170
Fax: (512)471-7681
Email: dbourell@mail.utexas.edu

David Brancazio (115)
Massachusetts Institute of Technology
77 Mass. Ave., Rm 35-011
Cambridge, MA 02139
Phone: (617)253-2606
Fax: (617)253-0209
Email: dbrancaz@mit.edu

Robert L. Brown
The Gillete Company
Prudential Tower Bldg.
49th floor
Boston, MA 02199
Phone: (617)421-7604
Fax: (617)421-8484
Email: robert_brown@gillette.com

Suzanne Buchele (593)
UT Austin/Argonne National Lab
Computer Sciences Department
Taylor Hall 2.124
Austin, Tx 78712
Phone: (512)471-9753
Fax: (512)471-7866
Email: buchele@cs.utexas.edu

Herb Caloud
Fiskars Inc Research & Development
2219 Eagle Drive
Middleton,WI 53590
Phone: (608)836-3133

Paul Calvert (11, 25, 473, 717)
University of Arizona
Arizona Materials Laboratories
4715 E. Fort Lowell Rd.
Tucson, AZ 85712
Phone: (520)322-2994
Fax: (520)322-2993
Email: calvert@engr.arizona.edu

Ian Campbell (551)
University of Nottingham
Dept. of Manufacturing Engineering
University Park
Nottingham NG7 2RD
UK
Phone: 44 115 951 4015
Fax: 44 115 951 4000
Email: Ian Campbell@nottingham.ac.uk

Joseph Cesarano (25)
Sandia National Laboratories
1001 University Blvd. NE, Ste. 100
Albuquerque, NM 87106
Phone: (505)272-7624
Fax: (505)272-7304
Email: jcesara@sandia.gov

Richard Chartoff
(247, 248, 325, 333, 537, 677)
University of Dayton
Rapid Prototype Development Laboratory
300 College Park Ave.
Dayton, OH 45469
Phone: (937)229-2517
Fax: (937)229-2503
Email: chartorp@udri.udayton.edu

Kenwei Chen
University of Texas at Austin
1648 W. 6th Apt. B
Austin, TX 78703
Phone: (512)474-0666

Uichung Cho (559)
University of Texas at Austin
Department of Mechanical Engineering
3358E Lake Austin Blvd.
Austin, TX 78703
Phone: (512)471-7347
Email: uichung@mail.utexas.edu

Michael Cima (115, 371)
Massachusetts Institute of Technology
Department of Mechanical Engineering
77 Mass. Ave., Rm 12-011
Cambridge, MA 01239
Phone: (617)253-6877
Fax: (617)258-6936
Email: mjcima@mit.edu

Richard Clancy (185)
AlliedSignal Research and Technology
Research and Technology
P. O. Box 1021
Morristown, NJ 07962-1021
Phone: (973)455-3794
Fax: (973)455-3008
Email: clancyR@mtomp201.research.allied.com

William Coblenz
DARPA/DSO
3701 N Fairfax Dr.
Arlington, VA 22203
Phone: (703)696-2288
Fax: (703)696-3999
Email: wcoblenz@darpa.mil

Alexander Cooper (133)
Stanford University
Mechanical Engineering
Bldg. 530, Rm. 128
Stanford, CA 94305-3030
Phone: (650)723-0565
Fax: (650)723-5034
Email: agcooper@leland.stanford.edu

Rich Crawford
University of Texas at Austin
Mechanical Engineering
C2200
Austin, TX 78712
Phone: (512)471-3030
Fax: (512)471-7682
Email: rhc@mail.utexas.edu

Jim Crocker (241, 481, 489)
University of Connecticut
Institute of Materials Science
97 N. Eagleville Rd., U-136
Storrs, CT 06269
Phone: (860)486-4410
Fax: (860)486-4745
Email: jec96001@uconnvm.uconn.edu

Robert Crockett
Milwaukee School of Engineering
Rapid Prototyping
1025 N. Broadway
Milwaukee, WI 53202
Phone: (414)277-7275
Fax: (414)277-7470
Email: crockett@msoe.edu

Stephen Danforth
(159, 185, 395, 403, 411, 421, 431, 689)
Rutgers - The State University of New Jersey
Center for Ceramic Research
Brett & Bowser Rds
P.O. Box 909
Piscataway, NJ 08855-0909
Phone: (732)445-2211
Fax: (732)445-3258
Email: danforth@rci.rutgers.edu

Gregory Danyo
Univesity of Texas
Mechanical Engineering
Austin, TX 78705
Email: gdanyo@mail.utexas.edu

Darius Daruwala
Milwaukee School of
Engineering
1025 N. Broadway
Milwaukee, WI 53202-3109
Phone: (414)277-7189
Fax: (414)277-7470
Email:
daruwala@warp.msoe.edu

Suman Das (81)
University of Texas at Austin
Mechanical Engineering
ETC 5.160
C2200
Austin, TX 78712
Phone: (512)471-5838
Fax: (512)471-8727
Email:
das@sffoffice.me.utexas.edu

Peter de Jager (585)
Delft University of Technology
Faculty of Industrial Design
Engineering
Jaffalaan 9
Delft 2628 BX
The Netherlands
Phone: 31-15-278 3437
Fax: 31-15-278 7316
Email: p.j.dejager@io.tudelft.nl

Carl Deckard (709)
720 Bastrop Hgw #108
Austin, TX 78741
Phone: (512)385-0388

Phill Dickens (267, 295, 307)
University of Nottingham
Dept. of Manufacturing Engg.
and Oper. Management
Nottingham, UK NG7 2RD
UK
Phone: 44-115-951-4063
Fax: 44-115-951-4000
Email: philip.dickens@
nottingham.ac.uk

Duane Dimos (33)
Sandia National Labs
MS 1411
P. O. Box 5800
Albuquerque, NM 87185
Phone: (505)844-6385
Fax: (505)844-9781
Email: dbdimos@sandia.gov

Nathanael Dolar (211)
Rensselaer Polytechnic Institute
Department of Mechanical
Engineering
Johnson Engineering Center
110 Eighth St., Rm 4026
Troy, NY 12180-3590
Phone: (518)276-6070
Fax: (518)276-2623

Patrick DuBois (1)
Automation & Robotics
Research Institute
Box 19045
7300 Jack Newell Blvd.
South Ft. Worth, TX 76118
Phone: (817)272-3092
Fax: (817)272-3406

Adrian DuPré
Sulzer Orthopedics Inc.
9900 Spectrum Dr.
Austin, TX 78717
Phone: (512)432-9330
Fax: (512)432-9250
Email: adupre@sous.com

Michael Durham
Accelerated Technologies, Inc.
12919 Dessau Rd.
Austin, TX 78754
Phone: (512)990-7199
Fax: (512)990-9726
Email:
mdurham@ariqustin.com

Deba Dutta (613, 661)
University of Michigan
Mechanical Engineering
Department
2250 G. G. Brown Labs
Ann Arbor, MI 48109
Phone: (313)936-3567
Fax: (313)647-3170
Email: dutta@unich.edu

Zwy Eliezer
University of Texas at Austin
Mechanical Engineering
Department
Austin, TX 78712
USA

William A. Ellingson (593)
Argonne National Laboratory
Energy Technology Division
9700 South Cass Ave., ET/212
Argonne, IL 60439
Phone: (630)252-5068
Fax: (630)252-4798
Email:
wa_ellingson@qmgate.anl.gov

Brett Engel
Univesity of Texas
Materials Science &
Engineering
ETC8.172 C2200
Austin, TX 78756
Phone: (512)454-4175
Email:
b.engel@mail.utexas.edu

Mark Ensz
Sandia National Labs
P. O. Box 5800
MS 0958
Albuquerque, NM 87185
Phone: (505)844-6873
Fax: (505)844-5589
Email: mtensz@sandia.gov

Marcelino Essien
Sandia National Labs
Dept. 1823 MS1411
Albuquerque, NM 87185
Phone: (505)845-0574
Fax: (505)844-9781
Email: messien@sandia.gov

Mike Ervin
DTM Corporation
1611 Headway Circle
Austin, TX 78754
Phone: (512)339-2922
Fax: (512)339-0634

Georges Fadel (569)
Clemson University
Mechanical Engineering
Department
202 Fluor Daniel Bldg.
Clemson, SC 29634
Phone: (864)656-5620
Fax: (864)656-4435
Email: gfadel@ces.clemson.edu

John Fessler (521)
Stanford University
Department of Mechanical
Engineering
Bldg. 500, Rm. 500K
Stanford, CA 94305
Phone: (650)723-4712
Fax: (415)723-4548
Email: fess@leland.stanford.edu

Kent Firestone
DTM Corporation
1611 Headway Circle Bldg. 2
Austin, TX 78754
Phone: (512)425-2860
Fax: (512)339-0634
Email: kentf@dtm_corp.com

S.G. Fishman
Office of Naval Research
800 N. Quincy St.
Arlington, VA 22217
Phone: (703)696-0285
Email: fishmas@onr.navy.mil

Tim Floy
DTM Corp.
1611 Headway Circle Bldg. 2
Austin, TX 78754
Phone: (512)425-2824
Fax: (512)634-0339
Email: floyt@dtm-corp.com

John Forsyth
Sanders Prototype, Inc.
P.O. Box 540
Pine Valley Mill, Elm St.
Wilton, NH 03086
Phone: (603)654-5100X220
Fax: (603)654-2616

Robert Franceschini (41)
University of Central Florida
Computer Science Department
4000 Central Florida Blvd
Orlando, FL 32816
Phone: (407)658-5519
Fax: (407)658-5059
Email: francesc@cs.ucf.edu

Doug Freitag
Bayside Materials Technology
21150 New Hampshire Ave
Brookeville, MD 20833
Phone: (301)570-3821
Fax: (301)570-3836
Email: dfreitag@ix.netcom.com

Craig Friedrich
Michigan Technological
University
MEEM Department
Houghton, MI 49931
Phone: (906)487-1922
Fax: (906)487-2822
Email: craig@mtu.edu

Tim Fuesting
Allison Engine Company
P.O. Box 420, Speed Code W-
08
Indianapolis, IN 46206
Phone: (317)230-5374
Fax: (317)230-4470

Paul Fussell (275, 521)
Aluminum Company of
America
Alcoa Technical Center
100 Technical Dr.
Alcoa Center, PA 15069
Phone: (412)337-2721
Fax: (412)337-2220
Email: paul.fussell@alcoa.com

Charles Gasdaska
Allied Signal
101 Columbia Rd. Bldg. ctc-2
Morriston, NJ 07962
Phone: (973)455-4022
Fax: (973)455-3008
Email:
gasdaska@research.allied.com

Erik Geiss
University of Connecticut
Institute of Materials Science
97 N. Eagleville Rd., U-136
Storrs, CT 06269
Phone: (860)486-1664
Email:
geiss@main.phys.uconn.edu

Vito Gervasi (141, 149)
Milwaukee School of
Engineering
Rapid Prototyping Center
1025 N. Broadway
Milwaukee, WI 53202
Phone: (414)277-4550
Fax: (414)277-7470
Email: gervasi@warp.msoe.edu

Ian Gibson (59)
The University of Hong Kong
Department of Mechanical
Engineering
Pokfulam Rd.
HONG KONG
Phone: +852 2859 7901
Fax: +85 2858 5415
Email: gibson@hkumea.hku.hk

Mike Gou
Cryco Quartz, Inc.
8107 Altoga Drive
Austin, TX 78724
Phone: (512)926-8931
Fax: (512)929-8257
Email: mgou@cryco.com

Tom Greaves
Delphi-GM
1401Crooks Rd.
MS-T1
Troy, MI 48084
Phone: (248)696-5145
Fax: (248)696-5150

Alair Griffin (603)
Lone Peak Engineering
12660 South Fort St.
Draper, UT 84020
Phone: (801)553-1732
Fax: (801)553-1734

Michelle Griffith (387, 699)
Sandia National Labs
P. O. Box 5800
MS 0958
Albuquerque, NM 87185
Phone: (505)284-2096
Fax: (505)844-5589
Email: mlgriff@sandia.gov

Joonwook Han (431)
Rutgers University
2217 Strawberry Rd.
Piscataway, NJ 08817
Phone: (732)572-8894
Email: jwhan@eden.rutgers.edu

Suresh Haridas (497)
Louisiana Tech University
911 Hergot Avenue
Ruston, LA 71272
Phone: (318)251-8312
Fax: (318)257-5104
Email: sha003@engr.latech.edu

Shay Harrison (241, 481, 489)
University of Connecticut
Institute of Materials Science
97 North Eagleville Rd., U-136
Storrs, CT 06269
Phone: (860)486-4410
Fax: (860)486-4745
Email:
slh95001@uconnvm.uconn.edu

Marge Hartfel
3M
3M Center
Building 235-BC-09
St. Paul, MN 55144
Phone: (612)737-2342
Fax: (612)736-1379
Email: mahartfel@mmm.com

Takeshi Hattori
University of Illinois at Chicago
Mitsubishi Chemical Co.
842 W. Taylor, 2039 ERF (M/C 251)
Chicago, IL 60607
Phone: (312)996-9620
Fax: (312)413-0457
Email: thattori@uic.edu

Uday Hejmadi
DTM Corporation
1611 Headway Circle
Austin, TX 78754
Phone: (51425-2932
Fax: (512)339-0634
Email: hejmadiu@dtm-corp.com

Jim Hertenstein
AutoFab Systems, Inc.
54 Wagonheel Road
Sudbury, MA 01776
Phone: (508)443-5110
Fax: (508)443-0320
Email: jimherten@aol.com

Kurt Hertzog
Delphi E - General Motors
PO Box 20366
Rochester, NY 14602-0366
Phone: (716)359-6735
Fax: (716)359-6578
Email:
lnushen.nzq355@gmeds.com

Arthur Heuer (379)
Case Western Reserve University
Dept. of Materials Science and Engineering
10900 Euclid Ave.
Cleveland, OH 44106-7204
Phone: (216)368-3868
Fax: (216)368-8932
Email: ahh@po.cwru.edu

Robert Hoffman (457)
Advanced Ceramics Research, Inc.
851 E. 47th St.
Tucson, AZ 85713
Phone: (520)792-2616
Fax: (520)792-2635
Email:
r.hoffman@acrtucson.com

Bernard Hon (653)
The University of Liverpool
Department of Engineering
P.O. Box 147
Liverpool L69 3BX
UK
Phone: +44(151)794-4680
Fax: +44(151)794-4693
Email: hon@liv.ac.uk

Paul Hooge
Louisiana Tech University
911 Hergot Avenue
Ruston, LA 71272
Phone: (318)255-9599
Email: pvhooge@linknet.net

Neil Hopkinson (267)
University of Nottingham
Dept. of Manuf. Eng. and Operations Management
University Park
Nottingham, UK NG7 2RD
UK
Phone: 44-115-951-4068
Fax: 44-115-951-4000
Email: epxnmh
@epn1.maneng.nott.ac.uk

Elaine Hunt (341, 725)
Clemson University
Department of Mechanical Engineering
100 Fluor Daniel Bldg.
Clemson, SC 29634
Phone: (864)656-0321
Fax: (505)656-4435
Email:
elaine.persall@ces.clemson.edu

Lori Jackson
Lockheed Martin
P.O. Box 748
Ft. Worth, TX 76101
Phone: (817)763-7264

Kevin Jakubenas
(241, 481, 489)
University of Connecticut
Institute of Materials Science
97 N. Eagleville Rd., U-136
Storrs, CT 06279-3136
Phone: (860)486-4410
Fax: (860)486-4745
Email:
kjakuben@mail.ims.uconn.edu

Vikram Jamalabad (159, 185)
AlliedSignal Research and Technology
Intelligent Systems and Technologies
101 Columbia Turnpike
Morristown, NJ 07962-1021
Phone: (973)455-3668
Fax: (973)455-5991
Email:
jamalabad@research.allied.com

Suresh Jayanthi (275)
DuPont Somos Solid Imaging Materials
Solid Imaging Group
Two Penn's Way, Ste. 401
New Castle, DE 19720
Phone: (302)328-5428
Fax: (302)328-5693
Email:
jayantss@esvax.dnet.dupont.com

Larry Jepson (67)
University of Texas at Austin
Department of Mechanical Engineering
ETC 5.160
Austin, TX 78712
Phone: (512)471-5838
Fax: (512)471-8728
Email:
larry@sffoffice.me.utexas.edu

Keith Jones (551)
The University of Texas at Arlington
Automation & Robotics Research
7300 Jack Newell Blvd
Ft. Worth, TX 76118
Phone: (817)272-5920
Email: djones@arrl.uta.edu

Hannu Kaikonen
Helsinki University of Technology
Lahti Centre
Niemenkatu 73
Lahti, FIN-15210
Finland
Phone: (+358) 3 8114266
Fax: (+358)3 7834512
Email:
hannu.kaikonen@ltk.hut.fi

N.P. Karapatis (317)
Swiss Federal Institute of Technology
Department of Mechanical Engineering
DGM-Ecublens, EPFL
CH-1015 Lausanne
SWITZERLAND
Phone: 41 21 693 3861
Fax: 41 21 693 3509
Email:
karapatis@imeco.dgm.epfl.ch

Satoshi Kawamura
Ebara Research Co. Ltd.
2-1, Honfujisawa 4-chome
251 Fujisawa-shi
JAPAN
Phone: 81 466 83 7627
Fax: 81 466 83 7635
Email:
kawamura03932@erc.ebara.co.jp

David Keicher
Optomec Design Company
13170B Central Avenue
Suite 310
Albuquerque, NM 87123
Phone: (505)761-8250
Fax: (505)761-6638
Email: dkeicher@flash.net

John Kietzman (133)
Stanford University
Mechanical Engineering
Bldg. 530, Rm. 128
Stanford, CA 94305
Phone: (650)723-0565
Fax: (650)723-5034
Email:
kietzman@leland.stanford.edu

Chuck Kirschman (569)
253 Knollview Rd.
Central, SC 29630
Phone: (864)868-3303

Jill Kirschman (569)
Clemson University
Industrial Engineering Department
Freeman Hall
Clemson, SC 29634
Phone: (864)656-4785
Email:
jkirsch@ces.clemson.edu

Jim Klos
Phillips Plastics
1201 Hanley Rd.
Hudson, WI 54016
Phone: (715)386-4320
Fax: (715)386-4326
Email: jimklos@phillips-origen.com

Don Klosterman
(247, 248, 537, 677)
University of Dayton
Rapid Prototype Development Laboratory
300 College Park Ave.
Dayton, OH 45469
Phone: (937)229-2794
Fax: (937)229-2503
Email:
Klosterman@udri.udayton.edu

Ron Knight
Lockheed Martin Vought Systems
M/S PT-91
P.O. Box 650003
Dallas, TX 75265-0003
Phone: (972)603-7868
Fax: (972)603-9052
Email: knight@vs.lmco.com

Martin Koch (195)
California Polytechnic State University
Industrial & Manufacturing Engineering
San Luis Obispo, CA 93407
Phone: (805)756-1114
Fax: (805)756-5439
Email: mkoch@calpoly.edu

Ken Kornele
3M
A141-1S-04
6801 River Place Rd.
Austrin, TX 78726-9000
Phone: (512)984-6567
Fax: (512)984-5064
Email: klkornele@mmm.com

Radovan Kovacevik
SMU
Dept. of Mechanical Engineering
PO Box 750337
Dallas, TX 75275-00337
Phone: (214)768-3200
Fax: (214)768-1473
Email: kovacevi@seas.smu.edu

Ramnath Krishnan (497)
Louisiana Tech University
Institute for Micromanufacturing
PO Box 8306
Ruston, LA 71272
Phone: (318)255-1185
Email:
kramnath@engr.latech.edu

Satoshi Kudo
Ebara Corporation
11-1, Haneda Asahi-cho
Ohta-ku
Tokyo 144
JAPAN
Phone: 81-3-3743-6549
Fax: 81-3-3745-3443
Email: ogawa04@ebara.co.jp

Donald Kupp (203)
Fraunhofer Resource Center Delaware
1 Innovation Way, Ste. 301
Newark, DE 19711
Phone: (302)369-6757
Fax: (302)369-6763
Email:
kupp@frc.de.fraunhofer.com

Jari Laine
Helsinki University of Technology
Lahti Centre
Niemenkatu 73
Lahti, FIN-15210
Finland
Phone: (+358)3 811 4266
Fax: (+358)3 783 4512
Email: jari.laine@ltk.hut.fi

Noshir Langrana (185, 411, 421)
Rutgers - The State University of New Jersey
Mechanical and Aerospace Engineering
Piscataway, NJ 08855
Phone: (732)445-3168
Fax: (732)445-3124
Email:
langrana@caip.rutgers.edu

Thomas Latham
United Technologies Research Center
99 Cathedral Rd.
Brewster, MA 02631
Phone: (508)896-3009
Fax: (860)610-7880
Email: lathamts@utrc.utc.com

Goonhee Lee
University of Texas
Department of Chemical Engineering
Austin, TX 78712
Phone: (512)471-6910
Fax: (512)475-7824
Email: jimin@marl.utexas.edu

Gary Lewis (513)
Los Alamos National Laboratory
Mail Stop G770
Los Alamos, NM 87544
Phone: (505)667-5268
Fax: (505)667-5268
Email: gkl@lanl.gov

John Lombardi (11, 133, 457)
Advanced Ceramics Research, Inc.
851 E 47th St.
Tucson, AZ 85713
Phone: (520)792-2616
Fax: (520)792-2635
Email:
j.lombardi@acrtucson.com

Tariq Manzur (99)
University of Connecticut
Photonics Research Center
260 Glenbrook Rd., U-192
Storrs, CT 06269
Phone: (860)486-1961
Fax: (860)486-1033
Email: tariq@eng2.uconn.edu

Harris Marcus
(99, 241, 481, 489, 669)
University of Connecticut
Institute of Materials Science
102 North Eagleville Rd., U-136
Storrs, CT 06269-3136
Phone: (860)486-4623
Fax: (860)486-4575
Email:
hmarcus@mail.ims.uconn.edu

Ann Marsan (661)
University of Michigan
2225 G. G. Brown Laboratory
2350 Hayward
Ann Arbor, Mi 48109
Phone: (313)763-4056
Fax: (313)647-3730

James Maxwell (497, 505)
Louisiana Tech University
Institute for Micromanufacturing
911 Hergot Avenue
Ruston, LA 71272
Phone: (318)257-5121
Fax: (318)257-5104
Email:
maxwell@engr.latech.edu

Joseph McIntosh (159)
Rutgers - The State University
of New Jersey
Center for Ceramic Research
Piscataway, NJ 08854
Phone: (908)637-4824
Fax: (908)637-8944

Scott McMillin (603)
Lone Peak Engineering
12660 South Fort St.
Draper, UT 84020
Phone: (801)553-1732
Fax: (801)553-1734

Tom McNulty (403)
Rutgers - The State University
of New Jersey
Center for Ceramic Research
Brett and Bowser Rds
Piscataway, NJ 08855
Phone: (732)445-5567
Fax: (732)445-3258

David Messia (49, 231)
Rensselaer Polytechnic Institute
Dept. of ME, Aeronautical Eng.
& Mechanics
JEC 5022
Troy, NY 12180
Phone: (518)274-5509
Fax: (518)276-2623
Email: messid@rpi.edu

Doyle Miller
Optomec Design Company
2655-A Broadbent Parkway
Suite 310
Albuquerque, NM 87107
Phone: (505)761-8250
Fax: (505)761-6638
Email: wdmiller@falsh.net

Farhad Mohammadi
Rutgers University
Dept. of Ceramic & Materials
Engineering
PO Box 909
Piscataway, NJ 08855-0909
Phone: (908)445-5675
Fax: (908)445-3258
Email: fmoha@eden.rutgers.edu

Hiroyuki Narahara (733)
Kyushu Institute of Technology
Dept of Mechanical Systems
Engineering
680-4 kawazu
Iizuka city, Fukuoka 820
JAPAN
Phone: 81-948-29-7766
Fax: 81-948-29-7751
Email: nara@mse.kyutech.ac.jp

Kesh Narayanan
National Science Foundation
4201 Wilson Blvd.
Room 590
Arlington, VA 22230
Phone: (703)306-1330
Fax: (703)306-0337
Email: Knarayan@NSF.gov

William Nebe
E.I. DuPont Co.
Wilmington Delaware
Experimental Statim E352/272
Phone: (302)695-4448

Christian Nelson
DTM Corporation
1611 Headway Circle, Bldg. 2
Austin, TX 78754
Phone: (512)425-2934
Fax: (512)425-2966
Email: nelson@dtm-corp.com

Ron Nemec (513)
SyntheMet Corporation
17 Pillar.
Los Alamos, NM 87544
Phone: (505)661-8879
Fax: (512)661-0510

Wyatt Newman (643)
Case Western Reserve
University
EEAP Department
Cleveland, OH 44106
Phone: (216)368-6432
Fax: (216)368-2668
Email: wsn@po.cwru.edu

Olli Nyrhila
Electrolux Rapid Development
Aholantie 17
21290 Rusko
FINLAND
Phone: 358-2-4365611
Fax: 358-2-4399620

Kurt O'Connor
Delco Electronics
One Corporate Center
M/S 9159 Box 9005
Kokomo, IN 46904
Phone: (765)451-9309
Fax: (765)451-7810

Chris O'Neill
Pratt & Whitney
400 Main St.
M/S 118-40
E. Hartford, CT 06108
Phone: (860)565-2729
Fax: (860)565-9614
Email: oneillcf@pweh.com

Toshiyuki Ogawa
Ebara Research Co. Ltd.
Production Engineering Office
11-1, Haneda Asahi-cho
Ohta-ku
Tokyo 144
JAPAN
Phone: 81-3-3743-6549
Fax: 81-3-3745-3443

Gunnar Palm
Swedish Institute of Prod. Engg.
Research
(IVF)
Brinellvagen 68
S-10044 Stockholm
SWEDEN
Phone: 46 8 2058 49
Fax: 46 8 2022 27
Email: gp@cadcam.kth.se

Thomas Pang (349)
Ciba Specialty Chemicals Corporation
Rapid Modeling Group
5121 San Fernando Road West
Los Angeles, CA 90039
Phone: (818)265-7151
Fax: (818)507-0167
Email: thomas.pang@usla.mhs.ciba.com

Alexandre Papadatos (709)
Clemson University
Department of Mechanical Engineering
EIB 250
Clemson, SC 29634
Phone: (864)656-7174
Email: apapada@clemson.edu

Chul Park (17)
University of Toronto
5 King's College Road
Toronto, Ontario M5S 3G8
CANADA
Phone: (416)978-3053
Fax: (416)978-3053
Email: park@mie.utoronto.ca

Joseph Pegna (49, 231)
Rensselaer Polytechnic Institute
Dept. of ME, Aeronautical Eng. & Mechanics
JEC 5022
110 8th St.
Troy, NY 12180-3590
Phone: (518)276-6999
Fax: (518)276-2623
Email: pegnaj@rpi.edu

Chadee Persad
Institute for Advanced Technology
University of Texas
4030-2 West Braker
Austin, Tx 78759
Phone: (512)471-9060
Fax: (512)471-9096
Email: persad@email.iat.utexas.edu

Reginald Ponder
Georgia Institute of Technology
Manufacturing Research Center
813 Ferst Drive
Atlanta, GA 30332-0406
Phone: (404)894-7688
Fax: (404)894-0957
Email: reginald.ponder@marc.gatech.edu

Matthew Pope (529)
Ceramic Composites, Inc
1110 Benfield Blvd.
Millersville, MD 21108
Phone: (410)224-3710
Fax: (410)224-4678
Email: markpat@techassess.com

Ty Posey
The University of Southern Mississippi
The Mississippi Polymer Institute/PMEC
P.O. Box 10003
Hattiesburg, MS 39406
Phone: (601)266-4607
Fax: (601)266-5635
Email: Ty.POSEY@usm.edu

Fritz Prinz (133, 521)
Stanford University
Mechanical Engg./Materials Science & Engg.
Bldg. 530, Rm. 220
Stanford, CA 94305
Phone: (415)723-0084
Fax: (415)723-5034
Email: fbp@cdr.stanford.edu

Sriram Rangarajan
(185, 395, 411, 421, 431)
Rutgers - The State University of New Jersey
Center for Ceramic Research
Brett & Bowser Rds.
P.O. Box 909
Piscataway, NJ 08855
Phone: (732)445-5616
Fax: (732)445-3258
Email: rangs@rci.rutgers.edu

A.C. Paul Raptis
Argonne National Lab
9700 S Cass Ave.
Argonne, IL 60516
Phone: (630)252-5930
Fax: (630)252-3250
Email: raptis@anl.gove

Anshuman Razdan
Arizona State University
PRISM
Box 875106
Tempe, AZ 85287-5106
Phone: (602)965-5368
Fax: (602)965-2910
Email: razdan@asu.edu

Floyd Roberts
NASA
EH32 MSFC
Huntsville, AL 35812
Phone: (205)544-1967
Fax: (205)544-8970
Email: fer3@bigfoot.com

Joe Rosales
3M
A141-1S-04
6801 River Place
Austin, TX 78726-9000
Phone: (512)984-2728
Fax: (512)984-5064
Email: jjrosales@mmm.com

David Rosen (627)
Georgia Institute of Technology
Rapid Prototyping and Manufacturing Institute
813 Ferst Dr.
Atlanta, GA 30332-0405
Phone: (404)894-9668
Fax: (404)894-9342
Email: david.rosen@me.gatech.edu

Emanuel Sachs (115, 371)
Massachusetts Institute of Technology
Department of Mechanical Engineering
77 Mass. Ave., Rm 35-136
Cambridge, MA 02139
Phone: (617)253-5381
Fax: (617)253-0209
Email: sachs@mit.edu

Ahmad Safari
(185, 395, 403 411, 421, 431)
Rutgers - The State University of New Jersey
Center for Ceramic Research
Brett & Bowser Rds
P.O. Box 909
Piscataway, NJ 08855
Phone: (908)445-4367
Fax: (908)445-3258
Email: safari@rci.rutgers.edu

Katsuhiko Sakamoto
University of Minnesota
Room 116, Burntside Hall
2408 Oakland Ave.
Duluth, MN 55812-2492
Phone: (218)726-8412
Fax: (218)726-6336
Email: ksakamot@d.umn.edu

Roy Sanders
Sanders Prototype, Inc.
P.O. Box 540
Pine Valley Mill, Elm St.
Wilton, NH 03086
Phone: (603)654-5100X232
Fax: (603)654-2616

Claus Schley (635)
University of Warwick, Rover Group
Advanced Power Train Technology
Mechanical Engineering Building
Coventry CV4 7AL
UNITED KINGDOM
Phone: (44)1203-524782
Fax: (44)1203-524796
Email: geoff@atc-4.WMG.warwick.ac.uk

John Schultz (325)
University of Dayton
Rapid Prototype Development Laboratory
300 College Park, KLA-11
Dayton, OH 45469-0131
Phone: (937)229-4363
Fax: (937)229-2503
Email: schultjw@main.udri.udayton.edu

James Serdy (115)
Massachusetts Institute of Technology
77 Mass. Ave., Rm 35-011
Cambridge, MA 02139
Phone: (617)253-2606
Fax: (617)253-0209
Email: serdy@mit.edu

Mohammed Shaarawi
University Of Texas
Mechanical Engineering/MS&E
MC2200
Austin, TX 78712
USA

Steven Shaffer
Milwaukee School of Engineering
Rapid Prototyping Center
1025 N. Broadway
Milwaukee, WI 53202
Phone: (414)277-4550
Fax: (414)277-7180
Email: shaffer@warp.msoe.edu

Jami Shah
Arizona State University
Mechanical Engineering
Mail Code 6106
Tempe, AZ 85287-6106
Phone: (602)965-6145
Fax: (602)965-2412
Email: jami.shah@asu.edu

Leon Shaw (481, 489)
The University of Connecticut
Institute of Materials Science
101 North Eagleville Rd., U-136
Storrs, CT 06269
Phone: (860)486-2592
Fax: (860)486-4545
Email: lshaw@mail.ims.uconn.edu

Charles Smith (1)
The University of Texas at Arlington
Electrical Engineering
Box 19016
Arlington, TX 76019
Phone: (817)272-3470
Fax: (817)272-2253
Email: smith@cc.uta.edu

Norman Smith (249)
Ford Motor Company
21500 Oakwood
Box 2053 Mail Drop 65
Dearborn, MI 48121-2053
Phone: (313)322-5094
Fax: (313)337-5808
Email: mron@wwnet.com

Geoff Smith-Moritz (635)
Rapid Prototyping Report
CAD/CAM Publishing, Inc.
1010 Turquoise Street
Suite 320
San Diego, CA 92109
Phone: (619)488-0533
Fax: (619)488-6052
Email: rpreport@cadcamnet.com

John Smugeresky (387, 699)
Sandia National Labs
MS9403/Dept 8712
Livermore, CA 94551
Phone: (510)294-2910
Fax: (510)294-3410
Email: smug@sandia.gov

Rupert Soar (307)
The University of Nottingham
Dept. of Manufacturing Engg.
and Oper. Management
University Park
Nottingham NG7 2RD
UK
Phone: 115 9515151 X8085
Fax: 115 9514000
Email: epxrs @epn1.
maneng.Nottingham.ac.uk

George Spanos
Naval Research Lab
ONR
4555 Overlook Ave S.W.
Washington, DC 20375-5000
Phone: (202)767-5799
Fax: (202)767-2623
Email:
spanos@anvil.nrl.navy.mil

Brian Spears
University of Texas at Austin
SLS Lab
2311 Nueces St #202
Austin, TX 78705
Phone: (512)481-1647
Email:
bkspears@mail.utexas.edu

Jim Stewart
Delco Electronics
P.O. Box 9005, MS9159
700 E. Firmin St.
Carmel, IN 46033
Phone: (765)451-9309
Fax: (765)451-7810

Brent Stucker (257)
University of Rhode Island
Dept. of Industrial &
Manufacturing Engr
Kingston, RI 02881
Phone: (401)874-5187
Fax: (401)874-5540
Email: stucker@egr.uri.edu

Lianchao Sun (481)
The University of Connecticut
Institute of Materials Science
97 North Eagleville Rd., U-136
Storrs, CT 06269
Phone: (860)486-4410
Fax: (860)486-4575
Email:
lis95001@uconnvm.uconn.edu

Douglas Taft (341)
Clemson University
Department of Chemical
Engineering
100 Fluor Daniel
EIB
Clemson, SC 29634
Phone: (864)656-3291
Fax: (864)656-4435
Email: dtaft@ces.clemson.edu

Mukul M. Takalkar
Louisiana Tech University
911 Hergot Avenue
Ruston, LA 71272
Phone: (318)255-0093
Fax: (318)257-5104
Email:
mmt003@engr.latech.edu

Charles Thomas (249, 577)
University of Utah
Department of Mechanical
Engineering
Salt Lake City, UT 84112
Phone: (801)585-6939
Fax: (801)585-9826
Email:
cthomas@me.mech.utah.edu

Jim Tobin
Proctor & Gamble
6110 Center Hill Ave.
Cincinnati, OH 45224
Phone: (513)634-2392
Fax: (513)634-4588
Email: tobin.jr@pg.com

Quyen Tong
University of Texas
Austin, TX 78712
Phone: (512)452-6061
Email:
qtong@armus.me.utexas.edu

Ampere Tseng
Arizona State University
Dept. of Mechanical and
Aerospace Engg
Box 876106
Tempe, AZ 85287-6106
Phone: (602)965-8201
Fax: (602)965-2412
Email: ampere.tseng@asu.edu

Neal Vail
BioMedical Enterprises, Inc.
Texas Research Park
14785 Omicron Dr., Suite 205
San Antonio, TX 78245
Phone: (210)677-0354
Fax: (210)677-0355
Email: vail@bme-tx.com

Douglas Van Putte
Eastman Kodak Company
1699 Lake Avenue
Building 604
Rochester, NY 14652-4102
Phone: (716)477-1492
Fax: (716)722-0810
Email: vanputte@kodak.com

Natesan Venkataraman
Rutgers University
Dept. of Ceramic & Materials
Engineering
Brett & Bowser Roads
PO Box 909
Piscataway, NJ 08855-0909
Phone: (732)878-0962
Email: vna@eden.rutgers.edu

Daniel Walczyk (211)
Rensselaer Polytechnic Institute
Department of Mechanical
Engineering
Johnson Engineering Center,
Room 4026
110 Eighth St.
Troy, NY 12180-3590
Phone: (518)276-2397
Fax: (518)276-2623
Email: walczd@rpi.edu

Yanshuo Wang (669)
University of Connecticut
Institute of Materials Science
102 North Eagleville Rd., U-136
Storrs, CT 06268
Phone: (860)486-4410
Email:
yaw94001@uconnvm.uconn.edu

Hongyun Wang (465)
University of Texas at Austin
Department of Mechanical
Engineering
2900 Cole St., Apt. 309
Austin, TX 78705
Phone: (512)471-3578
Email:
hongyun_wang@mail.utexas.edu

Timothy Weaver
Pennsylvania State University
118 Research Bldg West
University Park, PA 16802
Phone: (814)865-1308
Fax: (814)863-8211
Email: tjw112@psu.edu

Lee Weiss (133)
Carnegie Mellon University
217 Smith Hall
Pittsburgh, PA 15213
Phone: (412)268-7657
Fax: (412)268-5570
Email: lew@cs.cmu.edu

P. Whalen (185)
AlliedSignal Research and
Technology
Research and Technology
P. O. Box 1021
Morristown, NJ 07962
USA

Bernhard Wiedemann
Daimler Benz
Postfach 2360
Wilhem-Runge-Str. 11
Ulm 89013
GERMANY
Phone: 49-731-505-2925
Fax: 49-731-505-4212
Email: bernhard.wiedemann
@dbag.ulm.daimlerbenz.de

Martin Wohlert (81)
University of Texas at Austin
Department of Mechanical
Engineering
C2200
Austin, TX 78712
Phone: (512)471-3578
Fax: (512)471-7681
Email:
mwohlert@mail.utexas.edu

Sam Wood
University of Texas
Austin, TX 78712
Phone: (512)794-3998
Email:
wood@armus.me.utexas.edu

Joe Wright
Lockheed Martin Vought
Systems
PO Box 650003
Dallas, TX 75265-0003
Phone: (972)603-2507
Fax: (972)603-0419
Email: wrightjm@vs.lmco.co

Zhanping Wu (725)
Clemson University
Department of Mechanical
Engineering
Fluor Daniel RM#124
Clemson, SC 29634
Phone: (864)656-7177
Fax: (864)656-4435
Email: zwu@clemson.edu

S. Wu
(185, 395, 411, 421, 431)
Rutgers - The State University
of New Jersey
Department of Ceramic
Engineering
Brett and Bowser Rds.
Piscataway, NJ 08854
Phone: (908)445-5684
Fax: (908)445-3258
Email: swu@rci.rutgers.edu

Yi Xu (177)
University of Tokyo
Institute of Industrial Science
7-22-1, Roppongi, Minato-ku
Tokyo 106
JAPAN
Phone: +81 3 3402 6231
Fax: +81 3 5411 3908
Email: joe@iis.u-tokyo.ac.jp

Kenji Yamazawa (223)
The Institute of Physical and
Chemical Research
(RIKEN)
2-1, Hirosawa
Wako-Shi, Saitama-ken
JAPAN
Phone: +81 48 467 9578
Fax: +81 48 462 4621
Email:
kyama@postman.riken.go.jp

Walter Zimbeck (529)
Ceramic Composites, Inc
1110 Benfield Blvd.
Millersville, MD 21108
Phone: (410)224-3710
Fax: (410)224-4678
Email: zimbo@techassess.com